

SURFACES OF NANOPARTICLES AND POROUS MATERIALS

SURFACTANT SCIENCE SERIES

FOUNDING EDITOR

MARTIN J. SCHICK

Consultant

New York, New York

SENIOR ADVISOR

ARTHUR T. HUBBARD

Department of Chemistry

University of Cincinnati

Cincinnati, Ohio

ADVISORY BOARD

DANIEL BLANKSCHTEIN

*Department of Chemical Engineering
Massachusetts Institute of Technology
Cambridge, Massachusetts*

ERIC W. KALER

*Department of Chemical Engineering
University of Delaware
Newark, Delaware*

S. KARABORNI

*Shell International Petroleum
Company Limited
London, England*

CLARENCE MILLER

*Department of Chemical Engineering
Rice University
Houston, Texas*

LISA B. QUENCER

*The Dow Chemical Company
Midland, Michigan*

DON RUBINGH

*The Proctor & Gamble Company
Cincinnati, Ohio*

JOHN F. SCAMEHORN

*Institute for Applied Surfactant
Research
University of Oklahoma
Norman, Oklahoma*

BEREND SMIT

*Shell International Oil Products B.V.
Amsterdam, The Netherlands*

P. SOMASUNDARAN

*Henry Krumb School of Mines
Columbia University
New York, New York*

1. *Nonionic Surfactants*, edited by Martin J. Schick (see also Volumes 19, 23, and 60)
2. *Solvent Properties of Surfactant Solutions*, edited by Kozo Shinoda (see Volume 55)
3. *Surfactant Biodegradation*, R. D. Swisher (see Volume 18)
4. *Cationic Surfactants*, edited by Eric Jungermann (see also Volumes 34, 37, and 53)
5. *Detergency: Theory and Test Methods* (in three parts), edited by W. G. Cutler and R. C. Davis (see also Volume 20)
6. *Emulsions and Emulsion Technology* (in three parts), edited by Kenneth J. Lissant
7. *Anionic Surfactants* (in two parts), edited by Warner M. Linfield (see Volume 56)
8. *Anionic Surfactants: Chemical Analysis*, edited by John Cross (out of print)
9. *Stabilization of Colloidal Dispersions by Polymer Adsorption*, Tatsuo Sato and Richard Ruch (out of print)
10. *Anionic Surfactants: Biochemistry, Toxicology, Dermatology*, edited by Christian Gloxhuber (see Volume 43)
11. *Anionic Surfactants: Physical Chemistry of Surfactant Action*, edited by E. H. Lucassen-Reynders (out of print)
12. *Amphoteric Surfactants*, edited by B. R. Bluestein and Clifford L. Hilton (see Volume 59)
13. *Demulsification: Industrial Applications*, Kenneth J. Lissant (out of print)
14. *Surfactants in Textile Processing*, Arved Datyner
15. *Electrical Phenomena at Interfaces: Fundamentals, Measurements, and Applications*, edited by Ayao Kitahara and Akira Watanabe
16. *Surfactants in Cosmetics*, edited by Martin M. Rieger (see Volume 68)
17. *Interfacial Phenomena: Equilibrium and Dynamic Effects*, Clarence A. Miller and P. Neogi
18. *Surfactant Biodegradation: Second Edition, Revised and Expanded*, R. D. Swisher
19. *Nonionic Surfactants: Chemical Analysis*, edited by John Cross
20. *Detergency: Theory and Technology*, edited by W. Gale Cutler and Erik Kissa
21. *Interfacial Phenomena in Apolar Media*, edited by Hans-Friedrich Eicke and Geoffrey D. Parfitt
22. *Surfactant Solutions: New Methods of Investigation*, edited by Raoul Zana
23. *Nonionic Surfactants: Physical Chemistry*, edited by Martin J. Schick
24. *Microemulsion Systems*, edited by Henri L. Rosano and Marc Clausse
25. *Biosurfactants and Biotechnology*, edited by Naim Kosaric, W. L. Cairns, and Neil C. C. Gray
26. *Surfactants in Emerging Technologies*, edited by Milton J. Rosen
27. *Reagents in Mineral Technology*, edited by P. Somasundaran and Brij M. Moudgil
28. *Surfactants in Chemical/Process Engineering*, edited by Darsh T. Wasan, Martin E. Ginn, and Dinesh O. Shah
29. *Thin Liquid Films*, edited by I. B. Ivanov

30. *Microemulsions and Related Systems: Formulation, Solvency, and Physical Properties*, edited by Maurice Bourrel and Robert S. Schechter
31. *Crystallization and Polymorphism of Fats and Fatty Acids*, edited by Nissim Garti and Kiyotaka Sato
32. *Interfacial Phenomena in Coal Technology*, edited by Gregory D. Botsaris and Yuli M. Glazman
33. *Surfactant-Based Separation Processes*, edited by John F. Scamehom and Jeffrey H. Harwell
34. *Cationic Surfactants: Organic Chemistry*, edited by James M. Richmond
35. *Alkylene Oxides and Their Polymers*, F. E. Bailey, Jr., and Joseph V. Koleske
36. *Interfacial Phenomena in Petroleum Recovery*, edited by Norman R. Morrow
37. *Cationic Surfactants: Physical Chemistry*, edited by Donn N. Rubingh and Paul M. Holland
38. *Kinetics and Catalysis in Microheterogeneous Systems*, edited by M. Grätzel and K. Kalyanasundaram
39. *Interfacial Phenomena in Biological Systems*, edited by Max Bender
40. *Analysis of Surfactants*, Thomas M. Schmitt
41. *Light Scattering by Liquid Surfaces and Complementary Techniques*, edited by Dominique Langevin
42. *Polymeric Surfactants*, Irja Piirma
43. *Anionic Surfactants: Biochemistry, Toxicology, Dermatology. Second Edition, Revised and Expanded*, edited by Christian Gloxhuber and Klaus Kunstler
44. *Organized Solutions: Surfactants in Science and Technology*, edited by Stig E. Friberg and Bjorn Lindman
45. *Defoaming: Theory and Industrial Applications*, edited by P. R. Garrett
46. *Mixed Surfactant Systems*, edited by Keizo Ogino and Masahiko Abe
47. *Coagulation and Flocculation: Theory and Applications*, edited by Bohuslav Dobiáš
48. *Biosurfactants: Production • Properties • Applications*, edited by Naim Kossaric
49. *Wettability*, edited by John C. Berg
50. *Fluorinated Surfactants: Synthesis • Properties • Applications*, Erik Kissa
51. *Surface and Colloid Chemistry in Advanced Ceramics Processing*, edited by Robert J. Pugh and Lennart Bergsfrom
52. *Technological Applications of Dispersions*, edited by Robert B. McKay
53. *Cationic Surfactants: Analytical and Biological Evaluation*, edited by John Cross and Edward J. Singer
54. *Surfactants in Agrochemicals*, Tharwat F. Tadros
55. *Solubilization in Surfactant Aggregates*, edited by Sherril D. Christian and John F. Scamehom
56. *Anionic Surfactants: Organic Chemistry*, edited by Helmut W. Stache
57. *Foams: Theory, Measurements, and Applications*, edited by Robert K. Prud'homme and Saad A. Khan
58. *The Preparation of Dispersions in Liquids*, H. N. Stein
59. *Amphoteric Surfactants: Second Edition*, edited by Eric G. Lomax
60. *Nonionic Surfactants: Polyoxyalkylene Block Copolymers*, edited by Vaughn M. Nace

61. *Emulsions and Emulsion Stability*, edited by Johan Sjöblom
62. *Vesicles*, edited by Morton Rosoff
63. *Applied Surface Thermodynamics*, edited by A. W. Neumann and Jan K. Spelt
64. *Surfactants in Solution*, edited by Arun K. Chaifopadhyay and K. L. Mittal
65. *Detergents in the Environment*, edited by Milan Johann Schwuger
66. *Industrial Applications of Microemulsions*, edited by Conxita Solans and Hironobu Kunieda
67. *Liquid Detergents*, edited by Kuo-Yann Lai
68. *Surfactants in Cosmetics: Second Edition, Revised and Expanded*, edited by Martin M. Rieger and Linda D. Rhein
69. *Enzymes in Detergency*, edited by Jan H. van Ee, Onno Misset, and Erik J. Baas
70. *Structure-Performance Relationships in Surfactants*, edited by Kunio Esumi and Minoru Ueno
71. *Powdered Detergents*, edited by Michael S. Showell
72. *Nonionic Surfactants: Organic Chemistry*, edited by Nico M. van Os
73. *Anionic Surfactants: Analytical Chemistry, Second Edition, Revised and Expanded*, edited by John Cross
74. *Novel Surfactants: Preparation, Applications, and Biodegradability*, edited by Krister Holmberg
75. *Biopolymers at Interfaces*, edited by Martin Malmsten
76. *Electrical Phenomena at Interfaces: Fundamentals, Measurements, and Applications, Second Edition, Revised and Expanded*, edited by Hiroyuki Ohshima and Kunio Furusawa
77. *Polymer-Surfactant Systems*, edited by Jan C. T. Kwak
78. *Surfaces of Nanoparticles and Porous Materials*, edited by James A. Schwarz and Cristian I. Contescu
79. *Surface Chemistry and Electrochemistry of Membranes*, edited by Torben Smith Sørensen

ADDITIONAL VOLUMES IN PREPARATION

Interfacial Phenomena in Chromatography, edited by Emile Pefferkom

Solid-Liquid Dispersions, Bohuslav Dobiáš, Xueping Qiu, and Wolfgang von Rybinski

Modern Characterization Methods of Surfactant Systems, edited by B. P. Binks

Interfacial Forces and Fields, edited by Jyh-Ping Hsu

Silicone Surfactants, *edited by Randal M. Hill*

Surface Characterization Methods: Principles, Techniques, and Applications,
edited by Andrew J. Milling

SURFACES OF NANOPARTICLES AND POROUS MATERIALS

edited by
James A. Schwarz
Cristian I. Contescu

*Syracuse University
Syracuse, New York*

NEW YORK • BASEL

ISBN: 0-8247-1933-6

This book is printed on acid-free paper.

Headquarters

Marcel Dekker
270 Madison Avenue, New York, NY 10016
tel: 212-696-9000; fax: 212-685-4540

Eastern Hemisphere Distribution

Marcel Dekker AG
Hutgasse 4, Postfach 812, CH-4001 Basel, Switzerland
tel: 44-61-261-8482; fax: 44-61-261-8896

World Wide Web

<http://www.dekker.com>

The publisher offers discounts on this book when ordered in bulk quantities. For more information, write to Special Sales/Professional Marketing at the headquarters address above.

Copyright © 1999 by Marcel Dekker All Rights Reserved.

Neither this book nor any part may be reproduced or transmitted in any form or by any means, electronic or mechanical, including photocopying, microfilming, and recording, or by any information storage and retrieval system, without permission in writing from the publisher.

Current printing (last digit):
1 0 9 8 7 6 5 4 3

PRINTED IN THE UNITED STATES OF AMERICA

*They knew each other, they liked each other, and they
departed from their families and us almost at the same
time, in the last months of 1997.*

*They were our mentors. We dedicate this volume to
Edward J. Schwarz and Mihail I. Vass, with the
assurance that they knew the roles they have
played in our lives.*

Preface

So far as it goes, a small thing may give analogy of great things, and show the tracks of knowledge.

from *De Rerum Natura* (On The Nature of Things) Lucretius (99–55 BC)

In the world of nanoparticles and microporous materials, the interaction forces between nanosized particles and molecules from the surrounding medium, or the forces between particles themselves, may exceed the mechanical forces between bodies of the macroscopic world. This is caused by the high surface-to-volume ratio of nanoparticles and microporous materials. When familiar materials become mainly surface, they acquire new optical, magnetic, electrical, chemical, and transport properties. Thus, dispersions tend to agglomerate, fine particles show increased mechanical strength, and microporous solids develop tremendous sorption and molecular sieving properties.

Materials with a high surface-to-volume ratio have played important roles in evolution and in our own lives. Extensive surface area provides optimal conditions for chemical transformations to proceed with high reaction rates and high product selectivity. The organization and stability of nanosized structures are controlled by interactions at the molecular scale—chemical, electrical or magnetic—rather than by the mechanical forces that shape the macroscopic world. Our ability to control and use for our benefit all kinds of special properties developed at the extended surface that characterizes the objects of the nanoworld depends on our understanding of phenomena at and across the interfaces.

Nanoparticles and porous materials exist essentially as an extended surface. The line of structural similitude, however, ends at this point. Nanoparticles derive their properties from their small solid size in their condensed phase, while porous materials derive their properties from the absence of solid material in their condensed state. In other words, the shape of the nanoworld is either convex or concave,

depending on whether the object is a collection of microscopic particles or a collection of microscopic voids.

In either case, the surface can strongly influence the chemistry that occurs within the surrounding media. The gas–solid and liquid–solid interfaces of porous materials have been the focus of many studies, over decades. In recent years, nanodimensional materials have become the focus of many researchers. Such materials have interesting properties, but they do not definitively promise to change the state of science or technology. What might change is our use of design strategies for converting theoretical materials into practical materials for use.

The purpose of this volume, therefore, is to collect state-of-the-art procedures for construction and design of nanoparticles and porous materials, where their applications might be most appropriate. To that end, synthesis and characterization procedures are presented. The ultimate test is their practical utilization in “real world” environments that exist at the gas and liquid interfaces of these materials. Case studies are presented and, in some instances, conclusions and projections for optimal design procedures of nanoparticles and porous materials are offered. The scope of this volume is inherently multidisciplinary from the viewpoint of usage of materials. The common factor, however, is that their surface chemical behavior dominates, and thus, unification of purpose and scope becomes a reality.

The volume is organized into three sections, each of which addresses fundamental and practical realization of the production of nanostructured materials. The first section deals with the preparation, characterization, and transport properties of this unique class of materials. Structural and chemical heterogeneity are the result of preparation protocols, and various spectroscopies can be used to characterize these properties. Transport of adsorbates is affected by both intraparticle and interparticle resistance, which can greatly influence applications in practical processes. Each of these topics is represented as a case study that is general enough in scope that cautious application of the reported results can be extended to other systems of technological importance.

The remaining two sections deal with the fundamental and practical utilization of nanostructural materials in gaseous and liquid environments. The second section deals with the former case. A balanced blend of theoretical and practical applications is presented. Both theory and application emphasize the importance of structural and energetic heterogeneity and its influence on the performance of three-dimensional materials that are essentially only two-dimensional due to their high surface-to-volume ratio.

The final section presents case studies of the adsorption properties of surfaces under the influence of a solvent that can alter the surface and chemical heterogeneity by mechanisms that have been studied by colloidal scientists for many years. Again, in this section, there is a complimentary blend of theory and application. Applications involving both inorganic and organic adsorbates are considered.

The subject areas in all three sections are quite diverse, which is a reflection of the versatility of nanoparticles and porous materials in technologies that demand superior performance, yet still require latitude for optimization strategies. Each of the contributions has been peer-reviewed and we feel confident that the information contained is complete and can be used by seasoned researchers and newcomers

to the field to condition their own research objectives in alignment with their own expertise.

We wish to first acknowledge Professor Arthur Hubbard for the suggestion that a volume of this type was appropriate at this time. Each of the authors has responded under undue pressure from both of us to submit their contributions in a timely fashion. This has resulted in a final document that many should find of interest. We appreciate the assistance of Dr. Adriana Contescu in maintaining up-to-date folders of our correspondence with the contributors. Finally, the attention to detail and the electronic communication to get everything in place for publication came from Ms. Dawn Long. She has been responsible for helping us both remain honest and on time, so that the final submission to the publisher occurred on schedule and with minimum confusion.

James A. Schwarz
Cristian I. Contescu

Contents

Preface v

Contributors xiii

Part I Preparation, Characterization, and Transport Properties of Nanoparticles and Porous Solids

1. **Synthesis of a Polysilazane Coating on a Silica Gel via Chemical Surface Coating Comparing Liquid- and Gas-Phase Chlorosilylations** 1
Nathalie R. E. N. Ztnpens and Etienne F. Vansant
2. **Preparation of Molecular Sieves by Pillaring of Synthetic Clays** 15
Soon-Yong Jeong
3. **Engineering of Nanosize Superparamagnetic Particles for Use in Magnetic Carrier Technology** 31
Zhenghe Xu, Qingxia Liu, and James A. Finch
4. **Acid–Base Behavior of Surfaces of Porous Materials** 51
Cristian I. Contescu and James A. Schirarz
5. **Electro-Optical Spectroscopy of Colloidal Systems** 103
Maria Stoimenova and Tsuneo Okuho
6. **NMR Studies of Colloidal Oxides** 125
Edisson Morgado, Jr., Sonia Maria Cabral de Menezes, and Carlos Roberto Nogueira Pacheco
7. **Polymer Surface Dynamics Using Surface-Modified Glasses via Dynamic Contact Angle Measurements** 169
Joung-Mafz Park

8. Microporous Structure of Collagen Fibers 185
Keito Boki
9. Adsorption onto Oxides: The Role of Diffusion 199
Lisa Axe and Paul R. Anderson
10. Electrokinetic Phenomena in Porous Media and Around Aggregates 211
Pierre M. Adler, David Coelho, Jean-Francois Thoven, and Michael Shapu'o
11. Transport Processes in Microemulsions 259
Satya P. Moulik and Bidyut K. Paul
12. Structural Effects on Diffusivity Within Aggregates of Colloidal Zirconia 281
David H. Reeder, Alon V. McCormick, and Peter W. Carr

Part II Adsorption from the Vapor/Gas Phase onto Nanoparticles and Porous Solids

13. Characterization of Energetically Heterogeneous Surfaces from Experimental Adsorption Isotherms 295
James P. Olivier
14. Computer Simulations of the Structural and Thermodynamic Properties of Adsorbed Phases 319
William Stede
15. Surface Heterogeneity Effects on Adsorption Equilibria and Kinetics: Rationalizations of the Elovich Equation 355
Wladyslaw Rudzinski and Tornasz Panczyk
16. Single- and Multicomponent Adsorption Equilibria of Hydrocarbons on Activated Carbon: The Role of Micropore Size Distribution 391
K. Wang and D. D. Do
17. Surface and Structural Properties of Modified Porous Silicas 443
Michal Kruk and Mietek Jaroniec
18. Nanodimensional Magnetic Assembly of Confined O₂ 473
Katsumi Kaneko
19. Heat of Adsorption of Pure Gas and Multicomponent Gas Mixtures on Microporous Adsorbents 501
Shivaji Sircar and Madhukar B. Rao

Part III Adsorption from the Liquid Phase onto Nanoparticles and Porous Solids

20. Surface Chemistry of Activated Carbon Materials: State of the Art and Implications for Adsorption 529
Ljubisa R. Radovic
21. Charge Regulation at the Surface of a Porous Solid 567
Boris V. Zhrnud and Lennart Bergstrom

22. Surface Ionization and Complexation 593
Zhenghe Xu, Qingsong Zhang, and James A. Finch
23. The Surface Charge of Alkali Halides in Their Saturated Solutions 613
Jan D. Miller and Srinivas Veeraimsuneni
24. Ionic Adsorbates on Hydrophobic Surfaces 645
Richard L. Zollars
25. Adsorption of Metal Ions onto Humic Acid 661
Hideshi Seki and Akira Suzuki
26. Hydrous Metal Oxides as Adsorbents for Aqueous Heavy Metals 675
Russell Crawford, David E. Maimvaring, and Ian H. Hording
27. Adsorption of Ions onto Alumina 711
Edwin Baumgarten
28. Protein Adsorption onto Latex Particles 743
Jeffrey Leaver
29. Adsorption of Pharmaceutical Organic Compounds onto Porous Materials 763
Keiji Yamamoto and Siriporn Okonogi

Contributors

Pierre M. Adler Equipe Milieux Poreux, Institut de Physique du Globe de Paris, Paris, France

Paul R. Anderson Department of Chemical and Environmental Engineering, Illinois Institute of Technology, Chicago, Illinois

Lisa Axe Department of Civil and Environmental Engineering, New Jersey Institute of Technology, Newark, New Jersey

Edwin Baumgarten Institut für Physikalische Chemie und Elektrochemie, Heinrich-Heine-Universität, Düsseldorf, Germany

Lennart Bergstrom Institute for Surface Chemistry, Stockholm, Sweden

Keito Boki Department of Pharmaceutical Sciences, Kinki University, Osaka, Japan

Peter W. Carr Department of Chemistry, University of Minnesota, Minneapolis, Minnesota

David Coelho Equipe Milieux Poreux, Institut de Physique du Globe de Paris, Paris, France

Cristian I. Contescu Department of Chemical Engineering and Materials Science, Syracuse University, Syracuse, New York

Russell Crawford Centre for Applied Colloid and BioColloid Science, Swinburne University of Technology, Melbourne, Australia

D. D. Do Department of Chemical Engineering, University of Queensland, St. Lucia, Australia

James A. Finch Department of Mining and Metallurgical Engineering, McGill University, Montreal, Quebec, Canada

Ian H. Harding Centre for Applied Colloid and BioColloid Science, Swinburne University of Technology, Melbourne, Australia

Nathalie R. E. N. Impens Chemistry Laboratory of Adsorption and Catalysis, University of Antwerp, Antwerp, Belgium

Mietek daroniec Department of Chemistry, Kent State University, Kent, Ohio

Soon-Yong deong Chemical Process and Engineering Center, Korea Research Institute of Chemical Technology, Taejeon, Korea

Katsumi Kaneko Department of Chemistry, Chiba University, Chiba, Japan

Michal Kruk Department of Chemistry, Kent State University, Kent, Ohio

Jeffrey Leaver Molecular Recognition Group, Hannah Research Institute, Ayr, Scotland

Qingxia Liu Cominco Research. Cominco Ltd., Trail, British Columbia, Canada

David E. Mainwaring Department of Applied Chemistry, Royal Melbourne Institute of Technology, Melbourne, Australia

Alon V. McCormick Department of Chemical Engineering and Materials Science, University of Minnesota, Minneapolis, Minnesota

Sonia Maria Cabral de Menezes Chemistry Division, Petrobras Research and Development Center, Rio de Janeiro, Brazil

Jan D. Miller Department of Metallurgical Engineering, University of Utah, Salt Lake City, Utah

Edisson Morgado, Jr. Catalysts Division, Petrobras Research and Development Center, Rio de Janeiro, Brazil

Satya P. Moulik Center for Surface Science, Department of Chemistry, Jadavpur University, Calcutta, India

Siriporn Okonogi Department of Pharmaceutical Technology, Chiang Mai University, Chiang Mai, Thailand

Tsuneo Okubo Department of Applied Chemistry, Gifu University, Gifu, Japan

James P. Olivier Micromeritics Instrument Corporation, Inc., Norcross, Georgia

Carlos Roberto Nogueira Pacheco Chemistry Division, Petrobras Research and Development Center, Rio de Janeiro, Brazil

Tomasz Panczyk Department of Theoretical Chemistry, Marie-Curie-Sklodowska University, Lublin, Poland

Joung-Man Park Department of Polymer Science and Engineering, Gyeongsang National University, Chinju, Korea

Bidyut K. Paul Geological Studies Unit, Indian Statistical Institute, Calcutta, India

Ljubisa R. Radovic Department of Materials Science and Engineering, The Pennsylvania State University, University Park, Pennsylvania

Madhukar B. Rao Corporate Science and Technology Center, Air Products and Chemicals, Inc., Allentown, Pennsylvania

David H. Reeder Department of Chemical Engineering and Materials Science, University of Minnesota, Minneapolis, Minnesota

Wladyslaw Rudzinski Department of Theoretical Chemistry, Marie-Curie-Sklodowska University, Lublin, Poland

James A. Schwarz Department of Chemical Engineering and Materials Science, Syracuse University, Syracuse, New York

Hideshi Seki Department of Marine Bioresources Chemistry, Hokkaido University, Hakodate, Japan

Michael Shapiro Department of Mechanical Engineering, Technion—Israel Institute of Technology, Haifa, Israel

Shivaji Sircar Corporate Science and Technology Center, Air Products and Chemicals, Inc., Allentown, Pennsylvania

William Steele Department of Chemistry, The Pennsylvania State University, University Park, Pennsylvania

Maria Stoimenova Institute of Physical Chemistry. Bulgarian Academy of Sciences, Sofia, Bulgaria

Akira Suzuki Department of Marine Bioresources Chemistry, Hokkaido University, Hakodate, Japan

Jean-François Thovet Laboratoire de Combustion et de Detonique, Centre National de la Recherche Scientifique, Futuroscope, France

Etienne F. Vansant Chemistry Laboratory of Adsorption and Catalysis, University of Antwerp, Antwerp, Belgium

Srinivas Veeramasuneni Department of Metallurgical Engineering, University of Utah, Salt Lake City, Utah

K. Wang Department of Chemical Engineering, University of Queensland, St. Lucia, Australia

Zhenghe Xu Department of Chemical and Materials Engineering, University of Alberta, Edmonton, Alberta, Canada

Keiji Yamamoto Department of Pharmaceutical Technology, Chiba University, Chiba, Japan

Qingsong Zhang Hewlett Packard, Palo Alto, California

Boris V. Zhmud Institute for Surface Chemistry, Stockholm, Sweden

Richard L. Zollars Department of Chemical Engineering, Washington State University, Pullman, Washington

1

Synthesis of a Polysilazane Coating on a Silica Gel via Chemical Surface Coating Comparing Liquid- and Gas-Phase Chlorosilylations

NATHALIE R. E. N. IMPENS and ETIENNE F. VANSANT

Chemistry Laboratory of Adsorption and Catalysis, University of Antwerp,
Antwerp, Belgium

- I. Introduction
- II. Experimental
- III. Results and Discussion
 - A. Liquid-phase modification of silica gel with tetrachlorosilane and the first ammoniation
 - B. Second and higher reaction cycles
 - C. Porosity study
- IV. Conclusions
- References

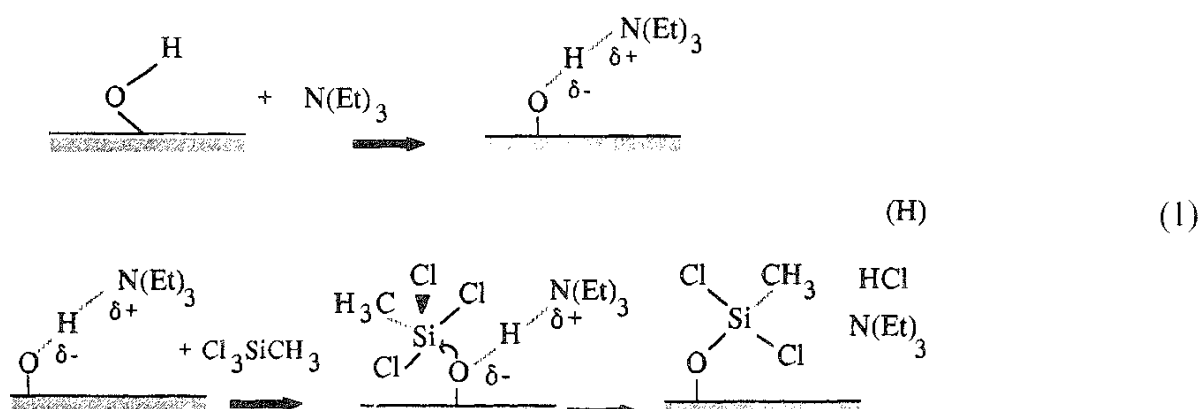
I. INTRODUCTION

Due to the widespread use of ceramic coatings, several synthesis techniques have been developed in recent decades. The majority of these techniques, such as chemical vapor deposition (CVD) and physical vapor deposition (PVD) and their variants, are focused on the synthesis of flat coatings. Recently, the preceramic polymeric synthesis route has offered the possibility to impregnate preceramic materials into porous matrices prior to pyrolysis in order to create coated or composite materials [1,2]. This technique, however, leads to pore filling and alterations of the original substrate texture. The impregnation does not guarantee a chemical bond between the substrate and the preceramic material. This can lead to an unstable composite material after pyrolysis. To avoid this, another technique, called chemical surface coating (CSC) [3], can be used. Based on the successive chemisorption of gaseous reagents in a cyclic way at relatively low temperatures, the technique offers clarity in the reaction mechanisms [4,5] and the evolution of porosity [6] during the preceramic synthesis. It has been shown that the preceramic

coating is chemically bound to the substrate surface and that it has grown in a very homogeneous way in spite of the very irregular substrate texture. The so-called coating precursor is afterwards pyrolyzed, and a chemically bound ceramic coating, e.g., Si_3N_4 or BN; is formed on silica gel. Characterization of the thermally converted Si—N or B—N polymer shows that a very thin homogeneous silicon oxynitride or boron nitride coating, respectively, is formed, whereas the original substrate texture is practically unchanged [7,8].

In the procedure described in this chapter, a preceramic polysilazane coating is synthesized on silica gel via CSC using SiCl_4 and NH_3 , but the chlorosilylations are performed in the liquid phase. In this way, a very small amount of the hazardous reagent is used in comparison with gas-phase reactions, and the total precursor synthesis can be performed at room temperature.

The solid–gas reaction of SiCl_4 with thermally pretreated silica gel has been optimized, and the reaction mechanisms were studied earlier [4]; a reaction temperature of 663 K is needed to modify all the surface hydroxyl groups. To reduce the reaction temperature, Tripp and Hair [9] studied the effect of the presence of triethylamine during reaction with trichloromethylsilane. At room temperature, a very high reaction yield was obtained. The reaction mechanism was deduced from the methoxysilylations of silica proposed by Blitz et al. [10] [see reaction (1)].



The nitrogen-containing base promotes the reaction by rendering the $\equiv\text{SiOH}$ group more nucleophilic. When the base strength is high enough (as in triethylamine), proton transfer is enabled. However, $[\text{HN}(\text{C}_2\text{H}_5)_3]^+\text{Cl}^-$ is formed at the substrate surface and must be removed by sublimation or dissolution in a water–methanol mixture, which results in the hydrolysis of $\equiv\text{SiCl}$ groups. This has to be avoided in the case of the CSC polysilazane synthesis, as these groups are especially created to enable a reaction with NH_3 that creates amine groups.

The effects of solvent and amine base on the solid–liquid reactions of trialkylchlorosilanes with the silica surface hydroxyls were thoroughly investigated by Kinkel and Unger [11]. They concluded that the best yield of silylation was obtained by using strong bases together with solvents with high Lewis donating and accepting properties. To our knowledge, none of the authors reported a pure chlorosilylation with the formation and conservation of $\equiv\text{SiCl}$ groups without the formation of ammonium salt on the silica surface.

In this study, the reaction parameters were chosen in such a way that the salt formed was dissolved in the solvent and the yield of $\equiv\text{SiCl}$ groups was comparable to that obtained with the gas–solid reactions at high temperature. For the reaction of SiCl_4 with the substrate in the following reaction cycles, a solvent was chosen that would not affect the precursor. A comparison of the chemical and morphological composition of the coating precursor using liquid- and gas-phase chlorosilylations synthesized in solid–gas and solid–liquid conditions was conducted using elemental analysis, Fourier transform infrared spectroscopy with photoacoustic detection (FTIR-PAS), and nitrogen porosimetry.

II. EXPERIMENTAL

The silica (KG60-Merckj, thermally pretreated at 973 K, was allowed to cool in an N_2 -purged glove box to avoid any possible rehydration of the sample. This treatment results in 0.7×10^{-3} mol isolated hydroxyl groups on the silica surface. This is determined by chemical probe reaction with hexamethyldisilazane as explained elsewhere [3]. The chlorosilylations were performed using Janssen products, which were stored in an N_2 atmosphere. Tetrachlorosilane (99.8%) was used as received, whereas the solvents toluene (99%), cyclohexane (99%), and dichloromethane (99.8%) were zeolite-dried prior to use 0.5 g of silica, and excess of 0.8 mL tetrachlorosilane, and varying amounts of amine base were added to 25 mL of solvent. After 3 h of stirring, the silica was filtered, then washed four times with 10 mL of pure solvent. Afterwards, the silica was dried using a cryogenic trap and a vacuum pump.

Ammoniation was carried out in a dynamic volumetric adsorption apparatus, as described elsewhere [3]. The ammonia uptake was measured volumetrically, whereas the surface chlorine concentration was determined argentometrically [5]. Extreme care was taken to prevent the samples from hydrolysis, by handling them in a N_2 glove box or in vacuo. The total chlorine concentration was determined argentometrically after direct hydrolysis of the modified surface following reaction.

FTIR-PA spectra were recorded on a Nicolet 5DXB FTIR spectrophotometer with photoacoustic detection. The PA detector is a prototype of the MTEC-100 cell constructed by J. F. McClelland. The photoacoustic cell was flushed with zeolite-dried helium in an N_2 glove box. The mirror velocity was 0.08 cm/s. Comparison of the amount of hydroxyls was performed by integrating the O—H band at 3747 cm^{-1} after Kubelka–Munk correction of the spectrum and normalizing the OH band by using the integrated reference band at 1850 cm^{-1} assigned to a Si—O—Si combination mode.

Nitrogen adsorption–desorption isotherms at 77 K were measured with a Quantachrome Autosorb 1 instrument. The sample surface area was calculated using the Brunauer–Emmett–Teller (BET) model [12], whereas the pore size distribution was obtained using the Barrett–Joyner–Halenda (BJH) model [13]. The t -plot method was used to check the microporosity [14].

III. RESULTS AND DISCUSSION

A Liquid-Phase Modification of Silica Gel with Tetrachlorosilane and the First Ammoniation

The creation of chlorosilyl groups on the substrate surface is very important in the synthesis of a chemically bound preceramic polysilazane coating, because the amounts and types of chlorosilyl species present influence the reaction behavior of the reactions. In Table 1, a comparison of the elemental analysis data is shown for the gas- and liquid-phase synthesis routes as a function of the number of reaction cycles. Infrared spectroscopy of the modified silica gel was used to study the reaction yield. In Figure 1, the infrared spectra of pure silica (973 K, spectrum a) and silica modified with SiCl_4 in both the gas and liquid phases (spectra b–f) are shown. When toluene (spectrum c) or cyclohexane were used as solvents, all the huge bands between 3000 and 2000 cm^{-1} and the sharp bands superimposed on the Si—O vibrations between 1500 and 800 cm^{-1} exactly correspond to triethylammonium chloride, which was formed on the silica surface and could not be removed by severe washing. When dichloromethane was used (lines d and e) no salt formation was detected, and very fast removal of the solvent was possible due to its volatility. This solvent's high Lewis accepting property is shown to promote the reaction of silica gel with octadecyldimethylchlorosilane at room temperature [15]. The nitrogen-containing base used in this study has to be a tertiary amine, avoiding any polymerization reactions with SiCl_4 . Triethylamine was chosen, as its conjugated base has a relatively high $\text{p}K_a$ value (10.8). When the base was added in a catalytic amount (5 μL , i.e., 1/20 relative to the OH groups present), the reaction amount was very low (Fig. 1, spectrum e). The reason is that after protonation the base has no further influence on the reaction, which implies that it does not act as a catalyst, as was erroneously reported in the literature [8]. An excess of base (800 μL) resulted in almost complete modification of the surface hydroxyl groups (Fig. 1, spectrum d). As a blank, the reaction was also carried out under similar conditions but

TABLE 1 Nitrogen and Chlorine Uptake (in mmol/g Unmodified Silica Gel) and N/Cl Ratio as a Function of the Number of Reaction Cycles for the Liquid- and Gas-Phase Synthesis Routes

| | | Reaction | | Cycle ³ | |
|--------------------|------|-------------|-------------|--------------------|-----------|
| | | 1 | 2 | 3 | 4 |
| Liquid phase route | Cl | 1.53 (0.05) | 2.7 (0.1) | 1.6 (0.1) | 1.6 (0.3) |
| | N | 3.05 (0.05) | 3.6 (0.1) | 3.3 (0.1) | 3.3 (0.4) |
| | N/Cl | 1.99 (0.07) | 1.33 (0.06) | 2.0 (0.1) | 2.0 (0.5) |
| Gas phase route | Cl | 2.00 (0.05) | 2.9 (0.1) | 3.1 (0.1) | 2.7 (0.3) |
| | N | 3.6 (0.05) | 4.4 (0.1) | 5.1 (0.1) | 4.9 (0.3) |
| | N/Cl | 1.8 (0.05) | 1.5 (0.2) | 1.65 (0.06) | 1.8 (0.2) |

^a Values in parentheses represent the absolute experimental errors.

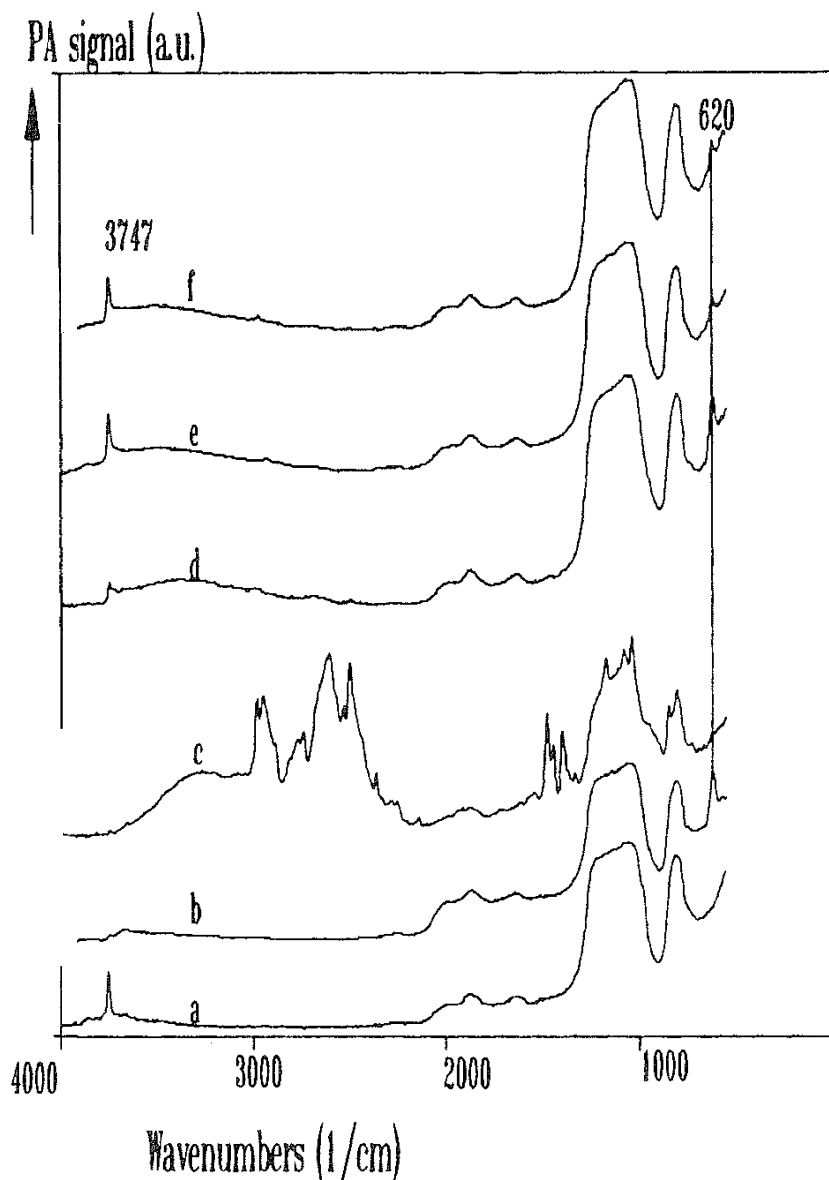


FIG. 1 FTIR-PA spectra of KG 60 (a) pretreated at 973 K, unmodified, and (b)–(e) modified with SiCl_4 ; (b) in gas phase, at optimal reaction conditions; (c) in liquid phase, using toluene and NEt_3 in excess; (d) in liquid phase, using CH_2Cl_2 and NEt_3 in excess; (e) in liquid phase, using CH_2Cl_2 and NEt_3 in catalytic amounts; (f) in liquid phase, using CH_2Cl_2 without NEt_3 . Relevant peak identification of silica gel: 3747 cm^{-1} , free $\equiv\text{SiO}-\text{H}$ stretch; 1850 cm^{-1} , $\equiv\text{SiOSi}\equiv$ combination; 1625 cm^{-1} , $\equiv\text{SiOSi}\equiv$ overtone; $1250\text{--}1050\text{ cm}^{-1}$, $\equiv\text{SiO}$ asymmetric stretch; 800 cm^{-1} , $\equiv\text{SiO}$ -symmetric stretch.

without triethylamine, resulting in no modification at all, as shown in Fig. 1, line f. In the liquid phase the highest yield is obtained with a high amine concentration in combination with a CH_2Cl_2 (spectrum d). The $\text{Si}-\text{Cl}$ vibration is positioned at the same frequency (620 cm^{-1}) for both a gas-phase reaction at 633 K (spectrum a) and a liquid-phase reaction at 298 K (spectrum d), indicating that monodentate binding occurs, resulting in $\equiv\text{SiCl}-\text{SiCl}_3$ groups [4]. The small $\text{SiO}-\text{H}$ band in the case of the liquid-phase modification (spectrum d) represents 25% of the total amount

of hydroxyl groups at the surface (0.53×10^{-3} mol of OH groups per gram of substrate are modified). As only —SiCl_3 groups are expected from IR data, the total chlorine content (Table 1) could be used to calculate the amount of —SiCl_3 groups created, being 0.51×10^{-3} mol of —SiCl_3 groups per gram of substrate. These two independently calculated values are in good agreement. Longer reaction times or higher amounts of reactants or amine base did not improve the reaction, probably due to steric hindrance, as both the amine and the SiCl_4 must be in the neighborhood in order to have any reaction.

Similar to the gas-phase chlorosilylated silica gel, the ammoniation was performed for 20 min at room temperature, as these were shown to be the optimal reaction conditions, resulting in the reaction [5]



After ammoniation, IR spectroscopy showed no difference between the gas and liquid synthesis routes. However, during the liquid-phase route, the nitrogen uptake is twice the chlorine uptake within the limit of experimental error, whereas only 90% of the chlorines are ammoniated after a gas-phase chlorosilylation (i.e., $\text{N/Cl} = 1.8$). From a steric point of view, this is a logical result, as in the liquid synthesis route both SiCl_4 and NEt_3 must be near the attacked SiOH group. Therefore, a smaller amount of chlorosilyl groups is formed in the liquid-phase synthesis route, situated at the most easily reached hydroxyls. After the liquid-phase reaction, NEt_3 leaves the reaction site, leaving an empty space that can be reached by NH_3 during the ammoniation. In the gas-phase synthesis route, no NEt_3 is needed for the silylation, and higher proton mobility is expected at the high temperature, resulting in silylation of OH groups at sterically hindered sites. Anyway, a significant fraction of these chlorosilyl groups synthesized in the liquid phase could not be modified by ammoniation due to steric reasons.

B. Second and Higher Reaction Cycles

In Fig. 2, the IR spectra of the samples after the first ammoniation (spectrum a) and the second liquid chlorosilylation are shown for different reaction conditions. From the second chlorosilylation on, dichloromethane could not be used and was replaced by cyclohexane, because dichloromethane reacts with the amino groups. The addition of triethylamine to the reaction mixture (spectrum b) leads to the deposition of triethylammonium chloride at the sample surface, which could not be removed with the solvent used or by sublimation, because thermal treatment also leads to condensation reactions of the amino groups [4]. Therefore, the chlorosilylations are performed without the addition of triethylamine. Spectrum c of Fig. 2 is that of the preceramic precursor after the second chlorosilylation. In the Si—Cl region, maxima are observed at 624 and 590 cm^{-1} . This means that both =SiCl_2 and —SiCl_3 groups are formed. The total disappearance of the asymmetric N-H bending vibration at 1544 cm^{-1} assigned to $\equiv\text{SiNH}_2$ groups indicates a total modification of these groups. Therefore, an estimation of the ratio of mono and bidentate reactions could be calculated [4]. Elemental analysis and iteration showed that 93% of the NH_2 groups are modified by bidentate binding and 7% by monodentate binding.

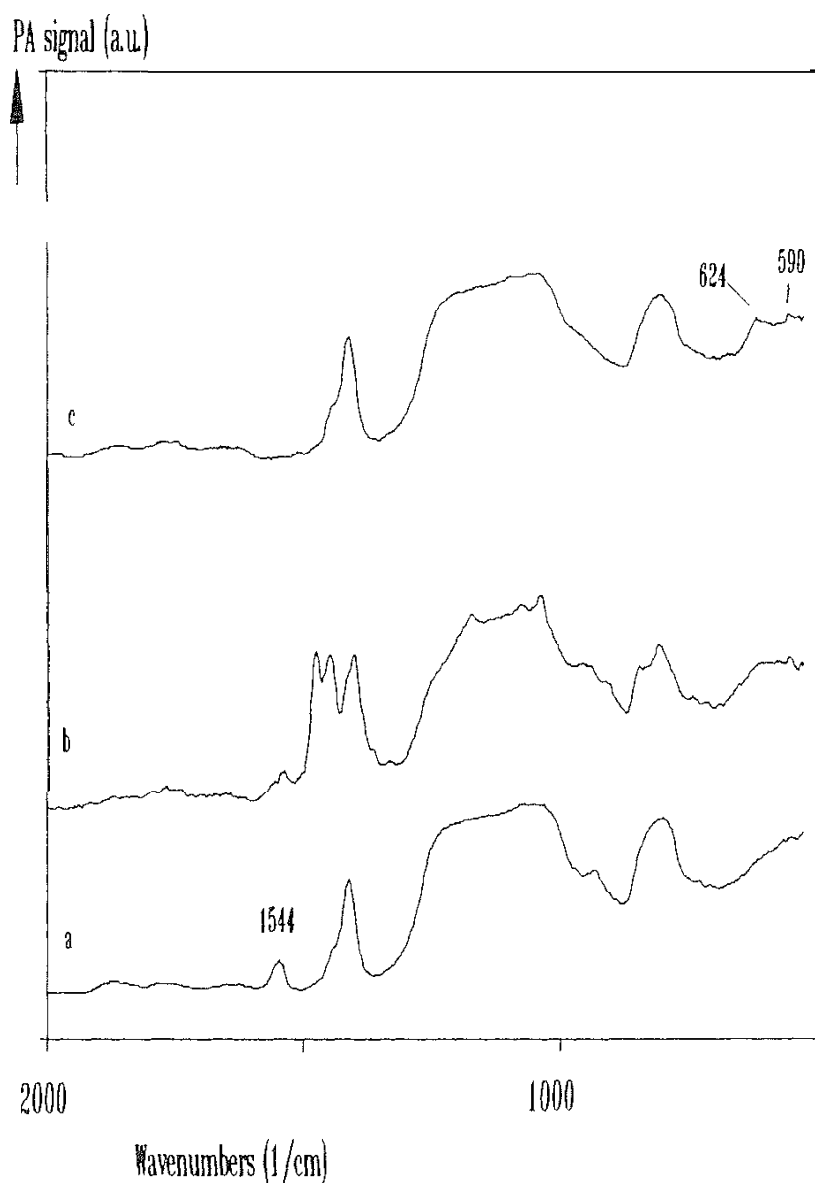


FIG. 2 FTIR-PA spectra of KG 60, pretreated at 973 K. (a) Reacted with SiCl_4 in CH_2Cl_2 and excess NEt_3 , and afterwards reacted with NH_3 in the gas phase. (b, c) Same as (a) but modified with SiCl_4 (b) in the presence of NEt_3 , using cyclohexane, and (c) without NEt_3 , using cyclohexane.

The second ammoniation does not lead to completion, as an N/Cl ratio of only 1.33 is reached. A similar phenomenon was observed in the gas-phase synthesis route, where an N/Cl ratio of 1.5 was found. In the gas-phase synthesis route, a higher uptake of Cl is observed during the third and fourth chlorosilylations than in the liquid phase. This is certainly due to the presence of the solvent in the liquid case, which leads to a sterically unfavorable situation. Therefore, chlorosilylation is expected only at the most easily reached sites. From the third reaction cycle on, the ammoniation leads to a complete modification of the $\equiv\text{SiCl}$ groups in the liquid-phase synthesis route, whereas the gas-phase synthesis route never leads to an N/Cl ratio of 2. After the solvent evacuation in the liquid case, there is enough space left for NH_3 to reach and react with all the $\equiv\text{SiCl}$ groups. The general trend of

nitrogen, chlorine, and weight uptake during the four reaction cycles for both the liquid- and gas-phase synthesis routes is shown in Fig. 3.. In general, all the curves are linear except for the chlorine uptake in the liquid-phase route, where a deflection is observed at two cycles. However, this trend is not followed by the NH_3 uptake, as the ammoniation is not disturbed by solvent hindrances. From this figure, it is clear that in the liquid case a smaller amount of polymer is formed on the silica surface, whereas all the gas-phase slopes are higher than in the case of liquid-phase modification. The total increase in weight gain after four reaction cycles is 0.55 and 0.8 g per gram of unmodified silica in the liquid and gas synthesis routes, respectively.

From the rough analytical data of Table 1, the amounts of SiCl , $\equiv\text{SiNH}_2$, $\equiv\text{SiNHSi}$, and NH_4Cl can be calculated (Table 2). These data can give an idea of the cross-linking in the polymeric preceramic material. The amount of NH_4Cl reflects roughly the ratio between the increasing weight of the two synthesis routes (weight: $0.55/0.8 = 0.69$; NH_4Cl : $6.6/9 = 0.73$), whereas the amount of unreacted SiCl groups is relatively lower in the liquid-phase synthesis route, even when the increased weight ratio is taken into account ($0.8/1.7 = 0.47$). This result was expected from the trend difference in the Cl and NH_3 uptakes. Another important factor is the percentage of primary amines that are not modified into silazanes: In the gas phase, only 26% of the total $\equiv\text{Si}-\text{N}=\text{}$ population has not reacted, whereas 36% is unreacted in the liquid-phase synthesis route. This means that a lower cross-linking efficiency is reached in the liquid-phase route. This value, in combination with the lower uptake of nitrogen in the liquid-phase synthesis route, shows that a gas-phase synthesis is more suitable for the synthesis of a dense cross-linked precursor.

C. Porosity Study

With each modification cycle during the synthesis of the polysilazane structure, the amount of product left at the silica pore walls increases. To study the effect on the substrate porosity of both types of precursors, N_2 adsorption–desorption isotherms are recorded at 77 K as a function of the number of reaction cycles. The isotherms presented in Fig. 4 are from the liquid-phase synthesis route and are all of type IV according to the Brunauer–Deming–Deming–Teller (BDDT) classification [16]. Therefore, both the substrate and the coated material are mesoporous materials. The total pore volume decreases with increasing number of reaction cycles. The type of hysteresis changes from type H_1 to H_2 according to the IUPAC classification [17]. Type H_1 corresponds to the pore shape of pure silica gel, whereas the H_2 type indicates ink-bottle or irregularly shaped pores. The evolution in the hysteresis shows the occurrence of pore shape modification during the formation of the polymer. This phenomenon earlier observed was for the gas-phase synthesis route [6]. The behavior of the C_{BET} constants for the liquid-phase reaction shows the same trend as in the gas phase; i.e., from the first cycle on, an important decrease is observed, indicating total monolayer coverage.

Using the calculation methods pointed out by Impens et al. [6], a difference between the theoretically expected and experimentally observed pore volume decreases can be used to calculate the amounts of pore blocking and regular

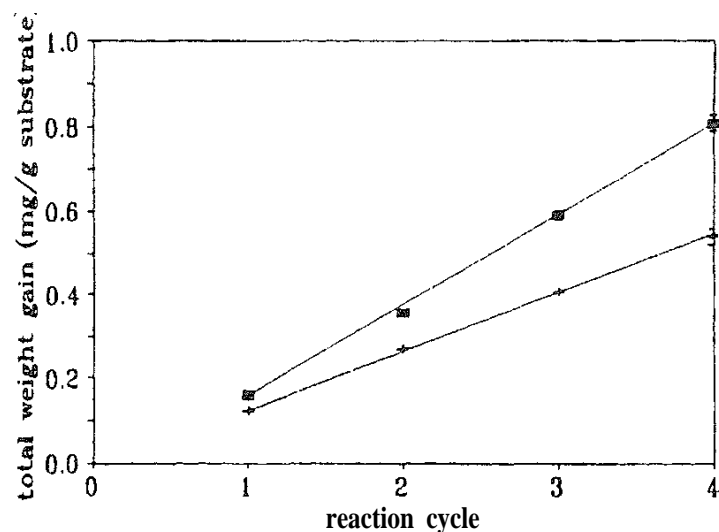
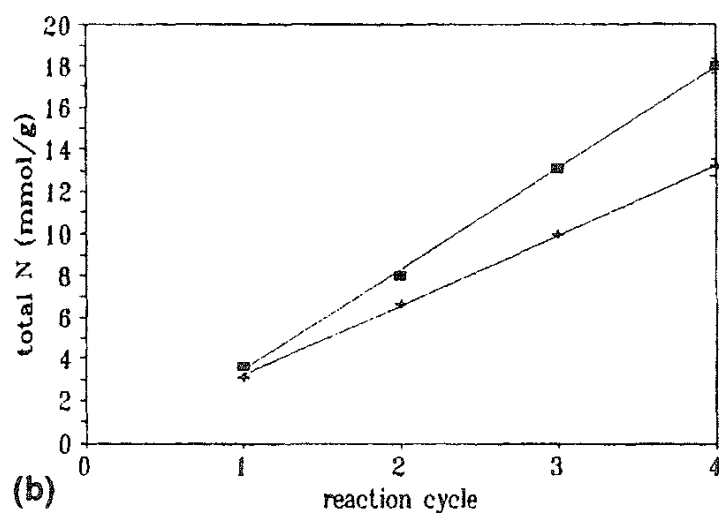
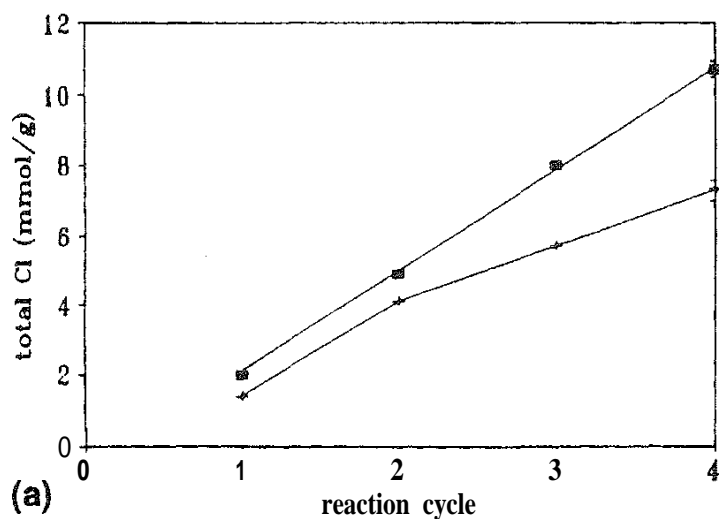


FIG. 3 Total (a) Cl, (b) N, and (c) weight uptakes as a function of the number of reaction cycles for (■) gas and (+) liquid synthesis routes, with corresponding linear regressions. A deflection point is introduced in the regression of the (+) curve of (a). The experimental errors for the first three reaction cycles are smaller than the symbols used.

TABLE 2 Composition of the Polysilazane Coating After Four Reaction Cycles for the Liquid- and Gas-Phase Synthesis Routes

| Species | Amount in coating (mmol/g unmodified silica gel) ^a | |
|-------------------------------|---|-----------------|
| | Liquid-phase route | Gas-phase route |
| $\equiv \text{SiCl}$ | 0.8 (0.4) | 1.7 (0.4) |
| NH_4Cl | 6.6 (0.2) | 9 (0.2) |
| $\equiv \text{SiNHSi} \equiv$ | 4.2 (0.4) | > 6.7 (0.3) |
| $\equiv \text{SiNH}_2$ | 2.4 (0.4) | < 2.4 (0.3) |

^aValues in parantheses represent the absolute experimental errors

pore narrowing. This method is independent of the pore shape [6]. In Figs. 5a and 5b, the theoretical and experimental pore volumes are shown as a function of the amount of NH_3 chemisorption for both synthesis routes. As an example, the amount of chemisorbed NH_3 is highlighted in the figures when a pore volume of $0.2 \text{ cm}^3/\text{g}$ is left. In the liquid-phase synthesis route (Fig. 5a), only 13 mmol/g NH_3 is chemisorbed. In the gas-phase synthesis route (Fig. 5b), the chemisorbed NH_3 is already 15 mmol/g. This indicates a higher amount of pore blocking in the liquid-phase synthesis route.

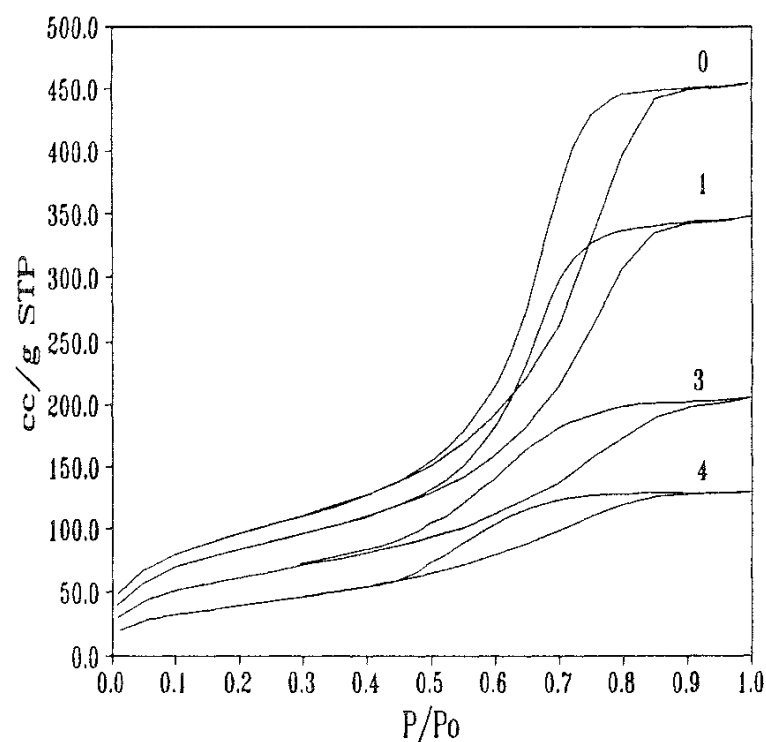


FIG. 4 Nitrogen adsorption–desorption isotherms at 77 K for the polysilazane-coated silica gel after zero, one, three and four reaction cycles of the liquid-phase synthesis route. The experimental error on the amount of N_2 adsorbed is $0.1 \text{ cm}^3/\text{g}$ STP.

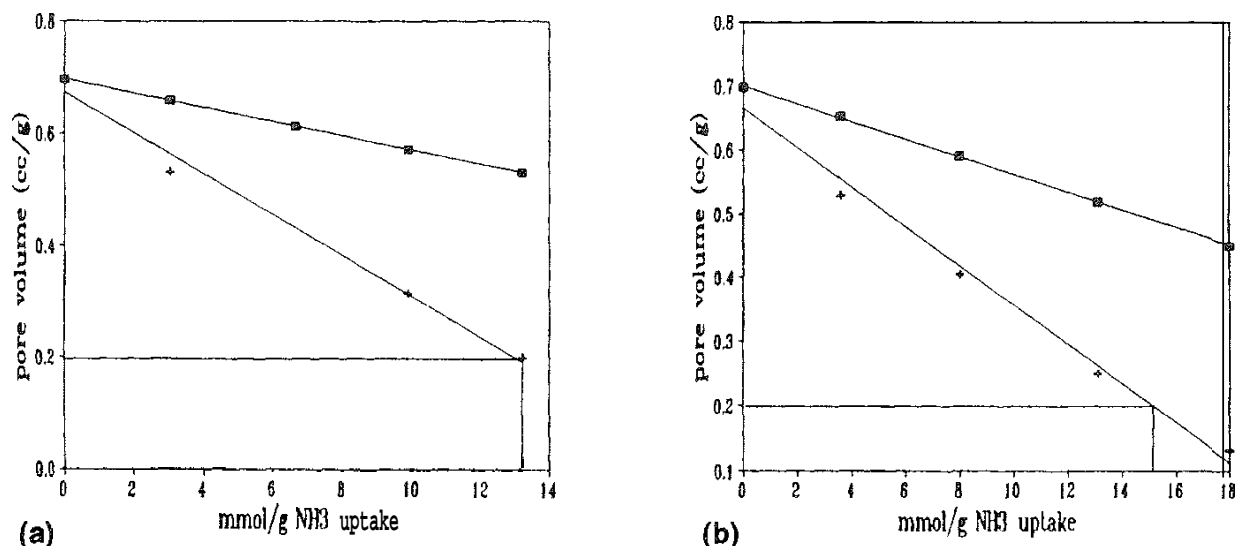


FIG. 5 Pore volume decreases as a function of the amount of NH_3 reacted. (■) Theoretical and (+) experimental values, (a) Liquid-phase synthesis route; (b) gas-phase synthesis route. The experimental errors are smaller than the symbols used. The linear regressions serve only as a guide for the eyes.

A similar trend was observed when the decreases in pore length were calculated using integration of the pore volume distributions obtained by the BJH method [13], as explained earlier [6]. However, this method is valid exclusively for cylindrical pores. The results are shown in Fig. 6. A systematically smaller pore length value is obtained for the liquid-phase route. These data show that more pore blocking occurs in this synthesis route.

The calculated amounts of pore-blocking and pore narrowing and their contribution to the total pore volume decrease are listed in Table 3. The results are based on the data of Fig. 5. Systematically higher absolute and relative amounts of pore blocking are seen for the liquid-phase synthesis route in spite of the lower uptake of N and Cl per reaction cycle, resulting in a lower coating homogeneity. Moreover, from the higher absolute and relative narrowing values in the gas-phase synthesis route, it can be concluded that a higher coating efficiency is obtained using the gas-phase synthesis route.

IV. CONCLUSIONS

Successive reactions of SiCl_4 in the liquid phase and NH_3 in the gas phase were performed on silica gel. The reaction parameters for the chlorosilylations (i.e., solvent choice and base promotion) were optimized to get as much $\equiv\text{SiCl}$ uptake as possible. The chemical composition of the polysilazane layer as a function of the number of reaction cycles is obtained by using a combination of elemental and infrared analysis.

A comparison of these results with the composition of a polysilazane coating fully synthesized in the gas phase showed less uptake of N and Cl and a greater number of $\equiv\text{SiNH}_2$ groups due to the presence of the solvent. This implies that the

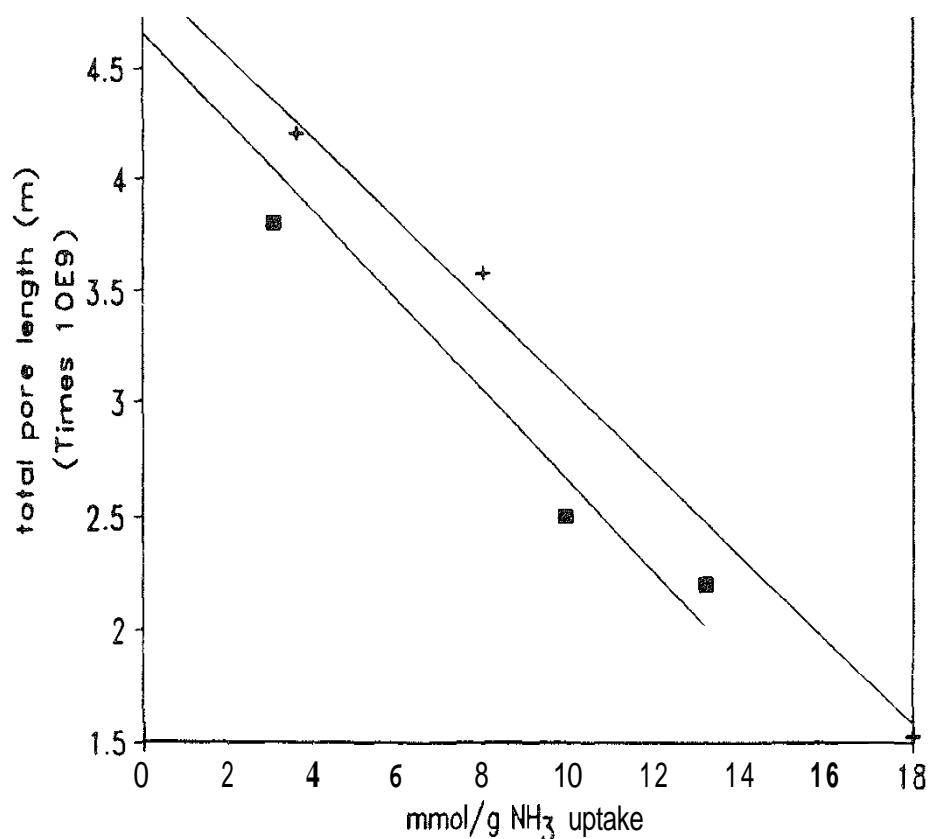


FIG. 6 Pore length decreases for (+) gas and (■) liquid synthesis routes, with respective linear regressions. The experimental errors are smaller than the symbols used. The linear regressions serve only as a guide for the eyes.

TABLE 3 Contribution of Pore Narrowing and Pore Blocking to the Decrease in Pore Volume^a

| Cycles | PV _{exp} (cm ³ /g) | PV _{theor} (cm ³ /g) | Blocking (cm ³ /g) | Narrowing (cm ³ /g) | Blocking (%) | Narrowing (%) |
|---------------------|---|---|----------------------------------|-----------------------------------|-----------------|------------------|
| Si-N (gas phase) | | | | | | |
| 0 | 0.70 | 0.70 | 0.00 | 0.00 | — | — |
| 1 | 0.53 | 0.65 | 0.12 | 0.05 | 71 | 29 |
| 2 | 0.41 | 0.58 | 0.17 | 0.12 | 59 | 41 |
| 3 | 0.29 | 0.49 | 0.20 | 0.21 | 49 | 51 |
| 4 | 0.13 | 0.39 | 0.26 | 0.31 | 46 | 54 |
| Si-N (liquid phase) | | | | | | |
| 0 | 0.70 | 0.70 | 0.00 | 0.00 | — | — |
| 1 | 0.53 | 0.66 | 0.13 | 0.04 | 77 | 23 |
| 2 | — | 0.61 | — | — | — | — |
| 3 | 0.31 | 0.57 | 0.26 | 0.13 | 67 | 33 |
| 4 | 0.20 | 0.53 | 0.33 | 0.17 | 67 | 33 |

PV = pore volume.

^aThe experimental errors on the pore volumes range from 0.0005 to 0.005 cm³/g. The errors in the percentages are smaller than 1%.

gas-phase synthesis route is more suitable for the creation of a dense, cross-linked polysilazane polymer on the silica surface.

The porosity was studied by using N₂ adsorption–desorption isotherms recorded at 77 K. A higher amount of pore blocking in the liquid–phase synthesis route was observed, although a smaller amount of product was chemisorbed. A combination of the pore blocking and pore narrowing results shows that the gas-phase synthesized polysilazane coating is more homogeneously spread on the silica surface.

REFERENCES

1. D. Seyferth, *Adv. Chem. Ser.* 224: 565.
2. D. Seyferth and G. H. Weiseman, *Polymer Prepr.* 25(1):10 (1984).
3. E. F. Vansant, P. Van Der Voort and K. C. Vrancken. *Characterization and Chemical Modification of the Silica Surface*, Elsevier. Amsterdam. 1995.
4. N. R. E. N. Impens, K. Possemiers, and E. F. Vansant, *J. Chem. Soc. Faraday Trans* 92(22):4285 (1996).
5. K. Possemiers, N. R. E. N. Impens, and E. F. Vansant, *J. Chem. Soc, Faraday Trans.* 93(13):2309 (1997).
6. N. R. E. N. Impens, K. Possemiers, K. Schrijnemakers, N. Maes, and E. F. Vansant, *J. Porous Mater.* 4:121 (1997).
7. N. R. E. N. Impens, K. Schrijnemakers, E. F. Vansant, P. Grobet, J. Riga and O. Brouxhon, *J. Mater. Chem.* 7(8):1467 (1997).
8. K. Possemiers, Ph.D. thesis, Antwerp, 1996.
9. C. P. Tripp, and M. L. Hair, *J. Phys. Chem.* 97:21 (1993).
10. J. P. Blitz, R. S. Murthy, and D. E. Leyden, *J. Colloid Interface Sci.* 127:387 (1988).
11. J. N. Kinkel and K. K. Unger, *J. Chromatogr.* 316:193 (1984).
12. S. Brunauer, P. H. Emmett, and E. Teller, *J. Am. Chem. Soc.* 60:309 (1938).
13. E. P. Barrett, L. G. Joyner, and P. P. Halenda, *J. Am. Chem. Soc.* 73:373 (1951).
14. B. C. Lippens and J. H. De Boer, *J. Catal.* 4:319 (1965).
15. J. N. Kinkel, and K. K. Unger, *J. Chromatogr.* 316:193 (1984).
16. S. Brunauer, L. S. Deming, W. S. Deming, and E. Teller, *J. Am. Chem. Soc.* 62:1723 (1940).
17. S. J. Gregg, and K. S. W. Sing, *Adsorption, Surface Area and Porosity*, Academic, New York, 1976, p. 287.

2

Preparation of Molecular Sieves by Pillaring of Synthetic Clays

SOON-YONG JEONG Chemical Process and Engineering Center, Korea
Research Institute of Chemical Technology, Taejeon, Korea

- I. Introduction
- II. Experimental Methods
 - A. Synthesis of aluminum-free clays
 - B. Synthesis of H-magadiite and H-kenyaite
 - C. Silica-intercalated layered silicate
 - D. Analytical methods
- III. Results and discussion
 - A. Synthesis of aluminum-free clays
 - B. Octylamine/octylammonium layered silicate gel
 - C. Reactions with TEOS
 - D. Gelation effects
- IV. Conclusions
- References

I. INTRODUCTION

In recent years, the synthesis of aluminum-free clays such as magadiite ($\text{Na}_2\text{Si}_{14}\text{O}_{29} \cdot 9\text{H}_2\text{O}$), kenyaite ($\text{Na}_2\text{Si}_{22}\text{O}_{45} \cdot 10\text{H}_2\text{O}$) and kanemite ($\text{Na}_2\text{HSi}_2\text{O}_5 \cdot 2\text{H}_2\text{O}$) has been of increasing interest due to their catalytic, absorptive, and ion-exchange properties [1,2]. Synthetic aluminum-free clays are also called layered silicates because they have a layered structure. They have the characteristic of being free of aluminum, unlike zeolites, and exhibit acid-resistance and thermal stability. Magadiite and kenyaite were first found by Eugster [3] in the lake beds of Lake Magadi in Kenya. Since then they have been reported to occur in various regions [4,5]. Most of these deposits were found in sodium carbonate-rich alkaline lake waters. Also they have been successfully synthesized under hydrothermal

conditions. Their basic structures are composed of duplicated SiO_4 tetrahedral sheets and are similar to those of clay minerals with no aluminum [6,7]. Lagaly and Beneke [8] discussed the preparation of Na-magadiite in a hydrothermal system at 100°C employing 4 weeks of reaction. More recently, Muraishi [9] synthesized K-magadiite at $100\text{--}180^\circ\text{C}$ with 2–5 days of reaction in KOH solution containing various amounts of NaCl. Kosuge et al. [10] synthesized Na-magadiite at 170°C with 18 h of reaction in the presence of organic solvent. However, the preparation of kenyaite has rarely been reported. Beneke and Lagaly [11] indicated that the formation of kenyaite at 100°C required several months. At higher temperature, the reaction time for the formation of kenyaite was much decreased, but quartz was formed simultaneously. More recently, Fletcher and Bibby [12] preliminarily investigated the effects of anions on the formation of kenyaite.

Silica pillaring of magadiite was reported by a few researchers. Landis et al. [13] found that the pillaring of magadiite could be facilitated by using a preswelling step in which the interlayers are exposed to organoammonium ion or amine. The calcined sample obtained from tetraethoxysilane (TEOS; $\text{Si}(\text{OC}_2\text{H}_5)_4$) pillaring exhibited a high surface area, $530\text{ m}^2/\text{g}$. Scholzen et al. [14] described the change in the ratio of $\text{Q}^3(\text{HOSiD}_3)$ to $\text{Q}^4(\text{SiO}_4)$ groups caused by silane coupling of silicate species with SiOH groups on the interlayered surface of magadiite. Sprung et al. [15] reported that pillared derivatives of magadiite can be obtained from the calcination of hydrolyzed phenyltrichlorosilane magadiites. Daily and Pinnavaia [16] synthesized supergallery derivatives on the basis of H-magadiite by gelation of TEOS with EtOH suspension. After calcining to remove organic compounds, pillared magadiite with surface areas of about $520\text{--}680\text{ m}^2/\text{g}$, depending on the amount of gelled TEOS, was formed. However, the pillaring of kenyaite has rarely been reported. Recently, Landis et al. [13] prepared pillared derivatives on the basis of H-kenyaite by gelation of TEOS with EtOH suspension. The calcined sample exhibited a high surface area, $600\text{ m}^2/\text{g}$.

In the sol-gel process, a solvent such as EtOH is added to prevent liquid-liquid separation during the initial stage of the hydrolysis reaction and to control the concentration of silicate species and water that influence the gelation kinetics [17]. However, the reaction of TEOS gelation by alcohol suspension occurs very slowly [17], and because TEOS is alcohol-soluble it can be released outside the layered phases during gelation. Aelion et al. [18] observed that the rate of hydrolysis of TEOS was influenced by the strength and concentration of the acid and base catalysts. Fast gelation using a catalyst such as acid or base can minimize the release of TEOS from the layered phases during gelation. Generally, TEOS gelation by acid- or base-catalyzed hydrolysis could diversify the interfacial properties of products and results in such products as bulk gel, film, fiber, powder, and catalyst support. In particular, gelation by acid and base catalyst into interlayers could bring out the pillaring effect as well as the diversity of interfacial properties of pillared layered phases. According to Brinker and Scherrer [17], the use of catalyst tends to develop the degree of polycondensation of the pillar in interlayers, so that gallery height can be increased.

We synthesized pure and well-crystallized Na-magadiite and Na-kenyaite under the carbonate system in a short reaction time. I report here the effects related to the compositions of reactants, reaction time, and temperature on the preparation of

these clays in the sodium carbonate system. Also, I report the effects of acid and base catalysts on the hydrolysis and condensation polymerization of intercalated TEOS in layered silicates.

II. EXPERIMENTAL METHODS

A. Synthesis of Aluminum-Free Clays

Na-magadiite and Na-kenyaite were prepared by the reaction of the SiO_2 -NaOH- Na_2CO_3 system under hydrothermal conditions. The materials used were silica gel (Wakogel Q-63) and NaOH and Na_2CO_3 of analytical reagent grade. Experiments were carried out in a stainless steel autoclave without stirring for the various reaction times and molar ratios of reactants at 150–180°C under autogenous pressure. The molar ratio of NaOH to Na_2CO_3 was fixed at 1/2 in all cases. The products were filtered, washed with deionized water to remove excess NaOH or Na_2CO_3 , and then dried at 40°C.

B. Synthesis of H-Magadiite and H-Kenyaite

H-magadiite was prepared by titrating Na-magadiite with 0.1 N HCl using the method of Beneke and Lagaly [11]. A suspension of 40g of Na-magadiite per 500mL of deionized water was stirred for 1 h. The suspension was then titrated with 0.1 N HCl to a final pH of 2.0 and then maintained at the same pH value for 1 week in a refrigerator. H-magadiite was recovered by filtering, washed with deionized water until chlorine free, and then dried in air at 40°C. The preparation of H-kenyaite was the same as that of H-magadiite.

C. Silica-Intercalated Layered Silicate

Octylamine/octylammonium magadiite gel was reacted for 24 h at room temperature by adding 10 g of excess octylamine to 2.0 g of air-dried H-magadiite. An organic pillar precursor, 40 g of TEOS, was added to octylamine/octylammonium magadiite gel and then stirred for 24 h at room temperature. TEOS was then absorbed into the organophilic interlayer region. TEOS-intercalated magadiite was separated by centrifugation from the mother liquid.

Octylamine/octylammonium kenyaite gel was formed by allowing air-dried H-kenyaite (2.0 g) to react at room temperature with excess octylamine (4.0 g) for 24 h. During octylamine addition, H-kenyaite absorbs the liquid amine, immediately forming a gelatinous mixture that will not flow. Silica-intercalated derivatives of kenyaite were prepared by the reaction of excess TEOS (40 g) with a gel composed of octylammonium kenyaite solvated by excess octylamine for 24 h at room temperature. The TEOS-intercalated product was separated by centrifugation from the mother liquid.

Gelation of the intercalated TEOS without catalyst was carried out by drying EtOH (10mL) suspension of TEOS-intercalated magadiite of kenyaite at 40°C in air. EtOH was mixed with 3 N NH_4OH and 0.1 N HCl in order to examine the effects of base and acid catalysts during the gelation. The compositions of acid and base catalysts are shown in [Table 1](#). Gelation was conducted with stirring for 60

TABLE 1 Compositions of Catalysts (wt%)

| | EtOH | H ₂ O | HCl | NH ₃ |
|---------------|------|------------------|------|-----------------|
| No catalyst | 95.0 | 5.0 | — | — |
| Base catalyst | 16.5 | 79.2 | — | 4.3 |
| Acid catalyst | 64.8 | 35.2 | 0.01 | — |

Source: Ref 29

min after addition of 10mL of each catalyst to the TEOS-intercalated magadiite or kenyaite at room temperature. The stoichiometry and methodology of gelation of TEOS are well known, and the physical characterization of gelled silicate has been studied by several researchers [17,19,20]. The gelled samples were filtered from the mother liquid, dried in air, and then calcined at 538°C for 4 h in air to remove water, intercalated organoammonium ion, and organic by products from TEOS hydrolysis.

D. Analytical Methods

Identification of samples was carried out by X-ray powder diffraction (Rigaku Rotaflex diffractometers equipped with CuK α radiation) and scanning electron microscopes (Jeol, JSM-840A). The chemical compositions of synthetic magadiite and kenyaite were determined with an energy-dispersive X-ray spectrometer (Link System AN10000-85S) and thermogravimetric analysis (TGA). EDX analysis was carried out using an electron beam with the sample of carbon-coated pellets. For the quantitative analysis of silica and sodium, quartz and sodium chloride were used as references. Thermogravimetric analyses were performed in air on a Dupont 9900 thermogravimetric analyzer. Basal spacings of samples were determined from the 001 X-ray powder diffraction using a Rigaku diffractometer equipped with Cu K α radiation. Samples of octylamine/octylammonium layered silicate gel and TEOS-intercalated layered silicate gels were prepared by smearing a thin film across a microscope slide and then recording diffraction patterns of wet samples. The products gelled by EtOH suspension, base-catalyzed reaction, and acid-catalyzed reaction were prepared by depositing a gelled suspension on a glass plate and allowing the suspension to air dry at 35°C. The calcined silica-pillared magadiite and kenyaite for X-ray diffraction analysis were prepared by calcining the gelled products on glass plates at 538°C in air for 4 h. Nitrogen adsorption-desorption isotherms were determined by Micrometrics ASAP 2000 at 77 K. All samples were outgassed at 300°C under a vacuum for 4 h. Surface area was determined by using the Brunauer-Emmett-Teller (BET) equation. The pore size distributions of silica-pillared products were determined by using the Barrett-Joyner-Halenda (BJH) equation [21].

III. RESULTS AND DISCUSSION

A. Synthesis of Aluminum-Free Clays

Figure 1 shows the development of crystalline magadiite with increasing reaction time at 150°C in the reactant compositions of $\text{SiO}_2/(\text{NaOH} + \text{Na}_2\text{CO}_3) = 5$ and

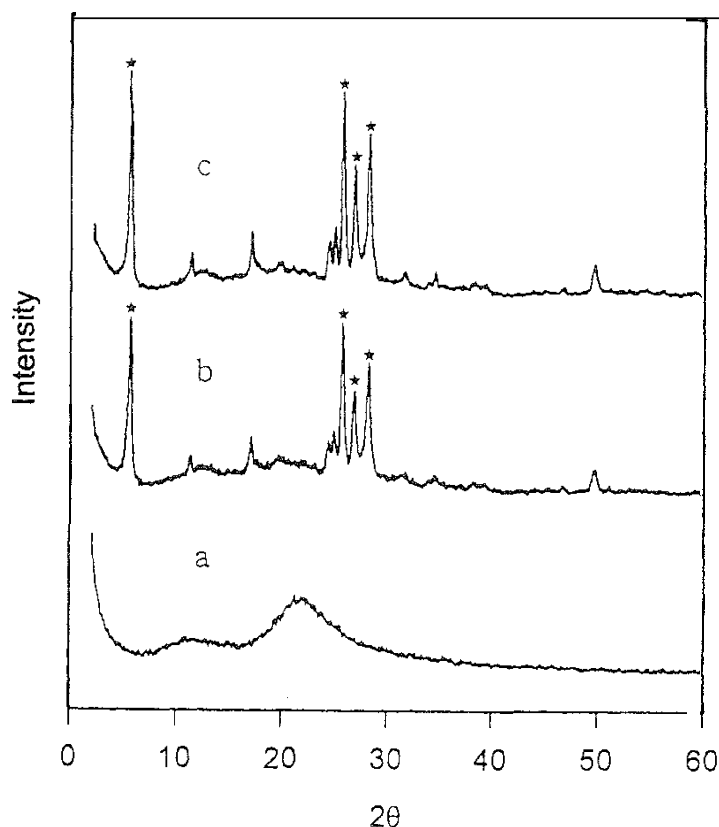


FIG. 1 X-ray diffraction patterns of synthetic magadiites at 150°C according to reaction time. Reactant molar ratio: $\text{SiO}_2/(\text{NaOH} + \text{Na}_2\text{CO}_3) = 5$; $\text{H}_2\text{O}/(\text{NaOH} + \text{Na}_2\text{CO}_3) = 100$. (a) 15 h; (b) 36 h; (c) 72 h. (★) Magadiite.

$\text{H}_2\text{O}/(\text{NaOH} + \text{Na}_2\text{CO}_3) = 100$. The X-ray diffraction (XRD) pattern of synthetic magadiite exhibited 001 X-ray reflections of the film sample corresponding to a basal spacing of 1.56 nm. The peak positions for synthetic magadiite agree well with values reported previously [13,15,16] for synthetic and natural magadiite. Pure magadiite is obtained after 36 h of reaction, and then the intensity of the peak increases as the reaction time increases from 36 to 72 h. Magadiite is synthesized directly from an amorphous form of silica, and the pure magadiite can be synthesized easily by adjusting reaction time and temperature. Figure 2 shows XRD patterns of synthetic samples at 170°C at fixed reactant compositions of $\text{SiO}_2/(\text{NaOH} + \text{Na}_2\text{CO}_3) = 5$ and $\text{H}_2\text{O}/(\text{NaOH} + \text{Na}_2\text{CO}_3) = 100$ for the different reaction times. As reaction time increases from 20 to 72 h, magadiite is transformed into kenyaite, and then kenyaite is transformed into quartz. Beneke and Lagaly [11] suggested that at 100°C, amorphous silica is transformed into magadiite and then into kenyaite. Above 100°C, the rate of kenyaite formation is much increased, and the rate of quartz formation is increased simultaneously. After 55 h, pure crystallized kenyaite is formed. The XRD pattern of synthetic kenyaite exhibits 001 X-ray reflections of the film sample corresponding to a basal spacing of 2.03 nm. The peak positions for synthetic kenyaite agree with values reported previously [10,11] for synthetic kenyaite. After 72 h, however, the quartz phase appears. This result indicates that it is very difficult to obtain pure kenyaite by controlling reaction

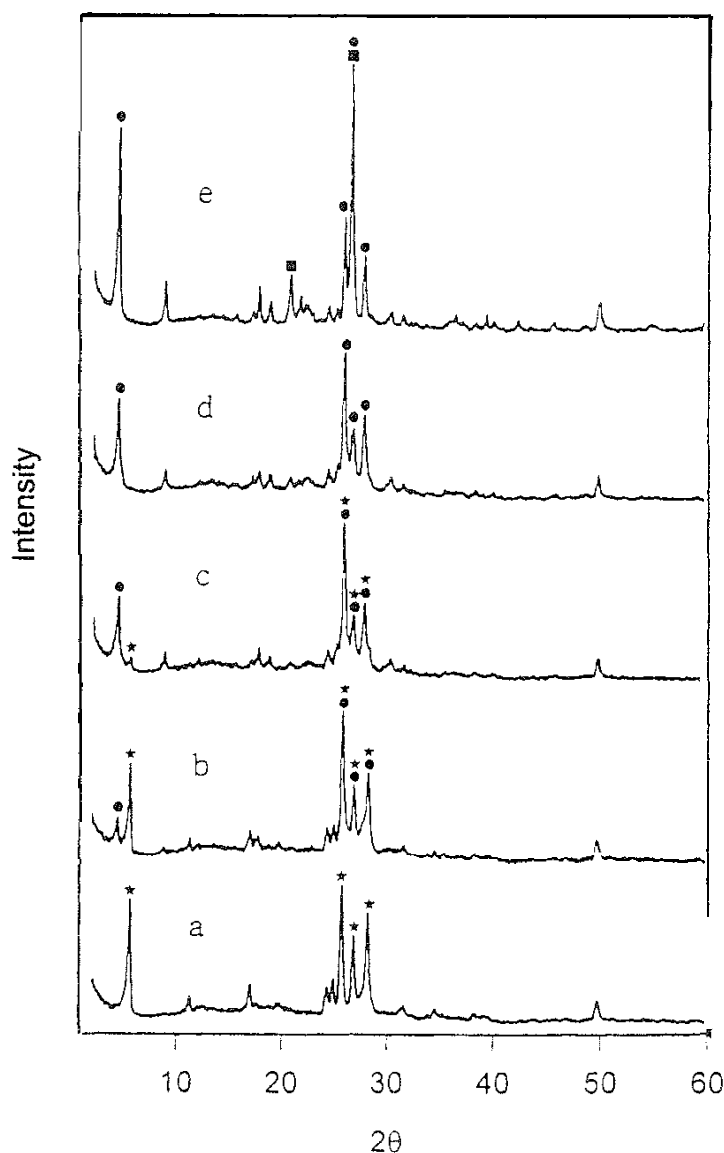


FIG 2 X-ray diffraction patterns of synthetic samples at 170°C according to reaction time. Reactant molar ratio: $\text{SiO}_2/(\text{NaOH} + \text{Na}_2\text{CO}_3) = 5$; $\text{H}_2\text{O}/(\text{NaOH} + \text{Na}_2\text{CO}_3) = 100$. (a) 20 h; (b) 45 h; (c) 50 h; (d) 55 h; (e) 72 h. (★) Magadiite; (●) kenyaite; (■) quartz. (From Ref. 30.)

time because pure kenyaite can be synthesized within only a short range of reaction time.

Figure 3 shows XRD patterns of synthetic samples obtained at 180°C in the higher molar ratio of Si/Na [$\text{SiO}_2/(\text{NaOH} + \text{Na}_2\text{CO}_3) = 20$ and $\text{H}_2\text{O}/(\text{NaOH} + \text{Na}_2\text{CO}_3) = 200$] with reaction time. Kenyaite can be synthesized directly from amorphous silica, and magadiite was not observed as an intermediate.

The higher Si/Na molar ratio accelerates the formation of kenyaite. Silica is first dissolved in alkali solution at elevated temperature, and then the nucleation of kenyaite occurs gradually. Therefore, the Si/Na ratio in the solution is a very important factor in the formation of kenyaite. Also, the higher content of silica in the composition of starting materials may cause a large Si/Na ratio in the solution. These conditions could accelerate the nucleation of kenyaite that has a

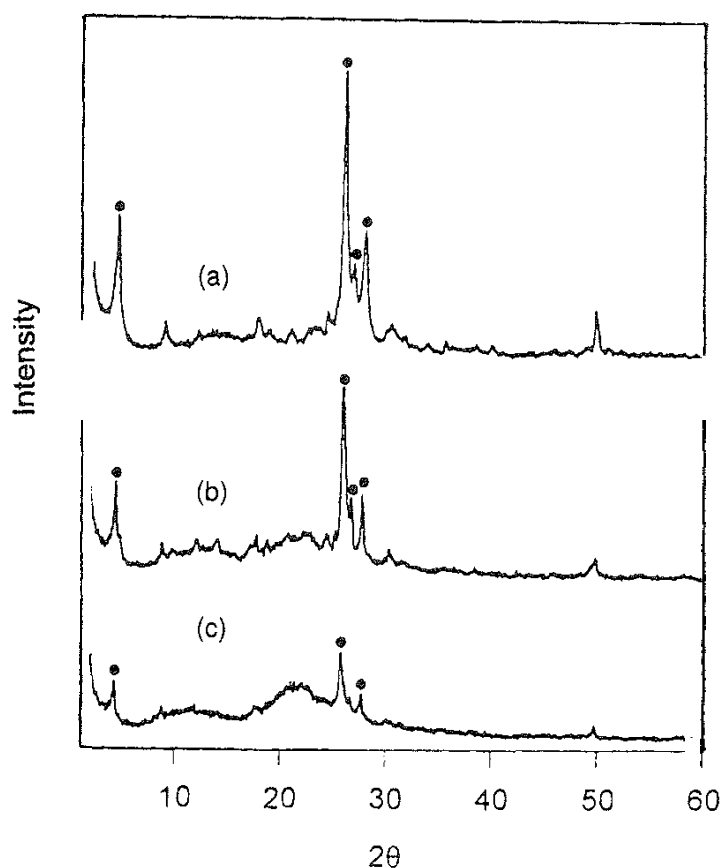


FIG. 3 X-ray diffraction patterns of synthetic samples at 180°C according to reaction time. Reactant molar ratio: $\text{SiO}_2/(\text{NaOH} + \text{Na}_2\text{CO}_3) = 20$; $\text{H}_2\text{O}(\text{NaOH} + \text{Na}_2\text{CO}_3) = 200$. (a) 96 h; (b) 65 h; (c) 45 h. (●) Kenyaite. (From Ref. 30.)

large Si/Na ratio. However, if the Si/Na ratio in the solution is large enough, kenyaite is capable of forming directly from amorphous silica without the formation of magadiite as an intermediate. The higher Si/Na molar ratio and the direct synthesis without an intermediate could be taken advantage of for obtaining pure kenyaite industrially.

Figure 4 shows scanning electron micrographs of the synthetic magadiite and kenyaite. Na-magadiite shows a particle morphology composed of silicate layers intergrown to form spherical nodules resembling rosettes. The shape of kenyaite is very similar to that of magadiite.

The chemical compositions of Na-magadiite and Na-kenyaite were obtained by TGA and EDS analyses for silica and sodium. TGA and EDS data obtained from Na-magadiite and Na-kenyaite are illustrated in Fig. 5 and Table 2. The weight losses from the two clays are coincident with an associated endotherm on a DTA scan from dehydration. The weight losses below 300°C are attributed to dehydration, while those above 300°C are presumably from water losses via condensation of the silanol groups to form siloxane bonds [22]. The water loss and sodium and silica contents give an approximate unit cell composition of $\text{Na}_{2.06}\text{Si}_{14}\text{O}_{29.03} \cdot 5.34\text{H}_2\text{O}$, which compares well with that given by Graces et al. [23]. (The degree of hydration can differ due to differences in sample treatment.)

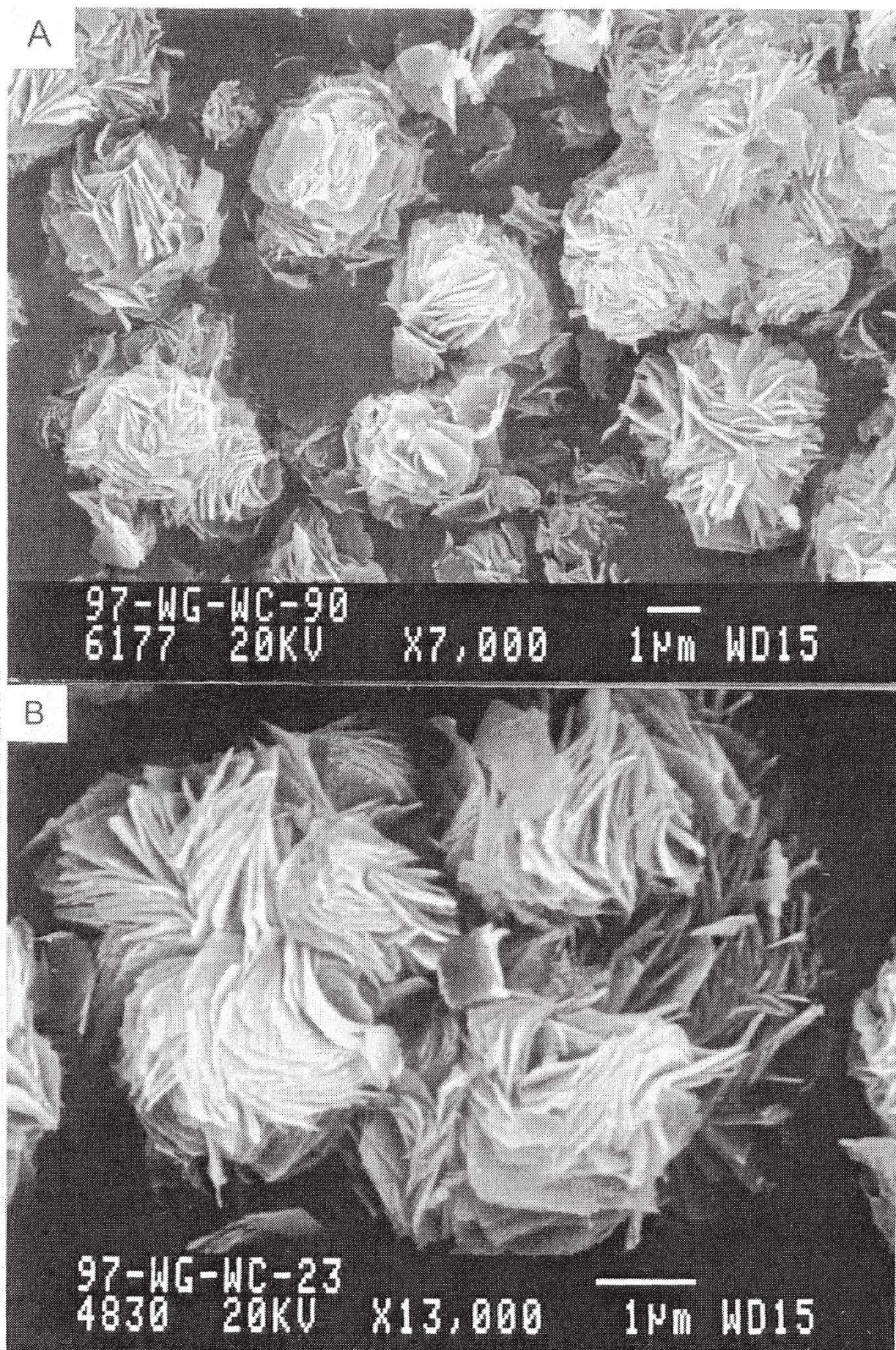


FIG. 4 Scanning electron micrographs of synthetic samples. (A) Magadiite; (B) kenyaite.

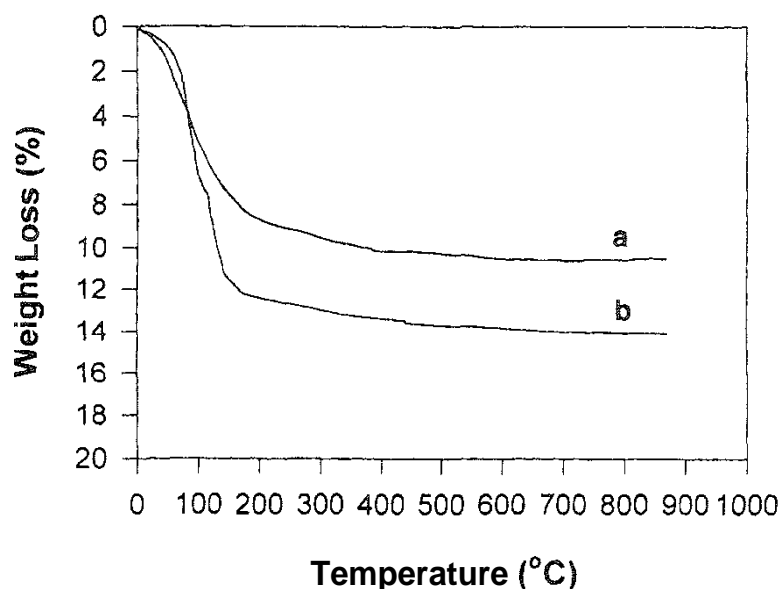


FIG. 5 Thermogravimetric analyses of (a) Na-magadiite and (b) Na-kenyaite. (From Ref, 30.)

The unit cell composition of Na-kenyaite deduced from TGA and the analyses of sodium and silica is $\text{Na}_{2.05}\text{Si}_{20}\text{O}_{41.03} \cdot 10.42\text{H}_2\text{O}$, which compares favorably with the approximate composition $\text{Na}_2\text{Si}_{20}\text{O}_{41} \cdot 10\text{H}_2\text{O}$ supported by the early work of Lagaly and Beneke [24].

B. Octylamine/Octylammonium Layered Silicate Gel

Lagaly and Beneke [24] reported that H-magadiite intercalated with dimethyl sulfoxide (DMSO) reacts with octylamines to form ordered bilayers of alkylammonium ions and alkylamine molecules between silicate layers. Daily and Pinnavaia [16] found that air-dried H-magadiite reacts directly with octylamine without the pre-intercalation with DMSO. In our experiment, air-dried H-magadiite and H-kenyaite reacted directly with excess octylamine. The X-ray diffraction pattern of the octylamine/octylammonium magadiite gel, as shown in Table 3, is indicative of 3.40 nm basal spacing. Since the layer thickness of magadiite is almost the same as the basal spacing of air-dried H-magadiite (1.12 nm), the corresponding gallery height can be calculated to be 2.28 nm. In the case of octylamine/octylammonium

TABLE 2 Compositions of Synthetic Magadiite and Kenyaite

| Synthetic sample | Weight percent | | | Atomic ratio | | |
|------------------|-------------------------|------------------|----------------------|---------------|---------------|----------------------|
| | Na_2O^a | SiO_2^a | H_2O | Na^a | Si^a | H_2O |
| Na-magadiite | 6.4 | 84.0 | 9.6 | 2.05 | 14 | 5.34 |
| Na-kenyaite | 4.4 | 82.8 | 12.8 | 2.05 | 20 | 10.42 |

E D X analysis.

Source: Ref. 30.

TABLE 3 Basal Spacings of Samples

| Sample | Basal spacings (nm) | Gallery height (nm) |
|--|------------------------|------------------------|
| Na-magadiite | 1.56 | 0.44 |
| Na-kenyaite | 2.03 | 0.23 |
| H-magadiite (air-dried) | 1.12 | 0 |
| H-kenyaite (air-dried) | 1.80 | 0 |
| Octylamine/octylammonium magadiite gel | 3.40 | 2.28 |
| Octylamine/octylammonium kenyaite gel | 3.95 | 2.15 |
| TEOS-intercalated magadiite | 3.80 | 2.68 |
| TEOS-intercalated kenyaite | 4.34 | 2.54 |

kenyaite gel, the gallery height is 2.15 nm, indicating that this value is similar to the gallery height of amine-solvated H-magadiite. This result indicates that the expansion of the gallery height of the layered phase is caused by the formation of laminar bilayers of octylammonium ion and octylamine molecules between the silicate layers.

C. Reactions with TEOS

The reactions of octylamine/octylammonium magadiite gel with TEOS afford TEOS-intercalated magadiite with well-ordered basal spacings. This product exhibits reflections corresponding to a basal spacing of 3.80 nm (gallery height, 2.68 nm). The gallery height for the siloxane intercalated derivative is about 0.4 nm larger than the gallery height of 2.28 nm observed in the octylamine/octylammonium magadiite precursor gel. In the case of TEOS-intercalated kenyaite, the basal spacing of this product is 4.34 nm (gallery height, 2.54 nm). The gallery height for the siloxane intercalated derivative is 0.39 nm larger than the gallery height of 2.15 nm observed in octylamine/octylammonium magadiite precursor gel. Kwon et al. [25] reported the effects of organic solvents on the intercalation of octylamine into H-magadiite. According to this result, the expansion of gallery height could be effected not only by the solvation of intercalated octylamine but also by the steric effects of solvated solvent molecules and solvent itself. In the octylamine/octylammonium layered silicate gel reacting with excess TEOS, TEOS could be exchanged with solvated free octylamine molecules in the interlayers and hydrogen-bonded octylammonium ion on the inner surface. The interlayer solvation and structure of TEOS could cause an increase in gallery height.

D. Gelation Effects

The gelation of intercalated TEOS by catalyst produces siloxane-intercalated derivatives with well-ordered basal spacings as well as the expansion of gallery height. The basal spacings of the products gelled by EtOH suspension, base-catalyzed reaction, and acid-catalyzed reaction are shown in Table 4. These products exhibit

TABLE 4 Basal Spacings of Gelled Products

| Sample | Basal spacing (nm) | Gallery height (nm) |
|---|-----------------------|------------------------|
| TEOS-intercalated magadiite by EtOH suspension | 2.50 | 1.38 |
| TEOS-intercalated magadiite by base-catalyzed reaction | 4.02 | 2.90 |
| TEOS-intercalated magadiite by acid-catalyzed reaction | 3.42 | 2.30 |
| TEOS-intercalated kenyaite by EtOH suspension | 3.09 | 1.29 |
| TEOS-intercalated kenyaite by base-catalyzed reaction | 4.23 | 2.43 |
| TEOS-intercalated kenyaite by acid-catalyzed reaction | 4.01 | 2.21 |

reflections corresponding to basal spacings of 2.50, 4.02 and 3.42 nm for magadiite and 3.09, 4.23, and 4.01 nm for kenyaite. The silica-pillared products gelled by base- and acid-catalyzed reactions exhibit a large increase in the gallery height, 0.9–1.6 nm, compared with the gallery height of the product gelled by EtOH suspension. A distinctive increase in the gallery height is related to the size and structure of pillared silica, which could be associated with the amount of intercalated TEOS, the gelation condition (catalyst type, solvent composition, pH, etc.), and the rate of gelation. The calcination of the siloxane intercalated derivatives at 538°C yields silica-intercalated products, showing a 1–3 Å reduction of basal spacings (Table 5).

Gelation by base and acid catalysts could minimize the release of TEOS outside the layered phase during the gelation of the intercalated TEOS, because gelation time is markedly reduced. The hydrolytic polycondensation of intercalated TEOS by acid or base catalyst could form silica clusters of a highly branched and stiff network structure. These conditions could bring about the effective gelation of intercalated TEOS in the interlayer and contribute to develop the size and structure of pillared silica clusters that bring about the large expansion of the gallery height of pillared kenyaite.

Adsorption–desorption isotherms of nitrogen were obtained at 77 K. Several pore characteristics calculated from them are listed in Table 5. The specific surface areas were calculated by using the BET equation from the adsorption isotherm below $P/P_0 = 0.1$. The calcined silica-pillared products have high surface areas of 533–845 m²/g, depending on the catalyst type. As the gallery height of the calcined sample decreases, the specific surface area is increased owing to the development of micropores. The total pore volume of the base-catalyzed sample is the largest

TABLE 5 Physical Properties of Silica-Pillared Magadiite and Kenyaite

| | Basal spacing (nm) | Gallery height (nm) | Specific surface area (m ² /g) | External surface area (m ² /g) | Total pore volume (cm ³ /g) |
|---------------------------|-----------------------|------------------------|---|---|---|
| Silica-pillared magadiite | | | | | |
| EtOH suspension | 2.30 | 1.18 | 587 | 126 | 0.60 |
| Base catalyst | 3.92 | 2.80 | 845 | 137 | 0.73 |
| Acid catalyst | 3.33 | 2.21 | 648 | 172 | 0.62 |
| Silica-pillared kenyaite | | | | | |
| EtOH suspension | 2.95 | 1.15 | 606 | 97 | 0.49 |
| Base catalyst | 3.99 | 2.19 | 533 | 106 | 0.52 |
| Acid catalyst | 3.95 | 2.15 | 584 | 91 | 0.46 |

Source: Adapted from Refs. 29 and 31

among the three pillared samples, indicating that the average pore size of that sample is the largest.

Figure 6 shows the pore size distributions of silica-pillared magadiite. The sample treated with the base-catalyzed gelation has the greatest microporosity (diameter < 2 nm) and shows a sudden increase in mesopore volume near 3.6 nm with a narrower pore size distribution. These results indicate that abrupt gelation by base catalyst is closely related to the formation of a more uniform pore. On the other hand, the sample gelled by the suspension of EtOH has a broader pore size distribution. In the case of gelation by an acid catalyst, microporosity decreases and mesoporosity increases between 4.0 and 10.0 nm compared with gelation with no catalyst. It is interesting that acid- and base-catalyzed products are very similar in physical properties to surfactant-templated mesoporous silica [26–28]. Figure 7 shows the pore size distributions of silica-pillared kenyaite. The base-catalyzed sample shows a sudden increase in mesopore volume near 2.2 nm with a compara-

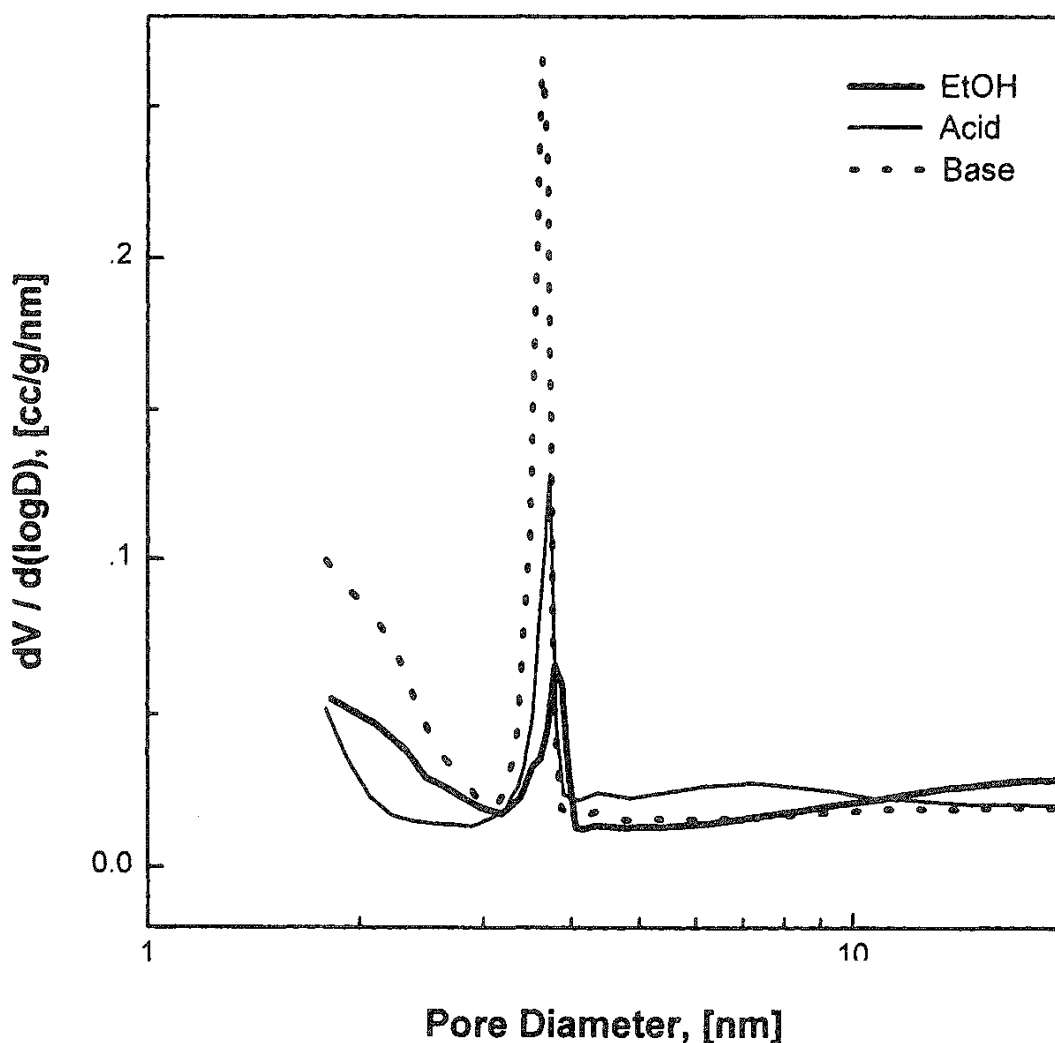


FIG. 6 Pore size distributions of the calcined silica-pillared inagadiite gelled by EtOH suspension, base-catalyzed reaction, and acid-catalyzed reaction. (Adapted from Ref. 31.)

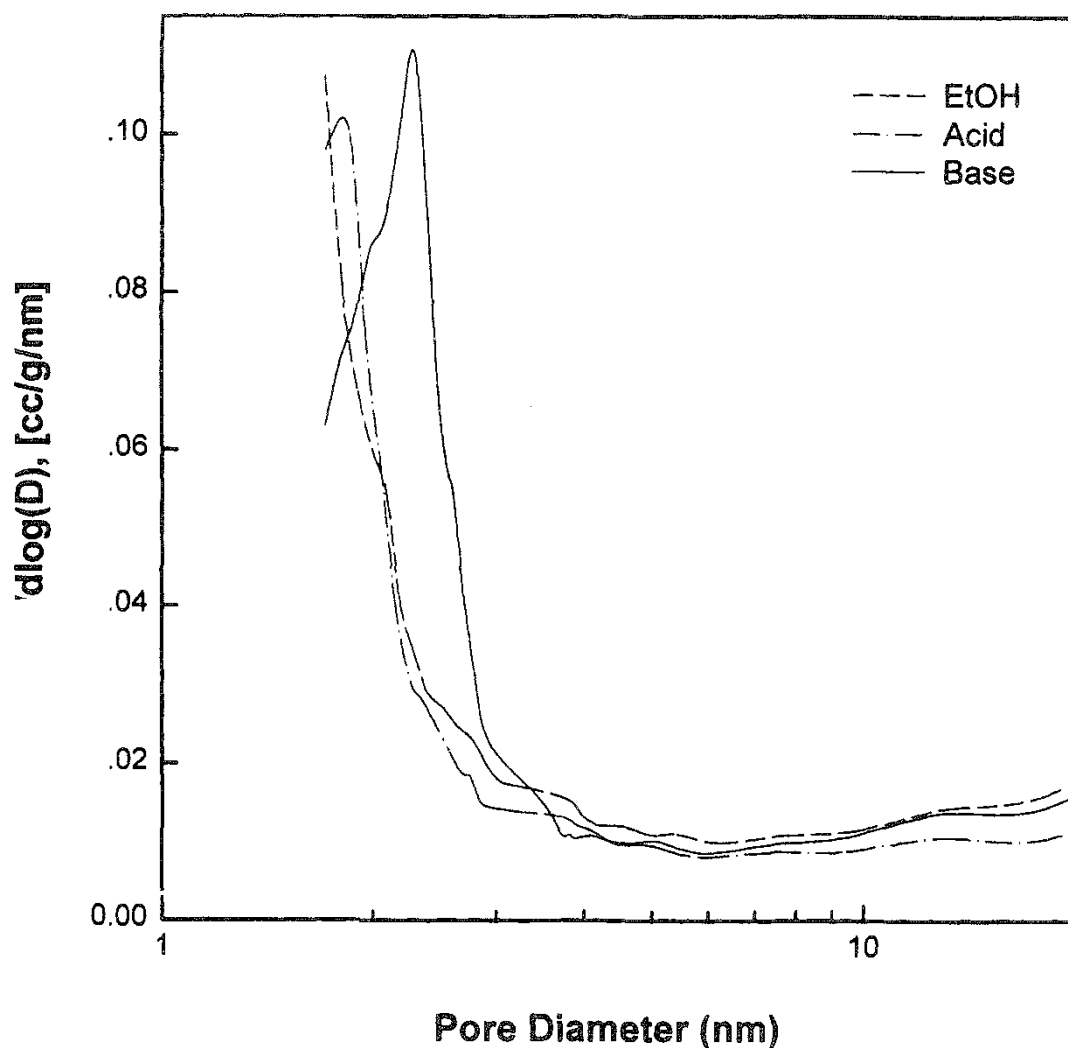


FIG. 7 Pore size distributions of the calcined silica-pillared kenyaite gelled by EtOH suspension, base-catalyzed reaction, and acid-catalyzed reaction. (Adapted from Ref. 29.)

tively narrow pore size distribution. The acid-catalyzed sample shows a narrow pore size distribution with a sharp peak near 1.8 nm. These values are similar to the gallery heights of the samples. These results indicate that the pore size of base- or acid catalyzed samples is closely related to the gallery height. The abrupt gelation of acid and base catalysts is closely related to the formation of more uniform pores. On the other hand, the sample gelled by the suspension of EtOH has a broader pore size distribution and more microporosity (diameter < 2.0 nm). Therefore, the acid- or base-catalyzed reaction not only allows for high surface area through optimization of silica pillaring but also permits the synthesis of materials with narrow pore size distributions.

IV. CONCLUSIONS

In the suspension of SiO_2 , NaOH , and Na_2CO_3 , the effects of the compositions of reactants, reaction time, and temperature on the formation of Na-magadiite and

Na-kenyaite were investigated. Magadiite was easily synthesized after a short reaction time of 36 h at various compositions of reactants and reaction temperatures. In the higher Si/Na molar ratio, kenyaite can be directly synthesized from amorphous silica without the formation of magadiite as an intermediate. A higher silica content in the composition of starting materials may cause a larger Si/Na ratio in the solution. These conditions could accelerate the nucleation of kenyaite, which has a large Si/Na ratio. These results indicate that the composition of reactant is an important factor in the formation of layered silicate.

The reaction of H-type layered silicate with octylamine results in a gel-like octylammonium intercalation with a basal spacing swollen by the intercalation of neutral octylamine. The solvated gel-like derivative has a bilayered structure. The reaction of octylamine/octylammonium-layered silicate gel with TEOS yields TEOS-intercalated layered silicate. The increase of basal spacing in the TEOS-intercalated layered silicate may be caused by interlayer solvation and the steric factor of TEOS molecules [25]. The gelation of intercalated TEOS by acid or base catalyst produces siloxane-intercalated derivatives with well-ordered basal spacing as well as an increase in the gallery. The calcined samples have high specific surface areas between 533 and 845 m²/g, depending on the catalyst type. Base- and acid-catalyzed samples exhibit narrow pore size distributions near 1.8 and 4.0 nm, respectively. The pore size distributions of the calcined samples are closely related to the gallery heights.

Finally, the acid- or base-catalyzed reaction of hydrolysis and condensation polymerization of TEOS into a layered silicate gallery could affect the physical properties of silica-pillared magadiite and kenyaite. The samples that were silica-pillared by acid- and base-catalyzed reactions show a large increase in basal spacing. Also, they exhibit relatively narrow pore size distributions and show high surface areas, depending on the type of catalyst and layered silicate. These results indicate that variations in the conditions of gelation contribute to the improvement in the physical properties of silica-pillared molecular sieves.

REFERENCES

1. K. H. Bergk, W. Schweiger, and M. Porsch, *Chem. Tech.* 39:508 (1987).
2. H. J. Werner, K. Beneke, and G. Lagaly, *Z. Anorg. Allgem. Chem.* 470:118 (1980).
3. H. P. Eugster, *Science* 157:1177 (1967).
4. J. McAtee, R. House, and H. P. Eugster, *Am. Mineral.* 53:2062 (1968).
5. T. P. Rooney, B. F. Jones, and J. T. Neal, *Am. Mineral.* 54:1026 (1969).
6. G. W. Brondley, *Am. Mineral.* 54:1583 (1969).
7. A. Brandt, W. Schweiger, and K. H. Bergk, *Rev. Chem. Miner.* 24:564 (1987).
8. G. Lagaly and K. Beneke, *Am. Mineral.* 60:642 (1975).
9. H. Muraishi, *Am. Mineral.* 74:1147 (1989).
10. K. Kosuge, A. Tsunashima, and R. Otsuka, *Chem. Soc. Jpn.* 10:1398 (1991).
11. K. Beneke and G. Lagaly, *Am. Mineral.* 63:818 (1983).
12. R. A. Fletcher and D. M. Bibby, *Clays Clay Minerals* 35:318 (1987).
13. M. E. Landis, A. B. Aufdembrink, P. Chu, I. D. Johnson, G. W. Kirker, and M. K. Rubin, *J. Am. Chem. Soc.* 113:189 (1991).

14. G. Scholzen, K. Beneke, and G. Lagaly, *Z. Anorg. Allgem. Chem.* 597:183 (1991).
15. R. Sprung, M. E. Davis, J. S. Kauffman, and C. Dybowski. *Ind. Eng. Chem. Res.* 29:213 (1990).
16. J. S. Daily and T. Pinnavaia, *Chem. Mater.* 4:855 (1992).
17. C. J. Brinker and G. W. Scherer, *Sol-Gel Science The Physics and Chemistry of Sol-Gel Processing*, Academic, London, 1990, pp. 97–160.
18. R. Aelion, A. Loebel, and F. Eirich, *J. Am. Chem. Soc.* 72:5705 (1950).
19. M. Nogami and Y. Moriya, *J. Non-Cryst. Solids* 37:191 (1980).
20. C. J. Brinker, K. D. Keefer, D. W. Schaefer, and C. S. Ashley, *J. Non-Cryst. Solids* 48:47 (1982).
21. P. B. Barrett, L. G. Joyner, and P. P. Halenda, *J. Am. Chem. Soc.* 73:373 (1951).
22. J. M. Rojo and E. Ruiz-Hitzky, *J. Inorg. Chem.* 27:2785 (1988).
23. J. M. Graces, S. C. Rocke, C. E. Crowder, and D. L. Hasha, *Clays Clay Minerals* 36:409 (1988).
24. G. Lagaly and K. Beneke. *Am. Mineral.* 60:642 (1975).
25. O. Y. Kwon, S. Y. Jeong, J. K. Suh, H. Jin, and J. M. Lee, *J. Colloid Interface Sci.* 177:667 (1996).
26. Q. Huo, D. I. Margolese, U. Ciesla, P. Feng, T. E. Gier, P. Sieges. R. Leon, P. M. Petroff, F. Schüth, and G. D. Stucky, *Nature* 368:317 (1994).
27. P. T. Tanev, M. Chibwe, and T. J. Pinnavaia, *Nature* 368:321 (1994).
28. C. Y. Chen, H. X. Li, and M. E. Davis, *Microporous Mater.* 2:17 (1993).
29. S. Y. Jeong, J. K., Suh, H. Jin, J. M. Lee, and O. Y. Kwon, *J. Colloid Interface Sci.* 180:269 (1996).
30. O. Y. Kwon, S. Y. Jeong, J. K. Suh, and J. M. Lee, *Bull. Korean Chem. Soc.* 16(8):737 (1995).
31. S. Y. Jeong, O. Y. Kwon, J. K. Suh, H. Jin, and J. M. Lee, *J. Colloid Interface Sci.* 175:253 (1995).

3

Engineering of Nanosize Superparamagnetic Particles for Use in Magnetic Carrier Technology

ZHENGHE XU Department of Chemical and Materials Engineering, University of Alberta, Edmonton, Alberta, Canada

QINGXIA LIU Cominco Research, Cominco Ltd., Trail, British Columbia, Canada

JAMES A. FINCH Department of Mining and Metallurgical Engineering, McGill University, Montreal, Quebec, Canada

- I. Introduction
- II. Molecular Self-Assembly
- III. Direct Silanization
- IV. Silica Coatings
- V. Applications
 - A. Self-assembled monolayers
 - B. Silanized monolayers
- VI. Summary
- References

I. INTRODUCTION

Magnetic particles have shown great promise as a base material for engineering carriers in separation science and technology. A potential area of application of magnetic particles is as supports for catalysts. Magnetic particles used in these areas are called magnetic carriers, although a distinction is sometimes made between magnetic carriers and magnetic tags. The former applies to magnetic particles significantly larger than the targets so that the targets coat on the particles (carriers) and the latter refers to magnetic particles smaller than the targets so they (the tags) deposit on the targets [1]. In this chapter, both are referred to collectively as magnetic carriers.

The objective of magnetic carrier technology is to confer the magnetic property to a naturally nonmagnetic target so that the target can be separated from the stream using magnetic separators. This is particularly important for separations

in a complex multiphase system. Figure 1 summarizes schematically the processes involved in a typical magnetic carrier technology application. To make a target magnetic, the target has to be recognized by and attached to a magnetic carrier. This requires the magnetic particles to be functionalized, usually by derivatizing a surface or putting a specific ligand on the particle (step I) [2], or by in situ formation of a magnetic core in a structured template such as micells, vesicles, porous silica, or polymer matrix (step II) [3–5]. The particles prepared in this way, termed magnetic carriers (b, Fig. 1), are added to a biological system containing unwanted targets such as infected cells (white circles in c). The selective attachment of infected cells to the magnetic carriers is accomplished through molecular recognition, which confers the magnetic property to the infected cells only (step III). By exposing the biological system to an external magnetic field, the labeled cells are directed to a desired location (the top of the system in this case), where they can be removed readily without disturbing the system (step IV). It should be noted that the application is not limited to biological cell separations. The targets can be toxic species of metal ions in industrial effluents. The use of magnetic separation in combination with magnetic carrier technology, as shown schematically in Fig. 1, makes isolation of targets in a complex system feasible and attractive.

For most applications, such as biological cell separation, effluent detoxification, ferrofluids, and the preparation of magnetic inks and magnetic recording media, the use of fine size carriers is either essential or beneficial. In biological cell separation, for example, it is important to avoid mechanical instability (i.e., sedimentation under gravity) of magnetic particles in a biological system in addition to the "invisibility" of the carriers to most biological cells. This requires the particles to be extremely small (in the submicrometer to nanometer range) to allow thermal energy

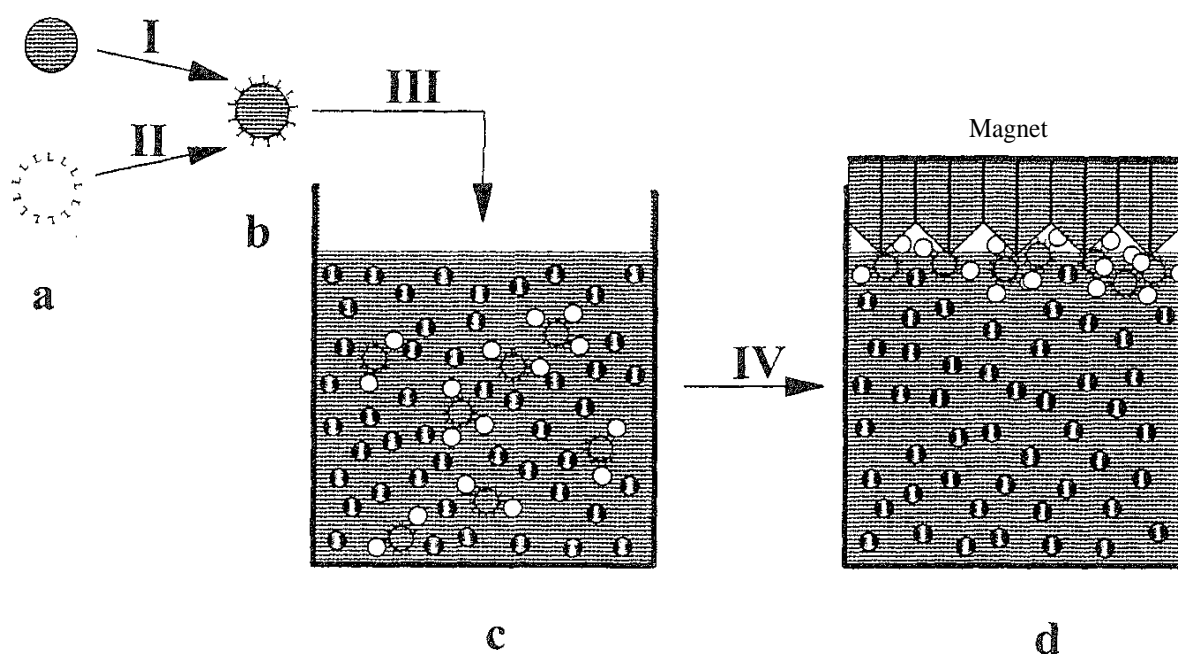


FIG. 1 Schematics of magnetic carrier technology in separation science and technology.

and surface forces to prevail. Another important requirement for these various applications is to avoid magnetic flocculation, a phenomenon in which magnetic particles agglomerate due to magnetic forces. With particles being in the submicrometer to nanosize range, the residual magnetic field can be considered negligible, so permanent magnetization can be avoided and magnetic flocculation minimized. The major challenge to the application of magnetic carrier technology in various areas, however, lies in the engineering of a robust, tailored surface functionality. A few methods have been developed to attach functional groups to magnetic particles, including surface precipitation of ferrihydrite [6], in situ polymerization [7], the formation of magnetic cores in porous media [8], molecular self-assembly using a bolaamphiphile [9], direct silanization [10,11], and silica coating followed by silanization on nanosize magnetic particles. In this chapter, two surface engineering technologies—molecular self-assembly and silanization developed in our research laboratory – are described. The particles prepared are characterized by Fourier transform infrared spectroscopy (FTIR), X-ray photoelectron spectroscopy (XPS), electrokinetics, and vibrating sample magnetometry (VSM) in combination with acid leaching.

II. MOLECULAR SELF-ASSEMBLY

Molecular self-assembly (SA) is a process of spontaneous formation of an organized organic molecular (surfactant) layer on an inorganic substrate from an organic solvent [12]. In SA, in contrast to Langmuir–Blodgett (LB) film deposition, molecules are anchored on the surface through chemical binding between functional groups of molecules and surface active sites, and assembled by hydrocarbon interchain associations. As a result, the organic film deposited on the substrate by SA is more stable than those produced by LB film deposition. The SA method has been used widely in preparing ultrathin organic films for developing optical sensors, electronic devices, biosensors, and corrosion- and wear-resistant coatings [12]. For example, SA has been used to deposit alkylsilane surfactant on hydroxylated surfaces such as silica and aluminum oxide; alkanethiolates on gold, silver, and copper; alcohol and amines on platinum; and carboxylic and hydroxamic acids on aluminum and silver oxides [13–21]. In these examples, the terminal group has been limited to either methyl ($-\text{CH}_3$) or trifluoromethyl ($-\text{CF}_3$) on flat substrates. Recently, SA has been used to fabricate other types of terminal groups [16, 22–26], including $-\text{COOH}$, $-\text{NH}_2$, $-\text{CONH}_2$, and halides (X) on flat gold, silica, and aluminum oxide surfaces. A bolaamphiphile of alkanethiols having a reactive functional group at the *in* position was used in these cases. The halide terminal group allows for further derivatization to a desired functionality. Most of the fabrications of SA monolayers are limited to flat substrates despite broad potential applications of SA monolayers on nanosize and submicrometer magnetic particles.

In our laboratory, 16-mercaptohexadecanoic acid [$\text{HS}(\text{CH}_2)_{16}\text{COOH}$; MHA] was assembled onto nanosize superparamagnetic particles (40 nm $\gamma\text{-Fe}_2\text{O}_3$) from either ethanol or chloroform solutions [9]. The XPS narrow-scan spectra of the particles with and without MHA coatings are shown in Fig. 2. For comparison, the

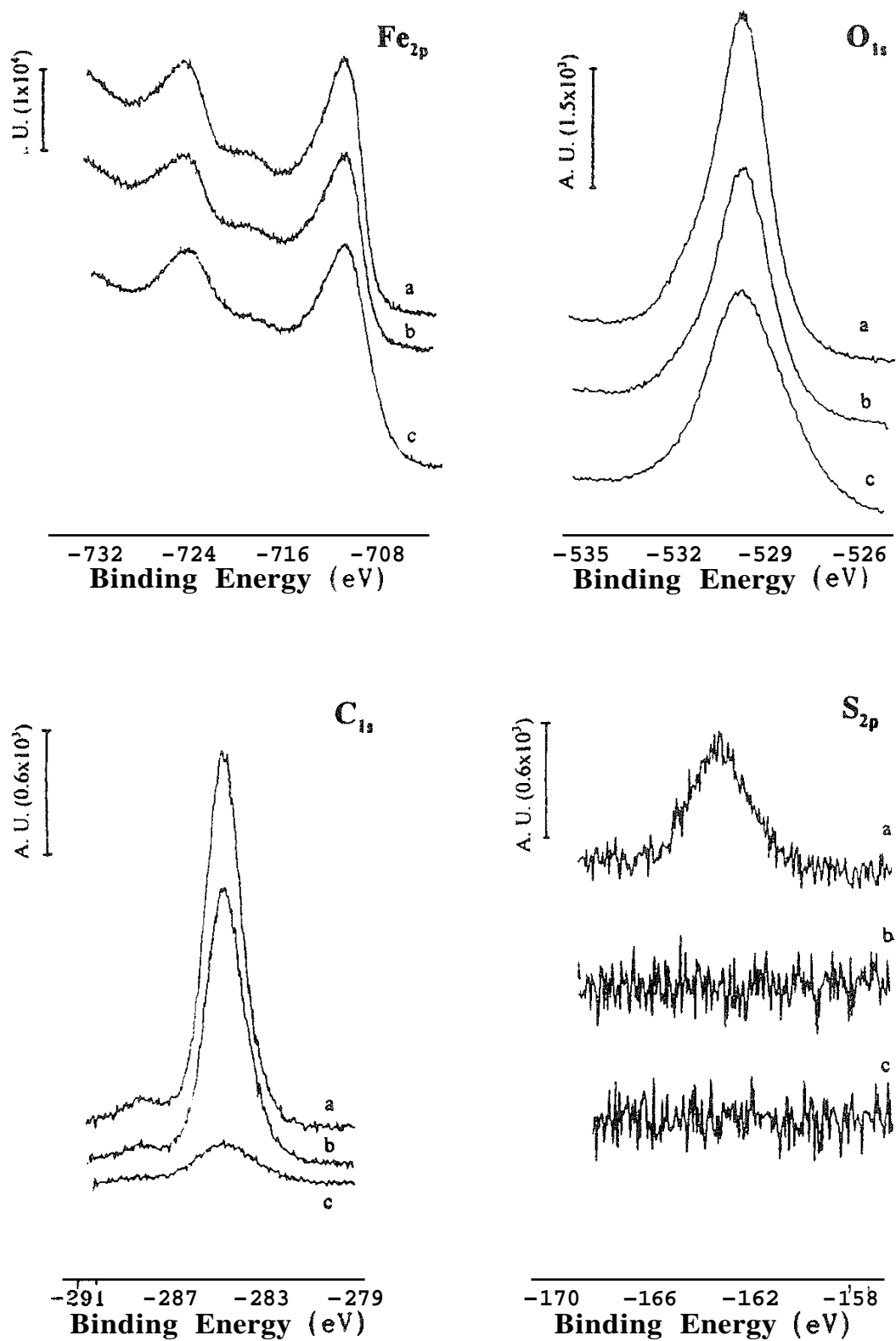


FIG. 2 Narrow-scan XPS spectra for the elements of interest on γ -Fe₂O₃ with self-assembled (a) MHA and (b) stearic acid, in comparison with (c) untreated γ -Fe₂O₃ particles.

spectra of $\gamma\text{-Fe}_2\text{O}_3$ with self-assembled stearic acid are also shown in this figure. Compared with uncoated particles, a significant increase in C_{1s} band intensity suggests the deposition of MHA (spectrum a) and stearic acid (spectrum b) on $\gamma\text{-Fe}_2\text{O}_3$. In addition, a sulfur band was detected on $\gamma\text{-Fe}_2\text{O}_3$ particles treated with MHA, further confirming the deposition of surfactant. A detailed analysis revealed two different carbon states, one at 284.6 eV as in a hydrocarbon chain (C—C) and the other at 288.3 eV, corresponding to a carbon in a carboxylic acid environment (COO). The area ratio of the C_{1s} band at high binding energy to that at low binding energy was found to be 1:17 and 1:15, respectively, for stearic and MHA coated on the particles, in excellent agreement with that derived from the molecular structure. It is interesting to note a similar $\text{C}_{1s}/\text{Fe}_{2p}$ band area ratio, 3.7 and 3.6 for $\gamma\text{-Fe}_2\text{O}_3$ coated with stearic acid and MHA, respectively, suggesting that the densities of stearic acid and MHA on $\gamma\text{-Fe}_2\text{O}_3$ are comparable.

To determine the orientation of surfactant molecules in the SA monolayers, a surface-sensitive, diffuse-reflectance infrared Fourier transform spectroscopy (DRIFTS) was used, and the spectra are shown in Fig. 3. Over the high wavenumber region, the CH_2 stretching vibration bands at 2924 and 2851 cm^{-1} are observed, suggesting the presence of a hydrocarbon chain as anticipated. The CH_2 bands appeared at the same band positions for bulk MHA and for MHA coated on $\gamma\text{-Fe}_2\text{O}_3$. However, the bands are sharper for the MHA on $\gamma\text{-Fe}_2\text{O}_3$ than for bulk MHA, indicating a more ordered polymethylene chain and confirming the assembly of a densely packed surfactant monolayer. Over the low wavenumber region, on the other hand, the MHA on $\gamma\text{-Fe}_2\text{O}_3$ resulted in a different spectral feature than bulk MHA. The absence of the carbonyl band at 1703 cm^{-1} and the presence of a carboxylate band at 1433 cm^{-1} for the MHA on $\gamma\text{-Fe}_2\text{O}_3$ suggest not only the anchoring of carbonyl groups on $\gamma\text{-Fe}_2\text{O}_3$, transferring a carbonyl to the carboxylate functionality, but also the absence of the second MHA layer, i.e., only a monolayer coverage. Should the second layer be present, a mixed functionality of carboxylate from the first layer (band at 1703 cm^{-1}) and carbonyl from the second layer (band at 1433 cm^{-1}) would be observed. From film flotation [9], a critical surface tension of MHA-coated $\gamma\text{-Fe}_2\text{O}_3$ surfaces was found to be 38 mN/m with a 10 mN/m difference between the surface tensions for complete wetting and nonwetting, compared to 30 mN/m with a difference of 5 mN/m for stearic acid-coated particles. These results further confirm that the terminal group of the MHA coated on $\gamma\text{-Fe}_2\text{O}_3$ is thiol or bisulfide, rather than a carbonyl, sulfate, or sulfonate functionality, which would result in a much higher critical surface tension (> 72.8 mN/m). Acid leaching tests in pH 2 solutions for 24 h showed that no iron was detected by atomic absorption in the leachate. It is important to note that a monolayer coating of MHA on $\gamma\text{-Fe}_2\text{O}_3$ only reduced the saturation magnetization (M_s) of magnetic particles marginally (2 emu/g) as determined by VSM. The particles remained superparamagnetic after coating, as anticipated. The characteristics of coatings on $\gamma\text{-Fe}_2\text{O}_3$ are summarized in Table 1. It is clear that the strong binding of the carboxyl groups of MHA with iron sites on $\gamma\text{-Fe}_2\text{O}_3$, compounded with the interchain association, allows MHA to be self-assembled on $\gamma\text{-Fe}_2\text{O}_3$, producing nanosize superparamagnetic particles with the desired characteristics for the biological and environmental applications.

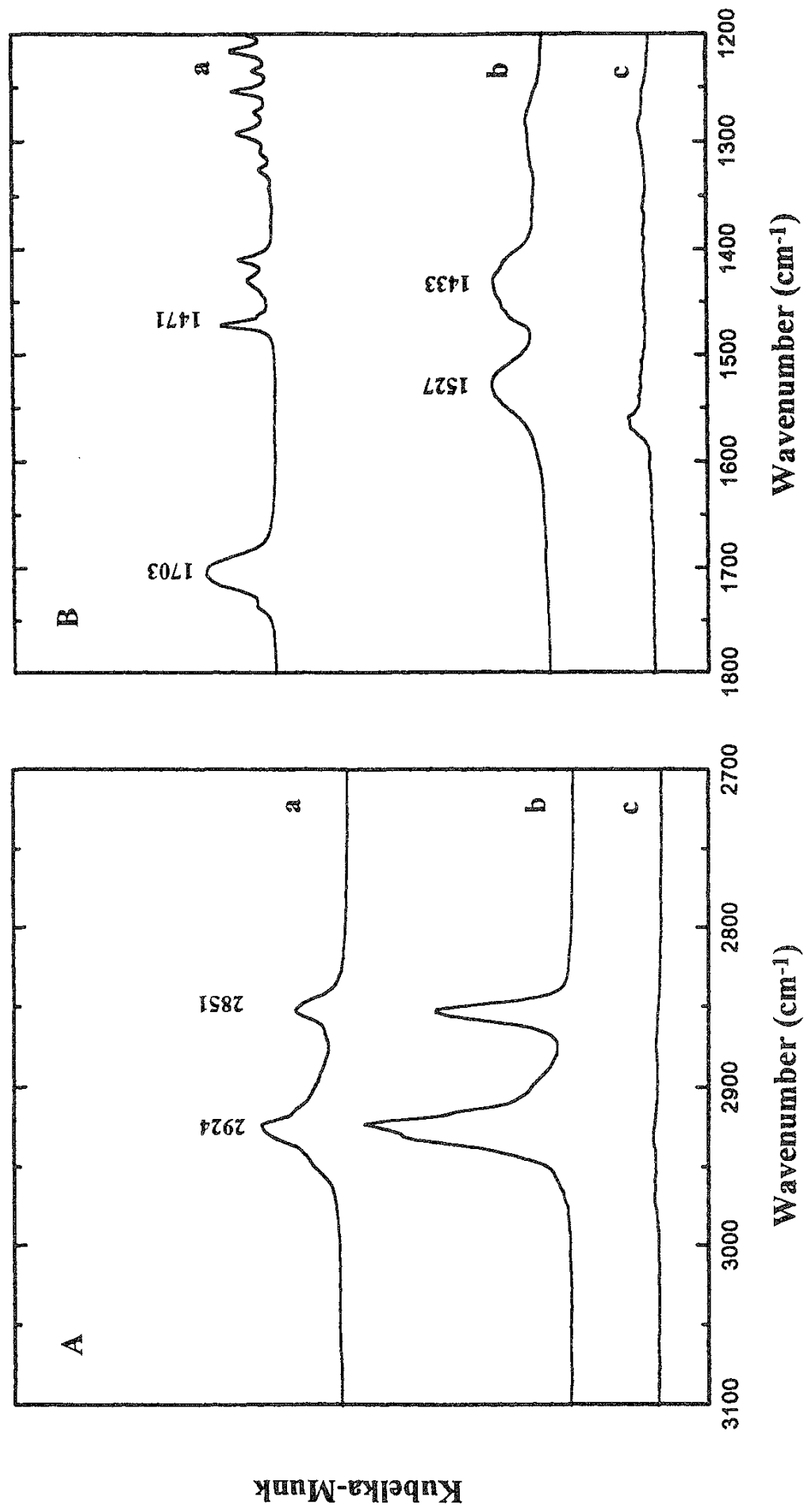


FIG. 3 DRIFTS spectra in the high (A) and low (B) frequency regions for (a) MHA in KBr, (b) MHA on γ -Fe₂O₃, and (c) untreated γ -Fe₂O₃ particles.

TABLE 1 Characteristics of Nanosize Superparamagnetic Particles Coated with Stearic Acid and 16-Mercaptohexadecanoic Acid Using Self-Assembly from Chloroform

| | C_{1s}/Fe_{2p} Area ratio | Fe in leachate (mg Fe/g particle) | γ_c (mN/m) | M_s (emu/g) |
|--------------------------------|--------------------------------|---|----------------------|------------------|
| $\gamma\text{-Fe}_2\text{O}_3$ | 0.2 | 60.3 | > 72.8 | 52.7 |
| MHA-coated | 3.6 | nil | 38 | 50.6 |
| Stearic acid-coated | 3.7 | nil | 30 | 50.6 |

III. DIRECT SILANIZATION

The SA method using bolaamphiphiles for preparing magnetic carriers appears attractive due to the stability of the monolayer and the high density of surface functional groups. However, control of the reactivity between the two functional groups and the substrate is crucial in determining the quality of the coatings. In the ideal case, one functional group anchors chemically to the surface while the other is relatively unreactive to the surface, which ensures a unique surface functionality. This requirement limits the types of functional groups that can be directly introduced onto the magnetic particles. A more general approach is to use a silane coupling agent of a general structure $Y-(CHC_2)_n-Si-X_3$, where X represents an alkoxy or halide group and Y an organic functional group, including amine, thiol, carboxylic, phosphate, vinyl, cyanide, or methacrylate. The strong reactivity between Si and surface metal hydroxyl groups causes silane coupling agents to condense readily on metal hydroxide surfaces, forming $Si-O-M$ bonds upon dehydration, whereas the free silanol groups polymerize laterally, forming a two-dimensional network. It is therefore clear that silanization is just a variation of SA, in that the interchain association that occurs in SA is replaced by lateral polymerization between condensed silane coupling agents through siloxane bonds.

Silanization was initially introduced to modify silica surfaces for use in synthetic transformation [27], preconcentration of trace metals [28], immobilization of artificial membranes [29], molecular recognition [30], chromatographic separations [31], and preparation of biomolecules [32–34]. It has since been extended to applications such as the protection of photocatalysts and the promotion of adhesion between different materials such as polymers, metals, glass fibers, and polymeric resins [35–39]. A large volume of literature is available on silanization using silane coupling agents to tailor the surface properties of metal oxides [40–42]. Whitehead et al. [10] used direct silanization in functionalizing paramagnetic particles. The functional groups they attempted include aminophenyl, amino, hydroxyl, sulfhydryl, aliphatic, and mixed functionalities. We examined the use of silanization in engineering nanosize superparamagnetic carriers [11]. For the purpose of illustration, the silanization of $\gamma\text{-Fe}_2\text{O}_3$ using 3-aminopropyl triethoxysilane (APTES) is presented below.

It is recognized that the coating of silane coupling agents by silanization is a multistep process [11]. The controlled hydrolysis of both surface and coupling agent is essential for successful coatings. The presence of nitrogen (N_{1s} at 399.4 eV) and silicon (Si_{2p} at 101.8 eV) XPS bands seen in Fig. 4 suggests that APTES can be deposited on $\gamma\text{-Fe}_2\text{O}_3$ from both water and toluene solutions. From Fig. 4, two different oxygen and nitrogen environments are seen. The bands centered at 399.4 and 401.3 eV are attributed to nitrogen in protonated and nonprotonated amines, respectively; those at 531.8 and 529.6 eV are assigned to oxygen from APTES film and $\gamma\text{-Fe}_2\text{O}_3$ particle matrix, respectively. Band fit analysis revealed that the proportion of oxygen in the Si — O environment is higher for the film silanized in water (24%) than in toluene (14%), suggesting a higher degree of APTES deposition on $\gamma\text{-Fe}_2\text{O}_3$ from water. Semiquantitative analysis of the XPS band area shows that a larger fraction of amines are protonated in the films silanized from water (26%) than in those silanized from toluene (17%). The higher APTES deposition is

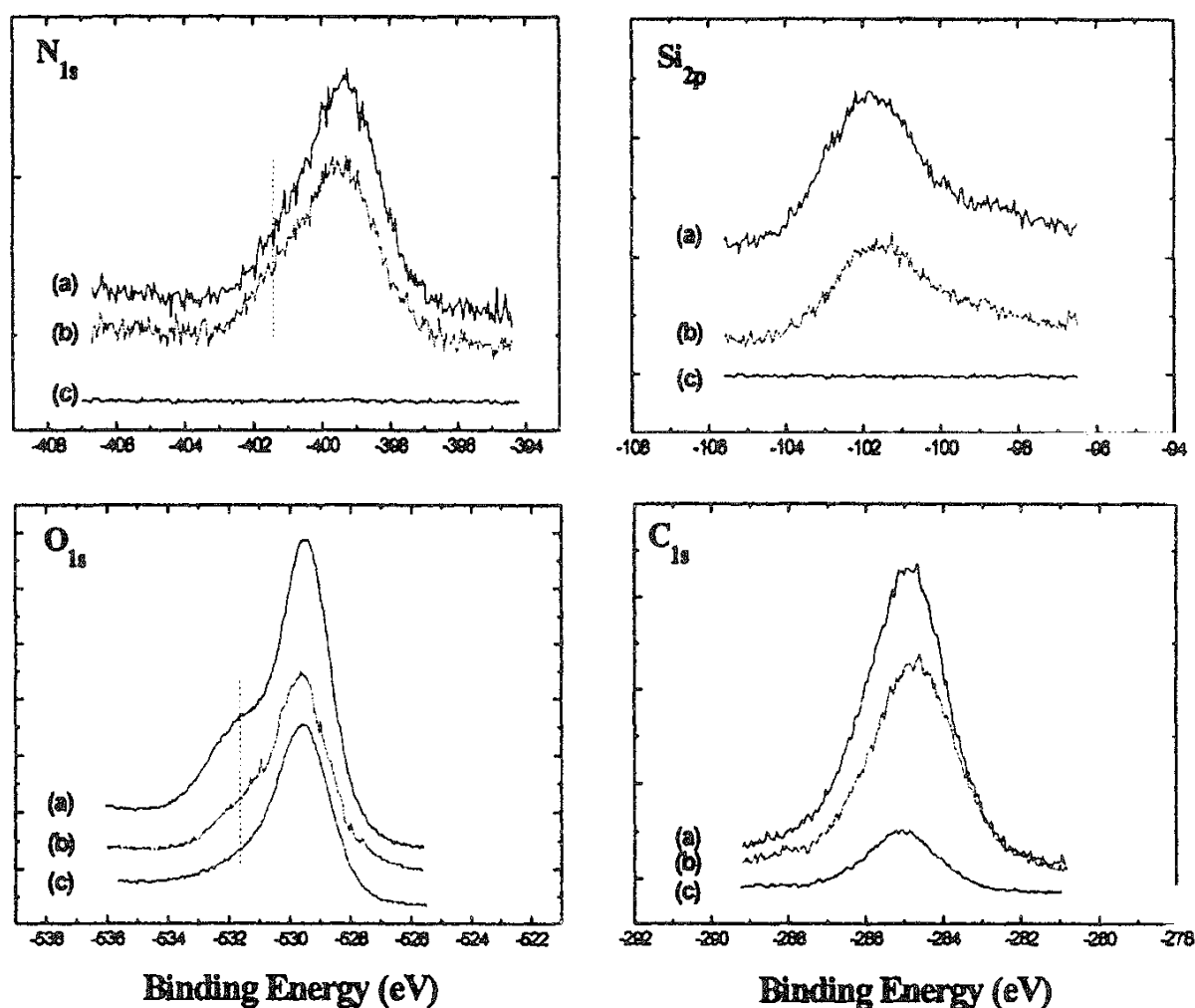


FIG. 4 Narrow-scan XPS spectra for the elements of interest on $\gamma\text{-Fe}_2\text{O}_3$ with silanized APTES (a) from water and (b) from toluene, in comparison with (c) untreated $\gamma\text{-Fe}_2\text{O}_3$ particles.

attributed to a higher degree of hydrolysis of APTES, while the higher fraction of amine protonation is related to the stronger interactions of amine groups with $\gamma\text{-Fe}_2\text{O}_3$ in water than in toluene. Also interesting to note is that the APTES forms a monolayer on $\gamma\text{-Fe}_2\text{O}_3$ from both solvents [11].

Although the XPS analysis confirmed the deposition of APTES on $\gamma\text{-Fe}_2\text{O}_3$, the technique is unable to determine the degree of hydrolyzation of ethoxy groups and subsequent cross-linking, which have a significant impact on the density and stability of the film. DRIFTS spectra were therefore collected. In contrast to silanization in water, DRIFTS spectra of the APTES film deposited from toluene solutions showed vibrational bands of methyl groups at 2974 and 2887 cm^{-1} , indicating the presence of small fraction of unhydrolyzed ethoxy groups in the film. The unhydrolyzed ethoxy groups are anticipated to inhibit the lateral polymerization of APTES, resulting in a poorer packing density and lower surface coverage than those of the films silanized from water in which the hydrolysis is more effective. This observation is consistent with the findings from XPS analysis, which showed a lower APTES coverage on $\gamma\text{-Fe}_2\text{O}_3$ from toluene.

To further confirm the orientation of APTES on $\gamma\text{-Fe}_2\text{O}_3$, the electrokinetics (zeta potentials) of the coated particles were measured. As shown in Fig. 5, an isoelectric point (iep), the point where zeta potential is zero, of the particles silanized with APTES from water and toluene was found at about pH 8.5 and

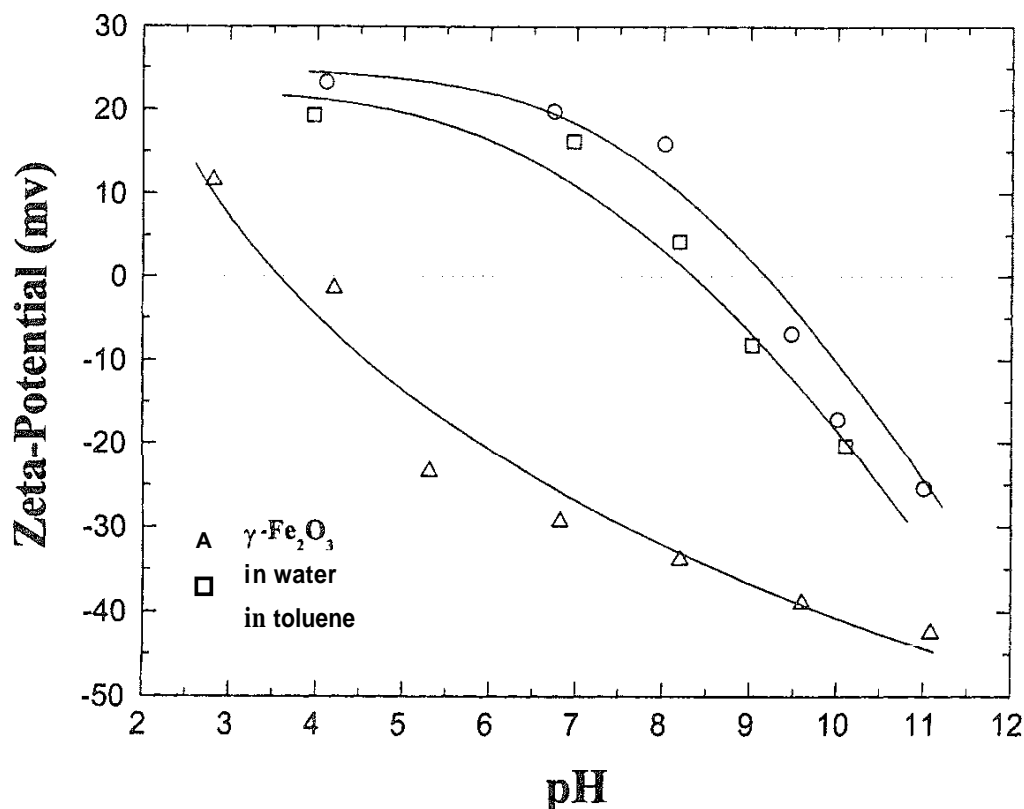


FIG. 5 Zeta potential of $\gamma\text{-Fe}_2\text{O}_3$ without silanization (Δ) and with silanization by APTES (\square) in water and (\circ) in toluene.

9.2, respectively, in contrast to pH 4.5 for uncoated $\gamma\text{-Fe}_2\text{O}_3$. The measured electrokinetics of the silanized particles resembles that of air bubbles in dodecylamine (a cationic surfactant) solutions, in which case the amine groups were exposed to water. This similarity confirms the condensation of APTES on $\gamma\text{-Fe}_2\text{O}_3$ from both water and toluene with amine groups facing the environment and remaining reactive. The difference in the measured zeta potentials using the particles silanized in water and toluene reflects mainly the variations of APTES orientation on $\gamma\text{-Fe}_2\text{O}_3$. Since more APTES was deposited on $\gamma\text{-Fe}_2\text{O}_3$ from water than from toluene, a slightly lower iep value observed for the particles silanized in water suggests that more amine groups were hidden inside the film compared to the silanization in toluene. As a result, the contribution from amine groups to the number of positive surface sites decreases while that from silanol groups to the number of negative sites increases. These two effects result in a lower iep as experimentally observed, consistent with XPS analysis, which showed a higher degree of protonation of amine groups considered to bind with the surface [43].

The stability of the silanized APTES films on $\gamma\text{-Fe}_2\text{O}_3$ was investigated by leaching the particles in pH 2 solutions for 20 h. It was found that the amount of iron leached out reduced from 60 mg/g for unsilanized $\gamma\text{-Fe}_2\text{O}_3$ to 34 mg/g for silanized $\gamma\text{-Fe}_2\text{O}_3$. Compared to the particles coated with MHA using the SA method, the amount of iron leached out is significant, suggesting that the original particles were not fully covered, compounded with some degree of detachment of APTES from the surface in acid solutions. As there was only a slight shift in iep from pH 9.2 to 8.7 upon leaching of the particles silanized from toluene, it is concluded that the $\gamma\text{-Fe}_2\text{O}_3$ surface was not fully covered by APTES as expected for insufficient lateral polymerization due to unhydrolyzed ethoxy groups. For particles silanized from water, a significant shift of iep from 8.6 to 6.2 was observed, although the amount of APTES deposited was greater than with silanization in toluene. It appears that the protonated APTES, presumably attached to the surface through hydrogen bonding was not stable, detaching readily in an acidic environment. After exposure to an alkaline environment, on the other hand, the electrokinetics of silanized $\gamma\text{-Fe}_2\text{O}_3$ approached that of unsilanized $\gamma\text{-Fe}_2\text{O}_3$, suggesting a much more significant detachment of APTES from $\gamma\text{-Fe}_2\text{O}_3$. Whether the detachment of APTES is due to the breakage of Si—O of Fe—O bonds remains to be further investigated. The damage appears to occur at the Fe—O linkage to account for the observed electrokinetics. (If the breakage were at the Si—O linkage, the attacked surface should have resembled a silica surface with an iep around pH 2.) The comparative information for the direct silanization is summarized in Table 2.

Clearly, the direct silanization of APTES from water and toluene solutions on $\gamma\text{-Fe}_2\text{O}_3$ described above is not suitable for engineering magnetic particles in biological and environmental applications. It is well documented that the Si—O bond is more stable than Fe—O bonds in acidic solutions. A well-known example is that silica (SiO_2) is insoluble but iron oxides dissolve in strong acids. One of the alternatives, therefore, is to coat a $\gamma\text{-Fe}_2\text{O}_3$ surface with a thin layer of silica, followed by the well-established silanization on silica, to improve the coating density and film stability.

TABLE 2 Coating Characteristics and Stability (in Acid) of APTES Films Silanized on γ -Fe₂O₃ from Water and Toluene Solutions

| | XPS | | | DRIFTS (-CH ₃) | Fe in leachate (mg/g) | iep | |
|--|--|--|-----|-------------------------------|--------------------------|-----------------|----------------|
| | O _{531.8} /O _{529.6} | N _{399.4} /N _{401.3} | | | | Before leaching | After leaching |
| γ -Fe ₂ O ₃ | — | — | — | — | 60.3 | 4.5 | — |
| Silanized in water | 0.32 | 2.85 | no | no | 34 | 8.6 | 6.2 |
| Silanized in toluene | 0.16 | 4.88 | yes | yes | 34.1 | 9.2 | 8.7 |

IV. SILICA COATINGS

Silica coating has been used on surfaces of carbon, steel, alumina, and polymer resins to promote adhesion, minimize photodegradation, or prevent material oxidation and corrosion. In view of the strong hydration of silica surfaces in aqueous solutions and hence high colloidal stability, silica coating has also been used to prepare stable ferrofluids. Silica-coated particles have been used for the synthesis of conductive polymer nanocomposites [44]. Dense liquid and sol-gel processes are the two principal methods used to coat silica films on finely dispersed particles. Silica coating using a dense liquid process is a complicated physicochemical process achieved by controlling the supersaturation level of silica in aqueous solutions. At least three competitive processes, homogeneous nucleation followed by surface growing and heterogeneous and homogeneous coating, are present simultaneously. In general, homogeneous coating requires the lowest supersaturation level, followed by heterogeneous coating and finally homogeneous nucleation, which requires excess energy as predicted by the Kelvin equation to account for the extremely high curvature of the nuclei. Although homogeneous nucleation can be avoided by carefully controlling the supersaturation level just above the critical concentration of heterogeneous coating, as desired, the homogeneous surface coating often presents a challenge to uniform surface coatings. It is evident that as soon as the substrate is coated with silica, the growth of the coated area, a process similar to homogeneous coating, prevails as it requires a lower supersaturation level, resulting in a nonuniform, patchwise (islands) coating as shown schematically in Fig. 6b.

Silica coating by the sol-gel process, on the other hand, is conducted in an organic solvent. The process is based on the hydrolysis of the precursors such as tetraethoxysilane (TEQS) in the presence of water and catalyst, followed by condensation with surface metal hydroxyls. With controlled hydrolysis of TEQS, an $M-O-Si$ chemical linkage is established between surface metal atoms (M) and TEQS, followed by lateral polymerization and finally the formation of a three-dimensional network via the formation of siloxane bonds ($Si-O-Si$) with increasing TEQS concentration and hydrolysis. A well-known drawback to the sol-gel process for engineering magnetic carriers is the porous nature of the silica

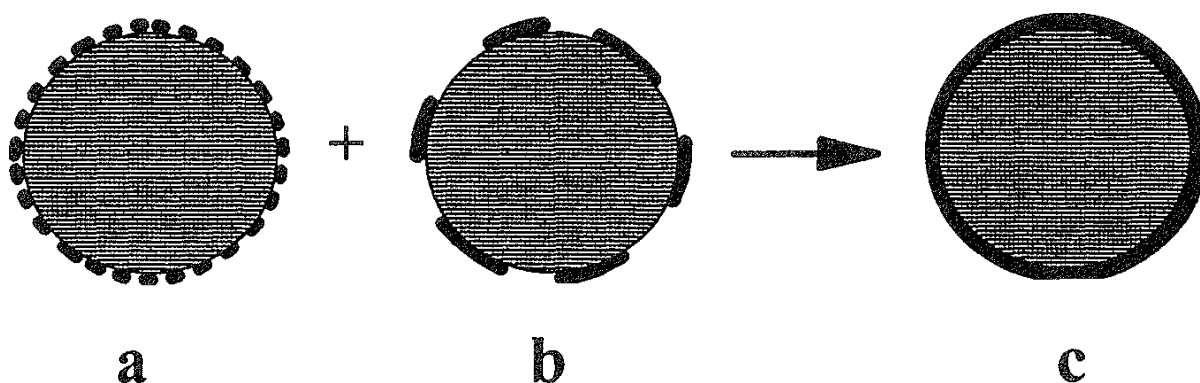


FIG. 6 Schematics of silica thin films coated on $\gamma\text{-Fe}_2\text{O}_3$ by (a) sol-gel, (b) dense liquid, and (c) two-step (i.e., a followed by b) processes.

film as shown schematically in Fig. 6a, although this could be advantageous for certain applications.

A compromise between these two methods is a novel two-step coating process developed in our laboratory [45]. This approach is based on the idea that the sol-gel process can coat a surface uniformly, although the film is often porous, as shown in Fig. 6a. In the second step, using the dense liquid process, the residual ethoxy groups in the silica films prepared using the sol-gel process are further hydrolyzed, and the pores are anticipated to be closed by and filled with silica under supersaturation conditions. It is clear that the two-step silica coating process integrates the advantages of uniform coatings by the sol-gel process and the low supersaturation levels required for homogeneous coating by the dense liquid process. As a result, a uniform thin silica layer as shown in Fig. 6c can be coated onto γ - Fe_2O_3 to protect the particles with a minimal reduction in saturation magnetization and to provide a surface for further functionalization by silanization.

For comparison, the silica was coated on γ - Fe_2O_3 at the 11% (by weight) silica level using these three methods. Narrow-scan XPS spectra of the coated particles are shown in Fig. 7. The presence of a silicon band at 103.4 eV and an additional oxygen band (O1) at 532.8 eV on the spectra of coated particles confirms the coating of silica on γ - Fe_2O_3 . Semiquantitative analysis showed an area ratio of silicon to iron bands (Si/Fe) of 0.7, 4.1, and 4.1 for particles coated using the dense liquid, sol-gel, and two-step processes, respectively. A higher Si/Fe ratio indicates a higher

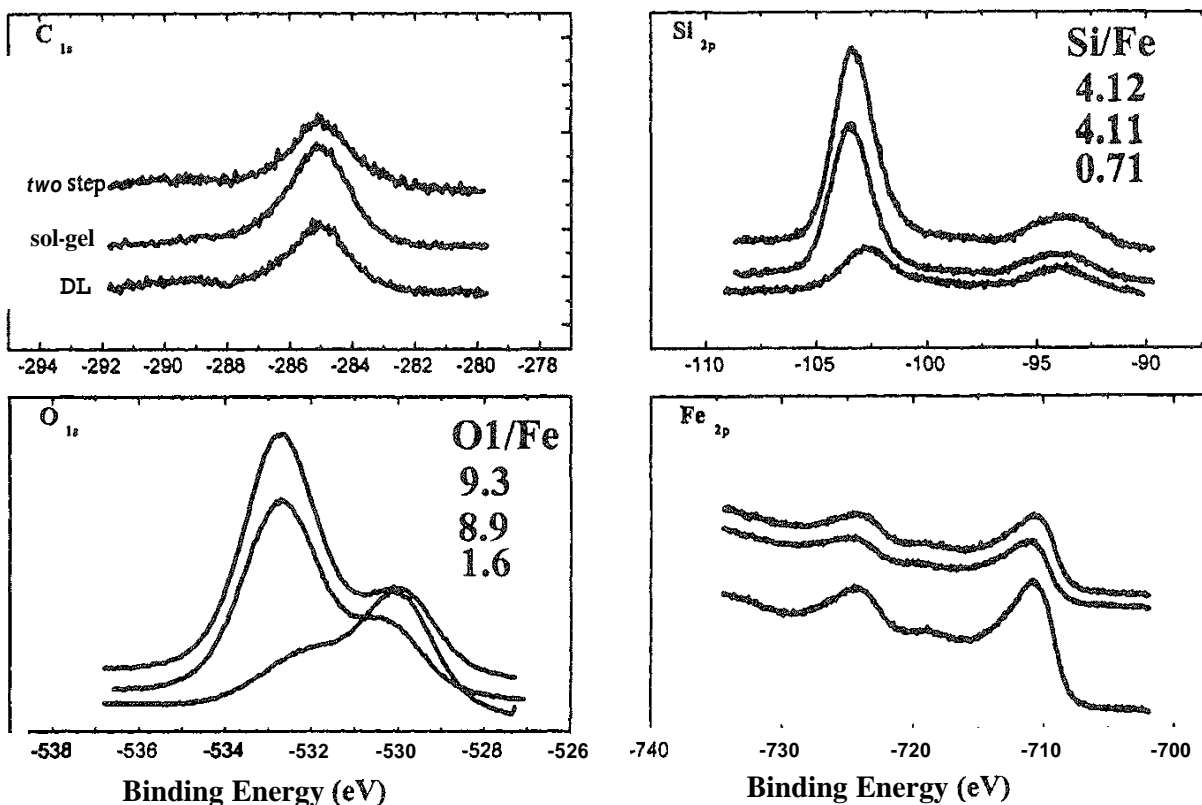


FIG. 7 Narrow-scan XPS spectra for the elements of interest on silica-coated γ - Fe_2O_3 particles.

degree of silica coating. It is evident that the silica coating efficiency is comparable for the sol-gel and two-step processes, higher than that of the dense liquid process. The DRIFTS spectra showed the formation of siloxane bonds in all three processes. In contrast to the dense liquid or two-step coating process, the unhydrolyzed ethoxy group was detected for the particles coated with the sol-gel process. The presence of Si-OEt terminal groups is partially responsible for the porosity of the films coated with the sol-gel process.

Leaching tests were conducted to further examine the state of silica film on γ -Fe₂O₃. The coated particles were dispersed in an acid solution of pH 2.5 for 20 h, and the amount of iron in the leachate was analyzed. The results are summarized in Table 3. Also shown in this table is the saturation magnetization of coated particles. It is evident that the amount of iron leached out became undetectable for the particles coated with the two-step process in contrast to the single-step, sol-gel, or dense liquid process, in which case, 1.1 or 2.8 mg of Fe per gram of particles was detected. However, the saturation magnetization is comparable for particles coated with silica using the sol-gel and two-step processes, suggesting that the amount of silica on the surface is virtually the same and confirming the important role of the film structure in protecting the matrix component of magnetic carriers for biological and environmental applications. It is evident that the two-step silica coating process is successful in making base materials that can be further functionalized by the conventional silanization process to produce magnetic carriers of a desired functionality.

V. APPLICATIONS

A. Self-Assembled Monolayers

The MHA coated γ -Fe₂O₃ particles prepared by the SA method contain reactive thion and/or disulfide groups that are known to have strong affinity to various metal ions such as gold, silver, and copper. The engineered carriers of large surface area can therefore be used to capture silver and copper present in industrial effluents. The metal-loaded particles can be readily separated from the effluent

TABLE 3 Stability as Measured by Amount of Iron Leached Out in Acid (pH 2.5) and Saturation Magnetization of Silica-Coated γ -Fe₂O₃ by Dense Liquid, Sol-Gel, and Two-step Coating Processes at 11% SiO₂

| Coating method | Fe in 0.01 N HCl (mg/g) | M _S (emu/g) |
|--|----------------------------|---------------------------|
| γ -Fe ₂ O ₃ | 60.3 | 52 |
| Dense liquid | 2.8 | 48.2 |
| Sol-gel | 1.1 | 43.2 |
| Two-step | nil | 42.5 |
| SiO ₂ | nil | — |

by using magnetic separation methods. This application is illustrated in our loading tests of Cu and Ag on MHA-coated γ -Fe₂O₃ particles from 10 mM CuSO₄ or AgCl solutions. The narrow-scan XPS spectra of the loaded particles separated with a hand magnet are shown in Fig. 8. The load of Ag and Cu on the MHA-coated particles is evident from the presence of Cu_{2p} (934 and 954 eV) and Ag_{3d} (368 and 374 eV) XPS bands on spectra c and d, respectively. The area ratio of the copper satellite band to its 2P_{3/2} band is lower than expected, suggesting that some of the copper ions are in the cuprous state. It appears that some of cupric ions were reduced to cuprous ions, accompanied by the oxidation of thiol to disulfide, which accounts for the presence of an additional sulfur band of higher binding energy but lower intensity. The surface metal-to-sulfur atomic ratio was found to be 0.6 and 0.8 for copper and silver, respectively. These results suggest a 1:2 (metal-to-sulfur) binding for divalent copper and 1:1 binding for monovalent silver. It is clear that the metal loading efficiency is sufficient for the MHA-coated magnetic carriers to be used in the removal or recovery of Ag and Cu from industrial effluents. For

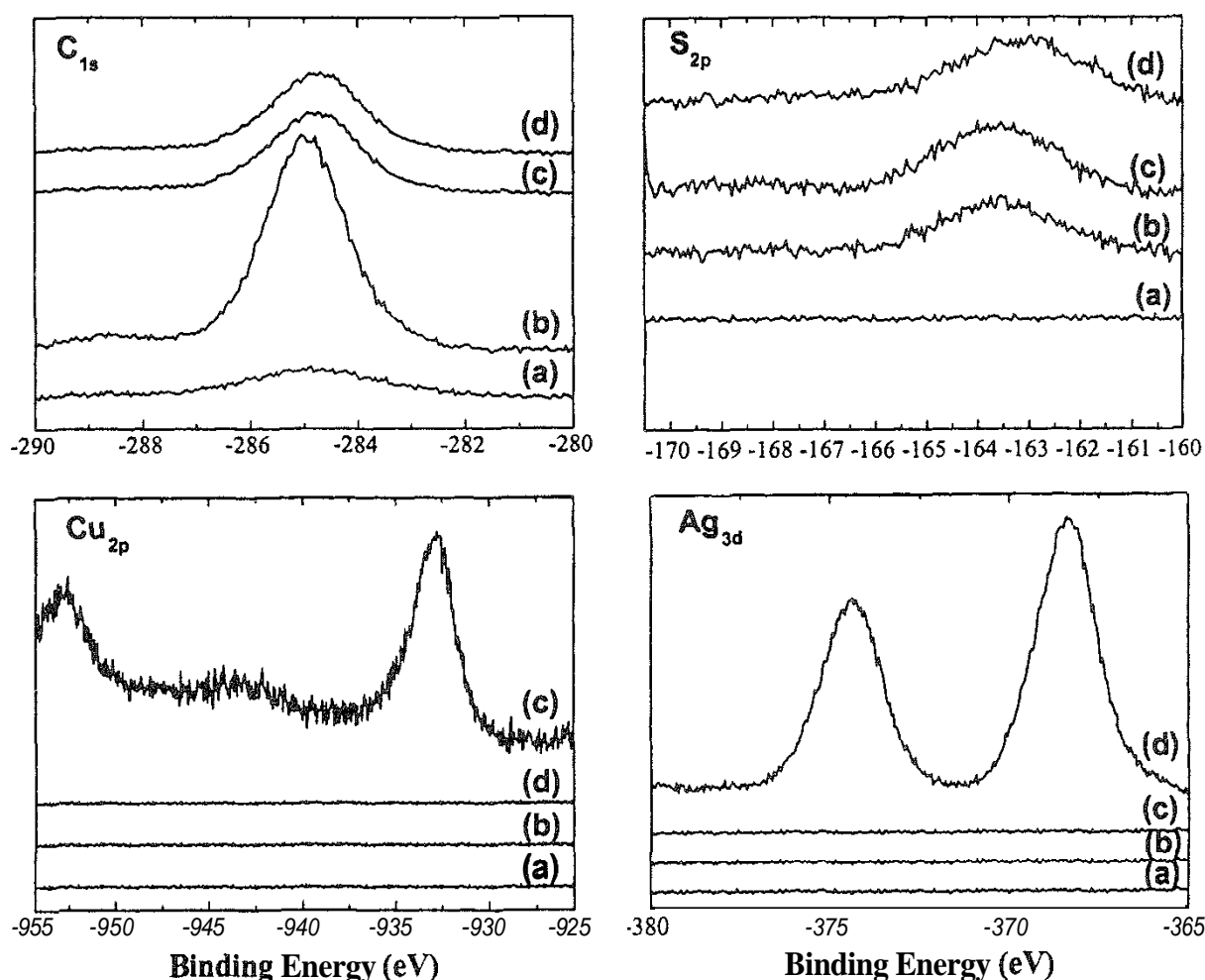


FIG. 8 Narrow-scan XPS spectra for the elements of interest on γ -Fe₂O₃ with various treatments: (a) Non; (b) MHA coating; (c) MHA coating followed by Cu loading; and (d) MHA coating followed by Ag loading.

other metal ions, the thio or disulfide group can be further oxidized to obtain the sulfonate or sulfate functionality [46].

Magnetic particles with reactive thiol and/or disulfide groups show special affinity to monoclonal antibodies (mAb's) containing disulfides in the basic unit [47]. Therefore, the magnetic carriers can be readily sensitized with an mAb of specific paratopes, such as antiglycophorin, which recognizes glycophorin, one kind of protein (M and N blood group antigens) in red blood cell membranes. When the carriers are introduced into a biological system, the cells containing glycophorin are captured and separated along with the carriers from the system by magnetic separation methods as shown in Fig. 1. A principal advantage of using magnetic carriers in cell separation applications is that there is no need to destroy the target cells in situ in biological systems. As a result, the side effects of conventional chemo treatments can be minimized.

B. Silanized Monolayers

It has been found that reactive amine groups are capable of attracting and adsorbing oxyanions such as arsenate, dichromate, selenate, molybdate, tungstate, and vanadate at the microgram per liter concentration level [48]. These species can then be removed effectively from an effluent by using magnetic separation with magnetic carriers to detoxify the effluent. The magnetic carriers with reactive amine groups are found to confer specific adsorption for heavy metal ions, including divalent mercury, lead, copper, zinc, manganese, and monovalent silver in contaminated aqueous and nonaqueous solutions [28]. Copper loading on the silanized magnetic particles of reactive amine groups is shown in Fig. 9. For comparison, copper loading on silica-coated magnetic particles is also shown in this figure. It is evident that at a given pH (pH 5.3), copper can be removed effectively from low concentration solutions (e.g., 100% removal from a 12 ppm solution). With increasing initial copper ion concentrations, the copper removal efficiency decreases as copper loading approaches the capacity limit of about 0.18 mmol of Cu per gram of particles. In contrast, the copper loading on the silica-coated magnetic particles is significantly lower than on the silanized particles, suggesting the important role of reactive amine groups in this application. It should be noted that the metal ion loading is pH-dependent. In a recent communication [49], we demonstrated the selective loading of various metal ions such as copper and zinc by varying the solution pH at which loading is performed.

It is evident that the use of magnetic carriers in separation science and technology, whether in the area of biological cell separation or industrial effluent detoxification, offers great flexibility. Other areas of potential applications of magnetic carriers with reactive amine groups include immobilization of enzymes, drug delivery, and biological sensors, among others. A detailed review of these applications can be found elsewhere [50]. The application can be extended further to other areas as long as a key-lock relationship (see Fig. 10) can be developed. The lock varies from antigen or streptavidin as in biological applications to metals or toxic species as in environmental applications, while the key could be an antibody or specific ligand. The most important consideration for these applications is to further improve the stability of coatings, which will significantly reduce the operating

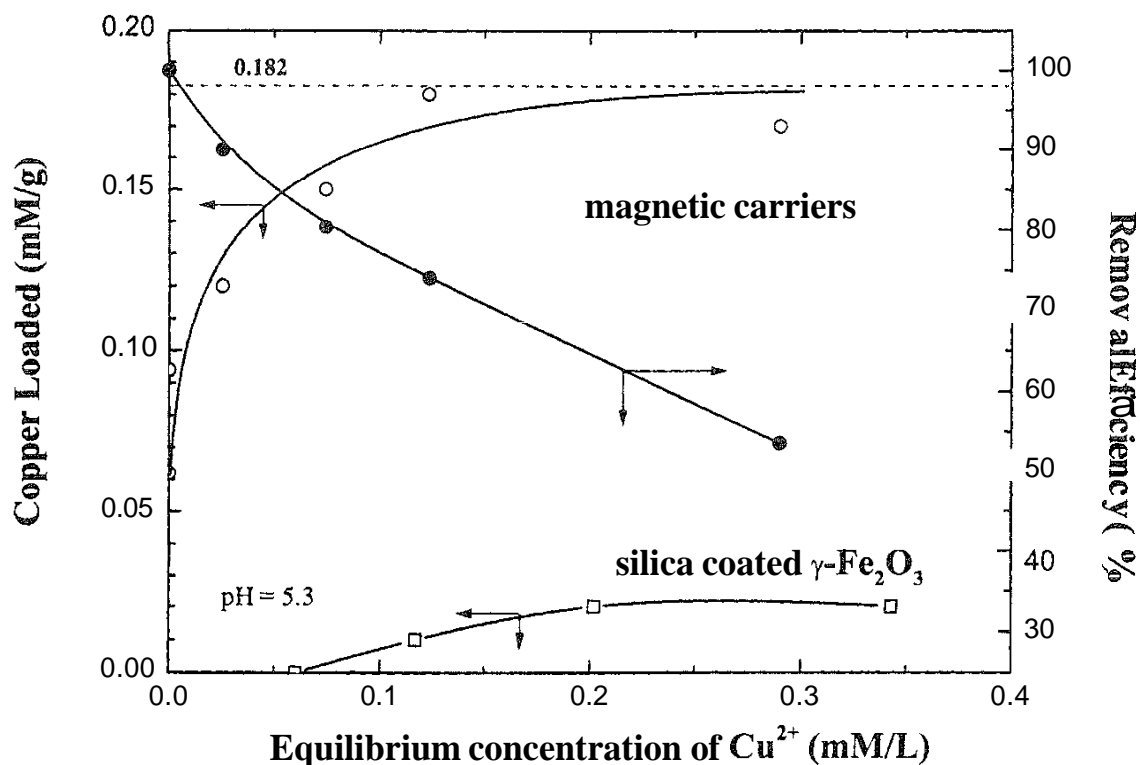


FIG. 9 Copper loading on ((○), left-hand axis) and removal by ((●), right-hand axis) APTES silanized on silica-coated $\gamma\text{-Fe}_2\text{O}_3$ particles in comparison to silica-coated $\gamma\text{-Fe}_2\text{O}_3$ particles ((□), left-hand axis) (loading at pH 5.3).

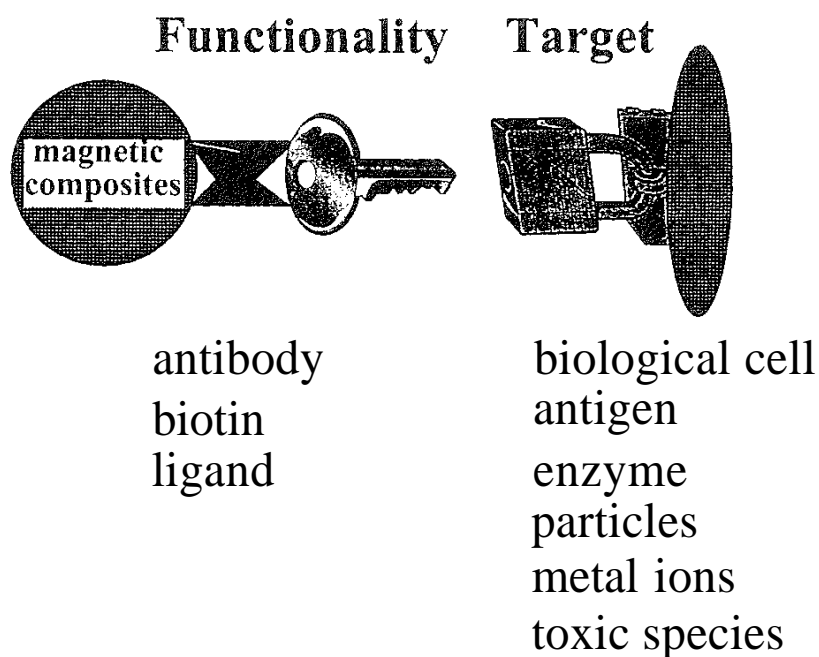


FIG. 10 Key–lock relation in potential applications of magnetic carriers.

cost by recycling magnetic carriers. The use of a silane coupling agent of longer hydrocarbon chain ($n \geq 14$) is anticipated to increase the film stability due to a stronger interchain association, forming a close-packed array through molecular self-assembly on substrate particles, magnetic carriers are expected to rapidly expand into other areas of application in the near future.

VI. SUMMARY

Three basic requirements for magnetic carriers in separation technology are fine particle size, superparamagnetism, and chemical stability in addition to tailored functionality. Two different approaches for engineering nanosize superparamagnetic carriers, molecular self-assembly and silica coating followed by silanization, have been described. Using molecular self-assembly, a bolaamphiphile of two different functional groups (16-mercaptohexadecanoic acid) was found to form a packed and stable monolayer on nanosize $\gamma\text{-Fe}_2\text{O}_3$, producing a surface of reactive thiol and/or disulfide functionality. Following a novel two-step silica coating process, reactive amino groups were successfully silanized on $\gamma\text{-Fe}_2\text{O}_3$ particles. Examples have been given for magnetic carriers of tailored functionalities in a variety of applications, including industrial effluent detoxification, metal recovery, biological cell separation, drug delivery, and the preparation of biological sensors.

REFERENCES

1. G. Moffat, R. A. Williams, C. Webb, and R. Stirling, *Miner, Eng.* 7:1039 (1994).
2. M. de Cuyper and M. Joniau, *Langmuir* 7:647 (1991).
3. S. Mann, J. P. Hannington, and R. J. P. Williams, *Nature* 324:565 (1986); S. Mann and J. P. Hannington, *J. Colloid Interface Sci.* 122:326 (1988).
4. J. H. Fendler, *Curr. Opinion Colloid Interface Sci.* 1:202 (1996).
5. N. S. Kommareddi, M. Tata, V. T. John, G. L. McPherson, and M. F. Herman, *Chem. Mater.* 8:801 (1996).
6. W. Y. Chen, P. R. Anderson, and T. W. Holsen, *Res. J. WPCF* 63:958 (1991).
7. R. J. Eldridge, *J. Macromol. Sci.-Chem.* A17:167 (1982).
8. J. Ugelstad, T. Ellingsen, A. Berge, and O. B. Helgee, U.S. Patent 4,654,267 (1987).
9. Q. Liu and Z. Xu, *Langmuir* 11:4617 (1996).
10. R. A. Whitehead, M. S. Chagnon, E. V. Groman, and J. Lee, U.S. Patent 4,695,393 (1987).
11. Z. Xu, Q. Liu, and J. A. Finch, *Appl. Surf. Sci.* 120:269 (1997).
12. A. Ulman, *An Introduction to Ultrathin Organic Films and Langmuir-Blodgett to Self-Assembly*, Academic, San Diego, 1991.
13. M. Pomerantz, A. Segmuller, L. Netzer, and J. Sagiv, *Thin Solid Films* 132:153 (1985); L. Netzer, R. Iscovici, and J. Sagiv, *Thin Solid Films* 99:235 (1983).
14. D. L. Allara and R. G. Nuzzo, *Langmuir* 1:52 (1985).
15. N. E. Schlotter, M. D. Porter, T. B. Bright, and D. L. Allara, *Chem. Phys. Lett.* 132:93 (1986).

16. P. E. Laibinis, J. J. Hickinan, M. S. Wrighton, and G. M. Whitesides, *Science*. 245:845 (1989).
17. C. D. Bain, E. B. Troughton, Y. T. Tao, J. Evall, G. M. Whitesides. and R. G. Nuzzo, *J. Am. Chem. Soc.* 111:321 (1989).
18. M. M. Walczak, C. Chung, S. M. Stole, C. A. Widrig, and M. D. Porter, *J. Am. Chem. Soc.* 113:2370 (1991).
19. A. N. Parikh, D. L. Allara, I. B. Azouz, and F. Rondelez. *J. Phys. Chem.* 98:7577 (1994).
20. R. H. Yoon, D. H. Flinn, and D. A. Guzonas, *Colloids Surf.* 87:163 (1994).
21. J. P. Folkers, L. B. Gorman, P. E. Laibinis, S. Boichholz, G. M. Whitesides, and R. G. Nuzzo, *Langmuir* 11:813 (1995).
22. D. L. Allara, A. F. Hebard, F. J. Padden, R. G. Nuzzo, and D. R. Falcone. *J. Vac. Sci. Technol.* A1:376 (1983).
23. A. Ihs and B. Liedberg. *J. Colloid Interface Sci.* 144:283 (1991); K. Uvdal, P. Bodo, and B. Liedberg, *J. Colloid Interface Sci.* 149:163 (1992).
24. C. A. Goss, D. H. Charych. and M. Majda, *Anal. Chem.* 63:85 (1991).
25. E. L. Smith, L. A. Alves, J. W. Andergg. M. D. Porter, and L. M. Siperko. *Langmuir* 8:2707 (1992).
26. Y. Okahata, K. Matsuura, K. Ito. and Y. Ebara, *Langmuir* 12:1023 (1996).
27. E. Angeletti, C. Canepa, G. Martinetti, and P. Venturello, *Tetrahedron Lett.* 29:2261 (1988).
28. D. E. Leyden and G. H. Luttrell, *Anal. Chem.* 47:1612 (1975).
29. R. J. Markovich, X. Qiu, D. E. Nichols, C. E. Pidgeon, B. Invergo, and F. M. Alvarez, *Anal. Chem.* 63:1985 (1991).
30. W. M. Heckl, F. M. Marrassi, K. M. R. Kallury, D. C. Stone, and M. Thompson, *Anal. Chem.* 62:32 (1990).
31. B. Buszewski and R. J. Lodkowski, *Liquid Chromatogr.* 14:1185 (1991).
32. H. Muramatsu, J. M. Dicks. E. Tamiya, and I. Karube. *Anal. Chem.* 59:2760 (1987).
33. E. Battistel, D. Bianchi, and G. Rialdi, *Pure Appl. Chem.* 63:1483 (1991).
34. M. D. Matteucci and M. H. Caruthers. *J. Am. Chem. Soc.* 103:3185 (1981).
35. A. V. Patsis and S. J. Cheng. *J. Adhes.* 25:145 (1988).
36. D. J. Ondrus, F. J. Boerio, and K. J. Grannen. *J. Adhes.* 29:17 (1989).
37. H. Ishida, *Poly. Compos.* 5:101 (1984).
38. C. J. Lund and P. D. Murphy, *J. Adhes. Sci. Technol.* 6:33 (1992).
39. C. Scott, H. Ishida, and F. H. J. Maurer, *J. Reinf. Plast. Compos.* 10:463 (1991).
40. E. P. Plueddemann, *Silane Coupling Agents*, Plenum, New York, 1982.
41. D. E. Leyden (ed.) *Silanes, Surfaces and Interfaces*, Gordon and Breach. New York. 1985.
42. K. L. Mittal (ed.), *Silanes and Other Coupling Agents*, Utrecht, The Netherlands, 1992,
43. F. M. Fowkes, D. W. Dwight, D. A. Cole, and T. C. Huang. *J. Non-Cryst. Solids* 120:47 (1990).
44. M. D. Butterworth, S. A. Bell, S. P. Armes. and A. W. Simpson, *J. Colloid Interface Sci.* 183:91 (1996).
45. Q. Liu, An innovative approach in magnetic carrier technology, PhD. Thesis, McGill University, Montreal, 1996.

46. R. J. Colloins and C. N. Sukenik, *Langmuir*, 11:2322 (1995).
47. T. E. Thomas, S. J. R. Abraham. A. J. Otter. E. W. Blackmore, and P. M. Lansdorp, *J. Immunol. Methods*. 154:245 (1992).
48. D. E Leyden, G. H. Luttrell, W. K. Nonidez, and D. B. Werho, *Anal. Chem.* 48:67 (1976).
49. Z. Xu, Q. Liu, and J. A. Finch., in *Composites at Lake Louise* (P. S. Nicholson, ed.), Trans. Tech Publications. Toronto, 1998.
50. R. A. Willians (ed.), *Colloid and Surface Engineering: Applications in the Process Industries*, Butterworth Heinemann, Oxford, UK, 1992.

4

Acid–Base Behavior of Surfaces of Porous Materials

CRISTIAN I. CONTESCU and JAMES A. SCHWARZ Department of Chemical Engineering and Materials Science, Syracuse University, Syracuse, New York

| | | |
|------|---|----|
| I. | Introduction | 52 |
| II. | Acid–Base Properties of Solid Surfaces | 53 |
| | A. General definitions | 53 |
| | B. Extension to solid surfaces | 56 |
| | C. The acid–base behavior of species confined in porous solids | 58 |
| III. | Origin of Acid–Base Properties of Solid Surfaces | 59 |
| | A. Ideally polarizable surfaces: metals | 60 |
| | B. Open surfaces: oxides | 61 |
| | C. Surfaces with variable composition: composite oxides | 71 |
| | D. Layered materials: clays | 75 |
| | E. Porous materials: zeolites and zeotypes | 76 |
| | F. Microporous materials: activated carbons | 78 |
| | G. Pseudo-liquid materials: heteropolyacids and salts | 80 |
| IV. | Measuring Acid–Base Properties of Solid Surfaces | 81 |
| | A. Nature, number, and strength of acid–base surface sites | 81 |
| | B. Experimental methods | 81 |
| | C. Theoretical concepts | 88 |
| V. | Manifestation of Acid–Base Properties of Microporous Solids | 91 |
| | A. Solid/gas interface: the role of acid–base sites in heterogeneous catalysis | 91 |
| | B. Solid/liquid interface: acid–base reactions in interlayers of layered minerals | 93 |
| VI. | Summary and Conclusions | 94 |
| | References | 95 |

I. INTRODUCTION

The concepts of acidity and basicity are used by scientists from all branches of theoretical, experimental, and engineering chemistry. They are fundamental in nature and are of unquestionable utility as a powerful classification tool. However, it is interesting to observe that the meaning of these two simple words may vary depending on the compounds or materials discussed, experimental conditions or methods of study, particular applications, state of matter or size of particles, and, in some instances, even the context in which the terms are used. Indeed, any discussion about acid–base properties is an assertion in comparative terms: a debate about relativity. By definition, acidity and basicity are opposite properties (or principles) that manifest themselves only in relationship to each other. Acids are revealed and measured by bases; the presence of bases is revealed and quantified by acids.

A simple, rarely mentioned rule requires that acids and bases to be compared be confined to a single, homogeneous phase, either liquid or gaseous. When this rule is adopted, there are numerous methods in chemistry and physics adequate for the identification and evaluation of the quality and quantity of either an acid or a base. As measurable properties, acidity and basicity are intrinsically connected. Indeed, all methods of quantitative characterization of acidity or basicity give only relative values; the strengths of acids measured in aqueous solutions differ from those measured in nonaqueous solvents, and the latter vary from one solvent to another. Two scales of acidity were selected for practical purposes, the aqueous scale and a scale based on gas-phase measurements, but they do not coincide. Both scales provide valuable theoretical insights into the molecular origin of acid–base properties. In fact, due to the inherent relativity of the measurements, any discussion of acid–base chemistry depends on the standards used or is specific to experimental conditions. Fortunately this fact is very well understood. As a result, the whole edifice of pure and applied chemistry was built upon the simple rule mentioned above: Acids and bases must be confined to the same homogeneous phase if they are to be compared. As long as this convention is observed, the reliability of analytical methods in acid–base chemistry or the meaning of their results is unquestionable.

This review focuses on the acid–base properties of surfaces of porous solids. In the context of the above discussion, it is inevitable that established practices will require some modifications. It is obvious that solids possess acidity and basicity. The challenge in characterizing their acid–base behavior results from the presence of two phases and from location of the acid–base sites at the interface between the solid and either a gaseous or liquid phase. Moreover, when acid–base chemistry occurs in spaces confined to the micropores or interlayers of nanostructured materials, the rules are broken a second time because all references to acid–base properties of macroscopically homogeneous phases based on the classical approach become inconsistent.

The surface chemistry of acid–base interactions in the nanospaces of solids comparable in size to the molecular dimensions of the reactants themselves is a new and fascinating subject. It has been approached from various angles; attempts were made to extend the concepts of classical chemistry, but new rules had to be developed. The consequence is that there is still no consensus regarding the significance of experimental results and their relationship to the theoretical notions.

An understanding of the acid–base properties of solid surfaces is extremely important in almost all fields of science and engineering. For example, the solid/gas interface intervenes when solid acids (or bases) are used as heterogeneous catalysts in the oil refining and chemical industries. The solid/liquid interface between rocks, minerals, and soils and natural waters is continuously transformed by weathering processes that result in the geohydrochemical circuit of elements. These are only two examples in which the primary reactivity factor is determined by the acid–base chemistry at solid interfaces, usually confined to molecule-sized spaces.

In the discussion that follows we attempt to organize the vast amount of information available on the acid–base behavior of porous solids. In Sec. I definitions from homogeneous systems are recalled and adapted to solid surfaces. Since the focus of this review is the molecular scale interactions and structure-determined acid–base properties at solid surfaces, the origin of these properties is discussed in [Sec. II](#) in relation to various types of solid interfaces. The discussion starts with the flat surfaces of clean metals, but most references are made to nanosized environments in porous and microporous solids in contact with a gaseous or aqueous phase. [Section III](#) deals with the experimental methods currently in use for characterization of surface acidity. The reader may discover contradictions and conflicting arguments in the subsection dedicated to the theoretical problem of finding a common scale for the acidity of solids. This unavoidable dilemma reflects the "confined" state of current understanding in this "heterogeneous" field and the inherently relative nature of most statements about acid–base properties.

II. ACID–BASE PROPERTIES OF SOLID SURFACES

A. General Definitions

1. Bronsted–Lowry

When Arrhenius formulated the classical views on acids and bases in 1887, his theory dealt exclusively with reactions in aqueous media [1]. He defined as acids all substances that upon reaction with *water* increase the concentration of hydronium ion (H_3O^+) in solution; those that increase the hydroxyl ion (OH) concentration were defined as bases.

In 1923 Bronsted [2] and Lowry [3] independently generalized these definitions and emphasized the crucial role of protons. Acids were defined as substances able to donate protons and bases as substances able to accept protons. Water was no longer required as a solvent, and bases no longer needed to donate hydroxyls.

The following equilibrium defines the pairs of conjugate acids and bases and is fundamental to the Bronsted–Lowry theory:



Acid A and its conjugate base B are two different but interrelated states in which a chemical system may exist. The acid is the proton-rich (and proton donor) state, while the base is the proton-deficient (and proton acceptor) state.

Because free protons do not exist in solution, the above scheme is only a simplification. A complete acid–base reaction actually takes place when two systems, let them be Systems 1 and 2, of conjugate acid–base pairs interact with each other. If most of the species of system 1 are in the proton-rich (acidic) state, their acidity can be manifested only if most of the species in system 2 are in the proton-deficient (basic) state. During the course of their interaction, a proton is transferred from the acidic species of system 1, A_1 , to the basic species of system 2, B_2 :



The reaction in the forward direction leads to the formation of a base in system 1 (B_1 , the conjugate base of A_1) and an acid in system 2 (A_2 , the conjugate acid of B_2). An important consequence is that the position of equilibrium depends on the relative acidity and/or basicity of conjugate acid–base pairs in the two systems, 1 and 2.

2. Lewis

In a further generalization, Lewis [4] advanced a definition that was no longer restricted to proton-exchange reactions. An acid was defined as any substance that can accept a pair of electrons from a donor substance, and a base as any substance able to donate an electron pair and form a "dative" covalent bond. In these more general terms, the acid–base interaction includes the formation of covalent bonds and applies to any chemical reaction in which an addition compound (adduct) is formed through a coordinative bond:



According to the above definition, both hydrogen bonding and π bonding are acid–base interactions.

Between Lewis acid–base adducts are possible displacement reactions that formally resemble the protolytic reaction (II) from the Bronsted–Lowry theory:



Thus the acids of the Bronsted–Lowry theory may be viewed as Lewis acid–base adducts in which the acidic component is H^+ (for example, H_3O^+ can be viewed as an $H_2O:H^+$ adduct). The Bronsted–Lowry bases are also Lewis bases. One can therefore conclude that the Lewis definition subsumes the *Bronsted–Lowry* definition of acids and bases.

3. Strength of Acids and Bases

In the Bronsted–Lowry theory all substances are considered, to some extent, amphoteric. Theoretically, the strength of individual acids can be expressed through the equilibrium constant of process (I), K_a , called the "acidity constant"; its reciprocal is termed the "basicity constant," K_b . Since neither acidity nor basicity of a system (system 1) manifest themselves without a proton acceptor or a proton donor (system 2), the individual constants K_a and K_b cannot be measured directly. One can, however, measure the equilibrium constant of the protolysis reaction (II):

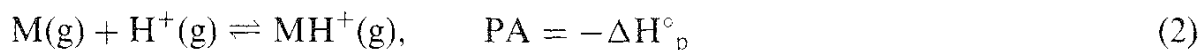
$$K = \frac{C_{B1} C_{A2}}{C_{A1} C_{B2}} = K_{a1} K_{a2} \quad (1)$$

It follows that the acidity of an acid can be measured only with reference to a base. If a common base is chosen, a relative acidity scale for several acids can be established. Water is a very common solvent. A scale of pK_a values ($pK_a = -\log K_a$) became very popular based on the convention that the common base B_2 is water. The pK_a scale is largely used as an acceptable and reproducible means for ranking the strength of acids (or of their conjugate bases) in dilute aqueous solutions. In water there cannot exist acids stronger than H_3O^+ ($pK_{a(H_3O^+)} = -1.7$) or bases stronger than OH^- ($pK_{a(OH^-)} = 15.7$). In nonaqueous solvents the acidity scales are different. Basic solvents (protophilic) enhance the strength of acids, and acidic solvents (protogenic) raise the strength of bases; thus the strength of acids (or bases) is leveled in highly basic or highly acidic solvents. Alkanes are inert solvents that do not accept or furnish protons; water is an amphiprotic solvent that either accepts or donates protons.

The strength of Lewis acid–base interactions cannot be expressed in terms similar to the acidity and basicity constants, K_a and K_b , of the Brønsted–Lowry theory. Consequently an equilibrium constant resembling the protolytic constant of Brønsted acid–base couples, Eq. (1), cannot be specified. Because of the broad variety of Lewis acid–base interactions there would be as many acid strength scales as there are interacting bases.

However, the strength of Lewis acid–base interaction can be expressed in energy terms, such as the exothermic molar heat, $-\Delta H^{AB}$, for the equilibrium (III) of adduct formation. The enthalpy term is preferred because entropy effects accompanying the formation of coordinative bonds are difficult to determine. Various models have been proposed for the theoretical estimation of the enthalpy term $-\Delta H^{AB}$ based on molecular properties of reactants and are reviewed in Ref 5. The most significant developments have been the hard and soft acid–base principle of Pearson [6], the E & C equation of Drago and Wayland [7], the donor and acceptor numbers of Gutmann [8], and the perturbation theory of Hudson and Klopman [9].

The heats of adduct formation with many Lewis acids have been measured experimentally in the gas phase using the technique of ion cyclotron resonance [10]. The absolute proton affinity (PA) of a gaseous base molecule has a precise thermodynamic definition in relation to the negative of the enthalpy variation for a hypothetical reaction of attachment of an isolated proton to a molecule M in the gas phase,



in the absence of any interactions with the medium. The corresponding free energy variation is referred to as the gas-phase basicity. Many compilations of various experimental results have been made [11], and several useful correlations for rationalizing the acid–base chemistry have been revealed. Quantum-mechanical calculations for the enthalpy of deprotonation in the gas phase generally give overestimated values [12].

The influence of a solvent complicates any understanding of acid–base interactions in solutions. The calculation of aqueous acidity constants would require the calculation of the free enthalpy of solvation of the acidic site, conjugate base, and proton, in addition to the gas-phase term for the change of free enthalpy during deprotonation and, of course, all entropy terms. While the entropy of deprotonation is nearly independent of the acid–base couple, the free enthalpy of solvation can be obtained only with difficulty from molecular dynamics calculations [13].

Although the importance of solvation effects for liquid-phase acid–base chemistry is evident, the experimental data are interpreted with difficulty. Thus, in aqueous solutions where the reference acid is H^+ , ammonia is a stronger base than triethylphosphine, while the opposite is true when the reference Lewis acid is CH_3Hg^+ . Examples of reversal in acid–base strength were also found for gas-phase adduct formation, where interactions should be free of any solvent effect [14]. Several factors are responsible for these inversions, such as the ease of formation of multiple hydrogen bonds in aqueous solutions or the occurrence of favorably oriented orbitals that maximize the mutual overlap for gas-phase intermolecular interactions.

B. Extension to Solid Surfaces

Bronsted and Lewis acids and bases are frequently encountered in the chemistry of solid surfaces, but in some instances these terms are used in a slightly different context from their original proposals. From the point of view of the Bronsted definition, a solid is acidic if it is able to donate (or at least transfer partially) a proton to a basic probe molecule to which the proton bonds (or with which it, at least, becomes partially associated). According to the Lewis definition, a solid is acidic if it is able to accept an electron pair from a basic molecule and also form a coordinative bond with it. The transfer of an electron pair in the meaning of the Lewis definition should be clearly distinguished from surface redox processes in which electron transfer (of one or two electrons) occurs without coordination.

Extension of the above definitions to acid–base processes on solid surfaces is further complicated by the "in between two phases" location of the acid–base sites.

For example, little is known about acid–base interactions at solid/solid interfaces. It has long been recognized that molecular interactions across the interface between condensed phases may be split into physical and chemical terms. Physical interactions (van der Waals forces) contribute to the non-ideality of fluids and have been traditionally considered for interfaces. However, modern theories explain interfacial phenomena on solid surfaces, such as adhesion or wetting, in terms of chemical interactions. Moreover, the Lewis definition of acidity is so comprehensive that it can easily be accepted that most chemical interactions at solid surfaces may be effectively described as acid–base interactions [15]. A continuously growing literature reinterprets interactions at solid/solid interfaces in terms of acid–base properties. For example, their role was shown in relation to solid/solid adhesion in film–substrate or fiber–matrix systems as well as in wood and paper processing, [16].

When solids interact with liquids and gases, the range of chemical interactions that can possibly occur between a solid surface and molecules of the fluid phase is very broad. For the solid/liquid interface and excluding from discussion all interactions that may be destructive for the solid, one can envisage local interactions that range from hydrogen bonding (such as between hydrogen atoms of chloroform and carbonyl groups of a solid polyester), to coordinative bonding (such as between nitrogen atoms of pyridine and electron acceptor sites that act as Lewis acids on the solid) to chemical interactions with exchange of H_3O^+ or OH on hydrated surfaces of oxides, mineral clays, or humic acids. The surface of activated carbon contains a variety of oxygen-containing complexes with either acidic or basic (Bronsted) character, and even the basal planes of graphene layers in activated carbons show properties of a Lewis base due to delocalized π electrons [17]. Moreover, for solids virtually free of functional groups, such as polyethylene, adsorbed impurities are almost always present on the surface and may readily react through specific chemical interactions. It is therefore warranted to consider that nearly all chemical interactions between solid surfaces and liquids, many of them responsible for wetting the solid, are acid–base reactions [15,18].

The solid/gas interface was traditionally studied with respect to adsorption and catalysis. Here the assertion that the Bronsted definition of acidity is a particular case of the Lewis definition is neither obvious nor even helpful. It suffices to say that many reactions in heterogeneous catalysis require specifically the presence of either Bronsted or Lewis acidic (or basic) sites, and the reaction mechanisms depend on the nature of the surface site. A long-term goal of surface studies for the characterization of solid catalysts was to distinguish and quantify the number of Bronsted or Lewis sites with potential catalytic activity for gas-phase reactants. For that reason, when discussing the acid–base behavior of solid surfaces, it is no longer possible, nor desirable, to adopt the viewpoint that subsumes Bronsted acid–base properties in the more general Lewis definition.

Similar to homogeneous one-phase systems, the acidity of solid surfaces manifests itself only in relation to a base that must be present; the strength of the acid–base interaction therefore depends on the particular base involved. This is true for both types of acid sites, Bronsted or Lewis. The reverse can be said, of course, for surface basic sites.

The special nature of the solid interface raises an additional practical problem: how to detect, in practice, the presence of acidity on solid surfaces. In general, any solid able to change the colour of a basic indicator, or on which a basic probe is chemically bound, should be regarded as a solid acid. Unfortunately, this very simple definition introduces, from the very beginning, a degree of uncertainty. How should those solid acids be classified that change the color of one indicator, I, but are indifferent to another indicator, I'? How should those solid acids be considered that strongly chemisorb a base, B, but interact weakly with another base, B'? Clearly, an important property of acids, their strength, is not uniquely recognized and defined. The lack of an acceptable scale of solid acidity comparable to the $\text{p}K_{\text{a}}$ scale for aqueous solutions or to proton affinities for gas-phase acid–base reactions is a primary problem that obscures the quantification of acidity on solid surfaces.

Another factor that makes difficult the assessment of acid–base properties on solid surfaces results from the intrinsic property of interfaces to serve as accumulation zones for adsorbed species. Returning to the above examples, one cannot take for granted that the change of color observed for indicator I on the surface of a solid acid is solely related to its acidity (in terms of classical definitions); the colour change could be attributed to side effects such as electrostatic polarization of the indicator induced by the local electric field on that particular surface. Also, if adsorption of base B' is weaker than that of base B, this may be the result of other surface-specific factors such as the presence of contaminants or steric hindrance of B' from access to specific binding sites on the solid adsorbent. The latter effect is most evident for microporous solids, where the number and strength ranking of acid sites detected experimentally may vary considerably with the nature of the basic probe molecules.

C. The Acid–Base Behavior of Species Confined in Porous Solids

The void space within porous materials constitutes a region with special properties, many of them not completely understood. At the level of molecular interactions in nanoscale-sized spaces it is difficult to distinguish between "pure" acid–base processes and perturbations due to the confined environment. Both the solid matrix and the molecules confined to the internal open spaces may show altered acid–base behavior in comparison with their "free-space" counterparts.

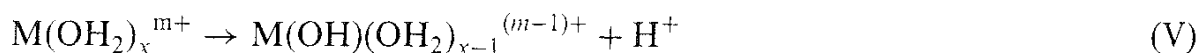
To illustrate this we select two examples that correspond to two classes of interfacial phenomena, both important from the practical point of view.

A gas/solid interface is present in the microporous environment inside the channels and cages characteristic of zeolite structures. All catalytic chemistry based on the acid properties of crystalline aluminosilicates (zeolites) is affected by two additional factors known as the "solvent" and "molecular sieve" effects. The chemical contribution, the solvent effect, describes the interaction at the molecular level between micropore-confined molecules and the coordination field created by all atoms that constitute the pore walls. The molecular sieve or geometrical effect accounts for the perturbation of the dynamics of confined molecules and is particularly important in relation to the selectivity of catalytic reactions occurring over this class of microporous solid acids. Both these effects may act concurrently to distort the intrinsic acid–base properties of molecules confined in the micropore spaces. In the case of alkane cracking, numerous observations demonstrate that various zeolites show very different specific rates for the same catalytic reaction. Two opposing views were expressed to account for this: (1) The Al—(OH)—Si positions in zeolite lattices span a very broad range of intrinsic acid strengths [19] that determine various reactivities, or (2) all acidic sites are virtually identical, and differences in reactivity result from geometric constraints in the micropores [20]. The perturbation due to geometrical factors may be so important that the existing experimental techniques cannot separate the effects, so any connection to the acid–base index of the solid zeolite surface becomes obscure [21]. It is known, for example, that the heat of adsorption of gaseous hydrocarbons on zeolites depends on the chain length or the diameter and shape of the micropores [22]. Catalysts with comparable numbers and strengths of acid sites but with different pore geometry

show completely different reactivities. In the one-dimensional pore system of mor-denite, the rates of monomolecular reactions are single-file diffusion-controlled, and bimolecular processes are virtually impossible [23]. Because the interaction with micropore walls is mainly due to dispersive van der Waals forces, which are typical for systems without covalent bonds, these effects should not be considered in relation to zeolites intrinsic acid–base properties [24].

As a second example, consider the liquid/solid interface in a nanosized environment representative of the interlayer space of clay minerals. The hydrophilic and swelling properties of these minerals is the result of structurally induced perturbations of acid–base chemistry in nanosized spaces.

The interlayer space in clays is bordered by oxygen from two planes of siloxane (Si—O—Si) groups. The oxygen atoms are electron pair donors (basic sites); their negative charge is compensated by exchangeable cations that are electron pair acceptors (acidic sites). When clays are hydrated, water in the interlayer spaces is structured. At the solid/liquid boundary of flat oxygen planes (zone A_o) and in the hydration atmosphere of exchangeable ions (zone A_m), water forms ordered structures; a disordered zone (B_{om}) occurs between the two ordered zones [25]. Depending on their position in the interlayer space, water molecules may act either as proton donors or as proton acceptors. Water acts as a hydrogen bond donor in zone A_o and may dissociate under the polarizing effect of metal cations in zone A_m:



Because of steric hindrance in the interlayer space, the hydration atmosphere of ions in interlayer zone A_m cannot extend as much as the hydration sphere of free ions in solution. Consequently, water in zone A_m is a stronger proton donor and interlayer protons are more mobile than in a liquid; the proton-donating tendency increases as the water content of the interlayer space decreases [26].

The wettability of the oxygen planes and the resulting structure of the interlayer water depend on the net balance between the kinetic energy of water molecules in the interlayer environment, the electrostatic forces between water molecules and exchangeable cations, and the attraction and dispersion forces between the layers [27]. The wettability increases with the tetrahedral substitution. In hectorite, where charge deficit occurs in the octahedral sheet, the negative charge of the oxygen plane is delocalized and no hydrogen bonds are formed with interlayer water. In vermiculite the charge deficit occurs mainly in tetrahedral sheets, and thus there is a greater localization of the negative charge that leads to the formation of strong hydrogen bonds in zone A_o [28]. Consequently, the interlayer of hectorite is the most expandable, while that of vermiculite is the most difficult to expand. Montmorillonite, saponite, and beidellite are intermediate between these extremes [25]. In the last section of this review we discuss additional examples of these effects.

III. ORIGIN OF ACID–BASE PROPERTIES OF SOLID SURFACES

The development of a scientific basis to describe the chemistry of solid surfaces has been impeded by their ill-defined nature; many factors can be responsible for observed effects. An understanding of surface chemistry at the same level develop-

ment in areas such as solution or gas-phase chemistry is desirable in that classical concepts proven useful for rationalizing chemical bonding and reactivity in traditional chemistry could be extended to the chemistry of solid surfaces,

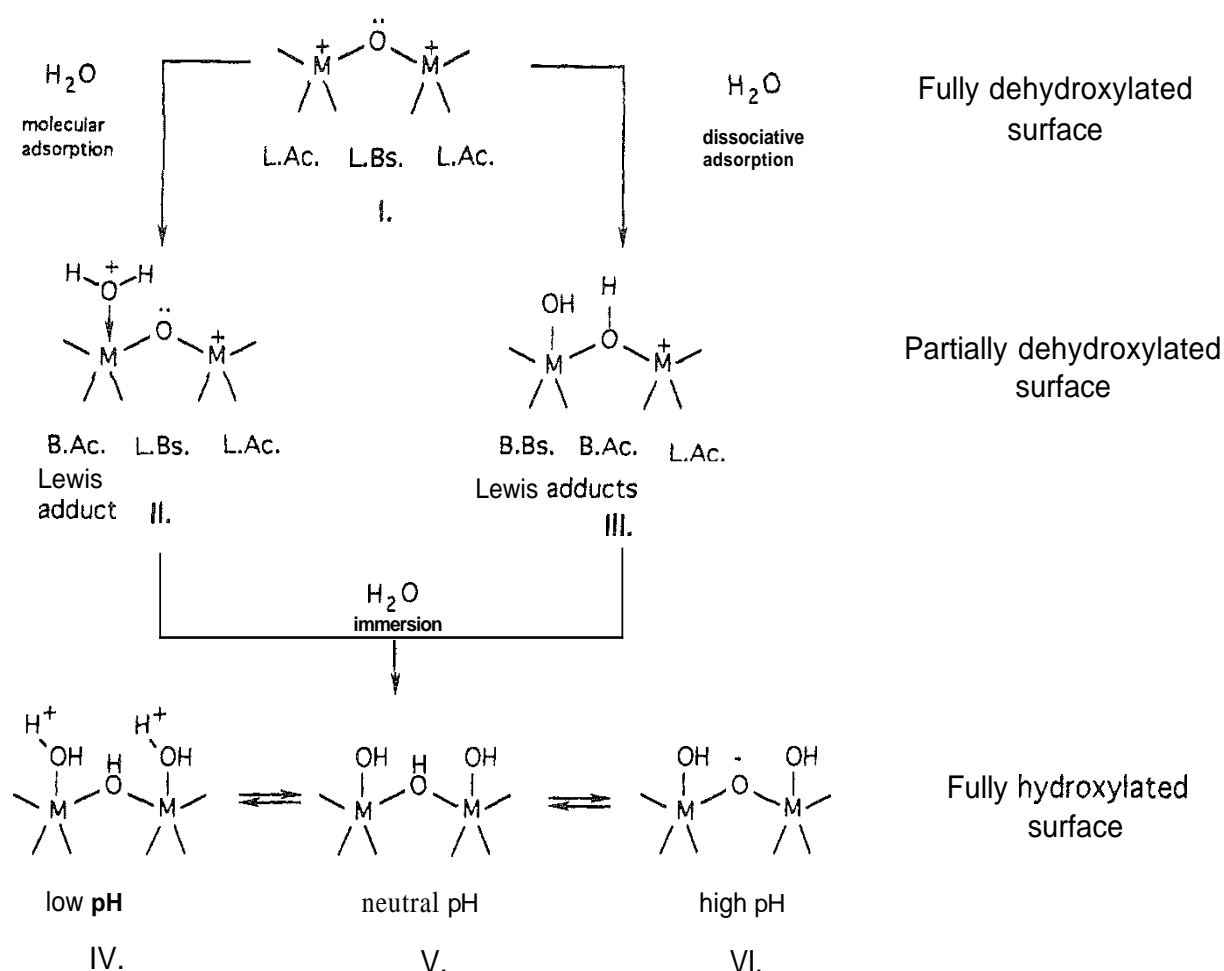
The acid–base concept, either in the limited interpretation of the Brønsted–Lowry theory or in the more general sense of the Lewis theory, is one of the most useful classification schemes in chemistry and a tool for systematizing the relationship between structure and reactivity. In this section we examine how this general concept can be applied to solid surfaces [29]. From the most general (Lewis) point of view, a surface is classified as acidic (electron acceptor) or basic (electron donor) according to the direction of net electron transfer that results in the formation of new chemical bonds with an adsorbed molecule.

A. Ideally Polarizable Surfaces: Metals

For clean metal surfaces, the direction of net electron transfer can be determined from measurements of the work function variation, $\Delta\phi$. A positive $\Delta\phi$ indicates net electron transfer from the surface to the adsorbed molecule (basic surface) while a negative $\Delta\phi$ indicates electron transfer in the opposite direction (acidic surface). As with all Lewis probes, a clean metal surface may act either as a base or as an acid, depending on the nature of the interacting molecules. For example, a clean Ni(111) surface is a Lewis base ($\Delta\phi < 0$) toward carbon monoxide [30] and a Lewis acid ($\Delta\phi < 0$) toward acetylene and benzene [31]. However, the criterion of net electron transfer is not always sufficient to define the acid or base character of clean metal surfaces. The reason is the substantial surface charge reorganization that may accompany chemisorption on metals. Because electronic states of metal surfaces are closely spaced in energy, acid–base interactions that require electron transfer and the formation of new chemical bonds are often delocalized.

Doping clean metal surfaces with either electronegative or electropositive elements produces changes in the acidic or basic properties that can be explained by inductive effects analogous to those in molecules [14]. Adsorbed foreign atoms may form either overlayers or incorporation structures. The latter may produce reconstruction of the top metal layer and strong decoupling of the metal atoms in the first layer from the bulk. This occurs, for example, during oxidation of metals and the growth of surface layers of metal oxides. Incorporation of oxygen in the top metal layer is accompanied by a significant electron transfer from metal atoms to the (more electronegative) oxygen atoms. This creates a large gap between the HOMO and LUMO energies of metal oxides and thus stabilizes the new charge distribution and inhibits charge reorganization during chemisorption. The result is the occurrence of localized Lewis acid–base sites (from a geometrical point of view) at the surface of oxidized metals.

The electron-rich oxygen anions at the top of oxide overlayers on metals show basic (electron donor) properties; the metal cations exposed in coordinately unsaturated sites (cus) show acidic (electron acceptor) character. This is depicted by structure I in Scheme 1. It is expected that the electron donors and acceptor orbitals are more localized on metal oxide surfaces than on clean metal surfaces. This forms the basis for the interpretation of the surface chemistry occurring on oxide surfaces



SCHEME 1 Transformation of surface structures and their acid–base characteristics on oxide surfaces with various degrees of dehydroxylation.

in terms of acid–base sites associated with individual surface ions located at various positions related to all possible terminations of the bulk crystal lattice.

B. Open Surfaces: Oxides

1. Surface Morphology

The morphology of oxide crystallites depends largely on their preparation method as well as on the prevailing crystalline phases. In general, the higher the temperature of calcination, the coarser and more crystalline is the final powdered oxide. For most transition metal oxides the surface area cannot exceed certain limits that reflect the microcrystalline organization of the solid [32]. For these materials of low porosity the average pore size is much larger than molecular diameters. Their surface is "open" for molecules impinging from the gas or liquid phase, and on the molecular scale the interaction zone can be viewed as a "flat" surface.

Materials with "open" surfaces are ideal for characterization of intrinsic acid–base properties of individual surface sites. The interaction of impinging molecules is essential bimolecular, and generally the surface does not show any peculiar

collective effect. Indeed, the electronic structure of most metal oxides is localized; oxygen atoms (both in bulk and at surface sites) can be considered as closed-shell O^{2-} ions that serve as ligands for metal cations [33]. This picture is strictly valid for highly ionic oxides (MgO is an example); it may require corrections only in the very few cases of semiconducting oxides (such as SiO_2) where bonding is largely covalent.

The metal and oxygen ions at the surfaces of oxides may or may not occupy the positions defined by simple extension of the bulk lattice. Surface reconstruction by atomic migration and relaxation of surface plane atoms from their position in the bulk stabilize the surface by minimizing the energy. Evidence exists that thermal stability of oxide surfaces may be correlated with the polarity of the surface and the degree of coordinative unsaturation of surface cations; the extent of surface relaxation depends on the presence of lone-pair electrons on the surface [34]. However, due to the paucity of existing experimental results gathered by techniques sensitive to surface geometry (such as LEED), it is in general difficult to say, with any certainty, where the atoms really are on the surface. Yet surface models that neglect surface reconstruction and relaxation can be regarded as valid.

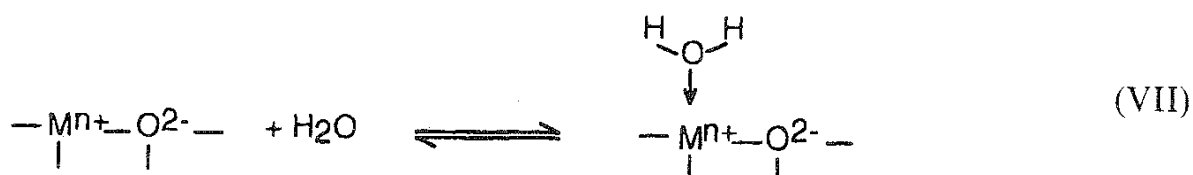
2. Fully Dehydroxylated Surfaces

The surface of a fully dehydroxylated ionic oxide can be considered as an extended array of coordinately unsaturated oxygen ions and metal cations. From the acid–base point of view, they act as Lewis base and Lewis acid centers, respectively (structure I in Scheme 1). The net charge on each surface center depends on the stoichiometry, ionicity, and local surface structure, which in turn vary from one crystal plane to another. A few positions that represent geometrical defects on the surface (corners, edges, dislocations) may be characterized by enhanced acid–base character, as their energy is further increased due to additional chemical unsaturation.

The molecules impinging on the surface can have either a Lewis base or Lewis acid character. For instance, CO with a filled orbital at the carbon end displays Lewis basicity, while CO_2 shows Lewis acidity [35]. The primary interaction is strictly localized on oxides, and surface adducts are formed with the acidic or basic centers of the solid. An example is the nondissociative adsorption of CO on exposed cationic centers on oxide surfaces:

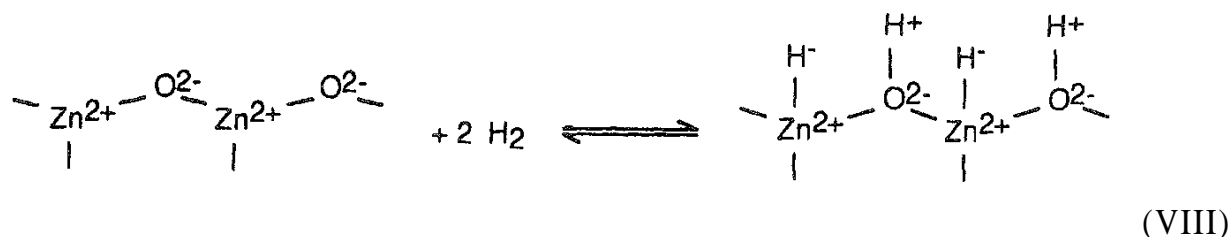


The adsorption of CO on oxides (ZnO) involves mainly a donation and little π bonding [36]. A similar character, though with a stronger interaction, is shown by the adsorption of NO, which has an electronic structure similar to that of CO except for one additional unpaired electron. Another example is the nondissociative adsorption of water on coordinately unsaturated cations:

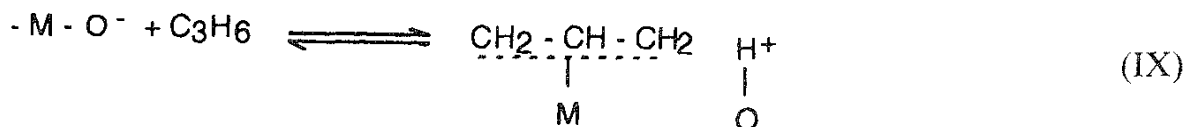


The newly formed adsorption complex (structure II in Scheme 1) is a Lewis adduct and at the same time a Bronsted acid site.

All important peculiarity of solid surfaces is the occurrence of adjacent Lewis acid (unsaturated cation) and Lewis base (unsaturated anion) sites in repetitive structures. If they interact in a concerted manner with the adsorbed species, the result is dissociative adsorption. For example, adsorption of hydrogen on ZnO is molecular at -195°C , but at room temperature adsorption is dissociative. The mechanism is most likely heterolytic, as suggested by new $\text{Zn}-\text{H}$ and $\text{O}-\text{H}$ vibrations observed in the IR spectrum [reaction (VIII)][37].



Another example of dissociative adsorption by concerted action of a Lewis acid–base couple is π bonding of alkenes on metal oxides, as in reaction (IX). However, dissociative adsorption of water on ideally dehydroxylated oxide surfaces is by far the most important example to cite, in view of the formation of surface hydroxyl groups and their tremendous impact on the reactivity of most oxides under ambient or close to ambient conditions [reaction (X)].



In Scheme 1, dissociative adsorption of water transforms the Lewis acid–base pair from structure I into a pair of Bronsted acid–base sites (structure III) that can be regarded, at the same time, as Lewis adducts. Also note the conversion of the Lewis acid into a Bronsted base and that of the Lewis base into a Bronsted acid.

3. Partially Dehydroxylated Surfaces

Fully dehydroxylated oxide surfaces, such as those considered above, can ideally be prepared either by treatment at elevated temperature under vacuum or by oxide cleavage in an inert atmosphere. These structures do not exist under normal conditions because Bronsted acidity is generated upon reaction with water after preparation. Under ambient conditions oxide surfaces are partially hydroxylated. They correspond to structures II and III of Scheme 1.

The validity of local models for acidic properties on oxide surfaces is supported by quantum-mechanical calculations. Brönsted acid sites are present only when

hydroxyl groups are present. The strength of Bronsted acid sites is controlled by the electrostatics of the system and is governed mainly by three structural parameters: the coordination number of the hydroxyl group, the charge on the cation(s), and the coordination number(s) of cations neighboring the hydroxyl group [38].

Surface hydroxyl groups may differ with respect to their coordination to underlying metal cations and the magnitude and sign of the uncompensated electron charge. In turn, this results in variations of the strength of O—H bonds at various surface oxygen sites. The acid–base properties of surface oxygen ions are therefore determined by surface structural factors. For example, the two Lewis adducts of structure III differ with respect to their Bronsted properties: The monodentate hydroxyl is basic whereas the bidentate hydroxyl is acidic. This fact can be recognized in the fine structure of O—H stretching vibrations in infrared spectra of partially dehydroxylated oxide surfaces.

The literature on infrared spectroscopy abounds with information that reveals the presence of several types of surface hydroxyls with various characteristic ν_{OH} stretching frequencies on partially dehydroxylated oxides. Structural considerations show that the number of all possible configurations for hydroxyl (and oxygen) groups on low index planes of oxides is limited [39]. For example, in silica the oxygen atoms are connected to two Si atoms, and therefore only one type of hydroxyl is likely to exist on the surface (silanol). In titania every oxygen ion is surrounded by three ions of Ti^{4+} , and therefore on the surface there may exist only terminal and bridging hydroxyls. Although the spinel structure of transitional alumina (η and γ) is more complex, structural considerations suggest that since the oxygen coordination number is 4, one can expect three types of surface hydroxyls. Cerium oxide also, with tetrahedral coordination of oxygen atoms, is expected to present three types of hydroxyl groups. Figure 1 illustrates the DRIFT spectra of several simple oxides in the region of deuterium-exchanged hydroxyl vibrations [40]. The spectra were collected using a Nicolet Impact 400 spectrometer equipped with a catalytic chamber. The O—D rather than O—H vibrations were investigated in order to isolate the contribution of oxide surface groups from other perturbing influences during the measurements.

Knozinger and Ratnasamy [41] assigned the ν_{OH} bands on alumina to surface groups in various configurations by assuming that only single-, double-, and triple-coordinated surface oxygen positions may exist in ratios and geometrical arrangements that differ from one surface plane to another. With some modifications [42] their scheme was generalized by Busca et al. [43] for surface sites on several oxides with spinel and corundum structures. In general, the ν_{OH} bands depend on the nature, coordination state, and number of directly neighboring cations. For OH groups bonded to the same element, the ν_{OH} frequencies decrease in the order: terminal over a tetrahedral cation > terminal over an octahedral cation > bridging > triple bridging; the breadth of the OH stretching band increases in the order terminal < bridging \ll triple bridging [43b].

The FTIR spectra shown in Fig. 1 are in fairly good agreement with the predictions based on structural arguments; small variations arise due to the particular structure of some oxides. Thus, a total of five bands or even more [44] (instead of

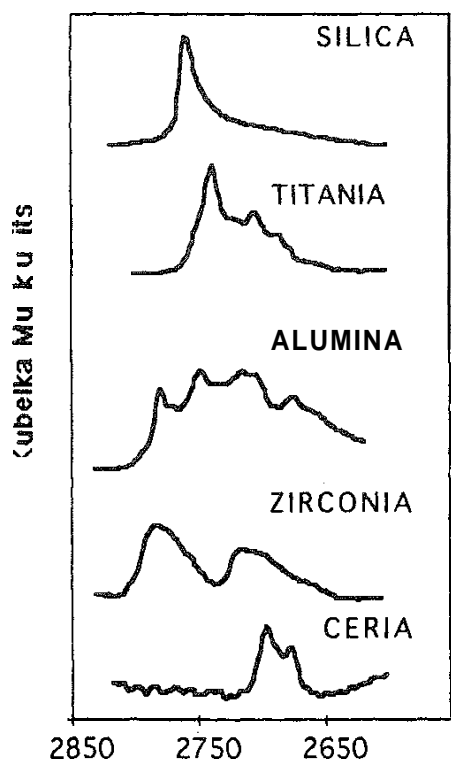


FIG. 1 Diffuse reflectance FTIR (DRIFT) spectra of the deuterioxy stretching vibrations for several oxides after partial surface dehydration at 500°C.

three) were regularly found on transitional aluminas; the larger number is the result of a distribution of Al^{3+} ions between octahedral and tetrahedral positions, which discriminates between $\text{O}-\text{H}$ vibrations. Also, ceria is likely to present only densely packed planes on its surface because of its CaF_2 type of lattice, and thus only two (instead of three) types of hydroxyl groups are revealed in IR spectra [39].

A dynamic, rather than static, picture of partially hydrated oxides is more appropriate, as confirmed by proton NMR [45] and dielectric spectroscopy studies [46]. The results of Pearson [45a] revealed two types of protons on partially dehydroxylated oxide surfaces: those associated with physisorbed water and those from chemisorbed water. About 85% of the total protons are present in the first two molecular layers. Subsequent ^{27}Al NMR studies [47] showed that a permanent proton exchange occurs between chemisorbed and physisorbed water.

In conclusion, partially dehydroxylated oxide surfaces exhibit a large inventory of surface OH groups and water molecules together with Lewis acidic and Lewis basic sites with coordinative unsaturation (structures II and III of Scheme 1). The hydroxyl population is the source of protons that cause enhanced surface electrical conductivity and catalytic activity. It is significant that the increase in the conductivity value is paralleled by increases in either the amount of weakly bound protons or their mobility [48]. Almost all metal oxides are active in catalytic isomerization of alkenes, which is one of the least demanding reactions in terms of the requirements for the acid strength of active sites [34]. Studies on several oxide systems show that the activity is lost after extensive dehydration and is partially restored by

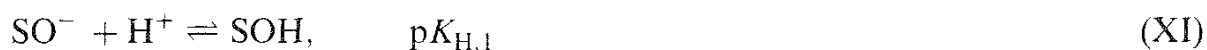
rehydration [49]. In all these examples the catalytically active sites were proton donors (Brönsted acids) of the oxide surface.

4. Fully Hydrated Surfaces

Complete hydration of oxides represented by structures II and III of Scheme 1 results in new surface structures (IV, V. and VI) at the oxide/solution interface. The interfacial phenomena at the solid/solution boundary include electrostatic adsorption, ion exchange, and ligand binding of species from solution. However, in most instances the species that count as charge-determining (in aqueous media) are always H^+ and O^- ions. As the concentration of these ions is pH-dependent in solution, the predominance of one or another of the surface structures IV, V, and VI is also pH-dependent.

From the liquid side of the solid/solution interface, the above phenomena are best approached by the electrostatic or ligand chemistry description or by a combination of both. However, from the solid side of the interface, the charge development depends on proton binding or release processes that occur at the outermost oxygen layer of the oxide lattice. On the solid side of the interface all proton transfer processes are localized. They can be regarded as acid–base interactions between the oxygen ions at the oxide boundary and one or two interface-structured layer(s) of hydrogen-bonded water molecules in the liquid phase.

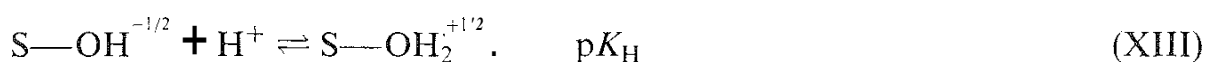
Which site-binding model is best suited to describe the adsorption of H^+ and O^- ions to specific sites at the oxide/water interface is still a matter of controversy. In the classical approach [50] the surface is assumed to be monofunctional and all surface oxygen ions are considered equivalent. Since most inorganic oxides show amphoteric acid–base properties, it was postulated that the charge buildup mechanism may be represented by the following two-step protonation process (“two- pK model”):



The two proton-binding constants are interrelated through an experimentally measurable quantity, the pH where the positive and negative charges compensate or the pH of zero charge (PZC):

$$PZC = \frac{pK_{H,1} + pK_{H,2}}{2} \quad (3)$$

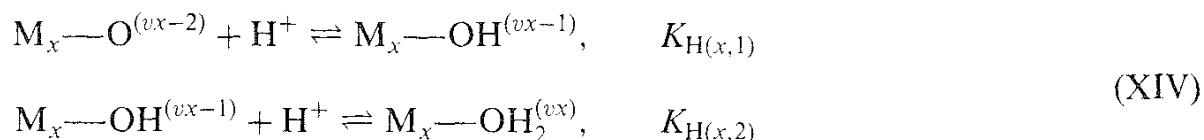
An alternative representation is the “one- pK model” proposed by Bolt and van Riemsdijk [51]. In this model only one protonation step and only one pK_H value are needed to describe the amphoteric character of surface oxygen groups:



It can be shown that the two- pK model reduces to the one- pK model if $\Delta pK = \log K_{H,1} - \log K_{H,2} \leq 2$ and the unique K_H value obtained corresponds to an experimental quantity, the point of zero charge: $PZC = \log K_H$.

The above approaches represent, of course, two idealized models. It has been recognized for a long time that the surfaces of real metal oxides and hydroxides

are nonuniform, i.e., several types of oxo and hydroxo groups are present. It has been assumed, as in the case of partially dehydroxylated surfaces, that the surface chemistry of the oxide/solution interface can be derived from the structure of solids using Pauling's concept of bond valence. Recently, Hiemstra et al. [52] and others [53] suggested an integrated approach based on the following protonation scheme:



This representation takes the form of a multisite complexation model (MUSIC). It is assumed that surface oxygens on different surface planes may bind to one or two protons, in separate equilibria, according to their $K_{\text{H}(x,1)}$ and $K_{\text{H}(x,2)}$ values (for oxo and hydroxo groups, respectively). In the above equations the bond valence v depends on the coordination number x of surface oxygens with metal cations, the formal charge per site may be any fractional number, positive or negative. The variability of surface groups, that may serve as sites for proton bonding is twofold: First, on different surface planes exposed to the solution, surface oxygens are in different coordination environments with respect to metal cations. Second, for each type of surface oxygen (terminal or type I, bridging or type II, triple bridging or type III) there are in principle two possible proton-binding equilibria, as shown by reactions (XIV), above. The MUSIC model incorporates, therefore, the "one-pK" and "two-pK" models as particular cases. In practice, however, it is possible that only one of the two reactions is "active" in the pH range of interest (about pH 3–11) for most applications. Thus, in practical terms, a "one pK, multisite" approach, as introduced by Contescu et al. [54], seems more appropriate for a description of proton-binding equilibria and of corresponding thermodynamic properties [55] at the oxide solution interface. In Scheme 1, the equilibrium between structures IV and V (deprotonation of monodentate water-bound complexes) occurs at a lower pH than the equilibrium between structures V and VI (deprotonation of bridging hydroxyl groups); proton dissociation of terminal hydroxyls of structures VI is possible at even a higher pH.

Originally, the MUSIC model assumed an even distribution of charge between metal cations and oxygens. A method was suggested for an a priori calculation of the intrinsic proton-binding constants of surface oxygens [52a] based on an estimate of the local electrostatic contributions to the standard Gibbs energy of proton adsorption. The method was calibrated with known values of equilibrium constants for protonation of oxo and hydroxo complexes in solution. In a later development [52c] the calculation of the undersaturation of oxygen valence at the surface was improved. Taking into account the structural details around surface oxygen ions resulted in asymmetrical charge distributions in the coordination environment. Following a suggestion by Bleam [56], the redefined MUSIC model emphasizes the role of hydrogen bonds (both donating and accepting) with neighboring water molecules at the interface. The model is able to predict the proton affinity constants for individual surface groups and can estimate correctly the PZC values of several metal oxides and hydroxides.

An important point of the original MUSIC model and its subsequent refinements [52] is that proton-binding constants at the solid oxide/solution interface are no longer regarded as free fitting parameters but as interface constants subjected to the constraints of physical and chemical reality, such as the distribution of oxygen ions on various crystallographic planes and the polarizing power of metal cations [57]. Even though the model may not be totally quantitative, the tabulated values of proton affinity constants [52a,53] have their own merit as reference values.

When experimental methods to measure proton affinity distribution spectra (PADs) from potentiometric titration data became available [54a], it was found by Contescu et al. [58] that the apparent values of proton binding constants identified from PADs were in semiquantitative agreement with log K values for H⁺ binding predicted by the MUSIC model (Table 1). The characteristic PADs for several oxides are shown in Fig. 2.

TABLE 1 Acidity Constants (pK_a) for Hydroxyl Groups with Different Coordination on Fully Hydrated Surfaces of Various Oxides

| Oxide | pK calculated from MUSIC model | pK from PAD measurements | Other pK estimates |
|--------------------------------|--|---|--|
| Al ₂ O ₃ | < 3 [54a] 4.5 [54a] 6.7 [54a] 10 [156]; 9.9 [57c] 12.3 [156] | < 3 [54a] 4.5 [54a] 6.7 [54a] 9.5–9.8 [54a] | |
| TiO ₂ (rutile) | 4.4 [52c] 5.3 [156]; 5.8 [52c] 6.3 [156]; 6.1 [15b] 7.5 [52c] | 5.6 [58b] 6.9 [58b] 9.2 [58b] | |
| TiO ₂ (anatase) | 4.7 [52c] 5.6 [52c] 6.3 [52c] 7.2 [52c] | 4.4 [58b] 5.4 [58b] 6.9 [58b] 8.7 [58b] 9.7 [58b] | 5.4 (CC) [159] 7.7 (CC) [157] 9.5 (CC) [159] |
| SiO ₂ | 7.5 [156]; 7.9 [52c] | 8.0 [140a] | 7.2 (S) [158] |
| ZrO ₂ | 4.2 [140a] 6.1 [140a] 9.2 [140a] | 4.5 [140a] 5.4 [140a] 6.7 [140a] 9.6 [140a] | 6.7–7.8 (DL) [155] |
| CeO ₂ | 5.5 [162] 10.4 [162] | 4.0 [160] 5.8 [160] 10.2 [160] | 3.1–3.3 (DL) [161] 6.0–6.3 (DL) [161] 11.1–11.2 (DL) [161] |

Data predicted theoretically by the MUSIC model and measured experimentally by PAD and other techniques.

DL = double-layer model; CC = constant capacitance model; S = spectroscopic methods.

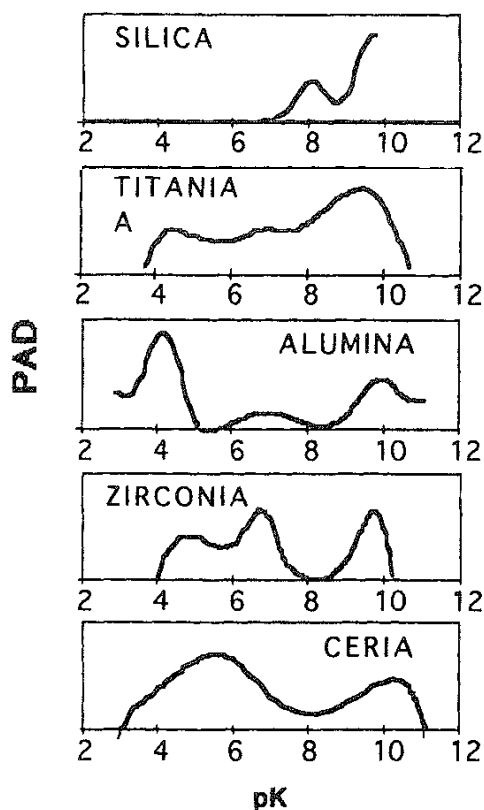


FIG. 2 Proton affinity distributions (PADs) measured for several oxides in 0.1 N NaNO_3 .

5. Factors that Determine Surface Acidity

What are the factors that determine the acid–base properties of solid surfaces such as metal oxides? On the basis of the discussion thus far it seems appropriate to relate the appearance of Lewis acidity and disappearance of Bronsted acidity to the increase in the degree of dehydroxylation. Indeed, the interconversion of Lewis and Bronsted acid sites has been demonstrated for some oxides, such as ZnO or supported MoO_3 , Cr_2O_3 , or WO_3 , by IR studies of pyridine or ammonia adsorption [59]. But which factors determine the strength of acid sites?

The chemical factor, i.e., the chemical nature of metal cations, must be considered first. The nature of metal cations, their electronegativity and oxidation state, determines the ionicity and geometry of the crystalline lattice.

Fully dehydroxylated covalent surfaces have a homopolar character, with no sensible charge separation. Adsorption on covalent solids is mainly physical; covalent surfaces tend to be hydrophobic, and extensive hydroxylation requires high temperatures. Hydroxyl groups present on partially dehydroxylated surfaces show very weak acidic character. They act as hydrogen bond donors with most bases and can protonate only very strong bases. A typical example is silica [35].

The acid–base properties of solid oxide surfaces with ionic character are controlled mostly by electrostatic factors. The stronger the ionic character, the stronger is the electric field pointing outward from the surface. The electric field of the surface may enhance (or diminish) the local electron donor (or acceptor) properties

of surface ions and thus modify their Lewis acid–base properties; inductive effects akin to those known for small molecules were proposed [14]. Various factors, such as electronegativity [60], effective charge on oxygen [61], and the polarizing power of metal ions [62] have been correlated with the acid–base properties of ionic oxides.

In stable oxide structures, the principle of electroneutrality requires that the charge of the cation be neutralized by the charge of surrounding oxygens. The distribution of charge over the surrounding ligands can be expressed per bond, leading to the concept of bond valence. Introduced by Pauling, the bond valence is defined as the charge of the cation divided by its coordination number:

$$v = z/\text{CN} \quad (4)$$

Pauling's bond valence rule has been used in various attempts to correlate acidic properties of surface hydroxyls with their formal charge, as expressed by the above relationship [41,52a,63]. For example, the assignment of stretching vibrations of surface hydroxyls ν_{OH} already mentioned [41] is based on calculations of the formal charge on surface hydroxyls using Pauling's rule. Based on the possible relationship between acidity and the stretching frequencies of hydroxyls in similar structures [64], the above reference to Pauling's rule illustrates, in fact, a relationship between structure and properties (acidity) for surface hydroxyls on partially dehydrated oxides. Pauling's valence bond rule served as a basis for the MUSIC model of proton binding to surface hydroxyls on fully hydrated oxides. The results of these semiempirical approaches are in remarkable agreement with exact quantum-mechanical calculations based on local Hartree–Fock models [38] and with many experimental trends.

A comparison of Figs. 1 and 2 shows that FTIR spectra of isolated hydroxyls on oxides have their counterpart in PADs of the fully hydroxylated surfaces. The parallelism is seen with respect to both the number and strength of hydroxyl groups present on the surface. A plot of stretching frequencies of O—D groups (from Fig. 1) versus the $\text{p}K$ values revealed by PADs of several oxides (Fig. 2) is shown in Fig. 3. Despite some scatter of the data, a linear trend is evident. At this stage one can only speculate that the slope of the straight line(s) describes the intensity of the electrostatic field(s) at the oxide surface. It apparently depends on the sample's chemical nature (possibly, through the cation's electronegativity or charge-to-radius ratio) and/or its surface structure (anion packing, preferential development of crystal planes, surface imperfections). In any case, the correlation shown in Fig. 3 is similar to a relationship found for zeolites in which the increase in Bronsted acidity correlates with decreasing O—H bond strength and can be monitored through the corresponding decrease in the stretching frequency in FTIR spectra [35].

Besides chemical factors, the role of physical factors in determining the acid–base properties of solid oxides should also be considered. Thus, the symmetry type of the crystalline lattice, the local geometry of surface ions, and the energetic stability (and relative occurrence) of densely packed planes depend on the ratio of the ionic radii of the cation and the O^{2-} ion. If polymorphic structures are likely, they may have different acidities depending on the packing density of surface O^{2-}

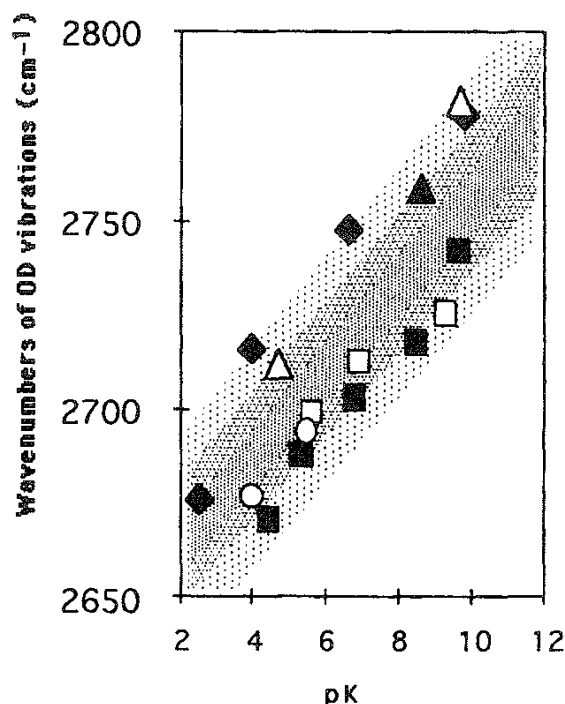


FIG. 3 The relationship between stretching frequencies of isolated deuterioxylys on partially dehydrated surfaces and the acidity constants determined by PAD at the oxide/solution interface for several oxides. (◆) Alumina; (▲) silica; (□) rutile; (■) anatase; (○) ceria; (△) zirconia.

ions, the degree of exposure of surface cations, and their preference for defect sites. For example, in η - Al_2O_3 the oxygen lattice is more loosely packed, the frequency of stacking faults is greater, and the fraction of cations in tetrahedral positions is slightly smaller than in γ - Al_2O_3 , although the local ionic configuration of Al^{3+} cations is the same in both modifications. Due to these structural differences, the acidity, surface reactivity, and catalytic activity of η - Al_2O_3 are significantly higher than those of γ - Al_2O_3 [41].

Surface imperfections of crystallographic structure may occur in small metal oxide crystallites. Metal or oxygen vacancies are typical imperfections that cause a local charge imbalance. Therefore, the acid properties may be strongly affected by the crystalline size, in parallel with (and perhaps as a consequence of) variation of electronic properties. For anatase particles with sizes in the range of 75–100 Å, the formation of new acid sites was observed with higher strength on smaller particles [65].

C. Surfaces with Variable Composition: Composite Oxides

1. Mixed Oxides

The acidity of materials can be controlled by mixing oxides with different properties and in various ratios. If phase separation does not occur, substitution of cations of the minor component oxide in the host oxide lattice results in bulk phases of true mixed oxides. Another method used to modify the acid–base properties of oxide

surfaces is surface deposition of "impurity" ions with limited substitutional incorporation. In the practice of catalyst preparation it is frequently found that the surface acidity (or basicity) of catalysts can be tuned by surface modifiers selected from the group of alkali or alkaline earth metals (to neutralize acidity) or from anions of oxyacids or electronegative elements (to promote acidity).

A number of models have been proposed for prediction of the generation of new acid sites in dilute oxide solid solutions. From the earliest models [66] it was understood that acid centers in mixed oxide structures owe their existence to localized electric charges created through isoinorphous substitution. The model proposed by Tanabe and coworkers [67,68] to explain acid site formation is among the most frequently cited. This model attributes the generation of surface acidity to the charge imbalance that develops along the $M-O-M'$ heterolinkages (where M and M' are different cations) due to the differences in cation valence and coordination number at the site of lattice substitution of the minor component cation. The model is based on two postulates: (1) The coordination number of cations from the substituting metal oxide and the matrix oxide are maintained even when mixed; and (2) all the oxygens in the binary oxide maintain the coordination number of oxygen in the matrix oxide. Based on Pauling's valence rule, the formal charge of each ion is assumed to be evenly distributed over the coordinating bonds. If the excess charge at the cation site is negative or positive, a Bronsted acid site or a Lewis acid site may appear. The former case is illustrated by, e.g., Ti substituted in a matrix of SiO_2 ; the latter by Si substituted in a matrix of TiO_2 . If there is no excess charge at the site of the substituting ion then no new acid sites are created, such as in the $Al_2O_3-Bi_2O_3$ system.

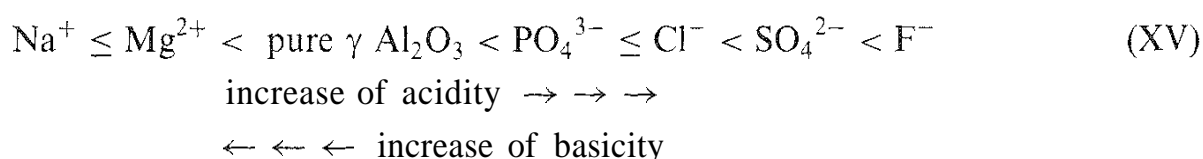
A different approach was taken by Kung [34,69]. This author proposed a model that accounts for variations in the electrostatic potential experienced by the guest cation from all ions in the oxide matrix. Although based on different assumptions, in most cases Kung's model gives the same prediction as Tanabe's model. However, an important difference exists between the two models: Tanabe's model is a localized model, whereas the model by Kung is delocalized. In other words, in Tanabe's model the site of acidity is fixed at the substituted cation, whereas in Kung's model the newly created acid sites may be located at any position with respect to the substitution site. Arguments supporting the localized model came recently from the works of Miller and Ko [70] on mixed oxide aerogels. Using preparation techniques of sol-gel chemistry that afford better control of molecular scale mixing, they demonstrated that well-mixed two-component oxides (zirconia-silica, titania-silica) display higher total site densities, larger Bronsted populations, and enhanced activity as acidic catalysts than less homogeneously mixed samples of the same composition. These observations were explained in terms of the much higher number of $M-O-M'$ linkages accessible in each well-mixed oxide pair.

2. Chemically Modified Oxides

A more efficient method for adjusting the surface acidity of solids is chemical modification of the outermost atomic layers. Connell and Dumesic [71] showed that acid centers (both Lewis and Bronsted) could be generated by doping small amounts (less than 1%) of a second metal cation on the surface of several oxides with various acid-base character, ranging from the very basic (MgO) to acidic

(Al₂O₃) or inert (SiO₂ and TiO₂). In these systems the "impurity" ions were not uniformly substituted in the bulk matrix oxide lattice but incorporated in defect cation positions at the surface of the host oxide. The model used by Connell and Dumesic to explain generation of acidity on chemically modified surfaces differs from Tanabe's or Kung's models for homogeneous solid oxide solutions. The important factors in their case are the electronegativity and coordination environment of dopant metal cations on the host oxide surface. The Connell–Dumesic model assumes that the formal charge on the deposited cation is balanced by coordinating oxygen ions from the surface lattice and that a deposited cation is coordinately unsaturated if its coordination number differs from that of cations in the host oxide. Thus, the origin of both Lewis sites and Brönsted sites was explained: The former are localized at coordinately unsaturated dopant cations; the latter are generated by substitution of a +3 cation in the tetrahedral environment of an SiO₂ matrix.

Scokart and Rouxhet [72] studied the influence of electropositive and electronegative dopants on various oxide adsorbents. They used Pauling's valence rule to evaluate the net charge of nonprotonic acid sites and found agreement with the strength of Lewis sites as measured by pyridine adsorption. For example, electronegative elements (such as fluorine [72–74]) enhance the acidity (both Bronsted and Lewis) of alumina; electropositive elements (such as sodium [75] or magnesium [72]) partially neutralize alumina acidity. A scale of the effects of various modifying ions on acid–base properties of alumina was summarized as follows by Delmon and coworkers [76]:



The discovery of strong nonzeolitic catalysts obtained by chemical modification was a breakthrough for the development of new solid acid catalysts. It was found that metal oxides, especially ZrO₂, TiO₂, Fe₂O₃, and zirconia-containing mixed oxides modified with sulfate ions show unusually strong acidity. Sulfate may be introduced either from a dilute solution of sulfuric acid or by impregnation with ammonium sulfate. The strong "catalytic" acidity of these materials is evident in their ability to activate paraffins at lower reaction temperatures than conventional acid catalysts. Several authors [77] denoted this property as "superacidity" and defined superacids as materials with an acid strength stronger than that of 100% sulfuric acid.

The mechanism for the generation of catalytically active centers in "superacidic" catalysts is not fully understood. In many cases the properties of the catalysts are strongly influenced by the preparation conditions. No agreement has been reached about the structure, strength, or nature of the acidic sites. Bronsted acidity is commonly observed on sulfated zirconia, although strong Lewis acidity has also been implicated in the high reactivity of these materials [78]. While nonsulfated zirconia exhibits two types of isolated OH groups, modification with sulfuric acid eliminates the terminal (most basic) OH group, enhances the acidity of the bridging

OH group, and introduces new, more acidic, Bronsted sites [79] in which the OH group is probably linked to sulfur and the proton is bridged to a neighboring oxide ion on the ZrO_2 support. It was also found that sulfur-containing species are bound through two or more $\text{S} - \text{O} - \text{Zr}$ bridges and carry $\text{S}=\text{O}$ or $\text{S} - \text{O}$ bonds.

It is important to emphasize that spectroscopic evidence shows that water transforms the Lewis acid sites of sulfated zirconia into Bronsted acid sites [80]. At the same time, water promotes isomerization reactions over sulfated zirconia for a moderate extent of catalyst dehydration. Similarities were reported between the effect of rehydration on the isomerization activity of sulfated zirconia [81] and on that of other oxide catalysts [49] that are consistent with the role of surface H^+ donor sites in hydrocarbon isomerization reactions. However, when spectroscopic methods using basic probes were used to compare sulfated zirconia and zeolites in terms of the strength of their acid sites, the results were inconsistent with all catalytic data. These findings illustrate the danger of comparing the acidity of catalyst systems that differ in structure and composition, such as zeolites and sulfated zirconia; in these systems the "catalytic" and the "physicochemical" scales for the strength of acid-base interaction may contain significantly different parameters.

3. Bidimensional Oxide Overlayers

Studies of bidimensional oxide overlayers has attracted increased interest in recent years as these overlayers are intermediates in the preparation of some of the most widely used industrial catalysts: hydrotreating catalysts [82].

Bidimensional overlayers may be formed by deposition of one metal oxide (CrO_3 , MoO_3 , WO_3 , Re_2O_7 , V_2O_5) on a second, high surface area oxide (Al_2O_3 , SiO_2 , TiO_2). A peculiarity of the oxides that may form bidimensional overlayers is their tendency to aggregate as polyoxoanions in acidic media and to disperse as monomeric oxoanions in basic media. Due to this fact, the factor that decisively determines the stability of bidimensional structures for various systems investigated so far is the match of acid-base properties between the dispersed and host oxide. Using Raman spectroscopy, Wachs and coworkers [83] showed that the bidimensional structures stable under ambient conditions correspond to the chemical species stable at the PZC of the composite oxide: Supports with basic character favor molecular species that are stable in basic solutions and vice versa.

Because supported oxide species follow the same chemistry as they do in aqueous solution as a function of pH, the structure of the overlayer is controlled by the PZC of the composite oxide in contact with the ambient; under these conditions the apparent PZC and the structural conformation of the overlayer oxide depend on the surface coverage [84]. For example, a strong increase in the proton acidity of alumina was found on addition of small amounts (maximum 5%) of MoO_3 , WO_3 , and CrO_3 [74,85]. Moreover, when exposed to aqueous solutions of variable pH, the structure of the overlayer changed with the solution's pH. Based on this property, Adachi et al. [86] showed that the number of protons released during potentiometric titration of $\text{MoO}_3\text{-Al}_2\text{O}_3$ correlated with the catalytic activity of sulfided catalysts in a typical hydrodesulfurization reaction.

D. Layered Materials: Clays

Clay minerals are hydrous layered aluminosilicates. The aluminosilicate layer is composed of two types of sheets: octahedral (O) and tetrahedral (T). Each sheet is composed of parallel planes of atoms, either oxygen or aluminum (silicon) in an alternating sequence. The large variability in the properties of clay minerals is related to the stacking sequence of the two basic types of sheets, T and O, and to the uncompensated charge that develops by isomorphous substitution of unevenly charged cations.

The hydration properties of clay minerals can be understood from the perspective of various types of acid–base interactions that may occur between several structurally defined sites in the clay matrix and surrounding water molecules. To facilitate discussion, a short description of clay structure is needed.

The tetrahedral sheet consists of a hexagonal network of corner-sharing SiO_4 tetrahedra with all their bases in the same plane. In this plane the oxygen atoms form an open hexagonal network, which is referred to as the hexagonal or "perforated" plane. Each oxygen of this plane is covalently bound to two silicon atoms. Substitution of Al for Si contributes a negative charge to the tetrahedral sheet, and the newly formed Al—O—Si groups are more basic than the original Si—O—Si (siloxane) groups were. However, the electron-donating strength of the siloxane oxygen depends on the existence of nonbonding electron pairs. Because of their asymmetric charge distribution, only nonbonding hybridized orbitals may serve as electron-pair donors. Consequently, structures with sp^3 hybridization on oxygen are expected to show greater hydrophilicity (because of the larger electron density in nonbonding hybridized orbitals) than structures with oxygen in sp^2 hybridization, whereas sp hybridization leads to hydrophobicity. Measuring the Si—O—Si angle in minerals provides a good estimate of the oxygen hybridization state. In good agreement with the above structural considerations, it was found that hydrophilicity of siloxane groups increases with decreasing Si—O—Si angle. In most silicates the Si—O—Si angle has values of $139\text{--}140^\circ$ indicative of an intermediate character between sp^2 and sp hybridization, for which the characteristic angles are 120° and 180° .

The octahedral sheet consists of a densely packed hexagonal plane of Al^{3+} ions (which in brucite is substituted by Mg^{2+}) sandwiched between two densely packed hexagonal planes of hydroxyls. The latter are called the hydroxyl planes and make an important contributions to the surface properties of minerals. The oxygen atoms in the hydroxyl layer have all their orbitals in the valence shell occupied and consequently cannot act as hydrogen bond acceptors with water molecules. Therefore, the hydrophilicity of the hydroxyl plane is solely determined by the interaction between protons of the hydroxyl layer and lone-pair electrons of adsorbed water. Thus the hydroxyl group must be acidic. Although the acid strength of M—OH groups increases from Mg—OH to Al—OH , it is believed that the proton-donating ability of the hydroxyl layer is not great enough to allow for the formation of hydrogen bonds with water molecules. In most minerals the hydroxyl layer is therefore a hydrophobic plane, although cationic substitution may change the hydration properties. Thus, substitution of Al for Mg increases the acid strength of M—OH groups and the hydrophilicity of the hydroxyl plane.

E. Porous Materials: Zeolites and Zeotypes

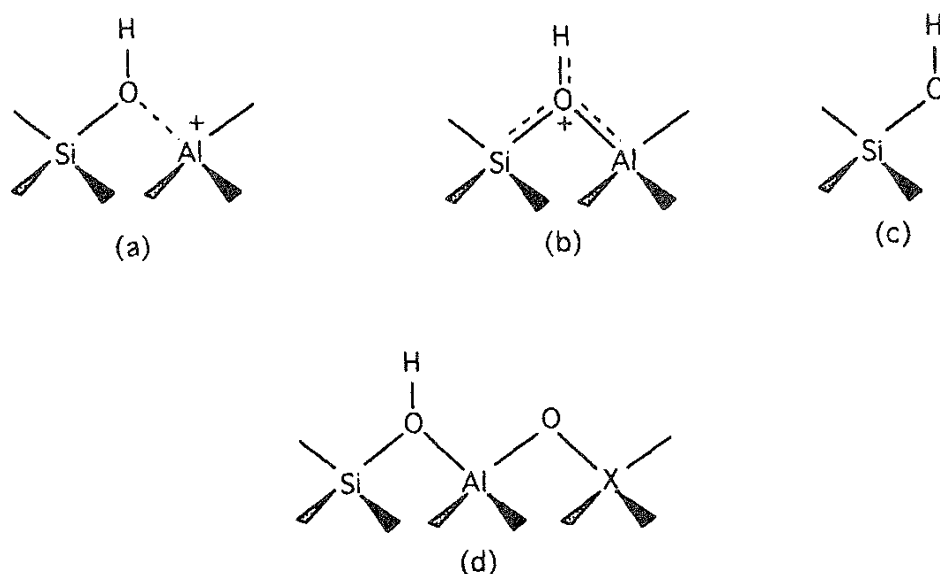
Natural aluminosilicates, such as clays, were the first solid acid catalysis commercially used on a large scale. They were the first cracking catalysts in the Houdry process and were prepared by acid leaching natural clays. The negative impact of impurities in natural clays stimulated research for new solid acid catalysts, and thus amorphous-like synthetic aluminosilicates were first prepared [87]. The natural evolution led to the synthesis of crystalline aluminosilicates (zeolites), aluminophosphates (ALPOs), and silica-alumina phosphates (SAPOs). Zeolites are crystalline aluminosilicates built from SiO_4 and tetrahedral AlO_4^- units. There is a virtually unlimited number of ways of linking tetrahedra, which give rise to zeolite crystals with pores, cavities, and channels with a wide variety of shapes and sizes. Today, crystalline zeolites and zeolite-type materials (zeotypes) are the most common acid catalysts used in the chemical industry. In addition to the strong acidic character of their amorphous predecessors, these materials have the benefits of high surface area and controlled pore sizes in the range of molecular dimensions.

The acidity of silica-aluminas is easily explained by Tanabe's model. Substitution of a Si atom by tetrahedral Al atom in a silica-rich host lattice generates AlO_4^- units with a localized negative charge that may be balanced by a cation or a proton. There exists an extensive body of literature on quantum-mechanical calculations of acidity from the proton affinity of small clusters [88] that confirmed this picture [89]; it was concluded that the $\text{O} \cdots \text{H}$ bond weakens and the proton is more easily ionized if the hydroxyl is located in bridging positions between Al and Si atoms. A general discussion on the acidity concept in zeolites can be found in Refs, 21 and 90.

In structure (a) of Scheme 2 the coordination of the O atom in the bridge position to tetrahedral Al corresponds to a Lewis acid–base interaction; the stronger the interaction, the stronger the Bronsted acid strength of the proton associated with the bridging oxygen. The model for Bronsted acidity in zeolites [91] shown as structure (a) of Scheme 2 has since been improved by assuming that the bridging oxygen atom is chemically bound to both Al and Si, making a real bridge between them [structure (b) in Scheme 2] [92]. Coordination of the bridging oxygen to both Al and Si causes an increase in the length of the $\text{O} \cdots \text{H}$ bond and therefore enhances the acidity of structure (b) with respect to the terminal silanols depicted in Scheme 2, structure (c). Silanol groups (terminal hydroxyls) are only very weakly acidic or nonacidic.

On the other hand, the increase in electronegativity in the neighborhood of the OH induces a transfer of electron density from H to O with a corresponding increase in acidity. Thus, in silica-alumina phosphate materials (SAPO) the substitution of Si^{4+} by P^{5+} creates a center of enhanced acidity as shown by structure (d) of Scheme 2, where $\text{X} = \text{P}$ [93].

The chemical composition of the framework has a definite impact on the acid strength of zeolites and zeotypes. The total number of Bronsted acid sites present in a zeolite depends on the framework Si/Al ratio or in general on the $\text{M}^{4+}/\text{M}^{3+}$ cations. The variation of stretching frequency of bridging hydroxyls [94] and results from H NMR spectra [95] suggest that the strength of Bronsted sites in HY zeolites increases with decreasing Si/Al ratio. This has been rationalized with the concept of



SCHEME 2 Structures proposed for the Bronsted acid sites in zeolites and substituted zeolites.

electronegativity: Any change in the composition of a zeolite would modify the electronegativity of the framework, and the higher the electronegativity, the greater the acid strength. A correlation was found between Sanderson's average electronegativity and the acid strength of zeolites [96] and zeotypes [97].

Geometrical effects, in addition to framework electronegativity, have a considerable influence on zeolite acidity. It was argued that the long-range order imposed by the crystalline structure is the reason the acid strength of crystalline zeolites is higher than that of their amorphous silica-alumina counterparts. The geometry of the crystalline lattice and the associated long-range interactions have a clear effect on the acidity of bridging hydroxyl groups in $\text{Al}-\text{OH}-\text{Si}$ linkages. Molecular orbital calculations [98] show that the deprotonation energy decreases (the acidity increases) with increase of the $\text{T}-\text{O}-\text{T}$ angle. Acidic zeolites have a range of $\text{T}-\text{O}-\text{T}$ angles larger than other, less acidic zeolites (cf. $137-177^\circ$ for ZSM-5, $143-180^\circ$ for mordenite, but only $138-147^\circ$ for HY) [90f]. By similar arguments, structure (a) of Scheme 2 could be more representative for amorphous silica-alumina, while structure (b) would be more appropriate for the acid site in a crystalline zeolite with long-range symmetry stabilization [90f].

Besides long-range effects, the local structure of cage or channel walls may cause preferential location of some particular oxygens. For example, in the faujasite structure of zeolite Y there are four different positions for covalent proton bonding on oxygen next to aluminum atoms; they correspond to two different stretching frequencies in infrared spectra, which indicates the occurrence of two groups with different acid strengths [90g].

The acid-base properties of zeolites are further complicated by the confinement of host molecules in narrow micropores. Several components of the interaction energy between (basic) host molecules and the walls or acidic sites of zeolite cages may be strongly enhanced in micropores with molecular dimensions.

Among them the most important are the attractive and repulsive contributions from van der Waals, dipole–dipole, and quadrupole–quadrupole interactions. Derouanne [99] suggested that sorbate molecules confined in zeolite micropores tend to organize themselves by optimizing their van der Waals interaction with the surroundings. In accordance with this rationale the guest molecules confined in micropores of sizes close to the molecular dimension of the guest should be regarded as "solvated" by the zeolite framework. The strong electric fields at the internal surface of molecule-sized spaces must strongly affect the properties of "solute" molecules, including the electronic energy levels of the guest molecule. The theory [100] predicts that confined guest molecules would show increased basicities with respect to their intrinsic basicity in the gas phase. However, this argument may equally be used to explain the unusually high acidity of zeolites [90f].

Lewis acidity may also be present on zeolites, but its precise nature remains an open question. Initially it was thought that Lewis acidity is generated by extensive dehydroxylation and corresponds to threefold coordinated Al ions on the surface. However, it is now established [35,101] that dehydroxylation is almost always accompanied by formation of extraframework aluminum species, $\text{Al}(\text{OH})_x$, that are non-acidic in the Brønsted sense and can be further dehydroxylated to form Lewis acid sites similar to those present in active aluminas [102]. The number of Lewis acid sites is a fraction (between 0.4 and 0.7, depending on dehydration temperature) of the total content of nonframework aluminum [103]. In cation-exchanged zeolites, another source of Lewis acidity is furnished by the exchanged cation; cations are electron acceptors and are able to act as Lewis acids in the broader sense. It was observed that the strength of Lewis acid sites in Na exchanged zeolites was dependent on crystallinity, whereas the strength of Lewis basic sites was less so; the collapse of the zeolite crystal caused a decrease in the numbers of both Lewis acids and Lewis bases [104].

F. Microporous Materials: Activated Carbons

Activated carbons consist of small graphene-like layers that are spatially distributed without regular organization and are separated by micropores, most of which are slit-shaped. The most reactive sites for the attack of molecular oxygen are the edges of the graphene layers and defect sites. Upon oxygen attack, and depending on reaction conditions, two types of carbon surface oxides are formed. Because of their practical importance, surface oxides of carbons have been the subject of many studies [105].

Basic carbon oxides are formed upon the exposure to oxygen of a clean carbon surface obtained by outgassing to 900–1000°C followed by cooling to room temperature. Aqueous suspensions of these carbons have a strongly basic pH, reducing properties toward noble metals, and anion-exchange properties. Acidic carbon oxides are formed when the carbon is oxidized at lower temperatures (300–400°C); the presence of water vapor during the oxidation process increases the amount of acids formed. When dispersed in water, these carbons have acidic pH and cation-exchange properties. Acidic surface oxides can also be formed by oxidation at room temperature with aqueous solutions of nitric acid, permanganate, hypochlorite, or hydrogen peroxide.

The reactivity of carbon surfaces is strongly influenced by their acid–base characteristics. The broad spectrum of applications for activated carbons arises from their wide range of chemical properties, which can be systematically controlled. Adsorbed oxygen makes the surface of carbon hydrophilic and aids dispersion in water [106]. Adhesion between carbon fibers and the polymer in carbon-fiber composites is vastly improved by the presence of carbon surface oxides [107]. Surface acidic groups may act as anchoring sites for metal particles of carbon-supported catalysts, limiting their growth, but they may also produce strong metal-support interactions and modifications of the electronic nature of supported metal particles [108].

The chemical nature of acidic and basic oxides on carbons has been widely investigated. The structure of basic oxides was first ascribed to cromene-like structures [109] and later to pyrone-type groups [110]. Other workers [17,111] assumed that carbon basicity of the Lewis type can be associated with the high concentration of π electrons on basal graphene layers where π bonding of water molecules may occur in oxygen-free media:



The acidic surface oxides obey a more complex chemistry [17,105,112]. A large variety of surface structures may occur. The most acidic are carboxyl groups, which may either be free or be condensed with neighboring hydroxyl groups to form lactones or with neighboring carbonyl groups to form lactols. At the other extreme are phenol-type hydroxyls, which are weakly acidic groups. All these groups have been identified by chemical reactions [112b].

In contrast with acidic groups of most other solids, the acidic groups of carbons as described above belong to well-established classes of chemical compounds described in any organic chemistry textbook. This fact permits their qualitative identification as well as their quantitative determination. Counting the number of acid sites on carbons poses fewer problems than with other solid acids, and a classical analytical method developed by Boehm [112a] is still in use today. The Boehm method uses the fact that carboxyl groups are strong enough to neutralize a very weak base like $NaHCO_3$ ($pK_{a(NaHCO_3)} = 6.37$). The less acidic lactols and lactones are neutralized by dilute Na_2CO_3 ($pK_{a(Na_2CO_3)} = 10.25$) but not by $NaHCO_3$, and the weakest acidic phenol groups are titrated only by $NaOH$ solutions ($pK_{a(NaOH)} = 15.74$). By titration with all Boehm titers in the presence of suitable indicators, it is therefore possible to quantitatively determine the content of acid functionalities with the acid strength (expressed as pK_a) in various acidity ranges.

Another method to access acidic groups on activated carbons is direct potentiometric titration, but it suffers from very slow exchange equilibria in solution [113] and the lack of definite endpoints. The latter fact reflects the spread of dissociation constants of most surface functionalities on carbons caused by interactions between neighboring groups and effects resulting from the limited size of the graphene sheets. Assuming a continuous, rather than discrete, distribution of pK_a values, Contescu et al. [114] showed that potentiometric titration data could be transformed to proton affinity distribution (PAD) curves and that the results were in

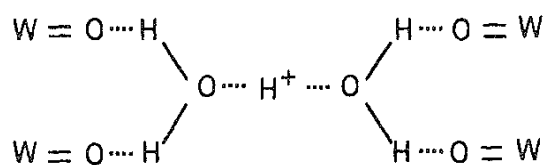
excellent agreement with the quantitative estimate of surface site concentrations obtained from the Boehm titration.

G. Pseudo-Liquid Materials: Heteropolyacids and Salts

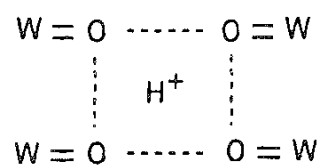
Heteropolyacids and their salts (heteropolymetalates) are formed by metal–oxygen octahedra as the main structural units linked by corner sharing and edge sharing. Of the wide variety of heteropoly compounds, those of the Keggin series are the most important as catalysts. The Keggin compounds, $\text{XM}_{12}\text{O}_{40}^{x-8}$, build around a central atom ($\text{X} = \text{Si}$ or P) with tetrahedral coordination by oxygen. The XO_4 unit is surrounded by MO_6 octahedra ($\text{M} = \text{W}, \text{Mo}, \text{V}, \text{Nb}, \text{Ta}$). They are arranged in four groups of three edge-shared octahedra, M_3O_{16} , which are linked by shared corners with the central tetrahedron. This is the primary structure of polyoxoanions that exists in solutions and in the solid state as well. In the solid state a secondary structure is formed by closepacking of the polyanions and is stabilized by counter-cations and water of hydration or, more precisely, protonated water dimers, $(\text{H}_2\text{O})_2\text{H}^+$. Several crystallographic arrangements may exist, depending on the degree of hydration and the nature and size of the counter-cations.

Heteropolyacids are strong Bronsted acids both in solution and in the solid state. Their strong acidity is related to the large size of the polyanion, which causes a low density of negative charge at its periphery and therefore weak interaction between adjacent polyanions and protons. The charge balance and hence the acidity are strongly affected by both the elements constituting the polyoxoanions and the nature of the counter-cations.

In the solid state, protons participate directly in the formation of the crystal structure [115]. The lattice is stabilized by H_5O_2^+ species hydrogen-bonded to oxygen atoms at the most exposed positions of four neighboring anions (structure XVII). Loss of water of crystallization gives rise to porosity (structure XVIII); thus solids with considerable surface area can be obtained by moderate heat treatments. The microporosity and the resulting surface area are largely controlled by the size of the counter-cations. The most effective are the bulky NH_4^+ , Rb^+ , and Cs^+ ions, for which surface areas of about $180 \text{ m}^2/\text{g}$ have been obtained. By controlled substitution of H^+ it is possible to produce solids with homogeneous and well-organized porosity [116].



(XVII)



(XVIII)

Solid-state heteropoly compounds have interesting catalytic properties [117] and have found applications in olefin and acetylene hydration and alcohol dehydration [90f]. Adsorption of nonpolar molecules (hydrocarbons) reaches saturation at amounts lower than monolayers ("surface-type" adsorption). However, it is characteristic of heteropoly compounds that adsorption of polar molecules (alcohols, ethers, amines) takes place in amounts that exceed by many times (10 – 10^2) mono-

layer surface capacity. This property of "bulk absorption" is clearly the result of acid–base interactions between the polar molecules and the solid heteropoly compound, since the amount absorbed depends on the polarity of sorbates and the nature of the counteranions.

The latter property is important for the catalytic activity of heteropoly compounds in acid-catalyzed reactions. With certain heteropoly salts and polar reactants, catalytic reactions such as alcohol dehydration occur in the bulk of the solid catalyst, not only on its surface. The solid behaves like a very concentrated acid solvation medium for the reactant, which allows these solid acids to be called pseudoliquids [118].

It has been clearly established that acid sites in heteropoly compounds are of the Bronsted type and that their strength, for dehydrated solids, is higher than that of concentrated sulfuric acid. The acidity increases with increasing cation electronegativity. For example, the partially exchanged $\text{Cs}_x\text{H}_{3-x}\text{PW}_{12}\text{O}_{40}$ is a superacid, and its performance depends on the degree of exchange, x [119].

IV. MEASURING ACID–BASE PROPERTIES OF SOLID SURFACES

A. Nature, Number, and Strength of Acid–Base Surface Sites

Because catalysis by solid acids and bases is central to a variety of industrial processes, relationships between solid acid–base behavior and catalytic properties have been explored [68,120]. However, many concepts, either qualitative or empirical, demand closer scrutiny.

A discussion of methods to quantify the surface acidity of solids, microporous or not, requires first the recognition of the fact that the term "acidity" is too vague. For catalytic applications, one should be able to identify the *nature*, either Bronsted or Lewis, of surface sites exposed by the surface of solids. On the other hand, even for the purpose of semiquantitative correlation with another property (such as catalytic activity), one should clearly distinguish the importance of measuring the *number* and assessing the *strength distribution* of acid sites. Both components cooperate to create the overall picture of "surface acidity," which is no more than a term used for a badly defined macroscopic property of solids. If improperly used, this term may generate misleading statements such as "catalyst A is more acidic than catalyst B." It would be more appropriate to compare, specifically, the *number* of acid sites in catalysts A and B, or their *acid strength*, assuming that it has been previously found that the *nature* of the acid sites is the same in both catalysts, either Bronsted or Lewis.

However, for several reasons it is difficult to compare the acidity of solids in definitive terms as demanded above. They are related to the experimental methods for characterizing surface acidity or to the theoretical definition of a common acidity scale.

B. Experimental Methods

A variety of methods have been suggested to characterize the acidity or basicity of solid surfaces in terms of the strength and number of surface sites they contain.

Some methods use the adsorption of acidic or basic probe molecules with the goals to (1) titrate the sites with opposite properties, (2) identify (and count, if possible) the sites with either Lewis or Bronsted character, and (3) determine the sites' strength in relation to a known property (i.e., the acid or base strength) of the probe molecules. A second group of methods uses standard catalytic reactions that are known to occur on surface sites of certain strength as a probe of acid–base characteristics.

These methods suffer from the lack of complementarity, and thus the significance of results provided by any of them is limited. A standard practice to detect the Bronsted or Lewis character of surface sites is pyridine adsorption combined with FTIR measurements; the number of Lewis or Bronsted sites is more difficult to count, however. Other titration methods use either color indicators and acid or base titrants in nonpolar solvents or the adsorption of gaseous acidic or basic probes. They do not, in general, give consistent quantitative information about the *number* of acid or base sites even when applied to the same sample. There are several reasons the applicability of titration methods is limited: Either the state of the surface is different for different methods or adsorption equilibrium is not always achieved. Another more serious source of discrepancies between titration methods is that probe molecules of different basicities "see" different surface sites. The lack of a uniquely defined thermodynamic scale of acid *strength* of surface sites makes difficult any correlation between results obtained with different probe molecules. The use of standard catalytic tests for probing the so-called catalytic acidity is not always a better approach, because the mechanistic assumptions involved are neither straightforward nor subject to experimental proof.

1. Identifying the Type of Acid Sites: Bronsted or Lewis?

There are several probe molecules for which infrared spectroscopy can differentiate between adsorption on Bronsted and Lewis acid sites and even estimate the amounts adsorbed. Pyridine is the most widely used because it gives well-resolved bands when protonated by Bronsted acid sites (e.g., 1540 and 1640 cm^{-1}) or when coordinated to Lewis acid sites (1450 and 1620 cm^{-1}). The values of extinction coefficients are available in the literature [121] for these bands, which makes possible semiquantitative measurements, separately, of Lewis and Bronsted sites. Ammonia, with a smaller kinetic diameter that enables it to reach more easily the acid sites in smaller pores, can also be used to distinguish between Bronsted and Lewis acid sites; however, the use of ammonia is less reliable, mainly because the resulting IR bands overlap each other [122]. Another base that can distinguish between Bronsted and Lewis acid sites is quinoline; because its size is greater than that of pyridine quinoline can also be used to differentiate between acid sites at the external surface and those in pores smaller than its kinetic diameter (6 Å). Bronsted sites can be selectively measured with IR methods by using substituted pyridines as probe molecules [123].

However, owing to their strong basicity, it is expected that most of these bases would adsorb nonspecifically, even on the weakest acid sites. Weaker bases are needed as probe molecules for IR spectroscopy, and studies have been reported in which CO, H₂S, acetone, benzene, olefins, acetonitrile, and even hydrogen have

been used [124]. Adsorption of CO at low temperatures is used extensively because infrared spectra can differentiate between CO molecules in interaction (by hydrogen bonding) with surface hydroxyls with Bronsted acid character and CO coordinated to unsaturated surface cations (Lewis sites) [125]. It appears that carbon monoxide is a highly specific probe molecule that enables the establishment of the order of relative acidities when different types of hydroxyls or coordinately unsaturated cations are present [90f].

NMR and MAS NMR methods can also be used to characterize the interaction of amines with acid sites, and the shift of ^{15}N or ^{31}P , rather than ^{13}C , is conveniently used to distinguish between Lewis and Bronsted sites.

2. Number and Strength of Acid–Base Sites

Counting the number (or measuring the concentration) of chemical species that may participate in acid–base reactions is a problem where traditional chemistry offers, in general, well-established solutions.

When the reaction medium is water (as it is in most analytical applications), the relative strengths of acids and bases can be compared by using a thermodynamically precise acidity scale, namely the $\text{p}K$ scale with water as a reference. In this case one can use titration methods. For example, an acid of known acid strength, $\text{p}K_{\text{A, titrant}}$, is added to the system and neutralizes all bases whose conjugate acids are weaker than the titrant, $\text{p}K_{\text{B}} > \text{p}K_{\text{A, titrant}}$. Similarly, when the titrant is a base of known strength, $\text{p}K_{\text{B, titrant}}$, all acids weaker than the titrant will be neutralized: $\text{p}K_{\text{A}} < \text{p}K_{\text{B, titrant}}$. The only experimental problem is recognition of the endpoint of titration; the amount of base (or acid) neutralized is then calculated from the amount of titrant consumed. Recall that all the $\text{p}K$ values just listed are acidity constants and the strength of bases $\text{p}K_{\text{B}}$ is compared using the strength of the corresponding conjugate acids, $\text{p}K_{\text{A}} = \text{p}K_{\text{water}} - \text{p}K_{\text{B}}$.

In aqueous solutions the principles of analytical chemistry established the protocol to use strong acids (or bases) as titrants; they "see" all bases (or acids) in the system, and the result of titration is a "total basicity" (or "acidity") number. If an additional method to measure the concentration of "free" acid at different titration points and under equilibrium conditions were available, then one could use aqueous titration methods to isolate bases (or acids) of different strengths that might be present in the system and evaluate their amount.

Extrapolation of the above principles to solid surfaces is not straightforward because of the strong interplay of the two fundamentally different notions: the strength and the number of acid–base sites. To accurately measure the number of acid sites of a solid acid, one should be able to define their "strength" and have available a "stronger" base to be used as a titrant. If the base titrant is not strong enough, some of the weakest acid sites will remain undetected. Titration in two-phase systems, and especially when one is a microporous solid, may be influenced by additional factors such as slow diffusion into the micropores and charge accumulation at the interface or at the pore mouth. In other words, even though a strong enough base was available, its access to the acidic sites on the internal surfaces might be hindered by geometrical constraints or its intrinsic basicity might be perturbed by intermolecular interactions in the confined space of the micropores.

3. Applications

The limitations of the experimental methods and potential methods to avoid misinterpretation of laboratory data are illustrated here with a few examples.

Benesi titration [126] is one of the oldest methods used for counting the acid sites of solid catalysts in different ranges of acid "strength." The use of quotation marks is necessary because the method is based on the convention that the pK_a scale in aqueous media can be extrapolated to very strong acid media by use of an appropriate series of color indicators. Thus, when a basic indicator (B) reacts with a surface Bronsted acid site (HA) to form a surface base (A) and the conjugated acid form of the indicator (HB^+), the acid strength is equated to the Hammett acidity function H_0 in the following way:

$$H_0 = pK_a + \log \frac{[B]}{[BH^+]} \quad (5)$$

Similarly, if interaction is with a Lewis acid site (A), the Hammett function is expressed as

$$H_0 = pK_a + \log \frac{[B]}{[AB]} \quad (6)$$

where [B] is the concentration of the unreacted base. The acid strength of surface sites is estimated by comparing the color of several indicators with different pK_a values adsorbed on the solid sample, while the number of sites in various $\Delta pK_a = pK_a^2 - pK_a^1$ ranges is estimated from the amount of base (in most cases, *n*-butylamine) needed to block the sites. The method suffers several limitations. The most serious is the fact that solid samples are titrated in nonaqueous media (e.g., benzene) but the pK_a values of indicators used for comparison are aqueous phase values, and the medium-transfer corrections for pK_a are ignored. Also, equilibrium may be achieved with difficulty [127], and the method does not distinguish between Bronsted and Lewis sites unless sterically hindered bases, which are selective for Bronsted sites, are used as titrants [128].

An alternative method proposed by Contescu et al. [54a] is aqueous titration combined with a suitable algorithm for deconvolution of the measured proton binding curve into a continuous spectrum of apparent pK_a values. Even neglecting corrections for charge accumulation at the solid/liquid interface, the content of the proton affinity distribution (PAD) function is complete with respect to both the number and the apparent strength of proton-binding sites at the solid/water interface. Agreement with the number of surface acidic sites was demonstrated [114] by comparing the PAD data for activated carbons with the results obtained independently using an established analytical method (Boehm titration [112a]). The validity of the evaluation of pK_a values was demonstrated by comparing the experimental results for oxides with "open" structures such as alumina with the acid strength of surface hydroxyls predicted by the MUSIC model [58a].

Another method for quantitative determination of acid sites on solid catalysts is calorimetric titration with amines [129]. This method uses the very simple concept that the enthalpy of adsorption for simple bases is a direct measure of acid strength. If a variation of the heat of adsorption with surface coverage is

observed, it demonstrates that the distribution of surface sites is nonuniform. However, with this method also there are difficulties with experimental procedures and the interpretation of results. In addition to the uncertainties due to effects other than acid-base interactions [130] and more than one proton being actually transferred [131], adsorption equilibrium may be slow [132] because the mobility of strong bases is low at low temperatures. For example, a microcalorimetric study of the adsorption of various amines on several high silica zeolites [129c] by Parillo and Gorte concluded that the structure of zeolites does not substantially affect their ability to transfer a proton to the reactants. Other factors such as confinement effects [20] may explain the discrepancies between the results of calorimetric measurements and catalytic activity data on zeolites.

Another methodology used to determine the number and strength of acid sites on solid catalysts is based on temperature-programmed desorption of adsorbed basic molecules (such as ammonia, pyridine, quinoline, or *n*-butylamine). In principle, an excess of base is adsorbed and the physically adsorbed species are removed by evacuation, in most cases combined with heat treatment. The amount that resists evacuation is attributed to the total number of acid sites. If thermodesorption is measured after heat treatment at several, progressively increasing temperatures, an approximate acid strength distribution can be established [133]. A linear correlation was found empirically [134] between the strength of acid sites expressed by the Hammett function (H_0) and the reciprocal temperature for the highest rate of thermodesorption (T_m):

$$H_0 = a + b/T_m \quad (7)$$

Alternatively, T_m can be used to calculate the activation energy of adsorption for the chemisorbed base, which is proportional to the heat of adsorption. However, determination of heats of adsorption from ammonia temperature-programmed desorption (TPD), although popular for its simplicity, may lead to inconsistent data because the experimental protocols may greatly influence the results [21].

Reactive amines other than ammonia have also been employed to distinguish Bronsted acid sites in various zeolites using a combination of TPD and thermogravimetric analysis (TGA) techniques [135]. The method is based on the fact that surface Bronsted sites may induce thermal decomposition of aliphatic amines to alkenes and ammonia over a narrow temperature range. The number of amine molecules reacted is equated to the number of strong Bronsted acid sites. By choosing amines of appropriate sizes it is possible to discriminate between acid sites located in pores of different diameters.

In general, when results obtained from titration methods are compared with the catalytic activity, the correlation is not necessarily good. One of the reasons is that only a small fraction of the total acid sites measured by titration are active for a given catalytic reaction. The low temperature at which amine adsorption is measured with the use of color indicators favors adsorption on all sites, including the weakest ones. Thermal desorption methods may discriminate between sites of different strength but are unable to distinguish between Lewis and Bronsted sites. When coupled with vibrational spectroscopy data, the TPD technique may, indeed, be adequate for analysis of surface acidity [136]. However, it is almost

always found that the use of a single technique is not sufficient for comprehensive characterization of the surface acidity of catalysts and predictions of catalytic activity.

The challenge is to identify the catalytically active sites for a specific acid-catalyzed reaction, to count them, and then to correlate the catalytic activity (expressed as reaction rate per unit catalyst surface) with the surface density of active sites. This task is quite easily solved in the case of zeolites, where it has been demonstrated that the number of Bronsted acid sites of a particular type (usually, those in Al—OH—Si bridges) could be quantitatively related to the rates of catalytic reactions [137].

A more challenging issue is to correlate the strength of acid sites with the rates of catalytic reactions [120c]. In homogeneous acid–base catalysis a relationship between the acid strength (pK_a) of an acid in solution and the rate of a catalytic reaction catalyzed by that acid was quantified first by Bronsted and Pedersen [138]: The stronger the acid, the easier it is to activate the bond to form a transition state complex and the faster is the catalytic reaction. The equation of Bronsted and Pedersen relates the effectiveness of a general acid catalyst to its acid–base strength:

$$k_A = G(K_a)^\alpha \quad (8)$$

where k_A is the specific rate constant for catalysis by an acid whose acid dissociation constant is K_a ; G and α are constants for a series of similar catalysts.

It was assumed by several authors that a similar correlation should exist for heterogeneous catalysis [139], but the difficulty of measuring the number and strength of Bronsted acid sites on solid catalysts at the same time hindered any experimental proof of a complementary relationship. Recently, the occurrence of a Bronsted-type relationship was demonstrated experimentally by Contescu et al. [140] for isomerization of 1-butene on a series of mixed oxide catalysts. The number and strength of Bronsted acid sites were simultaneously determined from the proton affinity distribution of solid acid catalysts by potentiometric titration [54a]. For a homologous series of catalysts, such as $\text{SiO}_2\text{--Al}_2\text{O}_3$, $\text{SiO}_2\text{--ZrO}_2$ or $\text{SiO}_2\text{--TiO}_2$, the areal reaction rates on catalysts of various molar compositions were directly correlated with the number of acid sites of a particular type (Fig. 4a), identified as the bridging hydroxyl in Si—OH—M structures. The significant fact was that active sites identified in each binary oxide system were characterized by nearly constant acid strength values (expressed on the pK scale of water), which shows that the acid strength in Si—OH—M structures is indeed determined by the electronegativity of M. Moreover, when the logarithms of specific reaction rate constants were plotted versus the pK values for the active sites found on catalysts from various binary systems, the linear correlations shown in Figs. 4b and 4c were found [140]. This is the equivalent in heterogeneous catalysis of the Bronsted relationship, Eq. (8), first developed in homogeneous catalysis.

The fact that a relationship similar to Eq. (8) was experimentally found for solid acid catalysts has both practical and theoretical significance. From a practical point of view, it demonstrates that at least one experimental method exists, namely the PAD method, that affords a direct and quantitative determination of both the number and strength of Bronsted acid sites on surfaces of porous oxide catalysts.

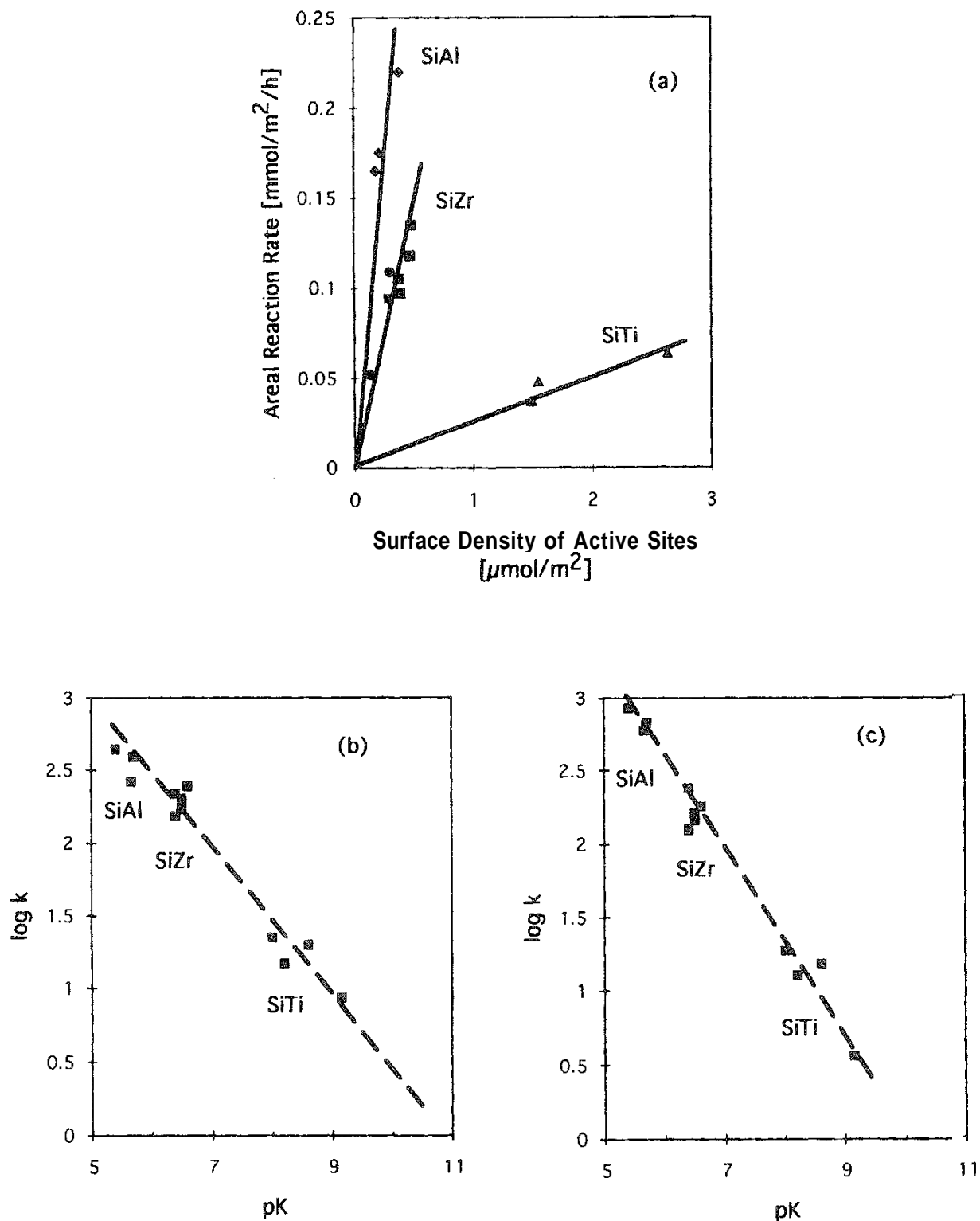


FIG. 4 Relationship between catalytic activity (isomerization of 1-butene to 2-cis- and 2-trans-butenes) on several mixed oxide catalysts and their surface acidity on the aqueous pK_a scale. (a) Linear dependence between specific reaction rates and the density of active sites from PAD data; (b) linear Bronsted relationship between the reaction rate of 2-cis-butene formation and the acid strength of corresponding active sites on different mixed oxides; (c) same relationship for formation of 2-trans-butene.

The fact that the results from potentiometric titration data for the solid/water interface could be used for correlation with the catalytic activity of the solid/gas interface (in similar systems) reopens the discussion of the relevance of one or another of possible acidity scales, either for gases or for water, in characterizing the surface acidity of solids.

C. Theoretical Concepts

In recent literature a considerable lack of agreement can be found as to which acidity scale is more suitable as a reference for molecules probing the acidity of a solid surface (gas-phase or aqueous-phase scale). This dichotomy presents a problem that is difficult to resolve and has interpretive implications for experimental results.

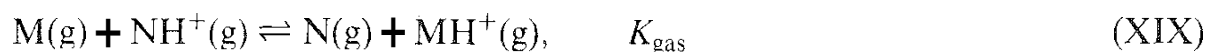
The difficulty of establishing a unique acidity scale for solid surfaces has been mentioned several times. Even the definition of "acid strength" of solid surface sites is not thermodynamically consistent. It is appropriate to analyze some of the theoretical concepts involved and to address some of the solutions advanced by various authors who tried to solve this problem.

The definition of acidity in terms of the Lewis theory has a broad meaning that encompasses the Bronsted definition as a particular case. In practice, especially in the field of heterogeneous catalysis, it is important to differentiate between Bronsted or Lewis acid sites on solid catalysts, since they may show completely different catalytic behavior.

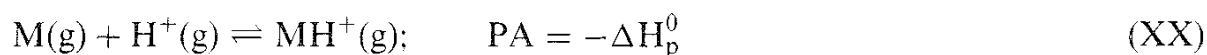
Limiting the discussion to Brönsted acidity, there have been two opposing views expressed regarding the question of which is the most appropriate acidity scale for solid surfaces. Some authors advocate the use of the acidity scale of gaseous species; others support the use of the pK scale of aqueous solutions.

1 Arguments for the Gas-Phase Acidity Scale

Acid–base properties determined for gas-phase molecular interactions are based on experimental measurements of equilibrium constants in proton transfer reactions between two gaseous bases:



The absolute proton affinity (PA) of a base molecule in the gas phase has a precise thermodynamic definition in relation to the enthalpy variation of the hypothetical reaction



in the absence of any interactions with the medium. The latter requirement is difficult to satisfy for accurate measurements even in vacuum. However, if the absolute proton affinity for a single base, M , could be measured independently in the gas phase, then a relative scale of basicities could be established by measuring the equilibrium constants K_{gas} , of a series of gas-phase reactions with

the participation of M. Again, conditions of total isolation from medium effects must be ensured, but this is less difficult for gas-phase reactions than for reactions with condensed media.

On the other hand, quantitative scales of Bronsted acidity available for aqueous solutions are based on measurements of equilibrium constants in proton transfer reactions like (II). The best-known scale of acidities, the pK_a scale, compares the relative proton-donating capacities of various molecules with respect to a unique base: water. The problem is that in this latter case the proton transfer cannot be regarded as isolated, because the aqueous medium contributes to the energetic stabilization (hydration) of all species, reactants and products, involved in the equilibrium.

It is possible, of course, to combine gas-phase proton affinities and solution-measured equilibrium constants (pK_a) in order to gain insight into the relative contribution of intrinsic (molecule-specific) versus medium-dependent effects while still using a perfectly rigorous thermodynamic approach [141]. Calculations showed that the solvation energy terms (medium effects), far from being a small perturbation, may be as important as the intrinsic terms (molecule-specific effects). When the reaction medium is water, the two types of effects are almost equally important, and the details of interaction of water with all species involved must be accounted for in order to derive first-principles-based acidity scales. However, the utility of the water-based pK_a scale has been demonstrated many times, and valuable insights into the molecule-specific effects have been gained by comparing pK_a values between the members of a homologous series of compounds.

In principle, a similar approach may be extended to Bronsted sites on solid surfaces. It is possible to design a thermochemical cycle that would permit an estimate of the enthalpy variations during protonation of a reference base on any solid surface site. All that is needed is a knowledge of gas-phase proton affinity for the base molecule and an estimate of the enthalpy variations when two systems, one with free base and the proton attached to the solid and the other with protonated base and the proton dissociated from the solid site, are brought from the solid state to a (hypotheical) gas-phase state. This enthalpy change is, however, very difficult to measure or calculate. The deprotonation energy of surface groups on solids can be obtained from quantum calculations and NMR data [142]. The real difficulty comes from the lack of any experimental data about transfer functions, i.e., the energetic terms involved in the interaction of the protonated base with the solid.

In other words, the medium-specific contribution is not easily measured or quantified for probe molecules in interaction with solid surfaces. Moreover, in the case of microporous solids, the short-distance interactions known as "confinement effects" are even more difficult to evaluate. In all comparisons of experimental data one should be aware that the reactivity of probe base molecules is largely influenced by the size of adsorbates and micropore dimensions. As a result, the acidity scales based on the free energy of proton transfer to a specific base are expected to depend on the choice of reference base. This fact has been confirmed experimentally, as calorimetric heats of adsorption of various bases on, e.g., zeolites, depend on the base chosen. For example, a ZH zeolite may be a stronger acid

than a Z'H one on a scale based on pyridine but a weaker acid on a scale based on ammonia [21].

2. Arguments for the Water-Based Acidity Scale

The advocates of the use of the aqueous pK_a scale for comparing the acidity of solids (mainly of oxides) invoke chemical, rather than thermodynamic, arguments. Their rationale is as follows. Since the protonation of a base probe molecule cannot be observed in total isolation from the environment, it is more logical to seek similarities with other systems instead of neglecting the serious perturbations that most solids induce on the state of the adsorbed base.

It is known that charged molecules are stabilized by different mechanisms in various media. In the gas phase, stabilization of a charged protonated species, such as $NH^+(g)$ from equilibrium (XIX), occurs by internal induction; in aqueous solutions the protonated $NH^+(aq)$ species is stabilized by interaction with water dipoles. Consequently, the same molecule may exhibit different acid strengths in different media. For example, in aqueous solutions ammonia is a stronger base (pK_a about 9) than pyridine (pK_a about 5); however, in the gas phase the basicity of pyridine is significantly higher.

It can be argued that the presence of oxygen ions (or of hydroxyl groups) on the surfaces of oxides, in interlayers of layered hydroxides, and in zeolite micropores creates a "waterlike" environment for adsorbed $NH^+(ads)$ species. In other words, the oxide may function as an aqueous solution, stabilizing the charge on the adsorbed molecules [34]. A series of titration or displacement experiments have shown, indeed, that the relative adsorption strength of various organic probes, including thiols, alcohols, acids, and alkynes, on various oxides reflects the order of their aqueous pK_a values and does not follow their order of acidity in the gas phase [143]. A similar conclusion was reached whereby the acidity and basicity of an amphoteric oxide like $\gamma-Al_2O_3$ was characterized by a combined volumetric-calorimetric technique with both basic and acidic probe molecules [144]. It was shown that the number and strength of acidic sites were related to the aqueous pK_a values of the adsorbed probe molecules.

A supplemental proof that metal oxide surfaces provide reaction environments that mimic conventional solvents emerged from studies on the reactivity of several organometallic compounds adsorbed on oxides. It is known from aqueous phase chemistry that the synthesis of iridium carbonyls is sensitive to the basicity of the solutions used. The same fact has been shown by Gates and coworkers [145] for metal carbonyl clusters on metal oxide surfaces (in the absence of solvents); their chemistry parallels that occurring in solvents with properties (such as basicity) analogous to those of the surface. For example, the environment on the surface of MgO and in the supercages of NaX zeolites is so highly basic that it allows the synthesis of a series of anionic iridium (or rhodium) carbonyl clusters that is possible only in basic solutions. In contrast, alumina and NaY zeolite are more neutral surfaces on which neutral iridium (or rhodium) carbonyl clusters form instead [145a]. The parallelism between the chemistry of carbonyls in solution and that on oxide surfaces demonstrates the importance of surface hydroxyl groups or a water association in the chemical environment offered by the oxide surface.

Comparing the nature of products synthesized on oxide surfaces with that of products formed in aqueous solutions allows an estimate of surface basicity. In the case of alumina the comparison suggests that thermal treatment (at 100°C) increases the basicity of the $\gamma\text{-Al}_2\text{O}_3$ surface.

These very new results are only preliminary and are not sufficiently accurate because neither the basicity of the organic solutions used for synthesis in organometallic chemistry nor that of solid surfaces are easily quantified. However, the conclusion that the *basicity* of $\gamma\text{-Al}_2\text{O}_3$ *increases* with decreasing surface hydroxylation [145d] agrees with the conclusion that the *Bronsted acidity* of alumina and several other mixed oxides ($\text{SiO}_2\text{-Al}_2\text{O}_3$, $\text{SiO}_2\text{-ZrO}_2$, $\text{SiO}_2\text{-TiO}_2$) *decreases* under similar conditions of thermal treatment [140].

The latter result was obtained from several catalytic activity studies for butene isomerization on mixed oxides dehydrated at various temperatures. Double-bond migration of 1-butene requires weak Bronsted acid sites on the surface of solid acid catalysts (with $\text{p}K$ values in the range from about 4 to 8 depending on oxide composition). Most oxides, especially mixed oxides, are active for this simple isomerization reaction if activated by mild dehydration. Infrared spectra show the occurrence of vast populations of surface hydroxyls on the active catalyst surface, which probably mediate the proton transfer from Bronsted acid sites on the catalyst surface to the reactant in the gas phase [140]. On the other hand, too high a dehydroxylation temperature decreases the activity, while rehydration partially restores the catalytic activity [49b,49d].

V. MANIFESTATION OF ACID-BASE PROPERTIES OF MICROPOROUS SOLIDS

To bring to closure the plethora of possible examples on this subject we cite two more. Each illustrates a specific domain of intrinsic practical importance in which the acid-base properties of microporous solids play a dominant role in determining a broad range of applications. The examples examine the gas/solid and liquid/solid interfaces, respectively. For the gas/solid interface, the interdependence of acid-base properties and microporous structure is revealed by the catalytic properties of zeolites, especially by their shape-selective properties. It is impossible to review all the literature in this area, and only a few recent views are summarized. For the liquid/solid interface, we focus on the role of acid-base chemistry in interlayers of clay minerals.

A. Solid/Gas Interface: The Role of Acid-Base Sites in Heterogeneous Catalysis

Zeolites are widely used as molecular sieve adsorbents and solid acid catalysts in the oil refining industry. The most important characteristic of these microporous solids is their acidity, in particular its interplay with the intracrystalline chemical environment.

There are many differences between traditional acid-base chemistry in solutions and acid functions on zeolites, but the general aspects of the chemistry between

proton acceptor reactants and proton donor sites on the solid's surface remain the same as those that occur in the aqueous phase. Therefore, the catalytic acidity of H-type zeolites is controlled by factors such as (1) the acid strength and concentration of zeolite hydroxyl groups, (2) the balance between media (solvation) and diffusion (geometrical) effects; (3) the nature of reactant molecules, especially their base strength or proton affinity; and (4) the stability and possible transformation routes of carbocation-like intermediates [146]. In zeolite micropores, the interaction between surface acid sites and reactant molecules involves not only the proton donor site localized at a given hydroxyl position but also the contribution from the surrounding crystal, or the solvent (medium) effect [147].

This insight is important in view of the large-scale use of these catalysts for alkane isomerization to increase the octane rating of motor fuels. It may help answer the question of which molecules become protonated by a particular catalyst and which do not. For example, one may infer that if water becomes protonated, stronger bases such as alcohols may also be protonated under similar conditions [90g].

SCHEME 3 Acidity centers in hydrated silica-alumina phosphates originating from water molecules and hydronium ions. (Adapted from Ref. 151.)

B. Solid/Liquid Interface: Acid–Base Reactions in Interlayers of Layered Minerals

An observation often made in the literature is that protonation of weak bases in clay suspensions frequently proceeds to a greater extent than that predicted from the pH of the bulk aqueous phase and the intrinsic constant $pK_{\text{BH}^+, \text{intr}}$ of the conjugated acid of the weak base [152]. This fact has important consequences for the reactivity of, e.g., pesticides or other organic contaminants in soil and may strongly modify their solubility, resistance to hydrolytic degradation, and long-term accumulation.

For example, it was reported that simetone and prometryne, two commercial herbicides with weakly basic amino groups ($pK_{\text{BH}^+, \text{intr}}$ about 4) develop higher apparent basicity when present at low concentration in dilute aqueous suspensions of natural clays (sepiolite and montmorillonite) [152a]. Depending on the experimental conditions (such as the presence of other electrolytes and their nature and concentration), the increase in the effective pK of these herbicides in water/clay suspensions amounted to up to two pK units. The effect has been accounted for by the electrostatic effects of the water/clay interface. In view of the fact that clays usually carry a net negative charge, their aqueous interface can significantly lower the potential of the protonated form of the organic molecule (BH^+) relative to that of the neutral form (B). This results in shifting the $\text{BH}^+ \rightleftharpoons \text{B} + \text{H}^+$ equilibrium to the left, which is equivalent to increasing the effective basicity of the herbicide in water/clay suspensions. The role of other metal cations, water, or other organic molecules in the aqueous phase is to control the accessibility and apparent number of negatively charged sites on the clay. Interestingly, the effects were not observed in water suspensions of a zeolite with pore size openings smaller than the protonated $\text{N}(\text{C}_2\text{H}_5)_4^+$ group of one of the herbicides, although the smaller $\text{N}(\text{CH}_3)_4^+$ protonated group had access and underwent exchange.

Modification of the acid–base chemistry of exchanged species in the interlayer spaces of minerals is supported by recent results in pillared clays, both anionic and cationic. The acid–base properties of pillared clays and of their thermal degradation products were characterized by potentiometric titration data from which the PAD functions were calculated [153]. It is generally accepted that the Bronsted and Lewis acidity of pillared clays is related to properties of both the mineral layers and the acidic sites introduced as pillars [154]. When pillars are composed of metal oxides or hydroxides (such as hydroxyaluminum or hydroxyzirconium polycations), the acidic properties of the clays are enhanced [155]. Similar changes were also observed as a result of thermal treatment of intercalated clays [153b] and were attributed to the rearrangements of pillars caused by dehydroxylation. However, the analysis of potentiometric titration data for nondehydrated samples revealed that OH groups in various surface coordinations attached to hydroxyaluminum pillars intercalated in cationic clays (montmorillonite) underwent shifts in their intrinsic pK_a values due to the influence of the clay sheets [153b]. This result was not reproduced for hydrotalcite-like anionic clays intercalated with molybdate and tungstate anions, which interact weakly with the brucite-like layer during ion exchange. In the latter case, the pK_a distribution of metalate-exchanged samples was close to that of concentrated aqueous solutions of the same metalate ions

[153a]. This is an indication that in the starting materials the intercalated oxoanions are monomeric WO_4^{2-} and MoO_4^{2-} ions and undergo a protonation mechanism in the interlayers during acid titration similar to that in water. This is not a trivial finding, because it further suggests that by adjustment of the pH of the water suspension one can modify the form of the intercalated anion and thus obtain pillared structures with different forms of the intercalated anions and thus with different acid–base surface properties [153a].

VI. SUMMARY AND CONCLUSIONS

The scope of this review was intentionally restricted to those gas/solid and liquid/solid interfaces where the acid–base properties at a molecular level can best be explained and related to particularly important applications.

In the field of heterogeneous catalysis, in which most solid acids or bases used as catalysts also have porous structure, the questions of primary interest are (1) how to characterize in a consistent manner the number and strength of surface acid–base couples, (2) how to distinguish between Lewis and Bronsted acid sites, and (3) how to prepare solids with high surface area, selected micropore size, and stable surface structures with desired acid properties. The progress made in this field is commensurate with its economic importance. Now it is possible to select and prepare catalysts with an acid strength adequate for almost any specific acid-catalyzed reaction. This has been made possible by the development of acid–base characterization methods that provided the basis for understanding the close relationship between the atomic-scale structure and the properties of surface acid sites. The progress in materials science and the development of molecularly engineering catalysts have extended the spectrum of inorganic materials used as solid acid catalysts. The new generation of zeolites and zeotypes with controlled molecular sieve properties and an acid strength as high as $H_0 = -10$ has induced a revolution in the field of oil refining and petrochemistry. When catalysts with even stronger acidities are required, the use of sulfated oxides is promising, although more work is needed to stabilize these “superacids” against premature deactivation.

Synthetic layered hydroxides with hydroxalite-like structures are used as heterogeneous catalysts for base-catalyzed reactions. One of their major drawbacks for technological application is their low stability during hydrothermal and/or thermal treatments. Recent attempts to incorporate large, preferably multicharged anions into their interlayer spaces introduced new routes for preparation of more stable materials. The effect of intercalated polymetalates or transition metal complex anions in the framework of layered hydroxides is twofold: They increase the gallery heights and thermal stability on one hand and introduce additional Lewis or Bronsted acidic sites in a basic framework on the other hand.

Oxides, especially those of Al, Si, Fe, and Mg, are essential components of the earth's minerals; their surface sites may have either Bronsted or Lewis acid–base properties. The weathering of rocks and the formation of soils are processes at the solid/liquid interface between minerals and natural waters or solutes from the medium in which solid phases are either formed, altered, or dissolved. Dissolution of solid minerals is controlled by slow surface reactions rather than

diffusion processes in the liquid phase and by acid–base reactions, either in the Bronsted sense (proton-promoted dissolution) or in the Lewis sense (ligand-promoted dissolution). Moreover, the hydrophilicity of natural clays and minerals, as well as their swelling and ion-exchange properties, originate in local acid–base interactions in the interlayer space. Thus the chemistry of natural waters and the quality of the environment are controlled by acid–base equilibria in multiphase systems of natural waters, solute, and minerals.

REFERENCES

1. S. Arrhenius, *Z. Phys. Chem.* 1:631 (1887).
2. J. N. Bronsted, *Rec. Trav. Chim. Pays-Bas* 42:718 (1923).
3. T. M. Lowry, *Chem. Ind. (Lond.)* 42:43 (1923).
4. G. N. Lewis, *Valence and the Structure of Atoms and Molecules*, The Chemical Catalog Col, New York, 1923.
5. (a) W. B. Jensen, *The Lewis Acid–Base Concepts: An Overview*, Wiley, New York, 1980; (b) W. B. Jensen, *J. Adhesion Sci. Tech.* 5:1 (1991).
6. (a) R. G. Pearson, *Hard and Soft Acids and Bases*, Dowden, Hutchinson and Ross, Stroudsburg, PA, 1973; (b) R. G. Pearson, *J. Am. Chem. Soc.* 85:3533 (1963).
7. (a) R. S. Drago and N. A. Matwiyoff, *Acids and Bases*, D. C. Heath, Lexington, MA, 1968; (b) R. S. Drago and B. B. Wayland, *J. Am. Chem. Soc.* 87: 3571 (1965).
8. (a) V. Gutmann, *The Donor – Acceptor Approach to Molecular Interactions*, Plenum, New York, 1982; (b) V. Gutmann, A. Steininger, and E. Wychera, *Monatsch. Chem.* 97: 460 (1966).
9. R. F. Hudson and G. Klopman, *Tetrahedron Lett.* 12:1103 (1967).
10. M. T. Bowers, D. H. Aue, H. M. Webb, and R. T. M. Iver, *J. Am. Chem. Soc.* 93:4314 (1971).
11. D. H. Aue and M. T. Bowers, in *Gas Phase Ion Chemistry*, Vol 2 (M. T. Bowers, ed.), Academic, New York, 1979, p. 2.
12. U. Fleischer, W. Kutzelnigg, A. Bleiber, and J. Sauer, *J. Am. Chem. Soc.* 115:7833 (1993).
13. W. L. Jorgensen and J. M. Briggs, *J. Am. Chem. Soc.* 111:4190 (1989).
14. P. C. Stair, *J. Am. Chem. Soc.* 104:4042 (1982).
15. J. C. Berg, in *Wettability* (J. C. Berg, ed.), Marcel Dekker, New York, 1993, p. 76.
16. (a) M. F. Finlayson and B. A. Shah, *J. Adhesion Sci. Tech.* 4:431 (1990); (b) H. F. Webster and J. P. Wightman, *J. Adhesion Sci. Tech.* 5:93 (1991); (c) T. S. Oh, L. P. Buchwalter, and J. Kim, *J. Adhesion Sci. Tech.* 4:303 (1990); (d) E. P. Papirer and H. Balard, *J. Adhesion Sci. Tech.* 4:357 (1990); (e) A. Larsson and W. E. Johns, *J. Adhesion* 25:121 (1988); (f) D. Ma, W. E. Johns, A. K. Dunker, and A. E. Bayoumi, *J. Adhesion Sci. Tech.* 4:411 (1990).
17. C. A. Leon y Leon and L. R. Radovic, in *Chemistry and Physics of Carbon*, Vol. 24 (P. A. Thrower, ed.), Marcel Dekker, New York, 1992, p. 213.
18. F. M. Fowkes, *J. Adhesion Sci. Tech.* 1:7 (1987).

- 19 J. G. Fripiat, F. Berger-Andre, J. M. Andre, and E. G. Derouane, *Zeolites* 3:306 (1983).
- 20 E. G. Derouane. in *Guidelines for Mustering the Properties of Molecular Sieves* (D. Barthomeuf, E. G. Derouane, W. Hölderich, eds.), Plenum, New York, 1990. p. 234.
- 21 W. E. Farneth and R. J. Gorte, *Chem. Rev.* 95:615 (1995).
- 22 H. Stach, K. Fiedler, and J. Jänchen, *Pure Appl. Chem.* 65:2193 (1993).
- 23 H. Liu, G. D. Lei, and W. M. H. Sachtler, *Appl. Catal. A* 137:167 (1996).
- 24 R. A. van Santen and G. J. Kramer, *Chem. Rev.* 95:637 (1995).
- 25 S. Yariv, in *Modern Approaches to Wettability: Theory and Applications* (M. E. Schrader and G. Loeb, eds.), Plenum, New York, 1992, p. 279.
- 26 R. Touillaux, P. Salvador, C. Vandermeersche, and J. J. Fripiat, *Isr. J. Chem.* 6:337 (1968).
- 27 G. Sposito and R. Prost, *Chem. Rev.* 82:553 (1982).
- 28 (a) H. Suquet, R. Prost, and H. Pezerat, *Clay. Miner.* 12:113 (1977); (b) J. Hougardy, W. E. E. Stone, and J. J. Fripiat, *J. Magn. Reson.* 25:563 (1977).
- 29 P. C. Stair, *J. Am. Chem. Soc.* 104:4044 (1982).
- 30 H. Conrad, G. Ertl, J. Küppers, and E. E. Latta, *Surf. Sci.* 57:475 (1976).
- 31 (a) J. E. Demuth and D. E. Eastman, *Phys. Rev. Lett.* 32:1123 (1974); (b) C. W. Seabury, T. N. Rhodin, R. J. Purtell, and R. P. Merrill, *J. Vac. Sci. Technol.* 18:602 (1981).
- 32 S. Soled, *J. Catal.* 81:252 (1983).
- 33 V. E. Henrich, *Rep. Prog. Phys.* 48:1481 (1985).
- 34 H. Kung, *Transition Metal Oxides: Surface Chemistry and Catalysis* (Stud. Surf. Sci. Catal. Vol. 45) Elsevier, Amsterdam, 1989.
- 35 A. Zecchina and C. O. Arean, *Catal. Rev. – Sci. Eng.* 35:261 (1993).
- 36 Yu, A. Lokhov and A. A. Davydov, *Kinet. Katal.* 21:1093 (1980).
- 37 R. P. Eischens, W. A. Plisken, and M. J. D. Low, *J. Catal.* 1:180 (1962).
- 38 P. Nortier, A. P. Borosy, and M. Allavena, *J. Phys. Chem B* 101:1347 (1997).
- 39 A. A. Tsyganenko and V. N. Filimonov, *J. Mol. Struct.* 19:579 (1973).
- 40 C. Contescu and J. A. Schwarz, unpublished results, 1995.
- 41 H. Knozinger and P. Ratnasamy. *Catal. Rev. – Sci. Eng.* 17:31 (1978).
- 42 (a) P. Nortier, P. Fourre, A. B. Mohammed Saad, O. Saur, and J. C. Lavalley, *Appl. Catal.*, 61:141 (1990); (b) A. B. Mohammed Saad, V. A. Ivanov, and J. C. Lavalley, *Appl. Catal. A: General* 94:71 (1993).
- 43 (a) G. Busca, V. Lorenzelli, V. Sanchez Escribano, and R. Guidetti, *J. Catal.* 131:167 (1991); (b) G. Busca, V. Lorenzelli, G. Ramis, and R. J. Willey, *Langmuir* 9:1492 (1993).
- 44 L. J. Alvarez, J. F. Sanz, M. J. Capitan, M. A. Centeno, and J. A. Odriozola, *J. Chem. Soc. Faraday Trans.* 89:3623 (1993).
- 45 (a) R. M. Pearson, *J. Catal.* 23:388 (1971); (b) L. B. Schreiber and R. W. Vaughan, *J. Catal.* 40:226 (1975).
- 46 V. M. Gunko, V. I. Zarko, V. V. Turov, E. F. Voronin, V. A. Tischenko, and A. A. Chuiko, *Langmuir* 11:2115 (1995).
- 47 B. A. Huggins and P. D. Ellis, *J. Am. Chem. Soc.* 114:2098 (1992).

48. (a) S. R. Morrison *The Chemical Physics of Surfaces*, Plenum, New York, 1977; (b) V. F. Kiselev and O. V. Krylov, *Electronic Phenomena in Adsorption and Catalysis on Semiconductors and Dielectrics*, Nauka, Moscow, 1979.
49. (a) S. G. Hindin, A. G. Oblad, and G. A. Mills, *J. Am. Chem. Soc.* **77**:535 (1955); (b) E. I. Ko, J. P. Chen, and J. G. Weissman, *J. Catal.* **105**:511 (1987); (c) M. R. Gonzales, K. M. Kobe, K. B. Fogash, and J. A. Dumesic, *J. Catal.* **160**:290 (1996); (d) K. H. Nam, M. S. Thesis, Syracuse University, 1997.
50. (a) T. W. Healy and R. L. White, *Adv. Colloid Interface Sci.* **9**:303 (1978); (b) R. D. James and G. A. Parks, in *Surface and Colloid Science*, Vol. 12 (E. Matijevic, ed.), Plenum, New York, (1990).
51. G. H. Bolt and W. H. van Riemsdijk, in *Soil Chemistry, B. Physico-Chemical Models* (G. H. Bolt, ed.), Elsevier, Amsterdam, 1982, p. 459.
52. (a) T. Hiemstra, J. C. M. De Wit, and W. H. van Riemsdijk, *J. Colloid Interface Sci.* **133**:91 (1989); (b) T. Hiemstra and W. H. van Riemsdijk, *J. Colloid Interface Sci.* **179**:488 (1996); (c) T. Hiemstra, P. Venema, and W. H. van Riemsdijk, *J. Colloid Interface Sci.* **184**:680 (1996).
53. L. K. Koopal, *Electrochim. Acta* **41**:2293 (1996).
54. (a) C. Contescu, J. Jagiello, and J. A. Schwarz, *Langmuir*, **9**:1754 (1993); (b) C. Contescu, J. Hu, and J. A. Schwarz, *J. Chem. Soc. Faraday Trans.* **89**:4091 (1993).
55. C. Contescu, A. Contescu, and J. A. Schwarz, *J. Phys. Chem.* **98**:4327 (1994).
56. W. F. Bleam, *J. Colloid Interface Sci.* **159**:312 (1993).
57. G. M. S. El Shafei, *J. Phys. Chem.* **97**:10127 (1993).
58. (a) C. Contescu, A. Contescu, and J. A. Schwarz, *J. Phys. Chem.* **98**:4327 (1994); (b) C. Contescu, V. T. Popa, and J. A. Schwarz, *J. Colloid Interface Sci.*, **180**:149 (1996).
59. (a) T. Morimoto, H. Yanai, and M. Nagao, *J. Phys. Chem.* **80**:471 (1976); (b) K. Segawa and W. Hall, *J. Catal.* **76**:133 (1982); (c) R. Groff, *J. Catal.* **86**:215 (1984).
60. (a) K. Tanabe and A. Ozaki, *J. Catal.* **8**:1 (1967); (b) K. Shibata, T. Kiyoura, J. Kitagawa, T. Sumiyoshi, and K. Tanabe, *Bull. Chem. Soc. Jpn.* **46**:2985 (1973).
61. (a) J. Take, N. Kikuchi, and Y. Yoneda, *J. Catal.* **21**:164 (1971); (b) T. Yamanaka and K. Tanabe, *J. Phys. Chem.* **80**:1723 (1976).
62. G. M. S. El Shafei, *J. Colloid Interface Sci.* **182**: 249 (1996).
63. (a) G. A. Parks, *Chem. Rev.* **65**:177 (1965); (b) R. H. Yoon, T. Salman, and G. Donnay, *J. Colloid Interface Sci.* **70**:483 (1979).
64. E. Knozinger, K. H. Jacob, S. Singh, and P. Hofmann, *Surf. Sci.* **290**:388 (1993).
65. H. Nakabayashi, N. Kakuta, and A. Ueno, *Bull. Chem. Soc. Jpn.* **64**:2428 (1991).
66. (a) C. L. Thomas, *Ind. Eng. Chem.* **41**:2564 (1949); (b) C. J. Plank, *J. Colloid Sci.* **2**:413 (1947).
67. K. Tanabe, T. Sumiyoshi, K. Shibata, T. Kiyoura, and J. Kitagawa, *Bull. Chem. Soc. Jpn.* **47**:1064 (1974).
68. K. Tanabe, M. Misono, Y. Ono, and H. Hattori, *New Solid Acids and Bases* (Stud. Surf. Sci. Catal. Vol. 51), Kodansha, Tokyo, 1989.
69. H. Kung, *J. Solid State Chem.* **52**:191 (1984).
70. (a) J. B. Miller, S. E. Rankin, and E. I. Ko, *J. Catal.* **148**:673 (1994); (b) J. B. Miller, S. T. Johnston, and E. I. Ko, *J. Catal.* **150**:311 (1994); (c) J. B. Miller and E. I. Ko, *J. Catal.* **159**:58 (1996).

71. (a) G. Connel and J. A. Dumesic, *J. Catal.* **101**:103 (1986); (b) G. Connel and J. A. Dumesic, *J. Catal.* **105**:285 (1987).
72. P. O. Scokart and P. G. Rouxhet, *J. Colloid Interface Sci.* **86**:96 (1982).
73. A. Corma, V. Fornes, and E. Ortega, *J. Catal.* **92**:284 (1985).
74. P. M. Boorman, R. A. Kydd, Z. Sarbak, and A. Somogyvary, *J. Catal.* **96**:115 (1985).
75. (a) J. M. Parera and N. S. Figoli, *J. Catal.* **14**:303 (1969); (b) C. M. M. Sachett, P. N. Da Silva, Y. L. Lam, M. Dufaux, R. Frety, and M. Primet, *Bull. Soc. Chim. France* **1989**:357; (c) S. Srinivasan, C. R. Narayanan, A. Biaglow, R. Gorte, and A. K. Datye, *Appl. Catal. A: General* **132**:271 (1995).
76. P. Berteau, M. A. Kellens, and B. Delmon, *J. Chem. Soc. Faraday. Trans.* **87**:1425 (1991).
77. (a) K. Arata, M. Hino, and N. Yamagata, *Bull. Chem. Soc. Jpn.* **63**:244 (1990); (b) F. R. Chen, G. Courdurier, J. Joly, and J. C. Vedrine, *J. Catal.* **143**:616 (1993); (c) T. Riemer, D. Spielbauer, M. Hunger, G. A. H. Mekhemer, and H. Knözinger, *J. Chem. Soc. Chem. Commun.* **1994**:1181; (d) V. Adeeva, J. W. de Haan, J. Janchen, G. D. Lei, V. Schunemann, L. J. M. van de Ven, W. M. H. Sachtler, and R. A. van Santen, *J. Catal.* **151**:364 (1995).
78. (a) J. H. Lunsford, H. Sang, S. M. Campbell, C. Liang, and R. G. Anthony, *Catal. Lett.* **27**:305 (1994); (b) F. Babou, G. Courdurier, and J. C. Vedrine, *J. Catal.* **152**:341 (1995); (c) A. Corma, V. Fornes, M. I. Juan-Rajadell, and J. M. Lopez-Nieto, *Appl. Catal. A* **116**:151 (1994); (d) F. Lonyi, J. Valyon, J. Engelhardt, and F. Mizukami, *J. Catal.* **160**:279 (1996).
79. L. M. Kustov, V. B. Kazansky, F. Figueras, and D. Tichit, *J. Catal.* **150**:143 (1994).
80. (a) C. Zhang, R. Miranda, and B. H. Davis, *Catal. Lett.* **29**:349 (1994); (b) D. A. Ward and E. I. Ko, *J. Catal.* **150**:18 (1994); (c) C. Morterra, G. Cerato, and V. Bolis, *Catal. Today* **17**:505 (1993).
81. M. R. Gonzales, J. M. Kobe, K. B. Fogash, and J. A. Dumesic, *J. Catal.* **160**:290 (1996).
82. I. E. Wachs and K. Segawa, in *Characterization of Catalytic Materials* (I. E. Wachs and L. E. Fitzpatrick, eds.), Butterworth-Heinemann, Boston, 1992, p. 69.
83. (a) G. Deo and I. E. Wachs, *J. Phys. Chem.* **95**:5889 (1991); (b) G. Deo and I. E. Wachs, *J. Catal.* **129**:307 (1991); (c) D. S. Kim, K. Segawa, T. Soeya, and I. E. Wachs, *J. Catal.* **136**:539 (1992).
84. F. J. Gil-Llambias, A. M. Escudey, J. L. G. Fierro, and A. Lopez Agudo, *J. Catal.* **95**:520 (1985).
85. W. Kania and K. Jurczyk, *Appl. Catal.* **61**:27 (1990).
86. (a) M. Adachi, C. Contescu, and J. A. Schwarz, *J. Catal.* **158**:411 (1996); (b) M. Adachi, C. Contescu, and J. A. Schwarz, *J. Catal.* **162**:66 (1996).
87. P. Courty and Ch. Marcilly, *Preparation of Catalysis III*, Amsterdam, Elsevier, 1983, p. 485.
88. (a) J. Sauer, *Chem. Rev.* **89**:199 (1989); (b) G. J. Kramer and R. A. van Santen, *J. Am. Chem. Soc.* **115**:2887 (1993); (c) S. P. Greatbanks, P. Sherwood, and I. H. Hillier, *J. Phys. Chem.* **98**:8134 (1994).

89. (a) W. Grabowski, M. Misono, and Y. Yoneda, *J. Catal.* **61**:103 (1980); (b) H. Hawakami, S. Yoshida, and T. Yonezawa, *J. Chem. Soc. Faraday Trans.* **280**:205 (1984); (c) G. M. Zhidomirov and V. B. Kazansky, *Adv. Catal.* **34**:131 (1986).
90. (a) J. A. Rabo (ed.), *Zeolites Chemistry and Catalysis* ACS Monograph No. 171, American Chemical Society, Washington DC, 1976; (b) W. J. Mortier and R. A. Schoonheydt, *Progr. Solid State Chem.* **16**:1 (1985); (c) D. Barthomeuf, *Mater. Chem. Phys.* **17**:49 (1987); (d) P. O. Fritz and J. H. Lunsford, *J. Catal.* **118**:85 (1989); (e) P. A. Jacobs, *Catal. Rev. — Sci. Eng.* **24**:415 (1982); (f) A. Corma, *Chem. Rev.* **95**:559 (1995); (g) R. A. van Santen and G. J. Kramer, *Chem. Rev.* **95**:637 (1995).
91. J. B. Uytterhoeven, L. G. Christner, and W. K. Hall, *J. Phys. Chem.* **69**:2117 (1965).
92. (a) I. D. Mikheikin, I. N. Senchenya, A. I. Lumpov, G. M. Zhidomirov, and V. B. Kazansky, *Kinet. Katal.* **20**:496 (1979); (b) W. J. Mortier, J. Sauer, J. A. Lercher, and H. Noller, *J. Phys. Chem.* **88**:905 (1984).
93. L. L. Smith, A. K. Cheetham, R. E. Morris, L. Marchese, J. M. Thomas, P. A. Wright, and J. Chen, *Science* **271**:799 (1996).
94. D. Freude, M. Hunger, H. Pfeifer, and W. Schwieger, *Chem. Phys. Lett.* **128**:62 (1986).
95. D. Barthomeuf and R. Beumont, *J. Catal.* **30**:288 (1973).
96. (a) W. Mortier, *J. Catal.* **55**:138 (1978); (b) P. A. Jacobs, *Catal. Rev. — Sci. Eng.* **24**:415 (1982).
97. (a) C. T. W. Chu and C. D. Chang, *J. Phys. Chem.* **89**:1569 (1988); (b) D. H. Dompas, W. J. Mortier, O. C. H. Kenter, M. J. G. Janssen, and J. P. Verduijn, *J. Catal.* **129**:19 (1991).
98. (a) J. Sauer, *Chem. Rev.* **89**:199 (1989); (b) E. Kassab, K. Seiti, and M. Allavena, *J. Phys. Chem.* **92**:6705 (1988).
99. E. G. Derouanne, *J. Catal.* **100**:541 (1986).
100. A. Corma, C. M. Zicovich-Wilson, and P. Viruela, *J. Phys. Chem.* **98**:10863 (1994).
101. (a) J. Dwyer, *Stud. Surf. Sci. Catal.* **37**:333 (1988); J. M. Thomas and J. Klinowski, *Adv. Catal.* **33**:199 (1985); (c) A. Martin, U. Wolf, S. Nowak, and B. Lucke, *Zeolites* **11**:85 (1991).
102. (a) M. H. W. Sonnemans, C. den Heijer, and M. Crocker, *J. Phys. Chem.* **93**:440 (1993); (b) D. Coster, A. L. Blumenfeld, and J. J. Fripiat, *J. Phys. Chem.* **98**:6201 (1994).
103. F. Yin, A. L. Blumenfeld, and V. Gruver, *J. Phys. Chem. B* **101**:1824 (1997).
104. M. Huang, S. Kaliaguine, and A. Auroux, *J. Phys. Chem.* **99**:9952 (1995).
105. (a) H. P. Boehm, *Carbon* **32**:759 (1994); (b) H. P. Boehm, *High Temp. Press.* **22**:275 (1990).
106. O. G. Taushkanova, E. P. Smirnov, and A. A. Novozhenets, *Russ. J. Phys. Chem.* **67**:671 (1993).
107. (a) J. B. Donnet and P. Ehrburger, *Carbon* **15**:143 (1977); (b) E. Fitzer and R. Weiss, *Carbon* **25**:455 (1987).
108. T. Tore, A. S. Arico, V. Alderucci, V. Antonucci, and N. Giordano, *Appl. Catal. A* **114**:257 (1994).
109. V. A. Garten and D. E. Weiss, *Aust. J. Chem.* **10**:309 (1957).

110. H. P. Boehm and M. Voll, *Carbon* 8:227 (1970).
111. C. A. Leon y Leon, J. M. Solar, V. Calemma, and L. R. Radovic, *Carbon* 30:797 (1992).
112. (a) H. P. Boehm, E. Diehl, W. Heck, and R. Sappok, *Angew. Chem. Int. Ed. Eng.* 3:669 (1964); (b) H. P. Boehm, *Adv. Catal.* 16:179 (1966); (c) J. B. Donnet, *Carbon* 6:161 (1968) (d) B. R. Puri, in *Chemistry and Physics of Carbon* (P. L. Walker, Jr., ed.), Vol. 6, Marcel Dekker, New York, p. 191.
113. (a) Y. Matsumura, S. Hagwiara, and H. Takahashi, *Carbon* 14:163 (1976); (b) S. Neffe, *Carbon* 25:441 (1987); (c) A. S. Arico, V. Antonucci, M. Minutoli, and N. Giordano, *Carbon* 27:337 (1989).
114. (a) A. Contescu, C. Contescu, K. Putyera, and J. A. Schwarz, *Carbon* 35:83 (1997); (b) A. Contescu, M. I. Vass, C. Contescu, K. Putyera, and J. A. Schwarz, *Carbon* 36:247 (1998).
115. (a) G. M. Brown, M. R. Noe-Spirlet, W. R. Bushing, and H. A. Levy, *Acta Crystallogr. Sect. B* 33:1038 (1977); (b) I. V. Kozhevnikov, A. Sinnema, R. I. Jansen, and H. van Bekkum, *Catal. Lett.* 27:187 (1994).
116. (a) G. B. McGarvey and J. B. Moffat, *J. Catal.* 130:483 (1991); (b) J. L. Bonardet, G. B. McGarvey, J. B. Moffat, and J. Fraissart, *Colloids Surf. A* 72:191 (1993).
117. I. V. Kozhevnikov, *Catal. Rev. — Sci. Eng.* 37:311 (1995).
118. (a) K. Y. Lee, T. Arai, S. Nakata, S. Asaoka, T. Okuhara, and M. Misono, *J. Am. Chem. Soc.* 114:2836 (1992); (b) T. Okuhara, A. Kasai, N. Ayakawa, Y. Yoneda, and M. Misono, *J. Catal.* 83:121 (1983); (c) M. Misono, *Catal. Rev. — Sci. Eng.* 29:269 (1987).
119. M. Misono and T. Okuhara, *CHEMTECH* 23:23 (1993).
120. (a) K. Tanabe, *Solid Acids and Bases*, Academic, New York, 1970; (b) O. Krylov, *Catalysis by Non-Metals*, Academic, New York, 1970; (c) D. Barthomeuf, in *Catalysis by Acids and Bases* (B. Imelik, C. Naccache, G. Cordurier, Y. Ben Taarat, and J. C. Vedrine, eds.), Elsevier, Amsterdam, 1985 p. 75; (c) M. S. Goldstein, in *Experimental Methods in Catalytic Research* (R. B. Anderson and P. T. Dawson, ed.), Vol. 1, Academic, New York, 1968, p. 354.
121. (a) T. R. Hughes and H. M. White, *J. Phys. Chem* 71:2192 (1967); (b) C. A. Emeis, *J. Catal.* 141:347 (1993); (c) S. Khabtou, T. Chevreau, and J. C. Lavalley, *Microporous Mater.* 3:133 (1994); (d) J. Datka, A. M. Tutek, J. H. Jehng, and I. E. Wachs, *J. Catal.* 135:186 (1992).
122. T. Barzetti, E. Selli, D. Moscotti, and L. Forni, *J. Chem. Soc. Faraday Trans.* 92:1401 (1996).
123. (a) H. Knozinger, H. Krilttenbrink, and P. Ratnasamy, *J. Catal.* 48:436 (1977); (b) A. Corma and V. Fornes, *Zeolites* 13:56 (1993); (c) A. Corma, C. Rodellas, and V. Fornes, *J. Catal.* 88:374 (1984).
124. (a) J. A. Lercher, H. Noller, and G. Ritter, *J. Chem. Soc. Faraday Trans. I* 77:621 (1981); (b) P. A. Jacobs, *Catal. Rev. — Sci. Eng.* 24:415 (1982); (c) G. Busca and V. Lorenzelli, *Mater. Chem.* 7:89 (1982).
125. (a) E. A. Paukshtis and E. N. Yurchenko, *React. Kinet. Catal. Lett.* 19:105 (1982); (b) C. Morterra, G. Cerrato, C. Emanuel, and V. Bolis, *J. Catal.* 142:349 (1993); (c) M. Maache, A. Janin, J. C. Lavalley, J. F. Joly, and E. Benazzi, *Zeolites*, 13:419 (1993).

126. (a) H. A. Benesi, *J. Am. Chem. Soc.* **78**:5490 (1950); (b) H. A. Benesi and B. H. C. Winquist, *Adv. Catal.* **27**:97 (1978).
127. (a) J. Take, Y. Nomizo, and Y. Yoneda, *Bull. Chem. Soc. Jpn.* **46**:3568 (1973); (b) M. Balikova, *React. Kinet. Catal. Lett.* **2**:323 (1975).
128. L. L. Murrell and N. C. Dispenziere, *J. Catal.* **117**:275 (1989).
129. (a) N. Cardona-Martinez and J. A. Dumesic, *Adv. Catal.* **38**:149 (1992); (b) M. B. Sayed, A. Auroux, and J. C. Vedrine, *Appl. Catal.* **23**:49 (1986); (c) D. J. Parillo and R. J. Gorte, *J. Phys. Chem.* **97**:8786 (1993).
130. D. J. Parillo and R. J. Gorte, *Catal. Lett.* **16**:17 (1992).
131. D. Farcasiu and A. Ghenciu, *J. Am. Chem. Soc.* **115**:10901 (1993).
132. N. Cardona-Martinez and J. A. Dumesic, *J. Catal.* **125**:427 (1990).
133. (a) N. Cardona-Martinez and J. A. Dumesic, *J. Catal.* **128**:23 (1991); (b) N. Cardona-Martinez and J. A. Dumesic, *Adv. Catal.* **38**:149 (1992); (c) D. J. Parillo and R. J. Gorte, *Catal. Lett.* **16**:17 (1992); (d) H. G. Karge, in *Catalysis and Adsorption by Zeolites* (G. Ohlman, H. Pfeifer, and R. Fricke, eds.), Elsevier, Amsterdam, 1991, p. 133.
134. J. C. Yori, L. M. Krasnogor, and A. A. Castro, *React. Kinet. Catal. Lett.* **32**:27 (1986).
135. C. Pereira and R. J. Gorte, *Appl. Catal. A* **90**:145 (1992).
136. P. Berteau, B. Delmon, J. L. Dallons, and A. Van Gysel, *Appl. Catal.* **70**:307 (1991).
137. (a) D. Barthomeuf, in *Molecular Sieves*, Vol. II (J. R. Katzer, ed.), ACS Symp. Ser. American Chemical Society, Washington, DC, 1977, p. 453; (b) G. Poncelet, M. L. Dubru, and P. A. Jacobs, in *Molecular Sieves*, Vol. II (J. R. Katzer, ed.), ACS Symp. Ser. American Chemical Society, Washington, DC, 1977, p. 607.
138. J. N. Bronsted and K. Pederson, *J. Phys. Chem.* **108**:185 (1924).
139. Y. Yoneda, *J. Catal.* **9**:51 (1967).
140. (a) C. Contescu, V. T. Popa, J. B. Miller, E. I. Ko, and J. A. Schwarz, *J. Catal.* **157**:244 (1995); (b) C. Contescu, V. T. Popa, J. B. Miller, E. I. Ko, and J. A. Schwarz, *Chem. Eng. J.* **64**:265 (1996).
141. (a) E. M. Arnett, in *Proton Transfer Reactions* (E. F. Caldin and V. Gold, eds.), Chapman and Hall, London, 1975, p. 88; (b) J. F. Wolf, P. Harch and R. W. Taft, *J. Am. Chem. Soc.* **97**:2906 (1975).
142. U. Fleischer, W. Kutzelnigg, A. Bleiber, and J. Sauer, *J. Am. Chem. Soc.* **115**:7833 (1993).
143. R. Spitz, J. Barton, M. Barteau, R. Staley, and A. Sleight, *J. Phys. Chem.* **90**:4067 (1986).
144. A. Gervasini and A. Auroux, *J. Phys. Chem.* **97**:2628 (1993).
145. (a) S. Kawi, J. R. Chang, and B. C. Gates, *J. Catal.* **142**:585 (1993); (b) S. Kawi, Z. Xu, and B. C. Gates, *Inorg. Chem.* **33**:503 (1994); (c) S. Kawi, J. R. Chang, and B. C. Gates, *J. Phys. Chem.* **97**:5375 (1993); (d) A. Zhao and B. C. Gates, *Langmuir* **13**:4024 (1997).
146. S. A. Rabo and G. J. Gajda, *Catal. Rev. — Sci. Eng.* **31**:385 (1989–90).
147. J. A. Rabo, *Catal. Rev. — Sci. Eng.* **23**:293 (1981).
148. A. G. Pelmeshnikov, R. A. van Santen, J. Janchen, and E. C. Meijer, *J. Phys. Chem.* **97**:11071 (1993).

149. L. Marchese, P. A. Wright, J. Chen, and J. M. Thomas, *J. Phys. Chem.* 97:8109 (1993).
150. P. Batamack, C. Dorieux-Morin, R. Vincent, and J. Fraissard, *J. Phys. Chem.* 97:9779 (1993).
151. L. Smith, A. K. Cheetham, R. E. Morris, L. Marchese, J. M. Thomas, P. A. Wright, and J. Chen, *Science* 271:799 (1996).
152. (a) J. R. Feldkamp and J. L. White, *J. Colloid Interface Sci.* 69:97 (1979); (b) R. D. Harter and J. L. Ahlrichs, *Soil. Sci. Soc. Am. Proc.* 33:859 (1969); (c) S. W. Karickhoff and G. W. Bailey, *Clays Clay Miner.* 24:170 (1974).
153. (a) K. Putyera, J. Jagiello, T. J. Bandosz, and J. A. Schwarz, *J. Chem. Soc. Faraday Trans.* 92:1243 (1996); (b) T. J. Bandosz, J. Jagiello, K. Putyera, and J. A. Schwarz, *J. Chem. Soc. Faraday Trans.* 93:3573 (1994).
154. (a) T. J. Pinnavaia, *Science* 220:365 (1983); (b) M. L. Occelli and P. M. Tindwa, *Clays Clay Miner.* 31:22 (1983); (c) S. Chevalier, R. Franck, H. Suquet, J. F. Lambert, and D. Barthomeuf, *J. Chem. Soc. Faraday Trans.* 90:667 (1994); (d) J. F. Lambert, S. Chevalier, R. Franck, H. Suquet, and D. Barthomeuf, *J. Chem. Soc. Faraday Trans.* 90:675 (1994).
155. W. Xu, Y. Yao, X. Xie, S. Liu, and T. Zhang, *Appl. Catal.* 75:33 (1991).
156. T. Hiemstra, J. C. M. de Wit, and W. H. van Riemsdijk, *J. Colloid Interface Sci.* 133:105 (1989).
157. C. Ludwig, P. W. Schindler, *J. Colloid Interface Sci.* 169:284 (1995).
158. K. Marshall, G. L. Ridgwell, and C. H. Rochester, *Chem. Ind. (Lond.)* 19:775 (1974).
159. W. Janusz, *J. Radioanal. Nucl. Chem., Articles* 125:393 (1988).
160. C. Contescu, unpublished results.
161. N. Sh. Petro, N. Z. Misak, and I. M. El-Naggar, *Coll. Surf.* 49:211 (1990).
162. M. Nabavi, O. Spalla, and B. Cabane, *J. Colloid Interface Sci.*, 160:459 (1993).

5

Electro-Optical Spectroscopy of Colloidal Systems

MARIA STOIMENOVA Institute of Physical Chemistry, Bulgarian Academy of Sciences, Sofia, Bulgaria

TSUNEO OKUBO Department of Applied Chemistry, Gifu University, Gifu, Japan

- I. Introduction
- II. Electro-Optical Effects in Suspensions of Spherical Particles
 - A. Electro-optical methods
 - B. Characterization of the samples
 - C. Electro-optical responses of spherical particles
 - D. Discussion
- III. Electro-Optical Effects in Suspensions of Anisometric Particles
 - A. Experimental results
 - B. Discussion
- References

I. INTRODUCTION

Colloidal electro-optical studies started with the discovery of the Kerr effect [1]. The theories of colloidal electro-optical phenomena were strongly influenced by the classical molecular electro-optics theory [2], particularly by the part concerning dipole molecules [3]. The latter explains the display of negative Kerr constants by the existence of permanent dipole moments perpendicular to the particle symmetry axis. The first formal theory [4] pretending to explain the extremely high values of the Kerr constant for colloids attributed them to particle volume. Experimental studies demonstrated that the processes causing electro-optical phenomena in colloids are much more diverse than those in molecular systems [5–8]. Deforming the ionic atmosphere surrounding the colloidal particle, the electric field, causes, on the one hand, particle electrokinetic motion (hence flow-induced particle orientation), while on the other hand it creates an induced dipole moment, i.e., polarization-induced particle orientation, the Kerr effect.

Low-frequency "anomalies" in the electro-optical responses of aqueous colloidal systems (sign reversal and accompanying deviations from Kerr behavior) have attracted scientific attention since the very beginning of colloidal electro-optical research. Starting in 1939 with the papers of Lauffer [9] on the tobacco mosaic virus, the phenomena were studied over the years on an impressive number of rigid colloids, biopolymers, polyelectrolytes, micelles, etc. [10–15]. This tendency continues to this day. It is sufficient to mention the systematic investigations on polyelectrolytes of Oppermann [16,17] and Kramer and Hoffmann [18], the numerous interesting results of Jennings et al. [19] and Hoffmann and coworkers [20,21] on micelles, the theoretical schemes on self-assembled rod-shaped particles [22], the attempts to find a model sample for analysis of the electro-optical phenomena [23], the impressive pictures obtained on gels concerning gel electrophoresis [24], as only a part of this activity. Actually, the history of colloidal electro-optics is a history of the investigations on the low-frequency electro-optical "anomalies."

The experimental observations gave birth to a series of theories competing to explain the phenomena. Treating the peculiar concentration dependencies of the low-frequency electro-optical responses, Lauffer was the first to indicate their more general character, citing the similar results on rod-shaped [9] and disk-shaped [25,26] particles and advancing the concept of "interaction forces." In the subsequent treatments of Sackmann [27] and Rabinovich [28], the colloidal surface double layer was considered responsible for the sign-reversal phenomena. Further, various concepts of particle properties and interaction forces were proposed to explain their origin: permanent dipoles, either inherent [29,30] or induced by interactions [31], asymmetry of surface charge [32], field-induced deformation [16,17], optical interactions [33], interaction-enhanced transverse conductivity [20,21], cluster orientation [34], etc.

The sign-reversal phenomena in the semidilute regime were demonstrated experimentally on a large variety of samples: rigid and flexible, of varying and constant size and axis ratio, and of various forms from disks to rods. In our recent papers we extended this list, reporting observations of similar effects on suspensions of rigid isotropic spherical particles [35,36]. Evidence was presented for the electroacoustic origin of the observed effects. Since all theoretical schemes constructed to explain the electro-optical sign reversal are based on the assumption of transverse particle orientation (or deformation), our results concern an essential problem in the understanding of the phenomenon. The observation of such effects on a stable suspension of isotropic particles signifies that particle optical anisotropy (or deformability) is not a necessary condition for the display of sign reversal. Actually, the basic concept applied in the analysis of colloidal electro-optical phenomena is their assignment to anisotropy fluctuations (Kerr effect or electrophoretic orientation), directed translation modes being ignored.

In the last decade the electroacoustic waves in colloids [37] attracted considerable attention. Electrically induced concentration fluctuations were detected by means of different experimental techniques. The Bragg diffraction technique was used to analyze the concentration gradients induced in colloidal crystals by dc electric pulses [38]. Density fluctuations in ac electric fields were observed with time-resolved reflection spectroscopy and transmitted light spectroscopy [39,40]. The conventional light scattering was also applied to detect the induced translation

modes [35,36]. Our research is directed to the possibility that they could grow to be large-scale and very significant in the hydrodynamic frequency range and could influence the optical response of the system both directly and through acoustic orientation of the particles. Thus for interacting systems self-orientation and collective orientation modes are coupled with self-translation and collective translation modes, resulting in a complicated frequency behavior of the electro-optical responses. Although the precise mechanism of low-field electro-optical sign reversal is not yet well understood and our studies are in the initial stage, we shall try to demonstrate here the close similarity of the electro-optical behavior in the hertz range of spherical and anisometric particles, hence the importance of electro-acoustic modes for the electro-optical anomalies in charged colloids.

An essential feature of this study is the choice of model samples. They are rigid particles in highly stabilized suspensions (liquid and crystal phases), hence interference of field-induced deformation and aggregation of particles is avoided. The highly monodisperse isotropic spheres are amorphous silica, thus neither form nor intrinsic optical anisotropy can be related to the particles, and surface effects attributed to latexes are also avoided. The anisometric particles are thin rods of the clay mineral paltgorskite of axis ratio 20. The sample is polydisperse, and its basic advantage is the great amount of electro-optical data accumulated in the course of its application as a model for research into the origin of the electro-optical phenomena. It displays a very large Kerr effect at high dilution and all features of low-frequency anomalous behavior in the semidilute regime.

The electro-optical responses of colloidal systems were detected by reflection spectroscopy and by the variations of scattered light intensity. Induced variations in the reflection spectra of colloidal crystals turned out to be very sensitive to electroacoustic effects, while the experimental setup of the second method permits direct comparison with numerous data on anisometric colloids. Investigations into reflection spectroscopy were carried out by Okubo and coworkers at Gifu University (Japan), and the light scattering studies by Stoimenova, Okubo, and coworkers at the Bulgarian Academy of Sciences. The essential parts of the results are due to our joint research.

II. ELECTRO-OPTICAL EFFECTS IN SUSPENSIONS OF SPHERICAL PARTICLES

A. Electro-Optical Methods

1. General Aspects

Conventionally the electro-optical effects of non interacting colloidal systems are presented by the statistical average of the product of the optical effect of a single particle $P(\Sigma_i)$ and the orientation distribution function Ω [40]:

$$a = \langle P(\Sigma_i) \Omega \rangle$$

where the optical part is a function of the components of the particle-scattering matrix. Thus, for field-induced birefringence and dichroism, the optical factor is determined by the diagonal elements of Σ_i at forward scattering:

$$A_n \approx [\text{Im}\Sigma_2(0) - \text{Im}\Sigma_1(0)]$$

$$A_n' \approx [\text{Re}\Sigma_2(0) - \text{Re}\Sigma_1(0)]$$

while the induced variations of scattered light intensity are followed by any preferred combination of the components (i.e., of light polarization) as a function of the observation angle:

$$\Delta I = I_E - I_0 \approx \Delta(|\Sigma_i(\theta)|^2)$$

For example, for light scattering observed from the side

$$\Delta I \approx \Delta(|\Sigma_i(90^\circ)|^2)$$

and for backward scattering.

$$\Delta I \approx \Delta(|\Sigma_i(180^\circ)|^2)$$

The above presentation illustrates the similar bases of the electro-optical methods [1]. The components of the scattering matrix can differ in their sensitivity to the various sources of particle anisotropy, but they yield similar information on the induced anisotropy fluctuations, particularly on their relaxation. This scheme is true in so far as noninteracting particles are concerned. Though the correlations in particle orientation [42] have been accounted for in recent electro-optical theories, the influence of the applied field on the space distribution of the scattering elements is generally neglected.

In interacting systems the optical and orientation factors are no longer separable quantities. The induced optical effect is determined both by the single particle scattering [form factor $P(q)$] and by the pair distribution function [structure factor $S(q)$], the latter being direction-dependent [42]. Since in addition to orientation the electric field causes particle translation, even for spherical particles the radial distribution function $g(q, t)$ and the "static" structure factor attain time-dependent induced anisotropy. The deformed surface potential also contributes to this effect.

Formally introducing modified values for $P(q)$ and $S(q)$ (in the general case the process involves nonequilibrium quantities), we can write for the steady-state electrical light scattering,

$$I_E \approx P_E(q)S_E(q)$$

The field-free decay of the electro-optical response, displaying relaxation of the induced anisotropy, can then be related to the dynamic structure factor,

$$S_E(q) = \frac{F_E(q, t)}{g_E(q, t)}$$

In the ideal case of noninteracting particles [$S_E(q) = S_0(q) = 1$]. $F(q, t)$ is the self-dynamic structure factor that describes the single-particle motion [for spheres, $P(q)$ is constant and no electro-optical effect is observed]. In the presence of interactions (including field-induced interactions), the decay process contains information on all single and collective motions caused by the field. The latter can be enhanced by appropriate choice of the applied field frequency and by the pulse duration. Basic

factors in this process are the area of observation (considerations with respect to this factor are similar to those presented for the photon correlation spectroscopy) and the pulse duration. The latter quantity actually determines the number of experimentally detected dynamic modes.

2. Electrical Light Scattering

The light scattering observations of the electrically induced changes in the colloidal systems were performed on a conventional apparatus used in numerous experiments on the anisotropic colloidal systems [43].

The measuring cell is shown schematically in Fig. 1. Attached to a sled, the cell is placed in a metal thermostated box. The movement of the sled in the box is restricted in the direction of the incident light beam. Scattered light intensity is measured at an observation angle of 90° using a photomultiplier or oscilloscope registration. The electric pulses are applied perpendicularly to the observation plane. The electrodes are platinum plates of radius 5.5 mm at a distance of 2.6 mm apart. The volume of the cell is about 10 mL, the diameter is 18 mm, and the distance between the front cell wall (of incidence) and the electrodes is about 5 mm.

The scattered intensity of the unperturbed system (I_0) is compensated, and the field-induced light-scattering variations ($\Delta I = I_E - I_0$) with time are observed directly on the oscilloscope. The dc component of the effect, ΔI is determined taking for I_E the middle of the modulated steady-state signal, the ac component – by the amplitude of the steady-state oscillations. The results presented in this chapter were obtained by the use of white unpolarized light.

Besides the advantage of direct comparison with previously obtained results, the construction of this cell permits the observation of propagating acoustic modes in the crystal colloidal samples.

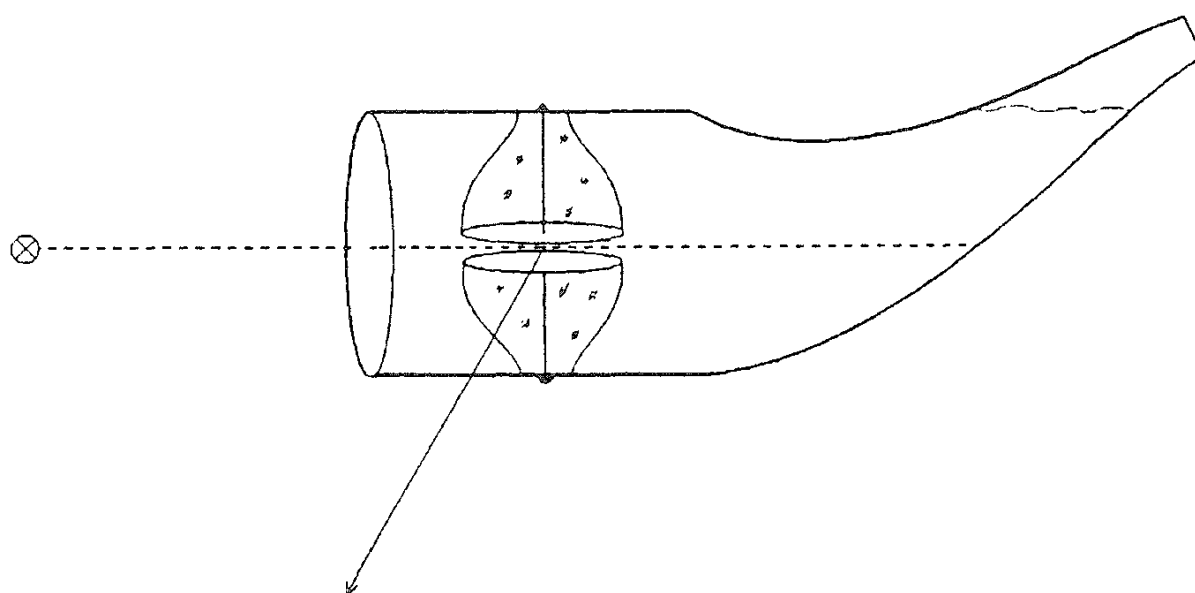


FIG. 1 Scheme of the measuring cell for electrical light scattering.

3. Electrical Light Reflection

Field-induced variations of reflected light intensities and spectra were recorded by the use of Y-type optical fiber cables. The measuring cell (rectangular, 248 x 185 mm) contains two parallel glass plates coated inside with electrically conducting membranes (Sanyo Shinku Kogio Co., Tokyo). The optical pathlength is 3 mm. The incident beam, (from a tungsten lamp) is introduced into the cell parallel to the electric field by a fiber cable, and reflected light is led in the same way to a photomultiplier/oscilloscope registration. The time-resolved reflection spectra were recorded on a PMA-50 photonic multichannel analyzer (Hamamatsu Photonics, Hamamatsu).

B. Characterization of the Samples

Highly monodisperse spherical particles were the main object of our studies. The colloidal silica spheres CS-81 and CS-91 used in the investigation are products of Catalyst & Chemicals Ind. Co. (Tokyo). By electron microscopy (TEM, JEOL Type JEM-2000FX), the spherical mean diameter and standard deviation were determined to be 103 ± 13.2 nm for CS-81 and 110 ± 4.5 nm for CS-91. The charge density of strongly acidic groups on the spheres determined by conductometric titration with a Wayne-Kerr autobalance precision bridge were 0.38 and $0.48 \mu\text{C}/\text{cm}$, respectively. Before use the samples were purified with an ultrafiltration cell and treated continuously on a mixed bed of cation- and anion-exchange resins [Bio-Rad, AG501-X8(D), 20-50 mesh]. The same resins were used for the deionization of water needed for the suspension preparation. The suspensions were obtained by dilution of the stock solution with water and were further kept in contact with the ion-exchange resins for a week in order to achieve the crystal state (conductivity below 10^{-6} ohm $^{-1}$ at 25°C). Crystals in the dilute suspensions were very large [44,45], which is an advantage for light scattering observations of the dynamic modes.

Turbidity of liquid like and crystal-like suspensions is very low compared to that of gaslike systems due to the diminished intensity of multiple scattering for visible light. Particularly low turbidity is observed for highly dilute and exhaustively deionized samples [46]. This made it possible to follow the static and dynamic light scattering behavior of the silica suspensions in gaseous, liquid, and crystalline states [47]. Data analysis was performed with the cumulant and histogram methods including Marquadt analysis. A single exponential decay was found only in the colloidal gases, corresponding to free particle translation diffusion. The diffusion coefficient is always lower than the value calculated with the Stokes–Einstein equation with the true diameter of spheres and correlates well with the effective diameter including the Debye atmosphere. The liquid samples display bimodal decay, corresponding diffusion coefficients (differing by a factor of 3) being related to short- and long-term self-diffusion of particles. The static light-scattering variations for the crystal state display very sharp peaks in their scattering vector dependence. The analysis of crystal structure dynamics yields three apparent diffusion coefficients that differ from each other by an order of magnitude: the basic one related to particle (restricted) Brownian diffusion, a slow mode assigned to propagating

shear waves in the crystal lattice, and a fast term possibly related to particle–electrolyte interactions.

C. Electro-Optical Responses of Spherical Particles

Typical electro-optical responses of the suspensions of spherical particles (CS81), recorded by the scattered light intensity are presented in Fig. 2. They are detected for the crystal state of the systems and for different intensities and frequencies of the applied sine-wave electric pulses. The low-frequency responses are modulated; they follow the field frequency at sufficiently low field intensity and exhibit a double frequency modulation at higher field intensity. Two different time scales are involved in the decay of the responses (10^{-4} and 1 s), which can be both exponential and oscillatory. At higher field intensity or frequency the effects cannot be distinguished by the responses of anisotropic colloids.

Figure 3 presents the frequency dependence of the electro-optical effects for suspensions of different volume fractions of spherical particles. The stock solution (8% sphere volume fraction) is highly deionized, and dilution is carried out with deionized water. Thus the highly dilute samples are in the liquid-phase state. Modulated responses are detected at low frequencies — for highly dilute samples

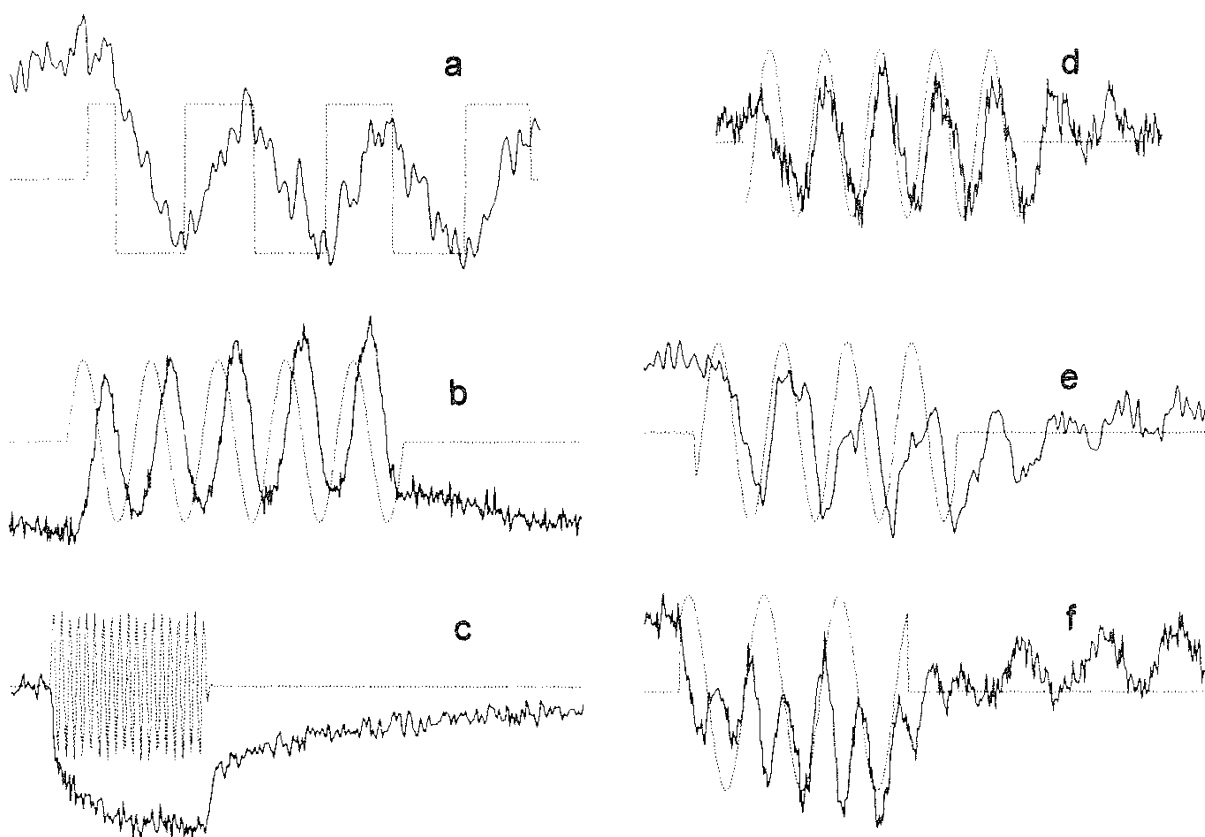


FIG. 2 Electrical light scattering (ELS) responses from highly deionized suspensions of silica spheres CS81 of volume fraction 1% (dotted line, electric field). (a) 5 Hz, 15 V/cm; (b) 0.5 Hz, 15 V/cm; (c) 1 kHz, 400 V/cm; (d) 10 Hz, 30 V/cm (outside the electrodes); (e) 10 Hz, 60 V/cm; (f) 10 Hz, 120 V/cm.

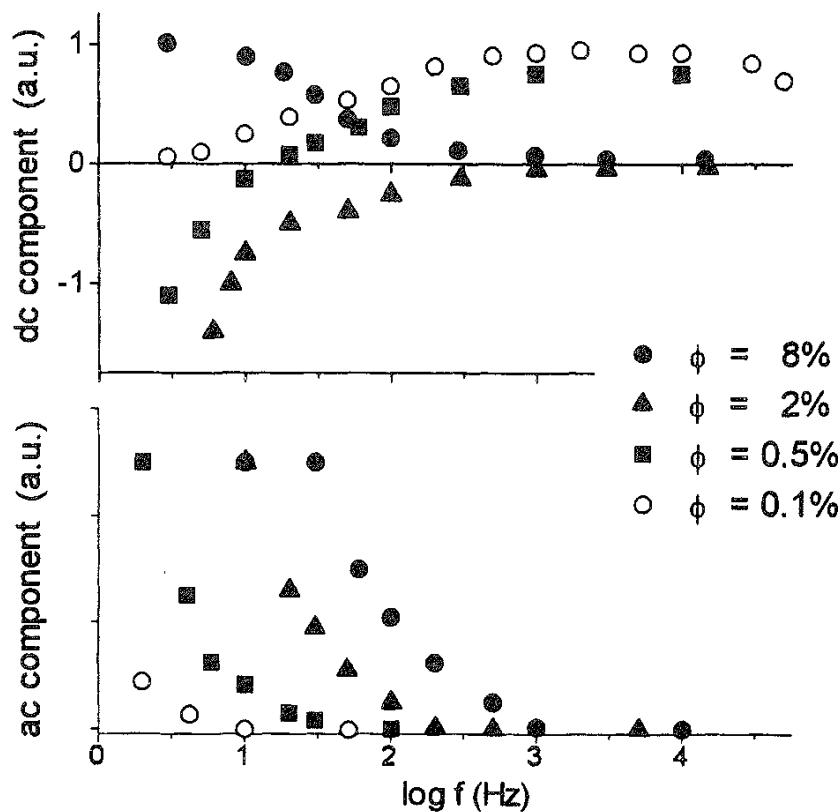


FIG. 3 Frequency dependence of the ELS responses from deionized suspensions of CS81 (field intensity 200 V/cm) for different sphere volume fractions.

(0.1%), below 1 Hz; for semidilute samples they cover the hertz interval, increasing to higher frequencies with increasing volume fraction. In parallel a dc component is observed, which, depending on volume fraction and ion content, can cover the entire frequency range (up to 100 kHz), typically related to orientation effects. In the semidilute regime the low-frequency sign reversal is observed, in close similarity to the low-field responses of anisotropic systems. At higher sphere concentrations (above 5% volume fraction), the responses are again positive.

The field intensity dependence of the ac and dc components of the responses in the intermediate concentration range are complicated: linear at very low fields and quadratic or rapidly saturating at higher fields [35]. On a larger scale they show oscillatory behavior. In Fig. 4 they are shown for the transition concentration of 0.5% sphere volume fraction for moderate field intensities. The ac component increases with field intensity and can be observed up to higher frequencies. Modulated signals are obtained up to 100 Hz, i.e., in the range of the negative dc component.

Figure 5 shows typical responses for this particular sample (0.5% sphere volume fraction). A basic difference in the electro-optical behavior of spherical compared to anisometric particles is the linear response at low field intensity. The modulated signal follows the frequency of the applied field with a phase difference of -90° . With an increase in frequency the ac component relaxes, changing in both amplitude and phase and passing to double frequency, while the dc component changes

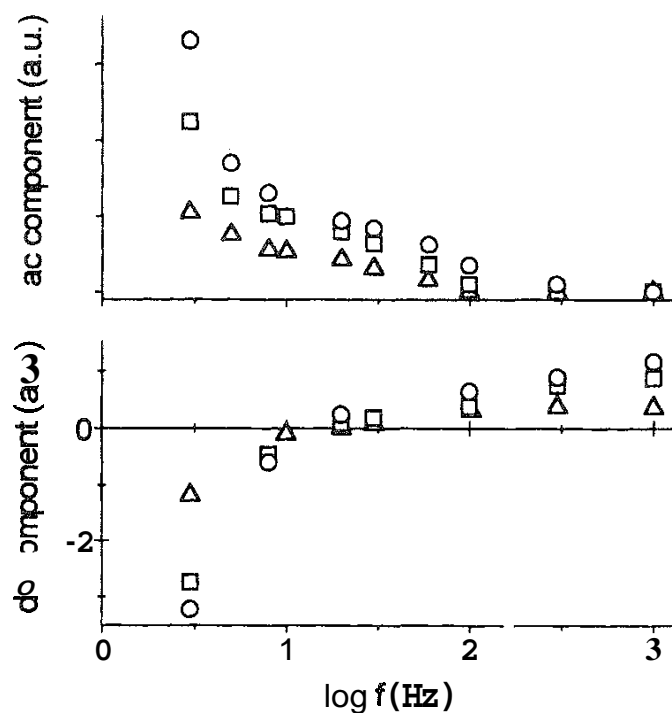


FIG. 4 Frequency dependence of the ELS responses from deionized suspensions of silica spheres (sphere volume fraction 0.5%) for different field intensities. (\triangle) 150 V/cm; (\square) 300 V/cm; (\circ) 420 V/cm.

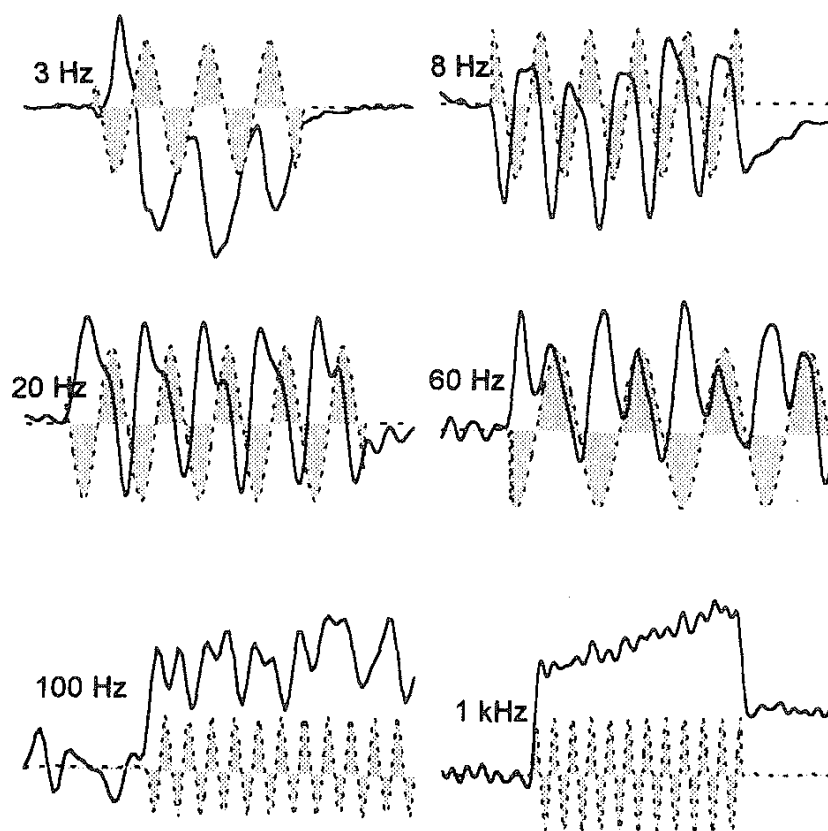


FIG. 5 ELS responses from deionized (liquid-state) suspensions of CS81 of volume fraction 0.5% (dotted line, electric pulses).

from a negative value to a small positive value. The decay process displays two basic relaxation times: one, associated with the positive kilohertz effect, on the order of milliseconds and the second, related to the low-frequency modulations, on the order of seconds. Additional slower modes can be observed upon application of longer pulses, as can be seen in the kilohertz response. This figure concerns the liquid state of the sample.

The electro-optical responses are strongly dependent on the phase state of the colloidal system. The transition of the same sample from the liquid to the crystalline state is accompanied by a considerable increase in the cutoff frequency of the ac component and a displacement of the dc curve to more negative values (Fig. 6). Similar variations can be observed by increasing of the sphere volume fraction, as demonstrated in Fig. 3, which shows that the effective volume fraction determines the process. In parallel, additional modes are observed to appear in the crystalline state. They introduce resonance peaks at frequencies depending on the sphere volume fraction (two volume fractions are presented in Fig. 6).

Typical responses of the crystal samples were shown earlier in Fig. 2. Below 1 Hz they are similar to the responses of the liquid phase (Figs. 2a and 2b) and are evidently related to induced longitudinal density waves. At low fields they follow the field frequency (Figs. 2d and 2e), and at higher fields a harmonic frequency appears (Fig. 2f). In the interval 1–100 Hz the responses show oscillatory decay. Estimating the parameters involved, we identified this mode as related to shear waves propagating in the crystal lattice [36]. Hence the registered peak frequencies are a relative measure of the elastic modulus of the system. The kilohertz effect is of reversed sign and displays distinctly two relaxation rates (Fig. 2c). The first one

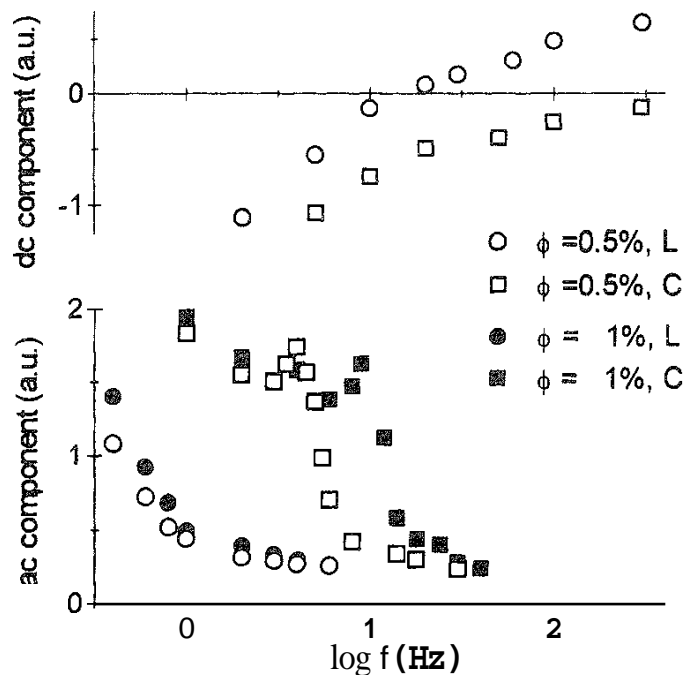


FIG. 6 Frequency dependence of the ELS responses from deionized suspensions of CS81 (field intensity 200 V/cm) for different sphere volume fractions at liquid and crystal states of the sample.

(milliseconds) is most probably related to particle self-diffusion, and the second one (on the order of seconds) concerns collective motion.

Detecting the scattered light while moving the measuring cell in the direction of the incident light beam permitted the observation of propagating shear waves in the cell outside the electrodes for the crystal samples [36]. The phenomenon is illustrated in Fig. 7, where the formation of standing waves upon application of lattice self-resonance frequencies can be observed.

Systematic investigations of the induced density waves in suspensions of silica spheres (CS91) in the low-frequency range (0.02–10 Hz) were performed by the use of light reflection techniques [48]. X–Y type plots and Fourier transforms of the reflection signals demonstrated the phase variations with both field frequency and intensity for a different experimental setup (incident and scattered light along the field direction). Detected phase changes seem to be relevant to inherent properties of the samples. Despite the differences in the phase variations of the responses obtained by the two techniques, a basic feature of the effects is preserved. In the linear low-field regime the electro-optical effects of aqueous systems display no harmonic components; the increase of field intensity changes the phase of the response and induces a double frequency component. The picture is quite similar to the responses obtained by electrical light scattering (Fig. 8).

Since time-resolved reflection spectroscopy allows for a more detailed study of the reflected intensity, it was used to investigate the origin of the harmonic

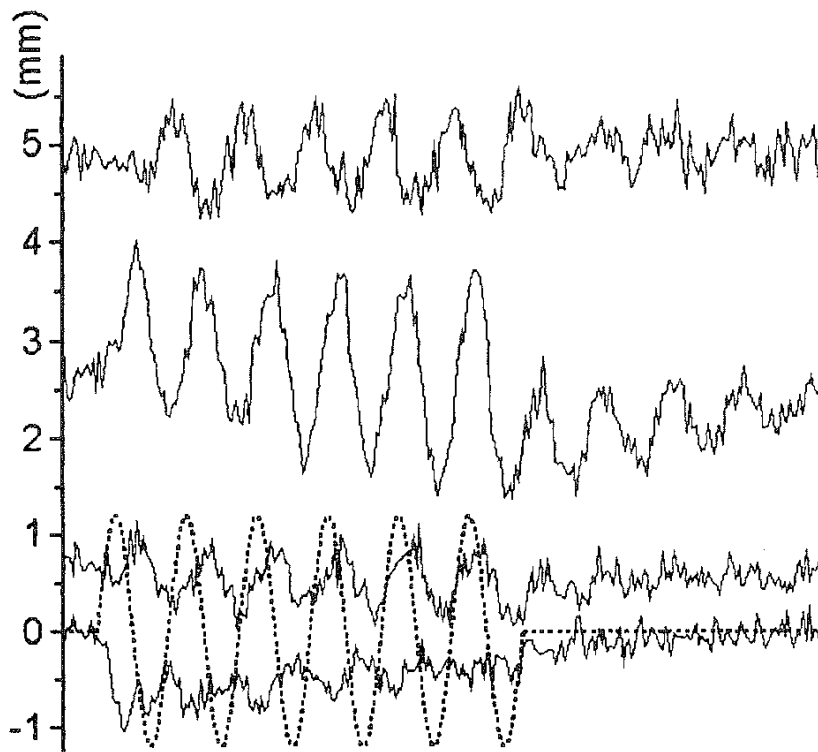


FIG. 7 ELS responses from deionized (crystal-state) suspensions of CS81 of volume fraction 1%, detected at different distances from the electrodes (dotted line, electric pulses; 0 mm denotes the center of the electrode space). (Adapted from Ref. 36.)

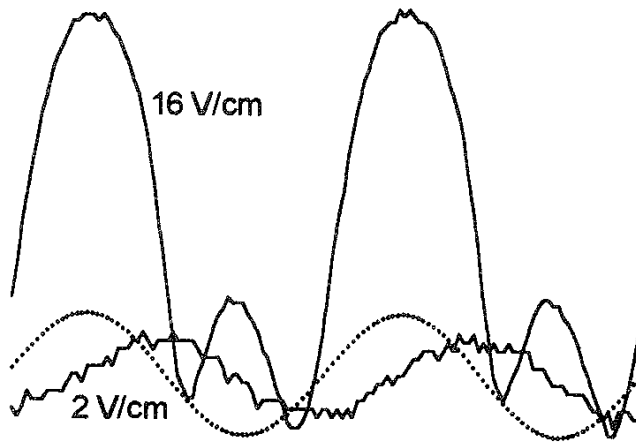


FIG. 8 Electric reflection (ER) responses from deionized (crystal-state) suspensions of CS91 of volume fraction 4.4% for pulses of 0.2 Hz and different field intensities (dotted line, electric field).

component in the electro-optical response [48]. Detailed investigations of the spectra of the responses of silica spheres in water and other solvents of different conductivity demonstrated that the method is informative for the analysis of the acoustic modes in colloids. [Figure 9](#) shows schematically the variations of the reflection spectra in the course of one cycle of the applied sine-wave electric field. They are compared to variations in the integrated reflected intensity. From the changes in the peak wavelength it is clear that the basic process at higher fields remains the same: oscillation of interparticle distance, i.e., density waves. A difference is seen in the variation in the integrated reflected intensity. While the peak wavelength variation follows the field frequency, the integrated intensity shows double frequency modulation. The transition between the extreme wavelengths is strongly asymmetric. The asymmetry is evidently due to different decay rates of the densified and rarefied states to equilibrium. The line half-width increases (particularly in the process of rarefaction), most probably due to reduced correlation length. The results obtained by reflection spectroscopy demonstrate that a double frequency optical response can be obtained by the electrically induced translation modes as well. The origin of the dc component (including sign reversal) can find similar explanation.

D. Discussion

Theoretical analyses predicted the propagation of low-frequency shear waves in both semidilute polymer solutions [49] and dilute colloidal crystals [50]. Different experimental techniques were applied for their detection and for the determination of the shear modules of colloidal samples [51–54]. The dispersion equation of the transverse waves for the low-frequency regime (wavelengths much larger than the interparticle distance) [55]

$$\omega^2 + i(\eta/\rho)\kappa^2\omega - (E/\rho)\kappa^2 = 0$$

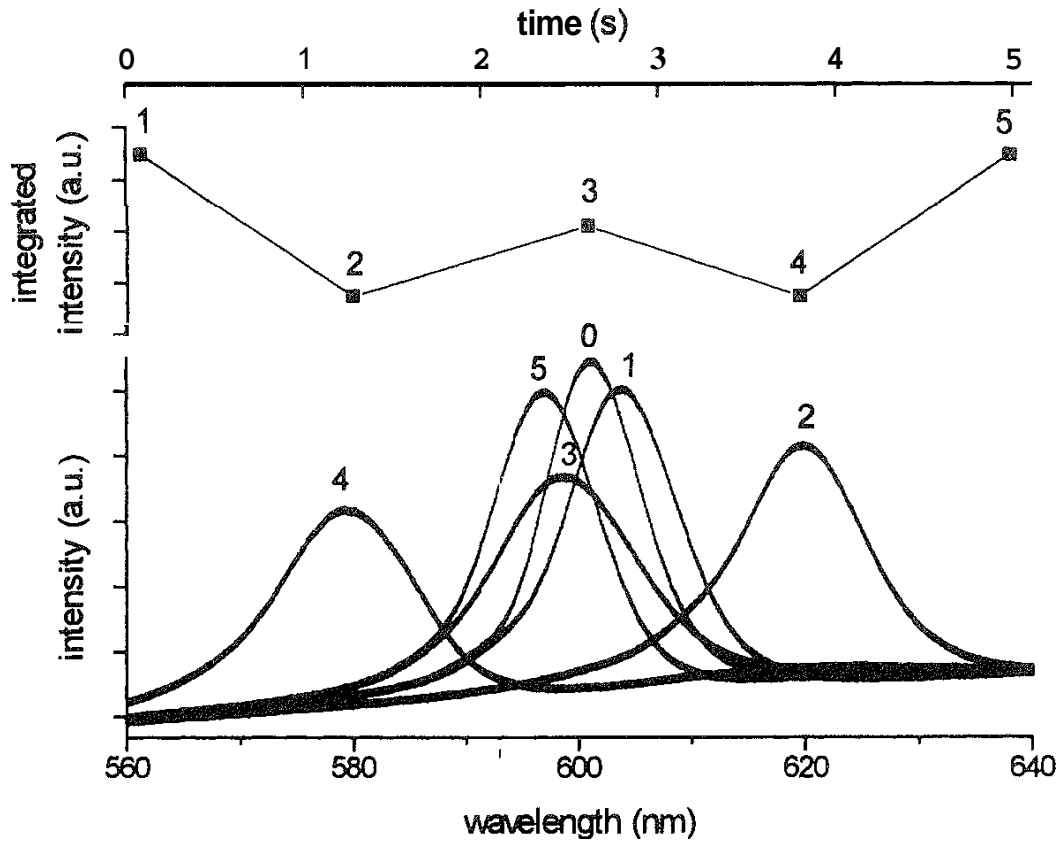


FIG. 9 Time-resolved reflection spectra for one cycle of the applied field (0.2Hz, 16 V/cm) for a deionized (crystal-state) suspension of CS91 of volume fraction 4.4%. Upper figure: Corresponding integrated intensities. (Adapted from Ref. 48.)

where $\rho (= 1 \text{ g/cm}^3)$ is the mass density, $\eta (= 10^{-2} \text{ poise})$ the viscosity of the solvent (water) and E the shear modulus of the sample.

For the volume fractions presented in Figs. (3–6) the shear modulus is on the order of 10 dyn/cm and the sound velocity $V (= \sqrt{E/\rho}) \cong 1\text{--}5 \text{ cm/s}$. The microscopic relaxation time $\tau (= \eta/E) \cong 1\text{--}10 \text{ ms}$, and the attenuation length $\lambda [= (\text{Im}\kappa)^{-1} = 2V/\omega^2\tau] \cong 1\text{--}10 \text{ cm}$. For frequencies below 1 kHz the dissipation is small and the shear waves are propagating. The dimensions of the measuring cell encourage the formation of standing waves.

The observed resonance-like behavior of our samples corresponds to the expected parameters of induced shear waves, thus giving evidence for the origin of the electro-optical effect. The decay rate of this mode corresponds to the slow mode detected by dynamic light scattering in the unperturbed system [47]. In the general case the analysis of light intensity scattered by electrically induced fluctuations would be complicated. It depends strongly on the area of observation. If the latter is sufficiently small, local density fluctuations are detected at low frequency and scattered intensity follows directly the variations in the acoustic pressure. For the gaseous state of the samples in the low-field regime it can be presented using O'Brien's equation [56,57]

$$\Delta\epsilon (\approx AP) \approx \phi(\Delta\rho/\rho)V$$

where ϵ is the system's complex dielectric constant, ϕ is the particle volume fraction, $\Delta\rho/\rho$ is the particle relative density, and V is the particle velocity in the applied field. An additional term should be written to account for the entropy fluctuations, which are evidently significant in the liquid state of the samples. The introduction of Coulomb interactions will add to the above equation terms accounting for correlations.

At higher frequencies, small-scale motions become predominant and light scattering is determined by average fluctuations. Higher field intensities (conventionally used to obtain electro-optical saturation) introduce nonlinear effects such as polarization of the system and interaction of acoustic waves. Thus the more general picture can become highly complicated. Nevertheless, the above equation displays several basic features of the process compared to Kerr electro-optical behavior. First, it predicts the linear dependence of the process on particle velocity, hence on field intensity and particle electrokinetic potential. It involves frequency-dependent particle mobility, which enhances significant phase variations of the optical response. Further, interparticle interactions could induce a considerable transverse component of particle mobility, thus giving rise to transverse density waves. Next, the equation predicts dependence on particle relative density that is much stronger than that expected for anisotropy fluctuations. Particle volume fraction influences the process both directly and through interactions. As can be seen from the figures, the electro-optical responses of spherical particles display the basic features of the low-frequency effects in anisometric colloids.

III. ELECTRO-OPTICAL EFFECTS IN SUSPENSIONS OF ANISOMETRIC PARTICLES

A. Experimental Results

Several figures are presented in this section to illustrate the similarity of the low-frequency behavior of spherical and anisometric particles. They were obtained by a conventional electro-optical method (electric light scattering) on a typical and well-studied colloidal sample [15,58,59]. The anisometric particles are rigid rods of the clay mineral palygorskite (attapulgate). Their average length and diameter are 200 nm and 10 nm, respectively. Particle surface charge in the aqueous suspensions is about $0.7 \mu\text{C}/\text{cm}^2$. A more detailed investigation of the sample is presented in Refs. 58–60.

Figure 10 is a typical picture of field intensity and frequency variations of the electro-optical responses of highly dilute aqueous colloids. The frequency curves of the anisotropic particles (below the overlap concentration) are significantly different from those of the spheres, due to the large effect in the kilohertz range. The decay of the responses of the investigated sample is nearly exponential, the time constant of several milliseconds (2–7 ms) corresponding to particle rotational diffusion. A tail on the order of 50 ms can still be detected. The high-frequency relaxation is proved to be related mainly to surface polarization of the particles, which causes their orientation. The low-frequency relaxation interval coincides with the cutoff frequency of the ac component (hydrodynamic range), where large variations

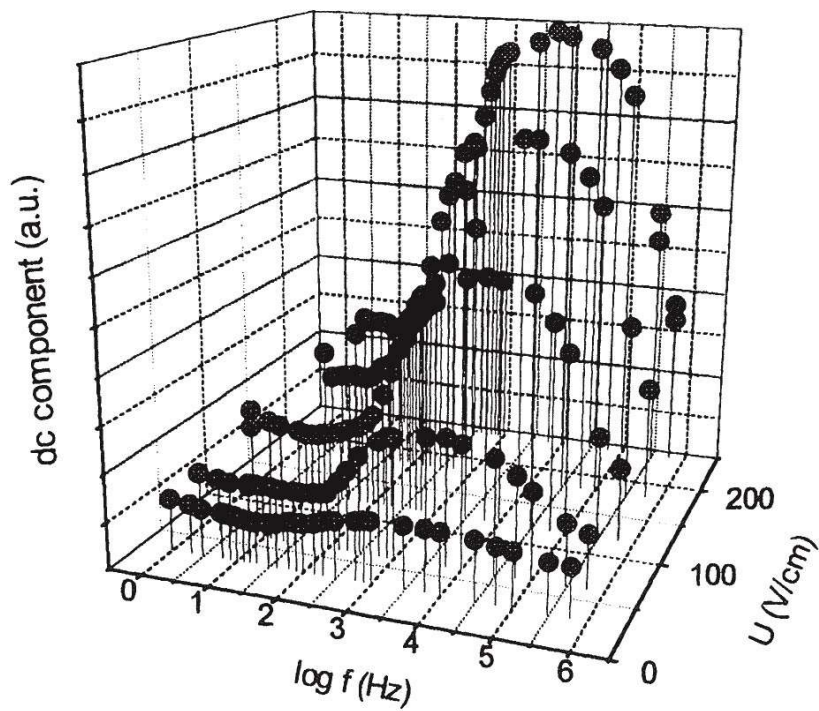
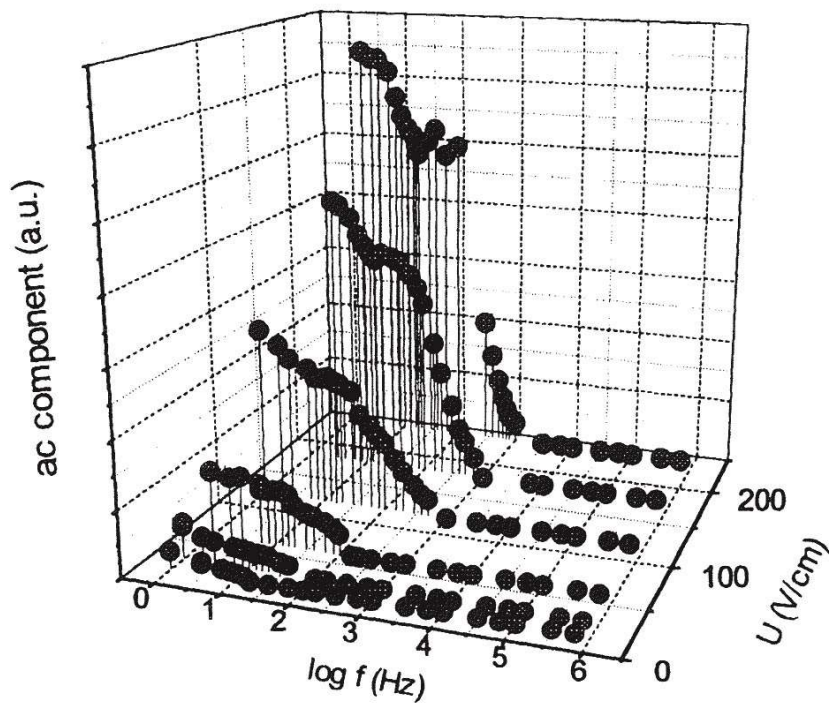


FIG. 10 Variation of the electro-optical responses of a highly dilute palygorskite suspension (volume fraction 0.001%) with frequency and intensity of the applied electric field.

in the effects (including sign reversal) are displayed in the semidilute regime or upon modifications of the ionic content of the systems.

Deionization of the sample for 1 month induces changes in the frequency curves as shown in Fig. 11. The decay of the kilohertz effect is biexponential. The short time, corresponding to self-rotation, remains almost unchanged (several milliseconds), and the long time increases drastically (200 ms), indicating collective rotation (further deionization of the sample diminishes the amplitude of the effect and further separates the time constants). The deionized suspension clearly shows a twofold relaxation of the ac component. The cutoff frequency of the latter increases similarly to the corresponding effect for spheres, and the width of the kilohertz line is reduced, as is typical of correlated motions. This is a basic feature of the considered low-frequency anomalies that is difficult to explain adequately by a transverse orientation scheme, since it is accompanied by a significant increase in the decay time of the responses. On the other hand, at low ionic strength, short-range orientation ordering can be observed in such systems far below the overlap concentration. It is accessible to static light-scattering observation, as demonstrated by the peaks in the static structure factor of tobacco mosaic virus samples under similar conditions [61].

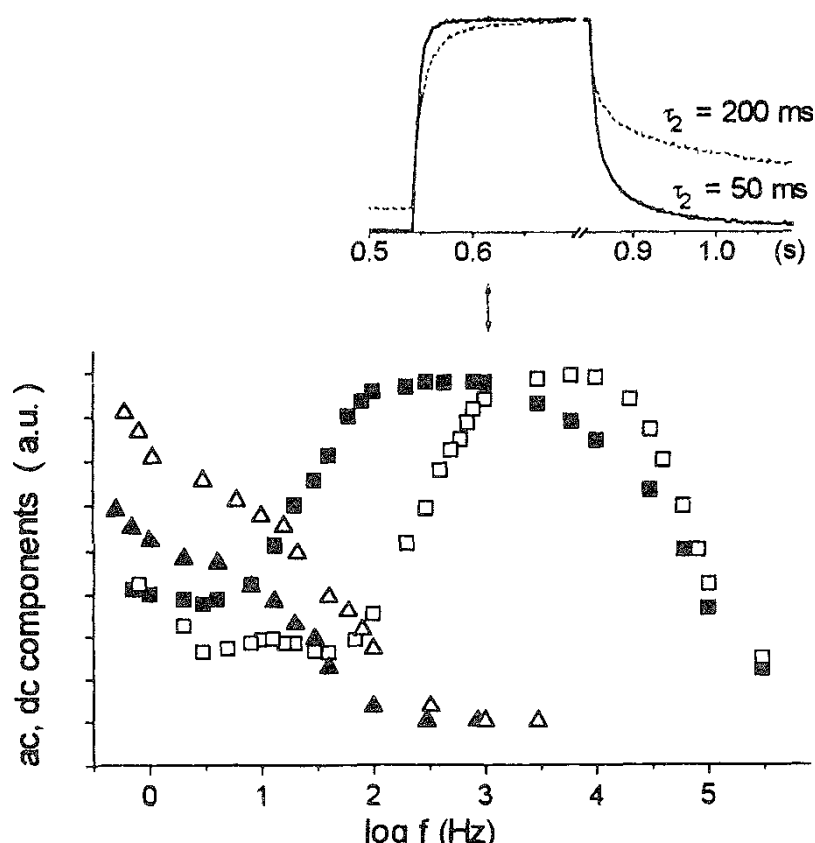


FIG 11 Frequency dependence of the ELS responses of a dilute palygorskite suspension (volume fraction 0.01%) for different ionic strengths of the sample ([■, □] dc compound; [▲, △] ac compound; filled symbols, 10^5 M NaCl; open symbols, about 10^{-6} M NaCl). Upper diagram: Electro-optical responses of the sample at field frequency 1 kHz (dotted line, deionized).

At low fields the quadratic and linear dependence of the effects in the two frequency ranges are clearly distinguished (Fig. 12). Modulated effects are observed up to 100 Hz, and they are asymmetric. The amplitude of the dc component displays a deep hollow around the same frequency, reaching to sign reversal.

Approaching the overlap concentration of the rods, the amplitude of the kilohertz response is reduced considerably and the sign reversal is observed at higher electrolyte concentration. Figure 13 is for a sample of ionic strength 10^{-5} MNaCl. The same sign reversal for the same sample, obtained by increasing the particle volume fraction, was reported in our previous papers [58,59]. Similarly to the effects of spheres, the effective particle volume fraction determines the process. Responses of the sample to dc pulses in the same range of field intensities are shown in the same figure. The decay time constants are strongly dependent on pulse duration. At pulse lengths below 100 ms the time constants extracted by biexponential fitting of the decay are approximately 1 and 60 ms. The increase in pulse length leads to multiexponential decay involving additional slow modes. Further deionization of the sample annihilates the Kerr line and turns the low-frequency effects positive, stable, and single-frequency [60]. They are similar to the

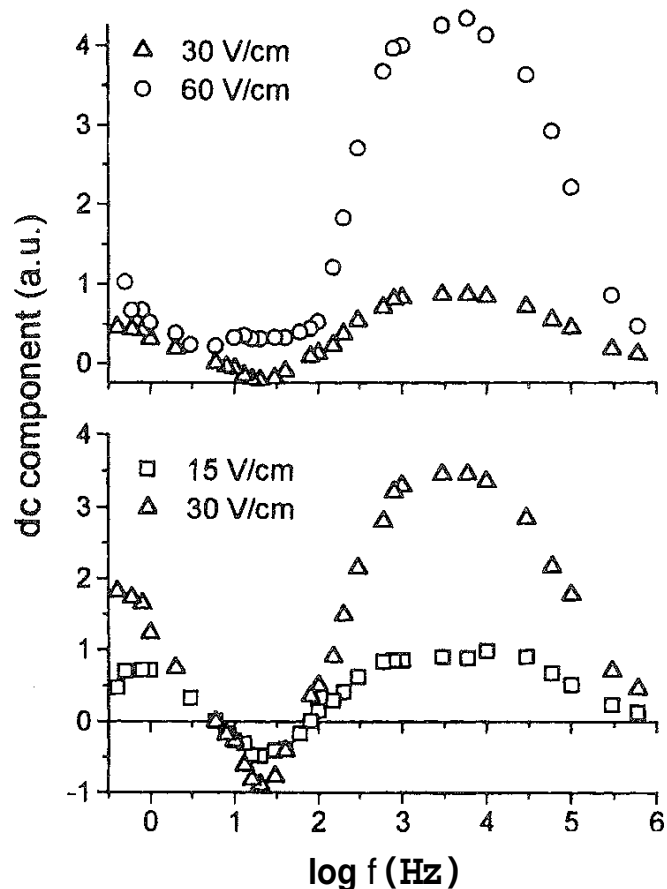


FIG. 12 Frequency dependence of the steady component of the ELS response from palygorskite suspension (volume fraction 0.01%) for different intensities in the low-field range.

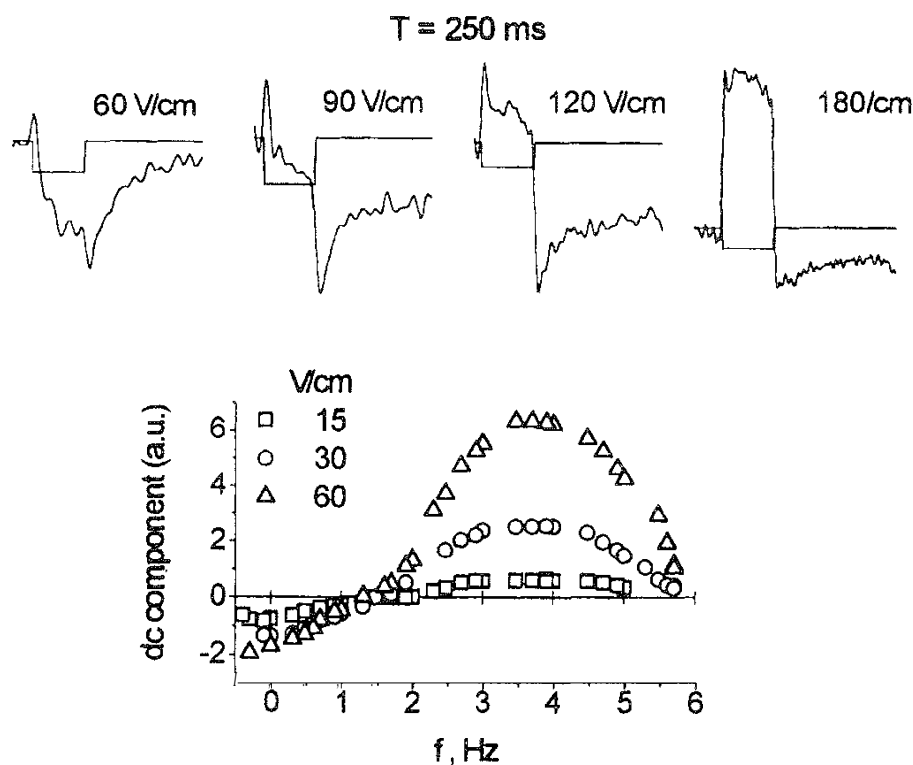


FIG. 13 Frequency dependence of the steady component of the ELS response from palygorskite suspension (volume fraction 0.15%) for different intensities in the low-field range. Upper figures: ELS responses to dc pulses.

effects shown by the more concentrated silica samples. [Figure 14](#) shows several typical responses of the anisometric particles.

B. Discussion

Generally speaking, three frequency ranges are clearly distinguished in the electro-optical dispersion curves of anisometric particles:

1. Below 1 Hz — the range of large-scale density fluctuations, which are not averaged in the optical response and can be detected both directly and by the induced flow orientation
2. The region around 100 Hz — on the order of particle reorientation frequency, where translation motions reduce particle orientation
3. The Kerr line, which dominates at higher fields but only until the particle self-rotation is not restricted by interaction forces

Hence, two basic factors are to be taken into account in the analysis of electro-optical data. First is the pulse duration. At certain values of the pulse length the response shows steady-like behavior, which is due to the separation of the time scales involved and the restricted sensitivity of the optical response to induced changes in the system. Second is the choice of frequency range for the determination of the Kerr constant. The latter is related to the low-field regime, where the acoustic modes contribute significantly. Adequate separation of orientation and

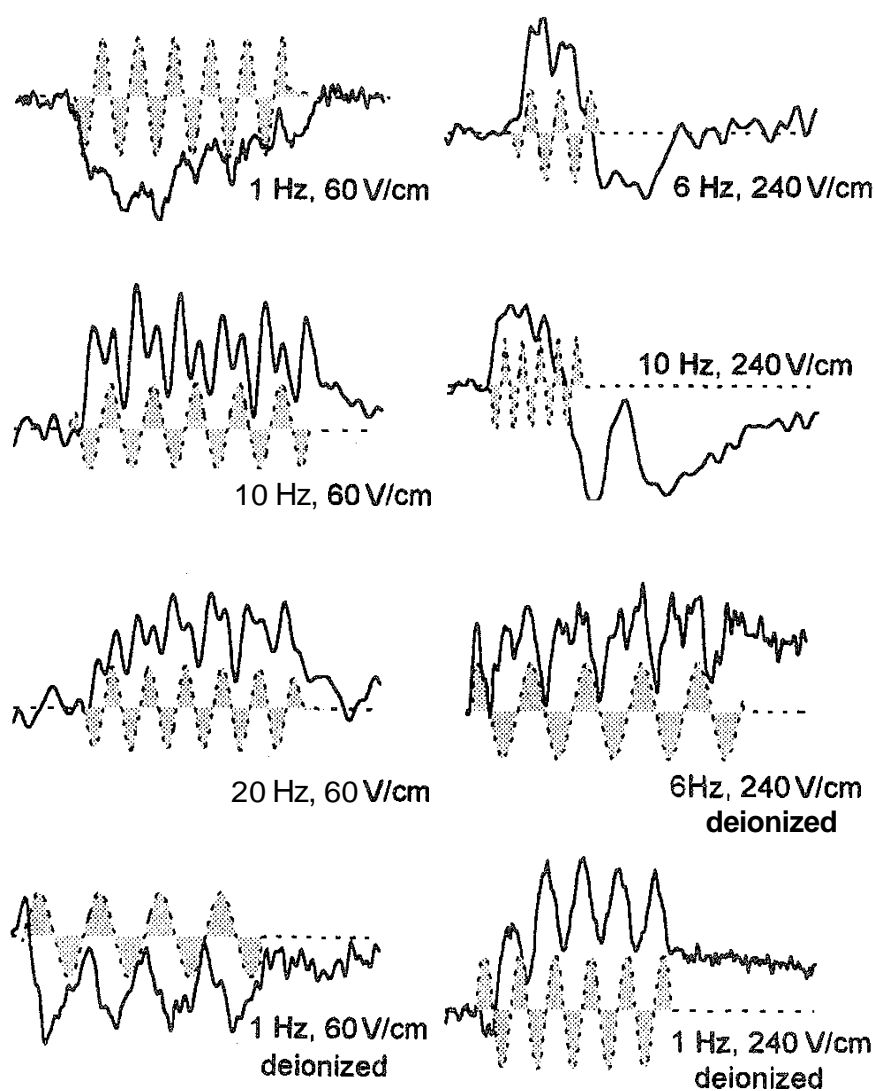


FIG 14 ELS response from palygorskite suspensions of volume fraction 0.15% (dotted line. electric field).

translation effects requires analysis of the responses over a wide range of field intensities and frequencies.

The results presented for spheres reject a general view lying at the basis of all schemes proposed for explanation for the low-frequency sign reversal in colloidal electro-optics — the necessary presence of anisotropic or deformable species in the disperse system as a condition for the detection of electro-optical responses. This is not a necessary condition for the observation of low-frequency negative electro-optical responses either. The essential role of particle electrophoretic mobility (giving rise to electroacoustic effects) for the latter is evident. The results presented concern a series of phenomena in different systems widely studied by researchers involved in the field of colloids, (bio)polymers, (bio)polyelectrolytes, etc. Below we turn our attention to some of these phenomena.

It is to be noted, in the first place, that the acoustic modes in semidilute polymers and colloids are quite similar [49,50], hence the optoelectroacoustic phenomena can

also be observed in polymer and polyelectrolyte solutions. Abundant experimental data on the electro-optical behavior of micelles [20,21] confirm the general similarity of the electro-optical spectra. Our basic objection to the developing views in this area concerns the interpretation of the volume fraction intervals (display of positive effects, anomalous sign reversal, return to positive effects). We have demonstrated similar observations on silica spheres, which could hardly be explained by the Odjik theory. As pointed out by Cates [34], several main features should be explained by a theoretical scheme for the sign reversal effect: the anomalous sign and the concentration dependence of the steady response; the disappearance of the anomaly at high fields; the concentration dependence of the decay times; and the chain length dependence of the steady response. We should add to the above several more.

First is the increase with volume fraction of the cutoff frequency of the alternating response (closely related to the cutoff frequency of the sign reversal) [36] (see Figs. 3 and 11). The latter feature strongly contradicts the idea of cluster orientation, since the correlation length of particle rotation (and therefore the cluster size) are expected to increase with volume fraction. The relation of this frequency to the elastic modulus of the system is consistent with experimental data. It explains both the universality of the phenomenon and its relation to interaction forces.

Second is the strong influence of the particle/medium density ratio on the concentration dependence of the sign reversal [33]. This fact is always ignored in proposed schemes and can simply be assigned to the influence of particle density on the electro-acoustic pressure.

Third, the decay times of the electro-optical responses at dc pulses are systematically lower than those of the responses in the kilohertz range. This is true for polyelectrolytes, as shown by the detailed investigations of Oppermann [16,17], it is also true for the rigid rodlike particles discussed here [58–60]. Assignment of the larger time constants to (collective) rotation is consistent with the fact that translation motions are restricted at higher frequency.

A considerable number of papers have been and are being devoted to the electro-optical determination of particle permanent dipoles [10–14]. This is a topic of everlasting discussions and contradictory views. Since the electro-acoustic effects display many features of permanent dipole behavior, they are evidently relevant to the problem. They should be taken into account even in the case of purple membranes, where the relation of the negative electro-optical response to the permanent dipole of the fragments seems generally accepted and beyond any doubt (See, e.g., Ref 62 and papers cited therein). Having in view the universality of the phenomenon and the display of its basic characteristics (concentration dependence of amplitude, frequency, and decay time of the negative effect) in the responses of purple membranes [63], their difference from the other colloidal systems might turn out to be rather quantitative.

The acoustic modes deserve particular attention in studies of gels. The results presented here for spheres are quite similar to the results reported for the low-frequency electro-optical behavior of agarose gels [32], particularly the single frequency of the alternating component. Some of the figures presented in Ref. 24 for bipolar pulses of unequal duration evidently indicate resonance amplifying of the electro-optical signal. It is therefore not surprising that the molecular weight separations observed in FIGE (field inversion gel electrophoresis) are highly

sensitive to pulse amplitude and duration [64]. Experiments directed to the determination of the self-resonance frequencies of the gel matrix might help to achieve better control of gel electrophoresis.

The above examples constitute only a brief illustration of the very wide range of phenomena and problems that may be relevant to electroacoustic effects in colloids.

REFERENCES

1. J. Kerr, *Phil. Mag.* 50:337 (1875).
2. P. Langevin, *Radium* 7:249 (1910).
3. M. Born, *Ann. Phys.* 55:177 (1918).
4. A. Peterlin and H. Stuart *Z. Phys.* 112:1 (1930).
5. W. Heller, *Rev. Mod. Phys.* 14:390 (1942).
6. M. V. Volkenstein, *Molecular Optics*, GITTL, Moscow, 1951 (in Russian).
7. C. T. O'Konski and B. H. Zimm, *Science* 111:113 (1950).
8. C. T. O'Konski, *J. Phys. Chem.* 64:605 (1960).
9. M. A. Lauffer, *J. Am. Chem. Soc.* 61:2412 (1939).
10. C. T. O'Konski (ed.), *Molecular Electro-Optics*, Marcel Dekker, New York, 1976.
11. B. R. Jennings (ed.), *Electro-Optics and Dielectrics of Macromolecules and Colloids*, Plenum, New York, 1979.
12. S. Krause (ed.), *Molecular Electro-Optics*. Plenum, New York, 1981.
13. H. Watanabe (ed.), *Macromolecules, Colloids, Liquid Crystals and Biological Systems*, Hirokawa, Tokyo, 1988.
14. B. R. Stoylov and S. P. Stoylov (eds), *Colloid and Molecular Electro-Optics* 1991 IOP Publishing, London, 1992.
15. S. P. Stoylov, *Colloid Electrooptics* (R. H. Ottewill and K. L. Rowell, eds), series 'Colloid Science,' Academic. New York, 1991.
16. W. Oppermann, *Macromol. Chem.* 189:927 (1988).
17. W. Oppermann, in *Colloid and Molecular Electro-Optics* 1991 (B. R. Stoylov and S. P. Stoylov, eds.), IOP Publishing, London, 1992, p. 93.
18. U. Kramer and H. Hoffman, *Macromolecules* 24:256 (1991).
19. B. R. Jennings, M. E. Nash, and G. J. T. Toddy, *J. Colloid Interface Sci.* 127:537 (1989).
20. M. Angel, H. Hoffmann, U. Kramer, and H. Turn, *Ber. Bunsenges. Phys. Chem.* 93:184 (1989).
21. H. Hoffman, U. Kramer. and H. Turn, *J. Phys. Chem.* 94:2027 (1990).
22. T. J. Grye and M. E. Cates, *J. Chem. Phys.* 98:9790 (1993).
23. F. Mantegazza, M. Giardini. R. Piazza, and V. Degiorgio, *J. Phys.: Condens. Matter* 4:8683 (1992).
24. J. S tellwagen and N. Stellwagen, in *Colloidand Molecular Electro-Optics* 1991 (B. R. Jennings and S. P. Stoylov, eds.), IOP Publishing, London, 1992, pp. 213–222.
25. F. J. Norton, *Phys. Rev.* 55:668 (1939).
26. H. Mueller, *Phys. Rev.* 55:508, 792 (1939).
27. B. W. Sackmann, *J. Opt. Soc. Am.* 35:66 (1945).
28. J. Rabinovich, *J. Phys. Rad.* 7:228 (1946).
29. M. J. Shah, D. C. Thompson, and C. M. Hart, *J. Phys. Chem.* 67:1170 (1963).

30. M. J. Shah, *J. Phys. Chem.* 67:2215 (1963).
31. H. Asai and N. Watanabe, *Biopolymers* 15:383 (1976).
32. S. P. Stoylov, *Ferroelectrics* 86:245 (1988).
33. M. Stoimenova and M. Buleva, *J. Colloid Interface Sci.* 152:483 (1992).
34. M. E. Cates, *J. Phys. France* 2:1109 (1992).
35. M. Stoimenova and T. Okubo, *J. Colloid Interface Sci.* 176:267 (1995).
36. M. Stoimenova, V. Dimitrov, and T. Okubo, *J. Colloid Interface Sci.* 184:106 (1996).
37. T. Oja, G. L. Petersen and D. C. Cannon, U.S. Patent 4,497,208 (1985).
38. M. Tomita and T. G. M. van de Ven, *J. Opt. Soc. Am. A: Opt. Image Sci* 1:317 (1984); *J. Phys. Chem.* 89:1291 (1985).
39. H. Fujita and K. Ametany, *Jpn. J. Appl. Phys.* 18:753 (1979).
40. T. Okubo, *J. Chem. Soc. Faraday Trans. 1* 84:3377 (1988).
41. M. Stoimenova and S. Stoylov, *J. Colloid Interface Sci.* 76:502 (1980).
42. B. Wejerich, B. D'Aguanno, E. Canessa, and R. Klein, *Faraday Discuss. Chem. Soc.* 90:1 (1990).
43. S. P. Stoylov, *Adv. Colloid Interface Sci.* 3:45 (1971).
44. T. Okubo, *Naturwissenschaften* 79:317 (1992).
45. T. Okubo, *Colloid Polym. Sci.* 271:190 (1993).
46. T. Okubo, *Langmuir* 10:1695 (1994).
47. T. Okubo, K. Kiriyama, N. Nemoto, and H. Hashimoto, *Colloid Polymer, Sci.* 274:93 (1996).
- T. Okubo, A. Tsuchida, S. Okada, and S. Kobata, *J. Colloid Interface Sci.*, 199:83 (1998).
49. P. G. de Gennes and P. Pincus, *J. Chim. Phys.* 74:616 (1977).
50. J. F. Joanny, *J. Colloid Interface Sci.* 71:622 (1979).
51. E. Dubois-Violette, P. Pieranski, F. Rothen, and L. Strzelecki, *J. Phys. (Paris)* 41:369 (1980).
52. D. W. Benzing and W. B. Russell, *J. Colloid Interface Sci.* 83:178 (1981).
53. H. M. Lindsay and P. M. Chaikin, *J. Chem. Phys.* 76:3774 (1982).
54. A. J. Hurd, N. A. Clark, R. C. Mockler, and W. J. O'Sullivan, *Phys. Rev. A* 26(5):2869 (1982).
55. P. Pieranski, *J. Phys. (Paris)* 41:369 (1980).
56. R. W. O'Brien, *J. Fluid Mech.* 190:71 (1988).
57. R. W. O'Brien, B. R. Midmore, A. Lamb, and R. J. Hunter, *Faraday Discuss. Chem. Soc.* 90:301 (1990).
58. V. Peikov, T. Radeva, and M. Stoimenova, *J. Colloid Interface Sci.* 168:1 (1994).
59. M. Stoimenova and T. Radeva, *J. Colloid Interface Sci.* 169:329 (1995).
60. V. Dimitrov, A. Alekov, and M. Stoimenova, *J. Colloid Interface Sci.*, submitted.
61. E. E. Maier, S. F. Schulz, and R. Webber, *Macromolecules* 21:1544 (1988).
62. G. Todorov, S. Sokerov, and S. P. Stoilov, *J. Colloid Interface Sci.* 165:154 (1994).
63. G. Todorov, S. Sokerov, and S. P. Stoilov, *Biophys. J.* 40:1 (1982).
64. G. F. Carle and M. V. Olson, *Nucleic Acids res.* 12:5647 (1984).

6

NMR Studies of Colloidal Oxides

EDISSON MORGADO, JR. Catalysts Division, Petrobras Research and Development Center, Rio de Janeiro, Brazil

**SONIA MARIA CABRAL DE MENEZES and
CARLOS ROBERTO NOGUEIRA PACHECO** Chemistry Division, Petrobras Research and Development Center, Rio de Janeiro, Brazil

- I. Introduction
- II. Special Considerations
 - A. Nuclear properties
 - B. NMR signal narrowing effect in colloids
 - C. Relaxation rates in colloidal species
 - D. Free solution species in the colloidal system
 - E. Adsorption phenomena
- III. NMR Studies on Colloidal Oxides and Hydroxide Systems
 - A. Colloidal silicas
 - B. Colloidal aluminas
 - C. Other colloidal oxides
- IV. Conclusions
- References

I. INTRODUCTION

Colloids are of considerable industrial importance and have intrinsic scientific interest. Generally they consist of a sol system, i.e., submicrometer-sized solid particles dispersed in a liquid phase that can polymerize into a continuous three-dimensional network called a gel. In particular, colloidal sols of oxides and hydroxides, either as such or as precursor dispersions, have numerous and wide-ranging applications in catalysis, coatings, optics, microelectronics, and ceramics and other composite materials. The importance of investigations on such systems is unquestioned, and many articles on this field are issued every month in the several periodicals on colloid science and materials science. Among these colloidal systems, silicon and aluminum oxopolymers, which transform into an oxide

network upon calcination, have been the most investigated [1–5] owing to the ready availability of these elements in nature and thus to their practical importance. TiO_2 [6], V_2O_5 [7], WO_3 [8], and ZrO_2 [9] sols through multicomponent oxosystems such as those of Si-Al [10] and Y-Ba-Cu [11] are important examples of other colloidal oxides that have also been studied. Special attention has been given to the development of the sol-gel process in the last 20 years [3,12].

Among the several experimental techniques for studying colloid and sol-gel chemistry, perhaps the most powerful one is nuclear magnetic resonance (NMR) spectroscopy. NMR allows investigation of these systems by a combination of structural information, obtained through lineshape analysis and chemical shift data, and indirect information from dynamic measurements of spin relaxation and diffusion.

Multinuclear magnetic resonance spectroscopy has been extensively used to study aqueous solutions (e.g., silicates, aluminates), providing information on the types of polymeric species in solution after partial hydrolysis. Indeed, high resolution NMR technique has been successfully used to follow the time evolution of the various chemical species in solution and has yielded detailed information on the kinetics and mechanisms of the involved reactions [13,14]. These are certainly important to understand the transformations that occur toward the resultant colloidal species formed in the later stages of polymerization. On the other hand, the magic angle spinning (MAS) technique in solid-state NMR has supported a large number of studies of gels, xerogels, and aerogels [5,15,16], providing valuable but indirect information on the sol precursors. In this case, the colloidal system is inevitably disrupted with the evaporation or extraction of the solvent for the solid-state analysis, and the original sol species may have undergone structural changes. In contrast to the large use of NMR for analysis of chemical species in solution and in the solid state, the use of liquid NMR for in situ investigation of colloidal systems has not been extensively exploited.

Studies on adsorbed species and the surface chemistry of oxides in their normal state have been carried out to a great extent by high resolution solid-state NMR [17], especially due to the widely growing area of heterogeneous catalysis. A relatively small contribution is found for the use of NMR for probing adsorption phenomena in colloidal oxides, and it is only briefly discussed here. Colloidal systems such as organic polymers, proteins, and microemulsions are relatively well covered in the literature and therefore are out of the scope of this chapter. Metal colloids are not considered either.

The purpose of this chapter is to show the applicability of liquid multinuclear NMR spectroscopy to the in situ characterization of some colloidal inorganic oxides and hydroxides. In Sec. II the features and advantages of using the NMR technique on such specific systems are summarized. In Sec. III some recent applications are presented, focusing on the characterization of alumina sols. It is not our intention to provide a comprehensive review; rather we seek to highlight some applications of NMR in this important field of study.

II. SPECIAL CONSIDERATIONS

A. Nuclear Properties

The nuclear properties of the nuclei usually found in colloidal oxides and/or hydroxides probed by NMR are shown in Table 1. ^{13}C NMR and ^1H NMR are often instructive of structural modifications in solution or colloidal precursors containing organic ligands, such as the metal alkoxides during their hydrolysis in sol-gel processes, as we briefly discuss in Sec. III. The properties of these two nuclei are very well known [18] and are not discussed here. The two most investigated nuclei in oxosystems — ^{29}Si and ^{27}Al — are quite different in their properties. The natural abundance and sensitivity of ^{29}Si are considerably lower than those of ^{27}Al . Furthermore, the spin-lattice relaxation time (T_1) of silicon is much longer than that of aluminum, which sometimes requires that either the sample be pulsed less frequently or a paramagnetic relaxation agent be employed. Despite these apparent disadvantages for observation of ^{29}Si , the chemistry of silicon-based sol-gels and aqueous silicates seems to be much better understood than that of similar systems based on alumina. The main reason for this contrast is the strong quadrupolar nature of ^{27}Al . For most ^{29}Si nuclei, the dominant relaxation process is the dipole-dipole interaction between the observed nuclei and other nearby magnetic nuclei. In the case of ^{27}Al nuclei, which have a quadrupole moment ($I > 1/2$) and only a moderately large magnetogyric ratio, the relaxation is dominated by the quadrupolar term due to the interaction with the fluctuating electric field gradient experienced by the nucleus. This phenomenon causes the resonance lines to be considerably broadened or even to vanish into the baseline when the nucleus is not in a highly symmetric site. A specific approach of this relaxation mechanism for colloidal species is summarized in Sec. II.C.

TABLE 1 Comparison of Nuclear Spin Properties

| Isotope | Spin | Natural abundance (%) | Magnetogyric ratio $\gamma/10^7$ rad/(T·s) | Quadrupole moment (10^{28} Q m ²) | Comparative sensitivity (D_p) relative to ^1H |
|-------------------|------|-----------------------|--|--|--|
| ^1H | 1/2 | 99.98 | 26.75 | 0 | 1.0 |
| ^{13}C | 1/2 | 1.11 | 6.72 | 0 | 1.8×10^{-4} |
| ^{17}O | 5/2 | 0.037 | -3.63 | -0.026 | 1.1×10^{-5} |
| ^{27}Al | 5/2 | 100 | 6.98 | 0.15 | 2.1×10^{-1} |
| ^{29}Si | 1/2 | 4.70 | -5.32 | 2 | 3.7×10^{-4} |
| ^{31}P | 1/2 | 100 | 10.84 | 0 | 6.7×10^{-2} |
| ^{47}Ti | 5/2 | 7.28 | -1.51 | 0.29 | 1.5×10^{-4} |
| ^{49}Ti | 7/2 | 5.51 | -1.51 | 0.24 | 2.1×10^{-4} |
| ^{51}V | 7/2 | 99.76 | 7.04 | -0.05 | 3.8×10^{-1} |
| ^{183}W | 1/2 | 14.4 | 1.12 | 0 | 1.1×10^{-5} |
| ^{207}Pb | 1/2 | 22.6 | 5.54 | 0 | 2.0×10^{-3} |

The quadrupolar ^{51}V nucleus presents features similar to those of ^{27}Al , ^{183}W and ^{207}Pb show magnetic properties closer to ^{29}Si , although the former is not easily observed due to the low sensitivity. ^{31}P is the most appropriate nucleus to be analyzed by NMR of those listed in Table 1. However, the use of ^{31}P NMR in the subject under consideration is restricted to the study of some colloidal hydroxyphosphates [19] or phosphorus-based molecules adsorbed on colloidal oxides [20].

Oxygen-17 shows all the negative aspects of both ^{29}Si and ^{27}Al allied with a very low natural abundance, which usually requires isotopic enrichment. Hence, ^{17}O NMR has not been used very often in the characterization of colloidal oxides, although there are notable exceptions described in the literature [21,22].

Unfortunately, the properties of the magnetically active nuclei ^{47}Ti and ^{49}Ti are very unfavorable for NMR measurements. These nuclei show a relatively low natural abundance, low sensitivity, and a high quadrupole moment. In fact, titanium has received little attention from the NMR spectroscopist. Therefore, despite the great practical importance of TiO_2 and associates in the colloid state, it is hardly possible to find any reference on the use of ^{47}Ti or ^{49}Ti NMR for the characterization of these oxides.

B. NMR Signal Narrowing Effect in Colloids

Colloidal sols are arbitrarily regarded as particles falling anywhere in the range of 1–1000 nm in diameter. However, a smaller upper limit will probably be required if the colloidal oxide species has to be observed and interpreted in a spectrum by means of conventional Fourier transform NMR in the liquid state. First, the particles must form a stable colloidal suspension ensuring the homogeneity of the medium. This is a basic condition to avoid a gradient of concentration in the volume being analyzed and guarantee equal excitation of the nuclei within the spectral range. Furthermore, the size of the particles should be sufficiently small to allow their incoherent isotropic tumbling motions so that both dipolar couplings and chemical shift anisotropy can be eliminated. Therefore, Brownian motion is expected to sharpen the signals of the colloidal particle and also of related surface-adsorbed species. In fact, the use of colloidal suspensions for NMR analysis in specific cases has been claimed as an alternative tool for NMR analysis of solids [19,23] replacing the magic angle sample spinning method where rapid mechanical rotation of the solid sample is applied.

C. Relaxation Rates in Colloidal Species

For a basic knowledge of NMR relaxation processes, which is needed for comprehension of the following paragraphs, the reader is referred to the basic NMR literature [24,25], including a recent article by Traficante [26]. The two main relaxation processes related to the nuclei discussed in this chapter are due to the dipole–dipole and quadrupole interactions. They are briefly reviewed as follows.

1. Dipole–Dipole Relaxation

As the only property of a nucleus of spin 1/2 that depends on orientation is its magnetic moment, transitions between nuclear spin levels can be induced only by magnetic fields. A nucleus in a liquid will experience a fluctuating field due to the magnetic moments of nuclei in other molecules as they execute Brownian motion. This chaotic random motion has a time scale that depends on a number of factors and is characterized by a somewhat loosely defined term, the rotational correlation time τ_c . This is the time interval after which the molecular motion contains no vestige of its earlier angular momentum. The relaxation field intensity due to the fluctuations of the magnetic fields in a liquid sample is related to the resonance frequency ν_0 and to the correlation time (Fig. 1). The intensity of the relaxation field is constant over the usual NMR frequency range (flat portion of the curves) and increases with increasing τ_c . This condition is ensured when the correlation time is much shorter than one Larmor period of the nuclei, that is, when $\nu_0\tau_c \ll 1$. This is known as the region of extreme narrowing, and small molecules that tumble rapidly in solution (very short τ_c) will be in this region. However, when τ_c is sufficiently long, the relaxation field (and so the relaxation rate) starts to decrease with increasing NMR frequencies. Hence, for relatively large particles, where the rate of molecular reorientation is lower than the spectrometer frequency, the extreme narrowing condition is not fulfilled.

The effect of varying τ_c and ν_0 is also shown in Fig. 2a, where the behavior of the intramolecular dipole–dipole longitudinal (T_{1DD}) and transverse (T_{2DD}) relaxation times is depicted for the homonuclear case. The main feature to note is the T_1 minimum, which marks the limit of extreme narrowing region ($\nu_0\tau_c \ll 1 \Rightarrow T_{1DD} = T_{2DD}$) and the way this minimum moves with spectrometer frequency. The higher this frequency, the shorter becomes the maximum allowed τ_c . To the right of the T_{1DD} minimum, the motion is too slow to cause an effective T_1 relaxation, and the contribution of the transverse relaxation time to the global relaxation process is enhanced. Moreover, T_{2DD} becomes shorter, resulting in increased linewidths [$\Delta\nu_{1/2} = (\pi T_2)^{-1}$].

For the heteronuclear case (Fig. 2b), where Si atoms are relaxed by neighboring protons, the relaxation behavior is similar to that shown in Fig. 2a. It can be inferred from Fig. 2b that both the longitudinal and transverse relaxation rates are two orders of magnitude faster than in the homonuclear case. Similarly, the T_1 minimum moves left with increasing magnetic field strength. In comparison, with the homonuclear case, the relaxation of Si caused by protons is the dominant relaxation process and has a minimum allowed τ_c slightly greater than that in the homonuclear case.

The correlation time can be estimated from the particle size on the basis of the Debye theory of electrical dispersion [24]:

$$\tau_c = 4\pi a^3 \eta / 3kT \quad (1)$$

where η is the viscosity of the liquid, T is the temperature, k is the Boltzmann constant, and a is the radius of the particle. Assuming colloidal particles in an aqueous system (room temperature) and with diameters greater than 1 nm, τ_c values larger than 10^{-10} s are calculated. From Figs. 1 and 2, this means that

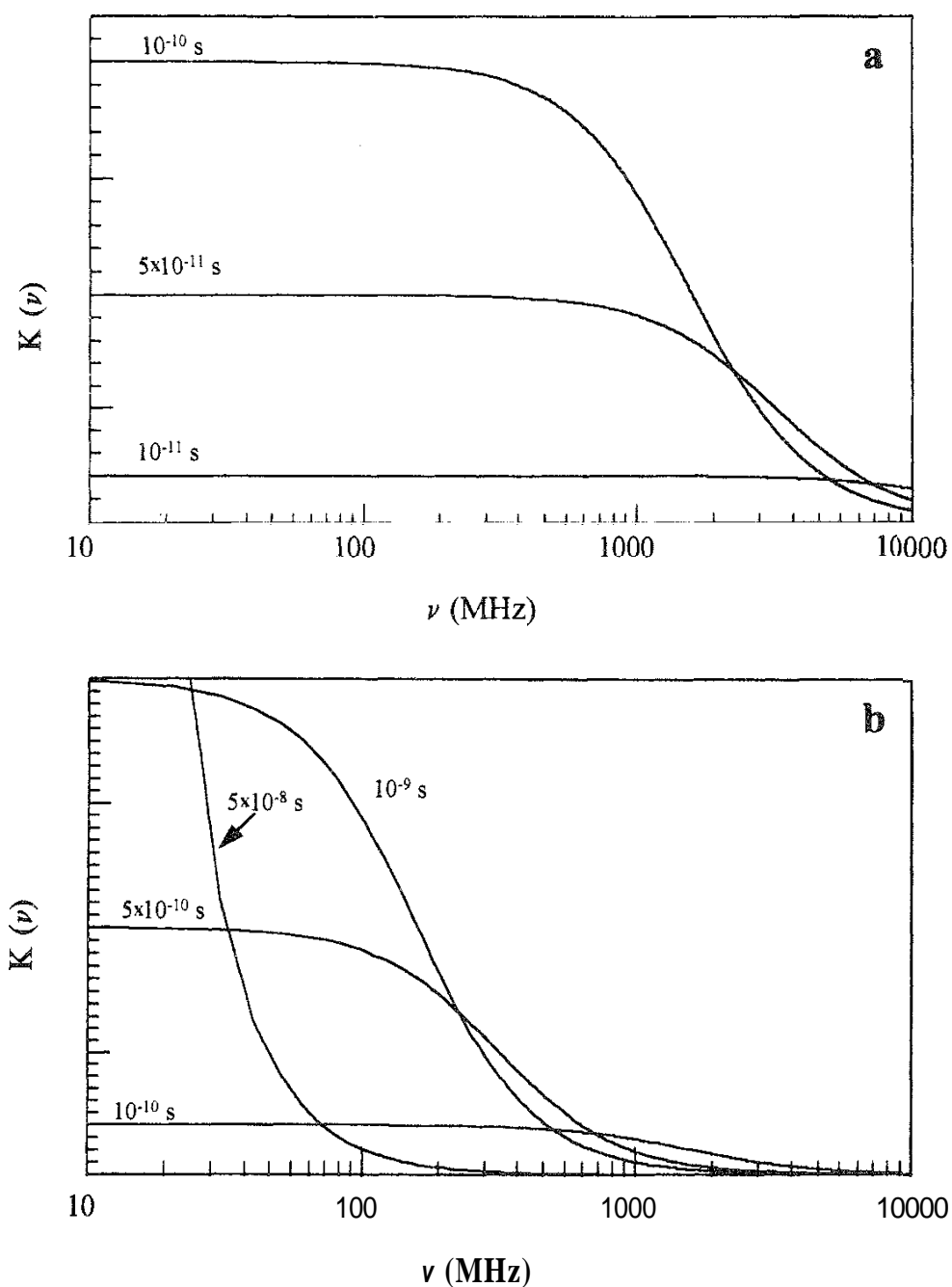


FIG. 1 Intensity of fluctuations. $K(\nu)$, in magnetic fields in a liquid sample due to Brownian motion as a function of the frequency, for different correlation times.

spin 1/2 nuclei of such particles will often be in the threshold region of the extreme narrowing or far from that. Furthermore, within the usual range of **NMR** frequency (60–750 MHz), the magnitude of ν_0 may be of crucial importance for the relaxation behavior, especially in the range of τ_c between 10^{-8} and 10^{-10} s.

2. Quadrupole Relaxation

For the case of quadrupolar nuclei in molecules in the extreme narrowing region, the quadrupole coupling constant χ influences **NMR** spectra through very efficient

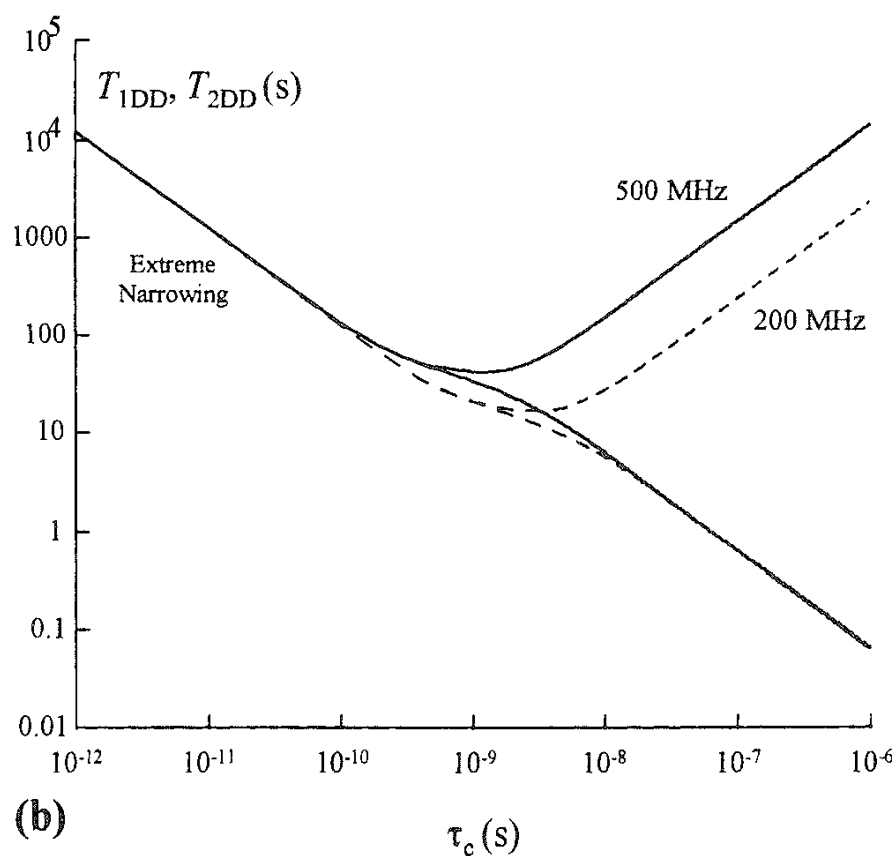
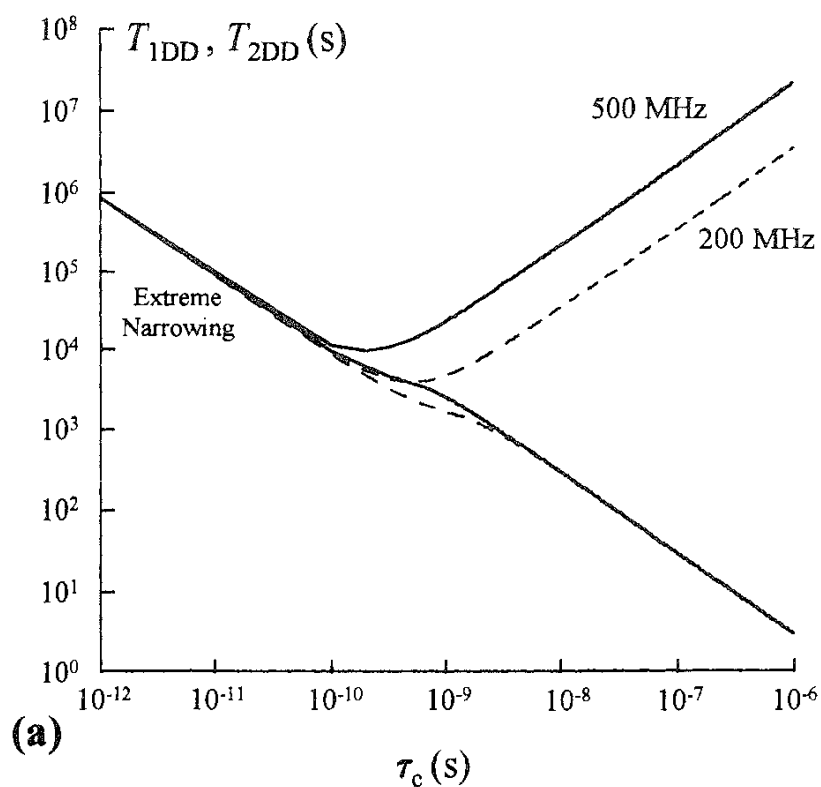


FIG. 2 Plots of dipole–dipole relaxation times T_{1DD} and T_{2DD} versus correlation time at spectrometer frequencies of 200 MHz (dashed line) and 500 MHz. (a) Homonuclear case: two silicon nuclei separated by 324 ppm in a Si—O—Si substructure; (b) heteronuclear case: a silicon and a proton separated by 258 ppm in a Si—O—H— substructure. (Bond lengths from Ref. 70; T_1 , T_2 calculations according to equations provided in Ref. 71.)

relaxation processes and is related to the equivalent longitudinal T_{1Q} and transverse T_{2Q} quadrupole relaxation times by equation

$$\frac{1}{T_{1Q}} = \frac{1}{T_{2Q}} = \pi \Delta \nu_{1/2} = \frac{3\pi^2(2I+3)}{10I^2(2I-1)} \left(\frac{1+\eta^2}{3} \right) \chi^2 \tau_c \quad (2)$$

where η is the asymmetry parameter and $\chi = e^2 q Q / h$ (eq = electric field gradient tensor; eQ = nuclear quadrupole moment; h = Planck's constant). In this case, the linewidth ($\Delta \nu_{1/2}$) of a resonance corresponding to a site that experiences an electric field gradient is proportional to the rotational correlation time for molecular motion (τ_c).

The simple exponential relaxation behavior dictated by Eq. (2) for molecules in the "extreme narrowing" conditions cannot be applied to molecules of limited mobility. Outside the region of extreme narrowing the behavior is reminiscent of that of spin 1/2 dipole-dipole relaxation (Fig. 2), but it is complicated by the fact that several nuclear transitions are possible. Thus for a nucleus like ^{27}Al with $I = 5/2$ there are five transitions, $3/2 \leftrightarrow 5/2$, $1/2 \leftrightarrow 3/2$, $1/2 \leftrightarrow -1/2$, $-1/2 \leftrightarrow -3/2$, and $-3/2 \leftrightarrow -5/2$, and the relaxation rates for nuclei undergoing external transitions differ from those of nuclei undergoing the central $1/2 \leftrightarrow -1/2$ transition. This produces what is called nonexponential relaxation. Bull *et al.* [27] presented numerical solutions for the nonexponential quadrupole relaxation of spin 5/2 and spin 7/2 nuclei. They found that the longitudinal relaxation (T_{1Q}) of nuclei with both 5/2 and 7/2 spin may be described approximately as a single exponential for all correlation times. However, the transverse relaxation (T_{2Q}) is governed by three and four contributions for the 5/2 and 7/2 cases, respectively, and the weights of the different contributions all have similar magnitudes for longer correlation times. This can be seen in Fig. 3, which shows the transverse relaxation behavior of the spin 5/2 nuclei as a function of $\nu_0 \tau_c$. The limiting values of the coefficients of the exponentially decaying contributions for large $\nu_0 \tau_c$ corresponds to 25.7%, 45.7%, and 28.6% for components I, II and III, respectively, in the spin 5/2 case and similarly for nuclei of spin 7/2. Curve I corresponds to the central transition $-1/2 \leftrightarrow +1/2$. For values of $\nu_0 \tau_c$ less than 1, the transverse relaxation is approximately a single exponential. For $\nu_0 \tau_c > 1$, a mixture of exponentials is observed, but the very rapid decay (short T_{2Q} and large relaxation rate) of the spin 5/2 component III may allow the analysis in terms of just two exponentials. For $\nu_0 \tau_c \gg 1$, single exponential analysis is allowed because the contribution of component II decays very rapidly too. In this case, the signal due to the central transition of the quadrupolar nucleus can give rise to a relatively narrow resonance, while the remaining transitions broaden dramatically, corresponding to a loss of the NMR signal up to 74.3% (cf. decaying contribution of the components). Care must be taken to avoid confusion between loss of intensity at the chemical shift frequency through rapid relaxation of the remaining components, indicating long correlation times, and the loss of intensity through quadrupole splitting caused by, for example, anisotropic molecular motion,

If the quadrupole nucleus is situated in a colloidal particle of limited mobility, it may be sensitive to second-order quadrupolar effects, and the central transition signal is thought to be shifted to lower frequency ("second-order dynamic shift").

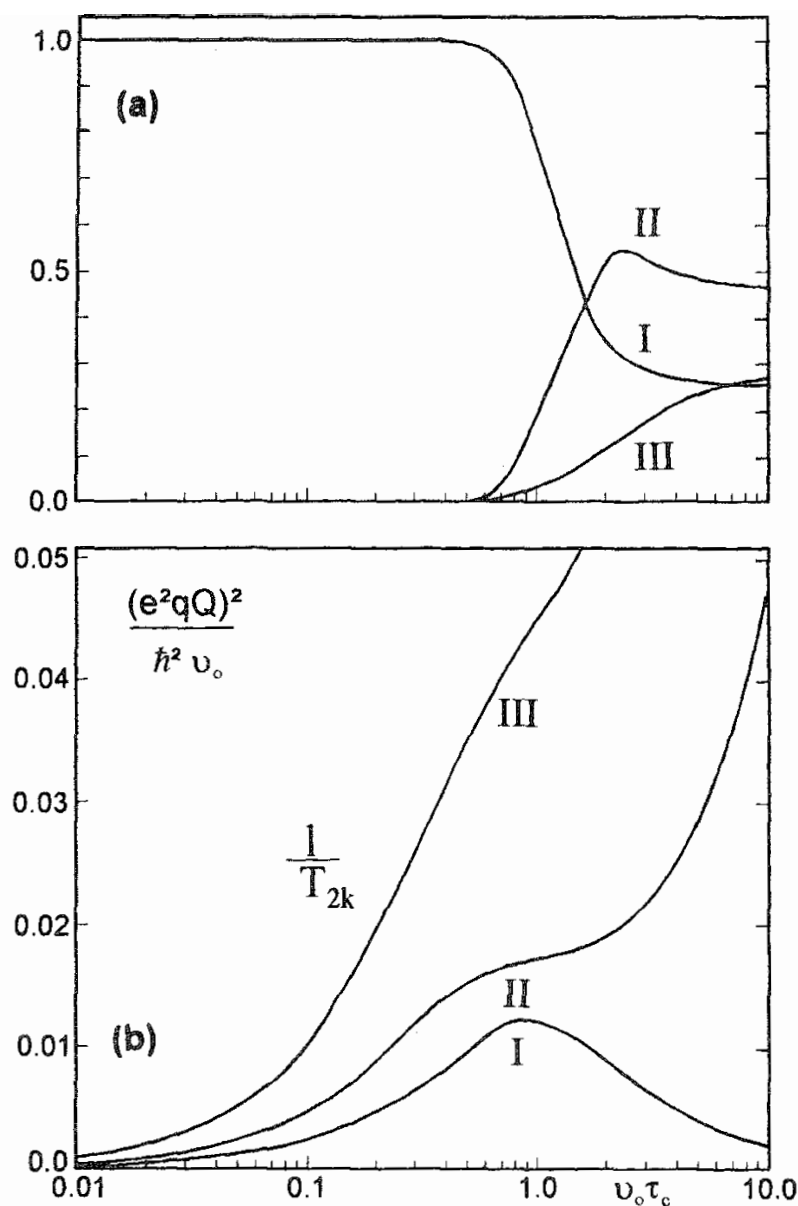


FIG. 3 Transverse relaxation of spin 5/2 nuclei in the absence of chemical exchange. (a) The normalized amplitudes of the three exponentially decaying components, and (b) their relaxation rates, both as a function of $\nu_0 \tau_c$. Note that for the longer correlation times, all three components are of similar amplitude. (From Ref. 27.)

The magnitude of this shift is related to the quadrupole coupling constant and decreases with increasing field. For $I = 5/2$ nuclei [28], it is given by

$$\delta - \delta_{\text{iso}} = -6 \times 10^3 \left(1 + \frac{\eta^2}{3} \right) \left(\frac{\chi^2}{\nu_0^2} \right) \quad (3)$$

where η , the asymmetry parameter, is usually assumed to be zero as a reasonable approximation.

The linewidth of the signal is also dependent on the resonance frequency of the nucleus and has been derived by Aramini and coworkers [29] for the same $I = 5/2$ nuclei as

$$\frac{1}{(\pi T_2)} = \Delta\nu_{1/2} = (4.9 \times 10^{-3}) \left[\frac{\chi^2}{\nu_0^2 \tau_c} \right] \quad (4)$$

It is worth noting that the linewidth of this resonance decreases with increasing τ_c . This behavior is in sharp contrast to the situation described by Eq. (2) and to the dipolar relaxation process, where the linewidth increases with increasing $\nu_0 \tau_c$. From the field dependence of the chemical shift and linewidth described in Eqs. (3) and (4), the values of χ and τ_c for spin $5/2$ nuclei in the slow motion limit can be obtained. As the parameter χ provides a measure of the coupling between the nuclear quadrupole and the electric field gradient at the nucleus, it reflects the symmetry of the local environment of the nucleus and thus can give information on the nature of the colloidal species, τ_c is a measure of the mobility of the species involved and, in principle, can provide information on the magnitude of the particle size when Eq. (1) is used.

D. Free Solution Species in the Colloidal System

The colloidal state inevitably brings about difficulties for the experimentalist when separation of the disperse phase from the dispersion medium is needed. This is the case when the speciation and concentration of only the free soluble species have to be determined. Separation of the ionic solution from the small colloidal particles for conventional chemical analysis is nontrivial, although separation techniques such as ultracentrifugation, dialysis, and field-flow fractionation have been successfully used. If the soluble species of interest have an active nuclear spin, the liquid **NMR** technique will constitute an alternative and simpler way to characterize and quantify those species without being affected by the disperse phase. An exception is the case where the colloidal species gives a signal that fully overlaps the sharp resonance of the solution entity. As NMR is quantitative, the absolute concentration of the species can be estimated based on an internal reference of known concentration but different chemical shift relative to the sample signals. Alternatively, a calibration curve can be established from a set of external standard solutions (preferably the same substance found in the sample) measured under the same experimental **NMR** conditions as those applied to the sample.

Care should be taken when the soluble species show a significant interaction with the surface of the disperse phase. In this case, a modification in the **NMR** spectrum profile may reflect an adsorption phenomenon, which should be properly interpreted.

E. Adsorption Phenomena

Adsorption of solution species in colloidal oxides and associates will probably involve attractions between hydroxyl groups at the surface and a specific group of the adsorbed molecule. If the latter contains a magnetically active nucleus, the

perturbation of its electron density can induce a shift in the NMR signal and qualitative information can be obtained. However, the molecule becomes less mobile and the relaxation rates increase. so NMR will also provide further information about the structure of the adsorbed layers, which allows one to investigate the interfacial properties of these colloidal systems. The interactions of the colloidal particles with either the dispersion medium (solvent) or other small molecules, surfactants, or polymers present in the dispersion medium can be investigated by NMR; a brief review focusing on this area has been published by Cosgrove and Obey [30]. As mentioned before, this aspect is not stressed here. Instead, we show a small number of applications in which colloidal oxides are involved. As these colloids are usually in aqueous dispersions, information about the dynamics of water molecules is quite important and can be obtained through water spin relaxation.

The particles of colloidal size are ideally suited to provide a high surface area per unit mass of substrate, which in turn is a highly desirable condition for obtaining NMR spectra of interfacial species. Another factor determining the sensitivity of the measurement is the existence of dynamic exchange of the dispersion medium (water) between the bulk and the surface. In the fast exchange limit, the average relaxation rate of the solvent will depend on the accessible area and its residence time/interaction mechanism at the particle surface. The residence time of the solvent is also sensitive to competitive solutes. The measured relaxation rates, R_i , in the fast exchange limit may be simplified by the equation [31]

$$R_i = P_F R_{F,i} + P_B R_{B,i} \quad i = 1, 2 \quad (5)$$

where P_F and P_B are the fractions of free and bound water and $i = 1, 2$ stands for longitudinal and transverse relaxations, respectively. The average relaxation rate of water molecules in the corresponding colloidal dispersions will give information about the particle structure and affinity of the surface for the solvent molecule. This is illustrated in Fig. 4, where the specific water proton spin-spin relaxation rate is plotted as a function of surface area (different particle size) of silica and alumina sols [30]. [The specific relaxation rate $R_{2sp} = (R_2 - R_2^0)/R_2^0$, where R_2^0 is the relaxation rate of pure water and R_2 is related to the overall colloidal dispersion given by Eq. (5).] The fact that the data fall on the same line is a clear demonstration that NMR can be used to monitor the total available surface area in a dispersion in situ, which is not straightforwardly achieved by other means. The straight line dependencies indicate that the samples satisfy the fast exchange limit. Besides, the higher slope of the alumina line indicates a stronger solvent–surface interaction than that for silica. More detailed studies of the water layer can be made by using ^{17}O and ^2H relaxation measurements, which are sensitive to changes in intramolecular motion [31]. Moreover, quadrupolar splitting of ^{17}O and ^2H NMR signals in surface-bound water molecules can elucidate structural modifications on oriented particle systems as in sol-gel transition [32]. NMR relaxation studies of water protons using paramagnetic probes as relaxation rate enhancers also provide a convenient way to investigate ion adsorption onto the surface of colloidal oxides [33].

When surface species are not in fast exchange, direct observation of the spectra can be used to probe both the surface orientation and the dynamics of the adsorbed species.

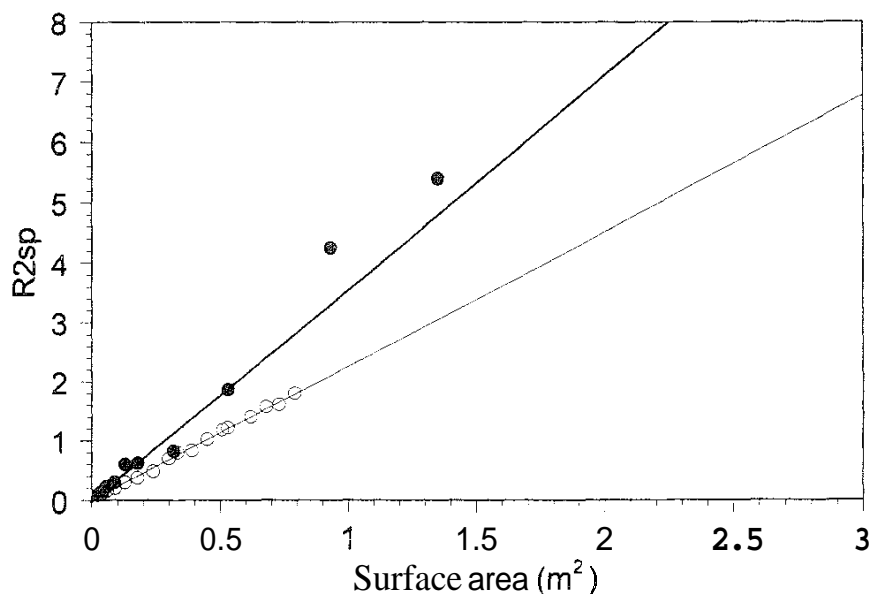


FIG. 4 Specific solvent (water) relaxation rates for oxide surfaces as a function of surface area. (●) Alumina; (○) silica. (From Ref. 30.)

III. NMR STUDIES ON COLLOIDAL OXIDES AND HYDROXIDE SYSTEMS

A. Colloidal Silicas

Since the introduction of pulsed Fourier transform NMR techniques, ^{29}Si NMR has become a powerful and routine tool for gathering knowledge of the complex nature of aqueous silicate solutions. This is due to the characteristic and mostly well-separated signals for the SiO_4 groups in different structural surroundings and the possibility of estimating the relative concentrations of the various structural entities [34]. A successive shift of the ^{29}Si resonance is observed to lower frequencies on replacement of $\text{Si}-\text{OH}$ bonds in silicate species by siloxane bonds ($\text{Si}-\text{O}-\text{Si}$). For every siloxane bond less, there is a shift of about 10 ppm to higher frequency. The Q^n notation introduced by Engelhardt et al. [35] for the assignment of the resultant building units has been widely used. In this notation, Q (quaternary) represents a silicate atom bound to four oxygen atoms forming a tetrahedron and the superscript n indicates the number of other Q units attached to the SiO_4 tetrahedron under study (Fig. 5). Q^4 is the fully condensed tetrafunctional species that lies around -110 ppm, and Q^0 is the fully hydrolyzed monomer with $5 \sim -70$ ppm $- 10 \pm (4 \times 10)$. The same notation has been used for the characterization of the degree of condensation of silicon species in the colloidal and solid states.

The studies with liquid ^{29}Si NMR spectroscopy for investigation of the chemistry and kinetics of the hydrolysis and condensation reactions either in alkali metal silicate solutions or in alkoxide sol-gel precursors are abundant and have been very well covered in reviews [3,13,34,36,37]. It is intended here to point to a few recent results and draw attention to the application of ^{29}Si NMR on colloidal silicas as stable particulate sols, which has rarely been exploited.

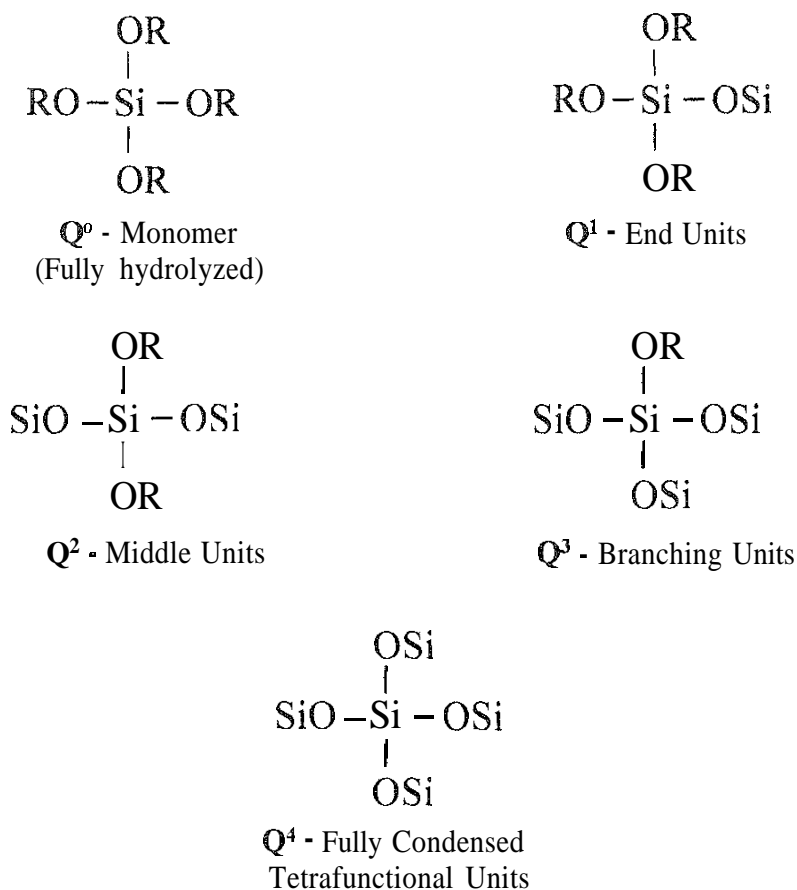


FIG. 5 Qⁿ building units in silicon environments. R can denote either H atoms or alkyl ligands.

The condensation mechanisms elucidated by ²⁹Si NMR are particularly important for understanding the formation of silica colloids. A common condensation reaction sequence of monosilicic acid in aqueous systems proceeds via monomer, dimer, trimer, and cyclic di-, tri-, and tetrameric species (rings) to polymeric products. In silicate solutions containing initially di- or trisilicic acid, partial hydrolysis to monomer and dimer, respectively, occurs simultaneously with the condensation reactions [34]. The ²⁹Si NMR spectra of polysilicates formed by hydrolysis of tetraalkoxysilanes can also be complex, as hydrolysis and condensation occur concurrently [3]. In general it is accepted that intramolecular reactions leading to the formation of rings and/or cages play a significant role in the polymerization sequence. Moreover, the condensation reaction pathway (conversion of Si—OH to Si—O—Si) is quite dependent on the synthesis conditions particularly the pH of the medium.

In a recent paper [38], Muñoz-Aguado and Gregorkiewicz reported the preparation of silica sols by neutralization of sodium silicate solution with HCl. They used ²⁹Si NMR to monitor the polycondensation reaction under acidic and basic pH. It was found that polycondensation sets in immediately after the reagents are mixed, as evidenced by the disappearance of the monomer (Q⁰) and a progressive continuous increase of the fraction of 4-connected silicate tetrahedra (Q⁴) at the expense of Q¹ and Q² species (Fig. 6). However, for base-catalyzed reactions Q¹

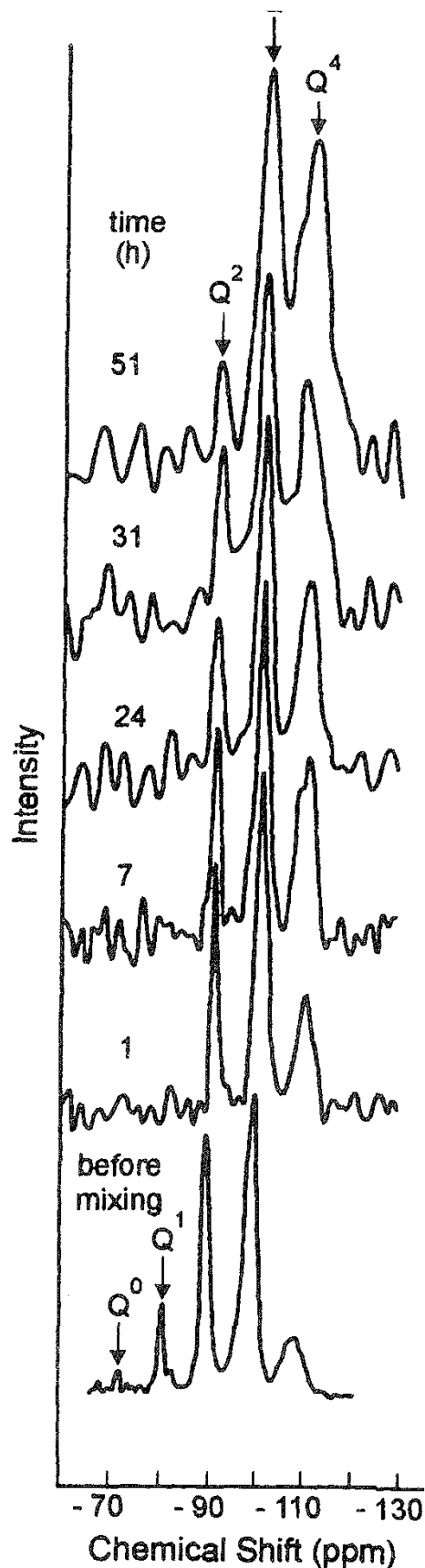


FIG. 6 ^{29}Si NMR spectra showing the polycondensation reaction in a silica (pH 1, $[\text{Si}] = 0.9 \text{ mol/L}$) produced from neutralization of sodium silicate solutions with hydrochloric acid. Spectra taken at different moments after preparation. The last spectrum (51h) was obtained immediately after gelation; the first ($t = 0$) is given for comparison, referring to the starting solution ($[\text{Si}] = 6 \text{ mol/L}$, pH ~ 11). (From Ref. 38.)

and Q^2 still exist in significant amounts throughout the polycondensation. Besides, there was an indication that polycondensation (towards Q^4 species) continued beyond the gelation point for acidic pH but not for the basic pH condition. Similar pH dependence effects have been observed in the time evolution ^{29}Si NMR analysis of tetraethylorthosilicate (TEOS) hydrolyzed systems [37,39], although at more basic pH, hydrolysis was still found to be complete at gelation with a significant amount of Q^0 species remaining. The results reported in both works suggest that acidic conditions promote hydrolysis but inhibit full condensation (Q^4). In basic conditions the reverse effect occurs, and hydrolysis is the rate-determining step. For strongly acidic media, where rapid hydrolysis takes place, liquid-state ^{29}Si NMR has made it possible to follow the silicon site distribution past the gel point without any apparent discontinuity or loss of ^{29}Si signal, indicating that even after gelation polymer segments are still quite mobile. At strongly basic conditions, however, significant loss of ^{29}Si NMR signal is observed [37], probably due to the insufficient rotational mobility (large τ_c) of the silicon in highly condensed forms (cf. Sec. II.B).

Complementary NMR measurements such as ^1H , ^{17}O , ^{13}C NMR can provide information on the hydrolysis that is not immediately visible from ^{29}Si NMR spectra [39] and can be used to monitor the behavior of water and organic ligand in sol-gel systems [3]. For instance, ^1H NMR studies on the effects of pH in a TEOS sol-gel [40] showed that in an acid-catalyzed process all the ethoxy groups were hydrolyzed long before the sample gels, whereas in a base-catalyzed process some ethoxy groups remained attached to the silicon at the gelation point. It is evident that this observation supports the above-mentioned mechanism according to ^{29}Si NMR. An indirect estimation of the remaining ethoxy groups on colloidal silica by ^{29}Si NMR has also been reported [41] based on the relative intensities of the Q^n species in the spectra and the respective OR/Si ratio (see Fig. 5).

By comparison, ^{29}Si NMR spectra of four commercial silica sols of different particle sizes are shown in Fig. 7. Commercially produced colloidal silicas are usually alkali-stabilized and consist of amorphous silica particles suspended in water that are kept in suspension due to the negatively ionized surface. The spectra of these particulate silica sols show the presence of the silicon species Q^2 , Q^3 , and Q^4 with the clear prevalence of the fully condensed species Q^4 (Table 2). In the interpretation of Ramsay et al. [42], the Q^4 resonance corresponds to the silica core of the sol particles, and the Q^3 and Q^2 components to polyhydroxy units, either bound to the silica surface or existing as oligomers free or associated at the sol surface. However, this last hypothesis seems to be more consistent because the proportion of these hydroxylated species (32% in the case of the sol with the smallest particle size) is far in excess of that corresponding to a simple hydroxylated plane surface. The decrease of the relative proportion of oligomeric silica with the size of the sol particles might arise from the condensation of the available oligomers at the particle surface. This observation is in agreement with the base-catalyzed polycondensation in neutralized aqueous silicates, where the Q^4 species was claimed to be formed at the expense of Q^3 near gelation [38]. In the case of the base-catalyzed alkoxides, the conditions of growth appear to be dominated by the addition of the monomer to the highly condensed particles [43]. In both cases, the mechanism of particle growth proposed by Iler [1] is valid.

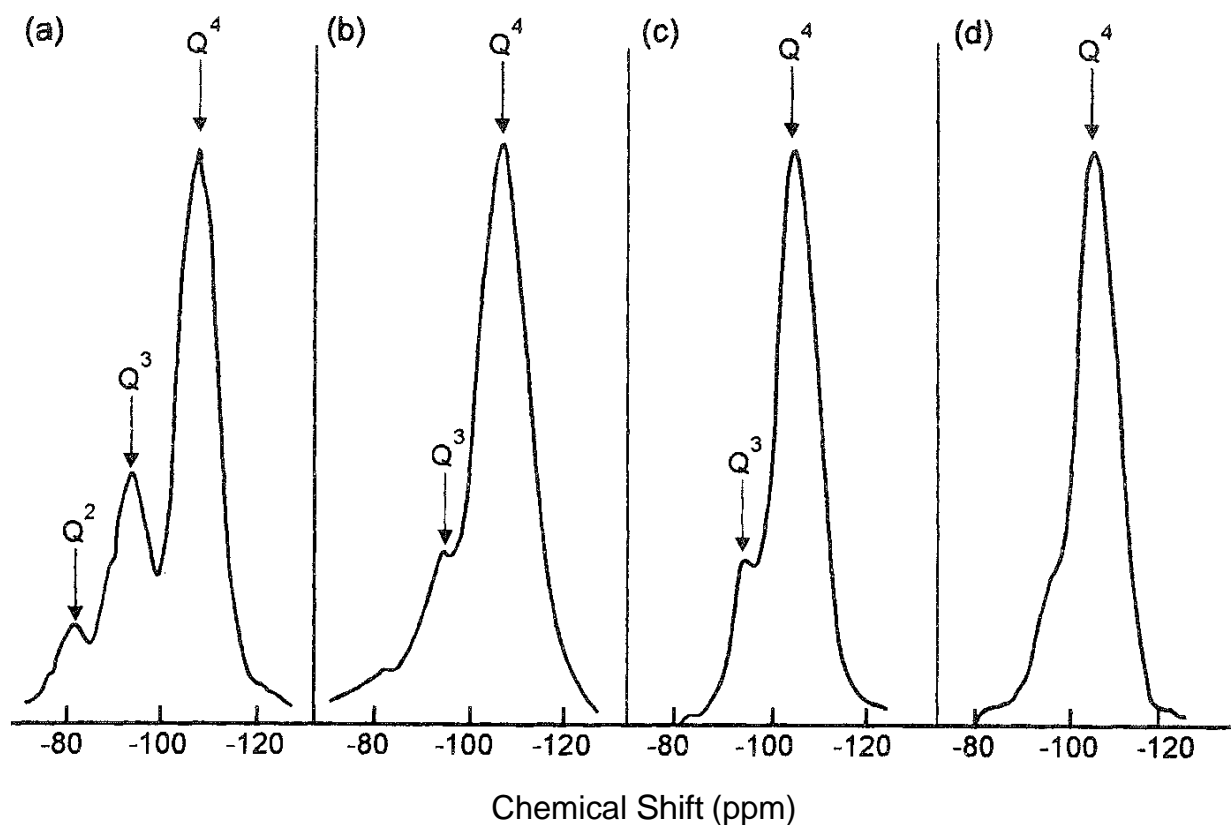


FIG. 7 ^{29}Si NMR spectra at 39 MHz of commercial colloidal silicas (see also Table 2). (a) S1; (b) S2; (c) S3; (d) S4 (From Ref. 42.)

Despite Ramsay's assignment of Q^4 species for the core silicon, the observation of ^{29}Si nuclei buried in the colloidal particles was questioned by Siedle and Newmark [44]. They pointed out that the dipole–dipole relaxation time T_1 of the "internal" ^{29}Si should be very long (Fig. 2a). Thus, the only ^{29}Si nuclei observable in NMR would be those on the outside of the silica sphere, which can be relaxed by protons from the solvent or which participate in chemical reactions such as exchange of silanol protons or equilibria involving siloxane linkages. This indeed may be true for particulate silica sols. Alternatively, the proximity of protons from Q^2 and Q^3 species might enhance the relaxation rate of Si in the buried Q^4 species

TABLE 2 Proportions of Q^n Species in Commercial Silica Sols

| Sol | Article code | Concentration (% w/w SiO_2) | Particle diameter (nm) | Q^2 | Q^3 | Q^4 |
|--------------|--------------|---------------------------------------|------------------------|--------------|--------------|--------------|
| Nalcoag 1115 | S1 | 16.1 | 8 | 9 | 23 | 68 |
| Ludox SM | S2 | 32.8 | 12 | 4 | 20 | 76 |
| Ludox HS | S3 | 40.3 | 16 | 5 | 17 | 78 |
| Ludox TM | S4 | 47.2 | 30 | 1 | 13 | 86 |

Source: Ref. 42.

(Fig. 2b, Sec. II.C). However, the efficiency of this heteronuclear process is dependent on the angles and bond lengths involved. On the other hand, there are ways of suppressing the excessively long spin-lattice relaxation times of ^{29}Si , such as the use of a paramagnetic agent (Sec. II.A), which allows data acquisition at a reasonable pulse repetition time. This will also depend on the efficiency of the paramagnetic agent in reaching the core silicon.

Alkali-stabilized aqueous silica sols have also been studied by ^{17}O and ^2H NMR to determine the water spin relaxation in these colloidal systems. In the excellent articles of Piculles and Halle [31], the dynamics of the water molecules were analyzed as functions of particle diameter, alkali content, and particle concentration. They found differences between the longitudinal (R_1) and transverse (R_2) relaxation rates demonstrating contributions from slow motions to the relaxations (see Sec. II.C) and estimated that the slow motion occurred on a time scale of more than 10^{-8} s based on the frequency dependence of the relaxation rates. The fast and slow dynamics were independent of particle concentration. The longitudinal excess relaxation rates (where excess relaxation rate is defined as $R_{\text{lex}} = R_i - R_F$ with $i = 1, 2$ standing for longitudinal and transverse rates, respectively; R_F is the transverse rate of the free water) were independent of particle size, supporting the assumption that the surface structure of the silica particles is independent of their size. In contrast, the transverse rates R_2 , which contain contributions from slow dynamics, increased with particle size. It is worth noting that the relaxation rates were divided by a factor including surface area, so that the net effect of the bound water per unit surface area could be seen (see, in contrast, the non-normalized case in Fig. 4). However, the contribution most important to those interested in characterizing the colloidal silica was the different responses of the relaxation rates of the two nuclei, ^2H and ^{17}O , after addition of alkali. As expected of an increase in the number of charged groups on the surface, ^{17}O relaxation rates increased on addition of alkali, but the transverse relaxation of ^2H decreased monotonically. A reasonable explanation was that the ^2H transverse relaxation was not dominantly coming from the water molecules but from the surface silanol groups, exchanging deuterons very rapidly with bulk water. The reduction of $R_2(^2\text{H})$ on addition of alkali led to the mechanism of deprotonation of silanol groups, contrasting with the mechanism usually accepted in the literature of adsorption of hydroxide ions.

The NMR investigation of adsorbed compounds on colloidal silica can be illustrated with some examples. Siedle and Newmark [44] studied the adsorption of $\text{Pd}(\text{F}_6\text{acac})_2$ in a silica sol with a mean diameter of 35 nm dispersed in 2-ethoxyethanol (EEO) by means of ^{19}F NMR. In addition to a sharp peak at 73.3 ppm, whose position and width were the same as those of $\text{Pd}(\text{F}_6\text{acac})_2$ in EEO, there was a broad resonance at 75.4 ppm in the colloid-EEO but not in the pure solvent. This higher frequency shift could be related to a complex formed between the fluorinated adsorbate and basic sites on the surface of the colloidal particles. Besides, the observation of separate peaks was indicative of a slow exchange rate between the free and bound $\text{Pd}(\text{F}_6\text{acac})_2$ on the NMR time scale. The ^{19}F longitudinal relaxation times in the free and bound states were 1.01 and 0.26 s, respectively. Assuming an intramolecular dipole-dipole relaxation, the correlation time, τ_c , was calculated as 4×10^{-9} through appropriate equations. This was much shorter than the

3×10^{-5} s overall correlation time for tumbling of a particle of radius 17.5 nm [Eq. (1)], indicating a fast reorientation of the axially symmetrical CF_3 groups that would provide a relaxation mechanism independent of motion of the small particles bearing the surface compound. The characterization of adsorbed polymer layers over colloidal silica (Ludox) was reported [45] that focuses on the structure of the adsorbed layer through a criterion based on the solvent mobility as perceived by pulsed field gradient nuclear magnetic resonance (PFG NMR) [46]. By using this technique, based on the diffusion of the solvent, Cosgrove and Griffiths [45] were able to estimate the average concentration of adsorbed polymer layers in concentrated silica sols under various conditions. Böhmer *et al.* [47] used ^1H NMR as an important complementary technique to study the adsorption of nonionic surfactants on colloidal silica. From their relaxation measurements, they found a much more pronounced enhancement of the specific relaxation rate of the water as a function of the equilibrium surfactant concentration. This indicates a large reduction of water mobility compared to that of related polymers [e.g., polyethylene oxide (PEO)], so that the conformation of the adsorbed surfactants could be proposed.

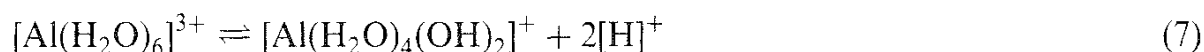
B. Colloidal Aluminas

Stable particulate alumina sols are precursors for many materials such as controlled porosity catalysts, ceramics, and coatings. They are commonly formed by peptization of pseudoboehmites ($\text{AlOOH} \cdot n\text{H}_2\text{O}$) by dilute monoprotic acids. They can be prepared either by the process developed by Yoldas [4] from hydrolyzed aluminum alkoxides or by acidic peptization of the precipitates derived from hydrolyzed aluminum salts [5,48]. As will be seen below, these alumina sols are usually multi-component fluids that also contain soluble aluminum species. Furthermore, colloidal aluminas can also be produced by the polymerization of hydrolyzed aluminum cations. Therefore, a brief review on the characterization of aluminum species in solution by ^{27}Al NMR is presented in Sec. III.B.1. The NMR studies on colloidal aluminas are then discussed in Sec. III.B.2.

1. NMR Studies on Hydrolyzed Aluminum Species

Aluminum exists in aqueous solutions solely as the monomeric $[\text{Al}(\text{H}_2\text{O})_6]^{3+}$ ion below pH 3 or as the $[\text{Al}(\text{OH})_4]^-$ ion above pH 11. At intermediate pH values, for an OH/Al molar ratio between 0 and 2.5, Al^{3+} is hydrolyzed by removal of H^+ from the coordinated water molecules, followed by condensation of the OH groups to form polynuclear ions. Ultimately, this process leads to the growth of large colloidal species and the formation of sol-gels, ^{27}Al NMR spectroscopic studies have contributed remarkably to establish speciation in hydrolyzed aluminum solutions. These studies were pioneered by Akitt *et al.* [49], and notable contributions have been made by Bottero *et al.* [50], Bertsch *et al.* [51], and more recently Klopogge and coworkers [52]. Many species with different degrees of polymerization and different internal hydrolysis ratios have been reported in this complex system. However, only the monomer $[\text{Al}(\text{H}_2\text{O})_6]^{3+}$ and the tridecameric ion $[\text{AlO}_4\text{Al}_{12}(\text{OH})_{24}(\text{H}_2\text{O})_{12}]^{7+}$ have been unequivocally assigned. These two species show sharp resonances in the ^{27}Al NMR spectrum at 0 ppm (octahedral region) and

63 ppm (tetrahedral region), respectively. The dimeric cation species $\text{Al}_2(\text{OH})_2(\text{H}_2\text{O})_8^{4+}$, was thought to be the source of a broadened NMR resonance at about 4 ppm in hydrolyzed aluminum solutions [49c,51a] but was later assigned to octahedral oligomeric species [49g,49h], possibly a precursor of the tridecameric ion [54]. The resonance at Oppm is in fact a weight-average contribution of the hexaaquo ion and its hydrolysates at a fast exchange rate,



which induces small changes in linewidth depending on the pH of the medium [49f,52b]. The tridecameric complex is usually expressed as “ Al_{13} ” and is composed of a central highly symmetric tetrahedrally coordinated aluminum atom (responsible for the sharp resonance at 63 ppm) surrounded by 12 octahedrally coordinated Al sites [16]. These latter are presumed not to have a symmetrical environment, thus causing a great broadening of the peak due to the large quadrupolar interaction (fig. 8b), so that the signal is not readily or completely detectable at room temperature, except with increasing temperature [49e,53].

The relative concentrations of these species, their interconversion mechanisms, and the rate at which they can convert to solid phases are largely dependent on the synthesis and aging conditions, as numerous workers have noted by means of ^{27}Al NMR. The degree of base hydrolysis, denoted by the molar ratio $[\text{OH}]/[\text{Al}]$, is particularly important in the speciation, as illustrated in Fig. 8. The mechanisms of condensation of the transient solution species, which eventually leads to crystalline aluminum hydroxides $[\text{Al}(\text{OH})_3]$ and oxyhydroxides $[\text{AlOOH}]$, have also been investigated in detail with ^{27}Al NMR. Besides the transient monomeric, oligomeric (4 ppm), and tridecameric species cited above, octahedral and tetrahedral broad resonances have been observed in some specific hydrolyzed aluminum systems by using liquid-state ^{27}Al NMR [14,49h,54]. These new species have been assigned to oligomers or mixtures of oligomers. Fu et al. [14] showed evidence that a broad resonance at 70 ppm formed due to dimerization of the Al_{13} species during its thermal treatment. In general, however, the aluminum species in the later stages of condensation are not detected by high resolution ^{27}Al NMR in the liquid state, since an appropriate colloidal state is likely not obtained for observation (cf. Sec. II.C). Alternatively, the corresponding amorphous solid phase can be separated from the solvent and analyzed by ^{27}Al MAS NMR as performed by Bottero and coworkers [16,55] and Morgado et al. [5]. Despite the removal of solvent, the presence of tetrahedral Al in the amorphous gel suggested the mechanism of aggregation of the tridecameric ion when the latter was present in the precursor solution.

Although hydrolysis and condensation proceed differently in alkoxide systems than in aqueous systems [3], similar ^{27}Al NMR speciation and sensitivity to the synthesis conditions are found in the hydrolyzed aluminum solutions that can be used as precursors to sol-gels. In comparison to silica (Sec. III.A), the rates of hydrolysis of aluminum precursors are very fast, and nonhydrolyzed $\text{Al}(\text{OR})_3$ oligomers are scarce in the resultant alumina sols. Therefore, the influence of organic

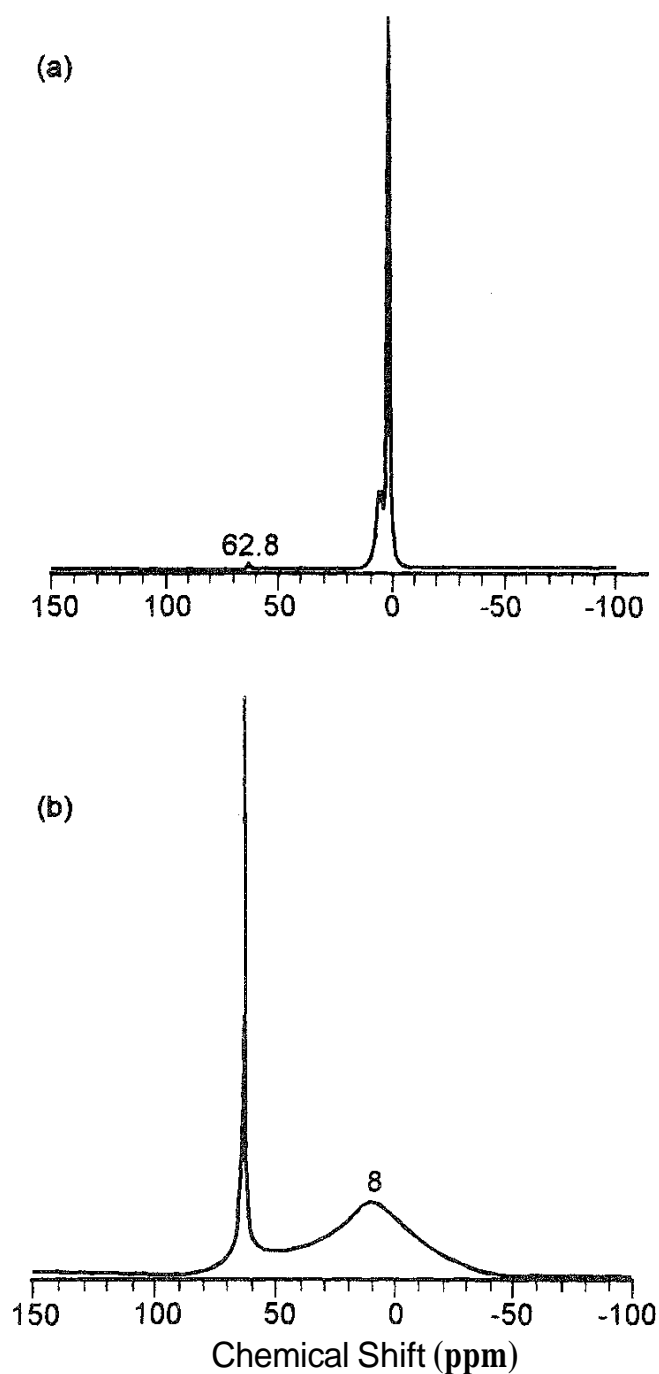


FIG. 8 ^{27}Al NMR spectra at 130.3 MHz of $[\text{Al}(\text{H}_2\text{O})_6]\text{Cl}_3$ hydrolyzed by base as a function of degree of hydrolysis. (a) $[\text{OH}]/[\text{Al}] = 1.0$; (b) $[\text{OH}]/[\text{Al}] = 2.2$. (From Ref. 53.)

versus inorganic precursors on the evolving structure appears to be minimized. Nazar and Klein [56] investigated alumina sols derived from hydrolysis of $\text{Al}(\text{OBu}^s)_3$ followed by acidic peptization ($>0.3 \text{ HNO}_3/\text{Al}$). The NMR data showed that in the clear sols processed at room temperature the aluminum is predominantly in the form of the Al_{13} polycation, with a minor contribution of the monomer at 0 ppm (Fig. 9a). Conversely, in the sols processed at 363 K, the monomeric species dominates the spectrum (Fig. 9b). Furthermore, heating the low

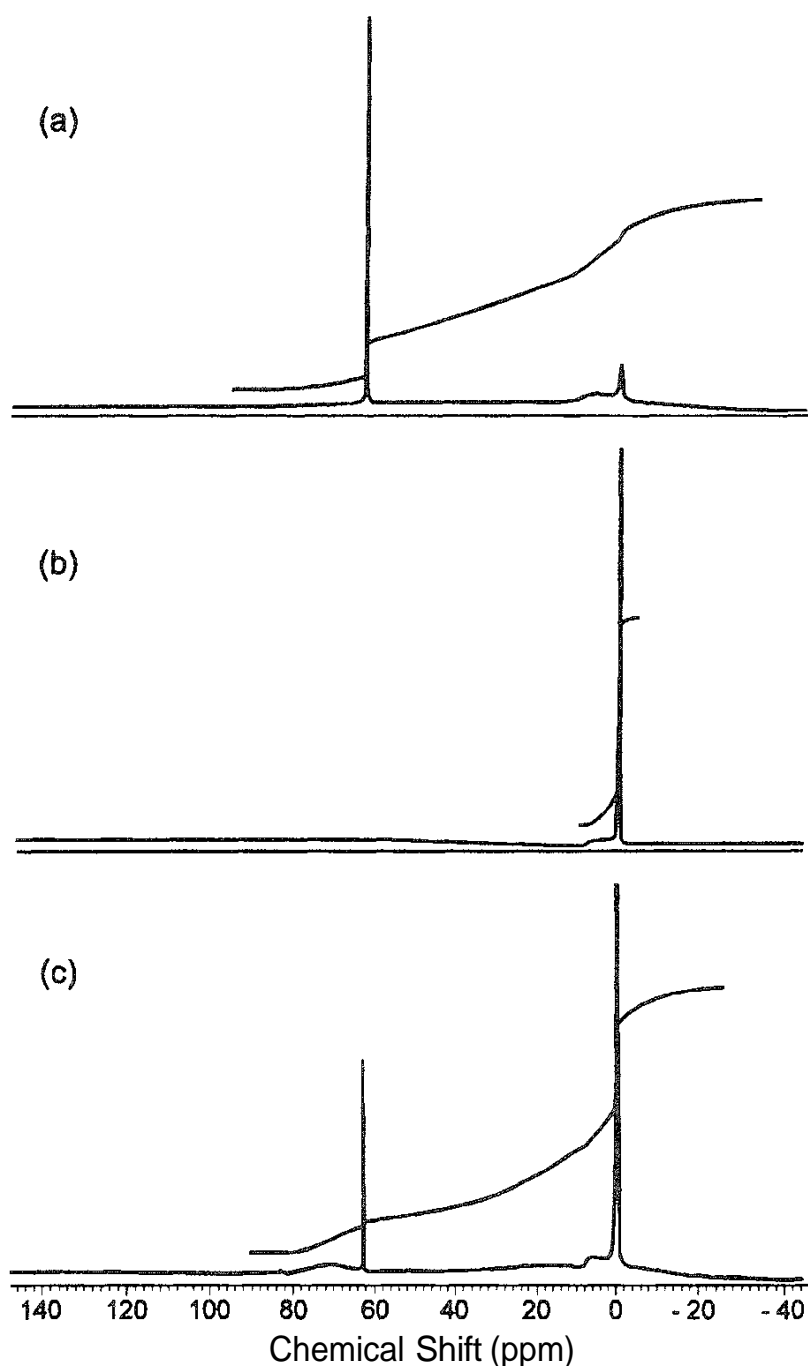


FIG. 9 ^{27}Al NMR at 104.2 MHz of alumina sols, 0.5 M HNO_3/Al , (a) hydrolyzed and aged at 293 K for 8 h; (b) hydrolyzed and aged at 363 K for 14 h; (c) hydrolyzed and aged at 293 K for 14 h, followed by aging at 363 K for 14 h. (From Ref. 56.)

temperature sols at 363 K does not transform them into the high temperature form directly but results in the growth of new tetrahedral and octahedral species (Fig. 9c), probably resulting from Al_3 condensation. A common feature of all spectra in Fig. 9 is a small broad peak at ~7 ppm which has been attributed by the authors to two overlapping peaks: one at 4.2 ppm tentatively assigned to the "dimeric" species and the other at 7.6 ppm, assigned to colloidal species.

2. NMR Studies on Peptized Boehmite Systems

Among the hydrated aluminum oxides only the oxyhydroxide in its nanocrystalline form ("pseudoboehmite") is expected to be converted into a clear or translucent sol by means of acidic peptization. In general, peptizable boehmites are known to be obtained by the Yoldas process [4], although they can also be produced from the hydrolysis of aluminum salt in aqueous solution [5]. The Yoldas process consists of hydrolyzing an aluminum alkoxide in a large excess of water at 353–373 K, resulting in the precipitation of a boehmite gel, which is peptized with a monoprotic acid (e.g., HNO_3) and yields a stable sol. Dos and Zahren [57] found that sols prepared by the Yoldas method consist of crystalline boehmite particles with dimensions on the order of nanometers and of amorphous or imperfectly crystallized clusters. In fact, the boehmite phase is thermodynamically favored at temperatures of 353 K or higher. ^{27}Al NMR studies by Olson and Bauer [58], Nazar and Klein ([56], Fig. 9b), and Kurokawa et al. [48] on alumina sols prepared by the Yoldas procedure at 373, 363, and 353 K, respectively, showed the presence of only octahedrally coordinated species. In sharp contrast, alumina sols obtained at similar conditions (353 K) showed an additional very broad tetrahedral resonance (60–70 ppm) in the ^{27}Al NMR spectra as obtained by Assih et al. [59] and more recently by Janosovits et al. [60] (Fig. 10). Assih assigned this new resonance to the tridecameric polycation adsorbed at the surface of colloidal boehmite particles being responsible for the stabilization of the sol. Although no direct evidence of the mentioned adsorption was demonstrated, the qualitative broadening of the tetrahedral resonance is indeed suggestive of adsorption (see Sec. II.E). Unfortunately, no detailed information on the width of the observed resonances was provided. However, it is remarkable that both the Assih and Janosovits groups combined ^{27}Al NMR with Raman spectroscopy, and the presence of tetrahedral aluminum could not be probed by the latter technique. The speciation discrepancy from previous results [48,56,58] using the same basic method of Yoldas might be explained by small differences in the experimental procedure, although such contrast cannot be easily explained. The extremely large resonance observed in the tetrahedral region by Assih and Janosovits is very similar to a broad asymmetric resonance ~ 7 KHz in width that was found by Akitt and Mann [49e] and Morgado et al. [61] and attributed to a background signal arising from aluminum in the probe head. This background signal varies in intensity depending on the experimental conditions and sometimes has to be subtracted from the sample spectra. If not considered, it may cause erroneous interpretation of the ^{27}Al NMR spectra and affect the deconvolution of overlapping peaks. In principle, however, the relative decrease in intensity of the band at ~ 70 ppm with acidic hydrolysis time observed by Janosovits and coworkers (Fig. 10) does not allow this supposition.

A detailed characterization of peptized boehmite sols by ^{27}Al NMR has been reported by Morgado et al. [61]. Alumina sols prepared from a commercial boehmite powder (produced by hydrolysis of aluminum alkoxides) were peptized at different water/ HNO_3 /Al ratios. The resulting sol systems containing 10 wt% Al_2O_3 were susceptible to sol-gel transformation following the addition of nitric acid ($\text{HNO}_3/\text{Al} > 0.06$) and were monitored by ^{27}Al NMR spectra recorded at periodic intervals up to the gel point (Fig. 11). The spectra of the sol recorded at

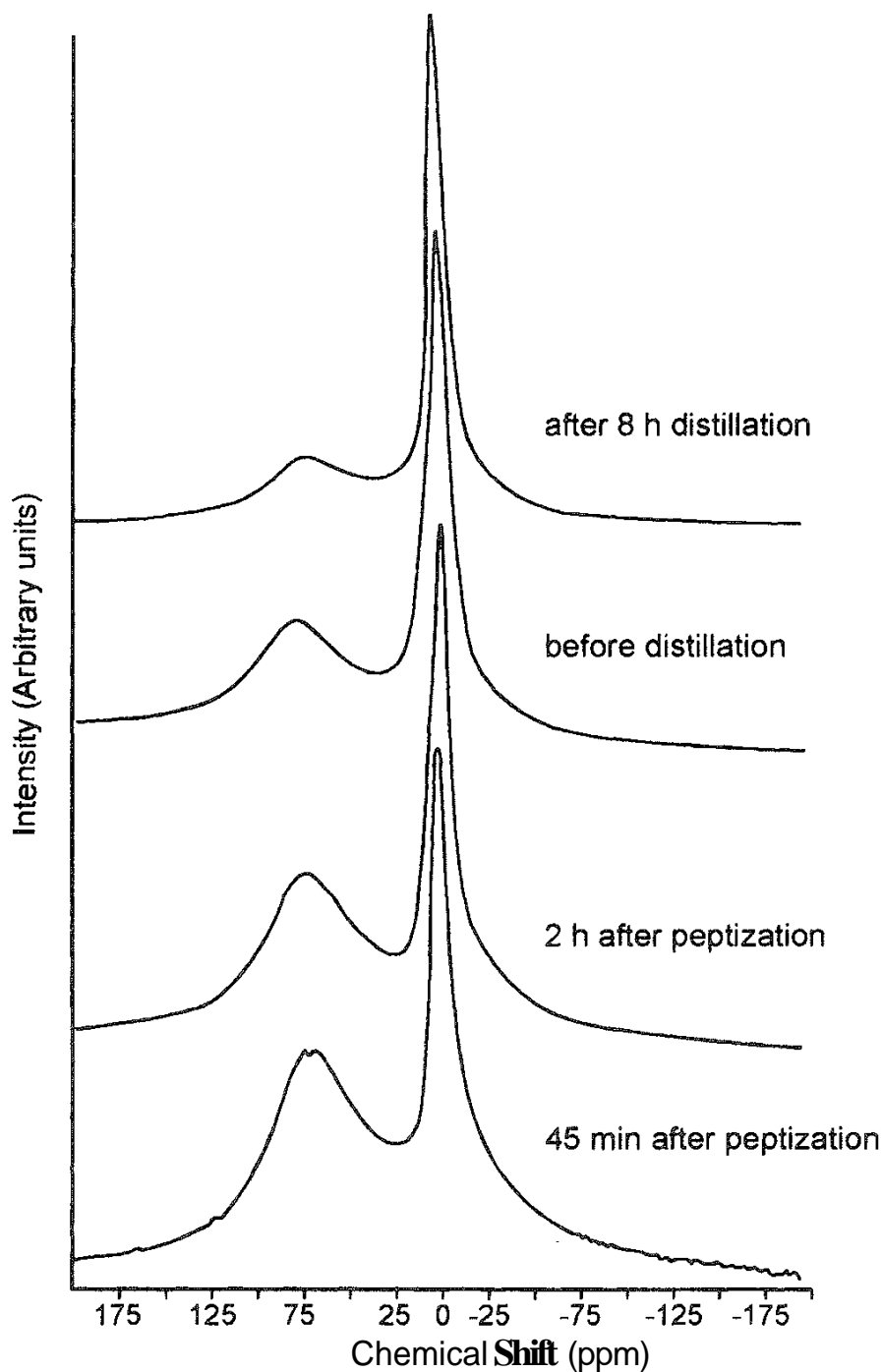


FIG. 10 ^{27}Al NMR spectra of the alumina sol synthesized by hydrolysis of aluminum *sec*-butoxide under molar ratios $\text{H}_2\text{O}/\text{Al}(\text{OC}_4\text{H}_9^s)_3/\text{HNO}_3 = 100:1:0.07$ for 3 days, followed by distillation for solvent removal (2-butanol). (From Ref. 60.)

130.3 MHz after 60 min (Fig. 11a) showed a sharp peak at 0 ppm assigned to the monomer $[\text{Al}(\text{H}_2\text{O})_6]^{3+}$ and its hydrolysates [Eqs (6) and (7)]. In addition, a relatively broad peak (linewidth ~ 470 Hz) at 8.5 ppm slightly overlapped with the monomer resonance. This latter, referred to as SB1, decreased in intensity with the gelation process, concomitant with the growth of another extremely broad octahedral resonance, referred to as SB2, centered at approximately 8 ppm (Figs.

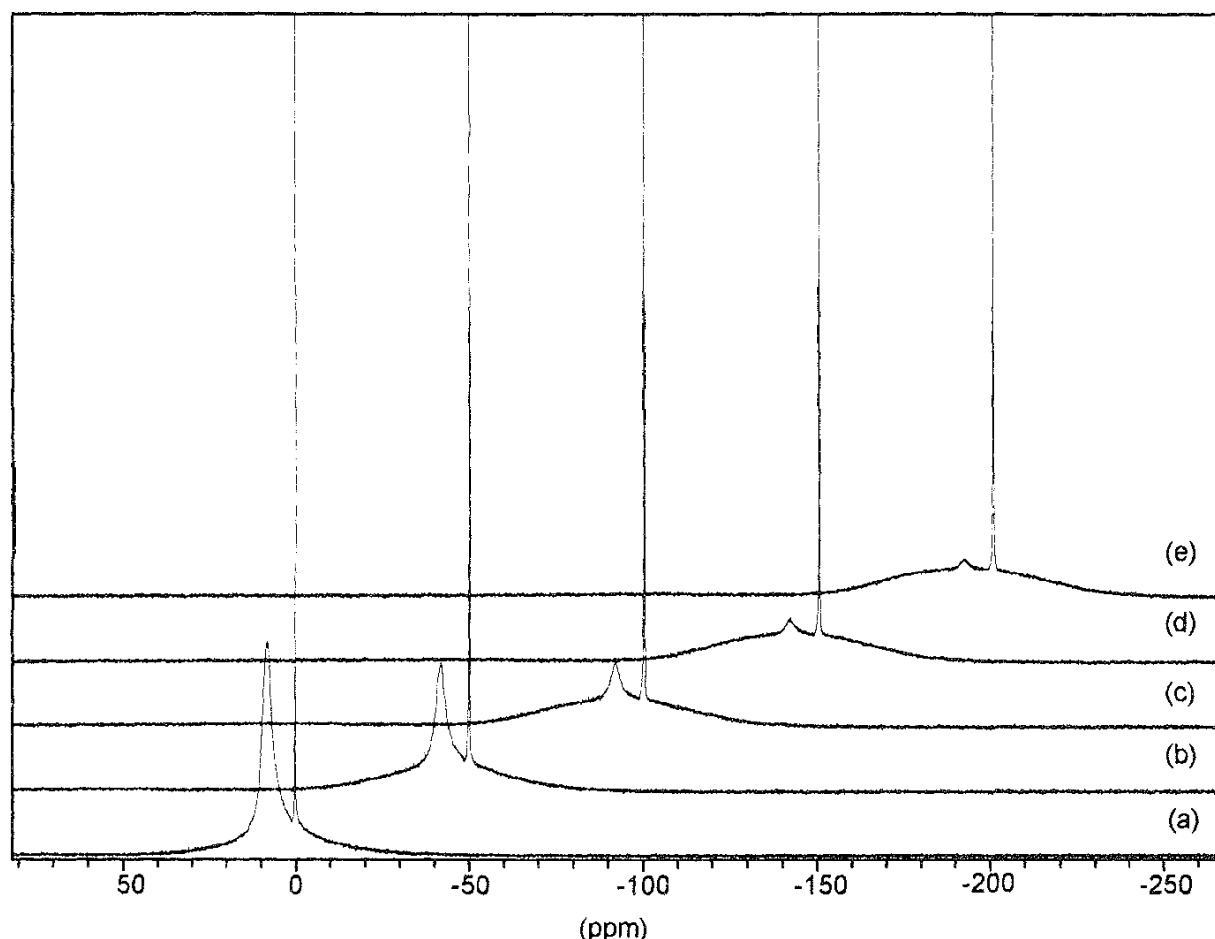


FIG. 11 ^{27}Al NMR spectra at 130.3 MHz of the boehmite SBS dispersion (10% Al_2O_3) peptized with $[\text{HNO}_3]/[\text{Al}] = 0.10$ for (a) 60 min; (b) 240 min; (c) 420 min; (d) 780 min; (e) 1200 min. Scale in x axis valid only for spectrum (a): other spectra were equally displaced in the x and y directions for better viewing of the broad resonance transformation during sol-gel transition. (From Ref. 61.)

11b–11e). The monomer, however, is relatively unaffected by gelation. Very similar spectral changes had already been observed by Olson and Bauer [58] in their peptized system ($\text{HNO}_3/\text{Al} = 0.08$), although their extremely broad peak (only visible by deconvolution) was not so well resolved as in the higher resolution spectra obtained by Morgado et al. [61]. Another interesting observation was the thermal reversibility of the sol-gel as monitored by ^{27}Al NMR. This can be seen in Fig. 12, where the original spectral profile of the sol (without the very broad resonance) is recovered after the semisolid gel is heated at 353 K. (A decrease of about 20% in the total resonance signal was found for spectrum of Fig. 12 acquired at 353 K relative to spectrum a. This is explained by the known inverse proportionality of the NMR signal to the temperature due to the decrease in the population difference between spins states [25].) The SB2 species responsible for the very broad resonance in the gel state is likely a larger structure derived from the SB1 species in a more anisotropic environment. However, due its thermal reversibility, weak attractive bonds are probably involved (e.g., van der Waals forces), in contrast

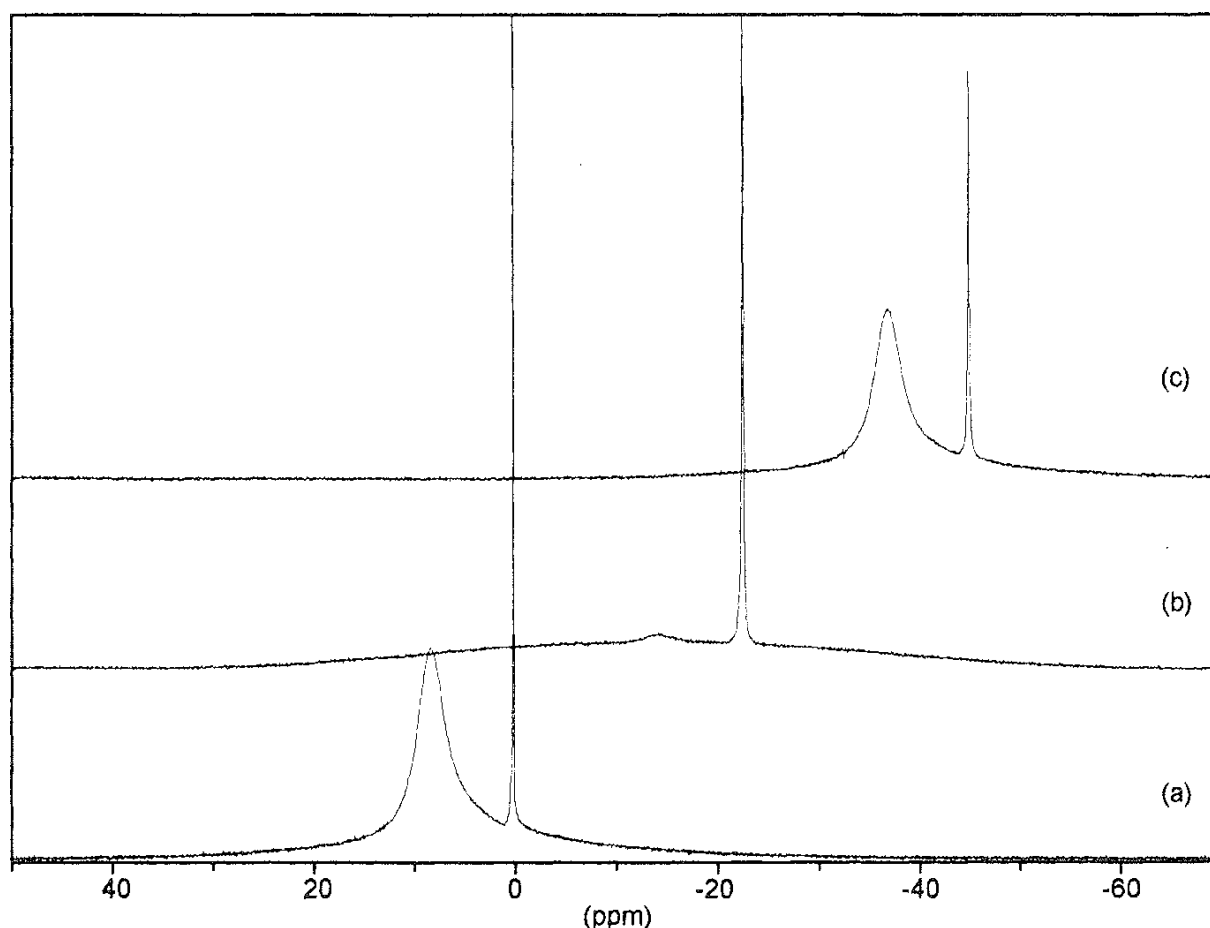


FIG. 12 ^{27}Al NMR spectra at 130.3 MHz of the boehmite SBS dispersion (10% Al_2O_3) peptized with $[\text{HNO}_3]/[\text{Al}] = 0.10$. (a) Sol after 60 min of peptization (298 K); (b) gel after 1200 min of peptization (298 K); (c) gel transformed to sol after 1260 min and recorded at 353 K. (From Ref. 61.)

with other more rigid structures such as those found in silica systems. It is also worth noting the presence of monomer even in the semisolid gel, probably moving freely in the interstitial water enclosed in the continuous solid structure.

It is obvious at this point that ^{27}Al NMR can be a powerful tool for examining the gelation chemistry of alumina sols, but the most interesting result obtained by Morgado et al. [61] was the unequivocal assignment of resonance SB1 to boehmite colloidal particles. This was possible only because of the field dependence shown by this species. The spectrum of the sol in Figs. 11a and 12a are seen to be quite similar to that in Fig. 8a (except for the very small signal at 63 ppm), and it would be tempting to assign the SB1 species as the solution oligomeric species discussed in the previous section. However, a remarkable shift to lower frequency and broadening of the SB1 resonance in the peptized boehmite sol were observed at lower magnetic fields, as depicted in Fig. 13. Morgado et al. could demonstrate that this field dependence was due to a second-order quadrupole-induced shift, which is commonly observed in solids but only for species of limited mobility in the liquid state, far from the extreme narrowing condition (cf. Sec. II.C.). The chemical shifts

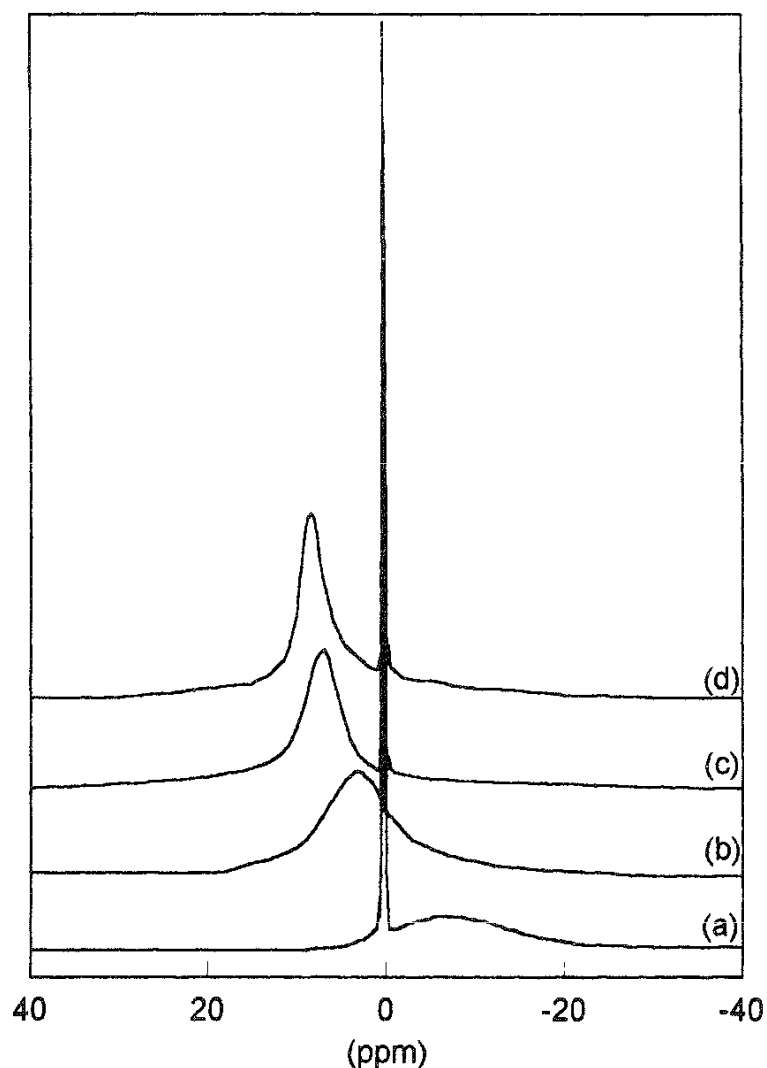


FIG. 13 Field dependence of the boehmite colloid resonance (SBI) in an aqueous peptized system. $\nu_0 =$ (a) 52.1 MHz, (b) 78.2 MHz. (c) 104.2 MHz. (d) 130.3 MHz. (From Ref. 61.)

and linewidths determined at four magnetic fields were plotted against the inverse of the square of the nuclear resonance frequency as shown in Fig. 14 (data denoted by solid squares). A quadrupolar coupling constant of $\chi = 22$ MHz and an isotropic chemical shift of 11.7 ppm were calculated respectively from the slope of the line and from the y intercept in the plot of δ vs. $1/\nu_0^2$, in accordance with Eq. (3) (assuming $\eta = 0$). A comparison of the χ value with those of other aluminum complexes described in the literature indicated that it was intermediate between those of sites of very high symmetry (such as the tetrahedral site of Al_{13} with $\chi = 0.65$ MHz) and those of sites of low symmetry (such as the octahedral site of Al_{13} with $\chi = 10$ MHz) but very close to 7 values for sites of reasonably high symmetry such as in $\text{Al}(\text{acac})_3$. Similarly, a value of $\tau_c = 3.5 \times 10^{-8}$ s was calculated from the slope of the line in the plot of $\nu_{1/2}$ vs. $1/\nu_0^2$ according to Eq. (4), by using the previously estimated value of 7. This value of correlation time was much higher than those observed for the soluble complexes $\text{Al}(\text{acac})_3$ ($\tau_c = 4.2 \times 10^{-11}$ s)

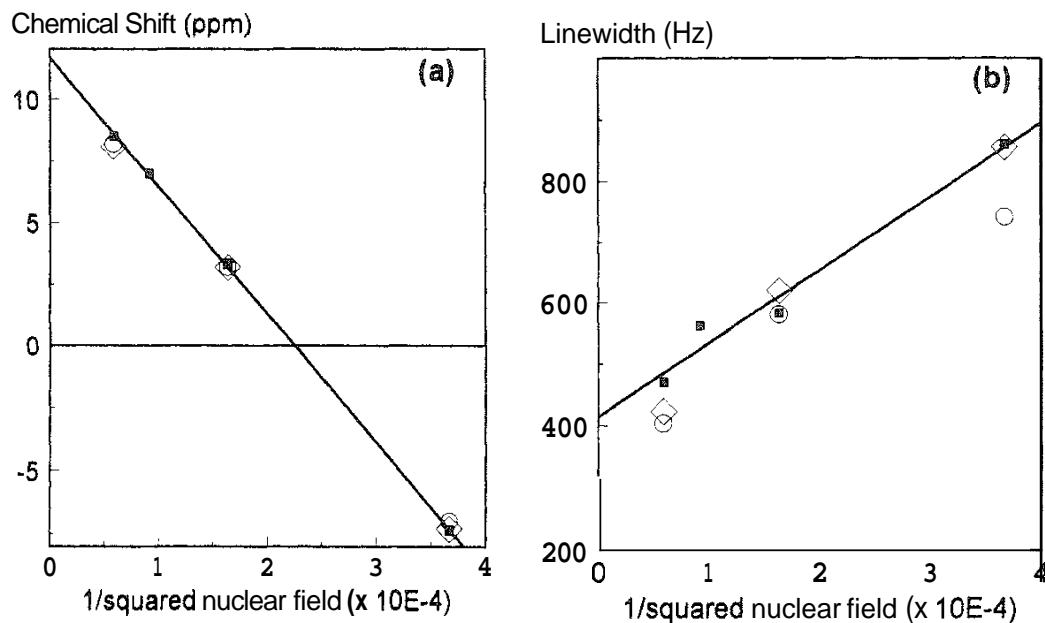


FIG. 14 Dependence of (a) chemical shift and (b) linewidth of the colloid (SB1) octahedral resonance as a function of the nuclear magnetic field (see also Table 4). (■ and line) SBS-HNO₃/Al = 0.10; (◇) SBF-HNO₃/Al = 0.08; (○) Disperal – HNO₃/Al = 0.06. (From Ref, 62.)

and Al₁₃ ($\tau_c = 1.3 \times 10^{-10}$ s) and of the same order of magnitude as that of an aluminum ion bound to large proteins [29]. Thus, the authors could confirm that species SB1 was not a small molecule in solution. In fact, the product $\nu_0\tau_c$ is 4.5 (130.3 MHz) and deviates from the extreme narrowing condition. From Fig. 3 this means that the contribution of the central transition should correspond to $\sim 26\%$ of the total Al signal. In their quantitative measurements (Fig. 15), Morgado and coworkers found that the signal of the resonance SB1 amounted to about 30% of the total aluminum, which is consistent with the complete contribution of the central transition (26%) plus a minor contribution from the transitions $m = \pm 1/2 \leftrightarrow \pm 3/2$ (in Ref. 61, there is a mistake in expressing such transitions of the Al nuclei), which has a considerably higher relaxation rate at $\nu_0\tau_c = 4.5$ (curve II in Fig. 3). This conclusion was reinforced by the fact that the corresponding contribution of the SB1 signal measured at 78.2 MHz was slightly higher ($\sim 35\%$ of the total Al) than that measured at 130.3 MHz. Indeed, $\nu_0\tau_c$ is 2.7 for the former frequency, and at this point the relaxation rate of transition II is closer to that of the central transition I, becoming more significant. Moreover, upon gelling, the contribution of the (SB1 + SB2) signal dropped slightly to 26% of the total Al. This is easily explained by the likely lower mobility of the SB2 species (larger τ_c), bringing the product $\nu_0\tau_c$ to higher values at the right-hand end of the plot in Fig. 3, where only the central transition accounts for the visible signal with a contribution of 25.7%. Therefore, the SB1 species along with the monomer accounted for all the aluminum in the sol system. All this evidence pointed to the assignment of SB1 resonance to the colloidal boehmite particles in the peptized system.

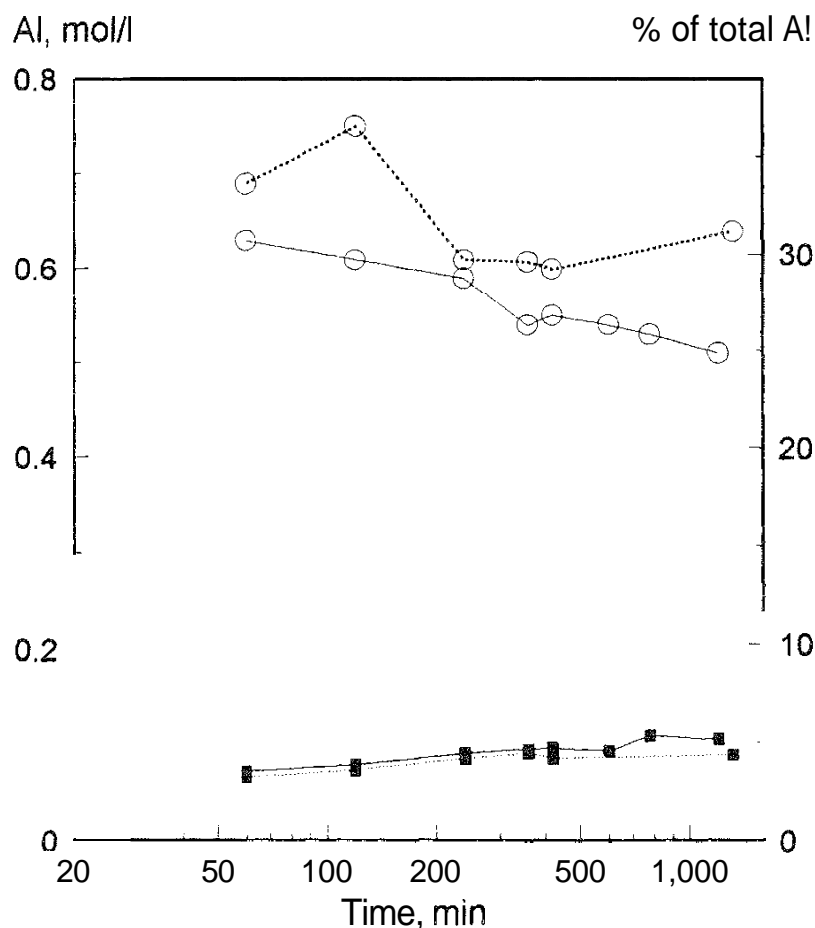


FIG. 15 Absolute and relative concentrations of (■) of the monomer and (○) the SB species in peptized boehmite systems (SBS – 10% Al_2O_3 – $\text{HNO}_3/\text{Al} = 0.10$), determined by ^{27}Al NMR spectral integration and comparison with standard $\text{Al}(\text{NO}_3)_3$ solutions. Solid lines denote results at 130.3 MHz, and dashed lines those at 78.2 MHz. Relative concentration is referred to the total Al present in the system. (From Ref. 61.)

The behavior and quantification of the monomeric species in their peptized boehmite systems have also been studied. Significant changes in linewidth of the monomer resonance were noted and were found to be dependent on the pH of the medium. This behavior was attributed to the differences in the composition of the hexaquo ion and its hydrolysates as shown by Eqs. (6) and (7). The dependence of the monomer line broadening on the pH and other experimental conditions followed the same relationship found in earlier ^{27}Al NMR studies of the hydrolysis of $\text{Al}(\text{III})$ in aqueous solutions [49f,52b]. This allowed Morgado et al. [61] to conclude that the monomeric species moves freely in the dispersion medium of their alumina sols without significant interaction with the surface of colloidal boehmite particles, which are probably stabilized by charging of the potential-determining ion H_3O^+ . As for the quantification of the monomeric species, those species were always present in their peptized systems, accounting for less than 10% of the total Al, indicating the partial dissolution of the boehmitic material. This was confirmed by the proportionality of the monomer concentration to the content of boehmite in the

slurry and to the $[\text{HNO}_3]/\text{Al}$ ratio. Besides, the amount of Al^{3+} released as monomers in solution increased continuously after the sol formation (Fig. 15), indicating that the dissolution process proceeds slowly after the first breakdown of the particles into the colloidal system. The monitoring of the Al^{3+} content by ^{27}Al NMR was certainly useful for the elucidation of the peptization mechanisms. This in situ measurement is particularly important considering that isolation of the dispersion medium for conventional determination of Al^{3+} in solution would not be trivial (see Sec. II.D).

Morgado and Pacheco [62] recently applied the same ^{27}Al NMR approach to investigate other types of colloidal aluminas. Three other commercial boehmites with different degrees of crystallinity were submitted to conditions of nitric peptization similar to those of the earlier study [61]. Table 3 shows the relative amorphous content and crystallite sizes determined by X-ray diffraction of the new boehmites SBF, Disperal, and Pural 200 (P-200), including the sample SBS used in the previous study. The aqueous suspensions with 10 wt% Al_2O_3 were acidified with nitric acid, and the resulting colloidal systems were analyzed with ^{27}Al NMR after 30 min of peptization. Different $[\text{HNO}_3]/[\text{Al}]$ ratios were used to achieve similar pH values, according to the type of alumina and their distinct acid uptake (Table 4). The samples SBS, SBF, and Disperal provided translucent sols, whereas a milky white dispersion was obtained with the highly crystalline boehmite P-200. This latter gave rise to a very ill-defined and broad peak in the NMR spectrum ($\nu_{1/2} \sim 7$ KHz, fig. 16) centered between 6 and 12 ppm, irrespective of the magnetic field employed. It is obvious that in this case a homogeneous system with sufficiently small particles could not be achieved for observation in liquid NMR (cf. Sec. II.C). However, an interesting aspect of the spectra was the detection of a very small sharp signal at 0 ppm due to a monomeric species in solution that was estimated as less than 0.05% of the total Al in the system. Indeed, the expectation

TABLE 3 Properties of the Boehmites

| Boehmite | Code | XRD data | |
|---------------------------|----------|----------------------------|--------------------------|
| | | % amorphous ^(c) | C.S. ^(d) (nm) |
| Pural SB-S ^(a) | SBS | 36 | 4.2 |
| Pural SB-F ^(a) | SBF | 27 | 5.4 |
| Disperal ^(a) | Disperal | 18 | 7.8 |
| Pural 200 ^(a) | P-200 | 0 | 20.1 |
| Si-25-2.7 ^(b) | B1 | 36 | 3.5 |
| Si-25-3.1 ^(b) | B2 | 39 | 3.4 |
| Si-25-5.4 ^(b) | B3 | 37 | 3.3 |

^(a)Commercial boehmites supplied by Condea GmbH (synthesis from hydrolysis of alkoxides)

^(b)Boehmite gels synthesized according to Ref. 5 by neutralization of $\text{Al}(\text{NO}_3)_3$ with NH_4OH .

^(c)Percent relative to the highly crystalline boehmite P-200, assumed as 100% crystalline (0% amorphous).

^(d)C.S. = crystallite size.

TABLE 4 Characteristics of the Peptized Colloidal Boehmites^(a)

| Boehmite | Total percent | | HNO ₃ /Al ratio | pH | MPR ^(b) (nm) | Monomer ^(c) | | Magnetic properties | | |
|----------|--------------------------------|--|-------------------------------|-----|-------------------------|------------------------|---------------------------|---------------------|--------------------------------|----------------------------------|
| | Al ₂ O ₃ | | | | | mol/L | % of total ^(c) | χ (MHz) | δ_{iso} (ppm) | τ_c (s) $\times 10^{-8}$ |
| SBS | 10 | | 0.06 | 3.6 | 26 | 0.048 | 2.3 | nd | nd | nd |
| SBS | 10 | | 0.08 | 3.0 | 24 | 0.052 | 2.5 | 2.93 | 11.5 | 3.1 |
| SBS | 10 | | 0.10 | 1.5 | 22 | 0.056 | 2.7 | 2.94 | 11.7 | 3.5 |
| SBF | 10 | | 0.06 | 3.0 | 16 | 0.033 | 1.6 | 2.95 | 11.7 | 3.4 |
| SBF | 10 | | 0.08 | 1.6 | 13 | 0.038 | 1.9 | 2.89 | 11.2 | 2.9 |
| Disperal | 10 | | 0.04 | 2.0 | 16 | 0.010 | 0.5 | nd | nd | nd |
| Disperal | 10 | | 0.06 | 1.6 | 15 | 0.019 | 0.9 | 2.87 | 11.2 | 3.6 |
| P-200 | 10 | | 0.04 | 1.4 | 100 | <0.001 | <0.05 | nd | nd | nd |
| B1 | 4 | | 0.11 | 3.6 | 19 | 0.029 | 3.6 | nd | nd | nd |
| B2 | 4 | | 0.11 | 3.6 | 12 | 0.036 | 4.5 | nd | nd | nd |
| B3 | 4 | | 0.11 | 3.5 | 13 | 0.039 | 4.9 | nd | nd | nd |

nd = not determined; spectrum acquired at only one magnetic field.

^(a)Sols of commercial boehmites and of boehmite gels characterized, respectively, 30 min and 24 h after HNO₃ addition.

^(b)MPR = mean particle radius determined by dynamic light scattering (hydrodynamic radius corrected by classical Mie equation).

^(c)Integration of the 0 ppm peak in the spectra acquired at 130.3 MHz. Concentration (mol/L) calculated from an external calibration curve. Integral vs.

[Al] of a series of Al(NO₃)₃ solutions measured with the same NMR conditions.

^(d)calculated from field-dependent chemical shifts and linewidths (see text).

^(e)Relative to the total aluminum present in the sol system.

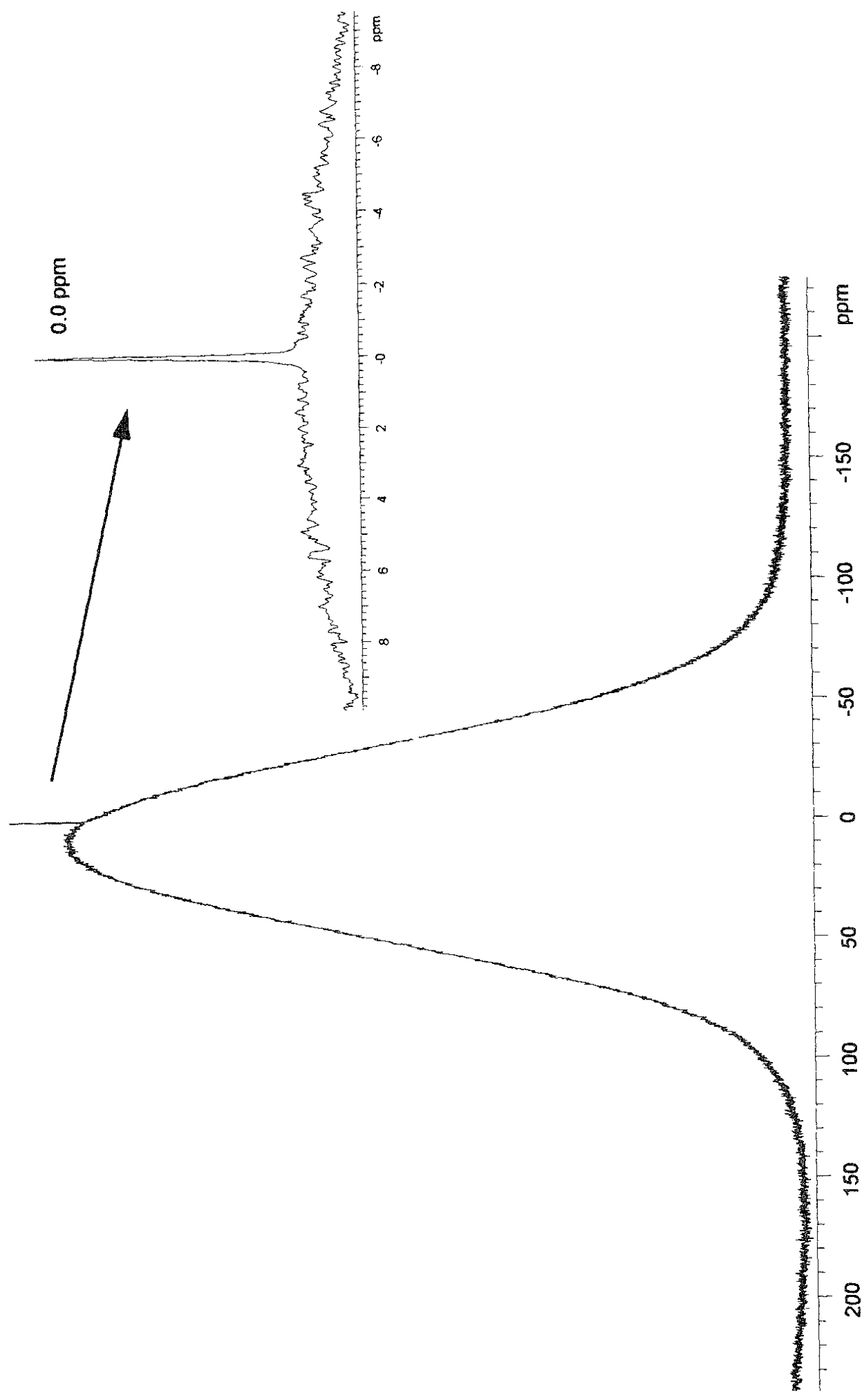


FIG. 16 ^{27}Al NMR spectra at 130.3 MHz of the white milky boehmite Pural 200 dispersion (10% Al_2O_3) peptized with $[\text{HNO}_3]/[\text{Al}] = 0.04$. Notice the very small peak of monomer over the broad band attributed to the colloid. (From Ref. 62.)

from this highly crystalline alumina was that practically no Al would be available for dissolution in the peptization. This fact illustrates the sensitivity of the technique.

The other alumina sols showed the same spectrum profile as that shown in Fig. 12a for the SBS sample, except for different relative intensities of the monomer signal to the colloidal (SB1) resonance. Indeed, the concentration of monomeric species was clearly dependent on the type of boehmite, as shown in Table 4. There is a direct relationship between the concentration of the monomer and the amount of amorphous phase in the original boehmite material (Table 3). It indicates that the monomeric species forms from dissolution of the amorphous phase associated with the dominating nanocrystalline part, which in turn is related to the colloidal resonance (SB1). For the new boehmite systems, the colloidal signal showed the same second-order quadrupole-induced shift as before. The results of the field-dependent chemical shifts and linewidths were also plotted against $1/\nu_n^2$ as shown in Fig. 14 (open symbols), along with the previous data reported by Morgado et al. [61] with the boehinite SBS. It is clear from Fig. 14a that the chemical shifts observed for all three types of boehmite lay on the same line, so that the same quadrupolar coupling constant χ and isotropic chemical shift δ_{iso} were calculated for the different boehmite systems, as shown in Table 4. This fact may provide some insight into the controversial crystal chemistry of the pseudoboehmites. Considering that the χ value reflects the local symmetry around the nucleus, it can be concluded that the chemical environment around the Al sites in the different boehmite colloids is not significantly different. It is in agreement with the theory of Tettenhorst and Hofmann [63] in which both poorly and well crystallized boehmites are continuous in their structure, i.e., they consist of the same or similar octahedral layers in the xz plane, although there is a lack of three-dimensional order for the materials of smaller crystallite sizes because of the restricted number of unit cells along the y axis. In Fig. 14b, the new data follow roughly the same trend as previously. The linewidths of the colloid resonance in the most crystalline boehmite (Disperal) were systematically lower than those of the other two. In all cases, the measured correlation times τ_c were of the same order of magnitude (Table 4). As τ_c is related to the mobility of the particle, the small differences in particle sizes (MPR in Table 4) are consistent with the lack of discrimination among the τ_c values, although Eq. (1) indicates a cubic dependence of τ_c on particle radius. In principle, an independent estimation of τ_c is possible from that equation. Using $\eta = 0.89 \times 10^{-3} \text{ Pa}\cdot\text{s}$ (298 K) and a particle radius of 15 nm as determined by dynamic light scattering, a value of $\tau_c = 3.1 \times 10^{-6} \text{ s}$ was obtained, which is two orders of magnitude higher than the values calculated through Eq. (4) (see Table 4). This deviation is partly explained by the fact that Eq. (1) assumes the rotational diffusion of a perfect sphere, whereas boehmite particles are known to be prolate or oblate spheroids whose rotational motion is therefore anisotropic. However, existing models for correcting such an assumption predict a maximum deviation of one order of magnitude from the classical theory [64]. Other sources of error may be derived from the determination of particle radius (MPR = a) by dynamic light scattering. Small errors in the estimation of particle size are enhanced in the calculation of τ_c through Eq. (1), since $\tau_c = f(a^3)$. The appropriate use of NMR for

obtaining information on the size of the particles and molecules is still a cloudy subject.

Alumina sols from peptization of boehmites obtained by an inorganic route have also been analyzed by ^{27}Al NMR at 130.3 MHz [65]. Boehmite precipitates were prepared by neutralization of $\text{Al}(\text{NO}_3)_3$ solution with NH_4OH according to the procedure described in Ref. (5). They were diluted with water to 4% Al_2O_3 and peptized with nitric acid, providing clear sols that did not gel, even 24 h after acid addition, when NMR analysis was carried out. Their spectra are shown in Fig. 17, and the concentration in monomeric species is shown in Table 4 (B1–B3). The spectra presented the same characteristic peaks as those of alumina sols from boehmite of hydrolyzed alkoxides (organic route). The colloid showed a resonance peak at 8.5 ppm and $\nu_{1/2} = 470$ Hz, similar to the spectrum of Fig. 12a. The monomer linewidth showed the same pH dependence of Al^{3+} in aqueous solution as observed for the alumina sols of commercial boehmites. The magnitude of the relative monomer concentration (percent of the total) is consistent with their high content of amorphous phase (Table 3), but it is larger than that shown by SBS of similar amorphous content by XRD. This can be explained either by the longer peptization time to which these boehmite sols were submitted or by a dif-

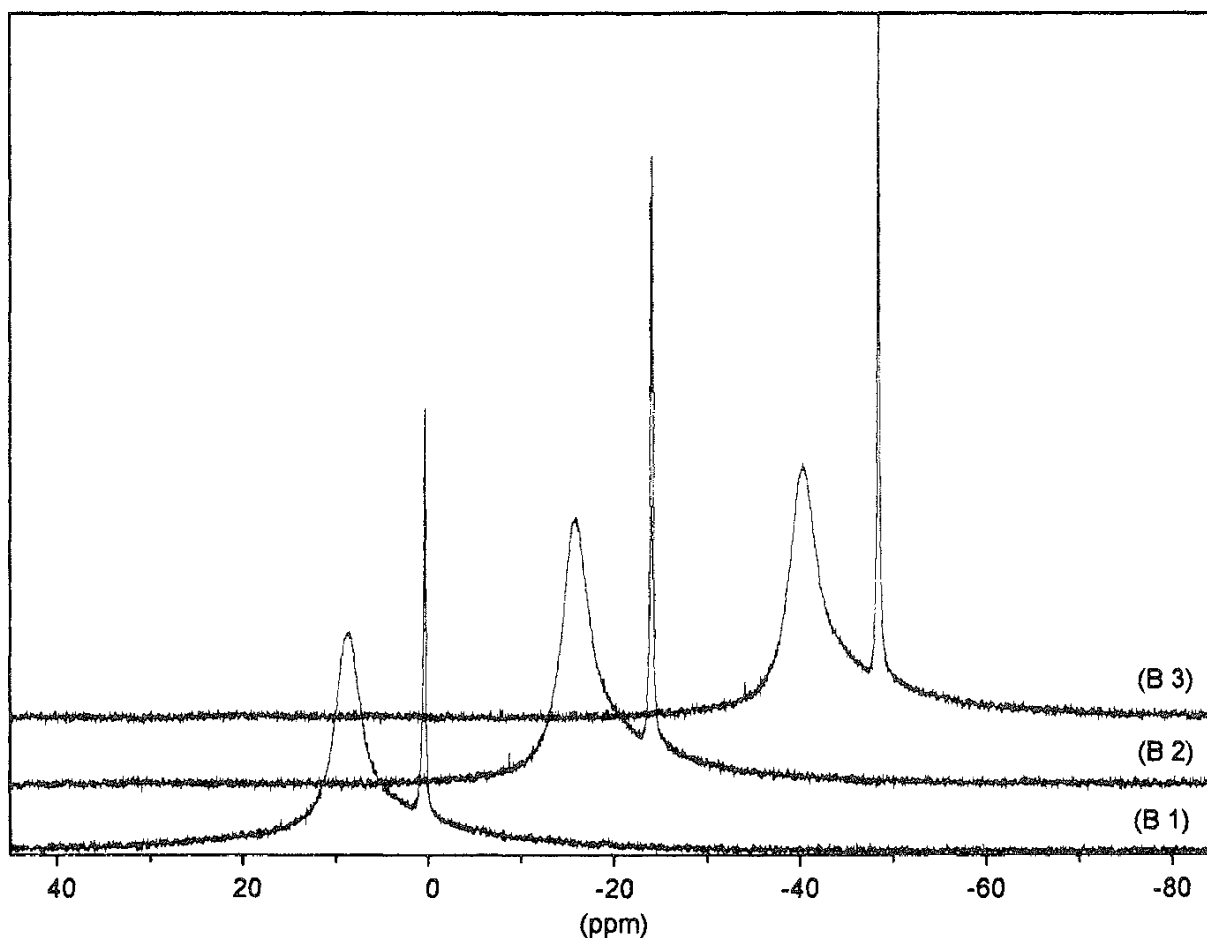


FIG. 17 Al NMR spectra at 130.3 MHz of boehmite sols (4% Al_2O_3) after peptization with $[\text{HNO}_3]/[\text{Al}] = 0.11$ of boehmite precipitates derived from inorganic route (see Tables 3 and 4). (From Ref. 65.)

ference in the nature of their amorphous phase, which might be more susceptible to dissolution by HNO_3 .

Another alumina sol from the inorganic route was studied by Kurokawa et al. [48]. Fresh precipitate produced by neutralization of AlCl_3 solution with NH_4OH was aged for 12 h and separated from the mother liquor to be peptized with acetic acid and by heating at 353 K. These researchers monitored the peptization process of the aluminum hydroxide precipitate toward a final alumina sol as a function of reflux period (Fig. 18). Although they used ^{27}Al (MAS) NMR with the sample rotating at 3.6 KHz, only soluble and colloidal Al species were observed, so that static ^{27}Al NMR would likely give the same spectra. It was found that the starting precipitate (before heating/peptization) was associated with disappearance of the NMR signal. Considering the amorphous nature of the material at this point (high quadrupole interaction with the electric field gradient), this fact is quite reasonable. It is also evident that the Al_{13} species that was present in the precursor hydrolyzed solution is still present with the precipitate (Fig. 18a). The tetrahedral species (Al_{13}) was decomposed upon acidic peptization at 353 K, while the sharp monomer peak and a broader resonance at 3.1–3.3 ppm increased with time of peptization. It was assumed that acetic acid is consumed by both peptization of the hydroxide and decomposition of the tetrahedral structure. It was not considered, however, that at their reflux conditions (353 K), colloidal boehmite is likely to be formed from the amorphous hydroxide along with peptization. The broader resonance at 3.1–3.3 ppm appearing after 1 h of reflux was assigned to oligomers of hydrous aluminum. However, from our previous discussion, such resonance is most probably due to colloidal boehmite. The spectral profile of their alumina sol (Fig. 18h) is very similar to the spectrum of the peptized boehmite system acquired at 78.4 MHz (Fig. 13b). In fact, their alumina sol showed particles in the range of a few tens of nanometers, and after solvent removal it showed an X-ray diffraction pattern with ill-defined reflections close to those of poorly crystallized boehmite. However, their NMR measurements were performed at $\nu_0 = 70.4$ MHz, and from Fig. 14 an apparent chemical shift of 1.3 ppm (instead of 3.1 ppm) would be expected for the colloidal boehmite. Either their assignment of soluble oligomers is correct or another colloidal species with χ sufficiently large, but different from that in commercial boehmites (Table 4), is involved. It should be stressed that the rotation (3.6 KHz) at the magic angle is not enough to remove the second-order quadrupolar effects.

3. Studies of Adsorbed Species

The use of NMR spectroscopy for probing molecules adsorbed on alumina dispersions is briefly cited. Söderlind and Blum [66] used deuterium NMR to probe the dynamics and structure of a surfactant (an alkylbenzenesulfonate, SHBS) adsorbed onto alumina. The phenyl ring was deuterium-labeled, and from the analysis of the lineshapes of ^2H spectra, valuable information on the degree of motional freedom in the adsorbed layer was obtained. As deuterium possesses a quadrupole moment, it is sensitive to the orientation of the molecule with respect to the external magnetic field. This sensitivity generates a quadrupolar splitting, which is defined as the separation between the two allowed transitions for the deuterium nucleus. In liquid systems, the quadrupole interaction is averaged out, but for static systems powder

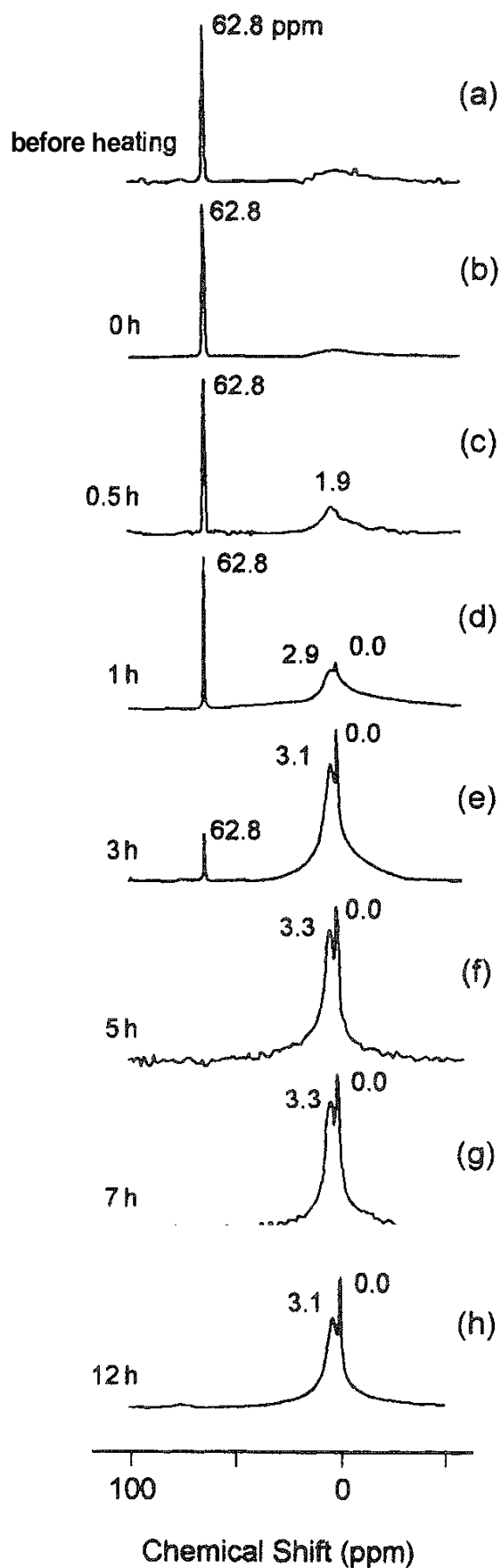


FIG. 18 ^{27}Al NMR spectra at 70.4 MHz of aluminum hydroxide precipitate [from neutralization of $(\text{Al}(\text{H}_2\text{O})_6)\text{Cl}_3$ with NH_4OH] peptized with acetic acid ($\text{H}/\text{Al} = 0.15$) at 353 K as a function of reflux period. (From Ref. 48.)

or Pake patterns are obtained. Molecular motions that are comparable to or faster than the quadrupole coupling constant will affect the lineshape and reduce the splitting from its rigid value.

Phosphorus-31 NMR was used by Burton et al. [20] to analyze polyphosphazenes (dispersants) bound to the surface of alumina ceramic particles. The differences between the spectra of the inorganic polymer in solution and in colloidal suspensions were used to probe the chemical interaction with the alumina. Their ^{31}P NMR results showed a small lower frequency shift associated with phosphazenes bound to alumina. Solution samples consistently displayed a broadening of the ^{31}P resonance upon cumulative addition of alumina to the suspension, indicating some degree of chemical adsorption (Sec. II.E). However, Burton et al. pointed out that this lineshape difference might be mistaken as an artifact caused by the amount of solids present in the NMR sample.

C. Other Colloidal Oxides

Nuclear magnetic resonance studies have proved valuable for the characterization of other colloidal oxides and hydroxides. Some selected examples of such studies are shown in the following paragraphs.

Pozarnsky and McCormick [7,22] used ^{51}V NMR to propose mechanisms for the synthesis of V_2O_5 aqueous sols. In contrast with the Al colloids discussed in the previous section, the ^{51}V NMR signal due to colloidal species (vanadate polymers) has mostly broadened beyond the detection limit, probably due to its very low symmetry, which enhances the problem of quadrupole interaction. Nevertheless, based on the solution chemistry associated with the sol, the gelation process could be rationalized in terms of the chain polymerization of the dioxovanadium cation, VO_2^+ (-545 ppm from VOCl_3). This polymerization could be rate-limited by the release of the VO_2^+ cations from decavanadate anions (-426 , -512 , -531 ppm) if these anions were initially present at high concentration. Using an external reference spectrum, Pozarnsky and McCormick found different starting concentrations of the decavanadate anion that were dependent on the synthesis method. In the slow gelation synthesis method, the decavanadate ion accounted for $\sim 80\%$ of the vanadium present, whereas in the fast synthesis method it accounted for only 20% . Therefore, a reaction scheme that explains the NMR data (after a brief initial transient period) could be obtained, thus rationalizing the polymerization mechanism.

Judeinstein and Livage [8] used ^1H and ^{13}C NMR to analyze molecular precursors formed during the sol-gel synthesis of WO_3 thin films but were not very successful in using ^{183}W NMR for their unequivocal characterization. Three ^{183}W broad resonance peaks appeared, but a definite conclusion was not possible because the chemical shifts might be related either to bonding distortions in a single oligomeric molecule or to different molecular species. In both cases the broadening of the NMR signals could be explained by short relaxation times arising from formation of oligomeric species and exchange reactions between different chemical species.

King et al. [21] applied ^{13}C , ^{15}N , and ^1H NMR to provide structural information on HTMA (hexamethylenetetramine) used as a gelation agent in the sol-gel syn-

esis of microspherical nuclear fuel (UO_2). Furthermore, they used ^{17}O NMR to monitor uranyl speciation during the hydrolysis and gelation processes. Léaustic et al. [6] used ^1H NMR to study the early stages in the preparation of TiO_2 colloids.

Most advanced ceramics are multicomponent materials having two or more cations in the oxide network such as mullite ($\text{Al}_6\text{Si}_2\text{O}_{13}$) and cordierite ($\text{Mg}_2\text{Al}_4\text{O}_{18}$). In particular, the sol-gel route may be applied in their synthesis to allow the homogeneous mixing of precursors at a molecular level. However, a major problem in forming homogeneous multicomponent gels is the unequal hydrolysis and condensation rates, as observed between silicon and aluminum precursor cases (Sec. III.B.1). Complexed aluminum alkoxide precursors with reduced reactivity have been used to overcome this drawback, and the effectiveness of this route has been studied by ^{27}Al NMR. By using this technique, Livage and coworkers [9,67] have followed the hydrolysis of TEOS in the presence of an aqueous (or ethanolic) solution of aluminum and magnesium nitrates and compared it with that in the presence of $\text{Al}(\text{O}^i\text{Bu})_3$ complexed by ethylacetoacetate (etac) and an aqueous solution of magnesium acetate. The ^{27}Al NMR spectra of these two precursor sols for cordierite are shown in Figs. 19a and 19b, respectively. For the first procedure (Fig. 19a), only a sharp peak at 0 ppm (solvated Al^{3+}) is noticed, indicating that no $\text{Si}-\text{O}-\text{Al}$ bonds are formed at this stage. In contrast, in case (b) when the aluminum precursor was complexed, the ^{27}Al NMR spectra showed the formation of transient species characterized by a sharp peak at ~ 51 ppm

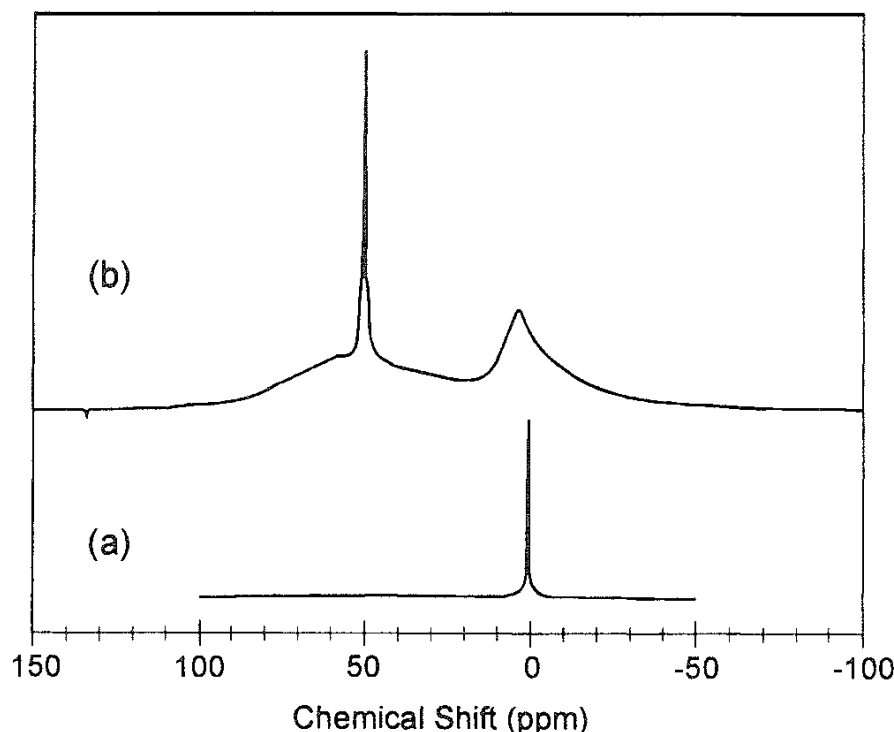


FIG. 19 ^{27}Al NMR spectra of two precursor solutions from cordierite. (a) TEOS hydrolyzed with an aqueous solution of aluminum and magnesium nitrates; (b) TEOS and $\text{Al}(\text{O}^i\text{Bu})_2$ (etac) hydrolyzed with an aqueous solution of magnesium acetate. (From Ref. 9.)

(similar to Al_{13} but not the same), which was assigned to $\text{Al}-\text{O}-\text{Si}$ bonds probably associated with $\text{Al}(\text{O}[\text{Si}(\text{OR})_3])_4$. Indeed, the corresponding ^{29}Si NMR spectrum showed a peak caused by $\text{Si}(\text{OAl})(\text{OR})_3$, suggesting such a structure. Upon sol-gel transformation, the sharp tetrahedral signal in the spectrum of Fig. 19b progressively disappears, giving rise to a broad resonance around 55 ppm along with the remaining broad peak at ~ 4 ppm. The main point is that the chemical shift of 55 ppm is typical of that found for cordierite, thus demonstrating the importance of the formation of $\text{Si}-\text{O}-\text{Al}$ bonds in the precursor sols as probed by ^{27}Al and ^{29}Si NMR. Another approach to ensure a good level of mixing of aluminate and silicate species was used by Jaymes and Douy [10] in the synthesis of mullite. They used urea decomposition to provide slow *in situ* generation of ammonia to hydrolyze and polycondense the aluminum species while promoting polycondensation of the silicic acid due to the slow increase in pH. In this process, a gel was formed within a few hours but was slowly disaggregated into a clear sol after 3 days, and finally a second gel was obtained after a week. The intermediate colloidal phase was formed at $0.8 < \text{OH}/\text{Al} < 2.7$. During this period of hydrolysis, static ^{29}Si and ^{27}Al NMR spectra were obtained and compared to the corresponding solid-state MAS NMR of the first and second gel phases. ^{29}Si NMR spectra of the sol phase showed that the remaining resonance peaks at -110 and -102 ppm, predominant in the first gel, progressively disappeared, being replaced by lines at -90 and -85 ppm. These lines in turn disappeared, giving rise to a single resonance at -78 ppm for a degree of hydrolysis (OH/Al) slightly higher than 2.4, remaining in the second gel. Surprisingly, ^{27}Al NMR studies of the sol phase showed only the peak at Oppm (like that of Fig. 19a), in contrast with a small additional tetrahedral Al signal in the first and second dried gels observed by ^{27}Al MAS NMR. The authors attributed the unexpected absence of Al^{IV} in the intermediate sol phase to aluminum species in highly distorted symmetry>probably not observable by NMR under static conditions. However, there is no reason to believe that the rotation of the sample at the magic angle would make visible such an asymmetric species. The MAS condition tends to eliminate anisotropy effects (CSA). Moreover, the small particles of 2 nm radius reported for their sol phase indicates that the colloidal species was probably moving rapidly enough to account for isotropic behavior so that it could be observed even in a static ^{27}Al NMR experiment (cf. SB1 species in the previous section). The authors attributed the predominant hexacoordinated aluminum and low condensed silicon species in the later stages of this sol-gel process to a chemical environment very close to that found in natural imogolite/allophane. In these minerals, each silicon atom is linked to hexacoordinated aluminum atoms via oxo bridges and to hydroxyl groups, showing a unique resonance at 78 ppm (^{29}Si NMR) and only octahedral aluminum. This work and many others [7,9,22] show the adequacy of the combination of liquid- and solid-state NMR to elucidate the complete transformation sequence in sol-gel processes. The same combination of techniques may be helpful in gaining a better understanding of adsorption phenomena in colloidal oxides [20].

Lead-207 NMR was employed to probe a $\text{PbO}-\text{TiO}_2$ sol-gel system [68]. A precursor was prepared by mixing lead acetate and isopropylorthotitanate solutions (1:1) in methoxyethanol and HCl. Only one ^{207}Pb signal appeared, around -883 ppm (from Me_4Pb), immediately on mixing, remaining unchanged with time

even during the gelation process. However, compared with the simple lead acetate in the solvent with a signal at -1248 ppm, there was a significantly higher frequency shift of the ^{207}Pb NMR signal in the two-component precursor. It indicated that an interaction between the two compounds happened very quickly and a new chemical environment with respect to the lead atom was established. On the other hand, ^{13}C and ^1H NMR spectra of the freshly prepared precursor showed that neither the $-\text{OPr}$ group of the titanium compound nor the $-\text{OAc}$ group of the lead compound were changed. So the chemical shift at -883 ppm could not be explained by a $\text{Pb}-\text{O}-\text{Ti}$ bonding at this stage. Based on additional information gained from infrared spectra, Lan et al. [68] suggested that the two compounds were rapidly interacting, forming a linkage or association through the bidentate acetate bridging, unchanged during solution reactions and gelation. $\text{Pb}-\text{O}-\text{Ti}$ bonds formed only upon calcination with the decomposition of the OAc groups.

Carbon-13 NMR was used for examination of $\text{YBa}_2\text{Cu}_3\text{O}_{6+x}$ precursor sols by Kramer et al. [11]. The interesting aspect of this work was the immediate broadening effect (without changing the chemical shift) in the methoxyethanol resonance when the copper(III) ethoxide toluene was added to the barium alkoxide solution. Because the initial copper solution was colloidal, it was suggested that the line broadening was due to the interaction of the quadrupolar copper nucleus with alkoxide. However, as hydrolysis proceeded, the signals became progressively narrower until the original aspect was recovered. This narrowing effect was coincident with a decrease in the particle size of the sol, indicating that yttrium and barium alkoxides react with copper ethoxide in such a way as to break up the colloidal particles. Duboudin et al. [69] used ^1H and ^3Li NMR to study the kinetics and structure of an LiTaO_3 material prepared by the sol-gel process.

An interesting example of simultaneous characterization of a colloidal hydroxide and surface-adsorbed species was studied by Yesinowski [19]. Calcium hydroxyapatite, $\text{Ca}_{10}(\text{OH})_2(\text{PO}_4)_6$, in colloidal suspension was analyzed by ^{31}P NMR in the liquid state. A stable colloidal suspension of this solid could be formed only with the addition of sodium diphosphonate (Na_2EHDP) acting as a peptizing agent. The ^{31}P NMR spectrum of the colloidal suspension is shown in Fig. 20b. The peak at 19.1 ppm (from H_3PO_4) arises from EHDP. In the phosphate region there are other two peaks. A sharp peak at 0.9 ppm arises from the orthophosphate ions liberated from hydroxyapatite into solution when EHDP was added. The broader peak at 2.8 ppm was assigned to the colloidal hydroxyapatite. Ultracentrifugation of the colloidal system and resuspension of the residue in pure water resulted in the nearly complete loss of the solution phosphate signal but not the colloidal signal (Fig. 20c). In addition, there was a reduction in size and a remarkable increase in the linewidth of the EHDP resonance, whereas the solution phosphate peak had no broadening. Yesinowski therefore concluded that the small broadened peak arose from EHDP chemisorbed on the hydroxyapatite surface. A closer look at the ^{31}P NMR spectrum of this sample before ultracentrifugation and resuspension (Fig. 20b) showed a sharp component arising from free EHDP over a broader one from the chemisorbed EHDP that is not in rapid exchange with free molecules in solution.

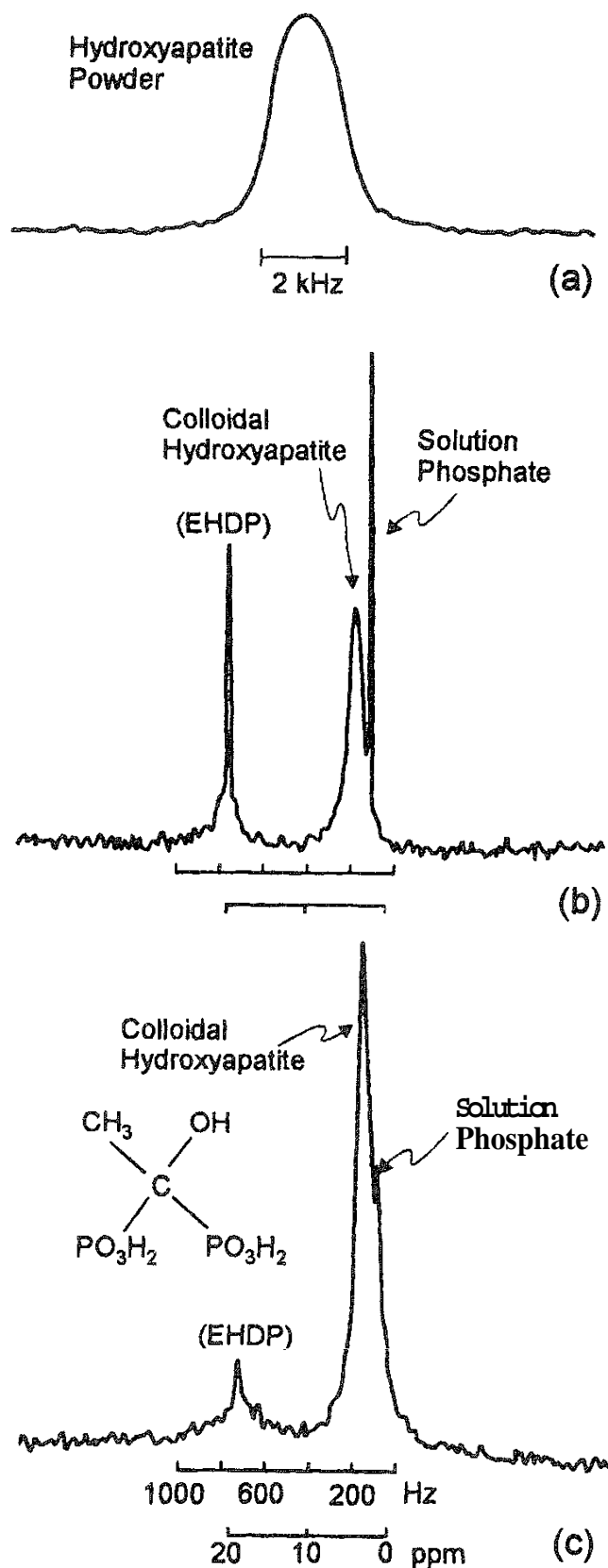


FIG. 20 ^{31}P NMR spectra at 36.4 MHz of (a) solid hydroxyapatite powder (undecoupled); (b) colloidal suspension of ≤ 0.6 g of hydroxyapatite in 2 mL of H_2O + 0.075 g of Na_2EHDP , 1.4 h data accumulation (proton-decoupled); and (c) colloidal suspension formed by ultracentrifuging sample (b) and resuspending pellet in 2 mL of H_2O , scale same as spectrum (b). (From Ref. 19.)

IV. CONCLUSIONS

All the studies described in Sec. III illustrate the ability of NMR to investigate the chemistry of a variety of colloidal oxides and associates in the liquid state. Due to the recent growth and attractiveness of sol-gel products derived from metal alkoxides, NMR spectroscopy has been extensively employed to study the chemical composition and kinetics of such systems from their initial formulation through their final processing stages. Nevertheless, similar results can be successfully obtained in colloidal dispersions by inorganic routes. The simultaneous analysis of the chemistry in both the dispersion medium and the disperse phase is a great advantage of liquid-state NMR of such colloidal systems. However, the disperse phase is investigated conveniently only when the particulate species meet a motional narrowing condition, where broadening interactions (typical of the solid phase) are eliminated. It seems that particles with effective diameters smaller than 50 nm are appropriate, although other parameters related to the particle motion, such as solvent viscosity and temperature, have to be considered as well. In the case of colloids containing quadrupolar nuclei such as ^{27}Al , studies of the field-dependent phenomena are particularly useful for qualitative and quantitative examination. The NMR spectra of adsorbed compounds on suitable colloidal oxides can easily be obtained and give structural information about the surface of the particle and adsorbate. In some cases, colloids will constitute useful models for bulk oxides. On the other hand, the use of NMR spectroscopy in fluid media furnishes a powerful tool in combination with MAS NMR to analyze the complete chemical pathway of sol-gel transformations.

REFERENCES

1. R. K. Iler, *The Chemistry of Silica*, Wiley, New York, 1979.
2. H. E. Bergna (ed.), *The Colloid Chemistry of Silica*. Adv. Chem. Ser., American Chemical Society, Washington, DC, 1994.
3. C. J. Bricker and G. W. Scherer, *Sol-Gel Science: The Physics and Chemistry of Sol-Gel Processing*. Academic, San Diego, CA, 1990.
4. B. E. Yoldas, Am. Ceram. Soc. Bull. 54:286 (1975).
5. E. Morgado, Jr., Y. L. Lam, and L. F. Nazar, J. Colloid Interface Sci, 188:257 (1997).
6. A. Leautic, F. Babonneau, and J. Livage, Chem. Mater. 1:248 (1989).
7. G. A. Pozarnsky and A. V. McCormick, J. Mater. Sci. Lett. 15:1526 (1996).
8. P. Judeinstein and J. Livage, J. Mater. Chem. 1:621 (1991).
9. J. Livage, F. Babonneau, M. Chatry, and L. Coury, Ceram. Int. 23:13 (1997).
10. I. Jaymes and A. Douy, J. Eur. Ceram. Soc. 16:155 (1996).
11. S. Kramer, G. Moore, G. Kordas, P. A. Kiefer, and T. G. Knight, Mater. Res. Soc. Symp. Proc. 121:643 (1988).
12. L. C. Klein (ed.), *Sol-Gel Technology for Thin Films, Fibers, Preforms, Electronics and Speciality Shapes*, Noyes, Park Ridge, NJ, 1988.
13. R. A. Assink and B. D. Kay, Annu. Rev. Mater. Sci. 21:491 (1991).
14. G. Fu, L. F. Nazar, and A. D. Bain, Chem. Mater. 3:602 (1991).
15. R. Joseph, S. Zhang, and W. T. Ford, Macromolecules 29:1305 (1996).

- 16 J. Y. Bottero, M. Axelos, D. Tchoubar, J. M. Cases, J. J. Fipriat, and F., Fiessinger, *J. Colloid Interface Sci.* 117:47 (1987).
- 17 I. D. Gay, in *Encyclopedia of Nuclear Magnetic Resonance*, Vol. 2 (D. M. Grant and R. K. Harris, eds.), Wiley, Chichester, UK, 1996, pp. 733–738.
- 18 R. J. Abraham and P. Loftus, *Proton and Carbon-13 NMR Spectroscopy, An Integrated Approach*, Heyden, London, 1978.
- 19 J. P. Yesinowski, *J. Am. Chem. Soc.* 103:6266 (1981).
- 20 S. D. Burton, W. D. Samuels, G. J. Exarhos, and J. C. Linehan, *Mater. Res. Soc. Symp. Proc.* 227:161 (1991)
- 21 (a) C. M. King, R. B. King, A. R. Garber, M. C. Thompson, and B. R. Buchanan, *Mater. Res. Soc. Symp. Proc.* 180:1075 (1990); (b) R. B. King, C. M. King, and A. R. Garber, *ibid.*, p. 1083,
- 22 G. A. Pozarnsky, PhD. Thesis, University of Minnesota, 1994.
- 23 K. Kimura and N. Satoh, *Chem. Lett.* 1989:271.
- 24 J. W. Akitt, *NMR and Chemistry — An Introduction to Modern NMR Spectroscopy*, Chapman & Hall, London, 1992, Chapter 4.
- 25 R. K. Harris, *Nuclear Magnetic Resonance Spectroscopy: A Physicochemical View*, Longmans, Avon, UK, 1986.
- 26 D. D. Traficante, in *Encyclopedia of Nuclear Magnetic Resonance*, Vol. 6 (D. M. Grant and R. K. Harris, eds.), Wiley, Chichester, UK, 1996, pp. 3988–4003.
- 27 T. E. Bull, S. Forsén, and D. L. Turnmer, *J. Chem. Phys.* 70:1306(1979).
- 28 A. C. Kunwar, A. R. Thompson, H. S. Gutowsky, and E. Oldfield, *J. Magn. Reson.* 60:467 (1984).
- 29 J. M. Aramini, M. W. Germann, and H. J. Vogel, *J. Am. Chem. Soc.* 115:9750 (1993).
- 30 T. Cosgrove and T. M. Obey, in *Encyclopedia of Nuclear Magnetic Resonance* (D. M. Grant and R. K. Harris, eds.), Vol. 2, Chichester, UK, 1996, pp. 1384–1390.
- 31 (a) L. Piculell, *J. Chem. Soc., Faraday Trans.* 1 82:387 (1986); (b) B. Halle and L. Piculell, *ibid.*, 415.
- 32 J. Ripmeester, L. S. Kotlyar, and B. D. Sparks, *Colloids Surf. A* 78:157(1993).
- 33 P. Roose, J. van Craen, G. Andriessens, and H. Eisendrath, *J. Magn. Reson. A* 120:206 (1996).
- 34 G. Engelhardt and D. Michel, *High-Resolution Solid-state NMR of Silicates and Zeolites*. Wiley, Chichester, 1987, Chapter III.
- 35 G. Engelhardt, H. Jancke, D. Hoebbel, and W. Wiecker, *Z. Chem.* 14:1109(1974).
- 36 B. K. Coltrain and L. W. Kelts, in *The Colloid Chemistry of Silica* (H. E. Bergna, ed.), *Adv. Chem. Ser.*, Am. Chem. Soc., Washington, DC, 1994, Chapter 19.
- 37 J. Sefcik and A. V. McCormick, *Catal. Today* 35:205 (1997).
- 38 M. J. Muñoz-Aguado and M. Gregoskiewitz, *J. Colloid Interface Sci.* 185:459 (1997).
- 39 L. W. Kelts, N. J. Effinger, and S. M. Melpolder, *J. Non-Cryst. Solids* 83:1375 (1986).
- 40 C. J. Brinker, K. D. Keefer, D. W. Shafes, R. A. Assink, B. D. Kay, and C. S. Ashley, *J. Non-Cryst. Solids* 63:45 (1986).
- 41 R. Badley, W. T. Ford, F. J. McEnroe, and R. A. Assink, *Langmuir* 6:1792 (1990).

42. J. D. F. Ramsay, S. W. Swanton, A. Matsumoto, and D. G. C. Goberdhan, in *The Colloid Chemistry of Silica* (H. E. Bergna, ed.), Adv. Chem. Ser., Am. Chem. Soc., Washington, DC, 1994, Chapter 3.
43. C. J. Brinker, in *The Colloid Chemistry of Silica* (H. E. Bergna, ed.), Adv. Chem. Ser. Am. Chem. Soc., Washington, DC, 1994, Chapter 18.
44. A. R. Siedle and R. A. Newmark, *J. Am. Chem. Soc.* **103**:1240 (1981).
45. T. Cosgrove and P. C. Griffiths, *Colloids Surf. A* **84**:249 (1994).
46. (a) R. E. Hurd, *J. Magn. Reson.* **87**:422 (1990); (b) R. E. Hurd, in *Encyclopedia of Nuclear Magnetic Resonance* (D. M. Grant and R. K. Harris, eds.) Vol. 3, Wiley, Chichester, UK, 1996, pp. 1990–2005.
47. M. R. Bohmer, L. K. Koopal, and R. Janssen, *Langmuir* **8**:228 (1992).
48. Y. Kurokawa, Y. Kobayashi, and S. Nakata, *Heterogen. Chem. Rev.* **1**:309–328 (1994).
49. (a) J. W. Akitt, N. N. Greenwood, and G. D. Lester, *J. Chem. Soc. A* **1969**:803 (1969); (b) J. W. Akitt and A. Farthing, *J. Magn. Reson.* **32**:345 (1978); (c) J. W. Akitt and A. Farthing, *J. Chem. Soc., Dalton Trans.* **1981**:1617 (1981); (d) J. W. Akitt and A. Farthing, *J. Chem. Soc. Dalton Trans.* **1981**:1624 (1981); (e) J. W. Akitt, and B. E. Mann, *J. Magn. Reson.* **44**:584 (1981); (f) J. W. Akitt, and J. M. Elders, *J. Chem. Soc., Faraday Trans. I* **81**:1923 (1985); (g) J. W. Akitt and J. M. Elders, *J. Chem. Soc., Dalton Trans.* **1988**:1347 (1988); (h) J. W. Akitt, J. M. Elders, X. L. R. Fontaine, and A. K. Kundu, *J. Chem. Soc. Dalton Trans.* **1989**:1889 (1989).
50. J. Y. Bottero, J. M. Cases, F. Fiessinger, and J. E. Poirier, *J. Phys. Chem.* **84**:2933 (1980); (b) J. Y. Bottero, D. Tchoubar, J. M. Cases, and F. Fiessinger, *J. Phys. Chem.* **86**:3667 (1982).
51. (a) P. M. Bertch, G. W. Thomas, and R. I. Barnhisel, *Soil Sci. Soc. Am. J.* **50**:825 (1981); (b) P. M. Bertch, *ibid.*, **51**:825 (1987).
52. (a) J. T. Klopogge, D. Seykens, J. B. H. Jansen, and J. W. Geus, *J. Non-Cryst. Solids* **142**:94 (1992); (b) J. T. Klopogge, D. Seykens, J. B. H. Jansen, and J. W. Geus, *J. Non-Cryst. Solids* **152**:207 (1993); (c) J. T. Klopogge, D. Seykens, J. B. H. Jansen, and J. W. Geus, *J. Non-Cryst. Solids* **160**:144 (1993).
53. A. R. Thompson, A. C. Kunwar, H. S. Gutowsky, and E. Oldfield, *J. Chem. Soc., Dalton Trans.* **1987**:2317 (1987).
54. T. E. Wood, A. R. Siedle, J. R. Hill, R. P. Skarjune, and C. J. Goodbrake, *Mater. Res. Soc. Symp. Proc.* **180**:97 (1990).
55. J. Y. Bottero, D. Tchoubar, J. M. Cases, J. J. Fipriat, and F. Fiessinger, in *Interfacial Phenomena in Biotechnology and Materials Processing* (Y. A. Attia, B. M. Moudgil, and S. Chander, eds.), Elsevier, New York, 1988, pp. 459–479.
56. L. F. Nazar, and L. C. Klein, *J. Am. Ceram. Soc.* **71**:C85 (1988).
57. C. J. Doss and R. Zahren, *Phys. Rev. B* **48**:626 (1993).
58. W. L. Olson and L. J. Bauer, *Mater. Res. Soc. Symp. Proc.* **73**:187 (1986).
59. T. Assih, A. Ayral, M. Abenoza, and J. Phalippou, *J. Mater. Sci.* **23**:3326 (1988).
60. U. Janosovits, G. Ziegler, U. Scharf, and A. Wokaum, *J. Non-Cryst. Solids* **210**:1 (1997).
61. E. Morgado, Jr., Y. L. Lam, S. M. C. Menezes, and L. F. Nazar, *J. Colloid Interface Sci.* **176**:432 (1995).
62. E. Morgado, Jr. and C. R. N. Pacheco, unpublished results, 1997.

63. R. Tettenhorst, and D. A. Hofmann, *Clays Clay Miner.* 28:373 (1980).
64. R. T. Boere and R. G. Kidd, *Annu. Rep. NMR Spectrosc.* 13:319 (1982).
65. E. Morgado Jr., M.Sc, Thesis, Federal Univ. Rio de Janeiro, 1995.
66. E. Söderlind, and F. D. Blum, *J. Colloid Interface Sci.* 157:172 (1993).
67. L. Bonhomme-Courty, F. Babonneau, and J. Livage, *Chem. Mater.* 5:323 (1993).
68. L. Lan, A. Montenero, G. Gnappi. and E. Dradi, *J. Mater. Sci.* 30:3137 (1995).
69. F. Douboudin, J. Dunogues, J. Senegas, N. Puyoo-Castaings, and J. Ravez, *Mater. Sci. Eng. B*5:431 (1990).
70. J. Sauer, in *Modelling of Structure and Reactivity in Zeolites* (C. R. A. Catlow, ed.), Academic, San Diego, CA, 1992, pp. 183–216.
71. W. R. Carper and C. E. Keller, *J. Phys. Chem.* 101:3246 (1997).

7

Polymer Surface Dynamics Using Surface-Modified Glasses via Dynamic Contact Angle Measurements

JOUNG-MAN PARK Department of Polymer Science and Engineering,
Gyeongsang National University, Chinju, Korea

- I. Introduction
- II. Experimental
 - A. Materials
 - B. Methods
- III. Results and Discussion
 - A. Surface density and wettability on alkyl-immobilized glass substrates
 - B. Effect of various alkyl chain lengths on contact angle and surface energies
- IV. Conclusions
- References

I. INTRODUCTION

Polymer surface dynamics or mobility at interfaces is an interesting and practically applicable subject [1,2]. Solid surfaces are assumed to be rigid and immobile due to surface chemistry. However, polymer molecules in the near surface or interfacial regions are really expected to exhibit motion and relaxation. Of course, these are not identical to the motion observed in the bulk because of the different interfacial environment. In general, given sufficient mobility, polymer surfaces and interfaces can be mobile and the surface can rearrange or reorient at interfaces to minimize the interfacial free energy with the surrounding phase.

For biomedical devices [3,4] and chromatographic supports [5], the nature of such surface motion can be applied. We know that polymer surfaces in aqueous solution can have different properties than in air or vacuum due to their different mobilities. The chromatographic properties of a reverse phase are dependent on the

conditions of the bonded phases. The motion of such alkyl-bonded chains is the key to understanding their chromatographic properties [6,7]. Many researchers, including Gilpin and Squires [8], have investigated dual models of monomeric alkyl surfaces ranging from a folded or "liquid-like" orientation to a rigid or bristly type in an aqueous environment.

Electron spectroscopy for chemical analysis (ESCA) [9] and Fourier transform infrared (FTIR) spectroscopy [10] with attenuated total reflectance (ATR) can also be used for routine surface studies. FTIR spectroscopy is known to have the sensitivity to determine the average orientation and reorientation of interfacial chains. But it does not directly provide information on the motion itself. The mobility of a solute in the neighborhood of an alkyl chain can be measured by fluorescence spectroscopy [11].

Direct measurement of molecular motion and dynamics is offered by ^{13}C NMR studies [12,13] using the spin-lattice (T_1) and spin-spin relaxation times (T_2). In a general sense, the changes in spin-lattice relaxation time (T_1) were consistent with increased segmental motion as a function of distance from the surface. Sindorf and Maciel [14] investigated the molecular motion of *n*-alkylsilane bonded to silica particles using ^{13}C NMR. Alkyl chain mobility might increase with chain length (i.e., up to $n = 8$) until the interactions between chains occur at longer chain length ($n = 18$, for example). However, the main disadvantage of ^{13}C NMR methods is that they are limited to fine particles having high surface areas and are not applicable to plate-type surfaces.

The Wilhelmy plate contact angle method might provide a sequential scanning curve or hysteresis loop that can be interpreted in terms of surface mobility, reorientation, solvent penetration, and intrinsic wettability under both water and air. Water is known to be a difficult liquid for use in contact angle studies due to its small molecular volume, resulting in penetration and local swelling of the solid surfaces [15].

According to Van Damme et al. [16], the receding contact angles on poly-*n*-alkyl methacrylate surfaces decrease in the range of $n = 6$ to $n = 12$, then increase to $n = 18$. Because of the increasing mobility due to the decreasing T_g , polymer surfaces with moderate-length alkyl side chains may reorganize, which may lead to a decreased number of hydrophobic segments exposed to water. In addition, as a minor factor, the hydrophilic ether groups may also reorient toward water surfaces. This result may be closely related to another study [17] of the brittle temperature for poly-*n*-alkyl acrylates and methacrylates. They showed a minimum in the brittle temperatures in the ranges of $n = 8$ – 12 due to increased side chain mobility. Judging by these cases, alkyl side chain bonded surfaces may have different motions with different chain mobilities and lengths.

It is not easy to measure such alkyl chain length effects directly on polymer substrates because of the packing density problem [18], polymer swelling effects [19], etc. Therefore, immobilized alkylsilanes on glass substrates can be used as a good model system for the study of alkyl surface dynamics. Because rigid glass surfaces are nondeformable, unlike polymer substrates, a rigid glass substrate may have a contact angle very different from that of a polymer substrate. Pure clean glass substrates contain silanol groups (i.e., high surface energy), and the contact angles are zero in a pure aqueous environment. Hence, we may be sure that the

contact angles obtained are indeed due to the alkyl side chains attached to the glass substrates.

In this work, we applied dynamic contact angle methods to the study of wetting and interfacial phenomena. The reaction of monofunctional silane reagents with silanol sites at the silica surface can result in a single monolayer, whereas di- and trifunctional silanes, especially if water is not completely excluded, hydrolyze and also polymerize, forming a polymeric bonded phase [7]. Therefore, a series of *n*-alkyl dimethyl monochlorosilanes of differing *n*-alkyl chain lengths ($n = 1, 4, 8$, and 18), available commercially, were bonded on the glass surfaces. We studied the effects of different alkyl chain lengths on borosilicate glass surfaces by varying the surface concentrations and using different solvents. In addition, using a non-linear programming method, surface energy terms, γ^d and γ^p were obtained from the data under both pure water solvent and mixed solvents of water and methanol.

II. EXPERIMENTAL

A. Materials

Trimethyl chlorosilane, *n*-butyldimethyl chlorosilane, *n*-octyldimethyl chlorosilane, and *n*-octadecyldimethyl chlorosilane were purchased from Petrarch Systems, Inc. and used without further purification (all $>99.5\%$). The chemical structures of these silanes are shown in Table 1. Dimers, present as minor constituents in reagents [e.g., $(\text{CH}_3)_3\text{SiOSi}(\text{CH}_3)_3$ for the $n = 1$ case], contain no reactive groups. Hence, they were removed during the rinsing procedure.

Prepurified water was further purified by passing through a Milli-Q reagent water system (Millipore Co.). Toluene was dried with molecular sieve particles for 24 h before use. Methanol and dehydrated ethyl alcohol were used as received.

Corning borosilicate cover glass (2940, No. 1 $1/2$, 24 x 50 mm, 0.16–0.19 mm thickness) was used as substrate. As determined by ESCA, surface elemental compositions of this borosilicate glass were B = 2.3, Si = 28, O = 63, C = 4.4 atomic percentages, respectively. Minor components below 1% were Na, Al, Zn, K, N, and Ti.

B. Methods

1. Cleaning Glasses

Glass slides were immersed in chromic-sulfuric acid solution at 80°C for 40 min, which supplied active oxygen atoms that oxidize carbonaceous materials on glass surfaces, rinsed extensively with purified water, and then dried overnight in a clean oven at 120°C in air. All other glassware used was also carefully cleaned by the same process.

We examined the cleanliness of the glass slides by measuring the surface tension of purified water ($72.6 \pm 0.5 \text{ dyn/cm}$) at room temperature (22°C) and by verifying that there was no water contact angle hysteresis and that the slides were perfectly wetted.

TABLE 1 Chemical Structures of *n*-Alkyl Silane Coupling Agents

| Designation ^a | Chemical name | Chemical structure |
|--------------------------|--|---|
| T2950 | Trimethyl chlorosilane | $\begin{array}{c} \text{Me} \\ \\ \text{CH}_3 - \text{Si} - \text{Cl} \\ \end{array}$ |
| B2785 | <i>n</i> -Butyldimethyl chlorosilane | $\begin{array}{c} \text{Me} \\ \\ n\text{-C}_4\text{H}_9 - \text{Si} - \text{Cl} \\ \end{array}$ |
| O9819 | <i>n</i> -Octyldimethyl chlorosilane | $\begin{array}{c} \text{Me} \\ \\ n\text{-C}_8\text{H}_{17} - \text{Si} - \text{Cl} \\ \end{array}$ |
| D5636 | <i>n</i> -Octadecyldimethyl chlorosilane | $\begin{array}{c} \text{Me} \\ \\ n\text{-C}_{18}\text{H}_{37} - \text{Si} - \text{Cl} \\ \\ \text{Me} \end{array}$ |

^aPetrach system designation

2. Preparation of Coated Surfaces

After verifying that the dried slide showed no contact angle hysteresis, clean glass slides were immersed in a suitable concentration of *n*-alkyldimethyl monochlorosilane in dried toluene and allowed to equilibrate for 15 min. Silanization reaction time was 30 min for the formation of monolayers at room temperature (22°C) [20]. The coupling chemical reaction of *n*-alkyl silanes with glass surfaces is shown in Fig. 1. Hydrolyzed alkyl silanes in aqueous solution can react with the silanol groups in the glass surfaces to produce immobilized alkyl chains.

The slides were then rinsed thoroughly four or five times with pure ethanol to remove unreacted silane materials. The treated slides were then heated in a vacuum oven at 70°C for 3 h under nitrogen to remove HCl and ethanol. The stability of the silane coating on the glass slides was tested by remeasuring the contact angle in purified water after drying in a vacuum oven at room temperature (22°C) and by verifying the reproducibility of the contact angle.

3. Dynamic Contact Angle Measurements

As soon as the coated slides were removed from the oven and cooled to room temperature, dynamic contact angles were measured by the Wilhelmy plate technique [21]. We obtained the wetting curve with an electrobalance (Cahn Model

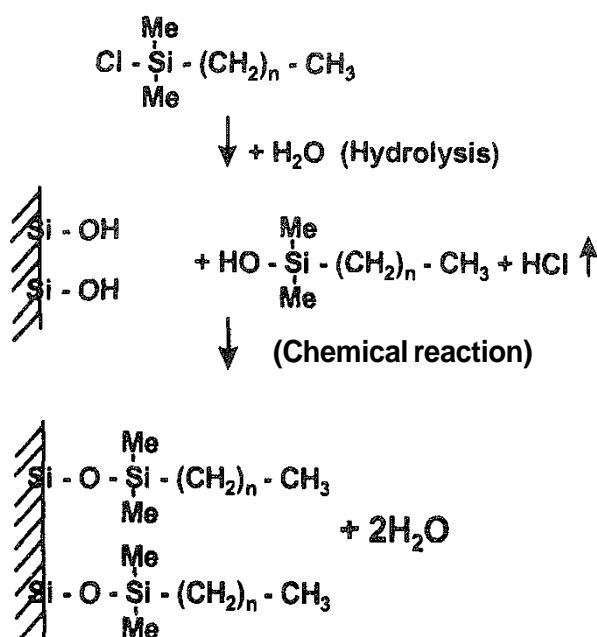


FIG. 1 Chemical reactions of *n*-alkyl silane coupling agents with glass surfaces for $n = 0, 3, 7$, or 17 .

RM-2) as a function of the immersion depth. A motor drives the shelf to advance or withdraw the water container at a controlled speed. The chamber is insulated and maintained at room temperature (22°C) and constant humidity (35% RH).

The output from the electrobalance measurement is fed to an X-Y recorder, with the balance output (force) feeding the Y axis and immersion depth feeding the X axis. To measure the contact angle, the silane-treated glass slides were immersed into or withdrawn from the purified water or mixed solvent at a constant speed of 40 mm/min. Dipping velocity was chosen to be fast enough for convenience of measurement but slow enough to avoid speed effects (such as hysteresis on the clean glasses) as shown in Fig. 2. Advancing contact angles were used for this study because they can show the surface energy condition directly, whereas receding contact angles can show the surface energy condition of the wetted surfaces.

Water-methanol solvents were made with increasing MeOH fraction. Each solution was kept for 15 min at room temperature to equilibrate; then its surface tension was measured. The contact angle and surface tension of each sample were measured three times, and their error ranges were within $\pm 3^\circ\text{C}$ and $\pm 0.5 \text{ dyn/cm}$, respectively.

4. Surface Energy Measurement

Young's equation, which describes the force balance of a liquid drop on a solid surface, is used with the usual symbols,

$$\gamma_{LV} \cos \theta = \gamma_{SV} - \gamma_{SL} \quad (1)$$

The total free energy is the sum of contributions from the different intermolecular forces at the surface,

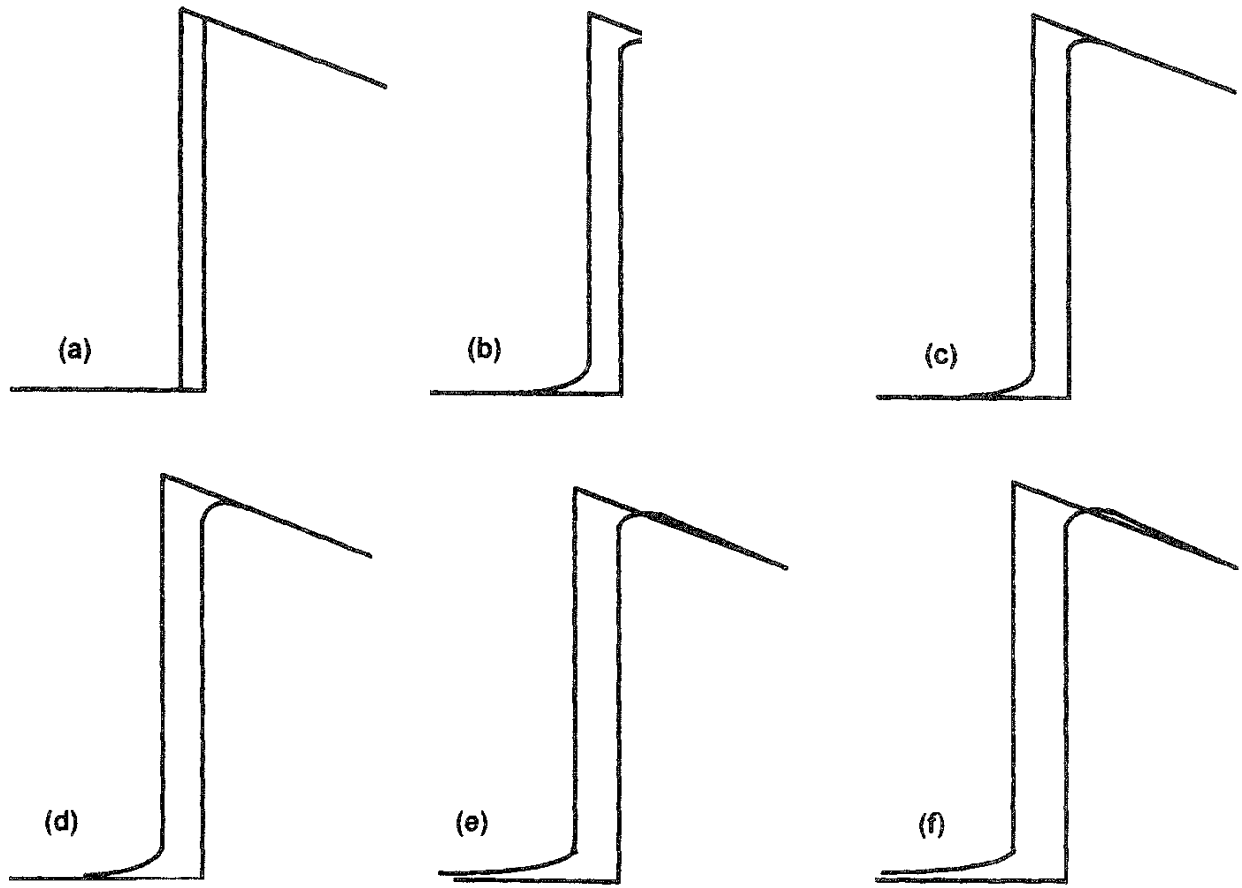


FIG. 2 Dipping velocity effect at various speeds using cleaned glass plates in the Wilhelmy plate technique: (a) 10 mm/min; (b) 30 mm/min; (c) 40 mm/min; (d) 60 mm/min; (e) 80 mm/min; (f) 120 mm/min.

$$\gamma_{LV} = \gamma_{LV}^d + \gamma_{LV}^p \quad (2)$$

where the superscripts d and p refer to the dispersion and polar force components, respectively.

The surface free energy of a solid/liquid interface can be described as a function of individual force components of the solid and liquid. For the relationship, the following equation, which was assumed by Owens and Wendt [21], is most reliable for polymeric solids:

$$\gamma_{SL} = \gamma_{SV} + \gamma_{LV} - (2\gamma_{SV}^d \gamma_{LV}^d)^{1/2} - (2\gamma_{SV}^p \gamma_{LV}^p)^{1/2} \quad (3)$$

Combining Eqs. (1) and (3) yields the well-known geometric mean equation,

$$\gamma_{LV}(1 + \cos \theta)/2 = (\gamma_{SV}^d \gamma_{LV}^d)^{1/2} - (\gamma_{SV}^p \gamma_{LV}^p)^{1/2} \quad (4)$$

By measuring the contact angle θ of two different liquids against a solid, simultaneous equations are obtained that can be solved for γ_{SV}^d and γ_{SV}^p if the values of γ_{LV}^d and γ_{LV}^p are known. With some organic liquids, the components of free energy were evaluated using reference solids. The result shows that the components deviated by over 10% from the mean, and they cannot be accepted as constant.

When more than two kinds of liquids are used, a useful technique introduced by Erbil and Meric [22] can be used. The method, based on a parameter identification problem, uses only the total surface free energy of liquids, which can be obtained precisely by experiment. For this method, an equation that shows the interaction between the solid and liquid surfaces is needed.

The work required to pull the liquid away from the surface (i.e., the work of adhesion) was given by Dupre as

$$W_A = \gamma_{LV}(1 + \cos \theta) \quad (5)$$

The work of adhesion was described as follows by Girifalco and Good [23] using the individual component of free energy,

$$W_A = 2\Phi(\gamma_{LV}\gamma_{SV})^{1/2} \quad (6)$$

where Φ is the interaction parameter. Combining Eqs. (4)–(6) yields

$$\Phi = (\gamma_{SV}^d\gamma_{LV}^d/\gamma_{SV}\gamma_{LV})^{1/2} + (\gamma_{SV}^p\gamma_{LV}^p/\gamma_{SV}\gamma_{LV})^{1/2} \quad (7)$$

When $\Phi = 1$, the network of adhesion W_A is maximized for a given value of γ_{SV} and γ_{LV} . This value of Φ corresponds to $\gamma_{LV}^d/\gamma_{LV} = \gamma_{SV}^d/\gamma_{SV}$ and $\gamma_{LV}^p/\gamma_{LV} = \gamma_{SV}^p/\gamma_{SV}$. Thus $\Phi = 1$ only when the fractional molecular force contributions from dispersion and polar components in both the liquid and the solid to the total surface tension are equal. This idealized condition is difficult to achieve during contact angle determination for most polymers due to the difference between the surface free energy properties of probe liquids and polymers. In this work, a new concept that involves the virtual liquid surface free energy components is introduced. With the known value of total surface free energy of liquid (γ_{LV}) and experimental data of the contact angle (θ), one can estimate the individual surface energy components of solids and virtual components of liquids with a parameter estimation algorithm using a nonlinear programming method. The method forces the interaction parameter Φ values close to 1 for each polymer–liquid pair under the constraint of the geometric mean relation, Eq. (4).

Because of some inevitable errors in measuring the contact angle, the geometric equation might show some deviation from the exact equality. With a value of acceptable error in Eq. (4), 3% or 5%, for example, one can optimize the free energy components to maximize the interaction parameter. We used a multivariable nonlinear regression algorithm developed by Marquadt (see Ref. 24) with some modification for constrained optimization. The result shows less than 3% error in the geometric mean relation and a mean value of over 0.95 for the interaction parameter in all cases.

III. RESULTS AND DISCUSSION

A. Surface Density and Wettability on Alkyl-Immobilized Glass Substrates

The samples of different alkyl chain lengths ($n = 1, 4, 8$, and 18) and different alkyl surface concentrations obtained by varying the silane concentration (10^{-4} – 0.5 mol/

100 mL toluene) in the treatment solution were characterized by contact angle measurements via the Wilhelmy plate method. Five different solvents were made up by mixing water and methanol.

Advancing contact angles measured for these modified glass substrates are shown in Table 2. For the monofunctional bonded phases ($n = 1, 4, 8$, and 18) in various solution environments, contact angles increase with both increasing alkyl silane concentration and increasing water fraction in the mixed solutions. With increases in the MeOH fraction, for $n = 4$ and 8 , contact angles decrease steadily to around 0° , whereas for the $n = 1$ and 18 cases, even with a pure MeOH environment, contact angles approach 10° due to the high hydrophobicity of silane on glass substrates. In an aqueous environment, the alkyl chain is "folded" and shows

TABLE 2 Advancing Contact Angles as a Function of Alkyl Chain Length and Log Concentration

| H ₂ O/MeOH (surface tension) ^b | Concentration (mol/100 mL toluene) | | | | | | |
|---|------------------------------------|-----|------------------|------------------|------------------|------------------|------------------|
| | 0.5 | 0.2 | 10 ⁻¹ | 10 ⁻² | 10 ⁻³ | 10 ⁻⁴ | 10 ⁻⁵ |
| $n = 1$ | | | | | | | |
| 100:0 (72.6) | 117 | 98 | 89 | 63 | 45 | 43 | 42 |
| 75:25 (48.5) | 95 | 85 | 77 | 51 | 37 | 33 | 31 |
| 50:50 (36.8) | 73 | 65 | 59 | 27 | 13 | 10 | 10 |
| 25:75 (29.5) | 41 | 39 | 35 | 10 | 7 | 0 | 0 |
| 0:100 (22.8) | 7 | 6 | 5 | 0 | 0 | 0 | 0 |
| $n = 4$ | | | | | | | |
| 100:0 (72.6) | 79 | 75 | 71 | 55 | 39 | 32 | — ^a |
| 75:25 (48.5) | 73 | 69 | 65 | 49 | 35 | 27 | — |
| 50:50 (36.8) | 53 | 51 | 44 | 25 | 13 | 7 | — |
| 25:75 (29.5) | 33 | 27 | 23 | 0 | 0 | 0 | — |
| 0:100 (22.8) | 0 | 0 | 0 | 0 | 0 | 0 | — |
| $n = 8$ | | | | | | | |
| 100:0 (72.6) | 76 | 71 | 69 | 63 | 49 | 41 | 41 |
| 75:25 (48.5) | 75 | 66 | 59 | 45 | 39 | 33 | 32 |
| 50:50 (36.8) | 59 | 49 | 41 | 27 | 17 | 10 | 3 |
| 25:75 (29.5) | 33 | 27 | 21 | 0 | 0 | 0 | 0 |
| 0:100 (22.8) | 0 | 0 | 0 | 0 | 0 | 0 | 0 |
| $n = 18$ | | | | | | | |
| 100:0 (72.6) | 99 | 93 | 85 | 72 | 64 | 57 | 57 |
| 75:25 (48.5) | 86 | 81 | 73 | 60 | 45 | 36 | 36 |
| 50:50 (36.8) | 66 | 62 | 57 | 44 | 28 | 16 | 0 |
| 25:75 (29.5) | 41 | 39 | 35 | 10 | 7 | 0 | 0 |
| 0:100 (22.8) | — | — | — | — | — | — | — |

^aDash (—) indicates no tested value

^bdyn/cm, error range within 0.5.

hydrophobicity, whereas in aqueous methanol solvent the chain is "brushlike" or "extended" as stated by Halasz and Sebastian [25]. Due to the lower surface tensions of mixed solvents, contact angles for glass surfaces modified with alkyl silane are low.

Using the above contact angle data, corresponding surface energies were obtained by using the nonlinear programming method as shown in Fig. 3. Figures 3a–3d show the surface energies of four different alkyl silane immobilized glass surfaces as a function of concentration. For all chain lengths the general trends for concentration are similar. As solution concentration decreases, contact angle values generally increase. Hence, total surface energies and the polar term increase, whereas the dispersion term gently decreases.

In this model system, we may change the relative surface concentration by preparing the samples with different silane solution concentrations. At low concentration, there may be less surface density and the surface may be nonuniform of an "island type" [26]. The predominance of the hydrophilic silanol phase causes low

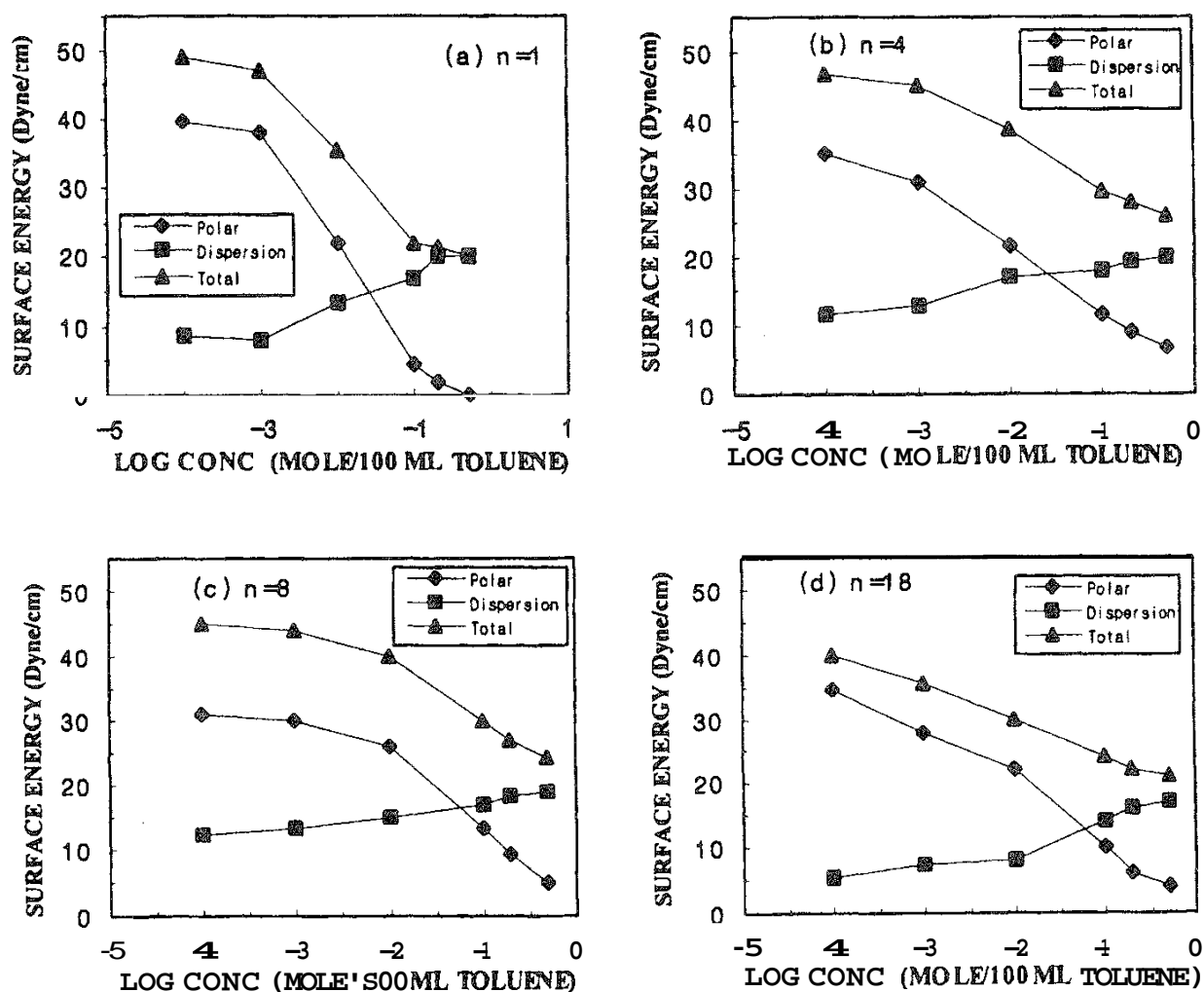


FIG. 3 Contact angles for four different alkyl lengths as a function of log concentration in pure water. (a) $n = 1$; (b) $n = 4$; (c) $n = 8$; (d) $n = 18$.

contact angles and high polar surface energy. Also the disperse surface energy term showed a lower value. However, the total surface energy exhibited higher values.

At high concentration the bonded alkyl chains are more prevalent and are probably relatively densely packed at the higher silane solution concentrations. Therefore, modified surfaces with alkyl chains can show a larger contact angle. Therefore a lower polar term of surface energy, like paraffin surfaces. However, a higher disperse term of surface energy was shown as expected, causing the total surface energy to decrease.

Water can usually be used as a unique solvent for the study of biomedical materials. In other applications such as reverse-phase liquid chromatography, however, different solvents such as water–methanol mixed solvents are used. As the MeOH fraction increases, the surface tension of the solution decreases. In mixed solvents, the trend of contact angles as a function of concentration was generally similar to that of the aqueous case. As the proportion of methanol increases, the contact angle decreases dramatically as in the case of decreased concentration.

B. Effect of Various Alkyl Chain Lengths on Contact Angle and Surface Energies

Several factors govern the exact nature of alkyl chain surfaces. First, the functionality of the silane materials may affect their monomeric or polymeric nature. Second, the degree of silanization and the surface concentration may influence the accessibility of water molecules to the unreacted hydrophilic silanol groups remaining on the underlying glass surfaces. Third, the length of the alkyl chain is a main factor in this work. It is expected that for moderate chain lengths, the chains are relatively mobile [16]. There are interactions between the chains (i.e., van der Waals forces) at long chain lengths [27]. These different chain types, folded or extended, may affect contact angles due to the different outermost groups exposed (e.g., CH_3- and $-\text{CH}_2-$) [28]. According to IR spectroscopic and ellipsometric studies by Porter et al. [29], the long *n*-alkyl thiols (about $n = 18$) form a densely packed, "crystal-like" assembly with fully extended alkyl chains. As the alkyl chain length decreases, the surface structure becomes increasingly disordered and liquidlike with lower packing density and coverage. Fourth, the effect of an aqueous environment is different from that of the aqueous methanol solvent environment. Although we usually use water for biomedical studies, for chromatographic studies the mixed solvent is very important. In a mixed solvent environment, the bonded alkyl chain can be "bristly" or brushlike [8].

Figure 4 show total surface energies as a function of concentration with four different chain lengths. Except for the $n = 18$ case, there are transitions in surface energies just below 10^{-2} mol. This results in two minimum contact angles for $n = 4$ and 8 in two different relatively high (0.1 and 0.5 mol) and low (10^{-2} and 10^{-3} mol) concentration ranges, and the possible reason is described below.

Figure 5 shows the advancing contact angles as a function of alkyl chain length at four different high and low surface concentrations (0.5 – 10^{-3} mol alkyl silane/100 mL toluene). With increasing carbon number the advancing contact angles decrease until $n = 8$ at relatively high concentrations (0.5 and 0.1 mol/100 mL) or decrease until $n = 4$ at relatively low concentrations (10^{-2} and

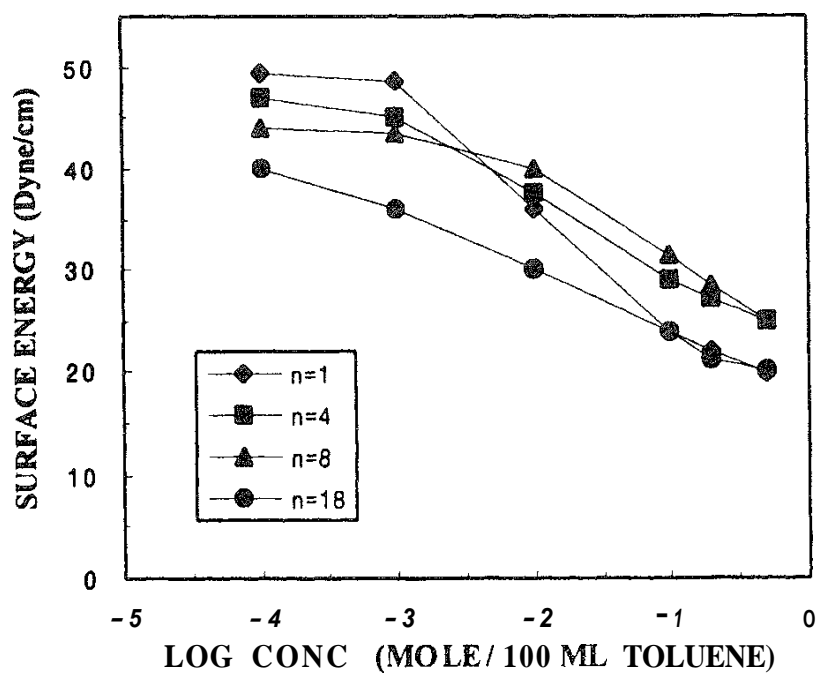


FIG. 4 Total surface energies as a function of concentration with four different chain lengths.

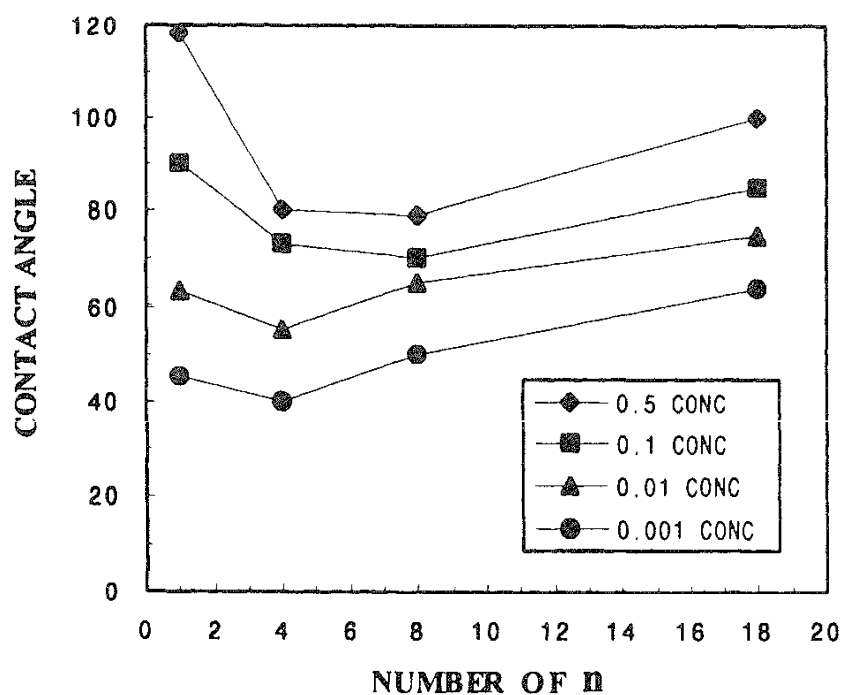


FIG. 5 Advancing contact angles for four different concentrations (0.5 , 0.1 , 10^{-2} , and 10^{-3} mol/100 mL) as a function of carbon number in the alkyl silanes.

10^{-3} mol/100 mL), then all cases increase until $n = 18$. The $n = 4$ and 8 cases, which are in the intermediate chain length ranges, showed lower surface energies than either the $n = 1$ or 18 cases.

Contact angle data are not presented for chain lengths in the range between $n = 8$ and $n = 18$ because silanes of these lengths were not available commercially. However, the van der Waals forces at intermediate chain lengths (e.g., $n = 12, 14, 16$) may be expected to increase continuously up to $n = 18$, well known to be capable of self-assembly. According to Johnson and Dettre [30], the advancing contact angle is associated with the low surface energy region (i.e., high contact angle). We can tell that the advancing angle may depend on the total hydrophobicity of surfaces, which also depends on the number and chain length of hydrophobic alkyl groups (i.e., CH_3- and $-\text{CH}_2-$) in the silane molecules adsorbed on the surfaces. ^{13}C NMR studies [14] show that the motion of terminal methyl carbons of n -alkyldimethyl monochlorosilanes on silica particles increases until $n = 8$; then at $n = 18$ it becomes almost constant.

Now we analyze the trends in Fig. 5 in two steps: (1) the silanization procedure in toluene solution and (2) contact angle measurement in an aqueous environment and their surface energies. In the $n = 1$ case, silane molecules can bind to reactive sites on the surfaces in a densely packed state but probably patchy style, due to the three bulky methyl groups per silane molecule.

For the longer $n = 4$ and 8 cases (e.g., their chain lengths are 0.71 and 1.20 nm, respectively), the adsorbed amount may decrease slightly until $n = 8$, probably due to an increased excluded volume effect. Therefore, the mean distances between chains may increase with n . In the $n = 18$ case (i.e., chain length is 2.47 nm), the adsorbed surfaces may be more densely packed due to van der Waals forces between the long chains. The reason for changing minimum contact angle at $n = 4-8$ with a decrease in concentration may be the contribution from the combination of van der Waals interaction due to different alkyl lengths and concentrations.

During measurement of contact angles, the expected behavior of hydrophobic alkyl chains in an aqueous environment is as follows. In the case of $n = 1$, because water molecules contact their rigid, hydrophobic, methyl groups on the surfaces, they exhibit a high advancing angle, which causes lower total and polar surface energies. In the $n = 4$ case, the advancing angle is lower than that of $n = 1$. Due to the folded style in an aqueous environment, it may expose the many methylene groups on the surface. We know that the methyl group has a lower critical surface tension (i.e., 24 dyn/cm) than that of the methylene group, 31 dyn/cm [28]. Therefore water molecules may touch methylene groups in chains, resulting in a lower contact angle. In the $n = 8$ case, the general trend is similar to that of the $n = 4$ case. However, the greater methylene numbers in a chain cause the advancing angle to decrease slightly. In addition, slightly decreased amounts of attached silane may contribute to the decreased contact angles until $n = 8$.

For such moderately longer alkyl chains (i.e., $n = 4$ and 8), due to the low degree of van der Waals interactions possible between the attached intermediate length alkyl chains, there may be an excluded volume for the folded alkyl chains to be relatively more mobile, disordered, and "liquid-like" than the self-assembling, crystal-like $n = 18$ case. Therefore, there may be a shielding effect of the folded chains

(i.e., $n = 4$ and 8) against water molecules approaching glass surfaces. For such intermediate alkyl lengths, total surface energies are relatively higher for the above reasons.

In the case of $n = 18$, the contact angle increases again. Due to alkyl chain interaction and packing, the water molecules may touch only the outermost alkyl chain methyl groups on the top of the surfaces, meaning that the water molecules find it difficult to penetrate into the silane bundles, giving less chance to contact methylene groups inside bundles. Hence, the advancing angle is high for $n = 18$. Therefore, surface energies become low again.

At lower concentration, 10^{-2} mol/100 mL, the general shapes are similar to those trends at higher concentration, 0.5. Minima near $n = 4$ and 8 are again observed at high concentrations; hence, we believe that at low surface coverages, the chain may be mobile and adopt folded styles at $n = 4$ and $n = 8$. At the long chain length, $n = 18$, these insufficiently covered surfaces from partially ordered "islands" rather than homogeneous layer [25]. Water molecules may contact most methyl groups on the top of these islands rather than methylene groups. Therefore, as in the high concentration case, the contact angle increases again at $n = 18$. The simplified model systems for these surfaces for four different alkyl chain lengths are shown in Fig. 6, based on the above descriptions.

IV. CONCLUSIONS

Contact angles obtained with the Wilhelmy plate method and near surface energies, γ_s^d and γ_s^p , obtained with nonlinear programming methods were varied with chain length surface concentrations for n -alkyldimethyl monochlorosilanes (i.e., $n = 1, 4, 8$, and 18) in various solvents.

As solution concentration decreases, total surface energy and the polar term increase, whereas the disperse term decreases, due to surface density with silanes.

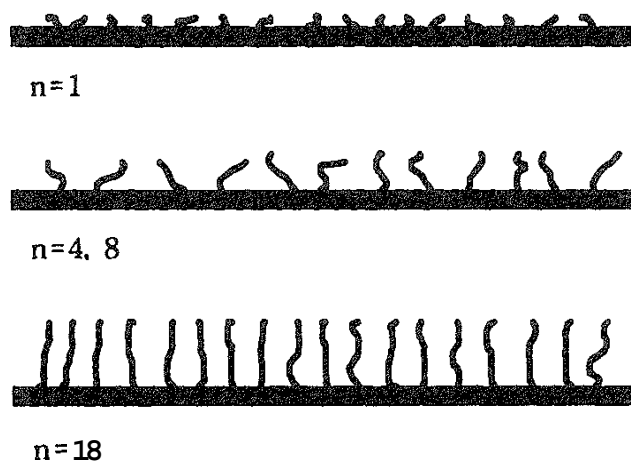


FIG. 6 Simplified model systems for four different alkyl chain lengths.

In the cases of chain lengths $n = 1$ and $n = 18$, contact angle and surface energy held high and low values due to patch-type terminal methyl groups and relatively high van der Waals interactions between long chains, respectively.

For both high and low surface concentrations, monomeric alkyl silanes in the range of $n = 4 - 8$ exhibit the minimum contact angle and higher surface energies, γ_s^{total} . This suggests that these chains may be relatively more disordered or liquidlike than the self-assembling, crystal-like, $n = 18$ case. This is probably because of the excluded-volume effect due to the low degree of van der Waals interactions possible between the attached intermediate length chains.

REFERENCES

1. J. D. Andrade, D.E. Gregonis, and L. M. Smith, in *Surface and Interfacial Aspects of Biomedical Polymers* (J. D. Andrade, ed.), Plenum, New York, 1985, p. 15.
2. H. Yasuda, A. K. Sharma, and T. Yasuda, *J. Polym. Sci. Polym. Phys.* **19**:1285 (1981).
3. R. S. Ward, *Org. Coat. Plast. Chem.* **42**:227 (1981).
4. J. D. Andrade, in *Polymers in Medicine*, Vol. II (E. Chiellini *et al.*, eds.), Plenum, New York, 1986, p. 29.
5. Z. Kessaissia, E. Papirer, and J. B. Dommet, *J. Colloid Interface Sci.* **79**:257 (1981).
6. L. C. Sander and S. A. Wise, *Anal. Chem.* **56**:504 (1984).
7. L. C. Sander, J. B. Callis, and L. R. Field, *Anal. Chem.* **55**:1086 (1983).
8. R. K. Gilpin and J. A. Squires, *J. Chromatogr. Sci.* **19**:195 (1981).
9. J. D. Andrade, in *Surface and Interfacial Aspects of Biomedical Polymers* (J. D. Andrade, ed.), Plenum, New York, 1985, p. 105.
10. E. J. Castillo, J. L. Koenig, C. K. Kliment, and J. Lo, *Biomaterials* **5**:186 (1984).
11. C. H. Lochmuller, A. S. Colborn, M. L. Hunnicutt, and J. M. Harris, *J. Am. Chem. Soc.* **106**:4077 (1984).
12. L. Faccini and A. P. Legrand, *Macromolecules* **17**:2405 (1984).
13. G. C. Levy, P. L. Rinaldi, J. J. Dechter, D. E. Axelson, and L. Mandelkern, *J. Am. Chem. Soc.* **106**:4077 (1984).
14. D. W. Sindorf and G. E. Maciel, *J. Am. Chem. Soc.* **105**:1848 (1983).
15. C. O. Timmons and W. A. Zisman, *J. Colloid Interface Sci.* **22**:165 (1966).
16. H. S. Van Damme, A. H. Hogt, and J. Feijen, *J. Colloid Interface Sci.* **114**:167 (1986).
17. C. E. Rehbreg and C. H. Fisher, *Ind. Eng. Chem.* **40**:1429 (1948).
18. J. J. Kirkland, *Chromatographia* **8**:661 (1975).
19. J. Gun and J. Sagiv, *J. Colloid Interface Sci.* **112**:457 (1966).
20. J. D. Andrade, S. M. Ma, R. N. King, and D. E. Gregonis, *J. Colloid Interface Sci.* **72**:488 (1979).
21. D. K. Owens and R. C. Wendt, *J. Appl. Polym. Sci.* **13**:1971 (1969).
22. H. Y. Erbil and R. A. Meric, *Colloid Surf.* **33**:85 (1988).
23. L. A. Girifalco and R. J. Good, *J. Phys. Chem.* **61**:904 (1957).
24. J. L. Kuester and J. M. Mize, *Optimization Techniques with FORTRAN*, McGraw-Hill, New York, 1973.

25. I. Halasz and I. Sebestian, *Angew. Chem. Int. Ed., Engl.* 8:453 (1969).
26. S. Garoff, H. W. Deckinan, and M. S. Alvarez. *Proc. Electrochem. Soc.* 85(8):112 (1985).
27. O. Levine and W. A. Zisman, *J. Phys. Chem.* 61:1068 (1957).
28. W. A. Zisman and R. F. Gould, *Adv. Chem. Ser.* 43:1 (1964).
29. M. D. Porter, T. B. Bright, and D. L. Allara, *J. Am. Chem. Soc.* 109:244 (1988).
30. R. E. Johnson and R. H. Dettre, *Surf. Colloid Sci.* 1:85 (1969).

8

Microporous Structure of Collagen Fibers

KEITO BOKI Department of Pharmaceutical Sciences, Kinki University, Osaka, Japan

- I. Introduction
- II. Hierarchical Structure of Collagen Fiber
 - A. Hierarchical structure of collagen fiber
 - B. Surface structure of collagen fiber
- III. Pretreatment and Inner Structure of Collagen Fiber
 - A. Pore size distribution determined from adsorption isotherm of water vapor on collagen fiber
 - B. Pore size distribution determined from adsorption isotherm of nitrogen gas on collagen fiber
- IV. Experimental Procedures
 - A. SEM, TEM, and AFM
 - B. Adsorption method
- V. Summary
- References

I. INTRODUCTION

Collagen, the essential component of the extracellular matrix, is present in the skin, bone, tendons, and connective tissues of the higher animals. The collagen fibril is functionally related to the tenacity in bone, the tensile strength in tendons, and the preservation of strength in skin or connective tissues. In the native state, collagen exists in a fibrillar form. Water is essentially related to the maintenance of collagen molecules in the native conformation. That is, the inner spaces inside the collagen fibers functionally maintain water in the native state.

Observations of the collagen fibril surface structure were performed using atomic force microscopy (AFM) [1], scanning electron microscopy (SEM) [2],

and transmission electron microscopy (TEM) [2]. These observations mainly give us visual information about the ultrastructure of the collagen fibril surface. On the other hand, the microporous structure, that is, the pore size distribution and pore volume, has been investigated by the adsorption method [3,4].

In this chapter, the structure of the collagen fiber, the surface and microporous structure of the collagen fiber, and experimental methods for the investigation of the microstructure are discussed.

II. HIERARCHICAL STRUCTURE OF COLLAGEN FIBER

A. Hierarchical Structure of Collagen Fiber

To understand the microporous structure of the collagen fiber, the structures of the collagen molecule, microfibril, collagen fibril, and collagen fiber must be recognized.

1. Collagen Molecule

Collagen molecules have a triple-helix and rodlike conformation. Their length and form depend on the type of collagen. The type I collagen molecule, tropocollagen, is approximately 300 nm long and 1.5 nm in diameter. It is composed of a triple-helix atelocollagen and N-terminal and C-terminal nonhelical telopeptides (Fig. 1).

From the results of calorimetric and mechanical experiments of hydration on rat tail tendons, it was proposed that water molecules are fixed by three hydrogen bonds inside the triple helix or by double hydrogen bonds in the available sites inside the triple helix [5]. This hypothesis indicates the existence of microspacing inside the tropocollagen structure that water molecules can enter.

2. Microfibrils

Five collagen molecules are aggregated to pack a microfibril. The microfibril scheme is shown in Fig. 2. A five-stranded microfibril is approximately 3.5 nm [6] or 3.8 nm [7] in diameter. Each tropocollagen is axially staggered by a D period with respect to its nearest neighbors. The D period includes one gap (hole) zone and one overlap (head and tail overlap) zone. The D period has been reported to be 67 nm [8], 64 nm [9] or 60–70 nm [10]. According to Pineri

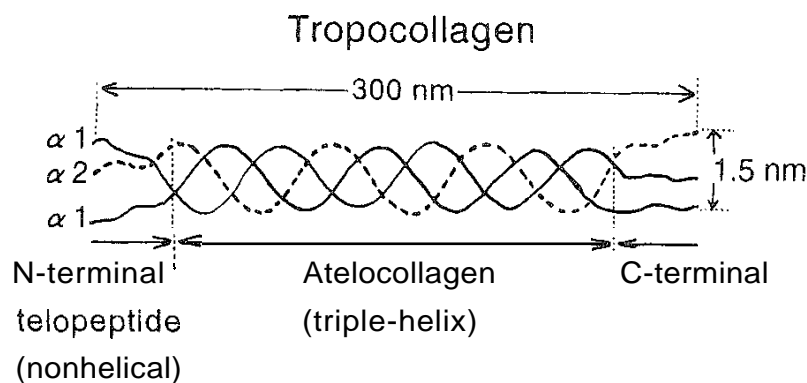


FIG. 1 Scheme of type I collagen molecule.

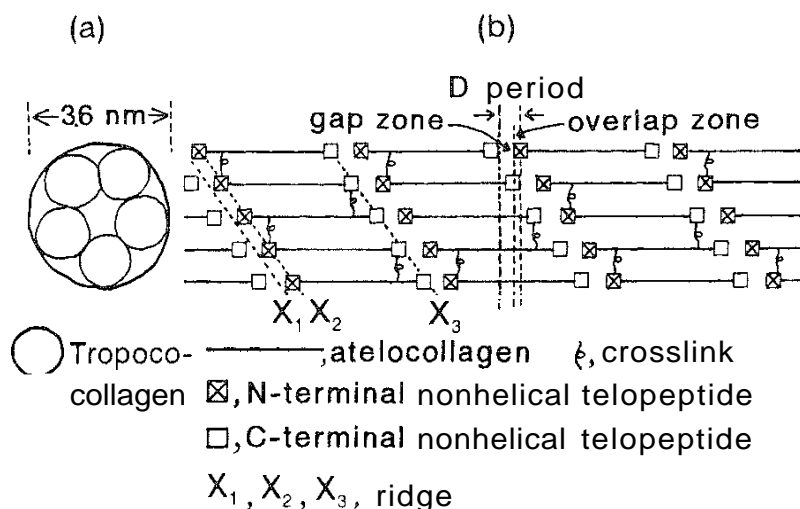


FIG. 2 Scheme of microfibril. (a) Cross section; (b) latitudinal section

et al. [5], water molecules are fixed in the microfibrils and in the hole zones adjacent to the end of the tropocollagen. It was reported that intermolecular space enclosed by the five tropocollagen molecules in a unit is 1.06 nm [11]. This indicates that there is microspacing inside the microfibril.

3. Collagen Fibril and Collagen Fiber

Microfibrils are packed on a tetragonal lattice [12] or quasi-hexagonal lattice [13] to form the collagen fibril. The collagen fibril is the fibrous entity observed by AFM [1,10] or SEM [2]. The diameters of the collagen fibrils are close to a multiple of 8.0 nm [14]. The collagen fibrils form a fiber, and the fibers are bundled together with elastic fibers and fibrocytes to form fibrous connective tissue.

B. Surface Structure of Collagen Fiber

1. Electron Microscopic Surface Observation of Collagen Fibril

Raspanti et al. [2] reported field emission electron gun (FEG)-SEM surface observations of collagen fibrils dehydrated by different procedures. Figures 3–6 are micrographs of air-dried (AD) fibrils, lyophilized (L) fibrils, critical point-dried (CPD) fibrils, and freeze-dried (FD) fibrils in tert-butyl alcohol, respectively. The AD fibrils appear flattened and distorted, and the D period is at times evidently altered and disrupted (Fig. 3). The L, CPD, and FD fibrils appear rather similar (Figs. 4–6). Their surface features show high porosity (Figs. 3–6). However, the micropore sizes or micropore shapes are not easily observed in these pictures. Three intraperiod ridges, X₁, X₂, and X₃, lie within the D period [15]. The X₁ ridge is located in the gap zone (Fig. 2). The X₂ and X₃ ridges are located on the gap—overlap transition and correspond in position to the N-terminal nonhelical telopeptide and C-terminal nonhelical telopeptide, respectively (Figs. 2 and 4). The L fibrils exhibit a sharp D banding and two evident ridges. The X₃ ridge is recognizable by its larger size (arrows in Fig. 4). The CPD fibrils show a gap—overlap alternation marked by two transverse ridges (Fig. 5). The FD fibrils show a D period, X₂ and X₃ ridges, and a sort of flaky and filamentous coating laid upon the fibril surface

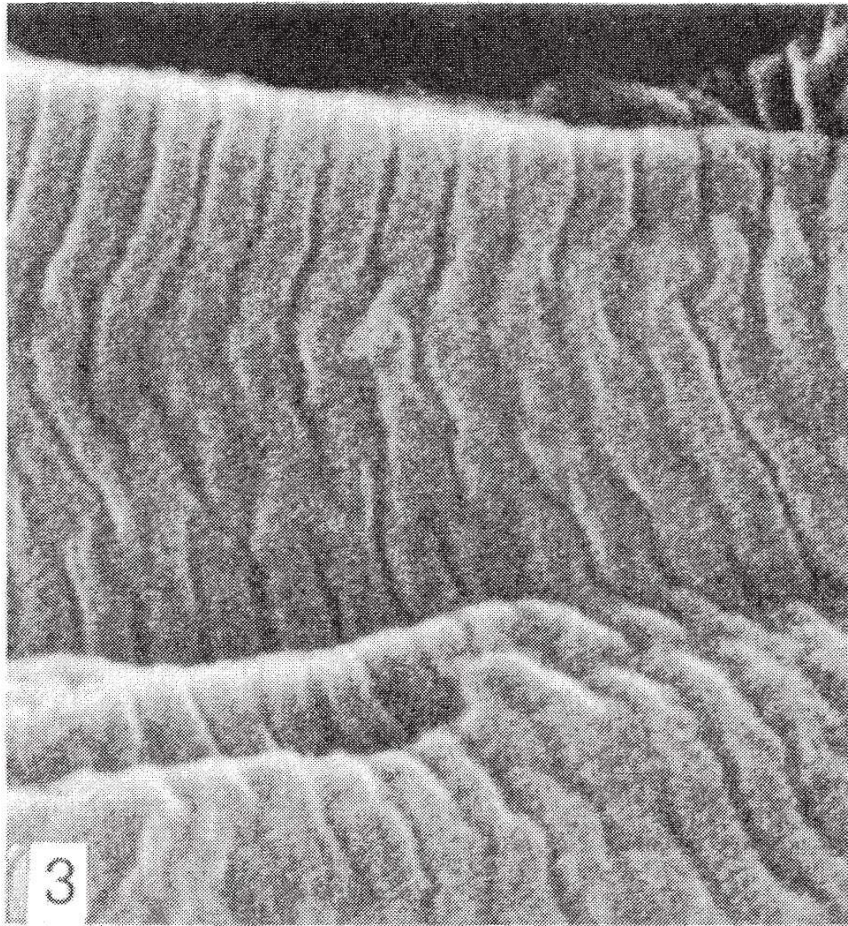


FIG. 3 Field emission electron gun–scanning electron microscope (FEG-SEM) picture of air-dried collagen fibrils (x 160,000). (From Ref. 2.)

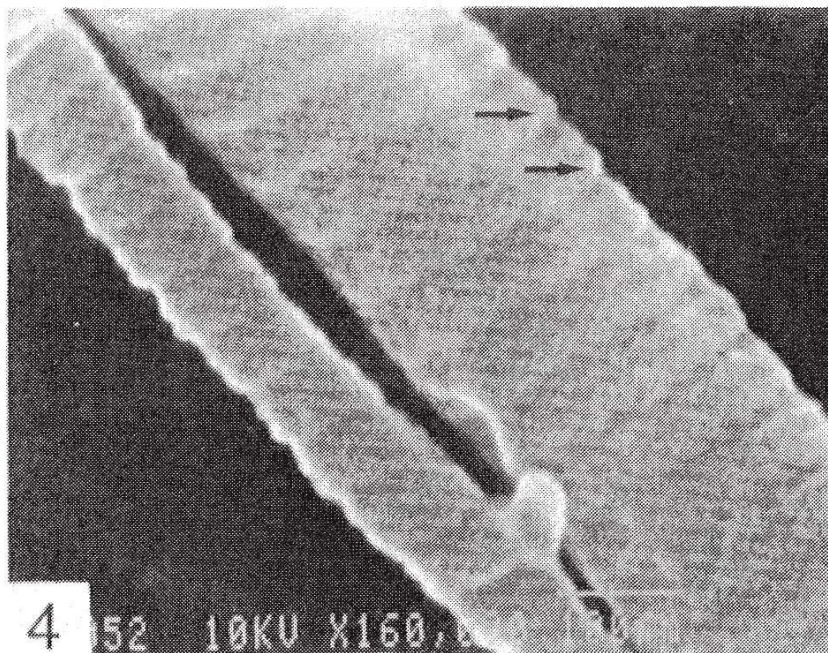


FIG. 4 FEG-SEM picture of lyophilized fibrils (x 160,000). (From Ref. 2.)

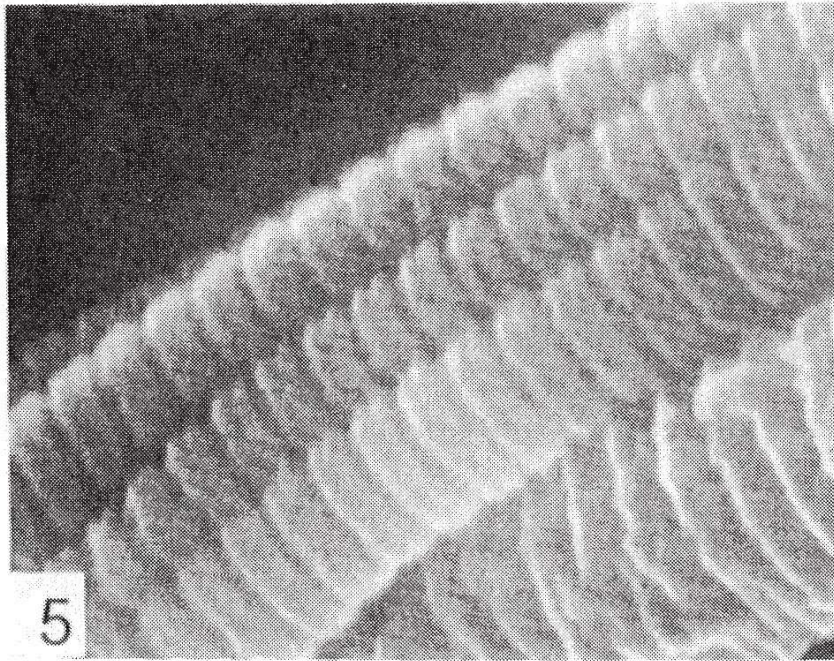


FIG. 5 FEG-SEM picture of critical point-dried fibrils ($\times 160,000$). (From Ref. 2.)

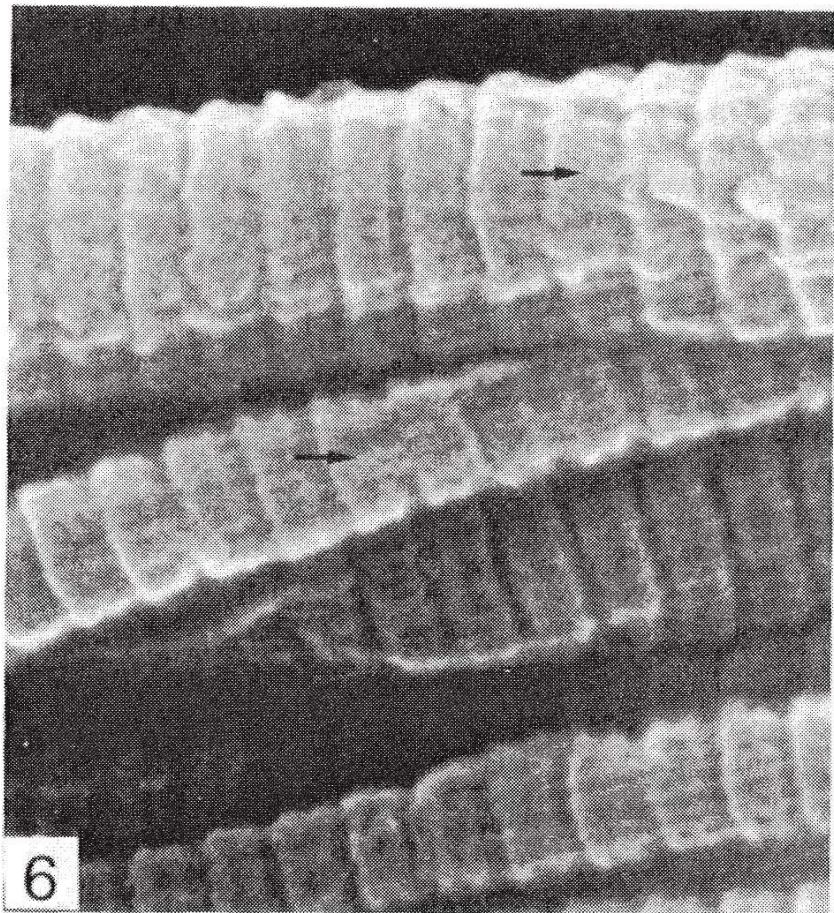


FIG. 6 FEG-SEM picture of freeze-dried fibrils in tert-butyl alcohol ($\times 160,000$). (From Ref. 2.)

(arrows) (Fig. 6). The fibril ultrastructure observed using transmission electron microscopy (TEM) shows three distinct beltlike ridges, X_1 , X_2 , and X_3 , which align in regular order from right to left, respectively (Fig. 7) [2]. All the ridges appear as a distinct row of globular subunits.

2. AFM Surface Observation of Collagen Fibril

Baselt et al. [10] imaged the AD native rat tail collagen by AFM. AFM is operated by lightly touching a tip to the sample and producing a topographic image by measuring the sample height as the tip scans over the sample. The cross sections of the AFM images are graphed in Figs. 8 and 9. The cross section shows the D periodicity, and groove widths are calculated by dividing the lateral distance by the groove number. Their values are approximately 63 nm (Fig. 8) or 60 nm (Fig. 9). From Figs. 8 and 9, we can observe the difference in height between the grooves and the ridges of the collagen fibril surface. The difference varies between ~ 5 nm on the small-diameter fibrils and ~ 15 nm on the large-diameter fibrils (Fig. 8). The difference between the overlap (elevated) zone and the gap (depressed) zone was 4 nm [1]. Two grooves per D period are observed on the smaller diameter sheath fibrils (Fig. 9). The deep grooves measure ~ 6 nm in depth, and minor grooves measure ~ 1 nm in depth. The minor grooves show hints of the presence of micropores on the microfibril surface.

III. PRETREATMENT AND INNER STRUCTURE OF COLLAGEN FIBER

The D period of the rat tail tendon collagen was reduced by dehydration from 68 to 64 nm [16]. The micropore volume of the collagen fiber was increased by acidification [17]. Therefore, the inner structure of the collagen fiber was also

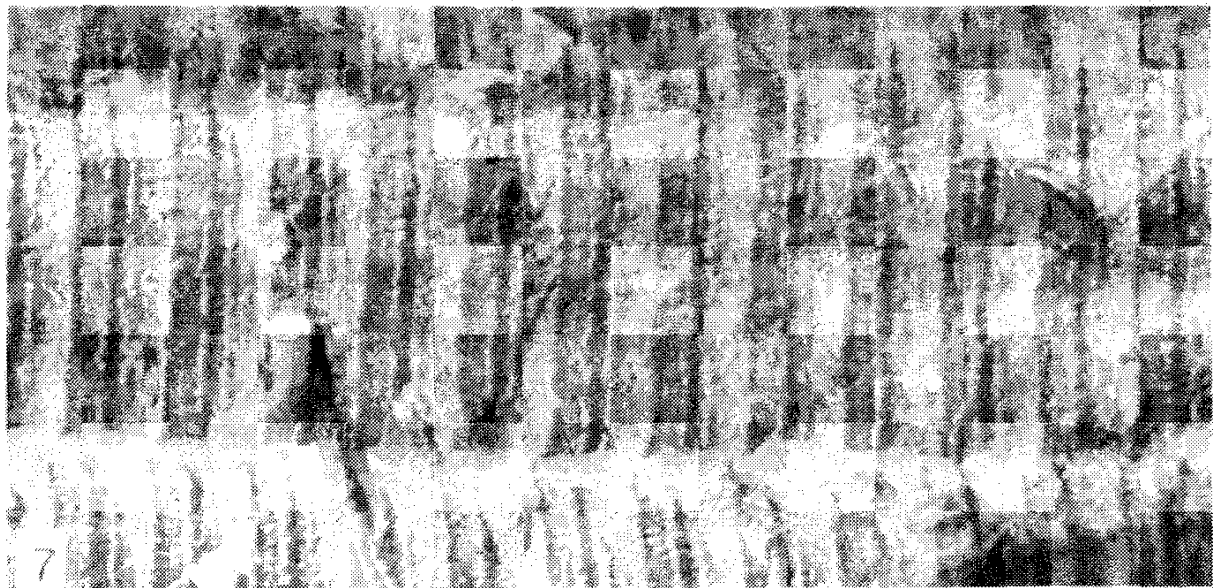


FIG. 7 Transmission electron micrograph of freeze-etched collagen fibrils; instrumental magnification of 40,000 \times . (From Ref. 2.)

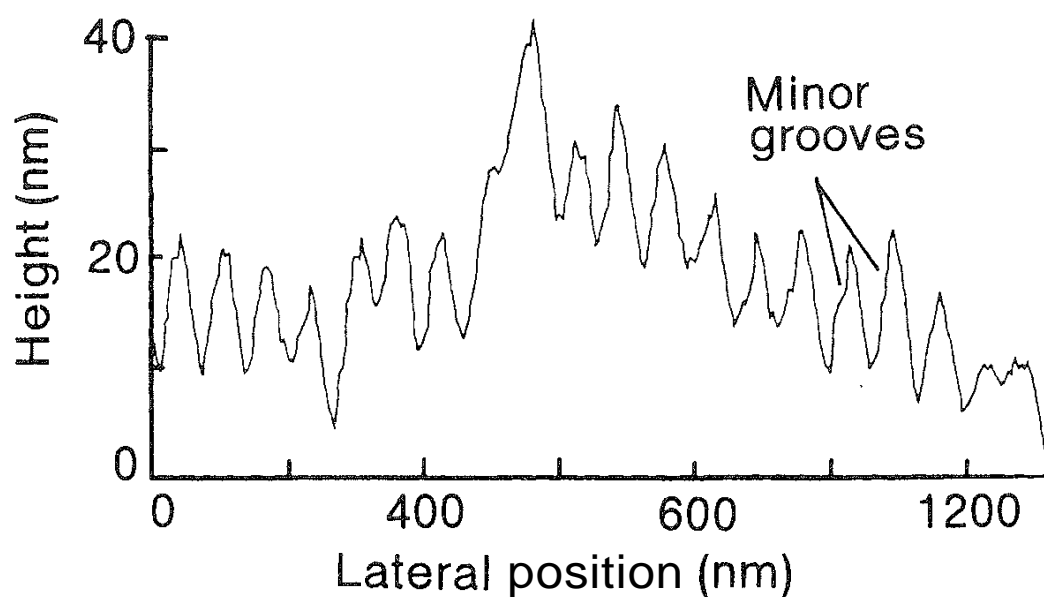


FIG. 8 Differences in height between grooves and ridges of D periodicity of microfibrils in cross section (native rat tail collagen fibril), Fibril height is ~ 300 nm (the zero points on both axes are arbitrary). (From Ref. 12.)

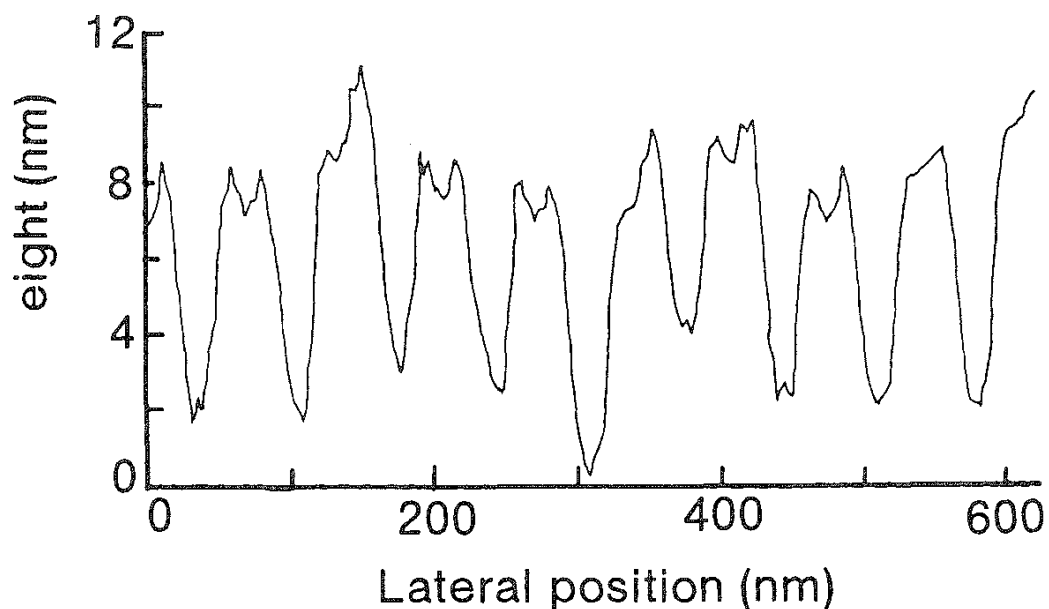


FIG. 9 Differences in height between grooves and ridges of D periodicity of microfibrils in cross section (native rat tail sheath fibril), Fibril height is ~ 22 nm (the zero points on both axes are arbitrary). (From Ref. 12.)

effectively varied by its pretreatments. The microspaces in the triple helix, microfibril, and collagen fibril are decreased or increased by chemical pretreatments and drying methods

The adsorption method has an advantage of quantitatively evaluating the ultrastructure of the collagen fiber. That is, the inner pore volume of the collagen fiber is determined by using the adsorption method. In this case, it is assumed that the pores are cylindrical and that capillary condensation occurs in the pores according to Kelvin's equation,

$$r_k = -2\sigma V \frac{\cos \theta}{RT} \ln \left(\frac{p}{p_0} \right)$$

where σ is the surface tension, V is the molar volume of the condensing vapor, θ is the angle of the liquid with the wall, r_k is Kelvin's radius, and p/p_0 is the relative pressure. The pores with widths of less than about 2.0 nm in Kelvin radius are termed "micropores," whereas pores with widths from 2.0 to 50 nm are referred to as "mesopores" or "transitional pores."

A. Pore Size Distribution Determined from Adsorption Isotherm of Water Vapor on Collagen Fiber

The differential pore size distributions obtained by Sanjeevi et al. [3] are shown in Figs. 10 and 11. The raw collagen fibers prepared from a portion of bovine belly hide have mesopores with radii of 3.9–7.7 nm and micropores with radii of 0.35–0.55 nm (mean, 0.45 nm). They suggested that a micropore diameter of 0.9 nm is

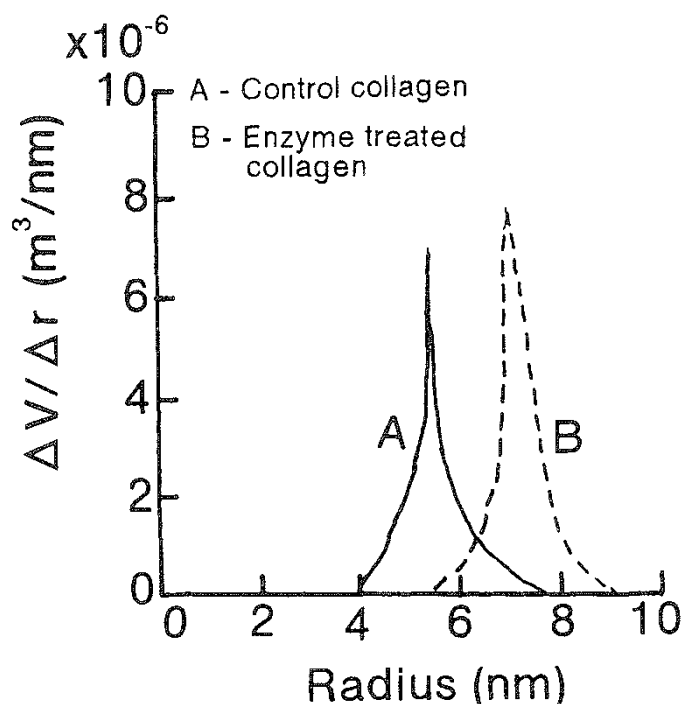


FIG. 10 Pore size distribution of raw and enzyme-treated collagen fibers. Mesopore volume was calculated using the BJH method. (From Ref. 5.)

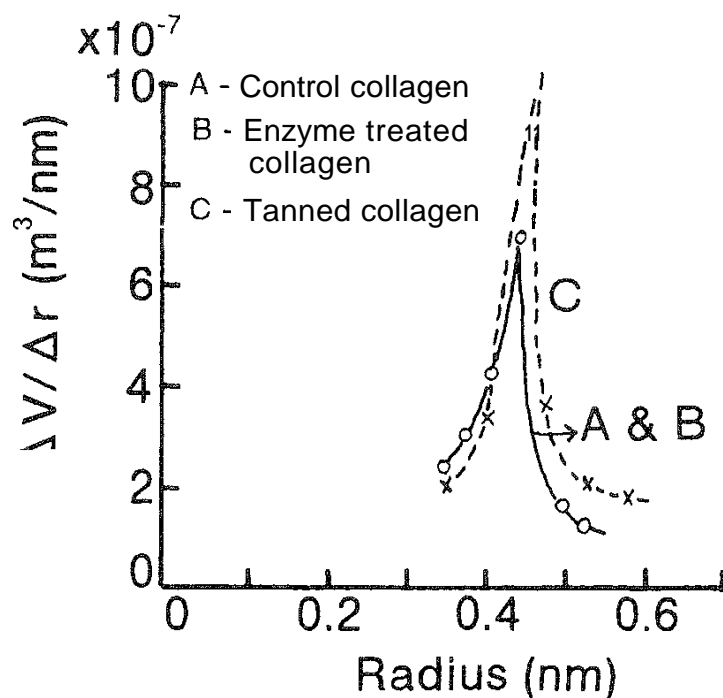


FIG. 11 Micropore size distribution of raw, enzyme-treated, and tanned collagen fibers. Micropore volume was calculated using the MP method. (From Ref. 5.)

near the intermolecular spacing (1.06 nm) inside the microfibril obtained by low-angle X-ray diffraction [11]. When the noncollagenous components are removed by the enzyme treatment, the 3.9–7.7 nm radii pores are widened to have radii of 5.0–9.2 nm (Fig. 10). When the raw collagen fiber is tanned, the 3.9–7.7 nm radii pores are absent (Fig. 10). However, neither the enzyme treatment nor the tanning causes any change in the micropores of radii 0.35–0.55 nm (Fig. 11).

B. Pore Size Distribution Determined from Adsorption Isotherm of Nitrogen Gas on Collagen Fiber

Boki et al. reported the structural analysis of alkali-treated [4] collagen fibers followed by preparation in acidic pH solution [17]. The cumulative pore size distributions are shown in Fig. 12. No micropores with radii less than 2.0 nm are found on the raw collagen fibers prepared from steer hide. However, micropores with radii of 1.2 nm or larger appear after the alkali treatment. These results are not in agreement with the data obtained by the moisture adsorption method [3] or low-angle X-ray diffraction [11].

The change in pore volume brought about by acidifying the alkali-treated collagen fibers was investigated [17]. The pore size distributions of the collagen fibers are shown in Fig. 13. Micropores with radii of 1.2 nm or larger appear after acidifying the raw collagen fiber with pores of radii larger than 2 nm. The increase in pore volume is greater with radii of 1.2–1.55 or 1.55–2.45 nm rather than with radii of 2.45–9.5 nm. It was suggested that the interspaces of the triple helix or microfibril are increased due to the formation of carboxylic acid moieties during the acid preparation [17].

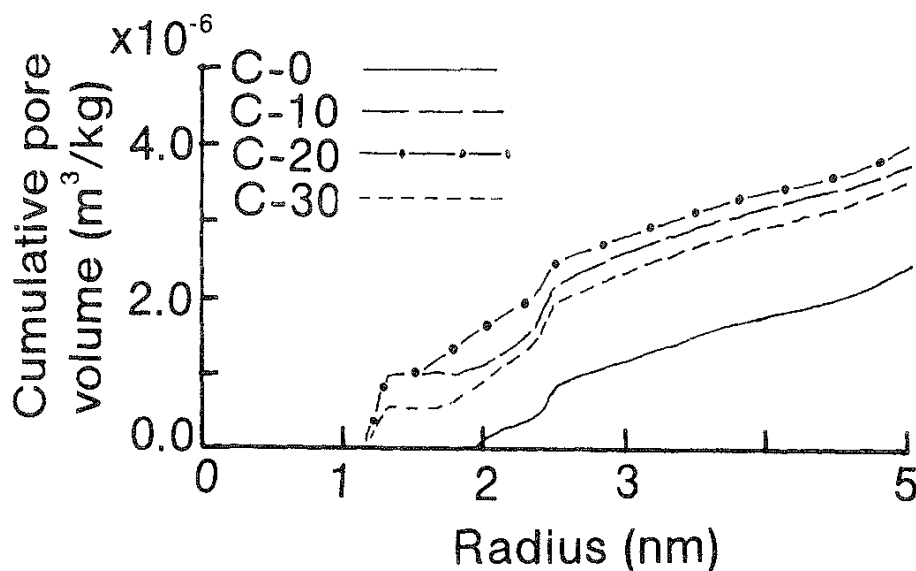


FIG. 12 Cumulative pore volume of alkali-treated collagen fibers. C-0, C-10, C-20, and C-30 are collagen fibers alkali-treated for 0, 10, 20, and 30 days, respectively. Micropore volume ($r < 1.55 \text{ nm}$) and macropore volume ($8.5 \text{ nm} > r > 1.55 \text{ nm}$) were calculated using the MP method and the DH method, respectively. (From Ref. 4.)

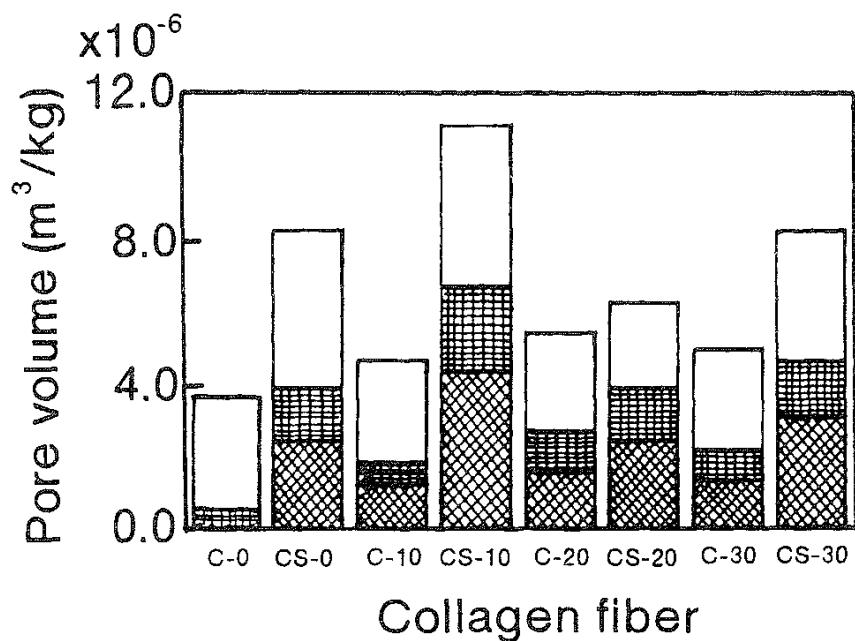


FIG. 13 Pore size distribution of collagen fibers. The labels C-0, CS-0, C-10, CS-10, C-20, CS-20, C-30, and CS-30 refer to the number of days the raw collagen fibers were alkali-treated. C denotes the alkali-treated and freeze-dried collagens. CS denotes the alkali-treated, freeze-dried, and acidified collagens. $1.2 \leq r < 1.55 \text{ nm}$; $1.55 \leq r < 2.45 \text{ nm}$; $2.45 \leq r < 9.5 \text{ nm}$. (From Ref. 17.)

IV EXPERIMENTAL PROCEDURES

A. SEM, TEM, and AFM

The air-dry preparation technique is inherently prone to artifacts [1,12]. Other dehydration procedures, including lyophilization, critical point drying, and freeze-drying, provide better results on biological specimens for SEM and AFM observation [2].

I am not experienced in the techniques of preparing a specimen, instrumentation, methodology, resolution, etc. References 1,2,12, and 18–21 may be useful for additional reading.

B. Adsorption Method

The pore size distribution of collagen fiber is determined by using adsorption isotherms of water vapor or nitrogen gas. The preparation of the sample, adsorption procedure, and calculation method are mentioned below.

1. Preparation of Sample

Collagen fibers are removed from an organic matrix. They are thoroughly washed in distilled water and prepared through a process of several steps. The sample should be dried. The fiber is dried in a vacuum desiccator over phosphorus pentoxide for 3 months to completely remove water from the collagen fiber [22]. The water inside the triple helix [5] must be removed. If the water inside the collagen fibers is not completely removed, then the amounts of nitrogen gas adsorbed will vary widely. This wide variation in the amount adsorbed may be caused by the phase change of the residual water inside the collagen fibers due to an extremely low adsorption temperature of -196°C .

2. Adsorption Procedure

The water vapor [23] and nitrogen gas [24] adsorption isotherms determined by using automatic adsorption apparatus have been reported. On the other hand, the manual adsorption method for the adsorption of water vapor and nitrogen gas is discussed in Refs. 25 and 4, respectively. The amount adsorbed is determined by using a Shibata moisture and surface area apparatus, Model P-850 (Shibata Scientific Technology, Ltd., Tokyo, Japan) [25]. The amounts of water vapor and nitrogen gas adsorbed are determined by the gravimetric method [25] and volumetric method [4], respectively.

The pore size distribution is calculated based on the water vapor or nitrogen gas adsorption isotherm. Before the calculation, it is essential to obtain an accurate adsorption isotherm. The amount of nitrogen gas adsorbed on the collagen fiber is extremely low in comparison to the amount of water vapor adsorbed on it. Approximately, 1×10^{-2} kg of collagen fiber, therefore, is put in the adsorption glass bulb. The amount adsorbed on the collagen fiber is measured at equilibrium pressures of 6.7, 13.3, 20.0, 26.7, 33.3, 40.0, 53.3, 66.7, 80.0, 93.3, and 101.3 kPa in order to get an accurate quantity. The adsorption isotherm for each

collagen fiber is performed in triplicate; therefore the reported amounts adsorbed are mean values [4].

3. Calculation of Pore Size Distribution

The pore size distributions are calculated using the micropore (MP) method [26] and the Dollimore–Heal (DH) method [27] based on the adsorption isotherm data. Prior to calculating the micropore distribution by the MP method, it is necessary to convert the adsorption isotherms into V_L – t plots [25]. The amount adsorbed at each relative pressure on the basis of the adsorption isotherms in Fig. 14 are converted into V_L and t values for the corresponding relative pressures calculated from deBoer's equation. The V_L – t plots, as shown in Fig. 15, begin to deviate

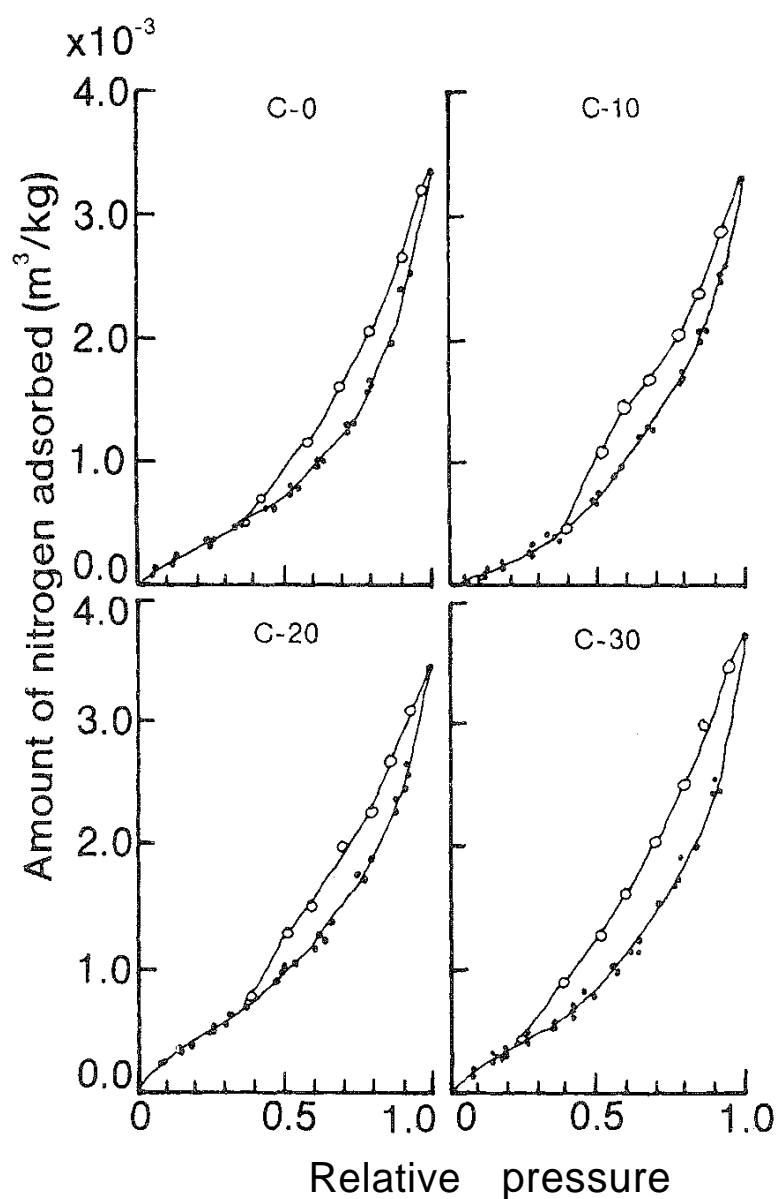


FIG. 14 Adsorption and desorption isotherms of nitrogen gas on collagen fibers. C-0, C-10, C-20, and C-30 are collagen fibers alkali-treated for 0, 10, 20, and 30 days, respectively. Experimental data of (●) adsorption and (○) desorption. (From Ref. 4.)

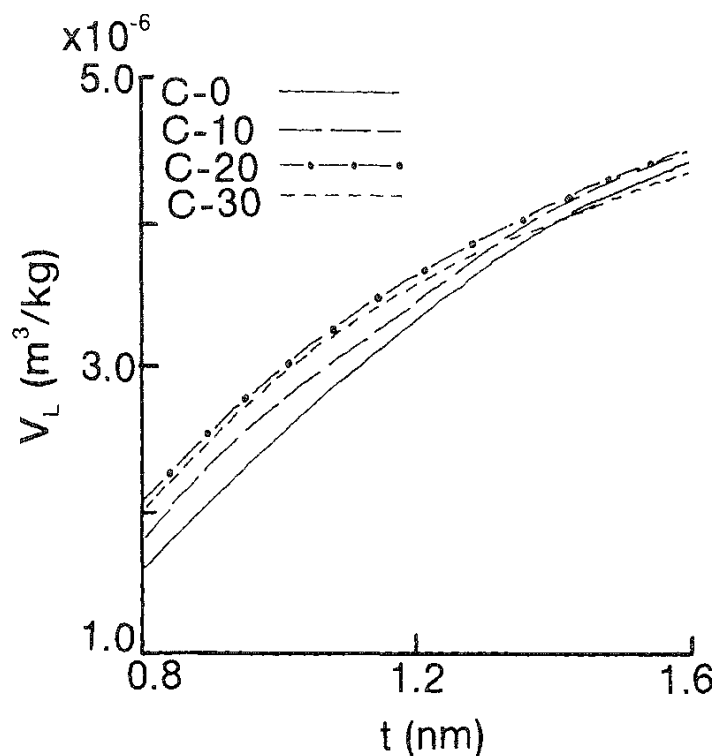


FIG. 15 Volume of nitrogen gas adsorbed versus statistical thickness. C-0, C-10, C-20, and C-30 are collagen fibers alkali-treated for 0, 10, 20, and 30 days, respectively. V_L = amount adsorbed converted into liquid; t = adsorbed thickness. (From Ref. 4.)

downward from straight lines. The downward deviations are used for the calculation of the cumulative pore volume and the pore size distribution of the micropores up to 1.55 nm [26]. The pore size distributions for radii of 1.55 nm or larger are calculated using the DH method [27]. The cumulative pore size distributions calculated using the MP and DH methods are shown in Fig. 12.

V. SUMMARY

The surface structure of collagen fibril is visually described using the SEM, AFM, and TEM observations. The ultrastructure of collagen fiber is quantitatively described using the pore size distribution calculated from adsorption isotherms. The former depends on the achievements of other researchers. The latter is mainly my work. It is regrettable that the SEM or AFM observation cannot be compared with the pore size distribution on the same collagen sample. The functions of micropores inside the collagen in the native state must be elucidated.

REFERENCES

1. I. Revenko, F. Somer, D. Tran Minh, R. Garrone, and J. M. Franc, *Biol. Cell.* 80:67 (1994).
2. M. Raspanti, A. Alessandrini, P. Gobbi, and A. Ruggeri, *Microsc. Res. Tech.* 35:87 (1996).

- R. Sanjeevi, N. Ramanathan, and B. Viswanathan, *J. Colloid Interface Sci.* 57:207 (1976).
- K. Boki, N. Kawasaki, K. Minami, and H. Takahashi, *J. Colloid Interface Sci.* 157:55 (1993).
5. M. H. Pineri, M. Escoubes, and G. Roche, *Biopolymers* 17:2799 (1978).
6. J. W. Smith, *Nature* 219:157 (1968).
7. A. Miller, and J. S. Wray, *Nature* 230:437 (1971).
8. A. J. Hodge, J. A. Petruska, and A. J. Bailey, in *Structure and Function of Connective and Skeletal Tissue* (S. Fitton-Jackson, R. D. Harkness, S. M. Partridge, and G. R. Tristram, eds.), Butterworths, London. 1965, pp. 31–41.
9. A. Veis, J. Anesey, and S. Mussell, *Nature* 215:1931 (1967).
10. D. R. Baselt, J.-P. Pevel, and J. D. Baldeschwieler, *Biophys. J.* 65:2644 (1993).
11. M. A. Rougvie, and R. S. Bear, *J. Am. Leather Chem. Assoc.* 48:735 (1953).
12. A. Miller and D. A. D. Parry, *J. Mol. Biol.* 75:441 (1973).
13. D. J. S. Hulmes and A. Miller, *Nature* 282:878 (1979).
14. D. A. D. Parry, and A. S. Craig, *Nature* 282:213 (1979).
15. A. Bairati, M. G. Petruccioli, and L. Torsi Tarelli, *J. Submicrosc. Cytol.* 1:113 (1969).
16. R. D. B. Fraser and T. P. Macrae, *Conformation in Fibrous Proteins and Related Synthetic Polypeptides*, Academic, New York. 1973, p. 628.
17. K. Boki, N. Kawasaki, and T. Tamura, *J. Colloid Interface Sci.* 173:249 (1995).
18. J. Yang, L. K. Tamm, A. P. Somlyo, and Z. Shao, *J. Microsc.* 171:183 (1993).
19. T. Inoue, and H. Osatake, *Arch. Histol. Cytol.* 51:53 (1988).
20. O. Ohtani, *Arch. Histol. Cytol.* 55:225 (1992).
21. M. Raspanti, A. Alessandrini, V. Ottani, and A. Ruggeri, *J. Struct. Biol.* 119:118 (1997).
22. A. C. Zettlemoyer, A. Chand, and E. Gamble, *J. Am. Chem. Soc.* 72:2752 (1950).
23. H. Naono and M. Hakuman, *J. Colloid Interface Sci.* 145:405 (1991).
24. H. Naono and M. Nakai, *J. Colloid Interface Sci.* 128:1146 (1989).
25. K. Boki, S. Ohno, and S. Shinoda, *J. Food Sci.* 54:487 (1989).
26. R. S. Mikhail, S. Brunauer, and E. E. Bodor, *J. Colloid Interface Sci.* 26:145 (1968).
27. D. Dollimore and G. R. Heal, *J. Colloid Interface Sci.* 33:508 (1970).

9

Adsorption onto Oxides: The Role of Diffusion

LISA AXE Department of Civil and Environmental Engineering, New Jersey Institute of Technology, Newark, New Jersey

PAUL R. ANDERSON Department of Chemical and Environmental Engineering, Illinois Institute of Technology, Chicago, Illinois

- I. Introduction
- II. A Conceptual Model for Sorption of Inorganic Substances at the Oxide/Water Interface
- III. The Diffusion Model
- IV. Implications from the Conceptual and mathematical Models
- V. Critical Review of Relevant Literature
- VI. Conclusions
- References

I INTRODUCTION

In natural aquatic systems and in many engineered processes, interactions with mineral surfaces can play an important role in determining the transport and fate of inorganic compounds. These interactions can influence nutrient availability and weathering processes, and in disturbed systems interactions with mineral surfaces can control the movement of hazardous chemicals. Among mineral surfaces, oxides probably play a dominant role because of their large surface areas and strong affinity for many trace elements. In this chapter we are especially interested in poorly crystallized porous oxides of aluminum, iron, and manganese. These minerals can exist both as discrete particles and as coatings on other mineral surfaces. Although not stable in a thermodynamic sense, aging and transformation of these minerals to more stable forms are often kinetically limited because of environmental conditions or the presence of other inhibiting compounds.

The chapter begins with a conceptual model describing sorption of inorganic materials onto oxides and a brief discussion about possible mechanisms for the often observed two-step sorption process. In many cases intraparticle diffusion is

the rate-limiting mechanism, and Sec. III includes a rate expression for that mechanism. Together, these conceptual and mathematical models suggest what should be observed in studies of these systems; we review those implications and then look into the literature for examples. Although there is some confirmation of these ideas, few of the existing studies were designed to test the hypotheses. Lastly, we present our conclusions.

II. A CONCEPTUAL MODEL FOR SORPTION OF INORGANIC SUBSTANCES AT THE OXIDE/WATER INTERFACE

Sorption of inorganics to oxides can be divided into a number of sequential and possibly parallel steps. (In this chapter we follow the suggestion of Sposito [1] and use the term sorption to represent adsorption, absorption, and surface precipitation.) The adsorbate must be initially transported from the bulk solution through the hydrodynamic boundary layer to the oxide external surface. Once at the surface, the adsorbate will try to find a desirable and/or available surface site to react with. Initially, sites are presumably readily available on or near the external surface. Eventually, however, the adsorbate must leave the surface and begin to move into the particle interior in search of an appropriate binding site. This intraparticle diffusion step is our main subject. Both of these first two steps involve some form of diffusion, and to maintain the electroneutrality condition the appropriate number of equivalents of counterions must diffuse in concert with the adsorbate. Once an appropriate binding site is found, and assuming the formation of an inner sphere complex, the adsorbate will lose its waters of hydration and then bind to that surface site. Most conceptual and mathematical models of that surface complexation reaction describe it as an exchange reaction. Assuming that no previous surface complexation reactions have occurred, sorption of cationic or anionic adsorbates implies that hydronium or hydroxide ions, respectively, will be released from the surface. These exchanged ions can either diffuse back into the bulk solution or find a desirable and/or available site to react with. Once again, electroneutrality must be maintained, so appropriate counterions will redistribute to balance the surface charge and/or diffuse along the hydronium or hydroxide ions. In summary>the overall sorption process can be divided into four major steps:

1. Diffusion through the hydrodynamic boundary layer to the external surface
2. Diffusion to a desirable and/or available surface site
3. Reaction with that surface site
4. Back-diffusion of ions released from the surface

Keep in mind, however, that each of these steps is more complex than the foregoing summary statements imply. Some of the complicating factors to consider include waters of hydration diffusing with the adsorbate and the counterions that diffuse with the adsorbate to maintain electroneutrality. Furthermore, adsorbate reaction with a specific surface site does not guarantee a permanent surface complex. It is possible that although reaction with the first site was kinetically favored, there is another, more energetically favorable site available to which the adsorbate could migrate.

Most studies of inorganic sorption by oxides report a two-step process [1,2]. Initial uptake, which is rapid and typically complete within hours, most likely involves sorption to external sites. However, following that initial uptake, secondary changes continue for weeks or months or longer. A variety of mechanisms have been suggested to explain the long, slow uptake process, including the formation of multinuclear surface complexes, the formation of solid solutions [3] or surface precipitates [4,5], particle–particle interactions [6,7], slow chemical reaction rates [8], and adsorbate diffusion into the interior of porous particles [9–12].

A review of the literature suggests that different mechanisms may play important roles in different systems. For example, results from pressure-jump studies of sorption reactions at nonporous surfaces have shown that the chemical reactions themselves are very fast [13–16], so that in most cases a slow chemical reaction rate is not likely a rate-limiting step. Spectroscopic evidence indicates that in some systems surface precipitation or solid solution formation does not occur even at high adsorbate loadings [17–20]. We believe, however, that intraparticle diffusion can be an important rate-limiting mechanism for all porous oxides.

III. THE DIFFUSION MODEL

Transport of an adsorbate through interior pores of an amorphous oxide involves intraparticle diffusion [21]. For macropores, transport occurs by bulk diffusion. Although the International Union of Pure and Applied Chemistry (IUPAC) defines micropores as pores of $d < 20 \text{ \AA}$, mesopores as having $20 \text{ \AA} < d < 500 \text{ \AA}$, and macropores as having $d > 500 \text{ \AA}$ this categorization is based on gas–solid systems. The average pore diameters for amorphous Al, Fe, and Mn oxides are $< 20 \text{ \AA}$ [10], 76 \AA [11], and $35\text{--}143 \text{ \AA}$ [22], respectively. In the aqueous phase, amorphous oxides are hygroscopic, which results in layers of water adsorbed on the particle surfaces—both external and internal surfaces [23]. These layers of adsorbed water on surfaces that are typically characterized as mesopores result in micropores. For the microporous amorphous oxides, flux into the particle is due to the concentration gradient [24]; this includes both surface and pore diffusion. In surface diffusion the adsorbate desorbs from one site and jumps to an adjacent vacant site. Concurrently, the adsorbate will diffuse in the aqueous phase of the pore. The overall rate of these parallel diffusion mechanisms will be determined by the fastest process.

The rate of metal removal in the porous oxide sorbents can be described with a film transfer process and either surface and/or pore diffusion models. To simplify the mass transfer of adsorbate from bulk solution to the adsorbent surface, some studies assume a linear concentration gradient existing in a hypothetical film surrounding the adsorbent particle [25]. When film transfer limits the rate, which, for example, is likely with nonporous particles, the following equation can be used to simulate the film transfer in a batch reactor:

$$\frac{dS}{dt} = \frac{3M}{V\varepsilon R\rho} k_f (S - S_s)$$

where

$S \equiv$ contaminant concentration in the aqueous phase

$S_s \equiv$ contaminant concentration in aqueous phase at external surface of particle

$k_f \equiv$ film transfer coefficient
 $M \equiv$ mass of adsorbent
 $R \equiv$ particle radius
 $t \equiv$ time
 $V \equiv$ solution volume
 $\varepsilon \equiv$ porosity in batch reactor
 $\rho \equiv$ apparent density of adsorbent

However, for amorphous Al, Fe, and Mn oxides, the microporous structure results in significant intraparticle diffusion resistance [10–12,26]. For Fe oxides, Axe and Anderson [24] showed that film transfer resistance is negligible compared to intraparticle diffusion resistance.

Assuming a spherical particle, the species mass balance yields the equation

$$\varepsilon \frac{\partial S}{\partial t} + \rho \frac{\partial C}{\partial t} = \frac{\rho}{r^2} \frac{\partial (D_s r^2 \partial C / \partial r)}{\partial r} + \frac{1}{r^2} \frac{\partial (D_e r^2 \partial S / \partial r)}{\partial r}$$

In this expression, C is the contaminant concentration in the sorbed phase and is a function of S through the adsorption process, ε is the porosity of the particle, D_s is the surface diffusion coefficient within the sorbent particle, ρ is the oxide bulk density, D_e is the pore diffusion coefficient within the sorbent, and r is the radial position within the sphere measured from the center. In aqueous environments, where contaminant concentrations are dilute, diffusivities are constant [23]. Also, the reaction is rapid or instantaneous for adsorption to amorphous oxides; the balance reduces to

$$\frac{\partial C}{\partial t} = \left(\frac{D_s + D_e dS / \rho dC}{1 + \varepsilon dS / \rho dC} \right) \left(\frac{1}{r^2} \right) \frac{\partial (r^2 \partial C / \partial r)}{\partial r}$$

where adsorption equilibrium (dC/dS) is described by the fitting isotherm. When the contaminant is not present upon oxide precipitation, the initial condition is

$$C(r, 0) = 0$$

At the center of the particle, the boundary condition is given by

$$\frac{\partial C}{\partial r}(0, t) = 0$$

and at the external oxide surface, $r = R$, one of two boundary conditions may exist, where, due to a turbulent hydraulic regime, the concentration at the surface is in equilibrium with the bulk aqueous phase or controlled by the flux of adsorbate to the surface:

$$C(R, t) = C_s$$

$$\frac{\partial C}{\partial r}(R, t) = \frac{k_f}{D_s} \left(\frac{dc}{ds} S - C_s \right)$$

Distinguishing between pore and surface diffusion, however, can be difficult if the surface boundary condition is unknown. However, molecular diffusion in

micropores is negligible when there is a strong affinity between the adsorbate and the surface, resulting in high adsorbate loadings [11,12,27,28]. The sorption of metal contaminants to amorphous Fe oxides is one example of a strong adsorbent–adsorbate system where surface diffusion dominates [11,12]. Diffusion obeys a random walk model where

$$D_s = \lambda^2 \nu_{\text{vib}} \exp\left(-\frac{E_A}{RT}\right)$$

In this expression, λ^2 defines the mean square hopping distance, and the probability that the adsorbate has the energy required to hop to the next site is the Boltzmann factor with E_A representing the activation energy. The adsorbate vibrational frequency, ν_{vib} , is a function of the molecular mass and the force constant, which is dependent on the potential energy on the pore surface.

In this chapter, we do not distinguish between surface and pore diffusion but instead talk about an overall effective diffusivity. In this way, we can include all the different approaches in our review. In summary, the mass balance model is based on the following assumptions: The adsorbent is composed of uniform, porous spheres with uniformly distributed sorption capacity, sorption is reversible, and diffusion is not a function of the particle dimension. These conceptual and mathematical models provide information about how sorption kinetics and the general system behavior can be influenced by changes in environmental conditions.

IV. IMPLICATIONS FROM THE CONCEPTUAL AND MATHEMATICAL MODELS

If inorganic sorption onto porous oxides follows the conceptual and mathematical models presented above, certain types of behavior should be observed. For example, in many aquatic environments, amorphous Al, Fe, and Mn oxides often precipitate in the presence of other dissolved ions. Under these conditions, adsorbates that have an affinity for oxide binding sites should have access to those sites during the formation process before they become sequestered in internal pores. Therefore, when coprecipitation occurs, intraparticle diffusion is probably not a rate-limiting step in the sorption process. Coprecipitation conditions, however, usually are not equilibrium conditions, because the amorphous oxides continue to age and transform into more stable mineral forms. During this aging process, adsorbates that are associated with the changing solid could become involved in several different reactions. If it does not fit well in the evolving mineral lattice, the adsorbate could be released to solution. Under these conditions, initial removal during coprecipitation would exceed the equilibrium conditions, and aging would cause an increase in adsorbate concentration in solution. In contrast, if it readily substitutes for major metal ions in the lattice, the adsorbate could become fixed in the oxide. In all cases, the rates of aging and transformation of the oxide, and possible release of adsorbate, would be controlled by intraparticle diffusion.

Adsorbate size relative to the size of pores in the oxides is also an important factor to consider. From the IUPAC classification, it seems reasonable that inorganic adsorbates should have access to binding sites in pores of the mesopore size

and larger. Micropores, however, may not be accessible to all adsorbates, especially the larger oxyanions such as phosphate, arsenate, and selenite. Furthermore, as mentioned earlier, these pore size categories were developed for gas–solid systems and may not be appropriate for oxides in aqueous systems. For example, oxides in solution have hydrated surfaces, and, depending on surface charge, an electrical double layer may be present. The form and extent of these surface phenomena within pores are not clear.

Another complicating factor involves the exchange reaction at the surface wherein cationic or anionic adsorbates form a surface complex and hydronium or hydroxide ions, respectively, are released. These released ions could diffuse back into bulk solution, but, depending on initial conditions, there may be desirable/available sites deeper within the particle. If so, during at least part of the sorption reaction there should be a pH front preceding the adsorbate front diffusing into the particle. In effect, available sites deeper within the particle would be titrated by the hydronium or hydroxide ions released during sorption. Eventually, the pore volume and quantity of available sites must become limiting and the released hydronium or hydroxide ions must diffuse out of the particle.

These surface charge effects could also influence other aspects of the physico-chemical behavior of the suspension. For example, depending on the solution ionic strength and the pH versus ZPC relationship, particles could aggregate, creating additional pore volume. Furthermore, surface charge and ionic strength must influence the counterion diffusion that is required to maintain electroneutrality.

In summary, although intraparticle diffusion is a rate-limiting mechanism for sorption in porous minerals, implications in using the diffusion model include accounting for such effects as coprecipitation, adsorbate type, potential exchange reactions, sorbent and solution chemistry, and the stability of the particle size distribution.

V CRITICAL REVIEW OF RELEVANT LITERATURE

Although the subsurface system is composed of a number of sorbents, amorphous oxides are an important phase in controlling metal contaminant distribution because they exist not only as discrete particles but also as coatings on other minerals. Sorption reactions between the bulk aqueous phase and organic matter and/or clay are generally readily reversible; as a result, adsorbates are eventually redistributed to porous amorphous oxides, where, in the slow sorption process of surface diffusion, the particle acts as a sink for the contaminant. In laboratory studies, Axe and Anderson [11,12] found that surface diffusivities range between 10^{-14} and 10^{-13} cm²/s, indicating that it may take years to reach equilibrium. Likewise, when the contaminant desorbs, a constant source of contaminant exists, which is presently not included in hydrogeochemical transport models and not accounted for during site remediation.

There are few studies that have examined configurational diffusion of metal contaminants diffusing in aqueous mineral systems. Furthermore, experimental methods and the conceptual and mathematical models used to represent diffusion vary widely. The diffusivities presented in Tables 1 and 2 are composite diffusivity

TABLE 1 A Summary of Diffusivity Values from Studies Involving Single-Phase Adsorbents with Significant Porosity

| Adsorbate | Adsorbent | Aporox. D ($\text{cm}^2 \text{ s}^{-1}$) ^a | Ref |
|-----------|------------------|---|-----|
| As(V) | HFO ^b | 5×10^{-11} | 26 |
| Cd | HFO (pH 7) | 8×10^{-14} | 12 |
| Cd | HFO (pH 6) | 6×10^{-13} | 12 |
| Cd | Alumina | 7×10^{-12} | 10 |
| Se(IV) | Alumina | 2×10^{-10} | 10 |
| Sr | HFO | 4×10^{-13} | 11 |

^aEffective diffusivities summarized here represent an average from each study; actual values were typically within an order of magnitude of these averages.

^bHFO = hydrous ferric oxide, also known as amorphous iron oxide or ferrihydrite.

values, which in some cases incorporate the effects of porosity, tortuosity, and adsorption. Also, some diffusivity values are estimates or averages from the information presented in the original paper. It is clear that pore size plays a significant role in diffusion. In general, diffusivity values for the adsorbents with what the IUPAC characterizes as micropores and mesopores (Table 1) are around $10^{-12} \text{ cm}^2/\text{s}$. In contrast, diffusivity values for adsorbents with macropores (Table 2) are typically up to six orders of magnitude larger. To better understand the effect of diffusion, diffusivities ranging from 10^{-14} to $10^{-10} \text{ cm}^2/\text{s}$ were used in the integrated analytical solution to the mass balance using a constant boundary condition at the particle surface and a particle diameter of $40 \mu\text{m}$ (Fig. 1). In systems with macropores, intraparticle diffusion approaches the rates expected for bulk diffusion. As pore size increases from micropores to mesopores to macropores, diffusion rates

TABLE 2 A Summary of Diffusivity Values from Studies Involving Single-Phase Adsorbents with Limited Porosity and Modified or Multicomponent Adsorbents^a

| Adsorbate | Adsorbent ^b | Approx. D (cm^2/s) | Ref. |
|------------|----------------------------------|--|------|
| Cd | Proprietary α -FeOOH | 1×10^{-8} | 29 |
| Cd | Fe oxide-coated GAC ^b | 2×10^{-8} | 30 |
| Cd | Mn oxide-coated GAC | 1×10^{-9} | 31 |
| Cr(VI) | Proprietary α -FeOOH | 1×10^{-6} | 29 |
| Cu | Fe oxide-coated GAC | 1×10^{-8} | 30 |
| Cu | Mn oxide-coated GAC | 9×10^{-11} | 31 |
| Pb | Proprietary α -FeOOH | 5×10^{-9} | 29 |
| Cd, Ni, Zn | α -FeOOH with 0.86% Si | 2×10^{-20} | 32 |

^aEffective diffusivities summarized here represent an average from each study; actual values were typically within an order of magnitude of these averages.

^bGAC = granular activated carbon.

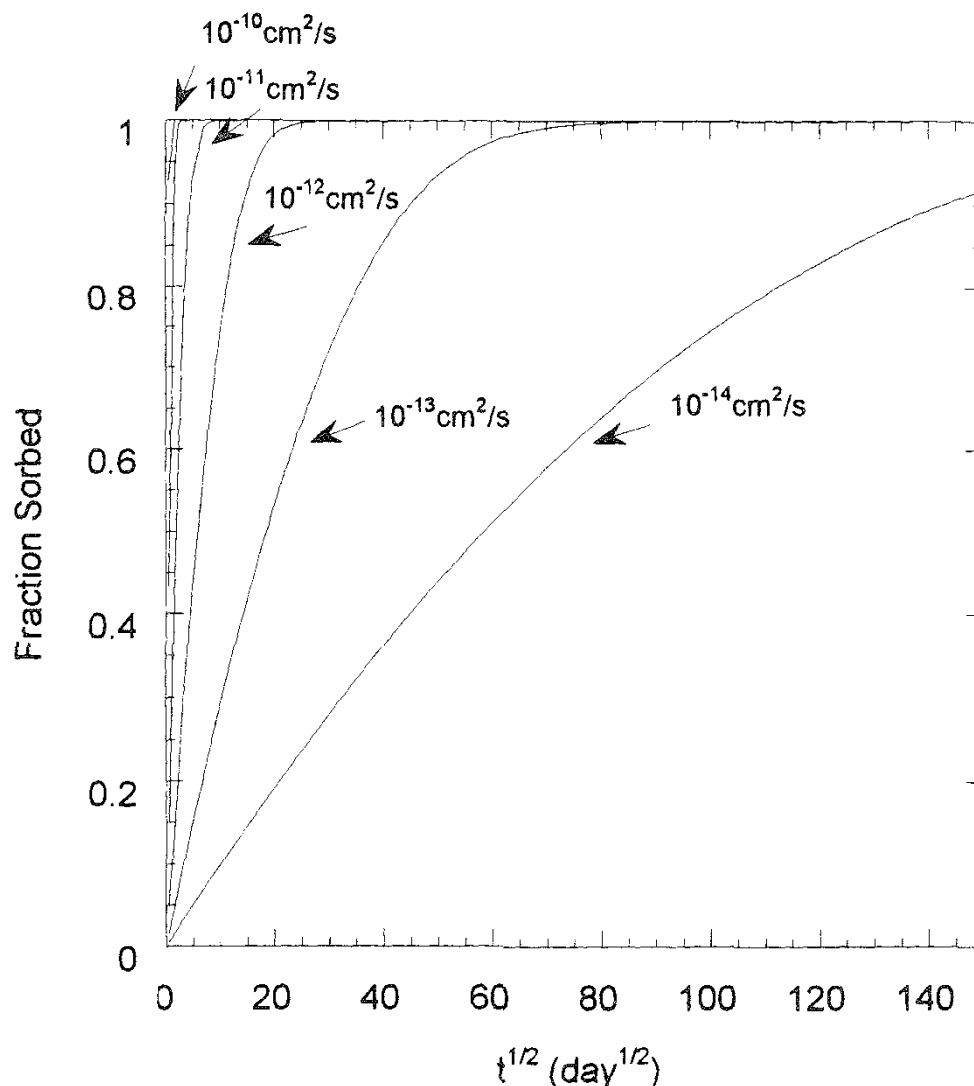


FIG. 1 Theoretical mass fraction sorbed versus the square root of time using a particle diameter of $40\text{ }\mu\text{m}$ and the integrated solution to the mass balance with a constant boundary condition.

can increase by from one to three orders of magnitude. Furthermore, although few data are available, it seems that these effects are more important for large oxyanions.

The adsorbate's charge and solution composition will determine its size, which affects the resulting type of intraparticle diffusion. Specifically, when pores are large relative to the diameter of the ion, bulk diffusion is possible. For pores that are small relative to the size of the ion, transport is limited to solid-state diffusion. When pore and ion are about the same size, the ion interacts with the pore wall as a result of physical forces, such as electrostatic and van der Waals forces [33]. Diffusion under these conditions is known as configurational diffusion [28,33]. In aqueous environments, layers of water adsorb in what is typically defined as mesopores, and interaction of the adsorbate with the pore wall results in configurational or surface diffusion. The size differences among anions compared to those among cations would suggest that anionic diffusion may fall into the solid-

state regime for certain cases, while the hydrated cation can move by both surface and pore diffusion.

Of the studies reviewed here, only the work by Papelis et al. [10] directly examined the effects of pore size. Under similar experimental conditions, they reported that when adsorbents with micropores and mesopores were compared, diffusivity values for Cd and Se(IV) increased by factors of about 2 and 33, respectively. As noted by those authors, the fact that Se(IV) is more sensitive to changes in the pore size is likely due to the fact that the hydrated selenite anion is large relative to Cd (diameters of about 6.5 Å and 4.5 Å, respectively). The larger selenite anion may be significantly hindered while diffusing through smaller diameter pores.

Waychunas et al. [20] noted that in contrast to postprecipitation adsorption tests, uptake of As(V) onto amorphous iron oxide was significantly greater and not diffusion-limited. Furthermore, with subsequent aging of the system, they observed desorption of As(V), presumably because it did not fit well in the structure of the aging oxide. In contrast, there apparently are some systems where the adsorbate does fit well into the structure of the aging oxide. For example, Kinniburgh et al. [34] reported increased uptake of Mg on Al gels aged for 205 days. The behavior could not be due to slow diffusion into the solid, however, because in the same systems the amount of Ca, Sr, and Ba decreased with aging. Trade-offs between diffusion and incorporation into the solid can have interesting implications for the transformation pathways of these unstable solids. Baltpurvis et al. [35] reported a correlation between the relative affinities of anions for HFO and enhanced formation of hematite rather than goethite.

Because amorphous oxides are metastable minerals, over time they will crystallize into more stable forms. For example, amorphous Fe oxide, also known as ferrihydrite, will restructure to hematite. However, upon dissolution of the amorphous Fe oxide, it would reprecipitate to goethite. These structural changes in the oxide, which are a function of time and solution chemistry, will affect the intraparticle diffusion process. However, Axe [36] studied amorphous Fe oxide aging with experiments that included spectroscopic analyses of the sorbent before, during, and at the conclusion of sorption experiments. X-ray diffraction was used to observe the oxide aging, with and without contaminant present. The diffraction pattern of freshly precipitated amorphous Fe oxide (Fig. 2) showed little or no crystallization; however, as it aged, more structure could be seen. Over time, the patterns were analyzed for the peak widths at half-height. After 7 weeks, there is evidence of both hematite and goethite minerals, but the oxide without Sr had more goethite present than the one with Sr. This crystallization increased with time; after 14 weeks diffraction pattern peaks narrowed and increased in height (less noise). At 14 weeks, there were no significant differences between the Fe oxide with and without Sr. The fresh, 7-week, and 14-week patterns were from one set of samples, but in the final time series, 22 weeks, a different sample was used. For the 22-week samples, the diffraction pattern of the Fe oxide without Sr has stronger, narrower peaks than does the pattern of oxide with Sr. An analysis of the peak widths indicates that for the oxide without Sr there is evidence of more hematite crystallization. As a result, the 5.5-month-old samples suggest that the presence of contaminant inhibited the crystallization of the amorphous oxide. Interestingly, the 22-week-old samples showed less crystallization than the samples at 14 weeks. Overall,

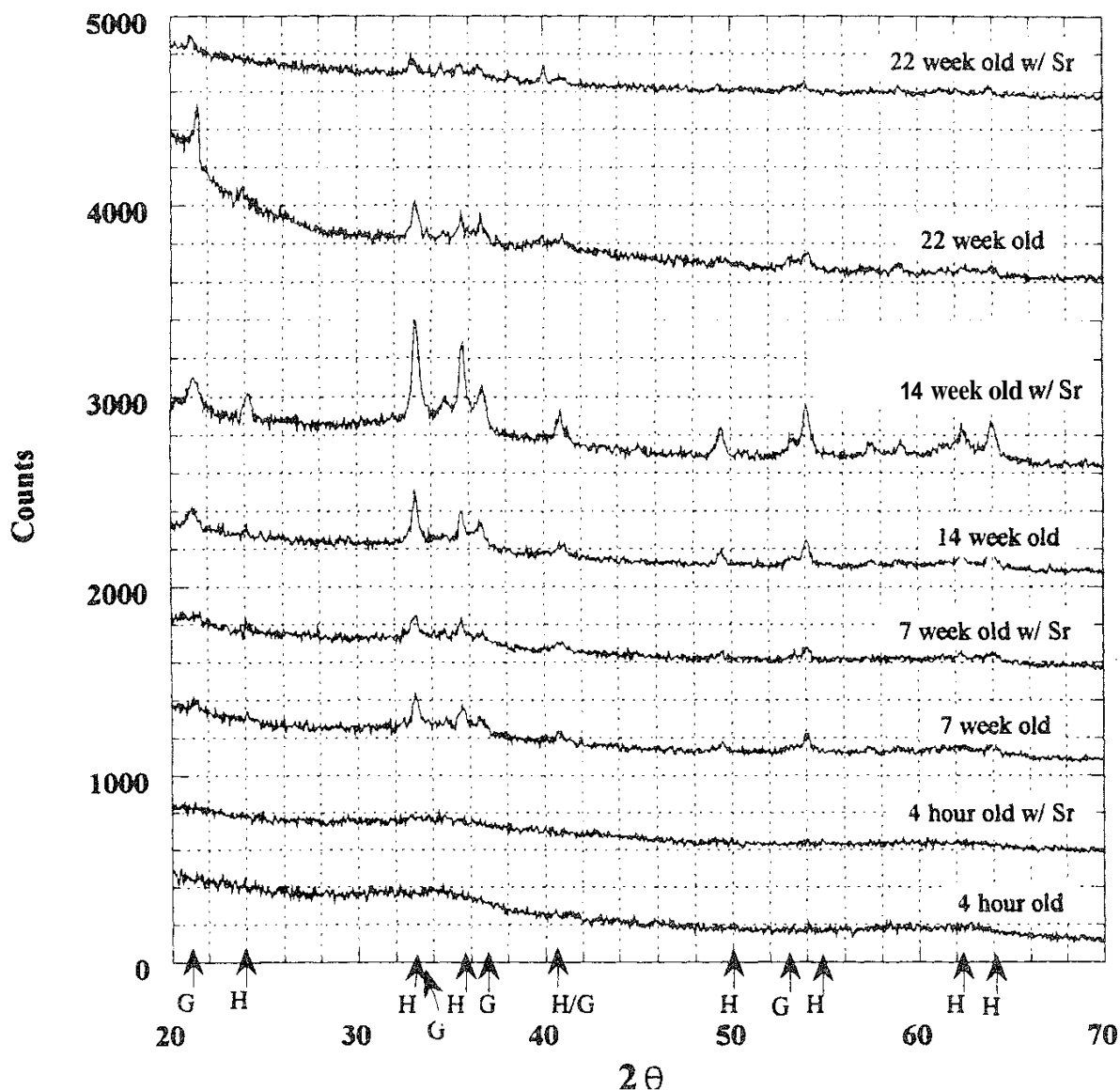


FIG 2 X-ray diffractograms of amorphous Fe oxide with and without contaminant present and as a function of time. H = hematite; G = goethite. (From Refs. 11 and 36.)

however, all diffraction patterns have substantial noise, indicative of an amorphous solid. While noise decreases, revealing crystallization, with time, there is still very little crystallization.

Amorphous Al, Fe, and Mn oxides are generally found with adsorbed inorganic ions and organic matter. Although amorphous oxides are metastable minerals, their aging to crystalline stable minerals can be retarded by the sorption of organic and inorganic species [35–38]. As a result, amorphous oxide minerals that have high surface areas, porous structure, and a high affinity for inorganic species are effective sorbents for inorganic contaminants. Further studies are needed to investigate the crystallization (or not) of amorphous oxides as a function of contaminant loading and time for better understanding the oxide stability as well as for potentially modeling the effect of the contaminant's presence.

VI. CONCLUSIONS

To accurately model contaminant transport when Al, Fe, and Mn oxide minerals are present, intraparticle diffusivities are needed. Additionally, as we tried to point out in this chapter, there are a number of implications in using the diffusion model with amorphous oxides. Some of these implications of intraparticle diffusion have been observed by researchers in macroscopic studies of both model and real systems. However, as only a small number of studies have been conducted on metal contaminant diffusion in aqueous oxide systems, many implications need yet to be addressed such as the long-term effect of contaminants sorbed in micropores of metastable minerals and desorption of contaminants from both coprecipitated oxides and oxides exposed to contaminants over long periods of time. Therefore, future studies are needed to study and improve our understanding of this slow sorption process, intraparticle diffusion.

REFERENCES

1. G. A. Sposito, in *Geochemical Processes at Mineral Surfaces* (J. A. Davis and K. H. Hayes, eds.), Am. Chem. Soc. Symp. Ser. 323, Am. Chem. Soc., Washington, DC, 1986, pp. 217–228.
2. J. A. Davis and D. B. Kent, in *Mineral–Water Interface Geochemistry* (M. F. Hochella and A. F. White, eds.), Mineralogical Society of America, Washington, DC, 1990, pp. 177–260.
3. B. R. Coughlin and A. T. Stone, *Environ. Sci. Technol.* 29(9):2445–2455 (1995).
4. D. A. Dzombak and F. M. M. Morel, *J. Colloid Interface Sci.* 112:588–598 (1986).
5. J. A. Davis, C. C. Fuller, and A. D. Cook, *Geochim. Cosmochim. Acta*, 51:1477–1490 (1987).
6. M. A. Anderson, M. I. Tejedor-Tejedor, and R. R. Stanforth, *Environ. Sci. Technol.* 19(7):632–637 (1985).
7. B. D. Honeyman and P. H. Santschi, *Environ. Sci. Technol.* 25:1739–1747 (1991).
8. T. L. Theis, T. L. Iyer, and L. W. Kaul, *Environ. Sci. Technol.* 22:1013–1017 (1988).
9. K. G. Stollenwerk and K. L. Kipp, in *Chemical Modeling of Aqueous Systems II* (D. C. Melchior and R. L. Bassett, eds.), A. C. S. Symp. Ser. 323, Am. Chem. Soc., Washington, DC, 1990, pp. 243–257.
10. C. Papelis, P. V. Roberts, and J. O. Leckie, *Environ. Sci. Technol.* 29(4):1099–1108 (1995).
11. L. Axe and P. R. Anderson, *J. Colloid Interface Sci.* 175:157–165 (1995).
12. L. Axe and P. Anderson, *J. Colloid Interface Sci.* 185:436–448 (1997).
13. K. Hachiya, M. Sasaki, T. Ikeda, N. Mikami, and T. Yasunaga, *J. Phys. Chem.* 88:27–31 (1984).
14. K. F. Hayes and J. O. Leckie, in *Geochemical Processes at Mineral Surfaces* (J. A. Davis and K. H. Hayes, eds.), A. C. S. Symp. Ser. 323, Am. Chem. Soc., Washington, DC, 1986, pp. 114–141.
15. P. Zhang and D. L. Sparks, *Environ. Sci. Technol.* 24:1848–1856 (1990).
16. P. R. Grossl, and D. L. Sparks, *Geoderma* 67:87–101 (1995).

17. K. F. Hayes, A. L. Roe, G. E. Brown, Jr., K. O. Hodgson, J. O. Leckie, and G. A. Parks. *Science* 238:783 (1987).
18. G. E. Brown, in *Mineral-Water Interface Geochemistry, Review in Mineralogy* (M. F. Hochella and A. F. White, eds.), Vol. 23, Mineralogical Society of America, Washington, DC. 1990, pp. 309--363.
19. S. Combes, C. J. Chisholm-Brause, G. E. Brown, Jr., and G. A. Parks, *Environ. Sci. Technol.* 26:376 (1992).
20. G. A. Waychunas, B. A. Rea, C. C. Fuller, and J. A. Davis. *Geochim. Cosmochim. Acta.* 57:2251--2269 (1993).
21. H. S. Fogler, *Elements of Chemical Reaction Engineering*, 2nd ed., Prentice-Hall, Englewood Cliffs, NJ. 1992.
22. K. Parida, P. K. Satapathy, A. K. Sahoo, and N. Das, *J. Colloid Interface Sci.* 173:112--118 (1995).
23. J. Kärger, and D. M. Ruthven, *Diffusion in Zeolites and Other Microporous Solids*, Wiley, New York. 1992.
24. L. Axe and P. Anderson. in *Adsorption of Metals by Geomedia: Variables, Mechanisms, and Model Applications* (E. Jenne, ed.). Academic Press, New York, 1998. pp. 193--208.
25. U. K. Traegner and M. T. Suidan, *Water Res.* 23(3):267--273 (1989).
26. C. C. Fuller, J. A. Davis, and G. A. Waychunas, *Geochim. Cosmochim. Acta*, 57:2271--2282 (1993).
27. L. D. Trowbridge, Isotopic selectivity of surface diffusion: an activated diffusion model, DE90 003473, U. S. DOE, Oak Ridge, TN, 1989.
28. G. F. Froment and K. B. Bischoff, *Chemical Reactor Analysis and Design*, 2nd ed., Wiley, New York, 1990.
29. T. L. Theis, R. Iyer, and S. K. Ellis, *Environ. Prog.* 13(1):72--77 (1994).
30. T. Wang, Copper(II) and cadmium(II) removal and recovery by iron oxide-coated granular activated carbon. Ph.D. Dissertation. Illinois Institute of Technology, Chicago, IL, 1995.
31. H.-J. Fan, Removal and recovery of Cu(II) and Cd(II) by Mn oxide-coated composite adsorbent, Ph.D. Dissertation, Illinois Institute of Technology. Chicago, IL, 1996.
32. G. W. Bruemmer, J. Gerth, and K. G. J. Tiller, *J. Soil Sci.* 39:37 (1988).
33. J. Xiao and J. Wei, *Chem. Eng. Sci.* 47(5):1123--1141 (1992).
34. D. G. Kinniburgh, J. L. Jackson, and J. K. Syers. *Soil Sci. Soc. Am. J.* 40:796--799 (1976).
35. K. A. Baltupurvis, R. C. Burns, and G. A. Lawrence. *Environ. Sci. Technol.* 39(3):939--944 (1996).
36. L. Axe, Sr and Cd diffusion and reaction within Fe oxides. Ph.D. Dissertation, Illinois Institute of Technology, Chicago, IL, 1995.
37. E. A. Jenne, in *Trace Inorganics in Water*. *Adv. Chem.* 73 (R. A. Baker, ed.), Am. Chem. Soc., Washington, DC. 1968, Chapter 21.
38. U. Schwertmann and W. R. Fischer, *Geoderma* 10:237--247 (1973).

10

Electrokinetic Phenomena in Porous Media and Around Aggregates

PIERRE M. ADLER and DAVID COELHO Equipe Milieux Poreux, Institut de Physique du Globe de Paris, Paris, France

JEAN-FRANÇOIS THOVERT Laboratoire de Combustion et de Detonique. Centre National de la Recherche Scientifique. Futuroscope, France

MICHAEL SHAPIRO Department of Mechanical Engineering, Technion— Israel Institute of Technology, Haifa, Israel

- I. Introduction
- II. Electrokinetic Equations
 - A. Flux of the ionic species
 - B. Flow velocity field
 - C. Electric potential
 - D. Boundary conditions
 - E. Equilibrium ion density distribution
 - F. Equilibrium ion density distribution in spatially periodic porous media
- III. Linearized Equations
 - A. Perturbations
 - B. Simplified equations
 - C. Dimensionless formulation
- IV. Examples
 - A. Porous medium submitted to external pressure and potential gradients
 - B. Semi-infinite void space
 - C. Plane Poiseuille configuration
 - D. Circular Poiseuille configuration
- V. Numerical Simulation of Electro-Osmotic Phenomena
- VI. Porous Media
 - A. Regular packings of spheres and ellipsoids
 - B. Random packings of spheres and ellipsoids
 - C. Reconstructed porous media
 - D. Discussion
- VII. Fractal Aggregates

| | |
|--|-----|
| A. Cluster generation | 245 |
| B. Macroscopic conductivity of suspensions of uncharged aggregates | 247 |
| C. Macroscopic conductivity of suspensions of charged aggregates | 250 |
| D. Electrophoretic mobility | 252 |
| VIII. Concluding Remarks | 253 |
| References | 255 |

I. INTRODUCTION

Consider an N -component dilute electrolyte filling the interstices of a porous medium. This medium is composed of electrically charged smooth solid particles arranged in a spatially periodic lattice structure. Far from the particles the solute may be considered neutral. However, in the vicinity of the particles' surfaces the distribution of ions within the electrolyte is affected by the particles' surface charge. For example, positively charged particle surfaces attract negative ions from the solution and repel positive ions. In the absence of external electric fields, pressure gradients, or body forces, the electrolyte rests in equilibrium. In this state there exists a region close to the particle surfaces with a nonzero volumetric charge distribution within the electrolyte. This region is called a Debye sheath layer [1]; its thickness may vary from hundreds of nanometers to several micrometers [2].

When the porous medium saturated with the electrolyte is embodied in an external electric field \mathbf{E} , there appears a nonzero volumetric body force within the Debye layer, which sets the ions in that region into motion. Far from the particle surfaces, this volumetric force is zero, since the solute there is neutral. However, the electrolyte is brought into motion also in the latter region as a result of the solute's viscosity. These processes lead to the appearance of an interstitial flow velocity field $\mathbf{u}(\mathbf{R})$. This velocity field, when integrated over a representative volume of the porous medium, yields a nonzero seepage velocity \mathbf{U} *in the absence of any macroscopic pressure gradient* applied to the porous medium. This process is called electro-osmosis, and the velocity \mathbf{U} is called the electro-osmotic velocity.

Hence, application of an external electric field results in two processes: the flow of electric current \mathbf{I} (which is typical of any continuum possessing free electric charges), and the electro-osmotic velocity \mathbf{U} . Both are proportional to the electric field intensity \mathbf{E} if the latter is sufficiently weak.

On the other hand, when a macroscopic pressure gradient ∇P is applied to the porous medium, the fluid percolates through it with a Darcy velocity \mathbf{U} . Additionally, the electrolyte flowing in the interstices affects the equilibrium ion distribution within the Debye layer, so that these ions are also set into motion. This results in a macroscopic electric current density \mathbf{I} flowing through the porous medium *in the absence of any external electric field*.

When the two "forcing factors" (or generalized forces) \mathbf{E} and ∇P are applied to the porous medium, there ensue corresponding responses (or generalized fluxes) \mathbf{I} and \mathbf{U} , which are related by

$$\mathbf{I} = \boldsymbol{\sigma} \cdot \mathbf{E} - \boldsymbol{\alpha} \cdot \nabla P \quad (1a)$$

$$\mathbf{U} = \boldsymbol{\beta} \cdot \mathbf{E} - \frac{\mathbf{K}}{\mu} \cdot \nabla \zeta \quad (1b)$$

where $\boldsymbol{\sigma}$ is the electric conductivity tensor, \mathbf{K} is the permeability tensor, and \mathbf{a} , $\boldsymbol{\beta}$ are the electro-osmotic tensor coefficients.

One can imagine limiting circumstances for which the latter equations are decoupled. Explicitly, for an almost ion-free (almost nonconductive) solution, one can see that $\mathbf{I} = 0$, while Eq. (1b) reproduces Darcy's law. In the other extreme case of a solid (infinitely viscous) electrolyte, one has $\mathbf{U} = 0$, and Eq. (1a) reduces to the familiar Ohm's law. In general, one can show that $\mathbf{a} = \boldsymbol{\beta}'$, by virtue of the Onsager thermodynamic theorem [3]; $\boldsymbol{\beta}'$ denotes the transpose of the tensor $\boldsymbol{\beta}$.

These coupled charge and mass transports have given rise to a vast literature that started with Smoluchowski [4], Huckel [5], Debye [6], Henry [7], and Booth [8], who considered limit cases (very thin or very thick double layers) in simple geometries (along a flat wall or around a single sphere) for small surface potentials. The relevant literature has been analyzed in detail by Coelho et al. [9], and it will be simply summarized here by giving some of the major landmarks.

There is, of course, an analogy between the study of a fixed and regular suspension and that of a spatially periodic medium. Dilute suspensions of particles have been intensively investigated by O'Brien and coworkers (cf., for instance, Ref. 10 for a recent review of these works). Only a few contributions deal with nondilute suspensions; an alternative and efficient approach is to use a cell model as Levine and Neale [11] did in order to take into account the effect of the finite solid volume void fraction.

Electrokinetic effects in porous media have been investigated by using either capillary tube models or, as mentioned before, concentrated suspensions or unconsolidated packings of particles.

A first important result was obtained by Overbeek [12], who extended Smoluchowski's [4] expression for the electrophoretic velocity beyond the double layer along a flat plate,

$$\mathbf{v}_s = - \frac{\varepsilon \zeta}{\mu} \mathbf{E} \quad (2)$$

where ε is the fluid permittivity, μ the viscosity, ζ the surface potential, and \mathbf{E} the electric field parallel to the wall. Overbeek has shown that Eq. (2) applies locally everywhere in the pore space provided that \mathbf{E} represents the local electric field. If the double layer volume is negligible, this implies the following relation between the transport coefficients in Eqs. (1):

$$\frac{\boldsymbol{\beta}}{\boldsymbol{\sigma}} = \frac{\varepsilon \zeta}{\mu \sigma_\infty} \quad (3)$$

where σ_∞ is the electrolyte conductivity.

The transport properties of circular capillaries were initiated by Osterle and coauthors (Ref. 2 and references therein). Various limitations were successively suppressed in these papers; the model was extended to account for nonvanishing double layer thickness, for concentration gradients, and for strong surface potentials.

Packed beds or concentrated suspensions of particles were mostly addressed in the limit of thin double layers. In this situation, the convected charge flux is

confined within the double layer and is determined by the local electrochemical potential gradients. Thus, it is only necessary to solve for the potential distribution, which can be done by matching outer and inner solutions. For the inner problem, the particle surface can be viewed as locally planar. In this framework, O'Brien and Perrins [13] and O'Brien [14] determined the conductivity and electro-osmosis coefficients, respectively, in three types of cubic close packings of equal spheres. The equation for the potential was numerically solved with a multipole expansion.

Aside from these theoretical studies, a large set of data has also been accumulated since the first observation of electrokinetic phenomena by Reuss [15], which is only very briefly reviewed here. Attention was focused on various problems, like the rheology of suspensions of charged particles [16], liquid transfers in soils [17], membrane separation [18], and various model situations of theoretical interest like suspensions of spheres [19,20] or streaming potential in specific geometries [21]. Recently, electrokinetic phenomena have been considered for interpreting the electrotelluric signals just before earthquakes [22]. Measurements of streaming potential and electro-osmosis coefficients have also been proposed as an easy and powerful alternative to direct permeability determination [23].

This review is organized as follows. The general electrokinetic equations that govern the flow of an electrolyte are presented in Sec. II along with a description of the infinite spatially periodic porous medium.

The influence of an external electric field and/or of an external pressure is studied in Sec. III. The equations that govern the perturbations of the ion distribution, the electric potential, the pressure, and the velocity are derived. They can be further simplified and linearized when the external electric field is small with respect to the local field induced by the zeta potentials and when the ionic distribution is not disturbed by the flow [24,25]. The linearized equations are made dimensionless by an adequate choice of basic units.

Some simple and useful examples are worked out in Sec. IV. First, the simultaneous motions of fluid and charges through a spatially periodic porous medium are analyzed: linearization enables us to summarize the results by means of four electro-osmotic tensors that relate the fluxes of charge and matter to the potential and pressure gradients. The cases of a semi-finite void space limited by a plane solid wall and of plane or circular channels are briefly addressed; the symmetry properties deduced from the general Onsager theorem are verified; these simple configurations are further used to check the numerical routines.

The general numerical method of solution is described in Sec. V. In the Debye-Hückel approximation, all the equations are linear. First, the equilibrium potential is solved; second, the ionic potential and the velocity field are alternately obtained in an iteration loop. These three systems are solved by means of classical iteration schemes such as the conjugate gradient for the potentials and a multigrid technique for the velocity. General estimates of the expected precision are given.

Results relative to porous media are presented and discussed in Sec. VI. Regular arrays of spheres and ellipsoids are addressed first. The influence of the surface potentials and that of the double layer thickness are systematically studied for a given choice of these two electrokinetic quantities.

Random packings of spheres and ellipsoids are simulated by a sequential deposition of particles under gravity. The influence of the surface potential and that of the

double layer have been systematically studied and discussed by comparison with the previously discussed ordered packings.

Reconstructed media based on Fontainebleau sandstones were generated and studied for three double layer thicknesses. These important data are discussed and compared with existing results [22,23].

Section VI ends with a general relation in the limit of large double layer thickness that, to the best of our knowledge, is novel. This property yields a single reduced representation of the electro-osmotic coefficients for all the studied configurations as functions of a dimensionless double layer thickness.

Section VII deals with suspensions made of fractal aggregates, because of the practical importance of such structures that may be present in many circumstances. The conductivity of such suspensions is determined for charged and uncharged clusters; the electrophoretic mobility is calculated in the dilute limit.

The chapter ends with some concluding remarks.

II. ELECTROKINETIC EQUATIONS

All the relevant microscopic equations that govern electro-osmotic phenomena are given in this section, as well as a general description of spatially periodic porous media.

A. Flux of the Ionic Species

Consider an A' -component Newtonian electrolyte of density ρ_f , dynamic viscosity $\mu = \text{constant}$, and dielectric constant ϵ , flowing with velocity $\mathbf{u}(\mathbf{R}, t)$ in interstices of a porous material. Let $\Psi(\mathbf{R}, t)$ be the electric potential prevailing within the solute. The flux \mathbf{j}_i of each i th ion species composing the solute is given by the constitutive equation [1]

$$\mathbf{j}_i = -D_i \nabla_R n_i - e z_i b_i n_i \nabla_R \Psi + n_i \mathbf{u}, \quad i = 1, 2, \dots, N \quad (4)$$

where $\nabla_R = \partial/\partial \mathbf{R}$, n_i is the ion's concentration in molecules per unit volume, Ψ is the electric potential, and D_i and b_i are the ion's diffusivity and electric mobility respectively, related by the Stokes–Einstein equation

$$D_i = b_i k T \quad (5)$$

Furthermore z_i is the ion's algebraic valence (greater or less than zero), e is the electron charge ($e > 0$), and \mathbf{u} is the flow velocity field. The flux \mathbf{j}_i and the concentration n_i obey the continuity (species conservation) equation

$$\frac{\partial n_i}{\partial t} + \nabla_R \cdot \mathbf{j}_i = 0 \quad (6)$$

B. Flow Velocity Field

We will be concerned with dense porous materials wherein the percolation flow velocity is normally small and the characteristic Reynolds number is much less than

unity. In these circumstances the (generally nonsteady) flow velocity field is governed by the Stokes equations

$$\mu \nabla_R^2 \mathbf{u} - \rho_f \frac{\partial \mathbf{u}}{\partial t} = \nabla_R p + \mathbf{F} \quad (7a)$$

$$\nabla_R \cdot \mathbf{u} = 0 \quad (7b)$$

where ρ_f is the electrolyte's density, p is the pressure, μ is the electrolyte's constant dynamic viscosity, and \mathbf{F} is the electric volumetric force density,

$$\mathbf{F} = \rho \nabla_R \Psi = \sum_{i=1}^N e n_i z_i \nabla_R \Psi \quad (8)$$

with

$$\rho = e \sum_{i=1}^N n_i z_i \quad (9)$$

being the electric charge density.

C. Electric Potential

The electric potential is given by the Poisson equation

$$\nabla_R^2 \Psi = -\frac{\rho}{\varepsilon} = -\frac{e}{\varepsilon} \sum_{i=1}^N n_i z_i \quad (10)$$

where ε is the dielectric constant of the electrolyte. It is assumed that for any nonsteady process of ion transport, transient phenomena associated with the electric potential occur so fast that one can use Eq. (4) in a quasi-steady approximation, i.e., assuming that $\Psi = \Psi(\mathbf{R}, t)$ satisfies Eq. (10) with time t being a parameter. This means that the electromagnetic wave propagation characteristic time L/c is much smaller than the characteristic time L^2/D_i associated with the diffusive species transport, L and c being the characteristic interstitial scale and velocity of light, respectively.

D. Boundary Conditions

Equations (6)–(10) have to be solved subject to the boundary conditions

$$\mathbf{v} \cdot \mathbf{j}_k = \mathcal{N} \quad (11a)$$

$$\mathbf{u} = 0 \quad (11b)$$

$$\Psi = \zeta \quad \text{or} \quad \mathbf{v} \cdot \nabla_R \Psi = -\frac{\sigma_s}{\varepsilon} \quad (11c)$$

where \mathbf{v} is the outer normal to the particle bed surface S_p , σ_s its surface charge density, and ζ its zeta potential. The two boundary conditions, namely the Dirichlet or Neuman condition on the electric field, are found in the literature.

E. Equilibrium Ion Density Distribution

Suppose that neither an external electric field nor a pressure (or concentration) gradient is imposed on the porous medium. Then one can rewrite Eq. (6) in the form

$$\nabla_R \cdot \mathbf{j}_i^0 = 0, \quad i = 1, 2, \dots, N \quad (12)$$

with the obvious zero-flux solution, which, with the help of Eqs. (4) and (5), may be written as

$$\mathbf{j}_i^0 = 0 = -D_i \nabla_R n_i^0 - \frac{e z_i}{kT} D_i n_i^0 \nabla_R \Psi^0, \quad i = 1, 2, \dots, N \quad (13)$$

In the above, the superscript 0, appearing on n_i and Ψ , refers to equilibrium conditions. From Eq. (13), one obtains the familiar Boltzmann distribution for n_i^0 ,

$$n_i^0 = n_i^\infty \exp\left(-\frac{e z_i}{kT} \Psi^0\right) \quad (14)$$

where n_i^∞ is a certain value of n_i^0 (at $\Psi^0 = 0$). To obtain the equilibrium potential distribution $\Psi^0(\mathbf{R})$, the introduction of Eq. (14) into Eq. (10) yields the Poisson-Boltzmann equation,

$$\nabla_R^2 \Psi^0 = -\frac{e}{\varepsilon} \sum_{i=1}^N n_i^\infty z_i \exp\left(-\frac{e z_i}{kT} \Psi^0\right) \quad (15)$$

This equation is to be solved subject to the equilibrium boundary condition

$$\Psi^0 = \zeta \quad \text{or} \quad \mathbf{v} \cdot \nabla_{\Psi^0} \mathcal{A} = -\frac{\sigma_s^{\mathcal{A}}}{\varepsilon} \quad \rho \pi \Omega_{\sigma} \quad (16a)$$

where ζ is the zeta potential of the particle surfaces. These two conditions are related by the condition that the sum of all the charges within the unit cell is equal to zero:

$$\sum_{i=1}^N \left(\int_{\tau} n_i^0 z_i dv + \int_S \sigma_i^0 dS \right) = 0 \quad (16b)$$

This condition will be called the macroscopic electroneutrality condition. In the most usual case, the surface potential is taken to be constant on S_p .

The flow velocity field equation (7) becomes, with the help of Eqs. (8) and (14),

$$\mathbf{0} = \nabla_R p^0 + \nabla_R \Psi^0 \sum_{i=1}^N n_i^\infty e z_i \exp\left(-\frac{e z_i}{kT} \Psi^0\right) \quad (17)$$

F. Equilibrium Ion Density Distribution in Spatially Periodic Porous Media

To complete the problem formulation, one should specify the porous microstructure of the material. Several types of ordered and disordered microstructures are considered here that are all characterized by the spatial periodicity property [26]. The porous medium is assumed to consist of a multitude of identical unit cells,

indefinitely reproduced within an infinite space (see Fig. 1). Therefore, the solution of Eqs. (6)–(11) is to be sought in the three-dimensional space \mathbb{R}^3 with

$$\mathbf{R} = \mathbf{R}_m + \mathbf{r} = n_1 \mathbf{I}_1 + n_2 \mathbf{I}_2 + n_3 \mathbf{I}_3$$

where $\{\mathbf{I}_1, \mathbf{I}_2, \mathbf{I}_3\}$ are the three basic vectors characterizing the unit cell of the porous medium and the trio of integers $\{n_1, n_2, n_3\}$ belongs to \mathbb{Z}^3 [26,27]. \mathbf{r} is the local position vector within the unit cell.

At equilibrium, all properties appearing in Eqs. (14) and (15) are spatially periodic functions, i.e., depend only on the intracell local position vector \mathbf{r} :

$$n_i^0(\mathbf{R}) = n_i^0(\mathbf{r}), \quad i = 1, 2, \dots, N; \quad p^0(\mathbf{R}) = p^0(\mathbf{r}); \quad \Psi^0(\mathbf{R}) = \Psi^0(\mathbf{r}) \quad (18)$$

and may be considered only within the unit cell τ , on the external faces of which the periodicity conditions should be imposed. These will be formulated in the form [27]

$$[\Psi^0] = 0 \quad [|\nabla_r \Psi^0|] = 0 \quad (19)$$

where $[\dots]$ denotes the difference between the values of a function at the opposite points $\mathbf{r}, \mathbf{r} + \mathbf{I}_j$, lying at the corresponding unit cell boundaries.

III. LINEARIZED EQUATIONS

A. Perturbations

The general system of equations, Eqs. (6) and (7), is nonlinear, which greatly complicates its solution in the general case, where the external fields \mathbf{E} and ∇P

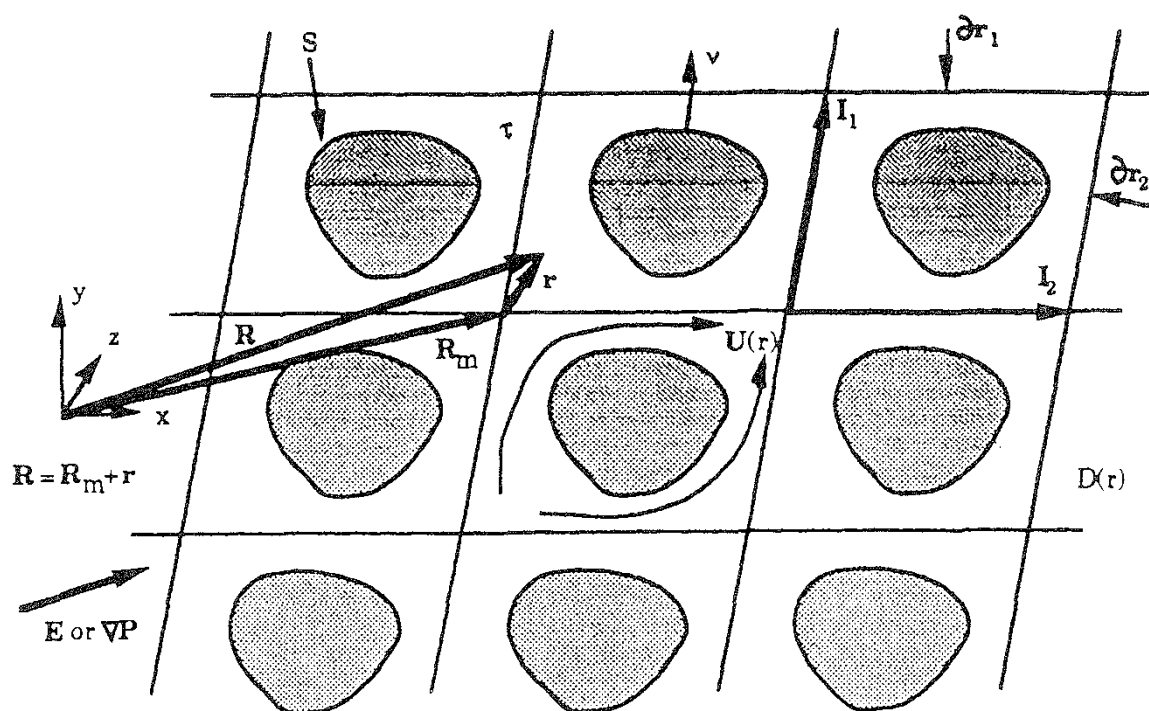


FIG. 1 Schematic view of a spatially periodic medium

are applied to the medium. One technique, generally accepted in most studies, is to assume that these external fields are small, as specified by appropriate nondimensional criteria. Accordingly, the ion concentration distributions and other quantities do not differ significantly with respect to their equilibrium values n_i^0 , Ψ^0 , p^0 , $\mathbf{u}^0 = \mathbf{0}$. This makes it possible to formulate the transport problem by linearized equations written in terms of corresponding small perturbation quantities $\delta n_i(\mathbf{R}, t)$, $\delta \Psi(\mathbf{R}, t)$, $\delta p(\mathbf{R}, t)$, $\delta \mathbf{u}(\mathbf{r}, t)$:

$$n_i = n_i^0(\mathbf{r}, t) + \delta n_i(\mathbf{R}, t), \quad i = 1, \dots, N \quad (20)$$

$$\Psi = \Psi^0(\mathbf{r}, t) + \delta \Psi(\mathbf{R}, t), \quad [|\delta \Psi|]_j = -\mathbf{E} \cdot \mathbf{I}_j \quad (21)$$

$$p = p^0(\mathbf{r}, t) + \delta p(\mathbf{R}, t), \quad [|\delta p|]_j = \nabla P \cdot \mathbf{I}_j \quad (22)$$

$$\mathbf{u} = \delta \mathbf{u}(\mathbf{r}, t), \quad [|\delta \mathbf{u}|] = 0 \quad (23)$$

In the above, the j subscript on jump conditions signifies that the component of the jump condition along the unit vector \mathbf{I} , is written for any value of j .

Introduce the ionic potentials Φ_i by means of the relationship (cf. [28])

$$n_i = n_i^0 \exp\left(-\frac{ez_i}{kT}(\Psi^0 + \delta \Psi + \Phi_i)\right) = n_i^0 \exp\left(-\frac{ez_i}{kT}(\delta \Psi + \Phi_i)\right) \quad (24)$$

Because of Eq. (14), the combination of Eq. (24) with Eqs. (4) and (13) for the flux of ionic species yields

$$\mathbf{j}_i = n_i D_i \frac{ez_i}{kT} \nabla_r \Psi_i + n_i \mathbf{u} \quad (25)$$

Since the ionic flux across a particle surface is nil as well as the fluid velocity, ionic potentials Φ_i are subject to the boundary conditions

$$\mathbf{v} \cdot \nabla_r \Phi_i = 0 \quad (26)$$

This condition is independent of the precise boundary condition (11c).

Equations (10) and (6) may be rewritten as

$$\nabla_r^2(\delta \Psi) = -\frac{\delta \rho}{\varepsilon} = -\frac{e}{\varepsilon} \sum_{i=1}^N \delta n_i z_i \quad (27)$$

$$\frac{\partial n_i}{\partial t} + n_i D_i \frac{ez_i}{kT} \left[\nabla_r^2 \Phi_i - \nabla_r(\Psi^0 + \delta \Psi + \Phi_i) \cdot \left(\frac{ez_i}{kT} \nabla_r \Phi_i + \frac{\mathbf{u}}{D_i} \right) \right] = 0 \quad (28)$$

Development of the velocity field equation leads to

$$\mu \nabla_r^2 \mathbf{u} - \rho_f \frac{\partial \mathbf{u}}{\partial t} = \nabla_r(p^0 + \delta p) + \rho \nabla_r(\Psi^0 + \delta \Psi) \quad (29)$$

Differentiating Eq. (24) gives

$$\nabla_r \left(\sum_{i=1}^N \right) = -\frac{1}{kT} \nabla_r(\Psi^0 + \delta \Psi) \rho - \sum_{i=1}^N \frac{ez_i}{kT} n_i \nabla_r \Phi_i \quad (30)$$

and using the solution for the flow velocity field at equilibrium, Eq. (17), one can show that

$$\mu \nabla_r^2 \mathbf{u} - \rho_f \frac{\partial \mathbf{u}}{\partial t} = \nabla_r \left(\delta p - kT \sum_{i=1}^n \delta n_i \right) - \sum_{i=1}^N e z_i (n_i^0 + \delta n_i) \nabla_r \Phi_i \quad (31a)$$

$$\nabla_r \cdot \mathbf{u} = 0 \quad (31b)$$

Thus, the $2N + 5$ perturbation fields (δn_i , $\delta \Psi$, Φ_i , δp , \mathbf{u}) are given by the $2N + 5$ equations (24), (27), (28), and (31), along with the jump conditions in Eqs. (21)–(23).

B. Simplified Equations

We will further assume that all the perturbing quantities are small, which is valid only when \mathbf{E} is small with respect to the electric field prevailing in the double layer. A comparable condition for VP will be established below. In addition, only stationary situations are considered. Accordingly, the time derivatives and the second-order perturbation terms are dropped in (24)–(31).

Then the conservation equation for the ionic species, Eq. (28), is reduced to a linear differential equation.

$$\nabla_r^2 \Phi_i = \nabla_r \Psi^0 \left(\frac{e z_i}{kT} \nabla_r \Phi_i + \frac{1}{D_i} \mathbf{u} \right) \quad (32a)$$

$$\mathbf{v} \cdot \nabla_r \Phi_i = 0 \quad (32b)$$

In the absence of any macroscopic gradient of ionic concentration [$n_i(\mathbf{r}) = n_i(\mathbf{r} + \mathbf{R}_n)$], the ionic potentials are subject to jump conditions. $[[\Phi_i]] + [[\delta \Psi]] = 0$ implies

$$[[\Phi_i]]_j = \mathbf{E} \cdot \mathbf{I}_j \quad (33)$$

Similarly, the equations governing the fluid motion become

$$\begin{aligned} \mu \nabla_r^2 \mathbf{u} &= \nabla \left(\delta p - kT \sum_{i=1}^N \delta n_i \right) - e \sum_{i=1}^N n_i^0 z_i \nabla_r \Phi_i \\ \nabla_r \cdot \mathbf{u} &= 0, \quad [[\mathbf{u}]] = 0, \quad \mathbf{u} = 0 \text{ on } S \end{aligned} \quad (34)$$

If there is no macroscopic gradient of ionic concentration [$n_i(\mathbf{r}) = n_i(\mathbf{r} + \mathbf{R}_n)$], then

$$\left[\left(\delta p - kT \sum_{i=1}^N \delta n_i \right) \right] = [[\delta p]] \quad (35)$$

The $N + 4$ equations (32), (34a) and (34b) allow the determination of the $N + 4$ quantities $\nabla_r \Phi_i$, \mathbf{u} , and $\delta p - kT \sum_{i=1}^N \delta n_i$. Equation (25) can be linearized by dropping second-order perturbation terms; this yields

$$\mathbf{j}_i = n_i^0 \left[D_i \frac{e z_i}{kT} \nabla_r \Phi_i + \mathbf{u} \right] \quad (36)$$

Hence, the solvent and solute fluxes can be deduced from $\nabla_r \Phi_i$ and \mathbf{u} only. Therefore it is not necessary to solve for δn_i and $\delta \Psi$.

C Dimensionless Formulation

In this subsection, the electro-osmosis problem is written in a nondimensional form. To this end, dimensionless variables are introduced as follows.

The average ionic strength n^* is used as a characteristic concentration,

$$n^* = \sum_{i=1}^N n_i^\infty z_i^2 \quad (37)$$

From the Poisson–Boltzmann equation, Eq.(15), potentials are scaled with Ψ^* :

$$\Psi^* = \Phi^* = \frac{kT}{e} \quad (38)$$

Distances are normalized by the characteristic length of potential variations.

$$\kappa^{-1} = \left(\frac{\epsilon kT}{e^2 n^*} \right)^{1/2} \quad (39)$$

This length is called the Debye–Hückel length. Therefore the electrostatic field is scaled with E^*

$$E^* = \frac{kT\kappa}{e} \quad (40)$$

The pressure is scaled in accordance with the van't Hoff formula

$$p^* = n^* kT = \epsilon \left(\frac{kT}{e} \right)^2 \kappa^2 \quad (41)$$

From the equations governing the flow velocity field (34). one can devise a characteristic velocity

$$u^* = \frac{p^*}{\kappa \mu} \quad (42)$$

Finally, the diffusion coefficients are scaled by

$$D^* = \frac{u^*}{\kappa} \quad (43)$$

These scales are used to define the reduced quantities, which are denoted by a prime:

$$\begin{aligned} \mathbf{I}'_j &= \kappa \mathbf{I}_j, & \nabla &= \kappa^{-1} \nabla_r \\ \mathbf{u}' &= \frac{\mathbf{u}}{u^*} & D'_i &= \frac{D_i}{D^*} \end{aligned}$$

$$p' = \frac{\delta p - kT \sum_{i=1}^N \delta n_i}{p^*}, \quad n_i^\infty = \frac{n_i^\infty}{n^*} \quad (44)$$

$$\begin{aligned} \Psi^{0'} &= \frac{\Psi^0}{\Psi^*}, & \Phi_i' &= \frac{\Phi_i}{\Phi^*} \\ \zeta' &= \frac{\zeta}{\Psi^*} & \sigma_s' &= \frac{\sigma_s}{\epsilon \kappa \Psi^*} \end{aligned}$$

Using the above scaling relationships, we write the following set of reduced equations:

$$\nabla^2 \Psi^{0'} = - \sum_{i=1}^n n_i^{\infty'} z_i \exp(-z_i \Psi^{0'}) \quad (45)$$

$$\nabla^2 \Phi_i' = \nabla \Psi^{0'} \cdot \left(z_i \nabla \Phi_i' + \frac{1}{D_i'} \mathbf{u}' \right) \quad (46)$$

$$\nabla^2 \mathbf{u}' = \nabla p' - \sum_{i=1}^N n_i^{\infty'} z_i \exp(-z_i \Psi^{0'}) \nabla \Phi_i' \quad (47a)$$

$$\nabla \cdot \mathbf{u}' = 0 \quad (47b)$$

This system (44)–(47) is to be solved subject to the boundary conditions inside the unit cell,

$$\left. \begin{aligned} \Psi^{0'} &= \zeta' & \text{or} & & \mathbf{v} \cdot \Phi' &= -\sigma^{0'} \\ \mathbf{v} \cdot \nabla \Phi_i &= 0, & \mathbf{u}' &= \mathbf{0} \end{aligned} \right\} \text{on } S \quad (48)$$

The system has still to be completed by the boundary conditions at the surface of the unit cell:

$$\begin{aligned} [[\Psi^{0'}]] &= \mathbf{0}, & [[\Phi_i']]_j &= \mathbf{E}' \cdot \mathbf{I}'_j \\ [[\mathbf{u}']] &= \mathbf{0}, & [[p']]_j &= \nabla p' \cdot \mathbf{I}'_j \end{aligned} \quad (49)$$

In addition, under the assumption that either the surface zeta potential ζ' or the surface charge $\sigma^{0'}$ is small, the Debye–Hückel approximation [5,6] can be used to linearize Eqs. (45) and (47a) with respect to $\Psi^{0'}$. This was done in the numerical implementation. This approximation is generally of the second order with respect to ζ' . In the particular case of two symmetric species with $n_1^\infty = n_2^\infty$, the order of approximation is 3.

IV. EXAMPLES

A. Porous Medium Submitted to External Pressure and Potential Gradients

Consider first an external electric field of intensity E applied to a porous material. In its dimensionless form, the flux of ionic species is given by

$$\mathbf{j}'_i = n_i^{0'} z_i D'_i \nabla \Phi'_i + n_i^{0'} \mathbf{u}' \quad (50)$$

The electric current density flowing through the porous medium, resulting from the application of E' , is

$$\mathbf{I}' = \frac{1}{\tau} \int_{\tau} \sum_{i=1}^N z_i \mathbf{j}'_i d\tau = \frac{1}{\tau} \int_{\tau} \sum_{i=1}^N n_i^{0'} z_i^2 D'_i \nabla \Phi'_i d\tau + \frac{1}{\tau} \int_{\tau} \sum_{i=1}^N n_i^{0'} \mathbf{u}' d\tau \quad (51)$$

The electro-osmotic velocity \mathbf{U}' can be calculated by integrating the velocity \mathbf{u}' throughout the unit cell volume:

$$\mathbf{U}' = \frac{1}{\tau} \int_{\tau} \mathbf{u}' d\tau \quad (52)$$

Because of the linearity of the previous system of equations and boundary conditions, all solutions should be proportional to E . The conductivity tensor σ of the medium is defined by

$$\mathbf{I}' = \sigma' \cdot \mathbf{E}'; \quad \sigma = \sigma^* \cdot \sigma', \quad \text{with } \sigma^* = \frac{en^* u^*}{E^*} = \frac{\epsilon k T n^*}{\mu}$$

and the electro-osmosis tensor β by

$$\mathbf{U}' = \beta' \cdot \mathbf{E}'; \quad \beta = \beta^* \cdot \beta' \quad \text{with } \beta^* = \frac{u^*}{E^*} = \frac{\epsilon k T}{\mu e}$$

In the following, the conductivity σ is sometimes normalized by the conductivity σ^∞ of the undisturbed fluid, instead of σ^* , as is customary for porous media. These two quantities are related by

$$\sigma^\infty = \sigma^* \sum_{i=1}^N n_i^{\infty'} z_i^2 D'_i \quad (53)$$

Let us consider now an external pressure gradient VP applied to the same porous material. Again, the solvent and charge fluxes are proportional to the driving force VP . Thus, the permeability tensor K and the electro-osmosis tensor α are defined by

$$\mathbf{U}' = K' \cdot \nabla P'; \quad K = K^* \cdot K' \quad \text{with } K^* = \frac{\mu u^*}{\kappa p^*} = \frac{1}{\kappa^2}$$

$$\mathbf{I}' = -\alpha' \cdot \nabla P'; \quad \alpha = \alpha^* \cdot \alpha', \quad \text{with } \alpha^* = \frac{\epsilon \pi^* \omega^*}{\kappa \sigma^*} = \frac{\epsilon \mu}{\mu \epsilon}$$

Since both problems considered in this section are linear, a superposition of the two generalized forces, i.e., simultaneous application of the pressure gradient and the electric field, leads to relationship (1) with the electro-osmotic tensors (σ , α , β , and K). This is true only under the assumption that the ion distribution is slightly distorted, by application of either VP or E . The condition imposed on the latter quantity is obviously

$$E' \ll \zeta' \quad (54)$$

The comparable condition to be imposed on VP can also be obtained. Application of VP results in a force that must be much smaller than electric forces near the walls ($en^*\kappa\zeta$). Therefore, the restriction on VP is

$$\|\nabla P'\| \ll \zeta' \quad (55)$$

A last physical situation may be of general interest. Previously, the jump condition for the ionic potentials Φ_i was calculated from Eq. (24) assuming that the ionic concentrations have no macroscopic gradient [$n_i(\mathbf{r} + \mathbf{R}_n) = n_i(\mathbf{r})$],

$$[\Phi_i]_j = -[\delta\Psi]_j = \mathbf{E} \cdot \mathbf{I}_j$$

If this condition is not fulfilled, for example with

$$[\Psi + \delta\Psi]_j = \mathbf{V} \cdot \mathbf{I}_j$$

then the ionic concentrations are subject to a jump condition.

$$n_i(\mathbf{r} + \mathbf{R}_n) = n_i(\mathbf{r}) \exp\left[-\frac{ez_i}{kT} (\mathbf{V} \cdot (\mathbf{I}_1 + \mathbf{I}_2 + \mathbf{I}_3))\right] \quad (56)$$

This expression is equivalent to a macroscopic gradient of unperturbed concentration and, under the restriction that $V \ll \kappa\zeta$, it may be reduced to

$$[n_i^\infty]_j = \left(-\frac{ez_i}{kT}\right) \mathbf{V} \cdot \mathbf{I}_j, \quad i = 1, \dots, N$$

In the presence of an externally imposed concentration gradient, the modified pressure field ($\delta p - kT \sum_{i=1}^N \delta n_i$) in the Stokes equation, Eq. (34), has a jump condition that depends on $\Psi^0(\mathbf{r})$.

B. Semi-Infinite Void Space

In a semi-infinite space bounded by a plane charged surface (cf. Fig. 2a), the equation for the undisturbed potential can be solved analytically [29]. It may be useful to reproduce this derivation here. For a symmetric electrolyte, $z_1 = -z_2 = 1$, $n_1^\infty = n_2^\infty = \frac{n^*}{2}$, the equation for the undisturbed potential reads as when x is the direction normal to the plane,

$$\frac{d^2 \Psi^{0'}}{dx'^2} = \sinh(\Psi^{0'}) \quad (57a)$$

Integrating (57a) twice while accounting for the boundary conditions at the walls ($\Psi^{0'} = \zeta'$) and far from it (uniform $\Psi^{0'}$), we get finally

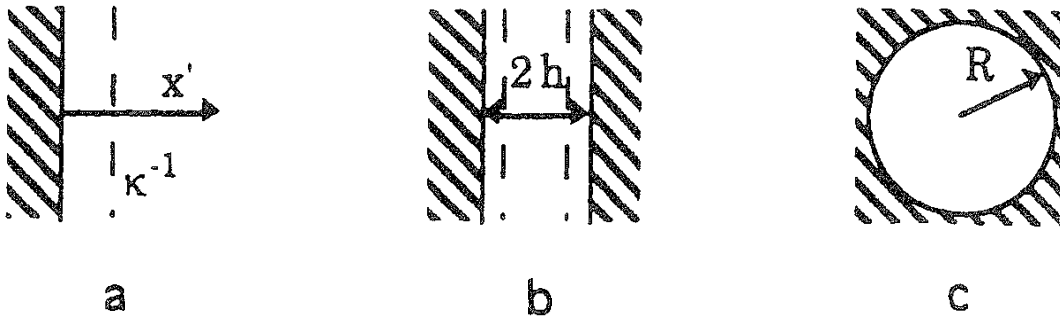


FIG. 2 (a) Semi-infinite void space, (b) plane, and (c) circular Poiseuille flows.

$$\Psi^{0'} = 2 \ln \left(\frac{1 + \gamma \exp(-x')}{1 - \gamma \exp(-x')} \right), \quad \gamma = \tanh \left(\frac{\zeta'}{4} \right) \quad (58a)$$

Note that for small potentials ($\zeta' < 1$), (57a) can be linearized into

$$\frac{d^2 \Psi^{0'}}{dx'^2} = \Psi^{0'} \quad (57b)$$

which yields the solution

$$\Psi^{0'} = \zeta' e^{-x'} \quad (58b)$$

This expression could also be obtained by a first-order expansion of the exact solution (58a). The surface charge can be obtained from (16a) and (58a) or (58b) as

$$\sigma'_s = 2 \sinh \frac{\zeta'}{2} \quad (59a)$$

$$\sigma'_s = \zeta' \quad (59b)$$

Consider now the application of an external electric field \mathbf{E} parallel to the y direction along the wall without any global pressure gradient. Equations (46)–(49) yield

$$\Phi'_i = E' y' \quad (60)$$

$$u'_{//}(x') = E' [\Psi^{0'}(x') - \zeta']$$

The tangential velocity $u'_{//}$ increases from 0 at the wall to the value u'_∞ far from it, which is given by Schmoluchofsky formula [4]

$$u'_\infty = -\zeta' E' \quad (61a)$$

or dimensionally

$$u_\infty = -\frac{\varepsilon}{\mu} \zeta E \quad (61b)$$

C. Plane Poiseuille Configuration

If the height $2h$ of a plane channel (see Fig. 2b) is assumed to be very large compared to the Debye thickness ($\kappa h \gg 1$), then Eq. (58) is a solution for the undisturbed potential distribution $\Psi^{0'}$. Under this condition, the conductivity and electrokinetic tensors can be calculated analytically.

On the other hand, if the channel is not very thick compared to the Debye layer, Poisson's equation must be linearized to be solved analytically when the surface potential is assumed to be low ($\zeta' \ll 1$).

Two species are present in the fluid with $z_1 = -z_2 = 1$ at the same initial concentration ($n^{\infty'} = \frac{1}{2}$). Therefore, Eq. (45) becomes

$$\frac{\partial^2 \Psi^{0'}}{\partial x'^2} = \Psi^{0'} + O(\zeta'^2) \quad (62a)$$

$$\Psi^{0'}(x' = \pm \kappa h) = \zeta' \quad (62b)$$

The solution of this system is

$$\Psi^{0'}(\kappa x) = \zeta' \frac{\cosh(\kappa x)}{\cosh(\kappa h)} + O(\zeta'^3) \quad (62c)$$

The surface charge on the walls deduced from (16a) and (62) is

$$\sigma'_s = \zeta' \tanh(\kappa h) \quad (63)$$

The average velocity induced by an axial external electric field can be calculated analytically, as well as the electric flux induced by a pressure gradient,

$$U'_{//} = \frac{E'_{//} \zeta'}{\kappa h} \int_0^{\kappa h} \left(\frac{\cosh(\kappa x)}{\cosh(h)} - 1 \right) d(\kappa x) = \zeta' E'_{//} \left(\frac{\tanh(\kappa h)}{\kappa h} - 1 \right) \quad (64)$$

$$I'_{//} = \int_0^{\kappa h} \left(-\zeta' \frac{\cosh(\kappa x)}{\cosh(\kappa h)} \right) \left(\frac{\kappa^2}{2} (h^2 - x^2) \nabla_{//} p' \right) d(\kappa x) = -\zeta' \nabla_{//} p' \left(\frac{\tanh(\kappa h)}{\kappa h} - 1 \right) \quad (65)$$

In the above, the subscript $//$ denotes the components of the vectors along the direction of the channel. From Eq. (65), we deduce the coefficients α' and β' , which are equal, in agreement with Onsager's theorem:

$$\alpha' = \beta' = \zeta' \left(\frac{\tanh(\kappa h)}{\kappa h} - 1 \right) \quad (66)$$

These coupling coefficients are very small ($\alpha' = 3' \ll \zeta'$) in a narrow channel and tend towards ζ' in a wide one ($\kappa h \gg 1$).

The electric flux under a given electric field gives the conductivity coefficient,

$$\sigma'_{//} = \frac{D'_1 + D'_2}{2} + \frac{1}{2} \zeta' (D'_1 - D'_2) \frac{\tanh(\kappa h)}{\kappa h} + \frac{\zeta'^2}{2} \left[\frac{\tanh(\kappa h)}{\kappa h} - \frac{1}{\cosh^2(\kappa h)} \right] \quad (67)$$

In Eq. (67). the first term corresponds to the fluid conductivity with uncharged walls. The second term is due to the difference between the concentrations of the ionic species, which have different mobilities. The third one results from the convection of the local charge disequilibrium; since this disequilibrium and the solvent velocity field are proportional to ζ' , this is a second-order contribution. However, since expression (36) for \mathbf{j}_i' is only first-order accurate, the last term in (67) accounts only partly for the ζ'^2 contribution.

D. Circular Poiseuille Configuration

Assume that the porous medium is composed of a series of parallel tubes (bundle of tubes model) each of diameter $2a$ (Fig. 2c). The unit cell is now formed by the region $0 < r < a$, $0 < z < L$, where L is an arbitrary length. The external field \mathbf{E} and the pressure gradient ∇P are applied parallel to the tube axis. The capillary axis is z , and the distance to this axis is r .

Owing to the cylindrical symmetry, Eq. (44) for $\Psi^{0'}$ reads, for two symmetrical species with $N = 2$, $z_1 = -z_2 = 1$, and $n_1^\infty = iff = \frac{n^*}{2}$,

$$\frac{1}{r'} \frac{\partial}{\partial r'} \left(r' \frac{\partial \Psi^{0'}}{\partial r'} \right) = \sinh(\Psi^{0'}) = \Psi^{0'} + O(\zeta'^3) \quad (68a)$$

with

$$\begin{aligned} \Psi^{0'} &= \zeta' \quad \text{at } r' = \kappa a \\ \frac{\partial \Psi^{0'}}{\partial z} &= \frac{\partial \Psi^{0'}}{\partial \theta} = 0 \end{aligned} \quad (68b)$$

The solution of the linearized equation involves the modified Bessel function of the first kind I_0 [30],

$$\Psi^{0'}(r') = \zeta' \frac{I_0(r')}{I_0(\kappa a)} + O(\zeta'^3) \quad (69a)$$

It can be given in a power series representation,

$$\Psi^{0'}(r') = \zeta' \frac{\sum_{p=0}^{\infty} \left[\frac{r'^p}{2^p p!} \right]^2}{\sum_{p=0}^{\infty} \left[\frac{(\kappa a)^p}{2^p p!} \right]^2} + O(\zeta'^3) \quad (69b)$$

Note that

$$I_0(r') \sim \frac{e^{r'}}{\sqrt{2\pi r'}} \quad \text{if } r' \gg 1 \quad (70)$$

Therefore, for wide capillaries ($\kappa a \gg 1$), the potential along the tube axis is

$$\Psi^{0'}(0) = \zeta' \sqrt{2\pi \kappa a} e^{-\kappa a} \quad (71)$$

The surface charge on the walls deduced from (16a) and (69) is

$$\sigma'_s = \zeta' \frac{I_1(\kappa a)}{I_0(\kappa a)} \quad (72)$$

The cylindrical symmetry also imposes that \mathbf{u}' reduces to its axial component u'_z . Equation (46) and the jump condition (49) for Φ_i yield

$$\frac{\partial \Phi'_i}{\partial z'} = E'_z \quad \frac{\partial \Phi'_i}{\partial r'} = \frac{\partial \Phi'_i}{\partial \theta} = 0 \quad (73)$$

Thus, from the r' and θ components of (47) we have

$$\frac{\partial p'}{\partial r'} = \frac{\partial p'}{\partial \theta} = 0 \quad (74)$$

Finally, u'_z is obtained from the z' component of (47):

$$\frac{1}{r'} \frac{\partial}{\partial r'} \left(r' \frac{\partial u'_z}{\partial r'} \right) = \frac{\partial p'}{\partial z'} + E'_z \frac{1}{r'} \frac{\partial}{\partial r'} \left(r' \frac{\Psi^{0'}}{\partial r'} \right) \quad (75)$$

Integration of (75) yields

$$u'_z = -\frac{(\kappa a)^2 - r'^2}{4} \frac{\partial p'}{\partial z'} + E'_z [\Psi^{0'}(r') - \zeta'] \quad (76)$$

and by averaging over the capillary cross section,

$$u' = -\frac{(\kappa a)^2}{8} \frac{\partial p'}{\partial z'} + \frac{2E'_z}{(\kappa a)^2} \int_0^{\kappa a} [\Psi^{0'}(r') - \zeta'] r' dr' \quad (77)$$

Finally, the four global transport coefficients are

$$\sigma' = \frac{D'_1 + D'_2}{2} + \zeta' \frac{I_1(\kappa)}{\kappa a I_0(\kappa a)} (D'_1 - D'_2) \quad (78a)$$

$$\alpha' = \beta' = \zeta' \left[\frac{2I_1(\kappa a)}{\kappa a I_0(\kappa a)} - 1 \right] \quad (78b)$$

$$K' = (\kappa a)^2 / 8 \quad (78c)$$

Again, Onsager's symmetry is verified.

The expression for σ' is truncated to order $O(\zeta'^2)$, since our expression for $\Psi^{0'}$ is only first-order accurate as in the previous case of a plane channel. For wide capillaries ($\kappa a \gg 1$).

$$\sigma' = \frac{D'_1 + D'_2}{2} + \frac{\zeta'}{\kappa a} (D'_1 - D'_2) \quad (79a)$$

$$(79b)$$

V. NUMERICAL SIMULATION OF ELECTRO-OSMOTIC PHENOMENA

The simplified equations that govern electro-osmotic phenomena are Eqs. (45)–(49). Apart from some simple situations [31] such as Poiseuille flow, isolated spheres, these equations cannot be solved analytically. Hence, it was found useful to start a systematic numerical analysis, which is summarized below.

In this first numerical approach to electro-osmotic phenomena, Eqs. (45) and (47a) were linearized by making the classical assumption that the potential $\Psi^{0'}$ is small; it is equivalent to assuming that either the surface zeta potential ζ' or the surface charge $\sigma^{0'}$ is small. Hence, (45) and (47a) are replaced by

$$\nabla^2 \Psi^{0'} = - \sum_{i=1}^n z_i n_i^{\infty'} (1 - z_i \Psi^{0'}) + O(z_i \Psi^{0'})^2 = \Psi^{0'} + O(z_i \Psi^{0'})^2 \quad (80)$$

$$\nabla^2 \mathbf{u}' = \nabla p' - \sum_{i=1}^n z_i n_i^{\infty'} \nabla \Phi_i' (1 - z_i \Psi^{0'}) + O(z_i \Psi^{0'})^2 \quad (81)$$

Note that these approximations are generally second-order. They are third-order if there are two symmetric species with $n_1^{\infty} = n_2^{\infty}$. This linearization is generally called the Debye–Hückel approximation [5,6].

The geometry of the porous medium is discretized into an array of $N_{Cx}N_{Cy}N_{Cz}$ elementary cubes of size a filled with fluid or solid. These cubes are subgridded by n^3 mesh points. The equations are solved in a finite difference formulation with a second-order discretization, which yields linear problems of the generic form

$$\hat{A} \cdot \hat{X} = \hat{B} \quad (82)$$

The vector \hat{X} is the unknown field (Φ_i' or \mathbf{u}'); the matrix \hat{A} results from the operator in the transport equation and from the local boundary conditions (48), and the right-hand term \hat{B} results from the driving force, i.e., from the global boundary conditions (49) and from the current value of \mathbf{u}' when solving for Φ_i' or the current value of Φ_i' when solving for \mathbf{u}' .

The fields $\Psi^{0'}$ or Φ_i' are determined by a program that solves in any geometry any linear differential equation of the general form

$$\nabla^2 f = \mathbf{A} \cdot \nabla f + Bf + C \quad (83)$$

with the mixed boundary conditions

$$0 = a \cdot \nabla f + bf + c \quad \text{on } S \quad (84)$$

by the use of a conjugate gradient method [32]. The convergence criterion is based on the global residue

$$\|\hat{A}\hat{X} - \hat{B}\| < \eta \|\hat{B}\| \quad (85)$$

with η generally taken smaller than 10^{-5} .

Equations (47) are solved by means of a routine derived from the one used for solving the Stokes equation [33]. The so-called artificial compressibility is applied

with a staggered marker-and-cell (MAC) mesh. Thus, a given pressure field is used to calculate the velocity field. The resulting velocity field does not fit the incompressibility equation (47b), and the pressure field must be modified to minimize the local velocity divergence. These steps are repeated until Eq. (47b) is satisfied. This corresponds to the equality of the total fluxes through all the cross sections of the sample, within the same accuracy η as in Eq. (84).

The general iterative scheme is illustrated by the flowchart in Fig. 3. Note the iteration loop on the determination of the coupled fields Φ'_i and u . The equilibrium potential $\Psi^{0'}$ is determined first. Then Eqs. (46) and (47) are solved alternately until convergence of the global electric and mass fluxes I and U . An estimate of the velocity is given (zero velocity when the routine enters the loop); an estimate of Φ'_i is determined by solving (46); the velocity field is then updated by solving Eqs. (47). The stabilization criterion for the fluxes is generally set to 10^{-3} .

These alternate computations usually converge in a few iterations. In the presence of a macroscopic electric field E without a macroscopic pressure gradient, one solves first for Φ'_i assuming $u' = 0$. Then u' is determined from (47), and reinjected into (46). However, the corrections to Φ'_i resulting from the presence of u' are very small, as it is a secondary effect. Similarly, if a macroscopic pressure gradient is imposed without an electric field, one first solves (47) for the flow field assuming

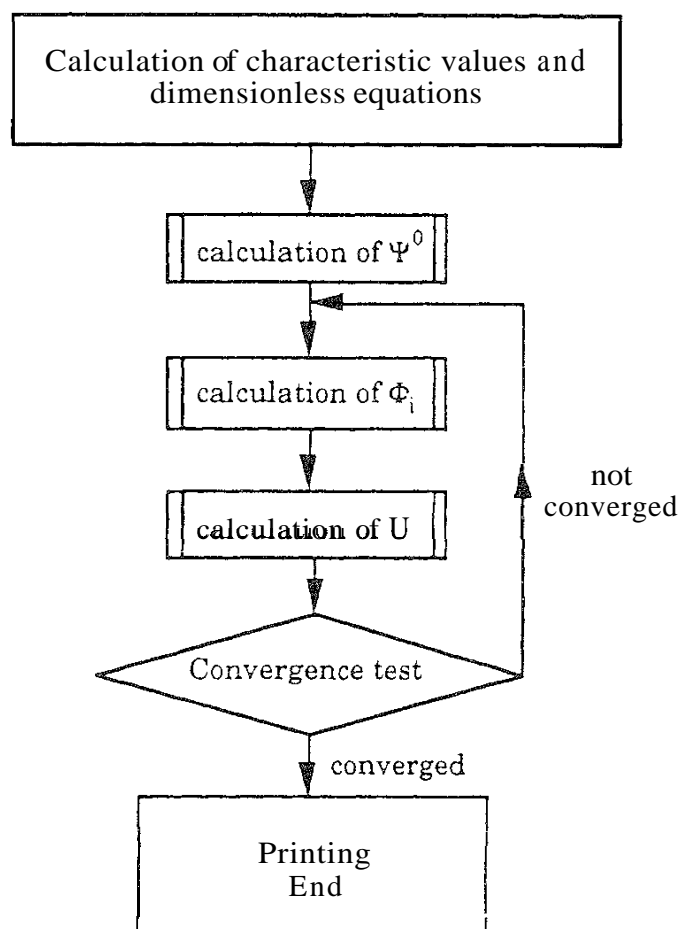


FIG. 3 Flowchart of the computing program.

constant Φ'_i . Then \mathbf{u}' is injected into (46) to compute $\nabla\Phi'_i$. The potential in (46) yields only a very small correction to \mathbf{u}' .

A large number of tests have been conducted to check these complex routines. They are detailed in Ref. (9) and can be summarized as follows.

Several non physical parameters have been introduced when implementing the numerical solution. The first one is the arbitrary choice of the unit cell to generate the periodic medium. It has been checked that it has absolutely no influence on the results, by performing similar runs with shifted unit cell boundaries. The same holds for rotations of the geometry by permutation of the coordinate axes.

There are also two discretization parameters. The elementary cube size a for discretizing the geometry is to be compared to a characteristic length scale L of the porous medium. Large or small ratios a/L correspond to coarse or fine descriptions of the geometry, respectively. The grid size a/n is the spatial resolution for the discretization of the transport equations, and it must be compared to the Debye thickness. Roughly speaking, the ratio $n/\kappa a$ is the number of grid points in the electrical double layer.

All the following computations are conducted for an aqueous solution of HClO_4 at 25°C , where species 1 is the proton with $D_1 = 9.31 \times 10^{-9} \text{ m}^2/\text{s}$ and species 2 is ClO_4^- with $D_2 = 1.79 \times 10^{-9} \text{ m}^2/\text{s}$; this corresponds to a ratio $D_1/D_2 = 5.2$. Plane and circular Poiseuille flows have been obtained with good precision, as well as the conductivity and the coefficient β' of suspensions of spheres, which were compared to the results found in the literature.

The results of all these tests can be summarized in a few simple statements. For a given geometry, with a fixed ratio R/a or h/a , the accuracy of the predictions critically depends upon the ratio κa (or $\kappa a/n$) of the grid spacing to the double layer thickness. For $\kappa a \leq 1$, the errors on all the perturbation quantities ($\sigma_s, \tilde{\sigma}, \beta, \dots$) do not exceed a few percent of $(\kappa a)^2$. When discretization is too coarse ($\kappa a > 1$), the predictions become grossly inaccurate, as could be expected since the double layers are overlooked by the discretization grid.

Moreover, the ratio R/a or h/a of the characteristic length scale of the medium to the discretization step determines the quality of the description of the geometry. Therefore, it affects equally the transport coefficients for uncharged solid walls and their disturbance by the electrokinetic effects. For example, the precision on $\tilde{\sigma}$ is about 2–3 times $(a/R)^2$, irrespective of the surface potential.

VI. POROUS MEDIA

Porous media can be classified as unconsolidated and consolidated materials. Soils, clays, and packings of various sorts belong to the first class, while rocks such as sandstones and limestones belong to the second. Both classes are investigated in this section. The first two subsections are devoted to ordered or random systems of particles, and the third to a different model of consolidated rocks, based on the classical reconstruction technique [26,34]. Finally, a formula valid in the thick double layer limit is used to gather all the numerical results and also some experimental results found in the literature.

A. Regular Packings of Spheres and Ellipsoids

Computations were conducted for simple cubic arrays of spheres and ellipsoids for various solid concentrations in an aqueous solution of HClO_4 . Of course, the conductivity and permeability of cubic sphere packings are isotropic, as may be reasoned from linear superposition. The external electric field is applied along one of the main directions of the cubic lattice. The double layer thickness was kept equal to $\kappa R = 1.65$. The ratio of the sphere radius to the particle separation l was varied from $R/l = 0.2$ to $R/l = 0.5$, which correspond to a dilute suspension ($\phi = 0.034$) and close packing ($\phi = 0.524$), respectively. The size a of the elementary cube was set to obtain a good discretization of the particle geometry and of the double layer, with $R/a \geq 4$ and $\kappa a \leq 1/3$.

The dimensionless conductivity σ/σ^∞ and coupling coefficients depend linearly upon ζ' . The conductivity and electro-osmotic coefficients $\beta = (\sigma/\sigma^\infty - 1)/\phi$ and β'/ζ' are plotted in Figs 4a and 4b, respectively, versus the solid volume concentrations ϕ for the three reduced surface potentials $\zeta' = -1, 0, +1$. For $\zeta' = 0$, one can see that β tends to $-3/2$ as $\phi \rightarrow 0$. Moreover, for uncharged particles, the values of $\tilde{\sigma}$ are very close to $-3/2$ in the whole range of ϕ . The corresponding analytical results of Sangani and Acrivos [35] are also plotted in Fig. 4a. For uncharged particles, the reduced conductivity significantly depends upon the packing density, which is explained by the effect of interactions between the double layers of adjacent particles.

Basically, the effect of increasing ϕ is to reduce the relative volume of the conducting matter and to diminish the absolute value of σ/σ^∞ , as may be observed for uncharged particles. This trend is also observed for positively charged particles. For negative ζ values, one can note the existence of a critical concentration at which $\tilde{\sigma} = 0$ ($a = \sigma^\infty$), where the above trend is counterbalanced by the excess of more mobile positive ions within the double layer. Due to this effect, the electrical conductivity of suspensions of negatively charged particles is always greater than for positively charged particles.

For any given ζ' , the electro-osmotic coefficient β' is a decreasing function of the solid volume fraction, as may be seen in Fig. 4b. In the dilute limit, the fluid in the bulk of the pore space is driven by the slip velocity at short distances of the particles. For lower porosities, the double layers overlap, and the free streaming zone shrinks and ultimately disappears.

The data for β'/ζ' are compared in Fig. 4b with similar results of Levine and Neal [11] computed with a cell model. The values of β'/ζ' differ by about 0.05 throughout the whole range of solid fractions. This implies that for dilute suspensions the agreement is satisfactory ($\cong 10\%$) where the cell model is applicable. Coelho et al. [9] showed that for $\phi \cong 0.01$, these two results agree to within a few percent. However, the relative error is large for close packing. This is because the cell model ignores the contacts between particles and assumes that the double layers surrounding different grains do not overlap. Accordingly, the departure worsens when κR increases.

Computations were also performed for simple cubic arrays of oblate ellipsoids of revolution with aspect ratio 5/1 and with solid concentrations varying from 0.02 up to 0.524. The double layer thickness was kept equal to $\kappa R = 2.81$. The geometry is

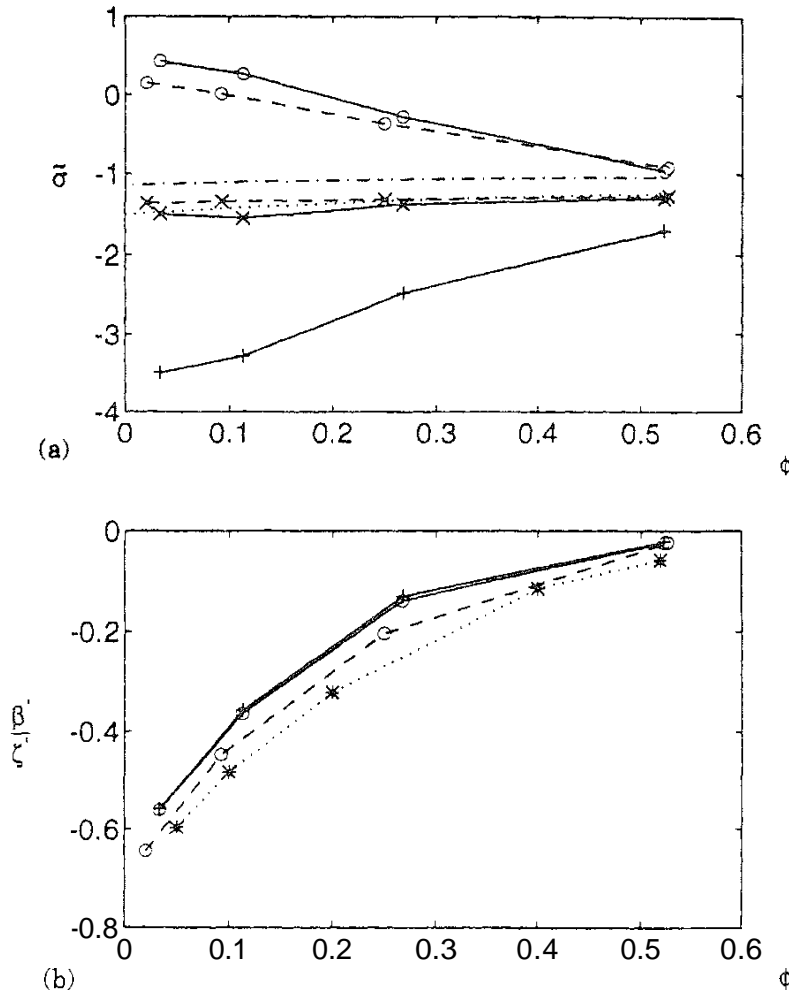


FIG. 4 (a) Conductivity coefficient $\tilde{\sigma}$ and (b) coupling coefficient β'/ζ' as functions of the solid volume fraction ϕ in a cubic array of spheres (solid lines) or ellipsoids (dashed lines). Data are for $\kappa R = 1.65$, $\zeta' = -1$ (\circ), 0 (\times) and $+1$ ($+$). The dotted line in (a) was obtained for uncharged particles [35], and the dash-dotted line for uncharged ellipsoids [36]; the dotted line in (b) results from a cell model [11].

discretized with $R_1/a = R_2/a = 22.5$ and $R_3/a = 4.5$ where R_1, R_2, R_3 are the semi-axes of the ellipsoids. The double layer thickness ranged from $\kappa R = 1.3$ up to 13, where R is the equivalent radius,

$$R = (R_1 R_2 R_3)^{1/3} \quad (86)$$

The electrical conductivity σ/σ^∞ and the electro-osmotic coefficient β' evaluated along the x direction were found to be within about 15% of the comparable data for spheres calculated for the same porosity. This does not quite agree with the approximate prediction of Tinga et al. [36] for the conductivity at $\zeta = 0$ from a cell model, which differs more significantly from the conductivity for spheres (see Fig. 4). In the dilute limit, Tinga et al. [36] obtained $\tilde{\sigma} = -1.14$ for uncharged aligned $5 \times 5 \times 1$ ellipsoids versus $\tilde{\sigma} = -1.5$ for spheres.

The results for both geometries at maximal solid fraction are recast in terms of the slopes $d(\sigma/\sigma^\infty)/d\zeta'$ of the reduced conductivity and β'/ζ' of the coupling coefficient as functions of κR in Fig. 5, where data for the vertical direction in packings of ellipsoids are also included. Identical trends are observed for the conductivities for both types of grains. The slopes $d(\sigma/\sigma^\infty)/d\zeta'$ for ellipsoids along the x and z directions are smaller and larger, respectively, than for spheres. For the thinner double layers ($\kappa R \geq 10$), our data for spheres converge with the results obtained by O'Brien and Perrins [13] or Kang and Sangani [37] using matched asymptotic expansions in the limit of vanishing Debye-Hückel length. The electro-osmotic coefficients β'/ζ' for ellipsoids are different along the two directions, since they are related to the corresponding permeabilities, as shown by Fig. 5b. The comparison with the results of matched asymptotic expansions for spheres with

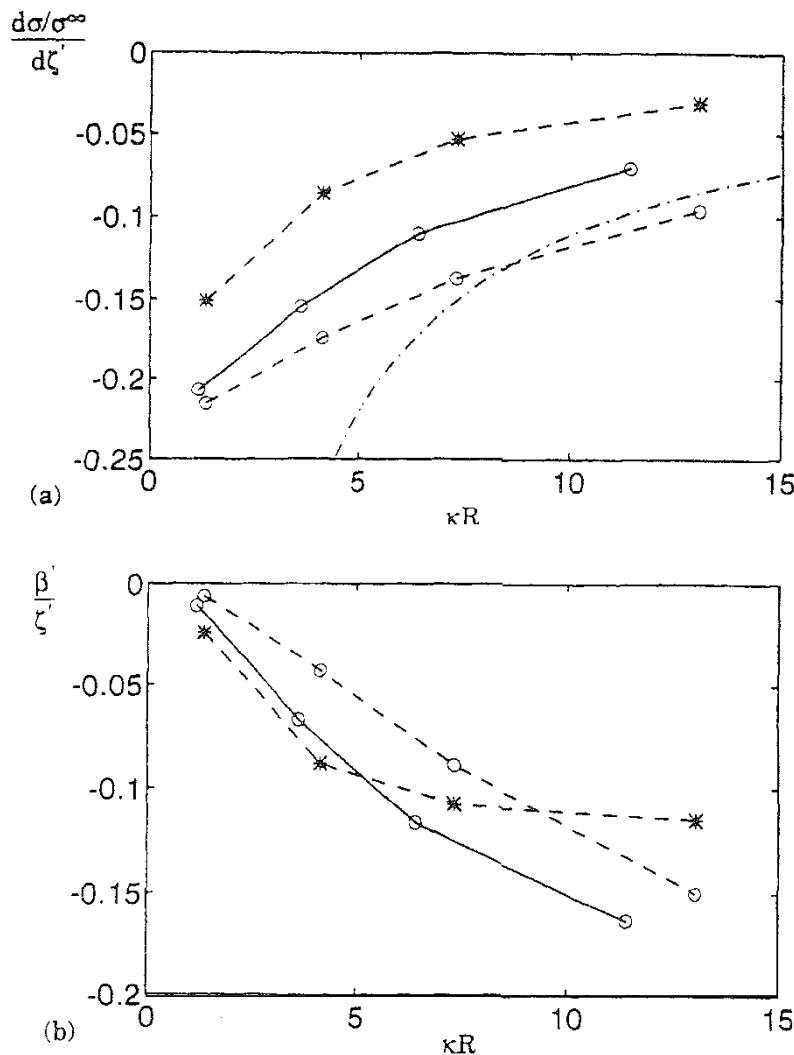


FIG. 5 (a) Derivative of the reduced conductivity $(d\sigma/\sigma^\infty)/d\zeta'$ and (b) coupling coefficient β'/ζ' in a cubic array of contacting spheres (solid lines) or oblate ellipsoids (dashed lines) along the horizontal (\circ) and vertical ($*$) directions as functions of the inverse dimensionless double layer thickness κR . The dash-dotted line in (a) is the result for spheres of a matched asymptotic expansions technique [13,27].

thin double layers [14,37] is bad in this range of κR . Ratios of about 3 and 2 are found for $\kappa R = 5$ and 10, respectively. Thus, the matched asymptotic expansion results converge more rapidly toward the limit $\beta'/\zeta' = -0.345$ than predicted by the numerical resolution of the full system of equations.

Finally, Coelho et al. [9] provided detailed results for orthorhombic arrays of ellipsoids of revolution with an aspect ratio of 5/1 in an attempt to describe the porous geometric structure of clays that are composed of platelike particles.

B. Random Packings of Spheres and Ellipsoids

The random packings were built by simulating the sequential deposition of particles in a parallelepiped cell with periodicity conditions along the two horizontal directions. After a particle is introduced at a random location from above the cell, it settles vertically along the z axis until it touches a grain already in place. Then it rolls and glides until it reaches an equilibrium position, where it sits on at least three supporting points. While reaching its equilibrium position, it undergoes rotations and translations (without bouncing) along the bed surface until it reaches the lowest position. The numerical procedure is described in detail in Ref. 38. An example of such a packing of ellipsoids with an aspect ratio $5 \times 5 \times 1$ is displayed in Fig. 6.

The transport properties of these random beds were investigated along the two horizontal x and y directions. The packings obtained in the above procedure are statistically isotropic in a horizontal plane. Accordingly, the results obtained for the two directions differed by at most 1%. In contrast with this, differences (up to 10%) between the values of the two coupling parameters a' and β' were observed stemming from the insufficiently fine discretization. In such cases, the arithmetic averages between these coefficients are presented.

Flat ellipsoids tend to settle with their largest section parallel to the xy plane (see Fig. 6), as in the orthorhombic arrangements of the previous paragraph. The average solid fraction is equal to 0.595 for spheres and 0.596 for ellipsoids. Since the unit cell used for the computations contained numerous particles, in order to be statistically representative, discretizations coarser than those for the previous regular packings were used. The unit cell contained about 30 spheres with $R/a = 4.27$, or 90 ellipsoids with $R_1/a = R_2/a = 6.4$ and $R_3/a = 1.28$. Note that discretizations were performed a posteriori, when the packing had been built in a continuous description.

The conductivity and permeability for uncharged particles are

Spheres:

$$\sigma_0/\sigma^\infty = 0.186, \quad K/R^2 = 2.9 \times 10^{-3} \quad (87a)$$

Ellipsoids:

$$\sigma_0/\sigma^\infty = 0.208, \quad K/R^2 = 2.5 \times 10^{-3} \quad (87b)$$

The above permeabilities roughly constitute the averages of the values obtained along the various directions considered in the orthorhombic packings, while the conductivities are closer to the smallest conduction.

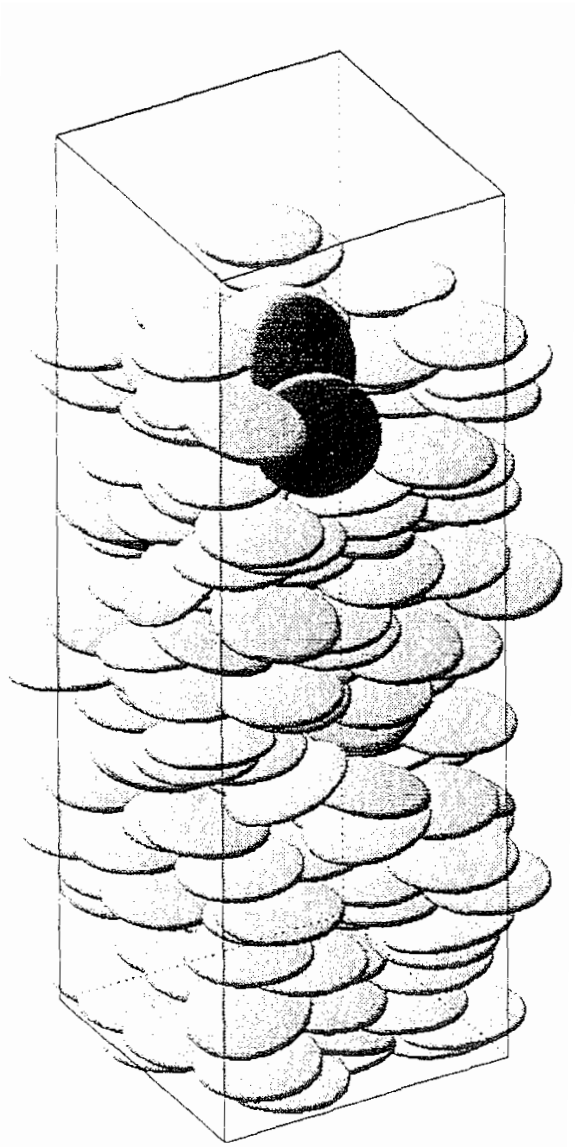


FIG. 6 Example of a bed of 5 x 5 x 1 ellipsoids obtained by sequential deposition.

The dimensionless conductivity σ/σ^∞ and coupling coefficients depend linearly on ζ' similarly to the comparable dependence of the ordered arrays (cf. Ref. 9). For $\kappa R = 2.46$, the initial slopes for the conductivity,

$$\frac{d\sigma/\sigma^\infty}{d\zeta'} = -0.88 \quad (\text{spheres}) \quad \text{or} \quad \frac{d, a/\sigma^\infty}{d\zeta'} = -0.12 \quad (\text{ellipsoids}) \quad (88a)$$

are somewhat smaller than for the orthorhombic arrays due to a larger overlap of the double layers. The ratios $\beta'/\zeta'K'$ are within the range

$$\frac{\beta'}{\zeta'K'} = -0.790 \quad (\text{spheres}) \quad \text{or} \quad \frac{\beta'}{K'} = -0.860 \quad (\text{ellipsoids}) \quad (88b)$$

The influence of the double layer thickness in these random packings was also investigated by Coelho et al. [9] and follows the same trends as those calculated for orthorhombic packings.

C. Reconstructed Porous Media

Finally, electro-osmotic transport coefficients for reconstructed porous media, based on Fontainebleau sandstones, were calculated. Since these materials contain only quartz mineral, no physicochemical interaction occurs during percolation of water. Therefore, the permeabilities measured in water and in air are almost identical. The Fontainebleau sandstones have only open (interstitial) porosity (no pore space inside the grains). These media are generated randomly, according to statistical geometrical characteristics measured on real materials. The reconstruction procedure has been described elsewhere [26,34], and only the main lines are given here. First, measurements were performed on a thin section of a given porous medium. A phase function $Z(\mathbf{x})$ is introduced:

$$Z(\mathbf{x}) = \begin{cases} 1 & \text{if } \mathbf{x} \text{ belongs to the pore space} \\ 0 & \text{otherwise} \end{cases} \quad (89)$$

where \mathbf{x} denotes the spatial position with respect to an arbitrary origin.

The porosity ε and the correlation function $R_z(\mathbf{u})$ can be defined by the statistical averages (denoted below by an overbar)

$$\varepsilon = \overline{Z(\mathbf{x})} \quad (90a)$$

$$R_z(\mathbf{u}) = \overline{[Z(\mathbf{x}) - \varepsilon][Z(\mathbf{x} + \mathbf{u}) - \varepsilon]} / \overline{[Z(\mathbf{x}) - \varepsilon]^2} \quad (90b)$$

or equivalently, because $Z^2(\mathbf{x}) = Z(\mathbf{x})$,

$$R_z(\mathbf{u}) = \overline{[Z(\mathbf{x}) - \varepsilon] \cdot [Z(\mathbf{x} + \mathbf{u}) - \varepsilon]} / [\varepsilon - \varepsilon^2] \quad (90c)$$

On a given sample, these measurements were performed using image analysis [26,34] in a single arbitrarily chosen plane, since the considered materials were isotropic. Hence, \mathbf{u} can be replaced by its absolute value u .

The process of reconstruction of a three-dimensional homogeneous and isotropic random medium of a given porosity ε and a given correlation function $R_z(u)$ is equivalent to generating a random discrete function $Z(\mathbf{x})$ that satisfies the properties specified in Eqs. (90). It can be shown that such $Z(\mathbf{x})$ can be devised from a Gaussian field $X(\mathbf{x})$ when the latter is passed successively through a linear and a nonlinear filter.

For the present investigation, porous media have been reconstructed using the data measured on two samples of Fontainebleau sandstones with porosities $\varepsilon = 0.21$ and $\varepsilon = 0.31$, respectively. Geometries of the reconstructed samples were discretized using N_c^3 solid or fluid elementary cubes of size a using $N_c = 12$ and $L/a = 1.58$ for $\varepsilon = 0.21$ or $L/a = 1.89$ for $\varepsilon = 0.31$. The length scale L is the correlation length deduced from the correlation function by

$$L = \int_0^\infty R_z(u) du \quad (91)$$

An example of a reconstructed sample with $\varepsilon = 0.31$ is displayed in Fig. 7.

The correlation length scale L as measured by image analysis was about $20 \mu\text{m}$, which exceeds the Debye layer thickness by at least two orders of magnitude. Nevertheless, we performed calculations with the dimensionless parameter

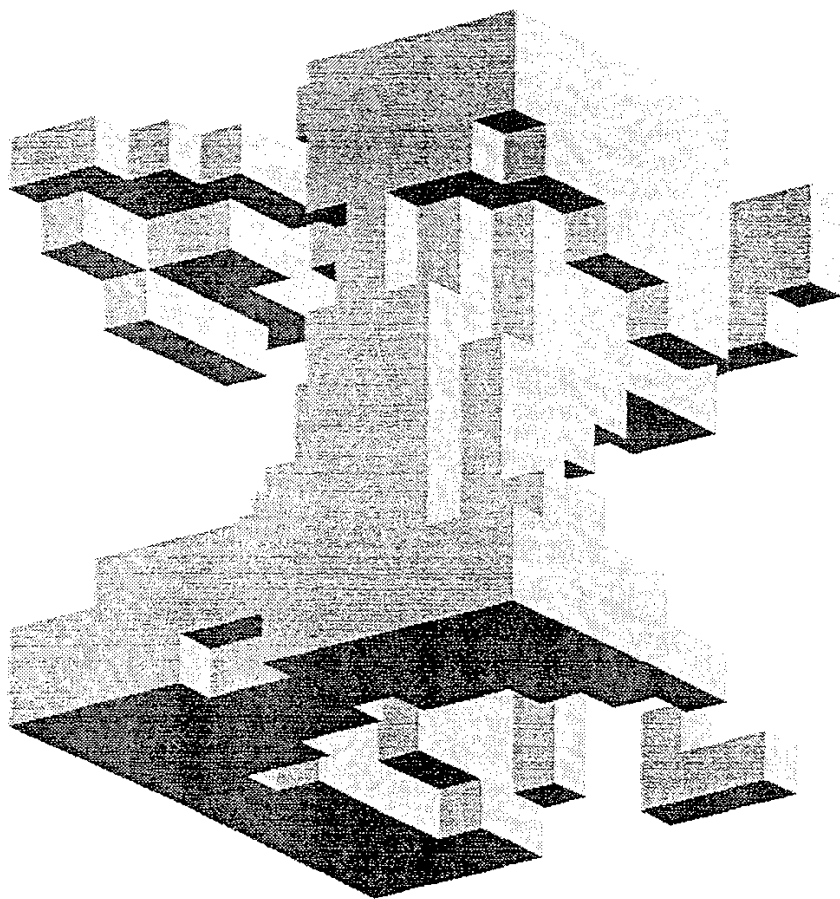


FIG. 7 Example of a reconstructed sample with $\varepsilon \approx 0.31$.

$\kappa L = 1/\sqrt{10}$, 1, and $\sqrt{10}$. This corresponds to the situation where the geometry of the reconstructed samples was scaled down about 100 times.

For the computations, the elementary cubes were subdivided into n^3 mesh cubes with $n = 1, 2$, or 4. We started with the coarsest grid, $n = 1$, and passed to finer subdivisions until the results were reproduced within about 5%. For $\kappa L \leq 1$, it was generally sufficient to take $n = 2$. For the smallest double layers ($\kappa L = \sqrt{10}$) or for the sample $\varepsilon = 0.21$, whose primary transport coefficients are the smallest, $n = 4$ was necessary. Even under these conditions, the results could be reproduced only to within about 10% in a few cases, corresponding to the least conducting directions. As a general rule, our data are believed to be accurate to within a few percent multiplied by $(\kappa L)^2$.

The properties of two reconstructed samples for each sandstone were measured along the three directions x , y , and z . One of the samples for $\varepsilon = 0.31$ did not percolate along the x axis. The results are presented in [Table 1](#), including the derivatives of σ measured between $\zeta' = 0$ and $\zeta' = -1/2$; the conductivity was indeed checked to be a linear function of ζ' in the range $\zeta' = 0$ to $\zeta' = -1$. The primary coefficients σ_0/σ^∞ and A'' are very scattered, and each individual sample is strongly anisotropic. However, when normalized by the medium effective conductivity along the same direction σ^0 , a significantly lower scatter is observed. In particular, for thick double layers, a remarkably constant value is obtained:

TABLE 1 Length Scale Λ for the Various Models

| Model" | Direction | Λ |
|------------------|-----------|---------------|
| SC, spheres | x, y, z | $0.754R$ |
| SC, ellipsoids | x, y | $0.372R$ |
| 0-1. spheres | x | $0.837R$ |
| | y | $0.723R$ |
| | z | $0.329R$ |
| 0-1, ellipsoids | x | $0.236R$ |
| | y | $0.235R$ |
| O-II, ellipsoids | x | $0.196R$ |
| | y | $0.466R$ |
| RP, spheres | x, y | $0.414R$ |
| RP, ellipsoids | x, y | $0.328R$ |
| RM. CJ | x, y, z | $0.51-0.706L$ |
| RM, 2A3 | x, y, z | $0.47-0.88L$ |
| Plane channel | | $\sqrt{8/3}h$ |
| Circular channel | | R |

^aSC = simple cubic; 0-1, O-II = orthorhombic types I and II; RP = random packings; RM = reconstructed media.

$$\frac{d}{d\zeta'} \left(\frac{\sigma}{\sigma^0} \right) = -0.67 \pm 0.005, \quad \kappa L = 1/\sqrt{10} \quad (92a)$$

The data for $\kappa L = 1$ are slightly more scattered:

$$\frac{d}{d\zeta'} \left(\frac{\sigma}{\sigma^0} \right) = -0.62 \pm 0.044, \quad \kappa L = 1 \quad (92b)$$

For thin double layers ($\kappa L = \sqrt{10}$), the data are still more scattered. Three values are far below the others and correspond to the least accurate computations. When these are excluded, one obtains

$$\frac{d}{d\zeta'} \left(\frac{\sigma}{\sigma^0} \right) = -0.42 \pm 0.12, \quad \kappa L = \sqrt{10} \quad (92c)$$

It is interesting to note that the variations in the relative conductivity for the reconstructed media are comparable to those in the granular media. For all the arrangements of spherical or ellipsoidal grains considered above, including random packings, we obtained for $\kappa R = 2.46$

$$-0.671 \leq \frac{d}{d\zeta'} \left(\frac{\sigma}{\sigma^0} \right) \leq -0.585, \quad \kappa R = 2.46 \quad (92d)$$

These numerical results agree with the theoretical value of $(d/d\zeta')(\sigma/\sigma^0)$ obtained for a constant ζ potential applied over all the pore space.

$$\lim_{\kappa L \rightarrow \infty} \left[\frac{d}{d\zeta'} \left(\frac{\sigma}{\sigma^0} \right) \right] = \frac{D'_1 - D'_2}{D'_1 + D'_2} = -0.6772 \quad (93)$$

The data for the coupling coefficient β are also easier to analyze in comparison with the corresponding permeabilities. Again, the ratio β'/ζ' tends to -1 for thick double layers. These results are discussed in the next section.

Since most sandstones have a relatively coarse microstructure with typical pore sizes of about $10\mu\text{m}$, the experimental data in the literature concerning electrokinetic effects in sandstones are beyond the range of double layer thicknesses investigated in these numerical computations. Jouniaux and coworkers [22,39,40] measured streaming potentials in various samples of Fontainebleau sandstones saturated with NaCl brines. From their values for the brine resistivity, κ^{-1} is likely to range from 10 nm to 30 nm. This corresponds to $\kappa L \geq 10^3$. Accordingly, the streaming potential obeys Eq. (3), and the ratio $\beta'/\zeta'K'$ is very small (<0.01). They also report the value of the surface potential $\zeta' \cong -0.88$. Similar results were obtained by Li et al. [41], who analyzed sandstones, limestones, and beds of fused glass beads, since the brine was more concentrated (0.1 M NaCl), which yields $\kappa \cong 1\text{ nm}$.

D. Discussion

A new important result of these computations is the relation between the coupling coefficients and the permeability for thick double layers [cf. Eq. (88b)]. The case of relatively thick double layers (fine porous media) was largely overlooked in the literature. Attention was generally focused on the opposite limit of vanishing Debye length, where the matching technique of inner and outer developments was extensively used (see Sec. I), which yielded the general relation (3) of Overbeek [12].

The analytical treatment for thick double layers is a formidable task because of the layers' overlap, which requires full resolution of the governing equations. However, for plane and circular channels, one can use formulas (66) and (78) to obtain

$$\frac{\beta'}{\zeta'K'} = \frac{3}{\kappa^2 h^2} \left(\frac{\tanh(\kappa h)}{\kappa h} - 1 \right) \quad \text{for a plane channel} \quad (94a)$$

$$\frac{\beta'}{\zeta'K'} = \frac{8}{\kappa^2 R^2} \left(\frac{2I_1(\kappa R)}{\kappa R I_0(\kappa R)} - 1 \right) \quad \text{for a circular channel} \quad (94b)$$

The thick double layer limits can be easily deduced:

$$\frac{\mu}{\varepsilon} \left(\frac{\beta}{\zeta} \right) \rightarrow -\kappa^2 K \quad \text{or} \quad \frac{\beta'}{\zeta'} \rightarrow -K', \quad \kappa \rightarrow 0 \quad (95)$$

This result can be generalized to any porous medium. It is more convenient to consider a macroscopic pressure gradient VP applied to the porous medium, thus aiming to obtain the comparable limit of the coupling coefficient a instead of the equivalent coefficient β . Suppose that VP induces a flow with velocity \mathbf{u} . The convected electric current is

$$\mathbf{I} = -\alpha \cdot \nabla P = \frac{1}{\tau} \int \rho \mathbf{u} dv \quad (96)$$

Using the same hypotheses and approximations as before, namely that the equilibrium ion concentrations n_i^0 are slightly distorted by the flow, that the electrolyte is symmetric, and that the surface potential is small enough to linearize the Poisson–Boltzmann equation, Eq. (96) can be recast into

$$\alpha \cdot \nabla P = \epsilon \kappa^2 \frac{1}{\tau} \int \Psi^0 \mathbf{u} dv \quad (97a)$$

Moreover, for thick double layers, with κ^{-1} larger than the characteristic pore size, Ψ^0 is nearly uniform and approximately equal to the surface potential ζ' . Therefore, replacing Ψ^0 by ζ and using the definition of permeability, one gets

$$\alpha \cdot \nabla P \approx \zeta \epsilon \kappa^2 \frac{1}{\tau} \int \mathbf{u} dv = \frac{\zeta \epsilon \kappa^2}{\mu} \left(\frac{\mu}{\tau} \right) \int \mathbf{u} dv = -\frac{\zeta \epsilon \kappa^2}{\mu} \mathbf{K} \cdot \nabla P, \quad \kappa L \ll 1 \quad (97b)$$

Since ∇P is arbitrary, one obtains

$$\alpha \rightarrow -\frac{\zeta \epsilon \kappa^2}{\mu} \mathbf{K} \quad \text{or} \quad \frac{1}{\zeta'} \alpha' \rightarrow -\mathbf{K}', \quad \kappa L \rightarrow 0 \quad (98)$$

Note, however, that the convergence in Eq. (98) is not necessarily uniform along different directions, as illustrated below.

The limit (95) has already been pointed out in several cases in the previous section. Since in most practical situations the Debye length is unlikely to exceed widely the typical pore size, it is essential to study the rate of convergence of the coupling coefficients toward the limit (95) to determine how far off this limit is from the actual value in an intermediate range, and possibly to introduce a correction factor. To this end, all the results of the previous section for all the investigated directions in all the geometric models were gathered.

In order to plot ratios $\beta'/\zeta'k'$ against a normalized double layer thickness, a length scale applicable to all the directions and geometries has to be defined. As already pointed out above and also shown by Eq. (97), the criterion for convergence toward (98) corresponds to the covering of the pore space by the electrical double layer rather than its thickness relative to a typical grain size. Thus, an adequate length scale should be a measure of the characteristic pore size. Such a length scale Λ was introduced in Ref 42. It is essentially a pore volume to pore surface ratio, with a measure weighted by the local value of the electric field $\mathbf{E}(\mathbf{r})$ in the conduction process:

$$\Lambda = 2 \frac{\int_{\tau} \mathbf{E}^2(\mathbf{r}) dv}{\int_s \mathbf{E}^2(\mathbf{r}) ds} \quad (99)$$

This length scale Λ is derived from the correction to σ due to the interfacial conductivity in thin layers.

An electrokinetic method [23] was proposed to measure Λ , as an alternative way to determine the permeability via

$$K = \frac{\sigma^0}{\sigma^\infty} \left(\frac{\Lambda^2}{8} \right) \quad (100)$$

This relation was shown [23,43] to provide excellent predictions for various models or real porous media. Note that for a plane channel, Eqs. (99) and (100) yield slightly different results, namely, $A = 2h$ and $A = \sqrt{2/3}(2h)$, respectively. For a circular channel, both expressions give $A \approx R$. For all the media considered here, A was evaluated by solving the Laplace equation in the pore space of the unit cell with insulating boundary conditions. For the ordered and random packings, A ranges from $A = 0.20R$ up to $A = 0.84R$ (Table 2). Our data are compared to Eq. (100) in Fig. 8. Note that the points that are significantly above the dotted line correspond to the orthorhombic and simple cubic packings of ellipsoids.

All the electro-osmotic data from our simulations are thus gathered in Fig. 9 and compared with the theoretical results, Eq. (94), for channels. For all anisotropic configurations, A was evaluated along each direction. All the data cluster around a single curve, with very little dispersion considering the variety of geometric configurations. As expected $\beta'/\zeta'K'$ tends to -1 for vanishing $\kappa\Lambda$. For intermediate Debye thicknesses, $\beta'/\zeta'K'$ is very well approximated by Eq. (94b) valid for a circular channel.

It is tempting to modify Eq. (99) to obtain an even better agreement with the numerical data. A least squares fit yields a modified expression for A ,

$$\Lambda = 1.544 \frac{\int_{\tau} \mathbf{E}^2(\mathbf{r}) dv}{\int_s \mathbf{E}^2(\mathbf{r}) ds} \quad (101)$$

The prediction with Eq. (94b) with R replaced by A in Eq. (101) is also plotted in Fig. 9. For an easier evaluation, expression (94a) for a plane channel could be substituted into (94b).

Alternatively, β can be deduced from the primary coefficients σ^0 and K measured along the same direction:

$$\beta = \frac{8\varepsilon\zeta K}{\mu\Lambda'^2} \left(\frac{2I_1(\kappa\Lambda')}{\kappa\Lambda'I_0(\kappa\Lambda')} - 1 \right) \quad (102)$$

$$\Lambda' = \left(\frac{12.5 K \sigma^\infty}{\sigma^0} \right)^{1/2} \quad (103)$$

The constant in (103) results from a least squares fit of our data (Fig. 10). Note that Eq. (102) can be recast into

$$\beta = \frac{\varepsilon\zeta}{\mu} \left(\frac{\sigma^0}{\sigma^\infty} \right) \left(\frac{2I_1(\kappa\Lambda)}{\kappa\Lambda I_0(\kappa\Lambda)} - 1 \right) \quad (104)$$

which underestimates Overbeek's [12] formula (3) for large $\kappa\Lambda$ by a factor of 0.64.

Finally, this model was compared with some experimental data for a porous material when the double layer thickness is comparable to the typical pore size [17,44–46]. Coupled charge and mass transport were measured in a plug of

ABLE 2 Macroscopic Properties for Reconstructed Samples of Fontainebleau Sandstones^a

| Direction | Porosity σ^0/σ^∞ | 10^3 K/L^2 | Λ/L | $-10^3(d/d\zeta')(\sigma/\sigma^\infty)$ | | $-(d/d\zeta')(\sigma/\sigma^0)$ | | $10^3\beta'/\zeta'$ | | $\beta'/\zeta'K'$ | | | | | |
|-----------|--------------------------------------|-------------------|-------------|--|----------------------------------|---------------------------------|----------------------------------|---------------------|----------------------------------|-------------------|----------------------------------|---------|--------|--------|--------|
| | | | | $\kappa L = 1$ | $\kappa L = \frac{1}{\sqrt{10}}$ | $\kappa L = 1$ | $\kappa L = \frac{1}{\sqrt{10}}$ | $\kappa L = 1$ | $\kappa L = \frac{1}{\sqrt{10}}$ | $\kappa L = 1$ | $\kappa L = \frac{1}{\sqrt{10}}$ | | | | |
| 0.208 | | | | | | | | | | | | | | | |
| x | 15.0 | 0.33 | 0.508 | 8.23 | 9.99 | 10.2 | 0.547 | 0.664 | 0.676 | -2.24 | -0.309 | -0.324 | -0.679 | -0.936 | -0.982 |
| y | 37.4 | 1.13 | 0.585 | 18.9 | 24.5 | 25.2 | 0.506 | 0.656 | 0.675 | -7.01 | -1.047 | -0.111 | -0.620 | -0.927 | -0.982 |
| z | 19.1 | 0.509 | 0.585 | 9.87 | 12.6 | 12.9 | 0.517 | 0.658 | 0.675 | -3.1 | -0.464 | -0.0496 | -0.609 | -0.911 | -0.974 |
| 0.206 | | | | | | | | | | | | | | | |
| x | 68.5 | 4.09 | 0.706 | 29.0 | 43.2 | 46.1 | 0.422 | 0.630 | 0.672 | -18.2 | -3.5 | -0.392 | -0.445 | -0.856 | -0.958 |
| y | 28.8 | 1.49 | 0.664 | 12.7 | 18.3 | 19.3 | 0.443 | 0.636 | 0.673 | -7.1 | -1.29 | -0.142 | -0.477 | -0.866 | -0.953 |
| z | 33.6 | 0.877 | 0.524 | 18.3 | 22.3 | 22.7 | 0.543 | 0.662 | 0.676 | -5.1 | -0.789 | -0.0834 | -0.582 | -0.900 | -0.951 |
| 0.313 | | | | | | | | | | | | | | | |
| x | 0 | 0 | --- | --- | --- | --- | --- | --- | --- | --- | --- | --- | --- | --- | --- |
| y | 58.1 | 1.88 | 0.472 | 28.5 | 37.8 | 39.2 | 0.490 | 0.651 | 0.674 | -10.5 | -1.66 | -0.172 | 0.559 | -0.883 | -0.915 |
| z | 115 | 6.4 | 0.632 | 45.8 | 71.4 | 77.0 | 0.400 | 0.622 | 0.671 | -27.7 | -5.46 | -0.614 | -0.433 | -0.853 | -0.959 |
| 0.314 | | | | | | | | | | | | | | | |
| x | 78.6 | 6.41 | 0.731 | 29.0 | 48.3 | 52.7 | 0.368 | 0.614 | 0.670 | -25 | -5.38 | -0.619 | -0.390 | -0.838 | -0.966 |
| y | 124 | 14.3 | 0.852 | 40.4 | 73.6 | 83.0 | 0.325 | 0.592 | 0.667 | -46 | -11.42 | -1.37 | -0.322 | -0.798 | -0.958 |
| z | 144 | 21.3 | 0.879 | 43.3 | 82.9 | 95.0 | 0.301 | 0.576 | 0.665 | -59.6 | -16.52 | -2.06 | -0.280 | -0.776 | -0.967 |

^aTwo different porosities were investigated.

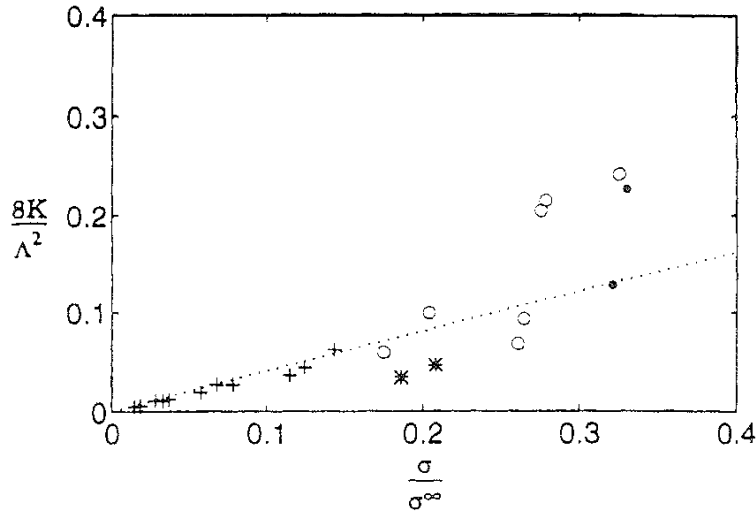


FIG. 8 Conductivity and permeability for regular close simple cubic (●) or orthorhombic (○) packings, random packings (*), and reconstructed sandstones (+). The slope of the least squares fit (dashed line) is 0.41.

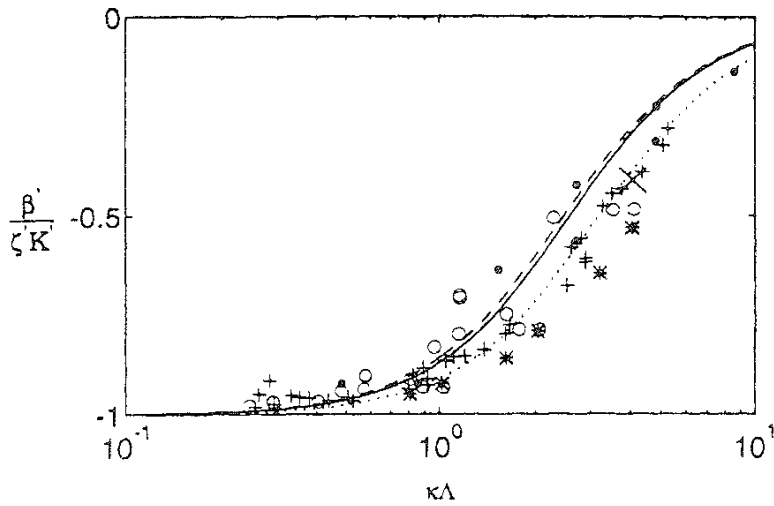


FIG. 9 Reduced coupling coefficients $\alpha'/\zeta K'$ and $\beta'/\zeta K'$ as functions of $\kappa\Lambda$ for all the configurations studied in Sec. VI. Data are for regular packings (●), orthorhombic packings (○) random packings (*), and reconstructed sandstones (+). Theoretical results from Eq. (93a) with $A = \sqrt{8/3}h$ (solid line), Eq. (93b) with $A = R$ (dashed line), and Eq. (100) (dotted line). (+) Experimental results for montmorillonite from Refs. 17 and 44-46.

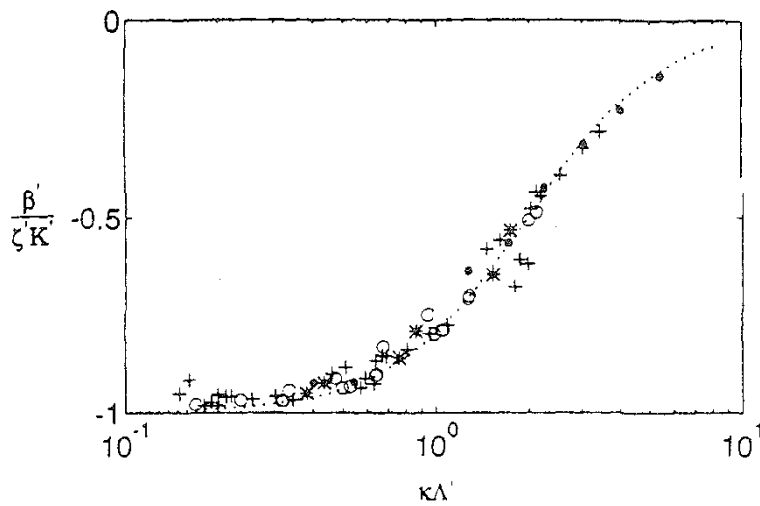


FIG. 10 The reduced coupling coefficients $\alpha'/\zeta'K'$ and $\beta'/\zeta'K'$ as functions of $\kappa\Lambda'$ for all the configurations studied in Sec. VI. Data are for (●) regular packings, (○) orthorhombic packings, (*) random packings, and (+) reconstructed sandstones. The dotted line is the least squares fit. Eqs. (101) and (102).

montmorillonite saturated with NaCl brine. The measurements were interpreted by regarding the pore space between the clay platelets as plane channels. The effective half thickness b of the water layer is also deduced from the measurements. These data were interpreted by Coelho et al. [9] and are displayed in Fig. 9, where they are seen to compare well to the numerical predictions.

VII. FRACTAL AGGREGATES

The transport properties of aggregates are of interest in a number of processes such as sedimentation, filtration, and electrophoresis whenever they are charged and submitted to an external electric field. Industrial applications include the determination of the settling velocity of sludge particle aggregates [47–49].

So far most efforts have been devoted to the determination of the drag force exerted by the surrounding fluid on a translating aggregate. The literature that has been devoted to this topic is already quite impressive and has been recently summarized by Coelho et al. [38]. The purpose of this section is to extend the analysis to electrophoretic mobility, i.e., to isolated particles to which an electric field is applied. As previously stated, the same formalism as for porous media can be applied to suspensions.

A. Cluster Generation

A cluster can be characterized by its gyration radius, which may be defined as

$$R_G^2 = \frac{1}{2N^2} \sum_{n,m=1}^N (\mathbf{r}_n - \mathbf{r}_m)^2 \quad (105)$$

where N is the total number of particles of the cluster, n and m denote the numbers of any two particles, and \mathbf{r}_n is the position vector of a particle. Each elementary particle is cubic of size a .

The fractal dimension D_F may be introduced by the relation

$$N = SR_G^{D_F} \quad (106)$$

where S is the compacity of the cluster.

Many procedures have been proposed in the literature [e.g., 50] for generating clusters with various fractal dimensions. Three of them have been selected for brief discussion here.

A modified Witten–Sander scheme was used to accelerate the convergence to the asymptotic regime [51]. The random particle does not stick to the cluster when it is on a site adjacent to occupied sites. but it is moved until it is on an occupied site; then its final position is assumed to be the previous one. Such a scheme yields a fractal dimension of 2.6, which is slightly larger than the 2.5 obtained with the original Witten–Sander scheme.

The hierarchical model with linear trajectories was applied without any modification [52]; two clusters are assumed to stick together when they occupy adjacent sites. Such a model is much less time-consuming than cluster–cluster aggregation with Brownian trajectories. The resulting fractal dimension is difficult to measure with precision because of the large statistical fluctuations due to the model itself: it was found to be close to 1.9.

The last model is a hierarchical model where the fractal dimension is tuned by selecting the orientation and the sticking point of clusters of size 2^{p-1} [53], where p is the iteration number. Four values of the fractal dimension were studied: 1.6, 1.9, 2.2, and 2.5. Two of these values were chosen close to the values of the Witten–Sander aggregate and to the standard hierarchical model. for reasons that will be clear in the next section.

The numerical results relative to these aggregates are summarized in [Table 3](#).

To compute the transport properties of these aggregates, a spatially periodic pattern of such particles was created. For the sake of convenience, one can say that the center of gravity of each aggregate is located at the center of each unit cell of size $N_c a$; however, because of the periodicity condition, the precise position of the cluster inside the unit cell does not matter. N_c was chosen equal to 32, 48, 64, and 96; usually, $N_c a$ is large with respect to the gyration radius, and the resulting solid concentration ϕ is smaller than 0.02. The structure of the suspension is represented in [Fig. 11a](#).

To determine the hydrodynamic radius R_H of the clusters, one has to solve the Stokes equations that govern the low Reynolds number flow of Newtonian fluids. By taking two opposite limits (namely, the solid concentration goes to zero and the size of the aggregates goes to infinity), it could be shown that the hydrodynamic drag F on an aggregate scale is

$$F = 6\pi\mu R_G(0.3D_F + 0.4)v \quad (107)$$

TABLE 3 Fractal Dimension and Compacity of the Various Types of Clusters

| | WS ^a (modif.) | Hierarch. ^b | Thouy and Jullien | | | |
|-----------------|--------------------------|------------------------|-------------------|------|-------------|------|
| <i>D</i> | 2.64 | 1.90 | 1.6 | 1.9 | 2 . 2 2 . 5 | |
| <i>N</i> = 64 | 4.13 ± 0.22 | 3.80 ± 0.07 | 3.83 | 4.23 | 4.03 | 4.40 |
| <i>A'</i> = 256 | 4.34 ± 0.14 | 3.71 ± 0.12 | 3.82 | 4.19 | 3.96 | 4.26 |
| <i>N</i> = 1024 | 4.48 ± 0.13 | 3.66 ± 0.26 | 3.82 | 4.18 | 3.94 | 4.20 |

^aWS = Witten–Sander model.

^bHierarch. = hierarchical model with linear trajectories.

where v is the translational velocity of the aggregate and R_G its gyration radius. This formula is in agreement with the classical Stokes formula. since for a solid sphere $D_F = 3$ and $R_G = (3/5)^{1/2} R$.

B. Macroscopic Conductivity of Suspensions of Uncharged Aggregates

To have a complete overview of conductivity, it was found useful to determine the macroscopic conductivity σ_0 of a suspension of uncharged aggregates, which requires solving a simple Laplace equation in the spatially periodic geometry described in Sec. II.

An analogous situation was considered in the literature. The Laplace equation was solved between an aggregate at a given potential and infinity with potential zero. This is actually equivalent to determining the growth rate and the distribution of absorbing sites in the cluster during the aggregation process [54]. This was done with random walk methods by Meakin et al. [55] and Halsey et al. [56] and with renormalization methods by Cates and Witten [57]. The incident flux has a scaling structure characterized by an infinite family of independent scaling exponents. The Laplace equation was also solved in two dimensions between two clusters at constant potentials by Evertsz and Mandelbrot [58].

Here, the boundary condition at the surface of the aggregate is a Neumann condition since it is considered perfectly insulating.

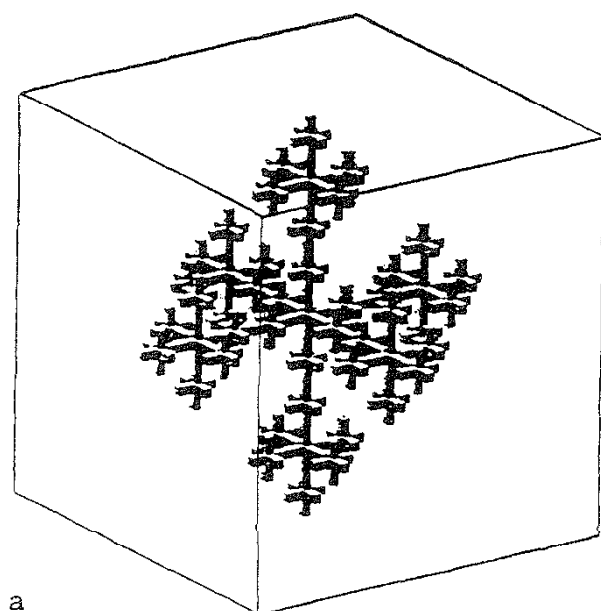
The results are represented by using the coefficient

$$\tilde{\sigma}_0 = 1 - \frac{\sigma_0}{\sigma_\infty} \quad (108)$$

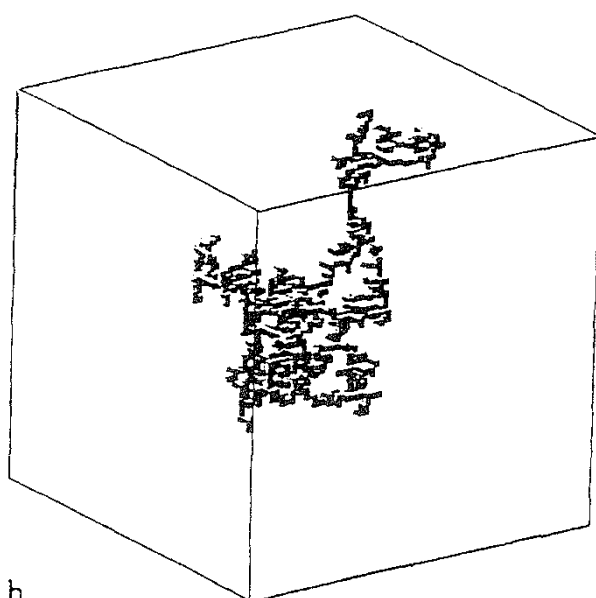
According to Maxwell [59], this coefficient is proportional to the solid concentration; for solid spheres, it is given by

$$\tilde{\sigma}_0 = \frac{3}{2} \Phi \quad (109a)$$

The proportionality is well verified in Fig. 12. Moreover, all the results relative to fractal aggregates are gathered around a single curve, whatever their fractal dimensions and their gyration radius. The equation of this curve is



a



b

FIG. 11 Spatially periodic suspensions of fractal aggregates. The aggregate in (a) contains 1024 cubic particles of size a ; it was built with the hierarchical model with linear trajectories. The deterministic self-similar flake in (b) is at the third-generation stage with $b = 5$.

$$\tilde{\sigma}_0 = 2.4\phi, \quad D_F \neq 3 \quad (109b)$$

These unexpected results are in a sense confirmed by the fact that Eq. (109a) is indeed well verified by the numerical data for solid spheres. Similar calculations were conducted with spheres with a uniform porosity. Their solid fraction ϕ_1 was set to equal to 0.25, 0.50, and 0.75, yielding $\tilde{\sigma}_0/\phi = 2.6$, 2.5, and 2.05, respectively. In this situation, σ_0 can be estimated by replacing the porous spheres with solid homogeneous ones with conductivity $\sigma_1 = \alpha\sigma_\infty$. Their volume fraction in

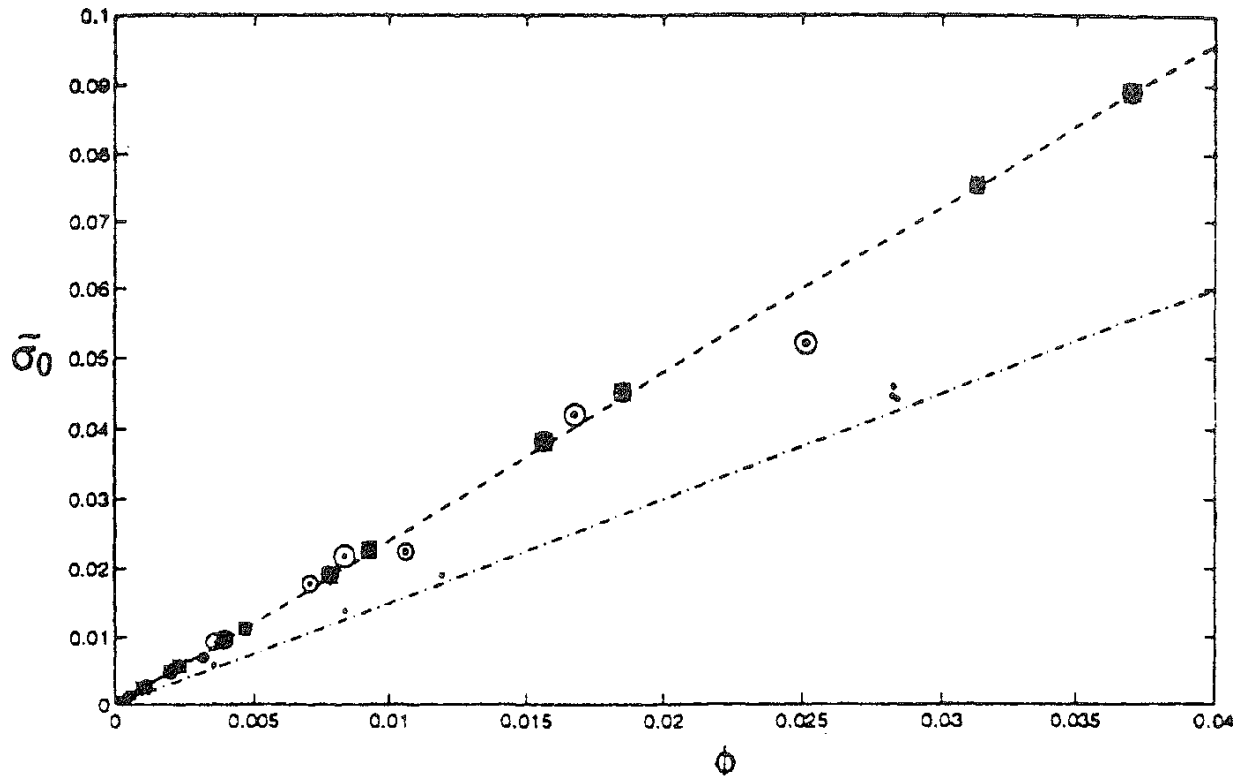


FIG. 12 The coefficient $\tilde{\sigma}_0$ for uncharged aggregates as a function of the solid fraction ϕ . Each point represents an average over 10 realizations. Data are for (*) Witten-Sander (modified: see text), $D = 2.5$; (\oplus) hierarchical with linear trajectories, $D = 1.9$; (•) Thouy and Jullien, $D = 1.6$; (+) Thouy and Jullien, $D = 1.9$; (x) Thouy and Jullien, $D = 2.2$; (*) Thouy and Jullien, $D = 2.5$; (••) spheres, $D = 3.0$; (O) porous spheres, $D = 3.0$; (•••) Sangani and Acrivos [35], $D = 3.0$.

the suspension would be $c = \phi/\phi_1$. The conductivity is then given by the general form of Maxwell's [59] formula for the conductivity of a random dilute suspension of spheres with conductivity $\alpha\sigma_\infty$,

$$\frac{\sigma_0}{\sigma_\infty} = 1 + 3\beta c, \quad \beta = \frac{\alpha - 1}{\alpha + 2} \quad (110)$$

a for random porous solids was determined independently by Thovert et al. [60]. It is equal to 0.55, 0.14, and 0 for $\phi_1 = 0.25$, 0.50, and 0.75, respectively, which yields $\tilde{\sigma}_0/\phi = 2.12$, 2.41, and 2.0. The predictions are in good agreement with the numerical data, except for the looser porous spheres ($\phi_1 = 0.25$); since their internal correlation length is comparable to their radii, such porous spheres cannot be represented by an equivalent effective material; note that the correlation length is defined as usual [61] as the average size of the connected solid clusters.

It may be worth noting, although there is no physical substantiation, that in view of (109b) and (110), all the aggregates considered here behave like porous

spheres with identical solid content and $\phi_1 = 1/2$. They may also be viewed as solid spheres of identical volume and a pseudo relative conductivity $\alpha = -1/3$.

C. Macroscopic Conductivity of Suspensions of Charged Aggregates

Complete systematic computations cannot be achieved here because they are extremely long. Hence, a complete picture cannot be presented as for the hydrodynamic radius.

Let us restrict ourselves in the following to a two-component electrolyte with valences $z_1 = -z_2 = 1$. The conductivity σ_∞ of the solution at equilibrium is [see Eq. (53)]

$$\sigma_\infty = \frac{e^2}{kT} n_\infty (D_+ + D_-) \quad (111)$$

where n_∞ is the electrolyte concentration and D_\pm the diffusion coefficient of the positive and negative ions. When the local potential of the solution is equal to Ψ , the ionic concentrations are derived from the Boltzmann equation as

$$n_\pm = n_\infty (1 \pm \Psi'), \quad \Psi' = \frac{e\Psi}{kT} \quad (112)$$

The fluid conductivity is denoted as

$$\sigma_\Psi = \sigma_\infty \left[1 + \frac{D_- - D_+}{D_- + D_+} \Psi' \right] \quad (113)$$

This relation suggests an adequate representation of the conductivity of a suspension of charged aggregates. The dimensionless coefficient $\hat{\sigma}$ is defined as

$$\sigma = \sigma_0 \left[1 + \hat{\sigma} \frac{D_- - D_+}{D_- + D_+} \zeta' \right] \quad (114)$$

In the two extreme cases of vanishing or infinite double layer thickness, the potential Ψ becomes uniform throughout the fluid, equal to 0 or ζ , respectively. The fluid conductivity, Eq. (113), is then also uniform. Accordingly, the coefficient $\hat{\sigma}$ in Eq. (114) tends to 0 and 1, respectively, in these two limits.

The coefficient $\hat{\sigma}$ defined by (114) is expected to depend on the four dimensionless quantities ϕ , R_G/a , κa , and D_F . We are interested in the limiting behavior when ϕ and aR_g tend to 0.

Let us restrict the presentation of our numerical results to the only case that could be completely worked out, i.e., $\kappa a = 1$. The first simplifying feature is that the coefficient $\hat{\sigma}$ is found to be proportional to the solid concentration, as can be seen in Fig. 13.

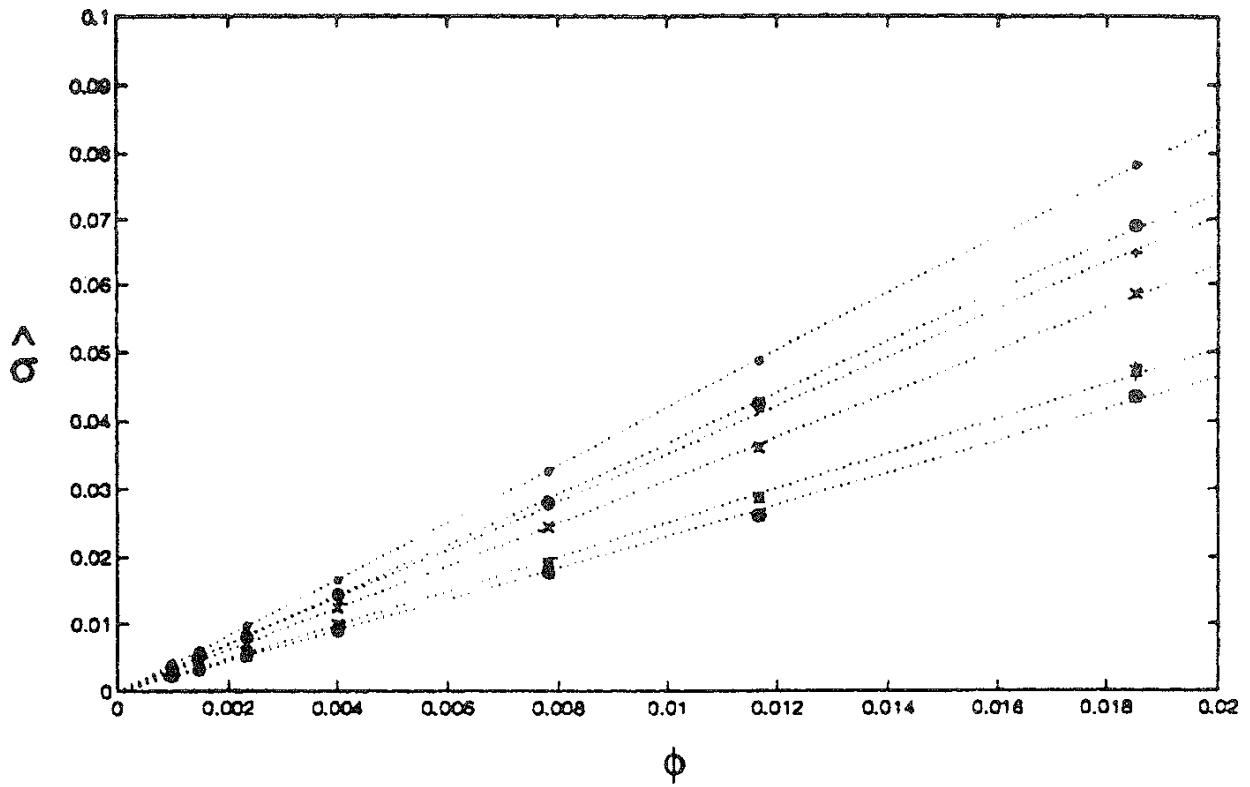


FIG. 13 The coefficient $\hat{\sigma}$ for charged aggregates as a function of the solid fraction ϕ . Same conventions as in Fig. 12. Data are for $\kappa a = 1, N = 256$.

Then, for a fixed value $\phi = 2.315 \times 10^{-3}$, $R_G \hat{\sigma} / \phi$ is represented as a function of the gyration radius. For all the aggregates, the data are very well fitted by a relation of the form

$$\hat{\sigma} = (a'(D_F)R_G + b'(D_F)]\phi/R_G \quad (115)$$

with a correlation coefficient $r \geq 0.99$.

As R_G tends to infinity, b' becomes negligible in (115) and $\hat{\sigma}/\phi$ tends to a constant value for each type of aggregate. This could be expected from a dimensional analysis argument. Since R_G/a is the only dimensionless group in the problem involving a length scale, with the exception of κa , which is kept constant here, its influence can vanish only when it tends to infinity.

Finally, a linear fit of the coefficient a' in (115) for the various types of aggregates yields

$$\hat{\sigma}/\phi = 7.86 - 2.43D_F, \quad Re, \rightarrow \infty \quad (116)$$

with a correlation coefficient $r = 0.991$. The decrease of $\hat{\sigma}/\phi$ with D could also be expected on a physical basis. From its definition in Eq. (114), $\hat{\sigma}$ is a measure of the fraction of the suspending fluid whose conductivity is disturbed by the surface potential of the particles, which is approximately a layer of thickness on the order of κ^{-1} around the solid. For the same solid volume, aggregates with a lower fractal dimension develop a larger surface, and thus the volume of disturbed fluid is larger.

To summarize, for the aggregates considered in this paper and for $\kappa a = 1$, Eqs. (114), (108), (109b), and (116) combine into

$$\frac{\sigma}{\sigma_\infty} = 1 - \left[2.4 - (7.86 - 2.43 D_F) \frac{D_- - D_+}{D_- + D_+} \zeta' \right] \phi + O(\phi^2), \quad \kappa a = 1 \quad (117)$$

Of course, the numerical coefficients in (116) are relative to $\kappa a = 1$, and another double layer thickness would yield different values.

Relation (117) has the same form as the prediction of O'Brien [24] for solid spheres,

$$\frac{\sigma}{\sigma_\infty} = 1 - \left[\frac{3}{2} - 3L'(\kappa a) \frac{D_- - D_+}{D_- + D_+} \zeta' \right] \phi + O(\phi^2) \quad (118)$$

where $L'(1) \approx 2.1$ and L' increases when κa decreases. The asymptotic analysis leading to (116) was not repeated for other values of κG . However, for a moderate aggregate size $N = 128$, $\hat{\sigma}/\phi$ for $\kappa a = 1/2, 1/4$, and $1/8$ was found to be larger than for $\kappa G = 1$ by a ratio of about 2.4, 6, and 17, respectively. The corresponding successive values of $L'(\kappa a)/L'(1) = 2.9, 9.6$, and 34 are of comparable magnitudes.

D. Electrophoretic Mobility

Let us apply to a suspension an electric field \mathbf{E} : it will induce electrophoretic motion of the particles with velocity \mathbf{v}_p . This is used to define the reduced electrophoretic mobility μ_E as

$$\mathbf{v}_p = -\frac{\varepsilon}{\mu} \zeta \mu_E \mathbf{E} \quad (119)$$

When the particle concentration ϕ is sufficiently small, \mathbf{v}_p is equal and opposite to the fluid seepage velocity.

Since computations are very long, the investigations on μ_E were also restricted to $\kappa a = 1$. Furthermore, the extrapolation to infinite cluster sizes was also impaired by this limitation.

The reduced electrokinetic mobility μ_E defined by Eq. (119) is again expected to depend on the set of dimensionless parameters ϕ , R_G/a , κG , and D_F . Its dependence on ϕ can be analyzed with the help of the calculations of Levine and Neale [11,62]. By use of a cell model, these authors generalized Henry's [7] prediction of the mobility of a single spherical particle with radius a to concentrated systems. Their result is cast in the form

$$\mu_E = f(\kappa a, \phi) \quad (120)$$

Although Eq. (120) is not expected to apply directly to suspensions of fractal aggregates, the function f is a natural candidate to describe the dependence of μ_E on the concentration ϕ , with a replaced by some characteristic radius R_μ . Thus the following form was tried:

$$\mu_E = \mu_{E0} \frac{f(\kappa R_\mu, \phi)}{f(\kappa R_\mu, 0)} \quad (121)$$

where μ_{E0} would be the aggregate mobility in the dilute limit.

The analytical expression for f is too cumbersome to allow a determination of R_μ by a least squares fit. Various simplified expressions have been proposed [62], but none is applicable in the present range, since κR_μ is always close to 1.

Therefore, κR_μ was determined for each type of aggregate and for $N = 256$ from the ratio of μ_E for $\phi = 10^{-3}$ and $\phi = 0.0185$:

$$\frac{\mu_E(\phi = 0.0185)}{\mu_E(\phi = 0.001)} = \frac{f(\kappa R_\mu, \phi = 0.0185)}{f(\kappa R_\mu, \phi = 0.001)} \quad (122)$$

It turns out that R_μ is close to a in all cases, even though R_G/a ranges from about 5 to 14. For a constant size $N = 256$, R_μ is even a slightly decreasing function of R_G . This indicates that the particle interaction effects on mobility result mostly from interactions between the elements of the aggregates and that the cluster pair interactions are negligible. The value of R_μ depends on the relative arrangement of the particle within the aggregates. For $N = 256$, R_μ/a can be represented by the linear fit

$$R_\mu/a = 0.32 + 0.335D \quad (123)$$

with a correlation coefficient $r = 0.989$. Unfortunately, no asymptotic analysis in the limit of infinite R_G could be performed; however, since the relevant interactions are short-range within the aggregates, Eq. (123) is probably a good approximation for any large cluster.

It appears also that the variations of f in this range of κa for small ϕ are very close to linear. The adjusted form, Eq. (121), is plotted in Fig. 14 together with the numerical data.

Moreover, it was found that the mobility μ_{E_0} in the dilute limit has very small variations with D_F compared to the error bars of the statistical averages (see Fig. 11). Hence, the electrophoretic mobility of fractal aggregates for $\kappa a = 1$ is given within $\pm 2\%$ by the model (121) with (123) and $\mu_{E_0} \cong 0.55$.

A few additional computations were run with $A' = 128$, $\phi = 3.9 \times 10^{-3}$, and $\kappa a = 1$. The data compare within 1.3% with the predictions of (121), (123), and $\mu_{E_0} \approx 0.55$, which supports the assumption that $A' = 256$ is close to the asymptotic regime. In addition, κa was set to $1/2$, $1/4$, and $1/8$ with $N = 128$ and $\phi = 3.9 \times 10^{-3}$ for the six types of aggregates. The data are compared to the model, Eqs. (121), (123), in Fig. 15. The deviations are significant and systematic. This suggests that a proper analysis should allow the extension of (123) for $\kappa a \neq 1$, with the same general form, Eq. (121).

VIII. CONCLUDING REMARKS

The electrokinetic properties of porous media, suspensions, and isolated particles can be determined within the same theoretical framework, which essentially assumes that the basic governing equations can be linearized. The resulting system can be solved numerically when the double layer thickness is not too small compared to a characteristic dimension of the medium under consideration. Hence, these results are applicable to finely divided media of submicrometric dimensions.

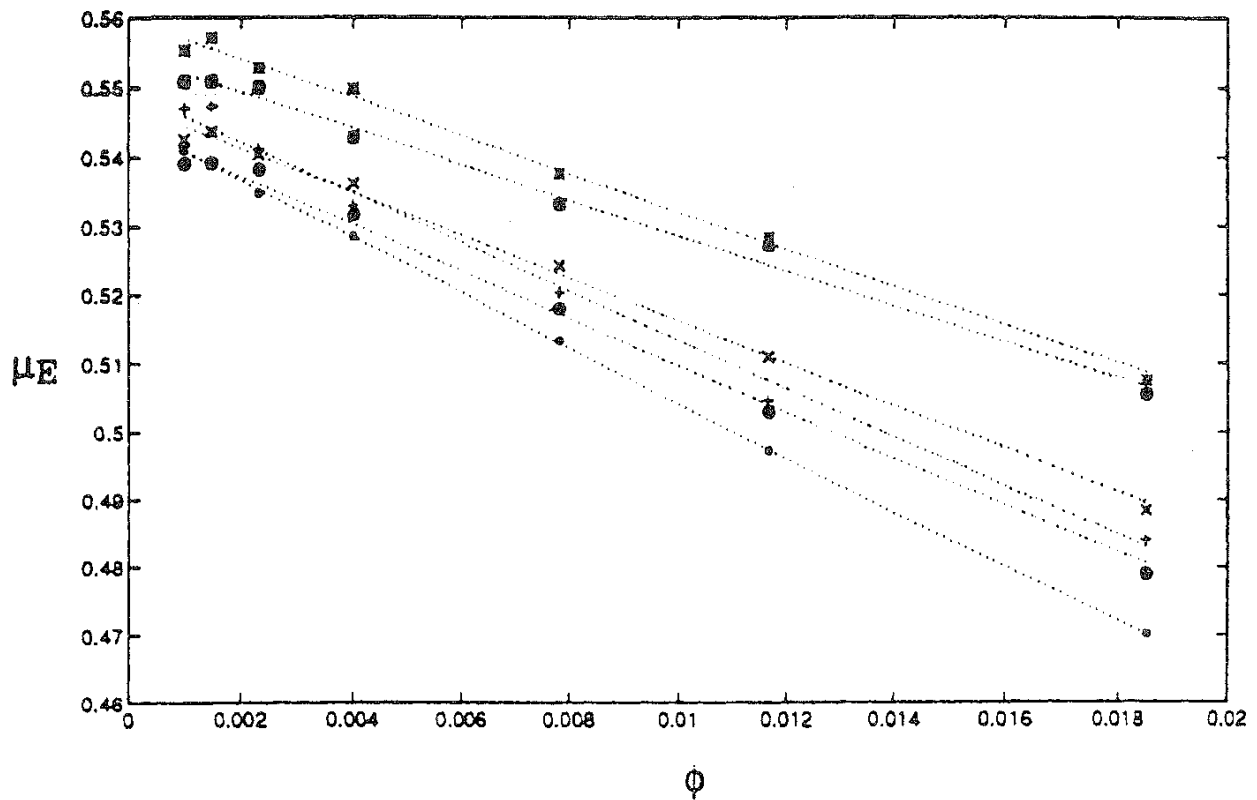


FIG. 14 Mobility μ_E of fractal aggregates as a function of the solid fraction ϕ . Same conventions as in Fig. 12. Data are for $N = 256$, $\kappa a = 1$. The dotted lines are the fit, Eq. (121).

$$\mu_E / \left[\mu_{E0} f(\kappa R_\mu, \phi) / f(\kappa R_\mu, 0) \right]$$

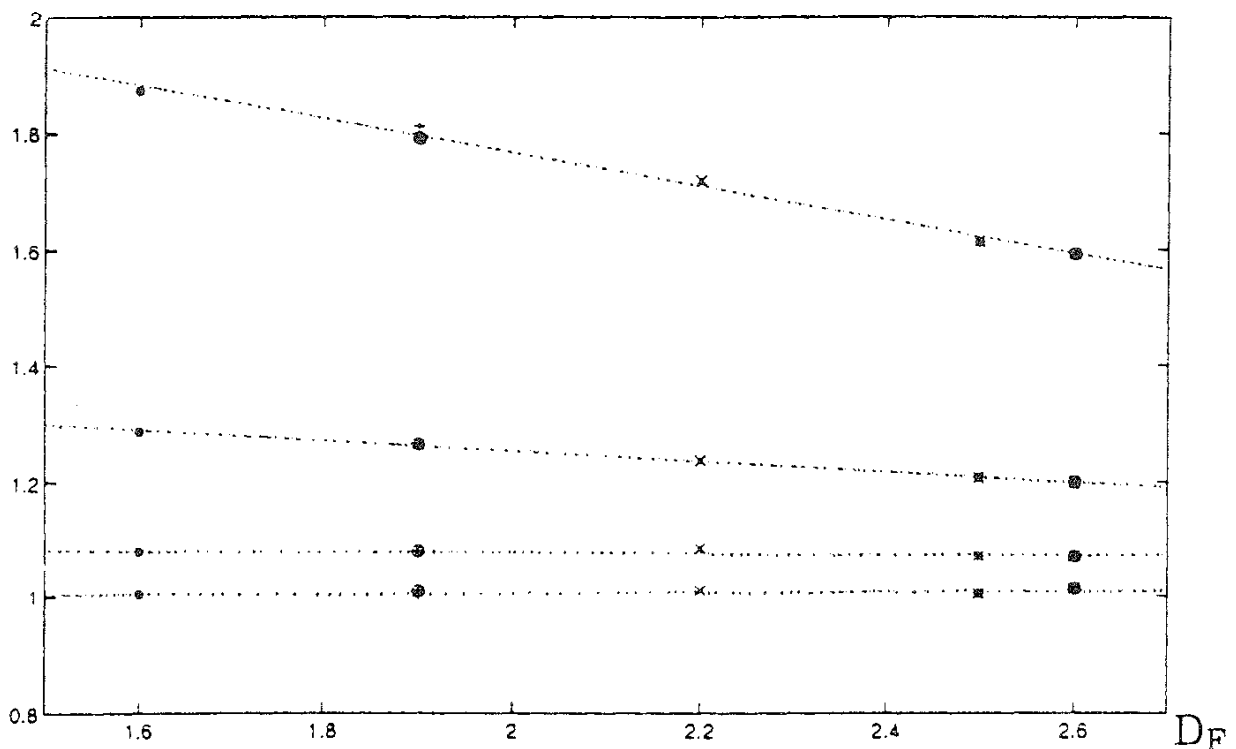


FIG. 15 Mobility μ_E of fractal aggregates divided by the prediction of Eqs. (122) and (123) as a function of the fractal dimension D_F . Data are for $N = 128$ and

This approach can be extended to many situations such as polyelectrolytes and porous particles.

The present set of investigations also needs to be completed with another numerical code able to address the opposite limit where the double layers are thin with respect to a characteristic length of the porous medium.

ACKNOWLEDGMENTS

Most computations were performed at CNUSC. whose support is gratefully acknowledged.

REFERENCES

- V. G. Levich, *Physico-chemical Hydrodynamics*, Prentice-Hall. Englewood Cliffs, NJ, 1962.
2. J. C. Fair and J. F. Osterle, *J. Chem. Phys.* 54:3307 (1971)
3. S. R. de Groot and P. Mazur, *Nan-Equilibrium Thermodynamics*, North-Holland, Amsterdam. 1969.
4. M. Smoluchowski, *Z. Phys. Chem.* 93:129 (1918).
5. E. Hückel, *Phys. Z.* 25:204 (1924).
6. P. Debye, *Polar Molecules*, Reinhold, New York, 1929,
7. D. C. Henry, *Proc. Roy. Soc. Lond. A* 133:106 (1931).
8. F. Booth, *Proc. Roy. Soc. Lond. A* 203:514 (1950).
9. D. Coelho, M. Shapiro, J.-F. Thovet, and P. M. Adler, *J. Colloid Interface Sci.* 181:169–190 (1996).
10. R. W. O'Brien, and D. N. Ward, *J. Colloid Interface Sci.* 121:402 (1988).
11. S. Levine and G. H. Neale, *J. Colloid Interface Sci.* 47:520 (1974).
12. J. T. G. Overbeek, in *Colloid Science* (H. R. Krug, ed.). Vol. 1, Elsevier, Amsterdam, 1952.
13. R. W. O'Brien, and W. T. Perrins, *J. Colloid Interface Sci.* 99:20 (1984).
14. R. W. O'Brien, *J. Colloid Interface Sci.* 110:477 (1986).
15. F. F. Reuss, *Mem. Soc. Imp. Natl. Moscou* 2:3227 (1809).
16. C. F. Fryling, *J. Colloid Interface Sci.* 18:713 (1963).
17. D. E. Elrick, D. E. Smiles, N. Baumgartner, and P. H. Groenevelt, *Soil. Sci. Soc. Am. J.* 40:490 (1976).
18. S. M. Sims, W. I. Higuchi, V. Srinivasan, and K. Peck, *J. Colloid Interface Sci.* 155:210 (1993).
19. A. G. Van der Put and B. H. Bijsterbosh, *J. Colloid Interface Sci.* 92:499 (1983).
20. R. Midmore, and R. W. O'Brien, *J. Colloid Interface Sci.* 123:486 (1988).
21. R. A. Van Wagenen, and I. D. Andrade, *J. Colloid Interface Sci.* 76:305 (1980).
22. L. Jouniaux, Effets électriques et magnétiques liés aux circulations de fluides dans les roches sous contraintes, PhD. Thesis, Paris, 1994.

23. D. B. Pengra, S. Li, S. X. Li. and P. Z. Wong, in *Dynamics in Small Confining Systems II* (J. M. Drake, J. Klafter. R. Kopelman, and S. M. Troian, eds.), Mater. Res. Soc. Symp. Proc. Vol. 366, 1995.
24. R. W. O'Brien, J. Colloid Interface Sci. *81*:234 (1981).
25. W. B. Russel, J. Fluid. Mech. *85*:209 (1978).
26. P. M. Adler. *Porous Media: Geometry and Transport*, Butterworth, Heinemann, Stoneham, MA, 1992.
27. H. Brenner. Phil. Trans. Roy. Soc. Lond. *297*:81–133 (1980).
28. R. W. O'Brien and L. R. White, J. Chem. Soc. Faraday Trans. II *74*:1607 (1978).
29. J. D. Sherwood, J. Fluid Mech. *101*:609 (1980).
30. C. L. Rice and R. Whitehead, J. Phys. Chem. *69*:4017 (1965).
31. R. J. Hunter, *Foundations of Colloid Science*, Vol. 1, Clarendon Press, Oxford, UK, 1987.
32. J. F. Thovert. F. Wary, and P. M. Adler, J. Appl. Phys. *68*(8):3872 (1990).
33. R. Lemaître, and P. M. Adler. Transp. Porous Media *5*:325 (1990).
34. P. M. Adler, C. G. Jacquin, and I. A. Quiblier, Int. J. Multiphase Flow *16*:691 (1990).
35. A. S. Sangani and A. Acrivos, Int. J. Multiphase Flow *8*:343 (1982).
36. W. R. Tinga, W. A. G. Voss, and D. F. Blossey, J. Appl. Phys. *44*:3897 (1973).
37. S.-Y. Kang and A. S. Sangani. J. Colloid Interface Sci. *165*:195 (1994).
38. D. Coelho, J. F. Thovert, and P. M. Adler. Phys. Rev. E *55*:1959 (1997).
39. L. Jouniaux and J. P. Pozzi, J. Geophys. Res. *100*(B6):197 (1995).
40. J. P. Pozzi, and L. Jouniaux, C. R. Acad. Sci. Paris *318*:73 (1994).
41. S. X. Li, D. B. Pengra, and P. Z. Wong, Phys. Rev. E *51*:5748 (1995).
42. D. L. Johnson, J. Koplik. and L. Schwartz, Phys. Rev. Lett. *57*:2564 (1986).
43. N. Martys and E. J. Garboczi. Phys. Rev. B *46*:6080 (1992).
44. P. H. Groenevelt. D. E. Elrick. and T. J. M. Blom, Soil. Sci. Soc. Am. J. *42*:671 (1978).
45. P. H. Groenevelt. D. E. Elrick, and K. B. Laryea, Soil. Sci. Soc. Am. J. *44*:1168 (1980).
46. D. J. A. Williams. and K. P. Williams, J. Colloid Interface Sci. *65*:79 (1978).
47. D. Li, and J. J. Ganczarczyk. Water Environ. Res. *64*:236 (1992).
48. B. E. Logan and D. B. Wilkinson, Biotechnol. Bioeng. *38*:389 (1991).
49. J. Namer and J. J. Ganczarczyk. Water Pollut. Res. J. Can. *29*:441–455 (1994).
50. R. Jullien and R. Botet, *Aggregation and Fractal Aggregates*, World Scientific, Singapore, 1987,
51. T. A. Witten. Jr. and L. M. Sander. Phys. Rev. Lett. *47*:1400 (1981).
52. D. N. Sutherland. Nature *226*:1241 (1970).
53. R. Thouy and R. Jullien, J. Phys. *A27*:2953 (1994).
54. T. A. Witten, Random kinetic aggregation. in *Physics of Finely Divided Matter* (N. Boccara and M. Daoud. eds.), Springer. New York, 1985.
55. P. Meakin. H. E. Stanley, A. Coniglio, and T. A. Witten, Phys. Rev. A *32*:2364–2369 (1985).
56. T. C. Halsey, P. Meakin, and I. Procaccia. Phys. Rev. Lett. *56*:854–857 (1986).
57. M. E. Cates and T. A. Witten, Phys. Rev. Lett. *56*:2497–2500 (1986).
58. C. J. G. Evertsz and B. B. Mandelbrot, Physica A *177*:589–592 (1991).
59. J. C. Maxwell, *Electricity and Magnetism*, Clarendon, Oxford, 1873.

60. J.-F. Thovert, F. Wary, and P. M. Adler, *J. Appl. Phys.* 68:3872–3883 (1990).
61. D. Stauffer and A. Aharony, *Introduction to Percolation Theory*, Taylor and Francis, London, 1991.
62. S. Levine and G. H. Neale, *J. Colloid Interface Sci.* 49:330–332 (1974).

11

Transport Processes in Microemulsions

SATYA P. MOULIK Center for Surface Science, Department of Chemistry,
Jadavpur University, Calcutta, India

BIDYUT K. PAUL Geological Studies Unit, Indian Statistical Institute, Calcutta,
India

| | |
|---|-----|
| I. Introduction | 259 |
| II. Transport Processes | 261 |
| A. Self-diffusion in microemulsions | 261 |
| B. Conductance of microemulsions | 263 |
| C. Transport across microemulsion acting as liquid membrane | 272 |
| References | 275 |

I. INTRODUCTION

Microemulsions are a unique class of microheterogeneous systems in which either water or oil disperses in a microfine state, being surface coated with organized amphiphiles in an otherwise incompatible continuum of either oil or water. Here a liquid that is immiscible with water is considered an oil and the amphiphiles are surfactants present alone or mixed with cosurfactants (normally lower alkanols, amines, etc.) In nonaqueous microemulsions, polar liquids such as glycol, glycerol, formamide, and dimethylformamide replace water. Microemulsions are of two categories: water-in-oil (w/o) and oil-in-water (o/w). They are isotropic, normally of low viscosity, and thermodynamically stable, having particle dimensions falling in the range of 10–200nm. The w/o microemulsions are grossly differentiated from reverse micelles in terms of the content of water in the pool. If the water content exceeds the solvation requirement of the amphiphile head groups, the term "reverse micelle" is replaced by "microemulsion." A pictorial representation of different types of microemulsions is given in Fig. 1.

The formation of a microemulsion is fundamentally controlled by the much lowered oil/water interfacial tension (of the order of 0.001 mN/m or less) by the

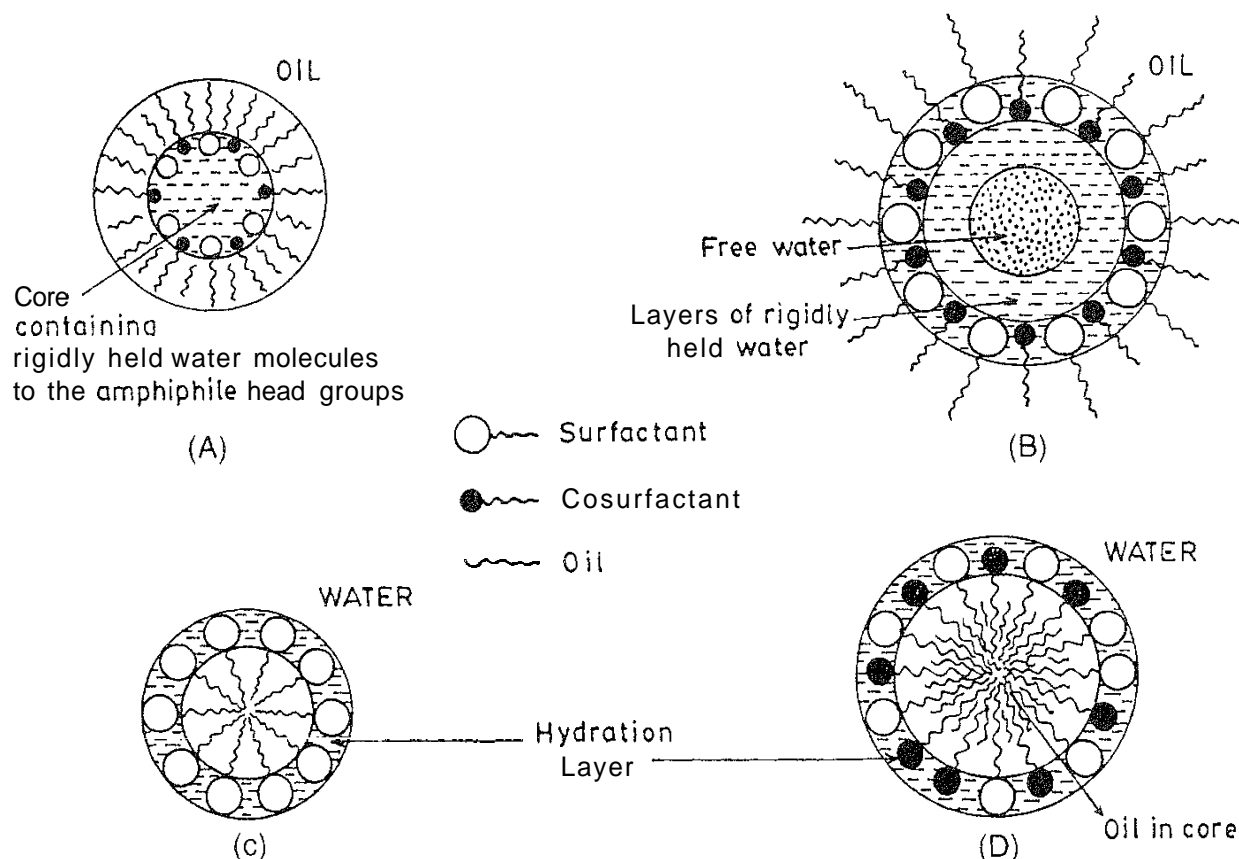


FIG. 1 Pictorial representations of reverse micelles and microemulsions

action of the interfacially adsorbed amphiphiles. The interfacial tension is not lowered to such an extent in emulsions; they are thus “thermodynamically unstable” and exist in much larger dimensions (200–3000 nm). Appreciable work (positive free energy) is required for their formation. The work for microemulsion formulation is insignificant, and they are said to be thermodynamically stable. Much depends on the types of amphiphiles used and their combination. For easy formation, the chemistry of formulation should be right.

The internal structure of microemulsions can be of three different types:

1. Isolated dispersed droplets of water in oil or oil in water.
2. Clusters of droplets of the above types in a continuum.
3. Both w/o and o/w dispersions simultaneously present to form a bicontinuous state in solution

These structures can be located in the phase diagrams essentially constructed to study the composition-dependent phase behaviors of ternary or quaternary systems.

For a general understanding of microemulsions, books and review articles on the subject may be consulted [1–20].

The overall physical state and function of a liquid can be understood by examining transport processes in it. Microemulsions are compartmentalized liquids; transport in them can help to reveal their internal consistency, interparticle interaction, overall particle geometry and stability, etc. In line with the scope of this review, concise descriptions and discussions of investigations related to (1) self-

diffusion of components in microemulsions, (2) transport of ions (conductance) in them, and (3) mass transport across microemulsions employed as liquid membranes are herein presented.

II. TRANSPORT PROCESSES

A. Self-Diffusion in Microemulsions

The components of a microemulsion constantly self-diffuse. The process is intimately related to the internal structural state of the system. The surfactant and cosurfactant molecules diffuse back and forth between the interfacial layer and the bulk, the water and oil molecules self-diffuse in the medium, and the droplets self-diffuse in the continuum. This dynamic process is influenced by the self-association or clustering of the droplets. Self-diffusion studies in microemulsions are therefore of considerable importance.

1. Measurements by NMR Method

The method of NMR based on physical properties of molecular spin provides an elegant way to investigate molecular degrees of freedom [21]. It has been used to determine micellar characteristics such as critical micellar concentration (CMC); aggregation number; counterion association; shape, size, and hydration of aggregates (micelles); structure of micellar solution; and monomer-micelle equilibria. The self-organized system of a microemulsion can be intrinsically understood by determining the self-diffusion coefficients of the constituent species, water, oil, and amphiphile as well as the dispersed droplets. The two or three phase domains of the system can also be understood by this method along with the degree of anisotropy and the presence of long-range discontinuities and continuities. In a microemulsion, the self-diffusion characteristics (manifested as the diffusion constant D) can have the following distinctions:

1. Winsor I (o/w) system: $D_{\text{oil}} \ll D_{\text{water}}$ and $D_{\text{amp}} \sim D_{\text{oil}} \sim D_{\text{droplet}}$
2. Winsor II (w/o) system: $D_{\text{water}} \ll D_{\text{oil}}$ and $D_{\text{amp}} \sim D_{\text{water}} \sim D_{\text{droplet}}$
3. Winsor III (bicontinuous) system: $D_{\text{water}} > D_{\text{amp}}$; $D_{\text{oil}} > D_{\text{amp}}$ (D_{amp} is lower because the amphiphiles exist in large aggregates)

The self-diffusion coefficients of the constituents can thus provide information about their domain-controlled states of aggregation and deaggregation. Typical self-diffusion behavior of the different species in microemulsion is illustrated on an arbitrary scale in Fig. 2,

The self-diffusion process of the constituent species in a microemulsion can speak in favor of their degrees of freedom and hence their residential status in different domains. For highlighting information on the process by the NMR method, the articles of Zana and Lang [21], Nilsson and Lindman [22], Lindman and Wennerström [23], and others [24–27] may be consulted.

For microemulsion systems, the Fourier transform nuclear magnetic resonance (FTNMR) method has been used extensively for self-diffusion studies of the components [28]. The nature of the composition-dependent self-diffusion coefficients of the constituents of the system saline water/SDS/butanol/toluene was determined by

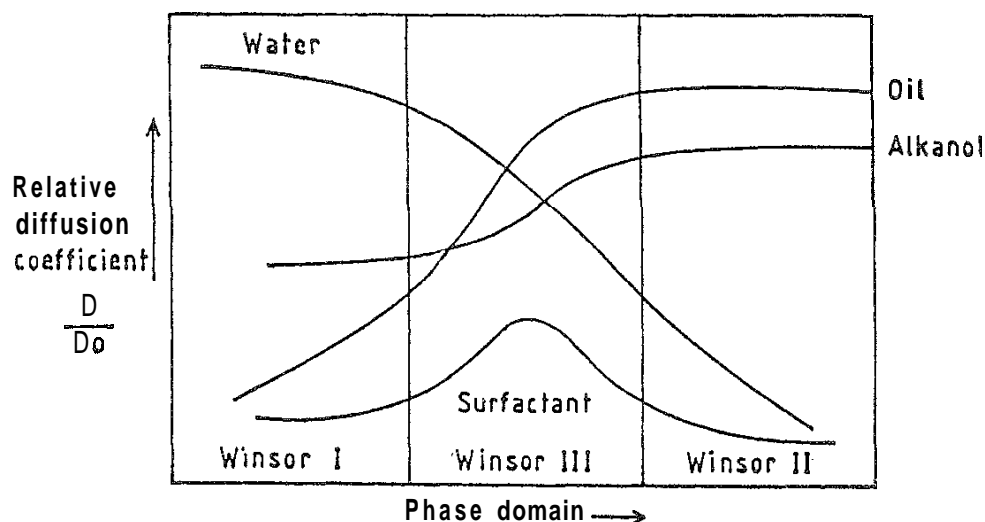


FIG. 2 Self-diffusion characteristics of different species in microemulsion drawn on an arbitrary scale.

Guering and Lindman [29]. The results support Winsor I \rightarrow Winsor III \rightarrow Winsor II transformations with increasing salinity of the system. Martino and Kaler [30] used NMR in the study of the bicontinuous structure of nonaqueous microemulsions where glycol, propylene glycol, and glycerol were used as polar solvents, with pentaethylene glycol mono-*n*-ether and straight-chain alkane as the amphiphile and oil, respectively. Dilute formulations in oil showed the presence of microstructures. The system brine/dodecyltrimethyl ammonium bromide (DTAB)/styrene in concentrated form gave evidence of the presence of spherical aggregates [31]. NMR studies of three different polar solvent/surfactant/oil systems were made by Jonstromer et al. [32]; the surfactants used were AOT, DDAB (didodecyl dimethyl ammonium bromide), and $C_{12}E_4$ (tetraethylene glycol dodecyl ether). In the AOT-derived systems, isolated reverse micelles closely aggregate at lower temperature; the structure changes toward the bicontinuous state at higher temperature. The DDAB- and $C_{12}E_4$ -derived systems did not provide evidence in favor of aggregate formation. The aggregates did not show a dominating diffusion phenomenon. Self-diffusion studies by the NMR technique indicated that the glycerol/SDS/hexanol system is structureless [33,34].

A number of other NMR-probed w/o microemulsions have appeared in recent literature. The diffusion coefficients in water/SDS/pentanol and ammonium hydroxide/SDS/pentanol microemulsions investigated by Olsson et al. [35] established that replacement of water by ammonium hydroxide destabilizes the liquid crystalline phase and reduces the size of the colloidal association structure in the isotropic liquid region. Olsson and Schurtenberger [36] worked on nonionic microemulsions prepared from D_2O , pentaethylene glycol dodecyl ether and decane. Discrete oil-swollen micelles have been evidenced by NMR self-diffusion measurements; the preparations are in conformity with the hard-sphere model. The NMR self-diffusion measurements on a water/octyl glucoside/pentanol/decane microemulsion system advocated a progressive decrease in the mean curvature of the surfactant film with water addition at a constant level of the oil [37]. It was concluded that the

microstructure changes from w/o to o/w via a bicontinuous state. From self-diffusion measurements, Leaver et al. [38] observed that in a water/pentaethylene glycol dodecyl ether/decane system prior to the bicontinuous state, limited growth occurs from spherical to oil-swollen prolate micelles. By NMR measurements Hendrikx et al. [39] explored the local properties of the AOT monolayer for brine/AOT/*n*-alkane systems. A lamellar phase was observed for alkanes with carbon number < 11; for longer chains, depending on salinity, the bicontinuous state appears. There can be chain penetration in the AOT monolayer for lower alkanes: the matter is inconclusive for higher alkanes. Microemulsions have the prospect of use as fire-resistant hydraulic fluids. A model study on water/octaethylene glycol mono-*n*-dodecyl ether/1-pentanol/*n*-dodecane was studied by the ^1H NMR method by Waysbort et al. [40]. An inversion from w/o to o/w type was found to occur with water in the range of 55–60% as corroborated from microviscosity measurements. A composition-dependent distinction between free and aggregated water was established. The Fourier transform pulse gradient spin echo ^1H NMR technique was used by Olsson et al. [41] in a dynamic study of water/pentaethylene glycol dodecyl ether/mixed oil (cyclohexane + hexadecane, 1:1 w/w). Rapid fusion–fission of the microdroplets was observed at low oil content and at low temperature; o/w microemulsion dominates in the system. A slight increase in temperature results in significant growth in the micellar size.

Self-diffusion measurements using the NMR technique have also elucidated the matter of water structure in the pool; up to 10–15 water molecules per $-\text{SO}_3^-$ group (when AOT is the surfactant) were shown to be structurally perturbed [42]. From self-diffusion NMR studies of AOT-induced w/o microemulsions, Maitra proposed several regions of bound water in the water pool domain [43]. The state of water in the pool for cationic surfactant-containing microemulsions (water/dodecyldimethyl ammonium bromide or didodecyldimethyl ammonium bromide/chloroform or cyclohexane) was examined by NMR self-diffusion studies at different $[\text{H}_2\text{O}]/[\text{amphiphile}]$ ratios or ω values. Three types of water molecules—bound, aggregated, and free—in various proportions have been envisaged [44].

The account given above illustrates that the transport phenomenon of self-diffusion is useful for the study of the internal states and dynamics of microheterogeneous microemulsion systems.

B. Conductance of Microemulsions

The ion conductance in a microemulsion depends on its type. In an o/w (Winsor I) microemulsion, the conductance is almost like that of an aqueous medium; in a w/o (Winsor II) microemulsion, it is very low, whereas in the bicontinuous (Winsor III) condition, the conductance can be conspicuously large. Depending on the composition and temperature, a dramatic increase in conductance may occur; this phenomenon is called percolation.

The very low conductance in a dilute w/o microemulsion system has been explained on the basis of migration of statistically charged droplets with charge fluctuation features [45–48]. In the ternary systems of water/ionic surfactants/alkanol, benzyl alcohol, polypropylene glycol, etc., the compositions toward the oil corner in the ternary phase diagram (called the L-phase), show an increase in

conductance with increasing alcohol concentration that passes through a maximum and then decreases. The increase and decrease have been attributed to the ionization of the surfactant by incorporation of alcohol in the micelle and the formation of mixed reverse micelles as well as a change in the shape of the aggregates [49–54]. In this context, the conductance behaviors of perfluoropolyether microemulsions is noteworthy.

The conductance of the water/ammonium salt of perfluoropolyether carboxylic acid/perfluoropolyether system as a function of water content at different oil/surfactant mass ratios has shown a well-shaped maximum in the curve [55]. The initial rise in conductance has been considered to be due to the increased dissociation of counterions from the head groups by their solvation with water. The formation of water droplets (reverse micelles) begins at the conductance maximum, which has been supported by scattering measurements. A working model and quantitative analysis for this distinct system have been attempted.

Unexpected conductance behaviors have been shown by w/o microemulsions obtained from mixed surfactants and mixed cosurfactants [56–62]. The transport property depends on the mixing ratio. This is discussed in [Section II.B.5](#).

1. Percolation of Conductance

Binary inclusions containing conductors and insulators after a threshold volume fraction of the conductors can exhibit a rapid rise in conductance followed by its leveling off. This phenomenon is called static percolation and has been critically studied by a number of researchers [63–69]. In colloidal solution as in w/o microemulsion, droplets can approach their neighbors by diffusion, and after reaching a threshold distance they can transfer charge to augment a sharp rise in conductance; this is called dynamic percolation [70–77]. Such a conductance manifestation can occur after a threshold dispersant concentration at a constant temperature (volume percolation) is reached as well as after a threshold temperature is reached at a constant dispersant concentration (temperature percolation). Conductance percolation can also occur in w/o microemulsions with nonionic surfactants containing soluble salts in the aqueous core [78]. The origin, nature, and mechanistic behavior of various percolating systems and quantification of the results can be found in the literature [79–83]. The [water]/[amphiphile] mole ratio (ω) plays an important role in the process of percolation. The threshold volume fraction of the disperse phase (ϕ_t) depends on ω , below which the change in conductance with volume fraction of the dispersed phase is only minimum. In the case of temperature percolation, the threshold temperature for percolation depends on ω , which is clearly demonstrated in the works of Mukhopadhyay et al. [84] and Alexandradis et al. [85].

Kurumada et al. [86] investigated the structure and percolation of water/oil microemulsions employing sodium bis(2-ethylhexyl)sulfosuccinate (AOT) and sodium bis(2-ethylhexyl) phosphate (SDEHP). The sulfosuccinate-derived microemulsions have produced spherical aggregates, whereas those derived from the phosphate are composed of cylindrical aggregates. But the preparations have shown percolation in conductance; the conductance increase with the phosphate system is 10–100 times more than that with the succinate system. Moreover, for the former, $\phi_t \sim 0.06$, and for the latter $\phi_t \sim 0.4$ – 0.5 . In the region of $\phi_t \geq 0.2$, the electrical conductivity of the phosphate system has been found to be 1000-fold

greater than that of the AOT system. The higher values in electrical conductivity have been considered to be a consequence of the presence of elongated aggregates in the system, inside which the charge can move for a long distance without much hindrance.

2. Mechanism of Percolation

The threshold volume fraction of percolation (ϕ_t) is guided by the amphiphile shell length and the overall volume fraction of the dispersed phase. For zero shell length and no interparticle attractive interaction, according to the randomly close-packed hard sphere model, $\phi_t = 0.65$; systems with strong attractive interactions end up with ϕ_t being lowered from 0.65 to 0.10.

During percolation, the transfer of charge may occur in two ways: (1) by the mechanism of "hopping" of surfactant ions from one droplet to another [73, 87–90] and (2) by the mechanism of transient fusion, ion transfer, and fission [91, 92]. While Maitra et al. [93] are in favor of the hopping mechanism, Mukhopadhyay et al. [84] support transient fusion and the mass transfer mechanism. The dynamics of the fusion model have been amply treated by use of the time-resolved fluorescence quenching (TRFQ) method [94–98]. The formation of the bicontinuous state by droplet association has also been suggested for augmenting percolation [99]. The evidence for the existence of the globular form of droplets in concentrated water/AOT/oil microemulsions given by the dynamic light scattering (DLS) method does not support the necessity of a bicontinuous structure for the occurrence of percolation [100]. Spherical droplets with strong short-range attractive interaction can produce percolation. The hopping, transient fusion, and mass transfer mechanisms are modeled in Fig. 3.

A thorough recent study on conductance percolation of water AOT/alkane (hexane, isooctane, decane, and dodecane) systems with regard to ω and temperature is due to Alexandradis et al. [85]; their observations on ω -dependent percolation are in agreement with the reports of Mukhopadhyay et al. [84].

According to Feldman et al. [101]; the conductivity and dielectric polarization below the percolation threshold arise from the motion of counterions through water channels and are not due to the hopping of ions. Above the threshold, the same mechanism still dominates.

3. Theory of Percolation

The w/o microemulsions with ionic amphiphiles or added electrolyte in the case of nonionic amphiphiles can be considered equivalent to mixtures of conductor and insulator. At a constant temperature in the percolation range, the conductance (σ) of the system on the whole is guided by the scaling law [102–104],

$$\sigma = k(\phi - \phi_t)^\mu \quad (1)$$

where k and μ are constants and k is related to the conductance of the dispersed phase.

According to a report of Feldman et al. [105], the exponent μ is 1.9 for both static and dynamic percolations. The scaling law for temperature percolation has the form [106–108]

$$\sigma = P(\theta - \theta_t)^n \quad (2)$$

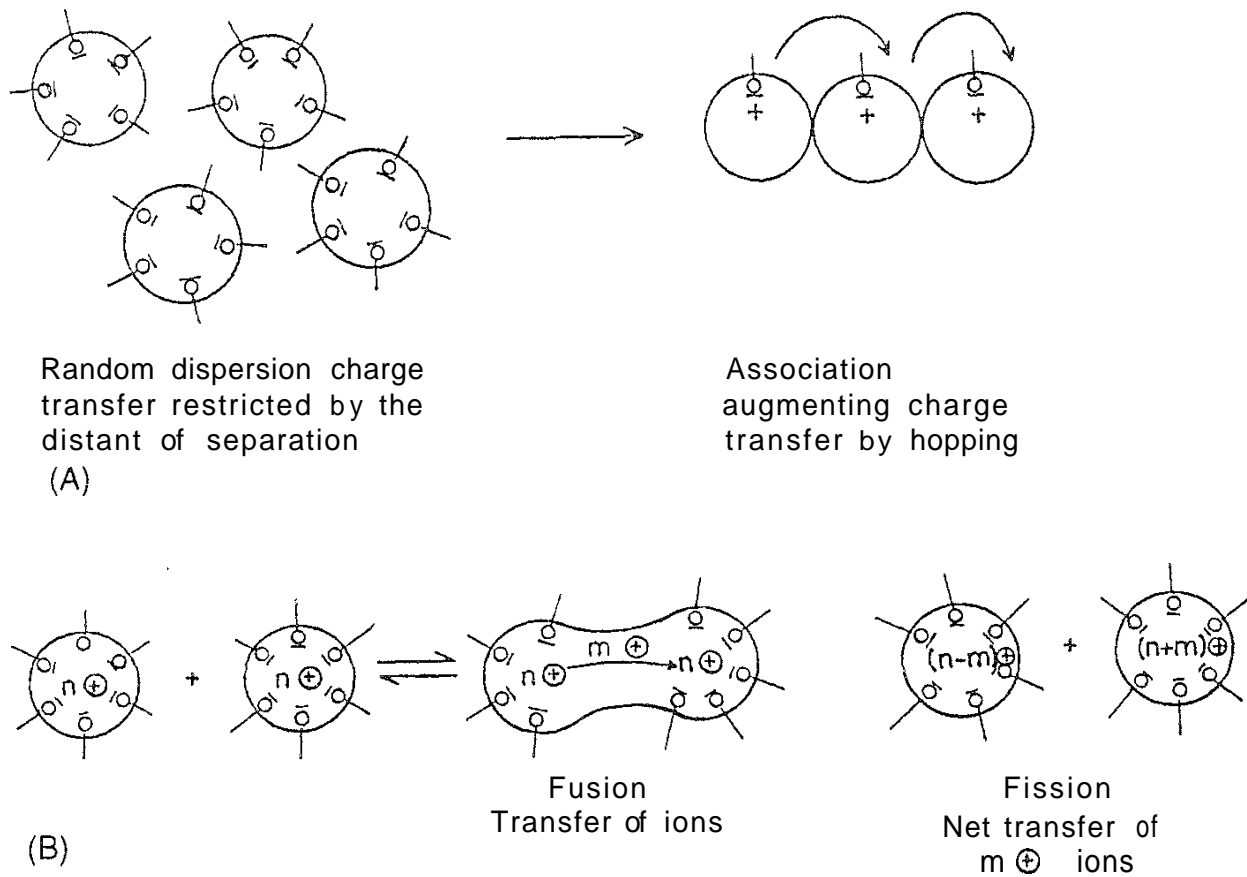


FIG. 3 (A) Hopping mechanism. Ions hop in the direction indicated by the curved arrows. (For simplicity, only one surfactant ion is shown.) (B) Ion transfer by fusion and fission. n cations are in each droplet; m cations are transferred.

where σ is the conductance of the solution at temperature 0, 0 , is the threshold temperature for transition, and P and n are constants.

The plots of ϕ and θ versus $\ln \sigma$ depicted in Fig. 4 are used to detect the transition values ϕ_t and θ_t respectively.

The expected value of n , like that of μ , is 1.9 [105,106]. But the values usually realized in actual experiments differ from 1.9, especially in the presence of additives.

The conductance of w/o microemulsions can be examined in the light of effective medium theories (EMTs) of binary inclusions [65,109,110]. The EMT is not adequate to deal with microheterogeneous dispersions of metals and metal oxides in a continuous medium, and Granqvist and Hunderi [111] proposed an effective medium theory considering dipole-dipole interaction among the dispersed entities (EMTDD). The dipolar interactions give rise to the formation of chains and clusters of spheroids. A percolation equation for the microheterogeneous dispersion of solids in a suitable medium was also proposed by Bernasconi and Wiesmann [112]. Under practical conditions, for a nonconducting dispersion medium ($\sigma_m = 0$), the equation of Bottcher [110] transforms into the scaling form with the exponent $\mu = 1$. Thus,

Bottcher:

$$\frac{\sigma - \sigma_m}{3\sigma} = \frac{\sigma_d - \sigma_m}{\sigma_d + 2\sigma} \quad (3a)$$

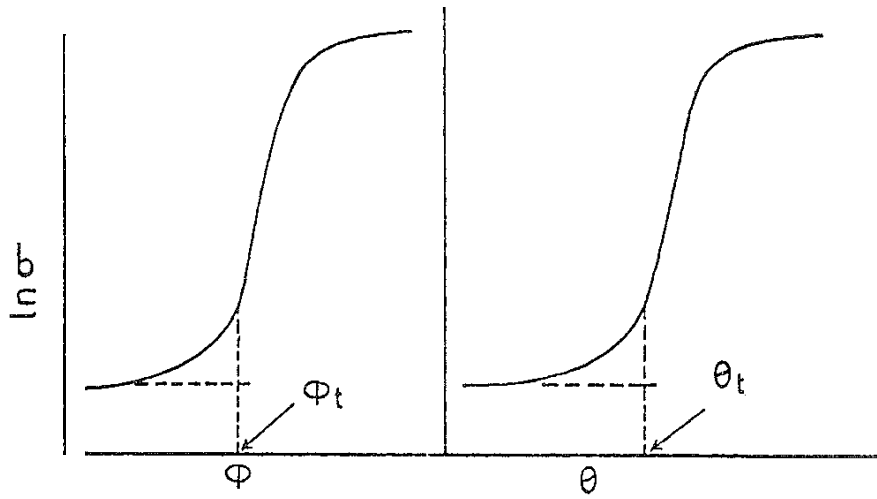


FIG. 4 Schematic representations of volume- and temperature-induced percolation. ϕ_t and θ_t are indicated by arrowheads.

Scaling form:

$$\sigma = 1.5 \sigma_d (\phi - 0.333) \quad (3b)$$

where σ_d is the conductance of the dispersed phase and the other terms have already been defined. 0.333 is the threshold volume fraction (ϕ_t); for nonspherical dispersions $\phi_t < 0.333$. From mass balance and the rationale put forward by Venable and Fang [113] and Bisal et al. [114], structural information (particle size and population, aggregation number of surfactant and cosurfactant per droplet, etc.) on w/o microemulsions can be realized. A set of typical results is presented in Table 1. The influence of oil, surfactant, and cosurfactant in determining the droplet size and amphiphile aggregation number is apparent from the table.

Pal et al. [115] simplified the EMTDD theory of Granqvist and Hunderi [111] for dispersed particles of different states of aggregation:

For spheres,

$$\sigma = 1.5 \sigma_d (\phi - 0.333) \quad (3b)$$

For chains,

$$\sigma = -0.1519 \sigma_d + (0.1566 \phi + 1.722 \phi^2 - 0.729 \phi^3) \sigma_d \quad (4)$$

For clusters,

$$\sigma = -0.0984 \sigma_d + (0.539 \phi + 0.568 \phi^2) \sigma_3 \quad (5)$$

The EMTDD (cluster) and Bernasconi–Wiesmann equations have been found not to be valid for all 29 systems examined by Pal et al. [115]. The EMT and EMTDD (chain) formulations have been found to be applicable to most of the systems examined. It can be mentioned that the threshold volume fraction $\phi_t = 0.157$ proposed by Bernasconi and Wiesmann (considering clustering of droplets) is in exact agreement with the ϕ_t^{EMTDD} for clusters when the conductance of the continuous medium is zero.

TABLE 1 Conductometrically Estimated Water Pool Size (R_w), Overall Droplet Dimension (R_e), Surfactant Aggregation Number (A_s), and Cosurfactant Aggregation Number (A_{cs}) per Droplet for a Number of W/O Microemulsions at 293 K at Constant Weight Fraction of Water = 0.2 and Surfactant Cosurfactant Weight Ratio = 0.5

| System' | R_w (nm) | R_e (nm) | A_s | A_{cs} |
|------------------|------------|------------|-------|----------|
| Water CTAB Hp Bu | 4.52 | 5.34 | 257 | 636 |
| Water CTAB Dc HA | 5.35 | 6.27 | 477 | 475 |
| Water CTAB Dc Bu | 4.45 | 5.26 | 241 | 636 |
| Water SDS Hp Bu | 6.90 | 7.85 | 1360 | 612 |
| Water SDS Xy Bu | 7.75 | 8.84 | 474 | 270 |
| Water SDS Dc Bu | 7.48 | 8.47 | 1781 | 401 |
| Water SDS Dc H4 | 6.30 | 7.25 | 1057 | 517 |
| Water AOT Hp Bu | 5.80 | 6.61 | 523 | 340 |
| Water AOT Dc Bu | 5.68 | 6.49 | 493 | 357 |
| Water AOT Dc HA | 5.56 | 6.38 | 474 | 270 |

'Hp = heptane; Dc = decane; Bu = butanol; HA = hexylamine; Xy = xylene

Source: Adapted from Ref. 114.

The equation is valid up to $\phi \leq 0.75$; for higher values of ϕ it assumes the form of the EMT. Pal et al. [115] also examined the possible correlation between the performance of EMT and EMTDD (chain) in terms of r (the structural ratio $[\text{cosurf}]/[\text{surf}]$ at the droplet interface) and σ_d . They further observed that the systems that give $r_{\text{EMT}} \geq 1$ satisfy both EMT and EMTDD (chain) formalisms. They further noticed that EMT and EMTDD (chain) propositions are obeyed in the presence of cosurfactant; without cosurfactant, the EMTDD (cluster) and Bernasconi–Wiesmann propositions are valid.

4. Effects of Additives on Percolation

The phenomenon of percolation has been found to be affected by the presence of additives; both enhancement and retardation of the percolation threshold have been witnessed. This phenomenon is related to the consistency of the oil/water interface of the water microdroplets. Softening of the interface by butanol [70] and its rigidification by cholesterol and its derivatives [116] have been demonstrated. According to one report [92], toluene blocks the transfer of charge carriers (ions), suppressing the conductance, i.e., prevents percolation. Mukhopadhyay et al. [84] made a detailed study of the additive effect using alkanols, cholesterol, esters of cholesterol, benzyl alcohol, and a crown ether in a water/AOT/decane microemulsion. Except for benzyl alcohol and the crown ether, other additives increased ϕ_t and also lowered the energy of activation for percolation. ϕ_t increased with the increasing chain length of the alkanols. The mechanism of transient fusion followed by mass transfer and fission as demonstrated by the TRFQ method [91,97,98,117] has been considered to be valid; the rate constant for fruitful droplet collision in the absence of additive has been shown to be of the same order as the

bimolecular exchange rate constant realized by the TRFQ method. The nonpercolating w/o microemulsion system of water/AOT/xylene (here xylene itself is a blocker, like toluene [92]) can be rendered percolating by the progressive addition of butanol. In the presence of butanol, cholesterol reduces the percolating efficacy [118]. Pileni et al. [119] reported that cytochrome c can induce significant temperature percolation in a nonpercolating water/AOT/isooctane w/o microemulsion system. Ray et al. [120] made an elaborate study of the effects of 29 additives of different kinds (electrolytes, nonelectrolytes, and surfactants) on the temperature as well as volume percolation of the water/AOT/heptane system. Bile salts, sodium cholate, and deoxycholate were observed to lower both ϕ_c and θ_c ; the other additives either remained indifferent or increased the percolation threshold. The exponent μ of Eq. (1) was found to be ≈ 1.0 , less than the expected value of 1.9. A special droplet fusion model was proposed to explain the percolation-assisting effects of the bile salts. In a subsequent study, Ray et al. [107] extended the additive effects on the percolation of the water AOT heptane system, demonstrating a unique effect of sodium cholate, the conversion of a nonpercolating w/o microemulsion system (water AOT/xylene) to a percolating one. In addition to this, the scaling laws were tested, and activation energies for percolation were evaluated. Like toluene and xylene, benzene and naphthalene increased the percolation threshold; the aromatic rings are considered to block the droplet fusion process, thus hindering the phenomenon. A representation of typical results is given in Table 2. It is seen from the table that at $\omega = 33$ the threshold percolation temperature of 35°C ((without additive) is lowered to 9.0°C by the presence of 0.1 mol/dm³ NaC, whereas NaDHC of same strength does not affect the threshold temperature. Tetraethylammonium iodide (TEAI) at 0.1 mol/dm³ NaC increases θ_c to 43°C, which decreases to 19.5°C in the presence of 0.08 mol/dm³ of NaC and 0.02 mol/dm³ TEAI. Xylene, toluene, benzene, and naphthalene at comparable weight percents (11.5) increase θ_c to 43.0, 46.5, 46.5, and 51.0°C, respectively. With 0.10 mol/dm³ NaC, θ_c for 11% (w/w) xylene diminishes to 17.5°C. From the analysis of the results, the values of μ and n of Eqs. (1) and (2) were found to be much lower than the expected value of 1.9 in the presence of additives. The modes of action of the bile salts (assister) and aromatics (blocker) on the droplet fusion–fission process are presented in Fig. 5. For establishing the proposed model on a firm basis, further investigations are needed.

The dependence of the percolation temperature of a w/o microemulsion (H₂O/AOT/isooctane) on the concentration of triblock copolymers (*b*-POE-*b*-PI-*b*-POE) and water droplets was straightforwardly suggested by Eicke et al. [121] on the basis of a thermodynamic model. Two distinct ranges of the [copolymer]/[nanodroplet] ratio were observed to correlate the percolation temperature.

5. Miscellaneous Conductance Studies

Ajith et al. [56,57] reported the unusual conductance behavior of water/Brij 35 *n*-propanol alkane and water SDS *n*-propanol cyclohexane microemulsions in the presence of NaCl. The conductance was found to decrease with increasing temperature. At lower ω , the conductance decline has been attributed to the difficulty encountered by ions in hopping from droplet to droplet. At higher ω , the conductance increases due to the clustering of droplets in the water/SDS/mixed alkanol/cyclohexane microemulsions [58]. The binary mixtures of lower alkanols

TABLE 2 Temperature Percolation Parameters for W/O Microemulsion System Water/AOT/Heptane in the Presence of Additives

| Additive (mol'dm ³) | ω | $\theta_i(^{\circ}\text{C})$ | $\ln P$ | n | E_p (kJ/mol) |
|---------------------------------|----------|------------------------------|---------|------|----------------|
| 0 | 33 | 35 | 2.0 | 1.80 | 1480 |
| NaC (0.10) | 33 | 9.0 | 1.70 | 2.50 | 1451 |
| NaC (0.08)+TEAI (0.02) | 33 | 14.0 | 0.43 | 3.01 | 882 |
| TEAI (0.10) | 33 | 43.0 | 2.10 | 1.90 | 379 |
| NaC (0.08)+TEAI (0.02) | 15 | 19.5 | -2.31 | 2.78 | 295 |
| TEAI (0.10) | 15 | 35.5 | -5.75 | 3.60 | 222 |
| SDS (0.20) | 33 | 33.5 | -1.70 | 3.45 | 608 |
| NaDHC (0.10) | 33 | 34.0 | 1.20 | 2.57 | 1028 |
| Xy 11% w/w in Hp | 33 | 43.0 | — | — | 790 |
| Xy 11% w/w in Hp + NaC (0.10) | 33 | 17.5 | — | — | 867 |
| Tl 11.23% w/w in Hp | 33 | 46.5 | — | — | 532 |
| Bz 11.37% w/w in Hp | 33 | 46.5 | — | — | 532 |
| Np 12.1% w/w in Hp | 33 | 51.0 | — | — | 538 |

NaC = sodium cholate; NaDHC = sodium dehydrocholate; TEAI = tetraethylammonium iodide; Xy = xylene; Tl = toluene; Bz = benzene; Np = naphthalene; Hp = heptane.

Source: Ref. 107.

(cosurfactants) were observed to behave like alkanols of carbon chain lengths intermediate between those of the two individual components. The system also showed a fair degree of percolation.

Structural and conductivity studies of mixed surfactants of anionic–nonanionic, cationic–nonionic, and cationic–anionic types were also examined by Seedher and Manik [60] and Li et al. [61,62]. The former authors observed that the threshold volume fraction of percolation for water/AOT/TX 100/*n*-heptane and water/CPB/TX 100/heptane depends on the mixing ratio; it increases with increasing proportion of the ionic component. The formation of bicontinuous phases for AOT/TX100, CTAB/TX 100, and Na oleate/CTAB combinations together with lower alkanols (*n*-butanol, *n*-pentanol, and *n*-hexanol) was reported by Li et al. [61,62] with diesel oil and heptane as the continuous media. The systems showed conspicuous conductance behavior.

Eicke and Meier [122] studied the interfacial charge transport in w/o microemulsions with mixed surfactants (AOT/pentaethylene monododecyl ether) and *n*-octane and observed unusual reductions in conductance producing a percolation type of pattern in the conductance versus temperature course. The diffuse double layer at the water/oil interface of the droplets was considered to be highly compressed, which accounts for reduced mobility and surface conductivity.

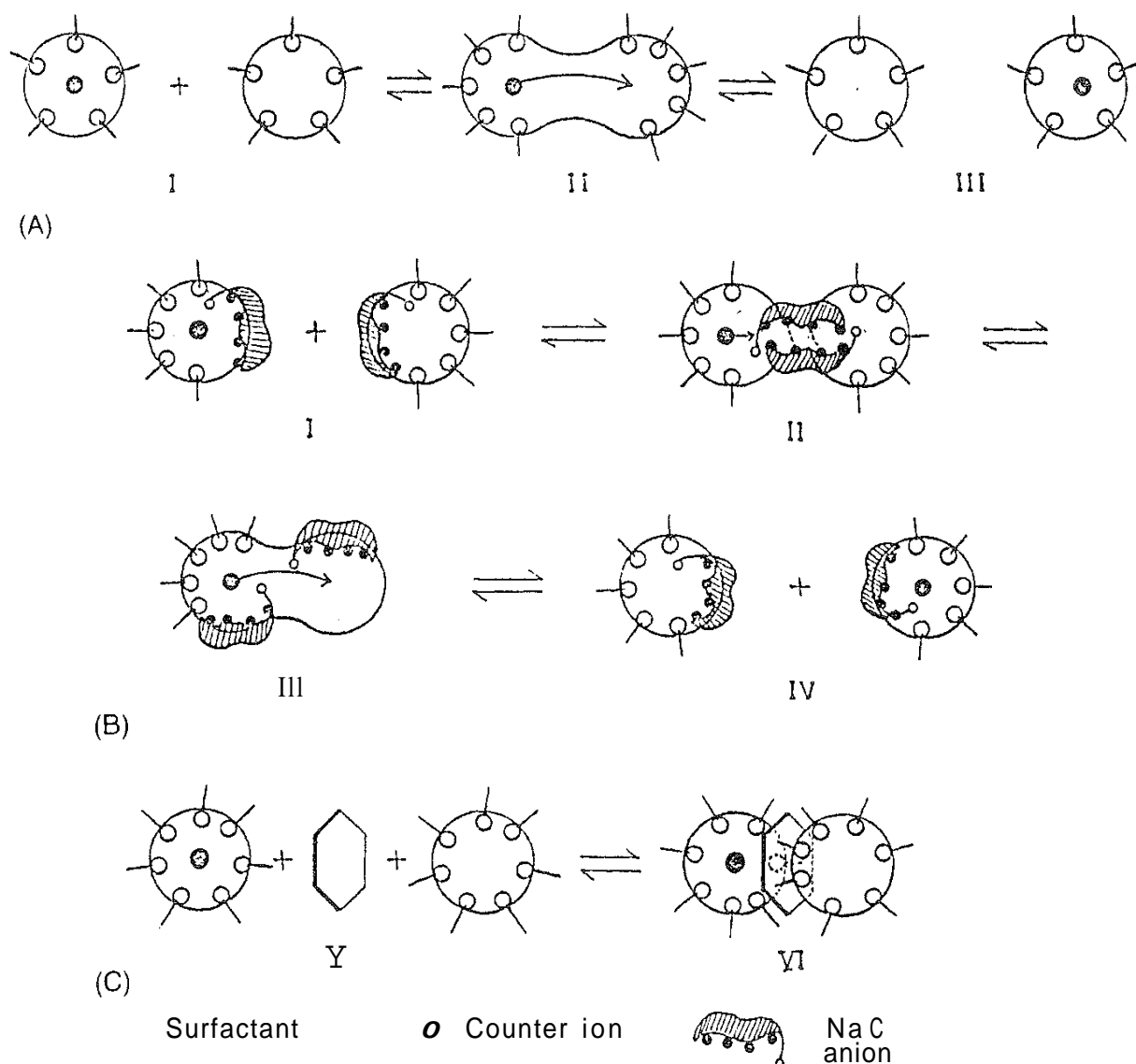


FIG. 5 Dynamics of events in percolation. Fusion-fission process for mass transfer (A) without additive; (B) in the presence of bile salt (NaC), favored mass transfer or percolation; (C) in the presence of aromatics, unfavored mass transfer or percolation.

The area of microemulsion research employing mixed amphiphiles and mixed oils has been only sparsely studied. For practical applications of microemulsions, this area needs elaborate exploration.

6. Pressure Effect on Conductance Percolation

On the whole, the phenomenon of droplet association augments percolation, which is manifested in the physical properties of conductance, viscosity, and permittivity. Like thermal energy at a constant pressure and composition, variable pressure at a constant temperature and composition can also initiate percolation. The droplet density required for pressure percolation is normally lower than that required for temperature percolation. Pairwise droplet attraction with increasing pressure that does not affect the droplet geometry was reported by Eastoe et al. [123]. The

pressure-independent droplet size was also reported by Kaler et al. [124]; the increasing pressure enhances the formation of aggregates without altering the dimension of the contributing droplets [125,126].

The work of Boned et al. [127] on pressure-induced conductance percolation of different microemulsion systems (water/AOT/undecane and glycerol/AOT/isooctane) is of fundamental importance. They varied pressure up to 1000 bar and explained their results on viscosity and conductance in terms of percolation theory. The percolation threshold ϕ_t decreased with pressure (P) for the water/AOT/undecane system, suggesting increasing interdroplet attraction; for the glycerol/AOT/isooctane system, ϕ_t varied insignificantly. The forms of scaling equations considered for the solution conductance (a) are

$$\begin{aligned}\sigma &= C_1(P)\sigma_1(P)[K(P_t)(P_t - P)]^\mu & \text{for } P > P_t + \delta P \\ \sigma &= C_2(P)\sigma_2(P)[K(P_t)(P - P_t)]^{-S} & \text{for } P < P_t - \delta' P\end{aligned}\quad (6)$$

In Eq. (6), C_1 and C_2 are prefactors, σ_1 and σ_2 are conductances of the dispersed phase, P_t is the threshold pressure, K is the pressure derivative of ϕ_t and $(\delta P + S'P)$ is the "crossover regime" or the transitional interval, which is of the order of $(\sigma_2/\sigma_1)^{1/(\mu+S)}$. The analysis of the dependence of σ on P is simple: if K is independent of P_t and if σ_1 , σ_2 , C_1 , and C_2 are also independent of P , the equation then takes the simplified form

$$\ln \sigma = f(\ln[P - P_t]) \quad (7)$$

Tingey et al. [128] reported an "antipercolation" feature of a water/dodecyltrimethylammonium bromide/supercritical propane microemulsion in the pressure range of 80–400 bar; the conductance decreased by three orders of magnitude. The interconnected channels of the studied bicontinuous system were anticipated to break down into dispersed droplets.

The pressure effect on percolation has been only limitedly studied. More thorough and more meaningful works on different categories of systems under varied environmental conditions are wanted.

C. Transport Across Microemulsion Acting as Liquid Membrane

In the recent past liquid membranes were employed for the separation and extraction of materials, and they can be conveniently employed for separating biological materials [129–137]. Microemulsions of Winsor I (o/w) and Winsor II (w/o) types are considered dispersed liquid membranes that can augment the transfer of oil-soluble and water-soluble compounds, respectively, across them by trapping them in microdroplets for convenient uptake and subsequent release. The microemulsions (Winsor I and II) are called bulk liquid membranes. They are recent additions in the field of separation science and technology. This field has been fundamentally explored and advanced by Tondre and coworkers [138–147], who worked out the fundamentals of the transport process by studying the transfer of alkali metal picrates and other compounds across the w/o microemulsions [140–142]. They also studied the transport of lipophilic compounds (pyrene, perylene, and anthracene) across o/w liquid membranes [138,139].

Their investigations were elaborate and extensive in terms of cell design, solute choice, amphiphile selection, additive effects, and data analysis. The transfer of Ni^{2+} , Co^{2+} , and Cu^{2+} as well as the nonionic compounds pyrene, perylene, and anthracene rapidly increases with time. Wiencek and Qutubuddin [148] also reported sharp separation of acetic acid from water. In Table 3, results of transport of Ni^{2+} by a w/o microemulsion liquid membrane are presented.

Tondre and coworkers proposed elaborate mechanisms of transport of both hydrophilic and lipophilic compounds across microemulsion liquid membranes [140,143]. This is not presented here due to lack of space.

On the basis of picrate ion transport across a w/o microemulsion, the flux (F) of the transported solute is given by the general equation

$$F = \frac{DK' C_G}{L} \left(\frac{[\text{S}]_{ss}^n}{1 + K' [\text{S}]_{ss}^n} \right) \quad (8)$$

In this equation, $n = 1$ and 2 for neutral solute and alkali metal picrate, respectively, the subscript "s" stands for the operating concentration of S in the source phase at steady-state conditions; C_G is the droplet (carrier) concentration, D the diffusion coefficient of the droplets, and L the cumulative thickness of the diffusion layer; and K' is either the extraction constant or the product of a partition constant times the equilibrium constant for solubilization inside the droplets.

The usefulness of Eq. (8) under varied experimental conditions has been examined; the measurement of flux compared with the classical procedure of direct contact has shown that membrane pore diameters of about 2.4 nm do not affect the interfacial transfer mechanism that occurs in microemulsion systems.

The transport flux for lipophilic substances through an o/w microemulsion has been shown by Xenakis and Tondre [139] in the light of reasonings of Ward [149] and Cussler [150] to be

$$F = \frac{DK''k''C_D}{L} \left(\frac{C_{p0}}{1 + K''k''C_{p0}} \right) \quad (9)$$

where D is the diffusion coefficient of the droplet, K'' is the equilibrium constant for binding of the solute with the droplet, k'' is the partition coefficient of solute

TABLE 3 Co-Ion-Dependent Transport of Ni^{2+} by Tetraethylene Glycol Dodecyl Ether Hexanol Decane W/O Microemulsion System

| Anion | Transport rate (ppm min) | 10^{10} Flux [mol (cm ² min)] |
|--------------------|-----------------------------|---|
| ClO_4^- | 0.347 | 301.00 |
| NO_3^- | 0.0897 | 77.60 |
| Cl^- | 0.0373 | 32.40 |
| Acetate | 0.0341 | 29.60 |
| SO_4^{2-} | 0.0080 | 6.94 |

Source: Adapted from Ref. 143

between the oil and water, C_D is the total droplet concentration, C_{p0} is the concentration of the solute outside the membrane, and L is the thickness of the diffusion layer.

Equation (9) has been experimentally verified; information regarding structural organization and thermodynamics of the solubilization–desolubilization process of the solutes in a microemulsion droplet have been also obtained.

In the case of separation of Ni^{2+} ions, 8-hydroxyquinoline and the industrial extractant Kelex 100 were used in water/SDS/butanol or pentanol/dodecane microemulsions. The kinetic and mechanistic formalisms in the extraction process were worked out by Tondre and coworkers [144,147]. To understand the coupled transport, crown ether or Kelex 100 were used by Derouiche and Tondre [143]. In several instances of metal ion transport, synergistic effects were observed: the results were explained on the basis of carrier diffusion in the stagnant layers.

Hebrant et al. [151] investigated the transport of amino acids (*p*-iodophenylalanine and tryptophan) through AOT/isooctane reverse micelles, and the rates of transport were compared and analyzed in relation to partition coefficients between water and the AOT palisade layer. The rate of uptake of amino acids by the reverse micelles and the influence of the ionization states of the acids on the extent of transport were also presented. Enantioselective transport using chiral AOT was also attempted, but the rigidity of the interfacial film according to them is not sufficient for chiral recognition for enantiomeric enrichment.

The two ways to extract copper ions in micellar compartments, i.e., association through ion exchange and complexation with micelle-solubilized hydrophobic extractants, were reported by Tondre et al. [152]. From the electrochemical behavior of Cu^{2+} ions they concluded that the Cu^{2+} /Kelex 100 complex is too stable to recover by electrolysis from water/CTAB/butanol microemulsion droplets.

The overall efficacy of microemulsion-based extraction of heavy metals (particularly mercury) from contaminated water involving oleic acid was reported and successfully modeled by Wiencek and coworkers [153,154], who used experimentally determined equilibrium extraction, stripping, and the initial reaction kinetics. This model accurately predicts both the initial extraction kinetics and final mercury extraction equilibrium. Good agreement between theory and experiment on the mechanism of extraction using a microemulsion to that of coarse emulsions has been found. Electrostatic coalescence and butanol addition were evaluated as potential demulsification techniques for recovery of the components from mercury-rich microemulsions [155].

The works on microemulsion liquid membranes have come mainly from the laboratory of Tondre and coworkers. Only a limited number of studies have appeared from other laboratories [156–163]. Further elaborate investigations in this potent field are needed for versatile applications in the area of separation, purification, and extraction.

1. Advantages and Limitations of Microemulsion Liquid Membranes

The advantages of microemulsion liquid membranes are the following:

1. Lower interfacial tension produces smaller droplets with large surface area per unit volume.

2. They are thermodynamically stable and can be conveniently handled,
3. Easy emulsification and demulsification with change of temperature aids in transfer and recovery of solute.
4. The rates of transfer are faster than with synthetic membranes.

The following features constitute the limitations of microemulsion liquid membranes:

1. For high efficiency of transport, the receiving end should contain a significant concentration of the separating component.
2. For versatile separation, the membrane should withstand a wide range of pH, which can be a driving force for the process.
3. The microemulsion-forming constituents should have minimum solubility in the feed phase (this limits the use of cosurfactants).
4. The extraction is limited by the attainment of equilibrium as in all passive transport processes.
5. Detailed knowledge about the phase behavior, stability, and so on of microemulsions is needed prior to putting them to use.

ACKNOWLEDGMENT

Support from the Department of Science and Technology, New Delhi (GOI) and the Indian Statistical Institute, Calcutta in the preparation of the manuscript is gratefully acknowledged.

REFERENCES

1. T. P. Hoar and J. H. Schulman, *Nature (London)* 152:102 (1943).
2. J. H. Schulman, W. Stoekenius, and L. M. Prince, *J. Phys. Chem.* 63:1677 (1959).
3. K. Shinoda and S. Friberg, *Adv. Colloid Interface Sci.* 4:281 (1975).
4. M. Kahlweit, *Science* 240:617 (1988).
5. K. V. Schubert and E. W. Kaler, *Ber. Bunsenges. Phys. Chem.* 100:190 (1996).
6. M. L. Robbins and J. Bock, *J. Colloid Interface Sci.* 124:462, 486 (1988).
7. G. J. Verhoeckx, P. L. de Bruyn, and J. Th. G. Overbeek, *J. Colloid Interface Sci.* 119:409 (1987).
8. P. L. de Bruyn, J. Th. G. Overbeek, and G. J. Verhoeckx, *J. Colloid Interface Sci.* 127:244 (1989).
9. K. Shinoda and B. Lindman, *Langmuir* 3:135 (1987).
10. S. P. Moulik and K. Mukherjee, *Ind. Natl. Sci. Acad.* 62A:215 (1996).
11. B. K. Paul and S. P. Moulik, *J. Dispersion Sci. Technol.* 18:301 (1997).
12. P. A. Winsor, *Solvent Properties Of Amphiphilic Compounds*, Butterworths, London, 1954, p. 68.
13. L. M. Prince (ed.), *Microemulsions: Theory and Practice*, Academic, New York, 1977.
14. G. Gillberg, in *Emulsions and Emulsion Technology* (K. J. Lissant, ed.), Marcel Dekker, New York, 1984, pp. 1–43.
15. I. D. Robb (ed.), *Microemulsions*, Plenum, New York, 1977.

16. D. O. Shah, (ed.), *Macro and Microemulsions: Theory and Applications*, ACS Symp. Ser. 272, Am. Chem. Soc. Washington, DC, 1985.
17. S. E. Friberg and P. Bothorel (eds.), *Microemulsions: Structure and Dynamics*, CRC Press, Boca Raton, FL, 1987.
18. M. Bourel and R. S. Schechter, *Microemulsions and Related Systems*, Marcel Dekker, New York, 1988.
19. K. Mittal and B. Lindman (eds.), *Surfactants in Solution*, Plenum, New York, 1984.
20. S. H. Chen and R. Rajagopalan (eds.), *Micelles and Microemulsions*, Springer-Verlag, New York, 1990.
21. R. Zana and J. Lang, in *Microemulsions: Structure and Dynamics* (S. E. Friberg and P. Bothorel, eds.), CRC, Boca Raton, FL, 1987, pp. 154–172.
22. P. G. Nilsson and B. Lindman, *J. Phys. Chem.* 86:271 (1982).
23. B. Lindman and H. Wennerström, in *Solution Behaviors of Surfactants* (K. L. Mittal and E. J. Fendler, eds.), Plenum, New York, Vol. 1, 1982.
24. O. Söderman and U. Olsson, in *Encyclopedia of NMR* (D.M. Grant and R. K. Harris Chichester, eds.), Wiley, New York, 1995, p. 3046.
25. O. Söderman and P. Stilbs, *Prog. NMR Spectrosc.* 26:445 (1994).
26. B. Lindman, U. Olsson, and O. Söderman, in *Dynamics of Solutions and Fluid Mixtures by NMR* (J. J. Delpuech, ed.), Wiley, New York, 1995.
27. B. Lindman and U. Olsson, *Ber Bunsenges Phys. Chem.* 100:344 (1996).
28. B. Lindman and P. Stilbs, in *Microemulsion Systems* (H. L. Rosano and M. Clause, eds.), Marcel Dekker, New York, 1987, p. 129.
29. P. Guering and B. Lindman, *Langmuir* 7:464 (1985).
30. A. Martino and E. W. Kaler, *Langmuir* 11:779 (1995).
31. A. Full and E. W. Kaler, *Langmuir* 10:2929 (1994).
32. M. Jonströmer, U. Olsson, and W. O. Parker, Jr., *Langmuir* 11:61 (1995).
33. K. P. Das, A. Ceglie, B. Lindman, and S. E. Friberg, *J. Colloid Interface Sci.* 116:390 (1987).
34. K. P. Das, A. Ceglie, and B. Lindman, *J. Phys. Chem.* 91:2938 (1987).
35. U. Olsson, K. Shinoda, and B. Lindman, *J. Phys. Chem.* 90:4083 (1986).
36. U. Olsson and P. Schurtenberger, *Langmuir* 9:3389 (1993).
37. W. O. Parker, Jr., C. Genova, and G. Carignano, *Colloids Surf. A* 72:275 (1993).
38. M. Leaver, I. Furo, and U. Olsson, *Langmuir* 11:1524 (1995).
39. Y. Hendrikx, H. Kellay, and J. Meunier, *Europhys. Lett.* 25:735 (1994).
40. D. Waysbort, S. Ezrahi, A. Aserin, E. Givati, and N. Garti, *J. Colloid Interface Sci.* 188:282 (1997).
41. U. Olsson, K. Nagai, and H. Wennerström, *J. Phys. Chem.* 92:6675 (1998).
42. H. Hauser, G. Haering, A. Pande, and P. L. Luisi, *J. Phys. Chem.* 93:7869 (1989).
43. A. N. Maitra, *J. Phys. Chem.* 88:5122 (1984).
44. T. Kawai, K. Hamada, and K. Kon-No, *Bull. Chem. Soc. Jpn.* 66:2804 (1993).
45. A. Jada, J. Lang, S. J. Candau, and R. Zana, *Colloids Surf.* 38:25 (1984).
46. H. F. Eicke, M. Borkovec, and B. Dasgupta, *J. Phys. Chem.* 93:314 (1989).
47. D. G. Hall, *J. Phys. Chem.* 90:429 (1990).
48. N. Kallay and A. Chittofrati, *J. Phys. Chem.* 94:4755 (1990).
49. G. Montalvo, M. Valiente, and E. Rodenas, *J. Colloid Interface Sci.* 172:495 (1995).

50. I. Molinero, M. L. Sierra, and E. Rodenas, *J. Colloid Interface Sci.* 188:239 (1997).
51. M. L. Sierra and E. Rodenas, *Langmuir* 10:4440 (1990); 12:573 (1996).
52. M. L. Sierra and E. Rodenas, *J. Phys. Chem.* 97:12387 (1993).
53. M. Valiente and E. Rodenas, *J. Colloid Interface Sci.* 127:52 (1989), *Colloid Polym. Sci.* 271:494 (1993).
54. E. Rodenas and E. Perez-Benito, *J. Phys. Chem.* 95:4552, 9496 (1991).
55. A. Chittofrati, A. Sanguineti, M. Visca, and N. Kallay, *Colloids Surf. A* 63:219 (1992).
56. S. Ajith, A. C. John, and A. K. Rakshit, *J. Pure Appl. Chem.* 66:509 (1994).
57. A. C. John and A. K. Rakshit, *Langmuir* 10:2084 (1994).
58. A. C. John and A. K. Rakshit, *Colloid Surf. A* 95:201 (1995).
59. S. Ajith and A. K. Rakshit, *J. Surf. Sci. Technol.* 8:365 (1992).
60. N. Seedher and M. Manik, *J. Surf. Sci. Technol.* 9:81 (1993).
61. X. Li, G. Zhao, E. Lin, and S. Qin, *J. Dispersion Sci. Technol.* 17:111 (1996).
62. X. Li, E. Lin, G. Zhao, and T. Xiao, *J. Colloid Interface Sci.* 184:20 (1996) and references therein.
63. H. Scher and R. Zallen, *Chem. Phys.* 53:3759 (1970).
64. R. Blanc and E. Guyon, in *Percolation, Structures and Processes—Annals of the Israel Physical Society* (G. Deutcher, R. Zallen, and J. Alder, eds.), Israel Physical Society, Jerusalem. Vol. 5. 1983, p. 229.
65. D. A. G. Burggeman, *Ann. Phys. (Leipz.)* 24:636, 665 (1935).
66. S. Kirkpatrick, *Phys. Rev. Lett.* 27:1722 (1971); *Rev. Mod. Phys.* 45:574 (1973).
67. J. Bernasconi, *Phys. Rev. B* 7:2252 (1973); 9:4575 (1974).
68. R. J. Elliott, J. A. Krumhansl, and P. L. Leath, *Rev. Mod. Phys.* 46:465 (1974).
69. D. Stroud, *Phys. Rev. B* 12:3368 (1975).
70. H. F. Eicke, R. Kubik, R. Hasse, and I. Zschokkel, in *Surfactants in Solution* (K. L. Mittal and B. Lindman, eds.), Plenum, New York, 1984, p. 1533.
71. A. M. Cazabat, D. Chatenay, F. Guering, D. Langevin, J. Mennier, D. Sorba, J. Lang, R. Zana, and M. Paillette, in *Surfactants in Solution* (K. L. Mittal and B. Lindman, eds.), Plenum, New York, 1984, p. 1737.
72. A. M. Cazabat, D. Langevin, J. Mennier, and A. Puchelon, *J. Phys. Lett.* 43:L 89 (1982).
73. M. W. Kim and J. S. Huang, *Phys. Rev. A* 34:719 (1986).
74. A. L. Bug, S. A. Safran, G. S. Grest, and J. Webman, *Phys. Rev. Lett.* 55:1896 (1986).
75. S. Bhattacharya, J. Stokes, M. W. Kim, and J. S. Huang, *Phys. Rev. Lett.* 55:1884 (1985).
76. M. A. Van Dijk, *Phys. Rev. Lett.* 55:1003 (1985).
77. S. A. Safran, G. S. Grest, and A. L. R. Bug, in *Microemulsion Systems* (H. L. Rosano and M. Clausse, eds.), Marcel Dekker, New York, 1987, p. 235.
78. H. F. Eicke, W. Meier, and H. Hammerich, *Langmuir* 10:2223 (1990).
79. M. Lagues, *J. Phys. Lett. (Paris)* 40:L331 (1979).
80. H. F. Eicke, S. Geiger, R. Hilfiker, F. A. Saner, and H. Thomas, in *Time Dependent Effects in Disordered Systems* (R. Pynn and T. Riste, eds.), Plenum, New York, 1987, p. 219.
81. S. Friberg, I. Lapezynska, and G. Gillberg, *J. Colloid Interface Sci.* 56:19 (1976).

82. M. Borkovec, H. F. Eicke, H. Hammerich, and B. Dasgupta, *J. Phys. Chem.* 92:206 (1988).
83. C. Cametto, P. Codastefano, P. Tartaglia, S. H. Chen, and J. Rouch, *Phys. Rev. A* 45:R 5358 (1992).
84. L. Mukhopadhyay, P. K. Bhattacharya, and S. P. Moulik, *Colloids Surf. A* 50:295 (1990).
85. P. Alexandradis, J. F. Holzwarth, and T. A. Hatton, *J. Phys. Chem.* 99:8222 (1995).
86. K. Kurumada, A. Shioi, and M. Harada, *J. Phys. Chem.* 98:12382 (1994).
87. G. S. Grest, I. Webman, S. A. Safran, and A. I. R. Bug, *Phys. Rev. A* 33:2842 (1986).
88. J. S. Huang, S. A. Safran, M. W. Kim, G. S. Grest, M. Kotlarchyk, and N. Quirke, *Phys. Rev. Lett* 53:593 (1984).
89. R. Hilfiker, H. F. Eicke, S. Geiger, and G. Furler, *J. Colloid Interface Sci.* 105:378 (1985).
90. J. Peyrelasse, M. Moha-Quchane, and C. Boned, *Phys. Rev. A* 38:904 (1988).
91. A. Jada, J. Lang, and R. Zana, *J. Phys. Chem.* 93:10 (1989); 94:381 (1990).
92. E. Dutkiewicz and B. H. Robinson, *J. Electroanal. Chem.* 251:11 (1988).
93. A. N. Maitra, C. Mathew, and M. Varshney, *J. Phys. Chem.* 94:5290 (1990).
94. F. Grieser and C. J. Drummond, *J. Phys. Chem.* 92:5580 (1988).
95. P. P. Infelta, M. Gratzel, and J. K. Thomas, *J. Phys. Chem.* 78:190 (1963).
96. M. Tachiya, *Chem. Phys. Lett.* 33:289 (1976).
97. J. Lang in *The Structure, Dynamics and Equilibrium Properties of Colloidal Systems* (D. M. Bloor and E. Wyn-Jones, eds.), Kluwer Academic, Amsterdam, The Netherlands, 1990, p. 1 and references therein.
98. J. Lang, N. Lalem, and R. Zana, *Colloids Surf.* 68:199 (1972).
99. D. Chatenay, M. Urbach, A. M. Cazabat, and D. Langevin, *Phys. Rev. Lett.* 54:2253 (1985).
100. M. Kotlarchyk, S. H. Chen, J. S. Huang, and M. W. Kim, *Phys. Rev. Lett.* 53:941 (1984).
101. Y. Feldman, N. Kozlovich, I. Nir, N. Garti, V. Archipov, Z. Idiyatullin, Y. Zuev, and V. Fedotov, *J. Phys. Chem.* 100:3745 (1996).
102. B. Lagourette, J. Peyrelasse, C. Boned, and M. Clause, *Nature (London)* 281:60 (1979).
103. M. Lagues, R. Ober, and C. Taupin, *J. Phys. Lett. (Paris)* 39:L487 (1978).
104. M. Clause, J. Peyrelasse, C. Boned, J. Heil, L. Nicoles, and A. Zradha, in *Solution Properties of Surfactants* (K. L. Mittal ed.), Plenum, New York, 1983.
105. Y. Feldman, N. Kozlovich, I. Nir, and N. Garti, *Phys. Rev. E* 51:478 (1995).
106. C. D. Mitescu and M. J. Mulsof, *J. Phys. Lett. (Paris)* 44: L679 (1983).
107. S. Ray, S. Paul, and S. P. Moulik, *J. Colloid Interface Sci.* 183:6 (1996).
108. S. Ray, S. Bisal, and S. P. Moulik, *Proc. Natl. Conf. Physical and Chemical Aspects of Organized Biological Assemblies*, Ind. Soc. Surf. Sci. and Techno],, Jadavpur University (Calcutta) 1991, p. 85.
109. R. Landauer, *J. Appl. Phys.* 23:779 (1952).
110. J. C. F. Bottcher, *Recl. Trav. Chim.* 64:47 (1945).
111. C. G. Granqvist and O. Hunderi, *Phys. Rev. B* 18:1554 (1976).
112. J. Bernasconi and H. J. Wiesmann, *Phys. Rev. B* 13:1131 (1976).

113. R. L. Venable and J. Fang, *J. Colloid Interface Sci.* 116:269 (1987).
114. S. R. Bisal, P. K. Bhattacharya, and S. P. Moulik, *J. Phys. Chem.* 94:350 (1990).
115. S. Pal, S. R. Bisal, and S. P. Moulik, *J. Phys. Chem.* 96:896 (1992).
116. C. Mathew, P. K. Patanjali, A. Nabi, and A. N. Maitra, *Colloids Surf.* 30:253 (1988).
117. R. Zana, in *Surfactant Solutions: New Methods of Investigation* (R. Zana, ed.), Marcel Dekker, New York, 1987, p. 241.
118. L. Mukhopadhyay, P. K. Bhattacharya, and S. P. Moulik, *Ind. J. Chem.* 32A:485 (1993).
119. M. P. Pileni, J. P. Huruguen, and C. Petit, in *The Structure, Dynamics and Equilibrium Properties of Colloidal Systems* (D. M. Bloor and E. Wyn-Jones, eds.), Kluwer Academic, Amsterdam, The Netherlands, 1990, p. 355.
120. S. Ray, S. R. Bisal, and S. P. Moulik, *J. Chem. Soc., Faraday Trans.* 89:3277 (1993).
121. H. F. Eicke, M. Gauthier, and H. Hammerich, *J. Phys. II France* 3:255 (1993).
122. H. F. Eicke and W. Meier, *Biophys. Chem.* 58:29 (1996).
123. J. Eastoe, B. H. Robinson, D. C. Steytler, and D. Thron-Lesson, *Adv. Colloid Interface Sci.* 36:1 (1991).
124. E. W. Kaler, J. F. Billmann, J. L. Fulton, and R. D. Smith, *J. Phys. Chem.* 95:458 (1991).
125. J. Eastoe, W. K. Young, B. H. Robinson, and D. C. Steytler, *J. Chem. Soc., Faraday Trans.* 86:2883 (1990).
126. D. Smith, J. P. Blitz, and J. L. Fulton in *Super Critical Fluid Science and Technology*, ACS Symp. Ser. 406, Am. Chem. Soc., Washington, DC, 1989, p. 165.
127. C. Boned, Z. Saidi, P. Xans, and J. Peyrelasse, *Phys. Rev. E* 49:5295 (1994).
128. J. M. Tingey, J. L. Fulton, D. W. Matson, and R. D. Smith, *J. Phys. Chem.* 95:1445 (1991).
129. H. L. Rosano, P. Dubey, and J. H. Schulman, *J. Phys. Chem.* 65:1704 (1961).
130. R. Ashton and L. K. Steinrauf, *J. Mol. Biol.* 49:547 (1970).
131. W. I. Higuchi, A. H. Ghanem, and A. B. Bikhazi, *Fed. Proc. Fed. Am. Soc. Exp. Biol.* 29:1327 (1970).
132. K. H. Wong, K. Yagi, and J. Smid, *J. Membr. Biol.* 18:379 (1974).
133. J. D. Lamb, J. J. Christensen, S. R. Izatt, K. Bedke, M. S. Aston, and R. M. Izatt, *J. Am. Chem. Soc.* 102:3399 (1980).
134. C. F. Reusch and E. L. Cussler, *AIChE J.* 19:736 (1973).
135. Y. Kabuke, K. Hanji, K. Horiguchi, M. Asada, Y. Nakayama, and J. Furukawa, *J. Am. Chem. Soc.* 98:7414 (1976).
136. M. Kirch and M. Lehn, *Angew. Chem. Int. Ed. Engl.* 14:535 (1975).
137. E. Pefferkorn and E. Varoqui, *J. Colloid Interface Sci.* 52:89 (1975).
138. C. Tondre and A. Xenakis, *Colloid Polym. Sci.* 260:232 (1982).
139. A. Xenakis and C. Tondre, *J. Phys. Chem.* 87:4737 (1983).
140. C. Tondre and A. Xenakis, *Faraday Discuss. Chem. Soc.* 77:115 (1984).
141. A. Xenakis and C. Tondre, *J. Colloid Interface Sci.* 117:442 (1987); *Talanta* 34:589 (1987).
142. A. Derouiche and C. Tondre, *J. Chem. Soc., Faraday Trans.* 1 85:3301 (1989).
143. A. Derouiche and C. Tondre, *Colloids Surf.* 48:243 (1990).

144. C. Tondre and M. Boumezioud, *J. Phys. Chem.* 93:846 (1989).
145. M. Boumezioud, A. Derouiche, and C. Tondre, *J. Colloid Interface Sci.* 128:422 (1989).
146. H. S. Kim and C. Tondre, *Sep. Sci. Technol.* 24:485 (1989).
147. M. Ismael and C. Tondre, *J. Membr. Sci.* 72:181 (1992).
148. J. Wiencek and S. Qutubuddin, *Sep. Sci. Technol.* 27:1211 (1992).
149. W. J. Ward, *AIChE J.* 16:405 (1970).
150. E. L. Cussler, *Multicomponent Diffusion*, Elsevier, New York, 1976.
151. M. Hebrant, P. Mettelin, C. Tondre, J. P. Joly, C. Larpent, and X. Chasseray, *Colloids Surf. A* 75:257 (1993).
152. C. Tondre, H. Hebrant, M. Perdicakis, and J. Bessiere, *Langmuir* 13:1446 (1997).
153. K. Larson and J. Wiencek, *Environ. Prog.* 13:253 (1994).
154. K. Larson, B. Raghuraman, and J. Wiencek, *Ind. Eng. Chem. Res.* 33:1612 (1994).
155. K. Larson, B. Raghuraman, and J. Wiencek, *J. Membr. Sci.* 91:231 (1994).
156. E. Paatero, J. Sjoblom, and S. K. Datta, *J. Colloid Interface Sci.* 138:388 (1990).
157. D. Bauer and J. Komornicki, *Int. Solvent Extraction Conf.* 315, (1983).
158. M. L. Robbins, U.S. Patent 3641181 (1972).
159. T. Flaim and S. E. Friberg, U.S. Patent 16, 467 (1981).
160. K. Osseo-Asare, *Colloids Surf.* 29:403 (1988); *Sep. Sci. Technol.* 23:1269 (1988).
161. A. G. Gaonkar and R. D. Neuman, *J. Colloid Interface Sci.* 119:251 (1987).
162. P. Fourre, D. Bauer, and J. Lemerle, *Anal. Chem.* 55:662 (1983).
163. P. Fourre and D. Bauer, *Solv. Extr. Ion Exch.* 1:463 (1983).

12

Structural Effects on Diffusivity Within Aggregates of Colloidal Zirconia

DAVID H. REEDER and ALON V. McCORMICK Department of Chemical Engineering and Materials Science, University of Minnesota, Minneapolis, Minnesota

PETER W. CARR Department of Chemistry, University of Minnesota, Minneapolis, Minnesota

| | |
|-------------------------------|-----|
| I. Introduction | 281 |
| II. Chromatographic Materials | 282 |
| A. Chromatographic zirconia | 282 |
| B. Colloidal aggregates | 283 |
| C. Other materials | 286 |
| III. Diffusion | 286 |
| A. Definitions of diffusion | 286 |
| B. Porous media | 287 |
| C. Large solutes | 290 |
| IV. Conclusion | 291 |
| References | 292 |

I. INTRODUCTION

The successful design of structured materials for separations depends on an understanding of the structural and chemical properties that are necessary and desirable for a given process. Reproducibility of manufacture and performance depend on adequate characterization of the chemical, physical, and process characteristics of the materials. An ideal chromatographic support would have a high solute load capacity, be highly selective between solutes, and allow complete solute recovery. These place specific requirements on the chemical and physical properties of any chromatographic support.

The outcome of a separation depends on fluid dynamics, mass transfer, and chemical kinetics within the system, with the relative importance of each changing with experimental conditions [1]. Porous chromatographic supports are commonly used because they present more surface area per bed volume than nonporous

supports. increasing the retention and the bed capacity for a given solute without the costs associated with a longer column (higher pressure drops, greater capital investment, longer separation times). However, resistance to mass transfer between the extraparticle and intraparticle fluid and intraparticle diffusion rates, which may be significantly reduced from those in the surrounding extraparticle fluid, can reduce the efficiency of a separation. In this chapter we focus on intraparticle diffusion.

This review is intended to familiarize the reader with an important class of chromatographic materials that are made by aggregating colloids. We review the literature relevant to predicting the diffusivity of large molecules within these materials. For design of material pore structures, rigorous theories and calculations incorporating explicit solute–support hydrodynamic and electrostatic interactions are desired. A rigorous level of understanding does exist for hindered transport in straight cylindrical pores such as are found in track-etched membranes. Researchers have explored the fundamental solute–pore interactions and have incorporated them into models that are successful in predicting both partition and transport coefficients [2]. However, an important limitation is the difficulty in relating fundamental geometric properties of solutes in a generalized porous medium (e.g., solute size and shape, pore geometry and topology) to those of solutes in cylindrical pores.

This discussion focuses on chromatographic materials made from aggregated spherical colloids. The interstitial space between the packed colloids forms a pore network within the chromatographic particle. Colloid aggregation is not the only way to produce porous materials; however, technologies for generating porous ceramics by colloid aggregation are accessible in terms of equipment, time, and starting materials, and they produce particles of appropriate pore size, surface area, particle size, and mechanical strength [3]. One example of a chromatographic material made by aggregating colloids is porous zirconia spheres made in our laboratories over the last few years.

II. CHROMATOGRAPHIC MATERIALS

A. Chromatographic Zirconia

Rigorously alkaline conditions—up to 0.5 M NaOH with alcohol and elevated temperature—are commonly used to certify sterilization in large-scale commercial bioseparations [4,5]. Zirconia is orders of magnitude less soluble than most other metal oxides, especially at elevated pH [6,7]; only harsh acidic conditions have caused detectable dissolution of zirconia, likely assisted by chelation/complexation with a solution anion [8]. The chemical stability of zirconia has motivated the development of zirconia-based supports using a variety of chromatographic modes, including size-exclusion, affinity, ion-exchange, and reverse-phase [9–14].

Zirconia is the only pure metal oxide that possesses four different chemical properties on its surface: acidic and basic as well as oxidizing and reducing [15–17]. The surface concentration of hydroxyls is higher than $20\ \mu\text{mol OH/m}^2$ [18,19].

Reports of the surface concentrations of acidic and basic sites vary. The highest results indicate about 5 pmol of Lewis acid sites per square meter and about 4 pmol of Lewis base sites per square meter [3]. Thus for zirconia to be useful as a chromatographic support, surface treatment is necessary to prevent the binding of any available molecule to compete the surface coordination, in particular to block the strong adsorption of carboxylate groups on proteins and peptides. Zirconia surfaces have been modified dynamically within chromatographic columns by the addition of competing Lewis bases to the mobile phase or by covering the zirconia surface with polymers or elemental carbon [9–14].

B. Colloidal Aggregates

In spray-drying processes, a stable suspension of colloids, which may contain a binder, is forced through a nozzle [20]. The resulting droplets are dried by hot air to yield particles as they sediment. The resulting structure is assumed to be a random packing of spheres, although in some cases gross heterogeneity has been observed, notably hollow or doughnut-shaped particles at rapid drying rates [21,22]. An oil emulsion process is conceptually similar to spray drying, with droplets formed by mechanical mixing or agitation and drying accomplished by extraction into hot oil [23].

In polymerization-induced colloidal aggregation (PICA) processes, a reactive monomer, generally urea formaldehyde, is mixed with a stable, submicrometer diameter metal oxide sol and undergoes an acid-catalyzed polymerization that results in porous, uniformly sized polymer–oxide composite microspheres [24,25]. PICA has been applied to a variety of metal oxide systems, primarily silica, but also alumina, titania, zirconia, ferric oxide, and antimony pentoxide [24,25]. The process is affected strongly by solution acidity [26]. At lower pH, polymerization is more rapid and a more porous but mechanically weaker particle is formed.

Particles made by oil emulsion drying and by PICA are significantly different [27–30]. Each produces particles of distinct size ranges. Recently PICA has been used to produce zirconia aggregates in the range of 1–5 μm in diameter (final sintered size) [26]. In oil emulsion processing, particle size and dispersity are easier to control at larger sizes, 20 μm and greater. Particles made by PICA processing are more uniformly spherical and monodisperse, while those made by oil emulsion processing tend to be more irregularly shaped (Fig. 1). The microscopic pore structure of particles made by the PICA process is more resilient to high temperature sintering than particles made by oil emulsion [30].

Microscopic examination of particle interiors reveals a gross difference in internal structure between particles made by oil emulsion processing and those made by PICA processing [28,31]. Materials made by PICA processing exhibit characteristic void spaces within the particles (Fig. 2). The particles appear to contain a spherical core around which is an approximately concentric void space; the appearance is reminiscent of an overripe peach in which the flesh has begun to pull away from the pit. These voids are not observed in materials made by oil emulsion processing and are an interesting and poorly understood feature of the mechanisms of particle formation and growth PICA.

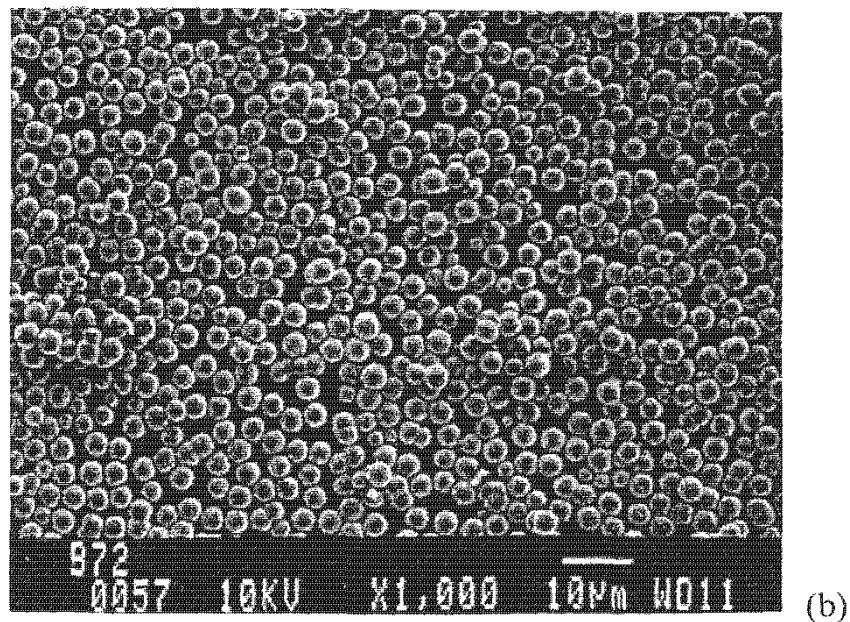
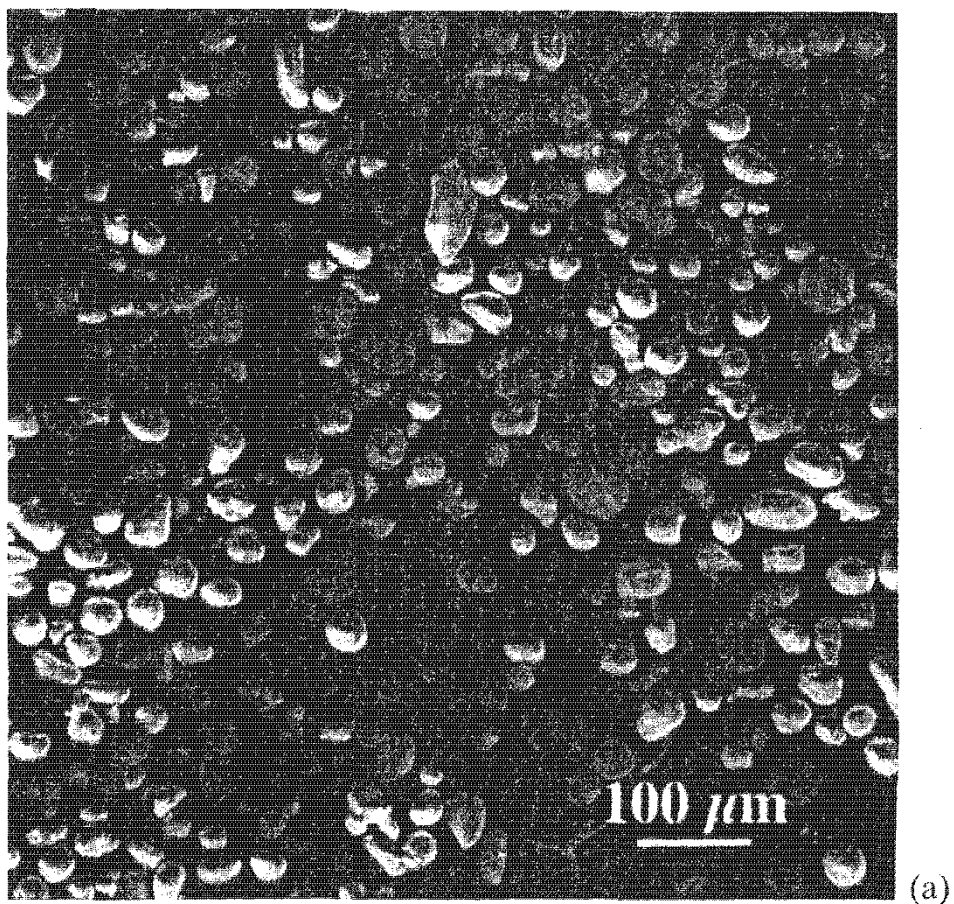
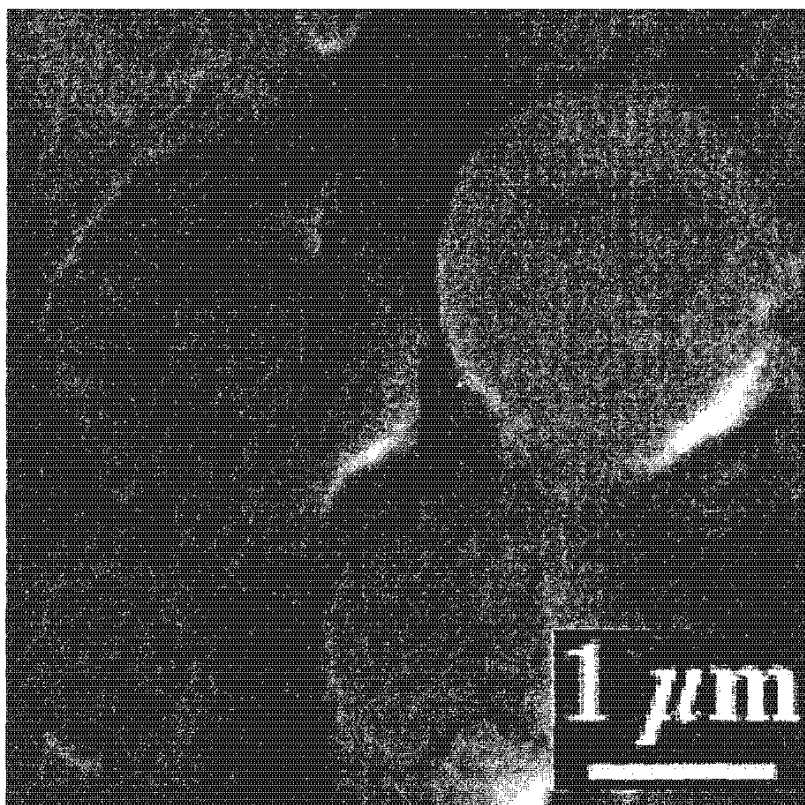
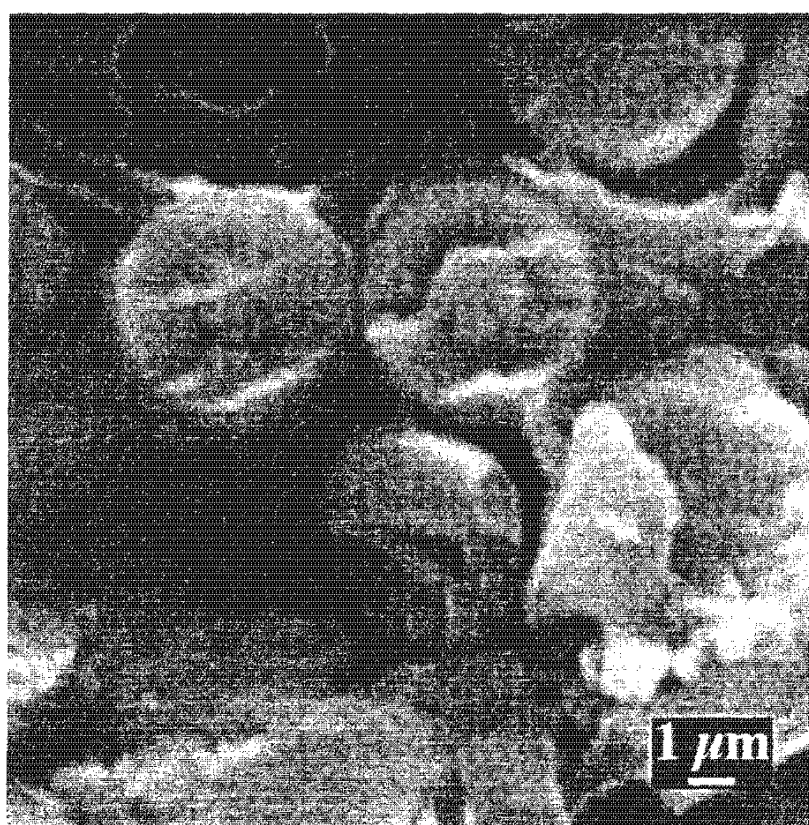


FIG. 1 Scanning electron microscopic images of zirconia colloidal aggregates made by (a) oil emulsion processing (batch OE-10) and (b) polymerization-induced colloid aggregation (batch B-72). (From Ref. 28.)



(a)



(b)

FIG. 2 Scanning electron microscopic images of particle interiors for particles made by polymerization-induced colloid aggregation. Sections were made by dispersing particles in epoxy resin and slicing with a microtome. Damage to the resin from the electron beam is visible in the images. (a) Zirconia, batch PICA-7; (b) zirconia, batch PICA-4. (From Ref. 28.)

C. Other Materials

Inorganic sol-gel polymerization processes are not yet a feasible alternative to colloid aggregation. These typically produce highly porous gels with small pores and low mechanical strength [32,33]. Mesoporous materials have also been produced by inorganic polymerization in the aqueous phase of an aqueous/micellar emulsion. The micellar phase is then extracted with an appropriate solvent. The most widely reported work has been on materials with unconnected cylindrical pores [34,35], but bicontinuous materials have also been reported [36]. These materials also generally lack sufficient mechanical strength for use in high pressure applications and have not been widely used, although a few reports exist [37].

Highly porous polymer gels are widely used in laboratory-scale purification of proteins, but they tend to deform under high pressure gradients and to shrink and swell upon solvent changes and may be stable over only a narrow range of pH—features that make them undesirable for use in large-scale or high-speed processes. Advances in polymer chemistry have improved the chemical and mechanical properties of these materials, but the syntheses do not result in gel structures. These non-gel materials are made either by hardening a biphasic emulsion, where the porogen is later removed to form the pore space, or by aggregating smaller, rigid polymer particles [38].

We show in Sec. III that the pore space of colloidal aggregates can be analyzed to yield diffusivity predictions for large molecules. It is hoped that similar models can be produced for the wider variety of materials just discussed.

III. DIFFUSION

A. Definitions of Diffusion

According to Fick's first law, the rate at which a species diffuses in a given direction is proportional to the concentration gradient in that direction.

$$\mathbf{j}_A = -\mathbf{D}_{AB} \cdot \nabla c_A \quad (1)$$

In Eq. (1), \mathbf{j}_A is the diffusive flux of species A (mass or moles per unit area per unit time), a vector quantity; \mathbf{D}_{AB} is the binary or mutual diffusion tensor describing the diffusion of A in a mixture of A and B; and ∇c_A is the spatial concentration gradient of A. If diffusion is isotropic, then it may be characterized by a scalar value \mathcal{D}_{AB} . Fick's law is a phenomenological description of diffusion on a macroscopic scale. It is useful in the design and analysis of processes like chromatography that involve nonequilibrium mass transport, as mathematical models of chromatography concern themselves with how fast a solute penetrates into the stationary phase, i.e., the flux.

Another definition of diffusion is given by the intradiffusion coefficient, which quantitatively describes how far an average molecule A will travel with time [39].

$$D_A = \lim_{t \rightarrow \infty} \frac{\text{trace}\langle \mathbf{r}\mathbf{r} \rangle}{6t} \quad (2)$$

In Eq. (2), D_A is the intradiffusion coefficient of species A, a scalar quantity obtained from the trace of the dyadic made from \mathbf{r} , the vector displacement of A. The brackets with subscript A indicate that this represents an average over a large number of A molecules. Here there is no concentration gradient. Movement occurs due to random momentum transfer during the frequent interactions between molecules. The intradiffusion coefficient is thus a thermodynamic quantity determined by the specific state of the system. Binary diffusion involves primarily solvent–solute interactions. Intradiffusion is the result not only of solute–solvent interaction but also of solute–solute interactions; thus in the limit of an infinitely dilute solution, where essentially only solute–solvent interactions occur, the binary diffusion coefficient and intradiffusion coefficient become identical [40].

The term "tracer diffusion" is often used to refer to measurements in which two forms of the species of interest diffuse into each other. The difference between the two forms is typically in isotopic composition or optical rotation: it should have a negligible effect on the chemical properties but allow for detection of a concentration gradient between the two forms. If the two forms of the solute are sufficiently similar, then the measured value is the same as the intradiffusivity. In actuality, though, this is a nonequilibrium ternary system [40].

B. Porous Media

Phenomenological descriptions of Fickian diffusion in porous media assume that there is some degree of homogeneity to the diffusivity within the system. In order to write the differential equations describing the mass transport, it is necessary to assume that the quantities involved can be treated as smoothly varying point functions. This is done by defining appropriate statistical averages over some distance that is large relative to the level of the pore structure but small relative to that of the entire system [41,42]. Thus a critical issue in any study of transport within a porous medium is the degree of microscopic detail that is necessary or useful to predict the desired macroscopic properties of the pore space.

Because a nonequilibrium diffusivity (including the tracer diffusivity) is defined by a flux, it is important on a macroscopic scale to consider how much of the plane through which the flux is being measured actually permits the passage of the diffusing species. The simplest description of diffusion in a porous medium (assumed here to be isotropic) relates the flux within the porous medium to that in the bulk solution with which it would be in equilibrium by introducing the fractional porosity ε and the tortuosity τ .

$$\mathcal{D}_{AB\text{apparent}} = \frac{\varepsilon}{\tau} \mathcal{D}_{AB\text{bulk}} \quad (3)$$

The fractional porosity accounts for the reduction in the flux due solely to the reduced area available for diffusion. It is customary to use the fractional volume porosity, but it has been argued that the fractional area porosity at the material's surface is more appropriate [43]. The definition given by Eq. (3) uses the tortuosity to account for all other effects that alter the binary diffusivity, and it lacks any inherent mechanistic or predictive detail.

The porosity is not a separate factor for diffusion measurements using techniques such as pulsed field gradient nuclear magnetic resonance spectroscopy and some modes of quasielastic light scattering in which the diffusivity is determined from the mean-square displacement of solutes:

$$D_{\text{apparent}} = \frac{D_{\text{bulk}}}{\tau'} \quad (4)$$

Here diffusion is measured only within regions that are permeable to diffusion. e.g., the liquid-filled pore space, rather than spatially averaged over permeable and impermeable regions as with Eq. (3). The tortuosity in Eq. (4), τ' , is not identical to τ in Eq. (3). As will be discussed below, partitioning and steric hindrance affect the two measurements differently.

When diffusing molecules are of a size comparable to that of a confining liquid-filled pore, the measured diffusivity may be significantly less than that measured in free solution due to frictional drag, steric hindrance, and differences between the solute concentration within the pore and in the free solution (partitioning) [2]. There are many quantitative predictions for rigid and flexible particles in variously shaped pores [44–47]. Partitioning affects both equilibrium and nonequilibrium measures of diffusion. Because the average concentration within the pore is different from that outside, the thermodynamic state of solutes within the pore differs from that of the bulk solution in important thermodynamic quantities like activity and partial molar volume [48]. Nonequilibrium measures of diffusion are further reduced by steric hindrance. In addition to the area through which there is no diffusive flux because it is occupied by the solid, there is a portion of the area near the pore surface that is inaccessible to the center of mass of the solute because of the finite size of the solute.

Numerous models also exist for the contribution of hydrodynamic or frictional drag in straight cylindrical pores. These are well reviewed in Ref. 2. If a solute adsorbs onto the pore surface and spends some portion of its time immobile, its net rate of transport will be reduced. Additionally, in some cases adsorption of the solute can significantly diminish the size of the pore and may even block the pore, preventing passage of another solute [49]. However, less is known about how to model the hydrodynamic drag in the convex, multiply connected pores provided by colloidal assemblies.

There is also the effect of the structure of the porous material. For a non-equilibrium measurement of diffusion, one can consider that there is no straight path for solutes to travel in the direction of the flux. In an equilibrium measurement of intradiffusion, this represents the fact that solutes are not longer subject to a purely random walk. When a solute is near a pore surface, the probabilities for moving in each direction are no longer uniform; certain directions are prohibited by the pore wall. For technical precision, then, one should differentiate between a structure factor and a tortuosity. A tortuosity, τ , quantitatively describes experimental results in which multiple interactions affect the diffusion. A structure factor, q , quantitatively describes only the effect of pore space geometry and topology on diffusion. Note that for limited conditions — when studying diffusion of small molecules and a passive pore surface — this allows for $\tau \approx q$.

The geometry and topology of real porous media tend to be very complex, making a complete description impractical. The challenge then is to determine the amount and type of information necessary to adequately and concisely describe transport within the material. Network models have demonstrated that diffusion within a pore network depends strongly on the mean pore coordination number and the pore size distribution [50,51]. Luckily, irregular networks have transport properties identical or nearly identical to those of regular networks as long as they have equal average coordination numbers and pore volume distribution [50]. For any regular lattice of identical pores, $q = 3$ [51]; this result is also obtained for randomly oriented uniform pores [52]. If the pore size is distributed, values of $q > 3$ are predicted. These predictions are much higher than experiments indicate for diffusion within colloidal aggregates [27,31]. These errors arise because these models erroneously assume that diffusion is unidimensional in a direction parallel to the pore axis and that the nodes connecting the pores have no volume—assumptions that are evidently invalid for highly or moderately porous materials. Efforts have been made to correct for the nonzero aspect ratio of the pores, with partial success [53]. Superlattice models [54] have the potential to account for the capacity of pore bodies but would be computation-intensive and would require the development of a method to generate the appropriate conductivity distributions from experimental data.

In the cell model [55,56] the macroscopic system is divided into smaller cells whose properties are assumed to be the same as those of the macroscopic system. This model gives

$$q = 1 + \phi/2 \quad (5)$$

where ϕ is the volume fraction of solids ($\phi = 1 - \varepsilon$). Equation (5) is valid for low volume fractions of solids placed periodically [40]; the dispersed solid is treated as a perturbation to the continuous liquid phase. Other than the required periodicity, the structure is not specified.

Exact prediction of the diffusivity requires solution of the continuity equations [57]. For an arbitrary structure, this is not feasible. However, for randomly placed, overlapping spheres, a statistical argument provides a closed-form analytical solution as a limiting case to a more general series solution [58]:

$$q = 1 - \frac{1}{2} \ln[1 - \phi] \quad (6)$$

For periodic structures, the continuity equations may also be solved explicitly by multipole expansion to yield tractable series solutions [59,60]. To a first approximation, these treatments are equivalent at low volume fractions of solids. Experimental studies of diffusion of small nonadsorbing solutes within ordered assemblies of colloids has been well predicted by these treatments [31,59,60]. However, these theories do not consider solutes of nonzero size, and another method is necessary to examine this.

C. Large Solutes

Travel under a random walk is described by Eq. (7), where $\langle r^2 \rangle$ is the mean square displacement of the walker, l is the length of the steps, and n is the number of steps taken.

$$\langle r^2 \rangle = l^2 n \quad (7)$$

Likewise, $w >$ intradiffusion can be mathematically described as a random walk [39],

$$\langle r^2 \rangle = 6Dt \quad (8)$$

where, when stepping is at a constant rate, time t is proportional to the number of steps. In a porous medium, the distance traveled will be reduced due to obstruction by the solid,

$$\langle r^2 \rangle = q^{-1} l^2 n \quad (9)$$

A random walk simulation thus provides the structure factor for any geometry that one defines. This technique has been used to examine the structure factor for an infinitely small solute within random arrays of freely overlapping cylinders with various orientation distributions [61], to study the effect of the distribution of reactive sites within a porous catalyst [62], and to study the effect of solute size on the structure factor within ordered assemblies of spherical colloids [31].

While the random walk simulation is straightforward in concept and in implementation, it is limited in application. The simulation does not contain time or energy; thus forces cannot be incorporated, and solutes and pore surfaces cannot interact other than to prevent overlap. For hydrodynamically interacting Brownian particles, the apparent intradiffusivity that would be measured at long times is expressible as the product of a hydrodynamically determined short-time diffusivity and a contribution that accounts for the distortion of the equilibrium dispersion structure caused by the diffusing particle [63]. The short-time diffusivity, D_0 , is an ensemble-averaged quantity that accounts for hydrodynamic forces between particles and can be evaluated from the hydrodynamic diffusion tensor using Monte Carlo simulation [64–66]. It has subsequently been postulated that diffusion in a porous medium can be described analogously as a product of a factor accounting for structure, q^{-1} , a factor accounting for hydrodynamic forces between diffusing solutes and the pore walls, f , and the diffusivity of the solute in a bulk solution [67],

$$D_{\text{apparent}} = q^{-1} f D_{\text{bulk}} \quad (10)$$

The friction coefficient f has been determined either from the hydrodynamic diffusion tensor using Monte Carlo simulation [67] or by using one of several simple analytical expressions for a sphere translating through a right cylindrical pore [31, 68–70]. The most commonly used is Eq. (11) [71], where λ is the characteristic ratio of solute size to pore size

$$f(\lambda) = 1 - 2.104\lambda + 2.089\lambda^3 - 0.948\lambda^5 \quad (11)$$

This and alternative expressions are well reviewed in Ref. 2.

NMR and light-scattering techniques as well as computer simulation have been used to measure the diffusion of large molecules within porous media. Both simulation and experimentation support the general form of Eq. (10) in the absence of solute adsorption or reaction for a variety of solutes and pore networks, including proteins within randomly oriented fiber systems [67], polystyrene in controlled-pore glasses [68–69], proteins in polymer-based chromatographic supports [70], and polystyrene within colloidal aggregates [31]. In most investigations, q has been assumed to be an empirical constant, independent of solute size [68–70], though for colloidal aggregates it has been predicted by computer simulation to be a function of solute size [31]. Values (or functions) for q reported in the literature vary between 1 and approximately 0.3 depending on the type of material and its porosity. Of the materials reported, fiber arrays generally have the highest porosities and the highest values for q , followed by aggregated ceramic colloids and aggregated polymer colloids, with controlled-pore glasses generally having the lowest values of q [31,66,68–70,72]. There is, however, general agreement that λ should be defined using the hydrodynamic radius of the solute and the mean pore constriction radius, such as one would measure by mercury porosimetry [31,68,69,72].

IV. CONCLUSION

To aid in the design of the aggregates we make in our laboratories, we have sought to understand the diffusion of large molecules within these porous materials as well as other materials. NMR and light-scattering techniques have allowed researchers to directly measure diffusion in porous media that were previously inaccessible to experimental measurement due to small length and time scales. We have summarized here the framework providing a general relation between the measurement of a diffusivity and its use in a macroscopic design equation. Hydrodynamic theories and computer simulations have led to significant advances in quantitative prediction of large molecules within porous materials that possess a periodic or statistical regularity, which we have applied to our own materials made of aggregated spherical colloids; however, these results have underscored the necessity of having at least a qualitative knowledge of the pore geometry—generally related to the synthesis method.

ACKNOWLEDGMENTS

This work has been supported by grants GM 45988 from the National Institutes of Health and CHE 917029 from the National Science Foundation. Additional support has come from the Biotechnology Training Program of the National Institutes of General Medical Sciences (IT32-GM08347), the Institute for Advanced Studies in Bioprocess Technology at the University of Minnesota, and the Regional Instrumentation Facility for Surface Analysis at the University of Minnesota.

REFERENCES

1. S. Golshan-Shirazi and G. Guiochon, *J. Chromatogr. A* 658:149 (1994).
2. W. M. Deen, *AIChE J.* 33:1409 (1987).
3. J. Nawrocki, M. P. Rigney, A. V. McCormick, and P. W. Carr, *J. Chromatogr. A* 657:229 (1993).
4. A. R. Barry and R. Chojnacki, *BioPharm* 7:43 (1994).
5. Pharmacia, Inc., *Downstream News and Views for Process Biotechnologists*, No. 2, Pharmacia, Inc., Piscataway, NJ, 1986.
6. K. K. Unger, *Porous Silica* (*J. Chromatogr. Silica Library*, Vol. 16), Elsevier, Amsterdam, 1977.
7. M. P. Rigney, T. P. Weber, and P. W. Carr, *J. Chromatogr.* 484:272 (1989).
8. P. W. Carr, J. A. Blackwell, T. P. Weber, W. A. Schafer, and M. P. Rigney, in *Chromatography in Biotechnology* (Cs. Horváth and L. S. Etter, eds.), American Chemical Society, Washington, DC, 1993.
9. M. Kawahara, H. Nakamura, and T. Nakajima, *J. Chromatogr.* 515:149 (1990).
10. J. A. Blackwell and P. W. Carr, *J. Chromatogr.* 549:59 (1991).
11. M. H. Glavanovich and P. W. Carr, *Anal. Chem.* 66:2584 (1994).
12. C. McNeff and P. W. Carr, *Anal. Chem.* 67:3886 (1995).
13. L. Sun and P. W. Carr, *Anal. Chem.* 67:2517 (1995).
14. C. Dunlap, P. W. Carr, and A. V. McCormick, *Chromatographia* 42:273 (1996).
15. M. A. Blesa, A. J. G. Maroto, S. I. Passaggio, N. E. Figliolia, and G. Rigotti, *J. Mater. Sci.* 20:4601 (1985).
16. A. Ayril, T. Assih, M. Abenoza, J. Phalippou, A. Lecomte, and A. Danger, *J. Mater. Sci.* 25:1268 (1990).
17. H.-C. Wang and K.-L. Lin, *J. Mater. Sci.* 26:2501 (1991).
18. H. Kita, N. Henmi, K. Shimazu, H. Hattori, and K. Tanabe, *J. Chem. Soc., Faraday Trans.* 77:2451 (1981).
19. J. Randon, A. Larbot, C. Guizard, L. Cot, M. Lindheimer, and S. Partyka, *Colloids Surf.* 52:241 (1991).
20. M. J. Wax and R. K. Grasselli, *E.U. Patent Appl.* EP 0 490 226 A1 (1991).
21. K. Masters, *Spray Drying Handbook*, 3rd ed., Wiley, New York, 1977.
22. C. Roth and R. Kobrich, *J. Aerosol Sci.* 19:939 (1988).
23. P. W. Carr, E. F. Funkenbusch, M. P. Rigney, P. L. Coleman, D. A. Hanggi, and W. A. Schafer, U.S. Patent 5,015,373, to Regents of the University of Minnesota (1991).
24. R. K. Her and H. J. McQueston, U.S. Patent 4,010,242, to E.I. DuPont de Nemours (1977).
25. L. Sun, M. J. Annen, C. F. Lorenzano-Porras, P. W. Carr, and A. V. McCormick, *J. Colloid Interface Sci.* 163:464 (1994).
26. M. J. Annen, R. Kizhappali, P. W. Carr, and A. McCormick, *J. Mater. Sci.* 29:123 (1994).
27. C. F. Lorenzano-Porras, M. H. Annen, M. C. Flickinger, P. W. Carr, and A. V. McCormick, *J. Colloid Interface Sci.* 170:299 (1995).
28. D. H. Reeder, P. W. Carr, M. C. Flickinger, and A. V. McCormick, presented by A. V. McCormick, American Chemical Society Spring National Meeting, San Francisco, CA, 1997.

29. C. F. Lorenzano-Porras, P. W. Carr, and A. V. McCormick, *J. Colloid Interface Sci.* 164:1 (1994).
30. C. F. Lorenzano-Porras, D. H. Reeder, M. J. Annen, P. W. Carr, and A. V. McCormick, *Ind. Eng. Chem. Res.* 34:2719 (1995).
31. D. H. Reeder, Pore structure and mass transport in colloidal aggregates for liquid chromatography, Ph.D. Thesis, Univ. Minnesota, Minneapolis, MN, 1997.
32. Q. Xu and M. A. Anderson, *J. Am. Ceram. Soc.* 76:2093 (1993).
33. J. B. Miller, S. E. Rankin, and E. I. Ko, *J. Catal.* 148:673 (1994).
34. C. T. Kresge, M. E. Leonowicz, W. J. Roth, J. C. Vartuli, and J. S. Beck, *Nature* 359:710 (1992).
35. M. Grun, I. Lauer, and K. K. Unger, *Adv. Mater.* 9:254 (1997).
36. J. C. Vartuli, K. D. Schmitt, C. T. Kresge, W. J. Roth, M. E. Leonowicz, S. B. McCullen, S. D. Hellring, J. S. Beck, J. L. Schenker, D. H. Olson, and E. W. Sheppard, *Chem. Mater.* 6:2317 (1994).
37. A. Kurganov, K. K. Unger, and T. Issaeva, *J. Chromatogr. A* 753:177 (1996).
38. F. Svec and J. M. J. Fréchet, *Science* 273:205 (1996).
39. A. Einstein, *Untersuchung uber di theorie der 'Brownschenbewegung'*, Akademische Verlagsgesellschaft, Leipzig. 1922.
40. E. L. Cussler, *Diffusion: Mass ~~Transfer~~ in Fluid Systems*, Cambridge Univ. Press, Cambridge, UK, 1984.
41. M. Sahimi, *J. Chem. Phys.* 96:4718 (1992).
42. L. Zhang and N. A. Seaton, *Chem. Eng. Sci.* 49:41 (1994).
43. R. N. Foster, J. B. Butt, and H. Bliss, *J. Catal.* 7:191 (1967).
44. J. C. Giddings, E. Kucera, C. P. Russell, and M. N. Meyers, *J. Phys. Chem.* 72:4397 (1968).
45. E. F. Casassa and Y. Tagami, *Macromolecules* 2:14 (1969).
46. E. D. Glandt, *AIChE J.* 27:51 (1981).
47. J. M. Nitsche and K. W. Limbach, *Ind. Eng. Chem. Res.* 33:1391 (1994).
48. J. L. Anderson and J. H. Brannon, *J. Polym. Sci.: Polym. Phys.* 19:405 (1981).
49. J. H. Petropoulos, A. I. Liapis, N. P. Kolliopoulos, J. K. Petrou, and N. K. Kanellopoulos, *Bioseparation* 1:69 (1990).
50. G. R. Jerauld, Flow and transport in chaotic media, Ph.D. Thesis, Univ. Minnesota, Minneapolis, MN, 1985.
51. M. Sahimi, G. R. Gavalas, and T. T. Tsotsis, *Chem. Eng. Sci.* 45:1443 (1990).
52. F. L. Johnson and W. E. Stewart, *J. Catal.* 4:248 (1965).
53. S. P. Friedinan and N. A. Seaton, *Chem. Eng. Sci.* 50:897 (1995).
54. D. Keffer, A. McCormick, and H. T. Davis, *J. Phys. Chem.* 100:967 (1996).
55. J. C. Maxwell, *A Treatise on Electricity and Magnetism*, Vol. 1. Clarendon Press, Oxford, 1873.
56. B. Jönsson, H. Wennerström, P. G. Nilsson, and P. Linse, *Colloid Polym. Sci.* 264:77 (1986).
57. R. B. Bird, W. E. Stewart, and E. N. Lightfoot, *Transport Phenomena*. Wiley, New York, 1960.
58. H. Weissberg, *J. Appl. Phys.* 34:2636 (1963).
59. P. Venema, R. P. W. J. Struis, J. C. Leyte, and D. Bedeaux, *J. Colloid Interface Sci.* 141:360 (1991).
60. M. H. Blees and J. C. Leyte, *J. Colloid Interface Sci.* 166:118 (1994).

61. M. M. Tomadakis and S. V. Sotirchos, *J. Chem. Phys.* 98:616 (1993).
62. H. P. G. Drewry and N. A. Seaton, *AIChE J.* 41:880 (1995).
63. J. F. Brady, *J. Fluid Mech.* 272:109 (1994).
64. G. Bossis and J. F. Brady, *Annu. Rev. Fluid Mech.* 20:111 (1988).
65. R. J. Phillips, J. F. Brady, and G. Bossis, *Phys. Fluids* 31:3462 (1988).
66. R. J. Phillips, J. F. Brady, and G. Bossis, *Phys. Fluids* 31:3473 (1988).
67. D. S. Claque and R. J. Phillips, *Phys. Fluids* 8:1720 (1996).
68. Z. Zhou, I. Teraoka, K. H. Langley, and F. E. Karasz, *Macromolecules* 27:7402 (1994).
69. M. T. Bishop, K. H. Langley, and F. E. Karasz, *Macromolecules* 22:1220 (1989).
70. J. L. Coffman, E. N. Lightfoot, and T. W. Root, *J. Phys. Chem. B* 101:2218 (1997).
71. J. L. Anderson and J. A. Quinn, *Biophys. J.* 14:130 (1974).
72. D. M. Smith, *AIChE J.* 32:1039 (1986)

13

Characterization of Energetically Heterogeneous Surfaces from Experimental Adsorption Isotherms

JAMES P. OLIVIER Micromeritics Instrument Corporation, Inc., Norcross, Georgia

- I. Introduction
 - A. Real and ideal surfaces
 - B. Origin of the adsorptive potential
 - C. Thermodynamic meaning of the adsorptive potential
- II. Theoretical Background
 - A. A short history of the integral equation of adsorption
 - B. Solving and using the integral equation of adsorption
- III. Application of Density Functional Theory
 - A. The deconvolution method
 - B. Parameters of the model matrix
 - C. Results
- IV. Discussion
- V. Conclusions
- References

I. INTRODUCTION

A. Real and Ideal Surfaces

A heterogeneous surface is one described by a distribution of adsorptive potentials [1].

In the formative years of adsorption theory, it was usual to assume that a solid surface presented a set of equivalent sites for the attachment of an adsorbate molecule. Such was the idealized picture used by Langmuir [2] in developing his classic equation. Even when the model was extended to include adsorbate-adsorbate interaction as was done by de Boer [3] in developing his nonideal

two-dimensional gas model for mobile adsorption and by Fowler and Guggenheim in their statistical thermodynamic derivation [4] for the case of localized adsorption, the assumption of an energetically homogeneous, or *homotattic* [5], surface was retained, as was the assumption of monolayer adsorption,

Today, there is probably universal agreement that almost all real surfaces are significantly heterogeneous. The importance of physical adsorption in chemical engineering processes involving separations and catalysis has led to increased interest in this subject and to the need to explore ways to characterize the surfaces of engineering adsorbents in terms of their adsorptive potential distributions.

In addition to providing a measure of the specific extent of a surface, the adsorption isotherm conveys a great deal of information about the energetic heterogeneity and geometric topology or porosity of a solid substrate. As a source of information for the characterization of materials, the gas adsorption isotherm has much to recommend it: It is quite easily measured, it is highly reproducible from laboratory to laboratory, and it provides a very sensitive indicator of surface properties. Using graphite at cryogenic temperature, for example, a 5% variation in adsorptive potential would correspond to a twofold change in the pressure required to maintain the same amount of argon adsorbed [1].

B. Origin of the Adsorptive Potential

The adsorptive potential is a measure of the net attractive force between a solid surface and an adsorbed molecule. For physical adsorption, these forces arise chiefly from London-type dispersion interactions (van der Waals forces) resulting from induced dipole–induced dipole and higher multipolar attractions, which in turn depend on the size, polarizability, and magnetic susceptibility of the interacting particles (atoms or molecules). Additional contributions may come from Coulombic interactions or from induction forces brought about by the operation of a surface electric field on induced or permanent dipoles of resident molecules. The net potential due to these forces acting on an adsorbed molecule is generally short-range and is the summed effect from all nearby surface atoms.

The contribution of the dispersion forces to the total potential can be well approximated by the Lennard-Jones equation for pairwise interaction,

$$\phi(s, \varepsilon) = 4\varepsilon \left[\left(\frac{\sigma}{s} \right)^{12} - \left(\frac{\sigma}{s} \right)^6 \right] \quad (1)$$

where ϕ is the potential. ε the depth of the potential well. s the molecular separation. and σ the separation at which $\phi = 0$. For an adsorptive molecule at the surface, the total dispersion potential, U^{LJ} , is the sum of its pairwise interactions with each atom of the solid:

$$U^{LJ} = \sum_j \phi(s_{ij} \varepsilon_j) \quad (2)$$

In Eq. (2), s_{ij} is the distance from the adsorbed molecule to the solid atom j having energy parameter, ε_j . It is readily shown that over 90% of the value of U^{LJ} is provided by the surface atoms within three to four molecular diameters of the adsorbed molecule. It is clear that any irregularity in the local chemical

composition, density, or geometry of the surface will cause a variation in the adsorptive potential at that point. If the surface topography is locally reentrant, so as to constitute a fine pore of molecular dimensions, then the adsorptive potential can be more than doubled. Since the effects of surface energetic heterogeneity and the effects of porosity on the adsorption isotherm are both expressed through this same adsorptive potential, we can anticipate some difficulty in separating the two. We shall see that such a separation is possible when the smallest pores in the material to be characterized are large enough to have negligible effect on monolayer formation.

C. Thermodynamic Meaning of the Adsorptive Potential

In the preceding section, we presented the idea that real surfaces can be, and usually are, "energetically heterogeneous" in that they provide regions of varying attractive force or potential to physically adsorbed molecules. In describing a surface energy characteristic, an energy function that is independent of temperature and concentration is desirable. Such a quantity is conveniently defined by the potential energy difference between the lowest energy state of the adsorptive molecule in the gas phase and its lowest energy state in the adsorbed phase, both at infinite dilution. In this way we obtain a quantity that is independent of the kinetic states of the molecule in either phase and that measures most directly the adsorptive potential of the system. The adsorptive potential, U_0 , is therefore defined for a homotactic surface [1, p. 23] as

$$U_0 = {}_aP^{\text{ads}} - {}_aE_0^{\text{vib}} \quad (3)$$

where ${}_aP^{\text{ads}}$ is the potential energy per mole lost by an isolated molecule in moving from a distant point to its equilibrium adsorbed position. The second term on the right is the zero-point vibrational energy of the adsorbed molecule with respect to the surface. Note that ${}_aP^{\text{ads}}$ may differ from U^{LJ} if mechanisms other than dispersion forces are at work.

When a molecule is adsorbed, the process is accompanied by a liberation of heat that can be measured calorimetrically. The experimentally measured heat can be related to a thermodynamic quantity, the differential heat of adsorption, by relationships that depend on the specifics of the calorimeter used [1, Ch. III]. The differential heat of adsorption, q^{diff} , on a homotactic surface at any isotherm point is related to U_0 by

$$q^{\text{diff}} = U_0 - ({}_aE^{\text{vib}} - {}_aE_0^{\text{vib}}) - \Delta E^{\text{tr}} - \Delta E^{\text{rot}} + {}_aP^{\text{ia}} \quad (4)$$

where the term $({}_aE^{\text{vib}} - {}_aE_0^{\text{vib}})$ is the thermal vibrational energy per mole of adsorbate in excess of the zero-point energy, ΔE^{tr} and ΔE^{rot} are the kinetic energy changes on adsorption due to loss in translational and rotational degrees of freedom, and ${}_aP^{\text{ia}}$ the energy of interaction with all neighboring adsorbed molecules. This latter term is clearly dependent on surface concentration and could be estimated by an equation analogous to Eq. (2).

Another thermodynamic quantity, q^{st} , the isosteric heat of adsorption, can be calculated from the temperature dependence of the adsorption isotherm by obtaining the slope of the adsorption isostere and is defined by

$$\frac{q^{\text{st}}}{T({}_gV - {}_aV)} \quad (5a)$$

where na is the moles adsorbed and ${}_gV$ and ${}_aV$ are the molar volumes of the gas and adsorbed phases, respectively. Neglecting the molar volume of the adsorbed phase and assuming that the gas phase is ideal gives the more familiar expression

$$\left(\frac{\delta \ln p}{\delta (1/T)} \right)_{na} = \frac{q^{\text{st}}}{R} \quad (5b)$$

It can be shown that the differential and isosteric heats are related by

$$q^{\text{diff}} = q^{\text{st}} - RT \quad (6)$$

The importance of Eq. (4) is that it expresses the differential heat of adsorption in terms of a number of concepts that have a readily visualized physical basis; it reasserts and emphasizes that the differential heat of adsorption contains inter alia separate expressions for the adsorbate–adsorbent interaction and the adsorbate–adsorbate interaction; and since all the other experimentally determined heats of adsorption are related to q^{diff} , the same conclusion holds true for them. The quantity U_0 , expressing as it does the adsorbate–adsorbent interaction stripped of all other incidental energy changes such as lateral interaction, work terms, and kinetic and vibrational energy changes, is more suitable than any of the experimentally measured heats as an index of the fundamental "affinity" of a solid surface for adsorbing a particular gas molecule.

The relation of the various heats of adsorption to the adsorptive potential is shown schematically in Fig. 1. It should be noted that although heat lost from a system is thermodynamically a negative quantity, it is a custom of long standing in adsorption science to employ a positive sign. This is frequently confusing to newcomers to adsorption studies.

For a more complete and detailed discussion of the thermodynamic quantities of interest in physical adsorption, the reader is referred to Chapter III of Ref. 1.

II. THEORETICAL BACKGROUND

A. A Short History of the Integral Equation of Adsorption

Although the concepts are somewhat older, the most widely used model for describing adsorption on an energetically heterogeneous surface was first explicitly stated by Ross and Olivier [6,7]. The model postulates that the surface of a real solid is composed of small patches of different adsorptive potential that adsorb independently of one another. The distribution of adsorptive energies, U_0 , among these patches can be represented by a continuous distribution function:

$$f_a = \frac{1}{A} \frac{da}{dU_0} = f(U_0) \quad (7)$$

where f_a is the patch (or site) frequency per unit energy interval on a surface of area A . The distribution function must normalize to unity, as was pointed out by Hill [8],

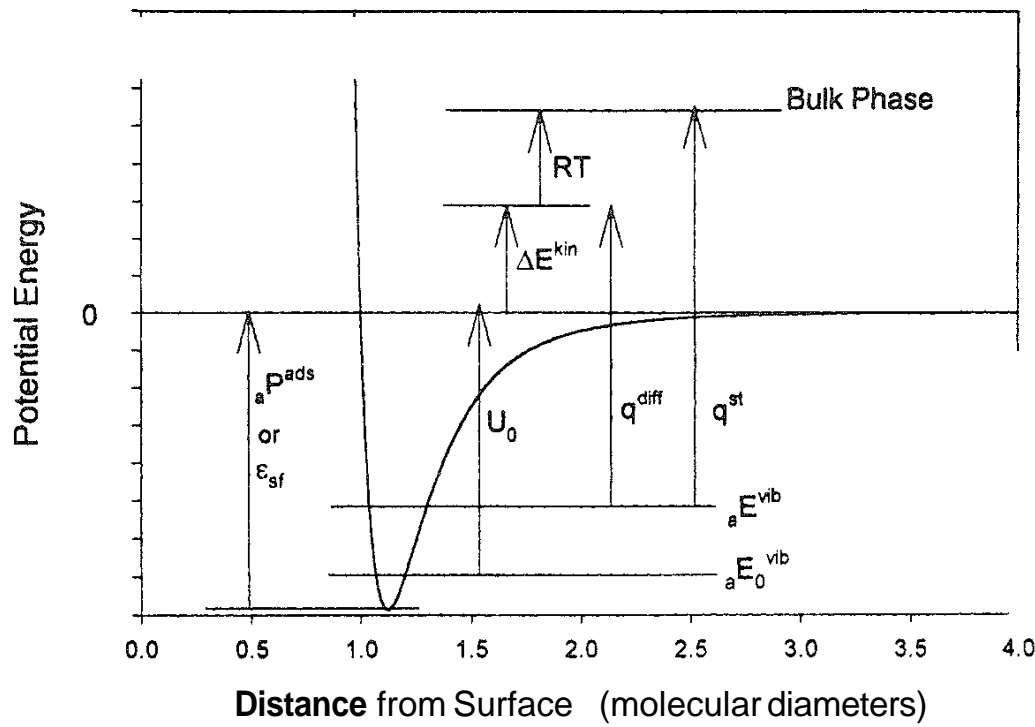


FIG. 1 Potential energy well for adsorbate-adsorbent interaction, showing the relation of the various heats of adsorption.

since we are dealing with a surface of finite extent; that is, $\int f(U_0) dU_0 = 1$ over the range of energies considered significant,

At any equilibrium pressure p under isothermal conditions, the quantity adsorbed per unit area, q , on a given surface patch will depend only on the adsorptive potential of that patch according to the function

$$q_a = q(p, U_{0a}) \quad (8a)$$

or, more generally,

$$q = q(p, U_0) \quad (8b)$$

The observed total amount adsorbed, Q , at pressure p is then the sum of contributions from each patch of surface, i.e.,

$$Q(p) = \int q(p, U_0) f(U_0) dU_0 \quad (9)$$

Equation (9) is therefore the general form for any adsorption isotherm and corresponds to Eq. (IV-4) of Ref. 1. The function $q(p, U_0)$ is called the kernel function or the local isotherm. Equation (9) is now often referred to as "the integral equation of adsorption".

B. Solving and Using the Integral Equation of Adsorption

1. Analytical Methods

Referring to Eq. (9), we see that in any treatment of surface heterogeneity we have to deal with three functions, any two of which, if known, assumed, or determined, can be used in theory to obtain the third. Equation (9) represents a Fredholm integral of the first kind. The solution of equations of this type is well known to present an ill-posed or ill-conditioned problem. For our purposes, this means that the data, $Q(p)$, can be "well represented" by many function pairs in the integrand; therefore, simply fitting the data does not guarantee that the kernel function or the distribution is individually "correct." In addition, the mathematical difficulties of handling Eq. (9) analytically has severely restricted the number of possible variations that have hitherto been published. In Table 1 are given mathematical descriptions of some models of adsorption on homotactic surfaces. We note that the function $q(pU_0)$ must be an explicit expression for the quantity adsorbed in terms of p and U_0 . This restriction alone means that of all the common theoretical monolayer isotherm equations, only the two-dimensional ideal gas (Henry's law) equation and the Langmuir equation are usable. The Hill-de Boer equation and the Fowler equation cannot be solved explicitly for quantity adsorbed.

TABLE 1 Mathematical Description of Some Models of Adsorption on Homotactic Substrates

| Description of adsorbed film | | Isotherm equation | |
|---|--|-------------------|------|
| Mobile film, two-dimensional ideal gas, Henry's law | $p = K\theta$ | | (10) |
| Mobile film, hard sphere particle, Volmer equation | $p = K \frac{\theta}{1-\theta} \exp\left[\frac{\theta}{1-\theta}\right]$ | | (11) |
| Mobile film, van der Waals gas interaction. Hill-de Boer equation | $p = K \frac{\theta}{1-\theta} \exp\left[\frac{\theta}{1-\theta} - \frac{2\alpha\theta}{kT\beta}\right]$ | | (12) |
| Localized film no interaction. Langmuir equation | $p = K \frac{\theta}{1-\theta}$ | | (13) |
| Localized film, interaction, Fowler equation | $p = K \frac{\theta}{1-\theta} \exp\left[-\frac{\omega\theta}{kT}\right]$ | | (14) |
| Mobile film, nonideal gas, interaction, virial equation | $p = K\theta \exp\left[\frac{2\theta}{\sigma_0} B(T) + \frac{3\theta^2}{2\sigma_0^2} C(T) + \frac{4\theta^3}{3\sigma_0^3} D(T) + \dots\right]$ | | (15) |

The Henry's law equation can be written $q = p/K$, where K , a function of U_0 and T only, is given by

$$K = A^0 e^{-U_0/RT} \quad (16)$$

Substituting into Eq. (9) gives the adsorption isotherm equation

$$Q = p \int \frac{f(U_0) dU_0}{K(U_0 T)} = \frac{p}{K'_0} \quad (17)$$

where K'_0 is a constant corresponding to an average surface potential U'_0 . This result shows that regardless of the form of the distribution function, Henry's law yields an adsorption isotherm that is a straight line through the origin. All theoretical equations for adsorption on homotactic surfaces must reduce to Henry's law at low surface concentration; therefore all experimental isotherms must reduce to Eq. (17) at sufficiently low uptake. The zero pressure limiting slope of any isotherm allows us to calculate the limiting differential or isosteric heat of adsorption through Eqs. (4), (6), and (16). In practice, the pressure at which this occurs may be immeasurably small, as the requirement is for a low surface concentration on even the highest energy patches.

Langmuir himself was the first to propose the form that the Langmuir equation [Eq. (13)] would take for a set of sites of different energies:

$$\theta = \sum_i \Delta\delta_i \theta_i \quad \text{or} \quad \theta = \sum_i \frac{\Delta\delta_i p}{K_{i+p}}$$

where $\Delta\delta_i$ is the fraction of the surface characterized by K_i [Eq. (16)] and θ is the fraction of the surface occupied at pressure p .

Zeldowitch [9] and later Roginsky [10] and Halsey and Taylor [11], still using the Langmuir equation, replaced the concept of a set of sites with a continuous distribution of energies, thus permitting the summation to be replaced with an integral. It was found that by selecting an exponential energy distribution of the form

$$f_i = \frac{d\delta}{dU_0} = C e^{-U_0/U'_0}$$

over the whole range of U_0 , both positive and negative, the integral yielded the Freundlich equation in the form

$$\theta = A(p/p_0)^{k'/U'_0}$$

In these early efforts, the goal was to find an analytical description of $Q(p)$ using a specific theoretical model for adsorption on a homotactic surface and an assumed distribution function. An alternative way to use Eq. (9) is to assume the form of both $Q(p)$ and $q(p, U_0)$ and thence derive the distribution function $f(U_0)$ by inversion. That this can be done and that a unique solution exists for $f(U_0)$ was demonstrated rigorously by Sips [12]. To describe the experimental isotherm, Sips chose for $Q(p)$ an empirical equation of the form

$$Q(p) = Ap^c / (1 + Ap^c)$$

and for $q(p, U_0)$ took once more the Langmuir equation. He inverted the integral equation by means of a Stieltjes transform and obtained for $f(U_0)$ a unique distribution function that he showed to be nearly equivalent to a Gaussian distribution of adsorptive energies.

An effort to evade the Langmuir equation and model mobile adsorption was made by Harkins and Stearns [13]. The results were marred by the simplifications needed to solve their model function $q(p, U_0)$ explicitly for the quantity adsorbed.

Another way to avoid introducing the Langmuir equation with its mechanism of localized adsorption and no lateral interaction was pointed out by Morrison et al. [14]. By differentiating Eq. (9) one obtains

$$f_i = \frac{1}{q_i} \frac{dQ}{dU_0} \quad (18)$$

For the solution of this equation, a new set of experimental results are demanded, namely q^{diff} , the differential heat of adsorption, as a function of Q . Equation (18) still contains the unknown function $q(p, U_0)$. This function can, however, be eliminated when we know q^{diff} as a function of Q at absolute zero. At that temperature, every surface patch is filled in the serial order of its adsorptive potential, beginning with the greatest. A surface patch is therefore either completely filled or completely empty. The function $q(p, U_0)$ can be replaced with the Dirac delta function, sometimes called in this context the condensation isotherm. This results in

$$f(U_0) = \lim_{T \rightarrow 0} \left(\frac{dQ}{dq^{\text{diff}}} \right) \quad (19)$$

The relation between U_0 and q^{diff} is given in Eqs. (4)–(6). In order to use this method, the heat adsorption and the heat capacity of the adsorbed film must be measured at a series of low temperatures for various surface concentrations and the zero degree heats calculated by extrapolation. In spite of this tremendous experimental effort, the results are flawed, as we see from Eq. (4) that at absolute zero, $q^{\text{diff}} = U_0 + aP^{\text{ia}}$. The interaction term is of the same magnitude as q^{diff} and not easily determined. The distribution obtained, while of the correct shape, is displaced by the molar value of the adsorbate–adsorbate interaction at 0 K.

The replacement of the kernel function $q(p, U_0)$ with the condensation isotherm has been used by several authors, invoking the so-called condensation approximation at experimental temperatures far from absolute zero. These efforts generally use Eq. (18) without observing the temperature limitation. The condensation approximation can also be applied in Eq. (9) directly:

$$Q(p) = \int q_{ca}(p, U_0) f(U_0) dU_0 \quad (20)$$

where q_{ca} represents the condensation isotherm. This can be shown to give

$$f(U_0) = - \left[\left(\frac{\delta Q}{\delta p} \right) \left(\frac{\delta p}{\delta U_0} \right) \right]_{p=p_i} \quad (21)$$

where $\delta Q/\delta p$ is the slope of the adsorption isotherm and $\delta p/\delta U_0$ is obtained from the relation between the condensation pressure and the adsorptive potential.

Applications of the condensation approximation have been well reviewed by Rudzinski and Everett [15]. In general we can say that ignoring the equilibrium thermal distribution of the adsorbate among the surface patches of different values of U_0 can result in a seriously distorted picture of the adsorptive potential distribution.

No analytic solution of Eq. (9) has yet been made based on reasonable models of adsorption incorporating adsorbate–adsorbate interaction. Such a solution may not be possible.

2. Early Nonanalytic Solutions of the Integral Equation of Adsorption

The period of renewed adsorption research activity in the decade of the 1950s happened at a time when high speed electronic computing was just becoming available to researchers in this field. This made the numerical solution of Eq. (9) a feasible undertaking. For the first time, it was possible to at least calculate the numerical values of $Q(p, U_0)$ from the integral equation of adsorption using more theoretically sophisticated kernel functions that incorporated adsorbate–adsorbate interaction, together with a reasonable distribution function.

The first such solutions were carried out by Ross and Olivier [1, p. 129; 6,7]. Using Gaussian distributions of adsorptive potential of varying width, they computed tables of model isotherms using kernel functions based on the Hill–de Boer equation for a mobile, nonideal two-dimensional gas and on the Fowler–Guggenheim equation [Eq. (14)] for localized adsorption with lateral interaction. The fact that these functions are implicit for quantity adsorbed was no longer a problem since they could be solved iteratively in the numerical integration.

It was not actually possible to fit data to the computed models using numerical methods in 1957; while computer speeds were astonishing at the time, they were at least 1×10^4 slower than today's desktop personal computers and had very limited memory. Ross and Olivier developed a technique to find the best-fitting model for an experimental isotherm data set by means of graphical overlays. They found that excellent fits to the experiment data could be obtained provided that the degree of heterogeneity was not too great. As pointed out in Sec. II.B.1, a good fit to the data does not in itself verify a kernel function or the distribution. However, as the adsorbent becomes more and more homotactic, its isotherms should approach agreement with the kernel function itself. This was shown to be the case for adsorption measurements on a series of carbons graphitized at increasing temperatures, culminating in the highly graphitized carbon black P-33, whose isotherms of argon and nitrogen at 77 and 90 K are closely fitted by the Hill–de Boer equation in the monolayer region. By also correctly describing the heat of adsorption as a function of quantity adsorbed for heterogeneous surfaces, this work confirmed Eq. (9) as a powerful tool for investigating surface heterogeneity and the validity of the two-dimensional nonideal gas model for the kernel function.

In later work, Ross and Morrison [16,17] and Sacher and Morrison [18] were able to make several advances. The van der Waals equation of state for real gases, which is the basis of the Hill–de Boer equation, is known to be rather inaccurate. Morrison and coworkers based their kernel function on a two-dimensional form of the much better virial equation of state [Eq. (15)]. But importantly, advances in

computing resources made it possible to solve Eq. (9) for the unknown distribution function rather than assuming a form a priori.

Again, it was found to be difficult to fit uniquely isotherm data for very heterogeneous surfaces. A limitation lies in the fact that the kernel functions used were only models for monolayer adsorption, yet it is well known that adsorption proceeds to multilayers as pressure is increased. To ensure that the more strongly adsorbing portions of the surface remained in the monolayer range, only the lowest pressure portion of the isotherm could be used. This means that the low adsorptive energy portions of the surface are contributing little information in the total amount adsorbed, making their estimation uncertain. If higher pressure data are included in $Q(p)$, then multilayers exist on some surface patches; hence these are not correctly modeled by the kernel function.

III. APPLICATION OF DENSITY FUNCTIONAL THEORY

While good descriptions of adsorption on uniform surfaces in the submonolayer region are available, only recently has accurate calculation of the whole isotherm, including the multilayer region, been demonstrated [19]. These calculations use a modified nonlocal density functional theory (MDFT). The first use of multilayer local isotherms calculated by MDFT in obtaining a measure of surface energetic heterogeneity for several solid adsorbents was reported in 1996 [20].

The formalism of density functional theory (DFT) has received considerable attention as a way to describe the adsorption process at the fluid/solid interface. The older approach was to treat the adsorbate as a separate, two-dimensional phase existing in equilibrium with the bulk gas phase. This model works well in the monolayer region, but at higher surface concentrations the formation of multilayers requires the adoption of some sort of three-dimensional model to account for increasing adsorbate–adsorbate interaction and diminishing adsorption potential.

Using density functional theory, the adsorbative can be treated as a single, inhomogeneous fluid phase. The fluid varies in density from that of the bulk gas to a much higher value at the adsorbent surface in response to the strength and configuration of the surface adsorptive forces. In this paradigm, there is no separate adsorbed phase; indeed, the concept of a monolayer capacity, fundamental to the two-phase paradigm, has disappeared as well. The benefit of this approach is that the isotherm can be modeled from the Henry's law region through to saturation, or even above the adsorbative's critical temperature.

In particular, the ability with DFT to model physical adsorption in a pore space of slitlike or cylindrical geometry has led to potentially useful methods for extracting surface area and pore size distribution information from experimental adsorption isotherms [21]. The predictions of density function theory have been reported to compare well with the results of simulations [22,23] using Monte Carlo or molecular dynamics methods. We have made stringent comparisons to real data [19] for the adsorption of nitrogen and argon on the near-homotactic surface of a highly graphitized carbon, Sterling FT-G(2700). In performing such comparisons, the only unknown intensive parameter is the Lennard-Jones pairwise interaction energy ϵ_{sf} between the adsorbate and adsorbent atoms. Using the customary

Tarazona [25] prescription (with corrected weight functions) for the free energy density functional, we found that the experimental isotherm data in the monolayer region of coverage can be moderately well described by DFT calculations; however, in the multilayer region of the isotherm, the quantity adsorbed per unit area is significantly overpredicted. Recent work [19] showed that a modification to the mean field approximation used to calculate the attractive component of the configurational chemical potential leads to the theoretical isotherms that agree closely with experiment over a six-decade range of pressure. An example is shown in Fig. 2.

A. The Deconvolution Method

The integral equation of adsorption, Eq. (9), can be rewritten in specific units as

$$Q(p) = \int d\varepsilon q(p, \varepsilon) f(\varepsilon) \quad (22)$$

where $Q(p)$ is the total quantity of adsorbate per gram of adsorbent at pressure p ; $q(p, \varepsilon)$, the kernel function (the local isotherm), describes the adsorption isotherm for an ideally homotattic surface characterized by an interaction energy ε as quantity of adsorbate per square meter of surface; and $f(\varepsilon)$ is the surface area distribution function with respect to ε . The quantity ε [Eq. (1)], as we shall see, is closely

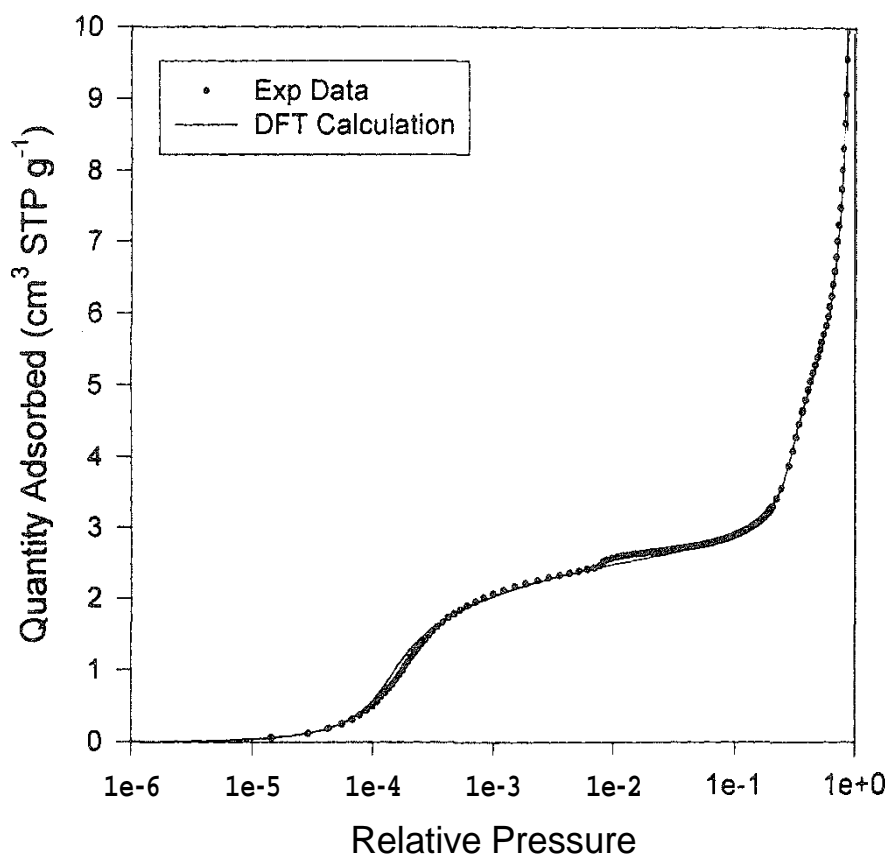


FIG. 2 Experimental data for nitrogen at 77 K on Sterling FT-G(2700) compared to MDFT calculation.

related to the adsorptive potential and can be related to the quantity aP^{ads} in Eq. (3) and in Fig. 1.

While DFT allows us to calculate values for $q(p, \varepsilon)$, it of course provides no analytic form for the function, and in general the form of $f(\varepsilon)$ is also unknown. However, by using carefully designed numerical methods, model isotherms calculated by MDFT can be used in carrying out the inversion of the discretized form of the integral equation of adsorption. In this way one can determine the effective adsorptive potential distribution of the adsorbent from the experimental adsorption isotherm. The method used can be expressed by

$$Q(\mathbf{p}) = \sum \mathbf{q}(\mathbf{p}, \varepsilon_i) \mathbf{f}(\varepsilon_i) \quad (23)$$

where $Q(\mathbf{p})$ is the experimental adsorption isotherm interpolated onto the vector \mathbf{p} of pressure points, $\mathbf{q}(\mathbf{p}, \varepsilon_i)$ is a matrix of quantity adsorbed per square meter, each row calculated by MDFT for a value of ε at pressures \mathbf{p} , and $\mathbf{f}(\varepsilon_i)$ is the vector of positive or null values whose terms represent the area of surface in the sample characterized by energy ε_i . The total surface area of the sample is given by $A^s = \sum_i f(\varepsilon_i)$. The solution values desired are those positive numbers that most nearly, in a least squares sense, solve Eq. (23). Additional constraints on the solution may be required to stabilize the deconvolution process [26].

Equation (23) differs from previous work in an important way. In previous attempts, $Q(\mathbf{p})$ was the amount adsorbed at the experimental pressures \mathbf{p} . This required that $\mathbf{q}(\mathbf{p}, \varepsilon_i)$ be calculated for that specific set of pressures and that the size of $\mathbf{f}(\varepsilon_i)$ be no greater than the number of experimental points. Not only does this result in a large computing task, it also causes the evaluation of $\mathbf{f}(\varepsilon_i)$ to be subject to a varying bias depending on the number of isotherm points and where on the pressure scale they were measured. The automatic adsorption equipment available today permits a large number of experimental points to be measured, and the isotherm can be interpolated accurately onto a predetermined optimized set of pressures. Hence the vector \mathbf{p} can be chosen to best represent the kernel function over the wide pressure range required by the set of ε_i .

If we consider m members of the set of ε and a vector \mathbf{p} of length n , it is clear that $n \geq m$ must hold. If $n = m$, the solution vector $\mathbf{f}(\varepsilon)$ can be "noisy" because of even small imperfections in the data or model. For $n > m$, the solution is smoother because of the additional data constraints. Various other regularization techniques have been proposed to mitigate the inversion problem; in this work we use the method of cominimization of the second derivative of $\mathbf{f}(\varepsilon)$ together with an over-determined matrix for which $n > 2m$.

B. Parameters of the Model Matrix

For use with Eq. (23), a model matrix was calculated by the MDFT method [19] using the parameters suitable for nitrogen at 77.3 K. For convenience, the values of ε were specifically the values of ε_{sf}/k used to calculate the wall potential $V(z)$ of that reference, and ranged from 20 to 100 K in steps of 2.0 K. Relative pressure points were chosen in geometric progression from 1×10^{-6} to 0.6 with 40 points per decade. Model isotherms were normalized to 1 m^2 of surface.

C. Results

The data reported here were obtained using a Micromeritics ASAP 2010 equipped with an optional 1 torr pressure transducer. Low pressure data were corrected for thermal effusion.

1. Graphitic Carbons

To confirm the deconvolution algorithm, we show in Figs. 3a and 3b the result of applying Eq. (23) to the experimental data of Fig. 2. Since this data set was used in developing the MDFT model, we would expect to recover a monomodal energy distribution with $e_{sf}/k = 57.0$ K, as used in the fit shown in Fig. 2. The best fit contained contributions from the classes representing $e_{sf}/k = 56$ and 58, with an area-weighted mean of 56.7 K, which is satisfactory agreement. The total surface area obtained is $12.4 \text{ m}^2/\text{g}$. The BET area of this certified reference material is $11.1 \text{ m}^2/\text{g}$. Because the MDFT model ignores the slight corrugation of the wall potential, the commensurate film transition seen at 0.008 relative pressure is not reproduced.

Figures 4a and 4b illustrate the application of Eq. (23) to the nitrogen isotherm obtained with Vulcan 3-G(2700). While graphitized at the same temperature as the Sterling FT, Vulcan has previously been reported as less uniform than the Sterling material [24]. As additional evidence, note that the commensurate film transition near $0.008 p_{\text{rel}}$ seen in Figs. 2 and 3 is not experimentally detected on the Vulcan surface. The area-weighted mean value of ε_{sf}/k is 56.1 K, and the total surface area is $80.78 \text{ m}^2/\text{g}$. The surface area by BET is $73.5 \text{ m}^2/\text{g}$.

2. Nongraphitized Carbon

An example of a much more heterogeneous surface is shown in Fig. 5. The adsorbent in this case is a nonporous carbon black designated C4, used by ASTM Committee D24 as a reference reinforcing black.

The total surface area by the present method is $138.60 \text{ m}^2/\text{g}$; the BET method gives $129.63 \text{ m}^2/\text{g}$. The weighted mean value of ε_{sf}/k is 53.61 K. The central mode of the distribution is somewhat lower than that for the graphites.

3. Noncarbon Adsorbents

Candidate adsorbents for the present method must not be microporous; that is, the adsorption isotherm must be that of a free surface at least through near completion of the monolayer. Zeolitic adsorbents and activated carbons are excluded by this requirement, but mesoporous materials are usually appropriate.

Figure 6 shows the interaction parameter distribution and the goodness of fit for a sample of controlled pore glass, CPG-120. Again we see a multimodal distribution with rather more of the surface having a low interaction value compared to carbon. The mean value of the interaction parameter is 51.54, and the indicated surface area is $133.25 \text{ m}^2/\text{g}$. The BET area is calculated to be $124.82 \text{ m}^2/\text{g}$. Fitting the data up to a relative pressure of 0.6 was possible because pore filling is negligible below about 0.8 relative pressure with this sample.

The isotherm for a yet more complex surface is shown in Fig. 7a. The adsorbent is an extruded silica-alumina catalyst support used by Micromeritics Instrument

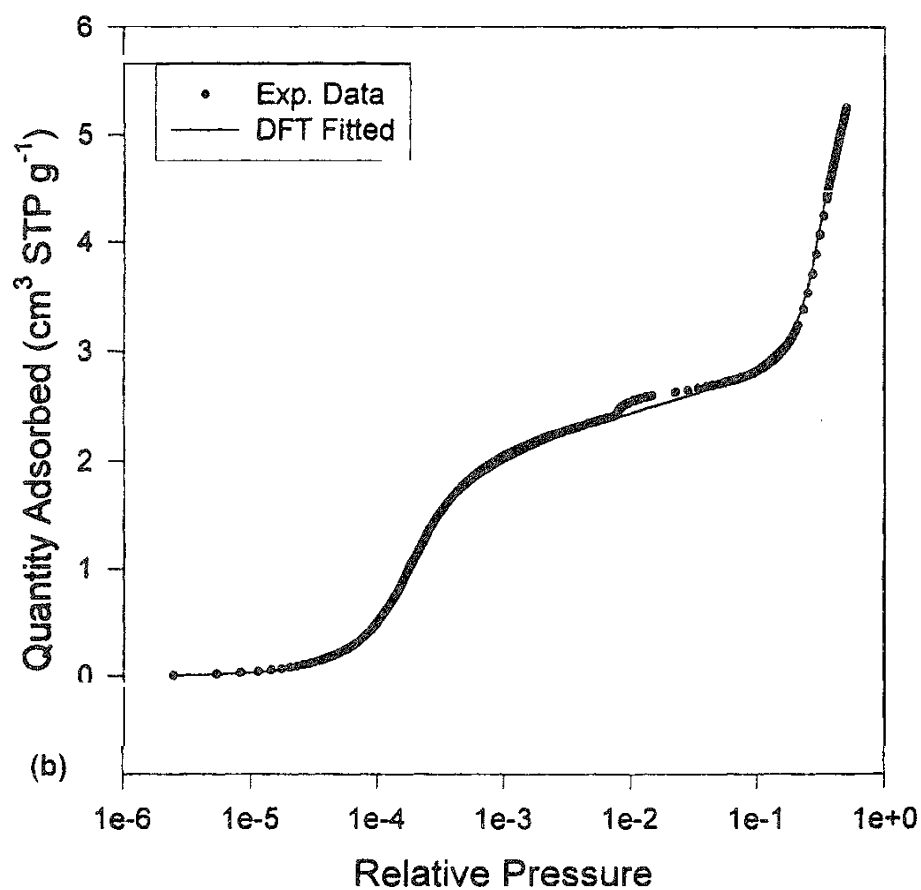
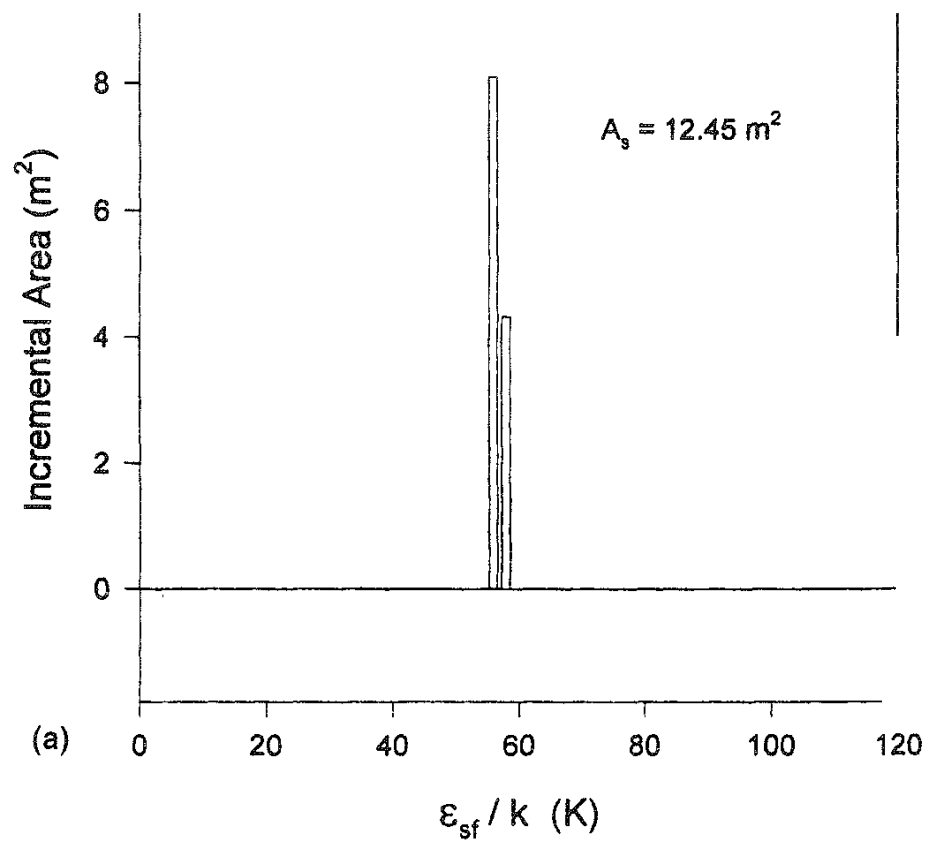


FIG. 3 (a) Expected recovery of a monoenergetic surface from the application of Eq. (20) to the experimental isotherm of nitrogen adsorbed at 77 K on Sterling FT-G(2700), shown in (b).

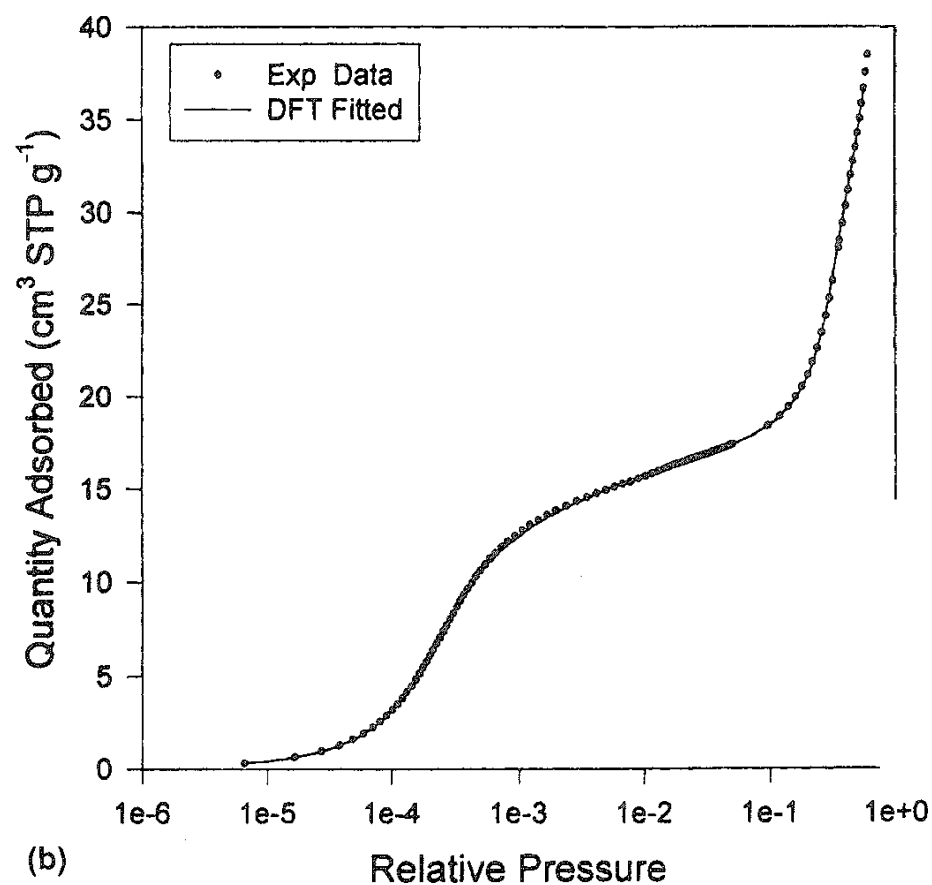
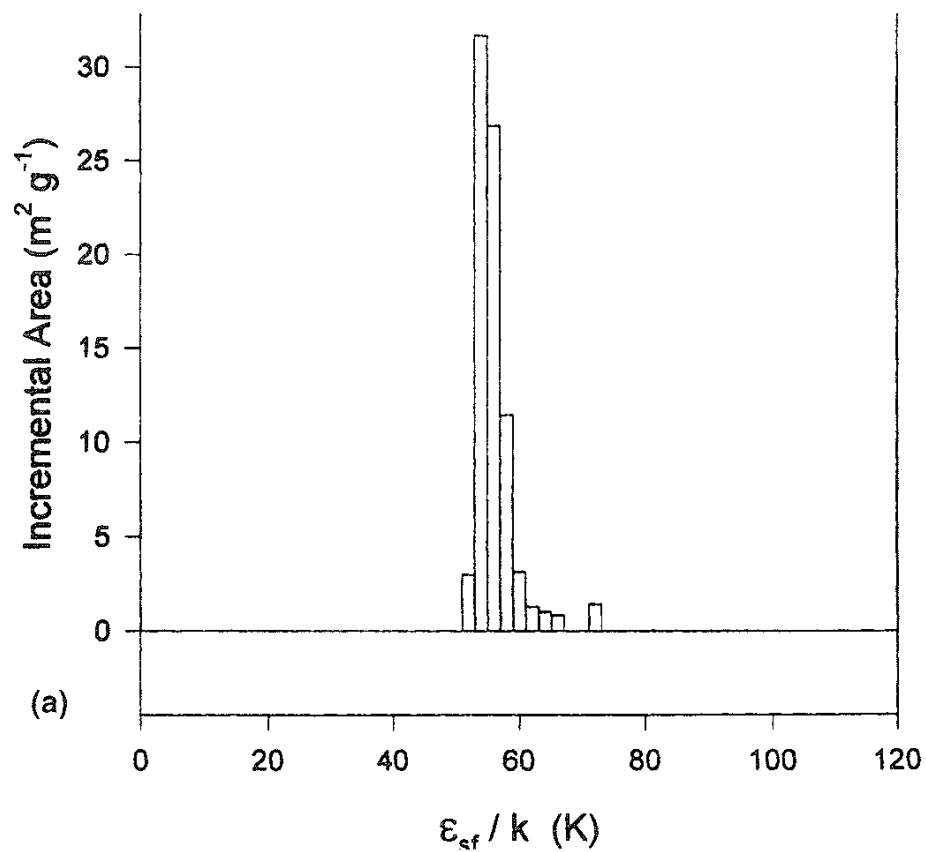


FIG. 4 (a) Distribution of ϵ_{sf}/k for Vulcan 3-G(2700) from the nitrogen isotherm at 77 K. (b) Nitrogen isotherm data showing the excellent DFT fitted result,

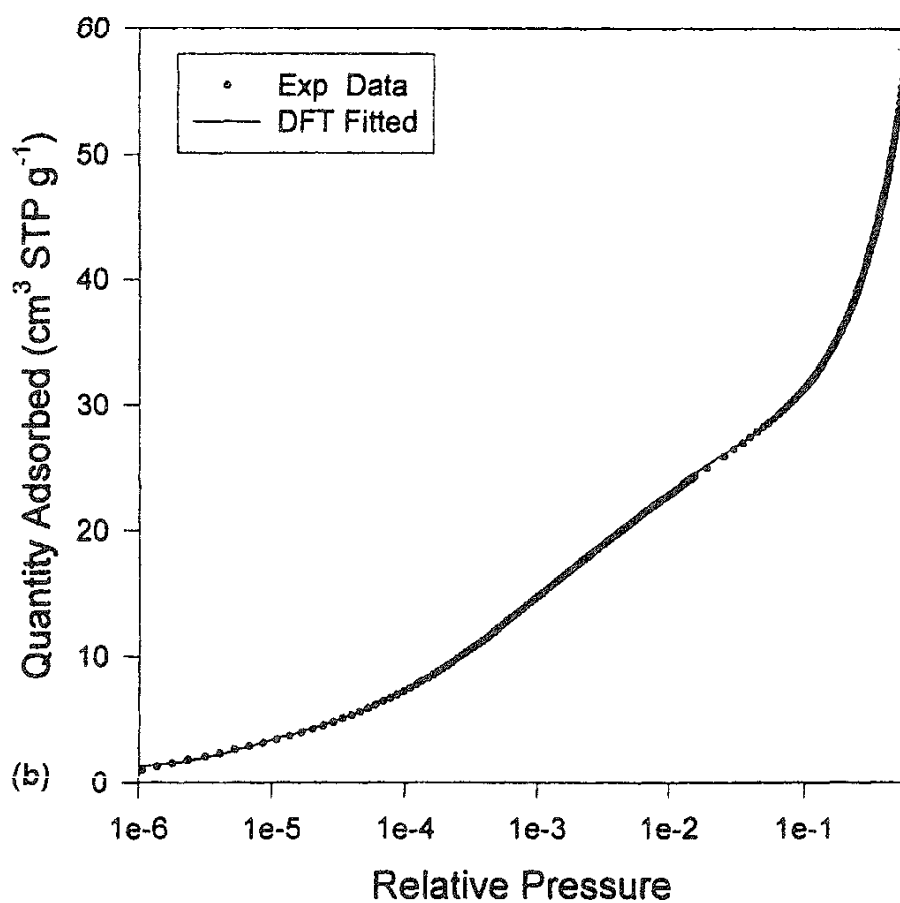
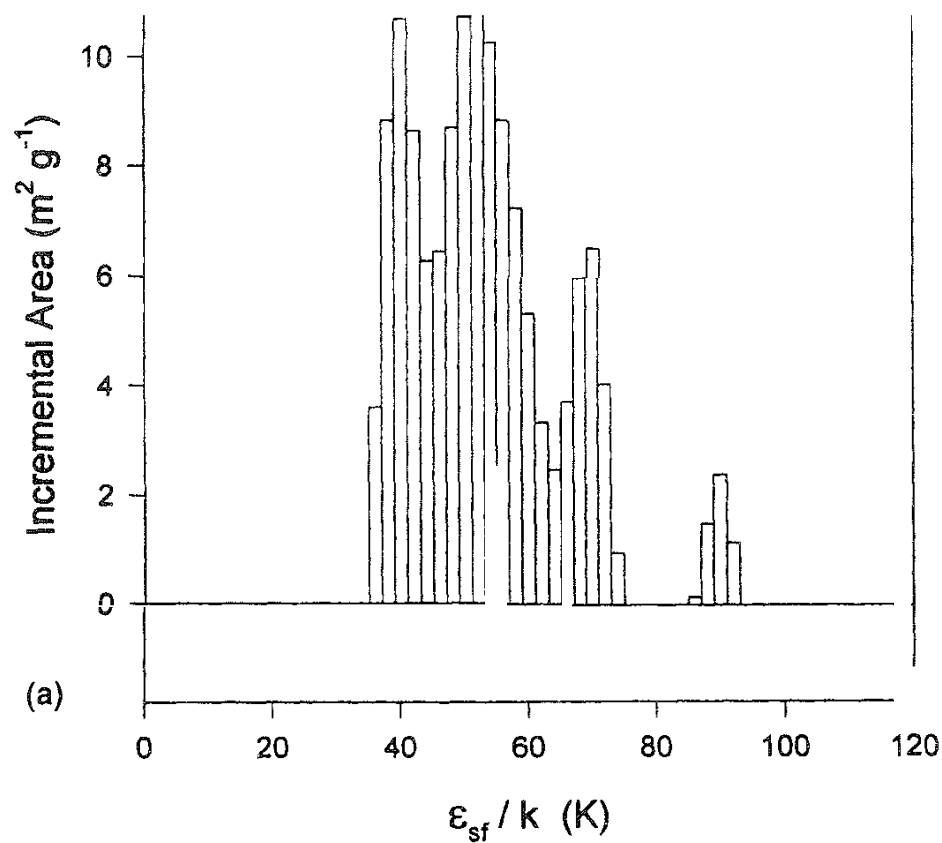


FIG. 5 (a) Distribution of ε_{sf}/k for ASTM carbon C4 from the nitrogen isotherm at 77 K. (b) Nitrogen isotherm data showing the DFT fitted result.

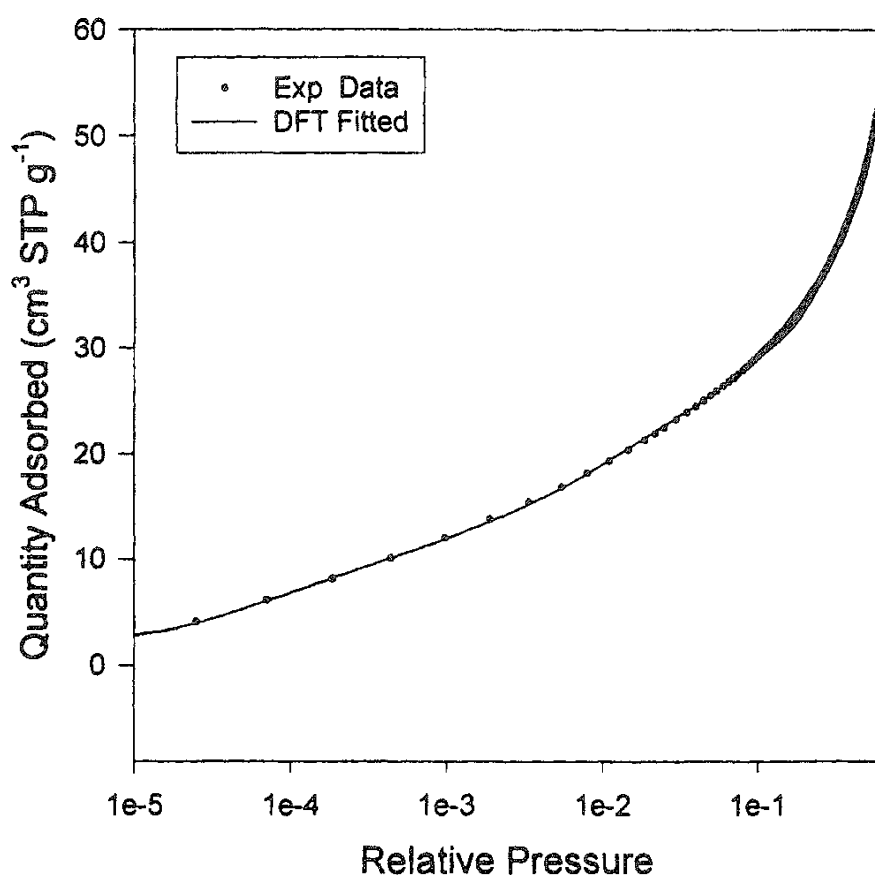
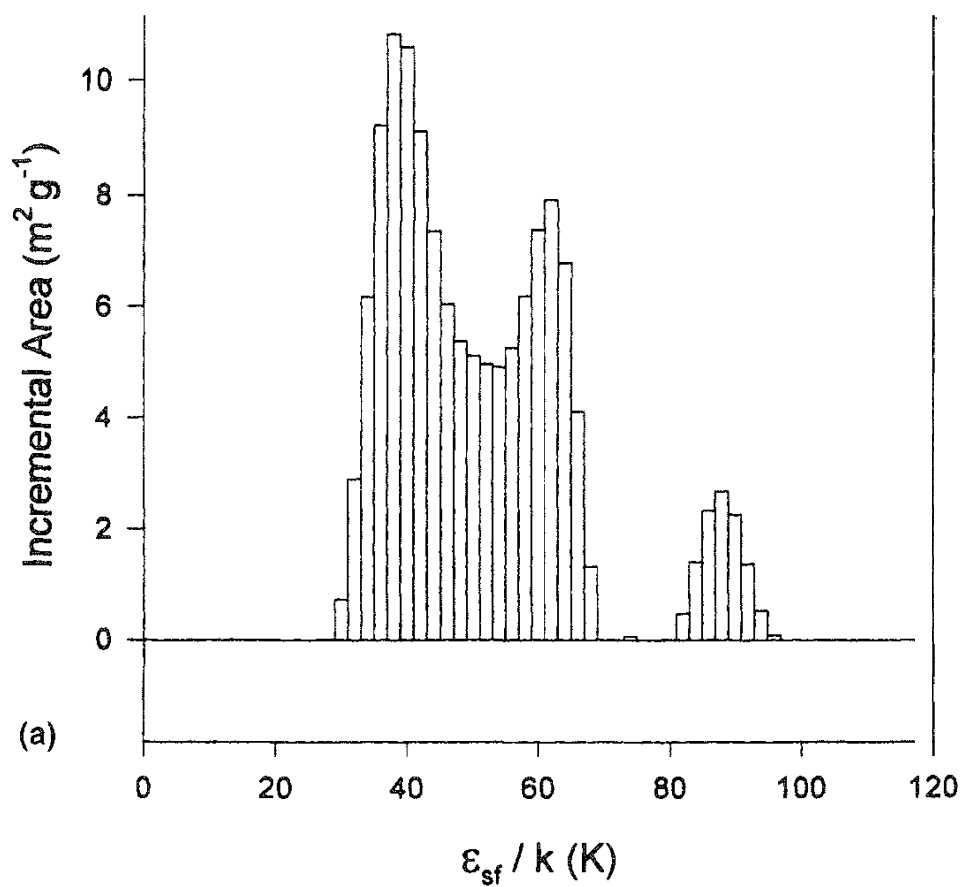


FIG. 6 (a) Distribution of ϵ_{sf}/k for CPG-120 from the nitrogen isotherm at 77K (b) Nitrogen isotherm data showing the DFT fitted result

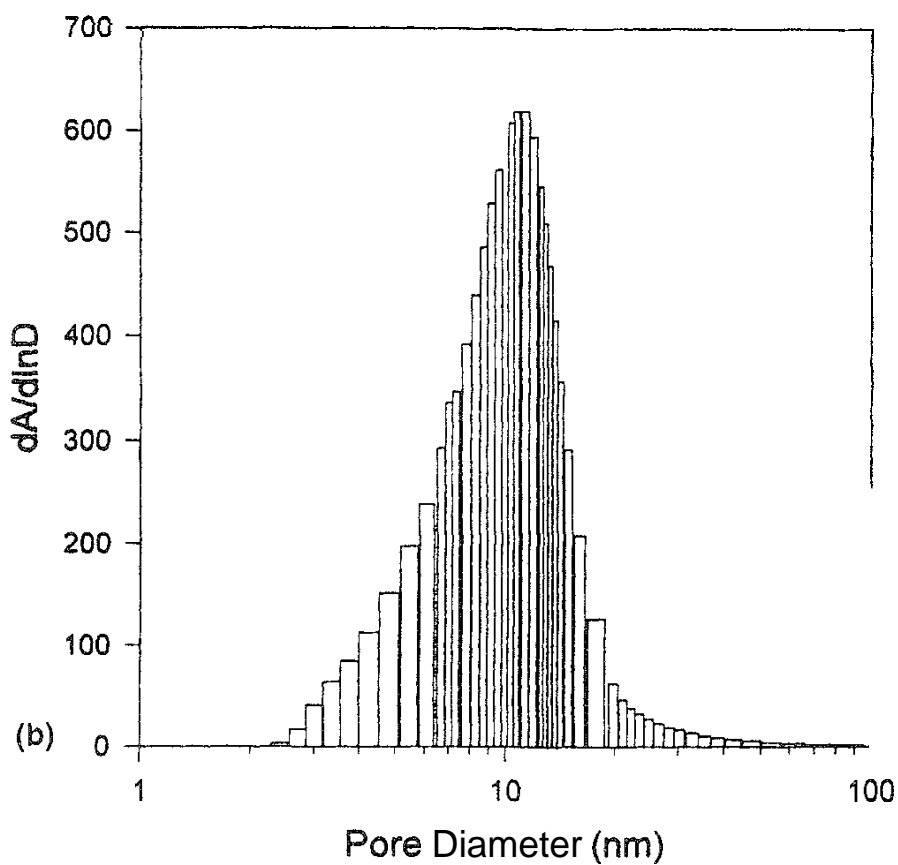
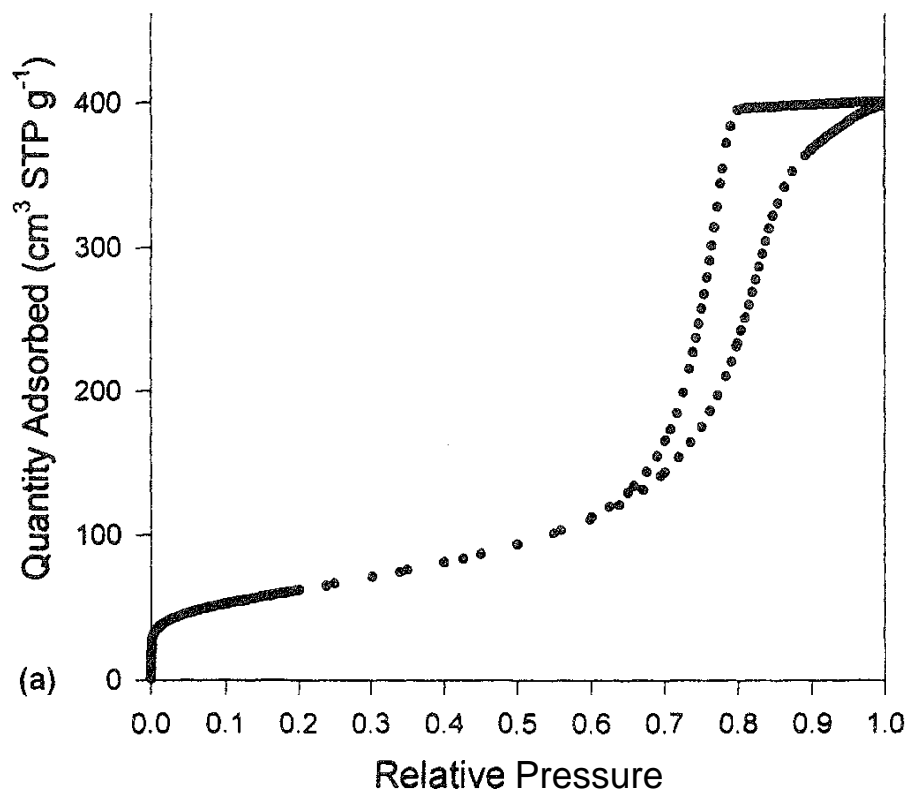


FIG. 7 (a) Adsorption isotherm of nitrogen at 77 K on a catalyst support reference material. (b) Mesopore area distribution by BJH method using Harkins and Jura thickness curve.

Corp. as a surface area and porosity reference material. The sample is quite obviously mesoporous. The pore area distribution shown in Fig. 7b obtained with the BJH method, based on the Kelvin equation, with the Harkins and Jura thickness curve shows porosity extending upward from just below 3.0 nm. To avoid the effect of pore capillary condensation in this size range, the surface parameter analysis was performed with only the isotherm data below 0.4 relative pressure. The surface parameter distribution shown in Fig. 8a displays at least four modes that are resistant to high levels of regularization; there may indeed be two maxima in the ϵ_{sf}/k range between 45 and 65 K. Figure 8b shows the goodness of fit obtained from this distribution.

The mean value of the interaction parameter for the catalyst surface is 55.58 K, and the surface area is calculated to be 225.68 m²/g. The BET surface area calculated from these data is 223.26 m²/g; 247.14 m²/g is obtained from the BJH calculation.

IV. DISCUSSION

The magnitude of the surface adsorptive potential for an adsorbed nitrogen molecule depends on two major factors: (1) the local density or proximity of the constituent atoms of the adsorbent at the site of adsorption and (2) the chemical nature of those atoms; for instance, their size, polarizability, susceptibility, and ionic charge. We have extracted the energy parameter distribution in the preceding examples in terms of ϵ_{sf}/k ; however, we must realize that it represents the net adsorptive energy variation arising from all factors. Even for a chemically pure graphite surface, a step dislocation will create a region along its base where the adsorptive potential will approximate 1.5 times the value for a plane and a region at its top edge with a potential about 0.5 the flat surface value. The thermodynamic meaning of the magnitude of the interaction parameter value is determined in the following way.

Although DFT yields no general analytic form for the adsorption isotherm, we know that in the limit of low amount adsorbed it must converge to Henry's law,

$$p = Kq/q_m, \quad q \ll q_m \quad (24)$$

q_m is the "monolayer capacity." The limiting slope, K , of the model isotherms can readily be calculated from the numerical results at very low pressure at each ϵ_{sf}/k value. The definition of K is given by Eq. (16):

$$K = A^0 e^{-U_0/RT}$$

To determine U_0 in terms of ϵ_{sf}/k , we plot $\ln(K)$, vs. ϵ_{sf}/k as shown in Fig. 9. From the slope of the regression line we obtain

$$U_0 = 0.2450RT(\epsilon_{sf}/k) \quad (25)$$

where U_0 is the adsorptive potential on a patch characterized by ϵ_{sf}/k . From this we can obtain the limiting isosteric heat of adsorption for the patch, since by Eq. (4) $q^{st} = U_0 + (3/2)RT$. The zero pressure limit of the isosteric heat of adsorption for

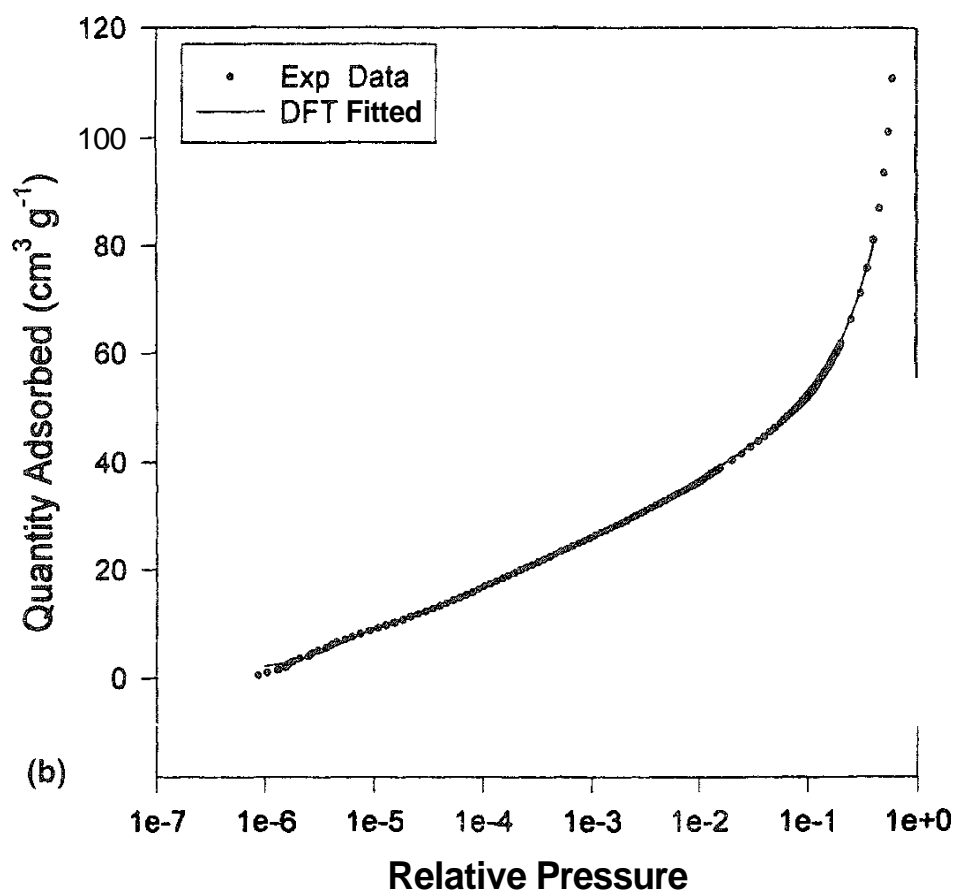
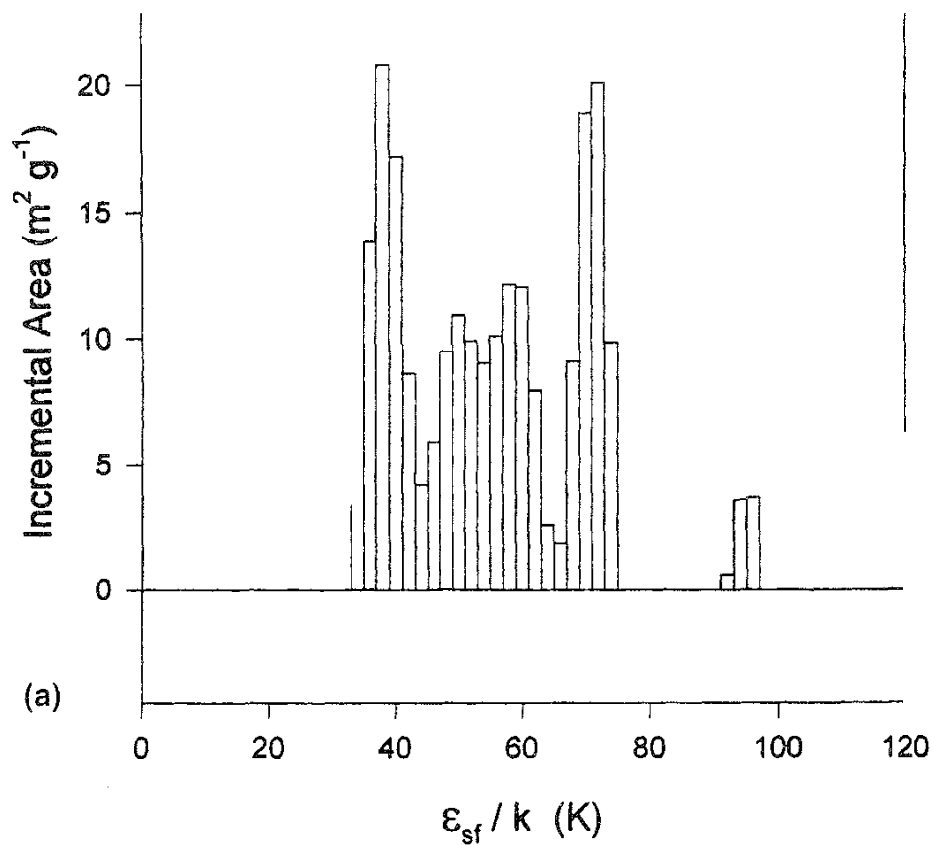


FIG. 8 (a) Distribution of ε_{sf}/k for a silica-alumina catalyst support from the nitrogen isotherm at 77 K. (b) Nitrogen isotherm data showing the MDFT fitted result.

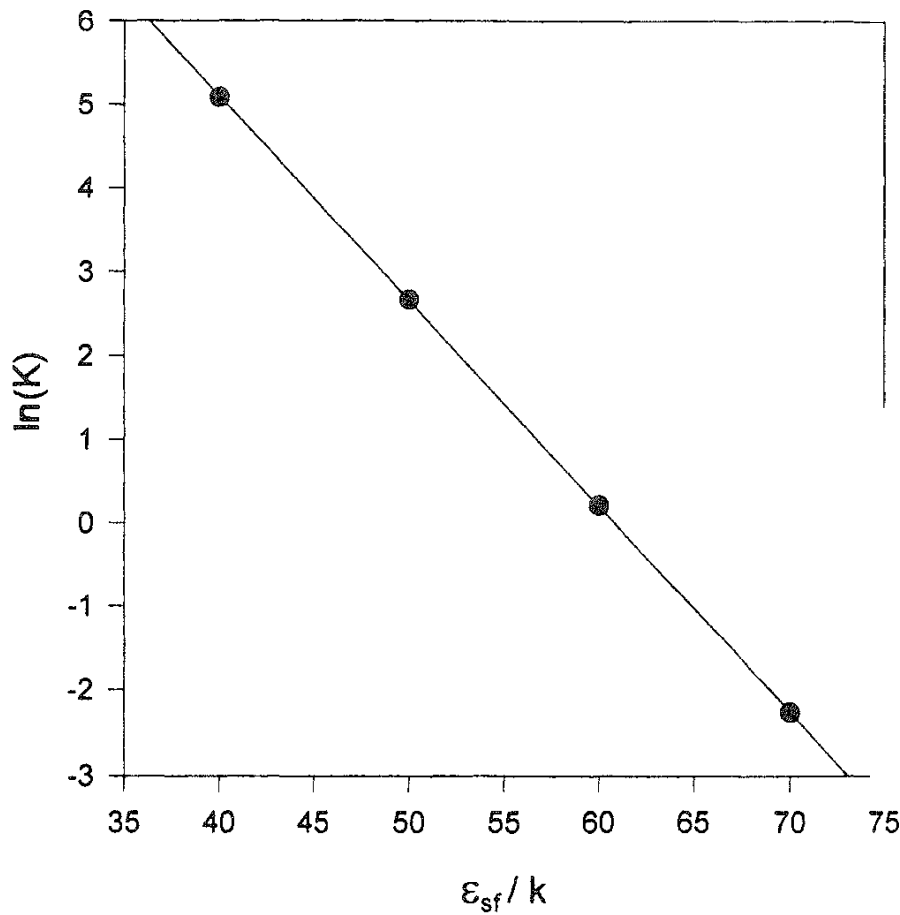


FIG. 9 Plot showing the logarithmic relation between the Henry's law constant and ϵ_{sf}/k .

the whole surface can be calculated from the reported distributions of ϵ_{sf}/k using Eqs. (24) and (25) together with Eq. (16):

$$U_0 = \frac{\sum U_{0i} a_i / K_i}{\sum a_i / K_i} \quad (26)$$

where a_i is the area of the i th patch. The results of this calculation are shown in Table 2, together with total surface areas determined with the present method. The BET values are included for reference.

The value of U_0 for Sterling FT-G(2700) from this work, corresponding to 2.15 kcal/mol, compares very well with the best estimate of Ross and Olivier [1, p. 228] of 2.16 kcal/mol. We see from Eq. (25) that the surface parameter intervals of 2.0 K correspond to about $(1/2)RT$.

V. CONCLUSIONS

Most previous attempts to employ Eq. (9) to extract a surface interaction distribution used a local isotherm function that describes only monolayer formation. Some, such as the Langmuir equation, are manifestly inappropriate, as they do not include adsorbate–adsorbate interaction, hence cannot describe an isotherm

TABLE 2 Calculated Heats at Zero Coverage with Surface Area Comparisons

| Adsorbent | Fig No | U_0 (kJ mol) | q^{st} (kJ mol) | A' (m ² /g) | A^s (BET m ² g) |
|-------------------------|--------|----------------|-------------------|--------------------------|------------------------------|
| Sterling FT-G(2700) | 3 | 9 | 9.96 | 12.4 | 11.1 |
| Vulcan 3 - G(2700) | 4 | 10.02 | 10.98 | 80.8 | 73.5 |
| ASTM - C4 | 5 | 14.12 | 15.09 | 38.7 | 129.6 |
| CPG-120 | 6 | 14.9 | 15.18 | 133.2 | 124.8 |
| Silica-alumina catalyst | 8 | 14.9 | 15.86 | 225.7 | 223.2 |

with a sigmoidal shape, as in Fig. 2. Others, such as the Hill–de Boer equation, Eq. (12), and the virial equation, Eq. (15) [16], can provide good descriptions of monolayer formation on moderately uniform surfaces yet have difficulty when applied to surfaces with a wide distribution of adsorptive potential.

A reason for the failure of previous methods was discussed in Sec. II.B.2. It can be better seen by inspection of the set of model isotherms shown in Fig. 10. As a reference, an approximate value of v_m is indicated at 0.2 cm³/m². If the range of heterogeneity of the sample surface is narrow, all surface patches can be sampled adequately without danger of multilayer formation on the higher energy portions. We can see, however, that if a significant part of the surface were characterized by a maximum value of ε_{sf}/k of 70, one would need to obtain data at pressures no greater than, say, 1 torr. At this pressure, patches with $\varepsilon_{sf}/k < 50$ would barely be contributing information to the total isotherm, and areas with $\varepsilon_{sf}/k > 70$ would be building multilayers, thus making a monolayer kernel function invalid. It is also clear from Fig. 10 that a multilayer model that incorrectly predicts the pressure range for the formation of a second layer relative to the monolayer will also fail to yield a good fit. The unmodified nonlocal DFT [25] is such an example [24].

The modifications to the DFT calculations that bring about the agreement seen in Fig. 2, while empirical in magnitude, have a plausible theoretical basis. For the present, the modifications assume that the surface of Sterling FT-G(2700) deviates undetectably from uniformity. To the extent that this is not true, we must point out that the parameter distributions obtained through Eq. (9) and reported here should be viewed as relative to that graphite surface.

The patchwise model underlying the integral equation of adsorption assumes that each patch adsorbs independently of others—that is, there are no "edge effects"—and the local isotherm function is assumed to account for all lateral, or adsorbate–adsorbate, interaction. If the patches are large, this assumption is valid. However, if adjacent patches are small and have quite different adsorptive potentials, then their occupancy at a given pressure will be different and also many adsorbed molecules will be near patch edges. A molecule at the boundary between patches of high and low occupancy will experience a kind of average lateral interaction different from that given by its local isotherm function, hence not be truly

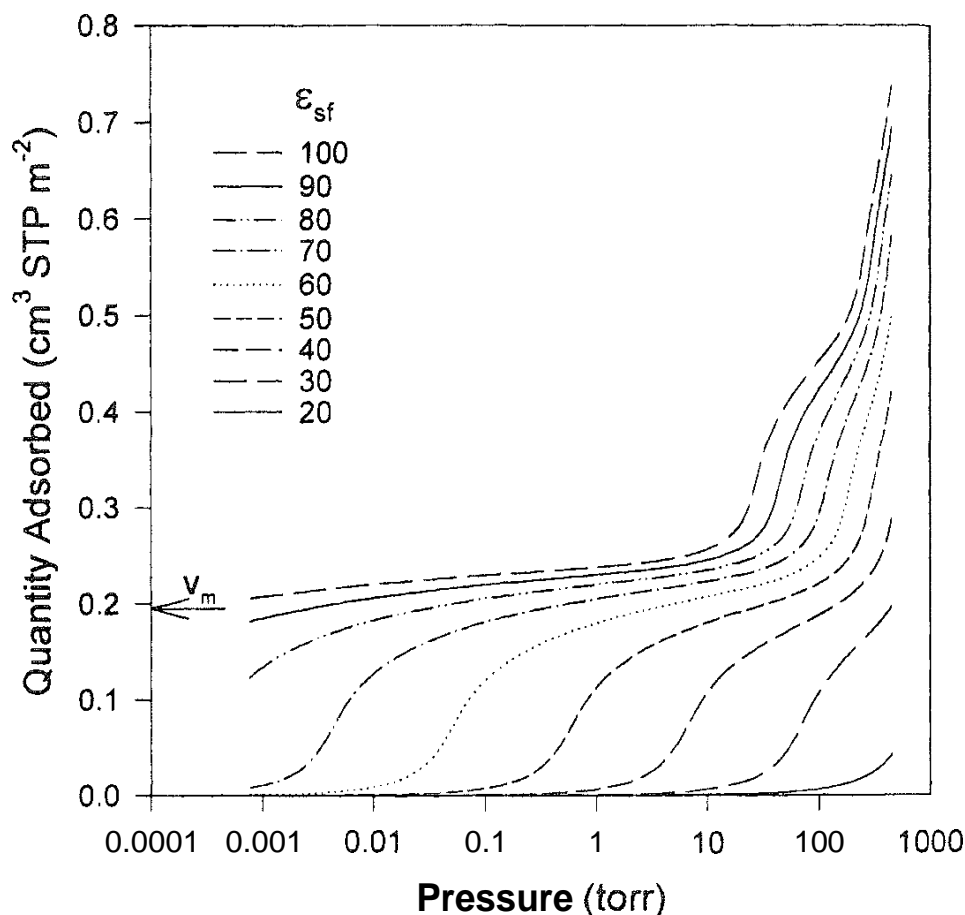


FIG. 10 Representative model isotherms for nitrogen on surfaces characterized by the indicated values of ϵ_{sf}/k .

independent of how adsorptive energy is distributed. This limitation of the patch-wise model is well known, so a question remains as to why it can work so well in reproducing the data. A tentative hypothesis is that the energy distributions of real surfaces are not random but tend to be correlated to the extent that neighboring patches differ but little in energy and occupation, thus greatly reducing edge effects.

REFERENCES

1. S. Ross and J. P. Olivier, *On Physical Adsorption*, Interscience, New York, 1964, p. 123.
2. I. Langmuir, *J. Am. Chem. Soc.* 38: 2267 (1916); 40:1361 (1918); *Phys. Rev.* 8:149 (1916).
3. J. H. de Boer, *The Dynamical Character of Adsorption*, The Clarendon Press, Oxford, 1953.
4. R. H. Fowler and E. A. Guggenheim, *Statistical Thermodynamics*, Cambridge Univ. Press, Cambridge, UK, 1949, p. 431.
5. C. Sanford and S. Ross, *J. Phys. Chem.* 58:288 (1954).
6. S. Ross and J. P. Olivier, *J. Phys. Chem.* 65:608 (1961).
7. J. P. Olivier and S. Ross, *Proc. Roy. Soc. (Lond.)* 265A:447 (1962).

8. T. L. Hill, *J. Chem. Phys.* 17:762 (1949).
9. J. Zeldowitch, *Acta Physicochim. URSS* 1:961 (1934).
10. S. A. Roginsky, *Compt. Rend. Acad. Sci. URSS* 45:61, 194 (1944); *Bull. Acad. Sci. URSS* 14 (1945); *Acta Physicochim. URSS* 20:227 (1945); 22:61 (1947).
11. G. D. Halsey, Jr. and H. S. Taylor, *J. Chem. Phys.* 15:624 (1947); G. D. Halsey, Jr., *J. Chem. Phys.* 16:931 (1948).
12. R. J. Sips, *J. Chem. Phys.* 16:490 (1948); 18:1024 (1950).
13. W. D. Harkins and R. S. Stearns, *J. Phys. Chem.* 58:292 (1954).
14. J. A. Morrison, J. M. Los, and L. E. Drain, *Trans. Faraday Soc.* 47:1023 (1951); L. E. Drain and J. A. Morrison, *Trans. Faraday Soc.* 48:840 (1952); 49:654 (1953).
15. W. Rudzinski and D. E. Everett, *Adsorption of Gases on Heterogeneous Surfaces*, Academic, London, 1992.
16. S. Ross and I. D. Morrison, *Surface Sci.* 52:103 (1975).
17. I. D. Morrison and S. Ross, *Surface Sci.* 39:21 (1973).
18. R. S. Sacher and I. D. Morrison, *J. Colloid Interface Sci.* 70:153 (1979).
19. J. Olivier, *J. Porous Mates*, 2:9 (1995).
20. J. Olivier, in *Proceedings of the Fifth International Conference on Fundamentals of Adsorption* (M. D. LeVan, ed.), Kluwer Academic, Boston, 1996, p. 699.
21. N. A. Seaton, J. P. R. B. Walton, and N. Quirke, *Carbon* 27:853 (1989).
22. C. M. Lastoskie, K. E. Gubbins, and N. Quirke, *Langmuir* 9:2693 (1993).
23. C. M. Lastoskie, K. E. Gubbins, and N. Quirke, *J. Phys. Chem.* 97:4786 (1993).
24. J. P. Olivier, W. B. Conklin, and M. v. Szombathely, in *Studies in Surface Science and Catalysis* 87, *Characterization of Porous Solids III (COPSI-III)* (J. Roquerol et al., eds.), Elsevier, Amsterdam, 1994, p. 81.
25. P. Tarazona, *Phys. Rev. A* 31:2672 (1985); 32:3148 (1985); P. Tarazona, U. M. B. Marconi, and R. Evans, *Mol. Phys.* 60:573 (1987).
26. C. L. Lawson and R. J. Hanson, *Solving Least Squares Problems*, Prentice-Hall, Englewood Cliffs, NJ, 1974.

14

Computer Simulations of the Structural and Thermodynamic Properties of Adsorbed Phases

WILLIAM STEELE Department of Chemistry, The Pennsylvania State University, University Park, Pennsylvania

- I. Introduction
- II. Algorithms
- III. Modeling the Interactions
- IV. Specific Examples
 - A. Elementary systems
 - B. Lennard-Jones atoms on various surfaces
 - C. Adsorption the critical region of the bulk fluid
 - D. Freezing of adsorbed layers
 - E. Energies of adsorption
 - F. Wetting and drying
- V. Discussion
- References

I. INTRODUCTION

Beginning about 40 years ago, algorithms that allow one to use computers to simulate the thermodynamic, structural, and dynamic properties of bulk molecular fluids began to appear in the scientific literature. The early studies based on these algorithms were limited to the simplest possible model fluids because of limitations imposed by the crude computers available at that time. Thus, hard sphere fluid properties were the first to be evaluated using this method. Both two- and three-dimensional systems were investigated. Inasmuch as these systems did not exist in reality, the results of these studies were a cornerstone of the development and testing of theories of the hard sphere and hard disk fluids. As computers increased in power and availability, the complexity of the systems investigated increased rapidly. At the same time, the variety of the algorithms developed to simulate

various thermodynamic ensembles increased from the initial Metropolis Monte Carlo method [1,2], which yields a simulated canonical ensemble by generating a Markov chain of states with appropriate probability rules, and the first molecular dynamics (MD) algorithms [3], which simulated the microcanonical ensemble by solving Newton's equations of motion for the particles that made up the ensemble,

In this early work and in nearly all subsequent computer studies, the success of a calculation that treats only a few hundred molecules in a box of volume equal to a few thousand cubic nanometers required that one eliminate the effects of the box walls on the fluid properties and also find a way to calculate the interactions between a molecule and the surrounding fluid when the molecule in question is near the box wall and so is lacking neighbors on one or more sides. The techniques of doing this begin with imposing periodic boundary conditions in which the box is surrounded by images of itself and the molecules in it. The walls of the box are made permeable to tile passage of molecules in (and out) by eliminating any trace of interaction between a molecule and the box wall. Because of the surrounding images, a molecule passing out through a wall will be accompanied by an image molecule passing in through the opposite wall, thus conserving the number of molecules N and minimizing finite-size effects. At the same time, the interactions of a molecule with its surroundings are evaluated by summing the (usually pairwise) interactions with both its real and its image neighbors out to some cutoff distance chosen to maximize precision while minimizing the time required to perform these sums. Both of these techniques have been described in detail in many review articles and books [4–7]. Their success relies on the decay of intermolecular spatial correlations over a distance that is significantly less than the box dimension. For fluids containing several hundred molecules this is usually not a problem (in three dimensions, the number 256 is often taken; in quasi-two-dimensional systems, 100 is frequently adequate), but of course the long-range spatial correlations present in solid phases can give rise to problems in the accuracy of the periodic boundary and minimum image conventions.

The application of these techniques to the simulation of adsorbed phases began to appear in the 1960s. The great majority of such studies are based on the idea that the solid adsorbent can be treated as a rigid, inert field of force that produces an inhomogeneous fluid when adsorbate molecules are in its vicinity. Clearly, the success of such simulations depends on the quality of the model used to represent the adsorbate–adsorbent (gas–solid) interactions. These models are discussed in Sec. III.

Although both molecular dynamics and Monte Carlo algorithms have been used in simulations of physical adsorption, this review is devoted primarily to the Monte Carlo simulations, since these provide better routes to the chemical potential (which gives the adsorption isotherm), among other thermodynamic and structural properties. In Sec. II, a brief discussion of some of the most useful Monte Carlo computer simulation algorithms is given. In Sec. IV, typical results from such simulations are presented. Conclusions are given in Sec. V.

It should first be noted that the introduction of a rigid solid adsorbent clearly alters the periodic boundary conditions for the fluid to be simulated. If the adsorbent is a nominally planar free surface, one has periodic boundary conditions and minimum image interaction calculations in only the two dimensions parallel to the

solid surface. In order to confine the adsorbate in the third dimension, i.e., in a region near the surface, it is conventional to introduce a hard wall that is parallel to the solid surface and at a rather large distance from it—large enough that changes in structure (i.e., density) due to its presence will be negligible. In practice, this amounts to a separation of 5–10 molecular diameters (of the adsorbed molecules) between the adsorbing surface and the hard boundary. Of course, this is not the only geometry encountered in sorption studies. In particular, sorption in porous solids is presently an active research area. If the pore is cylindrical, it is obvious that the only periodic condition will be in the direction parallel to the pore axis, as will also be the case with other pores with a closed cross section (triangular, elliptical, or rectangular, for instance). The frequently studied case of pores with parallel planar walls will be periodic in two dimensions and can be considered as an alternative to the free surface–hard wall system mentioned above, with the primary differences being that the two walls are usually assumed to be identical in their interactions with the sorbed fluid and that the properties of such fluids are frequently studied as a function of the wall separation. Finally, the case of sorption in the interstices of a packed powder or in a three-dimensional network of connected cavities such as those in zeolites are modeled with three-dimensional periodic boundary conditions.

Once the gas–solid energy and the gas–gas (adsorbate–adsorbate) interaction energies are chosen, one must pick a suitable algorithm from the large number that are now available. If transport, particularly surface diffusion, is of interest, molecular dynamics is usually the best starting point. (Transport can also be evaluated from Monte Carlo simulations [5,6], but this approach has the disadvantage that the elapsed time is taken to be proportional to the number of Monte Carlo trials attempted. While this seems to be reliable, the constant of proportionality is hard to estimate.) The original microcanonical molecular dynamics algorithm has now been supplemented by a number of approaches based on constrained dynamics that yield other ensembles [8–11]. For example, addition of the constraint that the total kinetic energy of all the molecules remains constant can be imposed on the Newtonian equations of motion (which then means that the total energy is no longer a conserved quantity). The result is a mechanical system with constant N , V , T , since temperature is proportional to the total kinetic energy of a fluid.

A variety of Monte Carlo algorithms are now available [4], and the choice is determined by the thermodynamic quantities that one wishes to simulate. In particular, an adsorption isotherm can be viewed as a determination of the chemical potential of the fluid as a function of the number of adsorbed molecules. This interpretation is based on the fact that adsorbed phases are usually studied when they are in equilibrium with the bulk phase that is generally the ideal adsorbate gas. This means that the chemical potentials μ_{bulk} and μ_{ads} of the two phases are equal. Since μ_{bulk} is equal to $\mu^0 + RT \ln p$ for an ideal gas (p should be replaced by the fugacity at high pressures where the bulk phase is nonideal), one has a straightforward method of relating the isotherm pressure p to the chemical potential of the adsorbed phase. The constant μ^0 can be calculated from molecular properties by standard methods [12]. In this way, grand canonical Monte Carlo (GCMC) algorithms in which the constant quantities are T , V , μ can be used to simulate the adsorption isotherm, which is now obtained from μ as a function of $\langle N \rangle$, where the brackets denote the ensemble average of a fluctuating quantity. A second thermo-

dynamic property of interest is the energy of the adsorbed phase or, more specifically, ΔU_m , the molar energy of adsorption from the gas. If this gas is ideal, the energy change will be due entirely to the potential energy acquired by the adsorbed molecules when they are transferred from the bulk gas to a location that is at or near the adsorbate surface. This energy is due to the interactions of the adsorbate molecules with each other and with the solid, and these two contributions can easily be evaluated separately in the simulation (and summed to give the experimental energy of adsorption). The molar energy of adsorption is related to the enthalpy change by an additive factor $RT = pV/N$. However, it should be noted here that these energy and enthalpy changes are not the partial molar quantities usually reported in experimental studies. For example, the isosteric heat q_{st} is the partial molar enthalpy change upon adsorption. If \bar{U}_m and \tilde{U}_m are the molar and partial molar energy, respectively, then \tilde{U}_m is equal to $\bar{U}_m + \partial \bar{U}_m / \partial N$. Thus, to evaluate the partial molar quantities from the molar quantities, one must either simulate the molar energy to a sufficiently high precision to allow one to differentiate it with respect to N or take the alternative route of evaluating the partial molar energy from the appropriate fluctuation formula in the GCMC ensemble. Theory gives [7,13]

$$\tilde{U}_m = \frac{\langle u_N N \rangle - \langle u_N \rangle \langle N \rangle}{\langle N^2 \rangle - \langle N \rangle^2} \quad (1)$$

where u_N is the total potential energy of N adsorbed molecules. Neither of these calculations is easy to perform accurately.

Equation (1) is an example of the evaluation of derivatives of thermodynamic quantities from fluctuation expressions valid for particular ensembles (Ref. 12, Chap. 3). Heat capacities can be obtained from fluctuations in the canonical (most convenient) and grand canonical ensembles; isothermal compressibilities (which are related to the slope of the adsorption isotherm) can be obtained from number fluctuations.

Two types of thermodynamic invariance of the local properties of an inhomogeneous fluid should be mentioned at this point. These arise from the mechanical and chemical equilibrium of such a fluid. The pressure tensor is a controlling factor in the mechanical equilibrium. For nonflowing fluids, this tensor is diagonal with elements p_{zz} , p_{xx} , and p_{yy} . If the z coordinate is taken to be perpendicular to the adsorbing surface, one can average over the x and y coordinates to obtain $p_{\tau\tau}$, the in-plane pressure tensor element. Mechanical equilibrium requires that there be no gradients in these elements in the direction of the force of the pressure element. Thus, for any x, y , $\partial p_{zz} / \partial z$ must be zero for all z in the fluid. A similar relation holds for the in-plane pressure tensor element. Clearly, this implies that a local pressure tensor must exist and that simulations of the local pressure tensor elements must obey these requirements. Such calculations rest upon expressions for the local pressure tensor elements in a small volume element δV located at \mathbf{r} in the fluid. It has been shown that the elements of the pressure tensor are given by a sum of three terms: the contribution due to molecules moving toward the solid (the ideal gas term); the contribution due to the intermolecular forces between pairs of adsorbate molecules, denoted here by 1 and 2; and the contribution due to the gas-solid

force on a molecule denoted here by 1. The explicit expression for the q th diagonal element of the tensor can be written as

$$p_{qq} = \frac{\langle \delta N \rangle kT}{\delta V} - \int_{q_l}^q dq_2 \int_{q_l}^{q_u} dq_1 \left\langle \frac{\partial u_{gg}(r_{12})}{\partial q_{12}} \right\rangle - \int_q^{q_1} dq_1 \left\langle \frac{\partial u_{gs}(x_1, y_1, z_1)}{\partial q_1} \right\rangle \quad (2)$$

where q can denote x , y , or z and q_l and q_u are the lower and upper limits of the position variables that define the adsorbed layer. Ordinarily, these are taken to be zero and l for z , where l is the thickness of the adsorbed layer, and $-\infty$ and $+\infty$ for x and y , the in-plane size variables. The brackets indicate an average over the configurations generated in the simulation. Note that the invariance in p_{zz} leads to an integral equation for the number density $n(\mathbf{r})$ in the fluid (Ref. 7, eq. 3.131).

Chemical equilibrium in an inhomogeneous fluid requires that the local chemical potential $\mu(\mathbf{r})$ be independent of \mathbf{r} . For a fluid in a canonical ensemble (either molecular dynamics or Monte Carlo), one considers a particular configuration of N molecules. An additional molecule is inserted at \mathbf{R}_1 ; this molecule interacts with the N molecules and the solid initially there but does not affect the simulated molecular configuration in any way. If the energy of this interaction is denoted by $u(1, N)$, where the added particle is at \mathbf{R}_1 and the A' particles are at positions denoted by \mathbf{R}_N , it can be shown that [14]

$$\mu - \mu^0 = RT \ln \frac{\langle \exp[-u(1, N)/kT] \rangle}{n(1)} \quad (3)$$

where $n(1)$ is the density of the fluid at point \mathbf{R}_1 . The average is taken over many computer-generated configurations of the adsorbed molecules in the ensemble. Insertion points can be chosen at any point in the fluid. The chemical potential of the fluid must be independent of location, or there could be a spontaneous transfer of molecules from the elements with higher chemical potentials to those with lower, which would mean that such systems would not be at the lowest global chemical potential and thus would not be in thermodynamic equilibrium. This method of simulating μ has been used successfully for many bulk model fluids, including nonspherical molecules where the coordinate \mathbf{R} includes orientational as well as translational variables. In the literature, one can see definitions of quantities such as the electrochemical potential for a fluid in an external electric field or the intrinsic pressure in which the contribution of the gas–solid force is omitted from the definition. These quantities will depend on position, but one still has the requirement that their values plus the contributions due to the external potential must be constant.

The expressions for the pressure tensor at a surface can be integrated to give the solid–fluid surface tension, which we here denote as γ (also called the spreading pressure):

$$\gamma A = \int_V \left[\frac{1}{2} (p_{xx} + p_{yy}) - p_{zz} \right] dV \quad (4)$$

where V is the volume of adsorbed fluid. This integral can be evaluated analytically to give [7,15]

$$\gamma A = - \left\langle \frac{1}{2} \left(x \frac{\partial u_{gs}}{\partial x} + y \frac{\partial u_{gs}}{\partial y} \right) - z \frac{\partial u_{gs}}{\partial z} \right\rangle - \frac{1}{4} \left\langle \frac{(r_{12}^2 - 3z_{12}^2)}{r_{12}} \frac{\partial u_{gg}(r_{12})}{\partial r_{12}} \right\rangle \quad (5)$$

The first ensemble average on the right-hand side of Eq. (5) is taken over all particles in the fluid, and the second is taken over all pairs of particles. Here, the gas–solid energy u_{gs} depends on the position of a particle in the fluid, and the gas–gas energy u_{gg} depends on the separation distance between particles 1 and 2. It has been suggested that the term involving the transverse derivatives of u_{gs} does not contribute to γA after averaging [16,17], but the universality of this argument is not completely clear at present.

Note that Eqs. (4) and (5) are valid only for a fluid adsorbed on a free surface where $p_{zz} = p_{\text{bulk}}$. In the general expression for γ that is as valid for pore fluids as for fluids on free surfaces, p_{zz} must be replaced for p_{bulk} . In the notation of Magda et al. [18], Eqs. (4) and (5) are actually for a quantity denoted by γ^* that becomes equal to γ only in the limit of large pore size. For a fluid in a slit pore of width h , $\gamma = \gamma^* - \Pi h$ and the disjoining pressure $\Pi = p_{\text{bulk}} - p_{zz}$. Note that p_{zz} for a slit pore is called the solvation force because it is the force on unit area of pore wall due to the presence of fluid between the walls.

II. ALGORITHMS

The canonical Monte Carlo method has been altered to give averages in any ensemble of interest. The basic idea is to generate a chain of Markov states (molecular configurations) for the fluid that will eventually produce configurations that characterize the desired statistical ensemble. To do this, one must specify the transition matrix a that takes the system from state m to state n by making a trial change in state m and then testing to see if the change leads the system toward one with the desired properties for the ensemble that is to be simulated. This means that many of the trial changes will be rejected, and one of the goals of the algorithm is to maximize their acceptance probability. It can be shown [1,2,4] that this probability is $\exp(-\delta V_{mn}/kT)$, where δV_{mn} is a molecular quantity that depends on the particular ensemble being simulated. To accept a trial change, a random number ξ between 0 and 1 is generated. If the random number is less than $\exp(-\delta V_{mn}/kT)$, the trial change is accepted (note that the trial is always accepted if δV_{mn} is negative), and if it is greater, the change is rejected. Even for acceptance ratios on the order of 0.1 or more, a chain of changes can contain upward of 10^6 trials, depending on the accuracy desired.

To generate a canonical ensemble, all the trials consist in changes in a position variable for molecules in the computer box, and δV_{mn} is the change in the energy of the molecule that is moved due to its interactions with the other molecules in the fluid and with the solid. The scale of these moves is adjusted to be small enough that δV_{mn} is not always large and positive (i.e., so that molecules do not overlap too much in the new state) but large enough that the phase space of the system is explored in a reasonable number of trials.

Ensembles other than canonical ones can be generated by adding to the types of moves that define the Markov chain. In the case of particular interest here, the

grand canonical Monte Carlo simulation is based on supplementing δV_{mn} with other moves that yield δD_{mn} and δC_{mn} for the creations and destructions that change the number of molecules in the system. Specifically, δD_{mn} is equal to $\delta V_{mn} + \ln(N/V) - (p - p^0)$ and δC_{mn} is equal to $\delta V_{mn} - \ln[N/(V + 1)] - (\mu - p^0)$, where N is here the number of molecules present in the initial state. Thus, there are three different types of moves in the GCMC simulation. Ordinarily, these are attempted with equal frequency (1/3) because this gives the most rapid convergence of the chain.

A number of alternative adsorption simulation methods have been proposed and tested, including algorithms for other ensembles such as the isobaric, isothermal [19], and alternatives to the GCMC. One such method is the Gibbs ensemble [20–22]. For example, adsorption isotherms have been evaluated using the potential distribution theory [23–25], which is based on Eq. (3) for the local chemical potential. Simulations of the Gibbs ensemble (which in adsorption simulations consists of two systems, one a dilute gas and one the actual dense adsorbed fluid, that are in equilibrium due to exchange of molecules between the two) have proved useful in studies of adsorbed fluids [26]. Variants on this method include those in Refs. 27 and 28.

III. MODELING THE INTERACTIONS

The gas–solid interaction laws explored in the numerous simulation studies of physisorption vary considerably in their complexity and level of realism. One starts from the simplest case, which is that of the hard wall, which can be planar, either as a free surface or as the boundaries of a slit pore. Of course, other geometries such as the straight-walled cylindrical pore can be studied. These systems are, of course, not very realistic, but they are very valuable in helping one understand the effect of confinement on the properties of a fluid without the complications of an attractive interaction at the wall. In fact, the hard wall idea can be extended by the addition of an attractive square well next to the hard wall that gives a relatively simple representation of the adsorption process as it might be observed in real systems. Still, both the hard wall and the hard wall plus square well models yield only the basic principles of adsorption, and one must go to more realistic representations if comparisons with experimental data are the goal,

Modeling of gas–solid interactions for real solids and gases is still done mostly at the semiempirical level. Much of this work has been reviewed in the 1990s [29,30] and is not discussed in detail here. It is based on an idea that is widely used in the simulation of bulk molecular fluids. In it, the shape of a nonspherical molecule is accounted for by assuming that its interactions with surrounding molecules can be expressed as the sums of pairwise spherically symmetric functions for a collection of sites that are most often located at the positions of the atoms that make up the molecule in question. Variations on this theme have been explored—in particular, by expressing the interactions of the methyl or methylene groups in hydrocarbons in terms of single sites rather than C plus two or three H sites. However, recent work on the structures of the dense arrays of hydrocarbon chains in many self-assembled monolayers indicates that the all-atom potentials give results that are significantly closer to experiment than the simpler

approximation by chains of methyl and methylene groups [31,32]. (The differences appear mainly at high densities, where the chains are in intimate contact.) In any case, the success of these site–site models for the modeling of bulk phases leads one to the idea the gas–solid potential energy might be represented in a similar fashion—namely, that the total interaction of a site in an adsorbate molecule with the solid can be given by a sum of spherically symmetric interactions with the sites associated with the atoms in a rigid adsorbent. Most often, the potential $u(r_{ss})$ for a pair of sites separated by a distance r_{ss} is taken to be a Lennard-Jones inverse 12-6 function:

$$u_{ss}(r_{ss}) = 4\varepsilon_{ss} \left[\left(\frac{\sigma_{ss}}{r_{ss}} \right)^{12} - \left(\frac{\sigma_{ss}}{r_{ss}} \right)^6 \right] \quad (6)$$

where ε_{ss} and σ_{ss} are the well depth and size parameters for the pair of sites under consideration. It is the choice of values for these parameters that is the most serious problem in devising a potential to represent a specific system such as a gas-phase molecule interacting with carbon black or silica (two of the most popular adsorbents in the experimental literature), whose bulk phase properties have often been simulated using this kind of model. The problem is that one has cross interactions for the adsorption energy functions with potential parameters for the sites in the solid that are unknown. Even if one were to guess these parameters (for C–C or O–O interaction, for instance), approximate combining rules such as the Lorentz–Berthelot rule are needed. More often than not, the validity of the results obtained is tested by comparison of experimental and calculated low-coverage limits of the isotherm slopes and heats of adsorption, and, if necessary, the parameters are adjusted to give agreement. [Low-coverage limiting data are used because theory shows that in this limit the calculations involve only isolated molecules on the surface (see Ref. 15, Secs. 3.6–3.8)]. At first glance, the summations over the semi-infinite numbers of sites in the solid would seem to be a sufficiently formidable task to prevent one from successfully carrying out simulations based on such models. However, there are ameliorating factors: In the first place, the Lennard-Jones functions are sufficiently short-ranged to allow one to truncate the sums after the nearest 100 (or so) sites have been included; for higher precision, the long-range parts of these sums can be replaced by integrals. Also, the atomic arrangements at planar surfaces of crystalline materials that are made up of a single Miller plane are periodic and thus will give site–site gas–solid interactions that have the same periodicity as the exposed crystal face. This can be exploited to give useful expressions for the interaction of a gas molecule site over a surface unit cell [15, Sec. 2.2; 33]. The two-dimensional vectors that define the size and shape of this unit cell can be defined as \mathbf{a}_1 and \mathbf{a}_2 with reciprocal lattice vectors \mathbf{b}_1 and \mathbf{b}_2 such that $\mathbf{a}_1 \cdot \mathbf{b}_1 = 1$, $\mathbf{a}_2 \cdot \mathbf{b}_2 = 1$ and $\mathbf{a}_1 \cdot \mathbf{b}_2 = 0$, $\mathbf{a}_2 \cdot \mathbf{b}_1 = 0$. If the vector connecting the gas-phase atomic site and the center of the unit cell in the α th layer of solid atoms is denoted by (z_α, τ, ϕ) , where ϕ denotes the orientation of the in-plane vector τ , one can show that

$$u_{sS}(z_\alpha, \tau, \phi) = \frac{2\pi\epsilon_{ss}\sigma_{ss}^2}{a_s} \left\{ \left[\frac{2}{5} \left(\frac{\sigma_{ss}}{z_\alpha} \right)^{10} - \left(\frac{\sigma_{ss}}{z_\alpha} \right)^4 \right] + f(z_\alpha, \tau, g, \phi) \right\} \quad (7)$$

where sS denotes the site-surface interaction with the α th plane of solid atoms, a_s is the unit cell area, and

$$f(z_\alpha, \tau, g, \phi) = 2 \sum \exp[ig\tau \cos \phi] \left[\frac{\sigma_{ss}^{10}}{60} \left(\frac{g}{2z_\alpha} \right)^5 K_5(gz_\alpha) - \sigma_{ss}^4 \left(\frac{g}{2z_\alpha} \right)^2 K_2(gz_\alpha) \right] \quad (8)$$

In this expression, ϕ is the angle between the vectors \mathbf{g} and $\boldsymbol{\tau}$, the K , are modified Bessel functions of the second kind, and $\mathbf{g} = 2\pi[g_1\mathbf{b}_1 + g_2\mathbf{b}_2]$, where g_1 and g_2 are integers. Here we have given a simplified version of the theory for the case where there is only one atom per surface unit cell and the solid atoms are all of the same kind. Extensions to deal with these problems are straightforward but give rather complicated expressions. To obtain the total energy of interaction, these energies should be summed over all values of a , but the sums converge very quickly and convenient approximations to their values can be derived. A convenient approximation to the value of the term with $g = 0$ in Eq. (7) can be written [33]

$$u_{gs}^0(z) = \frac{2\pi\epsilon_{ss}\sigma_{ss}^2}{a_2} \left[\frac{2}{5} \left(\frac{\sigma_{ss}}{z} \right)^{10} - \left(\frac{\sigma_{ss}}{z} \right)^4 - \frac{\sigma_{ss}^4}{d(z + 0.71d)^3} \right] \quad (9)$$

where d is the distance between layers.

The terms in the expression for u_{gs} with \mathbf{g} not equal to zero represent the periodic part of the gas-solid energy for a single crystal adsorbing surface, and the inverse $10 - 4$ term in Eq. (9) gives the surface-averaged "smooth" interaction, which is clearly independent of the position τ relative to the surface lattice of atoms. Although the form of Eq. (8) tends to obscure its physical significance, it is easy to show that a surface lattice whose unit cells are large compared to the size of the gas atom site will have a large periodic component, especially when the site is close to the surface.

Note that these results have been obtained for the inverse power law Lennard-Jones potential. If electrostatic interactions are present, expressions of this form that give the electrostatic energy in the form of a Fourier series are known [34]. Perhaps the easiest way to see this is to represent the dipole, quadrupole, etc. of a gas molecule by discrete charges attached to various sites in the molecule. the charges having magnitudes chosen to correctly give the known multipole moments. The electrostatic energy is then written as a sum of Coulomb interactions over charged species in the solid and the charge sites in the gas molecule. For a Coulomb interaction depending upon (distance)', the index of K is $1/2$, and, since $K_{1/2}(x) = (\pi/2x)^{1/2} \exp(-x)$, one can derive closed-form expressions for the electrostatic part of the interaction for polar molecules adsorbed on charged (i.e., ionic) solids.

For other types of surfaces, one must either adapt the methods that lead to the energy expressions shown here or, if all else fails, do a brute force summation over sites. Evidently, models of the interaction in porous solids require that one rethink

the ideas presented here, since few if any porous materials exhibit internal surfaces made up of single crystal planes.

Besides its accessibility for experimental work involving large-area adsorbents, one of the reasons for the great popularity of materials whose adsorbing surface is made up of the graphite basal plane is the great simplicity of their surface. This popularity extends not just to the free surface but also to porous materials such as parallel-walled slits and even to the buckytubes that are presently under intense scrutiny. In the first approximation, the atomic spacing in the graphite basal plane is so small compared to adsorbate site sizes that the periodic component of the gas–solid energy can be completely neglected. If one keeps only the integrated site–site energies that lead to the inverse 10^{-4} power part of the gas–solid energy for the infinite plane, interesting modifications are available; in particular, it is possible to derive an analytic expression for the interaction of a gas atom with a truncated graphite basal plane that is useful in a number of problems [35]. For example, a stepped graphite surface can be modeled [36]; pores that are more realistic than the parallel-walled case can be treated, including those with rectangular or triangular cross sections [37, 38]. Although the grooved graphite surface that uses truncated planes to make the grooves in the outermost surface layers might be considered to be of minor interest, one could take two such surfaces facing each other to make parallel-walled pores with alternating narrow and wide regions (i.e., with constrictions).

Finally, the planar graphite surface can be rolled into a cylinder to model a buckytube. The integrations that led to a 10^{-4} function for the infinite plane are more difficult in this case, but an analytic expression for the site–wall interaction in a smooth cylindrical tube can indeed be derived for use in the simulations of adsorption in this material [39].

Well-known and widely used adsorbents that are amorphous include many preparations of high-area oxides such as silica and titania. Models of the adsorbing surfaces of these materials have been proposed that are based on the ideas that first, the cations can be omitted for the site–site gas–solid potentials, at least for nonpolar adsorbates, and second, that the arrangements of the oxides is essentially that of a random close-packed array of hard spheres. An algorithm is available that will generate such arrays with periodic boundary conditions in two directions. If the hard spheres are then transformed into Lennard-Jones sites with interaction that represent the oxide–gas site potentials, the nonperiodic surface can be taken to be the adsorbing plane. In this case, the brute force approach of summing over these oxides can be used to evaluate the gas–solid interaction for such amorphous materials. The results of this modeling have been analyzed in a number of papers [40, 41]. (References to earlier work are given in Ref. 40.) In addition, variants on this procedure have been explored: One can roughen the surface by randomly deleting atoms from the outermost layer or two, or pores can be created by deleting the oxides from a volume of appropriate size and shape in the computer-generated random solid [42,43]. This allows one to model pores of arbitrary shape and even pore networks of varying connectivity (if a computer of sufficient power is available to handle such large systems).

IV. SPECIFIC EXAMPLES

The adsorption systems simulated to date range from elementary examples to some that are rather complex. We begin with cases that do not exist in nature but that exhibit features that may be encountered in other, more physically realistic systems. These solid–fluid systems involve hard interactions, either gas–solid or gas–gas or both.

A. Elementary Systems

By "hard interactions", one means interaction energies that jump from zero to infinity at a specific separation distance σ_{gg} or σ_{gs} , where gg denotes gas–gas and gs , gas–solid. Obviously, such systems have no interaction energies that could give energies of adsorption that differ from zero, regardless of the geometry of the confining wall. Nevertheless, the presence of the wall or walls produces profound changes in the properties of a fluid of hard spheres in the vicinity of the walls. Adsorption occurs with an adsorbed amount denoted by $\Gamma(p)$, the excess number of atoms (relative to the bulk) per unit area of surface when the pressure of the bulk fluid is p . This is always greater than zero, which means that the hard sphere fluid always wets the wall in these systems. At first this might appear to be a surprising result, because there are no attractive interactions between the wall and the fluid, but of course these interactions are absent in the adsorbed fluid as well. The number of atoms adsorbed per unit area is given by the general expression

$$\Gamma = \int [n(z) - n] dz \quad (10)$$

where n denotes the density of atoms per unit volume and adsorption on a smooth planar surface is assumed. Simulations are needed to evaluate $n(z)$, the number density in the fluid at a distance z from the wall. [Figure 1](#) shows the results of such a simulation [44] for a high density hard sphere fluid in a large hard-wall box with walls $16.2\sigma_{gg}$ apart. In this case, n , the density of the fluid far from the walls (and thus the bulk fluid density) is $n\sigma^3 = 0.90$. We see in the bottom panel that $n(z)$ is essentially equal to the bulk density for $z/\sigma_{gg} > 5$, which means that this system behaves as if it were adsorption on a free surface.

Specializing to planar walls for the moment, one has the exact relation [45] that $p/kT = n_w$, where n_w is the local density of the adsorbate in contact with the wall when the pressure of the hard sphere fluid is p . For hard sphere mixtures [46–49] n_w is the sum of the individual densities for each of the components in the fluid. Thus, the pressure of the fluid can be obtained from estimates of the intercept of the curve of $n(z)$ versus z : for example, [Fig. 1](#) indicates that $p\sigma_{gg}^3/kT$ is between 8 and 9 for this system. This result, taken together with the calculation of Γ at a given n from [Eq. \(10\)](#), allows one to construct the isotherm $\Gamma(p)$. [Figure 2](#) shows the adsorption of a hard sphere fluid on a hard wall as a function of the bulk-phase density [44]. The simulation points compare well with results of two theoretical calculations based on the scaled particle theory.

One also has an exact expression for the hard wall–hard sphere fluid surface tension γ , which is [44]

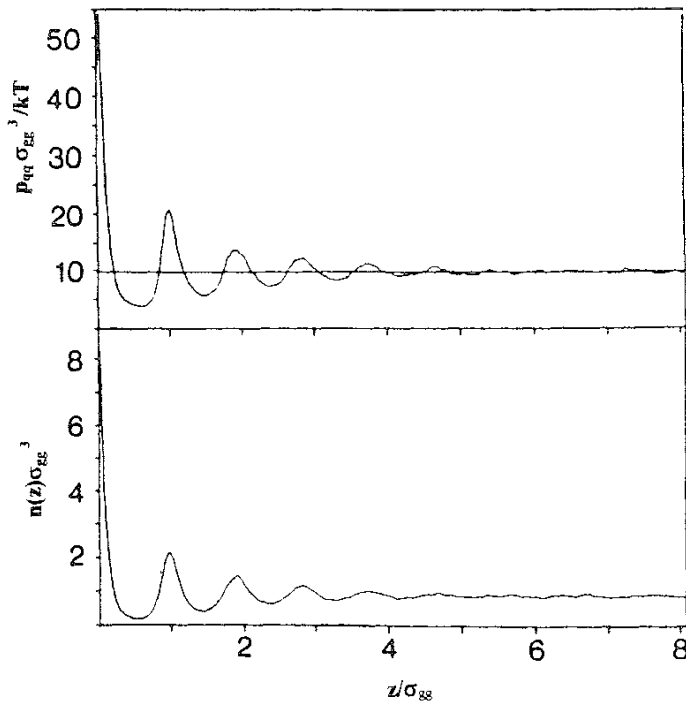


FIG. 1 Lower panel: Local density in reduced units for the hard sphere–hard wall system discussed in the text. Upper panel: Local pressure tensor component perpendicular (constant line) and parallel (oscillating curve) to the surface. These properties are plotted as a function of z/σ_{gg}^3 , the distance from the surface in reduced units. The bulk density for this system is 0.90 in reduced units, which is close to the freezing value. (From Ref. 44.)

$$\frac{\gamma}{kT} = \frac{n_w}{4} \int 2\pi\tau^3 [g_w(\tau) - 1] d\tau \quad (11)$$

where τ is the separation distance between a pair of hard spheres, $g_w(\tau)$ is the pair correlation function for a pair of fluid particles, both of which are in contact with the wall, ($g(\tau, z_1, z_2)$ is the pair correlation function for atoms 1 and 2 in the fluid). A second general route to the surface tension (or spreading pressure) has been given in Sec. I as the integral of the difference between the components of the pressure tensor parallel and normal to the surface. The local values of both of these pressure tensor components for a bulk-phase fluid density that is close to freezing are shown in the top panel of Fig. 1. The perpendicular pressure tensor element is independent of z , as required for mechanical equilibrium. The transverse component (which is not uniquely defined even though its integral with respect to z is [44]) oscillates and approaches p_{zz} at large z , as it should. All integral over these functions gives the gas–solid surface tension [see Eq. (4)]. The alternative route to this surface tension via Eq. (11) requires a simulation of the pair correlation function for spheres in contact with the hard wall. Figure 3 gives a comparison between this function and that for the bulk fluid, and Fig. 4 shows surface tensions as a function of the bulk fluid density.

Finally, a number of pair correlation functions with $z_1 = z_2$ but with varying z are shown in Fig. 5 [49] and compared with the bulk pair correlation functions for

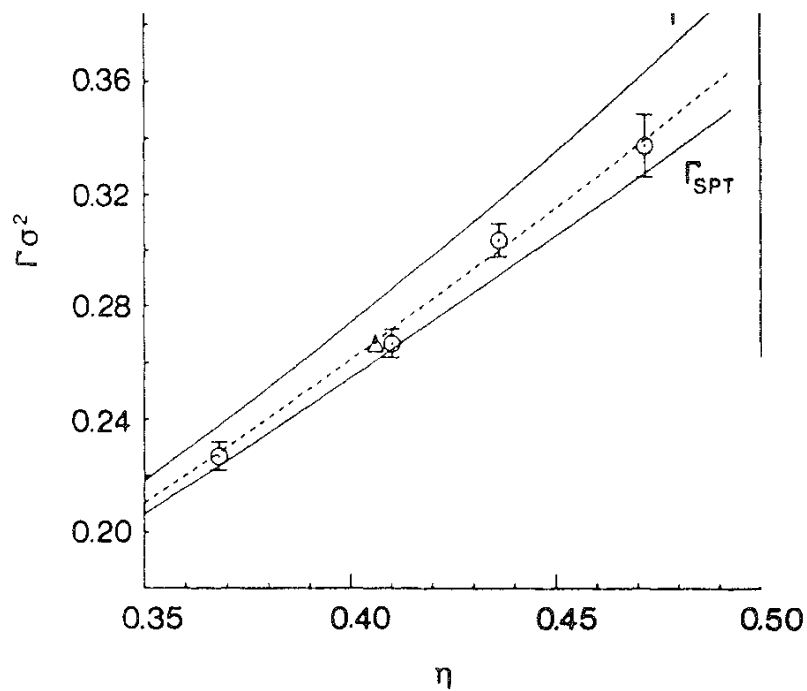


FIG. 2 Adsorption (molecules adsorbed per unit area) for the hard sphere–hard wall system plotted in reduced units as a function of the bulk density $\eta = (\pi/6)n\sigma_{gg}^3$. The points show the simulations, and the lines show theoretical calculations based on the scaled particle theory. (From Ref. 44.)

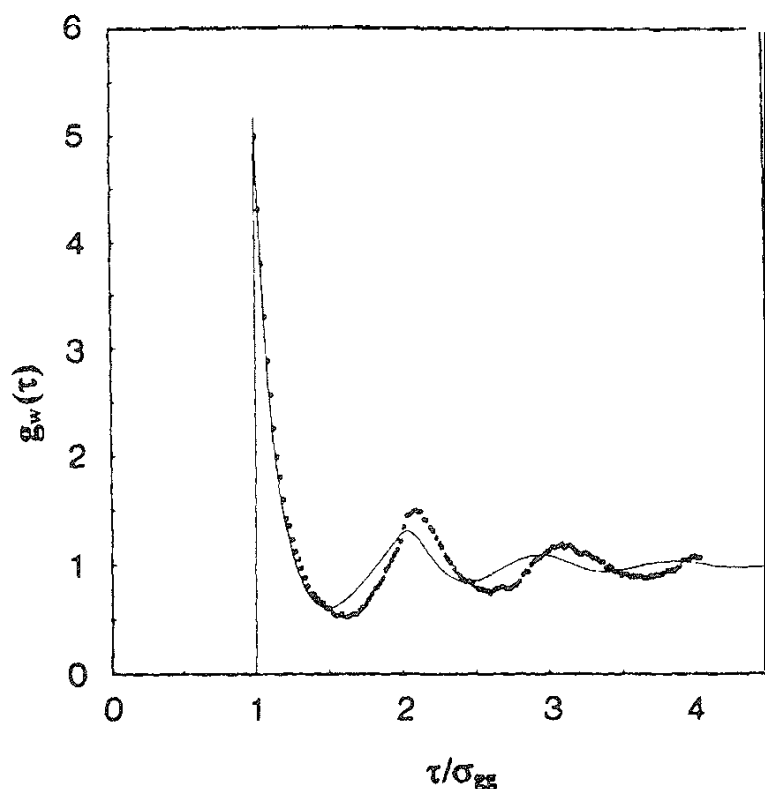


FIG. 3 The pair correlation function for hard spheres at a hard wall plotted as a function of the reduced separation distance between the pair of spheres for a reduced density of 0.90. The points show the simulations; the curve is for the bulk hard sphere fluid at the same reduced density. (From Ref. 44.)

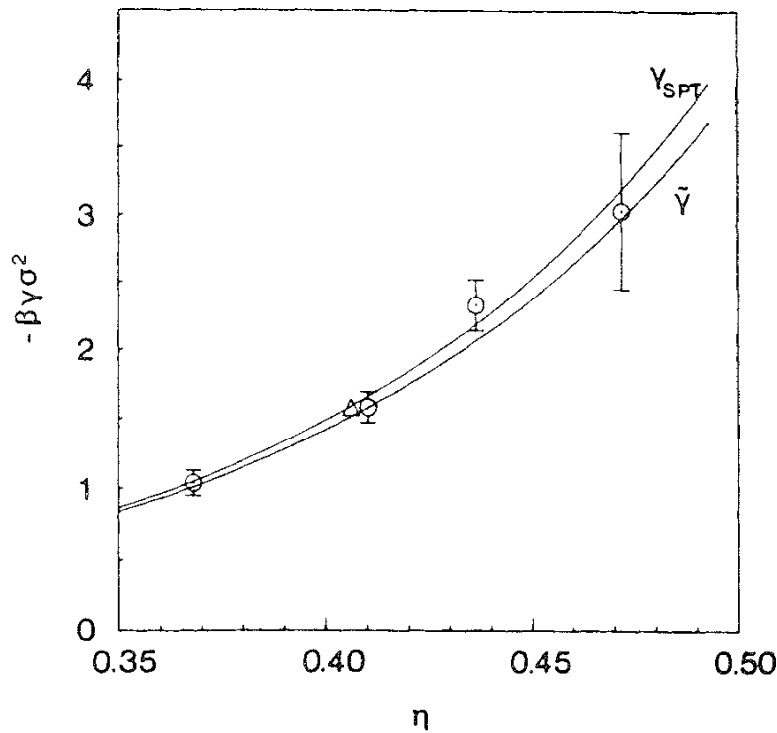


FIG. 4 The gas–solid surface tension in reduced units ($\beta = 1/kT$) for the hard sphere–hard wall system plotted as a function of the reduced density $\eta = (\pi/6)n\sigma_{gg}^3$. The points are simulated, and the two curves are calculated from different scaled particle theory expressions, (From Ref. 44.)

the same density. (The density profile for this system is shown in Fig. 6.) In general, the simulations indicate that hard sphere pair correlation functions near a hard wall with the two z values equal are rather close to those for the bulk fluid. Figure 7 shows the dependence of the pressure of the hard sphere fluid in a slit pore on the wall spacing h for a fixed value of the bulk-phase density [50]. The oscillatory behavior of the pressure is due to the layering in the fluid induced by the walls. The minima occur when h has a value that easily accommodates an integral number of fluid layers. Maxima are produced when an integral number of layers cannot be readily accommodated. Note that the periodicity in this function is slightly larger than σ_{gg} .

Other hard sphere–hard wall simulation studies include pair correlations [51], fluids in cylindrical pores [52], planar walls and spherical pores [53], isotherms in slit pores [54], and slit and cylindrical pores [55] as well as hard chains on hard walls [56] and in slit pores [57,58]. (Reference 58 gives references to other such studies.)

To this point, we have discussed only the adsorbed hard sphere fluid, but it is well known that hard spheres undergo freezing in both two and three dimensions. One expects to find analogous behavior in adsorption systems, especially when the fluid is confined to a monolayer or several layers (i.e., stratified). This can occur in a very narrow hard-wall slit pore, or it can be produced by the presence of a strong holding potential at the surface (which we discuss below). In fact, there has been great interest in the melting behavior of simple two-dimensional systems,

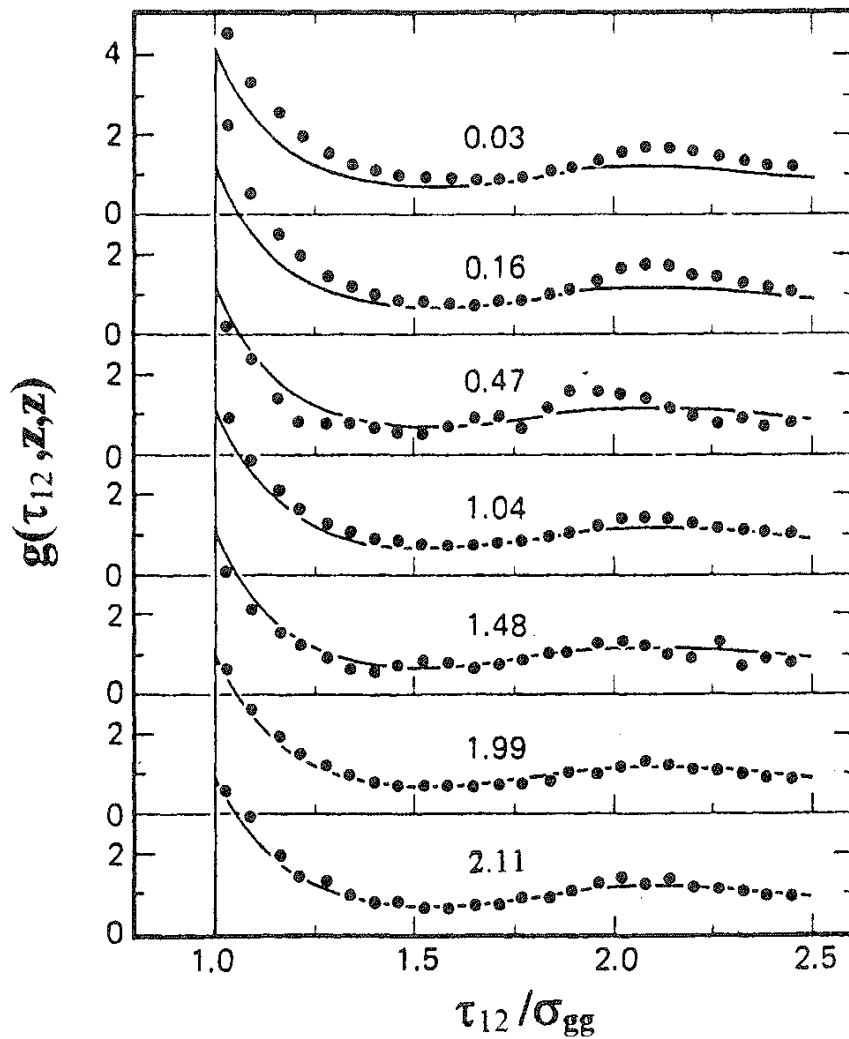


FIG. 5 Pair correlations plotted as a function of the reduced sphere separation distance for the system of Fig. 6. For these curves, each sphere is at the same distance from the surface so $z_1 = z_2$. The number above each curve indicates the value of this distance. The points are simulated, and the solid curves are the pair correlation functions for the bulk hard sphere fluid at the same reduced density (0.81) as that of the simulation. (From Ref. 49.)

stimulated by the Kosterlitz-Thouless-Halperin-Nelson-Young (KTHNY) theory, which predicts that two-dimensional melting will not be a first-order transition but will occur as two continuous transitions, the first being solid→hexatic and the second, hexatic→liquid, where the hexatic phase is one with short-range translational order but long-range bond orientational order. (The bonds are vectors between neighboring atoms in the fluid.) Many simulation studies of these 2D systems have been carried out in the effort to confirm or deny the theoretical predictions. These include various interaction potentials, Lennard-Jones inverse 12-6 [59–62], repulsive inverse 12 [63,64], screened Coulomb [65], and hard disks [66–68]. [References to previous studies are given in Ref. 59, and references to experiments and simulations are provided in Ref. 64.] Although the outcome of all this work is still not entirely clear, it is clear that if 2D melting is first-order, it is very weakly first-order.

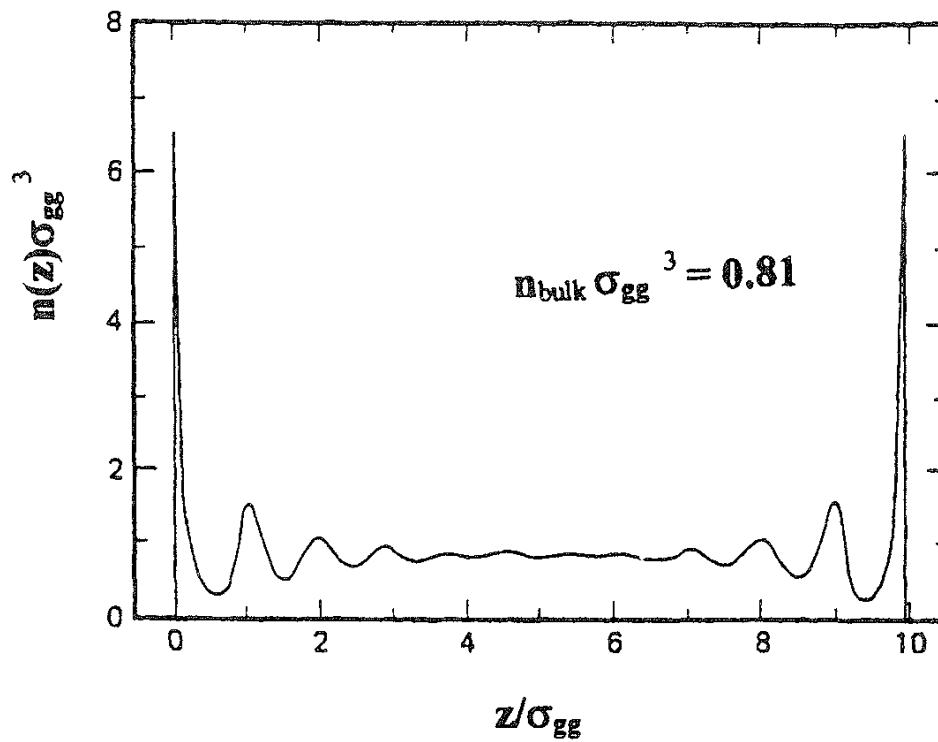


FIG. 6 Same as the local density in Fig. 1, except that the reduced bulk density here is 0.81 and the wall separation is $11\sigma_{gg}$. (From Ref. 49.)

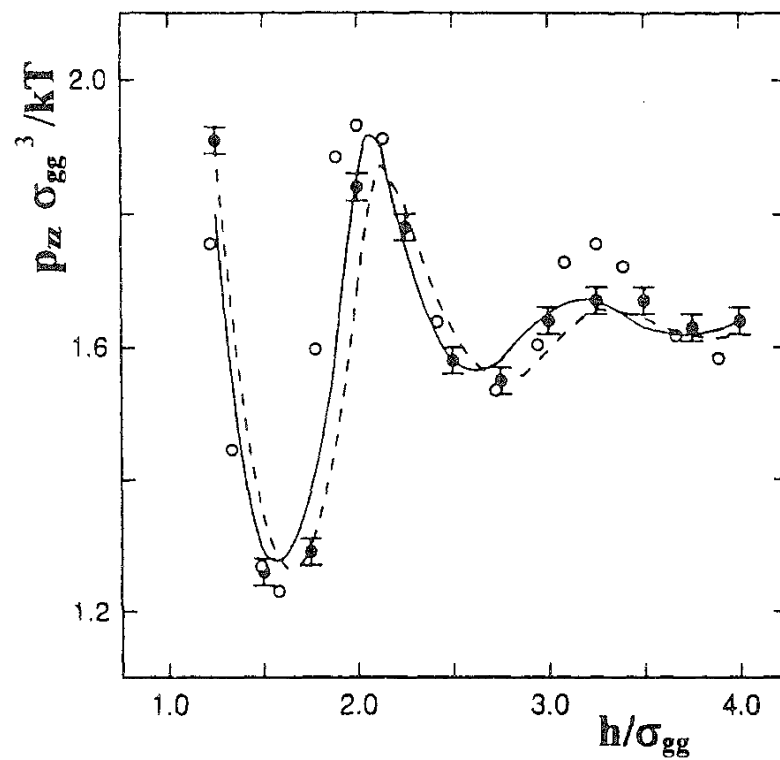


FIG. 7 Pressure normal to the wall plotted in reduced units as a function of the wall separation in reduced units (h/σ_{gg}). The points are simulated values, and the curves are theoretical, based on different integral equations. (From Ref. 50.)

Recently, two molecular dynamics simulations were published in which hexatic phases were observed for particular systems. In one [69], the phase was observed for a particular concentration in a two-component mixture of Lennard-Jones atoms, and in the other [70], the hexatic phase appeared for an inverse 12th-power potential at a particular value of the pressure. It is unclear why these special conditions should produce the hexatic phase, so extensions of these studies would appear to be necessary.

In any case, one should expect freezing in the hard sphere–hard wall systems that are under discussion, and indeed this is the case in slit pores. Schoen et al. [71] observed stratification in very thin films (two or three layers) in which the film atoms rearrange within their layer to pack more efficiently for certain values of the wall spacing. In a detailed study, Schmidt and Löwen [72] determined the phases present in thin multilayer hard sphere films as a function of the density for wall separations starting at the strictly 2D system of zero wall separation in excess of σ_{gg} and varying up to σ_{gg} . As can be seen in Fig 8, a remarkably rich phase diagram was obtained, starting from the triangular packing expected for a 2D system, followed by a "buckled" phase analogous to that deduced by Schoen et al. for excess wall separations slightly greater than zero. As the separation continues to increase, a two-layered square structure [(110) surface] is observed, followed by a two-layered rhombic phase and finally a two-layered triangular phase. The layers of atoms in the buckled and two-layered phases are all dovetailed to

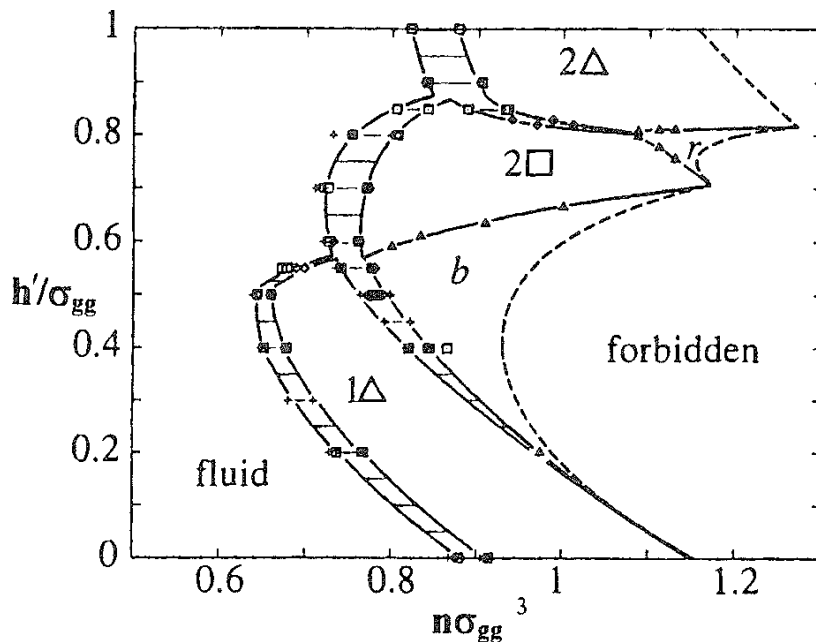


FIG. 8 The phase diagram for hard spheres enclosed in a hard-walled slit with excess width h'/σ_{gg} ranging from a value allowing one layer of fluid (or solid) ($h' = 0$) to two layers ($h' = \sigma_{gg}$) shown as a function of the sphere density n . Phase boundaries and coexistence regions are indicated. The nature of the ordered phases observed is discussed in Sec. IV.A. (From Ref. 72.)

obtain maximum packing densities. The forbidden region in Fig. 8 covers the range of densities higher than those allowed for the various close-packed hard sphere structures.

B. Lennard-Jones Atoms on Various Surfaces

We now proceed to more realistic models of adsorption systems. As a preliminary step, comparative simulations of various gases on various model surfaces should be mentioned. These include hard spheres at a soft repulsive wall [73] and hard spheres, soft repulsive spheres, and Lennard-Jones atoms between hard, soft repulsive, and soft attractive walls [74]. For coverages greater than one monolayer, these simulations show that the local density $n(z)$ is relatively insensitive to the detailed nature of the interactions [74]. It is the repulsive cores of the adsorbed atoms that are the determining factor. This point is illustrated in Fig. 9.

Several studies of the two-dimensional phase diagram for Lennard-Jones atoms have been reported [26,75]. In particular, the 2D liquid-vapor coexistence curve has been determined together with the critical temperature and density ($kT_{cr}/\epsilon_{gg} = 1.316$, $\rho_{cr}\sigma_{gg}^3 = 0.304$) (Fig. 10). These studies are relevant to monolayer adsorption of atoms on smooth surfaces with strong holding potentials, since the submonolayer films on such surfaces form quasi-two-dimensional systems. Theoretical analysis (Ref. 15, Chap. 4) reveals that the effect of this gas-solid potential can be taken into account by replacing \mathbf{p} by pK_H , with the Henry's law constant given by

$$K_H = \frac{A}{kT} \int \left\{ \exp \left[\frac{-u_{gs}(z)}{kT} \right] - 1 \right\} dz \quad (12)$$

where A is the area of the wall. The remainder of the calculation relies on the 2D equation of state of the model gas. In the case of hard spheres on an adsorbing surface, the simulated 2D equation of state is very well fitted by a simple expression given by scaled particle theory. When this result is used in the 2D approximation to the adsorbed monolayer, one finds

$$pK_{H*} = \frac{\Gamma^*}{1 - \Gamma^*} + \exp \left[\frac{\Gamma^*(3 - 2\Gamma^*)}{(1 - \Gamma^*)^2} \right] \quad (13)$$

where $K_{H*} = K_H/(\pi\sigma_{gg}^2/4)$ and $\Gamma^* = \Gamma(\pi\sigma_{gg}^2/4)$. This expression resembles the Langmuir equation, but the definitions of coverage are different in the two cases and, of course, the exponential factor, which will strongly affect the equation at high coverage, is missing from the Langmuir equation.

The two-dimensional approximation also applies to Lennard-Jones gases adsorbed on smooth surfaces such as those presented by the basal plane of graphite. Thus, the classic experiments of Thoisy and coworkers [76,77] show coexistence and critical points for several simple gases adsorbed on graphite that appear to be in good agreement with theory.

A number of GCMC simulations of the multilayer adsorption of classical rare gases on graphite have appeared. In many cases, the potential of Eq. (9) was used, with parameters chosen to represent the graphite-gas system under investigation.

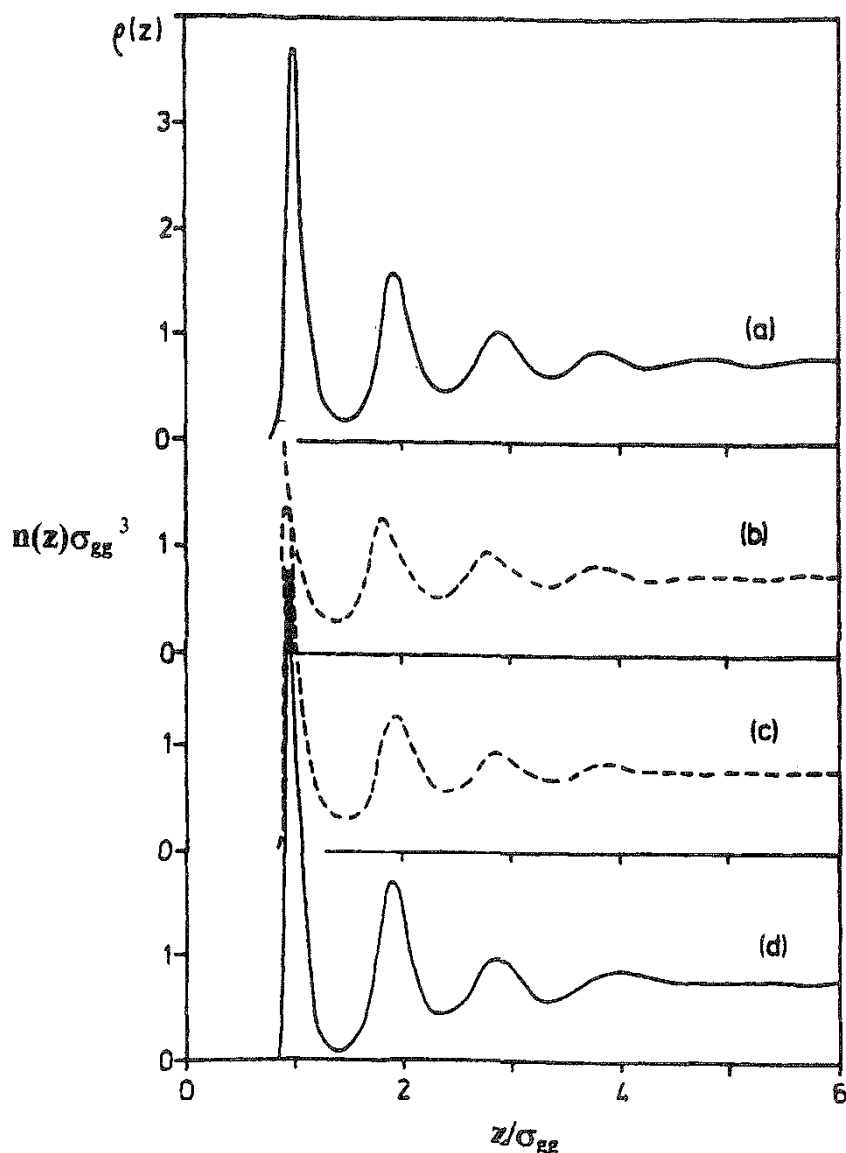


FIG. 9 Local densities for (a) a Lennard-Jones fluid at $n_{\text{bulk}}\sigma_{gg}^3 = 0.76$ on an atomically structured wall; (b) a hard sphere fluid with $n_{\text{bulk}}\sigma_{gg}^3 = 0.75$ on a smooth hard wall; (c) a hard sphere fluid on a wall with a soft repulsive potential; (d) a hard sphere fluid on a wall with gas–solid potential given by Eq. (9). In all cases, $kT/\varepsilon_{gg} \approx 1$. (From Ref. 74.)

Argon [25,78], krypton [79,80], and methane [81] (in attempts to reproduce the ordered monolayers commensurate with the graphite lattice that have been observed experimentally) and mixtures of argon and atomic models of methane and a larger atom were studied [82]. As an example, simulated multilayer isotherms are shown in Fig. 11 for argon on graphite at two temperatures. Analysis of the configurations gave unambiguous values for the coverage in each of the adsorbed layers (which were shown to be well stratified) and, with less precision, for the isosteric heat of adsorption. The waviness in the low temperature simulated isotherm is a remnant of stepwise layer formation that can be seen more clearly in the experimental data shown in the figure.

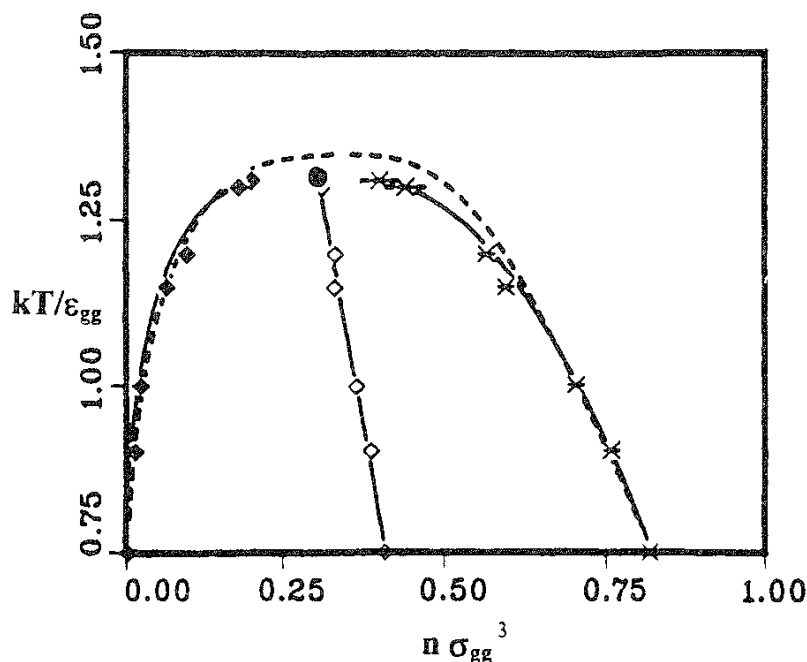


FIG. 10 The coexistence curve for a two-dimensional Lennard-Jones fluid, showing the estimated critical point as the filled circle (●). The points are simulation results, and the solid lines are fits to the 2D scaling law and the rectilinear diameter law; the dashed line is from an earlier equation of state. (From Ref. 75a.)

The gradual increase to very thick layers as p/p_0 approaches unity is normal behavior for adsorption on a free surface; however, when the adsorption occurs in a pore [83], the isotherm terminates at a coverage corresponding to a liquid-filled pore. Vertical jumps in coverage are seen (for adsorption in a single pore with a simple geometry) that are associated with capillary condensation and evaporation, and hysteresis is usually present in which the capillary condensation and evaporation occur at different pressures. Examples of this behavior are shown in Fig. 12 for a simulation of argon in a slit pore with walls made up of graphite basal planes [84]. The submonolayer isotherms in these systems are very similar to those with a single adsorbing wall, and this generalization holds good down to wall spacings that are small enough that the gas–solid potential fields overlap significantly. The two panels in Fig. 12 show capillary condensation at pressures that are much smaller than the bulk vapor pressures at the slit widths taken for the simulations, but only the large slit width isotherm shows hysteresis. In both cases, the jumps in coverage start at values slightly larger than the monolayer and end at nearly full pores. These two values can be viewed as those for coexisting capillary vapor and liquid phases. As the temperature is changed in a pore of fixed width and potential function, a capillary coexistence curve is traced out that has a critical temperature that is less than the bulk-phase value—how much less depends on the slit width and the gas–solid wall potential. (If the holding potential is strong, it may be convenient to treat the monolayer adsorption as separate from the pore fluid phase when it comes to calculating the pore fluid densities.) The detailed nature of the hysteresis loop is still not very well understood even after a good deal of theoretical and simulational

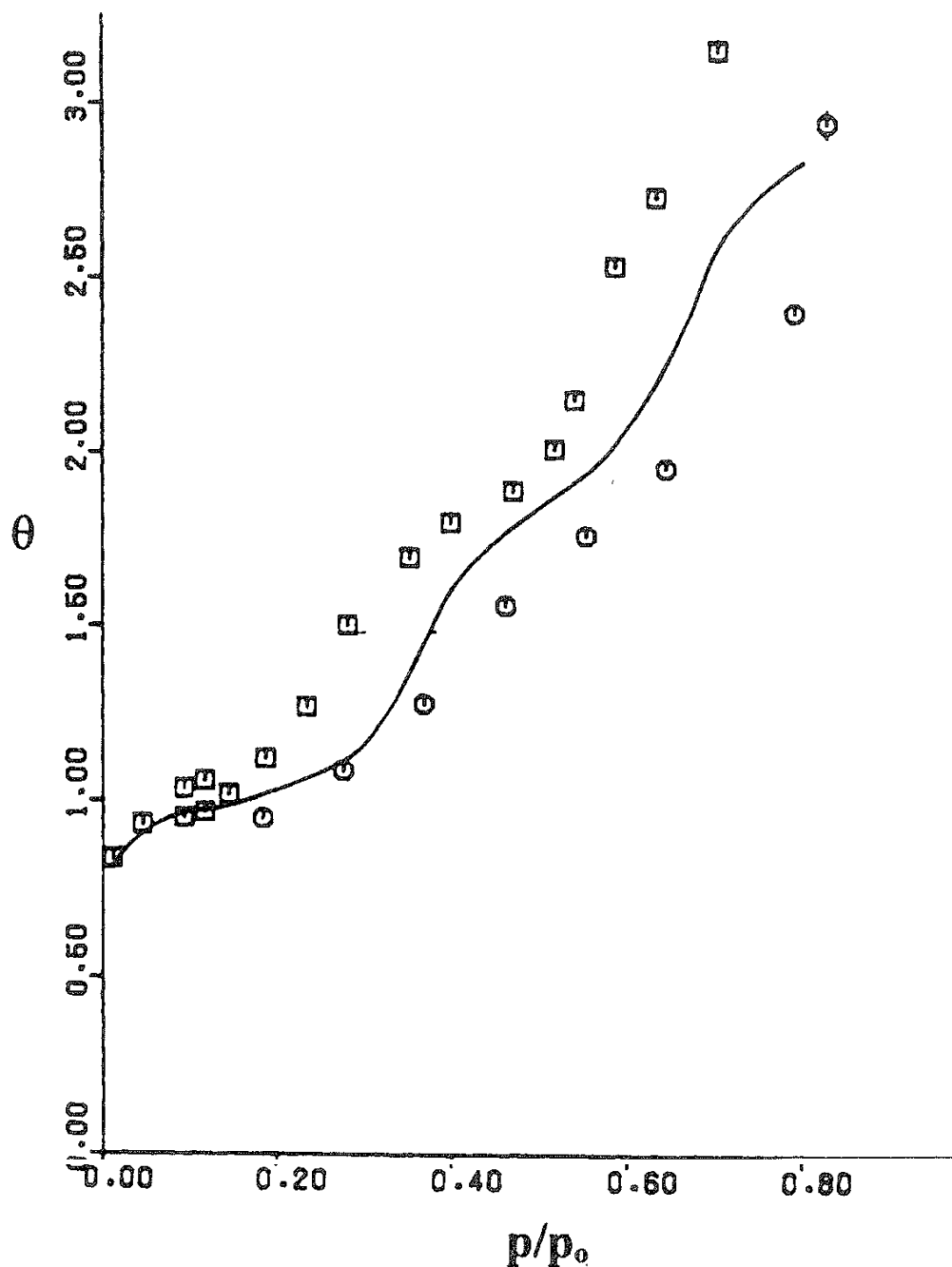


FIG. 11 Grand canonical Monte Carlo isotherms are shown for argon on the graphite basal plane modeled by the potential of Eq. (9). Surface coverage is given in terms of θ , the number of layers of gas on the surface, and p_0 denotes the bulk vapor pressure of the Lennard-Jones argon at the two temperatures of the simulation. Simulation points are for (\square) $kT/\epsilon_{gg} = 0.668$ and (\circ) $kT/\epsilon_{gg} = 1.002$; the solid curve is an experimental isotherm for argon on graphite at 78 K. (From Ref. 78.)

effort. The width of the loop clearly depends on temperature, pore geometry, and the gas–solid interaction potential. This phenomenon is a manifestation of meta-stable behavior. Densities at the tops and bottoms of the hysteresis loops may be considered as corresponding to points on the temperature-dependent spinodal lines for the pore fluid, and the equilibrium densities can be obtained by calculating the

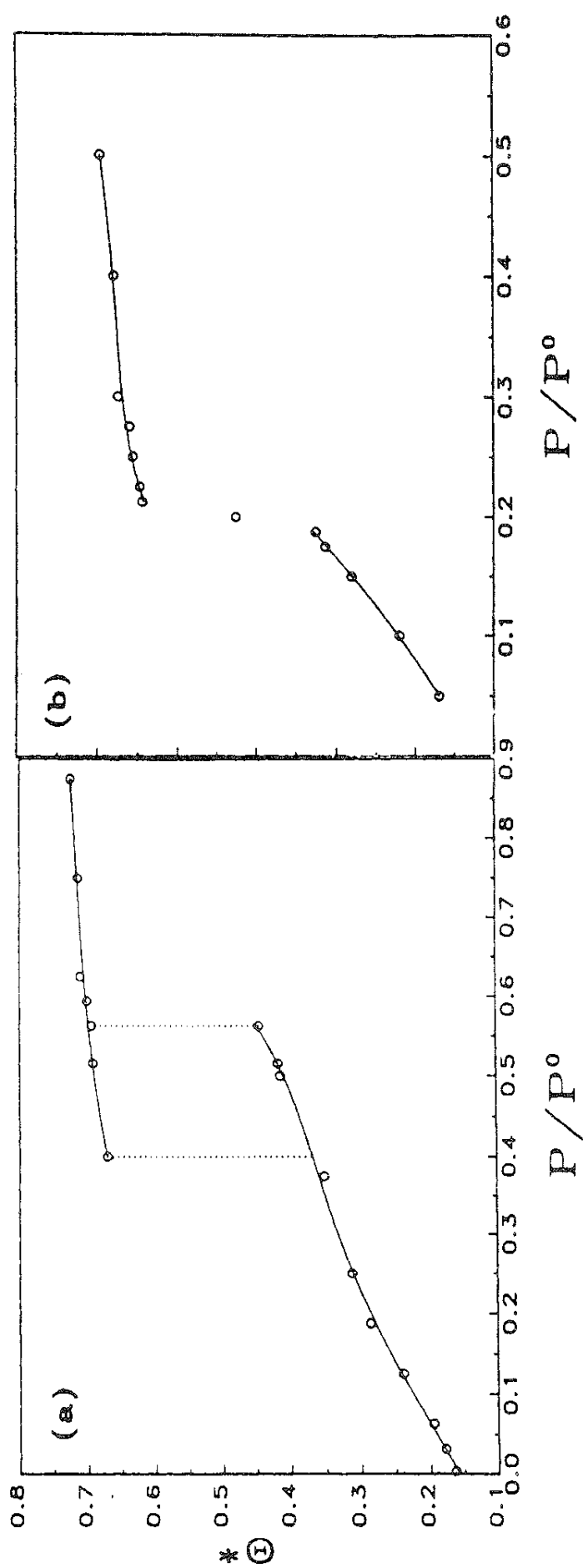


FIG. 12 Isotherms for argon in graphitic slit pores of width $h/\sigma_{gg} = 10$ (a) and 7 (b), both at $kT/\epsilon_{gg} = 0.8$. The coverage Θ^* is number of atoms per unit pore volume, in reduced units ($\Theta^* = \Theta \sigma_{gg}^3$). (From Ref. 84.)

grand potential (the free energy in the grand canonical ensemble) by thermodynamic integration along the isotherms starting from a low density point (which is known to be at equilibrium) [26,85]. Then the most stable thermodynamic states are those with the lowest grand potentials. A detailed theory has been given that fleshes out this picture [86]. Coexistence diagrams, which depend on pore size, geometry, and interaction potentials as well as temperature, are now beginning to appear [87–89]. (Liquid–vapor, liquid–liquid, and layering transitions in pores are reviewed by Gubbins et al. in Ref. 87.) One such diagram is shown in Fig. 13 for a Lennard-Jones fluid argon in a slit pore with width/ $\sigma_{gg} = 5.9$ and a repulsive ninth power gas–solid interaction function [89]. The capillary critical temperature kT_{cr}/ϵ_{gg} is 0.99 for this pore width, compared to the three-dimensional Lennard-Jones value of 1.25. This particular system is nonwetting because of the absence of attraction between the pore fluid and the walls. There can be problems with this approach when the pore fluid is strongly attracted to the walls, as is shown in Fig. 14. Here the low density fluid is not homogeneous but is rather two layers of dense liquidlike fluid that do not fill the entire pore volume. This is not what is expected for the coexisting "gaseous" pore fluid even though it has been taken from the simulation of an isotherm point that is very close to the coexistence line.

Another pair of isotherms [90] are shown in Fig. 15. Here a Lennard-Jones model of methane has been used in a simulation of sorption in a graphitic slit pore. The two sets of curves in the figure are for a single pore width but for two

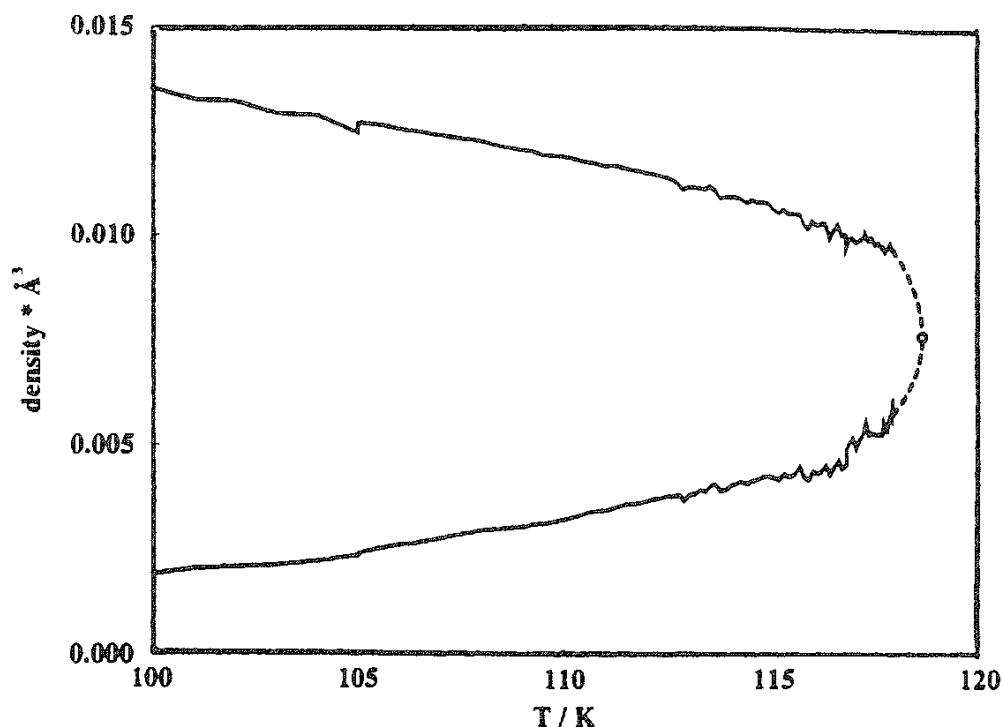


FIG. 13 Coexisting liquid- and gas-phase densities of argon in a slit of width $h/\sigma_{gg} = 5.9$ are shown as a function of temperature. For bulk argon, $T_{cr} = 151\text{ K}$, $n_{cr} = 0.008\text{ Å}^{-3}$. The capillary critical point is shown by the circle. (From Ref. 89.)

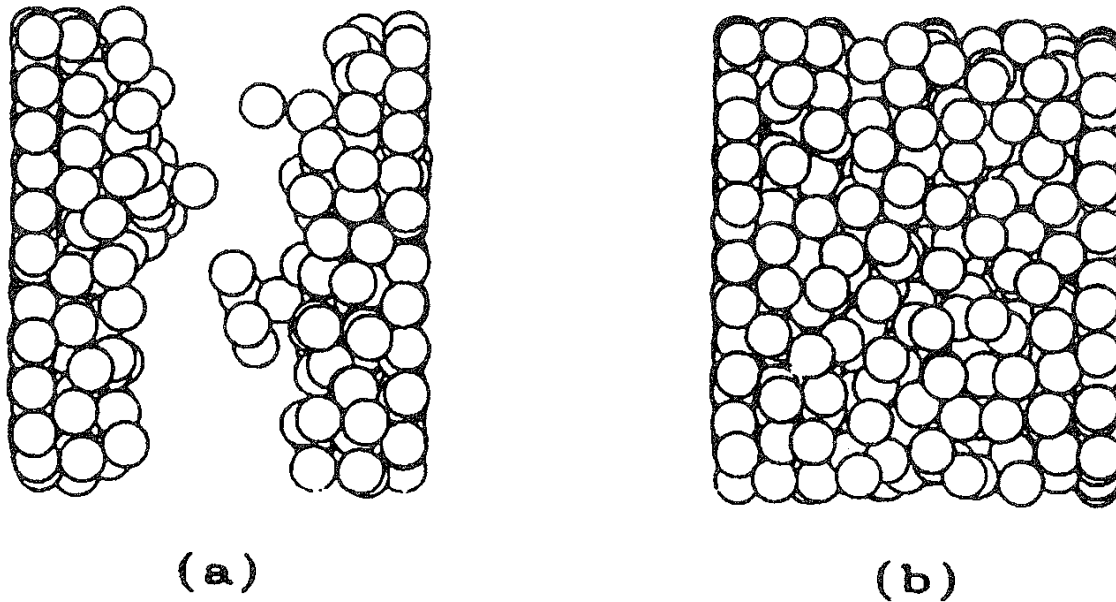


FIG. 14 Side views of the configurations of the adsorbed atoms in the system of Fig. 12a. Both panels are for pore fluid at $p/p_0 = 0.516$, which is in the hysteresis region of the isotherm of Fig. 12: thus, panel (a) shows a configuration for the low density "gas" in the pore, and panel (b) shows a configuration for a pore that is nearly full of liquidlike fluid. Note that the "gas" state is actually made up of liquidlike layers on each wall. (From Ref. 84.)

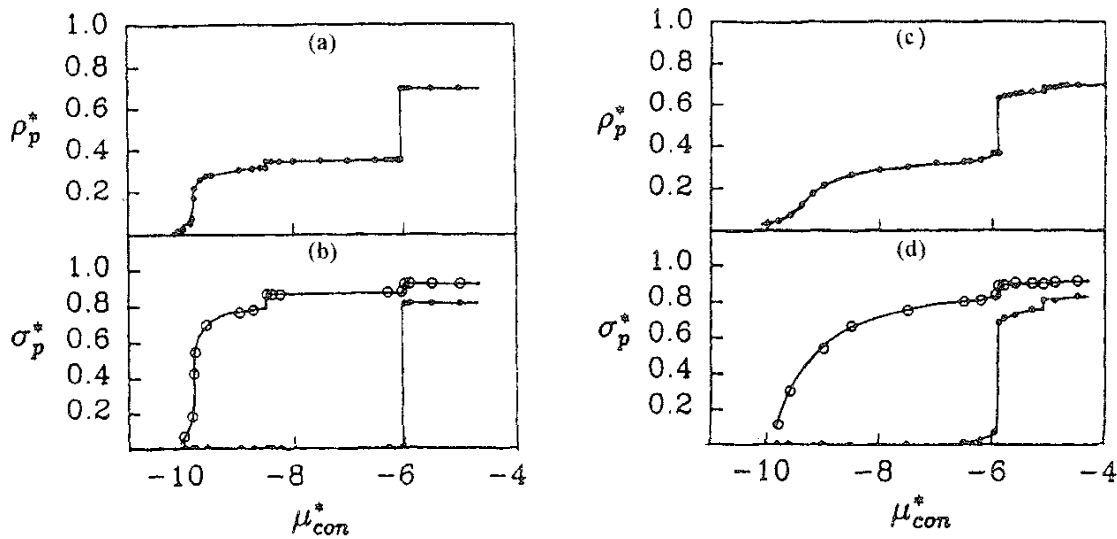


FIG. 15 Simulated isotherms for a spherical Lennard-Jones methane model in a graphite slit pore of width $h/\sigma_{gg} = 5.0$. (a, b) $h/\epsilon_{gg} = 0.5$; (c, d) $h/\epsilon_{gg} = 0.7$. The isotherms are given as ρ_p^* , the total number of pore atoms per unit pore volume [in reduced units obtained by multiplying by σ_{gg}^3 in (a) and (c) and by σ_p^* , the number of adsorbed atoms per unit area (in reduced units) in a given layer, in (b) and (d)]. (○) Layer 1; (●) layer 2. The isotherm data are plotted as a function of the configurational chemical potential in reduced units [equal to a constant plus $(kT/\epsilon_{gg}) \ln p$]. (From Ref. 90.)

temperatures, both of which are low enough to show freezing. This becomes visible when one takes the overall isotherm data and splits them into separate first and second layer isotherms, as shown in parts (b) and (d). With one exception, the small jumps in coverage are due to freezing, while the large jumps are due to monolayer and second layer condensation. The exception is the second small jump in the first layer isotherm at $kT/\varepsilon_{gg} = 0.5$. This is probably a consequence of the large change in density of the second layer, which then provides a potential field for the first layer atoms that allows them to become slightly more dense.

Other simulations of the sorption of Lennard-Jones fluids in parallel-walled graphitic slits include methane [91,92], argon and nitrogen [93], and CCl_4 [94] as well as methane–ethane mixtures [95] and argon and Lennard-Jones mixtures in slits with walls of rare gas atoms [96–99]. Simulations of Lennard-Jones fluids in straight-walled cylindrical pores include argon and argon–krypton mixtures in a “ CO_2 -walled” pore (weakly interacting compared to graphite) [100–103]. All these simulations have been carried out at temperatures near the bulk boiling points of the adsorbates where the density of the bulk vapor in equilibrium with the adsorbate is quite small, and freezing of the adsorbate can occur when the density of an adsorbed layer becomes sufficiently high (and the temperature sufficiently low).

C. Adsorption in the Critical Region of the Bulk Fluid

If one measures or simulates adsorption at temperatures near the critical region of the bulk adsorbate, new features appear in the isotherms, for adsorption both on the free surface [104,105] and in pores [106]. At slightly supercritical temperatures where bulk-phase condensation is absent, multilayer formation can be observed, as is shown by the local densities in Fig. 16. This simulation was for a simple model of ethylene on a graphitic surface (chosen so that comparison with experiment [107] was facilitated) at a temperature roughly 3% higher than the bulk critical value. Not surprisingly, the density maxima for the multilayers are not sharp as they are at lower temperatures, and these layers build up gradually compared to the low temperature behavior. In addition, the simulated isotherm in Fig. 17 shows the characteristic cusp in coverage versus pressure that is observed experimentally. The position and height of this cusp in the excess amount adsorbed depend on the choice of dividing plane that defines the adsorption excess; its existence is believed to be due to a slow increase in absolute amount adsorbed compared to the more rapid increase in the density of the bulk fluid with increasing pressure, thus yielding adsorption excesses that decrease with increasing pressure. The analogous simulation [106] for a graphitic slit pore shows the same phenomena, but with quantitative features that depend on slit width. In a more recent simulation [108], the critical behavior of fluid adsorbed in a graphitic slit pore was carefully studied. Although not in contradiction to the earlier simulations, this high precision study revealed that the pore fluid density for a rather large wall separation ($h/\sigma_{gg} = 20$) did not approach the bulk-phase density in the core region of the pore (i.e., far from the walls). The explanation suggested for this is based on the observation that the compressibility for the confined fluid was not the same as that for the bulk for a temperature very near T_{cr} , probably due to the fact that the capillary critical temperature is slightly different from that for the bulk even for the large slit

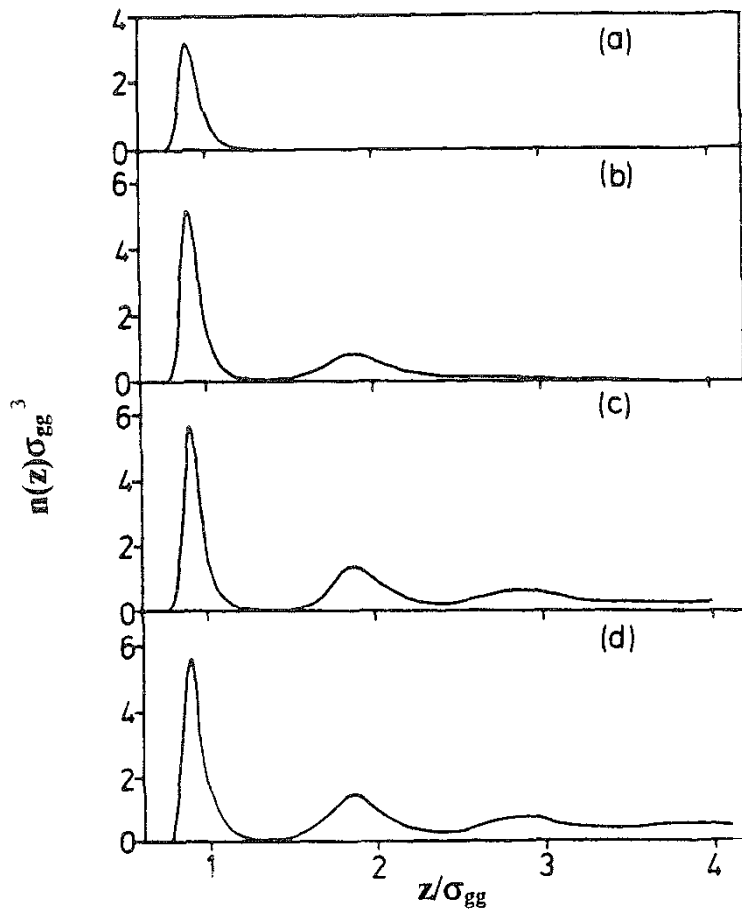


FIG. 16 The local density $n(z)$ (in reduced units) for an adsorbed gas slightly above its bulk critical temperature is shown here for bulk densities $n\sigma_{gg}^3$ equal to (a) 0.0015; (b) 0.0405; (c) 0.1395; and (d) 0.1935. Multilayer formation is clearly indicated at all but the lowest density. (From Ref. 104.)

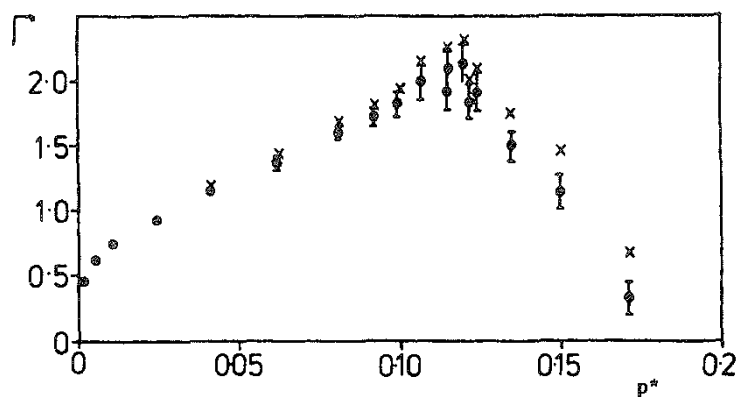


FIG. 17 Simulated excess adsorption in atoms per unit area (in reduced units) as a function of pressure $p^* = p\sigma_{gg}^3/\epsilon_{gg}$ for an adsorbed gas slightly above its bulk critical temperature. The points show the adsorption for two slightly different definitions of the excess adsorption Γ . (From Ref. 104.)

width taken in this work. In other words, the core fluid is effectively different from the bulk, with the slight difference significantly magnified by proximity to the critical point. This work did produce an interpretation of the experimental observations of near critical behavior in a system analogous to that of the simulation [109–111].

D. Freezing of Adsorbed Layers

At low temperature and high density, an adsorbed fluid with attractive interactions such as those for the Lennard-Jones potential will freeze. We have already discussed the ordered phases that have been simulated for hard sphere fluids in slit pores with small wall spacings. The 2D Lennard-Jones fluid also forms an ordered solidlike phase at high density, so there is every reason to expect that such phases will be formed from adsorbed fluid. Indeed, this is the case. Experimental and simulation studies of this behavior have been reviewed elsewhere [112,113] and need not be repeated here. It is worthy of note that the periodic boundary conditions used in simulations for fluids can give problems when a solidlike phase with long-range order in the directions parallel to the surface is formed. Unless the computer box happens to match perfectly with the lattice of the solidlike adsorbed phase, there will be difficulties in matching up the images with the real sample. A possible way of avoiding this problem is to simulate in the isobaric ensemble (for the pressure components parallel to the surface), since this causes the area of the computer box to fluctuate in order to hold the parallel pressure constant. Nevertheless, questions remain concerning the correct expression for this pressure in the presence of an adsorption potential that varies with position parallel to the surface. A more reliable but more expensive method is to simulate a large isolated patch of material on the periodic surface [114]. Simulations of the effects of periodic variations in the gas–solid potential energy on the freezing transition do reveal some interesting features. Many of these simulations have been done with molecular dynamics because of the power of this algorithm in revealing structures even at low temperatures where Monte Carlo simulation becomes difficult. However, we have chosen not to cover molecular dynamics simulations in the present review on the grounds that this will be done in the near future [115].

Starting with an early paper [116] in which it was shown that an argon monolayer on a graphitic surface at 131.7 K was ordered while the same system in a considerably weaker inverse 9-3 potential was not (see also Ref. 117), a study [118] of the argon–graphite monolayer at 77.5 K with and without the periodic terms in the *gs* potential revealed that the periodicity had only a minor effect on the incommensurate solidlike monolayer. This is definitely not the case for krypton–graphite, where a commensurate layer does form in the presence of the periodic potential [79,80,114,116,117,119]. It is clear that the difference arises from the different sizes of the two adatoms. Krypton with $\sigma_{gg} = 3.60$ Å, $r_{\min} = 4.04$ Å (r_{\min} is the distance for the minimum in the *gg* pair potential) matches up rather well with the commensurate lattice spacing of 4.26 Å, whereas r_{\min} for Ar is 3.82 Å. In fact, the solid Kr monolayer undergoes an incommensurate→commensurate transition driven by thermal expansion at a temperature that depends on the magnitude of the periodic part of the *gs* potential. Simulations of atoms on surfaces made up of exposed

planes of a crystal have also been reported for both the free surface [120–122] and a narrow slit pore [123]. Methane is similar in size to Kr ($\sigma_{gg} \approx 3.81$ Å for methane) and the phase transitions for this molecule on graphite have been simulated [90] with results that are quite similar to experiment and to those obtained for the Kr/graphite system. Ordering in 2D systems with periodic potentials due to vicinal crystal planes has also been studied [124]. These molecular dynamics simulations of ordered multilayer films will be discussed elsewhere [115].

E. Energies of Adsorption

Another kind of information obtainable from adsorption simulations is the average energy of interaction of the adsorbed atoms with each other (u_{gg}) and with the solid (u_{gs}). The sum of these two energies is essentially equal to the thermodynamic molar energy of adsorption, but the coverage dependence of the two separate terms gives a revealing view of the energetics of formation of a submonolayer (and more) film. As an example, these energies are shown in Fig. 18 for krypton adsorbed at 120 K in an atomically rough-walled cylindrical pore [125]. The decay in $-u_{gs}$ shown there is due to the successive adsorption on the areas of the surface with the strongest interactions, followed by coverage of the areas with weaker and weaker interactions. The linear increase in $-u_{gg}$ with coverage nearly cancels the decay in $-u_{gs}$ when the two are added to give the total. Experiment gives q_{st} , the isosteric heat, which is equal to RT minus the partial molar energy. For the nearly linear variations in energy shown in the figure, the molar energies are related to the partial

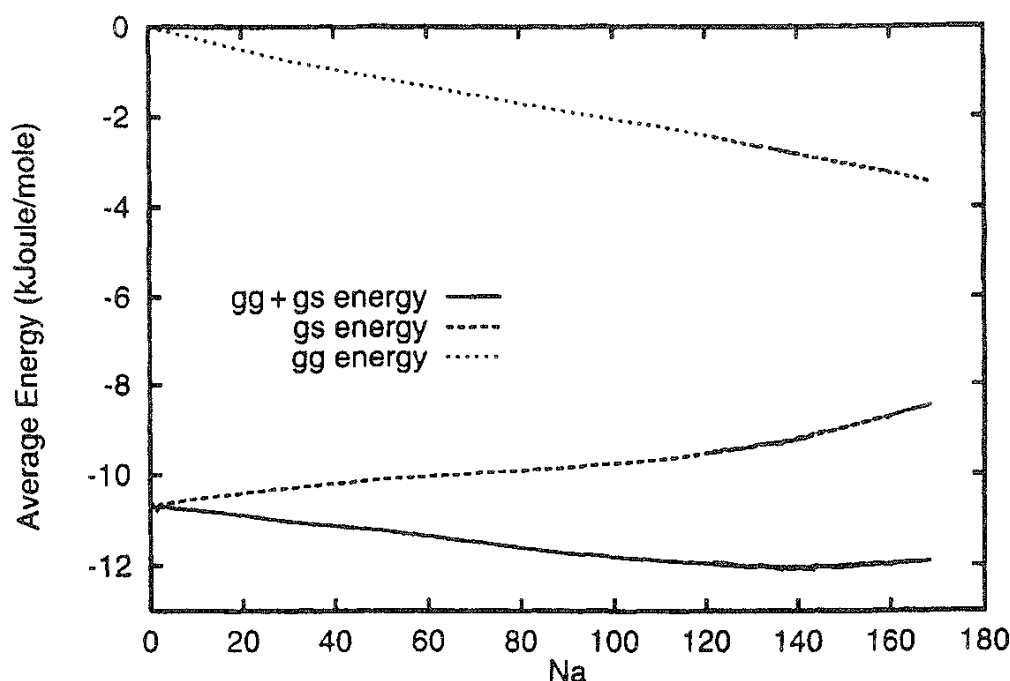


FIG. 18 Average energies for krypton adsorbed at 120 K in a rough-walled cylindrical pore. The dependence of the Kr–Kr (gg) and the Kr–pore wall (gs) energies on the number of atoms adsorbed, N_a , are shown separately, together with their sum. The Kr monolayer capacity under these conditions is about 130 atoms. (From Ref. 125.)

molar energies by the fact that they are equal in the limit of zero coverage, but the slopes of the partial molar quantities are double those of the molar quantities.

Significant conclusions can be drawn from these simulated curves. First, the submonolayer total energies of adsorption are nearly constant because of the compensation of the changing u_{gg} and u_{gs} . The frequent assumption that the signature of heterogeneity is a decaying negative energy (or enthalpy) of adsorption is seen to be incorrect in this case. Second, the linear change in u_{gg} (which is often found in simulations) implies that a mean field (or van der Waals) theory may be adequate to account for the interactions between neighboring atoms in the monolayer. The extension of these simulations into the multilayer regime is capable of producing physical insights into the nature of the average gg interactions in thick films as well as into the continuing decay in the gs part. Thus, this straightforward evaluation of the separate parts of the total energy helps elucidate the nature of film formation at a solid surface.

F. Wetting and Drying

As the holding potential for a gas on a solid surface or in a pore becomes weaker and weaker, a point is reached where the competition between monolayer adsorption and the condensation of the adsorbate gas into a bulk liquid (or solid) is no longer won by the adsorption process. In effect, this describes the changeover from wetting to nonwetting. In this simple picture, drying is a special case of adsorption and can occur when the potential energy in the bulk phase is sufficiently negative compared to that in the monolayer to stabilize the bulk relative to the adsorbed film. Since these two energies change differently with temperature and density, there is the strong possibility that marginal systems will undergo wetting \Rightarrow drying transitions along some line in the temperature–density plane (evidently, other thermodynamic variables can also be used to characterize the transition). The nature of this transition (first-order or continuous) is a question of considerable interest. A nonwetting film comprises a thin layer (usually, a fraction of a monolayer) in equilibrium with the bulk fluid, and the transition to the wetting film corresponds to the formation of a layer of fluid on the surface whose thickness approaches infinity as p approaches p_0 . Other transitions are possible such as thin film \rightleftharpoons thick film (but not infinitely thick) at a p less than p_0 , which is called prewetting.

A study [126] of argon on a weakly interacting surface (an inverse 9-3 potential with parameters characteristic of solid “CO₂”) gives the local density curves for $kT/\epsilon_{gg} = 1.1$ that are shown in Fig. 19. The isotherm for this system, given in the inset of the figure, indicates only small adsorption up to a value of the bulk density of about 0.048 (in reduced units) in equilibrium with the adsorbed film. When the bulk-phase density exceeds this, a pronounced change in the nature of the local density of the adsorbed phase occurs that is reflected in the jump in the amount adsorbed. Thick layers appear, and the density of the monolayer is much greater than that found for the thin films. Such behavior corresponds to a prewetting transition. In contrast to this, Fig. 20 shows that the isotherm and the local densities for this system at $kT/\epsilon_{gg} = 0.95$ grow continuously until saturation is reached. However, the slope of the isotherm at saturation is finite, so that the coverage is also finite at saturation, indicating partial wetting.

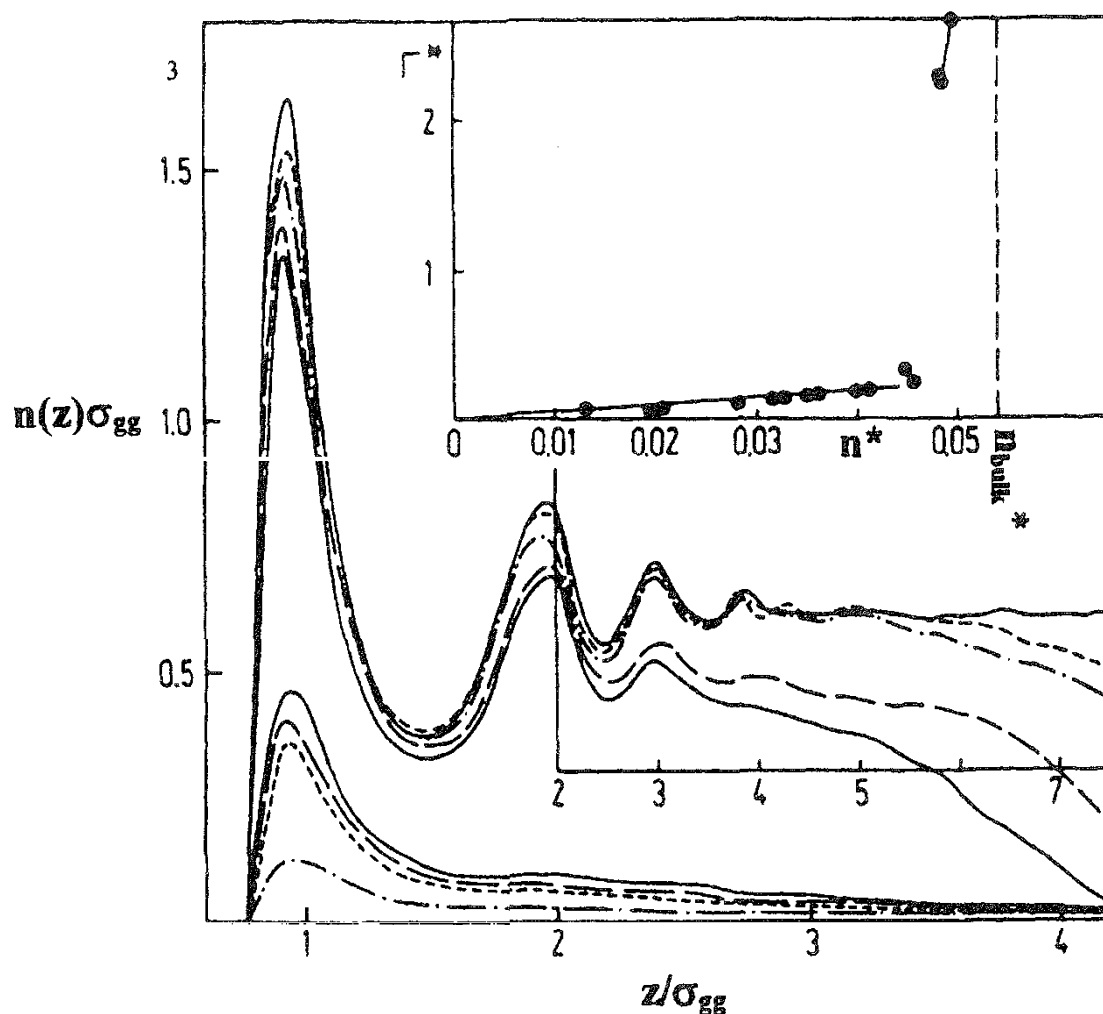


FIG. 19 Local densities of argon at $kT/\epsilon_{gg} = 1.1$ on a solid “CO₂” surface. The inset shows the adsorption isotherm, and the curves show the local densities for bulk-phase densities of (starting from the lowest) 0.0133, 0.0287, 0.0357, 0.0457, 0.0487, 0.0502, 0.0521, 0.0537, and 0.0656 (in reduced units = $n\sigma_{gg}^3$). The vertical dashed line in the inset figure is the saturated fluid density. A distance scale change is indicated for several of the density curves. (From Ref. 126.)

A number of such simulations have been reported, including the prewetting of Ar on solid CO₂ [127–129]; wetting and drying on a weakly interacting surface made up of Lennard-Jones atoms [130–132] (molecular dynamics was employed to obtain density profiles and surface tensions); wetting and drying in a square-well fluid–square-well wall system [133] that was simulated at various temperatures, densities, and well depths; and the wetting behavior of solutions [134]. In addition to deriving a number of useful exact expressions, the wetting properties of the square-well systems have been obtained for several well depths. It was found that the transition from a partially wetted to a dry surface is sharp; a combination of theory and simulation data indicates that it is in fact first-order. Much of this work has relied on evaluations of the solid-adsorbed fluid surface tension γ_{sf} . This quantity varies with film thickness and allows one to calculate the solid–fluid contact

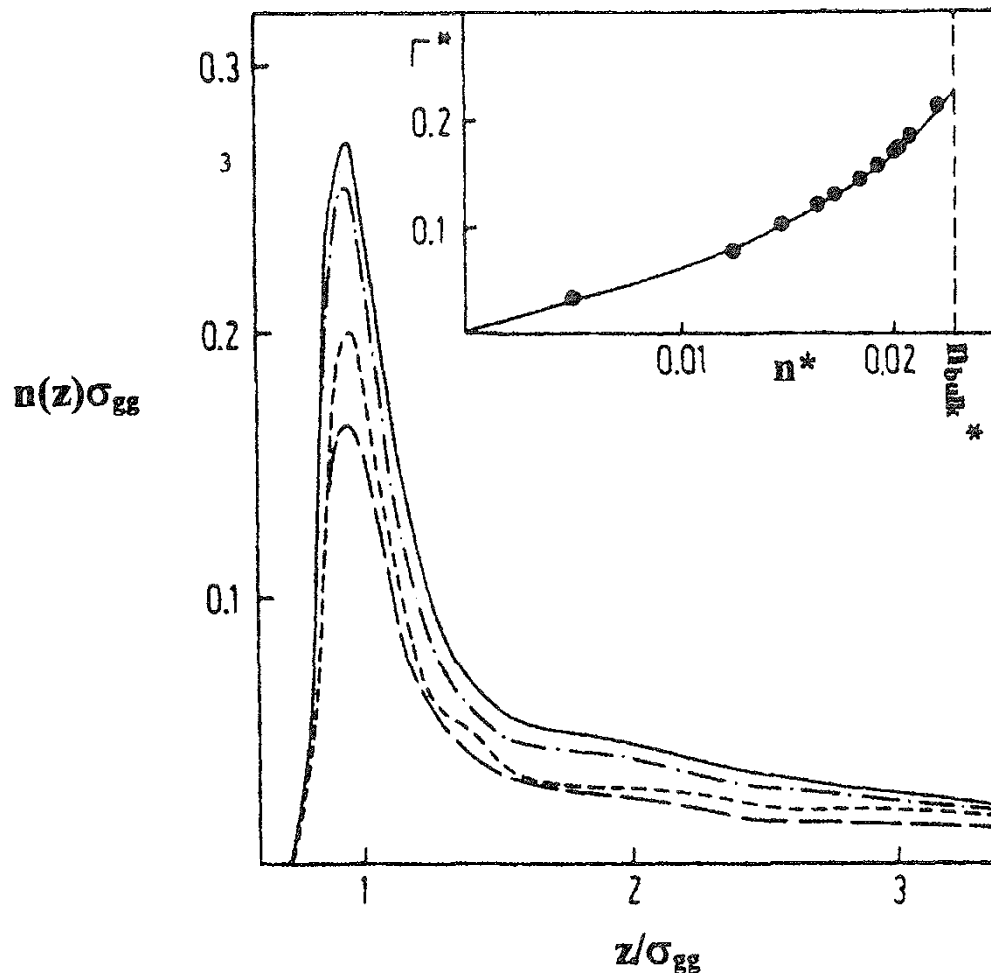


FIG. 20 Same as Fig. 19 but for partial wetting at $kT/\varepsilon_{gg} = 0.95$. The local density curves are for bulk densities of 0.0126, 0.0189, 0.0212, and 0.0226. (From Ref. 126.)

angle θ from Young's equation: $\gamma_{sv} - \gamma_{sl} = \gamma_{lv} \cos \theta$, where sv and sl denote the solid interfaced with the vapor and with the coexisting adsorbed fluid, respectively, and lv denotes the bulk liquid and coexisting vapor phases. Since this contact angle has a value of zero for the completely wetted surface and 180° for the nonwetting case (wetted by vapor only), with partially wetted surfaces having θ values between these limits, evaluations of the contact angle can provide an alternative route to the determination of wetting behavior.

V DISCUSSION

In this review, we have tried to show three aspects of the computer simulations of condensed matter:

1. The study of extremely simple systems, as exemplified by hard spheres. In this case, the computational power needed is relatively small, and the results are of primary interest as tests of theories. They are at best in qualitative agreement with experiment.

2. Studies based on the introduction of interaction potentials that are sufficiently realistic to produce results comparable with experimental data. In the adsorption case, these have been rare gases adsorbed on the graphite basal plane. The agreement with experiment, while of theoretical interest, primarily serves to validate the model potentials used.
3. Simulation outputs that give new physical insights not available otherwise. For example, the adsorbate local densities near the surface give information at the atomic level concerning the temperature and density of the distributions of the atoms near the surface that help reveal the mechanism of film growth. Splitting the adsorption energy into its gas–solid and gas–gas components is helpful, but not as helpful as the histograms that give the distributions of these energies.

The number of simulation studies of fluids physically adsorbed on solid surfaces and in model porous materials is too large for them to be reviewed here in their entirety. As stated above, most molecular dynamics studies have been omitted here on the grounds that these will be reviewed in the near future [115]. Unfortunately, this excludes much of the work on frozen (i.e., ordered) layers in monolayer and multilayer films. We have also excluded simulations on heterogeneous surfaces. These are normally modeled by introducing imperfections that are either geometric (such as cracks, steps, or amorphous surfaces rather than perfectly planar crystalline surfaces) or chemical (where impurity atoms are added to an initially chemically pure adsorbing surface). In fact, such studies are in their initial stages, and a great deal more work is needed before these systems are well understood. Many of the simulations of adsorption in porous materials, particularly in model zeolites, have also been omitted, as have the studies of solutions in pores and of nonspherical molecules adsorbed on simple surfaces and in pores [87,134,135]. In this last case, orientational ordering in monolayers and its changes with temperature and density have recently been reviewed elsewhere [113,136]. Simulations of nonspherical molecules in pores are scarce.

Consequently, the systems discussed here have been mostly limited to one-component atomic adsorbates on completely smooth or mildly corrugated surfaces such as the graphite basal plane. The large amount of experimental work carried out with the graphite basal plane as an adsorbent certainly warrants the theoretical and simulation studies reported for this system, and it seems fair to say that this particular adsorption problem is now essentially solved. Indeed, when one looks back to the 1960s when the pioneering experiments of the adsorption on atoms on the graphite basal plane were first reported by Thomy and Duval [76] and Thomy et al. [77], it is clear that enormous progress has been achieved in the understanding of fluid and solid adsorbed phases on simple surfaces and in simple pores. Much of this progress was at least assisted by computer simulation, which seems uniquely suited for the investigation of complex systems such as physical adsorption. There certainly remain many more problems in this area that will benefit from the insights afforded by thoughtful simulation studies.

REFERENCES

1. N. Metropolis, A. W. Rosenbluth, M. N. Rosenbluth, A. H. Teller, and E. Teller, *J. Chem. Phys.* **21**:1087 (1953).
2. W. W. Woods, in *Physics of Simple Liquids* (H. N. V. Temperley, J. S. Rowlinson, and G. S. Ruslibrooke. eds.), North-Holland, Amsterdam, 1968, Chap. 5.
3. A. Rahman, *Phys. Rev. A* **136**:405 (1964).
4. M. P. Allen and D. J. Tildesley. *Computer Simulation of Simple Liquids*, Clarendon Press, Oxford, UK, 1987.
K. Binder, *Monte Carlo Methods in Statistical Physics*. 2nd ed. (Topics Curr. Phys., Vol. 7), Springer-Verlag, Berlin, 1986,
6. K. Binder, *Applications of the Monte Carlo Method in Statistical Physics* (Topics Curr. Phys., Vol. 36), Springer-Verlag, Berlin, 1986.
D. Nicholson and N. Parsonage. *Computer Simulation and the Statistical Mechanics of Adsorption*, Academic. New York, 1982.
8. D. J. Evans and G. P. Morris, *Comp. Phys. Rep.* **1**:297 (1984).
9. S. Nose, *J. Chem. Phys.* **81**: 511 (1984); *Mol. Phys.* **57**:187 (1986).
10. D. J. Evans and B. Holian, *J. Chem. Phys.* **83**:4069 (1985).
11. W. Hoover, *Phys. Rev. A* **34**:2499 (1986).
12. T. L. Hill, *Statistical Mechanics*, McGraw-Hill, New York, 1958, Chap. 3.
13. T. Vuong and P. Monson, *Langmuir* **12**:5425 (1996).
14. J. S. Rowlinson and B. Widom, *Molecular Theory of Capillarity*, Oxford Univ. Press, New York, Sec. 4.2, 1987.
15. W. A. Steele, *The Interaction of Gases with Solid Surfaces*, Pergamon, New York, 1974. Chap. 3.
16. M. J. P. Nijmeijer and J. M. J. Bruin, *J. Phys. A.* **23**:4211 (1990).
17. M. J. P. Nijmeijer and C. Bruin, *J. Chem. Phys.* **105**:4889 (1996).
18. J. J. Magda. M. Tirrell, and H. T. Davis, *J. Chem. Phys.* **83**:1888 (1985).
19. J. E. Finn and P. A. Monson, *J. Chem. Phys.* **84**:1909 (1986).
20. A. Z. Pangiatopoulos, *Mol. Phys.* **61**:813 (1987).
21. A. Z. Pangiatopoulos, N. Quirke, M. Stapleton, and D. J. Tildesley, *Mol. Phys.* **63**:527 (1988).
22. B. Smit, in *Computer Simulations in Chemical Physics* (M. P. Allen and D. J. Tildesley, eds.), Elsevier, Amsterdam, 1993.
23. A.-L. Cheng and W. A. Steele, *Langmuir* **5**:1600(1989); *Mol. Sim.* **4**:349 (1990).
24. V. Bhethanabotla and W. A. Steele, *J. Chem. Phys.* **92**:3285 (1988).
25. J. E. Finn and P. A. Monson, *Mol. Phys.* **65**:1345 (1988).
26. S. Jiang and K. E. Gubbins, *Mol. Phys.* **86**:599 (1995).
27. B. Svensson and C. E. Woodward, *J. Chem. Phys.* **100**:4575 (1994).
28. M. Schoen, D. J. Diestler, and J. H. Cushman, *Mol. Phys.* **78**:1097 (1993).
29. W. A. Steele. *Chem. Rev.* **93**:2355 (1993).
30. G. Vidali, G. Ihm, H.-Y. Kim, and M. W. Cole, *Surf. Sci. Rep.* **12**:133 (1991).
31. C. M. Knobler and R. C. Desai, *Annu. Rev. Phys. Chem.* **43**:207 (1992).
32. G. Kaminski and W. L. Jorgenson, *J. Phys. Chem.* **100**:18010 (1996).
33. W. A. Steele. *Surf. Sci.* **36**:317 (1973).
34. J. E. Lennard-Jones and R. M. Dent. *Trans. Faraday Soc.* **24**:92 (1928).
35. M. J. Bojan and W. A. Steele, *Langmuir* **5**:625 (1988).

36. M. J. Bojan and W. A. Steele, *Langmuir* 9:2569 (1993); *Mol. Phys.*, (1998).
37. M. J. Bojan, E. Cheng, M. W. Cole. and W. A. Steele, *Adsorption* 2:53 (1996).
38. M. J. Bojan and W. A. Steele. *Carbon*, in press.
39. G. J. Tjatjopoulos, D. L. Feke, and J. A. Mann, Jr., *J. Phys. Chem.* 92:4006 (1988).
40. V. A. Bakaev and W. A. Steele, *Langmuir* 8:148 (1992).
41. V. A. Bakaev and W. A. Steele. *Langmuir* 8:910 (1992).
42. M. J. Bojan and W. A. Steele, in *Proc. 5th Conference on Fundamentals of Adsorption*. Asilomar, 1995 (M. D. LeVan, ed.), Kluwer, Amsterdam, 1996. p. 17.
43. M. J. Bojan and W. A. Steele, in *Characterization of Porous Solids IV* (T. Mays and B. MacEnaney, eds.), Elsevier, Amsterdam, 1998. p. 49.
44. J. R. Henderson and F. van Swol, *Mol. Phys.* 51:991 (1984).
45. I. Z. Fisher. *Statistical Theory of Liquids*, Univ. Chicago Press, Chicago, 1967, Chap. 6.
46. G. Rickayzen and A. Augousti, *Mol. Phys.* 52:1355 (1984).
47. M. Moradi and G. Rickayzen. *Mol. Phys.* 66:143 (1989).
48. Z. Tan, U. M. B. Marconi, and K. Gubbins, *J. Chem. Phys.* 90:3704 (1989).
49. I. K. Snook and D. Henderson, *J. Chem. Phys.* 68:2134 (1978).
50. R. Pospíšil, A. Malijevský, P. Jech. and W. R Smith, *Mol. Phys.* 78:1461 (1993).
51. M. Plischke and D. Henderson, *J. Phys. Chem.* 88:6544 (1984).
52. A. Antonchenko, V. V. Ilyin, N. N. Makovsky. and V. M. Khryapa, *Mol. Phys.* 65:1171 (1988).
53. R. D. Groot, N. M. Faber, and J. P. van der Eerden, *Mol. Phys.* 62:861 (1987).
54. S. Labik and W. R. Smith, *Mol. Phys.* 88:1411 (1996).
55. J. Alejandre. M. Lozada-Cassou. and L. DeGrève, *Mol. Phys.* 88:1317 (1996).
56. F. Holovko and E. V. Vakarin. *Mol. Phys.* 87:1375 (1996).
57. A. Yethiraj and C. K. Hall, *J. Chem. Phys.* 91:4827 (1989).
58. A. Yethiraj and C. K. Hall. *Mol. Phys.* 73:503 (1991).
59. K. Chen, T. Kaplan, and M. Mostoller, *Phys. Rev. Lett.* 74:4019 (1995).
60. F. Abraham, *Phys. Rev. B* 23:6145 (1981).
61. J. A. Barker, D. Henderson, and F. Abraham. *Physica* 106A:226 (1981).
62. M. P. Allen, D. Frenkel, W. Gignac, and J. McTague, *J. Chem. Phys.* 78:4206 (1983).
63. D. J. Evans. *Phys. Lett.* 88A:48 (1982).
64. K. J. Naidoo, J. Schnitker, and J. D. Weeks, *Mol. Phys.* 80:1 (1993).
65. K. J. Naidoo and J. Schnitter, *J. Chem. Phys.* 100:3114 (1994).
66. H. Weber, D. Marx, and K. Binder, *Phys. Rev. B* 51:14636 (1995).
67. J. A. Zollweg and G. V. Chester. *Phys. Rev. B* 46:1190 (1992).
68. B. J. Alder and T. E. Wainwright, *Phys. Rev.* 127:359 (1962).
69. M. Li, W. L. Johnson. and W. A. Goddard III, *Phys. Rev. E* 54:12067 (1996).
70. K. Bagchi, H. C. Anderson, and W. Swope, *Phys. Rev. E* 53:3794 (1994).
71. M. Schoen, D. J. Diestler, and J. H. Cushman. *J. Chem. Phys.* 101:6865 (1994).
72. M. Schmidt and H. Löwen, *Phys. Rev. E* 55:7228 (1997).
73. F. F. Abraham and Y. Singh, *J. Chem. Phys.* 67:2384 (1977).
74. I. Snook and W. van Megen, *J. Chem. Phys.* 70:3099 (1979).
75. (a) B. Smit, *J. Chem. Phys.* 96:8639 (1992); (b) B. Smit and D. Frenkel, *J. Chem. Phys.* 94:5663 (1991).

76. A. Thomy and X. Duval, *J. Chim. Phys.* 66:1966 (1970); 67:286 (1970).
77. A. Thomy, X. Duval, and J. Regnier, *Comptes Rend. Ser. C* 268:1416 (1969).
78. L. A. Rowley, D. Nicholson, and N. G. Parsonage, *Mol. Phys.* 31:365 (1976); 31:389 (1970).
79. J. S. Whitehouse, D. Nicholson, and N. G. Parsonage, *Mol. Phys.* 49:829 (1983).
80. D. Nicholson, N. G. Parsonage, and L. A. Rowley, *Mol. Phys.* 44:629 (1981).
81. S. Jiang, K. E. Gubbins, and J. A. Zollweg, *Mol. Phys.* 79:373 (1993).
82. J. E. Finn and P. A. Monson, *Mol. Phys.* 72:661 (1991).
83. S. J. Gregg and K. S. W. Sing, *Adsorption, Surface Area and Porosity*, 2nd ed., Academic, New York, 1982.
84. J. P. R. B. Walton and N. Quirke, *Mol. Sim.* 2:361 (1989).
85. B. K. Peterson and K. E. Gubbins, *Mol. Phys.* 62:215 (1987).
86. R. Evans, U. M. B. Marconi, and P. Tarazona, *J. Chem. Phys.* 84:2376 (1986).
87. K. Gubbins, M. Sliwinski-Bratkowiak, and S.-H. Suh, *Mol. Sim.* 17:333 (1996).
88. A. Panagiotopoulos, *Mol. Phys.* 62:701 (1987).
89. J. Forsman and C. E. Woodward, *Mol. Phys.* 90:637 (1997).
90. S. Jiang, C. L. Rhykerd, and K. E. Gubbins, *Mol. Phys.* 79:373 (1993).
91. E. M. Piotrovskaya and E. N. Brodskaya, *Langmuir* 11:2121 (1995).
92. P. N. Aukette, N. Quirke, S. Riddiford, and S. R. Tennison, *Carbon* 30:913 (1992).
93. D. Nicholson, in *Characterization of Porous Solids II* (F. Rodriguez-Reinoso, J. Rouquerol, K. S. W. Sing, and K. K. Unger, eds.), Elsevier, Amsterdam, 1991, p. 11.
94. T. Suzuki, K. Kaneko, and K. E. Gubbins, *Langmuir* 13:2545 (1997).
95. R. F. Cracknell, D. Nicholson, and N. Quirke, *Mol. Phys.* 80:885 (1993).
96. M. Schoen, C. L. Rhykerd, Jr., J. H. Cushman, and D. J. Diestler, *Mol. Phys.* 66:1171 (1989).
97. M. Schoen, D. J. Diestler, and J. H. Cushman, *J. Chem. Phys.* 87:5464 (1987).
98. J. E. Curry, J. H. Cushman, M. Schoen, and D. J. Diestler, *Mol. Phys.* 81:1059 (1994).
99. J. E. Curry and J. H. Cushman, *Mol. Phys.* 85:173 (1995).
100. B. K. Peterson, J. P. R. B. Walton, and K. E. Gubbins, *Proceedings of the 2nd International Conference on Fundamentals of Adsorption* (A. I. Liapis, ed.), Engineering Foundation, New York, 1987, p. 463.
101. G. S. Heffelfinger, F. van Swol, and K. E. Gubbins, *Mol. Phys.* 61:1381 (1987).
102. P. C. Ball and R. Evans, *Mol. Phys.* 63:159 (1988).
103. Z. Tan, F. van Swol, and K. E. Gubbins, *Mol. Phys.* 62:1213 (1987).
104. W. van Megen and I. K. Snook, *Mol. Phys.* 45:629 (1982); 47:1417 (1982).
105. J. Vermesse and D. Levesque, *J. Chem. Phys.* 101:9063 (1994).
106. W. van Megen and I. K. Snook, *Mol. Phys.* 54:741 (1985).
107. J. Specovius and G. M. Findenegg, *Ber. Bunsenges. Phys. Chem.* 82:174 (1978).
108. M. Schoen and M. Thommes, *Phys. Rev. E* 52:6375 (1995).
109. M. Thommes and G. M. Findenegg, *Langmuir* 10:4270 (1994).
110. M. Thommes, G. H. Findenegg, and H. Lewandowski, *Ber. Bunsenges. Phys. Chem.* 98:477 (1994).
111. M. Thommes, G. H. Findenegg, and M. Schoen, *Langmuir* 11:2137 (1994).

112. N. D. Shrimpton, M. W. Cole, and W. A. Steele. in *Surface Properties of Layered Materials* (G. Benedek. ed.), Kluwer, Amsterdam, 1991, p. 219.
113. W. A. Steele, *Langmuir* 12:145 (1996).
114. J. M. Houlrik, D. P. Landau. and S. J. Knak Jensen, *Phys. Rev. E* 50: 2007 (1994).
115. W. A. Steele. in *Molecular Dynamics* (P. Balbuena and J. M. Seminario, eds.), Elsevier, Amsterdam, in press.
116. J. E. Lane and T. Spurling. *Aust. J. Chem.* 29:2103 (1976).
117. J. E. Lane and T. Spurling, *Aust. J. Chem.* 31:933 (1978); 34:1 (1981).
118. D. Nicholson and N. G. Parsonage. *J. Chem. Soc., Faraday Trans. 2* 82:1657 (1986).
119. F. F. Abraham. *Adv. Phys.* 35:1 (1986).
120. F. F. Abraham, *J. Chem. Phys.* 68:3713 (1978).
121. J. F. Knight and P. A. Monson, *J. Chem. Phys.* 84:1909 (1986).
122. A. Patrykiewicz, S. Sokolowski, T. Zeintarski, and K. Binder. *J. Chem. Phys.* 102:8221 (1995).
123. M. Schoen, D. J. Diestler, and J. H. Cushman, *Mol. Phys.* 78:1097 (1993).
124. A. Patrykiewicz. in *Adsorption on New and Modified Inorganic Sorbents*, A. Dabrowski and V. A. Tertyleh, eds. Elsevier New York, 1996, p. 599.
125. M. J. Bojan and W. A. Steele, *Adv. Colloid Interface Sci.* 76–77:153 (1998) Vol. 76–77 p. 153.
126. S. Sokolowski and J. Fischer *Phys. Rev. A* 41:6866 (1990).
127. J. E. Finn and P. A. Monson, *Phys. Rev. A* 39:6402 (1989).
128. Y. Fan and P. A. Monson, *J. Chem. Phys.* 99:6897 (1993).
129. P. Adams and J. R. Henderson. *Mol. Phys.* 73:1383 (1991).
130. J. H. Sikkenk, J. O. Indeku, J. M. J. van Leeuwen, and E. O. Vossnack, *Phys. Rev. Lett.* 59:98 (1987).
131. J. H. Sikkenk, J. O. Indeku, J. M. J. van Leeuwen, E. O. Vossnak, and A. F. Bakker. *J. Stat. Phys.* 52:23 (1988).
132. M. P. J. Nijmeijer, C. Bruin, A. F. Bakker, and J. M. J. van Leeuwen. *Mol. Phys.* 72:927 (1991).
133. F. van Swol and J. R. Henderson, *J. Chem. Soc., Faraday Trans. 2* 82:1685 (1986).
134. Y. Fan, J. E. Finn, and P. A. Monson. *Fluid Phase Equil.* 75:163 (1992).
135. R. F. Cracknell, K. E. Gubbins, M. Maddox, and D. Nicholson, *Acc. Chem. Res.* 28:281 (1995).
136. D. Marx and H. Weichert, *Adv. Chem. Phys.* 95:213 (1996).

15

Surface Heterogeneity Effects on Adsorption Equilibria and Kinetics: Rationalizations of the Elovich Equation

WLADYSŁAW RUDZINSKI and TOMASZ PANCZYK Department of Theoretical Chemistry, Marie-Curie-Sklodowska University, Lublin, Poland

| | |
|--|-----|
| I. Introduction | 355 |
| II. Theory | 357 |
| A. Principles of the absolute rate theory and of adsorption equilibria | 357 |
| B. The condensation approximation approach to adsorption equilibria and kinetics | 359 |
| C. Generalization of ART for energetically heterogeneous solid surfaces | 364 |
| D. Theories relating the rate of adsorption/desorption processes to the chemical potential of adsorbed molecules | 374 |
| References | 388 |

I. INTRODUCTION

Most frequently the Elovich equation is written in its differential form,

$$\frac{dN}{dt} = ae^{-\alpha N} \quad (1)$$

describing the dependence of the amount adsorbed N on time t . Here, a and α are constants characteristic of the adsorption system under investigation. Assuming that at $t = 0$, $N = 0$, one arrives at the following integral form of the Elovich equation:

$$N = \frac{1}{\alpha} \ln[a\alpha t + 1] \quad (2)$$

which is also frequently used. However, the meaning of the Elovich equation should be sought in its differential form, which was first used by Tamman and Köster in 1922 to describe the kinetics of oxidation of metals [1]. Later Roginsky and Zeldovich [2–4] were the first to report on the applicability of Eq. (1) to describe chemisorption kinetics. As a result, Eq. (1) is also sometimes called the Roginsky–Zeldovich equation. However, it was Elovich and coworkers [5–7] who later demonstrated the wide applicability of Eq. (1) and proposed a rationalization for that empirical equation, and in the end the name of Elovich became attached to the form.

That equation and its integral form soon gained enormous popularity among scientists investigating the kinetics of gas adsorption on solid surfaces. Correlations of experimental data usually started with the application of that equation, and the frequently noted deviations from "Elovich behavior" were the form of analysis in dozens of published papers. Even reviews followed that general trend, discussing the Elovich equations and "deviations" from it.

Thus, in the introduction to a 1960 review, Low [8] explained that "the Elovich equation has been adopted for the present use in order to express, compare, and contrast with precision the otherwise chaotic data of chemisorption kinetics." That exhaustive review reflected a generally poor understanding of the phenomena behind that equation. Ten years later an excellent monograph published by Aharoni and Tompkins [9] was oriented toward a theoretical study of the origin of the Elovich equation. These authors pursued an idea proposed by Elovich in 1936, elaborated further in the 1940s by Temkin [10,11], and later discussed by Roginski in his 1949 monograph [12]. The proposal was that the Elovich equation describes the kinetics of adsorption on solids where the adsorption equilibrium is described by a Temkin isotherm. Two excellent reviews published by Tovbin [13] and Cerofolini [14] have appeared in the 1990s that shed more light on the problem.

According to the latter authors the rationalization of the Elovich equation is simple. It is based on the application of the absolute rate theory (ART) to adsorption on an energetically heterogeneous surface with a rectangular distribution of activation energies for adsorption. An implicit assumption is then made that the adsorption process is at quasi-equilibrium, that the process proceeds in a stepwise fashion, and that the activation energy for adsorption increases linearly with surface coverage.

Recently, Rudzinski and Aharoni [15,16] presented a new development of the equation, based on the statistical rate theory of interfacial transport (SRTIT) published by Ward and coworkers [17,18]. The new development is more rigorous in a thermodynamic sense and shows that the Elovich equation neglects the kinetics of simultaneous desorption.

A neglect of desorption kinetics may be the source of the deviations from the "Elovich behavior" observed in real adsorption systems. The new theoretical approach based on SRTIT also allows us to develop in a easy way a more general form of the Elovich equation, taking into account desorption kinetics. The form thus derived can now be tested against previously deviant adsorption kinetics data.

II. THEORY

A Principles of the Absolute Rate Theory and of Adsorption Equilibria

We start with a brief review of the approaches used to describe adsorption and desorption kinetics. First we consider the oldest, the still popular ART approach.

According to ART, in order for a molecule to take part in a reaction it must first form an activated complex. This can be accomplished by an input of energy—the "activation energy." It is assumed that molecules in the activated state are in equilibrium with the reactants and that the rate of reaction is the rate at which molecules pass through the activated state. In the case of adsorption, the reactant is a gas-phase molecule, and the activation energy for adsorption ε_a is the energy difference between that of the gas-phase molecule and the energy of molecules in the "activated" or "transition" state. The most exhaustive and clearest development of the ART expression for the rate of adsorption R_a is probably the one given by Clark [19],

$$R_a = \alpha v F(\theta) \exp\left[\frac{-\varepsilon_a}{kT}\right] \quad (3)$$

where $v = p/(2\pi mkT)^{1/2}$ is the rate of collision of gas molecules of mass m with the surface, p is the pressure, k and T are the Boltzmann constant and absolute temperature, respectively, and $F(\theta)$ is the fraction of surface available for adsorbing molecules. The product $vF(\theta) \exp[-\varepsilon_a/kT]$ is the rate at which molecules with sufficient energy strike vacant adsorption sites, and α , the condensation coefficient, is the fraction of molecules meeting this condition that actually adsorb.

For desorption, it is assumed that the desorbing molecule must pass through an activated state before desorbing. The activation energy for desorption, ε_d , is defined as the difference in energy between the adsorbed molecules and those in the activated state for desorption, and it is assumed that the adsorbed molecules are in equilibrium with the molecules in the activated state. The absolute rate theory offers the following expression for the desorption rate, R_d :

$$R_d = \gamma G(\theta) \exp\left[\frac{-\varepsilon_d}{kT}\right] \quad (4)$$

where γ is a constant and $G(\theta)$ is another unspecified function of the surface coverage θ . The change of the surface coverage with time ($d\theta/dt$) is thus given by

$$\frac{d\theta}{dt} = R_a - R_d \quad (5)$$

The absolute rate theory does not lead to explicit expressions for the functions $F(\theta)$ and $G(\theta)$ and does not suggest that α , γ , ε_a , ε_d might depend on the surface coverage θ .

First a coverage dependence of the preexponential factors was introduced on an empirical basis, leading to the following expression for $d\theta/dt$:

$$\frac{d\theta}{dt} = K_a p (1 - \theta)^s \exp\left[\frac{-\varepsilon_a}{kT}\right] - K_d \theta^s \exp\left[\frac{-\varepsilon_d}{kT}\right] \quad (6)$$

where s is the number of adsorption sites involved in an elementary adsorption-desorption process. In the case of $s = 1$, i.e., when one molecule occupies one adsorption site, at equilibrium when $d\theta/dt = 0$, Eq. (4) yields the Langmuir isotherm equation,

$$\theta^{(e)}(p, T) = \frac{Kp^{(e)} \exp(\varepsilon/kT)}{1 + Kp^{(e)} \exp(\varepsilon/kT)} \quad (7)$$

where $K = K_a/K_d$ and $\varepsilon = \varepsilon_d - \varepsilon_a$, and where the superscript e refers to equilibrium.

The strategy of experimental studies in adsorption has long hindered progress in understanding the nature of adsorption-desorption processes. This is because experimental studies have proceeded along three quite separate paths with only a minor interchange of ideas.

One group working on adsorption kinetics soon discovered the inapplicability of ART in describing the kinetics of adsorption in real adsorption systems. Instead, the empirical Elovich equation was used, aided sometimes by other empirical expressions. The Elovich equation was justified in using ART assuming that the activation energy for adsorption ε_a changes linearly with the surface coverage. At the same time it was assumed that the constant K_a does not depend on the surface coverage. The latter assumption is to be emphasized for reasons that will soon be explained.

The second group investigating desorption kinetics also discovered the inapplicability of the ART expression for correlating experimental data. Experiments on isothermal desorption kinetics were rarely reported, and almost all experimental studies were oriented toward the kinetics of thermodesorption. This was stimulated by the development of the temperature-programmed desorption (TPD) technique, which is easy to use [20-25]. The inapplicability of the ART expression to describe TPD experiment was solved by the assumption that the activation energy for desorption also varies with surface coverage [26-34]. Also, the assumption had to be made that the desorption constant K_d varies with surface coverage. The necessary procedures of deducing the functions $\varepsilon_d(\theta)$ and $K_d(\theta)$ were reviewed by Zhdanov [35] in his intriguing review, which collected a large variety of results from the literature. Zhdanov showed that the $\varepsilon_d(\theta)$ and $K_d(\theta)$ functions obtained by applying different assumptions were different as a rule rather than as an exception: $K_d(\theta)$ varied with θ by several orders of magnitude. This, as we will see, raises serious questions concerning the applicability of the ART approach. To show this, we first have to consider studies of adsorption equilibria.

The third group of scientists reported on the inapplicability of the Langmuir equation for describing adsorption equilibria in real adsorption systems, starting as early as the 1920s. Instead, empirical isotherm equations such as the Temkin, Freundlich, Toth, or Langmuir-Freundlich equations were widely used [36-39]. As a matter of fact, it was Langmuir himself who first emphasized [40] that there may exist various sites on solid surfaces that are characterized by various values of the adsorption energy ε . This idea was developed further by Roginski [12], who argued that in most cases the spectrum of adsorption energies will be so dense that one can use a continuous function $\chi(\varepsilon)$ to describe the differential distribution of the

number of sites with corresponding values of adsorption energy. That function is usually used in its form normalized to unity,

$$\int_{\Omega_a} \chi(\varepsilon) d\varepsilon = 1 \quad (8)$$

where Ω_a is the physical domain of the adsorption energies found in a given gas–solid system. At the same time it was assumed that the variation of the preexponential constant K with surface coverage should be so small that it can safely be neglected. The experimentally monitored surface coverage $\theta_i(p^{(e)} T)$ was represented by the integral

$$\theta_i^{(e)}(p^{(e)}, T) = \int_{\Omega_a} \theta^{(e)}(\varepsilon, p^{(e)}, T) \chi(\varepsilon) d\varepsilon \quad (9)$$

where $\theta(\varepsilon, p^{(e)}, T)$ is an isotherm equation describing the adsorption on sites characterized by adsorption energy ε . Most commonly the Langmuir isotherm was used to represent the "local" adsorption isotherm $\theta^{(e)}(\varepsilon, p^{(e)}, T)$. In the interest of simplicity we first consider this isotherm equation, neglecting lateral interactions between adsorbed molecules. Application of the Langmuir equation, along with a Gaussian-like adsorption energy distribution $\chi(\varepsilon)$ in Eq. (9) leads to the result that $\theta_i^{(e)}(p^{(e)}, T)$ takes the form of the well-known Langmuir–Freundlich empirical isotherm equation. That isotherm has been successfully applied to describe experimental isotherms in a variety of gas–solid systems [37]. In systems where strong surface heterogeneity is assumed to exist, the rectangular function

$$\chi(\varepsilon) = \begin{cases} \frac{1}{\varepsilon_m - \varepsilon_l} & \text{for } \varepsilon_l \leq \varepsilon \leq \varepsilon_m \\ 0 & \text{elsewhere} \end{cases} \quad (10)$$

is commonly applied to represent the dispersion of adsorption energies. Its application in Eq. (9) yields an expression for $\theta_i^{(e)}(\varepsilon, p^{(e)}, T)$ similar to the well-known Temkin isotherm.

B. The Condensation Approximation Approach to Adsorption Equilibria and Kinetics

There is one approach in the theories of adsorption that is extremely useful in considering the effects of solid surface energetic heterogeneity. It has been used mainly to study adsorption equilibria, but it can also be applied to the study of adsorption kinetics, as we will soon show. For that reason we repeat briefly the principles of that approach, called the CA (condensation approximation) approach.

We rewrite Eq. (7) in the form

$$\theta^{(e)}(\varepsilon, p, T) = \frac{\exp[(\varepsilon - \varepsilon_c^{(e)})/kT]}{1 + \exp[(\varepsilon - \varepsilon_c^{(e)})/kT]} \quad (11)$$

where

$$\varepsilon_c = -kT \ln[Kp^{(e)}] \quad (12)$$

Figure 1 shows the temperature dependence of the function $\theta^{(e)}(\varepsilon, \varepsilon_c)$,

$$\theta(\varepsilon) = \frac{\exp[\varepsilon_r/\tau]}{1 + \exp[\varepsilon_r/\tau]} \quad (13)$$

where $\varepsilon_r = (\varepsilon - \varepsilon_c)/kT_0$, and $\tau = T/T_0$ are appropriate dimensionless values.

Figure 1 shows that the kernel $\theta(\varepsilon)$ becomes a step function in the hypothetical limit $T \rightarrow 0$,

$$\lim_{T \rightarrow 0} \theta(\varepsilon, \varepsilon_c) = \theta_c(\varepsilon, \varepsilon_c) = \begin{cases} 0, & \varepsilon < \varepsilon_c \\ 1, & \varepsilon \geq \varepsilon_c \end{cases} \quad (14)$$

This means that at moderate temperatures, adsorption (desorption) on a heterogeneous solid surface proceeds in a stepwise fashion.

In the limit $T \rightarrow 0$ the kernel $\theta(\varepsilon)$ in Eq. (9) becomes the step function (14), so θ_t takes the simple form

$$\theta_t = \int_{\varepsilon_c}^{\infty} \mathcal{X}(\varepsilon) d\varepsilon = -\mathcal{X}(\varepsilon_c) \quad (15)$$

where $\mathcal{X}(\varepsilon)$ is the integral of $\mathcal{X}(\varepsilon)$,

$$\mathcal{X}(\varepsilon) = \mathcal{X}(\varepsilon) d\varepsilon \quad (16)$$

and the integration constant is chosen in such a way that $\mathcal{X}(\infty) = 0$. The assumption that the limits are $(0, +\infty)$ is commonly made in adsorption literature for the purpose of mathematical convenience. It does not affect the calculations until extremely low ($\theta_t \rightarrow 0$) or extremely high ($\theta_t \rightarrow 1$) coverages are considered [37].

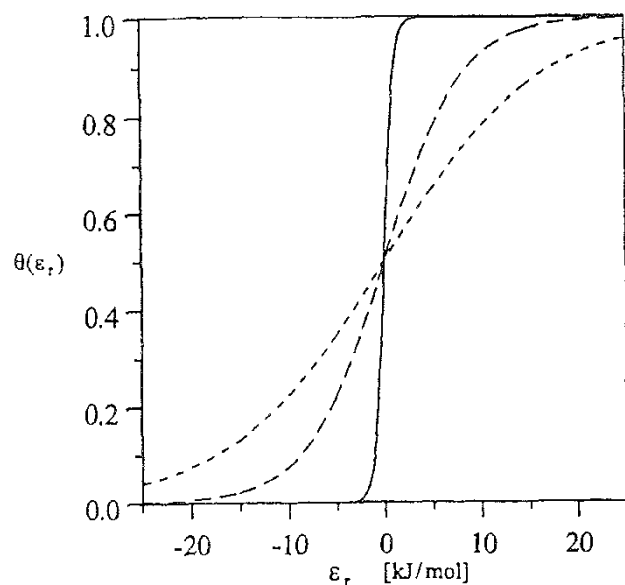


FIG. 1 Temperature dependence of the function $\theta(\varepsilon)$ in Eq. (13). The dimensionless temperatures are $\tau_1 = 0.5$ (—), $\tau_2 = 4$ (---), and $\tau_3 = 8$ (- · -).

Calculating θ_t in this way has been known for a long time in theories of adsorption equilibria and is called the condensation approximation.

At finite temperatures, $\theta(\varepsilon, \varepsilon_c)$ is not exactly a step function, but it is a frequent practice to replace the true kernel θ under the integral of Eq. (9) by a step function θ_c located at $\varepsilon = \varepsilon_c$ defined by the condition

$$\left(\frac{\partial^2 \theta}{\partial \varepsilon^2} \right)_{\varepsilon = \varepsilon_c} = 0 \quad (17)$$

Thus, ε_c is the value of ε at which the isotherm derivative $\partial\theta/\partial\varepsilon$ reaches its maximum. Figure 2 shows the derivatives $\partial\theta/\partial\varepsilon$ of the isotherms $\theta(\varepsilon, \varepsilon_c)$ drawn in Fig. 1.

Surprisingly, the above-described practice leads to pretty exact values of θ , for many adsorption systems (adsorption regimes) reported in the literature. The reason for that is that $\mathcal{X}(\varepsilon_c)$ appears to be the leading term of a certain expansion for θ_t at finite temperatures [37]. For a better understanding of the forthcoming considerations and the approximation made, we repeat briefly the principles of that expansion.

The integral of Eq. (9) is evaluated by parts:

$$\theta_t(p, T) = \theta(\varepsilon, p, T) \mathcal{X}(\varepsilon)|_0^\infty - \int_0^\infty \left(\frac{\partial \theta}{\partial \varepsilon} \right) \mathcal{X}(\varepsilon) d\varepsilon \quad (18)$$

It can be shown that the first term on the right-hand side of Eq. (18) is negligible compared to the second except for very small and very high values of θ , [37]. Therefore the second term is evaluated by expanding $\mathcal{X}(\varepsilon)$ into its Taylor series around the point $\varepsilon = \varepsilon_c$, at which $\partial\theta/\partial\varepsilon$ reaches its sharp maximum,

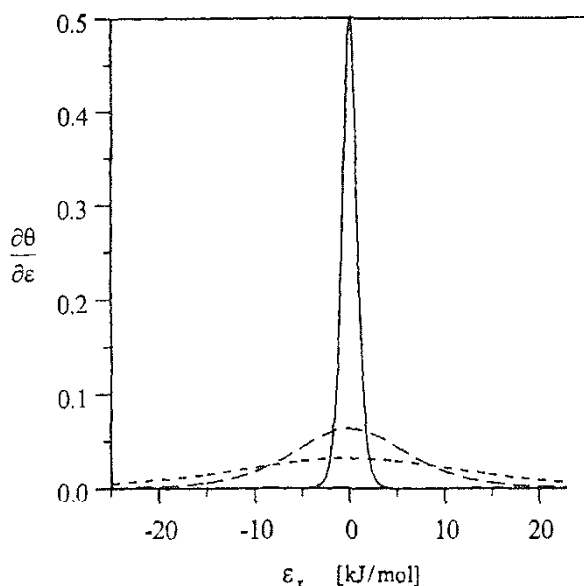


FIG. 2 The derivatives $\partial\theta/\partial\varepsilon$ of the function $\theta(\varepsilon)$ in Eq. (13) for the three dimensionless temperatures $\tau_1 = 0.5$ (—), $\tau_2 = 4$ (---), and $\tau_3 = 8$ (- - -).

$$\begin{aligned}
& - \int_0^\infty \left(\frac{\partial \theta}{\partial \varepsilon} \right) \mathcal{X}(\varepsilon) d\varepsilon = \\
& - \int_0^\infty \left(\frac{\partial \theta}{\partial \varepsilon} \right) \left[\mathcal{X}(\varepsilon_c) + \left(\frac{\partial \mathcal{X}}{\partial \varepsilon} \right)_{\varepsilon_c} (\varepsilon - \varepsilon_c) + \frac{1}{2} \left(\frac{\partial^2 \mathcal{X}}{\partial \varepsilon^2} \right)_{\varepsilon_c} (\varepsilon - \varepsilon_c)^2 + \dots \right] d\varepsilon
\end{aligned} \tag{19}$$

Thus

$$\begin{aligned}
\theta_t = & -\mathcal{X}(\varepsilon_c) - \left(\frac{\partial \mathcal{X}}{\partial \varepsilon} \right)_{\varepsilon_c} \int_0^\infty \left(\frac{\partial \theta}{\partial \varepsilon} \right) (\varepsilon_c - \varepsilon) d\varepsilon \\
& + \frac{1}{2} \left(\frac{\partial^2 \mathcal{X}}{\partial \varepsilon^2} \right)_{\varepsilon_c} \int_0^\infty \left(\frac{\partial \theta}{\partial \varepsilon} \right) (\varepsilon_c - \varepsilon)^2 d\varepsilon + \dots
\end{aligned} \tag{20}$$

The first term on the right-hand side of Eq. (20) is just the result obtained by applying the condensation approximation, i.e., assuming the hypothetical limit $T \rightarrow 0$. Because of the symmetry of the function $\partial\theta/\partial\varepsilon$, the second term on the right disappears, and the first nonvanishing correction to $-\mathcal{X}(\varepsilon_c)$ is the second correction term. For the Langmuir model of adsorption, to a good approximation [37],

$$\int_0^\infty \left(\frac{\partial \theta}{\partial \varepsilon} \right) (\varepsilon_c - \varepsilon)^2 d\varepsilon = \frac{\pi^2}{3} (kT)^2 \tag{21}$$

$\mathcal{X}(\varepsilon)$ is not the only function that may appear in the theoretical considerations of adsorption on heterogeneous solid surfaces. However, one assumes that

$$\int_0^\infty \left(\frac{\partial \theta}{\partial \varepsilon} \right) \phi(\varepsilon) d\varepsilon = \phi(\varepsilon_c) \tag{22}$$

This is equivalent to accepting the accuracy level corresponding to the condensation approximation. As in the case of calculating θ_t , $\phi(\varepsilon_c)$ will always be a leading term, thus usually approximating pretty well the exact value of the integral. It can also be shown that at all finite temperatures $\phi(\varepsilon_c)$ yields a fairly exact value of integral (8) if the variance of $\phi(\varepsilon)$ is reasonably larger than the variance of $\partial\theta/\partial\varepsilon$ [37].

The function $\mathcal{X}_c(\varepsilon_c)$ calculated from the relation

$$\mathcal{X}_c(\varepsilon_c) = -\frac{\partial \theta_t}{\partial s} = -\frac{1}{N_m} \frac{dN_t(\varepsilon_c)}{ds} \tag{23}$$

is usually called the condensation approximation for the actual adsorption energy distribution $\mathcal{X}(\varepsilon)$ and is defined as

$$\mathcal{X}_c(\varepsilon_c) = \int_0^\infty \left(\frac{\partial \theta}{\partial \varepsilon} \right) \mathcal{X}(\varepsilon) d\varepsilon \tag{24}$$

In the limit $T \rightarrow 0$, the derivative $\partial\theta/\partial\varepsilon$ becomes the Dirac delta function $\delta(\varepsilon - \varepsilon_c)$, and $\mathcal{X}_c(\varepsilon_c)$ becomes the exact function $\mathcal{X}(\varepsilon)$.

As we have mentioned, the Elovich equation for adsorption kinetics is associated mainly with the systems in which the equilibrium adsorption isotherm is described by Temkin's equation [3],

$$\theta_i(p, T) = C_1 + C_2 \ln p \quad (25)$$

where C_1 and C_2 are constants. Temkin's equation is obtained by accepting the CA equation (15) along with the rectangular adsorption energy distribution. Eq. (10). The expression for $\theta_i(p, T)$ then takes the explicit form

$$\theta_i^{(e)}(p^{(e)}, T) = \frac{\varepsilon_m}{\varepsilon_m - \varepsilon_l} + \frac{kT}{\varepsilon_m - \varepsilon_l} \ln(Kp^{(e)}) \quad (26)$$

For the rectangular adsorption energy distribution, CA becomes applicable when $(\varepsilon_m - \varepsilon_l)/kT \gg 1$. In this limit the exact result of the integration in Eq. (9) becomes the Temkin equation, Eq. (26). To show this, let us consider the exact result of integration in Eq. (9) when $\chi(\varepsilon)$ is the rectangular adsorption energy distribution, Eq. (10). Then the expression for $\theta_i^{(e)}(p^{(e)}, T)$ reads

$$\theta_i^{(e)}(p^{(e)}, T) = \frac{kT}{\varepsilon_m - \varepsilon_l} \ln \left[\frac{1 + Kp^{(e)} \exp[\varepsilon_m/kT]}{1 + Kp^{(e)} \exp[\varepsilon_l/kT]} \right] \quad (27)$$

For physical reasons. when $(\varepsilon_m - \varepsilon_l)/kT \gg 1$, ε_l is expected to take relatively small values, because ε_m cannot be unreasonably high. Then, except for very high pressures $p^{(e)}$, $Kp^{(e)} \exp[\varepsilon_l/kT]$ is small compared to unity, whereas $Kp^{(e)} \exp[\varepsilon_m/kT]$ is expected to be much larger than unity. Under such conditions Eq. (27) reduces to Temkin's isotherm, Eq. (26).

We now note the following important fact: The assumption that only ε is different for different adsorption sites is sufficient to describe the behavior of adsorption equilibria. We must not assume that K must also vary from site to site; i.e., it must also depend on the surface coverage $\theta_i^{(e)}(\varepsilon, p, T)$.

On the basis of the ART approach, $K = K_a/K_d$ and $\varepsilon = \varepsilon_a - \varepsilon_d$. On the other hand, the Elovich equation for adsorption kinetics was obtained by assuming that only ε_a changes with surface coverage whereas K_a is constant. This means that $K_d = K/K_a$ should be the same for all surface coverages, contrary to what is found in the analysis of thermodesorption experiments [35,41]. This inconsistency can be shown by carrying out an analysis of data obtained in studies of kinetics of adsorption, of the kinetics of (thermo)desorption, and of adsorption equilibria at the same time. Such comparative studies are, unfortunately, extremely rarely reported in the adsorption literature

We must point out another difficulty. In trying to find an interpretation for the physical meaning of the activation energy of desorption. it is frequent practice [41–43] to identify it with the isosteric heat of adsorption q_{st} , corresponding to the same surface coverage. at equilibrium conditions.

$$q_{st} = -k \frac{\partial \ln p^{(e)}}{\partial (1/T)} \quad (28)$$

For the Langmuir model of adsorption.

$$q_{st} = -k \frac{\partial \ln K}{\partial (1/T)} + \varepsilon_d - \varepsilon_a \quad (29)$$

This is so only if the kinetics of adsorption is "nonactivated," i.e., $\varepsilon_a = 0$, and the first term on the right-hand side of Eq. (29) is negligible. Meanwhile the Elovich equation assumes that ε_a exists and is a linear function of surface coverage.

These perceived difficulties in explaining the observed kinetics of adsorption/desorption in terms of ART have led to attempts to modify its fundamentals.

In 1957 Kisliuk [44] launched his idea of "precursor states." He assumed that before being adsorbed molecules form a weakly bound precursor phase. Molecules that do not strike an empty adsorption site but an already adsorbed molecule may still have a chance to be adsorbed by entering the precursor state on the adsorbed molecule and then jumping to a neighboring empty site.

Twenty years later, in 1977 King [45] made further efforts to improve that approach by assuming that two states may exist: one over a filled adsorption site and one over an empty site. Still another edition of that idea was proposed in 1978 by Gorte and Schmidt [46]. Other versions of the precursor state theory have been proposed [47], and their description can be found in a review by Lombardo and Bell [48].

The concept of precursor states and the corresponding expression for the rate of desorption did not gain the attention of researchers using TPD. Nor did it solve the problem of the large variations in the preexponential factor with surface coverage. Seebauer et al. [49] reviewed the existing theoretical interpretations of preexponential factors; none of them was able to explain the large variations found in the analysis of experimental data.

C. Generalization of ART for Energetically Heterogeneous Solid Surfaces

The procedures used to generalize the ART expressions for the case of energetically heterogeneous solid surfaces are discussed in the excellent review by Tovbin [41]. The rate expressions $d\theta_i/dt$ were written in the following form. For adsorption,

$$\frac{d\theta_i}{dt} = \int_{\Omega_c} K_a P [1 - \theta(\varepsilon)] \exp\left[-\frac{\varepsilon_a(\varepsilon)}{kT}\right] \mathcal{X}(\varepsilon) d\varepsilon \quad (30)$$

and for desorption,

$$\frac{d\theta_i}{dt} = - \int_{\Omega} K_d \theta(\varepsilon) \exp\left[-\frac{\varepsilon_d(\varepsilon)}{kT}\right] \mathcal{X}(\varepsilon) d\varepsilon \quad (31)$$

Contrary to what is found in the analysis of TPD spectra based on ART, the preexponential coefficients K_a and K_d were considered to be independent of surface coverage and of adsorption energy ε . Also, the assumption was made that the activation energies for adsorption and desorption, ε_a and ε_d , are linear functions of the adsorption energy ε [41].

$$\varepsilon_a = -\gamma_a \varepsilon \quad \text{and} \quad \varepsilon_d = \gamma_d \varepsilon \quad (32)$$

On the basis of the ART approach, the relation $\varepsilon = \varepsilon_d - \varepsilon_a$ must be obeyed. However, let us accept the assumptions in (32) and investigate their consequences for adsorption kinetics. Let us also assume that $\chi(\varepsilon)$ is the rectangular adsorption energy distribution, Eq. (10). This means that when $\theta_i^{(e)}(\varepsilon, p^{(e)}, T)$ is the Langmuir isotherm, Eq. (7), the experimentally observed ("total") isotherm $\theta_i^{(e)}(p, T)$ will be the Temkin isotherm, Eq. (26).

Now we are going to check whether we can use Eq. (30) to arrive at the Elovich equation by assuming that $\chi(\varepsilon)$ in Eq. (30) is the same rectangular adsorption energy distribution as Eq. (10) leading to the Temkin isotherm equation for adsorption equilibria. For that purpose, $d\theta_i/dt$ in Eq. (30) has to be expressed in terms of the overall adsorption coverage θ_i .

Like other authors using Eq. (30) or (31), we assume that adsorption is running at quasi-equilibrium conditions, so the chemical potential μ^s of adsorbed molecules is the same across the whole surface and is a function of θ_i . This means that the function $\theta(\varepsilon)$ appearing under the integral in Eq. (30) is

$$\theta(\varepsilon) = \theta(\varepsilon, \mu^s(\theta_i)) \quad (33)$$

A convenient way to express μ^s using θ_i , is to express μ^s through the equilibrium pressure $p^{(e)} = p^{(e)}(\theta_i)$ corresponding to the surface coverage θ_i . In practice this means that the isotherm $\theta(\varepsilon)$ under the integral in Eq. (30) is taken to be the Langmuir isotherm, Eq. (7), and $Kp^{(e)}$ is expressed by the $Kp^{(e)}$ value appearing in Eq. (26).

We now rewrite Eq. (26) in the form

$$\frac{1}{Kp^{(e)}} = \exp \left[\frac{\varepsilon_m - (\varepsilon_m - \varepsilon_l)\theta_i^{(e)}}{kT} \right] \quad (34)$$

Consider now the rate of the experimentally observed adsorption $d\theta_i/dt$ when $\chi(\varepsilon)$ is the rectangular adsorption energy distribution leading to the Temkin isotherm for adsorption equilibria. With including assumptions (32).

Simple analytical expressions for $d\theta_i/dt$ can be obtained for the cases $\gamma_a = 0, 1/2, 1$. For the case $\gamma_a = 1/2$, the solution was given in Tovbin's review [41]. Here we consider the two cases $\gamma_a = 0$ and $\gamma_a = 1$.

When $\gamma_a = 0$, the adsorption is not "activated" at all. The integral (30) takes the form

$$\begin{aligned} \frac{d\theta_i}{dt} &= K_a p \int_{\varepsilon_l}^{\varepsilon_m} [1 + Kp^{(e)} e^{\varepsilon/kT}]^{-1} \frac{1}{\varepsilon_m - \varepsilon_l} d\varepsilon \\ &= -K_a p \frac{kT}{\varepsilon_m - \varepsilon_l} \ln \left[\frac{1 + (1/Kp^{(e)}) \exp(-\varepsilon_m/kT)}{1 + (1/Kp^{(e)}) \exp(-\varepsilon_l/kT)} \right] \end{aligned} \quad (35)$$

where $p^{(e)}$ is the value of the equilibrium pressure at which the surface coverage is equal to θ_i . This is the same pressure that appears in Eq. (34). So we replace $1/Kp^{(e)}$ in Eq. (35) by its value calculated from Eq. (34),

$$\frac{d\theta_t}{dt} = K_{ap} \frac{kT}{\varepsilon_m - \varepsilon_l} \ln \left[\frac{1 + \exp \left[\frac{\varepsilon_m - \varepsilon_l}{kT} - \frac{\varepsilon_m - \varepsilon_l}{kT} \theta_t \right]}{1 + \exp \left[-\frac{\varepsilon_m - \varepsilon_l}{kT} \theta_t \right]} \right] \quad (36)$$

The Temkin equation, Eq. (26), was obtained as the limiting form of the related expression when $(\varepsilon_m - \varepsilon_l)/kT \gg 1$. In the interest of consistency this limit has to be accepted in Eq. (36). Then for $\theta_t \rightarrow 0$, the exponent in the denominator is small compared to unity, and for $\theta_t \rightarrow 1$, the exponent in the numerator is much greater than unity. Thus, except for very small and very high coverages, $d\theta_t/dt$ in Eq. (36) reduces to

$$\frac{d\theta_t}{dt} = K_{ap}(1 - \theta_t) \quad (37)$$

which is simply the ART expression in which 9 is replaced by 9,.

Now let us consider the other extreme case when the coupling parameter γ_a in Eq. (32) is equal to unity, i.e., when adsorption is strongly "activated." Then similar simple algebraic exercises lead us to

$$\frac{d\theta_t}{dt} = \frac{K_{ap}}{Kp^{(e)}} \left(\frac{kT}{\varepsilon_m - \varepsilon_l} \right), \left[\frac{1 + Kp^{(e)} \exp(\varepsilon_m/kT)}{1 + Kp^{(e)} \exp(\varepsilon_l/kT)} \right] \quad (38)$$

Replacing $Kp^{(e)}$ by the expression in Eq. (34), we obtain

$$\frac{d\theta_t}{dt} = K_{ap} \frac{kT}{\varepsilon_m - \varepsilon_l} F(\theta_t) \quad (39)$$

where $F(\theta_t)$ is a function of the surface coverage 6,:

$$F(\theta_t) = \exp \left[\frac{\varepsilon_m - (\varepsilon_m - \varepsilon_l)\theta_t}{kT} \right] \ln \left[\frac{1 + \exp \left(\frac{\varepsilon_m - \varepsilon_l}{kT} \theta_t \right)}{1 + \exp \left[\frac{\varepsilon_m - \varepsilon_l}{kT} (\theta_t - 1) \right]} \right] \quad (40)$$

Now when $\theta_t \rightarrow 0$ or $\theta_t \rightarrow 1$, in the limit $(\varepsilon_m - \varepsilon_l)/kT \gg 1$, $F(\theta_t)$ reduces to

$$F(\theta_t) = e^{\varepsilon_m/kT} \frac{\varepsilon_m - \varepsilon_l}{kT} (1 - \theta_t) \quad (41)$$

Thus, in the limit of a strong surface heterogeneity leading to the Temkin equilibrium isotherm, the assumption of a strongly "activated" adsorption leads us to the rate expression

$$\frac{d\theta_t}{dt} = K_{ap} e^{\varepsilon_m/kT} (1 - \theta_t) \quad (42)$$

which is essentially the ART expression in which $\varepsilon_a = -\gamma_a \varepsilon_m$ and 9 is replaced by θ_t . Thus, the generalization of ART based on Eq. (30) does not lead to the Elovich equation as the kinetic equation corresponding to the Temkin isotherm if $\theta(\varepsilon, p, t)$ is assumed to be the Langmuir isotherm. Eq. (7).

However, the Elovich equation can be obtained in another way by using the ART and the condensation approximation. That method was first used in the theoretical work of Roginski [12] and reviewed later by Aharoni and Tompkins [9].

Let us neglect the second (desorption) term on the right-hand side of Eq. (6), assume that $s = 1$, and carry out the integration of the resulting first-order differential equation, to arrive at the function $\theta(t)$,

$$\ln(1 - \theta) = -K_{ap} e^{-\varepsilon_a/kT} t + \text{constant} \quad (43)$$

Because at $t = 0$, $\theta = 0$, we have constant = 0, so that

$$\theta = 1 - \exp(-K_{ap} t e^{-\varepsilon_a/kT}) \quad (44)$$

Figures 3 and 4 show the function $\theta(\varepsilon_a)$ and its change with temperature

When $T \rightarrow 0$ the function θ tends to the step function θ_c ,

$$\theta_c = \begin{cases} 0, & \varepsilon_a > \varepsilon_{ac} \\ 1, & \varepsilon_a \leq \varepsilon_{ac} \end{cases} \quad (45)$$

The value of ε_{ac} is given by the condition

$$\left(\frac{\partial^2 \theta}{\partial \varepsilon_a^2} \right)_{\varepsilon_{ac}} = 0 \quad (46)$$

which for the function θ expressed in Eq. (44) yields

$$\varepsilon_{ac} = kT \ln[K_{ap} t] \quad (47)$$

In the CA limit $T \rightarrow 0$,

$$\theta_t = \int_0^{\varepsilon_{ac}} \chi(\varepsilon_a) d\varepsilon_a \quad (48)$$

Now let us assume that $\chi(\varepsilon_a)$ is the rectangular function,

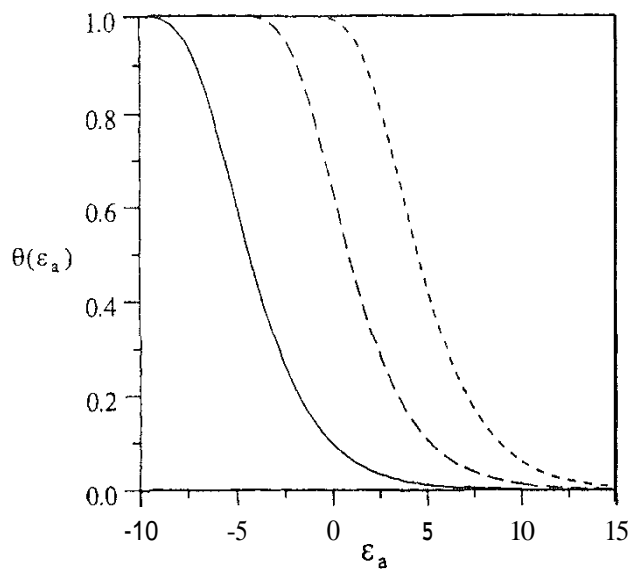


FIG. 3 The behavior of the function $\theta(\varepsilon_a)$ defined in Eq. (44) for three values of the parameters $K_{ap} t = K_{ap} t$, $K_{ap} t = 0.1$ (—), $K_{ap} t = 1$ (---), and $K_{ap} t = 5$ (- · -).

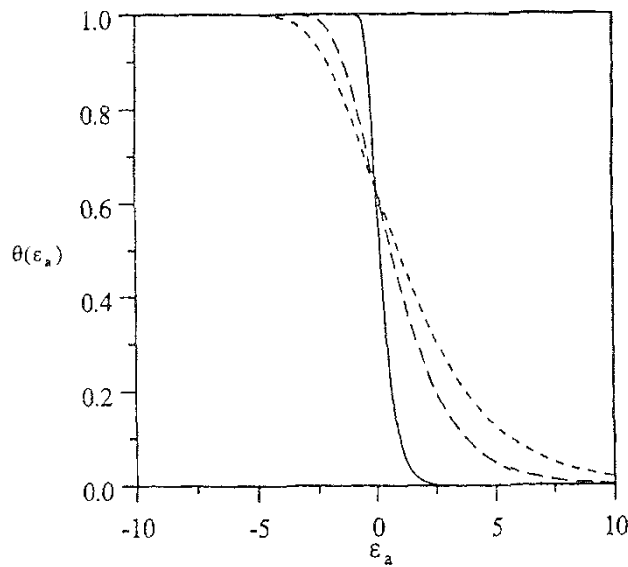


FIG. 4 The behavior of the function $\theta(\varepsilon_a)$ defined in Eq. (44) for three different temperatures: $T = 50$ K (—), $T = 200$ K (- - -), $T = 300$ K (- · -).

$$\chi(\varepsilon_a) = \begin{cases} \frac{1}{\varepsilon_{am} - \varepsilon_{al}} & \text{for } \varepsilon_a \in (\varepsilon_{al}, \varepsilon_{am}) \\ 0 & \text{elsewhere} \end{cases} \quad (49)$$

From Eqs. (47)–(49) we obtain

$$\theta_t = \frac{kT}{\varepsilon_{am} - \varepsilon_{al}} \ln[K_a p t] \quad (50)$$

Differentiation with respect to t yields

$$\frac{\partial \theta_t}{\partial t} = \frac{kT}{\varepsilon_{am} - \varepsilon_{al}} K_a p \exp\left[-\frac{\varepsilon_{am} - \varepsilon_{al}}{kT} \theta_t\right] \quad (51)$$

Equations (50) and (51) are the integral and differential form, respectively, of the Elovich equation.

Note that when linear relationship (32) between ε_a and ε is assumed, Eqs. (50) and (51) still preserve the form of the Elovich equation. This raises the question as to why Eq. (30), along with the assumption that $\varepsilon_a = -\gamma_a \varepsilon$ and $\chi(\varepsilon)$ as a rectangular function, Eq. (10), does not lead to the Elovich equation in the CA limit $(\varepsilon_m - \varepsilon_l)/kT \gg 1$. This inconsistency has not been discussed to date. It seems that the source of this problem lies in the use of the Langmuir equation $\theta(\varepsilon, p, T)$ with the ART expression for adsorption kinetics.

We note here that there are other theories of adsorption/desorption kinetics that offer expressions for the adsorption/desorption rate that are different from the ART expression but also lead to the Langmuir isotherm when $d\theta/dt = 0$. It is rather strange that adsorption systems with different kinetics of the adsorption/desorption processes have the same form at equilibrium.

Let us consider the situation when adsorption runs at quasi-equilibrium conditions. This means that at a surface coverage θ , all the surface correlation functions

are the same as at equilibrium at the same surface coverage. That is, the chemical potential of adsorbed molecules is the same across the whole solid surface.

For the Langmuir model of adsorption on a homogeneous solid surface, the surface chemical potential of the adsorbed molecules, μ^s , is given by

$$\mu^s = kT \ln \left[\frac{\theta}{1 - \theta} \right] - kT \ln q^s \quad (52)$$

where q^s is the molecular partition function of adsorbed molecules, consisting of the product

$$q^s = q^{int} q^{xy} q^z \exp \left[\frac{\varepsilon}{kT} \right] = q_0^s \exp \left[\frac{\varepsilon}{kT} \right] \quad (53)$$

In Eq. (53), q^z is the partition function for the vibrations normal to the surface, q^{xy} is the vibrational partition function for vibrations parallel to the surface, and q^{int} stands for rotations, vibrations due to hindered rotations, and electronic and spin degrees of freedom. Equation (52) can now be rewritten in the form

$$\theta(\varepsilon, \mu^s) = \frac{\exp[(\varepsilon - \varepsilon_c)/kT]}{1 + \exp[(\varepsilon - \varepsilon_c)/kT]} \quad (54)$$

where

$$\varepsilon_c = -\mu^s - kT \ln q_0^s \quad (55)$$

When the surface is heterogeneous, μ^s will be related to the total surface coverage θ_t , and Eq. (54) will give the "local" surface coverage of sites having adsorption energy ε . The features of the function $\theta(\varepsilon, \mu^s)$ will be the same as those of function (11) shown in Fig. 1. For instance, the derivative $\partial\theta/\partial\varepsilon$ will have its maximum value $(1/4kT)$ at $\theta = 1/2$.

Meanwhile the derivative $\partial\theta/\partial\varepsilon_a$ of the function defined in Eq. (44) reaches its maximum value, $1/ekT = 0.368/kT$, at $\theta = 1/e = 0.368$.

Although a comparison of these two pairs of values does not show dramatic differences, it points to an inconsistency when combining ART kinetic expressions with the Langmuir model for adsorption equilibria. We can always imagine the adsorption process running so slowly that quasi-equilibrium conditions can be assumed. However, even stranger is the necessity of invoking the existence of an activation energy for adsorption and its variation on various adsorption sites. In processes involving chemisorption, an activation energy for adsorption can be expected. However, an activation energy of adsorption processes of physical adsorption is less certain. We will show that the apparent activation energy for physical adsorption is the result of neglecting the readsorption term in the ART expression, Eq. (6). Since the Langmuir isotherm is obtained from Eq. (6), a fully rigorous consideration of adsorption kinetics should take into account both the adsorption and desorption terms.

Integration of Eq. (6) now yields

$$\theta = \frac{\bar{K}_a}{\bar{K}_a + \bar{K}_d} \{1 - \exp[-(\bar{K}_a + \bar{K}_d)t]\} \quad (56)$$

where

$$\bar{K}_a = K_a p \exp\left[-\frac{\varepsilon_a}{kT}\right] \quad (57)$$

and

$$\bar{K}_d = K_d \exp\left[-\frac{\varepsilon_d}{kT}\right] \quad (58)$$

We can now rewrite Eq. (56) in the form

$$\theta = \frac{\bar{K}}{1 + \bar{K}} \{1 - \exp[-\bar{K}_d(\bar{K} + 1)t]\} \quad (59)$$

where

$$\bar{K} = \frac{\bar{K}_a}{\bar{K}_d} = K_p \exp\left[\frac{\varepsilon}{kT}\right] = K_p \exp\left[\frac{\varepsilon}{kT}\right] \quad (60)$$

We next accept the assumption that the activation energy for adsorption does not exist, i.e., $\varepsilon_a = 0$, and that ε_d is equal to the isosteric heat of adsorption within the accuracy to a constant. Then,

$$\bar{K}_d t = K_{dt} \exp\left[-\frac{\varepsilon}{kT}\right] \quad (61)$$

Figures 5 and 6 show the behavior of the function $\theta(\varepsilon)$ defined in Eq. (59) for various values of the parameters $K_p = K_p$ and $K_{dt} = K_{dt}$.

Figure 7 shows the behavior of $\theta(\varepsilon)$ in Eq. (59) at three different temperatures. We can see in Fig. 7 that once again we could use the condensation approximation

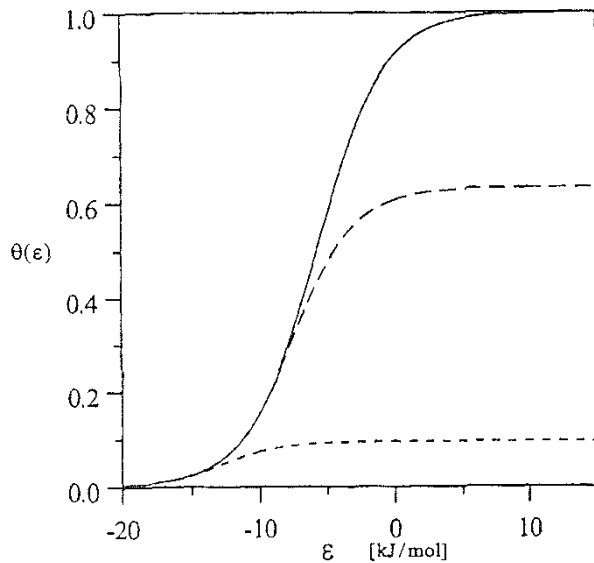


FIG. 5 The effect of the parameter K_{dt} on the behavior of the function $\theta(\varepsilon)$ defined in Eq. (59) for the fixed value of the parameter $K_p = 10$. $K_{dt} = 10$ (—), $K_{dt} = 0.1$ (---), and $K_p = 0.01$ (- - -).

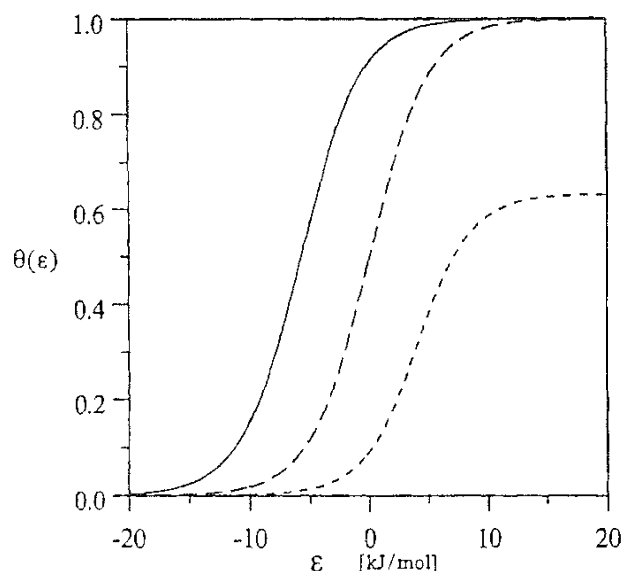


FIG. 6 The effect of the parameter K_p on the behavior of the function $\theta(\varepsilon)$ defined in Eq. (59) when the parameter K_{dt} is fixed and equal to 10. $K_p = 10$ (—), $K_p = 1$ (---), and $K_p = 0.1$ (- - -).

to calculate $\theta_t = \theta_t(t)$ and then subsequently calculate $d\theta/dt$ by putting the derivative $\partial^2\theta/\partial\varepsilon^2$ calculated from Eq. (59) to zero. Let y and Exp denote the following functions:

$$y(\varepsilon) = \frac{\bar{K}}{1 + \bar{K}}, \quad \text{Exp} = 1 - \exp[-\bar{K}_d(\bar{K} + 1)t] \quad (62)$$

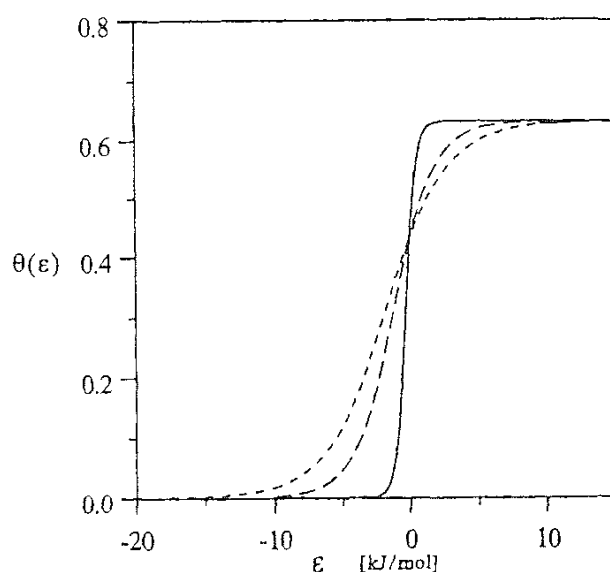


FIG. 7 The behavior of $\theta(\varepsilon)$ defined in Eq. (59) at three different temperatures: 300 K (—), 200 K (---), and 50 K (- - -), when $K = 1$ and $K_{dt} = 1$.

Then the first derivative reads

$$\frac{\partial \theta}{\partial \varepsilon} = \frac{1}{kT} [y(1-y)\text{Exp} + y\bar{K}_d t(\text{Exp} - 1)] \quad (63)$$

whereas the second derivative takes the form

$$\begin{aligned} \frac{\partial^2 \theta}{\partial \varepsilon^2} = & \left(\frac{1}{kT} \right)^2 [y(1-y)(1-2y)\text{Exp} + 2y(1-y)\bar{K}_d t(\text{Exp} - 1) \\ & + y\bar{K}_d t(1 - \bar{K}_d t)(\text{Exp} - 1)] \end{aligned} \quad (64)$$

We see that Eq. (17) cannot now be solved analytically to obtain the function ε_c ,

$$\left(\frac{\partial^2 \theta}{\partial \varepsilon^2} \right)_{\varepsilon=\varepsilon_c(K_p, K_{dt})} = 0 \quad (65)$$

In view of the fact that $\theta(\varepsilon)$ in Eq. (59) does not go to unity as $\varepsilon \rightarrow \infty$, Eq. (14) has to be modified by replacing unity on the right-hand side by the maximum value of 8, θ_{\max} , which is reached in the limit $\varepsilon \rightarrow \infty$. Now Eq. (14) takes the form

$$\lim_{T \rightarrow 0} \theta(\varepsilon, \varepsilon_c) = \theta_c(\varepsilon, \varepsilon_c) = \begin{cases} 0, & \varepsilon < \varepsilon_c \\ \theta_{\max}, & \varepsilon \geq \varepsilon_c \end{cases} \quad (65a)$$

From Eqs. (59)–(61) one can easily deduce that θ_{\max} is given by

$$\theta_{\max} = 1 - \exp[-K_p K_{dt}] \quad (65b)$$

Thus the generalized equation for $\theta_t(t)$ takes the form

$$\begin{aligned} \theta_t &= [1 - \exp(-K_p K_{dt})] \int_{\varepsilon_c(K_p, K_{dt})}^{\varepsilon_m} \frac{1}{\varepsilon_m - \varepsilon_l} d\varepsilon \\ &= [1 - \exp(-K_p K_{dt})] \frac{\varepsilon_m - \varepsilon_c(K_p, K_{dt})}{\varepsilon_m - \varepsilon_l} \end{aligned} \quad (66)$$

where $\varepsilon_c > 0$ must be taken.

The time dependence of θ_t in Eq. (66) is in fact a function of the variable $K_{dt} = K_d t$ and of the parameter K_p .

Thus, on the basis of ART one cannot arrive at a simple analytical generalization of the Elovich equation that takes simultaneous desorption into account.

The generalized Elovich equation for $\theta_t(t)$ can be evaluated by using numerical methods. It consists of two steps:

1. Solve Eq. (17) for a pair of values K_p and K_{dt} when $\partial^2 \theta / \partial \varepsilon^2$ is given by Eq. (64).
2. Use the calculated value of ε_c in Eq. (66) to calculate $\theta(t) = \theta(K_{dt})$.

The choice of a particular value of K_{dt} will not affect the "Elovich plot," i.e., θ_t plotted against $\ln t$. It will only shift it on the time axis. Therefore, in presenting our illustrative model calculations, we plot θ_t against $\ln K_{dt}$. Figure 8 shows three such Elovich plots for various values of the parameter K_p .

One can see in Fig. 8 that the linear dependence of θ_t on $\ln t$ typical Elovich behavior is observed over a region of moderate surface coverages, where read-

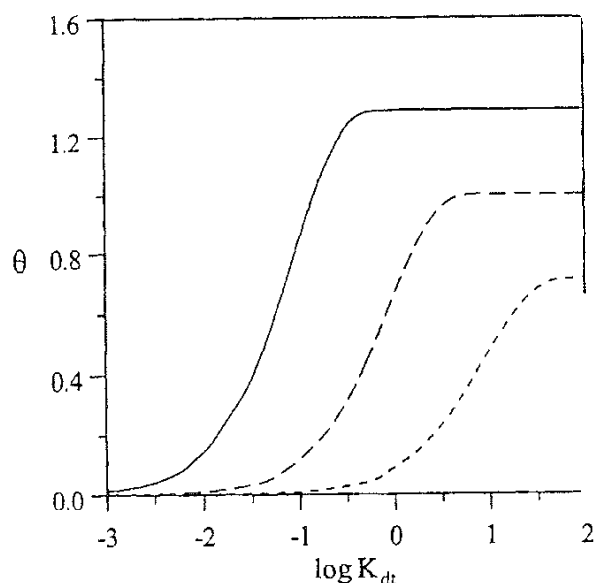


FIG. 8 The "Elovich plot" of θ vs. $\ln K_{dt}$, calculated from Eq. (66) for three values of the parameter K_s : 10 (—), 1 (---), and 0.1 (- - -). It is assumed that $\varepsilon_l = 0$, $\varepsilon_m = 20$ kJ/mol, and $T = 300$ K.

sorption kinetics do not play an important role. What is important here is that we have arrived at the "Elovich behavior" without invoking the concept of activation energy of adsorption.

In this way we have eliminated one assumption in developing the Elovich equation on the basis of ART. However, there are other inconsistencies in the generalization of the ART approach to suit the case of heterogeneous surfaces, using Eq. (30) or (31). Namely, the assumptions underlying the ART approach do not involve a particular mechanistic model of adsorption, for instance, the one leading to the Langmuir isotherm. To be fully consistent, one has to use expression (44) for θ in Eq. (30). In using the Langmuir equation for θ , one uses, in fact, the function $y(\varepsilon)$ defined in Eq. (62), which is the limiting form of θ defined in Eq. (59) when $t \rightarrow \infty$ and is obtained in addition by integrating the full ART expression, Eq. (6). Thus, it will also not be consistent to use for θ in Eq. (30) any one generalization of the Langmuir equation, taking into account interactions between the adsorbed molecules. The same inconsistency, of course, must be observed in all the papers on temperature programmed desorption based on applying Eq. (31) when $\theta(\varepsilon)$ is represented by the Langmuir isotherm or its generalizations (Bragg-Williams, quasi-chemical, etc.).

Therefore we would summarize the results of our foregoing analysis of the ART approach as follows:

1. The ART approach is not related to a particular mechanistic model of adsorption systems.
2. The fact that at equilibrium the ART approach yields the Langmuir isotherm is not sufficient proof that this isotherm should be used to represent $\theta(\varepsilon)$ in the generalizations of ART for the case of heterogeneous solid surfaces. Other

approaches to adsorption/desorption kinetics different expressions for $d\theta/dt$, but they also lead to the Langmuir isotherm at equilibrium.

3. On the basis of ART it can be proved that the Langmuir equation cannot be used to represent $\theta(\varepsilon)$ except for the limit $t \rightarrow \infty$.
4. Consequently, it is not consistent to use, in the ART approach for $\theta(\varepsilon)$, generalizations of Langmuir equation that take into account interactions between adsorbed molecules.
5. It is not easy to generalize the full ART expression. taking into account readorption, for the case of energetically heterogeneous surfaces, because one does not arrive at simple analytical solutions.

In the following sections we show that almost all these difficulties related to the use of the ART approach disappear when we use one of the new approaches relating the rate of adsorption desorption kinetics to the chemical potential of adsorbed molecules.

D. Theories Relating the Rate of Adsorption/Desorption Processes to the Chemical Potential of Adsorbed Molecules

At the beginning of the 1980s a new family of approaches to adsorption/desorption kinetics appeared. A common fundamental feature of these approaches is that they relate the rate of adsorption/desorption kinetics to the chemical potential of the adsorbed molecules, μ^s . Although all these approaches appeared at approximately the same time. the one proposed by Nagai [50,51] in 1985 could, for historical reasons, be considered first. This arises because the idea behind that approach can be traced back to de Boer [52] in 1956. In this approach the rate of desorption R_d is represented by

$$R_d = \zeta \exp\left[\frac{\mu^s - \varepsilon_d}{kT}\right] \quad (67)$$

where μ^s is the chemical potential of an adsorbed molecule and ζ is a constant. Nagai's approach, as well as two other approaches that are discussed soon, is especially useful for describing adsorption/desorption processes that take place not far from equilibrium.

It has often been assumed that the chances of doing an experiment at quasi-equilibrium conditions depend on how fast the surface diffusion is. However, computer simulations reported by Talbot and coworkers [53] show that the essential condition is rather the speed of the adsorption–desorption events. There is, in fact, a body of evidence that a quasi-equilibrium condition is achieved in a majority of reported TPD and isothermal adsorption/desorption experiments.

Nevertheless, Nagai's approach raised objections [54–57]. Later, however, Nagai presented proof [58] that his expression, our Eq. (67), is superior to the R_d expression derived from the ART approach. Using the hard hexagon adsorption model, Nagai showed that the ART approach underestimates the role of entropy changes as a factor affecting the kinetics of adsorption/desorption processes.

Since we have taken the Langmuir model for consideration, the chemical potential μ of the adsorbed molecules is given by expression (52). Therefore R_d in Eq (67) now takes the form

$$R_d = \frac{\zeta}{q_0^s} \left(\frac{\theta}{1-\theta} \right) \exp \left[-\frac{\varepsilon + \varepsilon_d}{kT} \right] \quad (68)$$

Another member of the new family of approaches using the chemical potential of adsorbed molecules, μ^s , is the approach proposed by Kreuzer and Payne in 1988 [42,43,59,60]. They followed the assumption made by Kobukowa [61] in 1938, that the rate of adsorption should be proportional to the difference between the actual (nonequilibrium) pressure p and the equilibrium pressure $p^{(e)}$ corresponding to the same surface coverage. On this basis they wrote the expressions for R_a and R_d in the form

$$R_a = S(\theta)p \frac{\alpha_s}{(2\pi mkT)^{1/2}} \quad (69)$$

and

$$R_d = S(\theta)p^{(e)} \frac{\alpha_s}{(2\pi mkT)^{1/2}} \quad (70)$$

where $S(\theta)$ is a "sticking coefficient." The equilibrium pressure $p^{(e)}$ is now expressed in terms of the gas-phase chemical potential, μ^g ,

$$p^{(e)} = kT \left(\frac{(2\pi mkT)^{1/2}}{h} \right)^3 q_0^g \exp \left[\frac{\mu^g}{kT} \right] \quad (71)$$

where q_0^g is the partition function of gas molecules due to the internal degrees of freedom. At equilibrium, $\mu^g = \mu^s$, so R_d takes the form

$$R_d = S(\theta)\alpha_s kT \frac{2\pi mkT}{h^3} q_0^g \exp \left[\frac{\mu^s}{kT} \right] \quad (72)$$

which is similar to Nagai's expression, Eq. (67). The sticking coefficient $S(\theta)$ is intended to account for the efficiency of energy transfer between the solid and the adsorbate. It cannot be obtained from thermodynamic arguments and must be calculated from microscopic theory or be derived from experimental data for a particular system. If we postulate that $S(\theta) = S_0(1 - \theta)$, then the Kreuzer-Payne expressions for R_a and R_d take the form of the classical ART expressions, with zero activation energy for adsorption. For the rate of adsorption we have

$$R_a = \frac{S_0 \alpha_s p (1 - \theta)}{(2\pi mkT)^{1/2}} \quad (73)$$

By replacing μ^s in Eq. (72) by expression (52), we obtain

$$R_d = S_0 \alpha_s kT \left(\frac{2\pi mkT}{h} \right) \left(\frac{q_0^g}{q_0^s} \right) \theta \exp \left[\frac{\varepsilon}{kT} \right] \quad (74)$$

On the other hand, since the physical meaning of the sticking coefficient is obscure, we may also put it equal to unit. Then, instead of Eq. (74), we have

$$R_d = K_0 q^z \frac{\theta}{1 - \theta} \exp\left[\frac{\varepsilon}{kT}\right] \quad (75)$$

where

$$K_0 = S_0 \alpha_s kT \frac{2\pi mkT}{h} \left(\frac{q_0^g}{q^{\text{int}} q^{\text{xy}}} \right) \quad (76)$$

If we assume that it is proper to accept the low-temperature limit for the vibrational partition function q^z , then R_d will be an expression in which ε in the exponent is increased by a constant, just as it is in Eq. (68).

We wrote that both for the case when the sticking coefficient S is assumed to be constant and when it is assumed to be equal to $S_0(1 - \theta)$, Kreuzer's approach leads to the Langmuir isotherm at equilibrium, i.e., when $R_a = R_d$. Ward and coworkers [17,18,62,63] present a different idea that applies the statistical rate theory to the kinetics of adsorption.

When a molecule coming from a gas phase adsorbs on a solid surface, it must both cross a gas-phase boundary and form an adsorptive bond when it encounters the solid. Similarly, when a molecule desorbs, it must break the adsorptive bond and enter the gas phase. Although the collision of a molecule with a solid surface can be treated by using either classical or quantum mechanics, the prediction of the rate of bond formation or breaking requires a quantum-mechanical description because this process involves the probability of an event occurring.

Based on quantum mechanics and thermodynamics, Ward and Findlay [62] developed a new approach to adsorption/desorption kinetics called the statistical rate theory of interfacial transport. The objective of this SRT approach is to obtain an explicit dependence of the rate expressions on coverage so that the other properties appearing in the rate expressions are molecular properties. The SRT approach leads to the rate expressions

$$R_a = K'_{gs} \exp\left[\frac{\mu^g - \mu^s}{kT}\right] \quad (77)$$

and

$$R_d = K'_{gs} \exp\left[\frac{\mu^s - \mu^g}{kT}\right] \quad (78)$$

where K'_{gs} is a constant.

The physical meaning of K'_{gs} is discussed in the paper by Ward and Findlay [62] as well as in the more recent publications of Ward and coworkers [17,18]. K'_{gs} is the exchange rate between the gas phase and the solid surface once an isolated system has reached equilibrium. All these approaches relating the kinetics of adsorption/desorption processes to the chemical potential of adsorbed molecules share an important feature. Because the expression for the chemical potential μ^s is determined from a mechanistic model of the adsorbed phase, one arrives at a

dependence of R_a and R_d on coverage without invoking the obscure concept of a sticking coefficient.

The problem that remains is to find a way of generalizing the expressions for R_a and R_d for the case of an energetically heterogeneous solid surface. The advantage of the new theoretical approaches to adsorption/desorption kinetics lies in the fact that $d\theta/dt$ is a function of ε . Thus the knowledge of the behavior of an adsorption system at equilibrium may be helpful in predicting the kinetics of the adsorption/desorption processes in that system.

The Elovich equation was successfully applied to a variety of kinetic data obtained using different techniques with constant or changing pressure [8]. This indicates that surface heterogeneity is a factor governing adsorption kinetics in these systems.

Now let us consider the kinetics of adsorption at lower surface coverages, where the desorption term R_d defined in Eq. (78) can be neglected, compared to the adsorption term R_a defined in Eq. (77). Then,

$$\frac{d\theta}{dt} = K'_{gs} \exp\left[\frac{\mu^g - \mu^s}{kT}\right] = K'_{gs} p q^s \exp\left[\frac{\mu_0^g}{kT}\right] \left(\frac{1 - \theta}{\theta}\right) \quad (79)$$

where μ_0^g is the standard chemical potential defined as

$$\mu^g = \mu_0^g + kT \ln p \quad (80)$$

Let

$$K = q_0^s \exp\left[\frac{\mu_0^g}{kT}\right] \quad (81)$$

Then Eq. (79) can be rewritten as

$$\theta = \left\{ 1 + \frac{\partial\theta/\partial t}{K'_{gs} p K} \exp\left[\frac{-\varepsilon}{kT}\right] \right\}^{-1} \quad (82)$$

The above equation describes the rate of adsorption on sites having adsorption energy ε . We also believe that the variation of ε from site to site is a factor governing the kinetics of adsorption on the energetically heterogeneous surfaces. In two previous publications, we showed how the statistical rate theory of interfacial transport can be generalized for the case of heterogeneous solid surfaces. Below we repeat briefly the principles of that method before we develop its generalization to take into account desorption kinetics.

The experimentally monitored surface coverage θ_t and the mean rate of adsorption $d\theta_t/dt$ are the values of 0 and $d\theta/dt$ averaged over all kinds of adsorption sites taken with an appropriate statistical weight. In the presence of a dense spectrum of adsorption energies, that statistical weight is well described by a continuous distribution function relating the number of adsorption sites to corresponding values of adsorption energy, $\chi(\varepsilon)$.

When the adsorption takes place at quasi-equilibrium conditions, the function $\theta(\varepsilon)$ in Eq. (82) can be written in the form

$$\theta(\varepsilon) = \left\{ 1 + \exp\left[\frac{\varepsilon_c - \varepsilon}{kT}\right] \right\}^{-1} \quad (83)$$

where

$$\varepsilon_c = -\mu^s(\theta_t) - kT \ln q_0^s \quad (84)$$

because the chemical potential of the adsorbed molecules will be the same throughout the surface phase and will be a function of the average surface coverage θ_t . The explicit form of this function will, of course, depend on the form of the adsorption energy distribution $\chi(\varepsilon)$.

Thus, in the case of a heterogeneous solid surface, the experimentally determined values θ_t and $d\theta/dt$ are given by the integral

$$\theta_t = \int_0^{+\infty} \left\{ 1 + \exp\left[\frac{\varepsilon_c - \varepsilon}{kT}\right] \right\}^{-1} \chi(\varepsilon) d\varepsilon \quad (85)$$

because ε_c is not a function of ε .

$$\varepsilon_c = kT \ln \left[\frac{d\theta/dt}{K'_{gs} p K} \right] = -\mu^s(\theta_t) - kT \ln q_0^s \quad (86)$$

When $T \rightarrow 0$, both θ and $\theta^{(e)}$ tend to the step function θ_c ,

$$\lim_{T \rightarrow 0} \theta(\varepsilon, \varepsilon_c) = \theta_c(\varepsilon, \varepsilon_c) = \begin{cases} 0, & \varepsilon < \varepsilon_c \\ 1, & \varepsilon \geq \varepsilon_c \end{cases} \quad (87)$$

The functions $\theta(\varepsilon, \varepsilon_c)$ and $\theta_c(\varepsilon, \varepsilon_c)$ have been discussed in previous sections.

At a given temperature T , pressure p , and $d\theta/dt$, the "adsorption front" is on the sites whose energy ε is equal to ε_c defined in Eq. (86). At that instant the overall adsorption rate $d\theta_t/dt$ is, in fact, governed mainly by the local rate of adsorption on the sites whose adsorption energy is equal to ε_c and will, of course, be proportional to the probability of finding such sites on the solid surface. Thus, the "local" and the "total" rates of adsorption will be linked as follows [16]:

$$\frac{d\theta_t}{dt} = \text{const} \times \chi(\varepsilon_c) \left(\frac{d\theta}{dt} \right)_{\varepsilon=\varepsilon_c} \quad (88)$$

Note that at $\varepsilon = \varepsilon_c$, $\theta = 1/2$, so that from Eq. (82) we have

$$\left(\frac{d\theta}{dt} \right)_{\varepsilon=\varepsilon_c} = K'_{gs} K p \exp\left[\frac{\varepsilon_c}{kT}\right] \quad (89)$$

and Eq. (88) takes the form

$$\frac{d\theta_t}{dt} = \tilde{K}_{gs} p K \chi(\varepsilon_c) \exp\left[\frac{\varepsilon_c}{kT}\right] \quad (90)$$

where

$$\tilde{K}_{gs} = \text{const} \times K'_{gs} \quad (91)$$

Equation (90) is fully correct only in the limit $T \rightarrow 0$, which represents the accuracy corresponding to the condensation approximation. This means that it

can be used at finite temperatures only when the solid surface is strongly heterogeneous, i.e., the variance of $\chi(\varepsilon)$ is larger than the variance of the derivative $\partial\theta/\partial\varepsilon$.

Equation (90) is an equation from which other equations can be developed to describe the kinetics of adsorption on surfaces characterized by various adsorption energy distributions.

The $d\theta_t/dt$ in turn is related to the surface coverage θ_t ,

$$\theta_t = \int_{\varepsilon_c}^{\infty} \chi(\varepsilon) d\varepsilon \quad (92)$$

For the particular case of the rectangular adsorption energy distribution,

$$\theta_t = \frac{\varepsilon_m - \varepsilon_c}{\varepsilon_m - \varepsilon_l} \quad (93)$$

Replacing ε_c in Eq. (90) by its value calculated from Eq. (93), we obtain

$$\frac{d\theta_t}{dt} = \tilde{K}_{gs} p K \frac{1}{\varepsilon_m - \varepsilon_l} \exp\left[\frac{\varepsilon_m}{kT}\right] \exp\left[-\frac{\varepsilon_m - \varepsilon_l}{kT} \theta_t\right] \quad (94)$$

Thus, Eq. (94) looks something like the Elovich equation and was developed here as the kinetic equation corresponding to a Temkin isotherm for adsorption equilibria. This agrees with common experimental observations. We see that the Elovich equation should apply at conditions where the desorption rate can be neglected, since we developed it by generalizing the adsorption rate term R_a in Eq. (77) and neglecting the desorption rate term R_d in Eq. (78).

As a matter of fact, most of the experiments on adsorption kinetics were done at lower coverages. In the literature we often find statements such as, "After the first very fast kinetics, a slower kinetics is observed, which follows the Elovich equation." The first fast kinetics, at very low surface coverages, is probably governed by purely kinetic (collision) factors, the effectiveness of the transfer of the energy excess to the solid phase as well as possible changes in the structure of the adsorbed phase. The last effect is due to the saturation of chemical bonds, which may be most essential for the first molecules adsorbed on a strongly "unsaturated," "empty" solid surface. After a certain first portion of molecules are adsorbed, the rate of adsorption falls to the limits where it runs as at quasi-equilibrium conditions.

In addition to the above-mentioned common deviations from the Elovich equation at very low surface coverages, the other common negative deviation was observed at higher coverages. To account for that negative deviation, Higuchi et al. [64] proposed the following modification of Eq. (I):

$$\frac{d\theta_t}{dt} = a(1 - \theta_t)e^{-\alpha\theta_t} \quad (95)$$

Other possible reasons for the deviations at higher surface coverages have also been put forward. From our derivation of the Elovich equation it follows that the main reason may be the neglect of the desorption kinetics inherent in the form of the Elovich equation. Moreover, there is the role of the lateral interactions between the adsorbed molecules.

As it happens, it can be shown that in the case of strongly heterogeneous surfaces characterized by a rectangular adsorption energy distribution, Eq. (10), the effects of the lateral interactions do not change the form of the Elovich equation.

As far as adsorption equilibria are concerned, the effects of the lateral interactions are included in the function $\varepsilon_c^{(e)}(\theta_t)$ given by the function ε_c in Eq. (86). The effects of the lateral interactions on $\theta_t^{(e)}$ were considered in much detail in a monograph by Rudzinski and Everett [37]. They depend on the way in which various adsorption sites are distributed on a solid surface. This two-dimensional spatial distribution of various adsorption sites on the surface is called "surface topography." To prove that lateral interactions do not change the form of the Elovich equation but only its parameters, we consider here the two extreme cases of surface topography.

In the case of high (infinite) spatial correlations, adsorption sites characterized by the same value of adsorption energy ε are grouped into "patches" that are so large that interaction between molecules adsorbed on different patches can be neglected. The whole adsorption system can then be considered to be a collection of independent subsystems in thermal and material contact. For such "patchwise" surface topography, the function $\varepsilon_c^{(e)}$ takes the form [37]

$$\varepsilon_c^{(e)} = -kT \ln Kp^{(e)} - \frac{1}{2}c\omega_{12} \quad (96)$$

where c is the number of nearest neighbors and ω_{12} is the energy of interaction between two molecules adsorbed on two neighboring sites. Equation (96) was obtained by applying the simplest mean-field (Bragg-Williams) approximation and including the effects of the lateral interactions between the adsorbed molecules.

The other extreme model of surface topography, "random topography," assumes that sites characterized by different values of ε are distributed on an energetically heterogeneous surface completely at random. The function $\varepsilon_c^{(e)}$ now takes the form [37]

$$\varepsilon_c^{(e)} = -kT \ln Kp^{(e)} - c\omega_{12}\theta_t \quad (97)$$

Now let us see how inclusion of the lateral interactions affects the form of the Temkin isotherm for adsorption equilibria and the Elovich equation for adsorption kinetics.

Using Eqs. (93), (96), and (97), we arrive at the isotherm $\theta_t^{(e)}$. For patchwise topography, we have

$$\theta_t^{(e)} = \frac{\varepsilon_m + c\omega_{12}/2}{\varepsilon_m - \varepsilon_l} + \frac{kT}{\varepsilon_m - \varepsilon_l} \ln Kp^{(e)} \quad (98)$$

whereas for random topography we obtain

$$\theta_t^{(e)} = \frac{\varepsilon_m}{\varepsilon_m - \varepsilon_l - c\omega_{12}} + \frac{kT}{\varepsilon_m - \varepsilon_l - c\omega_{12}} \ln Kp^{(e)} \quad (99)$$

By comparing Eqs. (98) and (99) with Eq. (26), we can see that including the effect of lateral interactions affects only the parameters in Temkin's iso-

therm, not its analytical form. Now let us consider equations for adsorption kinetics.

Including lateral interactions means introducing an additional term, μ_{int} , on right-hand side of Eq. (86). If we accept the mean-field approximation, this interaction term will become proportional to $c\omega_{12}\theta$ for patchwise topography or to $c\omega_{12}\theta_t$ for surfaces with random topography. So for patchwise topography Eq. (82) takes the form

$$\theta(\varepsilon) = \left\{ 1 + \frac{d\theta/dt}{K'_{gs}pK} \exp\left[-\frac{\varepsilon + c\omega_{12}\theta}{kT}\right] \right\}^{-1} \quad (100)$$

whereas for random topography we have

$$\theta(\varepsilon) = \left\{ 1 + \frac{d\theta/dt}{K'_{gs}pK} \exp\left[-\frac{\varepsilon + c\omega_{12}\theta_t}{kT}\right] \right\}^{-1} \quad (101)$$

To replace the true kernels $\theta(\varepsilon)$ by their corresponding step functions $\theta_c(\varepsilon)$, we use the Rudzinski–Jagiello criterion for choosing the value of ε_c ,

$$\left(\frac{\partial^2 \theta}{\partial \varepsilon^2} \right)_{\varepsilon=\varepsilon_c} = 0 \quad (102)$$

The problem is, in fact, similar to that in adsorption equilibria [37]. For both patchwise and random topography, criterion (102) leads to the condition

$$\theta_c(\varepsilon = \varepsilon_c) = \frac{1}{7} \quad (103)$$

Thus, from Eqs. (100) and (103), it follows that for patchwise topography,

$$\left(\frac{d\theta}{dt} \right)_{\varepsilon=\varepsilon_c} = K'_{gs}pK \exp\left[\frac{\varepsilon_c + c\omega_{12}/2}{kT}\right] \quad (104)$$

whereas for random topography we have

$$\left(\frac{d\theta}{dt} \right)_{\varepsilon=\varepsilon_c} = K'_{gs}pK \exp\left[\frac{\varepsilon_c + c\omega_{12}\theta_t}{kT}\right] \quad (105)$$

So, from Eqs. (90), (93), (104), and (105) we arrive at the following generalized forms of the Elovich equation. For patchwise topography.

$$\frac{d\theta_t}{dt} = K'_{gs}pK \frac{1}{\varepsilon_m - \varepsilon_l} \exp\left[\frac{\varepsilon_m + c\omega_{12}/2}{kT}\right] \exp\left[-\frac{\varepsilon_m - \varepsilon_l}{kT} \theta_t\right] \quad (106)$$

whereas for random topography we obtain

$$\frac{d\theta_t}{dt} = K'_{gs}pK \frac{1}{\varepsilon_m - \varepsilon_l} \exp\left[\frac{\varepsilon_m}{kT}\right] \exp\left[-\frac{\varepsilon_m - \varepsilon_l + c\omega_{12}}{kT} \theta_t\right] \quad (107)$$

Thus, including the lateral interactions between adsorbed molecules does not change the analytical form of the Elovich equation but does change the parameters of the equation. Deviations from the Elovich equation at higher surface coverages cannot, therefore, be attributed to lateral interactions between adsorbed molecules. Apart from peculiarities of some adsorption systems, the most probable source of these deviations may therefore be the neglect of the simultaneous desorption rate, i.e., the term R_d in Eq. (4).

For R_a and R_d defined in Eqs. (77) and (78), along with the Langmuirian expression for the chemical potential of adsorbed molecules, Eq. (52), Eq. (4) takes the following particular form:

$$\frac{d\theta}{dt} = K_a p \frac{1-\theta}{\theta} \exp\left(\frac{\varepsilon}{kT}\right) - K_d \frac{1}{p} \left(\frac{\theta}{1-\theta}\right) \exp\left[-\frac{\varepsilon}{kT}\right] \quad (108)$$

where

$$K_a = K'_{gs} q_0^s \exp\left[\frac{\mu_0^b}{kT}\right] \quad \text{and} \quad K_d = \frac{K'_{gs}}{q_0^s} \exp\left[-\frac{\mu_0^b}{kT}\right] \quad (109)$$

At equilibrium, Eq. (108) yields the Langmuir equation, in which the constant $K = (K_a/K_d)^{1/2}$. So the meaning of the constants K_a and K_d is not the same as in ART.

First we check whether Eq. (109) predicts the existence of a sharp adsorption/desorption "front." For that purpose we solve Eq. (102) when 6 is given by Eq. (108).

The first derivative $\partial\theta/\partial\varepsilon$ is

$$\frac{\partial\theta}{\partial\varepsilon} = -\frac{\frac{\partial}{\partial\varepsilon}\left(\frac{\partial\theta}{\partial t}\right)}{\frac{\partial}{\partial\theta}\left(\frac{\partial\theta}{\partial t}\right)} = \left(\frac{1}{kT}\right) \frac{\bar{K}_a \frac{1-\theta}{\theta} \exp\left(\frac{\varepsilon}{kT}\right) + \bar{K}_d \frac{1-\theta}{\theta} \exp\left(\frac{-\varepsilon}{kT}\right)}{\bar{K}_a \frac{1}{\theta^2} \exp\left(\frac{\varepsilon}{kT}\right) + \bar{K}_d \frac{1}{(1-\theta)^2} \exp\left(\frac{-\varepsilon}{kT}\right)} \quad (110)$$

where $\bar{K}_a = K_a p$ and $\bar{K}_d = K_d/p$. Let D denote the function $\partial\theta/\partial\varepsilon$ in Eq. (110). Then the second derivative, $\partial^2\theta/\partial\varepsilon^2$, takes the form

$$\frac{\partial^2\theta}{\partial\varepsilon^2} = \frac{1}{kT} \left(\frac{G(\theta, \varepsilon)}{\bar{K}_a \frac{1}{\theta^2} \exp\left(\frac{\varepsilon}{kT}\right) + \bar{K}_d \frac{1}{(1-\theta)^2} \exp\left(\frac{-\varepsilon}{kT}\right)^2} \right) \quad (111)$$

where $G(\theta, \varepsilon)$ is the function

$$G(\theta, \varepsilon) = \frac{\frac{\bar{K}_a}{kT} \left(\frac{1-\theta}{\theta} \right) \exp\left(\frac{\varepsilon}{kT}\right) - \frac{\bar{K}_a}{\theta^2} D \exp\left[\frac{\varepsilon}{kT}\right] - \frac{\bar{K}_d}{kT} \left(\frac{\theta}{1-\theta} \right) \exp\left[-\frac{\varepsilon}{kT}\right] + \frac{\bar{K}_d}{(1-\theta)^2} D \exp\left[\frac{-\varepsilon}{kT}\right]}{\left\{ \frac{\bar{K}_d}{\theta^2} \exp\left[\frac{\varepsilon}{kT}\right] + \frac{\bar{K}_d}{(1-\theta)^2} \exp\left[\frac{-\varepsilon}{kT}\right] \right\}^{-1}}$$

$$\frac{\frac{\bar{K}_a}{kT} \left(\frac{1}{\theta^2} \right) \exp\left[\frac{\varepsilon}{kT}\right] - \frac{2\bar{K}_a}{\theta^3} D \exp\left[\frac{\varepsilon}{kT}\right] - \frac{\bar{K}_d}{kT} \left(\frac{1}{(1-\theta)^2} \right) \exp\left[-\frac{\varepsilon}{kT}\right] + \frac{2\bar{K}_d}{(1-\theta)^3} D \exp\left[\frac{-\varepsilon}{kT}\right]}{\left\{ \bar{K}_a \left(\frac{1-\theta}{\theta} \right) \exp\left[\frac{\varepsilon}{kT}\right] + \bar{K}_d \left(\frac{\theta}{1-\theta} \right) \exp\left[\frac{-\varepsilon}{kT}\right] \right\}^{-1}}$$
(112)

After some lengthy algebra, we arrive at the following form of the function $G(\theta, s)$:

$$G(\theta, \varepsilon) = \left\{ \bar{K}_a^2 (1-\theta)^4 \exp\left[\frac{2\varepsilon}{kT}\right] + \bar{K}_d^2 \theta^4 \exp\left[\frac{-2\varepsilon}{kT}\right] + 2\bar{K}_a \bar{K}_d \theta^2 (1-\theta)^2 \right\} (1-2\theta)$$
(113)

From Eq. (111), it follows that condition (102) is fulfilled when $G(\varepsilon_c, \theta(\varepsilon = \varepsilon_c)) = 0$. From Eq. (113) we can deduce that the above condition is fulfilled when $\theta(\varepsilon = \varepsilon_c) = 1/2$. We now check whether there may be some other solutions. For that purpose we examine the solutions of the equation

$$\bar{K}_a^2 (1-\theta)^4 \exp\left[\frac{2\varepsilon}{kT}\right] + \bar{K}_d^2 \theta^4 \exp\left[\frac{-2\varepsilon}{kT}\right] + 2\bar{K}_a \bar{K}_d \theta^2 (1-\theta)^2 = 0$$
(114)

We introduce a new variable, $x = \exp[2\varepsilon/kT]$, and multiply (114) by x so that

$$\bar{K}_a^2 (1-\theta)^4 x^2 + 2\bar{K}_a \bar{K}_d \theta^2 (1-\theta)^2 x + \bar{K}_d^2 \theta^4 = 0$$
(115)

Now we solve the above quadratic equation with respect to x . This has only one solution:

$$x = -\frac{\bar{K}_d}{\bar{K}_a} \left(\frac{\theta^2}{(1-\theta)^2} \right)$$
(116)

which is a nonphysical solution, because from its definition $[\exp(2\varepsilon/kT)]$, x can never be negative. Thus, the only physical solution is

$$\theta(\varepsilon = \varepsilon_c) = \frac{1}{2}$$
(117)

and Eq. (108) is consistent with the Langmuirian model for adsorption equilibria.

Equation (88) now takes the form

$$\frac{d\theta_t}{dt} = \text{const} \times \chi(\varepsilon_c) \left(\frac{\partial \theta}{\partial t} \right)_{\varepsilon=\varepsilon_c}$$
(118)

which takes both adsorption and desorption kinetics into account. The function $(\partial\theta/\partial t)_{\varepsilon=\varepsilon_c}$ is obtained from Eq. (108) by taking into account the fact that when $\varepsilon = \varepsilon_c$, $\theta = 1/2$. Then

$$\left(\frac{d\theta}{dt}\right)_{\varepsilon_c} = K_a p \exp\left[\frac{\varepsilon_c}{kT}\right] - K_d \frac{1}{p} \exp\left[-\frac{\varepsilon_c}{kT}\right] \quad (119)$$

and $d\theta_t/dt$ takes the form

$$\frac{d\theta_t}{dt} = \tilde{K}_a p \chi(\varepsilon_c) \exp\left[\frac{\varepsilon_c}{kT}\right] - \tilde{K}_d \frac{1}{p} \chi(\varepsilon_c) \exp\left[-\frac{\varepsilon_c}{kT}\right] \quad (120)$$

where

$$\tilde{K}_a = \text{const} \times K_a \quad \text{and} \quad \tilde{K}_d = \text{const} \times K_d \quad (121)$$

The first term on the right-hand side of Eq. (120) represents the adsorption rate and is identical with the expression on the right-hand side of Eq. (90). The second term on the right-hand side of Eq. (120) represents the rate of the simultaneous desorption. At quasi-equilibrium conditions, $\varepsilon_c = \varepsilon_c^{(e)}$, and $\partial\theta_t/\partial t$ can be expressed as a function of surface coverage. Equation (120) is a generalized form of Eq. (90), which allows us to calculate the rate of adsorption (desorption) if the adsorption energy distribution is known. The latter function can be determined from the observed equilibrium adsorption isotherms. For the rectangular adsorption energy distribution Eq. (10), replacing ε_c in Eq. (120) by $\varepsilon_c^{(e)}$ defined in Eq. (93) leads us to the following generalized form of the Elovich equation, taking into account both adsorption and desorption occurring simultaneously:

$$\begin{aligned} \frac{d\theta_t}{dt} = & \frac{\tilde{K}_a p}{\varepsilon_m - \varepsilon_l} \exp\left[\frac{\varepsilon_m}{kT}\right] \exp\left[-\frac{\varepsilon_m - \varepsilon_l}{kT} \theta_t\right] \\ & - \frac{\tilde{K}_d}{p(\varepsilon_m - \varepsilon_l)} \exp\left[-\frac{\varepsilon_m}{kT}\right] \exp\left[\frac{\varepsilon_m - \varepsilon_l}{kT} \theta_t\right] \end{aligned} \quad (122)$$

The generalized Elovich equation is a three-parameter equation.

$$\frac{d\theta_t}{dt} = a p e^{-\alpha \theta_t} - \frac{b}{p} e^{\alpha \theta_t} \quad (123)$$

where

$$a = \frac{\tilde{K}_a}{\varepsilon_m - \varepsilon_l} \exp\left[\frac{\varepsilon_m}{kT}\right], \quad b = \frac{\tilde{K}_d}{\varepsilon_m - \varepsilon_l} \exp\left[-\frac{\varepsilon_m}{kT}\right] \quad (124)$$

and

$$\alpha = \frac{\varepsilon_m - \varepsilon_l}{kT} \quad (125)$$

Parameter α can be determined in equilibrium measurements as the tangent of the adsorbed amount plotted against the logarithm of adsorbate pressure. The two other parameters, a and b , are treated as best-fit parameters while fitting experimental data with expression (123). [Figure 9](#) shows the fit of Eq. (123) to the

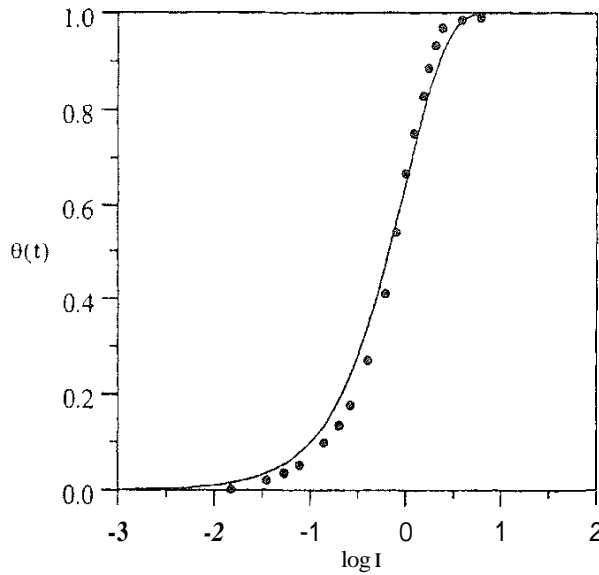


FIG. 9 The result of computer fitting of the experimental data for the kinetics of oxygen adsorption on polycrystalline tungsten reported by Lopez-Sancho and de Segovia, by our generalized Elovich equation, Eq. (132), assuming that $a = 0.394$, $a = 3.85 \times 10^6 \text{ torr}^{-1} \text{ s}^{-1}$, $b = 4.374 \times 10^{-7} \text{ torr}^{-1} \text{ s}^{-1}$. The pressure and temperature kept at the experiment were equal $5 \times 10^{-7} \text{ torr}$ and 77 K, respectively.

experimental data of the kinetics of oxygen adsorption on polycrystalline tungsten reported by Lopez-Sancho and de Segovia [65].

Now let us consider the integral form of the generalized Elovich equation, Eq. (123), which we write in the form

$$\frac{d\theta_t}{a p e^{-\alpha \theta_t} - (b/p) e^{\alpha \theta_t}} = dt \quad (126)$$

We now introduce the variable

$$x = e^{\alpha \theta_t}, \quad \text{so} \quad d\theta_t = \frac{dx}{\alpha x} \quad (127)$$

Then Eq. (126) takes the form

$$\frac{dx}{1 - (b/ap^2)x^2} = \alpha a p \, dt \quad (128)$$

and we get

$$\frac{\operatorname{arctanh} zx}{z} = \alpha a p t + C \quad (129)$$

where

$$z^2 = \frac{b}{ap^2} \quad (130)$$

Assuming that $\theta_t(t=0) = 0$, we get the equation

$$\theta_t = \frac{1}{\alpha} \ln \left| \frac{1}{z} \tanh[\alpha z a p t + \operatorname{arctanh} z], \quad |z| < 1 \quad (131)$$

$$\theta_t = \frac{1}{\alpha} \ln \left| \frac{1}{z} \left(\frac{\exp \left[\alpha z a p t + \frac{1}{2} \ln \left| \frac{1+z}{1-z} \right| \right] - \exp \left[-\alpha z a p t - \frac{1}{2} \ln \left| \frac{1+z}{1-z} \right| \right]}{\exp \left[\alpha z a p t + \frac{1}{2} \ln \left| \frac{1+z}{1-z} \right| \right] + \exp \left[-\alpha z a p t - \frac{1}{2} \ln \left| \frac{1+z}{1-z} \right| \right]} \right) \right|, \quad |z| < 1 \quad (132)$$

The features of the generalized Elovich equation, Eq. (132), are shown in Figs. 10–12.

Now let us remark that both the differential equation, Eq. (123), and its integral form, Eq. (132), correspond to the level of condensation approximation. Therefore, their application to the Langmuir equation

$$\theta(p, T, \varepsilon) = \frac{(\tilde{K}_a/\tilde{K}_d)^{1/2} p \exp[\varepsilon/kT]}{1 + (\tilde{K}_a/\tilde{K}_d) p \exp[\varepsilon/kT]} \quad (133)$$

obtained for equilibrium from Eq. (108) and the use of the rectangular adsorption energy distribution (10) should yield the Temkin isotherm. One can easily prove that this is true, by putting $d\theta_t/dt = 0$ into Eq. (122). The total equilibrium isotherm $\theta_t^{(e)}(p, T)$ then takes the form of the Temkin isotherm

$$\theta_t(p^{(e)}, T) = \frac{\varepsilon_m}{\varepsilon_m - \varepsilon_l} + \frac{kT}{\varepsilon_m - \varepsilon_l} \ln \left[\left(\frac{\tilde{K}_a}{\tilde{K}_d} \right)^{1/2} p^{(e)} \right] \quad (134)$$

to be compared with Eq. (26).

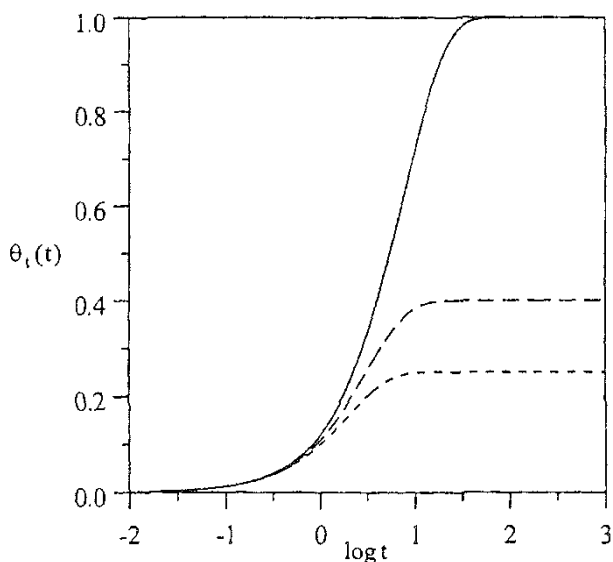


FIG. 10 The effect of the parameter a on the behavior of the generalized Elovich equation. Eq. (132), $a = 0.2$ (—), $\alpha = 0.5$ (---), and $a = 0.8$ (- · -). The calculations were done by assuming that $a = 10^7 \text{ torr}^{-1} \text{ s}^{-1}$, $b = 10^{-8} \text{ torr}^{-1} \text{ s}^{-1}$, and $p = 3.862 \times 10^{-8} \text{ torr}$.

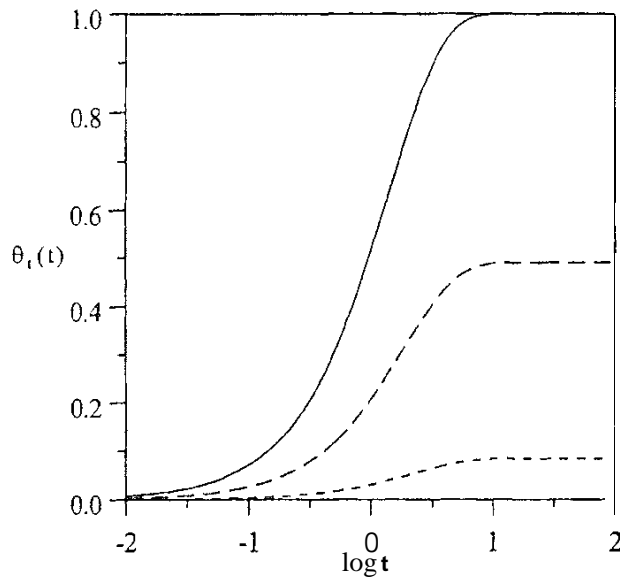


FIG. 11 The effect of the parameter a on the Elovich function $\theta_t(t)$ defined in Eq. (132). $a = 5 \times 10^7 \text{ torr}^{-1} \text{ s}^{-1}$ (—), $a = 3 \times 10^7 \text{ torr}^{-1} \text{ s}^{-1}$ (---), $a = 2 \times 10^7 \text{ torr}^{-1} \text{ s}^{-1}$ (- · -). The calculations were done by assuming that $\alpha = 0.5$, $b = 10^{-8} \text{ torr}^{-1} \text{ s}^{-1}$, and $p = 2.332 \times 10^{-8} \text{ torr}$.

The condition $|z| < 1$ in Eqs. (131) and (132) arises from the application of the condensation approximation and should not appear when, instead of Eq. (119), some exact solutions are applied. It can be easily checked that this condition is equivalent to the condition that $\theta_t(p^{(e)}, T)$ defined in Eq. (134) must be smaller than unity.

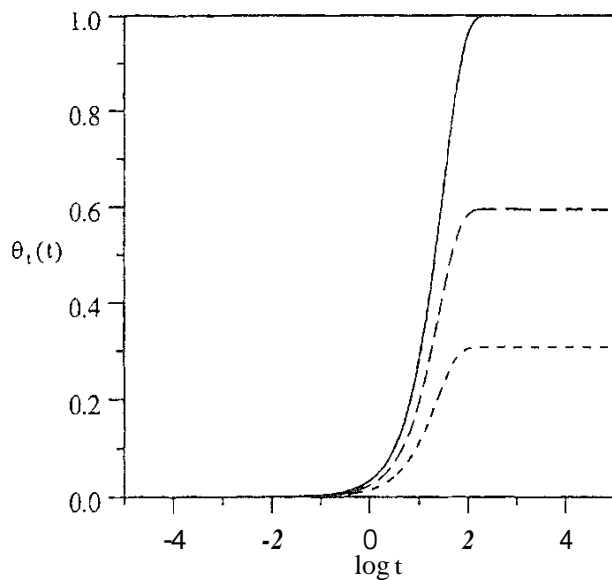


FIG. 12 The effect of the parameter b on the Elovich function, Eq. (132). $b = 10^{-10} \text{ torr}^{-1} \text{ s}^{-1}$ (—), $b = 1.5 \times 10^{-10} \text{ torr}^{-1} \text{ s}^{-1}$ (---), and $b = 2 \times 10^{-10} \text{ torr}^{-1} \text{ s}^{-1}$ (- · -). The calculations were done by assuming that $a = 0.5$, $a = 10^7 \text{ torr}^{-1} \text{ s}^{-1}$, and $p = 5.21 \times 10^{-9} \text{ torr}$.

REFERENCES

1. G. Tamman and W. Köster. *Z. Anorg. Allgem. Chem.* 123:146 (1922).
2. S. Z. Roginsky and Ya. B. Zeldovich, *Acta Phys. Chem. USSR* 1:554 (1934).
3. Ya. B. Zeldovich, *Acta Phys. Chem. USSR* 1:449 (1934).
4. Ya. B. Zeldovich, Ph.D. Thesis. Leningrad, 1936.
5. S. Yu. Elovich and F. F. Kharakorin, *Prob. Kinet. Catal*, 3:322 (1937).
6. F. F. Kharakorin and S. Ya. Elovich, *Acta Physicochim. USSR* 5:325 (1936).
7. S. Ya. Elovich and G. M. Zbrova, *Zh. Fiz. Khim.* 13:1775 (1939).
8. M. J. D. Low. *Chem. Rev.* 60:267 (1960).
9. C. Aharoni and F. C. Tompkins, *Adv. Catal.* 21:1 (1970).
10. M. I. Temkin. *Zh. Fiz. Khim.* 15:296 (1941).
11. M. I. Temkin, *Zh. Fiz. Khim.* 31:3 (1957).
12. S. Z. Roginsky. *Adsorption and Catalysis on Heterogeneous Surfaces*, Akad. Nauk USSR. Moscow, 1949.
13. Yu. K. Tovbin, *Theory of Physical Chemistry Processes at a Gas-Solid Interface*, Izd. Nauka, Moscow, 1990; English transl., CRC Press, Boca Raton, FL, 1991.
14. G. F. Cerofolini, in *Adsorption and Chemisorption on Inorganic Sorbents* (A. Dabrowski and V.A. Tertych, eds.), Elsevier. New York, 1996.
15. W. Rudzinski and C. Aharoni, *Langmuir* 13:1089 (1997).
16. W. Rudzinski, in *Equilibria and Dynamics of Gas Adsorption or Heterogeneous Solid Surfaces* (W. Rudzinski. W. A. Steele. and G. Zgrablich. eds.), Elsevier, New York, 1996.
17. C. A. Ward and M. Elmoselhi, *Surf. Sci.* 176:457 (1986).
18. C. A. Elliott and C. A. Ward, *J. Chem. Phys.* 106:5677 (1997).
19. A. Clark, *The Theory Of Adsorption and Catalysis*. Academic. New York, 1970.
20. R. I. Cvetanovic and Y. Amenomiya, *Adv. Catal.* 17:320 (1967).
21. R. I. Cvetanovic and Y. Amenomiya, *Catal. Rev.* 6:21 (1972).
22. I. I. Falconer and I. A. Schwarz, *Catal. Rev. Sci. Eng.* 25:141 (1983).
23. I. L. Lemaitre, in *Characterization of Heterogeneous Catalysis* (F. Delannay, ed.), Marcel Dekker, New York. 1984. Chap. 2.
24. S. Bhatia, I. Beltramini, and D. D. Do, *Catal. Today* 8:309 (1990).
25. Y. Amenomiya and R. J. Cvetanovic, *J. Phys. Chem.* 67:144 (1963).
26. A. W. Czanderna, J. R. Biegan, and W. J. Kollen, *J. Colloid Interface Sci.* 34:406 (1970).
27. G. Cater. *Vacuum* 12:245 (1962).
28. W. A. Grant and G. Cater. *Vacuum* 15:13 (1965).
29. D. T. Dawson and Y. K. Peng, *Surf. Sci.* 33:565 (1972).
30. Y. Tokoro, M. Misono, and Y. Yoneda, *Bull. Chem. Soc. Jpn.* 51:85 (1978).
31. D. A. King, *Surf. Sci.* 47:384 (1975).
32. Y. Tokoro. T. Uchijima, and Y. J. Yoneda, *Catalysis* 56:110 (1979).
33. H. Knözinger and P. Ratnasamy, *Catal. Rev. Sci. Eng.* 17:31 (1978).
34. P. Malet and G. Munuera, in *Adsorption at the Gas-Solid and Liquid-Solid Interface* (J. Rouquerol and K. S. W. Sing, eds.), Elsevier, Amsterdam, 1982, p. 383.
35. V. P. Zhdanov, *Surf. Sci. Rep.* 12:183 (1991).

36. M. Jaroniec and R. Madey, *Physical Adsorption on Heterogeneous Solids*, Elsevier, New York, 1988.
37. W. Rudzinski and D. H. Everett. *Adsorption Of Gases on Heterogeneous Surfaces*, Academic, New York, 1992.
38. J. Toth, *Adv. Colloid Interface Sci.* 55:1 (1995).
39. G. Cerofolini and W. Rudzinski, in *Equilibria and Dynamics of Gas Adsorption on Heterogeneous Solid Surfaces* (W. Rudzinski, W. A. Steele. and G. Zgrablich, eds.), Elsevier, New York, 1997, p. 1.
40. I. Langmuir. *J. Am. Chem. Soc.* 40:1361 (1918).
41. Yu. Tovbin, in *Equilibria and Dynamics of Adsorption on Heterogeneous Solid Surfaces* (W. Rudzinski, W. A. Steele, and G. Zgrablich. eds.), Elsevier. New York, 1997.
42. H. J. Kreuzer and S. H. Payne, in *Dynamics of Gas-Surface Interactions* (C. T. Rettner. and M. N. R. Ashfold, eds.), Royal Society of Chemistry, Cambridge, UK, 1991, Chap. 6.
43. H. J. Kreuzer and S. H. Payne, in *Equilibria and Dynamics of Gas Adsorption on Heterogeneous Solid Surfaces* (W. Rudzinski, W. A. Steele and G. Zgrablich, eds.), Elsevier, New York. 1997.
44. P. Kisliuk, *J. Phys. Chem. Solids* 3:95 (1957).
45. D. A. King, *Surf. Sci.* 64:43 (1977).
46. R. Gorte and L. D. Schmidt, *Surf. Sci.* 76:559 (1978).
47. W. H. Weinberg, in *Springer Series in Surface Sciences*, Vol. 8 (M. Granze and H. J. Kreuzer. eds.), Springer, Berlin. 1987. p. 94.
48. S. J. Lombardo and A. T. Bell, *Surf. Sci. Rep.* 13:1 (1991).
49. E. G. Seebauer, A. C. F. Kong, and L. D. Schmidt, *Surf. Sci.* 193:417 (1988).
50. K. Nagai, *Phys. Rev. Lett.* 54:2159 (1985).
51. K. Nagai, *Surf. Sci.* 176:193 (1986).
52. J. H. de Boer, *Adv. Catal.* 8:89 (1956).
53. J. Talbot, X. Jin, and N.-H. Wang, *Langmuir*, 10:663 (1994).
54. V. P. Zhdanov, *Surf. Sci.* 171:L461, L469 (1986).
55. K. Nagai and A. Hirashima. *Surf. Sci.* 171: L464 (1986).
56. A. Cassuto, *Surf. Sci.* 203:L656 (1988).
57. K. Nagai, *Surf. Sci.* 203:L659 (1988).
58. K. Nagai, *Surf. Sci.* 244:L147 (1991).
59. H. J. Kreuzer and S. H. Payne. *Surf. Sci.* 198:235 (1988); 200:L433 (1988).
60. S. H. Payne and H. J. Kreuzer, *Surf. Sci.* 205:153 (1988); 222:404 (1989).
61. M. Kobukowa, *Rev. Phys. Chem. Jpn.* 12:157 (1938).
62. C. A. Ward and R. D. Findlay, *J. Chem. Phys.* 76:5615 (1982).
63. J. A. Elliott and C. A. Ward, in *Equilibria and Dynamics of Gas Adsorption on Heterogeneous Solid Surfaces* (W. Rudzinski, W. A. Steele and G. Zgrablich, eds.), Elsevier, New York, 1996.
64. I. Higuchi, T. I. Ree, and H. Eyring, *J. Am. Chem. Soc.* 77:4969 (1955).
65. J. M. Lopez-Sancho and J. L. Segovia, *Surf. Sci.* 30:419 (1972).

16

Single- and Multicomponent Adsorption Equilibria of Hydrocarbons on Activated Carbon: The Role of Micropore Size Distribution

K. WANG and D. D. DO Department of Chemical Engineering, University of Queensland, St. Lucia, Australia

| | |
|---|-----|
| I. Introduction | 392 |
| II. Adsorbed Solution Theories | 393 |
| A. The ideal adsorbed solution theory | 393 |
| B. The nonideal behavior of the adsorbed phase | 396 |
| III. Equilibria Models Based on Potential Theory | 398 |
| A. Direct application of DR and DA equations | 400 |
| B. Potential theory approach | 403 |
| C. Other methods | 405 |
| IV. Other Models | 407 |
| A. The extended Sips model | 407 |
| B. Isostatic heat as a function of loading model | 408 |
| C. The heterogeneous extended Langmuir model | 409 |
| D. The multisite Langmuir model | 411 |
| E. The multispace adsorption model | 411 |
| F. Martinez's model | 412 |
| G. Keller's model | 413 |
| V. Microporous Structure and Adsorption Equilibria on Activated Carbon | 414 |
| A. The structure of activated carbon | 414 |
| B. Potential energy and slit pore configuration | 415 |
| C. Characterizing the PSD of activated carbon | 417 |
| D. Prediction of adsorption equilibria | 420 |
| VI. Microporous Structure and Adsorption Equilibria—the Micropore Size Distribution Model | 421 |
| A. MPSD model for a pure component system | 422 |
| B. MPSD model for a multicomponent system | 424 |

| | |
|---|-----|
| C. Comparison with experimental data—pure component equilibria | 426 |
| D. Comparison with experimental data—binary component equilibria | 430 |
| E. Discussion of the MPSD model | 430 |
| VII. Statistical Mechanical Methods and Multicomponent Equilibria | 433 |
| A. Pore selectivity isotherm | 434 |
| B. Test of the IAST at the microscopic level | 435 |
| VIII. Conclusion | 436 |
| References | 437 |

I. INTRODUCTION

Knowledge of multicomponent adsorption equilibria is critical to the design of practical gas separation processes based on adsorption mechanisms [1–4]. For pressure or thermal swing adsorption technology, information such as adsorption capacity, selectivity, driving force for mass transfer, and isosteric heat of adsorption are necessary for design and operation. This information can be conveniently obtained from an isotherm equation that properly represents the adsorption equilibria of the gas mixture in the system. However, finding a proper adsorption isotherm equation for a gas mixture system is not a simple task if this equation is meant to give good predictive results over a wide range of operating conditions. Two main factors contribute to our slow progress in this area: (1) The adsorbents of practical use such as activated carbon, carbon molecular sieve, zeolite, alumina, and silica gels are heterogeneous solids; and (2) multicomponent gas mixture adsorption data are scarce, and those that do exist are mostly incomplete [2–4].

Adsorption measurement for multicomponent systems is a function of the composition, temperature, pressure, and properties of adsorbate and adsorbent. As the number of components increases, the number of measurements needed to define the adsorption equilibrium increases rapidly and eventually becomes infeasible. Adsorption equilibrium models are therefore needed to correlate and predict the multicomponent adsorption equilibria. These models should be able to predict the mixture equilibria using the information available on pure component equilibria, as the latter are relatively easy to measure and furthermore there is an abundance of pure component isotherm data available in the literature. As a result, predictive models for gas mixture adsorption are necessary in the design and modeling of adsorption processes.

In the past 30 years, great efforts have been expended to develop techniques for predicting the multicomponent adsorption equilibria based on pure component data. However, until now only limited success has been achieved. Several publications provide good reviews of the work in this area [1,2,5]. Generally speaking, these models can be classified into four groups: (1) Vacancy solution theory, (2) statistical models, (3) ideal adsorbed solution theory (IAST), (3) Polanyi theory, and (4) various empirical or semiempirical models,

The vacancy solution theory or vacancy solution model (VSM) was proposed by Suwanayuen and Danner [6,7] and later modified by Cochran et al. [8]. The isosteric heat of adsorption of this model was obtained by Talu and Kabel [9]. In this theory,

the vacancy is an imaginary entity defined as the vacuum space that acts as the solvent for the system. Thus, the VSM treats pure component adsorption as a phase equilibrium between two binary vacancy solutions of different compositions. The detailed VSM and its modifications were reviewed by Yang [2]. The VSM was shown to be capable of predicting multicomponent equilibria at high surface coverage, and even the adsorption azeotrope in some circumstances, although it also presents some deviation for a number of systems [10,11].

The statistical models are based on thermodynamics arguments. But these models are normally specific to adsorbents with well-defined structures such as zeolites [12] or carbon black [13]. There was also a statistical model reported for the multicomponent adsorption equilibria of vapors on activated carbon, but it was validated only for a particular system [10].

This chapter reviews the progress in adsorption equilibrium models that have received some general interest in the literature. Particular emphasis is put on the role of the micropore size distribution in single- and multicomponent adsorption equilibria.

II. ADSORBED SOLUTION THEORIES

A. The Ideal Adsorbed Solution Theory

Among the theories of predicting mixed-gas adsorption equilibria from pure component adsorption isotherms, the ideal adsorbed solution theory (IAST) [14] has become the standard and often serves as a benchmark for the purpose of comparison by other models. IAST is a thermodynamically rigorous theory based on the mixing of individual components at constant spreading pressure to form an ideal solution. It has the advantages that (1) no mixture data are required and (2) the theory is independent of the actual model of physical adsorption.

The basic equation of IAST is analogous to Raoult's law for vapor-liquid equilibrium:

$$P_i = P_i^0(\pi_i)x_i \quad (1)$$

where x_i and π_i are the molar fraction and spreading pressure, respectively, of component i in the adsorbed phase. At adsorption equilibrium, the reduced spreading pressures

$$\pi_i^* = \frac{\pi_i}{RT} = \int_0^{P_i^0} \frac{n_i^0(P)}{P} dP, \quad i = 1, 2, 3, \dots, N \quad (2)$$

for each component and for the mixture are the same, i.e.,

$$\pi_1^* = \pi_2^* = \dots = \pi_N^* = \pi^* \quad (3)$$

The function $n_i^0(P)$ is the pure component equilibrium capacity, and P_i^0 is the pure component hypothetical pressure that yields the same spreading pressure as that of the mixture. By assuming ideal mixing at constant π and T , the total amount adsorbed, n_t , is found to be

$$\frac{1}{n_i} = \sum_{i=1}^N \left[\frac{x_i}{n_i^0(P_i^0)} \right] \quad (4)$$

with the constraint

$$\sum_{i=1}^N x_i = 1 \quad (5)$$

Thus, for a system consisting of N components with specified partial pressure in the gas phase, there are $2N + 1$ independent variables to be solved: $x(i)$, P and π . Equations (1)–(4) provide the $2N + 1$ necessary equations. Since the equations are nonlinear and the integrals in Eq. (2) cannot be solved analytically for most of the pure component isotherm equations, the $2N + 1$ equations have to be solved numerically.

The IAST has the advantage that no restriction exists for the type of pure component isotherm equation used for the prediction of multicomponent equilibria. The success of the IAST in predicting the multicomponent adsorption equilibria depends on three factors: (1) the quality of pure component equilibria data; (2) the correct choice of isotherm equation for the pure component, which should fit the experimental data well over the entire pressure range; and (3) the regression algorithm in deriving the parameters for pure component isotherm equations. Factors 2 and 3 were studied by Richter et al. [15]. Recently, Malek and Farooq [16] investigated the performance of a number of popular isotherm models in fitting pure component isotherms with various nonlinearities in a very comprehensive way. In the same article, they also examined the performance of each model equation and compared it with the IAST in predicting the multicomponent adsorption equilibrium on activated carbon (experimental data on the ternary system methane–ethane–propane were used).

1. The FastIAS Procedure

To avoid the numerical integration procedure and iterative scheme in the IAST, O'Brien and Myers [17] introduced an algorithm that allows for fast computation of multicomponent adsorption equilibria. The pure component isotherm equation was chosen as

$$n_i^0 = m_i \left[\frac{\eta_i}{1 + \eta_i} + \frac{\sigma^2 \eta_i (1 - \eta_i)}{2(1 + \eta_i)^3} \right] \quad (6a)$$

where σ_i is the variance of the adsorption energy distribution and

$$\eta_i = K_i P_i^0 \quad (6b)$$

Equations (6) can be analytically integrated for the spreading pressure π . The equilibrium amount adsorbed of each species can be obtained from the solution of a set of A' nonlinear algebraic equations [15]. This algorithm (called FastIAS) was improved by Moon and Tien [18] and later refined by O'Brien and Myers [19]. It is about one to several orders of magnitude faster than the IAST, depending on the nature of the problem,

Frey and Rodrigues [20] proposed a method for the explicit calculation of multi-component equilibria using IAST. They used a polynomial or Taylor series to approximate the relationship between π_i and $P_i^0(\pi_i)$. However, their method has limited application owing to the approximation used.

2. The Thermodynamics Requirement for the Isotherm Equation

Since the IAST has a rigorous thermodynamics basis, the pure component isotherms used are also expected to meet the thermodynamics requirement. Myers and coworkers [21,22] pointed out that the thermodynamic consistency for the single-component isotherm equations means that they should not have a singular value and be exact at the origin, i.e.,

$$\lim_{P \rightarrow 0} \frac{n_i^0(P)}{P} = \text{finite value} \quad (7)$$

This is required by the integration procedure of Eq. (2) in calculating the spreading pressure. For example, the Freundlich isotherm equation,

$$n = CP^t, \quad 0 < t < 1 \quad (8)$$

incorrectly gives a value of infinity in Eq. (7) and consequently may cause a large error in the calculation of spreading pressure.

Toth [23,24] recently suggested that additional criteria should be met for the thermodynamics consistency of an isotherm equation. He defined the function

$$\psi(\theta) = \frac{\theta}{P} \frac{dP}{d\theta} \quad (9)$$

where θ is the fractional coverage of the surface. The spreading pressure of Eq. (2) can then be rewritten as

$$\pi(\theta) = \frac{RT}{\phi_m} \int_0^\theta \psi(\theta) d\theta \quad (10)$$

where ϕ_m is the surface of adsorbent covered by 1 mol of adsorptive at $\theta = 1$. According to Toth, the criteria for thermodynamics consistency of an isotherm equation are

At $\theta = 0$,

$$\lim_{\theta \rightarrow 0} \psi(\theta) = 1 \quad (11)$$

At $\theta = 1$,

$$\pi_r = \frac{\pi}{RT\phi_m} = \int_0^1 \psi(\theta) d\theta = \text{finite value} \quad (12)$$

Equation (11) corresponds to Eq. (7), while Eq. (12) is the extra thermodynamics requirement that basically stipulates that at full surface coverage the change in the free energy of the adsorbed phase must be finite. According to the criteria of Toth, however, most of the currently used isotherm equations are "thermodynamically incorrect," since they cannot meet one or both conditions. Equation (12), however, is controversial. Toth [25] further pointed out that this inconsistency problem is

caused by the fact that most isotherm equations deal with the absolute amount adsorbed. If the excess amount adsorbed is used instead, this inconsistency problem can be avoided.

The thermodynamics consistency for binary adsorption equilibria isotherm equations was studied by Myers and Sircar [26]. Franses et al. [27] used similar thermodynamics arguments and proposed the following differential criterion for testing the thermodynamics consistency of adsorption isotherm equations of binary systems:

$$\frac{\partial}{\partial c_2} \left(\frac{\Gamma_1(c_1, c_2)}{c_1} \right) = \frac{\partial}{\partial c_1} \left(\frac{\Gamma_2(c_1, c_2)}{c_2} \right) \quad (13)$$

where c is the fluid phase concentration and Γ is the adsorbed phase density

B. The Nonideal Behavior of the Adsorbed Phase

The IAST is based on the assumption that the adsorbed phase is ideal. This is valid at low pressure, and the IAST is known to give good prediction of multicomponent adsorption equilibria at surface coverages up to about 50% [23]. At high pressure, the model prediction tends to diverge from the experimental data (normally underpredicting the experimental data), presumably due to the negative bias from Raoult's law. This is expected, because at high pressure the adsorbed phase becomes more like a liquid, and liquid mixtures of dissimilar molecules are generally nonideal (nonideality). Sometimes problems also arise regarding the spreading pressure when IAST is applied to binary systems consisting of strongly and weakly adsorbing components; i.e., when the partial pressure of the 'strongly adsorbing component approaches its saturation value, the spreading pressure of the mixture can well exceed the saturation pressure of the weakly adsorbing component.

The surface energetic heterogeneity further complicates this problem because micropores of different sizes or sites with different adsorption energies will present different adsorption affinities and selectivities toward different adsorbates. Interactions among adsorbed molecules of the same type and among those of different types also make this problem more complicated [28]. Sircar [29] demonstrated that either of the following two factors can cause erroneous predictions of IAST even in cases where there are no lateral interactions among adsorbed molecules: (1) a large difference in molecular size or (2) adsorbent heterogeneity. Under certain circumstances, these two factors could result in an azeotrope that cannot be accounted for by IAST, Dunne and Myers [30] studied molecules of unequal size adsorbing into a microporous cavity by using a computer simulation technique, and they found that the micropore size exclusion effect for larger molecules generates nonideal behavior in the system.

1. Real Adsorbed Solution Theory

There are two approaches to dealing with these nonideal behaviors in the adsorption process. One accounts for the nonideality of the adsorbed phase with the introduction of an activity coefficient; this method is called the real adsorbed solution theory, or RAST [31–33]. In RAST, Eq. (1) is replaced by

$$Py_i = \gamma_i P_i^0(\pi_i) x_i \quad (14)$$

The RAST has extra parameters to be extracted from a binary system. so it is not, in a strict sense, a predictive model. It has been suggested that γ_i can be correlated as a function of x_i at constant T by measuring a few data points for the binary gas adsorption isotherm. This approach, however, has found only limited success,

2. Energy Distribution Approach

The other approach considers the surface heterogeneity, in which the heterogeneous surface is considered to be patchwise. That is, adsorption sites having the same energy are grouped together; thus the adsorption system can be considered as a collection of independent subsystems. The surface heterogeneity is then represented by a distribution function of adsorption energy. The overall adsorption equilibria of a pure component is the integral of the local adsorption equilibrium on each patch over the complete energy distribution range [34–36].

For a multicomponent system with N components adsorbing onto a heterogeneous surface at temperature T , pressure P , and composition $y = [y_1, y_2, \dots, y_N]$, the overall amount of the i th component adsorbed, n_{it} , is

$$n_{it} = \int \int \cdots \int_{\Omega_n} n_i(T, P, y, e_1, e_2, \dots, e_N) F(e_1, e_2, \dots, e_N) de_1 de_2 \cdots de_N \quad (15a)$$

where

$$\int \int \cdots \int_{\Omega_N} F(e_1, e_2, \dots, e_N) de_1 de_2 \cdots de_N = 1 \quad (15b)$$

and $F(e_1, \dots, e_N)$ is the normalized N -dimensional distribution function in terms of all adsorption energies, $n_i(T, P, y, e_1, e_2, \dots, e_N)$ is the amount of component i adsorbed on a surface characterized by a set of adsorption energies (e_1, e_2, \dots, e_N) and Ω_n is the N -dimensional physical domain of (e_1, e_2, \dots, e_N) . This integral equation represents a general adsorption isotherm of a multicomponent adsorption system involving heterogeneous surfaces [37].

Equations (15) can be simplified with the assumption that the ordering of the sites from low to high energy is the same, i.e., the perfect positive correlation. In this case, Eq. (15a) reduces to

$$n_{it} = \int_0^\infty n_i(T, P, y, e_1, e_2, \dots, e_n) F_i(e_i) de_i \quad (16)$$

Equation (16) is the general integral equation from which many multicomponent equilibria models are derived [38,39]. Sircar [40] also used the binary selectivity S instead of energy e in Eq. (16) to study the role of adsorbent heterogeneity in adsorption from a binary liquid mixture.

The local interaction energy in the adsorbed phase (or energy matching) between different species in Eq. (16) is also an interesting problem. To simplify the integration, Valenzuela et al. [41] assumed that the cumulative energy distribution function was the same for all components in the system, i.e.,

$$f(e_i) = f(e_j) \quad (17)$$

and this is termed a cumulative energy matching scheme. Moon and Tien [42] assumed regular matching (congruent distribution) or complementary matching (opposite distribution) schemes, with binary data needed to obtain some relevant parameters. It was shown in their study that with their matching schemes the IAST can produce the nonideal behavior of some systems. The energy-matching scheme in the adsorbed phase is a fundamental issue in the multicomponent adsorption equilibria on a heterogeneous surface, and we discuss it further in Sec. VI.B. The role of adsorption energy heterogeneity and the local isotherm in the prediction of mixture adsorption equilibria was studied by Hu and Do [43].

Equation (16) has also been applied to IAST [41]. When it is assumed that the gas mixture obeys the perfect gas law and that the adsorbed phase on each patch is ideal, the resulting model is termed HIAST (heterogeneous IAST). Since the HIAST requires the evaluation of the local equilibria on each energy patch with IAST, much more computational effort is required, and yet the increase in performance over the original IAST is only modest for most cases. Therefore, this theory has not been widely used in practical applications.

The adsorbate–adsorbate interaction in the adsorbed phase was also considered in some models [44]. However, the current trend in the literature is focused on the surface heterogeneity resulting from (1) the size difference between adsorbate molecules [29,30,45] or (2) the structural heterogeneity of the adsorbent. Li and Talu [46] demonstrated that in a system where the lateral interactions are very significant, the assumption of a locally ideal mixture can still be applicable. The other example that strongly supports this point of view is the experimental results of binary equilibria of the methane–ethane system on BPL-activated carbon reported by Gusev et al. [47]. Figure 1 presents experimental results of the selectivity of ethane to methane at different pressures (dots) along with the model prediction from IAST (solid line). The selectivity is defined as

$$S = \frac{x_{\text{eth}}/y_{\text{eth}}}{x_{\text{meth}}/y_{\text{meth}}} \quad (18)$$

It can be seen that IAST predictions seriously deviate from the experimental data for this system even though the adsorbed phase is known to be very close to ideal under the experimental conditions. This deviation therefore points to the surface heterogeneity. To address this heterogeneity, new models continue to emerge in the study of multicomponent adsorption equilibria.

III. EQUILIBRIA MODELS BASED ON POTENTIAL THEORY

The potential theory of adsorption was introduced by Polanyi in 1914. Dubinin [48,49] and Stoeckli et al. [50] improved the theory and termed it the theory of volume filling of micropores (TVFM). This theory has been widely used in correlating the effect of temperature on the adsorption isotherms of pure gases. The modern formulation of TVFM is the Dubinin–Astakhov (DA) equation, which is expressed as

$$V = V_0 \exp[-(A/\beta E_0)^n] \quad (19a)$$

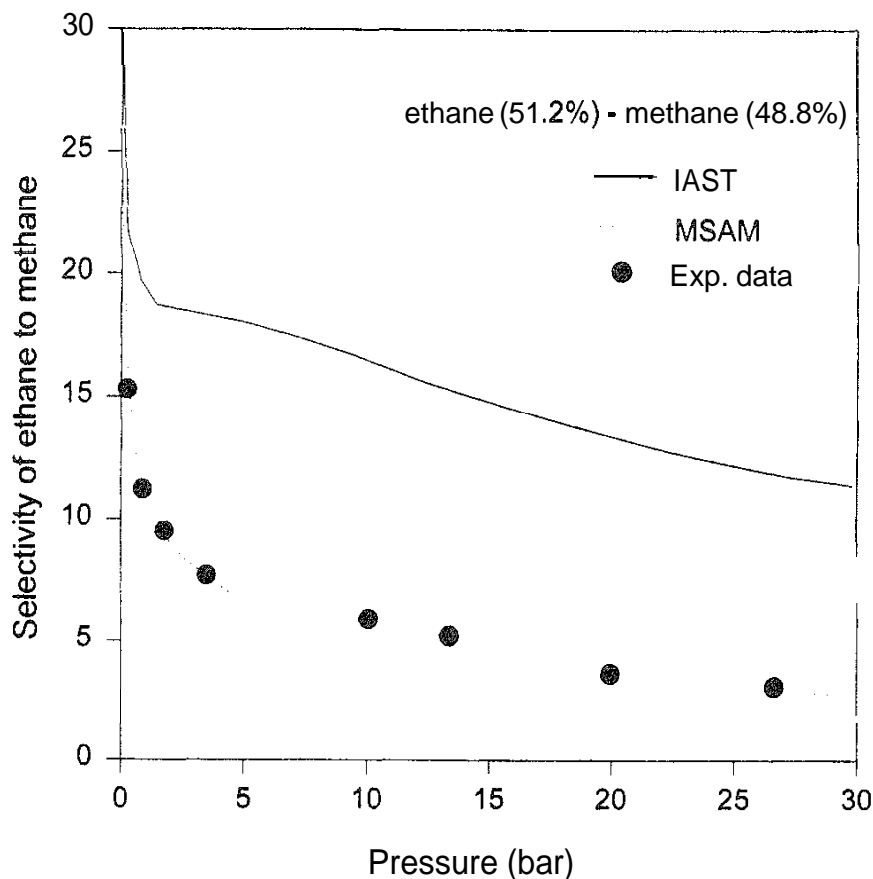


FIG. 1 Plot of selectivity of ethane to methane as a function of pressure. (From Ref. 47.)

where

$$A = RT \ln(P_s/P) \quad (19b)$$

is the adsorption potential, V is the volume adsorbed at the relative pressure P/P_s , P_s is the saturation pressure at temperature T , β is the affinity coefficient of the adsorbate, V_0 is the micropore volume, and E_0 is the characteristic energy of the adsorbent.

The plot of amount adsorbed versus A is defined as the characteristic curve. The relationship between E_0 and pore size for adsorption in micropores was studied by Chen and Yang [51]. The exponential term n , which lies in the range of 1–4, accounts for the structure of the adsorbent. Large n values are found to be associated with adsorbents that have a narrow micropore size distribution, while small n values relate to adsorbents with a wide range of micropore sizes and possibly with meso- and macropores as well.

The DA isotherm contains parameters related separately to the solid and the adsorbates. The advantage of using the potential theory for predicting gaseous mixture adsorption equilibria is that the pure component characteristic curves are generally independent of temperature. Thus having obtained isotherm information of a pure component at one temperature, the mixture equilibria at other temperatures and pressures can be predicted. The DA equation and its

modifications [52–56] have also been used extensively in the characterization of adsorbents.

Some difficulties are also met in the application of the TVFM under certain conditions, because

1. The liquid solution parameter molar volume is required to convert the volumetric adsorbed amount to molar adsorbed amount. When the adsorption temperature is above the normal boiling temperature of the solution, empirical correlations have to be used to obtain the liquid molar volume [57].
2. The adsorbate molar volume is normally assumed to be the same in both single- and mixed-gas adsorption.
3. The calculation of the saturation pressure at supercritical temperature also incurs some uncertainty.
4. The DA equation does not conform to Henry's law in the low pressure region. The Henry's law limit for pore filling models in multicomponent adsorption equilibrium was discussed by Rudisill and Le Van [58].

Various efforts have also been made to extend the DA equation for the study of the adsorption equilibria of gas/vapor mixtures. The models for multicomponent adsorption equilibria based on the DA equation can be roughly classified into three groups: (1) the direct extension or application of the DA (or DR) equation; (2) the potential theory approach, which is based on coalescing the potential curves of different components; (3) other methods, which link the DA equation to other adsorption properties, such as the adsorbed phase properties or adsorbate–pore interaction potentials.

A. Direct Application of DR and DA Equations

1. Bering et al.'s Model

Early efforts to extend the DR equation were largely empirical. Bering et al. [59] extended the DR equation to binary system in a direct manner. For binary systems, their model is

$$V_1 + V_2 = V_0 \exp \left\{ - \left(\frac{RT}{\beta_{12} E_0} \ln \left[\frac{P_1 + P_2}{P_{s12}} \right] \right)^2 \right\} \quad (20)$$

where V_1 and V_2 are volumes adsorbed for each species, and P_{s12} is the saturated vapor pressure for the adsorbed mixture over which the saturated vapor has the same composition as that of the equilibrium vapor over the adsorbent. The parameter β_{12} is the average affinity coefficient, taken as

$$\beta_{12} = A_1 \beta_1 + x_2 \beta_2 \quad (21)$$

To calculate V_1 and V_2 , the following Lewis relationship for a binary system [60] is used:

$$\frac{q_1}{q_1^0} + \frac{q_2}{q_2^0} = 1 \quad (22)$$

with the constraint

$$x_1 + x_2 = 1 \quad (23)$$

The Lewis relationship has its theoretical basis in micropore filling with the assumption that the adsorbed phase is ideal [2].

Thus the Bering et al. model must be solved iteratively. When the temperature is above the boiling point, it is difficult to justify the relationship between the partial pressure of each species and the saturation pressure of the system, P_{s12} . Hence this model is less attractive than other methods.

2. Doong and Yang's Model

Doong and Yang [61] proposed a simple way of predicting multicomponent equilibria by using the concept of TVFM. Their model is based on the idea that in the DA equation the total micropore volume of the adsorbent should be replaced by the "maximum available micropore volume" for each species. Other assumptions are that (1) the adsorbate-adsorbate interaction is negligible compared to the adsorbate-adsorbent interaction, (2) the parameters n and βE_0 for any species are independent of the other species, and (3) the adsorbed phase is ideal. With these assumptions, the DA equation for each species in a binary system can be written as

$$V_1 = (V_{01} - V_2) \exp \left[- \left(\frac{RT}{\beta_1 E_0} \ln \frac{P_{s1}}{P_1} \right)^{n_1} \right] \quad (24a)$$

$$V_2 = (V_{02} - V_1) \exp \left[- \left(\frac{RT}{\beta_2 E_0} \ln \frac{P_{s2}}{P_2} \right)^{n_2} \right] \quad (24b)$$

Solving for V_1 and V_2 yields the equations

$$V_1 = \frac{A_1(V_{01} - V_{02}A_2)}{1 - A_1A_2} \quad (25a)$$

$$V_2 = \frac{A_2(V_{02} - V_{01}A_1)}{1 - A_1A_2} \quad (25b)$$

where

$$A_1 = \exp \left[- \left(\frac{RT}{\beta_1 E_0} \ln \frac{P_{s1}}{P_1} \right)^{n_1} \right] \quad (26a)$$

$$A_2 = \exp \left[- \left(\frac{RT}{\beta_2 E_0} \ln \frac{P_{s2}}{P_2} \right)^{n_2} \right] \quad (26b)$$

Equations (25) and (26) are sufficient for predicting the equilibria of binary mixtures. The simplicity of this method constitutes an advantage over other methods based on TVFM. Besides, this model is not iterative and can be extended to N -component systems in a straightforward manner.

For practical purposes, the volumetric amount adsorbed (V) in Eqs. (25) should be converted into molar amount adsorbed, q , with the equation

$$q = V/V_a \quad (27)$$

where V_a is the liquid molar volume of the adsorbate. Doong and Yang [61] recommended the following relationships:

$$V_a = \begin{cases} V_{s, \text{sbp}} & \text{for } T < T_{\text{nbp}} \\ V_c - (V_c - V_{s, \text{nbp}}) \left(\frac{T_c - T}{T_c - T_{\text{nbp}}} \right) & \text{for } T_{\text{nbp}} \leq T < T_c \\ V_c (T/T_c)^{0.6} & \text{for } T \geq T_c \end{cases} \quad (28)$$

where

$$\begin{aligned} V_{s, \text{nbp}} &= \text{molar volume of the saturated liquid at its normal boiling point} \\ V_c &= \text{molar volume of the species at its critical temperature} \end{aligned}$$

This model is validated with the binary experimental data on several systems [22]: (1) alkane and alkene mixtures on Nuxit activated carbon; (2) O_2 – N_2 mixture on zeolite; (3) binary adsorption on BPL activated carbon. The model was compared with three other models (IAST, G-M, and Bering et al.'s model), and it was found that under most circumstances this model gives equivalent or even superior performance.

3. DR Equation Used with IAST

The application of the DR equation in IAST was studied by Richter et al. [15] and was used recently by Lavanchy et al. [62] to predict the binary adsorption equilibria of chlorobenzene–carbon tetrachloride vapor mixtures on activated carbon. This is simply a formal application of the IAST theory with the DR equation being used to describe the pure component isotherm. However, due to some special properties of the DR equation, this combination generates some unique features and deserves some elaboration here.

The DR equation is a special case of the DA equation, Eq. (19), with $n = 1$. When the DR equation is substituted into Eq. (2), the analytical form for the spreading pressure of component i is

$$\psi_i(P_i^0) = \int_0^{P_i^0} \frac{n_i(P)}{P} dP = \left(\frac{V_0}{V_{ai}} \right) \left(\frac{\beta_i E_0}{RT} \right) \left(\frac{\sqrt{\pi}}{2} \right) \left\{ \left[1 - \operatorname{erf} \left(\frac{RT}{\beta_i E_0} \right) \ln \left(\frac{P_i^0}{P_{is}} \right) \right] \right\} \quad (29)$$

where $P_i^0 = P_i/x_i$ is the hypothetical pressure for pure component i that gives the same spreading pressure as that of the mixture. The adsorbed phase concentration for a binary system is obtained by simply solving (assuming an ideal adsorbed phase)

$$\psi_1(P_1^0) = \psi_2(P_2^0) \quad (30)$$

The number of moles adsorbed at the hypothetical pressure can be calculated from the DR equation as

$$n_i^0 = \frac{V_0}{V_{ai}} \exp \left\{ - \left[\left(\frac{RT}{\beta_i E_0} \right) \ln \left(\frac{P_{is}}{P_i^0} \right) \right]^2 \right\} \quad (31)$$

It is seen in Eq. (29) that the DR equation requires two types of parameters: (1) properties of the adsorbent—micropore volume V_0 and characteristic energy E_0 ; (2) properties of the adsorbate — saturation pressure P_s , affinity coefficient β , and liquid molar volume V_{si} . Principally, the first group of parameters are temperature-independent and can be obtained from the adsorption of a reference adsorbate on the same adsorbent, while the second group of parameters are temperature-dependent but can be simply estimated from the thermodynamic properties of each species. Therefore, a limited set of data is required to describe binary adsorption over a wide range of pressure and temperature. Thus the advantages of using the DR equation deserve to be exploited.

The error in calculating the spreading pressure caused by the incorrect behavior of the DA equation in the Henry's law region was estimated by Richter et al. as

$$\Delta\left(\frac{\pi A}{RT}\right) \approx \frac{V_0}{V_{mi}} \exp\left[-\frac{\beta E_0}{4RT}\right] \quad (32)$$

This error is normally smaller than experimental error.

B. Potential Theory Approach

The basic assumption in the potential theory approach to predicting the adsorption equilibria of a gas mixture is that the adsorption data for all pure components on the same adsorbent will fall on the same line when plotted on some appropriate coordinate (coalescing) [39,63]. This principle is reflected in the Lewis method [64] and in the Grant–Manes (G–M) method [65] and its modification by Metha and Danner [66].

1. The Grant–Manes (G–M) Method

The G–M method for predicting the phase diagram of a binary system on activated carbon is based on the equation

$$\frac{RT}{\beta_1} \ln\left(\frac{x_1 f_{s1}^0}{f_1}\right) = \frac{RT}{\beta_2} \ln\left[\frac{(1-x_1)f_{s2}^0}{f_2}\right] \quad (33)$$

where f_1 and f_2 are the fugacities of components 1 and 2, and f_{s1}^0 and f_{s2}^0 are the fugacities of each component at its saturation vapor pressure and at system temperature T . Moon and Tien [67] showed that in most cases the bulk fugacity can be replaced by pressure. Equation (33) can be used to derive the adsorbed phase composition by using the concept of pseudoadsorbate pressure and its related saturated liquid molar volume in an iterative manner.

According to Grant and Manes [65], the affinity coefficient β_i that coalesces the potential curves of each species satisfies the relationship

$$\beta_1/\beta_2 = V_{b1}^0/V_{b2}^0 \quad (34)$$

where V_{bi}^0 is the saturated liquid molar volume of pure component i at its normal boiling point.

2. Metha–Danner Method

However, Metha and Danner [66] and Moon et al. [68] demonstrated that Eq. (34) is too crude and too unreliable for various adsorbates on adsorbents of practical interest. They pointed out that the potential curves of different pure gases on activated carbon are usually close but do not coincide. To overcome this, Metha and Danner suggested that Eq. (33) be replaced by the equation

$$\ln \left[\frac{x_1 f_{s1}^0}{f_1} \right] = \frac{M_{12} V_{s1}^0}{V_{s2}^0} \ln \left[\frac{(1 - x_1) f_{s2}^0}{f_2} \right] \quad (35)$$

where V_{si}^0 is the saturated liquid volume of the component i at the pseudoadsorbate pressure. The parameter M_{12} is the interaction parameter for the mixed adsorbate–adsorbent system, which is related to the coalescing factors of each species: k_1^0, k_2^0 . For different adsorbate–adsorbent interactions, the following relationships were proposed by Metha and Danner:

For nonpolar adsorbents such as activated carbon:

$$M_{12} = k_1^0 / k_2^0 \quad (36)$$

For polar adsorbents such as silica gel and molecular sieve:

$$M_{12} = [k_1^0 / k_2^0]^2 \quad (37)$$

Upon generalization of the potential approach for adsorption equilibria of gas mixtures, Rudzinski et al. [39] pointed out that the potential theory approach corresponds to a special case of IAST for adsorption on a heterogeneous surface and therefore it works better on strongly heterogeneous adsorbents such as activated carbon. Based on thermodynamic analysis, Rudzinski et al. also suggested that an extra coalescing factor be introduced in Eq. (35) and in this way the predictive accuracy of the potential theory approach could be further improved.

Sircar and Myers [69] used the same idea but proposed another way of coalescing the isotherms of different vapor adsorbates on a heterogeneous surface. Based on a comprehensive thermodynamic analysis, they suggested the characteristic equation

$$P(\theta) = \frac{m}{\Delta G} RT \ln x \quad (38)$$

where m is the adsorptive capacity at saturation, x is the reduced pressure, and ΔG is the free energy of immersion of the adsorbent in liquefied adsorbate, which can be obtained from binary mixture data or by fitting the pure component isotherm with Eq. (38). The factor $\Delta G/m$ is the molar free energy of immersion of the adsorbate vapor, which transforms the Polanyi potential $-RT \ln x$ into a dimensionless function that is the same for all adsorbates. Equation (38) is shown to work well for adsorbates of different sizes and structures.

C. Other Methods

1. Dobruskin's Model

Dobruskin [57] proposed a model for the adsorption equilibria of multicomponent vapor mixtures based on the concept of TVFM and an adsorbed phase model in which the adsorbate–adsorbent interactions predominate over the lateral interaction between adsorbed molecules. The proportions of the component in the adsorbed phase are determined by a statistical distribution based on Frenkel's [70] mechanism and kinetic gas theory [71,72]. In Dobruskin's study, the equilibrium is viewed as a dynamic process in which the average molecular residence time τ is the reciprocal of the rate constant for desorption, k . For adsorption of a binary mixture in an elementary volume dW , the ratio of the average times between two components is

$$\frac{\tau_1}{\tau_2} = \frac{\nu_2}{\nu_1} \exp\left[\frac{q_1 - q_2}{RT}\right] \quad (39)$$

where q and ν are the adsorption energy and vibration frequency, respectively. If the adsorption energies of the components are independent of each other, the following approximation is made:

$$\Delta q = \Delta A = \Delta \beta A \quad (40)$$

in which the similarity of the characteristic curves at constant fractional loading is taken into account.

At equilibrium of gas adsorbing onto a surface of area S , the number of molecules in the adsorbed phase is assumed to be equal to the product of the average time and the number of molecules striking the surface. The average ratio of the numbers of molecules n_1 to n_2 in this element W is

$$\bar{x} = \frac{n_1}{n_2} = \frac{N_1 S}{N_2 S} \left(\frac{\bar{\tau}_1}{\bar{\tau}_2} \right) \quad (41)$$

By using kinetics theory and inserting $N_i = P_i / (2\pi m_i kT)^{0.5}$ into Eq. (41), Dobruskin obtained the following equation for the selectivity of the binary system:

$$S = \left(\frac{\beta_1}{\beta_2} \right)^{0.5} \theta^{-1} \exp(b^2) \left(\exp \left\{ - \left[\left(\ln \frac{1}{\theta} \right)^{0.5} - b \right]^2 \right\} + \pi^{0.5} b \left\{ 1 - \operatorname{erf} \left[\left(\ln \frac{1}{\theta} \right)^{0.5} - b \right] \right\} \right) \quad (42)$$

where $b = \Delta \beta E / 2RT$. The adsorbed phase equilibrium composition can be obtained with further assumptions about the adsorbed phase, molar work, and special points in the potential curve. This model is capable of computing multicomponent equilibria by using single gas isotherm parameters only, while the use of liquid solution parameters is avoided.

2. Eiden and Schlunder's Model

Eiden and Schlunder [73] proposed a model for predicting the adsorption equilibria of a binary vapor mixture based on pure component parameters. The model

combines the TVFM and IAST on the basis of a multiphase mixture, i.e., the micropore space is divided into subvolumes that are related to the adsorption potential by means of the characteristic curves of pure components. Amount adsorbed and composition are evaluated separately in each subvolume by assuming that the adsorbate mixture forms ideal solutions.

Eiden and Schlunder used the modified DA equation,

$$V = V_{s0} \exp \left[- \left(\frac{A - A_{Gr}}{E_0} \right)^{n_1} \right] \quad (43)$$

where V_{s0} is the saturation micropore volume and A_{Gr} is the limiting potential. When the V_{s0} are the same for all species, the micropore volume is divided into z subvolumes, and each subvolume j corresponds to the adsorption potential

$$A_{ij} = A_{Gr,i} + E_{0i} \left(\ln \frac{z}{j} \right)^{1/n_i}, \quad i = 1, 2; j = 1, 2, \dots, z \quad (44)$$

With related thermodynamics properties of the modified DA equation, the following expression is derived for the molar fraction of component i in the subvolume j :

$$\frac{x_{1j}^{V_M}}{1 - x_{1j}} = \frac{\phi_1^{V_M}}{\phi_2} \exp \left[\frac{V_M A_{1j} - A_{2j}}{RT} \right] \quad (45)$$

where ϕ_i is the relative pressure P_i/P_{si} and V_M is the ratio of the molar liquid volumes, V_2/V_1 . With Eq. (44), the phase compositions of the j th subvolume can be calculated directly. The overall adsorbed quantity for a component is the sum of its related quantities in each subvolume, provided the adsorption potential of that component is larger than the limiting potential. It should be noted that this model can describe the real adsorption behaviors when the exponents n_1, n_2 are different.

In the case that V_{s0} are different owing to the steric effects, real adsorption behaviors are to be expected. The multiphase real adsorbed solution (MRAS) approach is used, considering the "real behavior" to comprise two factors: (1) adsorbate-adsorbent interactions, which are taken into account by the multiphase concept; (2) adsorbate-adsorbate interactions, which are considered by activity coefficients and are taken as the same for the same species in each subvolume. The MRAS model is

$$\frac{(x_{1j}\gamma_1)^{V_M}}{\gamma_2(1 - x_{1j})} = \frac{\phi_1^{V_M}}{\phi_2} \exp \left[\frac{V_M A_{1j} - A_{2j}}{RT} \right] \quad (46)$$

Their model was validated with the experimental data of benzene-hexamethyldisiloxane and dichloromethane-benzene systems on two activated carbons [74]. Satisfactory agreement was found between model predictions from Eq. (45) and the data for all the systems, even for one that showed strongly pressure-dependent azeotropic behavior.

IV. OTHER MODELS

In this section we review the models that do not fall within the scope of the previous two sections. Some of these models may bear more or less empiricism in their model development. However, their methodology and practical significance are of more interest to practicing engineers. A large number of models of this type are to be found in the literature, but here we cover only a few that exhibit some distinctive features.

A. The Extended Sips Model

Sips [75] proposed an empirical equation for the adsorption of a pure component system that is a combination of the Langmuir and Freundlich equations. This three-parameter equation has been widely used for fitting the isotherm data of numerous hydrocarbons on activated carbon [22]. The Sips adsorption isotherm for the pure component has the form

$$C_{\mu} = C_{\mu s} \frac{(bP)^{\alpha}}{1 + (bP)^{\alpha}} \quad (47)$$

If we used the same analogy as that for the generalization of the Langmuir equation, we would obtain for the extended Sips model the equation

$$C_{\mu,i} = C_{\mu s} \frac{(b_i P_i)^{\alpha_i}}{1 + \sum_{k=1}^N (b_k P_k)^{\alpha_k}} \quad (48)$$

However, this direct extension corresponds only to the ideal situation where the adsorption energies of the various components are completely uncorrelated [76]. Rudzinski et al. [39] demonstrated that if the adsorption energies of each component are highly correlated to each other by the relation

$$e_j = e_i + \Delta_{ji}, \quad j, i = 0, 2, \dots, N \quad (49)$$

then the generalized Sips equation for a multicomponent system will take the form

$$C_{\mu,i} = \frac{C_{\mu s} b_i P_i}{\sum_{k=1}^N b_k P_k} \frac{\left(\sum_{k=1}^N b_k P_k \right)^{\alpha_i}}{1 + \left(\sum_{k=1}^N b_k P_k \right)^{\alpha_i}} \quad (50)$$

This equation can also be derived by formally applying the IAST, using the Sips equation, Eq. (47), to describe pure component data. Hence, for adsorption of gas mixtures onto activated carbon, the use of Eq. (50) is generally justified.

Because the exponential term $a \neq 1$, the Sips equation does not have a correct low pressure limit, which is contrary to experimental observations. To overcome this problem and extend the range of applicability of isotherms of this type, Staudt et al. [77] introduced the pressure- and temperature-dependent exponents to ensure that Henry's law holds when pressure is sufficiently low. The new generalized form of Eq. (48) is

$$C_{\mu,i} = C_{\mu s} \alpha_{\infty,i} \frac{(b_i P_i)^{\alpha_i}}{1 + \sum_{k=1}^N (b_k P_k)^{\alpha_k}} \quad (51a)$$

where

$$a_i = \alpha_i(P, T) \quad (51b)$$

is the new pressure-dependent characteristic exponent, which satisfies the two limits

$$\lim_{P \rightarrow 0} a_i = 1 \quad \text{and} \quad \lim_{P \rightarrow \infty} a_i = \alpha_{i,\infty} \quad (51c)$$

Staudt et al. suggested the following functional form of a_i , which conforms to the above limits:

$$\alpha_i(P_i) = \frac{1 + \alpha_{\infty,i} P_i a_i}{1 + P_i a_i} \quad (51d)$$

where a_i is a constant. The temperature dependence of the exponential terms is

$$\frac{\alpha_{\infty,i}(T)}{\alpha_{\infty,i}(T_{c,i})} = \left(\frac{T}{T_{c,i}} \right)^{k_{\alpha,i}} \quad (51e)$$

where T_c is the critical temperature and k is a constant. With these corrections, the new model predictions were shown to be much improved for both single- and multicomponent adsorption equilibria. This method of Staudt et al. is also applicable to other isotherms. For example, for the Toth isotherm it is

$$C_{\mu i} = C_{\mu\infty} \alpha_{\infty,i} \frac{b_i P_i}{\left[1 + \sum_{k=1}^N (b_k P_k)^{\alpha_k} \right]^{1/\alpha_i}} \quad (52)$$

where a is defined in the same way as in Eq. (51d)

B. Isosteric Heat as a Function of Loading Model

Do and Do [78] proposed an adsorption equilibria model based on isosteric heat as a function of loading (IHFL). In their model the variation of isosteric heat with loading is regarded as the measure of the heterogeneity of the adsorbent. Since this model takes into account the surface heterogeneity and allows for the variation of the isosteric heat during the adsorption process, it gives an excellent fit to the equilibria of many species on the same adsorbent when fitted simultaneously. The model was tested successfully for many systems on various adsorbents such as activated carbon, zeolite, and H-mordenite. The model equation for a pure component is

$$\frac{\theta}{(1 - \theta^{t_k})^{1/t_k}} = \frac{\beta P}{\sqrt{M_k T}} \exp \left[\frac{E_k(0)[1 - \alpha f(\theta; c)] + u_k \theta}{RT} \right] \quad (53)$$

where θ is the surface coverage, t is the parameter specific to the adsorbent-adsorbate pair, β is a parameter characterizing the solid property, $E(0)$ is the isosteric heat at zero loading, α is the extent of energy heterogeneity, $f(\theta; c)$ is a function describing the pattern of heterogeneity, and u is the adsorbate-adsorbate interaction energy. Equation (53) has also been extended to study multicomponent adsorption equilibria. The general form of the extended equation is

$$\frac{\theta_i}{\left[1 - \left(\sum_{k=1}^N \theta_k\right)^{t_i}\right]^{1/t_i}} = \frac{\beta P_i}{\sqrt{M_i T}} \exp \left[\frac{E_i(0) \left[1 - \alpha f\left(\sum_{k=1}^N \theta_k; c\right)\right] + \sum_{k=1}^N (u_{i,k} \theta_k)}{RT} \right] \quad (54a)$$

where P_i is the partial pressure in bulk phase. and

$$P_i = P_T y_i \quad (54b)$$

The cross adsorbate–adsorbate interaction energy is assumed to take the form

$$u_{i,k} = (u_i + u_k)/2 \quad (54c)$$

The mole fraction of component i in the adsorbed phase is calculated from

$$x_i = \frac{\theta_i}{\sum_{k=1}^N \theta_k} \quad (54d)$$

The form for the pattern of heterogeneity for the solid is assumed to be the same for all components, and this pattern is assumed to take the form

$$f(\theta; c) = \frac{c\theta}{1 + (c-1)\theta} \quad (54e)$$

To reduce the number of parameters in the IHFL model. the following assumptions can be employed:

1. If the adsorbate–adsorbate interaction energy is negligible compared to that of the adsorbate–adsorbent interaction, then u is set to zero.
2. The saturation capacity is independent of temperature.
3. The saturation capacity is a function of the adsorbate.

Therefore. the number of parameters in the optimization can be reduced to $3 + 3N$ (N = number of adsorbates) without seriously compromising its performance.

C. The Heterogeneous Extended Langmuir Model

Kapoor et al. [79] proposed a heterogeneous extended Langmuir (HEL) model for the description of multicomponent equilibria on heterogeneous adsorbents. With the integral equation approach of Eq. (16), the general isotherm for a pure component system can be simplified as

$$\theta(T, P) = \int_{e_{\min}}^{e_{\max}} \theta(T, P, e) F(e) de \quad (55)$$

where $\theta(T, P, e)$ is the "local isotherm" representing the amount adsorbed on a homogeneous patch with an energy e ; $F(e)$ is the normalized distribution function; and e_{\min} and e_{\max} are the minimum and maximum energies, respectively. In one of the simplest cases where the local isotherm is described by the Langmuir equation and $F(e)$ follows the uniform energy distribution, Eq. (55) is analytically integrable, and the final form is the famous LUD (UniLan) isotherm equation [21]:

$$C_{\mu}(T, P) = \frac{C_{\mu s}}{2s} \ln \frac{1 + \bar{b}Pe^s}{1 + \bar{b}Pe^{-s}} \quad (56a)$$

where

$$\bar{b} = b_{\infty} \exp\left[\frac{\bar{e}}{RT}\right], \quad s = \frac{\sqrt{3}\sigma}{RT} \quad (56b)$$

In Eqs. (56), b_{∞} is the adsorption affinity at infinite temperature; \bar{e} and σ are the mean and square root of variance of energy, respectively; and s is the heterogeneity parameter related to the spread of the energy distribution.

When the system consists of a gas mixture containing N components, the overall adsorption equilibrium is described by the general integral equation, Eq. (16). Kapoor et al. applied the extended Langmuir equation as a local isotherm and a uniform energy distribution. The uniform distribution function is

$$F(e_i) = \begin{cases} \frac{1}{e_{i,\max} - e_{i,\min}} & \text{for } e_{i,\min} \leq e \leq e_{i,\max} \\ 0 & \text{elsewhere} \end{cases} \quad (57)$$

The cumulative energy matching scheme [41] is employed to address the energy matching between different adsorbates in the adsorbed phase. With the uniform energy distribution, it is

$$\frac{e_i - e_{i,\min}}{e_{i,\max} - e_{i,\min}} = \frac{e_j - e_{j,\min}}{e_{j,\max} - e_{j,\min}} \quad (58)$$

The HEL model then takes the form

$$C_{\mu i} = \int_{e_{i,\min}}^{e_{i,\max}} \left[\frac{C_{\mu s} P_i b_{\infty,i} \exp(e_i/RT)}{1 + \sum_{j=1}^N P_j b_{\infty,j} \exp(e_j/RT)} \right] \left[\frac{1}{e_{i,\max} - e_{i,\min}} \right] de_i \quad (59)$$

Equation (59) must be solved numerically. The analytical solution is available only under certain conditions (the variance of the energy distribution is the same for all components).

The HEL model is a noniterative model and has a reasonable prediction capability. With the pure component isotherm parameters derived from the LUD equation, the model can be employed to predict the adsorption equilibria of gas mixtures at any other temperature. Since the LUD equation is flexible in correlating the pure component data, the HEL model prediction for a gas mixture is generally good. Kapoor et al. [79] demonstrated in their study that the HEL model gave satisfactory results for a number of systems, which were comparable in many cases to the results from the IAST or even HIAST model.

However, some arbitrary assumptions such as the energy distribution and energy matching do exist in the HEL model. Meanwhile, the performance of the HEL model depends on the LUD parameters derived from pure component data. When the quality of pure component data is not good or there are too few data points, it is possible that the energy parameters (especially $e_{i,\min}$ and $e_{i,\max}$) derived from the LUD equation are meaningless or inconsistent between different species. In this case, the model prediction from the HEL model must be treated with care.

D. The Multisite Langmuir Model

The multisite Langmuir (MSL) model [80] is an extension of the Langmuir equation to adsorption on multiple sites. Component i is assumed to occupy a_i sites (a_i is not necessarily an integer) in the adsorbed phase. The specific saturation capacity of component i is m_i , and for different components on the same adsorbent it satisfies

$$a_i \times m_i = \text{constant} \quad (60)$$

The MSL equation can be derived from classical kinetics considerations [71] or from statistical mechanics. For a pure component, the MSL model equation is

$$K_i P = \frac{\theta_i}{(1 - \theta_i)^{a_i}}, \quad i = 1, 2, \dots, N \quad (61)$$

and for a gas mixture, it is

$$K_i P y_i = \frac{\theta_i}{\left[1 - \sum_{j=1}^N \theta_j\right]^{a_i}}, \quad i = 1, 2, \dots, N \quad (62)$$

MSL models present the correct Henry's law limit and obey the requirement of thermodynamic consistency. This model is often used to account for the effect of the size difference in the study of multicomponent adsorption equilibria [29,30]. The MSL model can be extended to include effects such as lateral interactions in the adsorbed phase as well as surface heterogeneity [80].

E. The Multispace Adsorption Model

Gusev et al. [47] recently proposed a multispace adsorption model (MSAM) for noncrystalline adsorbent. In this model, the pore volume is divided into two spaces: Space I is close to the surface of the adsorbent where the adsorbate–adsorbent interaction is strong, and space II is further from the adsorbent, where the adsorbates interact with those in space I but have no direct interaction with the adsorbent. The amount adsorbed in space II depends on the occupancy of space I. The heterogeneity of the adsorbed phase is then due to the proximity of an adsorbed molecule to the surface.

For species i in an N -component system, the amount adsorbed is then the contribution from both spaces, i.e.,

$$n_i = n_{i,I} + n_{i,II} \quad (63)$$

The fraction of space I in the total pore volume is defined as

$$R = \frac{\text{saturation capacity of } i \text{ in space I}}{\text{saturation capacity of } i \text{ on adsorbent}} = \frac{n_{i,I}^\infty}{n_i^\infty} \quad (64)$$

Hence the following equation holds:

$$\frac{n_i}{n_i^\infty} = R \frac{n_{i,I}}{n_{i,I}^\infty} + (1 - R) \frac{n_{i,II}}{n_{i,II}^\infty} \quad (65)$$

The overall isotherm for species i is

$$\frac{n_i}{n_i^\infty} = L_{i,I}(P)[R + (1 - R)L_{i,II}(P)] \quad (66a)$$

where

$$L_{i,I}(P) = \frac{K_{i,I}P}{1 + K_{i,I}P}, \quad L_{i,II}(P) = \frac{K_{i,II}P}{1 + K_{i,II}P} \quad (66b)$$

and $K_{i,I}$, $K_{i,II}$ are the Langmuir constants for species i in spaces I and II, respectively.

The adsorbed phases in spaces I and II are assumed to be ideal, and hence the IAST can be applied to each space separately (HIAST). The parameter R is the key parameter for the MSAM; it reflects the structure of the adsorbent and is independent of temperature and the adsorbing mixture. The value of R is determined by using the MSAM to fit a limited amount of mixture data for an arbitrary binary mixture. Because of this, the MSAM is more a corrective method than a predictive method.

It was demonstrated in the study of Gusev et al. [47] that the MSAM gives a good representation of both ideal and nonideal behavior of the adsorbed phase for a number of systems that cannot be described by the IAST. For example, the non-ideal adsorption behavior of the ethane–methane system on BPL carbon (Fig. 1) is successfully simulated by the MSAM (dotted line in Fig. 1). It is noted, however, that the MSAM does introduce some arbitrary assumptions and unrealistic pictures in describing the adsorbed phase; as the authors put it, "This model is intended for engineering application rather than for the fundamental mechanisms of multicomponent adsorption equilibria."

A similar method that treats the adsorbed phase as a combination of two phases or patches was used by Li and Talu [46] and Guo et al. [81]. Li and Talu [46] show that with the combination of HIAST and the multicomponent van der Waals (MvdW) model [36], the highly unusual behavior of benzene–p-xylene vapor mixtures adsorbing onto silicalite can be more than qualitatively predicted. The non-ideality of the system results in an S-shaped isobaric binary isotherm and a crossover point of selectivity curves at different pressures. Their results further support the view that surface heterogeneity is the major contribution to the 'observed' nonideality [82].

F. Martinez's Model

Martinez and Basmadjian [83] proposes a general isotherm model for the adsorption of both pure gas and gas mixtures. This model takes into account a broad range of factors such as adsorbate size r , loss of symmetry or chemical dissociation s , clustering u , and molecular interactions in the adsorbed phase W . The model is based on the combination of the kinetics arguments of Langmuir, which account for the molecular size effect, and statistical thermodynamics arguments [84], which account for other factors such as clustering and molecular interaction. This model has two forms: (1) the complete form and (2) the reduced form in the Flory limit. Only the latter form was investigated in detail by Martinez and Basmadjian [83]; it is

$$y_i P = M_i \frac{\theta^{s_i/m_i}}{(1 - \Theta)^{r_i}} \exp \left(r_i \sum_{j=1}^N \frac{W_{ij}}{kT} \theta_j \right) \quad (67)$$

where $\Theta = \sum_{i=1}^N \theta_i$ is the total coverage, M is the isotherm parameter, N is the number of components in the system, and P is the bulk pressure. This model was shown to reduce to simple isotherm equations such as those of Langmuir, Freundlich, Sips, Nitta, and Fowler and Guggenheim in various limiting forms. It can also be cast into a form similar to Raoult's law as

$$y_i P = P_i^* x_i \psi_i \beta_i \quad (68)$$

where P is the pure component vapor pressure of species i at the same surface coverage and temperature as the mixture. The parameters ψ_i and β_i are two distinct parts of the activity coefficient, with the former reflecting the contribution due to the size effect, segmentation, and clustering, while the latter addresses the molecular interaction.

To examine the model performance, Martinez and Basmadjian used the following experimental data in their study: (1) the pure component and binary gas mixtures of hydrocarbon on activated carbon and on silica gel [85–88]; (2) hydrocarbons and CO_2 on zeolite [11]; (3) propane, CO_2 , and H_2S and their binary mixtures on H-mordenite [30]. The adsorption nonideality of the binary systems increases from mild (group 1) to high (group 3), and the model performance is shown to be satisfactory for each group of data.

In spite of the merits of the model cited above, it suffers from the following problems:

1. It needs binary data to derive the molecular interaction parameter W ; thus it is again a corrective rather than a predictive model (indeed, most existing models require binary data to represent the nonideal adsorption behavior of the system).
2. It has five or more parameters to be optimized (depending on the simplification of the model), so there exist some uncertainties in the extracted parameters; for example, the optimized interaction energies may lack physical meaning and consistency.
3. In the simulation, the authors simplified the model according to the degree of nonideality of the experimental data; this may bear some empiricism.

G. Keller's Model

Keller and coworkers [89–91] proposed a class of thermodynamically consistent isotherm equations in which the size-scaling effects are encompassed by means of the fractal dimension of the adsorbent. One interesting property of the Keller model is that the influence of the adsorbent's geometry and roughness, expressed by fractal dimension D , and the influence of the energetic heterogeneity, expressed by the nonconstant behavior of the adsorption energies (E) with partial pressure, clearly appear in the isotherm equation. The decoupling of these two effects may enable us to achieve a clearer picture of the role of energeticgeometric heterogeneity in adsorption isotherms. The concept of fractal dimension was first

introduced by Avnir and Pfeifer [92] in characterizing the surface structure in adsorption processes and was recently investigated by Sahouli et al. [93], who used the standard adsorption isotherm on various adsorbents. The Keller isotherm is

$$C_{\mu i}(T, P_i) = C_{\mu \infty}(T) \Phi \left(\sum_{k=1}^N c_k f_k^{\alpha_k} \right) \left[\alpha_i c_i f_i^{\alpha_i} + \frac{f_i}{RT} \sum_{k=1}^N \alpha_k c_k f_k^{\alpha_k} \left(\frac{\partial E_k}{\partial f_i} \right) \right], \quad (69a)$$

$i = 1, 2, \dots, N$

where f is the fugacity and c is related to the adsorption energy E through the equation

$$c_k = [P_{k\infty} \exp(-E_k/RT)]^{-\alpha_k}, \quad P_{k\infty} = \text{constant} \quad (69b)$$

The exponent α depends on the molecular size r and the fractal dimension D of the adsorbent:

$$\alpha_i = \alpha_r (r_r/r_i)^D \quad (69c)$$

where the subscript r represents a reference species.

Φ is the characteristic function. In the case of Langmuir monolayer coverage, it is

$$\Phi(x) = 1/(1 + x) \quad (69d)$$

and in the case of BET multilayer adsorption, it is

$$\Phi(x) = F/[(1 - x)(1 + Fx - x)] \quad (69e)$$

Keller's model was investigated in detail by Giona and coworkers [94,95], and it was shown that the model is able to simulate the highly nonlinear adsorption behavior of the binary data provided by Talu and Zwiebel [32].

V. MICROPOROUS STRUCTURE AND ADSORPTION EQUILIBRIA ON ACTIVATED CARBON

A. The Structure of Activated Carbon

Activated carbon is produced from various carbonization and activation processes. Its structure is known to be very complicated [96–98]. Microscopically, it is generally composed of amorphous carbons and graphitic crystals. In the adsorption process, the former contain void space (macropores and mesopores) for intercrystalline transport, while the latter provide a microporous network in which most of the adsorption capacity resides. The basic structure of the graphite crystal is graphite-like aromatic micro-crystals that accommodate slit-shaped micropores between graphite layers (pore walls). The width of the micropores is of molecular dimension so that the interaction between adsorbate molecules and both sides of the pore walls is enhanced, resulting in strong adsorption potential [99,100]. Under a certain pore size, the adsorbate–pore interaction is highly sensitive to variation in pore size; i.e., a small variation in pore size can result in a significant change in the

potential energy of interaction. When the system consists of adsorbates with different molecular properties, the difference in interaction energies will lead to enhancement of one adsorbate relative to the others (selectivity). In physical adsorption, where the dispersive interaction is predominant over the other interactions, the micropore size distribution (MPSD) is the main source of surface heterogeneity, which dictates the overall adsorption equilibria of the system.

The slit shape of the micropore structure of activated carbon is supported by several experimental observations: (1) molecular sieving properties; (2) high resolution microscopy [101]; and (3) neutron diffraction and small-angle neutron scattering [102]. The most popular mathematical representation of the micropore configuration in activated carbon is the slit pore contained in parallel graphite layers of infinite extent. There are also other mathematical descriptions of the pore configuration in the literature; for example, Bojan and Steele [103,104] considered a pore with triangular section, and Segarra and Giant [105] used circular graphite platelets that are randomly oriented to represent the structure of activated carbon.

Other sources of surface heterogeneity also exist in activated carbon. These include functional groups and defects on the pore walls, the irregularity of the shape of micropores, pore networking and blocking, and electrostatic interaction, among others. These effects are too complicated to be quantified and treated individually at present. A useful approach is to combine these effects in the "equivalent" MPSD, in which the interaction is taken as purely dispersive.

The role of surface heterogeneity in adsorption equilibria is well recognized nowadays. The macroscopic equilibria properties such as the amount adsorbed, selectivity, and heat of adsorption of each species reflect in general the aggregate behavior of interaction between adsorbates and, more important, the interaction between adsorbate and microporous network. Thus to correctly represent the multicomponent adsorption equilibria on activated carbon, the surface heterogeneity has to be properly addressed.

In this section, we briefly introduce a mathematical configuration of a model micropore, the potential energy of adsorbate–adsorbate interaction, and the adsorption potential energy in micropores of different configurations. Then we demonstrate two major applications based on the concept of adsorption potential energy in slit-shaped micropores: (1) characterizing the pore size distribution (PSD) of activated carbon and (2) predicting the adsorption equilibria.

B. Potential Energy and Slit Pore Configuration

In physical adsorption, the main interaction between an adsorbate molecule and a carbon atom on the graphite layer is the dispersive force. This potential energy is adequately described by the Lennard-Jones 12-6 potential theory:

$$\phi(z) = 4\varepsilon_{sk}^* \left[\left(\frac{\sigma_{sk}}{z} \right)^{12} - \left(\frac{\sigma_{sk}}{z} \right)^6 \right] \quad (70a)$$

where z is the distance between the carbon atom and the adsorbate molecule k , and ε_{sk} and σ_{sk} are the cross LJ parameters, which are calculated using a geometric mean and arithmetic mean (Lorentz–Berthelot rule), respectively,

$$\varepsilon_{sk} = (\varepsilon_{ss} \times \varepsilon_{kk})^{1/2} \quad (70b)$$

$$\sigma_{sk} = \frac{\sigma_{ss} + \sigma_{kk}}{2} \quad (70c)$$

The interaction potential energy between an adsorbate molecule and all the carbon atoms on the pore wall is then the summation of all the pairwise interaction energies. This process of summation can be replaced by an integration operation if the shortest distance between the adsorbate molecule and the pore wall is greater than the distance between carbon-carbon centers. Three configurations are commonly used to describe the slit-shaped micropores in activated carbon: (1) The pore walls are two parallel lattice layers of infinite extent; (2) the pore walls are two parallel semi-infinite slabs; (3) the pore walls are a combination of many parallel lattice layers separated by a distance A . The overall potential energy of molecules confined in micropores with the above pore configurations is termed 10-4, 9-3 [99], and 10-4-3 potential energy [100], respectively. The equations describing these potential energies are described below.

1. The 10-4 Potential

$$\varphi(r, z) = \frac{5}{3} \varepsilon_{sk}^* \left[\frac{2}{5} \left(\frac{\sigma_{sk}}{r-z} \right)^{10} + \frac{2}{5} \left(\frac{\sigma_{sk}}{r+z} \right)^{10} - \left(\frac{\sigma_{sk}}{r+z} \right)^4 - \left(\frac{\sigma_{sk}}{r-z} \right)^4 \right] \quad (71a)$$

where

$$\varepsilon_{sk}^* = \frac{6}{5} \pi n_s \varepsilon_{sk} \sigma_{sk}^2 \quad (71b)$$

is the minimum interaction energy between the adsorbate molecule and a single lattice layer, z is the distance between the adsorbate and the central plane of the pore, and n_s is the number density of carbon centers per unit area of graphite surface (38.2 nm^{-2}).

2. The 9-3 Potential

$$\phi(r, z) = \frac{3}{\sqrt{10}} \varepsilon_{sk}^* \left[\frac{2}{5} \left(\frac{\sigma_{sk}}{r+z} \right)^9 + \frac{2}{15} \left(\frac{\sigma_{sk}}{r-z} \right)^9 - \left(\frac{\sigma_{sk}}{r+z} \right)^3 - \left(\frac{\sigma_{sk}}{r-z} \right)^3 \right] \quad (72a)$$

where

$$\varepsilon_{sk}^* = \frac{2\sqrt{10}}{9} \pi n'_s \varepsilon_{sk} \sigma_{sk}^3 \quad (72b)$$

is the interactive energy minimum between an adsorbate molecule and a single slab (pore wall) and n'_s is the number of carbon molecules per unit volume of the slab.

3. The 10-4-3 Potential

$$\varphi(r, z) = \frac{5}{3} \varepsilon_{sk}^* \left\{ \frac{2}{5} \left[\left(\frac{\sigma_{sk}}{r+z} \right)^{10} + \left(\frac{\sigma_{sk}}{r-z} \right)^{10} \right] - \left[\left(\frac{\sigma_{sk}}{r+z} \right)^4 + \left(\frac{\sigma_{sk}}{r-z} \right)^4 \right] - \left[\left(\frac{\sigma_{sk}^4}{3\Delta(0.61\Delta + r+z)^3} \right) + \left(\frac{\sigma_{sk}^4}{3\Delta(0.61\Delta + r-z)^3} \right) \right] \right\} \quad (73a)$$

where

$$\varepsilon_{sk}^* = \frac{6}{5} \pi \rho_s \varepsilon_{sk} \sigma_{sk}^2 \Delta \quad (73b)$$

is the interaction energy minimum between an adsorbate molecule and a single lattice layer, and ρ_s is the number density of carbon molecules per unit volume. The values of Δ and ρ_s are taken as 0.335 (nm) and 114 (nm⁻³), respectively [100].

These LJ potentials are temperature-independent, and among them the 10-4-3 potential is the most commonly used in the literature because its pore configuration is the closest to the real pore structure of activated carbon. The 10-4 potential was also found to be superior to the 9-3 potential in describing the microporous structure of activated carbon [56].

C. Characterizing the PSD of Activated Carbon

Characterizing the microporous structure of activated carbon is an important and yet very challenging issue. Until now there has been no method that was accepted as a general tool even though many methods have been proposed in the literature. Direct methods such as X-ray scattering, small-angle neutron scattering, and nuclear magnetic resonance have the disadvantages of being of high cost and doubtful interpretation. Classical adsorption methods such as MP [106], molecular probe, water adsorption, and TVFM [52,55] are based on phenomenological assumptions such as subcritical adsorbate homogeneity and incompressibility or volume filling of pores and Gaussian distribution (TVFM). The inhomogeneity of the adsorbed phase in smaller pores is not accounted for by these methods. More specific reviews regarding the above methods for characterizing the PSD are available in Refs. 107 and 108.

The LJ potential theory in the last section provides us with a useful functional link between adsorption potential energy and pore size, thus laying a foundation for characterizing the PSD of activated carbon [109] and for studying the molecular assembly formulation of simple gaseous molecules in graphitic micropores [110]. Methods based on LJ potential theory are available for describing the PSD of the activated carbon. Three methods are briefly discussed here.

1. Horvath–Kawazoe Method

The Horvath–Kawazoe (H-K) equation was developed by Horvath and Kawazoe [111] to characterize the microporous structure of an adsorbent. They used the 10-4 potential to describe the potential energy of adsorbate molecules in a slit pore and

assumed that the average potential energy is equal to the free energy change upon adsorption, i.e.,

$$RT \ln\left(\frac{P}{P_0}\right) = \frac{\int_{\sigma_{sk}}^{H-\sigma_{sk}} \varphi(z) dz}{\int_{\sigma_{sk}}^{H-\sigma_{sk}} dz}$$

$$= N_{AV} \frac{N_a A_a + N_A A_A}{\sigma_0^4 (H - 2\sigma_{sk})} \left[\frac{\sigma_0^4}{3(H - \sigma_{sk})^3} - \frac{\sigma_0^{10}}{9(H - \sigma_{sk})^9} - \frac{\sigma_0^4}{3\sigma_{sk}^3} + \frac{\sigma_0^4}{9\sigma_{sk}^9} \right] \quad (74)$$

where

$$\sigma_0 = (2/5)^{1/6} \sigma_{sk}$$

$$H = \text{pore width } (2r)$$

$$N_{AV} = \text{Avogadro's number}$$

$$N_a, N_A = \text{density per unit area}$$

$$A_a, A_A = \text{dispersion constants}$$

From the amount adsorbed at P , Eq. (74) yields the pore width H ; thus the pore volume at this pore size can be obtained.

The implicit assumption behind the H-K equation is that the adsorbed phase is a two-dimensional ideal gas, i.e., Henry's law region adsorption. Cheng and Yang [112] modified the H-K equation by including the nonlinearity of the isotherm. The modified H-K equation is

$$RT \ln\left(\frac{P}{P_0}\right) + \left[RT - \frac{RT}{\theta} \ln\left(\frac{1}{1-\theta}\right) \right]$$

$$= N_{AV} \frac{N_a A_a + N_A A_A}{\sigma_0^4 (H - 2\sigma_{sk})} \left[\frac{\sigma_0^4}{3(H - \sigma_{sk})^3} - \frac{\sigma_0^{10}}{9(H - \sigma_{sk})^9} - \frac{\sigma_0^4}{3\sigma_{sk}^3} + \frac{\sigma_0^4}{9\sigma_{sk}^9} \right] \quad (75)$$

where θ is the filling fraction. The modified H-K equation generally results in sharpening the PSD and shifting the peak position to smaller pore size.

2. Statistical Mechanical Methods

Statistical mechanics [113] provides the means of relating physical models for adsorption in individual pores, expressed in terms of solid–fluid or fluid–fluid interaction, to a single pore isotherm. Since it simulates the real adsorption process in micropores, statistical mechanics gives a more accurate description of the PSD of adsorbents and has been used widely in characterizing the PSD of activated carbon. Two methods are often seen in the current literature: (1) the approximate theory, represented by the density function theory (DFT) and (2) the full Monte Carlo simulation, represented by the grand canonical Monte Carlo (GCMC) or molecular dynamics (MD). The single pore isotherm is related to the overall adsorption equilibria according to the equation

$$n(P) = \int_{H_{\min}}^{H_{\max}} f(H) \rho(P, H) dH \quad (76)$$

where $n(P)$ is the number of moles adsorbed at pressure P , $f(H)$ is the differential volume distribution of pore width, $\rho(P, H)$ is the local molar density of adsorbate at P (the single pore isotherm), and H_{\min} and H_{\max} are the lower and upper limits, respectively, of the pore size range. In DFT, $\rho(P, H)$ is determined by the local mean field density functional theory, whereas in GCMC, $\rho(P, H)$ is obtained by taking the ensemble average. In both methods, the PSD is assumed to be the sole source of surface heterogeneity, the adsorbate–adsorbate interaction is described by the 12-6 potential, and the adsorbate–adsorbent interaction is normally described by the 10-4-3 potential. By inverting Eq. (76) with respect to experimental isotherm data, the PSD of the adsorbent can be derived.

(a) *DFT Method* The DFT is based on a mean field approximation of fluid–fluid interaction. It provides a good description of a simple fluid (hard sphere) confined in geometrically simple space and also has the advantage of being less computationally demanding than the full Monte Carlo simulation. Seaton et al. [114] calculated the single pore isotherm for nitrogen adsorption at 77 K and applied the results to obtain the micropore as well as the mesopore size distribution of the activated carbon. Lastoskie et al. [115] improved the DFT method and proposed the nonlocal density function theory (NLDF). However, the DFT method also has the problem of being inexact and cannot account for the steric effect of the adsorbate molecule.

The consistency test of DFT was carried out by Jing et al. [116] and more recently by Quirke et al. [117]. Quirke et al. used the PSD obtained from nitrogen adsorption data to predict the adsorption isotherm of methane at normal temperature. As a result, the methane isotherm is considerably overpredicted. This is attributed to several reasons, two of which are that (1) at higher temperatures other nondispersive molecular interactions are weakened and (2) the methane has no dipole or quadrupole, which may enhance the adsorbate–adsorbent interaction for N_2 adsorption.

(b) *GCMC Method.* The GCMC method can be conveniently applied to adsorption processes because its independent thermodynamic variables are temperature, system volume, and chemical potential (which is related to the bulk pressure via an equation of state). The adsorption isotherm for a given pore can be obtained by evaluating the ensemble average of the number of adsorbate molecules whose chemical potential equals that of the bulk phase at a given temperature and pressure [118]. The application of the GCMC method to characterize the PSD of adsorbent (especially activated carbon) has gained considerable popularity. Gusev and O'Brien [119] used this method to characterize the PSD of BPL activated carbon with a methane isotherm at supercritical temperature (308 K). This PSD is demonstrated to be capable of predicting the adsorption isotherm of methane at two other temperatures (333 and 373 K) with good accuracy. Later the PSD obtained from methane adsorption was employed to predict the adsorption of ethane on the same carbon [120]. Quantitative agreement was found between simulation results and experimental data if the ethane molecule is considered as the two-site LJ model. This is a strong indication of the consistency of the PSD thus obtained.

Lopez-Ramon et al. [121] applied a more rigorous method to characterize the PSD and pore connectivity (represented by the mean coordination number of the pore network) of the activated carbon using the GCMC technique. Their study was based on the idea that molecules of different sizes have access to different pore size ranges. By combining and analyzing the PSD information obtained for each species, the overall PSD for the adsorbent can be better represented. Three species were used in their studies: CH_4 , CF_4 , and SF_6 , which are all nonpolar and approximately spherical but are different in molecular diameter. By analyzing the size difference between the molecules, the obtained PSD is then represented by the nonoverlapping contribution of the PSD for each species. In their study, the temperature was found to have some effect on the PSD derived for each species, especially those for CF_4 and SF_6 .

It was also found in their studies that to characterize the PSD of the activated carbon at supercritical temperature, considerably higher pressure is needed to obtain information on micropores of larger sizes (near 2 nm).

D. Prediction of Adsorption Equilibria

With the adsorbate–pore interaction potentials defined earlier, some researchers attempted to predict the adsorption isotherm for some simple adsorbates based on the known thermodynamic properties of the adsorbate and macroscopic information of the adsorbent. So far only limited success has been achieved.

Fischer et al. [122] proposed a model to predict the adsorption isotherm of krypton in porous material at supercritical temperature. In their study, a model pore of infinite length is formed by concentric cylindrical surfaces on which the centers of solid atoms are located. The interaction between an adsorbate and an individual center on the pore wall is described by the LJ 12-6 theory, and the overall potential is the integral of this interaction over the entire pore surface. With thermodynamic relations, Fischer et al. obtained the functional dependence of the saturation adsorption excess and the Henry's law constant on the pore structure. The isotherm was then produced by the interpolation between Henry's law range and saturation range. They tested their theory with the adsorption of krypton on activated carbon. It was shown that, with information on the surface area of the adsorbent and thermodynamic properties of the adsorbate, their model gives more than qualitative agreement with experimental data. If a few experimental data such as the Henry's law constant at one temperature are available, the isotherms for all temperatures and pressures can be predicted with good quality.

Forbert and Schlunder [123] proposed a model that is able to predict the adsorption equilibria of arbitrary organic vapors on activated carbon at subcritical temperature by using information of a reference isotherm or a characteristic curve for the same adsorbent. The model is based on the idea that for organic vapor on carbonaceous adsorbents, the molar binding energy is a function of the volume of the adsorbed phase only while the characteristic curve can be regarded as an integral volumetric distribution of the binding energy. The molar binding energy between adsorbate and carbon surface is defined as the difference between heat of adsorption and enthalpy of evaporation:

$$\Delta h_b = \Delta H_{\text{ads}} - \Delta H_{\text{evap}} \quad (77)$$

In the case of a temperature-independent characteristic curve, the following equation is valid:

$$\Delta h_b = A\{v\} \quad (78a)$$

where v is the volume adsorbed and A is the adsorption potential

$$A = -RT \ln(f/f^*) \quad (78b)$$

So for organic vapors on carbonaceous adsorbents, Δh_b is a function of the volume of the adsorbed phase only. Forbert and Schlunder then made the key assumption that the interaction potential in the middle of the pore is crucial for the pore filling and derived this interaction potential on the basis of the 12-6 potential theory as

$$\begin{aligned} \Delta \Phi_{\text{ads}} = & 2 \left[-c_1 p_1 \left(\frac{H}{2} \right)^{-q_1} - c_2 p_2 \left(\frac{H}{2} \right)^{-q_2} + c_3 \left(\frac{H}{2} \right)^{-10} \right] \\ & - 4\pi D_A \left[-\frac{c_A}{12} \left(\frac{H - d_a + d_A}{2} \right)^{-3} - \frac{c'_A}{30} \left(\frac{H - d_a + d_A}{2} \right)^{-5} + \frac{c''_A}{90} \left(\frac{H - d_a + d_A}{2} \right)^{-7} \right] \end{aligned} \quad (79)$$

where

$d_A = 2 \times [2.277(\alpha_A - 2.78 \times 10^{-31} \text{ m}^3)]^{1/3}$ is the adsorbate diameter
 $d_a = 0.35 \text{ nm}$, the distance between layers of activated carbon
 p_i, c_i , and q_i can be calculated from known thermodynamics parameters
 H is the pore width

Following their assumption, $\Delta \Phi_{\text{ads}}$ is related to Δh_b by

$$\Delta h_b = -k_{\text{AV}} \Delta \Phi_{\text{ads}}\{H\} \quad (80)$$

Thus for a given adsorbate, the adsorption potential A is directly related to micropore size. However, due to its assumptions this model is valid only at subcritical temperature for the adsorption of vapor adsorbate with spherical geometry.

VI MICROPOROUS STRUCTURE AND ADSORPTION EQUILIBRIA—THE MICROPORE SIZE DISTRIBUTION MODEL

Many researchers [124–128] recognized the role of the micropore size distribution (MPSD) in the study of adsorption equilibria on activated carbon. The MPSD model [126] is based on the idea that adsorption energy heterogeneity is induced by structural heterogeneity, which can be characterized by the size distribution of the slit-shaped micropores. The MPSD is an intrinsic property of activated carbon, and in physical adsorption it dictates the adsorption equilibria through the dispersive interaction between adsorbate and the microporous network of activated carbon.

A. MPSD Model for a Pure Component System

If the MPSD of the activated carbon is represented by a distribution function $f(r)$ with $f(r) dr$ being the fraction of micropores having a half-width between r and $r + dr$, and the local isotherm is represented by $\theta(r)$, the overall adsorption equilibria of a species k at a pressure P and temperature T can be expressed as the integral of the local isotherm over the accessible micropore range:

$$\langle \theta_k \rangle = \int_{a_k}^{r_{\max}} \theta_k(P, r) f(r) dr \quad (81)$$

where r_{\max} is the maximum micropore half-width and a_k is the minimum pore half-width below which that species cannot penetrate.

Equation (81) suggests that the surface heterogeneity is induced solely by the MPSD. This approach is more fundamentally sound than the approach of energy distribution in Eq. (55), since the distribution of energy sites, $F(e)$, may not follow any particular type of distribution function. On the other hand, the microporous structure of the activated carbon results from the random processes of carbonization and activation and therefore may possibly be characterized by some distribution functions. Hence, assuming a function $f(r)$ is more reasonable than arbitrarily imposing a function $F(e)$. In the MPSD approach, $F(e)$ can be derived from $f(r)$ according to the relationship

$$F(E) dE = f(r) dr \quad (82)$$

For a given set of adsorption equilibrium data, Eq. (81) can be used (inverted) to derive the MPSD if a local isotherm is specified. But such an inverse has been known to be an ill-posed problem, and presents some difficulties in application [38]. For example, for a given adsorbate and a given local adsorption isotherm, one would find many different distribution functions that can yield the same overall adsorption capacity (within experimental error). Furthermore, if the isotherm equation, Eq. (81), is applied individually for each adsorbate, we might obtain very different MPSDs for the same activated carbon! This violates the basic premise that the MPSD is an intrinsic property of the given carbon, independent of what adsorbate is used. Realizing this inconsistency problem often seen in the literature, we propose a different approach here, applying Eq. (81) to multiple temperature data of many adsorbates simultaneously while constraining the MPSD as an intrinsic characteristic of the adsorbent. To achieve this, the functional dependence of interaction energy on micropore size has to be defined first.

1. Adsorption Potential and Slit Pore Configuration

For the physical adsorption of a nonpolar adsorbate on activated carbon, the adsorbate–adsorbent interaction is much stronger than the adsorbate–adsorbate interaction. This interaction potential is represented by Steele's 10-4-3 potential, and the adsorbate–adsorbent interaction energy can be taken as the negative of the potential energy minimum inside the slit-shaped micropore. This concept was first proposed by Jagiello and Schwarz [124,125] to characterize the MPSD of activated carbon, and later it was refined and found other applications [127,128]. Although this method does not take into account the adsorbate–adsorbate interaction, which

may be important at high surface coverage. it catches the essential feature of the adsorbate–pore interaction. There is also some justification for using it in the high pressure range; for example, Lopez-Ramon et al. [121] demonstrated that when the model pore isotherms obtained from Monte Carlo simulation are fitted to the Hill-de Boer isotherm, the variation of adsorption energy versus micropore size closely resembles the variation of the 10-4-3 potential minimum with pore size. Thus solving Eqs. (73) for the potential minimum, the functional dependence of interaction energy on pore size can be obtained, and for a given MPSD the corresponding energy distribution can be derived from Eq. (82).

2. The Model Equation

The local adsorption isotherm is assumed to take the form of the Langmuir-type equation

$$\theta(r, T, P) = \frac{Pb(r)}{1 + Pb(r)} \quad (83)$$

where $b(r)$ is the local adsorption affinity, which is assumed to take the form

$$b(r) = b_{\infty} \exp\left[\frac{E(r)}{RT}\right] \quad (84a)$$

If the adsorbate–adsorbate interaction is taken into account, $b(r)$ can take the form

$$b(r) = b_{\infty} \exp\left[\frac{E(r) + nu\theta}{RT}\right] \quad (84b)$$

where θ is the surface fractional coverage of the adsorbate. u is the adsorbate–adsorbate interaction energy, and n is the number of neighboring adsorbed molecules. With Eq. (84b), the local adsorption isotherm is known as the Fowler–Guggenheim equation. For the adsorption of hydrocarbon gases or vapors on activated carbon, Eq. (84a) is found to be adequate to describe the local adsorption affinity [126].

In physical adsorption, the adsorption affinity at the infinite temperature level (b_{∞}) of different species are correlated according to

$$b_{\infty} = \beta/\sqrt{MT} \quad (85)$$

This equation is derived by assuming the collision of gaseous molecules toward the pore mouth of micropores, and such a collision rate is known from the kinetic theory of gases to be inversely proportional to the square root of the molecular weight and to the square root of temperature. The affinity parameter β in Eq. (85) is specific only to the solid adsorbent. The theoretical value of β was reported as $4.26 \times 10^4 (\text{K} \cdot \text{g/mol})^{1/2}/\text{kPa}$ [129].

The maximum adsorption capacity of each species, $c_{\mu s}$, takes the temperature-dependent form

$$C_{\mu s}(T) = C_{\mu s}^0 \exp[\delta(T_0 - T)] \quad (86)$$

where $C_{\mu s}^0$ is the adsorption capacity at some reference temperature T_0 , and δ is the thermal expansion coefficient.

The MPSD is assumed to follow some distribution function. A nonnegative gamma distribution is used here:

$$f(r) = \frac{q^{\gamma+1} r^{\gamma} e^{-qr}}{\Gamma(\gamma+1)} \quad (87)$$

where q and γ are the two distribution parameters.

With all the parameters defined, the overall adsorption isotherm of Eq. (81) can be expressed explicitly in terms of the MPSD for adsorbate k as

$$\theta(k, T, P) = \int_{r_{\min}}^{r_{\max}} \frac{P b_k(r)}{1 + P b_k(r)} \left(\frac{q^{\gamma+1} r^{\gamma} e^{-qr}}{\Gamma(\gamma+1)} \right) dr \quad (88a)$$

where

$$b_k(r) = \frac{\beta}{\sqrt{M_k T}} \exp \left[\frac{E_k(r)}{RT} \right] \quad (88b)$$

The parameters r_{\min} and r_{\max} are the lower and upper limits, respectively, for the micropore size range. The lower limit r_{\min} is for a pore that has the same adsorption potential energy as that of a single lattice layer or for a pore that has zero potential energy. The volume of pores having sizes between these two values of r_{\min} is very small, and hence either value of r_{\min} will suffice. The upper limit r_{\max} is cut off at $3.5\sigma_{sk}$ for convenience, since the adsorption potential energy in pores with half-widths larger than this value is effectively zero,

The model equations have two distinct groups of parameters to be optimized: (1) the parameters characterizing the carbon structure (q, γ, β) and (2) the isotherm parameters ($C_{\mu s, i}, \varepsilon_{sk}^*$). By simultaneously optimizing the multiple temperature data of many adsorbates measured on the same activated carbon, it is possible to derive the results for the micropore size distribution as well as relevant adsorption parameters for all adsorbates.

B. MPSD Model for a Multicomponent System

The multicomponent adsorption equilibrium on a heterogeneous surface is more complicated than that of a pure component system. As discussed in previous sections, two fundamental issues need to be addressed properly: (1) the size difference between various adsorbate molecules and (2) the local interaction energy (or matching energy) between various adsorbate molecules. Issue 1 suggests that there possibly exists a certain pore range that adsorbates with larger molecular size cannot penetrate (size exclusion) but that is accessible to adsorbates of smaller sizes, while issue 2 requires a relationship between interaction energy of each adsorbate and the pore size. These two issues are well accounted for by the MPSD approach.

The MPSD model can be conveniently extended to describe the adsorption equilibria of a gas mixture with N components. The generalized MPSD model simply takes the extended Langmuir equation as the local isotherm while using the MPSD information obtained from pure component data:

$$\theta(k, T, P) = \int_{r_{\min,k}}^{r_{\max,k}} \frac{P_k b_k(r)}{1 + \sum_{j=1}^M P_j b_j(r)} \left(\frac{q^{\gamma+1} r^{\gamma} e^{-qr}}{\Gamma(\gamma+1)} \right) dr, \quad k = 1, 2, \dots, N \quad (89)$$

This model has two distinguishing features in addressing the two issues:

1. The equilibrium interaction between different adsorbates is confined within the same pore where they are accommodated; i.e., adsorbates inaccessible to a pore do not participate in the competition and hence are not accounted for in the local extended Langmuir equation for that pore ($M \leq N$). This effect of size exclusion is reflected in the lower integration limit.
2. The matching energies between different species are related to their own interaction strength with the local micropores. This matching scheme, which is termed the adsorbate–pore interaction scheme, introduces the physical condition for determining the matching energies between different species on a heterogeneous surface.

In comparison, the traditional cumulative energy matching scheme [Eq. (17)] lacks a fundamental basis.

The size exclusion and the energy matching for the binary pair ethane–propane is shown graphically in Fig. 2 as an example [126]. It is seen that for pores of half-width between 3.21 and 3.38 Å, only ethane is allowed whereas propane is excluded. Both ethane and propane can adsorb in pores of half-width larger than 3.38 Å. What is interesting is that in pores whose half-width is between 3.38 and 3.55 Å,

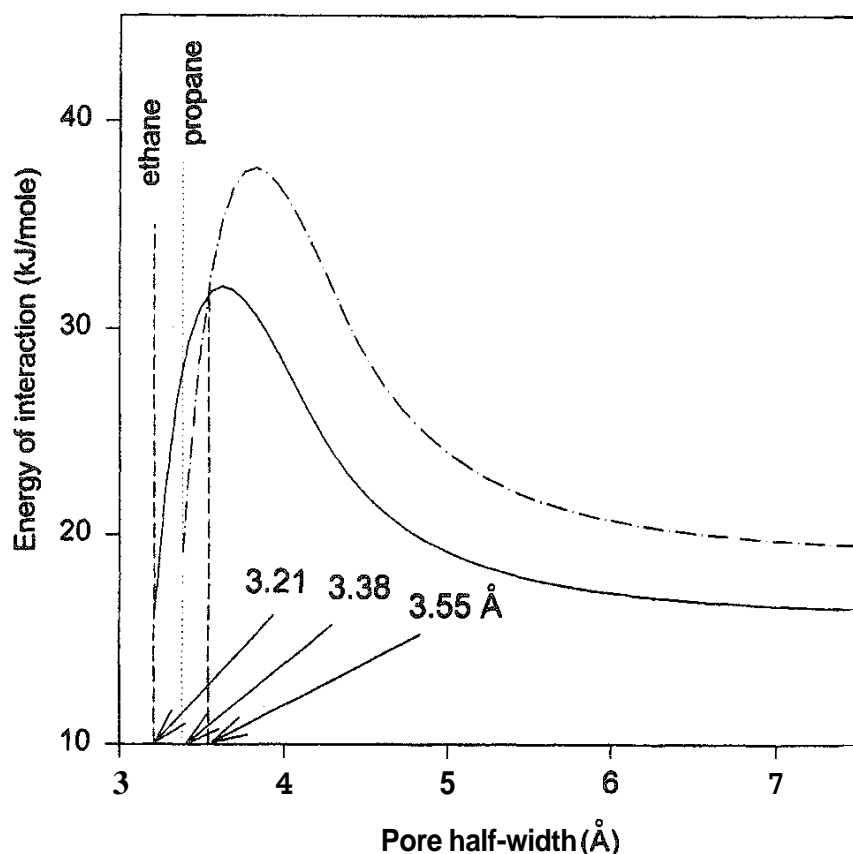


FIG. 2 Plots of energy of interaction of ethane and propane versus pore half-width

ethane actually has a higher affinity than propane, and it is only in pores whose half-width is greater than 3.55 Å that propane will have a higher adsorption affinity than ethane. This means that the separation factor of the binary system can change from pore to pore. This simple example demonstrates that in micropores of different sizes the local interaction energy is a function of not only the size of the micropore but also the size of the adsorbate molecule.

C. Comparison with Experimental Data— Pure Component Equilibria

In this section we compare the MPSD model with pure component adsorption data, that were measured for 11 species on two activated carbons, Ajax carbon [78] and Nuxit carbon [22]. The molecular properties of adsorbates and experimental temperatures for pure component system are listed in Tables 1 and 2 for Ajax activated carbon and Nuxit activated carbon, respectively.

In the MPSD model, the selection of the LJ diameter of the adsorbate is very important, since the LJ diameter dictates the accessibility of that species in the micropore network of the adsorbent. For inolecules having major and minor dimensions, we propose to use the minor dimension, as molecules tend to diffuse into micropores along their smallest configuration [130].

1. Ajax Activated Carbon

The MPSD model with the local Langmuir equation and 10-4-3 potential is optimized with respect to the isotherm data of eight species measured on Ajax activated carbon (Table 1) at at least three different temperatures for each species. The reference temperature for the adsorption capacity, T_0 , is chosen as 273 K. The model fitting (lines) and experimental data (symbols) for ethane and propane are plotted in Fig. 3. The fit of other adsorbates (methane, *n*-butane benzene, toluene,

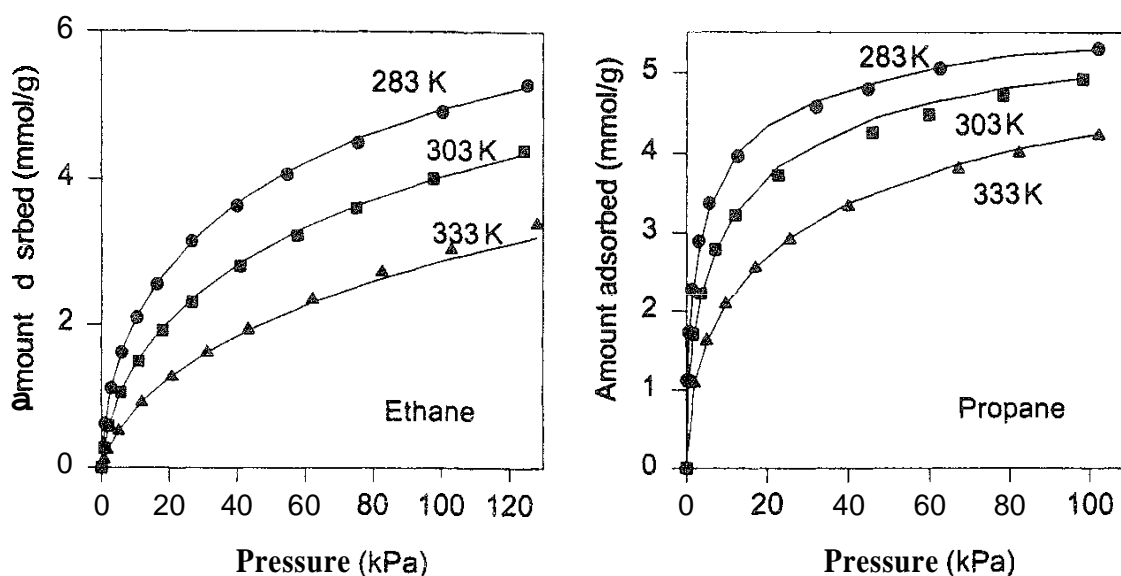


FIG. 3 Plots of MPSD model fitting and experimental data of ethane and propane on Ajax activated carbon. (From Ref. 12b.)

TABLE 1 Adsorbates and Adsorption Temperatures for Ajax Activated Carbon

| Property | CO ₂ | SO ₂ | Methane | Ethane | Propane | Butane | Benzene | Toluene |
|--------------------------|------------------|------------------|-----------------------|------------------|------------------|-----------------------|------------------|------------------|
| σ_k (Å) | 3.3 | 3.6 | 3.8 | 3.9 | 4.3 | 4.3 | 3.7 | 3.8 |
| ε/κ (K) | 195.2 | 335.4 | 148.6 | 300.0 | 237.1 | 331.4 | 412.3 | 457.1 |
| T (K) | 258, 273, 303 | 298, 323, 373 | 258, 273, 283, 303 | 283, 303, 333 | 283, 303, 333 | 283, 303, 333, 473 | 303, 333, 363 | 303, 363, 473 |

Source: Ref. 131.

TABLE 2 Adsorbates and Adsorption Temperatures for Nuxit Activated Carbon

| Property | CO ₂ | Methane | Acetylene | Ethylene | Ethane | Propylene | Propane | Butane |
|--------------------------|-----------------------|-----------------------|-----------------------|-----------------------|-----------------------|-----------------------|-----------------------|-----------------------|
| σ_k (Å) | 3.3 | 3.8 | 3.3 | 3.9 | 3.9 | 4.5 | 4.3 | 4.3 |
| ε/κ (K) | 195.2 | 148.6 | 231.8 | 224.7 | 300.0 | 248.9 | 237.1 | 331.4 |
| T (K) | 293, 313, 333, 363 | 293, 313, 333, 363 | 293, 313, 333, 363 | 293, 313, 333, 363 | 293, 313, 333, 363 | 293, 313, 333, 363 | 293, 313, 333, 363 | 293, 313, 333, 363 |

Source: Ref. 131

TABLE 3 Optimized Isotherm Parameters for Each Species on Ajax Carbon

| Property | Methane | Ethane | Propane | Butane | Benzene | Toluene | CO ₂ | SO? |
|-------------------------------|-----------------------|--------|---------|--------|---------|---------|-----------------|-------|
| C_{us}^0 (mmol/g) | 7 491 | 8 018 | 6 004 | 4 863 | 4 845 | 4 393 | 12 11 | 14 91 |
| ε_{sf}^* (kJ/mol) | 10 47 | 14 39 | 16 70 | 20 18 | 29 49 | 30 68 | 13 40 | 16 92 |
| δ (K ⁻¹) | 1.17×10^{-5} | | | | | | | |

Source Ref 121

carbon dioxide, and sulfur dioxide) is also very good [121]. This is regarded as excellent in the light of the fitting done on all isotherm data simultaneously (a total of 27 curves). The optimized structure parameters are $q = 19.59 \text{ \AA}^{-1}$, $\gamma = 88.69$, and $\beta = 1.04 \times 10^{-4} (\text{K} \cdot \text{g/mol})^{1/2} / \text{kPa}$. The optimized isotherm parameters are listed in Table 3.

The MPSDs derived for Ajax-activated carbon are shown in Fig. 4, with the average micropore width $\approx 9.2 \text{ \AA}$. This average value falls within the range of micropore size determined by experimental methods for many samples of activated carbon [132]. The affinity parameter for Ajax activated carbon, β , is approximately one-fourth of the theoretical value of $4.26 \times 10^{-4} (\text{K} \cdot \text{g/mol})^{1/2} / \text{kPa}$ [124].

Turning to the isotherm parameters optimally obtained, we found that

1. α (the thermal expansion coefficient) is very small, suggesting that the saturation capacity is not affected by the change of temperature, at least within the range studied.
2. ε_{sk}^* (adsorbate–lattice layer interaction minimum) increases with the carbon number for a given class of adsorbate family (ethane, propane, butane). Aromatics have higher values of ε_{sk}^* than those of paraffins, with toluene being a more strongly adsorbing species than benzene.
3. ε_{sk}^* of each species is very close to its theoretical value calculated by Eq. (73b).
4. The values of $C_{\mu s}^0$ (adsorption capacity at 273 K) for CO_2 and SO_2 are a little bit higher than those of the other species.

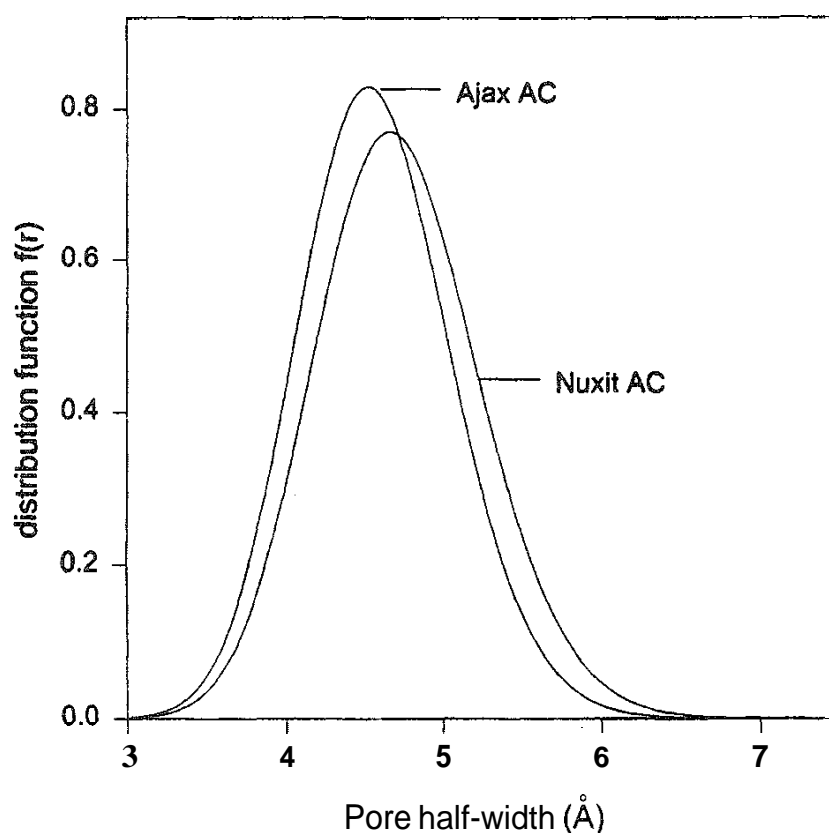


FIG. 4 Plots of the derived micropore size distribution for Ajax activated carbon and Nuxit activated carbon. (From Ref. 126.)

Figure 5 shows plots of the optimized interaction energy ε_{sk}^* obtained from the fitting versus the theoretical interaction energy calculated from Eq. (73b) for the 10-4-3 potential. The theoretical parameters are calculated using the molecular properties given by Reid et al. [133] and Steele [100]. It is noted that the optimal and theoretical values for ε_{sk}^* are very comparable to each other. On the other hand, such good agreement is not observed if the 10-4 or 9-3 potential is employed in the model equation (not shown in the figure). and this might suggest that the 10-4-3 potential is appropriate to describe the dispersive interaction in activated carbon.

Although the model fittings for SO_2 and CO_2 are good, we must be cautious about the applicability of the MPSD model to these polar adsorbates, because the dispersive force is not enough to describe the interaction between polar adsorbates and carbon surface.

2. Nuxit Activated Carbon

Next, the equilibrium data on Nuxit activated carbon are used to test the model. The data are collected for eight species at four temperatures (Table 2). To show the predictability of the model, we choose the data at three temperatures (283, 303, and 333 K) for optimization and then use the results to predict the remaining data at 363 K. Like the case of Ajax activated carbon, the fit between the model and all the

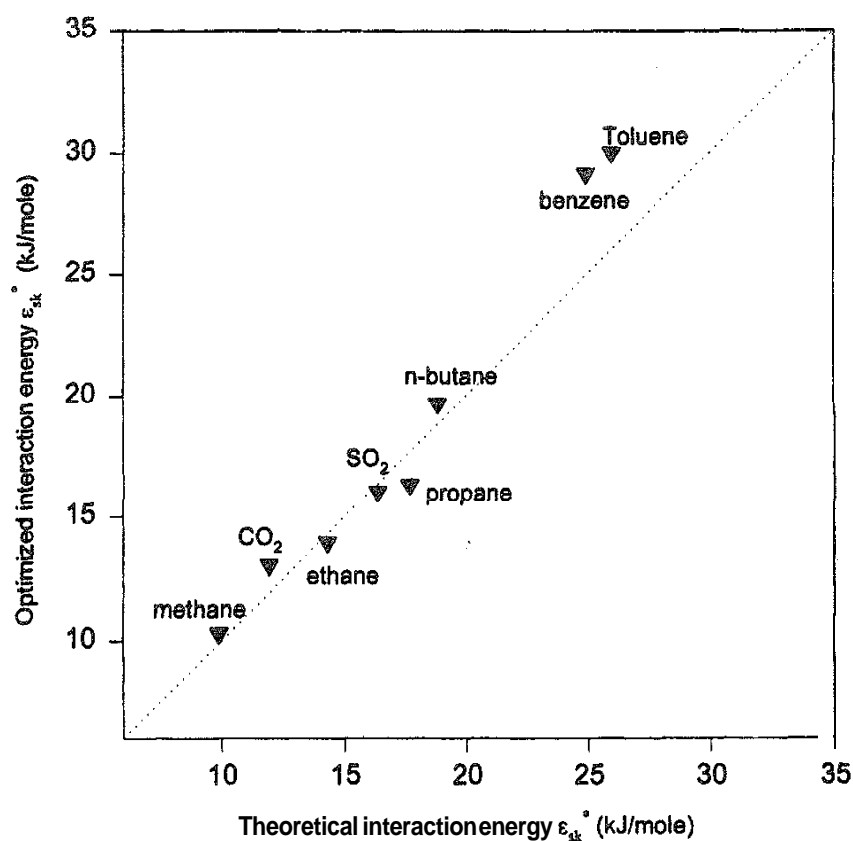


FIG. 5 Plot of the optimized interaction energy ε_{sk}^* versus the theoretical interaction energy calculated from Eq. (73b).

data is excellent [126]. The optimized structural parameters are $q = 17.93 \text{ \AA}^{-1}$, $\gamma = 81.11$, and $\beta = 3.84 \times 10^{-5} (\text{K} \cdot \text{g/mol})^{1/2}/\text{kPa}$. The optimized isotherm parameters are tabulated in Table 4.

As for Ajax carbon, the value of 5 is very small. The affinity parameter β for Nuxit carbon is a bit smaller than that of Ajax carbon, suggesting that the adsorption affinity at infinite temperature on Nuxit carbon is slightly lower than that on Ajax carbon. The MPSD for Nuxit carbon is also plotted in Fig. 4, and we see that the MPSDs of these two activated carbons are very comparable.

The optimized parameters are used in the model to predict the equilibria data of these eight species at 363 K. The predictions are excellent [126], clearly supporting the temperature dependence of the model.

D. Comparison with Experimental Data—Binary Component Equilibria

With the structural parameter and isotherm parameters obtained, we employ the extended MPSD model to simulate the binary adsorption equilibria. As a criterion to judge the model performance, the related simulation results from IAST are also presented for the related systems,

1. Ajax Activated Carbon

The binary adsorption equilibria on Ajax activated carbon are measured on a volumetric rig for the following systems [134]: (1) methane–ethane (303 K); (2) methane–propane (303 K); (3) methane–CO₂ (273 and 303 K). For each binary system, the total pressure for the bulk phase was kept at about 500 torr. Figure 6 shows a typical plot of the amount adsorbed versus the mole fraction of methane for the system methane–propane–Ajax activated carbon. The continuous lines are predictions from the MPSD model, and the dotted lines are from the IAST. As the figure shows, the predictions from the MPSD model are better than those from the IAST. This trend is also observed for other binary systems studied.

2. Nuxit Activated Carbon

For Nuxit activated carbon, the binary equilibria of the following systems were simulated: (1) methane–ethylene (293 K); (2) ethylene–propylene (293 K); (3) ethane–propane (293 and 333 K); (4) ethane–ethylene (293 K); (5) ethane–methane (293 K); (6) ethylene–CO₂ (293 K). Like the case of Ajax activated carbon, the model predictions from the MPSD model are again excellent, suggesting that the MPSD model is appropriate to study multicomponent equilibria of hydrocarbons on activated carbon.

E. Discussion of the MPSD Model

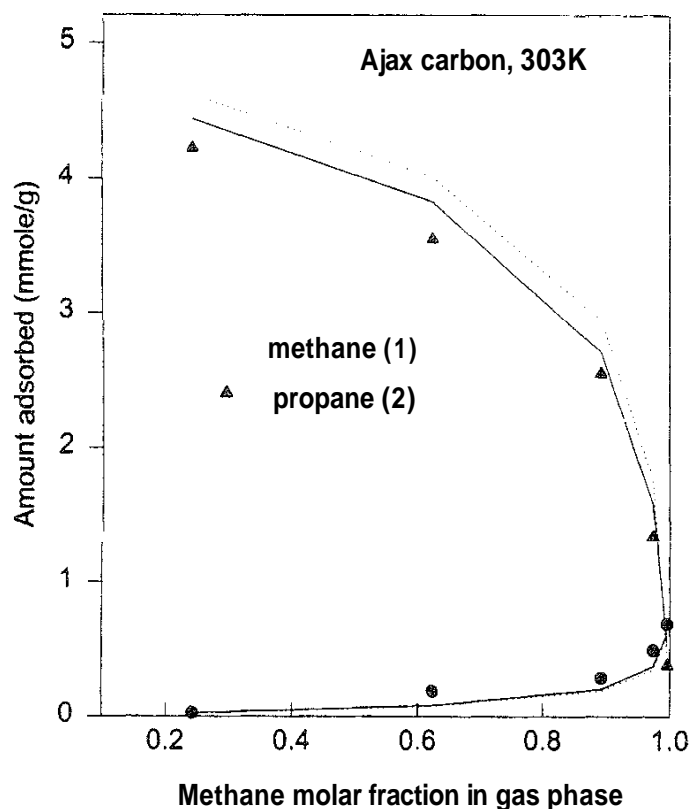
1. The MPSDs

A comparison of the MPSDs derived for the two activated carbons in Fig. 4 reveals that Nuxit activated carbon has slightly larger average pore size and variance than Ajax activated carbon does, although the difference is not significant. This observation may reflect the general feature of the commercial activated carbons. On the

TABLE 4 Optimized Isotherm Parameters for Each Species on Nuxit Carbon

| Property | Methane | Acetylene | Ethylene | Ethane | Propylene | Propane | Butane | CO ₂ |
|-----------------------------|------------------------|-----------|----------|--------|-----------|---------|--------|-----------------|
| $C_{\mu s}^0$ (mmol/g) | 5.778 | 7.176 | 6.687 | 6.435 | 5.556 | 5.220 | 4.242 | 10.52 |
| ϵ_{st}^* (kJ/mol) | 11.48 | 16.38 | 14.70 | 15.38 | 16.35 | 17.41 | 20.37 | 14.69 |
| δ (K ⁻¹) | 1.168×10^{-6} | | | | | | | |

Source: Ref. 121.



FIG, 6 Plots of the amounts of methane and propane adsorbed versus the mole fraction of methane for Ajax activated carbon. Total pressure is 500 torr, and the temperature is 303 K.

other hand, the MPSD derived from a KOH chemically activated nutshell-derived activated carbon shows considerable difference in MPSD from those of commercial carbons [134]. Thus the physical meaning and the reliability of the derived MPSD deserve further investigation. The microporous structure of activated carbon is very complex; the assumption of any form for $f(r)$ will impose some constraint in the inverse process of Eq. (81). Furthermore, the assumption of the slit-shaped model micropore of infinite extent is an oversimplified picture of a real micropore, in which the other sources of surface heterogeneity, as we stated before, are not accounted for. Due to the sensitivity of the LJ potential to the pore size, the MPSD obtained will locate mainly in the region of one to two LJ diameters. So the MPSD derived here represents the lumped effect of micropores of all sizes on the overall adsorption equilibria. Considering the complexity of the carbon structure and the two-parameter gamma distribution function, the MPSD obtained this way should be treated qualitatively rather than quantitatively, in spite of its significant role in describing both pure and binary adsorption equilibria on heterogeneous surfaces.

2. The Multicomponent MPSD Model

From the practical point of view, the extended MPSD model offers several advantages:

1. The MPSD derived is based on the extensive equilibria information of many pure component data, which is necessary to account for surface heterogeneity.
2. It gives a good fit for the equilibria of many species over a broad range of temperature.
3. The model has the predictive capability for multicomponent equilibria.
4. The model is noniterative and can be conveniently applied in the study of adsorption kinetics on a heterogeneous surface [135]. This is important because the application of a practical kinetic separation process depends critically on a model that reliably describes multicomponent equilibria,

In its theoretical aspect, the MPSD model also provides us with some insight into the role of surface heterogeneity. It takes into account the size exclusion effect and sets a physical criterion for the local matching energies between different adsorbate molecules in the micropore. Although the local extended Langmuir isotherm in the model is simplistic in its description of true equilibria, this problem can be overcome by applying the concept of IAST in each micropore, and the overall adsorption equilibrium is the contribution from the local equilibria over the complete MPSD range. However, the model will become iterative and very time-consuming while its performance improves only marginally. The significance of this sacrifice for purely theoretical purposes is questionable.

However, as we discussed before, the present model represents only a primitive, oversimplified picture of multicomponent equilibria in activated carbon. All other interaction mechanisms are also lumped into the potential minimum of the adsorbate–pore interaction, as the model does not account for interactions with the *same* adsorbate molecule, nor does it reflect the importance of surface loading as the pore filling progresses. These suggest that more fundamental work is needed for a full understanding of the multicomponent adsorption equilibria on heterogeneous solids.

VII. STATISTICAL MECHANICAL METHODS AND MULTICOMPONENT EQUILIBRIA

In recent years, the behavior of fluid molecules in small pores has been well studied by computer simulation [136,137]. Computer simulation can provide us with valuable information about the microscopic behavior of adsorbate molecules confined in small pores in terms of intermolecular and surface forces, thus enabling us to understand the fundamental behaviors of adsorbates in the potential field of the model pores. The current trend in the literature suggests that for physical adsorption in activated carbon, the adsorbate–adsorbate interaction and adsorbate–pore interaction are well represented by the LJ potential theory while the model micropore is a slit-shaped channel of infinite extent. This forms the basis for the application of the statistical method in adsorption processes.

A. Pore Selectivity Isotherm

Although the statistical mechanical method can provide us with more accurate descriptions of the PSDs of adsorbents and the microscopic behavior of adsorbates in micropores, it is still not feasible to use these methods to directly compute the multicomponent equilibria in practical processes because of the intensive computational requirement. What is valuable to us is that it enables us to have deep insight into the separation properties (especially selectivity) of certain systems in pores of various sizes, thus possibly providing us with some guidelines in making or selecting the right adsorbent. An example is the study of the adsorbent structure for natural gas storage [116,138]. Fundamentally, the adsorption selectivity for a multicomponent system depends on several factors: (1) the adsorbate–adsorbate interaction; (2) the adsorbate–adsorbent interaction; (3) the pore configurations, including the length and width of the micropore; and (4) the shape and size of the adsorbate molecules. All these factors fall within the capability of statistical mechanical methods. At present, studies are carried out mainly for the binary system consisting of species with simple molecular geometry in graphitic model pores,

Finn and Monson [139] first tested the predictability of IAS theory for binary systems using the isothermal isobaric Monte Carlo simulation on a single surface. However, this system does not represent real adsorption systems. Tan and Gubbins [140,141] conducted detailed studies on the binary equilibria of the methane–ethane system in slit-shaped micropores using the nonlocal density function theory (NLDFT). The selectivity of ethane to methane was studied in terms of pore width, temperature, pressure, and molar fractions.

The selectivity of ethane to methane is defined in terms of density or molar fraction as (p = pore phase, b = bulk phase; 1 = methane, 2 = ethane)

$$S = \frac{\rho_{p2}/\rho_{b2}}{\rho_{p1}/\rho_{b1}} = \frac{(1 - x_{p1})/x_{p1}}{(1 - y_{b1})/y_{b1}} \quad (90)$$

At the limit of zero pressure, the selectivity is S_0 :

$$S_0 = \lim_{p \rightarrow 0} S \quad (91)$$

which is determined by the ratio of Henry's law constants for each species and hence independent of the bulk fluid phase. With DFT theory, this S_0 is expressed as

$$S_0 = \lim_{p \rightarrow 0} \frac{\rho_{p2}/\rho_{b2}}{\rho_{p1}/\rho_{b1}} = \frac{\int_0^H \exp[-V_2^{\text{ext}}(z)/k_B T] dz}{\int_0^H \exp[-V_1^{\text{ext}}(z)/k_B T] dz} \quad (92)$$

where $V_i^{\text{ext}} = \phi(z) + \phi(H - z)$ is the external field experienced by a fluid molecule at z for a given pore size H . So S_0 is entirely determined by the ratio of the integrated Boltzmann factors of the external force of the two components, and this suggests that the selectivity at zero pressure limit for a certain system depends only on the temperature and pore size.

At various pore sizes, S_0 exhibits a maximum for each temperature, the position of which is approximately located at $H^*(H/\sigma_{11}) = 2$. When temperature increases, the position of this maximum shifts slightly to smaller pore size. In small pores, S_0 decreases quickly, as ethane is geometrically more restricted than methane. When $H^* < 1.7$, methane will be selectively adsorbed in comparison with ethane in such small pores.

When pressure is high, the fluid–fluid force also plays an important role in selectivity, and as a result the selectivity also depends on bulk-phase pressure and molar fraction. Tan and Gubbins introduced a classification scheme for the selectivity isotherm (selectivity versus pressure). They classified the shape of the selectivity isotherm at different temperatures into four types: Type I is for cases where the temperature is significantly higher than T_{cc} (T_{cc} = capillary critical temperature for the mixture), in which the selectivity isotherm shows a single maximum; type II occurs where the temperature is just above T_{cc} , in which the selectivity isotherm has double maxima; types III and IV occur when temperatures are below T_{cc} and are characterized by discontinuities corresponding to condensation and layering transition. Later, another type of selectivity isotherm was discovered by Cracknell and Nicholson [142] and was appended to this classification scheme as the type V selectivity isotherm. Type V selectivity presents a monotonic decrease with an increase in pressure, a phenomenon frequently observed experimentally.

B. Test of the IAST at the Microscopic Level

Cracknell and Nicholson first studied the selectivity of the same methane–ethane system using the GCMC technique in which the ethane molecule is treated as a spherical LJ fluid [143]. They also investigated the predictability of the IAST theory for the binary mixture in pores of different sizes. Their study was carried out at the supercritical temperature ($T = 296.2$ K), and the results were compared with those of Tan and Gubbins. It was found that in most cases the DFT overestimates the selectivities (of ethane), but there is qualitative agreement between the results from the two methods. The following reasons are attributed for the discrepancies: (1) The weighting function for density expansion does not have enough terms; (2) the mean field assumption for the attractive force is inadequate.

Cracknell and Nicholson further investigated the same binary system using a more realistic model for ethane, in which the ethane was treated as two LJ sites connected by a certain length of bond [144]. The simulation results showed that the elongated shape of ethane strongly influences the pore size dependence of selectivity and that the confinement in micropores may cause a significant decrease in the selectivity. Their studies were also extended to the ethane–propane system [142], in which the ethane and propane were considered as two- and three-site LJ fluids, respectively. Again, using the simulated single-component data as input, the IAST was found to be able to predict the selectivity with reasonable accuracy.

Gusev et al. [145] also studied the selectivity of the ethane–methane system with the GCMC method in model graphite micropores of various sizes at supercritical temperature and under a broad range of pressure. Both adsorbates were treated as

spherical LJ fluids. It was found that in the low pressure range the IAST describes the binary system behavior well for all pore size ranges. This is in accordance with our expectation, as IAST becomes exact in the Henry's law region. At the simulation temperature (308 K), the predictability of IAST is seen to be the best at pressures less than 10 bar, and it deteriorates sharply at higher pressure. This is partly attributed to the fact that the IAST calculation procedures require extrapolation of the simulated methane isotherm to pressures well above the mixture pressure and even the normal pore-filling pressure in many cases. The overall predicted selectivity on model solids (with different PSDs) is found to be reasonable and to be as good as that in a single pore.

VIII. CONCLUSION

The issue of multicomponent adsorption still poses a fundamental problem to researchers working in the adsorption area. Many mathematical models have been proposed to address this problem, and there have been reviews such as those cited in this chapter. The choice of an appropriate model rests on the balance of simplicity and capability of the model as well as the intended application of the model. For example, for quick calculation of the multicomponent equilibria of similar adsorbates (such as low-order paraffin gases), simple models such as the FastIAS and the extended Sips model are adequate. However, to study the influence of the porous structure of activated carbon on the adsorption equilibrium properties of nonpolar adsorbents, the MPSD model is complex enough, while still retaining some simplicity, to explain the effects of factors such as micropore size distribution and adsorbate molecular properties on the adsorption equilibria.

Two factors play important roles in the study of adsorption equilibria of mixtures on heterogeneous adsorbents like activated carbon and hence have received attention in the development of various models. They are (1) the size difference between the adsorbate molecules and (2) the adsorption energetic heterogeneity, or the structural heterogeneity of the adsorbent if the adsorbate is nonpolar. For many conditions, these two factors are adequate to account for the nonideal behavior of the adsorbed phase, and they are readily accounted for by the MPSD model. This model needs to be further applied and tested in many systems to verify its capability, and it needs to be modified (fine-tuned) to account for many factors such as the irregular structure of the micropore as well as the inclusion of functional groups to deal with polar adsorbates.

Statistical mechanical methods like GCMC or DFT have a good prospect in characterizing the PSD of activated carbon and in examining multicomponent adsorption equilibria at the microscopic level. However, the study of nonideal adsorption behavior with these methods is not a trivial task. The nondispersive interaction in the adsorption process also needs to be quantified.

Systematic and reliable experimental data of single adsorbates and binary and ternary mixtures on samples of activated carbon with various pore structures and surface chemistry are badly needed for the critical evaluation of models of multicomponent adsorption equilibria.

ACKNOWLEDGMENT

This work is supported by the Australia Research Council

REFERENCES

- D. M. Ruthven, *Principles of Adsorption and Adsorption Processes*. Wiley, New York, 1984.
2. R. T. Yang, *Gas Separation by Adsorption Process*. Butterworths, Boston, 1987.
3. S. Sircar, Ind. Eng. Chem. Res. 30:1032 (1991).
4. B. K. Kaul, Ind. Eng. Chem. Des. Dev. 23:711 (1984).
5. M. Jaroniec and R. Madey. *Physical Adsorption on Heterogeneous Solids*, Elsevier, Amsterdam. 1988.
6. S. Suwanayuen and R. P. Danner, AIChE J. 26:68 (1980).
7. S. Suwanayuen and R. P. Danner, AIChE J. 26:76 (1980).
8. T. W. Cochran, R. L. Kabel, and R. P. Danner, AIChE J. 31:268 (1985).
9. O. Talu and R. L. Kabel, AIChE J. 33:510 (1987).
10. W. Liedy and E. U. Schlunder, Ber. Bunsenges. Phys. Chem. 92:4 (1988).
11. S. H. Hyun and R. P. Danner, J. Chem. Eng. Data 27:196 (1982).
12. D. M. Ruthven and F. Wong, Ind. Eng. Chem. Fundam. 24:27 (1985).
13. M. Moredau, P. Valentin, C. V. Madjar, B. C. Lin, and G. Guiochon, J. Colloid Interface Sci. 141:127 (1991).
14. A. L. Myers and J. M. Prausnitz, AIChE J. 11:121 (1965).
15. E. Richter, W. Schurtz, and A. L. Myers. Chem. Eng. Sci. 44:1609 (1989).
16. A. Malek and S. Farooq. AIChE J. 42(11):3191 (1996).
17. J. A. O'Brien and A. L. Myers, Ind. Eng. Chem. Process Des. Dev. 24:1199 (1985).
18. H. Moon and C. Tien, Ind. Eng. Chem. Res. 26(10):2042 (1987).
19. J. A. O'Brien and A. L. Myers, Ind. Eng. Chem. Res. 27:2085 (1988).
20. D. D. Frey and A. E. Rodrigues, AIChE J. 40:182 (1994).
21. A. L. Myers. *Fundamentals of Adsorption*, p. 365. (A. L. Myers and G. Belfort, eds.) Engineering Foundation. New York (1984).
22. D. P. Valenzuela and A. L. Myers, *Adsorption Equilibrium Data Handbook*, Prentice-Hall, Englewood Cliffs. NJ, 1989.
23. J. Toth, J. Colloid Interface Sci. 163:299 (1994).
24. J. Toth. J. Colloid Interface Sci. 185:228 (1997).
25. J. Toth, J. Colloid Interface Sci. 191:449 (1997).
26. A. L. Myers and S. Sircar, J. Phys. Chem. 76:3412 (1972).
27. E. Frances, F. Siddiqui, D. J. Ahn, C. H. Chang, and N. H. L. Wang, Langmuir 11:3177 (1995).
28. A. L. Myers, G. Belfort, and M. Suzuki, Int. Chem. Eng. 32:585 (1992).
29. S. Sircar, AIChE J. 41:1135 (1995).
30. J. Dunne and A. L. Myers. Chem. Eng. Sci. 49:2941 (1994).
31. E. Costa, J. L. Sotelo, G. Calleja, and C. Marron, AIChE J. 27:5 (1981).
32. O. Talu and I. Zwiebel, AIChE J. 32:1263 (1986).
33. R. Paludetto, G. Gamba, G. Storti, S. Carra, and M. Morbidelli, Chem. Eng. Sci. 42:2713 (1987).

34. S. S. Roginski, *Adsorption and Catalysis on Heterogeneous Surfaces*, Acad. Sci. USSR, Moscow, 1948.
35. S. Ross and J. P. Oliver, *On Physical Adsorption*, Interscience. New York, 1964.
36. S. E. Hoory and W. Prausnitz, Chem. Eng. Sci. 22:1025 (1967).
37. M. Jaroniec and W. Rudzinski, Phys. Rev. Lett. 53A:59 (1975).
38. W. Rudzinski and D. H. Everett, *Adsorption of Gases on Heterogeneous Surfaces*, Academic, Orlando, 1992.
39. W. Rudzinski, K. Nieszporek, H. Moon, and H. K. Rhee, Chem. Eng. Sci. 50:2641 (1995).
40. S. Sircar, Langmuir 3:369 (1987).
41. D. P. Valenzuela, A. L. Myers, O. Talu, and I. Zwiebel, AIChE J. 34:3 (1988).
42. H. Moon and C. Tien, Chem. Eng. Sci. 43:2967 (1988).
43. X. Hu and D. D. Do, AIChE J. 41:1585 (1995).
44. L. K. Koopal, W. H. Rijnsdijk, C. M. Wit, and M. F. Benedetti, J. Colloid Interface Sci. 166:51 (1994).
45. M. Giustiniani, M. Giona, and D. K. Ludlow, Ind. Eng. Chem. Res. 34:3856 (1995).
46. J. Li and O. Talu, Chem. Eng. Sci. 49(2):189 (1994).
47. Y. V. Gusev, J. A. O'Brien, C. R. Jensen, and N. A. Seaton, AIChE J. 42:2773 (1996).
48. M. M. Dubinin, J. Colloid Interface Sci. 23:487 (1967).
49. M. M. Dubinin, Carbon 27:457 (1989).
50. H. F. Stoeckli, F. Kraehenbuehl, L. Balierini, and S. De Bernardini, Carbon 27:125 (1989).
51. S. G. Chen and R. T. Yang, J. Colloid Interface Sci. 177:298 (1996).
52. M. Jaroniec and J. Choma, in *Equilibria and Dynamics of Gas Adsorption on Heterogeneous Solid Surfaces* (W. Rudzinski, W. A. Steele, and G. Zgrablich, eds.) Elsevier, New York, 1997.
53. S. K. Bhatia and H. K. Shethna, Langmuir 10:3230 (1994).
54. F. Kraehenbuehl, H. F. Stoeckli, and V. M. Muller, Carbon 25:499 (1990).
55. M. Jaroniec, R. Madey, and J. Choma, Carbon 27:77 (1989).
56. B. McEnaney, Carbon 26:267 (1988).
57. V. K. Dobruskin, Langmuir 12:987 (1996).
58. E. N. Rudisill and M. D. Le Van, AIChE J. 34:12 (1988).
59. B. P. Bering, V. V. Serpinski, and S. I. Surinova, Dokl. Phys. Chem. (English translation) 153:949 (1963).
60. W. K. Lewis, E. R. Gilliland, B. Chertow, and W. P. Cadogan, Ind. Eng. Chem. 42:1319 (1950).
61. S. J. Doong and R. T. Yang, Ind. Eng. Chem. Res. 27:630 (1988).
62. A. Lavanchy, M. Stockli, C. Wirz, and F. Stoeckli, Adsorp. Sci. Technol. 13(6):537 (1996).
63. W. H. Cook and D. Basmadjian, Can. J. Chem. Eng. 42:146 (1964).
64. W. K. Lewis, E. R. Gilliland, B. Chertow, and W. P. Cadogan, Ind. Eng. Chem. 42:1326 (1950).
65. R. J. Grant and M. Manes, Ind. Eng. Chem. Fundam. 490 (1966).
66. S. D. Metha and R. P. Danner, Ind. Eng. Chem. Fundam. 24:325 (1985).
67. H. Moon and C. Tien, Chem. Eng. Sci. 43:2967 (1988).

68. H. Moon and C. Tien, *Sep. Technol.* 3:161 (1993).
69. S. Sircar and A. L. Myers, *AIChE J.* 32:650 (1986).
70. Y. I. Frenkel, *Kinetics Theory of the Liquid State*. Akad. Nauk, Moscow, 1945.
71. D. C. Henry, *Phil. Mag.* 44:689 (1922).
72. A. W. Adamson, *Physical Chemistry of Surfaces*, Wiley, New York, 1976.
73. U. Eiden and E. U. Schlunder, *Chem. Eng. Process.* 28:13 (1990).
74. W. Liedy, E. U. Schlunder, and T. Turek, *Chem. Eng. Process.* 22:177 (1987).
75. R. Sips, *J. Chem. Phys.* 16:490 (1948) 18:1024 (1950).
76. B. W. Wojciechowski, C. C. Hsu, and W. Rudzinski, *Can. J. Chem. Eng.* 63:397 (1985).
77. R. Staudt, F. Dreisbach, and J. U. Keller, 5th Int. Conf. Fundamentals of Adsorption, Kluwer, Boston, 1995.
78. D. D. Do and H. D. Do, *Chem. Eng. Sci.* 52:297 (1997).
79. A. Kapoor, J. A. Ritter, and R. T. Yang, *Langmuir* 6:660 (1990).
80. T. Nitta, T. Shigetomi, M. Kuro-oka, and T. Katayama, *J. Chem. Eng. Jpn.* 17:39 (1984).
81. C. J. Guo, O. Talu, and D. T. Hayhurst, *AIChE J.* 35:573 (1989).
82. J. A. O'Brien and A. L. Myers, in *Fundamental of Adsorption* (Liapis, ed.), p. 451, Engineering Foundation, New York, 1987.
83. G. M. Martinez and Diran Basmadjian, *Chem. Eng. Sci.* 51:1043 (1996).
84. G. M. Martinez, *Chem. Eng. Sci.* 49:2423 (1994).
85. W. K. Lewis, E. R. Gilliland, B. Chertow, and D. Bareis, *J. Am. Chem. Soc.* 72:1160 (1950).
86. W. K. Lewis, E. R. Gilliland, B. Chertow, and W. Miliken, *J. Am. Chem. Soc.* 72:1157 (1950).
87. L. Szepeszy and V. Illes, *Acta Chim. Hung.* 35:37 (1963).
88. L. Szepeszy and V. Illes, *Acta Chim. Hung.* 35:245 (1963).
89. J. U. Keller, *Ber. Bunsenges. Phys. Chem.* 92:1510 (1988).
90. J. U. Keller, *Physica A.* 166:180 (1990).
91. R. Staudt, G. Sailer, F. Dreisbach, and J. U. Keller. *AIChE Meeting*, St. Louis, Missouri, 1993.
92. D. Avnir and P. Pfeifer, *Nouv. J. Chim.* 7:71 (1983).
93. B. Sahouli, S. Blacher, and F. Brouers, *Langmuir* 13:4391 (1997).
94. M. Giona and M. Giustiniani, *Ind. Eng. Chem. Res.* 34:3848 (1995).
95. M. Giustiniani, M. Giona, and D. K. Ludlow, *Ind. Eng. Chem. Res.* 34:3856 (1995).
96. S. J. Gregg and K. S. W. Sing, *Adsorption, Surface Area and Porosity*, Academic, London, 1982.
97. P. J. M. Carrott, R. A. Roberts, and K. S. W. Sing, *Characterisation Of Porous Solids*, Elsevier, Amsterdam, 1994.
98. D. D. Do, *Chem. Eng. Sci.* 51(17):4145 (1996).
99. D. H. Everett and J. C. Powl, *J. Chem. Soc., Faraday Trans.* 72:619 (1976).
100. W. A. Steele, *The Interaction of Gases with Solid Surfaces*. Pergamon, New York, 1974.
101. H. Marsh, H. Crawford, T. M. O'Grady, and A. Wennerberg, *Carbon* 5:419 (1982).
102. K. Kaneko, R. F. Cracknell, and D. Nicholson, *Langmuir* 10:4606 (1994).

103. M. J. Bojan and W. A. Steele, *Surf. Sci.* 199:395 (1988).
104. M. Bojan and W. A. Steele, *Ber. Bunsenges. Phys. Chem.* 94:300 (1990).
105. E. I. Segarra and E. D. Glant, *Chem. Eng. Sci.* 49:2953 (1994).
106. B. Lippens and J. H. de Boer, *J. Catal.* 4:319 (1965).
107. B. P. Russell and M. D. LeVan, *Carbon* 32:845 (1994).
108. K. Kaneko, *J. Membrane Sci.* 96:59 (1994).
109. R. Evans and P. Tarazona, *J. Chem. Phys.* 84:2376 (1986).
110. K. Kaneko, *Colloids Surf.* 109:319 (1996).
111. G. Horvath and K. Kawazoe, *J. Chem. Eng. Jpn.* 16:470 (1983).
112. L. S. Cheng and R. T. Yang, *Chem. Eng. Sci.* 49:16 (1994).
113. R. F. Cracknell, K. E. Gubbins, M. Maddox, and D. Nicholson, *Acc. Chem. Res.* 28:7 (1995).
114. N. A. Seaton, J. P. R. B. Walton, and N. A. Quirke, *Carbon* 27:853 (1989).
115. C. Lastoskie, K. E. Gubbins, and N. Quirke, *J. Phys. Chem.* 97:4786 (1993).
116. S. Jiang, J. Z. Zollweg, and K. E. Gubbins, *J. Phys. Chem.* 98:5709 (1994).
117. N. Quirke and S. R. R. Tennison, *Carbon* 34:1281 (1996).
118. D. Nicholson and N. G. Parsonage, *Computer Simulation and Statistical Mechanics of Adsorption* Academic, Orlando, FL, 1982.
119. V. Y. Gusev and J. A. O'Brien, *Langmuir* 13:2815 (1997).
120. V. Y. Gusev and J. A. O'Brien, *Langmuir* 13:2822 (1997).
121. M. V. Lopez-Ramon, J. Jagiello, T. J. Bandosz, and N. A. Seaton, *Langmuir* 13:4435 (1997).
122. J. Fischer, M. Bohn, B. Korner, and G. H. Findenegg, *German. Chem. Eng.* 6:84 (1983).
123. R. Forbert and E. U. Schlunder, *Chem. Eng. Proc.* 34:49 (1995).
124. J. Jagiello and J. A. Schwarz, *J. Colloid Interface Sci.* 154:225 (1992).
125. J. Jagiello and J. A. Schwarz, *Langmuir* 9:2153 (1993).
126. K. Wang and D. D. Do, *Langmuir* 13:6226 (1997).
127. X. Hu and D. D. Do, *Langmuir* 10:3296 (1994).
128. J. Jagiello, T. Bandosz, and J. A. Schwarz, *Langmuir* 12:2837 (1996).
129. J. P. Hobson, *J. Chem. Phys.* 43:1934 (1965).
130. N. Rao, R. G. Jenkins, and W. A. Steele, *Langmuir*, 1:140 (1985).
131. D. W. Breck, *Zeolite Molecular Sieves: Structure, Chemistry and Use*, Wiley, New York, 1974.
132. R. W. Innes, J. R. Fryer, and H. F. Stoeckli, *Carbon* 27:71 (1989).
133. R. C. Reid, J. M. Prausnitz, and B. E. Polling, *The Properties of Gases and Liquids*, McGraw Hill, New York, 1987.
134. A. Ahmadpour, K. Wang, and D. D. Do, *AIChE J.* 44:740 (1998).
135. D. D. Do and K. Wang, *AIChE J.* 44:68 (1998).
136. M. P. Allan and D. J. Tildesley, *Computer Simulation of Liquids*, Clarendon, Oxford, 1987.
137. R. Evans, in *Inhomogeneous Fluids* (D. Henderson, ed.), p. 85. Marcel Dekker, New York, 1992.
138. K. R. Matranga, A. L. Myers, and E. D. Glandt, *Chem. Eng. Sci.* 47:1569 (1992).
139. J. E. Finn and P. A. Monson, *Mol. Phys.* 72:661 (1991).
140. Z. Tan and K. E. Gubbins, *J. Chem. Phys.* 90:3704 (1989).
141. Z. Tan and K. E. Gubbins, *J. Phys. Chem.* 96:845 (1992).

- 142. R. F. Cracknell and D. Nicholson, J. Chem. Soc., Faraday Trans. *90*:1487 (1994).
- 143. R. F. Cracknell and D. Nicholson, Mol. Phys. *80*:885 (1993).
- 144. R. F. Cracknell, D. Nicholson, and N. Quirke, Mol. Simu. *13*:161 (1994).
- 145. V. Y. Gusev, J. A. O'Brien, C. R. C. Jensen, and N. A. Seaton, in *Fundamentals of Adsorption* (M. D. LeVan, ed.) Kluwer, Boston, p. 337 1996.

Surface and Structural Properties of Modified Porous Silicas

MICHAL KRUK and MIETEK JARONIEC Department of Chemistry,
Kent State University, Kent, Ohio

- I. Introduction
- II. Methods of Characterizing Porous Silicas on the Basis of Nitrogen Adsorption Data
 - A. Introductory remarks
 - B. Evaluation of the specific surface area and pore volume
 - C. Calculation of the pore size and pore size distribution
 - D. Estimation of the adsorption energy distribution
- III. Studies of Porous Structures and Surface Properties of Organic-Modified Conventional and Ordered Mesoporous Silicas
 - A. Nitrogen adsorption properties of unmodified conventional and ordered mesoporous silicas
 - B. Physically coated mesoporous silicas
 - C. Conventional mesoporous silicas with bonded organosilanes
 - D. Ordered mesoporous silicas with bonded organosilanes
- IV. Conclusions and Future Research Perspectives
- References

I. INTRODUCTION

Porous silicas are widely used in many areas of modern science and technology as adsorbents, catalyst supports, additives, and chromatographic packings, to mention just a few [1–6]. Many of the applications result from their high surface area, tailored particle size and pore size, and high mechanical, thermal, and chemical stability [1–6]. Another advantage of porous silicas is their high surface reactivity toward some coupling agents, which makes it possible to obtain a broad range of materials with desired surface properties that are useful for the separation of

mixtures (high performance liquid chromatography, ion-exchange chromatography, size exclusion chromatography, gas chromatography), catalysis, and biochemical applications [4–27]. For instance, chemical bonding of organosilanes was found to be a very convenient procedure for attachment of various ligands of different size, surface coverage, and functionality [4]. The combination of a proper silica support and an organosilane used for the modification provides an opportunity to obtain materials with high mechanical and chemical stability; tailored particle size, pore size, and surface area; and the desired functionality and surface properties.

The discovery of ordered mesoporous materials (OMMs) [28–31] opened new perspectives in the field of synthesis and application of mesoporous silicas. OMMs were reported for the first time in 1990 by Kuroda and coworkers [28,29], who synthesized mesoporous molecular sieves using layered polysilicate precursors. However, it was the discovery of scientists from Mobil Oil published in 1992 [30,31] that attracted considerable attention and initiated a significant and still growing number of studies in the direction of synthesis, application, and characterization of ordered mesoporous materials [32–69].

The Mobil scientists reported details of the synthesis and structure of a new family of mesoporous silicas and aluminosilicas, called M41S, and put forward a hypothesis concerning the synthesis mechanism [30,31]. The M41S materials were obtained from inorganic precursors in the presence of alkyltrimethylammonium surfactants. Depending on the synthesis conditions, three different types of products were obtained: hexagonally ordered MCM-41, bicontinuous cubic MCM-48, and lamellar MCM-50. The MCM-41 structure exhibited a system of long straight, approximately cylindrical channels arranged in a honeycomb structure with no connections between the channels. MCM-48 featured a three-dimensional porous structure of cubic symmetry, exhibiting curved interconnected channels with approximately constant diameter. MCM-50 was a lamellar phase with silicate or aluminosilicate layers separated by surfactant layers. As-synthesized MCM-41 and MCM-48 materials had their pore voids filled with surfactant molecules, but after the surfactant was removed by calcination at elevated temperatures (typically about 823 K), porous structures of remarkable pore volumes (above $0.7\text{ cm}^3/\text{g}$) and surface areas (above $700\text{ m}^2/\text{g}$) were obtained. The structure of the lamellar MCM-50 collapsed during calcination. The Mobil scientists proposed that the synthesis of these remarkable materials proceeds via a liquid crystal templating mechanism. It is well known that surfactants in water form various kinds of micelles, which can assemble into liquid crystalline phases. For example, cylindrical micelles can be formed and aggregate in a honeycomb structure. It was speculated that silicate or aluminosilicate precursors condense on such preformed liquid crystalline matrices and, for instance, the MCM-41 phase results from the condensation of inorganic precursors around a honeycomb assembly of micelles. Alternatively, cylindrical micelles may first be covered by inorganic species and then assemble into the honeycomb structure.

Subsequent studies showed that the liquid crystal templating mechanism is generally correct, but its details are usually somewhat different from the two ways outlined above [32–35]. It was demonstrated [32] that in most cases the synthesis of novel mesoporous materials involves the formation of ion pairs between surfactant ions and inorganic precursors, their assembly into the liquid crystalline phase, and

subsequent condensation of the inorganic species. The liquid crystal templating mechanism was directly confirmed by a successful synthesis of several new phases [33–35,40,61–63], most of which have their counterparts in liquid crystalline surfactant–water systems.

In accord with the reports of Mobil scientists [30,31], novel mesoporous materials were found to exhibit surface areas of about $1000\text{ m}^2/\text{g}$, most of which was the surface area of the so-called primary mesopores, i.e., mesopore structures with uniform pore diameters. The external surface area was found to be about an order of magnitude smaller. In most cases, there was no evidence of the presence of micropores (pores of width below 2 nm) [39,54]. The primary mesopore sizes of typical MCM-41 materials range from about 2 to 4.5 nm, and synthesis procedures for good quality large-pore materials with pore diameters up to at least 6.5 nm have recently been developed [33,36–39]. Usually, the primary mesopore volume of ordered mesoporous materials is in the range of $0.5\text{--}1\text{ cm}^3/\text{g}$. The capillary condensation in primary mesopores of MCM-41 manifests itself as a pronounced and often almost vertical step on the adsorption isotherms [39,53,56,60,68]. Only in the case of small-pore samples with pore diameters close to 2 nm are there no noticeable condensation steps, and the increase in the adsorbed amount at higher pressures is very small, indicating that primary mesopores are filled with the adsorbate at low relative pressures (below about 0.2) [53].

The Mobil scientists reported that the surface properties of MCM-41 are close to those of silica gels [30], which is not surprising when one takes into consideration their composition and the lack of crystallinity of their pore walls [30–35]. Consequently, surfaces of MCM-41 and other ordered mesoporous silicas feature silanol groups (single or geminal) and siloxane bridges. Silanol groups may be hydrogen-bonded with one another or with physisorbed water molecules. Water adsorption studies revealed that the surface of both siliceous and aluminosiliceous MCM-41 samples is relatively hydrophobic [64,65] in comparison with that of conventional silica gels. Several adsorption studies indicated strong surface heterogeneity [53,54,58,65–67] in accord with well-known surface properties of silica gels and silica-aluminas [1,2,70,71].

The presence of silanol groups on the surface of MCM-41 and other ordered mesoporous silicas provides an opportunity to modify the surface via chemical bonding of organic ligands. Many surface modifications of ordered mesoporous materials by chemical bonding have been reported [30,44–52,59], and some of the resulting materials have been shown to be catalysts with interesting properties [51,52] or efficient adsorbents for the removal of heavy metal ions [47–49]. Moreover, it was demonstrated that surface modification via trimethylsilylation significantly improves the mechanical and hydrothermal stability of silica-based ordered mesoporous materials [44]. It is also interesting to note that mesoporous molecular sieves with covalently bonded organic groups can be synthesized via co-condensation of tetraethoxysilane and organotriethoxysilane in a one-step procedure [41–43].

The aim of this chapter is to provide the methodology for characterizing unmodified and modified porous silicas by using nitrogen adsorption. Owing to the significant and still growing interest in the synthesis, modification, and application of ordered mesoporous silicas, problems of their characterization are emphasized

and considered in detail. In Sec. II, a possibility of complex characterization of both porous structure and surface properties of modified porous silicas on the basis of nitrogen adsorption measurements in a wide pressure range is presented. Methods for determining the surface area, pore volume, and pore size distribution are discussed. Moreover, calculations of adsorption energy distributions from low pressure nitrogen adsorption data are outlined, because they provide new opportunities in characterization of surface properties of modified porous silicas. In Sec. III, several recent studies of modified conventional and ordered mesoporous silicas are presented to demonstrate the usefulness of the adsorption data analysis described in Sec. II. Conclusions are discussed in Sec. IV. Due to immense amount of literature about the characterization, modification, and application of porous silicas, the list of references is by no means complete and is focused mostly on the synthesis, characterization, and modification of ordered mesoporous materials, which currently attract a good deal of attention.

II. METHODS OF CHARACTERIZING POROUS SILICAS ON THE BASIS OF NITROGEN ADSORPTION DATA

A. Introductory Remarks

Nitrogen adsorption at 77 K is a standard and widely used method to determine the specific surface area and pore size distribution of mesoporous adsorbents [72,73]. This technique is also commonly applied to determine microporosity [72–75]. However, it is rarely appreciated that analysis of low pressure nitrogen adsorption data affords considerable insight into the surface properties of porous materials [75]. Adsorption instrumentation capable of performing low pressure measurements (down to relative pressures of about 10^{-7}) is currently commercially available. Therefore, it is convenient to carry out nitrogen adsorption runs over the entire pressure range in order to obtain information about surface area, porosity, and surface properties from a single adsorption isotherm. It is well known [75] that porous adsorbents usually exhibit strong structural and surface heterogeneities, the former caused by the presence of pores of different sizes and shapes, and the latter resulting from surface irregularity, roughness, and the presence of impurities and various functional groups. Adsorption processes on solid surfaces are influenced by both structural and surface heterogeneities, and it is often difficult to recognize which of these factors is responsible for adsorption properties observed experimentally.

Our recent studies of nitrogen adsorption on mesoporous silicas [39,46,53–55,59,70,71,76–79] were aimed at exploring the possibility of separating pore structure and surface functionality effects in order to develop better characterization procedures for these materials. The low pressure adsorption properties of porous silicas were found to be markedly different from those of many other adsorbents, such as graphitized and nongraphitized carbons and porous titania and zirconia or even alumina [78,79]. However, low pressure nitrogen adsorption on numerous conventional and ordered mesoporous silicas proceeds in essentially the same way, indicating that nitrogen probe molecules are quite insensitive to details of silica surface and mesoporous structure [39,53–55,70]. The similarity of the surface

properties of different silica samples allows for the easy detection of micropores, even if they are present in relatively small amounts [39]. Moreover, nitrogen adsorption was shown to be significantly affected by the introduction of organosilanes in chemical bonding modification procedures, and the changes in adsorption properties were clearly dependent on the structures of the bonded species [46,59,71,76,77]. These studies demonstrated that nitrogen adsorption is a powerful technique to analyze both the porous structure and surface functionality of unmodified and modified mesoporous silicas. Before the results of our studies are reviewed, it is important to discuss selected fundamental aspects of adsorption data analysis and to present characterization techniques that were found to be very useful in studies of porous silicas.

According to IUPAC recommendations [72,73], pores are classified with respect to their size as micropores (width below 2 nm), mesopores (width between 2 and 50 nm), and macropores (width greater than 50 nm). For mesoporous silica gels, nitrogen adsorption isotherms of type IV (IUPAC classification [72]) are commonly observed. These isotherms usually exhibit pronounced hysteresis loops at relative pressures above about 0.4, arising from capillary condensation of nitrogen in mesopores. However, if mesopores present in the material do not exceed a diameter of about 4 nm, there is no adsorption-desorption reversibility. If, in addition, the pore size distribution is narrow, which is the case for ordered mesoporous silicas, sharp reversible steps of capillary condensation are observed, and the resulting adsorption isotherms may be referred to as reversible type IV isotherms [68]. When a material has mesopores of sizes below 4 nm with a broad pore size distribution or the mesopore size approaches the micropore size limit (2 nm), an adsorption isotherm resembles type I behavior characteristic of microporous adsorbents (reversible adsorption isotherm, which is concave to the "relative adsorption" axis and levels off at low relative pressures). In this case, the mesoporous character of the sample can be verified by using the comparative plot method in the range of low pressure nitrogen data.

The IUPAC recommendations [72] classify hysteresis loops into four types (H1–H4), and two of them, H1 and H2, are typically observed for many mesoporous silicas. Hysteresis loops of the H1 type have two parallel, nearly vertical branches and were often reported for materials composed of agglomerates (assemblages of particles rigidly joined together) or compacts of approximately spherical molecules arranged in a fairly uniform way [72]. Recently, type H1 loops were also observed for materials of cylindrical pore geometry and a high degree of pore size uniformity [33,39,55]. Thus the presence of the H1 type of hysteresis loop on the adsorption isotherm for a porous solid appears to indicate high pore size uniformity and facile pore connectivity.

A type H2 hysteresis loop has a triangular shape and a very steep desorption branch. Such behavior was observed for many porous inorganic oxides and was attributed to pore connectivity effects [80], which were often defined as the presence of pores with narrow mouths (inkbottle pores), but the latter identification may be grossly oversimplified [50]. Indeed, triangular hysteresis loops were observed even for highly ordered MCM-41 materials with pore sizes of about 4–5 nm [39,55,57]. For such samples, desorption (capillary evaporation) of nitrogen from primary mesopores takes place at relative pressures of 0.4–0.5, i.e., in the region where

hysteresis loops usually close. This results in very steep desorption branches of nitrogen adsorption isotherms and triangular hysteresis loops. It can be concluded that the H2 hysteresis loops may result not only from poor pore connectivity but also from the transition from the irreversible to reversible adsorption–desorption behavior in a relative pressure range characteristic of a given adsorbate (0.4–0.5 in the case of nitrogen at 77 K).

B. Evaluation of the Specific Surface Area and Pore Volume

The Brunauer–Emmett–Teller (BET) method [81] provides a standard procedure to calculate the specific surface area of mesoporous materials [72–75]. However, if an adsorbent has an appreciable number of mesopores with sizes close to the micropore size range (2–3 nm), adsorption data from the region of capillary condensation in these mesopores should not be used in the BET calculations [53]. In such cases, the accuracy of surface area determination can be improved by using the comparative plot method [54], as described below. The total pore volume can be estimated from the amount adsorbed at a relative pressure close to the saturation vapor pressure (usually about 0.99) by converting the adsorbed amount to the corresponding volume of liquid adsorbate [74]. The conversion factor is equal to 0.0015468 for nitrogen at 77 K when the adsorbed amount and the pore volume are expressed in cubic centimeters at STP per gram and cubic centimeters per gram, respectively, and it is assumed that the density of condensed adsorbate is equal to the density of liquid adsorbate at the temperature of measurement. This procedure provides the volume of pores with widths below 100–200 nm, depending on the pressure value used in the calculations. In the case of adsorption isotherms, which exhibit a steep increase in the adsorbed amount at pressures close to the saturation vapor pressure, the estimation of the total pore volume may be quite inaccurate.

In many cases, information about structural properties of high surface area materials can be obtained by comparing the adsorption isotherm of a solid under study with the adsorption isotherm of a reference macroporous material of similar surface properties [74,82,83]. The comparison is made by plotting the amount adsorbed for the solid under study as a function of the amount adsorbed for the reference material (v_{ref}) at the same pressure. The adsorption for the reference is usually expressed either as the statistical film thickness t of the adsorbate on the surface (in the t -plot method) or as the standard reduced adsorption α_s (in the α_s -plot method) [74]. The quantity a , is defined as the ratio of the adsorbed amount at a given pressure to the adsorbed amount at a relative pressure of 0.4.

In the case when the solid under study and the reference material have the same surface and structural properties and differ only in the amount of surface area, the comparative plot is linear and starts from the origin of the graph. However, usually the plots obtained on the basis of experimental data exhibit deviations from linearity, which can be analyzed to obtain information about the structural and surface properties of a given solid. If the solid under study has micropores, they are filled at low relative pressures, and the amount adsorbed in them does not change significantly with further pressure increase. The increase in the gas uptake for higher pressures results mostly from adsorption on the external surface area of the sample,

which proceeds via multilayer adsorption, as is the case for the reference material. Therefore, the comparative plot curves for many microporous solids rise steeply at low pressures and then gradually level off and exhibit linearity at higher pressures. The linear part of the comparative plot can be extrapolated to the adsorbed amount axis, and the intercept provides the amount adsorbed in micropores, v_{mi} , which can be converted to the micropore volume by multiplying by a proper conversion factor. The slope of the linear part of the comparison plot can be used to calculate the external surface area of the sample, as described elsewhere [39,54,82,84].

Another type of comparative plot curve can be observed for mesoporous samples. In the region of low pressures, the adsorption on both the mesoporous solid and the reference adsorbent proceeds via the same mechanism, i.e., monolayer-multilayer formation, so the initial part of the plot is linear, and its slope can be used to calculate the total surface area of the mesoporous sample [39,54]. However, in the region of higher pressures, capillary condensation takes place in mesopores, and the increase in the adsorbed amount is relatively much larger for the mesoporous solid than for the macroporous reference, and consequently the comparative plot is bent upward. Subsequently, the comparative plot levels off when mesopores are already filled with condensed adsorbate. For ordered mesoporous solids, those higher pressure parts of the plots can be used to calculate the primary mesopore volume and the external surface area (the surface area of other pores present in these materials) in a way analogous to that described above for microporous adsorbents. If the material under study contains both micropores and mesopores, the deviations of the comparative plot from linearity can be observed in both low pressure and high pressure regions.

The considerations presented above are based on assumptions that surface properties of the reference adsorbent are close to those of the solid under study. However, it is also possible to use the comparative plot analysis to study the surface properties of adsorbents. It was recently reported [82] that the shape of the low pressure part of the plot reflects the differences in interactions of the adsorbate with the compared surfaces, provided microporosity is not present. This finding is important in the analysis of modified mesoporous silicas, whose surface properties are dramatically different from those of unmodified silicas due to the removal of surface silanols and the introduction of organic groups of certain functionalities. When macroporous silica gels are used as reference adsorbents, comparative plots for modified materials exhibit marked downward swings resulting from the decrease in nitrogen-surface interactions as a result of the modification with organic species. These results are discussed in detail in the next section.

C. Calculation of the Pore Size and Pore Size Distribution

Many methods to calculate the pore size are currently available (see Refs. 74, 75, and 84 and references therein), so it is important to choose a proper tool for the analysis of mesoporous silicas. Our studies showed that the Barrett-Joyner-Halenda (BJH) [85] method is a very useful characterization technique [76,77]. In the BJH approach, the adsorption process in mesopores was considered to consist of the formation of the adsorbed layer on pore walls and subsequent condensation of the adsorbate in the interior of the pore. The desorption process was assumed to

proceed in the opposite way, i.e., by capillary evaporation from the interior of the pore followed by a gradual decrease in the thickness of the adsorbed film on the pore surface. In order to develop a useful method for the analysis of porosity, the relationships between (1) the pore size and the capillary condensation/evaporation pressure and (2) the statistical film thickness and pressure need to be known. Barrett et al. [85] assumed that the formation of the adsorbed film is essentially independent of the pore size and used the statistical film thickness curve $t(p/p_0)$ for a macroporous reference adsorbent. To describe the relation between the capillary evaporation pressure and the pore radius (denoted here as r), the Kelvin equation with the correction for the statistical film thickness was used:

$$r\left(\frac{p}{p_0}\right) = \frac{2\gamma V_L}{RT \ln[(p_0/p)]} + t\left(\frac{p}{p_0}\right) \quad (1)$$

where V_L is the molar volume of the liquid adsorbate, γ is its surface tension, R is the universal gas constant, and T is the absolute temperature. In the case of nitrogen adsorption at 77 K, $\gamma = 8.88 \times 10^{-3}$ N/m and $V_L = 34.68$ cm³/mol.

In the BJH method, calculations are performed starting from the adsorption-desorption isotherm data for the highest pressures attained during the experiment, where it is assumed that all pores are completely filled with the condensed adsorbate. When the pressure is subsequently lowered, a certain number of the largest pores are emptied by the capillary evaporation, but the walls of these pores are still covered by the adsorbate film. The decrease in the amount adsorbed, which was caused by the lowering of pressure, can be recalculated to obtain the volume of these emptied pores. but in order to do that, assumptions need to be made about pore geometry and density of condensed adsorbate. The latter can be approximated by the density of liquid adsorbate at the saturation vapor pressure and temperature of the measurement [74]. As far as the geometry is concerned, Barrett et al. [85] assumed that pores are cylindrical in order to make calculations more tractable. Hence, the volume of the inner space in the pores that were emptied during the first evaporation step is equal to the volume of liquid adsorbate corresponding to the measured decrease in the adsorbed amount. To arrive at the total volume of those pores, one simply needs to account for the thickness of adsorbate on the pore walls. The pressure for which the considered decrease in adsorption took place can now be related to the pore radius through the Kelvin equation [Eq. (1)].

A reasoning similar to that described above for desorption from the largest pores during the first pressure-lowering step can be applied to subsequent decreases in the adsorbed amount. But in these cases, the decrease in adsorption is caused not only by the capillary evaporation but also by thinning of the adsorbed layer in pores in which the capillary evaporation has already taken place. The calculations are repeated until a sufficiently low pressure value is reached or the cumulative pore volume obtained using the procedure described above equals or exceeds the total pore volume. The BJH procedure follows the sequence of events during desorption measurements; it actually does not make any difference whether adsorption or desorption data are used. However, different relations between the pressure and the pore size may need to be used for capillary condensation and evaporation [74]. It needs to be noted that the Kelvin equation [Eq. (1)] was shown to underestimate

the size of pores below 7.5 nm [86], becoming increasingly inaccurate as the pore size decreases. Moreover, the assumptions of the BJH method are invalid for micropores (width below 2 nm), since the formation of the adsorbed film on the pore wall is affected by the proximity of the opposite pore wall and cannot be adequately described by the statistical film thickness curve for the macroporous reference adsorbent.

As was already mentioned, nitrogen adsorption–desorption at 77 K on the majority of porous solids is reversible at relative pressures below about 0.40 [55,72–74], and only above this pressure limit can the irreversibility, i.e., the presence of hysteresis loops, be observed. Therefore, lower closure points of hysteresis loops are often observed at pressures close to this limiting value. The existence of the pressure range for which crossover between irreversible and reversible adsorption behavior takes place has significant implications for characterization of porous solids on the basis of adsorption data. The most commonly used method to calculate pore size distributions (PSDs) is based on the Kelvin equation [72–74], which was shown to predict adsorption–desorption irreversibility during adsorption in pores of the most commonly encountered shapes (e.g., cylindrical, slitlike) [74]. Therefore, in the cases of materials for which experimentally measured hysteresis loops close at relative pressures of about 0.4–0.45, exhibiting steep desorption branches, calculations of the pore size distribution from desorption data will indicate narrow pore size distributions, which is likely to be grossly misleading [55,72,74].

In our studies of modified conventional mesoporous silicas [76,77] that had pore sizes greater than 10 nm, the BJH method was used, and calculations were performed on the basis of desorption data. These materials exhibited narrow HI hysteresis loops, which indicated facile pore connectivity and permitted the application of desorption data, which may be inappropriate for many other mesoporous silicas, as discussed above. The statistical film thickness curve used assumed the form of the Halsey equation: $t[\text{nm}] = 0.354[-5/\ln(p/p_0)]^{1/3}$.

A reliable assessment of pore size appears to be a major problem in the characterization of ordered mesoporous materials, for which pore sizes are monodisperse and can be precisely controlled in the range from 2 to at least 6.5 nm by using proper synthesis procedures. At the same time, traditional adsorption methods of pore size estimation, e.g., those based on the Kelvin equation, are expected to be inaccurate for such small mesopores [56,74,76,86]. Therefore, there is a need to develop new accurate and reliable approaches to the pore size analysis for unmodified and modified ordered mesoporous silicas and other nanostructured porous materials. In some cases, one can take advantage of the simple geometry of ordered porous structures (referred to as primary mesopores) of these materials. For instance, in the case of long, approximately cylindrical primary mesopores (MCM-41, HMS, etc.), one can calculate their diameter on the basis of their surface area S_p and pore volume V_p , using the formula $w = 4V_p/S_p$ [60]. The primary mesopore size of MCM-41 materials can also be calculated from X-ray diffraction (XRD) data and the primary mesopore volume using a simple formula based on geometrical considerations of the honeycomb structure characteristic of the MCM-41 materials [53,87]:

$$w = cd \left(\frac{\rho V_p}{1 + \rho V_p} \right)^{1/2} \quad (2)$$

where d is the (100) interplanar spacing obtained from X-ray diffraction, ρ is the density of siliceous pore walls (which can be assumed to be equal to that of amorphous silica, i.e., 2.2 g/cm³ [1,2,87]), and c is a constant dependent on the pore geometry assumed and equal to 1,213 for cylindrical pores. Calculations based on Eq. (2) were shown to be consistent and are expected to give very accurate results, especially for good quality MCM-41 samples [39,53,54]. Equation (2) can also be applied for such materials as SBA-15 [40]. It should also be noted that the assumption of a constant pore wall thickness for MCM-41 samples can be employed for approximate evaluation of the pore size, which can simply be estimated by subtracting the assumed pore wall thickness from the distance between pore centers [56]. The latter can be obtained from XRD measurements. Our extensive studies of MCM-41 materials [based on Eq. (2)] confirmed that in many cases the pore wall thickness is approximately constant (0.8 ± 0.2 nm), but such an assumption is not always valid, especially for samples that exhibit small primary mesopore volumes (below 0.5 cm³/g) [39,53,54].

The methods of pore size evaluation for ordered mesoporous silicas described above are not generally applicable for all kinds of ordered mesoporous structures, and some of them cannot be applied for modified samples. Therefore, computer simulation studies of ordered mesoporous materials were undertaken to improve the understanding of adsorption on these materials and improve the ability to characterize their porous structures [56–58]. Adsorption on MCM-41 was modeled using nonlocal density function theory (NLDFT) [56] and computer simulations [58] to establish the relation between the pore size and the pressure of the capillary condensation in primary mesopores. Based on NLDFT data [56], a program was developed to calculate pore size distributions for MCM-41 [57]. These advanced computational approaches seem to be very promising, but there are still some questions concerning the interpretation of computational adsorption isotherm data. Namely, there is no agreement in the literature [56–58] as to how the adsorption/desorption branches of the calculated isotherms and the point of equilibrium transition between these branches correspond to the experimental adsorption/desorption branches of adsorption isotherms. Moreover, the programs to calculate pore size distributions for ordered mesoporous materials on the basis of computer simulation or NLDFT data are still not available to the majority of the scientific community,

In response to the demand for an accurate method for evaluating pore size distributions of ordered mesoporous silicas and other materials, empirical equations were recently developed to describe relations between the capillary condensation pressure and the pore size in cylindrical siliceous mesopores. These formulas were derived using good quality MCM-41 materials with pores in the range of 2–6.5 nm as model adsorbents, and their pore size was estimated using Eq. (2). The following relation was found between the pore radius r and the pressure of nitrogen capillary condensation in the pores at 77 K [55]:

$$[\text{nm}] = 0.416 \left[\log \left(\frac{p_0}{p} \right) \right]^{-1} + t \left(\frac{p}{p_0} \right) + 0.3 \quad (3)$$

where p is the equilibrium vapor pressure, p_0 is the saturation vapor pressure, and the statistical film thickness curve t is described by the equation

$$t \left(\frac{p}{p_0} \right) [\text{nm}] = 0.1 \left[\frac{60.65}{0.03071 - \log(p/p_0)} \right]^{0.3968} \quad (4)$$

Equations (3) and (4) can conveniently be used in different methods of mesopore size evaluation, of which the BJH approach appears to be particularly suitable [55]. These relations were carefully tested on numerous MCM-41 samples and shown to be in excellent agreement with pore sizes calculated using Eq. (2), with differences usually below 0.1–0.2 nm. Pore size calculations based on Eqs. (3) and (4) can conveniently be performed for both modified and unmodified ordered mesoporous silicas and can be expected to provide highly accurate results, especially for siliceous samples with cylindrical pores. Therefore, the BJH method of calculations based on these equations was used in our recent studies of modified MCM-41 materials [46,59]. It needs to be noted that Eq. (3) was derived for nitrogen capillary condensation (adsorption) data and should not be used in calculations based on desorption data. Moreover, it was shown that the desorption data are not appropriate for the pore size evaluation for mesoporous materials with pore sizes in the range of about 4–5.5 nm, due to the transition between reversible and irreversible adsorption behavior at relative pressures of about 0.4, as already described above. Because of this behavior, the relation between the capillary evaporation (desorption) pressure and the pore size would have a more complicated and less useful form than Eq. (3) derived for the capillary condensation process [55]

D. Estimation of the Adsorption Energy Distribution

It is well known that the adsorption of a gas on a solid surface depends on the interactions between the surface and gas molecules [75,88–91]. These interactions can be described in terms of the adsorption energy distribution (AED) for a given adsorbate–adsorbent system. The AED can be analyzed to obtain information about the surface, i.e., about its structure and functional groups [46,59,70,71,75–77]. In order to calculate AEDs, one needs two fundamental pieces of information. First, adsorption isotherms for homogeneous surfaces interacting with the adsorbate with specified adsorption energies need to be known [75,90]. Second, one needs to account for the topography of adsorption sites (patchwise, random, or intermediate between these two extremes) [75,90,92]. The topography is expected to influence the adsorption on a heterogeneous surface unless lateral interactions (interactions between adsorbed molecules) are negligible. To deal with these problems, one needs to make suitable approximations. Under certain assumptions concerning the properties of the adsorbent and the adsorbed film (geometry of the surface, number of layers of adsorbed molecules, lateral interactions, mobility of adsorbed molecules, etc.), one can derive analytical expressions for adsorption isotherms on homogeneous surfaces [75,90]. For instance, the Fowler–Guggenheim (FG) equation was derived for monolayer localized adsorption with lateral inter-

actions on homogeneous surfaces. The FG equation appears to be particularly interesting, since it has a simple analytical form and yet accounts for lateral interactions in the adsorbed layer. During the last decade, it became possible to generate adsorption isotherms for homogeneous surfaces with specified adsorption energies by employing the nonlocal density function theory (NLDFT) [88] or computer simulations [93]. Therefore, accurate model adsorption data for homogeneous surfaces are now readily available. On the other hand, effects of topography of adsorption sites are rather difficult to account for adequately in calculations of adsorption energy distributions (e.g., using the integral equation of adsorption discussed below) and often have to be neglected to make the calculations feasible.

To obtain the adsorption energy distribution from experimental adsorption data, one can use a formalism of the integral equation for the overall adsorption [75,90]. This equation simply states that the overall adsorption is a sum of the contributions from adsorption on all of the adsorption sites present on the surface:

$$v_t(p) = \int_{\varepsilon_{\min}}^{\varepsilon_{\max}} \theta(p, \varepsilon) v^M(\varepsilon) d\varepsilon \quad (5)$$

where $v_t(p)$ is the total adsorbed amount, $\theta(p, \varepsilon)$ is the degree of surface coverage on sites of adsorption energy ε as a function of pressure (later referred to as the local adsorption isotherm), and $v^M(\varepsilon) d\varepsilon$ after integration is the monolayer capacity of adsorption sites with energies from the interval ε_{\min} to ε_{\max} . It is sometimes more convenient to use an alternative form of Eq. (5) that assumes the form

$$\Theta_t(p) = \int_{\varepsilon_{\min}}^{\varepsilon_{\max}} \theta(p, \varepsilon) F(\varepsilon) d\varepsilon \quad (6)$$

where the overall adsorption $v_t(p)$ and $v^M(\varepsilon)$ were divided by the monolayer capacity v_t^M of the adsorbent in order to obtain the overall degree of surface coverage $\Theta_t = v_t(p)/v_t^M$ and the fraction $F(\varepsilon) = v^M(\varepsilon)/v_t^M$ of adsorption sites of energy ε . The monolayer capacity v_t^M can be calculated using the standard BET method.

To calculate the population of adsorption sites as a function of adsorption energies (i.e., normalized AED), the integral equation for the overall adsorption [Eq. (5) or (6)] needs to be inverted. The required overall adsorption isotherm is directly measured experimentally, but the form of the local adsorption isotherm must be specified. The FG adsorption isotherm was used in our calculations, and the reasons for its selection are discussed elsewhere [75,89]. One of the useful features of the FG equation is that it can easily be modified to account for differences in lateral interactions in the cases of different topographies of adsorption sites. For patchwise topography, the standard expression for the FG adsorption isotherm can be used:

$$\theta(p, \varepsilon) = \frac{K_L p \exp(z\omega\theta/k_B T)}{1 + K_L p \exp(z\omega\theta/k_B T)} \quad (7)$$

where the lateral interaction energy [accounted for by the exponential term in [Eq. (7)] for a molecule located on a site with adsorption energy equal to ε is dependent on the average number of nearest neighbor molecules (assumed to be proportional to the degree of surface coverage θ) on the surface patch of this adsorption energy. In the case of random topography of adsorption sites, it is more realistic to assume that the lateral interactions of a molecule located on a certain adsorption site are dependent on the degree of the surface coverage on the whole surface rather than on adsorption sites of the same energy. Therefore, the local FG adsorption isotherm for the random topography of adsorption sites assumes the form

$$\theta(p, \varepsilon) = \frac{K_L p \exp(z\omega\Theta_i/k_B T)}{1 + K_L p \exp(z\omega\Theta_i/k_B T)} \quad (8)$$

In Eqs. (7) and (8), T is absolute temperature, k_B is the Boltzmann constant, z is the number of nearest-neighbor molecules in the monolayer, and ω is the interaction energy between two nearest-neighbor molecules. In our studies of mesoporous silicas, $z\omega/k_B$ was set to be equal to 380 K, and the random topography of adsorption sites was assumed. K_L is the Langmuirian constant,

$$K_L = K_L^0(T) \exp(\varepsilon/k_B T) \quad (9)$$

The preexponential factor K_L^0 can be calculated from partition functions for an isolated molecule in the gas and surface phases [75].

To invert Eq. (6) with respect to the normalized distribution of adsorption sites, the INTEG program was used [94]. This advanced numerical procedure is based on the regularization method, which is required to overcome the difficulty caused by the inherent numerical instability of the inversion of integral equations that have the general form of Eq. (6) [94,95]. It also should be noted that there is a commercially available program to calculate adsorption energy distributions, which is part of the DFT Plus package of software for the pore size and adsorption energy calculations developed by Micromeritics (Norcross, GA). It was reported [88] that the local adsorption isotherms were calculated using the NLDFT formalism and that the inversion of the integral equation for overall adsorption [Eq. (2)] was performed using the regularization method to provide numerically stable results.

III. STUDIES OF POROUS STRUCTURES AND SURFACE PROPERTIES OF ORGANIC-MODIFIED CONVENTIONAL AND ORDERED MESOPOROUS SILICAS

A. Nitrogen Adsorption Properties of Unmodified Conventional and Ordered Mesoporous Silicas

To successfully synthesize modified mesoporous silicas with the desired properties, it is important to characterize the structure of the silica support used for modifications. For that purpose, nitrogen adsorption is particularly useful, because it provides an opportunity to obtain such crucial data as the specific surface area, mesopore size distribution, and micropore volume. In addition, low pressure

adsorption data can be used to study the surface properties of porous materials, as was discussed in the previous section. However, in the case of mesoporous silicas, low pressure adsorption was rather insensitive to the details of their porous structure. Shown in Fig. 1 are adsorption isotherms for a macroporous silica gel LiChrospher Si-1000 (BET specific surface area of $25 \text{ m}^2/\text{g}$) [39,54] and an ordered mesoporous MCM-41 silica with a pore size of 5.0 nm [59, 69]. For LiChrospher Si-1000, nitrogen adsorption proceeds via multilayer formation up to pressures close to the saturation vapor pressure, where capillary condensation may also contribute to the observed steep increase in the amount adsorbed. In the case of the MCM-41 material, multilayer adsorption takes place on the surface of primary mesopores and on the external surface at relative pressures below about 0.4; then capillary condensation in primary mesopores is observed and the adsorption isotherm levels off. Despite completely different porous structures and the resulting differences in high pressure adsorption behavior, these two silicas exhibit very similar low pressure adsorption properties, which can be seen from the strong similarity of their adsorption energy distributions calculated from submonolayer adsorption data (see Fig. 2). One can conclude that the difference between the mesoporous and macroporous structures of silicas do not affect their surface properties with respect to nitrogen probe molecules [54]. This observation has two important implications. First, it opens an opportunity to obtain a detailed comparative plot analysis of not only high pressure data, which are quite insensitive to surface properties of adsorbents [74], but also low pressure data for mesoporous silica. Second, changes in low pressure adsorption properties that may result from surface modification can be attributed to different surface properties of the modified material rather than to changes in the mesoporous structures (the latter usually involve mainly a decrease in the pore diameter).

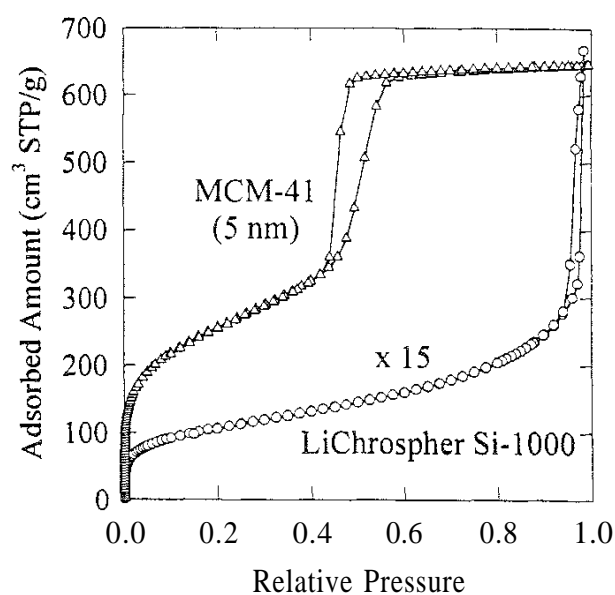


FIG. 1 Comparison of nitrogen adsorption isotherms for the macroporous silica gel LiChrospher Si-1000 and an ordered mesoporous MCM-41 material with pore size of 5 nm. (Data partially taken from Ref. 59.)

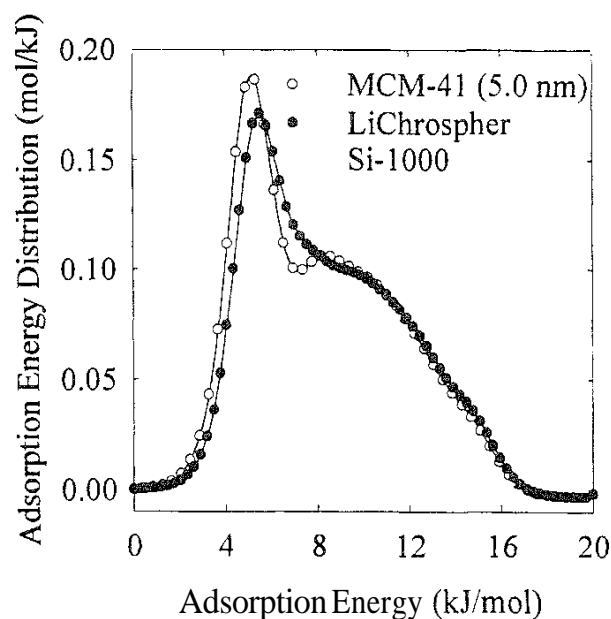


FIG. 2 Comparison of adsorption energy distributions for the macroporous silica gel LiChrospher Si-1000 and an ordered mesoporous MCM-41 material with pore size of 5 nm. (Data partially taken from Ref. 59.)

B. Physically Coated Mesoporous Silicas

Nitrogen adsorption was used to study the applicability of a physical coating procedure for surface modification of conventional [77] and ordered mesoporous [46] silicas. A LiChrospher Si-100 silica gel with an average pore diameter of 12.9 nm (estimated using the conventional BJH method on the basis of desorption data) was coated with 4'-cyano-4-biphenyl [4-(4-pentenyl)oxy] benzoate (CBPB) [77]. The samples are denoted as CBPB-AX, where A indicates the type of modification procedure (T, physical coating; B, chemical bonding; and BT, chemical bonding and subsequent coating) and X provides the weight percent of CBPB in a given material. For comparative purposes, a LiChrospher Si-100 material with bonded CBPB ligands was also prepared and will be referred to as CBPB-B22. Moreover, CBPB-B22 was coated with an additional amount of CBPB, and the resulting material is denoted as CBPB-BT33. The MCM-41 material chosen for the physical coating procedure had a pore size of 3.8 nm [46], and its properties are described in detail elsewhere [53]. The MCM-41 samples coated with CBPB are referred to as X% CBPB MCM-41, where X denotes the weight percent of CBPB.

As can be seen in Fig. 3, the introduction of physically coated species led to a significant decrease in the adsorbed amount and consequently in the pore volume and surface area [77], but the overall shape of the adsorption isotherms remained unchanged, indicating that the mesoporous structure of the silica support was not altered. However, the average BJH pore size decreased after the modifications, depending on the amount of the organic species introduced and the modification procedure used. The largest decrease was observed in the case of chemical bonding (from 12.9 for the unmodified silica gel to 10.8 nm for CBPB-B22) and was much

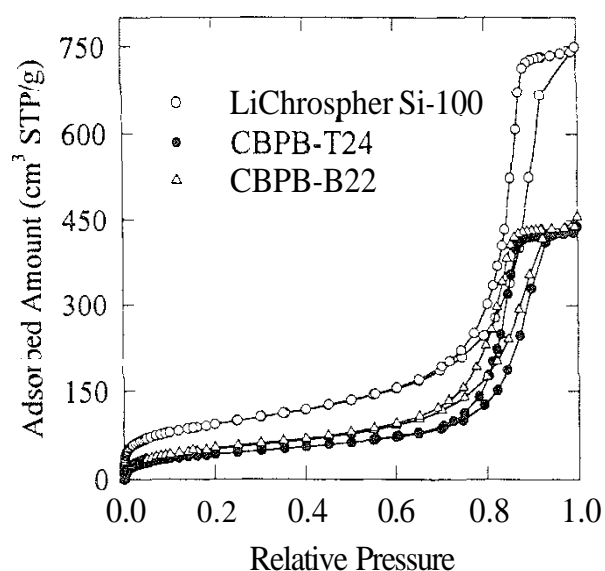


FIG. 3 Nitrogen adsorption isotherms for the unmodified mesoporous silica gel LiChrospher Si-100 and samples physically coated (CBPB-T24) and chemically bonded (CBPB-B22) with CBPB. (Data from Ref. 77.)

more pronounced than in the case of physical coating. For instance, CBPB-T24 with the CBPB loading similar to that of CBPB-B22 had a larger pore diameter (12 vs. 10.8 nm). The reasons of such behavior became clear when the pore size distributions (PSDs) for these samples were examined (Fig. 4). Namely, the physical coating resulted not only in a shift of PSD toward smaller pore sizes, but also in a depletion of smaller pores. Therefore, the physical coating procedure can be expected to provide much less uniform surface coverage than the chemical bonding

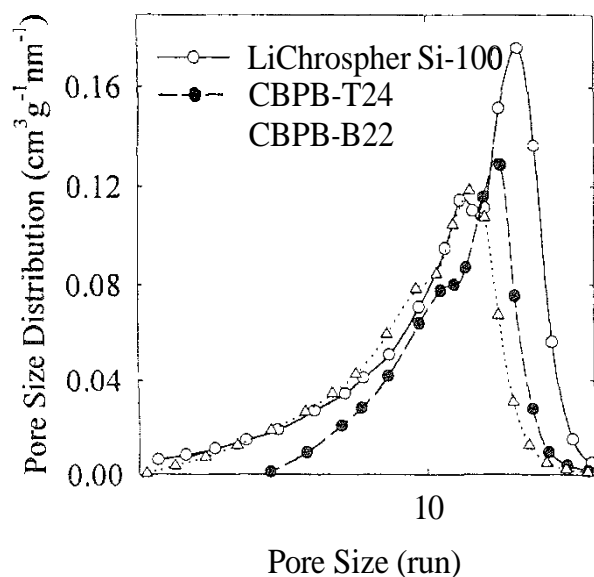


FIG. 4 BJH pore size distributions calculated using desorption isotherms for the unmodified mesoporous silica gel LiChrospher Si-100 and samples physically coated (CBPB-T24) and chemically bonded (CBPB-B22) with CBPB. (Data from Ref. 77.)

procedure. This conclusion was supported by examination of low pressure adsorption data, which is discussed below.

To show the influence of the modification procedure on the surface properties of the materials studied, the comparative plot method can be used to analyze low pressure adsorption data. As can be seen in Fig. 5, initial parts of the comparative plots for the modified silicas exhibit pronounced deviations from linear behavior, which was observed for the silica support, confirming that the latter has essentially the same surface properties as the macroporous reference silica (LiChrospher Si-1000). The plots for modified materials are bent downward to an extent dependent on the CBPB loading and the modification procedure. Increases in the amount of organic modifier caused a systematic decrease in the low pressure adsorption. Examination of the comparative plots for CBPB-T24 and CBPB-B22 shows that the plot for the chemically modified material is bent downward to a slightly larger extent, indicating somewhat more pronounced changes in surface properties. The latter may be due to a more uniform surface coverage, in agreement with the pore size data shown in Fig. 4 and/or due to removal of high energy adsorption sites in the course of chemical modification. The presented results indicate that in the case of a mesoporous silica with pore sizes much larger than the size of coating molecules, the physical coating procedure used may lead to the accumulation of the organic modifier in smaller pores, but still it provides a quite uniform surface coverage only slightly inferior to the chemical bonding procedure.

To quantify the gas-surface interactions for the materials under study, adsorption energy distributions (AEDs) were calculated. It was shown [77] that the highest energy adsorption sites (above 12 kJ/mol) gradually disappeared (see Fig. 6) as the amount of coated CBPB was increased up to 24 wt% in the case of CBPB-T24

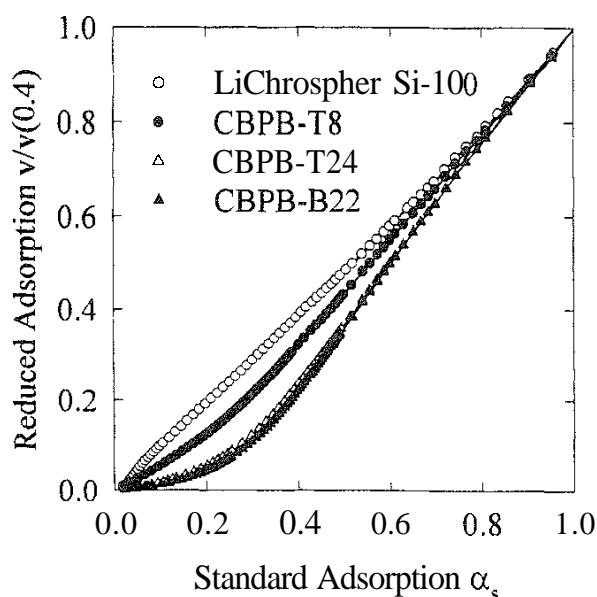


FIG. 5 Comparative plots for unmodified and modified LiChrospher Si-100 samples. The adsorbed amount for the samples was divided by the adsorbed amount at a relative pressure of 0.4 to allow for a better comparison. (Data partially taken from Ref. 77.)

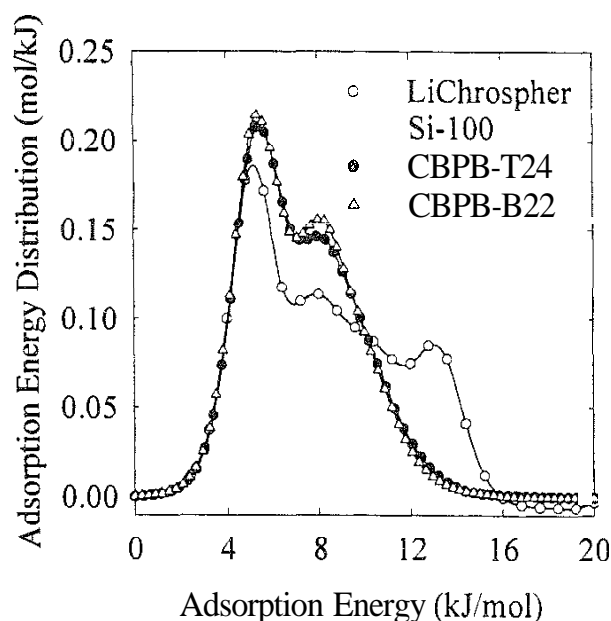


FIG. 6 Comparison of adsorption energy distributions for unmodified LiChrospher Si-100 silica gel and physically coated (CBPB-T24) as well as chemically bonded (CBPB-B22) samples with similar loadings of CBPB. (Data taken from Ref. 77.)

material, which corresponds to a surface coverage of $2.45 \mu\text{mol}/\text{m}^2$. Only a minor further decrease in the number of high energy sites was noted when the surface coverage was increased to $6.58 \mu\text{mol}/\text{m}^2$ (46 wt%). This indicated that the surface coverage of $2.45 \mu\text{mol}/\text{m}^2$ allowed a layer of coated CBPB to form on most of the silica surface, which is also supported by the fact that the sample with chemically bonded CBPB ligands had a similar loading and consequently the similar surface coverage ($2.15 \mu\text{mol}/\text{m}^2$) as that for the CBPB-T24 sample. The disappearance of high energy adsorption sites was explained as an effect of shielding (in the case of physical coating) or of removal and shielding (in the case of chemical modification) of surface silanols, which decreased their population accessible to nitrogen molecules [77]. It should be noted that even for the highest coating and/or chemical bonding levels, there was an appreciable population of 10–12 kJ/mol adsorption sites, which were not present on AEDs for silicas modified by octyldimethylsilyl groups with long aliphatic chains [71], as will be discussed later. Therefore, it was concluded that these sites are polar or aromatic segments of the organic modifier, such as ester, ether, or nitrile groups and benzene rings. However, it was impossible to perform a further identification, since, for example, the presence or absence of the nitrile group in the structure of organic modifiers did not result in any noticeable changes of the adsorption properties of the modified surface [77].

To further examine the usefulness of the physical coating procedure, a sample of MCM-41 material with pore size of about 3.8 nm was modified by introducing several different amounts of CBPB [46]. It was shown that in this case the physical coating procedure was not suitable for surface modification, probably because of the relatively large size of the organic modifier (CBPB) in comparison to the pore diameter of the MCM-41 material used, which did not allow for

successful deposition of the organic modifier inside the pores. After the coating procedure, samples exhibited a significant lowering of the primary mesopore volume, but at the same time the pore diameter and the surface properties did not change significantly. As can be seen in Fig. 7, the AED for the 36% CBPB MCM-41 is much closer to the AED for the unmodified MCM-41 than to the AED for the CBPB-BT33 sample (the surface of the latter is expected to be completely or almost completely covered by CBPB). It was concluded [46] that coating of the MCM-41 material under study resulted in a very nonuniform surface coverage of CBPB and that the organic modifier filled or blocked some of the pores, making them inaccessible to nitrogen adsorbate. As will be discussed later, the chemical bonding procedures have the potential to overcome the shortcomings of physical coating procedures, providing a means of modifying the surface of primary mesopores by bulky ligands without pore blocking.

An interesting problem was to assess the fraction of the surface covered by the physically coated organic modifier [46]. To do that, a patchwise model of a modified surface was employed. A part of the surface of the MCM-41 material that was not covered by the organic species was assumed to exhibit the same adsorption properties as the unmodified MCM-41, and the surface of the organic modifier (CBPB) coated on the silica surface was assumed to exhibit the same adsorption properties as pure CBPB. The latter is nonporous and is expected to have a very small surface area, so a direct measurement of its nitrogen adsorption was not attempted. Instead, adsorption data for the previously studied CBPB-BT33 silica gel chemically bonded and subsequently coated with high loading of the organic modifier were used. To test our model, the fitting procedure was applied to the

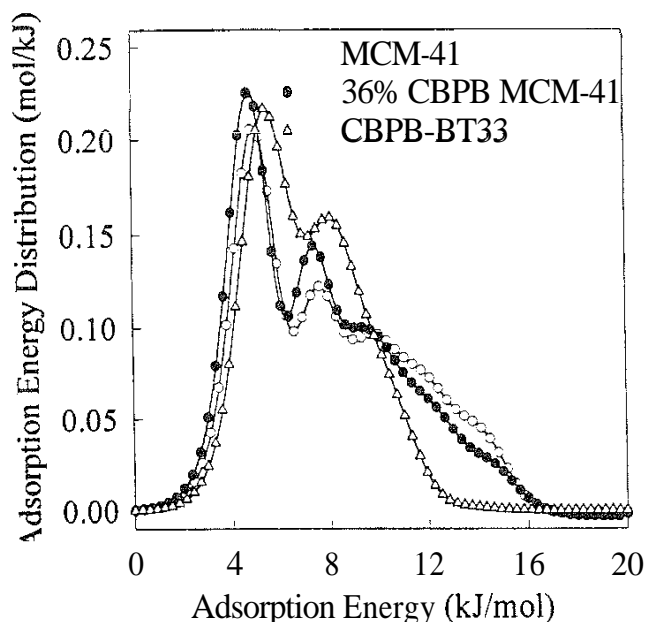


FIG. 7 Comparison of adsorption energy distributions for an unmodified MCM-41 material, MCM-41 sample coated with CBPB, and a silica gel sample that was chemically bonded and subsequently physically coated with CBPB. (Data from Refs. 46 and 77.)

LiChrospher Si-100 samples with physically coated CBPB that were described earlier. Calculations were performed using adsorption isotherm data for relative pressures below 0.1, and it was shown that the low pressure data for the physically coated samples can be fitted by a proper combination of data for the unmodified sample and the CBPB-BT33 (see Fig. 8). The results indicated that in the case of the samples with CBPB surface coverages (estimated from the elemental analysis) of $0.67\mu\text{mol}/\text{m}^2$ (CBPB-T8), $0.96\mu\text{mol}/\text{m}^2$ (CBPB-T11), and $2.45\mu\text{mol}/\text{m}^2$ (CBPB-T24), 37%, 52%, and 82%, respectively, of the surface was covered with CBPB. To reproduce these surface coverages on the basis of calculated percentages, an assumption about the monolayer surface coverage of CBPB must be made. When one assumes that the latter is equal to or smaller than about $1.83\mu\text{mol}/\text{m}^2$, surface coverages for CBPB-T8 and CBPB-T11 samples can readily be reproduced, and only in the case of CBPB-T24 would much lower surface coverage be obtained on the basis of adsorption data. This result can easily be explained, since it was already shown that the coverage of CBPB on the surface of CBPB-T24 is expected to be quite nonuniform and some CBPB molecules may lie on top of other CBPB molecules or fill smaller pores present in the sample, leaving some uncovered silica surface, even though potentially the amount of CBPB is enough to cover the entire surface of the support. In principle, calculations of the surface coverage on the basis of adsorption data make it possible to obtain the fractions of bare and covered silica surface. This provides the way to estimate the minimum surface coverage of CBPB molecules (i.e., the number of molecules forming a monolayer) that would result in the observed low pressure adsorption properties of the material. Consequently, one can compare the total surface coverage obtained from elemental

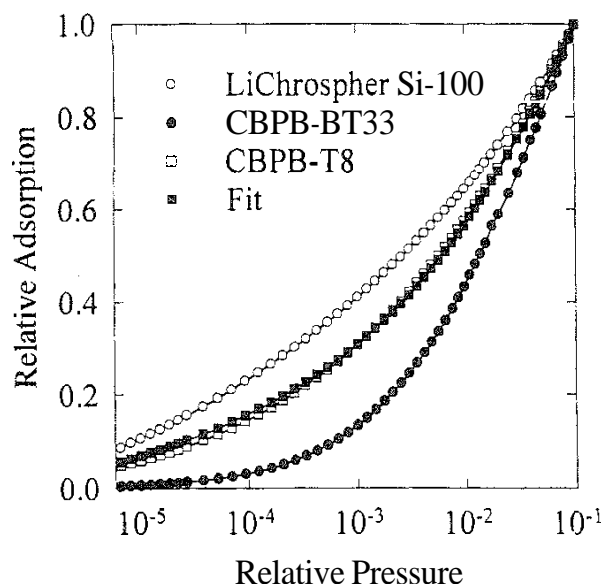


FIG. 8 Results of the fitting of low pressure adsorption data for a physically coated CBPB-T8 silica gel sample with a relatively low loading of CBPB using low pressure data for the unmodified silica gel and the modified sample (CBPB-BT33) with large amounts of CBPB chemically bonded and physically coated. Data for CBPB-BT33 are assumed to represent adsorption on pure CBPB. (Data from Refs. 46 and 77.)

analysis or other methods with the surface coverage assessed from adsorption data in order to estimate whether the coverage of physically coated molecules on the surface is uniform.

Since the fitting procedure was found to provide very reasonable results for modified silica gels, it was interesting to use it in studies of the MCM-41 materials coated with CBPB [46]. It was shown that the low pressure data for the modified samples can be well fitted by data for the unmodified MCM-41 and the selected reference material covered with CBPB (i.e., CBPB-BT33). The results obtained by fitting indicated that the surface coverages of CBPB molecules did not vary significantly for 11%, 28%, and 36% loadings of CBPB and were estimated to be less than or equal to 0.32, 0.40 and 0.48 $\mu\text{mol}/\text{m}^2$, respectively. Total surface coverages of CBPB estimated from the elemental analysis were 0.27, 0.86, and 1.1 $\mu\text{mol}/\text{m}^2$, respectively, which suggests a very nonuniform coverage of CBPB for the materials with higher CBPB loadings. The relatively small increase in surface coverage with a significant increase in the CBPB loading that was estimated from the adsorption data paralleled the observed changes in the primary mesopore size of the materials, which were also small and suggested that a limited amount of CBPB actually formed a monolayer on the surface of the primary mesopores. Therefore, it appears that the organic modifier either completely filled some of the pores or blocked them and/or deposited on the external surface area of the material. It can be concluded that low pressure nitrogen adsorption data can be useful for a qualitative estimation of the coverage of organic species on the surface of mesoporous silicas. To our best knowledge, similar estimations of the coverage of surface species using adsorption of nonpolar gas molecules have not been reported before.

C. Conventional Mesoporous Silicas with Bonded Organosilanes

As was discussed above, studies of conventional and ordered mesoporous silicas with coated organic species allowed us to examine the effects of surface coverage on the adsorption properties of modified materials. Another interesting problem was to investigate how the structure of organic surface groups influences low pressure nitrogen adsorption. First, a study of several silica gels with chemically bonded octyldimethylsilyl ligands was undertaken [71]. Surface coverages of octyl groups were in the range of 3.4–4.1 $\mu\text{mol}/\text{m}^2$. It was found that for all of the octyl phases, low pressure nitrogen adsorption was greatly reduced in comparison to that on unmodified silica gels. Consequently, adsorption energy distributions for the modified samples did not feature adsorption energy sites above about 10 kJ/mol (see Fig. 9), which are characteristic of the silica surface (Figs. 2, 6, 7). The high energy adsorption sites were hypothesized to be isolated silanol groups, and it was concluded that most of these sites reacted during the modification procedure. It was also suggested that nitrogen adsorption energy for silanols hydrogen-bonded with one another or with water molecules, for siloxane bridges, as well as for octyl ligands lies in the range from about 3 to 10 kJ/mol, but further identification appeared to be difficult. As will be shown in Sec. III.D, there is evidence [59] that for somewhat lower surface coverages of bonded ligands (2.5–3 $\mu\text{mol}/\text{m}^2$) there are still high energy adsorption sites present on the silica surface. and, depending on the size of the bonded ligands, they may be accessible or inaccessible

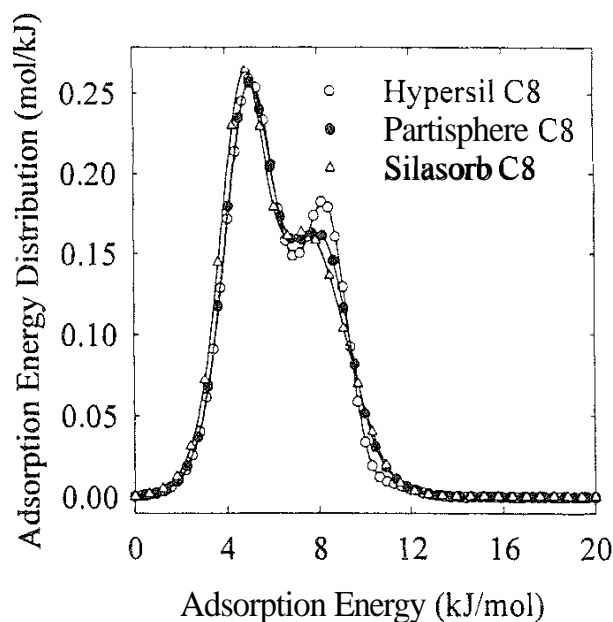


FIG. 9 Adsorption energy distributions for silica gel samples with bonded octyldimethylsilyl ligands. (Data from Ref. 71.)

to nitrogen molecules. Consequently, the lack of high energy sites on the AEDs for the octyl phases under study does not necessarily indicate the removal of these sites from the surface, as they could be effectively shielded by the long-chain alkyl groups.

In another study [76], low pressure adsorption properties of polymeric amine and amide bonded phases were examined. It was shown that the introduction of relatively small polymeric 3-aminopropylsilyl groups led to a decrease in the number of high adsorption energy sites in the range of 10–16 kJ/mol. A slight further decrease in the number of these sites was observed when the amine ligands were converted to amides with phenyl, cyanophenyl, acetylphenyl, and octyl groups, especially for the latter. The similarity of AEDs for phenylamide and cyanophenylamide bonded phases confirmed previous findings [77] that it is impossible to detect the presence of nitrile groups attached to aromatic rings of the ligands, which indicates that these two groups exhibit essentially the same interaction energies with respect to nitrogen molecules. However, it was possible to distinguish between adsorption properties of arylamide and alkylamide bonded phases, which is also consistent with the previous studies discussed in Secs. III.A and III.B [71,77].

It was shown earlier that polar parts of organic modifiers gave rise to adsorption energy sites with energies up to about 12 kJ/mol. However, the polymeric bonded phases exhibited adsorption sites with energies up to about 15 kJ/mol. One can expect that the latter sites are silanol groups present in the structure of the bonded phase due to hydrolysis of side alkoxy groups and/or on the silica surface. This idea was supported by the examination of the polymeric octyl phase [76], which exhibited a much smaller population of adsorption sites between 10 and 13 kJ/mol but showed a pronounced peak at about 13 kJ/mol. Since octyl chains interact with

nitrogen with adsorption energies below about 10 kJ/mol, it was concluded that the AED peak at 13 kJ/mol can be attributed to the presence of silanol groups accessible to nitrogen probe molecules. Moreover, these results confirmed that polar parts of organic modifiers give rise to adsorption energies in the range from about 10 to 12 kJ/mol.

D. Ordered Mesoporous Silicas with Bonded Organosilanes

Although it is possible to study pore size changes resulting from the modification of conventional mesoporous silicas, as was shown in Sec. III.B, such changes are much easier to analyze in the case of ordered mesoporous silicas due to their narrow pore size distribution and relatively small mesopore sizes. Moreover, there has recently been a significant and rapidly growing interest in studies of organic-modified ordered mesoporous materials [30,41–52,59]. It was therefore interesting to investigate the surface modification of a good quality large-pore MCM-41 material via chemical bonding of trimethylsilyl (TMS), butyldimethylsilyl (BDMS), and octyldimethylsilyl (ODMS) monomeric ligands and polymeric 3-aminopropyl (APS-P), hexanoyl-3-aminopropyl (HAPS-P), and octyl (OS-P) phases [59]. The obtained surface coverages were in the range of 2.5–3 $\mu\text{mol}/\text{m}^2$. It was shown that the increase in the size of bonded ligands led to a systematic shift of the step of capillary condensation in primary mesopores toward low pressures (Fig. 10). The overall shape of the adsorption isotherm remained unchanged, showing that the modification procedure did not change the structure of the ordered mesoporous support. Pore size distributions (PSDs) for unmodified MCM-41 and selected modified materials (Fig. 11) indicated that the modification procedures

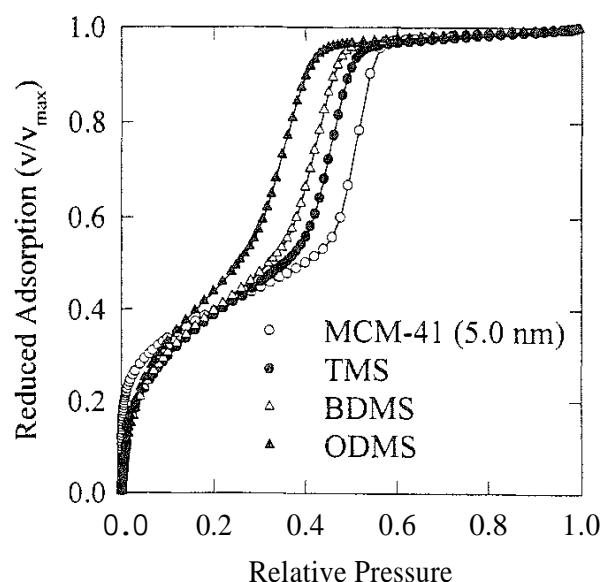


FIG. 10 Comparison of nitrogen adsorption isotherms on a large-pore MCM-41 with pore size of 5 nm, unmodified and chemically bonded with trimethylsilyl (TMS), butyldimethylsilyl (BDMS), and octyldimethylsilyl (ODMS) ligands. Adsorbed amounts for the materials were divided by the maximum adsorbed amount at a relative pressure of about 0.995. (Data from Ref. 59.)

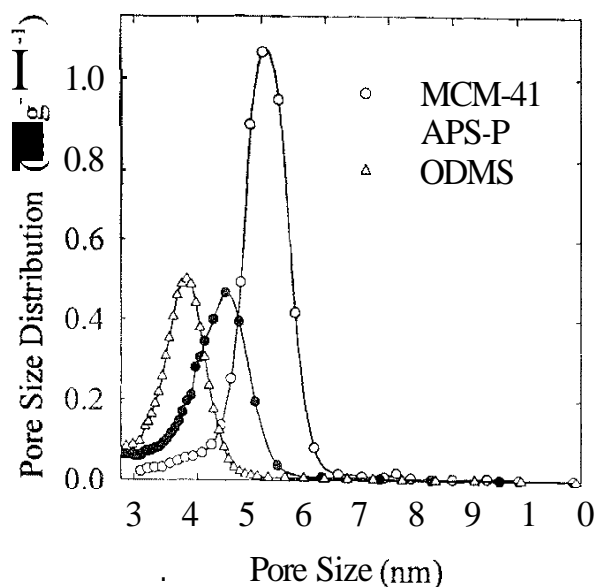


FIG. 11 Pore size distributions calculated from adsorption isotherms using the BJH method with Eqs. (3) and (4) for an unmodified large-pore MCM-41 and chemically bonded materials with polymeric 3-aminopropylsilyl (APS-P) and monomeric octyldimethylsilyl (ODMS) ligands. (Data from Ref. 59.)

used markedly decreased the pore size of the material but did not lead to an appreciable broadening of the PSD. It was shown that the increase in the size of bonded ligands resulted in a gradual decrease in the pore size. For example, the initial pore size of the support (5.0 nm) decreased to 4.5, 4.3, and 3.8 nm after modification with TMS, BDMS, and ODMS ligands, respectively. Moreover, there was good agreement between the pore size changes in the case of different ligands of similar sizes. For instance, the pore diameters of the materials with monomeric and polymeric octyl phases were 3.8 and 4.0 nm, respectively. Pore sizes of butyl and aminopropyl phases of similar organic chain length but different functionality were also very similar (4.3 and 4.4 nm, respectively). It was concluded that when reproducible surface coverages of bonded ligands can be achieved, it is relatively easy to predict the pore size of the modified materials on the basis of the pore diameter of the support and the size of the ligand. Such predictions can be based on the data, which were presented above and discussed in detail elsewhere [59].

Another interesting problem was to monitor changes in the surface properties of ordered mesoporous silicas caused by attachment of organic ligands. As can be seen from the linearity of its a_p plot, the unmodified MCM-41 (Fig. 12) exhibits surface properties typical of mesoporous silicas. The modifications via bonding of organo-silanes led to a decrease in the low pressure adsorption, which manifested itself in downward bends of the comparative plots. As expected, these deviations from linearity were especially pronounced for octyl bonded phases. Figure 13 shows adsorption energy distributions for selected modified materials. In comparison with the AED for the bare MCM-41 material, the AED for the 3-aminopropyl polymeric phase exhibited a smaller number of higher energy sites in the range

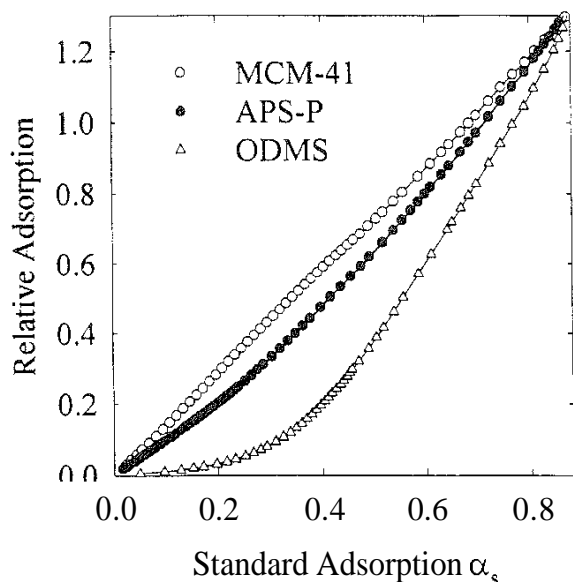


FIG. 12 High resolution a_r plots for an unmodified large-pore MCM-41 material and samples with chemically bonded polymeric 3-aminopropylsilyl (APS-P) and monomeric octyldimethylsilyl (ODMS) ligands. (Data from Ref. 59.)

10–16 kJ/mol, in agreement with previous studies reviewed in Sec. III.C. The comparison of AEDs for monomeric (ODMS) and polymeric (OS-P) octyl bonded phases indicated that in the case of the latter a small number of high energy adsorption sites are still accessible to nitrogen adsorbate. It should also be noted that the TMS MCM-41 had a significant number of high energy adsorption sites at

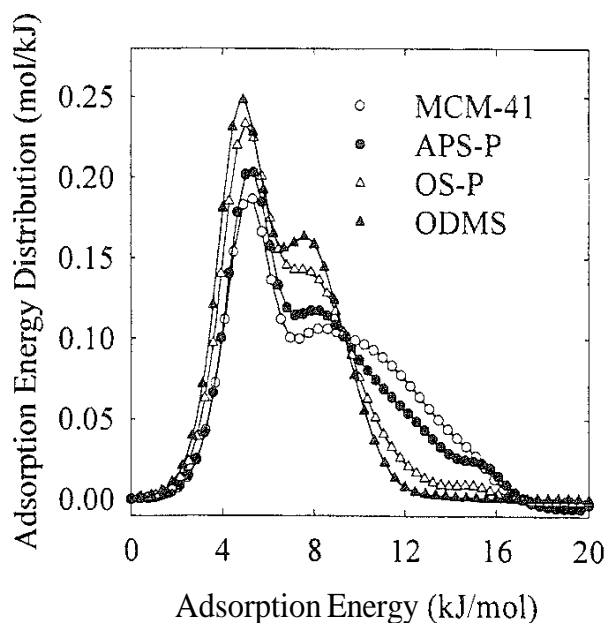


FIG. 13 Adsorption energy distributions for an unmodified large-pore MCM-41 material and samples modified with chemically bonded polymeric 3-aminopropylsilyl (APS-P) and octylsilyl (OS-P) ligands as well as monomeric octyldimethylsilyl (ODMS) groups. (Data from Ref. 59.)

11–16 kJ/mol. In contrast, only a small population of these sites were observed for BDMS and they were not present on the AED for ODMS MCM-41 (see Fig. 13). The surface coverage of the bonded groups was shown to slightly decrease with an increase in the size of bonded ligands. Consequently, the larger the size of the bonded groups, the fewer silanols had to react during the modification. This leads to the conclusion that the number of residual surface silanols is probably the greatest for the ODMS MCM-41 among the three materials considered. Since silanols are expected to be high energy adsorption sites with respect to nitrogen, one can conclude that the increase in the size of bonded ligands decreases the accessibility of nitrogen to sites on the silica surface, and for a sufficiently large surface coverage and size of bonded groups, the silica surface may become inaccessible to nitrogen adsorbate.

IV. CONCLUSIONS AND FUTURE RESEARCH PERSPECTIVES

The results presented here demonstrate the great usefulness of nitrogen adsorption measurements for the characterization of unmodified and modified mesoporous silicas. High pressure adsorption data allow for a detailed characterization of mesoporous structures of materials, providing their surface areas and pore size distributions. Low pressure measurements provide an opportunity to study the surface properties of materials and to monitor changes in these properties that result from surface modifications. For instance, it is possible to attribute the appearance of adsorption sites of certain energies in the adsorption energy distribution to the presence of some types of surface groups such as silanols, aliphatic chains, or aromatic or polar segments of organic ligands. Low pressure data can also be used to estimate the surface coverage of organic species on the silica surface. Therefore, nitrogen adsorption measurements carried out over a wide range of pressures make it possible to characterize both surface and structural properties of modified mesoporous silicas.

However, further studies are needed to improve our understanding of the relation between the adsorption properties of modified mesoporous silicas and their structure and surface functionality. First, additional studies of modified materials with different functional groups would be desirable to gain additional insight about the types of surface groups that can be detected and distinguished from one another by nitrogen probe molecules. Second, other nonpolar or weakly polar probe molecules need to be examined in order to assess their applicability and sensitivity to details of the surface, and it is very likely that some of them will exhibit properties very useful for surface characterization. Third, it is important to improve methods of pore size analysis. New approaches based on studies of model adsorbents with well-defined structures (e.g., MCM-41) appear to be promising and successful, but they require further refinement to improve their accuracy for materials with different pore geometries and surface properties. Finally, the currently proposed analysis of the effects of the pore structure and surface functionality on adsorption properties of mesoporous materials is relatively easy due to the possibility of separating these effects. Namely, high pressure adsorption data are influenced mostly by properties of the porous structure, whereas low pressure data reflect mainly the

nature of the surface. A major challenge will be to develop methods of pore structure and surface analysis suitable for materials for which separation of the surface and structural effects on adsorption properties is difficult, for instance, for modified microporous adsorbents.

REFERENCES

1. R. K. Iler, *The Chemistry of Silica*, Wiley, New York, 1979.
2. H. E. Bergna (ed.), *The Colloidal Chemistry of Silica*. American Chemical Society, Washington, DC, 1994.
3. C. J. Brinker and G. W. Scherer, *Sol-Gel Science: The Physics and Chemistry of Sol-Gel Processing*, Academic Press, San Diego, 1990.
4. E. F. Vansant, P. Van der Voort, and K. C. Vrancken. *Characterization and Modification of the Silica Surface*, Elsevier, Amsterdam, 1995.
5. K. K. Unger (ed.), *Packings and Stationary Phases in Chromatographic Techniques*, Marcel Dekker, New York, 1990.
6. R. P. W. Scott, *Silica Gel and Bonded Phases*, Wiley, Chichester, 1993.
7. M. J. Wirth, R. W. P. Fairbank, and H. Q. Fatunmbi. *Science* 275:44 (1997).
8. J. Blumel, *J. Am. Chem. Soc.* 117:2112 (1995).
9. S. V. Slavov, K. T. Chuang, and A. R. Sanger, *J. Phys. Chem.* 100:16285 (1996).
10. B. R. Guidotto, W. R. Caseri, and U. W. Suter, *Langmuir* 12:4391 (1996).
11. J. E. O'Gara, B. A. Alden, T. H. Walter. J. S. Walter, J. S. Petersen, C. L. Niederlander, and U. D. Neue, *Anal. Chem.* 57:3809 (1995).
12. A. Grabe, T. A. Michalske, and W. L. Smith, *J. Phys. Chem.* 99:4648 (1995).
13. K. C. Vrancken, P. Van der Voort, K. Possemiers, and E. F. Vansant, *J. Colloid Interface Sci.* 174:86 (1995).
14. K. C. Vrancken, L. De Coster, P. Van der Voort, P. J. Grobet, and E. F. Vansant, *J. Colloid Interface Sci.* 170:71 (1995).
15. C. P. Tripp and M. L. Hair, *Langmuir* 11:149 (1995).
16. M. L. Hair and C. P. Tripp, *Colloids Surf. A* 105:95 (1995).
17. D. J. Macquarrie and S. E. Fairfield, *J. Mater. Chem.* 7:2201 (1997).
18. T. Czajkowska, M. Jaroniec. and B. Buszewski, *J. Chromatogr. A* 728:213 (1996).
19. C. P. Jaroniec, R. K. Gilpin, and M. Jaroniec, *J. Chromatogr. A* 797:103 (1998).
20. R. K. Gilpin, M. Asif. M. Jaroniec, and S. Lin, *J. Liquid Chromatogr.* 19:2811 (1996).
21. V. Tittelbach, M. Jaroniec, and R. K. Gilpin, *J. Liquid Chromatogr.* 19:2943 (1996).
22. T. Czajkowska and M. Jaroniec, *J. Chromatogr. A* 762:147 (1997).
23. M. Jaroniec, *J. Chromatogr. A* 722:19 (1996).
24. B. Buszewski, M. Jaroniec, and R. K. Gilpin, *J. Chromatogr. A* 668:293 (1994).
25. P. Van der Voort and E. F. Vansant, *J. Liquid Chromatogr.* 19:2723 (1996).
26. T. L. Ascah, K. M. R. Kallury, C. A. Szafranski, S. D. Corman, and F. Liu, *J. Liquid Chromatogr.* 19:3049 (1996).
27. B. Buszewski, M. Jaroniec, and R. K. Gilpin, *J. Chromatogr. A* 673:11 (1994).
28. T. Yanagisawa, T. Shimizu, K. Kuroda, and C. Kato, *Bull. Chem. Soc. Jpn.* 63:988 (1990).

- T. Yanagisawa, T. Shimizu, K. Kuroda, and C. Kato, *Bull. Chem. Soc. Jpn.* 63:1535 (1990).
- J. S. Beck, J. C. Vartuli, W. J. Roth, M. E. Leonowicz, C. T. Kresge, K. D. Schmitt, C. T.-W. Chu, D. H. Olson, E. W. Sheppard, S. B. McCullen, J. B. Higgins, and J. L. Schlenker, *J. Am. Chem. Soc.* 114:10834 (1992).
- 31 C. T. Kresge, M. E. Leonowicz, W. J. Roth, J. C. Vartuli, and J. S. Beck, *Nature* 359:710 (1992).
- 32 Q. Huo, D. I. Margolese, U. Ciesla, D. G. Demuth, P. Feng, T. E. Gier, P. Sieger, A. Firouzi, B. F. Chmelka, F. Shüth, and G. D. Stucky, *Chem. Mater.* 6:1176 (1994).
- 33 Q. Huo, D. I. Margolese, and G. D. Stucky, *Chem. Mater.* 8:1147 (1996).
- 34 N. K. Raman, M. T. Anderson, and C. J. Brinker, *Chem. Mater.* 8:1682 (1996).
- 35 A. Sayari, *Stud. Surf. Sci. Catal.* 102:1 (1996).
- 36 D. Khushalani, A. Kuperman, G. A. Ozin, K. Tanaka, J. Garces, M. M. Olken, and N. Coombs, *Adv. Mater.* 7:842 (1995).
- 37 C.-F. Cheng, W. Zhou, D. H. Park, J. Klinowski, M. Hargreaves, and L. F. Gladden, *J. Chem. Soc., Faraday Trans.* 93:359 (1997).
- A Corma, Q. Kan, M. T. Navarro, J. Perez-Pariente, and F. Rey, *Chem. Mater.* 9:2123 (1997).
- 39 A. Sayari, P. Liu, M. Kruk, and M. Jaroniec, *Chem. Mater.* 9:2499 (1997).
- 40 D. Zhao, J. Feng, Q. Huo, N. Melosh, G. H. Fredrickson, B. F. Chmelka, and G. D. Stucky, *Science* 279:548 (1998).
- 41 S. L. Burkett, S. D. Sims, and S. Mann, *Chem. Commun.* 1367 (1996).
- 42 D. J. Macquarrie, *Chem. Commun.* 1961 (1996).
- 43 M. H. Lim, C. F. Blanford, and A. Stein, *J. Am. Chem. Soc.* 119:4090 (1997).
- 44 K. A. Koyano, T. Tatsumi, Y. Tanaka, and S. Nakata, *J. Phys. Chem. B* 101:9436 (1997).
- 45 X. S. Zhao, G. Q. Lu, A. K. Whittaker, G. J. Miller, and H. Y. Zhu, *J. Phys. Chem. B* 101:6525 (1997).
- 46 M. Jaroniec, M. Kruk, C. P. Jaroniec, and A. Sayari, *Adsorption*, in press.
- 47 X. Feng, G. E. Fryxell, L.-Q. Wang, A. Y. Kim, J. Liu, and K. M. Kemner, *Science* 276:923 (1997).
- 48 L. Mercier and T. J. Pinnavaia, *Adv. Mater.* 9:500 (1997).
- 49 J. Liu, X. Feng, G. E. Fryxell, L.-Q. Wang, A. Y. Kim, and M. Gong, *Adv. Mater.* 10:1 (1998).
- 50 D. Brunei, A. Cauvel, F. Fajula, and F. DiRenzo, *Stud. Surf. Sci. Catal.* 97:173 (1995).
- 51 A. Cauvel, G. Renard, and D. Brunei, *J. Org. Chem.* 62:749 (1997).
- 52 Y. V. Subba Rao, D. E. De Vos, and P. A. Jacobs, *Angew. Chem. Int. Ed. Engl.* 36:2661 (1997).
- 53 M. Kruk, M. Jaroniec, and A. Sayari, *J. Phys. Chem. B* 101:583 (1997).
- 54 M. Kruk, M. Jaroniec, R. Ryoo, and J. M. Kim, *Microporous Mater.* 12:93 (1997).
- 55 M. Kruk, M. Jaroniec, and A. Sayari, *Langmuir* 13:6267 (1997).
- 56 P. I. Ravikovitch, S. C. O. Domhnaill, A. V. Neimark, F. Schuth, and K. K. Unger, *Langmuir* 11:4765 (1995).

57. P. I. Ravikovitch, D. Wei, W. T. Chueh, G. L. Haller, and A. V. Neimark, *J. Phys. Chem. B* 101:3671 (1997).
58. M. W. Maddox, J. P. Olivier, and K. E. Gubbins, *Langmuir* 13:1737 (1997).
59. C. P. Jaroniec, M. Kruk, M. Jaroniec, and A. Sayari, *J. Phys. Chem. B*, 102:5503 (1998).
60. O. Franke, G. Schulz-Ekloff, J. Rathousky, J. Starek, and J. Zukal, *J. Chem. Soc., Chem. Commun.* 724 (1993).
61. P. T. Tanev and T. J. Pinnavaia, *Science* 267:865 (1995).
62. S. A. Bagshaw, E. Prouzet, and T. J. Pinnavaia, *Science* 269:1242 (1995).
63. R. Ryoo, J. M. Kim, C. H. Ko, and C. H. Shin, *J. Phys. Chem.* 100:17718 (1996).
64. C.-Y. Chen, H.-X. Li, and M. E. Davis, *Microporous Mater.* 2:17 (1993).
65. P. J. Branton, P. G. Hall, M. Treguer, and K. S. W. Sing, *J. Chem. Soc., Faraday Trans.* 91:2041 (1995).
66. P. J. Branton, K. S. W. Sing, and J. W. White, *J. Chem. Soc., Faraday Trans.* 93:2337 (1997).
67. P. L. Llewellyn, Y. Grillet, J. Rouquerol, C. Martin, and J.-P. Coulomb, *Surf. Sci.* 352–354:468 (1996).
68. P. J. Branton, P. H. Hall, and K. S. W. Sing, *J. Chem. Soc., Chem. Commun.* 1257 (1993).
69. M. Kruk, M. Jaroniec, and A. Sayari, *Microporous Mater.* in press.
70. Y. Bereznitski, M. Jaroniec, and M. Kruk, *J. Liquid Chromatogr.* 19:1523 (1996).
71. Y. Bereznitski, M. Jaroniec, M. Kruk, and B. Buszewski, *J. Liquid Chromatogr.* 19:2767 (1996).
72. K. S. W. Sing, D. H. Everett, R. A. W. Haul, L. Moscou, R. A. Pierotti, J. Rouquerol, and T. Siemieniewska, *Pure Appl. Chem.* 57:603 (1985).
73. J. Rouquerol, D. Avnir, C. W. Fairbridge, D. H. Everett, J. H. Hayness, N. Pernicone, J. D. F. Ramsay, K. S. W. Sing, and K. K. Unger, *Pure Appl. Chem.* 60:1739 (1994).
74. S. J. Gregg and K. S. W. Sing, *Adsorption, Surface Area and Porosity*. Academic Press, London, 1982.
75. M. Jaroniec and R. Madey, *Physical Adsorption on Heterogeneous Solids*, Elsevier, Amsterdam, 1988.
76. C. P. Jaroniec, R. K. Gilpin, and M. Jaroniec, *J. Phys. Chem. B* 101:6861 (1997).
77. M. Kruk, M. Jaroniec, R. K. Gilpin, and Y. W. Zhou, *Langmuir* 13:545 (1997).
78. C. P. Jaroniec, M. Jaroniec, and M. Kruk, *J. Chromatogr. A* 797:93 (1998).
79. M. Jaroniec, M. Kruk, and J. Choma, in *Characterization of Porous Solids IV* (B. McEnaney, T. J. Mays, J. Rouquerol, F. Rodriguez-Reinoso, K. S. W. Sing, and K. K. Unger, eds.), Royal Society of Chemistry, London, 1997, pp. 163–170.
80. H. Liu, L. Zhang, and N. A. Seaton, *J. Colloid Interface Sci.* 156:285 (1993).
81. S. Brunauer, P. H. Emmett, and E. Teller, *J. Am. Chem. Soc.* 60:309 (1938).
82. M. Jaroniec and K. Kaneko, *Langmuir* 13:6589 (1997).
83. K. Kaneko, C. Ishii, M. Ruike, and H. Kuwabara, *Carbon* 30:1075 (1992).
84. M. Jaroniec, in *Access to Nanoporous Materials* (T. J. Pinnavaia and M. F. Thorpe, eds.), Plenum, New York, 1995, pp. 255–272.
85. E. P. Barrett, L. G. Joyner, and P. P. Halenda, *J. Am. Chem. Soc.* 73:373 (1951).
86. R. F. Cracknell, K. E. Gubbins, M. Maddox, and D. Nicholson, *Acc. Chem. Res.* 28:281 (1995).

87. T. Dabadie, A. Ayrat, C. Guizard, L. Cot, and P. Lacan, *J. Mater. Chem.* 6:1789 (1996).
88. J. P. Olivier, in *Fundamentals in Adsorption* (M. D. LeVan, ed.), Kluwer, Boston, 1996, pp. 699–707.
89. M. Jaroniec and P. Brauer, *Surf. Sci. Rep.* 6:65 (1986).
90. W. Rudzinski and D. H. Everett, *Adsorption of Gases on Heterogeneous Solid Surfaces*, Academic Press, New York, 1992.
91. M. Jaroniec, in *Adsorption on New and Modified Inorganic Adsorbents* (A. Dabrowski and V. A. Tertykh, eds.), Elsevier, Amsterdam, 1996, pp. 411–433.
92. J. L. Riccardo, W. A. Steele, A. J. Ramirez Cuesta, and G. Zgrablich, *Langmuir* 13:1064 (1993).
93. W. A. Steele, *Chem. Rev.* 93:2355 (1993).
94. M. v. Szoinbathely, P. Brauer, and M. Jaroniec, *J. Comput. Chem.* 13:17 (1992).
95. M. Heuchel, M. Jaroniec, R. K. Gilpin, P. Brauer, and M. v. Szombathely, *Langmuir* 9:2537 (1993).

18

Nanodimensional Magnetic Assembly of Confined O₂

KATSUMI KANEKO Department of Chemistry, Chiba University, Chiba, Japan

- I. Introduction
- II. Solid Nanospace of Enhanced Molecular Field
- III. Magnetic Interaction of Molecular Spins
- IV. Magnetic Properties of Bulk O₂ and Two-Dimensional O₂
- V. Pore Structures and Magnetic Properties of Activated Carbon Fibers
- VI. Adsorption of O₂ in a Graphitic Nanospace
- VII. Magnetic Susceptibility of O₂ Confined in a Graphitic Nanospace
- VIII. Dependence of Magnetic Susceptibility of Confined O₂ on Pore Width
- IX. Effect of Coexistent H₂O on Magnetic Susceptibility of Confined O₂
- X. Magnetic Distinction of Weakly Interacting Molecules in Nanospace
- References

I. INTRODUCTION

The interaction energy of a simple molecule with a solid surface as it undergoes physical adsorption is quite small compared with that of chemical bonding. The physical adsorption mechanism changes according to the type of solid surface—flat or macropore surface, mesopore, or micropore [1–3]. The molecule–surface interaction increases in the order of adsorption on the flat surface, mesopore, or micropore. Adsorption on a flat or macropore surface leads to a type II adsorption isotherm, whereas adsorption on a mesopore gives type IV. An enhanced potential from opposite pore walls in the micropore is great enough to provide a

characteristic adsorption isotherm of Type I [3,4], which has a significant uptake within a low relative pressure region. Although lateral interaction between adsorbed molecules should be important, it is neglected in the well-known Brunauer–Emmett–Teller (BET) theory [5,6]. On the other hand, the so-called capillary condensation theory about adsorption on mesopores is based on lateral interaction. Capillary condensation theory presumes that the adsorbed layer is the same as the bulk liquid, that the lateral interaction is not specific but is the same as in the bulk [7,8]. Although the interaction of a molecule with a solid surface is markedly enhanced in micropores, an adsorbed layer in micropores has been believed to be identical to the bulk liquid. That is, no enhanced lateral interaction is presumed. Thus, the intermolecular interaction between physically adsorbed molecules is less understood than molecule–surface interaction [9]. Although recent computer simulation approaches have taken the lateral interaction into account using the Lennard-Jones potential, the importance of the intermolecular interaction in physical adsorption, particularly on micropores, is not sufficiently recognized [10–13]. If physical adsorption is used for controlling intermolecular interactions with the aid of various solid surfaces from flat surfaces to micropores, it should be helpful to understand special molecular behavior.

In the molecular sciences, elucidation of the structure and property of a van der Waals molecule is an important current research subject. The van der Waals molecule is unstable at room temperature, and it is quite difficult to get a concentrated system of van der Waals molecules [14,15]. There is another weakly interactive molecular complex compound, called a molecular clathrate. Usually, molecular clathrates are unstable at ambient conditions. Supercritical gas molecules such as N_2 and NO are said to tend to produce dimers in micropores [16–20]. In particular, NO molecules are adsorbed in micropores of activated carbon fiber (ACF) at ambient conditions in the form of dimers that are typical van der Waals molecules. Water molecules form an organized structure in the carbon micropore [21]. The formation of NO hydrate and CH_4 hydrate in micropores at a subatmospheric pressure has also been suggested [22,23]. Hence micropores accelerate the formation of van der Waals molecules or molecular clathrate hydrates. In the case of micropores that have a deep potential well, many molecules tend to be adsorbed in the deep potential well. Molecules confined in micropores should form the best dense structure according to the micropore geometry. Therefore, we can control the intermolecular structure with micropores even at supercritical conditions of the bulk gas. The molecular field of micropores can stabilize van der Waals molecules and molecular clathrates.

Even a weak intermolecular interaction is much stronger than a spin–spin interaction. A spin–spin interaction is so weak that it is sensitively affected by an intermolecular interaction. Therefore, magnetic measurement is a powerful method for the study of the weakly bound structure between molecules. Furthermore, in graphitic microporous carbons such as ACFs that are mainly composed of diamagnetic [23,24], the electronic state of O_2 is triplet, leading to paramagnetism in the gas phase. Hence, the magnetic properties of O_2 confined in micropores of ACF should provide essentially important information on the intermolecular structure of simple molecules [25,26]. In particular, we can compare the intermolecular structure of O_2 in a micropore with the intermolecular structure of O_2 on a graphite surface

which has been actively studied [27]. The formation of a linear dimer of O₂ in the cylindrical pore was suggested by magnetic susceptibility measurements at temperatures above 77 K [28]. Understanding the O₂ molecular assembly in a graphitic micropore should be helpful to the understanding of the specific role of O₂ in biological activities and new separation technologies.

II. SOLID NANOSPACE OF ENHANCED MOLECULAR FIELD

The interaction $\Phi(r)$ between a molecule (f) and a surface atom (s) as a function of the distance r between them can be expressed by the Lennard-Jones potential,

$$\Phi(r) = 4\varepsilon_{sf}[(\sigma_{sf}/r)^{12} - (\sigma_{sf}/r)^6] \quad (1)$$

where ε_{sf} and σ_{sf} are the well depth and effective diameter for the molecule-graphitic carbon atom complex. These cross parameters are calculated according to the Lorentz-Berthelot rules, $\varepsilon_{sf} = (\varepsilon_{ss}\varepsilon_{ff})^{1/2}$; $\sigma_{ss} = (\sigma_{ss} + \sigma_{ff})/2$. Here, $(\sigma_{ss}, \varepsilon_{ss})$ and $(\sigma_{ff}, \varepsilon_{ff})$ are the Lennard-Jones parameters for a surface atom and a molecule, respectively. The interaction potential $\Phi(z)$ for a molecule and a single graphite slab is given by the Steele 10-4-3 potential [29],

$$\Phi(z) = 2\pi\rho_C\varepsilon_{sf}\sigma_{sf}^2\Delta\left[\frac{2}{5}\left(\frac{\sigma_{sf}}{z}\right)^{10} - \left(\frac{\sigma_{sf}}{z}\right)^4 - \frac{\sigma_{sf}^4}{3\Delta(0.61\Delta + z)^3}\right] \quad (2)$$

where z is the vertical distance of the molecule above the surface, Δ is the separation between graphite layers ($= 0.335$ nm), and ρ_C is the number density of carbon atoms in a graphite layer ($= 114/\text{nm}^3$). As the micropores of activated carbon can be approximated by the slit spaces between the predominant basal planes of nano-graphitic units, the whole interaction potential $\Phi(z)_{\text{pore}}$ of a molecule with the micropore of an intergraphite surface distance H_p can be given by the equation

$$\Phi(z)_{\text{pore}} = \Phi(z) + \Phi(H_p - z) \quad (3)$$

Consequently, we can evaluate the potential profile of the molecule adsorbed in the graphitic micropore. Here H_p is not the effective pore width w determined by the adsorption experiment. The difference between H_p and w is a function of σ_{sf} and σ_{ff} [30]:

$$H_p - w = 0.85\sigma_{sf} - \sigma_{ff} \quad (4)$$

In the case of the O₂-graphite slit pore system, w is equal to $H_p - 0.26$ nm. Figure 1 shows potential profiles of an O₂ molecule in a slit-shaped graphite pore as a function of w using the one-center approximation. Here, the molecular position in Fig. 1 is expressed by the distance z from the central plane between two surfaces. The solid line shows the potential profile for the single graphite surface. The potential becomes deeper as w decreases. Thus, micropores have stronger adsorption fields than flat or mesoporous graphitic surfaces. However, the potential minimum for $w = 1$ nm is still 1500 K, which is not enough to induce predominant adsorption of O₂ at ambient conditions.

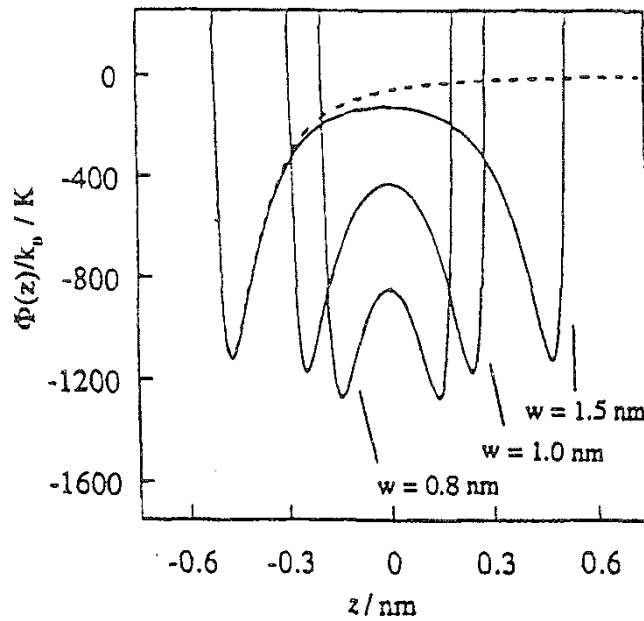


FIG. 1 Interaction potential profiles of O_2 with the graphitic slit pores of different widths. Here z denotes the vertical distance from the midplane of two graphitic surfaces. The broken line indicates the profile for the single surface.

We can estimate the effective pressure from the potential profile; molecules confined in a slit pore of 1 nm width are presumed to be exposed to the high pressure of 100 MPa. Therefore, the graphitic micropore can offer a high pressure field from the macroscopic view [18].

III. MAGNETIC INTERACTION OF MOLECULAR SPINS

When a homogeneous magnetic field H is applied to the sample, the magnetization M is induced.

$$M = \chi H \quad (5)$$

Here χ is the magnetic susceptibility. When the magnetic field is weak enough, χ is independent of H . In molecular magnetism the cgs emu system has been used instead of the SI system. The volume magnetic susceptibility is a dimensionless quantity traditionally expressed in emu/cm^3 ; the dimension of the electromagnetic unit (emu) is formally the cubic centimeter. The specific magnetic susceptibility (emu/g), which is obtained by dividing the volumetric magnetic susceptibility by the density, is often used. χ is the sum of the diamagnetic (χ^d) and paramagnetic (χ^p) susceptibilities.

$$\chi = \chi^d + \chi^p \quad (6)$$

The χ^d value is negative and χ^p is positive. When χ^d dominates, the sample is said to be diamagnetic; it is repelled by the magnetic field. When χ^p is the leading contribution, the sample is paramagnetic: it is attracted by the applied field.

Diamagnetism is an underlying property of matter. It is always present, even when it is masked by paramagnetism. Diamagnetism is due to the interaction of the magnetic field with the motion of electrons in their orbits. χ^d is independent of the temperature and the strength of the applied field. The diamagnetic susceptibility of a molecular compound can be approximated by the additive form of the constitutive corrections (Pascal's law). The additive method may be sufficient to estimate the diamagnetic contribution for paramagnetic compounds of low molecular weight. The observed susceptibilities are corrected for the diamagnetic contribution for a discussion of paramagnetic susceptibility χ^p .

Paramagnetic susceptibility characterizes the way in which an applied magnetic field H interacts with the angular momenta associated with the thermally populated states of a molecule. The magnetization is related to the energy variation under an external magnetic field.

$$M = -\frac{\partial E}{\partial H} \quad (7)$$

A molecule has a discontinuous energy E_n ($n = 1, 2, 3, \dots$) in the presence of a magnetic field. For each energy level we can define a microscopic magnetization μ_n as

$$\mu_n = -\frac{\partial E_n}{\partial H} \quad (8)$$

The macroscopic magnetization M is then obtained by summation of the microscopic magnetizations μ_n using the Boltzmann distribution.

$$M = \frac{N \sum_n (-\partial E_n / \partial H) \exp[-E_n / k_B T]}{\sum_n \exp[-E_n / k_B T]} \quad (9)$$

where T and k_B are the temperature and Boltzmann constant, respectively. This combines macroscopic and microscopic quantities. However, the application of the general equation (9) is difficult without the knowledge on $E_n = f(H)$. Van Vleck introduced the approximation

$$E = E_n^{(0)} + E_n^{(1)} H + E_n^{(2)} H^2 \quad (10)$$

where $E_n^{(0)}$ is the energy level n in zero magnetic field. $E_n^{(1)}$ and $E_n^{(2)}$ are called the first- and second-order Zeeman coefficients respectively. When $H/kT < 1$,

$$\exp\left[\frac{-E_n}{k_B T}\right] = \exp\left[\frac{E_n^{(0)}}{k_B T}\right] \left(1 - \frac{E_n^{(1)} H}{k_B T}\right) \quad (11)$$

When all energies E_n are linear in H , these approximations yield the equation

$$\chi = \frac{N \sum_n (E_n^{(1)})^2 \exp[-E_n^{(0)} / k_B T]}{k_B T \sum_n \exp[-E_n^{(0)} / k_B T]} \quad (12)$$

Here $E_n^{(1)}$ and the Zeeman operator \mathbf{H}_{ZE} are given by

$$E_n^{(1)} = \langle n | \mathbf{H}_{ZE} | n \rangle \quad (13)$$

$$\mathbf{H}_{ZE} = \beta_B \sum (\mathbf{I}_i + g_e \mathbf{s}_i) \cdot \mathbf{H} \quad (14)$$

where \mathbf{I}_i is the orbital momentum of electron i and \mathbf{s}_i is the spin momentum of the same electron. g_e is the g factor of the free electron ($= 2.0023$), and β_B is the Bohr magneton ($\beta_B = eh/4\pi m_e c = 0.9174 \times 10^{-20}$ erg gauss).

We assume the simplest situation in molecular magnetism of the molecule of the ground state $^{2S+1}\Gamma$ (Γ : irreducible representation). When the field is applied, the energies of the $2S+1$ Zeeman components are given by the equation

$$E_n = M_S g \beta_B H, \quad M_S = -S, -S+1, \dots, S-1, S \quad (15)$$

If the first excited states are assumed to be too high in energy to couple with the ground state, g is in principle isotropic and equal to g_e . As E_n is linear in H , the above Van Vleck formula [Eq. (12)] with $E_n^{(0)} = 0$ can be used.

$$E_n^{(1)} = M_S g \beta_B H, \quad M_S = -S, -S+1, \dots, S-1, S \quad (16)$$

which leads to

$$\chi = \frac{N_{Av} g^2 \beta_B^2 S(S+1)}{3k_B T} \quad (17)$$

Here N_{Av} is Avogadro's number. Thus the magnetic susceptibility varies as C/T , the constant C depending on the spin multiplicity of the ground state. This is the Curie law, which describes the representative paramagnetism of mutually isolated spins. In the cgs system, $N_{Av} \beta_B^2 / 3k_B = 0.12505$.

In real solid-state or molecular magnetic species, spins are not perfectly free. Hence the Curie law is modified to account for weak intermolecular interactions using the assumption that the molecular field approximation of a perturbation is added to the Zeeman term. This perturbation takes the form $-z_m \mathbf{J} \langle S_z \rangle \mathbf{S}_z$, where $\langle S_z \rangle$ is the mean value of the S_z component of the spin operator. \mathbf{J} is the interaction parameter between two nearest-neighbor magnetic species, and Z_m is the number of nearest neighbors around a given magnetic molecule. When \mathbf{J} is positive or negative, the intermolecular interaction is said to be ferromagnetic or antiferromagnetic, respectively. The neighboring spins tend to align in a parallel fashion in the case of the ferromagnetic interaction, while they tend to align in an antiparallel fashion in the antiferromagnetic interaction. The total spin Hamiltonian is

$$\mathbf{H} = g \beta_B \mathbf{S}_z \cdot \mathbf{H} - z \mathbf{J} \langle S_z \rangle \mathbf{S}_z \quad (18)$$

where the magnetic field is assumed to be along the z direction and the \mathbf{g} tensor is assumed to be isotropic. The eigenvalues $E(S, M_S)$ are given by

$$E(S, M_S) = M_S (g \beta_B H - z \mathbf{J} \langle S_z \rangle) \quad (19)$$

$\langle S_z \rangle$ is given by the Boltzmann distribution law and is expressed as

$$\langle S_z \rangle = - \frac{S(S+1) g \beta_B H}{3k_B T - z \mathbf{J} S(S+1)} \quad (20)$$

$\langle S_z \rangle$ is negative because the Zeeman components with negative M_S are more populated than those with positive M_S . M may be expressed as

$$M = -N_{\text{Av}} g \beta_B \langle S_z \rangle \quad (21)$$

Hence **7** can be derived using $\chi = \partial M / \partial H$.

$$\chi = \frac{N_{\text{Av}} g^2 \beta_B^2 S(S+1)}{3k_B T - zJS(S+1)} \quad (22)$$

χ is rewritten as

$$\chi = C / (T - \Theta) \quad (23)$$

This is the well-known Curie–Weiss law. C is the Curie constant, and Θ is the Weiss constant defined by $\Theta = zJS(S+1)/3k_B$ [31–34].

A plot of $\chi^{-1} = f(T)$ for a system obeying the Curie–Weiss law gives a straight line with a slope of C^{-1} . The intercept with the T axis yields both the sign and the value of Θ . In the framework of this model, a positive Θ indicates ferromagnetic interactions and negative Θ indicates antiferromagnetic interactions. Hence the χ^{-1} vs. T plot can determine the sort of magnetic interaction. In the case of ferromagnetic interactions ($\Theta > 0$), the Curie–Weiss law is limited to the temperature range $T > \Theta$. Accordingly, if we use a paramagnetic probe molecule such as an O_2 molecule, the low temperature magnetic susceptibility measurement can provide an essential information on the intermolecular states of confined molecules using this analysis.

IV. MAGNETIC PROPERTIES OF BULK O_2 AND TWO-DIMENSIONAL O_2

The ground state of an O_2 molecule is the triplet ($^3\Sigma_g^-$), and therefore O_2 gas shows the representative paramagnetism. The effective spin concentration and Weiss constant of bulk O_2 gas are 1.5×10^{22} spins/g and 0 K. O_2 gas liquefies at 90.2 K, and the liquid solidifies at 54.4 K. The solid oxygen has three polymorphs: α ($T < 23.9$ K), β ($23.9 < T < 43.6$ K), and γ ($43.8 \text{ K} < T < 54.4$ K) [35]. The magnetic properties of solid oxygen have been actively studied since the days of Kammerlingh Onnes. Solid oxygen ($s\text{-O}_2$) has two sharp magnetic transitions corresponding to α – β and β – γ crystallographic changes. Active studies [35–41] showed that the α phase ($\alpha\text{-O}_2$) is antiferromagnetic, with two-dimensional ordering. It is suggested that the β phase ($\beta\text{-O}_2$) has a "frustrated" antiferromagnetic nature [38,42]. It was indicated that the γ ($\gamma\text{-O}_2$) and liquid phases have a common feature [43]. Although $s\text{-O}_2$ is a simple elemental solid, there are still many obscure problems with respect to the properties and structures of $s\text{-O}_2$ [35].

Oxygen gas of high purity (99.99%) was sealed in a highly pure quartz tube. Its magnetic susceptibility was measured with a SQUID magnetometer system over a temperature range of 2–100 K under a magnetic field of 1 T. Figure 2 shows the temperature dependence of the magnetic susceptibility χ of condensed O_2 . The χ value in Fig. 2 was determined just after the equilibration of the measuring temperature. The χ – T relations on cooling and heating between 2 and 100 K almost coincide with each other. There are two anomalies at 23.8 and 43.8 K, which are ascribed to the well-known α – β and β – γ transitions [35].

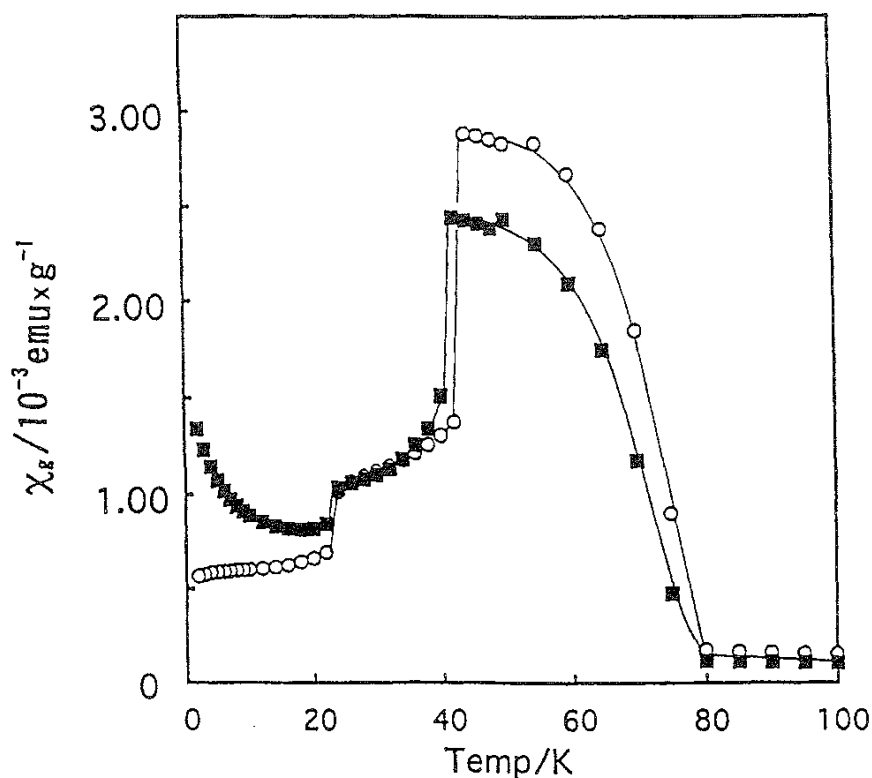


FIG. 2 Temperature dependence of the magnetic susceptibility of bulk condensed O_2 with and without coexistent H_2O . (○) O_2 , (■) $O_2 + H_2O$ (H_2O/O_2 molar ratio $R_H = 0.22$).

However, we observed a long time dependence of χ in the temperature range of 44–55 K over several hours upon cooling from liquid O_2 . Figure 3 shows the χ – T relation at equilibrium. Here the χ value at 44 K after 2.2×10^4 s is used in Fig. 3, which should be smaller than the perfect equilibrium χ value. The equilibrium χ values are smaller than nonequilibrium ones by one or two orders of magnitude (see Fig. 2). An obscure jump near 24 K and a very steep jump at 44 K are shown. The latter jump should become more pronounced if we measure it after a much longer time. The shape of χ – T relation near 44 K is close to a λ type [44]. Consequently, the well-known χ – T relation in Fig. 2 is obtained at nonequilibrium conditions.

It is presumed that both the α and β phases should form a single phase at perfect equilibrium. The obscure α – β transition at 24 K should stem from residual crystallites of the β phase due to a finite cooling rate from liquid O_2 . Marked time dependence is one of the characteristics of random magnetism, and therefore the higher temperature solid phase (> 24 K) should show random magnetism. As the χ value of the lower temperature phase (< 24 K) decreases with the decrease of temperature, it should be antiferromagnetic.

The effect of coexistent H_2O on magnetic susceptibility was examined under nonequilibrium conditions. The effect of coexistent H_2O on the χ – T relation is also shown in Fig. 2. The coexistent H_2O gives rise to a remarkable increase of χ in the α phase as temperature decreases, but it does not change that of the β phase. In contrast, χ of the γ phase becomes smaller due to the H_2O addition. The appearance of the paramagnetic behavior in the α phase is ascribed to the decoupling of

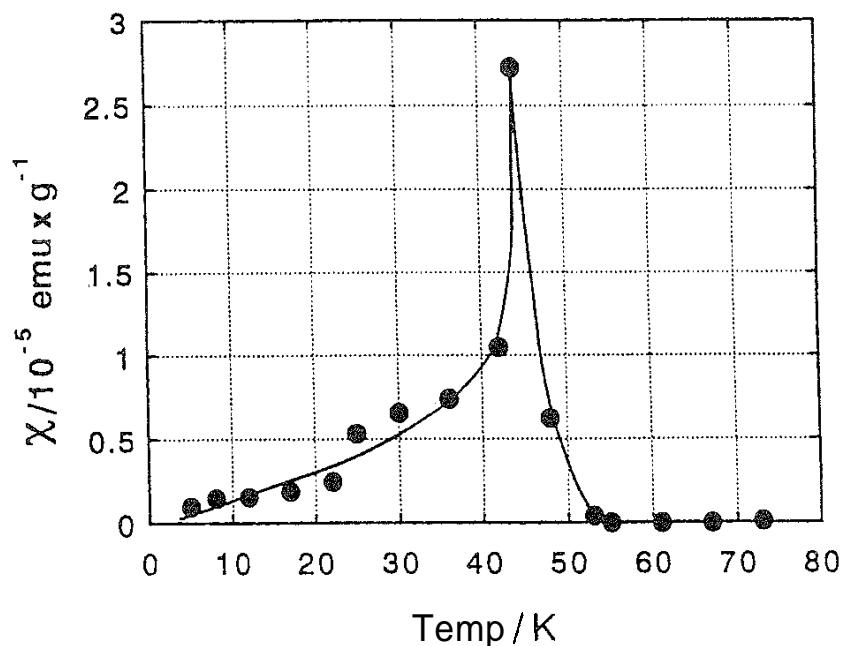


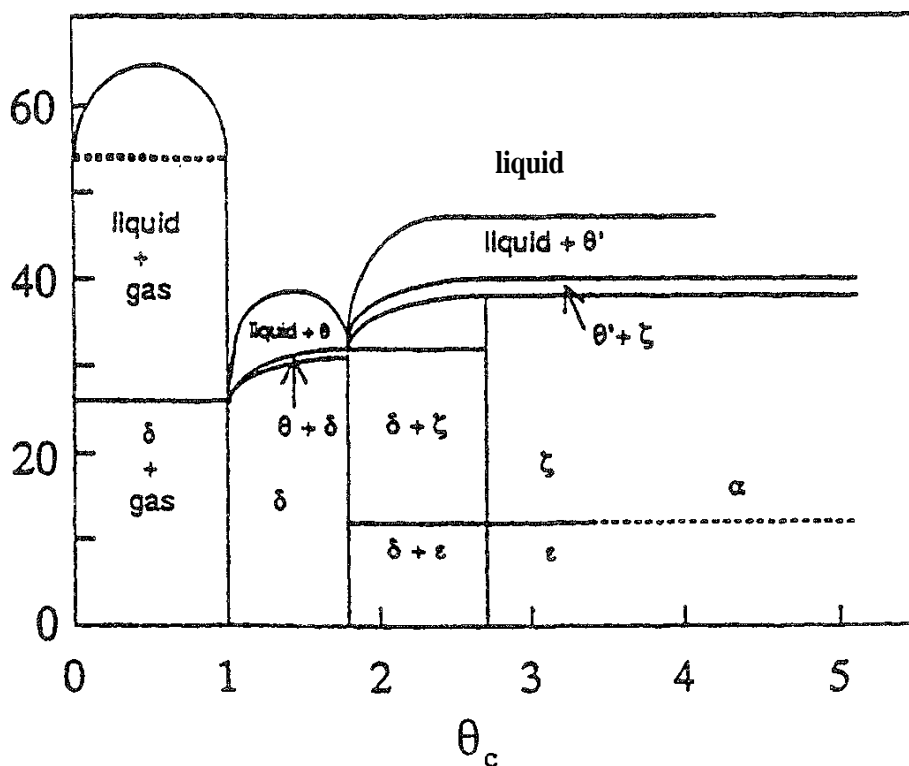
FIG. 3 Temperature dependence of the magnetic susceptibility of bulk O_2 at an equilibrium state.

spins by structural destruction. The insensitive behavior of the β phase may come from the disordered nature of the structure [35]. Jezowski et al. [45] reported that doping of N_2 or Ar in $\alpha\text{-O}_2$ had a drastic effect on the thermal conductivity, but the β phase was insensitive to the doping, which has a similarity to the effect of coexistent H_2O .

The magnetic interactions of O_2 adsorbed on the graphite surface have been extensively studied [46–49]. The mono- or bilayer of O_2 molecules adsorbed on the two-dimensional graphite surface has phases such as $\bar{5}$, ϵ , and ζ that are different from the bulk α , β , and γ phases; the phase change depends on both temperature and coverage. The α and β phases appear in the multilayer of adsorbed O_2 on the flat graphite surface. Also the ϵ to ζ phase transition leads to a magnetic anomaly. A diagram of the two-dimensional magnetic structure of O_2 on the graphite basal plane is shown in Fig. 4. This diagram was obtained at nonequilibrium conditions. In the following discussion, the magnetic properties of O_2 confined in nanospace obtained at nonequilibrium conditions are used for comparison with published results.

V. PORE STRUCTURES AND MAGNETIC PROPERTIES OF ACTIVATED CARBON FIBERS

Activated carbon fibers (ACFs) are mainly composed of nanographitic units that have sheet structures (stack height $L_c = 1\text{--}1.5 \text{ nm}$; stack width $L_a = 3.5 \text{ nm}$). The unit size depends on the degree of activation, and therefore a low-burnoff ACF has a greater nanographitic structure. There are many slit-shaped spaces between the nanographites, giving slit-shaped micropores with pore volume in the range of



4 Phase diagram of O₂ on graphite surface

0.3–1 mL/g. There are several kinds of ACFs depending on the precursors. Cellulose-based ACF contains a large number of oxygen groups, while polyacrylonitrile-based ACF has polar C—N bonds. Pitch-based ACF (PIT) is the purest carbon, and PIT samples of different pore widths are available. Therefore, PIT is the best ACF for elucidation of molecular states in carbon micropores. Three kinds of pitch-based ACFs were used. These are denoted P-0.75, P-0.96, and P-1.45, using the micropore width in this chapter. the L_c values were 0.8 nm for P-0.75, 0.8 nm for P-0.96, and 0.7 nm for P-1.45.

Figure 5 shows adsorption isotherms of N₂ on ACFs at 77 K [19]. The adsorption isotherms of N₂ on P-0.75 and P-0.96 are typical type I, indicating the presence of uniform micropores. The adsorption isotherm of P-1.45 has a steep uptake at the low P/P_0 range and a gradual adsorption until $P/P_0 = 0.4$. The initial adsorption uptake and the gradual adsorption at the medium P/P_0 range are ascribed to the monolayer adsorption on the micropore walls and to the second- and/or third-layer adsorption of N₂ on the monolayer-covered micropore walls, respectively. This adsorption behavior suggests that the pore width of P-1.45 corresponds to a thickness of more than four adsorbed layers. As the monolayer is completed below the relative pressure corresponding to adsorption on the flat surface, the routing BET evaluation of the surface area leads to an overestimation. The adsorption in micropores is composed of both an enhanced monolayer adsorption on the micropore walls and adsorption in the residual space between the monolayer-covered micropore walls (a kind of condensation). Hence the enhanced adsorption should be subtracted. A high resolution α_s plot of the isotherm is quite effective for evaluation of the specific surface area. The data of high resolution N₂ adsorption isotherms of

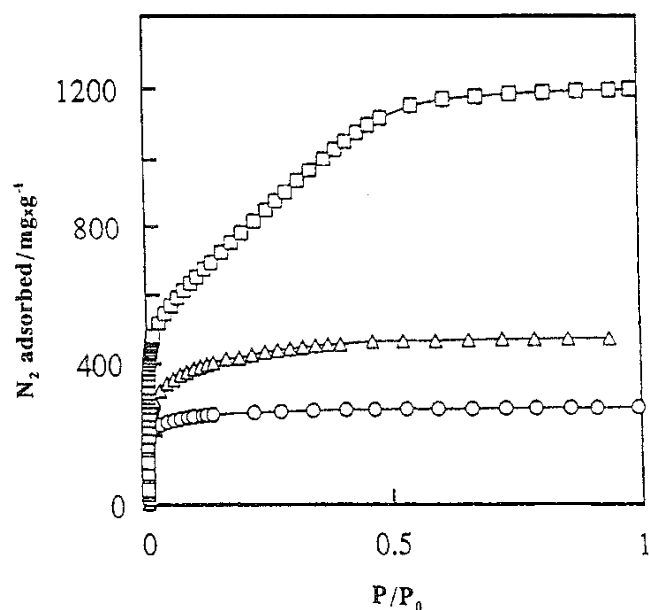


FIG. 5 Nitrogen adsorption isotherms of pitch-based ACFs at 77 K. (O) P-0.75; (Δ) P-0.96; (\square) P-1.45.

nonporous carbon black were used for the standard carbon. The subtracting pore effect (SPE) method for the high resolution a_s plot can remove the enhanced adsorption, giving the correct surface area [50–52]. The high resolution a_s plot for P-1.45 has two swings from linearity in the α_s regions of 0–0.3 and 0.7–1.0. The line between the two swings passes through the origin, and its slope provides the total surface area, that is, the sum of the microporous and external surface areas. The slope of the line of $\alpha_s = 1$ gives the external surface area, and its intercept leads to the micropore volume. Hence the high resolution α_s plot provides the total surface area, the microporous surface area, and the micropore volume. The micropore geometry of ACF can be approximated by the slit, and thus the average slit width (micropore width w) was determined from the microporous surface area and the micropore volume. The a_s plots of P-0.75 and P-0.96 had the only swing below $\alpha_s = 0.3$. Their surface area and micropore volume were determined in a similar way. Table 1 lists the total surface area, micropore volume, and average micropore width for the three ACFs.

TABLE 1 Micropore Structural Parameters of Pitch-Based ACFs

| ACF | Surface area (m^2/g) | Pore volume (ml/g) | Pore width (nm) |
|--------|---|----------------------------------|--------------------|
| P-0.75 | 900 | 0.34 | 0.75 |
| P-0.96 | 1247 | 0.61 | 0.96 |
| P-1.45 | 2110 | 1.42 | 1.45 |

Porous carbon is mainly composed of nanographites. The electronic structure of porous carbon is estimated from that of graphite. Carbon atoms in a graphite structure are combined with σ sp^2 hybrid orbital) and π ($2p_z$ orbital) bonds. π electronic wave functions extend over the basal plane, so π electrons can move freely in the basal plane. The conjugated π -electron system of the graphite sheet structure gives rise to the representative diamagnetism [53], which is associated with the extension of the conjugated π -electron system. Thus the magnetic susceptibility provides information on the electronic structure of nanographites in porous carbons. It was shown that the diamagnetic susceptibility of porous carbon at room temperature is proportional to the nanographitic unit size, as given by the equation. A unit nanographitic unit structure of about 60 carbon atoms for activated carbon was suggested [54]. Thus, most ACFs show representative diamagnetism, and the diamagnetism is associated with Eq. (24).

$$|\chi(10^{-6} \text{emu/g})| = 0.0090 \times (\text{number of carbon atoms}) + 0.47 \quad (24)$$

At the same time, the presence of an electronic defective structure in the π -conjugated structure and a dangling σ bond at the edge induces paramagnetism. Also, Volpilhac and Hoarau [55] studied the relationship between graphitic unit size and diamagnetism theoretically; they suggested that magnetic susceptibility decreases with increases in graphitic size until the stack width equals 30 nm and becomes constant thereafter. Hence, the magnetism of the porous carbon indicates sensitively the electronic states through the nanographitic unit and their stacking structures. In particular, the low temperature magnetic susceptibility measurement is useful. ACFs having very high surface area show paramagnetism near room temperature regardless of the absence of magnetic impurities [56–59]; they have electronic defect structures and dangling bonds due to the extremely minute graphitic unit structure. The mechanism of the paramagnetism of ACFs having very high surface area is itself an important research subject.

Figure 6 shows the temperature dependence of the magnetic susceptibility of PITs over a wide temperature range. Basically P-0.75 and P-0.96 are diamagnetic above 10 K. On the other hand, P-1.45 has positive magnetic susceptibility, being temperature-independent above 10 K. P-1.45 is highly activated, and it should have many dangling bonds at the edges of nanographites, giving rise to paramagnetism as suggested by Nakayama et al [56]. The magnetic susceptibility increases steeply below 20 K. This indicates clearly the presence of spins, which should be associated with the nanographitic structure. A preliminary electron spin resonance (ESR) study showed that there are two kinds of electron spins having π and σ character in ACFs, and only the spin of the σ electrons is affected by the adsorbed O_2 at low temperature [60]. The paramagnetic behavior below 20 K should be associated with the π -electron spin. As the magnetic susceptibility of these PIT samples is much lower than that of O_2 , the reliable magnetic susceptibility of O_2 confined in micropores of PIT can be determined, as shown later.

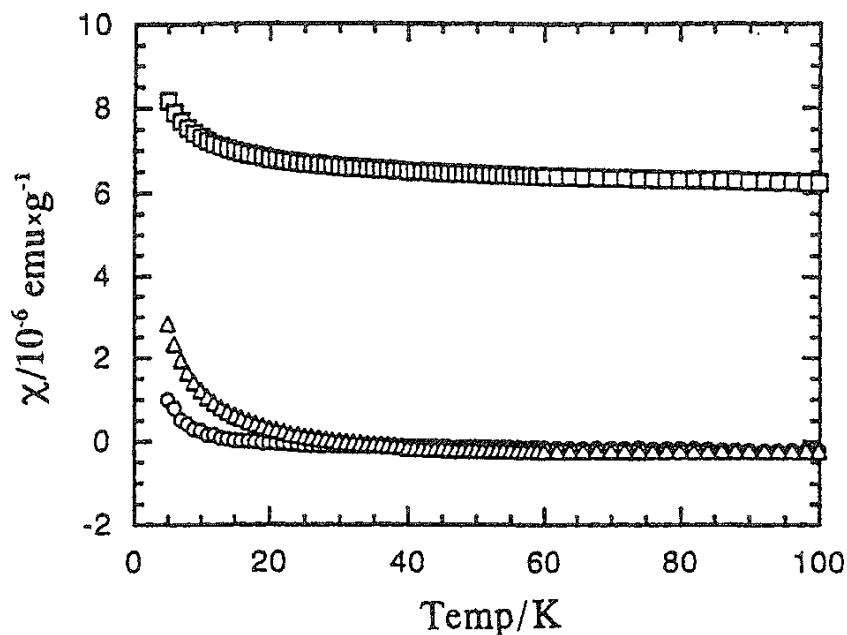


FIG. 6 Temperature dependence of the magnetic susceptibility χ of pitch-based ACFs at low temperature, (○) P-0.75; (△) P-0.96; (□) P-1.45.

VI. ADSORPTION OF O₂ IN A GRAPHITIC NANOSPACE

The adsorption isotherms of O₂ on ACFs at 77 K are close to those of N₂, as shown in Fig. 7 [61]. Although the adsorption isotherm was measured at 77 K, which is below the boiling temperature (90.18 K), no condensation occurred during the measurement. The O₂ adsorption isotherm was described by the Dubinin–Radushkevich (DR) equation [62]

$$\frac{W}{W_0} = \exp\left[\frac{-A^2}{E^2}\right], \quad A = RT \ln\left(\frac{P_0}{P}\right); E = \beta E_0 \quad (25)$$

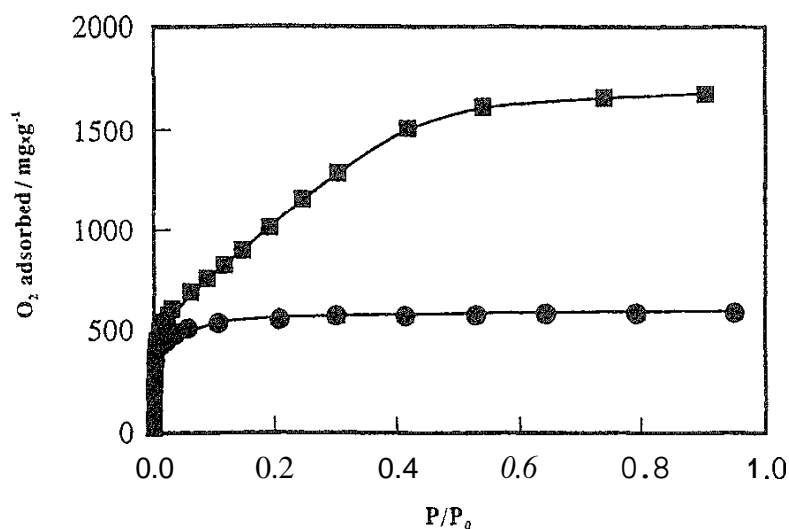


FIG. 7 Oxygen adsorption isotherms of pitch-based ACFs at 77 K. (●) P-0.96; (■) P-1.45.

Here W and W_0 are the amount of adsorption at P/P_0 and the micropore volume, respectively. β and E are the affinity coefficient and characteristic adsorption energy, respectively. A is the adsorption potential. The DR plot was almost linear, suggesting that O_2 molecules are filled homogeneously. The liquid density of 1.15 mL/g at 87 K was used for calculation of the volume of the adsorbed layer at 77 K. The micropore volume from the DR plot for O_2 adsorption was similar to that from N_2 adsorption. The isosteric heat of adsorption at $\phi = 1/e$, $q_{st,\phi=1/e}$, was evaluated with the equation

$$q_{st,\phi=1/e} = \beta E_0 + \Delta H_v, \quad (26)$$

Here ΔH_v , is the enthalpy of evaporation at the boiling temperature. The micropore volume and $q_{st,\phi=1/e}$ values for O_2 and N_2 are shown in Table 2. Here, 6.82 and 5.59 kJ/mol were used as ΔH_v , values for O_2 at 90 K and N_2 at 77 K, respectively. The two pore volumes are similar; the Gurvitch rule holds for O_2 and N_2 adsorption. The ΔH_v for O_2 is slightly greater than that for N_2 irrespective of differences in molecular size and quadrupole moments. Probably O_2 adsorbed in micropores is not ordinary liquid, but O_2 molecules should form an organized structure.

VII. MAGNETIC SUSCEPTIBILITY OF O_2 CONFINED IN A GRAPHITIC NANOSPACE

The magnetic susceptibility of O_2 adsorbed on ACF after sealing was measured with a SQUID magnetometer system over a temperature range of 1.7–100 K and at a magnetic field of 1 T. The magnetic susceptibility of O_2 confined in carbon nanospaces of PIT depends on the temperature, the coverage, and the pore width [25,26,63]. The coverage (θ_c) is defined as

$$\theta_c = \frac{n_{O_2} N_A}{6.36 a_s m_{ACF}} \times 10^{-18}$$

where n_{O_2} , is moles of oxygen dosed, 6.36 is the reference density (molecules/nm²) [12] for the registered $\sqrt{3} \times \sqrt{3}$ commensurate structure, a_s is the specific surface area (m²/g), and m_{ACF} is the weight of ACF (g). The commensurate structure is not observed for adsorbed O_2 layers in the ACF micropores but is used to define the standard unit for comparison with results in an O_2 –graphite system. Fractional filling ϕ , which is the volume fraction filled with adsorbed molecules, is calculated as $\phi = 0.63\theta_c$ using the pore volumes of ACFs and the liquid density of oxygen (1.14 g/cm³).

TABLE 2 Micropore Volume and $q_{st,\phi=1/e}$ for O_2 and N_2 from DR Plot

| ACF | O_2 | | N_2 | |
|--------|----------------------------|-------------------------------|----------------------------|-------------------------------|
| | Micropore volume (mL/g) | $q_{st,\phi=1/e}$ (kJ/mol) | Micropore volume (mL/g) | $q_{st,\phi=1/e}$ (kJ/mol) |
| P-0.96 | 0.49 | 12.4 | 0.45 | 11.52 |
| P-1.45 | 0.79 | 9.22 | 0.88 | 8.68 |

The temperature dependence of the magnetic susceptibility χ of O_2 molecules adsorbed in micropores of P-0.96 is shown as a function of the coverage in Fig. 8. No critical change in the $\chi-T$ curve for $\theta_c < 0.2$ is observed in the temperature range of 5–100 K. χ increases steeply with decreasing temperature, which is characteristic of paramagnetism. The $\chi^{-1}-T$ relation is well described by the Curie-Weiss equation. The Curie constant of 2.8×10^{-2} emu g $^{-1}$ K and the Weiss constant (O) of -7.4 K are obtained from the $\chi^{-1}-T$ curve for $\theta_c = 0.046$ (the average O_2-O_2 distance $d = 1.9$ nm). These Curie and Weiss constants are quite close to those for bulk gaseous O_2 ($C = 3.1 \times 10^{-2}$ emu g $^{-1}$ K and $O = 0$ K). Although the submonolayer O_2 on the graphite surface gives rise to a magnetic anomaly due to the melting of the 5 phase at 26 K for $\theta_c < 1$, the low coverage O_2 layer in micropores of P-0.96 at $\theta_c < 0.5$ provides no evidence of such a magnetic transition. Hence, the O_2 adsorbed layer of $\theta_c < 0.5$ is completely different from that on the flat graphite surface. Furthermore, the spin system of O_2 in the micropore behaves like a free spin regardless of the fact that O_2 is confined in the micropore by the strong surface-molecule interaction potential.

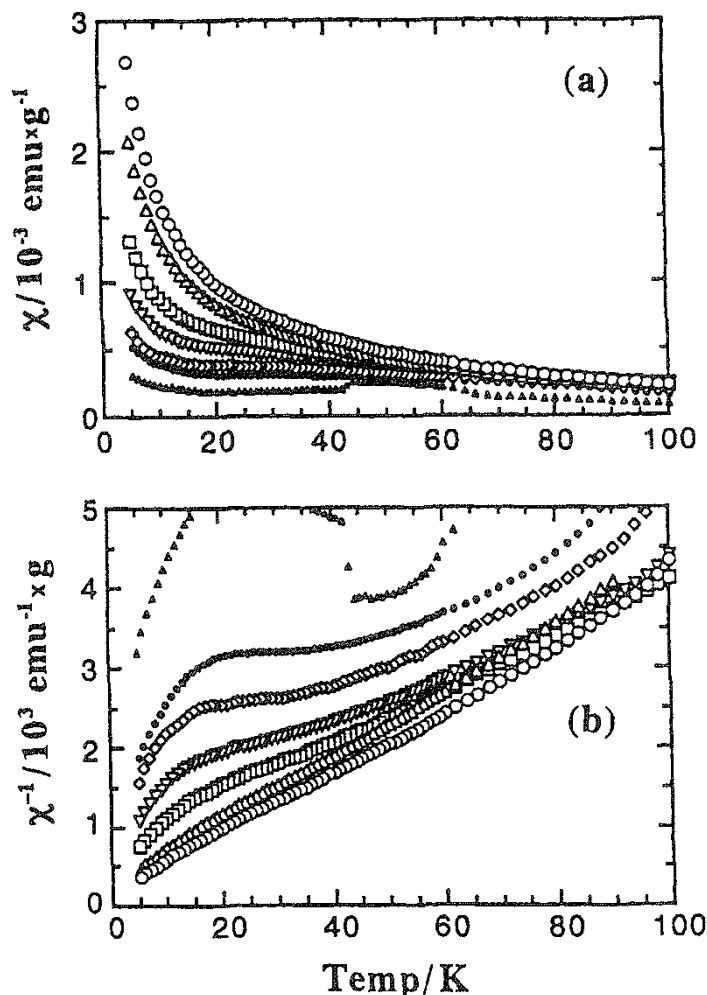


FIG. 8 Temperature dependence of magnetic susceptibility χ of O_2 adsorbed in micropores of P-0.96 at coverages (θ_c) of (\circ) 0.046, (\triangle) 0.11, (\square) 0.24, (∇) 0.46, (\diamond) 0.75, (\bullet) 1.1, and (\blacktriangle) 1.3. (a) $\chi-T$ curves; (b) $\chi^{-1}-T$ curves.

The temperature independence of 7 with the increase of θ_c is observed, especially for the temperature range of 20–50 K at $\theta_c > 0.46$. However, this change is not due to the effect of antiferromagnetism by the formation of 5, ε , or α phase but to the effect of the random magnetism developed in the micropore as described later. Clear jumps in the χ – T curve of $\theta_c = 1.3$ ($d = 0.35$ nm and $\phi = 0.82$) are observed at 24 and 44 K, which correspond to the α – β and β – γ transition temperatures of the bulk oxygen, respectively, whereas either phase corresponding to the bulk oxygen does not appear below $\theta_c = 3.5$ in the O_2 /graphite system [48]. This result shows that even trimolecular layers in the micropore can form a dense structure identical to that of the bulk solid, since the pore width of P-0.96 is almost three times the molecular diameter of O_2 . This phenomenon may be ascribed to the strong micropore field, which offers a high pressure effect [18].

The Curie (C_{TL-T_H}) and Weiss (Θ_{TL-T_H}) constants calculated in the several temperature ranges are plotted in Fig. 9 to illustrate how the intermolecular interaction changes with an increase in θ_c , since the χ^{-1} – T curve is not straight at $\theta_c > 0.2$. The $C_{T_L-T_H}$ and $\Theta_{T_L-T_H}$ values were evaluated from the linear approximation for the χ^{-1} – T curves in the temperature range of T_L to T_H K, where T_L and T_H represent the low and high temperature limits, respectively, in the temperature range. The C_{30-42} and Θ_{30-42} values change markedly at $\theta_c = 1.2$. The changes in these constants reflect the phase transition of the bulk solid (β to γ). Since the C_{44-54} and Θ_{44-54} values change steeply at 8, > 1.2 , these constants also correlate to the phase transition. C_{5-10} and Θ_{5-10} , however, show little change over the whole range of θ_c and indicate the values relatively close to those for gaseous O_2 . This may be because in the very low temperature region, contributions from free spins to the susceptibility are predominant but those from the antiferromagnetic phases or spin clusters are very small, provided that the mixed states of the free spins and interacting spins coexist. We can regard C_{5-10} and Θ_{5-10} as the parameters related to the amount of the free spins.

The χ – T curve for 6, $\theta_c = 0.75$ ($d = 0.46$ nm and $\phi = 0.47$) in the low temperature range is shown in Fig. 10a. The curve has a maximum at 2.1 K after zero-field cooling (ZFC), whereas it has no anomaly and can be described by the Curie–Weiss equation for the field cooling (FC) process. The time course after a temperature drop from 30 to 5 K is also shown in Fig. 10b. The magnetic moment slowly increases with time after the temperature drop. This magnetic behavior should be attributed to random magnetism such as spin glass or micromagnetism [64]. This is because O_2 molecules form clusters consisting of a few or several molecules and the cluster behaves as the system of an effective spin. Since such spins are frozen in the low temperature range, we can observe the relaxation phenomenon for spin orientation in the magnetic field. Similar results are obtained for $0.24 \leq \theta_c \leq 1.1$. The spin–spin interaction of the spin clusters gives increases in C_{30-42} and C_{44-54} and decreases in Θ_{30-42} and Θ_{44-54} before the bulk phase transition, as are shown at $0.2 < \theta_c < 1.0$ in Fig. 9. The random magnetic behavior is not observed for 9, $\theta_c < 0.2$, because a very small cluster or an isolated molecule behaves like a free spin. On the other hand, the busy packing of the molecules inhibits the free motion of the spin and facilitates the formation of the bulk solid phase, so that the adsorbed O_2 of $\theta_c > 1.3$ shows no random magnetism.

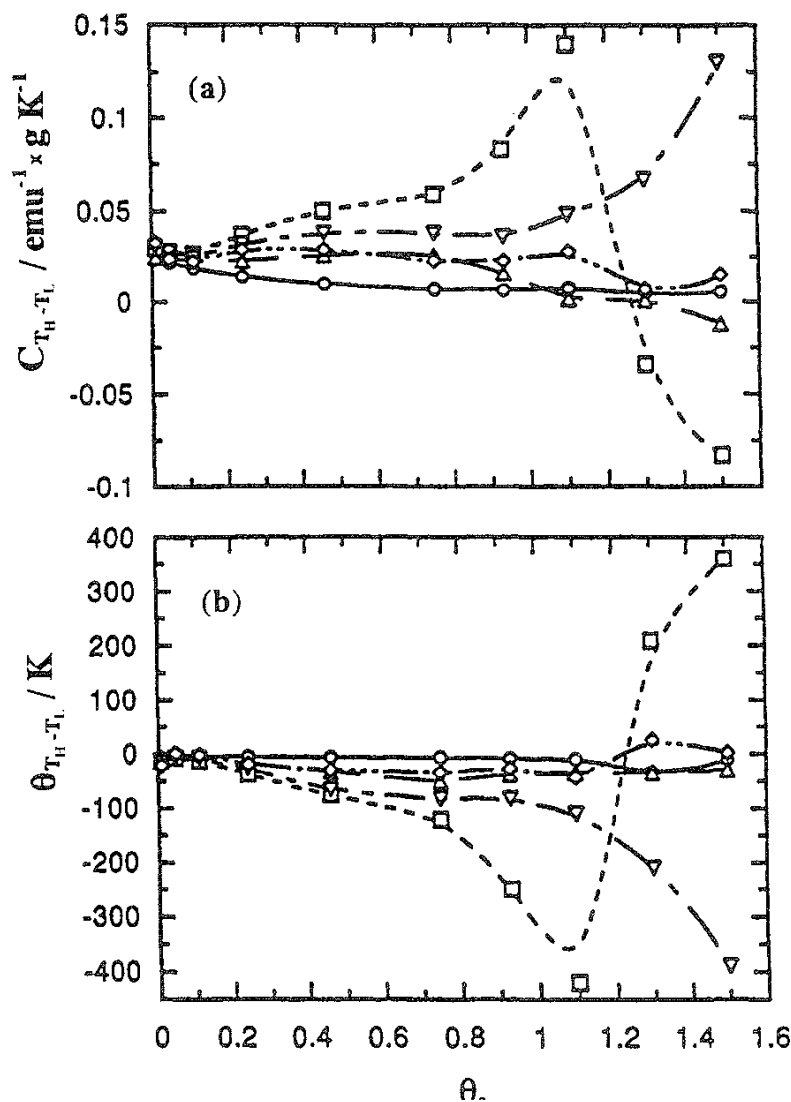


FIG. 9 The Curie ($C_{T_L-T_H}$) and Weiss ($\Theta_{T_L-T_H}$) constants in the several temperature ranges for the $O_2/P-0.96$ system at $\theta_c = 0.75$. The $C_{T_L-T_H}$ (a) and $\Theta_{T_L-T_H}$ (b) values were evaluated from the linear approximation for the $\chi^{-1}-T$ curves (Fig. 8b) in the temperature range of T_L to T_H K, where T_L and T_H represent the low and high temperatures limit, respectively, in the temperature range.

VIII. DEPENDENCE OF MAGNETIC SUSCEPTIBILITY OF CONFINED O_2 ON PORE WIDTH

The spin association of O_2 confined in micropores depends on the pore width. Results similar to those of ACF-0.96 are obtained for O_2 adsorbed in the micropores of P-0.75, although the dependence of the $\chi-T$ curve on θ_c differs from that of P-0.96. The $\chi-T$ curve for $\theta_c = 0.056$ ($d = 1.7$ nm) gives the constants of $C = 2.3 \times 10^{-2}$ emu g^{-1} K and $\Theta = -1.8$ K. No 2D magnetic lattice formation is observed at $\theta_c > 1.1$ ($d = 0.38$ nm and $\phi = 0.87$), but the bulk phases appear at $\theta_c > 1.1$. The changes in $C_{T_L-T_H}$ and $\Theta_{T_L-T_H}$ are not so great relative to those for P-0.96. The magnetic relaxation process of the spin cluster in the micropores of

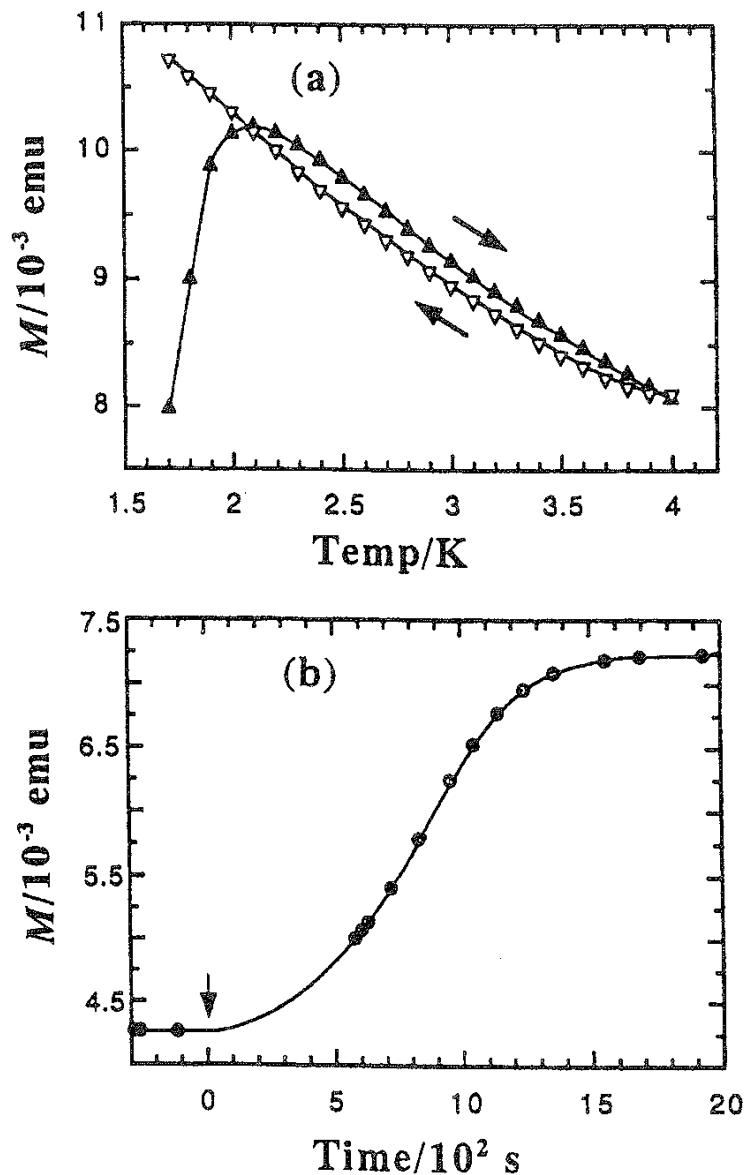


FIG 10 Magnetic moment (M) of the $\text{O}_2/\text{P-0.96}$ system at $\theta_c = 0.75$. (a) M - T curve. The measurement was carried out after cooling to 1.7 K with the magnetic field (H) of 0 T [zero-field cooling (ZFC)], followed by application of the field up to 1 T. (\blacktriangle) Heating after ZFC; (∇) field cooling (FC). (b) Time course after temperature drop from 30 to 5 K at $H = 1$ T. The temperature was dropped at the point indicated by an arrow.

P-0.75 is also observed at $0.3 < \theta_c < 1.2$, but the relaxation is much faster than that of P-0.96. Therefore, P-0.75 offers a restricted molecular environment less suitable for cluster formation than P-0.96.

The χ - T curve of O_2 adsorbed in the micropore of P-1.45 at $\theta_c = 0.021$ ($d = 2.7$ nm) satisfies the Curie-Weiss law ($C = 2.6 \times 10^{-2}$ emu g^{-1} K and $\Theta = 2.3$ K) as is shown in Fig. 11a. The curves for $\theta_c \geq 0.42$, however, give different features from those of the other two samples described above. The curves for $\theta_c = 0.42$, 0.60, and 0.78 have broad peaks at 28, 36, and 44 K, respectively. Moreover, the bulk phase appears at $\theta_c = 1.1$ ($d = 0.38$ nm and $\phi = 0.63$). This is a smaller coverage than with either P=0.96 or P-0.75. The changes in $C_{T_L-T_H}$ and

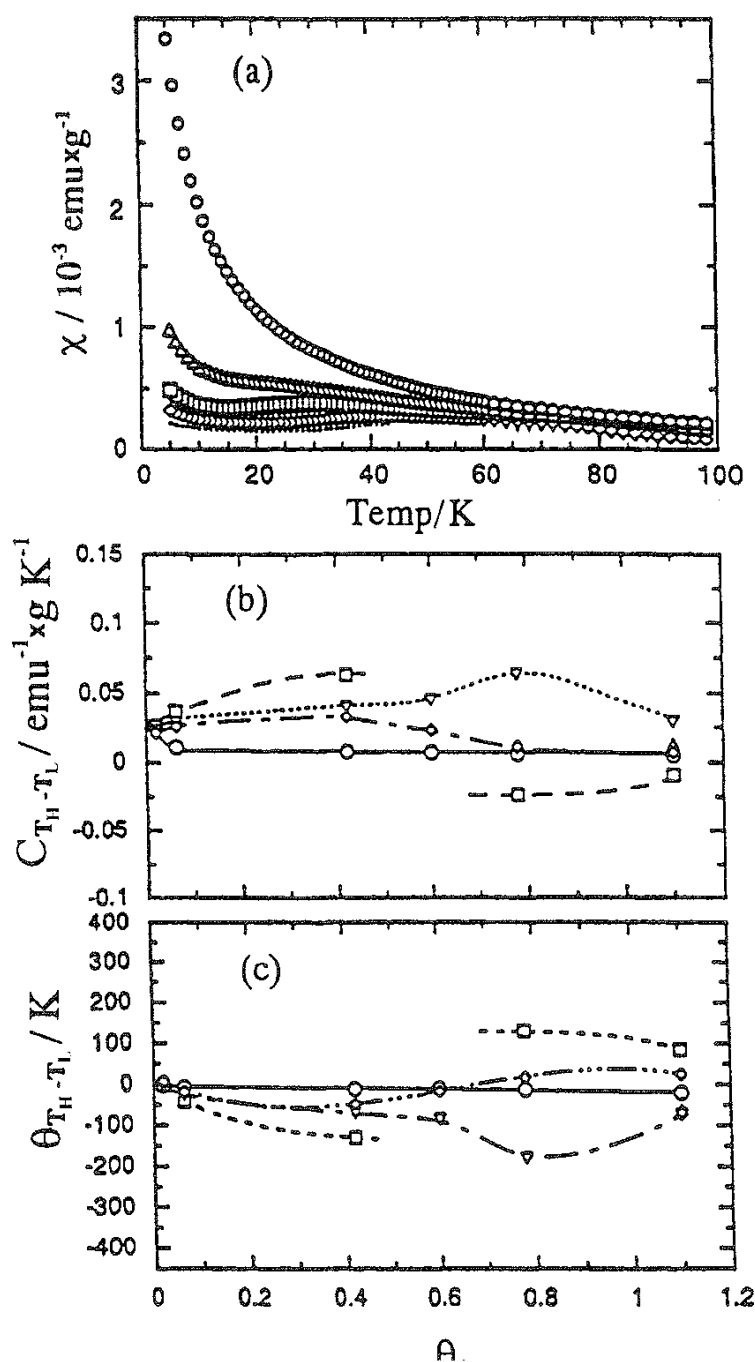


FIG. 11 $\text{O}_2/\text{P-1.45}$ system. (a) χ - T curves at coverages (θ_c) of (○) 0.021, (▲) 0.063, (□) 0.42, (▽) 0.60, (◇) 0.78, and (●) 1.1. (b) $C_{T_H - T_L}$ vs. θ_c ; (c) $\Theta_{T_H - T_L}$ vs. θ_c .

$\Theta_{T_H - T_L}$ are different from those for P-0.96 or P-0.75. Accordingly, C_{30-42} and Θ_{30-42} , especially, give discontinuous changes in the region $0.5 < \theta_c < 0.7$. The sample of $\theta_c = 1.1$ gave the slowest spin-relaxation phenomenon in the $\text{O}_2/\text{P-1.45}$ system regardless of the bulk phase formation at the coverage. A maximum of 2.0 K upon heating after ZGC and spin-relaxation after the temperature drop are observed. These results indicate the coexistence of the bulk phase and clusters in micropores of P-1.45, which is not observed in the micropores of P-0.75 or P-0.96. The detailed χ - T curves for $\theta_c = 0.42$, 0.60, and 0.78 are shown in Fig. 12. These

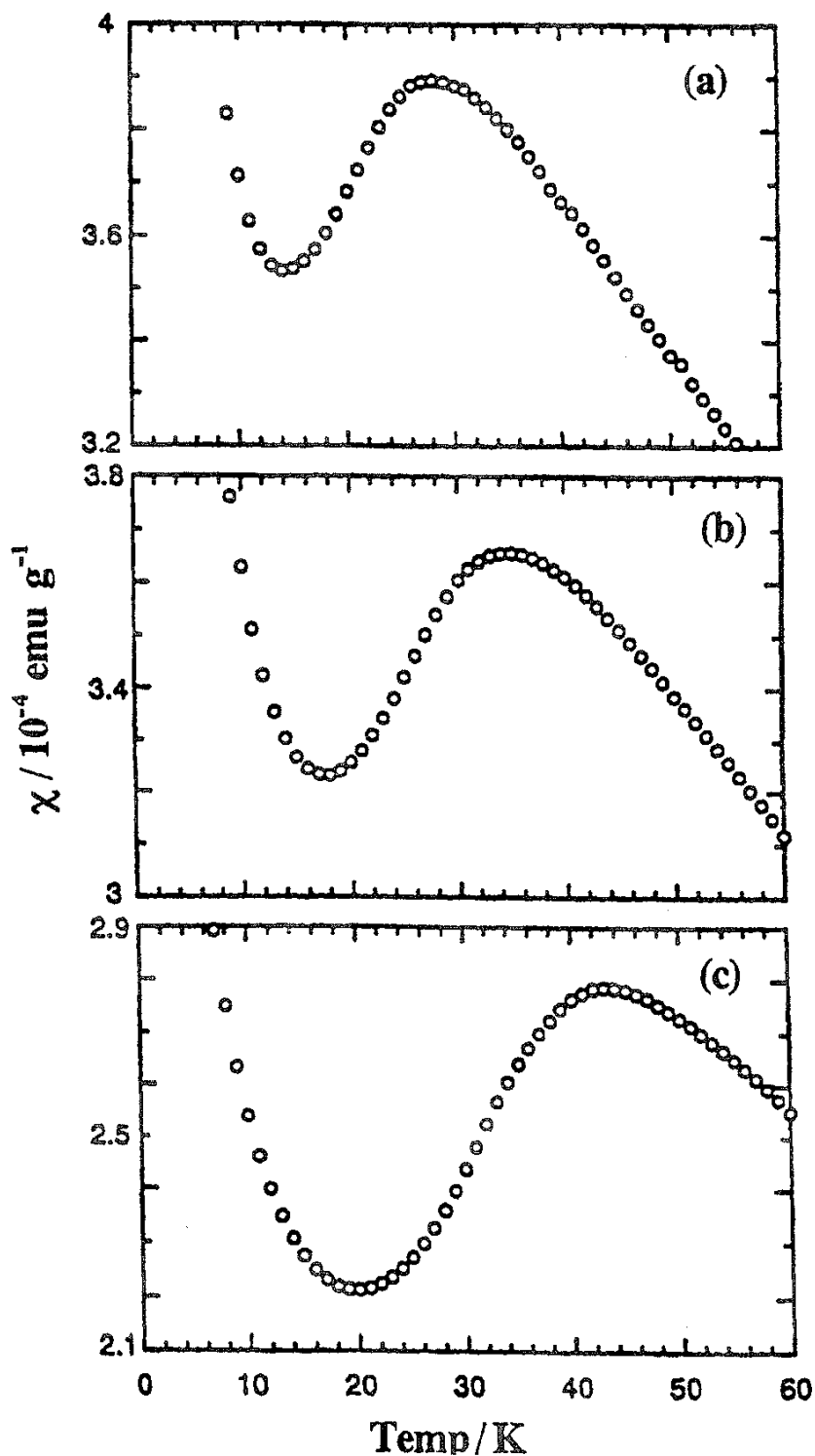


FIG. 12 χ - T curves of O_2 /P-1.45 system at coverages of θ_c of (a) 0.42, (b) 0.60, and (c) 0.78.

are somewhat similar to a curve for the 0 phase in the O_2 /graphite system obtained by Kobler and Marx [48]. These authors propose that liquid and θ phases coexist in the region of $1 \leq \theta \leq 1.8$ and $32 < T < 40$ (32 K is the melting point of the 8 phase; 40 K, that of the 0 phase) for the O_2 /graphite system. The θ phase is presumed to have a liquid crystalline structure in which molecular axes are ordered like those of

a smectic crystal, but the molecular centers are disordered in the 2D plane. The clusters formed in the micropores of P-1.45 should be in a less ordered state than that of the θ phase. The values of C_{30-42} and Θ_{30-42} at $\theta_c = 0.42$ are comparable to those for P-0.96 at $\theta_c = 0.75$, but the results of spin relaxation show that the cluster formation proceeds to a lesser extent than in the latter case. This is because the spins in the state of the 0-like phase also contribute to the two constants.

The magnetic behavior of the clusters formed in the micropores of ACFs depends on the pore width and tends to approach that of the O_2 /graphite system with an increase in the pore width. The C_{5-10} and Θ_{5-10} values are related to the amount of the free spins as described above and are shown in Fig. 13. These results indicate that the amount of free spins decreases with increasing θ_c at a constant pore width and with increasing pore width at a constant θ_c , although the Θ_{5-10} values for ACF-0.96 and ACF-1.45 deviate noticeably after the bulk phase formation owing to the influence of the antiferromagnetism of the α phase. Each extra-

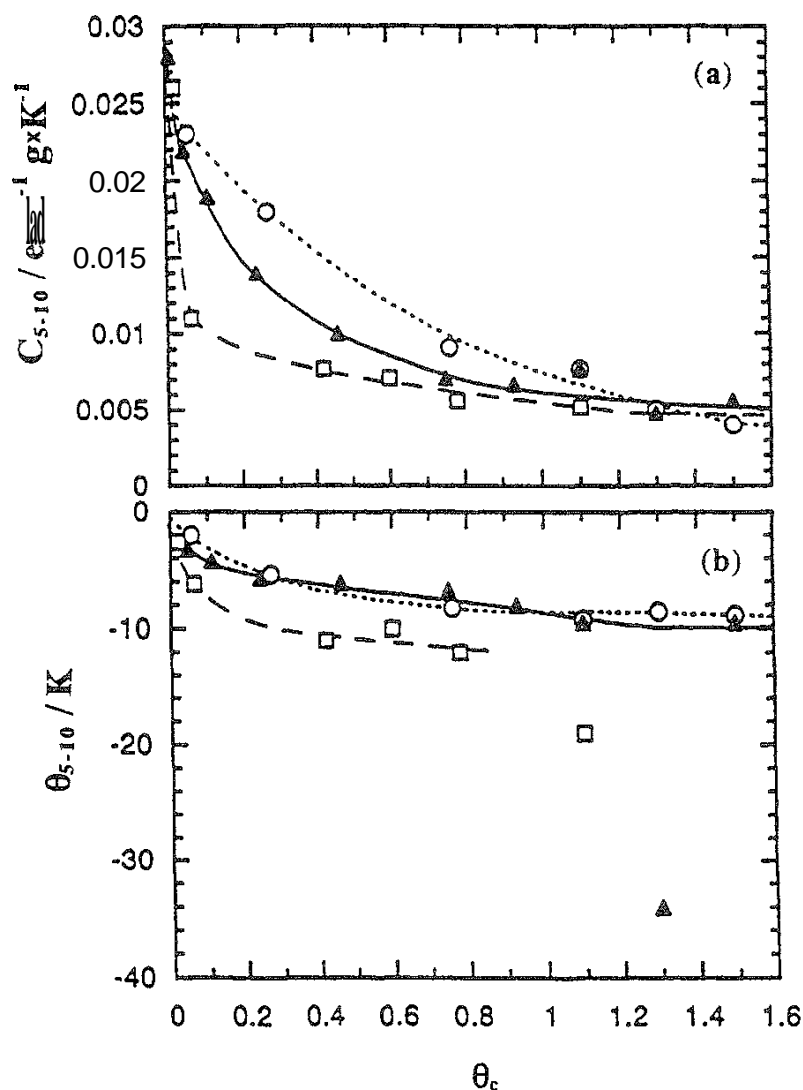


FIG. 13 Dependence of C_{5-10} and Θ_{5-10} on θ_c for three O_2 /PIT systems. (a) C_{5-10} vs. θ_c curve, (b) Θ_{5-10} vs. θ_c .

polation of θ_c to zero gives the Curie and Weiss constants of the free spins confined in the nanospace; $C_0 = 2.6 \times 10^{-2} \text{ emu g}^{-1} \text{ K}$ and $\Theta_0 = -0.2 \text{ K}$ for P-0.75; $C_0 = 3.0 \times 10^{-2} \text{ emu g}^{-1} \text{ K}$ and $\Theta_0 = -1.2 \text{ K}$ for P-0.96; and $C_0 = 2.9 \times 10^{-2} \text{ emu g}^{-1} \text{ K}$ and $\Theta_0 = -0.6 \text{ K}$ for P-1.45. All values obtained are very close to those of gaseous O_2 . The results for each O_2/ACF system also indicate that the spin cluster is formed at $C_{5-10} < 0.015$. The phase diagrams of the O_2/ACF systems deduced from the total data in this work are shown in Fig. 14. The phase diagram is simpler than that of the $\text{O}_2/\text{graphite}$ system because few phase transitions occur before the bulk phases appear in the two-dimensional system. It is very interesting that none of the liquid or solid phases are observed for the O_2 submonolayer in the

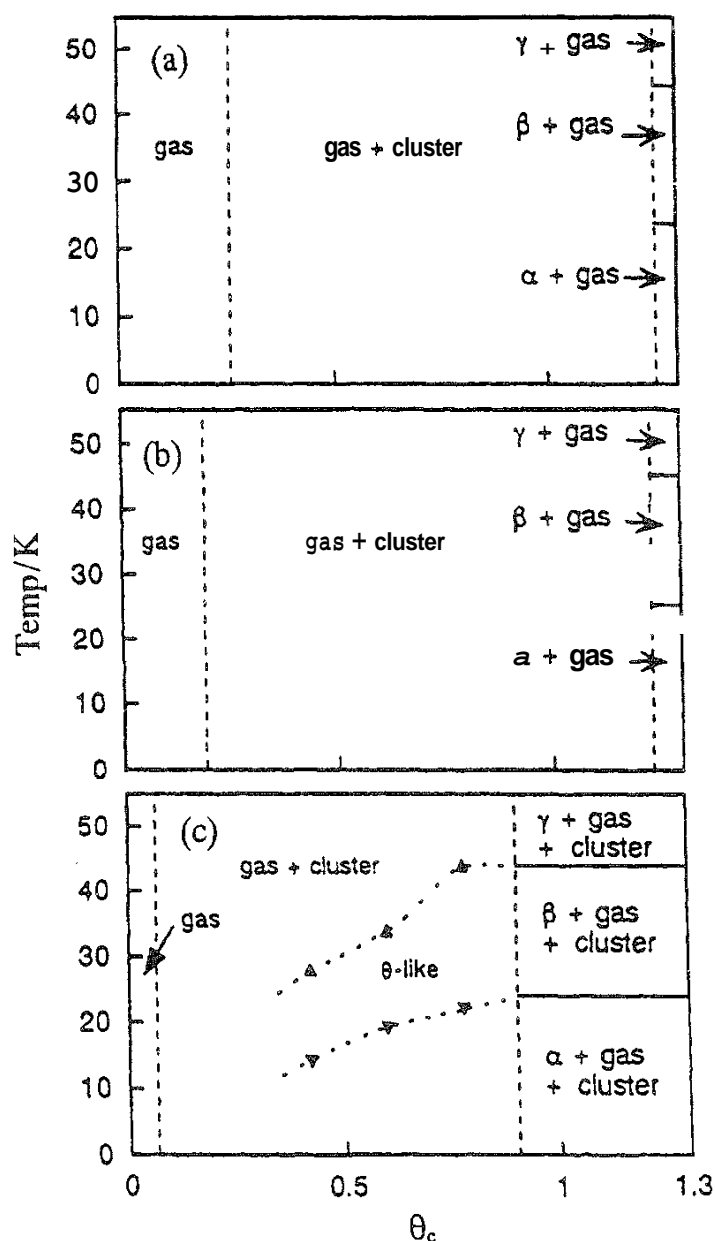


FIG. 14 Phase diagrams for O_2 confined in micropores of ACF. (a) P-0.75; (b) P-0.96; (c) P-1.45. ▲ and ▼ in (c) denote the value at the peak and at the trough, respectively, in Fig. 12.

low temperature range. It is plausible that O₂ molecules confined in the slit pore of 1 nm width cannot form a two-dimensional lattice similar to that on the flat graphite surface. The relationship between the disappearance of the 2D lattice formation and the slit width should shed light on the unusual state of molecules confined in a narrow space.

IX. EFFECT OF COEXISTENT H₂O ON MAGNETIC SUSCEPTIBILITY OF CONFINED O₂

Water molecules can form a network structure that accepts a guest molecule to produce a clathrate compound under application of high pressure or low temperature [65,66]. Recent in situ X-ray diffraction studies showed that H₂O molecules confined in the graphitic nanospace of ACF form an ice-like structure [21,67] and produce a clathrate compound different from the bulk one even near ambient conditions [22,23]. Such a clathrate structure can isolate an O₂ spin system. Thus, knowledge of the magnetic susceptibility of the H₂O–O₂ mixture confined in the nanospace of ACF at different compositions and fractional fillings ϕ over the temperature range of 2–100 K is necessary for understanding O₂ assembly.

The results for P-0.96 are shown here. The diamagnetic contribution of ice (-0.699×10^{-6} emu g) was subtracted from the observed value [68]. The coexistent H₂O affects seriously the magnetic structure of even the bulk condensed O₂, as mentioned earlier. Earlier studies [25,26] showed that the χ – T curve of confined O₂ for $\phi < 0.16$ ($\theta_c < 0.25$) has no critical change in the temperature range of 2–100 K, and confined O₂ shows paramagnetism within a low temperature range; an almost free O₂ spin state was confirmed by the Curie–Weiss parameters close to those of O₂ gas. Temperature independence of χ was observed in the temperature range of 20–50 K for $\phi > 0.16$ ($\theta_c > 0.25$), which is associated with random magnetism due to spin cluster formation having an explicit relaxation. The temperature dependence of χ of O₂ confined in the nanospace of ACF is shown in Fig. 15 as a function of ϕ in the presence and absence of H₂O. Here, the H₂O content is expressed in terms of the H₂O/O₂ molar ratio $R_{\text{H}_2\text{O}}$. Although the coexistent H₂O brings about a paramagnetic nature as mentioned above, it does not sensitively affect the magnetic behavior of confined O₂ for $R_{\text{H}_2\text{O}} \leq 0.35$ because of the free O₂ spin state even without the coexistent H₂O. On the other hand, the addition of excess H₂O noticeably changes the χ – T relation, which indicates the perfect isolation of O₂ by coexistent H₂O. Figures 16 and 16b show the Curie–Weiss plots for $R_{\text{H}_2\text{O}} \leq 0.35$ and $R_{\text{H}_2\text{O}} = 28.7$, respectively. The coexistent H₂O bends the plot upward markedly, indicating that the coexistent H₂O accelerates the spin cluster formation, inducing random magnetism. In the case of $R_{\text{H}_2\text{O}} \leq 0.35$, the Curie–Weiss plot bends down at 10 K for both cases, with and without H₂O. The spin concentration is decreased slightly by the presence of H₂O, while the Weiss constant does not change, as shown in Table 3. The decrease of the spin concentration by the presence of H₂O supports the formation of spin clusters. Association of H₂O molecules should lead to an island formation of O₂ molecules, producing the spin cluster. The Curie–Weiss plot in the absence of H₂O is linear, whereas that with an excess of H₂O is convex. The constants from the Curie–Weiss plot are also shown in Table 3. The spin

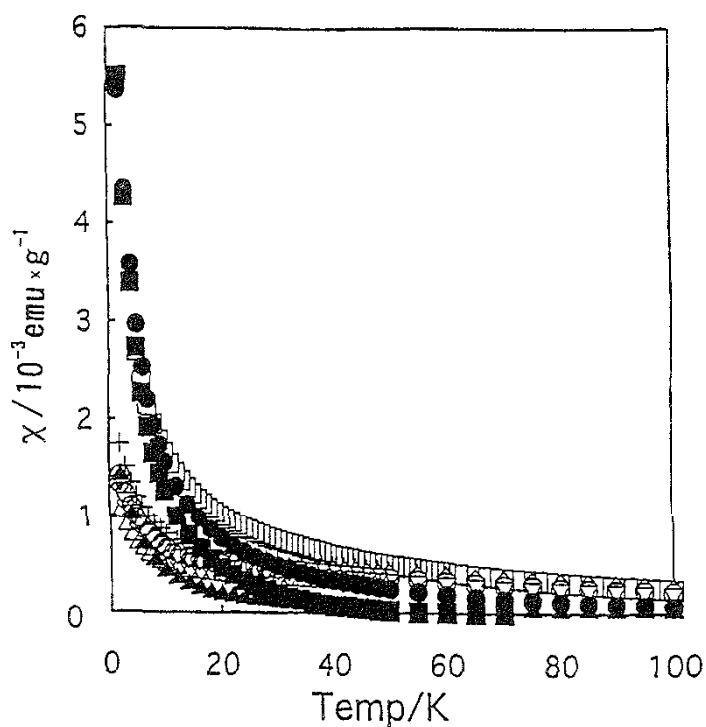


FIG. 15 Temperature dependence of the magnetic susceptibility of O_2 confined in the graphitic nanospace at different fractional fillings by O_2 (ϕ) and amounts of coexistent H_2O (R_w). (\square) $\phi = 0.029$, $R_w = 0$; (+) $\phi = 0.23$, $R_w = 0$; (\triangle) $\phi = 0.45$, $R_w = 0$; (\circ) $\phi = 0.18$, $R_w = 0.12$; (\diamond) $\phi = 0.30$, $R_w = 0.21$; (∇) $\phi = 0.20$, $R_w = 0.35$; (\blacktriangle) $\phi = 0.045$, $R_w = 8.7$; (\bullet) $\phi = 0.0057$, $R_w = 76$; (\blacksquare) $\phi = 0.0023$, $R_w = 172$.

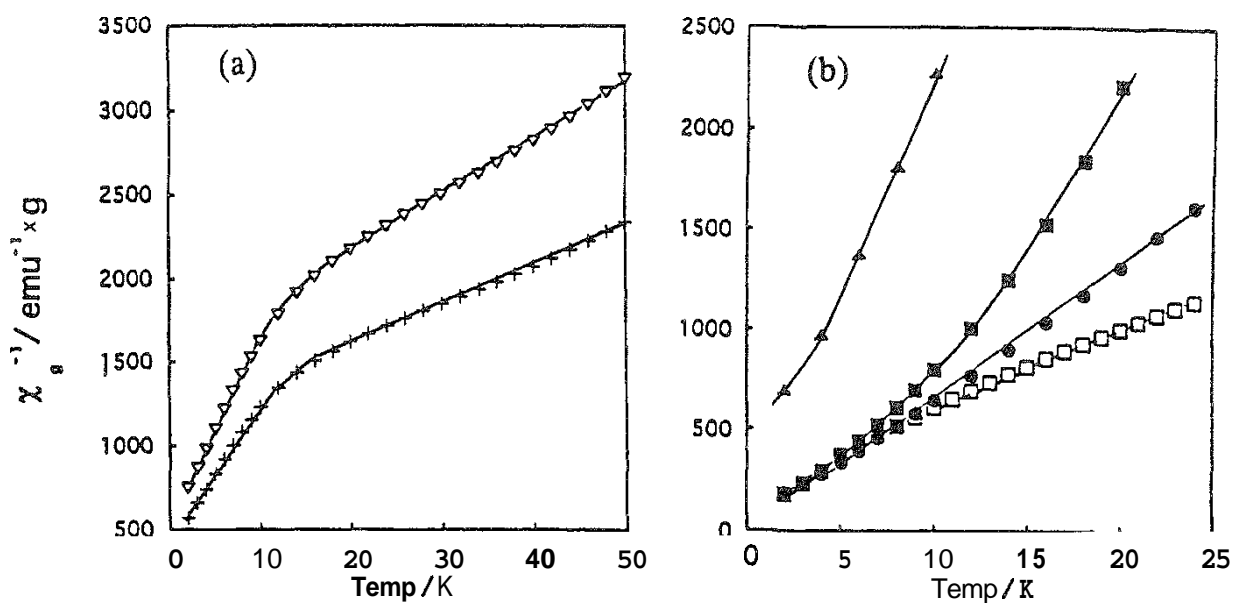


FIG. 16 The Curie-Weiss plot of O_2 - H_2O confined in graphitic nanospace. (a) A smaller content of H_2O . (∇) $\phi = 0.20$, $R_w = 0.35$; (+) $\phi = 0.23$, $R_w = 0$; (b) An excess amount of H_2O . (\square) $\phi = 0.029$, $R_w = 0$; (\blacktriangle) $\phi = 0.045$, $R_w = 8.7$; (@) $\phi = 0.0057$, $R_w = 76$; (\blacksquare) $\phi = 0.0023$, $R_w = 172$.

TABLE 3 Curie–Weiss Constants in the Temperature Range of 2–10 K

| Fractional filling by O ₂ , ϕ | H ₂ O/O ₂ ratio, R_{H} | Spin concentration (10 ²² spins/g) | Weiss constant (K) |
|--|--|--|-----------------------|
| 0.029 | 0 | 1.04 | −3.0 |
| 0.23 | 0 | 0.58 | −5.0 |
| 0.45 | 0 | 0.37 | −5.4 |
| 0.18 | 0.12 | 0.48 | −5.0 |
| 0.30 | 0.21 | 0.48 | −5.9 |
| 0.20 | 0.35 | 0.44 | −4.9 |
| 0.045 | 8.7 | 0.24 | −0.32 |
| 0.0057 | 76 | 0.84 | −1.01 |
| 0.0023 | 172 | 0.63 | 0.02 |

concentration of O₂ diluted by H₂O is smaller than that of the bulk O₂ gas, while the Weiss constant is close to zero. The decrease in the spin concentration suggests a strong interaction between O₂ molecules such as dimer formation and/or interaction of O₂ with H₂O molecules in the graphitic nanospace. The diamagnetic dimer [69] of O₂ surrounded by H₂O molecules should reduce the χ value. Accordingly, single O₂ and dimerized O₂ form a clathrate structure in the nanospace to give rise to almost perfect paramagnetism. Thus, the doping of H₂O molecules in an O₂ molecular assembly can control the magnetic interaction of O₂ in the graphitic nanospace.

X. MAGNETIC DISTINCTION OF WEAKLY INTERACTING MOLECULES IN NANOSPACE

Chemisorbed species on solid surfaces have been widely studied, and established methods are available for determination of the different chemisorbed species. For example, five representative species of chemisorbed oxygen—O, O₂[−], O₂^{2−}, O[−], and O^{2−}—have been evidenced with the aid of IR and ESR for oxygen chemisorbed on the surface of transition metal oxides [70,71]. However, interactions in physical adsorption, even micropore filling, are too weak, and we have no established method for assigning the different physisorbed states. The interaction potential profiles of an O₂ molecule with slit graphite are shown in Fig. 1. Although the potential minimum difference of three ACFs shown in Fig. 1 is only 150 K, which is very small, it is large enough for magnetic interaction. There is a possibility that a slight difference in a weakly interacting system can be measured by the magnetic method. The magnetic method is quite sensitive, and we identify different oxygen states in micropores with the aid of magnetic susceptibility measurements at low temperature, as described above. The magnetic behaviors of O₂ micropores can provide an adsorbed mechanism. The average intermolecular distance d is calculated from the fractional filling using the assumption of isotropic and homogeneous

distribution of O₂ molecules in the pore. Generally speaking, d of 1 nm is necessary for the spin dipole–spin dipole interaction. It has been recently elucidated that a new spin relaxation of bulk gaseous O₂ occurs through a quadrupole-mediated mechanism at the contact distance of Lennard-Jones molecules [60]. Consequently, the critical distances are 0.34 nm and about 1 nm in the magnetic interactions of O₂. Oxygen molecules do not magnetically interact with each other, and they are isolated at a distance of more than 1 nm below $\phi = 0.2$ ($\theta_c = 0.3$). In the middle fractional filling range of $0.2 < \phi < 0.6$ ($0.3 < \theta_c < 0.95$), some isolated molecules are associated with each other to form a cluster that causes random magnetism. Clusters are aggregated to produce an organized assembly near complete filling. The condensed phase in the micropore exhibits the same magnetic transitions as the bulk phase. However, the χ – T jump at the magnetic phase transition is not sharp, and therefore the condensed molecular layer should contain many defects due to geometrical restrictions.

The grand canonical Monte Carlo simulation of O₂ adsorption by a graphite slit at 100 K showed that O₂ molecules are orientationally ordered on the micropore walls [72]. If O₂ molecules have an orientationally ordered structure in the micropore as suggested by the simulation work, such an ordered structure coincides with the cluster and the organized assembly formation. Thus magnetic measurements are quite effective for identifying the weakly interacting molecular states in micropores.

ACKNOWLEDGMENT

I am grateful for Dr. H. Kanoh, Dr. C. Ishii, and Mr. J. Suzuki for collaborative works. This work was funded by a Grant-in-Aid for Scientific Research on Priority Areas No. 288, "Carbon Alloys," from the Japanese government.

REFERENCES

1. A. W. Adamson, *Physical Chemistry of Surfaces*, Wiley, New York, 1990.
2. S. J. Gregg and K. S. W. Sing, *Adsorption, Surface Area, and Porosity*, Academic, London, 1984.
3. K. S. W. Sing, D. H. Everett, R. A. Haul, R. A. Pierotti, J. Rouquerol, and T. Simieniewska, *Pure Appl. Chem.* 57:603 (1985).
4. D. H. Everett and J. C. Powl, *J. Chem. Soc., Faraday Trans. I* 72:619 (1976).
5. S. Brunauer, P. H. Emmett, and E. Teller, *J. Am. Chem. Soc.* 60:309 (1938).
6. S. J. Gregg and K. S. W. Sing, *Adsorption, Surface Area, and Porosity*. Academic, London, 1984, p. 113.
J. C. P. Broekhoff and B. G. Linsen, in *Physical and Chemical Aspects of Adsorbents and Catalysts* (B. G. Linsen, ed.), Academic, London, 1970, Chap. 1.
D. H. Everett, in *The Solid-Gas Interface* (E. A. Flood, ed.), Marcel Dekker, New York, 1967, Chap. 3.
9. W. Rudzinski and D. H. Everett, *Adsorption of Gases on Heterogeneous Surfaces*, Academic, London, 1992.
10. N. A. Seaton, J. R. P. B. Walton, and N. Quirk, *Carbon* 27:853 (1989).
11. A. V. Bakaev and W. A. Steele, *Langmuir* 8:148 (1992).

12. R. F. Cracknell, D. Nicholson, and K. E. Gubbins. *J. Chem. Soc., Faraday Trans.* 91:1377 (1995).
13. R. F. Cracknell, D. Nicholson, K. E. Gubbins, and M. Madox. *Acc. Chem. Res.* 28:281 (1995).
14. M. Rigby, E. B. Smith, W. A. Wakeham, and G. C. Maitland. *The Forces between Molecules*. Oxford Sci., Oxford, UK. 1986.
15. O. Kajimoto, *Cluster Chemistry* (in Japanese), Baihoukan, Tokyo, 1992.
16. K. Kaneko. *Langmuir* 3:357 (1987).
17. K. Kaneko, N. Fukuzaki, and S. Ozeki. *J. Chem. Phys.* 87:776 (1987).
18. J. Imai, M. Sounia, S. Ozeki, and K. Kaneko. *J. Phys. Chem.* 95:9955 (1991).
19. K. Kaneko, K. Shimizu, and T. Suzuki, *J. Chem. Phys.* 97:8705 (1992).
20. R. Moreh and D. Levant, *Mol. Phys.* 69:735 (1990).
21. T. Iiyama, K. Nishikawa, T. Otowa, and K. Kaneko, *J. Phys. Chem.* 99:10075 (1995).
22. K. Fujie, S. Minagawa, T. Suzuki, and K. Kaneko, *Chem. Phys. Lett.* 236:427 (1995).
23. J. Miyawaki, T. Kanda, T. Okui, Y. Maeda, and K. Kaneko, *J. Phys. Chem.* 102:2187 (1998).
24. T. Suzuki, T. Kasuh, and K. Kaneko, *Chem. Phys. Lett.* 93:2355 (1993).
25. K. Kanoh and K. Kaneko, *J. Phys. Chem.* 99:5746 (1995).
26. K. Kanoh and K. Kaneko, *Chem. Phys. Lett.* 237:329 (1995).
27. W. A. Steele, *Chem. Rev.* 93:2355 (1993).
28. T. Takaishi. *J. Chem. Soc., Faraday Trans.* 93:1257 (1997).
29. W. A. Steele, *Surf. Sci.* 36:317 (1973).
30. K. Kaneko, R. Cracknell, and D. Nicholson, *Langmuir* 10:4606 (1994).
31. J. H. Van Vleck, *The Theory of Electric and Magnetic Susceptibilities*, Oxford Univ. Press, Oxford, UK, 1932.
32. A. Weiss and H. Witte, *Magnetochemie* (Translated into Japanese by M. Sorai). Misuzu, Tokyo, 1980, Chap. 4.
33. O. Kahn, *Molecular Magnetism*, VCH, Weinheim, 1993.
34. T. Oguchi, *Statistical Theory of Magnetism* (in Japanese), Shyokabo, Tokyo, 1975.
35. G. C. DeFotis, *Phys. Rev.* 23:4717 (1981).
36. E. Kanda, T. Haseda, and A. Otsubo. *Physica* 20:131 (1954).
37. P. W. Stephens and C. F. Majkrzak. *Phys. Rev. B* 33:1 (1986).
38. C. Uyeda, K. Sugiyama, and M. Date, *J. Phys. Soc. Jpn.* 54:1107 (1985).
39. F. Dunstetter, V. P. Plakhti, and J. Schweizer, *J. Magn. Magn. Mater.* 72:258 (1988).
40. C. S. Barrett, L. Meyer, and J. Wesserman, *J. Chem. Phys.* 47:592 (1967).
41. R. J. Meier, J. H. P. Copla, and H. Sigg, *J. Phys. C* 17:4501 (1983).
42. A. J. R. da Silva and L. M. Falicov. *Chem. Phys. Lett.* 222:339 (1994).
43. J. E. Cahill and G. E. Leroi, *J. Chem. Phys.* 51:97 (1969).
44. K. Kaneko, J. Suzuki, and C. Ishii, *Phys. Rev. Lett.* to be submitted.
45. A. Jeowski, Yu. A. Freiman, J. Mucha, P. Stachowiak, and V. V. Sumarokov, *J. Phys. Condens. Matter* 7:L631 (1995).
46. S. Gregory. *Phys. Rev. Lett.* 40:723 (1978).
47. D. D. Awschalom, G. N. Lewis, and S. Gregory, *Phys. Rev. Lett.* 51:586 (1983).
48. U. Köbler and R. Marx, *Phys. Rev. B* 35:9809 (1987)

49. H. Suematsu and Y. Murakami, *J. Magnet. Magnet Mater.* 90/91:749 (1990).
50. K. Kaneko and C. Ishii, *Colloid Surf*, 67:203 (1992).
51. N. Setoyama, T. Suzuki, and K. Kaneko, *Carbon*, 36:1459 (1998).
52. M. Jaroniec and K. Kaneko, *Langmuir*, 13:6589 (1997).
53. J. W. McClure, *Phys. Rev.* 108:612 (1956).
54. K. Kaneko, K. Yamaguchi, C. Ishii, S. Ozeki, S. Hagiwara, and T. Suzuki, *Chem. Phys. Lett.* 176:75 (1991).
55. G. Volpihac and J. Hoarau, *Phys. Rev.* 104:666 (1978).
56. A. Nakayama, K. Suzuki, T. Enoki, C. Ishii, K. Kaneko, M. Endo, and N. Shindo, *Solid State Commun.* 93:323 (1995).
57. C. Ishii, N. Shindo, and K. Kaneko, *Chem. Phys. Lett.* 242:196 (1995).
58. C. Ishii and K. Kaneko, *Prog. Organic Coat.* 1 (1997).
59. C. Ishii, T. Suzuki, N. Shindo, and K. Kaneko, *J. Porous Solids* 4:1 (1997).
60. A. Zamma, K. Sugihara, and K. Kaneko, *J. Phys. Chem*, to be submitted.
61. H. Kanoh, A. Zamma, N. Setoyama, Y. Hanzawa, and K. Kaneko, *Langmuir* 13:1047 (1997).
62. B. McEnaney, *Carbon* 25:69 (1987).
63. K. Kaneko, C. Ishii, H. Kanoh, Y. Hanzawa, N. Setoyama, and T. Suzuki, *Adv. Colloid Interface Sci.* 76-77:295 (1998).
64. J. A. Mydosh, *Spin Glasses: An Experimental Introduction*, Taylor & Francis, London. 1993.
65. K. Sparks and J. W. Texter, *J. Phys. Chem.* 96:11022 (1992).
66. E. D. Sloan, Jr., *Clathrate Hydrate of Natural Gases*, Marcel Dekker, New York. 1990.
67. T. Iiyama, K. Nishikawa, T. Suzuki, and K. Kaneko, *Chem. Phys. Lett.*, 274:152 (1997).
68. J. Suzuki, C. Ishii, and K. Kaneko, *Chem. Phys. Lett.* 282:176 (1998).
69. A. Malakhovskii, E. Sominska, and A. Gedanken, *J. Chem. Soc., Farada Trans.* 92:1319 (1996).
70. H. H. Kung, *Transition Metal Oxides: Surface Chemistry and Catalysis*, Elsevier, Amsterdam, 1989, Chap. 7.
71. N. Uekawa and K. Kaneko, *J. Phys. Chem.* 100:4193 (1996).
72. S. Sokotowski, *Mol. Phys.* 75:999 (1992).

19

Heat of Adsorption of Pure Gas and Multicomponent Gas Mixtures on Microporous Adsorbents

SHIVAJI SIRCAR and MADHUKAR B. RAO Corporate Science and Technology Center, Air Products and Chemicals, Inc., Allentown, Pennsylvania

| | |
|--|-----|
| I. Introduction | 501 |
| II. Heats of Adsorption by Gibbsian Thermodynamic Model | 502 |
| III. Heat Removal from and Supply to an Isothermal Adsorption System | 506 |
| IV. GSE Model for Mass and Energy Balances in Adiabatic Adsorption Columns | 507 |
| V. Indirect Estimation of Isostatic Heat of Adsorption | 508 |
| A. Pure gas isosteric heat | 508 |
| B. Multicomponent gas isosteric heat | 510 |
| C. Shortcut method | 510 |
| VI. Direct Estimation of Isostatic Heat of Adsorption | 513 |
| VII. Characteristics of Pure Gas Isostatic Heat of Adsorption | 516 |
| A. Homogeneous adsorbent | 518 |
| B. Heterogeneous adsorbent | 518 |
| C. Limiting value of isosteric heat of adsorption | 520 |
| D. Special cases of adsorbent heterogeneity | 520 |
| E. Simple models for isosteric heat of adsorption | 521 |
| VIII. Characteristics of Multicomponent Gas Isostatic Heats of Adsorption | 521 |
| A. Limiting values of isosteric heat of adsorption | 524 |
| B. Simple models of multicomponent gas isosteric heats of adsorption | 524 |
| C. Example of model heterogeneity for a binary system | 526 |
| References | 527 |

I. INTRODUCTION

Adsorption and desorption are, respectively, exothermic and endothermic processes. Consequently, all practical adsorptive gas separation processes such as pressure swing adsorption (PSA) and thermal swing adsorption (TSA) are non-

isothermal. These processes are generally carried out using nearly adiabatic adsorbers, and the local temperatures of the gas and the solid adsorbent change continuously along the length of the adsorber during various steps of the PSA and TSA processes [1,2]. The local gas adsorption equilibria and kinetics within the adsorber depend on the local gas pressure (P), the gas and adsorbent temperature (T), and the gas-phase composition (mole fraction of component i , y_i). Thus, it is critical that accurate knowledge of the heats of adsorption and desorption of the adsorbates as a function of P , T , and y_i be available so that correct temperature changes within the adsorber can be estimated during the process steps. A theoretical sensitivity analysis of the performance of a simple PSA process (Skarstrom cycle) for separation of a binary gas mixture using a detailed mathematical process model showed that small errors in the estimation of heats of adsorption of the adsorbates and their variation with adsorbate loadings could significantly alter the process performance [2]. Furthermore, the study clearly demonstrated the pitfalls of ignoring adsorber non-isothermality.

Traditionally, a variety of heats of adsorption and desorption for pure and multicomponent gas–solid systems have been defined by using thermodynamic models [3–6]. Experimental techniques have also been developed to measure these heats [4,7]. These models generally use the actual amounts adsorbed as the primary variables for representing the extents of adsorption of the adsorbates. Unfortunately, the Gibbsian surface excesses (GSE), and not the actual amounts adsorbed, are the only true experimental variables for measuring the extent of adsorption [8–10]. In view of this fact, a detailed thermodynamic model for multicomponent gas adsorption equilibria using GSE as base variables has already been developed [9].

This chapter (1) elaborates on the thermodynamic properties of multicomponent heats of adsorption and desorption using the GSE framework, (2) demonstrates the practical utility of these heats by developing mathematical models to describe mass and energy balances in adsorption columns using GSE, (3) describes direct and indirect experimental methods for estimating the heats, (4) provides experimental and theoretical examples of the heat of adsorption of pure gas and binary gas mixtures on microporous adsorbents (energetically homogeneous and heterogeneous), and (5) comments on the complex nature of multicomponent heats of adsorption. Only microporous solids are considered in this chapter because of their practical values.

II. HEATS OF ADSORPTION BY GIBBSIAN THERMODYNAMIC MODEL

Figure 1 shows the GSE model for equilibrium adsorption from a bulk multicomponent gas mixture of i components ($i = 1, 2, \dots, N$) characterized by P , T , and y_i . The adsorption system contains a unit amount of an inert adsorbent whose total helium void volume is v^0 (cm³/g). It is assumed that all pores of the adsorbent are accessible to the nonadsorbing helium gas. The dotted line in Fig. 1 represents the Gibbs interface separating the Gibbsian adsorbed phase and the bulk gas phase. It is arbitrarily located inside the actual bulk gas phase. The adsorbed phase has a

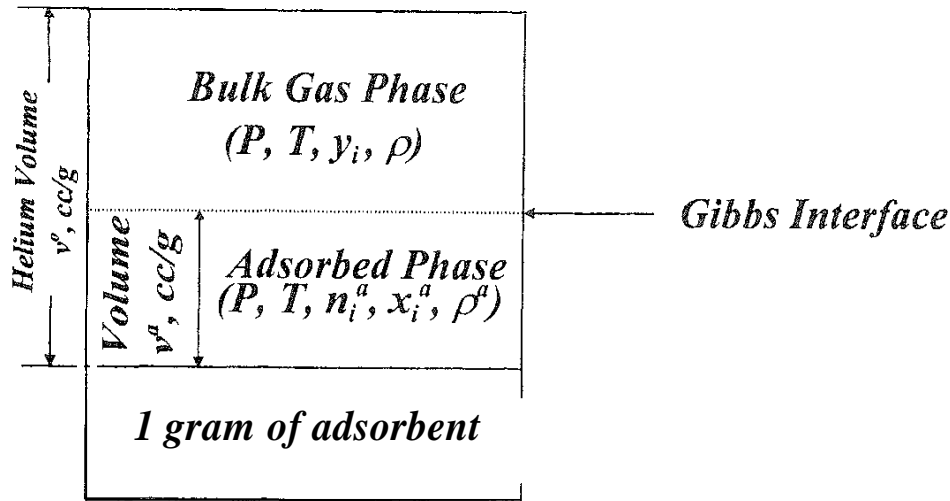


FIG. 1 Schematic of Gibbsian surface excess (GSE) model for multicomponent gas adsorption.

volume of $v^a(\text{cm}^3/\text{g})$, and the actual amount of component i adsorbed is n_i^a (mol/g). The molar density of the adsorbed phase is $\rho^a = (\sum_i n_i^a / v^a, \text{mol}/\text{cm}^3)$. The bulk gas-phase molar density is ρ (mol/cm³). The pressure (P) and temperature (T) of the bulk and adsorbed phases are the same, n_i^0 is the total amount of component i (mol/g) in the entire system.

The magnitudes of variables v^a , ρ^a , and n_i^a depend on the location of the Gibbs interface, and therefore the actual amount adsorbed cannot be unequivocally measured. On the other hand, the GSE for component i (n_i^m , mol/g) of the gas mixture is independent of the location of the Gibbs interface and can be estimated by measuring P , T , y_i , ρ , n_i^0 , and v^0 [9,10]. n_i^m is defined as

$$n_i^m = n_i^a - v^a \rho y_i = n_i^0 - v^0 \rho y_i \quad (1)$$

All conventional experimental techniques such as volumetric, gravimetric, closed-loop recycle, total desorption, and chromatographic techniques measure the GSE of a pure gas as functions of P and T or those of the components of a gas mixture as functions of P , T , and y_i . It can be easily demonstrated that $n_i^m \sim n_i^a$ only when (1) $\rho^a \gg \rho$ for pure gas adsorption and (2) $\rho^a x_i^a \gg \rho y_i$ for multicomponent gas adsorption, where $x_i^a (= n_i^a / \sum_i n_i^a)$ is the adsorbed phase mole fraction of component i . Otherwise, there may be a substantial difference between n_i^m and n_i^a [9,10].

An excess internal energy (u^m , cal/g), an excess enthalpy (h^m , cal/g), an excess entropy [s^m , cal/(g · K)], an excess Gibbs free energy (g^m , cal/g), and an excess volume (v^m , cm³/g) can also be defined for the thermodynamic system of Fig. 1 [9]:

$$v^m = v^a(\rho^a z^a - \rho z) \quad (2)$$

where z^a and z can be the molar internal energy (u), the molar enthalpy (h), the molar entropy (s), the molar Gibbs free energy (g), and the molar volume (v) of the adsorbed and bulk gas phases, respectively, z^m is the corresponding excess function. It should be noted that v^m is equal to zero by this definition, and thus $h^m (= u^m + Pv^m)$ is equal to u^m .

Integral and differential thermodynamic relationships between the different excess quantities defined by Eq. (2) and the set of experimental variables (P, T, y_i) or (T, n_i^m) can be derived analogously to those for conventional bulk-phase thermodynamic properties [9]. However, an additional intensive property called the surface potential $(\phi, \text{cal/g})$ is necessary to completely define the Gibbsian adsorbed phase. The surface potential can be calculated by using the relationship [9]:

$$\phi = -RT \int_0^P n^m d(\ln P) \quad (3)$$

For pure gas adsorption, Eq. (3) can be used to calculate $\phi(P, T)$ by measuring the pure gas surface excess (n^m) as a function of gas-phase pressure (P) at constant T (adsorption isotherm for pure gas). For a multicomponent gas mixture, Eq. (3) can be used to calculate $\phi(P, T, y_i)$ by measuring the surface excess of component i (n_i^m) as a function of total gas-phase pressure (P) at constant T and y_i [9]. The variable n^m of Eq. (3) in this case is the total surface excess for all components $(\sum_i n_i^m)$. R is the gas constant.

The total internal energy $(u^0, \text{cal/g})$ and the total enthalpy $(h^0, \text{cal/g})$ of the entire adsorption system of Fig. 1 at P, T , and y_i are given by [9]:

$$u^0 = u^m + v^0 \rho u + c_s(T - T_0) \quad (4)$$

$$h^0 = h^m + v^0 \rho h + c_s(T - T_0) \quad (5)$$

where c_s [cal/(g·K)] is the heat capacity of the adsorbent and T_0 is a reference temperature. Equations (4) and (5) can be combined for the case where the gas phase (pure or mixture) of Fig. 1 is ideal ($h = u + Pv$; $Pv = RT$; $\rho = P/RT$) to get

$$h^0 = u^0 + Pv^0 \quad (6)$$

Both u^0 and h^0 can be expressed as functions of P, T , and y_i or T and n_i^m . Thus, one can show by using the chain rule of calculus that

$$du^0 = \left(\frac{\delta u^0}{\delta T} \right)_{n_i^m} dT + \sum_i \left(\frac{\delta u^0}{\delta n_i^m} \right)_{T, n_{j \neq i}^m} dn_i^m \quad (7)$$

$$dh^0 = \left(\frac{\delta h^0}{\delta T} \right)_{n_i^m} dT + \sum_i \left(\frac{\delta h^0}{\delta n_i^m} \right)_{T, n_{j \neq i}^m} dn_i^m \quad (8)$$

One can now define the following thermodynamic variables [9]:

$$\left(\frac{\delta u^0}{\delta n_i^m} \right)_{T, n_{j \neq i}^m} = -q_i^d; \quad \left(\frac{\delta h^0}{\delta n_i^m} \right)_{T, n_{j \neq i}^m} = -q_i \quad (9)$$

$$\left(\frac{\delta u^0}{\delta T}\right)_{n_i^m} = C_A^d; \quad \left(\frac{\delta h^0}{\delta T}\right)_{n_i^m} = C_A \quad (10)$$

It can be shown by using the thermodynamic relationships between different extensive and intensive variables of the multicomponent system of Fig. 1 that [9]:

$$q_i = RT^2 \left[\frac{\partial \ln(Py_i)}{\partial T} \right]_{n_i^m} \quad (11)$$

$$q_i^d = q_i - RT \quad (12)$$

$$C_A = -T \left(\frac{\partial^2 \phi}{\partial T^2} \right)_{P, y_i} + \sum_i q_i \left(\frac{\partial n_i^m}{\partial T} \right)_{P, y_i} + \sum_i n_i^0 c_{gi}^* + c_s \quad (13)$$

$$C_A^d = C_A - Pv^0/T \quad (14)$$

where c_{gi}^* is the molar heat capacity [cal/(mol·K)] of pure gas i . It is assumed in the derivations of Eqs. (11)–(14) that the gas phase of Fig. 1 is ideal. The variables q_i^d and q_i , defined by Eq. (9), are two different forms of differential heats (cal/mol). They represent the differential changes in the total internal energy or the total enthalpy of the closed system of Fig. 1 due to a differential change in the surface excess of component i while the surface excesses of other components and the system temperature are held constant. They are related by Eqs. (11) and (12). They can be indirectly estimated from experimental adsorption equilibrium data using Eq. (11). q_i^d and q_i , respectively, are called the differential and isosteric heat of adsorption of component i from a gas mixture. For pure gas adsorption, q_i^d and q_i are simply obtained by setting $y_i = 1$ in Eq. (11). Traditionally, q_i^d and q , are defined by Eq. (11), substituting n_i^a for n_i^m . The present derivations show that these variables can be analogously defined by using GSE as the base variables. The isosteric heat of adsorption of component i can be a function of P , T , and y_i or of T and n_i^m .

The variables C_A^d and C_A , defined by Eq. (10), are two different heat capacities [cal/(g·K)] of the adsorption system of Fig. 1. They represent the changes in the total internal energy or total enthalpy of the closed system of Fig. 1 due to a differential change in the system temperature at constant n_i^m . Equation (14) relates these two different heat capacities.

Equation (13) can be used to calculate C_A from experimental adsorption equilibrium data. For pure gas adsorption, C_A^d or C_A can be obtained by simply setting $y_i = 1$ in Eq. (13). The summation terms of Eq. (13) are then replaced by a single term.

The total surface excess of all components of Fig. 1 ($n^m = \sum_i n_i^m$) can be expressed as functions of T and gas-phase partial pressures of component i , $p_i (= Py_i)$. Thus, by using the chain rule of calculus, one has

$$dn^m = \left(\frac{\partial n^m}{\partial T} \right)_{P, y_i} dT + \sum_i \left(\frac{\partial n^m}{\partial p_i} \right)_{T, p_j \neq i} dp_i \quad (15)$$

Equation (15) can be differentiated with respect to T at constant n_i^m and combined with Eq. (11) to get

$$\left(\frac{\partial n^m}{\partial T}\right)_{P, y_i} = - \sum_i \left(\frac{\partial n^m}{\partial p_i}\right)_{T, p_{j \neq i}} \frac{p_i q_i}{RT^2} \quad (16)$$

It can be shown from Eq. (1) that for a closed system (constant n_i^0) with an ideal gas phase, one has

$$\left(\frac{\partial n^m}{\partial p_i}\right)_{T, p_{j \neq i}} = \left(\frac{\partial n^m}{\partial P}\right)_T; \quad \left(\frac{\partial n_i^m}{\partial P}\right)_{T, y_i} = y_i \left(\frac{\partial n^m}{\partial P}\right)_T \quad (17)$$

Equation (3) can be differentiated with respect to T at constant P and y_i and combined with Eqs. (13), (16), and (17) to get

$$C_A = - \frac{\partial}{\partial T} \left[\int_0^{n_i^m} \sum_i q_i dn_i^m \right]_{P, y_i} + \sum_i q_i \left(\frac{\partial n^m}{\partial T}\right)_{P, y_i} + \sum_i n_i^0 c_{gi}^* + c_s \quad (18)$$

For the special case where q_i is not a function of T and n_i^m , Eq. (18) simplifies to

$$C_A = \sum_i n_i^0 c_{gi}^* + c_s \quad (19)$$

Equation (19) was previously derived for adsorption of a pure gas [9].

III. HEAT REMOVAL FROM AND SUPPLY TO AN ISOTHERMAL ADSORPTION SYSTEM

A certain amount of heat (dQ) must be supplied to or removed from the closed adsorption system of Fig. 1 to maintain system isothermality when the GSE of component i is changed by a differential amount (dn_i^m). By applying the conventional energy balance for the closed system [11], one gets

$$du^0 = -dQ \quad (20)$$

The negative sign for the quantity dQ in Eq. (20) represents the case where heat is removed from the system in order to maintain system isothermality. Equations (7), (9), (12), and (20) can be combined to obtain

$$dQ = \sum_i q_i^d dn_i^m = \sum_i q_i dn_i^m - n^m RT \quad (21)$$

Equation (21) was previously derived by many authors using the actual amount adsorbed (n_i^a) instead of the GSE as the base variable. The equation demonstrates the practical value of the differential heats defined by Eq. (9).

IV. GSE MODEL FOR MASS AND ENERGY BALANCES IN ADIABATIC ADSORPTION COLUMNS

It is demonstrated in this section that the GSE framework of adsorption system can be easily used to describe instantaneous unsteady-state mass and energy balances in an adiabatic adsorption column. Figure 2 is a schematic diagram of gas flow through a differential section (AZ) of an adiabatic adsorption column located at a distance Z from one end of the column at any given t . The column is packed with the adsorbent particles. The gas flow is in the direction of coordinate Z . It is assumed that (1) the gas flow through the adsorber is plug flow in nature, (2) there is instantaneous thermal equilibrium between the gas and the adsorbent, (3) there is no axial dispersion of mass or heat, including axial conduction of heat between the adsorbent particles, and (4) the column is adiabatic. The variable Q represents the instantaneous molar flow rate of gas per unit empty cross-sectional area of the adsorber [$\text{mol}/(\text{cm}^2\text{-s})$]. It can be a function of Z and t . P , T , and y_i are, respectively, the gas pressure, gas and adsorbent temperature, and gas-phase mole fraction of component i at Z and t . The instantaneous mass balance for component i across the differential section ΔZ at time t yields

$$\left[\frac{\partial \bar{n}_i}{\partial t} \right]_z = - \left[\frac{\partial \{Q y_i\}}{\partial z} \right]_i \quad (22)$$

where \bar{n}_i (mol/cm^3) is the total amount of adsorbate i per unit volume of the adsorber at Z and t :

$$\bar{n}_i = \rho_b n_i^m + \varepsilon \rho y_i, \quad i = 1, 2, \dots, N \quad (23)$$

where n_i^m (mol/g) is the instantaneous GSE of component i at Z and t . ε is the helium void fraction (cm^3/cm^3) of the adsorber, and ρ (mol/cm^3) is the gas-phase density at Z and t . ρ_b is the bulk density (g/cm^3) of the adsorbent.

The instantaneous energy balance across the differential section AZ (open adiabatic system, no shaft work) at time t yields [11]

$$\rho_b \left[\frac{\partial u^0}{\partial t} \right]_z = - \left\{ \frac{\partial}{\partial z} [Q c_g (T - T_0)] \right\}_t \quad (24)$$

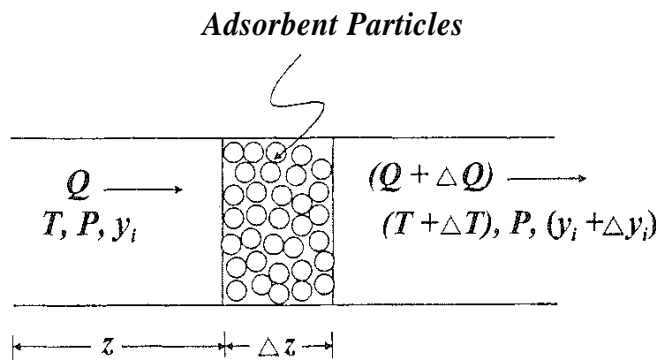


FIG. 2 Schematic of instantaneous mass balance across a differential section in an adsorbent column at time t .

where c_g is the molar heat capacity of the gas phase at Z and t . Equations (7), (9), (10), (12), (14), and (24) can be combined to get

$$C_A \rho_b \left(\frac{\partial T}{\partial t} \right)_z = - \left\{ \frac{\partial}{\partial z} [Q c_g (T - T_0)] \right\}_t + \rho_b \sum_i q_i \left(\frac{\partial n_i^m}{\partial t} \right)_z + \varepsilon \left(\frac{\partial P}{\partial t} \right)_z \quad (25)$$

Equation (25) represents the instantaneous column energy balance using the GSE framework. The key thermodynamic variables in the equation include q_i and C_A defined by Eqs. (9) and (10), respectively. The last term on the right-hand side of Eq. (25) vanishes for isobaric process steps (constant P).

The quantity $(\delta n_i^m / \delta t)_z$ in Eq. (25) represents the instantaneous rate of change of surface excess of component i at Z and t . This replaces the local rate of adsorption term in the conventional energy balance equation derived by using the actual amount adsorbed as the base variable. A simple model to describe the rate of change of GSE is the analog of the conventional linear driving force model [12].

$$\left(\frac{\partial n_i^m}{\partial t} \right)_z = k_i [n_i^{m*} - n_i^m] \quad (26)$$

where n_i^{m*} is the equilibrium GSE of component i at the local values of P , T , and y_i . k_i (s^{-1}) is the mass transfer coefficient for the i th component of the gas mixture.

Equations (22)–(26) show that the unsteady-state mass and energy balances within the adiabatic adsorber can be written using the surface excess of each component of the gas mixture as the primary variables to define the extent of adsorption. The isosteric heat of adsorption of component i (q_i) and the heat capacity of the adsorption system (C_A), defined using the GSE framework, become the appropriate thermodynamic properties to describe the energy balance.

V. INDIRECT ESTIMATION OF ISOSTERIC HEAT OF ADSORPTION

A. Pure Gas Isosteric Heat

For pure gas adsorption of component i , Eqs. (11) and (15) can be modified ($n^m = n_i^m$, $y_i = 1$, $p_i = P$) and differentiated with respect to T at constant n_i^m to obtain [13]:

$$\frac{q_i}{RT^2} = - \frac{(\partial n_i^m / \partial T)_P}{P(\partial n_i^m / \partial P)_T} \quad (27)$$

Equation (27) shows that the isosteric heat of adsorption (q_i) of pure gas i can be estimated at a given value of P and T or T and n_i^m by (1) measuring a set of pure gas adsorption isotherms (n_i^m as a function of P at constant T) at different temperatures, (2) generating a set of adsorption isobars (n_i^m as a function of T at constant P) from the isotherms or measuring them independently, and (3) estimating the isotherm and isobar slopes at the desired values of P and T . The use of Eq. (27) for calculating q_i for pure gas is, however, very sensitive to errors in measuring the isotherm and isobar slopes. On the other hand, it is very useful to develop analytical expressions for q_i as functions of T and n_i^m when the adsorption isotherms can be described by analytical models [14].

A more popular method of estimating a , for adsorption of pure gas ($y_i = 1$) is to integrate Eq. (11) by assuming that q_i is not a function of T . Thus,

$$\ln(P) = -\frac{q_i}{RT} + c(n_i^m) \quad (28)$$

where c is a constant or a function of n_i^m only. According to Eq. (28), a semilog plot of P against $1/T$ at constant values of n_i^m yields a straight line with a slope equal to $-q_i/R$. Thus q_i can be estimated as functions of n_i^m by measuring pure gas adsorption isotherms at different temperatures. The linearity of Eq. (28) is experimentally validated over a large range of T (100–400 K) for many pure gas adsorption isotherms on microporous adsorbents, indicating that q_i for a given n_i^m is indeed a very weak function of T . Figure 3 shows a family of linear plots according to Eq. (28) for adsorption of pure CO_2 on BPL carbon at different values of $n_{\text{CO}_2}^m$. These plots were generated from pure gas adsorption isotherm data at 212.7, 260.2, and 301.4 K [22].

One practical problem in using Eq. (28) to calculate q_i as a complete function of n_i^m is that the procedure requires very high pressure isotherm data at the higher temperatures [12].

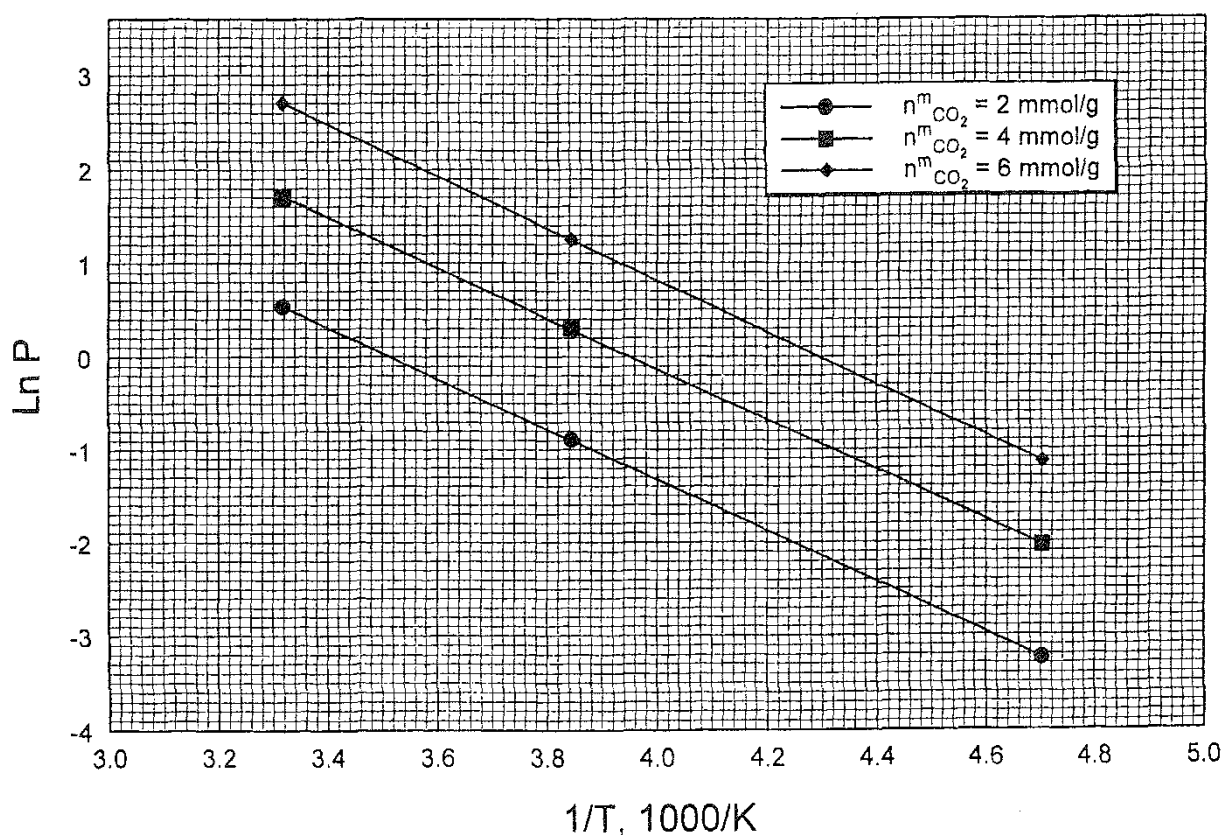


FIG. 3 Plots of $\ln P$ versus $1/T$ at constant n_i^m for adsorption of pure CO_2 on BPL activated carbon.

B. Multicomponent Gas Isostatic Heat

The common methods of measuring the extent of adsorption of multicomponent gas systems are to measure (1) n_i^m as functions of P at constant T and y_i , (2) n_i^m as functions of T at constant P and y_i , and (3) n_i^m as functions of y_i at constant P and T [9]. Adsorption thermodynamics can be used to generate expressions for multicomponent gas isosteric heats of adsorption using the slopes of the three functionalities described above. These expressions are analogous to Eq. (27) derived for pure gas adsorption. For a binary system ($i = 1, 2$) one gets [9]:

$$\frac{q_1}{RT^2} = \frac{(1/P)(n_{1T}^m n_{2y}^m - n_{1y}^m n_{2T}^m) + (1/y)(n_{1P}^m n_{2T}^m - n_{1T}^m n_{2P}^m)}{n_{1y}^m n_{2P}^m - n_{1P}^m n_{2y}^m} \quad (29)$$

$$\frac{q_2}{RT^2} = \frac{(1/P)(n_{1T}^m n_{2y}^m - n_{1y}^m n_{2T}^m) - [1/(1-y)](n_{1P}^m n_{2T}^m - n_{1T}^m n_{2P}^m)}{n_{1y}^m n_{2P}^m - n_{1P}^m n_{2y}^m} \quad (30)$$

where y is the gas-phase mole fraction of component 1, and

$$n_{iT}^m = \left(\frac{\partial n_i^m}{\partial T} \right)_{P,y}; \quad n_{iy}^m = \left(\frac{\partial n_i^m}{\partial y} \right)_{P,T}; \quad n_{iP}^m = \left(\frac{\partial n_i^m}{\partial P} \right)_{T,y} \quad (31)$$

It can be seen that the experimental protocol to generate data for use in Eqs. (29) and (30) can be extremely time-consuming and impractical. We are not aware of any such data in the published literature. The degree of complexity increases enormously when the gas phase has three or more components.

It is also unfortunate that Eq. (11) cannot be easily integrated for multicomponent adsorption as in the case of pure gas adsorption [Eq. (28)] because no multicomponent adsorption experiment can be designed to generate p_i as functions of T at constant n_i^m ($i = 1, 2, \dots, N$). Consequently, there is no easy way to estimate multicomponent ($i \geq 2$) isosteric heats of adsorption by measuring n_i^m as functions of P , T , and y_i .

C. Shortcut Method

A shortcut method for estimating the isosteric heat of adsorption of pure and multicomponent gas systems has been proposed [15,16]. It consists of packing a container with a unit amount of the adsorbent of interest and then saturating the adsorbent (initial state) with a pure gas at P^0 and T^0 or with a gas mixture at P^0 , T^0 and y_i^0 . The container is placed in a thermostated bath at T^0 and is equipped with a gas-mixing device (optional) and instruments for measuring the gas-phase pressure and composition. The amount of pure gas i or the amounts of the components ($i = 1, 2, \dots, N$) of a gas mixture introduced into the container to reach the initial state of saturation are measured. The temperature (T) of the thermostated bath is then periodically changed, and the changes in the P and y_i of the gas phase within the sealed container are measured after every new equilibrium state is achieved at different values of T . The total amount of each adsorbate inside the closed container ($\$, \text{ mol/g}$) remains constant during the process.

It is argued that n_i^m is approximately equal to n_i^0 , according to Eq. (1), provided that $n_i^m \gg v^0 \rho y_i$. This can be met by having a small specific helium void volume (v^0 , cm³/g) for the container and choosing appropriate values of P^0 , T^0 , and y_i^0 . Consequently, it is assumed in the shortcut method that

$$\frac{q_i}{RT^2} = \left[\frac{\partial \ln(Py_i)}{\partial T} \right]_{n_i^m} \sim \frac{\bar{q}_i}{RT^2} = \left[\frac{\partial \ln(Py_i)}{\partial T} \right]_{n_i^0} \quad (32)$$

The apparent isosteric heat of adsorption (\bar{q}_i) of component i (pure or multi-component gas) defined by Eq. (32) is estimated by the shortcut method. According to Eq. (32), a semilog plot of the pressure of pure gas ($y_i = 1$) or the partial pressure of component i (Py_i) against $1/T$ at a constant value of n_i^0 should yield a straight line with a slope equal to $-\bar{q}_i/R$ if \bar{q}_i is independent of T . The linearity of such plots has been experimentally verified for many systems using the experimental data obtained by the shortcut method [15,16]. Thus \bar{q}_i , and hence q_i , can be estimated as functions of n_i^m by the shortcut method.

Unfortunately, the approximation $\bar{q}_i \sim q_i$ assumed by Eq. (32) may not be valid even if the approximation $n_i^m \sim n_i^0$ is reasonable [13]. \bar{q}_i and q_i are equal only if v^0 is equal to zero, which is not practically possible. The minimum value of v^0 for a container tightly packed with the adsorbent particles is given by $(\rho_c - \rho_b)/\rho_c \rho_b$, where ρ_c and ρ_b are, respectively, the chemical and bulk densities of the adsorbent. Most practical microporous adsorbents (zeolites, activated carbons, aluminas, silica gels, etc.) exhibit a ρ_c value of ~ 2.0 g/cm³ and ρ_b values ranging between 0.4 and 1.0 g/cm³. Thus, the typical minimum values of v^0 range between 0.5 and 2.0 cm³/g.

The exact thermodynamic relationship between \bar{q}_i and q_i for closed system (constant n_i^0) can be derived by expressing n_i^m in functional form in terms of P , T , and y_i to estimate the change in n_i^m for differential changes in those variables and combining the result with the differential form of Eq. (1).

It can be shown that for adsorption of pure gas i , the difference between \bar{q}_i and q_i is given by [13]:

$$q_i - \bar{q}_i = \frac{(v^0/RT)(\bar{q}_i - RT)}{(\partial n_i^m / \partial P)_T} \quad (33)$$

Equation (33) shows that (1) the difference between \bar{q}_i and q_i increases as P or n_i^m increases (isotherm slope decreases) and (2) $q_i > \bar{q}_i$ because $(\bar{q}_i - RT)$ is generally positive.

For a binary system ($i = 1, 2$) one gets [13]

$$q_1 - \bar{q}_1 = \frac{(v^0/RT)[p_2(Pn_{1p}^m - yn_{1y}^m)(\bar{q}_2 - RT) - p_1(Pn_{2p}^m - yn_{2y}^m)(\bar{q}_1 - RT)]}{p_1(n_{1p}^m n_{2y}^m - n_{1y}^m n_{2p}^m)} \quad (34)$$

$$q_2 - \bar{q}_2 = \frac{(v^0/RT)[p_1\{Pn_{2p}^m + (1-y)n_{2y}^m\}(\bar{q}_1 - RT) - p_2\{pn_{1p}^m + (1-y)n_{2y}^m\}(\bar{q}_2 - RT)]}{p_2(n_{1p}^m n_{2y}^m - n_{1y}^m n_{2p}^m)} \quad (35)$$

where y is the gas-phase mole fraction of component 1 and variables n_{ip} and n_{iy} are given by Eq. (31).

Table 1 shows the differences between n_i^m and n_i^0 and q_i and \bar{q}_i for binary adsorption of CO₂ (component 1) + CH₄ (component 2) mixtures on BPL carbon at 303.1 K [13]. They were estimated at three different total gas pressure levels and at different gas-phase compositions. The table also gives the fractional adsorbate loadings (6,) of the components [$\theta_i = n_i^m(P, T, y_i)/m$]. m is the saturation capacity (surface excess) for both components. The pure and binary gas adsorption isotherms for this system can be described by the Langmuir model [17]. The model parameters are given in Table 1. A value of 0.80 cm³/g was used as v^0 for these calculations. It can be seen from Table 1 that the differences between n_1^m and n_1^0 are relatively small because CO₂ (component 1) is more selectively adsorbed than CH₄ on the carbon. The differences between n_2^m and n_2^0 are, however, much larger. Furthermore, the differences between q_i and \bar{q}_i are much larger than the corresponding differences between n_i^m and n_i^0 . The differences between q_i and \bar{q}_i get even bigger as the system pressure (P) and the mole fraction of component 1 (y) in the gas phase are increased. These examples demonstrate the weakness of the shortcut method.

Equations (33)–(35), on the other hand, show that a_i can be calculated using the \bar{q}_i values obtained by the shortcut method provided that n_{ip}^m and n_{iy}^m are estimated from some other data source. For pure gas adsorption, the denominator of Eq. (33) can be easily obtained by independently measuring the adsorption isotherm for the pure gas at the base temperature (T^0) of the shortcut method. For a binary gas adsorption system, n_{ip}^m and n_{iy}^m can be estimated by independently measuring the total surface excess ($n^m = n_1^m + n_2^m$) as functions of P at constant T^0 and y and as functions of y at constant P and T^0 [13]:

$$n_{ip}^m = y \left(\frac{\partial n^m}{\partial P} \right)_{T,y} + \frac{y(1-y)}{P} \left(\frac{\partial n^m}{\partial y} \right)_{T,P} \quad (36)$$

TABLE 1 Examples of Errors in Estimating q_i by Shortcut Method^a [CO₂(1) + CH₄(2) on BPL carbon at 303 K]

| Conditions | | Adsorbate loadings | | | Estimated error (%) | | | |
|------------|-------------------|--------------------|------------|----------|-------------------------------|-------------------------------|-------------------------------|-------------------------------|
| P (atm) | y | θ_1 | θ_2 | θ | $\frac{n_1^m - n_1^0}{n_1^m}$ | $\frac{n_2^m - n_2^0}{n_2^m}$ | $\frac{q_1 - \bar{q}_1}{q_1}$ | $\frac{q_2 - \bar{q}_2}{q_2}$ |
| 5.0 | $y \rightarrow 0$ | 0.0000 | 0.5454 | 0.5454 | 2.6 | 6.8 | 6.9 | 11.1 |
| | 0.10 | 0.1291 | 0.4522 | 0.5813 | 2.9 | 7.4 | 7.6 | 12.2 |
| | 0.50 | 0.4907 | 0.1907 | 0.6817 | 3.8 | 9.7 | 10.7 | 16.5 |
| | 0.90 | 0.7124 | 0.0308 | 0.7432 | 4.7 | 12.0 | 13.9 | 21.0 |
| | $y \rightarrow 1$ | 0.7551 | 0.0000 | 0.7551 | 4.9 | 12.6 | 14.8 | 22.2 |
| 2.0 | 0.50 | 0.3321 | 0.1292 | 0.4613 | 2.2 | 5.7 | 4.0 | 7.1 |
| 5.0 | 0.50 | 0.4907 | 0.1907 | 0.6817 | 3.8 | 9.7 | 10.7 | 16.5 |
| 10.0 | 0.50 | 0.5836 | 0.2271 | 0.8107 | 6.3 | 16.3 | 24.5 | 34.2 |

^aLangmuir parameters: $n = 4.35$ mol/kg; $K_1 = 2.682$ mol/(kg · atm); $K_2 = 1.044$ mol/(kg · atm); $q_1^0 = 5.29$ kcal/mol, $q_2^0 = 4.17$ kcal/mol.

$$n_{2p}^m = \left(\frac{\partial n^m}{\partial P} \right)_{T,y} - n_{1p}^m \quad (37)$$

$$n_{1y}^m = n^m + y \left(\frac{\partial n^m}{\partial y} \right)_{P,T} + (1 - 2y) \left(\frac{\partial F}{\partial y} \right)_{P,T} + y(1 - y) \left(\frac{\partial^2 F}{\partial y^2} \right)_{P,T} \quad (38)$$

$$n_{2y}^m = \left(\frac{\partial n^m}{\partial y} \right)_{P,T} - n_{1y}^m \quad (39)$$

$$F(P, y) = \int_0^P n^m d \ln P \quad \text{at constant } T \text{ and } y \quad (40)$$

Equations (36)–(40) are derived using adsorption thermodynamics [13]. Even though the above-described experimental protocols for a binary system are tedious, they provide the additional information to calculate q_i from \bar{q}_i using Eqs. (33)–(35). We are not aware of any work where the above-described method is tested. This thermodynamic approach has not yet been extended to systems containing more than two adsorbates.

VI. DIRECT ESTIMATION OF ISOSTERIC HEAT OF ADSORPTION

It must be very clear from the above discussions that the available indirect methods for estimation of q_i may not be very useful for multicomponent ($i \geq 2$) adsorption systems. A calorimetric method is necessary where the heat evolved (or consumed) due to specific changes in the adsorption system is directly measured. Recently, a Tian–Calvet heat flux microcalorimeter was developed to measure the heat of adsorption [18–21]. Figure 4a is a schematic diagram of the calorimeter. It consists of a thermostated cell whose walls are surrounded by thermopiles for directly measuring the heat flow signals through the cell walls. Figure 4b shows the typical profile of thermopile response (in microvolts) versus time during an experiment. The area under the curve of Fig. 4b gives the total energy (cal/g) removed from the calorimeter during an experiment. It is necessary to calibrate the response curve using a known heat generation system within the cell.

The cell is connected with instruments for measuring the gas-phase pressure and composition. It is also connected to a thermostated gas injection system (dosage side) through a valve. A unit amount of the adsorbent is placed in the cell (sample side), and it is initially saturated with pure gas i at P^0 and T^0 or a gas mixture at P^0 , T^0 , and y_i^0 . The experiment consists of very slowly introducing a very small quantity of pure gas i (AN., mol/g) into the sample side from the dosage side through the valve. The temperature of the gas entering the sample side [$T(t)$] is monitored as a function of time in conjunction with the thermopile response profile. The dosage side pressure and temperature are also monitored as functions of time. The system temperature is T^0 at both the start and end of the experiment.

The amount of pure component i introduced during the experiment is given by

$$\Delta N_i = \int_0^{t^*} \dot{N}_i dt; \quad \dot{N}_i = v^d \frac{d\rho^d}{dt} \quad (41)$$

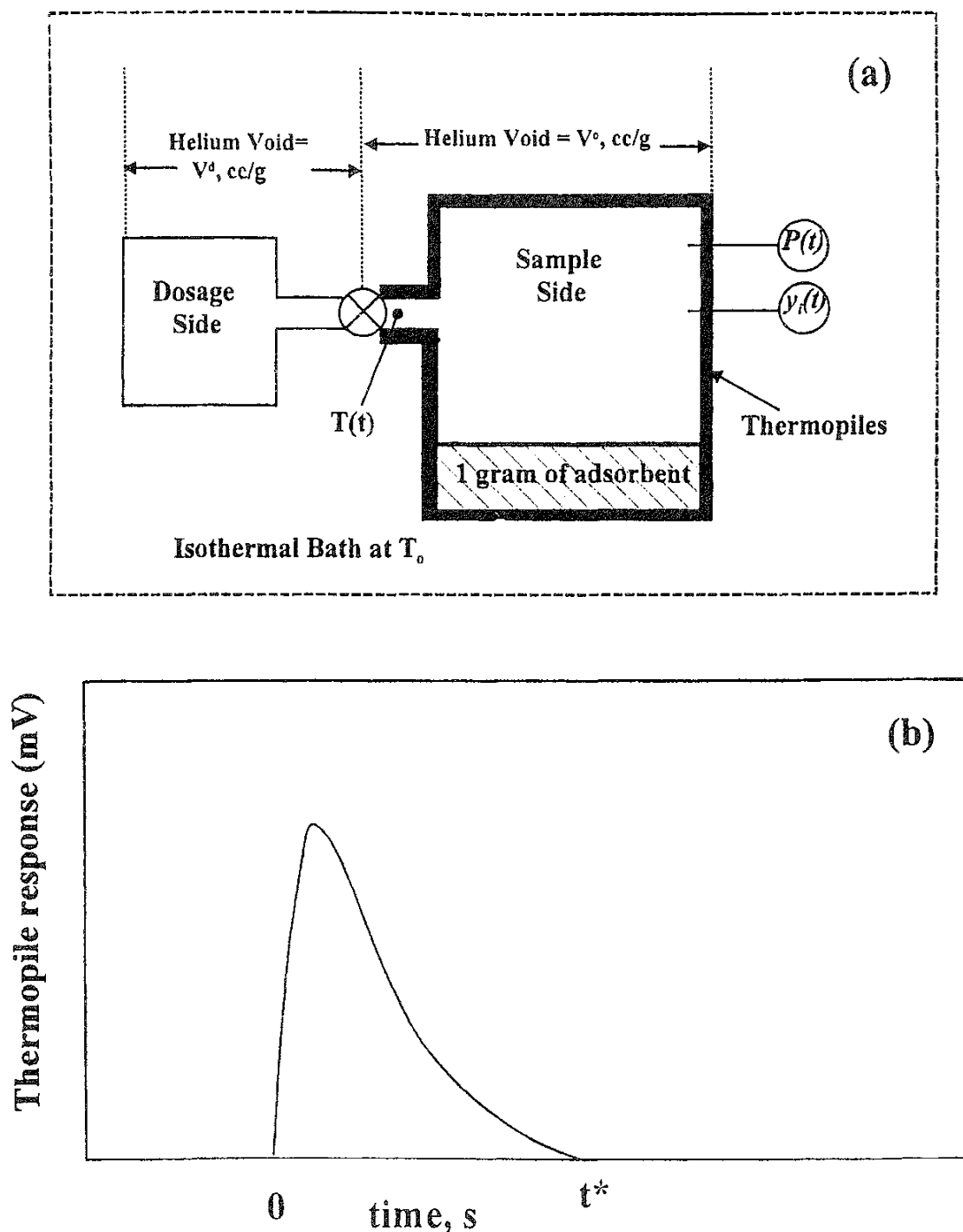


FIG. 4 (a) Schematic of Tian-Calvet type of calorimeter system and (b) thermopile response curve.

where \dot{N}_i (mol/s) is the rate of introduction of pure gas i into the sample side. It can be calculated by knowing the volume of the dosage side ($v^d, \text{cm}^3/\text{g}$) and the rate of change of gas density ($\rho^d, \text{mol}/\text{cm}^3$) in the dosage side during the experiment. t^* (s) is the time interval of the experiment. The amount of energy (enthalpy, cal/g) introduced into the sample side of the calorimeter (ΔH_{in}) during the experiment is given by

$$\Delta H_{\text{in}} = \Delta N_i \bar{h}_i \quad ; \quad \bar{h}_i = \frac{\int_0^{t^*} c_{gi}^* [T(t) - T^0] \dot{N}_i dt}{\int_0^{t^*} \dot{N}_i dt} \quad (42)$$

where \bar{h}_i is the average molar enthalpy (cal/mol) of pure gas i introduced into the sample side. \bar{h}_i is equal to zero if $T(t) \rightarrow T^0$ during the experiment.

The mass balance for the sample side of the calorimeter during the experiment can be described by

$$\Delta N_i = \Delta n_i^m + \frac{v^0}{RT^0} \Delta p_i \quad (43)$$

$$\Delta N_{j \neq i} = 0 = \Delta n_{j \neq i}^m + \frac{v^0}{RT^0} \Delta p_j \quad (44)$$

where Δn_i^m and Δp_i are, respectively, the changes in the surface excess and the gas-phase partial pressure of component i in the sample side. v^0 is the helium void volume (cm³/g) of the sample side.

An energy balance for the sample side of the calorimeter (open system, $H_{\text{out}} = 0$, no shaft work) yields [11]:

$$\Delta u^0 = \Delta H_{\text{in}} - \Delta Q_i \quad (45)$$

where Δu^0 is the total change in internal energy (cal/g) of the sample side of the calorimeter during the experiment. ΔQ_i (cal/g) is the total amount of heat removed from the sample side of the calorimeter through the thermopiles during the experiment. Equations (6), (7), (11), (12), and (42)–(45) can be combined to get

$$\frac{\Delta Q_i}{\Delta N_i} = q_i - \sum_j \frac{v^0 \Delta p_{ji}}{\Delta N_i} \left[\frac{q_j}{RT} - 1 \right] + \bar{h}_i, \quad i, j = 1, 2, \dots, N \quad (46)$$

where Δp_{ji} ($j = 1, 2, \dots, N$) is the change in the gas-phase partial pressure (p_j , atm) of component j in the sample side of the calorimeter when ΔN_i moles of pure gas i is introduced into the sample side.

For a multicomponent gas system ($i = 1, 2, \dots, N$), a total of N experiments must be carried out around the base saturation conditions of T^0 , P^0 , y_i^0 (corresponding surface excess of component $i = n_i^{m0}$), by separately introducing differential quantities (ΔN_i , mol/g) of each pure gas i into the sample side. This will generate N independent equations ($i = 1, 2, \dots, N$) analogous to Eq. (46) that relate N different unknowns (q_i). Consequently, the isosteric heat of adsorption of component i can be estimated as functions of T^0 and n_i^{m0} .

For adsorption of pure gas i , Eq. (46) simplifies to

$$\frac{\Delta Q_i}{\Delta N_i} = q_i - \left[v^0 \frac{\Delta P}{\Delta N_i} \left(\frac{q_i}{RT} - 1 \right) \right] + \bar{h}_i \quad (47)$$

The direct calorimetric method for measurement of q_i for multicomponent gas mixtures ($i \geq 2$) may still be tedious, but it is much simpler, more accurate, and less time-consuming than the indirect methods.

VII. CHARACTERISTICS OF PURE GAS ISOSTERIC HEAT OF ADSORPTION

Figures 5 and 6, respectively, show the isosteric heats of adsorption of pure CO_2 and C_2H_6 as functions of adsorbate loadings (surface excess) on three different microporous adsorbents (silicalite crystals, NaX zeolite crystals, and granular BPL activated carbon). Figure 7 shows similar plots for adsorption of three different pure gases (CH_4 , SF_6 , and CO_2) on NaX zeolite crystals and pellets. The data for adsorption of CO_2 and C_2H_6 on BPL carbon and those for adsorption of CH_4 on NaX zeolite pellets were calculated with Eq. (11) using the pure gas adsorption isotherms at different temperatures [22]. The CH_4 isotherms on the zeolite pellets were measured in our laboratory. All other data were measured by using a Tian-Calvet type of calorimeter [19,20].

Silicate is a crystalline, hydrophobic, nonpolar, microporous adsorbent. The NaX zeolite is a crystalline, hydrophilic, highly polar microporous adsorbent. The activated carbon is an amorphous, moderately polar, micro-mesoporous

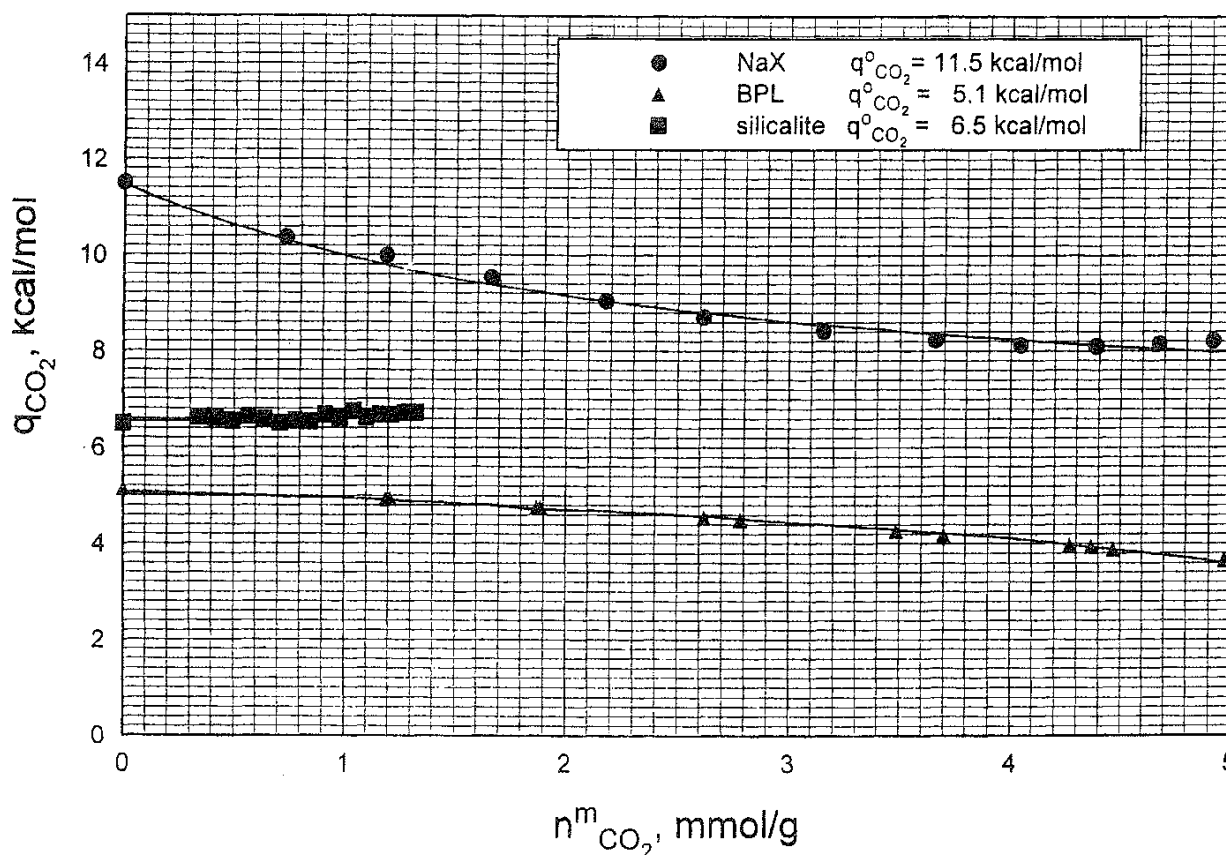


FIG. 5 Isosteric heats of adsorption of pure CO_2 as functions of adsorbate surface excesses on NaX zeolite, silicalite, and BPL activated carbon.

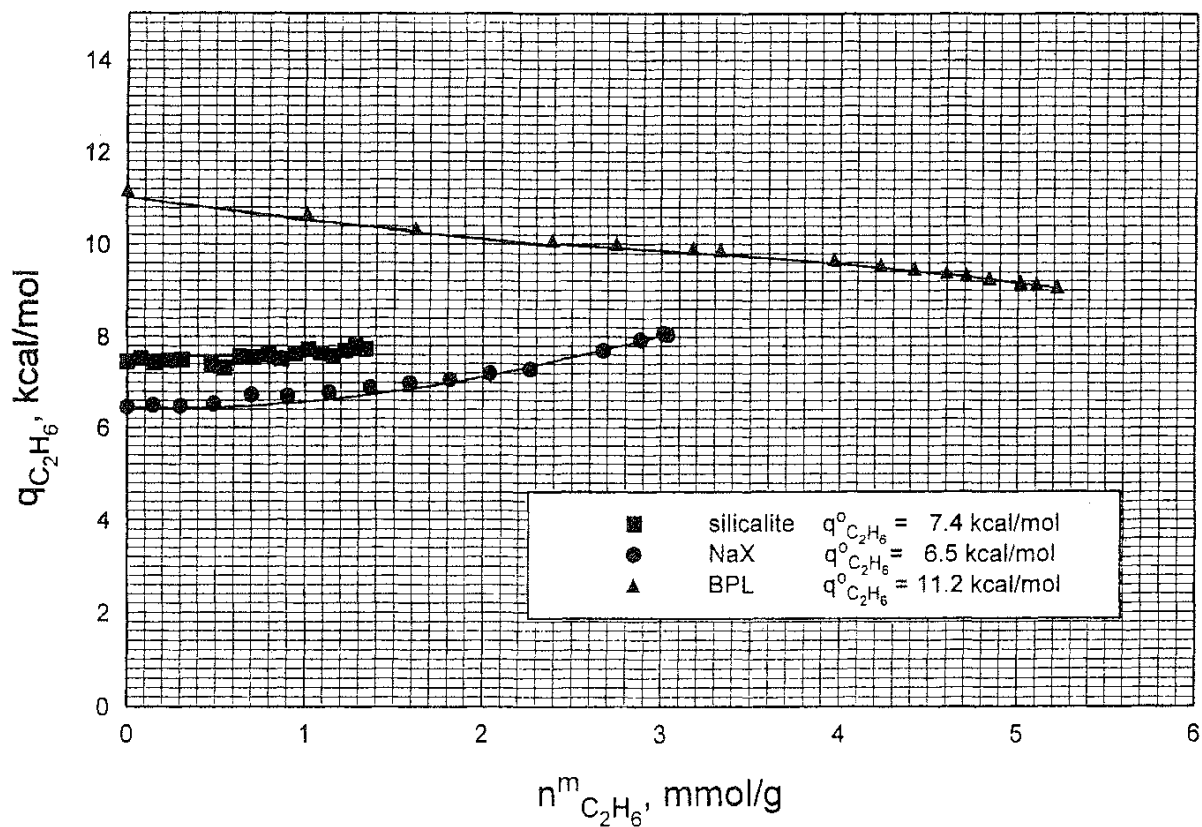


FIG. 6 Isosteric heats of adsorption of pure C_2H_6 as functions of adsorbate surface excesses on NaX zeolite, silicate, and BPL activated carbon.

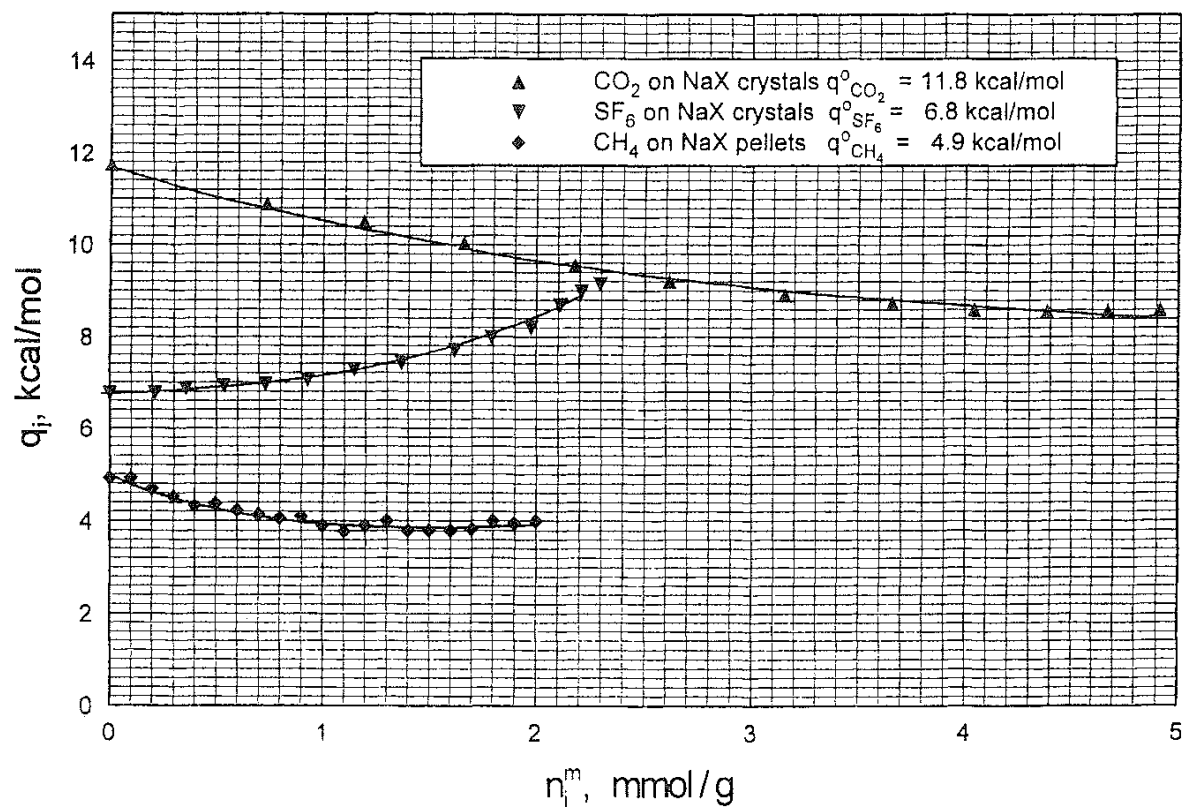


FIG. 7 Isosteric heats of adsorption of pure CH_4 , CO_2 , and SF_6 as functions of their surface excesses on NaX zeolite.

adsorbent. The pores of the silicalite and the NaX zeolite are extremely homogeneous and well defined, while the activated carbon has a network of various micro- and mesopores. The adsorbates range from nonpolar (CH_4 , SF_6) to weakly polar (C_2H_6) to polar (CO_2), and they have different sizes, molar volumes, and polarizabilities. Table 2 lists the key properties of the adsorbates.

A. Homogeneous Adsorbent

An adsorbent is said to be energetically homogeneous for adsorption of a pure gas if all the sites of adsorption for that gas have the same energy of adsorption. Consequently, the isosteric heat of adsorption of a pure gas i (q_i) on that adsorbent remains constant for all values of the surface excess (n_i^m). The data of Figs. 5 and 6 show that silicate is energetically homogeneous for adsorption of CO_2 and C_2H_6 within the range of the data.

Even for an energetically homogeneous adsorbent, q_i can vary with n_i^m if (1) the adsorbate–adsorbate lateral interactions in the adsorbed phase are significant, (2) the adsorbate orientation on the adsorbent surface changes with coverage; (3) there is multilayer adsorption or condensation of the adsorbate in the mesopores, and (4) there is a change in the physical structure of the adsorbed phase. The lateral interactions cause q_i to increase with increasing n_i^m particularly when the surface coverage is large. The adsorption of C_2H_6 (Fig. 6) and SF_6 (Fig. 7) on NaX zeolite are examples of significant lateral interactions in the adsorbed phase. The interactions between the adsorbed molecules can be very different from those in the corresponding bulk gas or liquid phase due to the presence of the adsorbent molecules, which create multibody interactions in the adsorbed phase.

B. Heterogeneous Adsorbent

An adsorbent is said to be energetically heterogeneous for adsorption of a pure gas if it consists of a distribution of sites of different adsorption energies. Even though all sites are populated by the adsorbate molecules at all gas pressures, the higher energy sites are predominantly occupied by the adsorbate molecules at the lower gas pressures. Lower energy sites are progressively occupied by the adsorbate molecules as the gas pressure increases. Consequently, q_i for pure gas adsorption decreases as n_i^m increases (P increases).

TABLE 2 Molecular Properties of Various Adsorbates

| Adsorbate | Liquid molar volume ^a (cm^3/mol) | Kinetic diameter (\AA) | Polarizability ($\times 10^{25} \text{ cm}^3$) | Dipole moment ($\times 10^{18} \text{ esu} \cdot \text{cm}$) | Quadrupole moment ($\times 10^{26} \text{ esu} \cdot \text{cm}^2$) |
|------------------------|---|---|---|---|--|
| CH_4 | 37.7 | 3.8 | 26.0 | 0.0 | — |
| C_2H_6 | 53.6 | 4.4 | 44.7 | 0.0 | 1.56 |
| SF_6 | 72.7 | 5.8 | 65.4 | 0.0 | — |
| CO_2 | 33.3 | 3.3 | 26.5 | 0.0 | 4.30 |

^aAt normal boiling point.

The adsorption of CO₂ on NaX zeolite and BPL carbon (Fig. 5) and the adsorption of C₂H₆ on BPL carbon (Fig. 6) indicate that these systems exhibit various degrees of adsorbent heterogeneity. The highly polar NaX zeolite is more heterogeneous for adsorption of polar CO₂ molecules than the less polar BPL carbon.

The data of Fig. 7 show that the same adsorbent can exhibit vastly different gas–solid interactions depending on the nature of the adsorbate. The adsorption of CH₄ on NaX zeolite is nearly homogeneous. The adsorption of SF₆ exhibits significant lateral interactions. The adsorption of CO₂ is significantly heterogeneous. These behaviors can be qualitatively explained by the properties of the adsorbates. The nonpolar adsorbates (CH₄ and SF₆) are not affected by the polar heterogeneity of the zeolite. However, the larger and more polarizable SF₆ molecules introduce significant lateral interactions within the zeolite cavities. The polar CO₂ molecules, on the other hand, experience the polar heterogeneity of the NaX zeolite.

The energetic heterogeneity of the adsorbent is physico-chemical in nature. For microporous amorphous adsorbents (activated carbons, aluminas, silica gels), the heterogeneity is caused by (1) the presence of a network of micro- and mesopores of different sizes and shapes, (2) the presence of different polar and nonpolar surface groups on the pore walls, and (3) the presence of strongly adsorbed trace impurities. For microporous crystalline adsorbents (zeolites), where the physical structure of the crystal lattice is well defined and uniform, the heterogeneity is caused by (1) structural defects, (2) the presence of different types of cations in the structure, (3) the location and accessibility of the cations, (4) hydration of the cations, and (5) variation in the silica/alumina ratio in the zeolite framework. It is not possible to a priori characterize the adsorbent heterogeneity at the microscopic scale (pore size distribution or surface chemistry) by using today's technology. Measurement of overall isosteric heats of adsorption of pure gases remains the best way to characterize the macroscopic heterogeneity of adsorption of gases on micro–mesoporous solids.

Despite the above-mentioned problem, numerous works have been published to micromodel adsorbent heterogeneity by assuming that the adsorbent comprises a patchwise distribution of homogeneous sites of different isosteric heats of adsorption [23]. According to this concept, the overall surface excess isotherm of a pure gas i on a heterogeneous adsorbent (n_i^m) is given by

$$n_i^m(P, T) = \int_0^\infty n_i^{ml}(P, T, q_i) \lambda(q_i) dq_i \quad \text{at constant } T \quad (48)$$

where n_i^{ml} is the local surface excess isotherm of pure gas i on a homogeneous patch of sites characterized by the isosteric heat of adsorption q_i . $\lambda(q_i)$ is the normalized probability density function for the distribution of isosteric heats of adsorption:

$$\int_0^\infty \lambda(q_i) dq_i = 1 \quad (49)$$

The lower and upper limits of q_i in the energy distribution function are generally assumed to be zero and infinity for mathematical convenience.

Equations (48) and (49) have been used (1) to calculate the pure gas isosteric heat probability distribution function $\lambda(q_i)$ for a heterogeneous adsorbent from

the experimental overall adsorption isotherm n_i^m by assuming a local homogeneous adsorption isotherm model n_i^{ml} such as the Langmuir equation, and (2) to develop analytical overall adsorption isotherm equations by assuming a functionality for $\lambda(q_i)$ in conjunction with a local homogeneous adsorption isotherm model n_i^{ml} . Some of the key works in these areas are described in Ref. 23. Unfortunately, as mentioned earlier, the estimated or assumed $\lambda(q_i)$ functions cannot be experimentally verified.

C. Limiting Value of Isostatic Heat of Adsorption

Statistical thermodynamics of adsorption dictate that the pure gas adsorption isotherm of component i be linear at the limit of $P \rightarrow 0$:

$$n_i^m = K_i P, \quad P \rightarrow 0 \quad (50)$$

where K_i [mol/(g·atm)] is called the Henry's law constant. It is a function of T only. It follows from Eq. (11) that q_i in the Henry's law limit (linear isotherm range) is given by

$$q_i^0 = -RT^2 \frac{d \ln K_i}{dT} \quad (51)$$

$$K_i = K_i^0 e^{q_i^0/RT} \quad (52)$$

where q_i^0 is the isosteric heat of adsorption of pure gas i in the Henry's law region. K_i^0 is a constant. Equation (52) is derived by integrating Eq. (51), assuming that q_i^0 is independent of T (generally valid). It follows from Eq. (51) that q_i^0 is a constant in the Henry's law region.

D. Special Cases of Adsorbent Heterogeneity

An adsorbent may not be homogeneous even if q_i remains constant as a function of n_i^m . For example, an adsorbent can be heterogeneous by having a distribution of adsorption patches with different Henry's law constants but with the same isosteric heats of adsorption for the sites. Thus the constant K_i^0 of Eq. (52) may vary from patch to patch while q_i^0 remains constant. The overall isosteric heat of adsorption of a pure gas in that case will not vary with n_i^m even though the local adsorption isotherms on different patches will be different. This was experimentally demonstrated by synthetically creating a heterogeneous adsorbent for adsorption of pure N_2 by (1) physically mixing crystals for pure BaX and NaX zeolites and (2) binary ion-exchanging Ba and Na ions into an X zeolite structure [24]. Both pure BaX and NaX zeolites were homogeneous adsorbents for pure N_2 . Both materials had practically the same isosteric heats of adsorption for N_2 , but the K_i^0 values were substantially different for these materials. The end result was that the synthetically produced mixed zeolite sample was a chemically heterogeneous adsorbent for which the isosteric heat of adsorption of N_2 did not vary with surface coverage.

It is sometimes argued that the observation of a constant isosteric heat of adsorption of a pure gas over a range of surface coverage is caused by mutual cancellation of two effects: (1) an increase of a , with increase of n_i^m due to lateral

interactions and (2) a decrease of q_i with increase of n_i^m due to adsorbent heterogeneity [19]. Although this is possible, such cancellation is fortuitous. The energy of adsorbate–solid interactions on practical adsorbents is generally much greater than that for lateral interactions in the adsorbed phase.

E Simple Models for Isostatic Heat of Adsorption

Table 3 lists several simple, analytical, adsorption isotherm models and the corresponding isosteric heats for pure gas adsorption. These models have been fairly successful in describing pure gas adsorption on microporous adsorbents (type I isotherms [4]).

The homogeneous multisite Langmuir (MSL) model [25,26] assumes that a_i adsorption sites are occupied by each molecule of adsorbate i . The saturation surface excess (mol/g) for the pure adsorbate i is given by m_i , which is not a function of T . $\theta_i (= n_i^m / m_i)$ is the fractional coverage for pure component i . b_i (atm^{-1}) is the gas–solid interaction parameter for component i . b_i is a function of T only (Table 3), and b_i^0 is a constant. The isosteric heat of adsorption of pure component i (q_i^0) for this model is independent of coverage. The MSL model reduces to the original homogeneous Langmuir model [4] when $a_i = 1$.

The MSL model has been extended to incorporate lateral interactions in the adsorbed phase [27]. In this case, the adsorbent is energetically homogeneous, but q_i increases linearly with increasing θ_i due to lateral interaction. w_{ii} is the pure gas lateral interaction energy parameter for component i . This model reduces to the original homogeneous Fowler–Guggenheim model [7] when $a_i = 1$. Furthermore, it reduces to the Langmuir equation when $a_i = 1$ and $w_{ii} = 0$.

The Toth model is derived for pure gas adsorption on a heterogeneous adsorbent without lateral interactions [28]. The parameters m_i and b_i are identical to those for the Langmuir model. The parameter k (≤ 1), which is a function of T only, is the heterogeneity parameter. The adsorbent is heterogeneous if $dk/dT > 0$. The adsorbent heterogeneity increases as the value of the parameter k decreases. The model reduces to the homogeneous Langmuir model when $k = 1$. The Toth model can be derived using Eqs. (48) and (49) by assuming that the adsorbent is patchwise homogeneous, consisting of a collection of Langmuir sites with a skewed Gaussian-like distribution of site isosteric heats of adsorption [28]. The q_i for the Toth model decreases as θ_i increase. An inconsistency of the Toth model is, however, that $q_i \rightarrow -\infty$ as $\theta_i \rightarrow 1$.

VIII. CHARACTERISTICS OF MULTICOMPONENT GAS ISOSTERIC HEATS OF ADSORPTION

There are very few published experimental data on multicomponent gas isosteric heats of adsorption [21,29]. Even those are limited to the study of binary gas adsorption systems. Figures 8 and 9, respectively, show the isosteric heats of adsorption of CO_2 and C_2H_4 from their binary mixture on NaX zeolite crystals measured as functions of CO_2 loading (surface excess) at approximately constant

TABLE 3 Simple Models for Pure Gas Isothermic Heats of Adsorption

| Model | Isotherm equation | Isothermic heat of adsorption |
|---|---|--|
| Multisite Langmuir model [25] | $b_i P = \frac{\theta_i}{(1 - \theta_i)^{a_i}}$ | $q_i(\theta_i) = q_i^0 = -RT^2 \frac{d \ln b_i}{dT};$ $b_i = b_i^0 e^{(q_i^0/RT)}$ |
| Multisite Langmuir model with lateral interactions [27] | $b_i P = \frac{\theta_i}{(1 - \theta_i)^{a_i}} \exp \left[-\frac{a_i w_{ii} \theta_i}{RT} \right]$ | $q_i(\theta_i) = q_i^0 + a_i w_{ii} \theta_i; \quad b_i = b_i^0 e^{(q_i^0/RT)}$ |
| Toth model [28] | $b_i P = \frac{\theta_i}{[1 - (\theta_i)^k]^{1/k}}$ | $q_i(\theta_i) = q_i^0 + \frac{RT^2}{k} \frac{d \ln k}{dT} F_i(\theta_i);$ $b_i = b_i^0 e^{(q_i^0/RT)}$ $F_i(\theta_i) = \frac{[1 - (\theta_i)^k] \ln[1 - (\theta_i)^k] + (\theta_i)^k \ln[(\theta_i)^k]}{1 - (\theta_i)^k};$ $F_i(\theta_i) < 0; \quad \frac{dk}{dT} > 0$ |

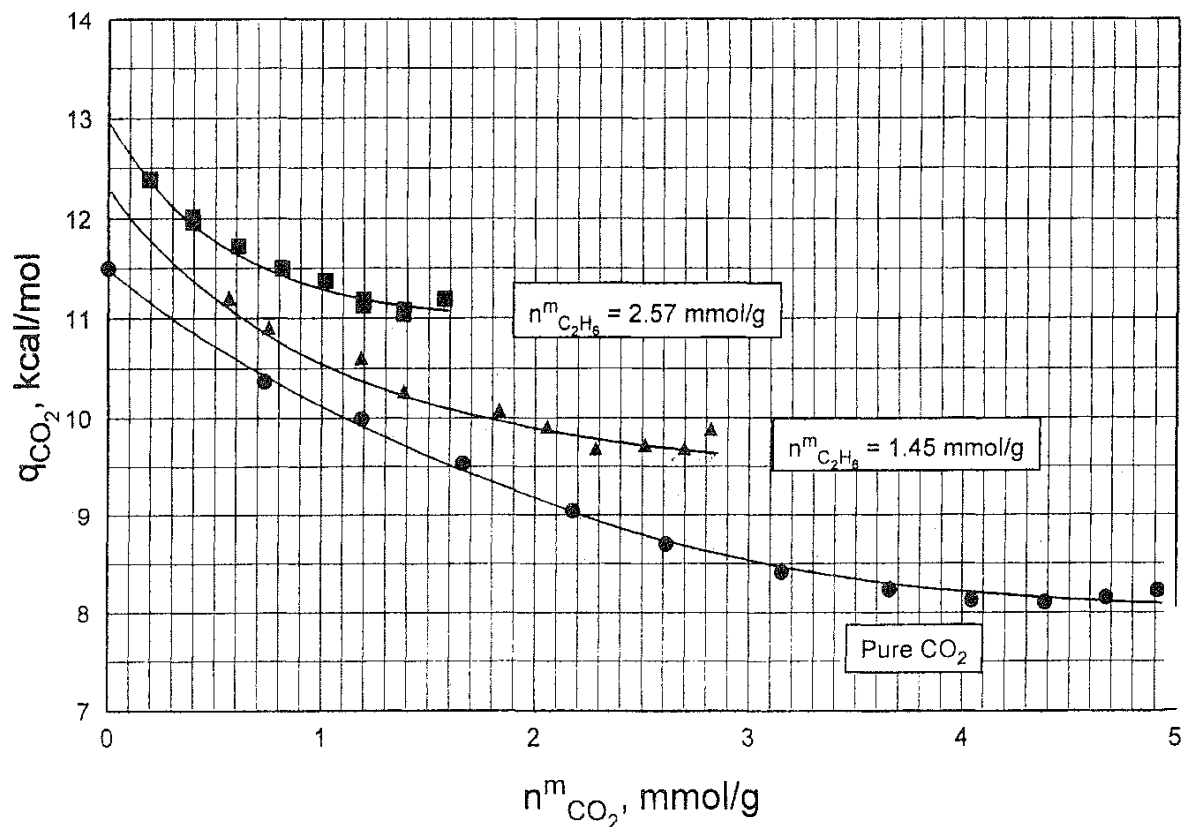


FIG. 8 Isosteric heats of adsorption of CO_2 from binary mixtures with C_2H_6 as functions of CO_2 surface excesses on NaX zeolite.

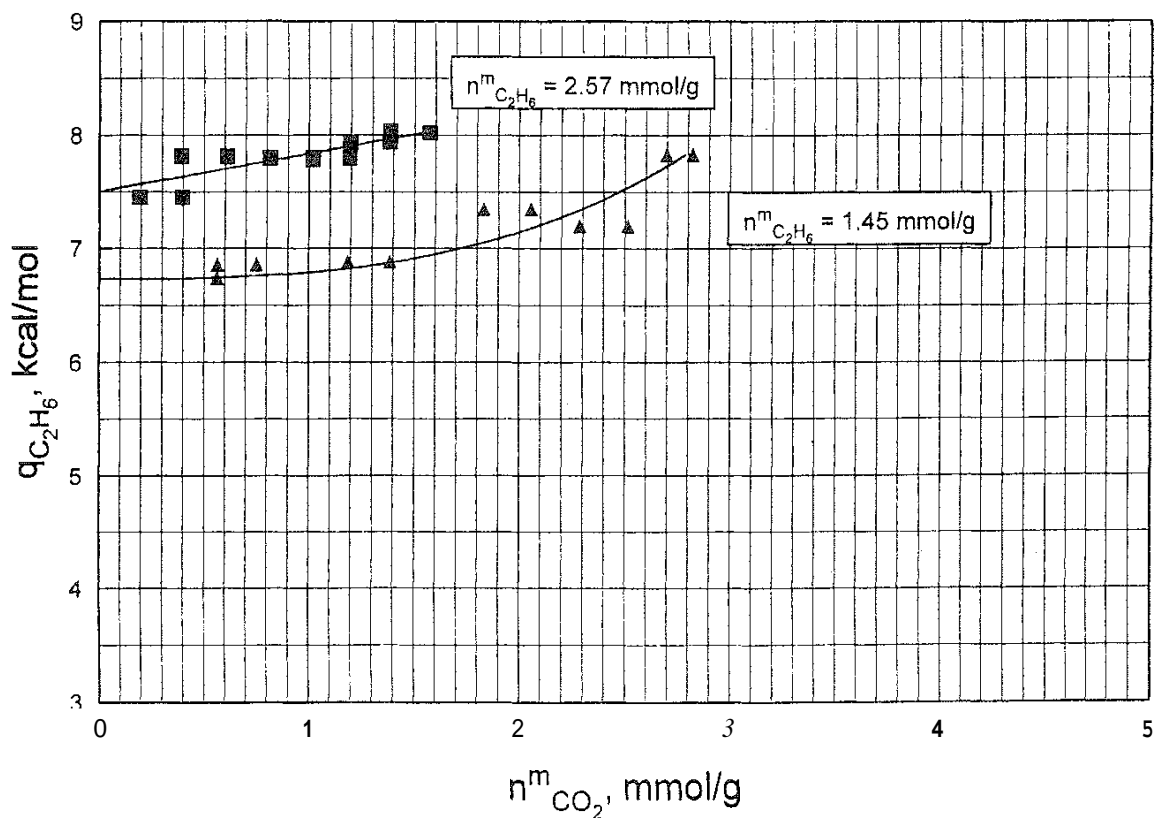


FIG. 9 Isosteric heats of adsorption C_2H_6 from binary mixtures with CO_2 as functions of CO_2 surface excesses on NaX zeolite.

C₂H₆ loadings at a temperature of 302 K. The data were measured using a Tian–Calvet type of calorimeter [21].

It can be seen from Fig. 8 that q_{CO_2} decreases significantly as $n_{\text{CO}_2}^m$ increases within the range of the data. It also shows that q_{CO_2} is larger at any given value of $n_{\text{CO}_2}^m$ when the coadsorption of C₂H₆ ($n_{\text{C}_2\text{H}_6}^m$) is increased. This result is counter-intuitive. Figure 8 also plots q_{CO_2} as functions of $n_{\text{CO}_2}^m$ for pure gas adsorption. The q_{CO_2} from the binary mixture is larger than that for pure CO₂ at any given value of CO₂ loading. Figure 9 shows that $q_{\text{C}_2\text{H}_6}$ slowly increases as $n_{\text{CO}_2}^m$ is increased at both levels of $n_{\text{C}_2\text{H}_6}^m$ reported in the figure. Again, these results are counterintuitive.

Clearly, the factors determining the isosteric heats of adsorption of gas mixtures are complex. Many more binary experimental data have to be gathered and analyzed before any acceptable theory to explain the observed behavior emerges. There is also an urgent need for generating a comprehensive and systematic database for multicomponent gas ($i \geq 2$) isosteric heats of adsorption for aiding practical adsorptive process designs.

A. Limiting Values of isosteric Heat of Adsorption

Statistical thermodynamics of adsorption dictates that the adsorption isotherm of component i from a mixture be a linear function of the partial pressure of that component ($p_i = Py_i$) in the Henry's law region ($p_i \rightarrow 0$):

$$n_i^m = K_i(T)Py_i, \quad P \rightarrow 0 \quad (53)$$

$$n_i^m = K_i^*(P, T)Py_i, \quad y_i \rightarrow 0; \text{ constant } P \quad (54)$$

The Henry's law constant (K_i) in Eq. (53) is equal to the Henry's law constant of pure gas [Eq. (50)], and it is a function of T only. The variable K_i^* in Eq. (54) is a different Henry's law constant, and it is a function of both P and T . It follows from Eqs. (11), (53), and (54) that

$$q_i = q_i^0 = -RT^2 \frac{d \ln K_i}{dT}, \quad P \rightarrow 0 \quad (55)$$

$$q_i = q_i^* = -RT^2 \frac{d \ln K_i^*}{dT}, \quad y_i \rightarrow 0; \text{ constant } P \quad (56)$$

Equation (55) shows that the isosteric heat of adsorption of component i of a mixture is equal to the pure gas isosteric heat of adsorption of component i (q_i^0) in the mixture's Henry's law region at the limit of $P \rightarrow 0$. On the other hand, the isosteric heat of adsorption of component i of a mixture is equal to q_i^* at the limit of $y_i \rightarrow 0$ (constant P).

B. Simple Models of Multicomponent Gas Isosteric Heats of Adsorption

The three pure gas adsorption models described by Table 3 have been extended to cover multicomponent adsorption equilibria. Table 4 gives the multicomponent

E 4 Simple Models for Multicomponent Gas Isothermic Heats of Adsorption

| | Isotherm equation | Isothermic heat of adsorption |
|---|--|---|
| Multisite Langmuir model [25] | $b_i P y_i = \frac{\theta_i}{(1 - \sum_i \theta_i)^{a_i}}$ | $q_i(\theta_i) = q_i^0 = -RT^2 \frac{d \ln b_i}{dT}$ |
| multisite Langmuir model with lateral interactions [27] | $b_i P y_i = \frac{\theta_i}{[1 - \sum_i \theta_i]^{a_i}} \exp \left[- \sum_j \frac{a_j w_{ij} \theta_j}{RT} \right]$ | $q_i(\theta_i) = q_i^0 + \sum_j a_j w_{ij} \theta_j$ |
| Toth model [28] | $b_i P y_i = \frac{\theta_i}{\left[1 - \left(\sum \theta_i \right)^k \right]^{1/k}}$ | $q_i(\theta_i) = q_i^0 + \frac{RT^2}{k} \frac{d \ln k}{dT} F(\theta);$ $F(\theta) = \frac{[1 - (\theta)^k] \ln[1 - (\theta)^k] + (\theta)^k \ln(\theta)^k}{1 - (\theta)^k};$ $\theta = \sum_i \theta_i; \quad F(\theta) < 0; \quad \frac{dk}{dT} > 0$ |

gas adsorption isotherm equations and the corresponding expressions for multicomponent isosteric heats of adsorption.

The saturation capacity (surface excess) of component i in the multicomponent MSL model [25] is given by in_{∞} , and the fractional coverage of component i is given by $\theta_i (= n_i^m/m_i)$. The total fractional coverage of all adsorbates is $\theta (= \sum_i \theta_i)$. The multicomponent MSL equation is thermodynamically consistent [26] provided that the constraint $m_i a_i = \text{constant}$ is obeyed. The isosteric heat of adsorption of component i is equal to that for the pure gas.

The multicomponent MSL model with lateral interaction [27] exhibits a linear increase in the isosteric heat of adsorption of component i with increase of $\theta_j (= n_j^m/m_j)$ of all components ($j = 1, 2, \dots, N$). w_{ij} is the adsorbate i –adsorbate j lateral interaction energy parameter in the adsorbed phase.

The multicomponent Toth model is thermodynamically consistent only when the variables m_i and k for all components are equal [13,14]. The mixed gas adsorption model is based on the criteria that the local site selectivity of adsorption for component i – j pairs ($S_{ij} = b_i/b_j$) is constant for all adsorption sites, but the gas–solid interaction parameters of component i (b_i) vary from site to site. The functions $F(\theta_i)$ and $F(\theta)$ of Tables 3 and 4, respectively, are identical except that the independent variables are θ_i and θ .

It should be noted here that all models of Tables 3 and 4 were originally developed by using the actual amount adsorbed (n_i^a) as the base variable. We adapted them to describe the actually measured surface excess variable (n_i^m) as functions of P , T , and y_i because they describe the experimental surface excess isotherm data very well.

C. Example of Model Heterogeneity for a Binary System

The Toth model describes the adsorption isotherms of pure C_2H_4 (component 1) and CH_4 (component 2) as well as those for their binary mixtures on Nuxit charcoal fairly well [14,30]. The multicomponent Toth model was used to calculate the binary gas isosteric heats of adsorption for a C_2H_4 – CH_4 mixture as functions of C_2H_4 gas-phase mole fraction (y_1) at a total pressure of 99.2 kPa and at a temperature of 293 K [14]. Figure 10 shows the results, $q_{\text{C}_2\text{H}_4}$ decreases as the mole fraction of that component in the gas phase increases. q_{CH_4} increases as the mole fraction of that component in the gas phase increases. This is a typical characteristic of the Toth model.

Figure 10 also shows the isosteric heats of adsorption of the pure gas i (dotted lines) at the same adsorbate loading (surface excess) as that of component i from the binary mixture at P , T , and y_i . It can be seen that the binary and pure gas isosteric heats are comparable for C_2H_4 only at the higher values of y_1 . There is a large difference between them at lower values of y_1 . On the other hand, the difference between the binary and pure gas isosteric heats are striking for CH_4 at all values of y_1 . The pure gas isosteric heats for component 2 are much larger than those from the mixture at the same values of θ_2 . The reason for these differences is that the isosteric heat of adsorption of the components of the mixture, according to the Toth model, depend on the total adsorbate loading θ . For this system, θ is closer to θ_1 at higher values of y_1 due to the high selectivity of adsorption of C_2H_4 .

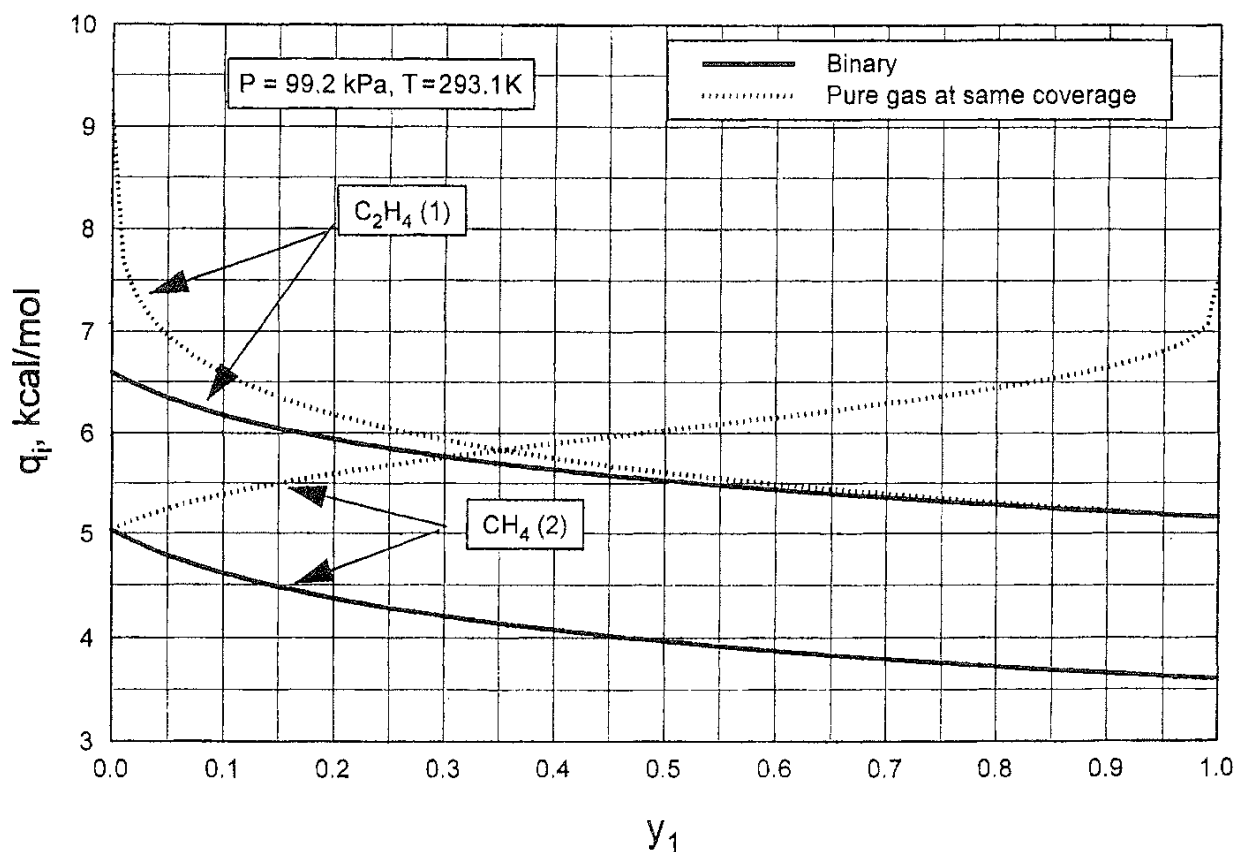


FIG. 10 Isosteric heats of adsorption of C_2H_4 (1) and CH_4 (2) from their binary mixtures at constant pressure and temperature on Nuxit charcoal, calculated with the Toth model. (Parameters: $m = 11.0 \text{ mol/kg}$; $b_1^0 = 7.802 \times 10^{-9} \text{ kPa}^{-1}$; $b_2^0 = 7.602 \times 10^{-9} \text{ kPa}^{-1}$; $q_1^0 = 9.122 \text{ kcal/mol}$; $q_2^0 = 7.560 \text{ kcal/mol}$; k at $293.1 \text{ K} = 0.34$; $dk/dT = 0.0015 \text{ K}^{-1}$).

compared to CH_4 . Thus the mixture and pure gas heats are comparable only for component 1 at higher values of y_1 . These results show that it may not be correct to use pure gas isosteric heats of adsorption as functions of its coverage to represent the isosteric heat of adsorption of the components from a gas mixture at the same coverage for process design purposes.

REFERENCES

1. S. Sircar, in *Fundamental of Adsorption*, Proceedings of Engineering Foundation Conference held at Sonthofen, Germany (A. B. Mersmann et al., eds.), Engineering Foundation, N.Y. 1991, p. 815.
2. D. G. Hartzog and S. Sircar, *Adsorption* 1:133 (1995).
3. T. L. Hill, *J. Chem. Phys.* 17:520 (1949).
4. D. M. Young and A. D. Crowell, *Physical Adsorption of Gases*, Butterworths, Washington, DC, 1962.
5. D. H. Everett, *Colloq. Int. CNRS* 201:45 (1971).
6. N. Cardona-Martinez and J. A. Dumesic, *Adv. Catal.* 38:149 (1992).

7. S. Ross and J. P. Olivier, *On Physical Adsorption*, Interscience, New York, 1964.
8. J. W. Gibbs, *The Collected Works of J. W. Gibbs*, Longmans and Green, New York, 1928.
9. S. Sircar, J. Chem. Soc., Faraday Trans. I 81:1527 (1985).
10. S. Sircar, Adsorption 2:327 (1996).
11. R. E. Balzhiser, M. R. Samuels, and J. D. Eliassen, *Chemical Engineering Thermodynamics*, Prentice-Hall, Englewood Cliffs, NJ, 1972, pp. 98–101.
12. S. Sircar, J. Chem. Soc. Faraday Trans. I 81:1541 (1985).
13. S. Sircar. Ind. Eng. Chem. Res. 31:1813 (1992).
14. S. Sircar, Langmuir 1:3065 (1991).
15. M. Bulow and P. Lorenz, *Fundamentals of Adsorption*, Proceedings of Engineering Foundation Conference held at Santa Barbara, CA (A. I. Liapis, ed.), Engineering Foundation, N.Y. 1987, p. 119.
16. P. Graham, A. D. Hughes, and L. V. C. Rees, Gas Separ. Purif. 3:56 (1989).
17. S. Sircar and R. Kumar, Sep. Sci. Technol. 21:919 (1986).
18. B. E. Handy, S. B. Sharma, B. E. Spiewak, and J. A. Dumesic, Meas. Sci. Technol. 4:1350 (1993).
19. J. A. Dunne, R. Mariwala. M. Rao, S. Sircar, R. J. Gorte and A. L. Myers, Langmuir, 12:5888 (1996).
20. J. A. Dunne, M. Rao, S. Sircar, R. J. Gorte and A. L. Myers, Langmuir 12:5896 (1996).
21. J. A. Dunne, M. Rao, S. Sircar, R. J. Gorte. and A. L. Myers, Langmuir. 13:4333 (1997).
22. R. Reich, Ph.D. Dissertation, Georgia Institute of Technology, 1974,
23. S. Sircar and A. L. Myers. Surf. Sci. 205:353 (1988).
24. T. C. Golden and S. Sircar, J. Colloid Interface Sci. 147:274 (1991).
25. T. Nitta, M. Shigetomi, M. Kuro-oka, and T. Katayama, J. Chem. Eng. Jpn, 17:39 (1984).
26. S. Sircar, AIChE J. 41:1135 (1995).
27. G. M. Martinez and D. Basmadjian, Chem, Eng. Sci. 51:1043 (1996).
28. M. Jaroniec and J. Toth, J. Colloid Polym. Sci. 254:643 (1976).
29. H. Kowalczyk, J. Thermal. Anal. 45:729 (1995).
30. L. Szepesy and V. Illes, Acta Chim. Hung. 35:37 (1963).

Surface Chemistry of Activated Carbon Materials: State of the Art and Implications for Adsorption

LJUBISA R. RADOVIC Department of Materials Science and Engineering, The Pennsylvania State University, University Park, Pennsylvania

- I. Introduction
- II. Surface Chemistry of Activated Carbons
- III. Adsorption of Inorganic Solutes
 - A. Adsorption of cations
 - B. Adsorption of anions
- IV. Adsorption of Organic Solutes
 - A. Role of electrostatic interactions
 - B. Role of dispersion interactions
 - C. Toward a comprehensive adsorption model
- V. Summary and Conclusions
- References

I INTRODUCTION

It is well known that the uptakes of gaseous, vapor, or liquid adsorbates by different carbon adsorbents can vary over a remarkably wide range. Many of these variations are due to differences in the physical surface properties, i.e., to surface area effects, as well as to different degrees of molecular sieving because of their widely varying pore size distributions. However, when such factors are allowed for, large uptake differences per unit of total (or accessible) surface area still remain [1]. These are especially important in liquid-phase adsorption; they have been well documented, but they are not well understood. They may also be important in vapor- and gas-phase applications. This undesirable state of affairs is surprising, having in mind the fact that of the four technologically relevant adsorbents activated carbon is by far the most important one, with estimated worldwide sales of about \$10⁹ being an order of magnitude higher than those of its competitors [2].

The results of a very recent study by Attia [3], summarized in Fig. 1, are a good illustration. Carbons of varying surface area were produced by carbonization and activation of date pits in steam, air, or carbon dioxide (at different temperatures and to different extents of burnoff). The correlations of water vapor and pyridine uptakes with the total surface area are seen to be very poor. The author concludes that "water vapour adsorption is related to the chemistry of the surface rather than to the extent of the surface area" but does not identify, let alone quantify, this chemistry. Regarding pyridine adsorption, the author notes that "activation of carbons at low temperatures created acidic sites while treatment at high temperatures led to the generation of basic sites on the surface," but she does not identify these sites.

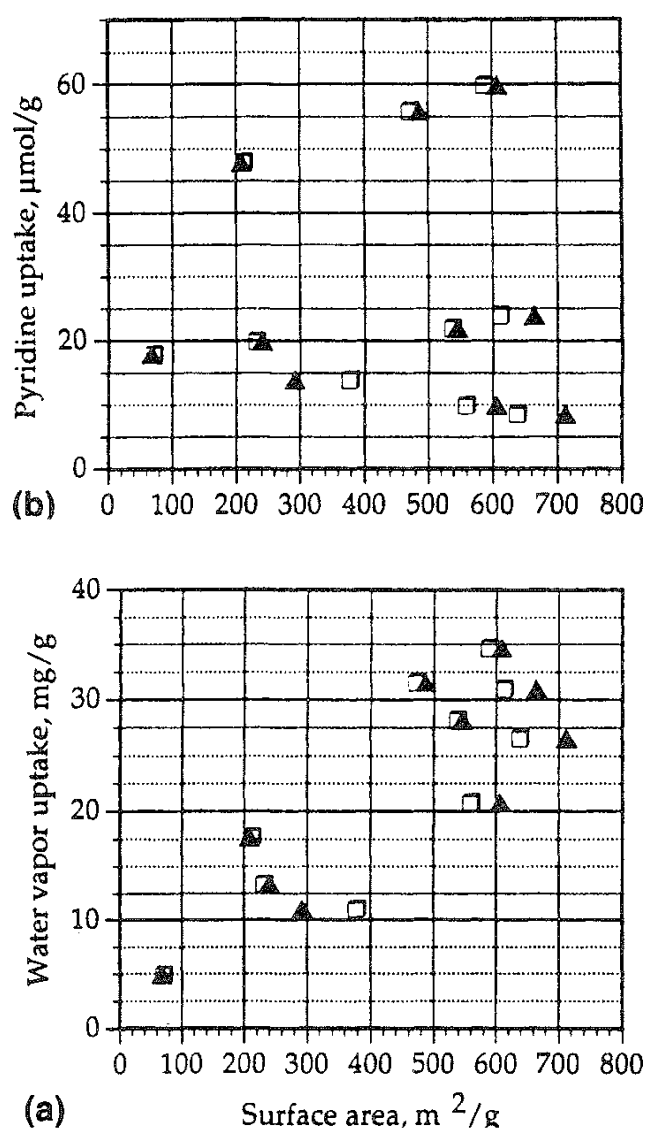


FIG. 1 Correlation (or lack thereof) between the surface area of an activated carbon and the uptake of (a) water vapor at 298 K and (b) pyridine at 423 K. (\blacktriangle) BET surface area (from N_2 adsorption at 77 K); (\square) Dubinin-Radushkevich (DR) surface area (from CO_2 adsorption at 298 K).

In this review I first present what is arguably the state of the art in the understanding of the surface chemistry of activated carbon (Sec. II). This knowledge is a necessary condition for rationalizing the varying uptakes of both inorganic (Sec. III) and organic (Secs. IV.A and IV.B) pollutants from the aqueous phase. I illustrate this general conclusion by presenting the results obtained in my research group and by analyzing those of others. Finally, in Sec. IV.C I rescue all appropriate quantitative model from undeserved oblivion, and I conclude that at long last real progress is being made toward achieving predictive capabilities and tailoring the chemistry of carbon adsorbents for the removal of specific pollutants from aqueous and other waste fluid streams.

II. SURFACE CHEMISTRY OF ACTIVATED CARBONS

It is not my intention to present an exhaustive review here. A comprehensive and critical review is provided elsewhere [4]. Boehm has also presented a brief but authoritative review [5]. Instead I summarize here the issues that are now known to be essential for predicting adsorption uptakes, especially in aqueous solutions. The main features of carbon surface chemistry are presented first, and the consequent acid–base behavior of carbons is briefly discussed to illustrate their unique amphoteric character. (These same features should be important in the adsorption of gases and vapors, but a discussion of the relevant evidence, beyond that presented in conjunction with [Fig. 1](#), is not within the scope of the present work.) In Sec. III it is shown that these phenomena govern the adsorption of inorganic compounds. In Sec. IV I argue that they are sometimes dominant in the adsorption of organic compounds, but more often they are only a part of the "whole story"!

The essential features of the surface chemistry of carbons, relevant to their behavior in aqueous solution, are summarized in [Figs. 2](#) and [3](#). Purists may argue that the two figures are (over)simplified representations that do not do justice to the acknowledged complexity and heterogeneity of carbon surfaces [6–8]. Obviously, the three-dimensional nature of the micropores, the details of their topology, the proximity of the pore walls, and the distribution of energies of the various surface functional groups should all be somehow taken into account if reliable adsorption potentials are to be obtained. However, a judicious selection of activated carbons for many practical applications (e.g., water treatment, removal of volatile organic compounds) requires the resolution of much more basic issues. Perhaps at the top of the list of such issues are the separability and relative importance of electrostatic and dispersion adsorbate–adsorbent interactions. I argue here that [Figs. 2](#) and [3](#) are necessary *and* sufficient for addressing this issue.

Figure 2 illustrates the macroscopic chemical features of the activated carbon surface, both internal and external. In response to pH changes in aqueous solution, the surface develops coexisting electric charges of opposite sign, whose prevalence depends on solution chemistry. Therefore, attractive or repulsive electrostatic interactions between the adsorbate and the adsorbent must be taken into consideration. The development of negative charge is well understood, well documented, and noncontroversial: It is the result of the dissociation of acidic surface functionalities such as carboxyl, lactone, and phenolic groups. Two controversial points in this

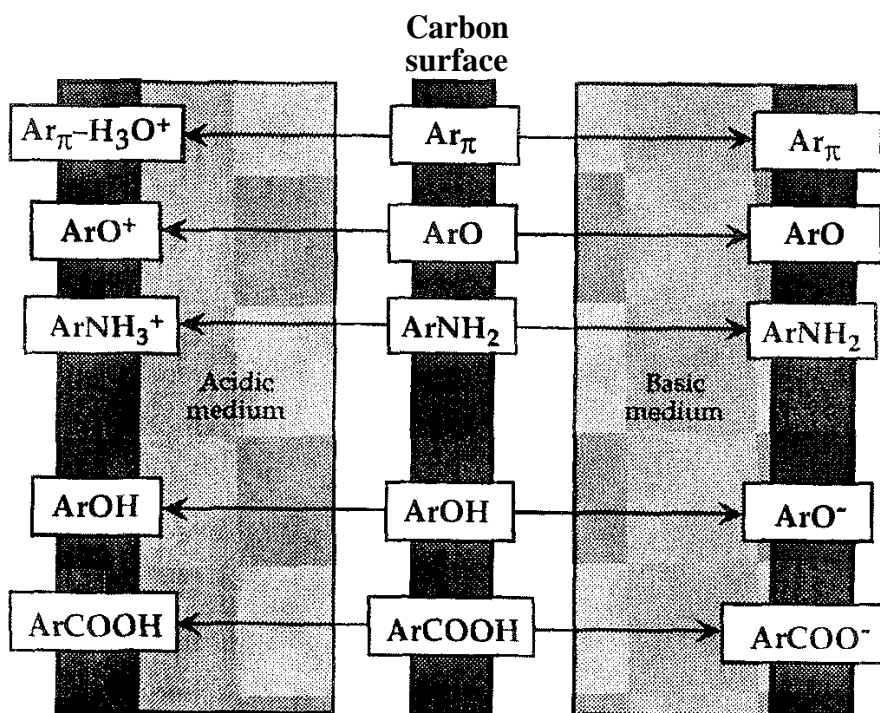


FIG. 2 Principal features of the activated carbon surface that give rise to surface charge development in aqueous solution.

figure deserve special attention: (1) the origin of the positive charge and (2) the relative contributions of functional groups vs. graphene layers to the development of surface charge. In Fig. 3 one such graphene layer is depicted, albeit in two dimensions only. It consists of (1) saturated basal plane sites, (2) unsaturated edge sites, (3) edge sites saturated with heteroatom-containing functional groups, and (4) π electrons delocalized over the entire graphene layer. The small size and poor alignment of the crystallites make them highly porous and reactive. The high porosity, especially in the micropore range (with equivalent diameters of 3–20 Å), exposes large surfaces to gaseous and liquid environments. The crystallite faces are composed of fused benzene rings (graphene layers). The functional groups at the crystallite edges are ubiquitous because of carbon's great affinity for oxygen; they possess a wide range of thermal and chemical stability. Most of them are acidic (e.g., carboxyl and lactone groups), but some may be basic (e.g., carbonyl plus ether, or pyrone, groups). Some edges are terminated by thermally stable C—H groups, while others are much more reactive because they are terminated either with free radicals (i.e., unpaired σ electrons) or with somewhat stabilized π – σ electron pairs. In contrast to more ordered carbons (e.g., heat-treated carbon blacks), where the overwhelming majority of the surface consists of basal planes, in activated carbons the ratio of edge to basal plane carbon atoms can be as high as 10–20%.

Three possible sources of the positive charge are highlighted in Fig. 2: basic oxygen-containing functional groups (e.g., pyrones or chromenes), protonated amino groups (for nitrogen-rich carbons), and graphene layers acting as Lewis bases and forming electron donor–acceptor (EDA) complexes with H_2O molecules. When nitrogen-containing functional groups are not abundant, which is the case in

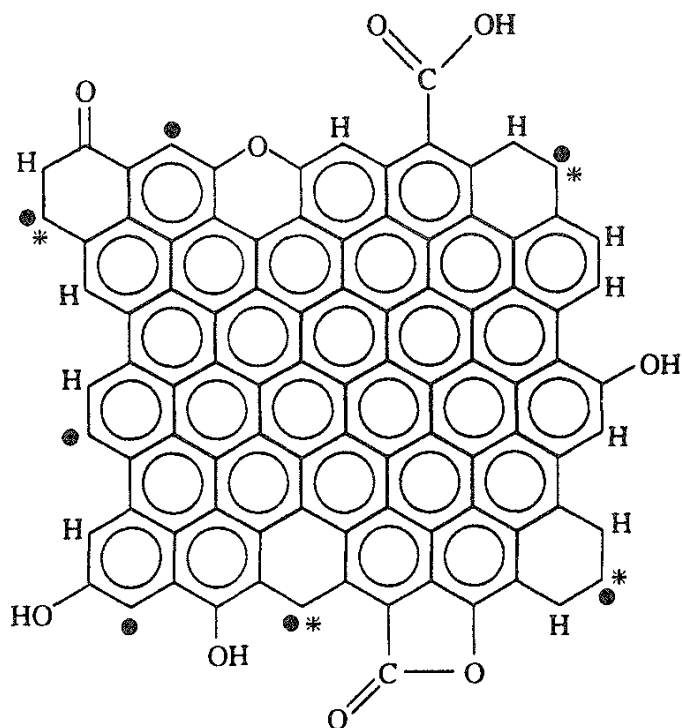


FIG. 3 Schematic representation of a graphene layer in a carbon crystallite including the various oxygen-containing functional groups (carboxyl, lactone, phenolic, carbonyl, pyrone) at the edges of graphene layers. Many such layers are stacked more or less parallel to each other to form carbon crystallites connected by a network of slit-shaped pores. The structure is representative of an activated carbon with a crystallite width of 15Å and an elemental analysis (by weight) of 87.5% C, 11.3% O, 1.2% H. (●) Unpaired sigma electron; (●*) an "in-plane sigma pair," where * is a localized π electron.

most practical situations (unless nitrogen is added deliberately, e.g., by treatment with ammonia), the relative contributions of basic oxygen and graphene layers to the positive charge are the key issue. Such information is not readily available in the literature, even though it has important practical implications (Just based on statistical arguments): In the absence of shielding effects, electrostatic repulsion of adsorbates from the graphene layers (where most of the surface area resides) is thought to be much more detrimental for adsorbent effectiveness than repulsion from the basic oxygen functional groups.

Electrophoretic studies on activated carbon and carbon black particles, and their comparison with the results for amphoteric oxides, contain clues about the contributions of functional groups and graphene layers to the development of surface charge. [Figure 4](#) illustrates a typical set of results. Electrophoretic mobilities of particles are measured as a function of pH and are seen to be an order of magnitude smaller than those of hydrogen ions under comparable conditions. They are commonly converted to either zeta potentials or surface charges using standard electrical double layer (EDL) equations. In theory, each graph represents "a titration of surface charged groups and as such is strictly comparable with a

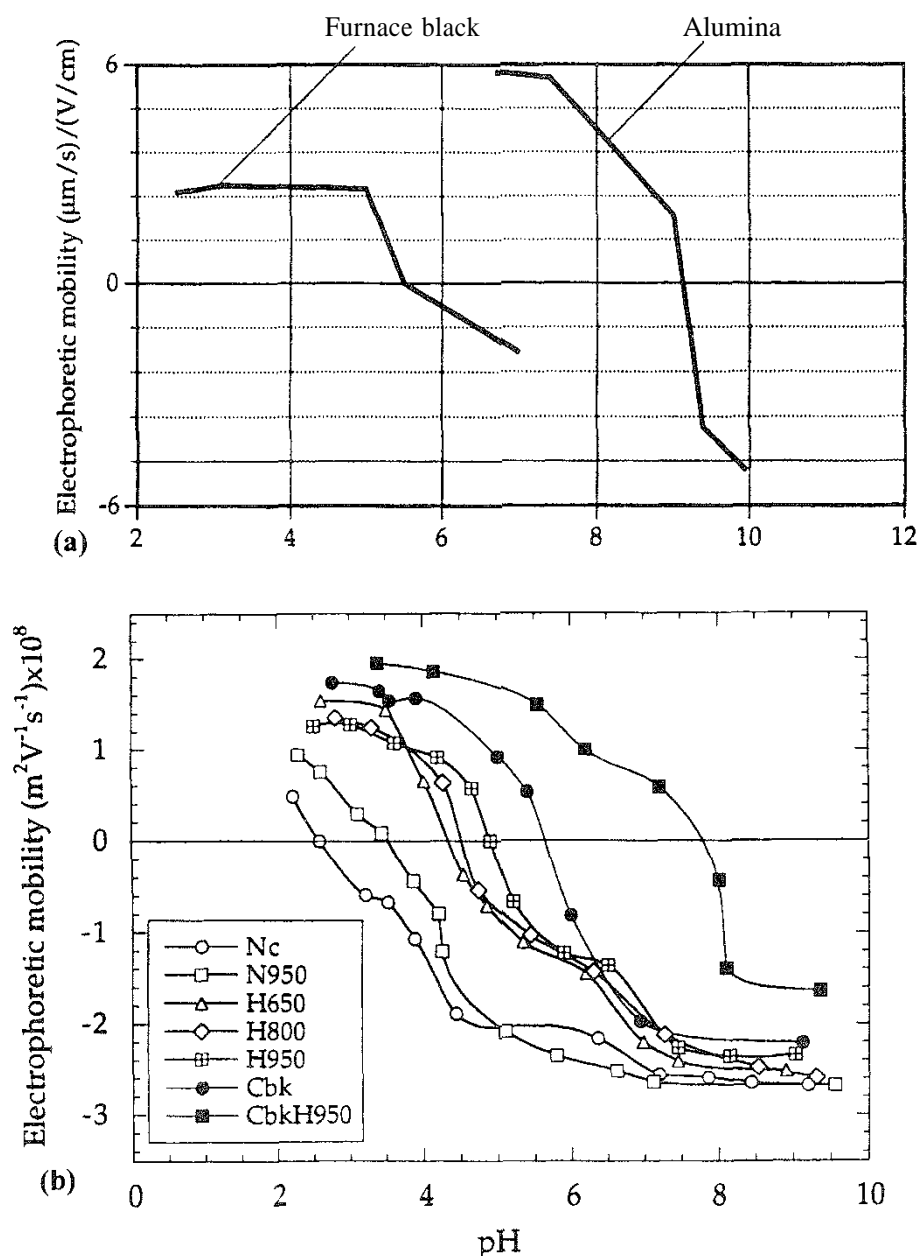
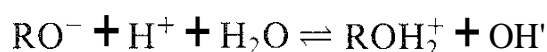


FIG. 4 Electrophoretic mobility as a function of pH for (a) a-alumina [146] and a furnace carbon black [24] and (b) an activated carbon [49].

potentiometric titration" [9]. The so-called H carbons [10] have a high isoelectric point (e.g., $\text{pH}_{\text{IEP}} > 7$), while the so-called L carbons [10] have a low isoelectric point (e.g., $\text{pH}_{\text{IEP}} < 7$). A common observation in the surface charge characterization of many carbon materials is that the absolute value of the positive charge is often much smaller than that of the negative charge [11–22]. This has been obvious for more than half a century [23], but its implications were not discussed until recent years; for example, from the data of Steenberg, as reproduced by Garten and Weiss [10], the uptake of NaOH on an L carbon (sugar-derived char activated at 400°C) was $\sim 700 \mu\text{mol/g}$, while the uptake of HCl on an H-type carbon (same char activated at 800°C) was $\sim 300 \mu\text{mol/g}$. In contrast, for carbon blacks the situation can be reversed [10], or the electrophoretic mobility vs. pH diagrams

tend to be much more "symmetric" [24]. More recently, for example, Dobrowolski et al. [15] reported the charges for a "basic" carbon (outgassed in argon at 1400 K) and an "acidic" carbon (oxidized in H₂O₂) of 15 mC/m² (at pH = 2.4) and -60 mC/m² (at pH = 8.4), respectively. To put these numbers in perspective, an activated carbon (-1000 m²/g) that is heavily oxidized (e.g., with HNO₃) may contain as much as 10 wt% oxygen; if all this oxygen is in the form of carboxyl groups, this is equivalent to ~3 mmol of C O O per gram, or 300 mC/m² (~1.5 V).

The comparison with amphoteric oxides [25–27] is also instructive. In an early review, Snoeyink and Weber [28] compared the surface functional groups on carbons and silicas but did not point out the resulting differences in the "symmetries" of their electrokinetic behavior. For amphoteric oxides containing ROH surface groups, the symmetry (see Fig. 4a) is a consequence of the equilibrium [25,29–34]



and at pH = pH_{iep}, [ROH₂⁺] = [RO⁻].

Taken together, these results strongly suggest that (1) there is an important contribution of the graphene layers to the positive surface charge of carbon adsorbents and (2) the widely held belief (especially reflected in the literature reviewed in Sec. III) that surface charge develops as a consequence of both deprotonation and protonation of the same oxygen functional groups should be discarded. Protonation of aromatic carboxyl groups in aqueous solution is highly unlikely. [Thus, for example, only acids whose strength exceeds $pK_a \sim -7$, e.g., HI ($pK_a = -10$), can protonate aromatic carboxyl groups, while ArCOOH₂⁺ is, of course, a much stronger acid than H₃O⁺ ($pK_a = -1.74$), and ArCOOH is the dominant species in water.] Instead, protonation of the basal plane [35] is considered to be much more important for the applications of interest here.

The use of titrations is commonly considered to be an alternative to electrophoresis for the estimation of surface charge. Actually, in the case of solid carbons, and especially in the case of high surface area activated carbons, this turns out to be a complementary method [20], and failure to make the distinction can be misleading. Electrophoretic mobility is considered to be a response to primarily external surface charge on the particles, while titrations probe both the external and internal surfaces of particles. For convenience I shall refer to the titration-derived parameter (pH_{pzc}) as the point of zero charge, while the electrokinetically derived parameter (pH_{IEP}) will be referred to as the isoelectric point. I acknowledge that a more fundamental distinction between these two parameters [34] requires a discussion of specific adsorption (in an ideal situation, the two should be identical in the absence of specific adsorption), but such a discussion is typically not included in adsorption studies, especially of organic compounds. In most cases of practical interest, pH_{IEP} < pH_{PZC} because of preferential (diffusion-controlled) ambient-air-induced oxidation (e.g., carboxyl group generation) on the external surfaces of carbon particles. Hence, the smaller the difference between the two values, the more homogeneous the distribution of surface charges. This is illustrated in Table 1. A dramatic example of this difference between pH_{PZC} and pH_{IEP} has been shown (albeit implicitly) by Dixon et al. [36] for the case of a commercial activated carbon, ~10.2 vs. ~3.5.

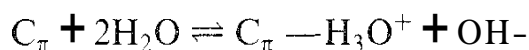
TABLE 1 Electrochemical Properties of As-Received and Chemically Modified Activated Carbons

| Carbon sample" | pH _{PZC} | pH _{IEP} | pH _{PZC} -pH _{IEP} |
|----------------------------|-------------------|-------------------|--------------------------------------|
| Nc (Norit C) | 2.5 | 2.6 | -0.1 |
| NcA | 2.2 | 2.2 | 0.0 |
| NcN | 5.2 | 3.5 | 1.7 |
| NcNA | 4.2 | 2.9 | 1.3 |
| NcH | 9.0 | 4.9 | 4.1 |
| NcH-1ox | 8.9 | 4.2 | 4.7 |
| NcH-7ox | 9.0 | 4.2 | 4.8 |
| NcH-20ox | 8.6 | 3.7 | 4.9 |
| NcH-30ox | 8.4 | 3.3 | 5.1 |
| NcH-HNO ₃ d16h | 3.9 | 3.5 | 0.4 |
| NcH-HNO ₃ cl/4h | 3.3 | 1.6 | 1.7 |
| NcH-HNO ₃ cl/2h | 2.8 | 1.4 | 1.4 |

"A = treatment in air at 250°C for 3 h; N = treatment in N₂ at 950°C for 3 h; NA = same as N but subsequently oxidized in air at 250°C for 7 min; H = treatment in H₂ at 950°C for 3 h; H-Xox = room temperature exposure of sample H to ambient air for X days; H-HNO₃XYh = treatment of sample H with concentrated (X = c) or dilute (X = d) HNO₃ for Yh.
Source: Ref. 20.

A compilation of pH_{PZC} and pH_{IEP} values for several commercial activated carbons [37] shows that the values for adsorbents commonly used in water treatment can vary by several pH units. This reinforces the point that was clearly illustrated by Lau et al. [38]: Because of the large affinity of carbon for oxygen, the storage and thermal history of the adsorbent often have a strong influence on its chemical surface properties.

Figure 3 is an attempt to synthesize and highlight the key molecular features of the edges and basal planes of graphene layers. Only some of the most prevalent surface functional groups are depicted [35]. Special attention should be given to the delocalized π -electron system that acts as a Lewis base in aqueous solution [35,39,40],



In addition to giving rise to a positive surface charge, the graphene layers participate in π - π interactions [41–44] with aromatic adsorbates. These are known to be sensitive to substituent effects on the aromatic ring [41, 45–48]. The substituent effects on the carbon adsorbents are examined in detail in Secs. IV.B and IV.C. Suffice it to note here that there are at least three ways in which the π -electron density of a graphene layer can decrease [49–51]: (1) deliberate “decoration” of the edges with oxygen functional groups, by controlled oxidative treatments; (2) accidental (and more or less inevitable) decoration of the edges with oxygen functional groups upon adsorbent exposure to ambient air; and (3) additional localization of π electrons at the edges by forming “in-plane σ pairs” with the

unpaired σ electrons (remnants of high temperature treatment of the material). The degree to which these processes take place can be fine-tuned by carbon pretreatment in inert or reactive gases, as illustrated in Fig. 5. The dramatic decrease in both the O_2 uptake (at room temperature) and the heat of O_2 adsorption upon H_2

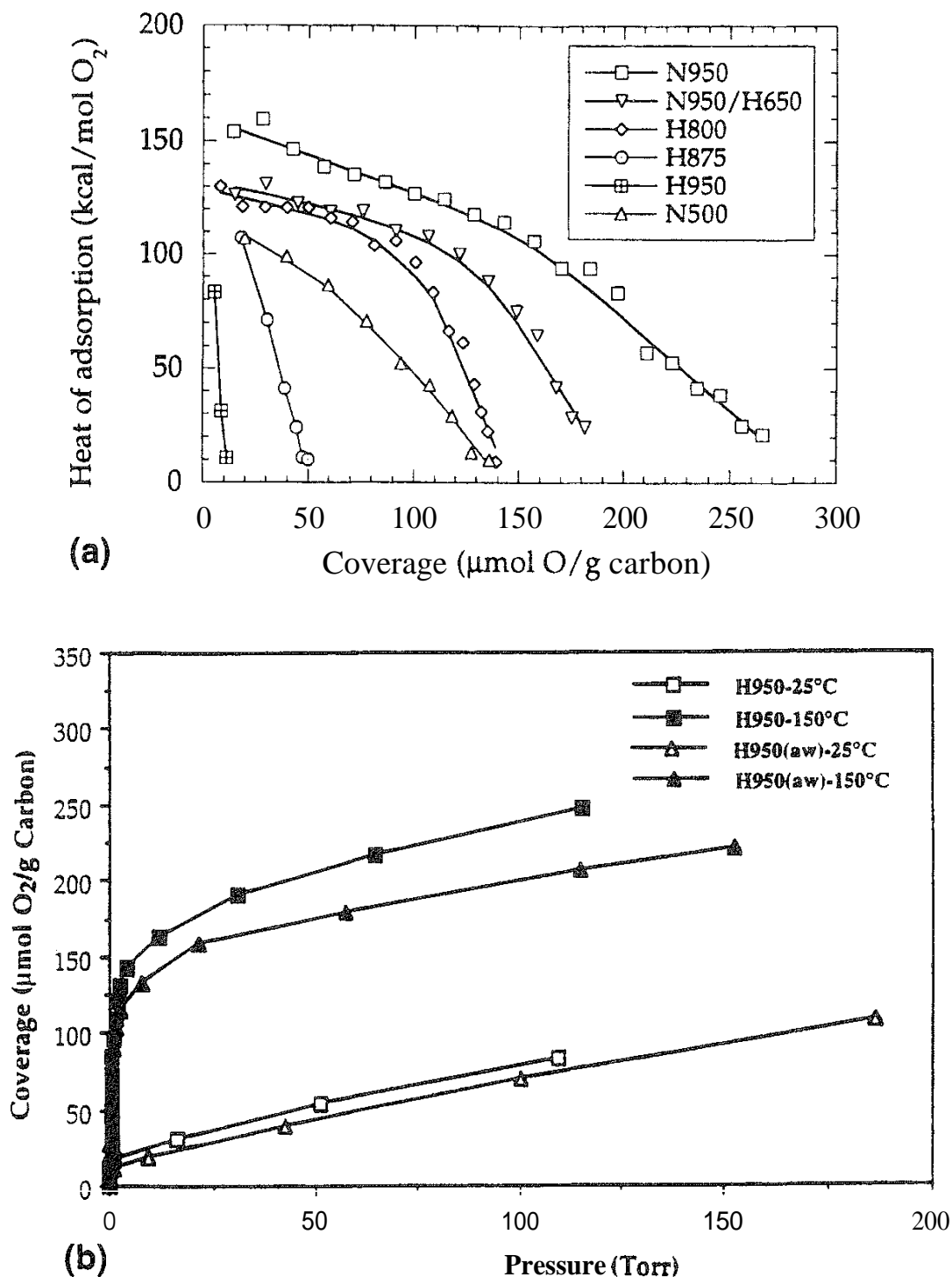


FIG. 5 Effects of treatments in H_2 at 650–950°C (H950, etc.) and N_2 at 500–950°C (N500, etc.) on the surface chemistry of a commercial activated carbon (Norit C extra). (a) Differential heats of adsorption of O_2 at 25°C; (b) adsorption isotherms of O_2 at 25 and 150°C (aw = acid-washed).

treatment at 950°C (Fig. 5a) is not a consequence of the creation of stable C—H groups at the edges of the graphene layers; rather, it is achieved by selective removal (hydrogasification) of the most (re)active carbon atoms. The resulting structure is less (re)active upon subsequent ambient air exposure even though it contains many unsaturated sites. Figure 5b confirms this interpretation; adsorption of O₂ on these less (re)active carbon sites does occur at the higher temperatures.

Interaction of π systems with water, as well as with cations, has been a topic of considerable fundamental [52–55] and practical [56] interest. Even though solid carbons are generally considered to have a hydrophobic character (which is certainly true in comparison with adsorbents such as most zeolites and clays), they can be very effective in removing both organic and inorganic acids and bases, especially from aqueous solutions [57]. A critical review of the carbon–water interactions has long been overdue, but space constraints do not allow me to offer it here. (The reader is referred to a recent review by Vartapetyan and Voloshchuk in *Russ. Chem. Rev.* 64, 985, 1995). Suffice it to say that progressive incorporation of acidic oxygen functional groups can transform a very hydrophobic carbon into a very hydrophilic one [58–60], while treatment at an optimum temperature in H₂ can result in both hydrophobic (basic) and stable carbon surfaces [49–51,61,62]. The latter point is illustrated in Fig. 6: A relatively high pH_{PZC} is maintained for this carbon over a period of several months, even though some external surface oxidation does occur.

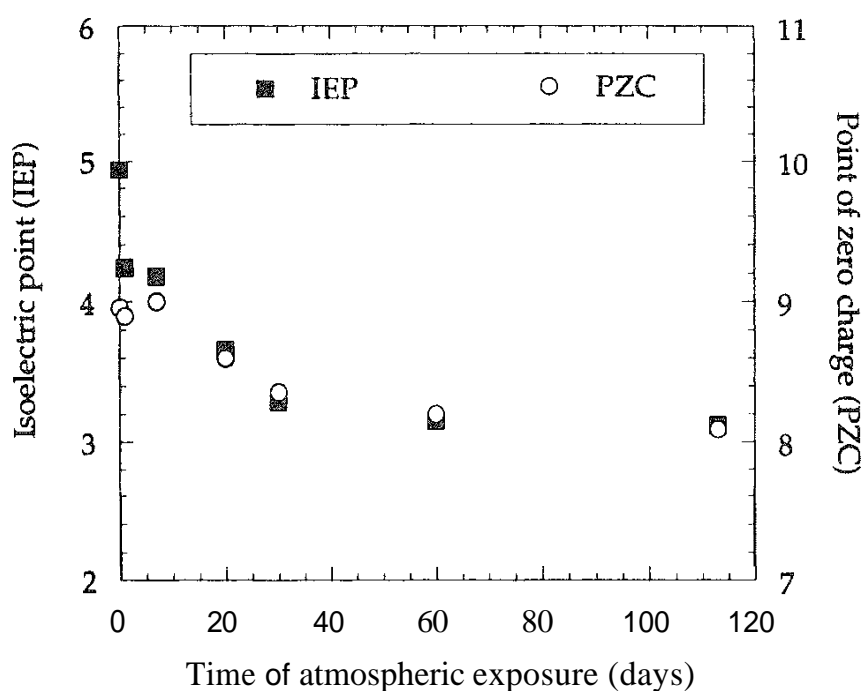


FIG. 6 Effect of atmospheric exposure on the isoelectric point (determined by electrophoresis) and point of zero charge (determined by mass titration) for an activated carbon treated in H₂ at 950°C.

III. ADSORPTION OF INORGANIC SOLUTES

The adsorption of inorganic solutes is a topic of great practical interest because of water treatment and metal recovery applications. In particular, the uses of activated carbons in mercury removal [63] and gold recovery [64] have been of interest for decades. The fundamental aspects of the process are also of interest in the preparation of carbon-supported catalysts [65]. A critical and comprehensive review is offered elsewhere [37]. Here I briefly discuss the removal of selected metals. In particular, I explore the "symmetry", or lack thereof, in the electrostatic attraction between a positively charged surface and adsorbate anions at $\text{pH} < \text{pH}_{\text{PZC}}$ and between a negatively charged surface and adsorbate cations at $\text{pH} > \text{pH}_{\text{PZC}}$. If such symmetry existed, then the uptake of, say, Pd^{2+} species would be equally maximized when $\text{Pd}(\text{NH}_3)_4^{2+}$ cations are contacted with a negatively charged carbon as when PdCl_4^{2-} anions are contacted with a positively charged surface. Early (albeit indirect) evidence against the existence of such symmetry was provided by Carrasco-Marín et al. [66] (see also Radovic and Rodriguez-Reinoso [65]) in a study of catalytic activity of carbon-supported palladium: The catalyst was much more active, and presumably adsorption of Pd occurred over a much greater surface (thus minimizing catalyst sintering), when PdCl_4^{2-} anions were contacted with a positively charged surface (at pH 0.1).

The key issue from both a practical and a fundamental viewpoint is whether or not the entire adsorbent surface is available for adsorption. (Multilayer adsorption or volume filling of micropores is not considered here, nor is the possibility of molecular sieving.) Its resolution depends on the answers to two questions:

1. Is the surface electrostatically accessible, i.e., has electrostatic repulsion been eliminated?
2. Is the affinity of the uncharged surface for the (usually charged) adsorbate species sufficiently strong to attract them from solution through van der Waals (e.g., dispersion) interactions?

These factors are considered in more detail elsewhere [37]. Here I analyze only one of the clues that contains the answers: the fraction of the carbon surface covered by selected cationic and anionic adsorbates.

A. Adsorption of Cations

Table 2, from the study of Ferro-Garcia et al. [67], provides the relevant information, which turns out to be typical for cationic adsorbate species (see, e.g., Refs. 68–70). The isotherms were obtained at pH 5 because a large increase in uptake was observed as the pH was raised from 3 to 5. The authors reasoned that the pH_{PZC} "lies between these two values," despite the fact that the pH of the slurry was much higher (see Table 2). Therefore, residual electrostatic repulsion of the Cd^{2+} , Zn^{2+} , and Cu^{2+} cations by the still positively charged surface ($\text{pH} < \text{pH}_{\text{slurry}}$ pH_{PZC}) may have counterbalanced the ion exchange that has increasingly taken place on some of the dissociated carboxyl groups at pH 5. Indeed, in the earlier work of Huang and Smith [12] using a chemically similar carbon ($\text{pH}_{\text{PZC}} = 7.1$), Cd^{2+} removal efficiency continued to increase well beyond pH 5, and especially so

TABLE 2 Physical and Chemical Surface Properties of Selected Activated Carbons and Their Metal Adsorption Capacities Expressed as a Fraction of Available Surface Area

| Carbon ^a | pH | $S_{\text{CO}_2}^b$ (m ² /g) | V_T^b (cm ³ /g) | V_{micro}^b (%) | Percent surface occupied ^c | | |
|---------------------|------|--|---------------------------------|-----------------------------|---------------------------------------|------------------|------------------|
| | | | | | Zn ²⁺ | Cd ²⁺ | Cu ²⁺ |
| A | 8.57 | 1103 | 0.707 | 38.2 | 4.1 | 0.7 | 3.9 |
| H | 8.23 | 1316 | 0.473 | 60.2 | 2.6 | 1.4 | 3.7 |
| P | 7.40 | 876 | 0.442 | 65.4 | 3.0 | 1.1 | 4.3 |

^aThe activated carbons A, H, P were prepared from almond shells, olive stones, and peach stones, respectively. Their aqueous suspensions all had pH > 7.0.

^bThe surface area, total pore volume, and micropore volume (in pores < 7.5 nm) were determined by CO₂ adsorption and mercury porosimetry.

^cCalculated using Langmuir adsorption capacities obtained at 293K and pH 5.

Source: Ref. 67.

when pH was above pH_{PZC} (even though some of this increase was attributed by the authors to hydroxide precipitation). The authors calculated for Cd(II) "a hydrated radius of approximately 25 Å which is larger than the reasonable size of hydrated cadmium ions."

These results indicate that a much smaller fraction of the adsorbent surface is typically covered by inorganic adsorbates than by organic (especially aromatic) adsorbates (see Sec. IV). A logical inference is that, in contrast to the mechanism of adsorption of organic solutes (see Sec. IV), the graphene layers are not involved in the adsorption of inorganic cations from dilute aqueous solution. Instead, cation-exchange processes or interactions with functional groups at the graphene layer edges are primarily responsible for the adsorption of metals. The study by Jayson et al. [71] is interesting in this context. These authors found that "saturation adsorption [of an activated charcoal cloth] increases slightly as the pH increases from 3 to 5.5," which is consistent with a decrease in electrostatic repulsion or a higher degree of ion exchange. They assumed that at the saturation adsorption capacity at pH 5.5, mercury exists as a cationic species (even though Baes and Mesmer [72] suggested that neutral $\text{Hg}(\text{OH})_2$ is predominant) and thus calculated a surface coverage of 3.5% for the unhydrated cation; however, when a single sphere of hydration was assumed to surround it, an unusually high coverage of ~ 90% was obtained. One possible reason for such a large uptake is that this carbon (whose surface chemistry was not described) had a very high surface functional group concentration; perhaps a more likely explanation is that the metal concentration used was much higher (by several orders of magnitude) than those typically encountered in wastewater streams.

Clearly, further fundamental studies are needed to confirm these conclusions. For example, it will be interesting to find out whether much higher surface coverages can be accomplished on a carbon whose maximum number of (cation-exchangeable) adsorption sites, e.g., ~ 3 mmol COO^-/gC , is not only created but also made electrostatically accessible by adjusting the solution chemistry (and in the

process distinguishing clearly between adsorption and precipitation). Under these conditions, for example, the theoretical (ion-exchange) capacity for a divalent cation is as much as 50% of the total surface area of a typical activated carbon ($\sim 1000 \text{ m}^2/\text{g}$).

Alternatively, it will be important to verify whether the highest uptakes can be achieved under conditions of electrical neutrality of both the adsorbate species and the adsorbent surface, for example, at some optimum pH. This has often been observed for organic adsorbates (see Sec. IV), because departure from these conditions has led more often to electrostatic repulsion than to electrostatic attraction. Not as many such reports are available in the literature on the adsorption of inorganic solutes, or if they are, their discussion does not follow this line of reasoning. I offer just one example to illustrate this point. Bhattacharyya and Cheng [73] studied the adsorption of Cd-Ni chelates on a commercial activated carbon ($\text{pH}_{\text{PZC}} = 9.0$) and reported a set of intriguing results: When the metals were complexed with ethylenediaminetetraacetic acid (EDTA), a maximum in uptake was observed at intermediate pH; in contrast, when they were complexed with a ligand that yields a positively charged species over the entire pH range (5–12), a monotonic increase in uptake was observed.

B. Adsorption of Anions

The adsorption of anions is a much more controversial topic than the adsorption of cationic species. It is quite intriguing that in many cases the uptake does not appear to be much higher, as one might expect if the positively charged graphene layers (see Figs. 2 and 3) were electrostatically accessible and "active" in adsorption. Indeed, in a review of anion adsorption by Hingston [74], the use of carbonaceous adsorbents is not even mentioned.

For example, McDougall and Hancock [75] cite and discuss a study of Clauss and Weiss in which it was "calculated that the surface coverage amounted to less than one gold atom per 5 nm^2 of available carbon surface." They thus "excluded basal planes, carboxylic acid groups and basic oxides as so-called 'points of attachment' and proposed that the adsorption sites were probably quinone-type groups" or "special type of micropore[s]." In sharp contrast, Klauber [76] notes that "it is difficult to convert the pmol g^{-1} loadings into a sensible figure for aurocyanide coverage" but proceeds to calculate (based on X-ray photoelectron spectroscopic results) that the "extrapolated loading of 2000 pmol g^{-1} approximately equates to a 0.65 monolayer equivalent"; he thus concludes that "the graphitic planes of the activated carbons [are] the location onto which the $\text{Au}(\text{CN})_2^-$ anions adsorb."

Table 3 summarizes the results of Solar et al. [18], which clearly illustrate the dramatic improvement in molybdenum adsorption once the electrostatic repulsion is eliminated. Thus, for example, the surface coverage of the as-received carbon black increased by more than an order of magnitude at $\text{pH} < \text{pH}_{\text{PZC}}$; despite the uncertainties regarding the surface area occupied by the adsorbed species and the complex speciation diagram of Mo^{6+} [72], these high values could well be interpreted to represent a large fraction of the adsorbent surface.

TABLE 3 Molybdenum Loadings on As-Received (M) and Chemically Modified Carbon Blacks

| Adsorbent ^a | pH | Mo adsorbed ^h (wt%) |
|--|-----|-----------------------------------|
| M (Monarch 700, Cabot Corp.) ($\text{pH}_{\text{IEP}} = 6.2$; $\text{pH}_{\text{PZC}} \approx 7.0$; $202 \text{ m}^2/\text{g}$) | 8.5 | 0.06 |
| | 2.6 | 1.39 |
| M-HNO ₃ ($\text{pH}_{\text{IEP}} = 1.3$; $\text{pH}_{\text{PZC}} \approx 2.6$; $246 \text{ m}^2/\text{g}$) | 8.5 | 0.02 |
| | 1.8 | 0.85 |
| M-2500-HNO ₃ ($\text{pH}_{\text{IEP}} = 3.0$; $\text{pH}_{\text{PZC}} \approx 5.6$; $131 \text{ m}^2/\text{g}$) | 8.5 | 0.02 |
| | 1.9 | 0.52 |

^aHNO₃ = treatment in boiling 6 N nitric acid for 1 h; 2500 = heat treatment at 2500°C in N₂.

^hFrom a solution of H₂(MoO₃C₂O₄), initial pH 2.0; determined by atomic absorption spectroscopy.
Source: Ref. 18.

IV. ADSORPTION OF ORGANIC SOLUTES

The need to purify both municipal and industrial wastewaters places increasingly stringent demands on the performance of activated carbon adsorbents. Reliance on the physical surface properties (e.g., high surface area, adequate pore size distribution) is thought to be particularly insufficient for the cost-effective removal of aromatic pollutants and the subsequent reactivation of the spent adsorbent. A thorough discussion of the opportunities that judicious design of surface chemistry offers in these applications is presented elsewhere [37], together with a comprehensive and critical review of the relevant literature. Here I summarize one of the key issues: the relative importance of electrostatic versus dispersive interactions in the adsorption of aromatics,

It is well known that methylene blue and other dyes are used to estimate the adsorption capacity of carbons and even to characterize their porous structure [77–80]. This implies that nonspecific dispersion adsorbate–adsorbent interactions are dominant in these systems and that the entire surface is accessible to the adsorbate. However, as Fig. 7 illustrates, the adsorption capacity depends very much on the chemistry of the carbon surface and the pH; unless the uptake by this carbon is determined at a relatively high pH, the measured surface area can be underestimated by a factor of 2 (e.g., from 500 to 1000 m²/g). This means that electrostatic interactions can be very important as well.

Based on extensive experimental evidence regarding the importance of pH and surface chemistry [37], there is no question that the arguments discussed in the previous section in the context of adsorption of inorganic solutes are applicable also—and indeed are required—for understanding the adsorption of organic solutes, many of which are weak electrolytes. What does need careful consideration here are the answers to the following two questions:

1. Which specific features of carbon surface chemistry need to be known, in both qualitative and quantitative terms, in order to be able to optimize an activated carbon for a specific pollution control task?

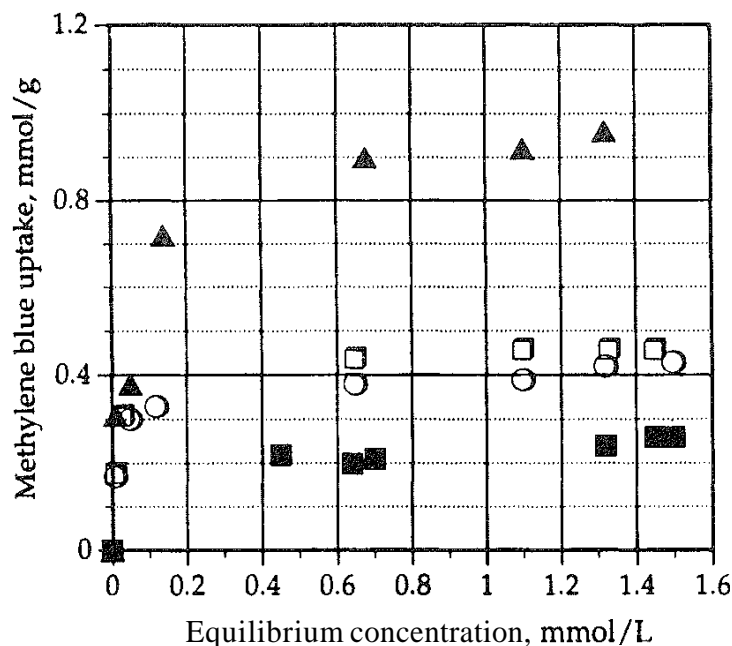


FIG. 7 Adsorption isotherms for methylene blue on BPL carbon (Calgon Carbon Corp.) under different pH conditions: (■) pH 3.1; (○) pH 6.29; (□) pH 9.0; (▲) pH 11.9.

2. What are the relative roles of electrostatic and dispersive interactions in the various adsorbate–adsorbent systems of interest?

In the preface to their landmark monograph, Mattson and Mark [81] wrote, "Carbon researchers have, for the most part, considered the surface chemistry of activated carbon to be in such a state of disarray that they want to avoid lengthy discussions of surface phenomena." More than two decades later, with vast improvements in our knowledge of the role of surface chemistry in carbon gasification [82] and in the use of carbons as catalyst supports [65], an argument is presented here that this is no longer true.

There are probably no more contentious issues in the use of activated carbons than the role of surface oxygen functional groups in the aqueous phase adsorption of weak aromatic electrolytes. In a 1980 discussion in print, Suffet (see Ref. 83) made the following (under)statement and posed the key question: "There is some confusion in the literature regarding the major sites of adsorption [on granular activated carbon]. Is an oxidized surface adsorbing material on the oxidized functional groups, or is it adsorbing on the nonpolar carbon surface?"

Even though the components of the total interaction potential between such complex adsorbents as solid carbons and a wide range of adsorbates can be grouped in many different ways [84,85], it is convenient to consider only the London dispersion (induced dipole) forces and the electrostatic (double layer) forces [43,44,86,87].

A. Role of Electrostatic Interactions

Elsewhere my coworkers and I discuss in detail the benefits of establishing connecting points, and thus achieving cross-fertilization, between the disciplines of surface chemistry, electrochemistry and liquid-phase adsorption [4,37]. Here I briefly review the effects of pH on surface chemistry (or vice versa) and on the uptake of weak organic electrolytes. (It should be noted, however, that there continue to appear published reports in which the pH of the adsorption experiment is not even mentioned, let alone controlled.)

In the pioneering work of Mattson et al. [88], a decrease in *p*-nitrophenol uptake with increasing pH was noted, but it was attributed to increasing solubility rather than electrostatic repulsion. Vaccaro [89] noted that the pH effects "originate from a variety of mechanisms, many of which remain inadequately understood" but chose not to address the relevant issues. Zogorski et al. [90] noted a decrease in the rate of adsorption of substituted phenols as pH increased. Peel and Benedek [91] noted that the "influence of pH is complex and potentially could have ... a significant effect on the results of studies conducted in the vicinity of the pK_a ." Fuerstenau and Pradip [92] reported a small but consistent decrease and a small but consistent increase in the uptake of *o*-cresol ($pK_a = 10.2$) for two coals with pH_{PZC} values of 3.6 and 4.6, respectively; they dismissed these trends by stating that "no effect of pH on adsorption was observed" and that this was "not surprising since *o*-cresol is a neutral molecule and presumably adsorption is occurring through hydrophobic interactions of the benzene ring with the coal surface." Puri [93] discussed the decrease in the pH values of the aqueous suspensions of oxidized activated carbons and its effect on the uptake of ammonia but did not consider this effect in the adsorption of aromatic species such as aniline. McGuire et al. [94] reported that as the pH was increased from 1.9 to 7.7 the uptake of phenol also increased slightly. Grant and King [95] reported a large suppression of reversible phenol uptake as the pH increased from 1.8 to 12.1, but they attributed this primarily to a solubility effect ("phenolate anion has more affinity for the aqueous phase than does phenol"); electrostatic repulsion was not associated with the charge on the adsorbent surface but rather to "anions in the surface layer." Vidic et al. [96] reported similar results for 2-chlorophenol uptakes under anoxic conditions but invoked the same unconvincing explanation offered by Rosene and Manes [97], "in terms of physical adsorption of the undissociated acid," which does not recognize the importance of carbon surface chemistry. Nakhla et al. [98] also studied the effect of pH on activated carbon adsorption of phenolics in both oxic and anoxic systems. Surprisingly, they stated that "little is known about the influence of parameters such as pH ... on the retention capacities" of activated carbons (under conditions when surface-promoted chemical reactions such as oxidative coupling are possible). Their findings confirmed those of Grant and King [95] and Vidic et al. [96], and the explanations offered are similar, eluding any reference to the role of carbon surface chemistry, especially under anoxic conditions. Analysis of pH effects on the kinetics of adsorption of phenols by the same research group [99] also ignores the role of surface chemistry. Similar findings and conclusions are reported by Cooney and Xi [100], with some notable exceptions. They do state that "ionized forms of species adsorb less effectively to activated carbon than do

their undissociated forms" but do not give an explanation for this fact; and they discuss the role of electron-donating substituent groups in accelerating oxidative coupling, an important issue that I address in Secs. IV.B and IV.C. Ha et al. [101] studied the adsorption equilibrium of the protein bovine serum albumin (BSA) on surface-modified carbon fibers. They report that "the saturation amount adsorbed is significantly affected by surface characteristics as well as pH." Maximum uptakes were typically observed at intermediate pH values "near the isoelectric point of BSA." Curiously, however, these authors affirm that carbon fibers usually possess a net negative charge over the pH range of their experiments (pH 3–9). They do conclude that the "surface charge attributed [to] the surface functional groups" or the "dissociability of the surface functional groups" is one of the "controlling factors for BSA adsorption," but they leave the reader somewhat confused about how exactly such control is exerted. Longchamp et al. [102] studied the effect of pH adsorption behavior of plasmin (Pln, an enzyme) on the surface of a Nujol–graphite paste. They also concluded that "maximal efficiency in the adsorption of Pln was attained at pH 7.7," which is close to the isoelectric point of the "major fraction of Pln," and the "local isoelectric potential distribution of the supporting surface is also of concern"; but they did not elaborate on this latter point. Dargaville et al. [103] state that the "pH of the adsorbent/adsorbate system could be critical in determining the amount adsorbed" and that "the affinity for adsorption increases (hence larger amounts adsorbed) as the acidity of the adsorbate increases," but they do not provide the explanation for these effects nor do they direct the reader to the appropriate references where such explanations are offered.

In these and many other [37] studies, the pH effect was noted, but its critical link to both surface chemistry and adsorption behavior had not been made. As early as 1937, however, in a paper whose dubious distinction is that it has zero citations in 35 years (according to the Science Citation Index, 1961–1997), Frampton and Gortner [23] studied charcoal surface chemistry using electrokinetic techniques. They did not report the variations in the point of zero charge as a function of charcoal pretreatment (e.g., H_2 at 1000°C, N_2 at 900°C, HNO_3 , etc.), but they did measure the electrophoretic mobilities in water and found them all to be negative [on the order of $3-4 (\mu m/s)/(V/cm)$] and insensitive to treatment conditions. They concluded therefore that (1) "electrokinetic data do not indicate a difference between 'basic' and 'acidic' charcoal" and (2) "apparently the adsorption of weak electrolytes from aqueous solution on charcoal is molecular rather than ionic." In the first edition of *Active Carbon* [104], Hassles cites this work to affirm that the "electrokinetic behavior of carbon does not appear to be altered by the adsorption of weak organic acids or bases"; in the subsequent edition [105], however, the same statement is made without any references. Also intriguing is the omission from the second edition of a graph showing the influence of pH on the electrophoretic mobility and amphoteric character of activated carbons. In fact, the relevant changes between the two editions appear (in hindsight) to have hindered our understanding of electrostatic interactions (see pp. 89–92 in the first edition and pp. 231–233 and 360 in the second), because for a long time (see below), when surface charge was invoked, if at all, carbonaceous adsorbents were assumed to possess only a negative charge.

The important work of Muller and coworkers [106–108] regarding pH effects on the adsorption of weak organic electrolytes has been ignored by the environmental electrochemistry community [37], but in the adsorption community it resonated clearly, albeit slowly (see below). Their model for single-solute systems is discussed in more detail in Sec. IV.C. Müller et al. [106] note that "certain combinations of solute pK , solute concentration, and surface charge" are predicted to result in "an adsorption maximum with hydrogen ion concentration," this being a frequently reported experimental finding. In particular, such an "adsorption maximum is found in a pH range where the solute exists mostly as a counterion and where the effect of pH on ionization of the solute is stronger than that on the decrease of the magnitude of the surface charge" [106]. Clearly, the emphasis here is on electrostatic adsorbate–adsorbent interactions. The authors do acknowledge that "aromatic solutes adsorb onto activated carbon by interaction of the aromatic ring with the carbon surface" and that "changes in the electron density of the aromatic ring affect the affinity to adsorb" [107], although their reference for the latter statement should be (see Ref. 37) the work of Coughlin and coworkers [109–111] and not the cited study of Mattson et al. [88]. The adjustable parameters in their model were not subjected, however, to a scrutiny that would reveal the importance of this non-electrostatic contribution to the overall adsorption potential (see Sec. IV.C). The dominant effect of electrostatic interactions was illustrated by showing (1) a dramatic decrease in the uptake of benzoic acid ($pK_a = 4.2$) as the pH was raised from 4.5 to 11.0 for a carbon whose pH_{PZC} was 6.7; (2) a gradual increase in the uptake of aniline ($pK_a = 4.6$) by the same carbon as the pH was raised from 2.0 to 10.8; and (3) a gradual decrease in the uptake of *p*-nitrophenol ($pK_a = 7.3$) as the pH was raised from 2.05 to 10.6 for a carbon whose pH_{PZC} was 5.8.

In the mainstream literature on the adsorption of organics, this appreciation of the importance of electrostatic interactions and its further development was a very slow process. It was hampered by uncertainties regarding the key aspects of the chemistry of the carbon surface and by efforts to find a direct relationship between specific features of this chemistry and carbon's adsorptive properties. In the pioneering work of Snoeyink and Weber [112], it was concluded that "there is strong indication of the need for continuing research on the definition of the nature of surface functional groups, and on the particular conditions of preparation which will produce an active carbon best suited for a specific application." Snoeyink et al. [13] were somewhat more specific a few years later, after establishing that the uptakes of both phenol and *p*-nitrophenol are suppressed as pH increases; but they still concluded that the "precise reasons for the capacity differences [of a coal-based versus a coconut-shell carbon] with respect to the two solutes are not known." Thirty years later, a much better understanding of surface chemistry has been achieved, but, as argued below, it was not necessary to wait for this development in order to be able to optimize the adsorption of organics on activated carbons. A brief historical development of the key ideas is presented below; it is discussed in more detail elsewhere [37].

Chapter 7 of the landmark review by Mattson and Mark [81] emphasized the pH dependence of the uptake of acetic acid, *n*-butylamine, substituted benzoic acids, anionic benzenesulfonates, and methylene blue. In particular, the suppression of methylene blue uptake at pH below the isoelectric point of the carbon was

explained by stating that "the formation of positive surface sites in that region certainly would not enhance cationic adsorption." The important work of Getzen and Ward [114,115] was also cited, in which the concept of the isoelectric point (or point of zero charge) was not mentioned (presumably because this work was based on the historically popular concept of hydrolytic adsorption), but which clearly emphasized the importance of electrostatic adsorbate-adsorbent interactions: "There is a distribution of residual forces on the surface of the charcoal (which may be varied by changes in pH) such that they may exert an attraction for both electropositive and electronegative ions as well as for the uncharged molecules.... They are, in the case of ions, the coulombic forces and, in the case of uncharged molecules, van der Waals and similar forces."

Even though Getzen and Ward [114] state that the "existence of such forces is recognized today and their description is generally understood," the subsequent three decades of published work in this area have shown too many examples to the contrary. A series of papers by Urano and coworkers [116-119] — in none of which is the work of Müller et al. [106] mentioned — is a good example. In an early paper on the adsorption of strong acids and bases [116], the authors provided a very useful determination of the pH_{PZC} of a commercial activated carbon. Subsequently, uptakes of a large number of both aliphatic and aromatic adsorbates by five commercial carbons were reported, but among the properties of the adsorbents there was no mention of their pH_{PZC} or of the pH of the solutions [118]. Instead, and surprisingly, emphasis was placed on the adsorbent's physical surface properties, and the authors concluded that they could "predict the adsorption capacities of organic compounds in aqueous solutions for any activated carbon whose pore size distribution is known." Even more surprising is the introduction of new arguments regarding the mechanisms of adsorption in the later papers [119,120], even though many of the same adsorbates are reconsidered. In particular, the authors [119,120] emphasize the " π -electron combination on the carbon surface" (see Sec. IV.B). They do acknowledge the influence of "several electrophilic groups ... on the surface of activated carbon" [120] and that "the influence of the pH on the adsorptions of organic compounds in water has not been made clear" [19] but then attribute the decrease in uptake of weak anionic electrolytes with ionization in basic solutions only to the fact that "the apparent solubilities of the ionized forms increase much more than those of the non-ionized forms" [119]. They emphasize the *sui generis* behavior of phenolic compounds and conclude, rather unconvincingly, that "the deviation of phenol [from predictions based on Freundlich isotherm parameters for the nonionized and ionized species] may be due to the combination of the hydroxide ion with the electrophilic groups on the surface of activated carbon."

By this time, a brief review from an authoritative industrial source [1] had identified the reason for the fact that "quite a number of phenomena [including adsorption of polar substances and electrochemical properties] cannot be explained at all with the usual carbon characterisations" and had postulated that "the presence and the configuration of oxygen-containing functional groups are responsible for the differences hitherto not explained." The author briefly discussed the zeta potential but concluded, rather anticlimactically, that oxidized carbons adsorb a polar compound such as methanol in preference to toluene and in proportion to

the amount of surface oxygen present. In a more comprehensive treatise on activated carbons, Bansal et al. [121] did not do justice to this issue either; their 17-page section on the removal of organic solutes from water in the active carbon applications chapter cites only 13 papers (from the pre-1983 period), none of which illustrate the important role of pH in the adsorption of weak organic electrolytes. The authors do point out "the importance of the surface chemistry of activated carbons for [the] removal [of organics]," but how exactly and which feature(s) of the surface chemistry is/are important was not settled. Even in the more fundamental chapter on the characterization of active carbons, electrostatic interactions are mentioned only in passing, as they relate to heat of immersion measurements. In this respect, Kinoshita's monograph [122] is more enlightening; it contains a detailed discussion of the zeta potential and surface charge, but not in the context of liquid-phase adsorption phenomena.

The relevant studies by Mazet and coworkers [123–127], published within a span of six years, are both illustrative and instructive. In the first of these papers, electrostatic interactions — between a powdered activated carbon (PAC) and calcium cations — and zeta potential measurements are discussed, but the emphasis is on the beneficial effect of Ca^{2+} in neutralizing the negative charge on the carbon surface. The last paper focuses much more on the chemical nature of the carbon surface and its impact on the adsorption of a wide range of organic compounds. Both positive and negative zeta potentials are reported, with pH_{IEP} values ranging from below 3 to above 6 [127]. Particularly instructive are the results for phenol and benzoic acid (see Table 4), both showing monotonically decreasing uptake with increasing pH in agreement with the reversal of zeta potential from positive to negative in the same pH interval. The authors attribute these results to the effects of solubility, adsorbate dissociation (ionization), surface charge, and electrostatic repulsion and conclude "that the electric charge of PAC is an important parameter for the adsorption of organic solutes." Table 4 also illustrates the neglected point

TABLE 4 Effects of pH on the Uptake of Phenol and Benzoic Acid for As-Received and Chemically Modified Activated Carbons

| Adsorbent ^a | pH | Zeta potential (mV) | Adsorption capacity (mmol/g) | |
|--------------------------------|-----|------------------------|------------------------------|--------------|
| | | | Phenol | Benzoic acid |
| Heat-treated Filtrisorb 400 | 3.0 | 14 | 0.99 | 1.16 |
| | 5.6 | 3 | 1.08 | 1.06 |
| | 7.2 | −4 | 0.93 | 0.82 |
| As-received Filtrisorb 400 | 3.0 | −4 | 1.02 | 1.0 |
| | 5.6 | −20 | 0.78 | 0.71 |
| | 7.2 | −28 | 0.73 | 0.65 |
| Oxidized Filtrisorb 400 | 5.6 | −26 | 0.43 | 0.57 |
| | 7.2 | −32 | 0.37 | 0.50 |

^a Heat treatment in N_2 at 800°C for 4 h; oxidation in boiling conc. HNO_3 for 1 h

Source: Ref. 127.

that, on a given adsorbent, the uptake of phenol is comparable to that of benzoic acid, despite the fact that the latter is much less soluble (see Sec. IV.C); the authors mention the "existence of a polarity due to π electrons (in phenol for example)," but they interpret this also as an electrostatic rather than a dispersion effect.

The recent studies of King and coworkers [128,129] have addressed the effects of pH and surface properties both on the uptake of lactic and succinic acids and on the adsorption and regeneration of phenol. In many cases, uptake decreased as pH increased, and all oxidized carbons "exhibited a significant reduction in uptake at the lower solute concentrations" [129]. Table 5 summarizes the relevant results. The observed uptakes [129] were interpreted as a complex net effect of several potentially conflicting trends: (1) a greater extent of oxidative coupling at high pH; (2) a lesser extent of oxidative coupling on oxidized surfaces; (3) a suppressed uptake at high pH "because of an increase in the negative charge on the adsorbent surface and an increased degree of phenol ionization"; (4) a decrease in available surface area upon surface oxidation due to preferential adsorption of water; and (5) a decrease in the adsorbate-adsorbent interaction energy for oxidized surfaces, presumably as a consequence of suppressed π - π overlap, as originally argued by

TABLE 5 Effect of pH and Carbon Surface Chemistry on the Freundlich Adsorption Parameters^a for Phenol

| Adsorbent | Treatment ^b | pH | K_F | n |
|-----------|------------------------|----|-------|-------|
| F400 | As-received | 2 | 51.1 | 0.198 |
| | As-received | 9 | 47.1 | 0.223 |
| | Acid-washed | 9 | 75.9 | 0.168 |
| | AW,H1 | 9 | 60.7 | 0.183 |
| | Ox 2/50 | 9 | 56.1 | 0.207 |
| | Ox 9/70 | 9 | 28.6 | 0.235 |
| | Ox 9/70,H6 | 9 | 57.7 | 0.189 |
| WVB | As-received | 2 | 12.7 | 0.345 |
| | As-received | 9 | 11.5 | 0.353 |
| | Acid-washed | 9 | 14.2 | 0.338 |
| | AW,H1 | 9 | 40.7 | 0.207 |
| | Ox 2/50 | 9 | 38.4 | 0.212 |
| RO | As-received | 2 | 57.4 | 0.185 |
| | As-received | 7 | 84.7 | 0.158 |
| | As-received | 9 | 68.7 | 0.179 |
| CG6 | As-received | 2 | 42.6 | 0.211 |
| | As-received | 9 | 41.3 | 0.231 |

^a K_F = adsorption capacity ("uptake at a solution phase concentration equal to unity"); n = "intensity of adsorption" (low values reflect high uptake at low concentration).

^b H1 and H6 = heat-treated at 1000°C and 650°C, respectively, for 24h in N₂; OxY/Z = acid-washed (AW), then heat-treated at 1000°C (in N₂), followed by oxidation in conc. HNO₃ for Y at temperature Z (in °C).

Source: Ref. 129.

Coughlin and coworkers [109–111] (see Ref. 37) and not, as the authors state, proposed by Mahajan et al. [130]. Thus, for example, even though the data shown in Table 5 are not unambiguous, the authors invoke the dominant effect of oxidative coupling for the observation that the "uptake at pH 9 was either higher (F400, RO, CG6) or remained essentially the same (WVB) as that at pH 2" [129]. They did characterize the surface chemistry of their carbons and did cite the work of Müller et al. [107] in this context, but they did not determine the surface charge variations with pH.

The recent studies by Newcombe and coworkers [131–135] concerning the complex fundamental issue of adsorption of natural organic matter (NOM) are important contributions to our understanding of electrostatic interactions. This is also an important practical issue in water treatment because NOM adsorption leads to carbon fouling. They performed measurements of both the isoelectric point and the point of zero charge and investigated their relationship with the adsorption and regeneration behavior of several commercial activated carbons. Table 6 summarizes the surface charge characteristics of virgin and spent commercial activated carbons. The significance of the differences between pH_{PZC} and pH_{IEP} was discussed earlier. Of interest here is the decrease in pH_{PZC} with increasing adsorption of humic and fulvic acids, as well as the increasing negative charge of the adsorbent. This result led Morris and Newcornbe [133] to conclude that "the surface charge properties of the GAC are largely determined by the adsorbed material, rather than the carbon surface itself." When applying these concepts to the chemical regeneration of GAC from an operating water treatment plant, Newcombe and Drikas [131] note that in prior studies "no attempt was made to investigate the surface chemistry of the interactions taking place at the carbon–water interface. As a result the findings have often been poorly understood, incorrect conclusions have been drawn and the possibility of chemical regeneration has not been fully explored." To remedy this situation, Newcornbe and coworkers [131,132] analyzed the surface chemistry of virgin, spent, and regenerated activated carbon and speculated that the effectiveness of the selected regeneration protocol was due to the creation of "an environment of lower pH within the pore structure, enhancing adsorption of organics" by virtue of "a large decrease in the electrostatic repulsion between the surface and

TABLE 6 Electrochemical Properties of a Granular Activated Carbon^a Before and After Adsorption of Natural Organic Matter

| Sample ^b | pH_{PZC} | pH_{IEP} | Surface charge (C/m^2) | |
|---------------------------|--------------------------|--------------------------|--|---------|
| | | | pH 7.0 | pH 8.0 |
| Virgin GAC | 7.3 | 3.0 | +0.0003 | −0.0006 |
| Spent GAC (3.5 mg DOC/g) | 6.4 | 2.7 | −0.0019 | −0.0046 |
| Spent GAC (10.0 mg DOC/g) | 4.5 | 2.4 | −0.0053 | −0.0084 |

^aFiltrisorb 300 (Calgon Carbon Corp.).

^bDOC = dissolved organic carbon (measure of concentration of NOM)

Source: Ref. 133.

the adsorbing species." In a more incisive study of the same issue, Newcombe [134] set out to determine "how surface concentration and pH affect the degree of ionization, the conformation, and the change in the free energy of dissociation of the adsorbed material, and how the effects may be explained in terms of the properties of both the humic material and the carbon surface." Most recently, the same research group tackled the key issue of the relative importance of electrostatic and nonelectrostatic effects [135] in the adsorption of NOM by studying the effectiveness of electrostatic screening (using an added salt) in the case of two chemically different commercial activated carbons. Those results are discussed in more detail elsewhere [37].

B. Role of Dispersion Interactions

Nonspecific dispersion interactions between the adsorbent and the adsorbate are the dominant driving force for the adsorption of gases and vapors. Therefore, in the absence of molecular sieving effects, the entire carbon surface is "active" in the removal of gaseous or vapor-phase pollutants. It was seen in Sec. III that adsorption of inorganic solutes takes place predominantly on specific sites on the carbon surface, e.g., by ion exchange, and that very high concentrations of solute or surface functional groups are necessary for achieving high removal efficiencies. Here I show how the interplay of electrostatic and dispersion interactions governs the uptake of aromatic pollutants on activated carbons.

My interest in this topic was sparked by intriguing initial results for the adsorption of benzoate, oxalate, and fumarate anions on chemically modified (oxidized vs. nitrified) activated carbons [136]. For example, both oxidation (which reduces the pH_{PZC} of the carbon) and nitrifying (which raises the pH_{PZC}) were found to suppress the uptake of benzoic acid; this is contrary to the expectations based on electrostatic arguments alone. On the basis of these and other findings, my co-workers and I proposed the following mechanisms of adsorption [136,137]:

1. Adsorption of benzoate (aromatic) anions occurs primarily on the basal plane of carbon, and the electron-withdrawing effects of nitrogen and carboxyl functional groups suppress the π - π interaction of the basal planes with the adsorbate's aromatic rings.
2. Adsorption of aliphatic anions occurs also predominantly on the basal plane, and the same electron-withdrawing effects enhance its interaction with the carboxyl anions.

More recently, we studied in more detail the relative importance of dispersion and electrostatic adsorbate-adsorbent interactions as we examined the uptake of methylene blue and nitrophenol as well as that of benzoic, oxalic, and fumaric acids [137]. In agreement with our earlier findings, we concluded that while electrostatic interactions are important, dispersion interactions appear to be dominant in the adsorption of aromatic solutes. On the other hand, electrostatic repulsion appears to be much more important for the adsorption of aliphatic anions.

Further validation of these conclusions was achieved [138] by contrasting the behavior of three chemically different carbons in adsorbing two vastly different aromatic solutes; nitrobenzene is a very weak Lewis acid that possesses the elec-

Iron-withdrawing NO₂ group. whereas aniline is a predominantly cationic species at pH < 4.6 that also possesses the electron-donating NH₂ group. The chemical differences among the carbons were produced by incorporating O- or N-containing functional groups on the carbon surface. While the effects of the former on the adsorption of phenol and other aromatics are well documented (though not necessarily well understood) [37], the effects of the latter, as well as the interplay of (1) surface groups, (2) solution pH, and (3) effective charge on the carbon surface, had not received adequate attention in the literature.

Table 7 summarizes some of the physical and chemical characteristics of the samples used. Only samples exhibiting minor changes in physical surface properties (which can be tailored to meet widely varying demands regarding surface area and pore size distribution) and major changes in chemical surface properties were used in subsequent adsorption tests.

Figure 8 shows the behavior of as-received and modified carbons in adsorbing aniline under widely varying solution chemistry conditions. A significant effect of solution chemistry (pH) on the uptake is observed. The effect of surface chemistry depends in turn on pH. At pH 2 (pH < pH_{PZC}), when the surface charge is predominantly positive and anilinium cations are dominant in solution, carbon oxidation is seen to enhance aniline adsorption whereas nitriding is seen to suppress it (with respect to the as-received and devolatilized carbons). This is exactly what one would expect if electrostatic adsorbate–adsorbent interactions were more important than the dispersive interactions. In contrast to oxidation, which does not lead to the formation of positively charged sites on the carbon surface and shifts the pH_{PZC} to a value that is close to solution pH, nitriding obviously enhances the adsorbate–adsorbent repulsion. Note that this behavior of the cation-forming aniline is in contrast to that of the anion-forming benzoic acid as the adsorbate, for which the dispersive interactions were found to be dominant even in highly basic aqueous solutions (pH = 10) [137]. (This again confirms the lack of "symmetry" in the

TABLE 7 Characteristics of Carbons Used in Figs. 8 and 9

| Sample | C (wt%) | H (wt%) | N (wt%) | O (wt%) | $S_{N_2}^b$ (m ² /g) | V_{mi}^c (cm ³ /g) | pH _{IEP} | pH _{PZC} |
|----------------------------|------------|------------|------------|------------|------------------------------------|------------------------------------|-------------------|-------------------|
| As received ^a | 96.5 | 0.57 | 1.29 | 1.64 | 859 | 0.62 | 4.0 | 8.0 |
| Devolatilized ^d | 98.0 | 0.41 | 1.46 | 0.13 | 858 | 0.58 | 5.5 | 10 |
| Oxidized ^e | 82.9 | 1.30 | 1.60 | 14.2 | 807 | 0.55 | 1.5 | 2.6 |
| Nitrided ^f | 90.5 | 0.47 | 5.81 | 3.22 | 869 | 0.59 | 5.2 | 8.9 |

^aHydrodarco GCW (Norit Americas),

^bBET surface area.

^cMicropore volume obtained from the Dubinin–Radushkevich equation applied to the N₂ adsorption isotherm.

^dHeat treatment in inert atmosphere at 1223 K.

^eTreatment in conc. HNO₃ at 363 K for 6 h.

^fReaction with NH₃ at 873 K for 3 h.

Source: Ref. 138.

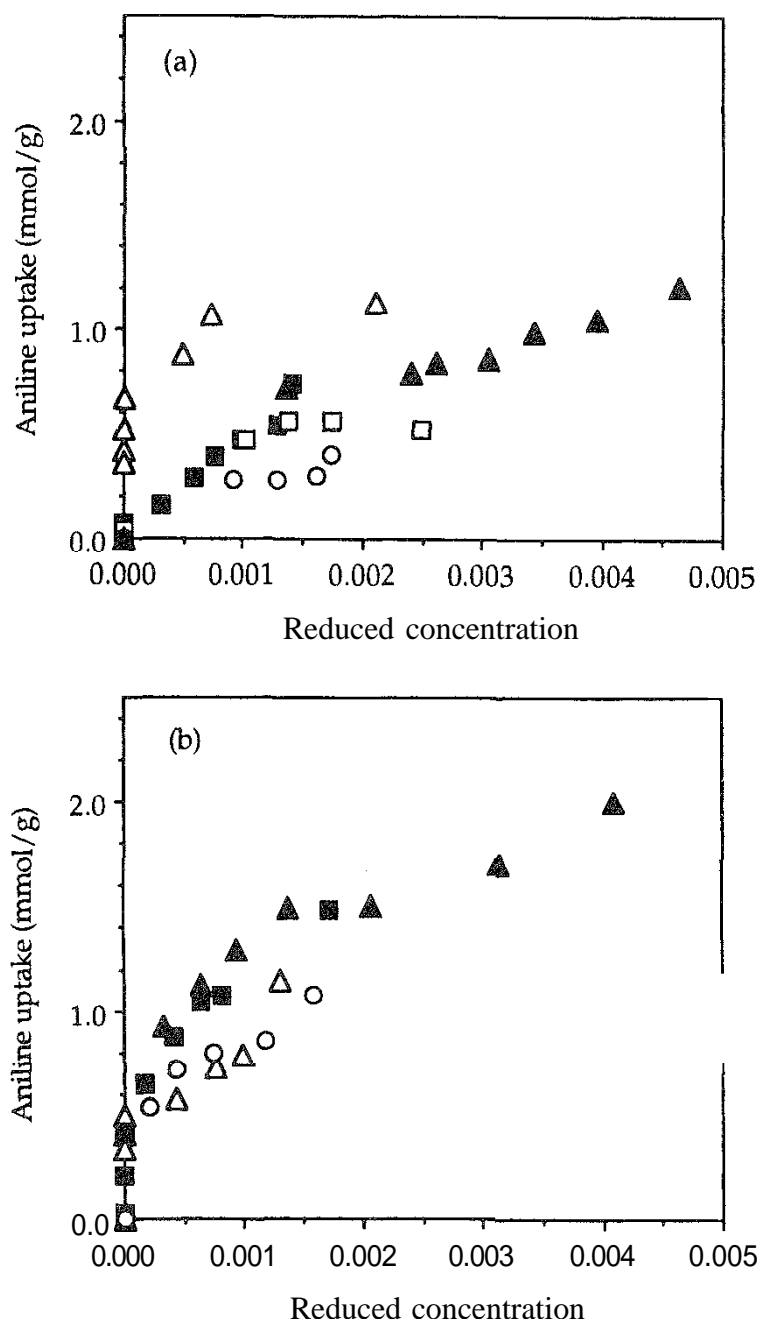


FIG. 8 Aniline adsorption isotherms at pH 2 (a) and pH 11 (b) for as-received and chemically modified Norit GCW carbons. (■, □) As-received; (○) nitrified; (△) oxidized; (▲) devolatilized.

adsorbate–adsorbent electrostatic attraction.) At the other extreme (pH 11, $\text{pH} > \text{pH}_{\text{PZC}}$), when the surface charge is predominantly negative and aniline molecules are dominant in solution, both oxidation and nitriding are detrimental. This suggests that dispersion forces control the adsorption process. In agreement with the behavior of benzoate anions [137], π – π interactions are not favored by the decrease in π -electron density on the graphene layers caused by π -electron localization and/or withdrawal due to the presence of oxygen-containing and some nitrogen-containing functional groups. At $\text{pH} \approx \text{pH}_{\text{PZC}}$ [138], aniline uptake is relatively

high on all adsorbents. This is consistent with the minimized electrostatic repulsion on the (overall) neutral surface. Closer inspection of the data also reveals the following trends as a function of pH: a monotonic increase for as-received, devolatilized, and nitrated carbons and a maximum (at $\text{pH} = \text{pH}_{\text{pzc}}$) for oxidized carbon. These results are discussed later in conjunction with those shown in Figs. 11 and 12.

Figure 9 shows the behavior of the same carbons in adsorbing nitrobenzene. In contrast to the findings for aniline, solution chemistry (pH) is seen to have little

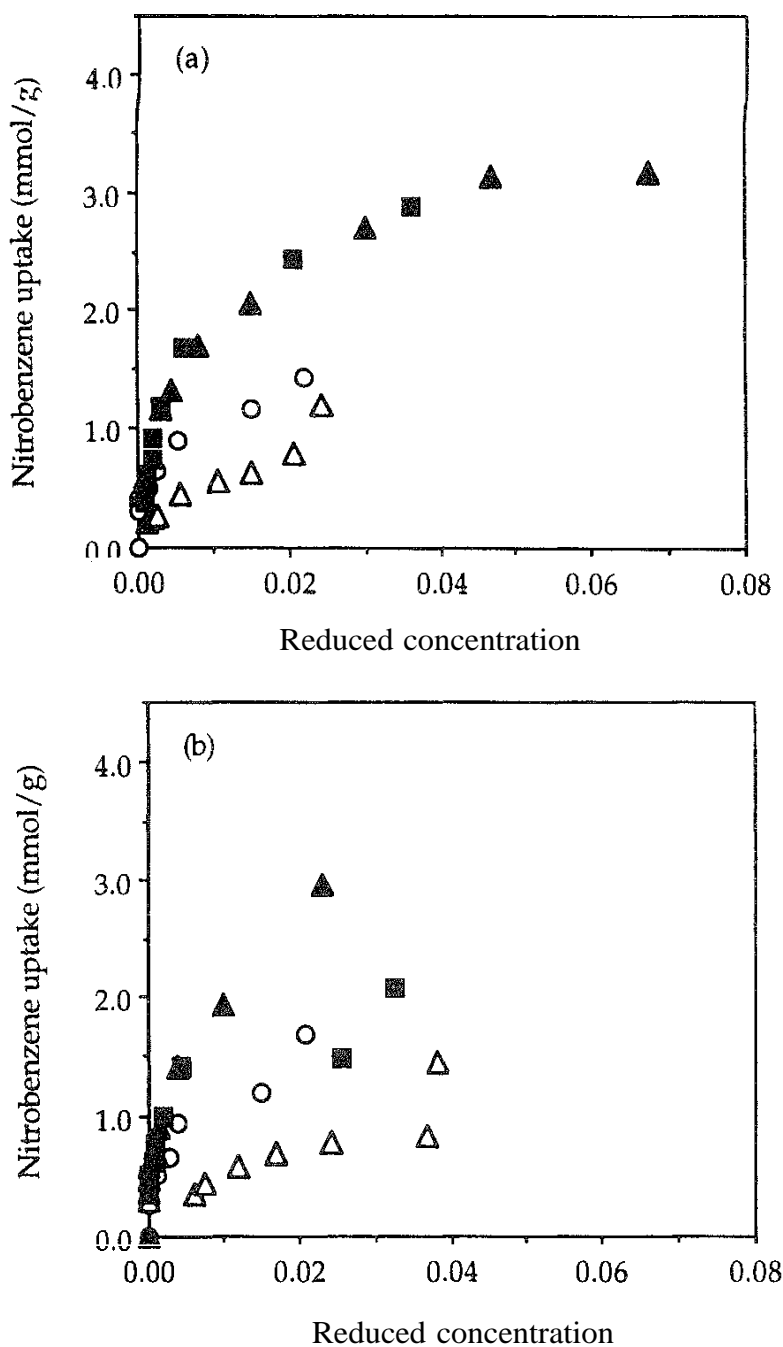


FIG. 9 Nitrobenzene adsorption isotherms at pH 2 (a) and pH 11 (b) for as-received and chemically modified Norit GCW carbons. (■) As-received; (○) nitrated; (△) oxidized; (▲) devolatilized.

effect on the equilibrium uptake. This is consistent with the fact that nitrobenzene is a very weak Lewis acid and molecular species are dominant in the entire pH range. The effect of surface chemistry is obviously much more important. The as-received and devolatilized carbons exhibit the highest uptake, while adsorption is suppressed for both nitrated and oxidized carbons. This behavior is consistent with that of aniline and benzoic acid at high pH ($\text{pH} > \text{pH}_{\text{PZC}}$). Dispersion forces are dominant once again; reduced adsorption is the consequence of withdrawal and/or localization of π electrons (i.e., decrease in π -electron density on the graphene layers) brought about by carbon oxidation and nitrating.

The importance of dispersive interactions is also apparent when the results shown in Fig. 8 are compared with those shown in Fig. 9. For example, aniline is much more soluble in water than nitrobenzene (35 vs. 2 g/L at 25°C), yet its uptake does not reflect this. A similar result was reported recently by Tamon and Okazaki [139]. In agreement with the foregoing arguments, this result can be attributed to the beneficial effect of the electron-donating NH_2 group. Enhanced adsorption of aniline is due to the resulting increase in the negative charge density on the graphene layers of the adsorbent.

C. Toward a Comprehensive Adsorption Model

There are several possible theoretical approaches to the formulation of a suitable model for the adsorption processes discussed above. The most fundamental one is based on the perturbation molecular orbital (PMO) theory of chemical reactivity [140,141] in which the wave functions of the products are approximated by using the wave functions of the reactants. A key issue in the use of Klopman's PMO theory is the relative importance of the two terms in the expression for the total energy change of the system, ΔE_{pert} , which is taken to be a good index of reactivity, ΔE_{react} [142,143]:

$$\Delta E_{\text{react}} \sim \Delta E_{\text{ch}} + \Delta E_{\text{orb}}$$

The question is whether the extent of adsorption is determined by charge control (ΔE_{ch} , i.e., Coulombic or electrostatic interactions) or by orbital control (ΔE_{orb} , i.e., attractive interactions between the filled orbitals of the adsorbate and the empty orbitals of the adsorbent).

In a recent interesting study, Tamon and coworkers [139,142,144] implicitly took the approach that orbital control is dominant. They analyzed the adsorption and desorption characteristics of a series of aromatic compounds at 308 K and uncontrolled pH. (They assume that "since the concentration of aromatic compounds is very low, pH seems to be almost equal to the value of distilled water" [139]. They do not mention, however, whether the presence of carbon modifies the pH of the suspension, as it often does.) They used the semiempirical MINDO/3 method to determine the HOMO energy levels (E_H) for these adsorbates and the LUMO levels (E_L) for several adsorbents (including chemically modified activated carbons). The range of calculated $|E_H - E_L|$ values for adsorbates ranging from p-nitrobenzoic acid to aniline on a commercial activated carbon was 6.7–9.0 eV. Low values (< 7.3 eV) coincided with those systems for which irreversible adsorption was found; those adsorbates that possess electron-donating groups (e.g., aniline), i.e.,

with the highest HOMO levels (or lowest ionization potentials), could not be desorbed easily (using distilled water at 308 K). In contrast, those aromatic species that possess electron-withdrawing groups (e.g., nitrobenzene) were more weakly (reversibly) adsorbed. These findings are in remarkable agreement with the conclusion [136,137,145] that when dispersion forces are dominant, the electron-withdrawing effects of nitrogen and carboxyl functional groups suppress the interaction of the basal planes with the adsorbate's aromatic rings. Based on these findings, Tamon et al. [142] proposed a two-state model to explain the appearance of irreversible adsorption of electron-donating compounds, according to which the barrier for going from the precursor (reversible) adsorption state to the irreversible state is higher for the electron-withdrawing aromatic compounds than for the electron-donating compounds. They do not provide a justification for this assumption; instead, they invoke the Hammond postulate according to which "the structure of the transition state will resemble the product more closely than the reactant for endothermic processes whereas the opposite is true for exothermic processes" [142]. How exactly this is related to the exothermic adsorption process is not clarified. A more straightforward alternative theory is offered below.

Functionalization of either the adsorbate or the adsorbent that increases the π -electron density leads to either enhanced or stronger adsorption when the adsorption process is governed by π - π (dispersion) interactions. The converse is also supported by available experimental evidence: Functionalization (of the carbon adsorbent or the aromatic adsorbate) that decreases the π -electron density leads to suppressed or weaker adsorption.

As shown in Secs. IV.A and IV.B, however, some adsorption systems involving aromatic adsorbates are very much influenced by electrostatic interactions. Additional examples are cited and discussed elsewhere [37]. Clearly, a model is needed that takes both electrostatic and dispersion interactions into account. Such a model has been presented by Müller and coworkers [106–108]. My coworkers and I [136,137,145] used this model to illustrate the possibly dramatic effects of modifications of carbon surface chemistry on equilibrium uptake of p-nitrophenol. We also extended it further to evaluate the relative importance of electrostatic and dispersive interactions [138,145].

The wide range of surface chemical properties of activated carbon adsorbents is illustrated schematically in Fig. 10. (The intriguing lack of "symmetry" between the low pH and high pH regions, observed for the vast majority of activated carbons has been mentioned earlier and will be addressed in more detail elsewhere.) The "acidic" (C1) and "basic" (C3) carbons, whose pH_{PZC} values are 3 and 10, respectively, can be easily designed to develop an electric charge on the order of $\sim 0.03 \text{ C/m}^2$, which corresponds typically to a surface potential of $\sim 150 \text{ mV}$. At the other extreme, high temperature treatment and stabilization in H_2 of an "acidic" carbon [49] or low-temperature treatment in the presence of hydrogen atoms [50,51] produces a "basic" carbon whose pH_{PZC} remains high and constant over extended periods of exposure to room temperature air, as illustrated in Figs. 5 and 6.

The key equation describing competitive Langmuirian adsorption on such amphoteric carbons in terms of fractional surface coverage θ of molecules (M) and ions (M^+ or M^-) of a partially dissociated organic solute on a homogeneous surface is

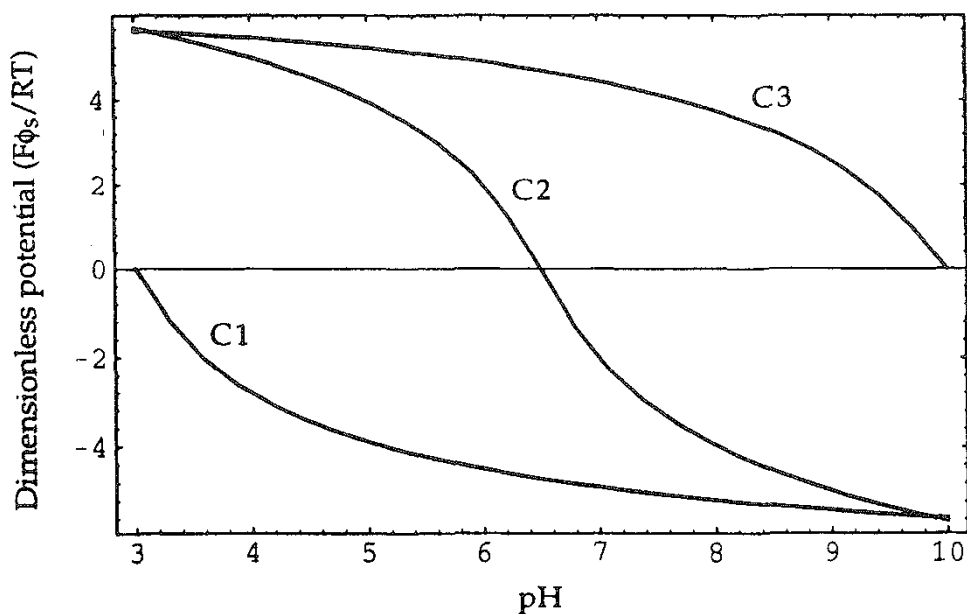


FIG. 10 Surface potential vs. pH for three (hypothetical) activated carbons: C1, "acidic" carbon ($\text{pH}_{\text{IEP}} = \text{pH}_{\text{PZC}} = 3.0$); C2, typical as-received (amphoteric) carbon ($\text{pH}_{\text{IEP}} = \text{pH}_{\text{PZC}} = 6.5$); C3, "basic" carbon ($\text{pH}_{\text{IEP}} = \text{pH}_{\text{PZC}} = 10.0$).

$$\theta = \theta_{\text{M}} + \theta_{\text{M}^{\pm}} = \frac{K[\text{M}] + K'[\text{M}^{\pm}]}{1 + K[\text{M}] + K'[\text{M}^{\pm}]}$$

In the above isotherm equation, K is the equilibrium constant for the molecules (due to London dispersion interactions), while K' is the equilibrium constant for the ions and has the form

$$K' = KK_q = K_0 \left[\exp\left(-\frac{U}{RT}\right) \right] \left[\exp\left(\frac{z_{\pm} F \phi_s}{RT}\right) \right]$$

In the above expression, which consists of two driving forces for adsorption, z_{\pm} is the valence of the charged species, F is the Faraday constant, ϕ_s is the interfacial electrical potential due to the development of surface charge, and U is the potential arising from the dispersive adsorbent–adsorbate interactions. Implicit in this expression is the realization that the co-ionic solute species (e.g., an anilinium cation interacting with the surfaces at $\text{pH} < \text{pH}_{\text{PZC}}$) can adsorb only if the (attractive) adsorption potential U is greater than the repelling electrostatic potential $z_{\pm} F \phi_s$. Explicit exclusion of co-ionic species from the surface is included in the model for a heterogeneous adsorbent surface, which conforms to the Freundlich isotherm:

$$\theta = \frac{C_{\alpha}}{C_1} \left(\frac{C_1}{C_1 + K} \right)^n$$

with

$$C_{\alpha} = [\text{M}] + \frac{\alpha[\text{M}^{\pm}]}{K_q} \quad \text{and} \quad C_1 = [\text{M}] + \frac{[\text{M}^{\pm}]}{K_q}$$

Here again it is assumed that the electrostatic potential is on the same order of magnitude as or lower than the dispersion potential, $(z_{\pm}F\phi_s)/RT \leq U/RT$.

The remarkable potential flexibility of activated carbon adsorbents is readily apparent from inspection of Figs. 10-12. As is intuitively obvious from simple electrostatic arguments, an "acidic" carbon is most appropriate for adsorbing the weakly basic aniline ($pK_a = 4.6$), especially at low pH, when a large fraction of the adsorbent surface is unavailable for adsorption of co-ionic species. These figures show the results of a parametric sensitivity study of the effects of modified dispersion potentials, as a consequence of the removal (Fig. 11) or incorporation (Fig. 12) of electron-withdrawing groups as well as the incorporation of electron-donating groups (Fig. 11) at the edges of graphene layers of an activated carbon.

Conversion of an "acidic" carbon (C1) to a "basic" carbon (C3-E) increases the point of zero charge from 3 to 10, and this is detrimental for the adsorption of anilinium cations at low pH; but it also enhances the π -electron density in the graphene layers and thus increases the dispersive potential, say, by a factor of 2 (C3-E-D x 2) to 10 (C3-E-D x 10). It is seen in Fig. 11 that the electrostatic effect is dominant in suppressing aniline uptake at low pH, but the dispersive effect both dampens the electrostatic effect at low pH and enhances the uptake at high pH.

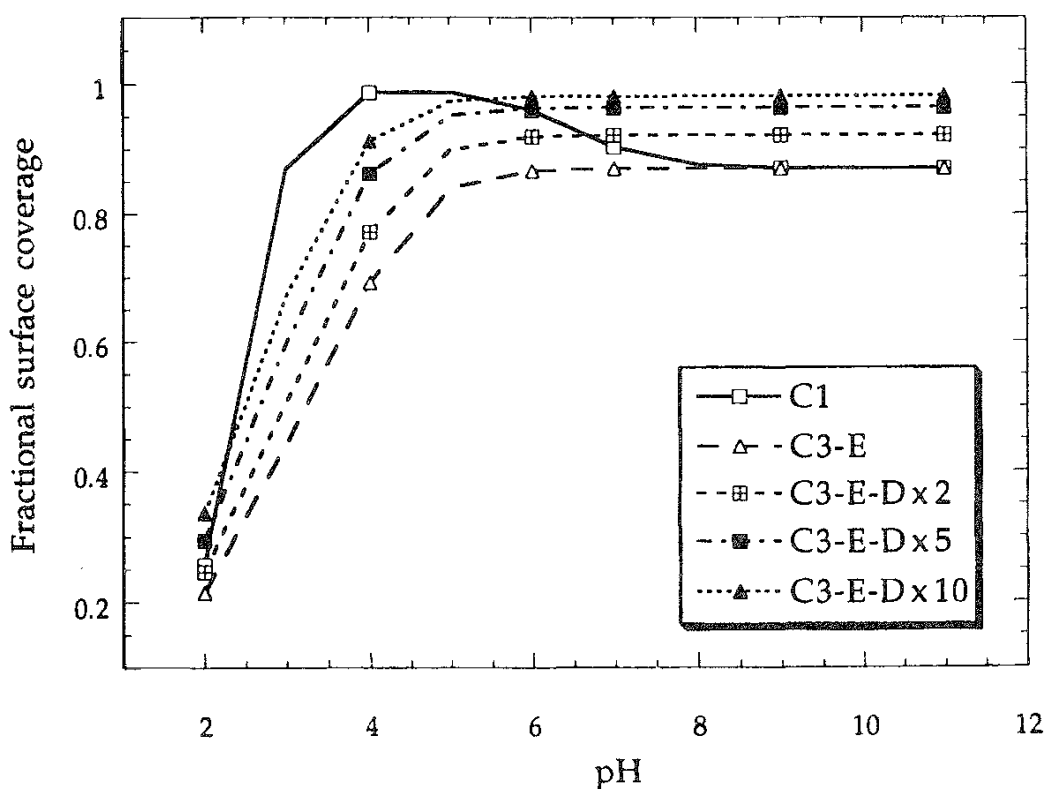


FIG. 11 Combined effects of electrostatic and dispersive interactions on changes in aniline uptake upon thermal treatment (e.g., in H_2 or NH_3) of an "acidic" carbon and its conversion to a "basic" carbon. C1, original "acidic" carbon; C3-E, "basic" carbon (only electrostatic interaction adjusted); C3-E-D x 2, "basic" carbon (dispersive attraction potential enhanced by a factor of 2); C3-E-D x 5, "basic" carbon (dispersive attraction potential enhanced by a factor of 5); C3-E-D x 10, "basic" carbon (dispersive attraction potential enhanced by a factor of 10).

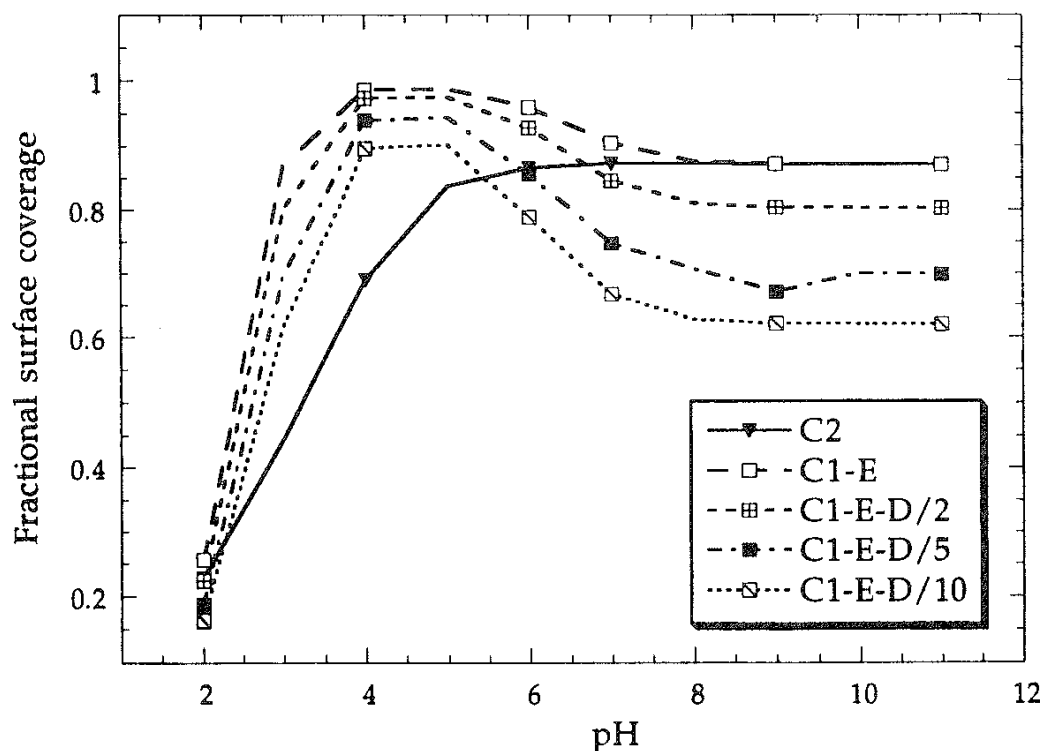


FIG. 12 Combined effects of electrostatic and dispersive interactions on changes in aniline uptake upon oxidation. C2, original (as-received) carbon; C1-E, oxidized carbon (only electrostatic interaction adjusted); C1-E-D/2, oxidized carbon (dispersive attraction potential reduced by a factor of 2); C1-E-D/5, oxidized carbon (dispersive attraction potential reduced by a factor of 5); C1-E-D/10, oxidized carbon (dispersive attraction potential reduced by a factor of 10).

Conversion of an amphoteric carbon (C2) to an "acidic" carbon (C1-E) decreases the pH_{PZC} from 6.5 to 3.0, and this is beneficial for the adsorption of anilinium cations at low pH; but it also reduces the π -electron density in the graphene layers and thus decreases the dispersive potential, say, by a factor of 2 (C1-E-D/2) to a factor of 10 (C1-E-D/10). The net result is shown in Fig. 12: enhanced adsorption at low pH, made less pronounced by the detrimental dispersive effect, and suppressed adsorption at high pH.

V. SUMMARY AND CONCLUSIONS

In contrast to the optimization of physical surface properties of activated carbons — where we know what is needed for a particular adsorption or water treatment task (an adequate surface area and a specific pore size distribution) and we also know how to achieve it — very few guidelines were available for the optimization of the chemical surface properties. Much progress has been made in our understanding of the surface chemistry of carbons and in developing techniques for modifying it for catalyst support applications. So, in using carbons for water treatment we have long known how to modify their surface chemistry, but only recently have we learned what kind of surface chemistry we need for a specific

task. Not unexpectedly, we have also realized that compromises need to be made to meet the sometimes conflicting demands imposed by electrostatic or dispersion forces.

In the adsorption of inorganic solutes, the main fundamental challenge remains how to "activate" the entire surface to achieve maximum removal efficiencies. In the adsorption of organic solutes, the influence of carbon surface chemistry is decidedly more complex. Both electrostatic and dispersive interactions can influence or control the equilibrium uptake of a weak aromatic electrolyte.

Typical modifications of carbon surface chemistry affect the extent of both electrostatic and dispersive interactions. For example, carbon oxidation not only lowers its point of zero charge; it also reduces the dispersive adsorption potential by decreasing the π -electron density in the graphene layers. And conversely, the removal of electron-withdrawing oxygen functional groups not only increases the point of zero charge, it also increases the dispersive adsorption potential by increasing the π -electron density.

A relatively simple theoretical model that accounts for both electrostatic and dispersive interactions successfully describes the qualitative trends observed in this study. In the particular case of aniline (a weak electrolyte), both theory and experiments indicate that maximum adsorption uptake is attained on oxidized carbon surfaces at a solution pH near the adsorbate's pH_{PZC} . Accordingly, aniline adsorption is deemed to involve two parallel mechanisms: (1) electrostatic interactions between anilinium cations and negatively charged carbon surface groups and (2) dispersive interactions between aniline molecules and graphene layers. On the other hand, for nondissociating nitrobenzene, maximum adsorption uptake is found on heat-treated carbon surfaces, particularly at a solution $\text{pH} \sim \text{pH}_{\text{PZC}}$. Therefore, adsorption results primarily from dispersive interactions between nitrobenzene molecules and graphene layers. Dispersive interactions in general are promoted by conducting the experiments at solution pH values near the adsorbate's pH_{PZC} , at which the repulsive interactions between charged surface groups and uncharged molecules are effectively minimized. The theoretical model invoked to account for all the above trends can in principle be used as a much needed predictor of the adsorbent and solution characteristics that will act in concert to maximize the adsorption uptake of aromatic compounds by activated carbons.

It is expected that similar considerations of both electrostatic and dispersive forces will be necessary for developing more reliable interaction potentials in the case of the adsorption of gases and vapors on chemically heterogeneous activated carbon surfaces.

ACKNOWLEDGMENTS

The collaboration of my colleagues, Joshua Ume, Isabel Santos-Silva, J. Angel Menendez, and Jonathan Phillips, as well as stimulating discussions with Carlos Moreno-Castilla and Jose Rivera-Utrilla (University of Granada, Spain) are gratefully acknowledged. Financial support was provided by the U.S. Department of Energy (DE-FG22-95PC95225) and the Carbon Research Center at Penn State University.

REFERENCES

1. J. van Driel, in *Fundamentals of Adsorption* (A. I. Liapis, ed.), AIChE, New York, 1986, p. 589.
2. J. L. Humphrey and G. E. Keller II, *Separation Process Technology*, McGraw-Hill, New York, 1997.
3. A. A. Attia, *Adsorp. Sci. Technol.*, 15:707 (1997).
4. C. A. Leon y Leon and L. R. Radovic, in *Chemistry and Physics of Carbon*, Vol. 24 (P. A. Thrower, ed.), Marcel Dekker, New York, 1994, p. 213.
5. H. P. Boehm, *Carbon* 32:759 (1994).
6. J. Jagiello, T. J. Bandosz and J. A. Schwarz, *J. Colloid Interface Sci.* 151:433 (1992).
7. T. J. Bandosz, J. Jagiello, and J. A. Schwarz, *Langmuir* 9:2518 (1993).
8. J. Jagiello, T. J. Bandosz, and J. A. Schwarz, *Carbon* 32:1026 (1994).
9. A. M. James, in *Surface and Colloid Science* (R. J. Good and R. R. Stromberg, eds.), Plenum, New York, 1979, p. 121.
10. V. A. Garten and D. E. Weiss, *Rev. Pure Appl. Chem.* 7:69 (1957).
11. C. P. Huang and F. B. Ostovic, *J. Environ. Eng.* 104:863 (1978).
12. C. P. Huang and E. H. Smith, in *Chemistry in Water Reuse* (W. J. Cooper, ed.), Ann Arbor Science, Ann Arbor, MI, 1981, p. 355.
13. M. M. Jevtitch and D. Bhattacharyya, *Chem Eng. Commun.* 23:191 (1983).
14. C. P. Huang and P. L. K. Fu, *J. Wat. Pollut. Contr. Fed. (WPCF)* 56:233 (1984).
15. R. Dobrowolski, M. Jaroniec, and M. Kosmulski, *Carbon* 24:15 (1986).
16. C. P. Huang and L. M. Vane, *J. Wat. Pollut. Contr. Fed. (WPCF)* 61:1596 (1989).
17. G. M. K. Abotsi and A. W. Scaroni, *Carbon* 28:79 (1990).
18. J. M. Solar, C. A. Leon y Leon, K. Osseo-Asare, and L. R. Radovic, *Carbon* 28:369 (1990).
19. M. V. Lopez-Ramon, C. Moreno-Castilla, J. Rivera-Utrilla, and R. Hidalgo-Alvarez, *Carbon* 31:815 (1993).
20. J. A. Menendez, M. J. Illán-Gómez, C. A. Leon y Leon, and L. R. Radovic, *Carbon* 33:1655 (1995).
21. B. M. Babic, S. K. Milonjic, M. J. Polovina, and B. V. Kaludjerovic, *Carbon* 1998, in press.
22. A. B. Garcia, A. Cuesta, M. A. Montés-Morán, A. Martinez-Alonso, and J. M. D. Tascon, *J. Colloid Interface Sci.* 192:363 (1997).
23. V. L. Frampton and R. A. Gortner, *J. Phys. Chem.* 41:567 (1937).
24. S. Kratochvil and E. Matijevic, *Colloids Surf.* 5:179 (1982).
25. D. W. Fuerstenau, *Pure Appl. Chem.* 24:135 (1970).
26. J. P. Brunelle, *Pure Appl. Chem.* 50:1211 (1978).
27. M. Schultz, S. Grimm, and W. Burckhardt, *Solid State Ionics* 63–65:18 (1993).
28. V. L. Snoeyink and W. J. Weber, Jr., in *Progress in Surface and Membrane Science*, Vol. 5 (J. F. Danielli, M. D. Rosenberg, and D. A. Cadenhead, eds.), Academic, New York, 1972, p. 63.
29. R. O. James and G. A. Parks, in *Surface and Colloid Science*, Vol. 12 (E. Matijevic, ed.), Plenum, New York, 1982, p. 119.
30. J. A. Mieth, J. A. Schwarz, Y.-J. Huang, and S. C. Fung, *J. Catal.* 122:202 (1990).

- 31 K. C. Akratopulu, C. Kordulis, and A. Lycourghiotis, *J. Chem. Soc. Faraday Trans.* 86:3437 (1990).
- 32 S. Zalac and N. Kallay, *J. Colloid Interface Sci.* 149:233 (1992).
- 33 P. Jayaweera, S. Hettiarachchi, and H. Ocken, *Colloids Surf. A* 85:19 (1994).
- 34 J. Lyklema, *Fundamentals of Interface and Colloid Science*, Vol. II, *Solid-Liquid Interfaces*, Academic, London, 1995.
- 35 C. A. Leon y Leon, J. M. Solar, V. Calemme, and L. R. Radovic, *Carbon* 30:797 (1992).
- 36 S. Dixon, E. H. Cho, and C. H. Pitt, *AIChE Symp. Ser.* 74(173): 75 (1978).
- 37 L. R. Radovic, C. Moreno-Castilla, and J. Rivera-Utrilla, *Chem. Phys. Carbon* 27 (1998). in preparation.
- 38 A. C. Lau, D. N. Furlong, T. W. Healy, and F. Grieser, *Colloids Surf.* 18:93 (1986).
- 39 T. J. Fabish and D. E. Schleifer, *Carbon* 22:19 (1984).
- 40 E. Papirer, S. Li, and J.-B. Donnet, *Carbon* 25:243 (1987).
- 41 C. A. Hunter and J. K. M. Sanders, *J. Am. Chem. Soc.* 112:5525 (1990).
- 42 C. A. Hunter, J. Singh, and J. M. Thornton, *J. Mol. Biol.* 218:837 (1991).
- 43 C. A. Hunter, X.-Y. Lu, G. M. Kapteijn, and G. van Koten, *J. Chem. Soc. Faraday Trans* 91:2009 (1995).
- 44 C. Chipot, R. Jaffe, B. Maigret, D. A. Pearlman, and P. A. Kollman. *J. Am. Chem. Soc.* 118:11217 (1996).
- 45 R. D. Topsom, *Prog. Phys. Org. Chem.* 12:1 (1976).
- 46 E. Grunwald, *CHEMTECH* 1984:698.
- 47 R. W. Taft and R. D. Topsom, *Prog. Phys. Org. Chem.* 16:1 (1987).
- 48 H. Tamon, K. Aburai, M. Abe, and M. Okazaki, *J. Chem. Eng. Jpn.* 28:823 (1995).
- 49 J. A. Menéndez, J. Phillips, B. Xia and L. R. Radovic. *Langmuir* 12:4404 (1996).
- 50 J. A. Menendez, L. R., Radovic, B. Xia, and J. Phillips, *J. Phys. Chem.* 100:17243 (1996).
- 51 J. A. Menendez, B. Xia, J. Phillips, and L. R. Radovic, *Langmuir* 13:3414 (1997).
- 52 J. L. Brédas and G. B. Street, *J. Chem. Phys.* 90:7291 (1989).
- 53 S. Suzuki, P. G. Green, R. E. Bumgarner, S. Dasgupta, W. A. Goddard III, and G. A. Blake. *Science* 257:942 (1992).
- 54 D. A. Dougherty. *Science* 271:163 (1996).
- 55 M. A. Montes-Morán, J. A. Menendez, E. Fuente, and D. Suarez, *J. Phys. Chem. B* (1998), in press,
- 56 J. Padin and R. T. Yang, *Ind. Eng. Chem. Res.* 36:4224 (1997).
- 57 V. L. Snoeyink and D. Jenkins, *Water Chemistry*, Wiley, New York, 1980.
- 58 P. L. Walker, Jr. and J. Janov, *J. Colloid Interface Sci.* 28:449 (1968).
- 59 Y. Kaneko, K. Ohbu, N. Uekawa, K. Fujie, and K. Kaneko, *Langmuir* 11:708 (1995).
- 60 E. A. Müller, L. F. Rull, L. F. Vega, and K. E. Gubbins, *J. Phys. Chem.* 100:1189 (1996).
- 61 R. W. Farmer, B. W. Dussert, and S. L. Kovacic, *Am. Chem. Soc. Div. Fuel Chem. Prepr.* 41(1):456 (1996).
- 62 R. A. Greinke and R. I. Bretz, U.S. Patent 5,582,811 to UCAR Carbon Technology Corp. (Dec. 10, 1996).

63. M. J. Humenick, Jr. and J. L. Schnoor. *J. Environ. Eng.* 100:1249 (1974).
64. R. J. Davidson, *J. S. Afr. Inst. Min. Metall.* 1974:67.
65. L. R. Radovic and F. Rodriguez-Reinoso, in *Chemistry and Physics of Carbon*, Vol. 25 (P. A. Thrower, ed.), Marcel Dekker, New York, 1997, p. 243.
66. F. Carrasco-Marín, J. M. Solar, and L. R. Radovic. *International Carbon Conference ('Paris)*, 1990, p. 672.
67. M. A. Ferro-Garcia, J. Rivera-Utrilla, J. Rodriguez-Gordillo, and J. Bautista-Toledo, *Carbon* 26:363 (1988).
68. N. Petrov, T. Budinova, and I. Khavesov, *Carbon* 30:135 (1992).
69. T. Budinova, K. M. Gergova, N. V. Petrov, and V. N. Minkova, *J. Chem. Technol. Biotechnol.* 60:177 (1994).
70. M. Polovina, A. Surbek. M. Lausevic. and B. Kaludjerovic, *J. Serb. Chem. Soc.* 60:43 (1995).
71. G. G. Jayson, J. A. Sangster, G. Thompson, and M. C. Wilkinson, *Carbon* 25:523 (1987).
72. C. F. Baes, Jr. and R. E. Mesmer, *The Hydrolysis of Cations*, Wiley, New York, 1976.
73. D. Bhattacharyya and C. Y. R. Cheng, *Environ. Prog.* 6:110 (1987).
74. F. J. Hingston, in *Adsorption of Inorganics at Solid-Liquid Interfaces* (M. A. Anderson and A. J. Rubin, eds.), Ann Arbor Science. Ann Arbor, MI, 1981, p. 51.
75. G. J. McDougall and R. D. Hancock, *Gold Bull.* 14:138 (1981).
76. C. Klauber, *Langmuir* 7:2153 (1991).
77. D. Graham, *J. Phys. Chem.* 59:896 (1955).
78. D. G. Duff, S. M. C. Ross, and D. H. Vaughan, *J. Chem. Educ.* 65:815 (1988).
79. J. H. Potgieter, *J. Chem. Educ.* 68:349 (1991).
80. N. E. Krupa and F. S. Cannon. *J. Am. Water Works Assoc.* 1996:94.
81. J. S. Mattson and H. B. Mark, Jr., *Activated Carbon: Surface Chemistry and Adsorption from Solution*, Marcel Dekker. New York, 1971.
82. J. Lahaye and P. Ehrburger (eds.), *Fundamental Issues in Control of Carbon Gasification Reactivity*, Kluwer, Dordrecht. The Netherlands, 1991,
83. Roundtable Discussion, in *Activated Carbon Adsorption of Organics from the Aqueous Phase*, Vol. 1 (I. H. Suffet and M. J. McGuire, eds.), Ann Arbor Science, Ann Arbor, MI, 1980, p. 483.
84. J. N. Israelachvili, *Intermolecular and Surface Forces*, Academic. London, 1992.
85. D. F. Evans and H. Wennerström, *The Colloidal Domain: Where Physics, Chemistry, Biology and Technology Meet*, VCH. New York, 1994.
86. S. R. Deshiikan and K. D. Papadopoulos, *J. Colloid Interface Sci.* 174:302 (1995).
87. S. R. Deshiikan and K. D. Papadopoulos, *J. Colloid Interface Sci.* 174:313 (1995).
88. J. S. Mattson, H. B. Mark, Jr., M. D. Malbin, W. J. Weber, Jr., and J. C. Crittenden, *J. Colloid Interface Sci.* 31:116 (1969).
89. R. F. Vaccaro, *Environ. Sci. Technol.* 5:134 (1971).
90. J. S. Zogorski, S. D. Faust, and J. H. Haas, Jr., *J. Colloid Interface Sci.* 55:329 (1976).
91. R. G. Peel and A. Benedek, *Environ. Sci. Technol.* 14:66 (1980).
92. D. W. Fuerstenau and Pradip, *Colloids Surf.* 4:229 (1982).

93. B. R. Puri, in *Treatment of Water by Granular Activated Carbon* (M. J. McGuire and I. H. Suffet, eds.), American Chemical Society, Washington, DC, 1983, p. 77.
94. J. McGuire, C. F. Dwiggin, and P. S. Fedkiw, *J. Appl. Electrochem.* 15:53 (1985).
95. T. M. Grant and C. J. King, *Ind. Eng. Chem. Res.* 29:264 (1990).
96. R. D. Vidic, M. T. Suidan, and R. C. Brenner, *Environ. Sci. Technol.* 27:2079 (1993).
97. M. R. Rosene and M. Manes, *J. Phys. Chem.* 81:1651 (1977).
98. G. Nakhla, N. Abuzaid, and S. Farooq, *Water Environ. Res.* 66:842 (1994).
99. N. S. Abuzaid and G. F. Nakhla, *J. Hazard. Mater.* 49:217 (1996).
100. D. O. Cooney and Z. Xi, *AIChE J.* 40:361 (1994).
101. K.-S. Ha, H. Hinago, A. Sakoda, and M. Suzuki, in *Fundamentals of Adsorption* (M. Suzuki, ed.), Kodansha, Tokyo, 1993, p. 251.
102. S. Longchamp, H. N. Randriamahazaka, and J.-M. Nigretto, *J. Colloid Interface Sci.* 166:444 (1994).
103. T. R. Dargaville, F. N. Guerzoni, M. G. Looney, and D. H. Solomon, *J. Colloid Interface Sci.* 182:17 (1996).
104. J. W. Hassles. *Active Carbon*, Chemical Publishing Co., Brooklyn, NY, 1951.
105. J. W. Hassles, *Activated Carbon*, Chemical Publishing Co., New York, 1963.
106. G. Muller, C. J. Radke, and J. M. Prausnitz, *J. Phys. Chem.* 84:369 (1980).
107. G. Muller, C. J. Radke, and J. M. Prausnitz, *J. Colloid Interface Sci.* 103:466 (1985).
108. G. Muller, C. J. Radke, and J. M. Prausnitz, *J. Colloid Interface Sci.* 103:484 (1985).
109. R. W. Coughlin and F. S. Ezra, *Environ. Sci. Technol.* 2:291 (1968).
110. R. W. Coughlin, F. S. Ezra, and R. N. Tan, *J. Colloid Interface Sci.* 28:386 (1968).
111. R. W. Coughlin and R. N. Tan, in *Water-1968*, AIChE, New York, 1968, p. 207.
112. V. L. Snoeyink, and W. J. Weber, Jr., *Environ. Sci. Technol.* 1:228 (1967).
113. V. L. Snoeyink, W. J. Weber, Jr., and H. B. Mark, Jr., *Environ. Sci. Technol.* 3:918 (1969).
114. F. W. Getzen and T. M. Ward, *J. Colloid Interface Sci.* 31:441 (1969).
115. T. M. Ward and F. W. Getzen, *Environ. Sci. Technol.* 4:64 (1970).
116. K. Urano, M. Sonai, R. Nakayama, and Y. Kobayashi, *Nippon Kagaku Kaishi* 1976:1773.
117. K. Urano, Y. Koichi, and Y. Nakazawa, *J. Colloid Interface Sci.* 81:477 (1981).
118. K. Urano, Y. Koichi, and E. Yamamoto, *J. Colloid Interface Sci.* 86:43 (1982).
119. K. Urano and H. Kano, *Bull. Chem. Soc. Jpn.* 57:2051 (1984).
120. K. Urano, H. Kano, and T. Tabata, *Bull. Chem. Soc. Jpn.* 57:2307 (1984).
121. R. C. Bansal, J.-B. Donnet, and F. Stoeckli, *Active Carbon*, Marcel Dekker, New York, 1988.
122. K. Kinoshita, *Carbon: Electrochemical and Physicochemical Properties*, Wiley-Interscience, New York, 1988.
123. M. Mazet, A. Yaacoubi, and P. Lafrance, *Water Res.* 22:1321 (1988).
124. P. Lafrance and M. Mazet, *J. Am. Water Works Assoc.* 81:155 (1989).
125. M. Allali-Hassani, O. Dusart, and M. Mazet, *Water Res.* 24:699 (1990).
126. O. Dusart, H. Bouabane, and M. Mazet, *J. Chim. Phys.*, 88:259 (1991).
127. M. Mazet, B. Farkhani, and M. Baudu, *Water Res.* 28:1609 (1994).
128. L. A. Tung, and C. J. King, *Ind. Eng. Chem. Res.* 33:3217 (1994).

129. J. E. Kilduff and C. J. King, *Ind. Eng. Chem. Res.* 36:1603 (1997).
130. O. P. Mahajan, C. Moreno-Castilla, and P. L. Walker, Jr., *Sep. Sci. Technol.* 15:1733 (1980).
131. G. Newcombe and M. Drikas, *Water Res.* 27:161 (1993).
132. G. Newcombe, R. Hayes, and M. Drikas, *Colloids Surf.* 78:65 (1993).
133. G. Morris and G. Newcombe, *J. Colloid Interface Sci.* 159:413 (1993).
134. G. Newcombe, *J. Colloid Interface Sci.* 164:452 (1994).
135. G. Newcombe and M. Drikas, *Carbon* 35:1239 (1997).
136. J. I. Ume, A. W. Scaroni, and L. R. Radovic, *21st Biennial Carbon Conference*, Buffalo, NY, 1993, p. 468.
137. L. R. Radovic, J. I. Ume, and A. W. Scaroni, in *Fundamentals of Adsorption* (M. D. Le Van, ed.), Kluwer Academic, Norwell, MA, 1996, p. 749.
138. L. R. Radovic, I. F. Silva, J. I. Ume, J. A. Menendez, C. A. Leon y Leon, and A. W. Scaroni, *Carbon* 35:1339 (1997).
139. H. Tamon and M. Okazaki, *J. Colloid Interface Sci.* 179:181 (1996).
140. G. Klopman, *J. Am. Chem. Soc.* 90:223 (1968).
141. W. B. Jensen, *The Lewis Acid-Base Concepts*, Wiley-Interscience. New York, 1980.
142. H. Tamon, M. Atsushi, and M. Okazaki, *J. Colloid Interface Sci.* 177:384 (1996).
143. Y. Jean and F. Volatron, *An Introduction to Molecular Orbitals*, Oxford Univ. Press, New York, 1993.
144. H. Tamon, M. Atsushi, and M. Okazaki, in *Fundamentals of Adsorption* (M.D. Le Van, ed.), Kluwer Academic, Norwell, MA. 1996, p. 961.
145. I. F. Silva, J. I. Ume, A. W. Scaroni, and L. R. Radovic, *ACS Prep. (Div. Fuel Chem.)* 41(1):461 (1996).
146. J. A. Yopps and D. W. Fuerstenau, *J. Colloid Sci.* 19:61 (1964).

21

Charge Regulation at the Surface of a Porous Solid

BORIS V. ZHMUD and LENNART BERGSTRÖM Institute for Surface Chemistry, Stockholm, Sweden

- I. Introduction
- II. Characterization of Porous Structure
 - A. Nitrogen adsorption
 - B. Mercury porosimetry
 - C. Limitations of the cylindrical pore model
 - D. Determination of surface charge density and surface potential
- III. Thermodynamic Background of Charge Regulation
- IV. Surface ionization
 - A. Protolytic properties of partly oxidized silicon nitride: Heuristic ideas
 - B. Distribution of surface potential and surface charge over pore sizes
 - C. Application of charge regulation model for determination of equilibrium constants of surface reactions
- References

I. INTRODUCTION

When two different phases containing some carriers of electricity, such as electrons or ions, are brought into contact with each other, charge separation occurs, leading to the formation of an electrical double layer [1]. This is a rather general contact phenomenon that occurs in a variety of systems, not necessarily involving a solid. Known examples are emulsions containing an ionogenic surface-active component, metal/vacuum, metal/solution, or dielectric/electrolytic solution systems. Indeed, the origin of the charge and the mechanism of charge transfer may be different,

but the driving force is always the same: a difference in the energy levels of the charge carriers in the different phases.

This chapter is concerned with the mechanisms of formation of the electrical double layer at a dielectric solid/electrolytic solution interface. When such a contact occurs, the solid's surface acquires a certain charge due to the dissociation of surface ionizable groups and adsorption of ions from solution. Since the whole system is assumed to be electroneutral, the solution has to bear an equal charge of opposite sign. This charge is effectively confined to a thin layer near the dividing surface, termed the diffuse double layer. Its thickness is characterized by the reciprocal Debye length,

$$\kappa = \left(\frac{2e^2 n_0}{\epsilon \epsilon_0 k T} \right)^{1/2} \quad (1)$$

where n_0 is the number density of uni-univalent background electrolyte ions, and other symbols have their conventional meaning.

For aqueous solutions, the diffuse double layer will have a decay length varying from a few up to a few thousand angstroms, depending on the concentration of the background electrolyte. However, taking into account that the Debye–Hückel theory fails for electrolyte concentrations higher than about 0.01 M and that it is difficult to maintain a constant ionic strength below about 0.0001 M for water-based colloidal systems—mainly because of some solubility of solids and autodissociation of soluble species—a much narrower range, from about 30 up to about 300 Å, appears to be of practical importance.

When the surface charge is formed, its sign and magnitude are governed by thermodynamic factors such as the affinity of adsorbed ions for the surface and their activity in the bulk solution and conservation laws, including the charge and mass balance, making the whole process self-regulated. This is, basically, where the term "charge regulation" comes from. Many facets of this phenomenon have already been studied in detail and summarized in several reviews [2–5]. Other aspects have remained untouched until recently. In particular, this concerns charge regulation at the surface of porous solids.

II. CHARACTERIZATION OF POROUS STRUCTURE

When talking about a "porous solid", it is usually meant that the pore system has a fixed geometry that is not affected by the surrounding environment. Although more alleged than proven and not thermodynamic at all, this assumption of absolute rigidity makes it possible to bring together results of porosimetric measurements normally performed with a dry solid with potentiometric and electrokinetic data that bring information about the surface charge and potential of the solid in contact with an aqueous electrolytic solution.

Compared to nonporous solids, charge regulation at the surface of porous solids reveals some new features if the mean pore size is (1) large enough to justify consideration of the surface charge, which is discrete by its very nature, as continuously smeared over the surface, but (2) small enough to ensure sufficient over-

lapping of diffuse double layers that extend from opposite walls of a pore. These requirements are met whenever the mean pore size happens to be much greater than the mean distance between surface ions, being at the same time comparable in magnitude with the Debye screening radius, $1/\kappa$. For dilute aqueous electrolytes, it is the mesoporous region of pore sizes (20–200 Å) that is of interest with respect to the charge regulation problem. Consequently, the following discussion is, for the most part, limited to systems of this type.

Since an analysis of the charge regulation problem is intimately related to certain parameters used to characterize the porous structure of solids, it is useful to start with an elementary description, outlining the most common experimental routines used for characterization of porous solids and elucidating the involved model assumptions and limitations. For more details on the subject, the reader is referred to special monographs, Refs. 6–8.

A. Nitrogen Adsorption

Gas adsorption is by far the most common technique used to gain information about the porous structure from the adsorption/desorption isotherms. As adsorbent, nitrogen is the most commonly used. The treatment of results here is based on a cylindrical pore model.

The adsorption isotherm is measured at 77 K, gradually increasing the nitrogen pressure, p , from zero up to the saturation pressure, p_0 . Indeed, the boundary points are excluded because of instrumental limitations. When the relative pressure p/p_0 exceeds a certain limit, capillary condensation commences, resulting in filling pores with liquid adsorbate. As p/p_0 continues to increase, larger and larger pores are filled, until all porous space is flooded at $p/p_0 \approx 1$. Then, by reversing the course of events, the desorption isotherm can be obtained.

Assuming that the surface is perfectly "wetted" by adsorbate, i.e., the contact angle is zero, the maximum pore radius, r_i , filled at the i th point of the isotherm, corresponding to the relative pressure p_i/p_0 , can be found from the Kelvin equation,

$$r_i = \frac{2\gamma V_L}{RT \ln(p_0/p_i)} \quad (2)$$

where $\gamma = 8.9 \text{ mN/m}$ is the surface tension and $V_L = 34.7 \text{ cm}^3/\text{mol}$ is the molar volume of liquid nitrogen, and other symbols have their standard meaning.

Take any two neighbouring points, the i th and $(i+1)$ th, on the adsorption isotherm. By the moment the first point is reached, all pores having radius less than or equal to r_i are filled. Accordingly, at the second point, all pores with radius less than or equal to r_{i+1} are filled. Hence, the volume of pores with radius between r_i and r_{i+1} is given by

$$\Delta v_i = (n_{i+1} - n_i) V_L \quad (3)$$

where n_i stands for the mole amount of nitrogen (per unit mass of solid) adsorbed at relative pressure p_i/p_0 .

Next, from Eq. (2) it follows that

$$\begin{aligned}\Delta r_i = r_{i+1} - r_i &= \frac{2\gamma V_L}{RT} \left(\frac{1}{\ln(p_0/p_{i+1})} - \frac{1}{\ln(p_0/p_i)} \right) \\ &\cong \frac{2\gamma V_L}{RT} \left(\frac{\Delta p_i}{p_i \ln^2(p_0/p_i)} \right)\end{aligned}\quad (4)$$

Plotting $\Delta v_i/\Delta r_i$ vs. r_i yields the so-called differential pore size distribution, probably the most widely used characteristic of a porous solid.

In a more rigorous treatment, a correction should be made to account for the finite thickness of a multilayer molecular film preadsorbed on the pore walls prior to the capillary condensation. Most modern instruments automatically execute all these routines.

The same data can be used for an evaluation of the specific surface area. On noting that the internal surface area of cylindrical pores with radius in the range r_i to $r_i + \Delta r_i$ is

$$As_i = 2\Delta v_i/r_i \quad (5)$$

and substituting expressions (2) and (3) for r_i and Δv_i , respectively, the well-known Kiselev formula for the specific surface area, S_{sp} , follows at once:

$$S_{sp} = \sum_i \Delta s_i = \frac{RT}{\gamma} \sum_i \ln \frac{p_0}{p_i} \Delta n_i \quad (6)$$

which more commonly is expressed in an integral form, useful if the experimental points are interpolated by a continuous function.

B. Mercury Porosimetry

Mercury porosimetry makes use of the fact that the pressure, p_i , required to intrude liquid mercury into a cylindrical pore with nonwetttable walls is inversely proportional to the radius, r_i , of the pore. This is a direct consequence of the Young–Laplace equation,

$$p_i = \frac{2\gamma \cos(180 - \theta)}{r_i} \quad (7)$$

where θ is the contact angle of mercury with solids, normally taken to be 130 – 140° , and $\gamma = 480 \text{ mN/m}$ is the surface tension of mercury. Here, the interpretation of results is also based on the cylindrical pore model.

By measuring the volume, v_i , of mercury intruded into pores under pressure p_i , the differential pore size distribution, $\Delta v_i/\Delta r_i$ vs. r_i , can be arrived at by noting that

$$\Delta r_i = 2\gamma \cos \theta \left(\frac{1}{p_i} - \frac{1}{p_{i+1}} \right) \cong \frac{2\gamma \cos \theta \Delta p_i}{p_i^2} \quad (8)$$

and expressing r_i from Eq. (7). Further processing of data follows essentially in the same ways as in the case of nitrogen capillary condensation described in the previous section.

It is worth noting that in mercury porosimetric measurements, the finest pores are accessed the last at the highest pressure allowed by instrument design, whereas in nitrogen adsorption measurements they are accessed first, as soon as the capillary condensation commences. As a result, the accuracy of nitrogen adsorption data progressively deteriorates with increasing pore size, basically because of the destructive effect of small pressure fluctuations while approaching the saturation limit, whereas the accuracy of mercury porosimetric data has the opposite tendency. For this reason, mercury porosimetry is deemed to be a useful complementary tool for scanning the upper part of the mesoporous region of pore sizes.

C. Limitations of the Cylindrical Pore Model

Like any idealized model, the cylindrical pore model has many limitations, knowledge of which is essential for proper interpretation of experimental data. In particular, the following should be kept in mind:

1. Except when cylinders are plugged at one end, the model fails to explain the existence of hysteresis between the adsorption and desorption branches of isotherm. The pore size distributions calculated from these two branches may differ considerably. A typical example is given in [Fig. 1](#). The desorption branch always gives a more narrow distribution shifted to the fine-pore region, which is, in general, in better agreement with that calculated from mercury intrusion data. At the same time, unless different pores are isolated, the desorption isotherm may be influenced by some network effects, such as pore blocking, which do not affect the adsorption branch.
2. The actual pore size may be underestimated at the lower end of the mesoporous region because of some decrease in surface tension of capillary liquid with increasing curvature of its meniscus.
3. In gas adsorption measurements, there is a critical lower value of relative pressure, e.g., $p/p_0 \approx 0.4$ for nitrogen, below which capillary condensate cannot exist as a separate phase, no matter whether the pore system extends to finer pores or not; this is a consequence of the existence of so-called tensile strength limit [6]. As a result of this, a very narrow false maximum may appear on the differential pore size distribution at its fine-pore end, typically between 17 and 20 Å in the case of nitrogen.

Last, it should be realized that although it is not impossible to build up a crystalline structure with a close to ideal geometry of the porous space—a computer-generated example can be seen in [Fig. 2](#)—it is rather unlikely to find something like that in existing porous materials. In most cases, including precipitated silica gels and related metal oxide systems, a porous solid is represented by an agglomerate of primary particles, of micrometer size or less, rigidly joined together—by fusion, by sintering, by application of pressure, or otherwise. A molecular model of such an agglomerate produced by irreversible random coagulation of a few primary spherical particles, each one having the structure of high cristobalite, is shown in [Fig. 3](#). The voids between the particles form a pore system.

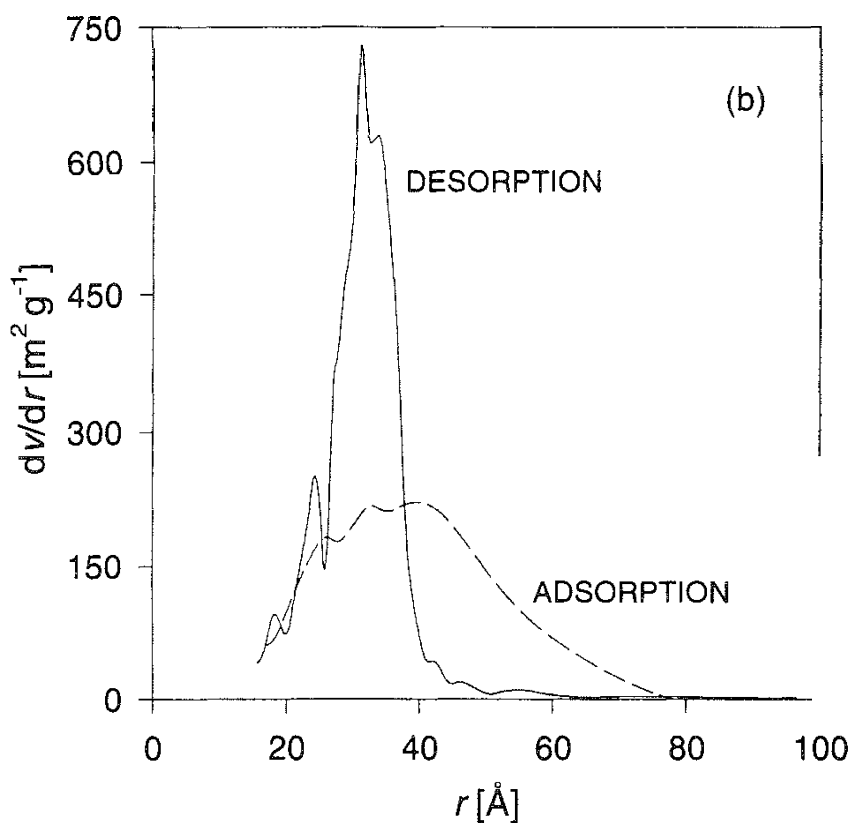
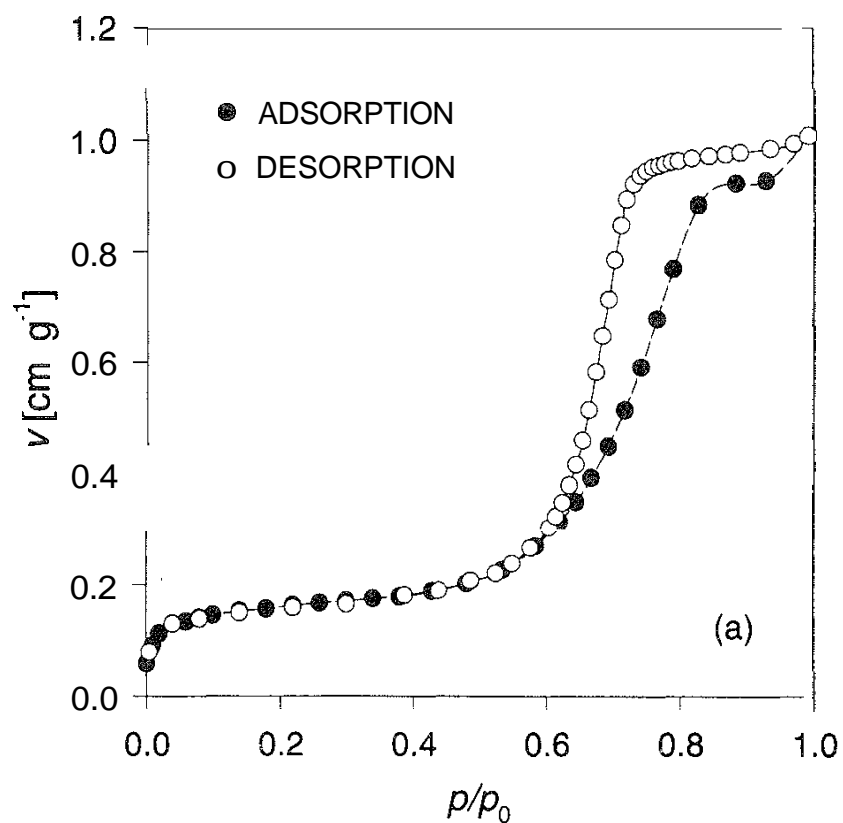


FIG. 1 (a) Adsorption (●) and desorption (○) isotherms of nitrogen at the surface of mesoporous silical gel with the specific surface area $436 \text{ m}^2/\text{g}$ and specific pore volume $0.801 \text{ cm}^3/\text{g}$. Experimental points are continuously interpolated by cubic splines. (b) Differential pore size distributions obtained from the adsorption (---) and desorption (—) branches.

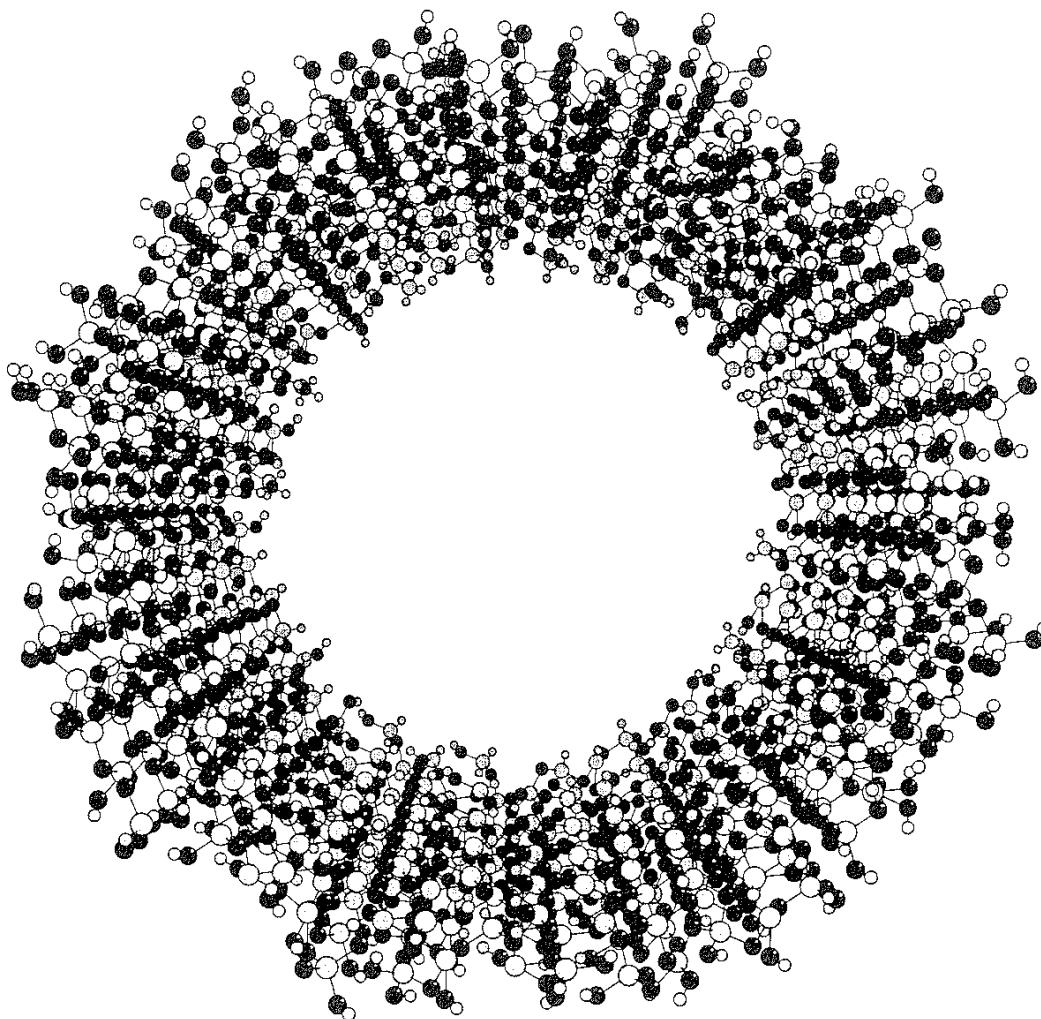


FIG. 2 Hypothetical silicon oxide structure (molecular formula $\text{Si}_{660}\text{O}_{1521}\text{H}_{756}$) shaped in the form of an empty cylinder with internal radius 16Å and external radius 23 Å. Constituent Si and O atoms are situated in the lattice of β -cristobalite, and the remaining atomic valences are filled with hydrogen atoms to simulate a hydroxylated surface.

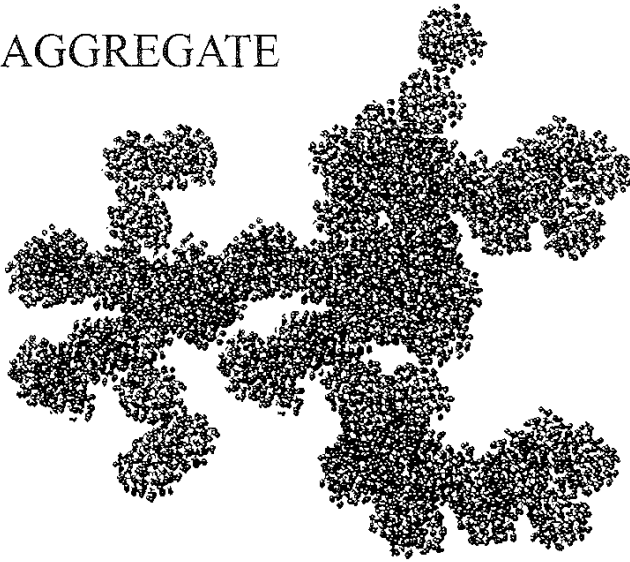
D. Determination of Surface Charge Density and Surface Potential

Neither the surface charge density nor the surface potential at the solid/liquid interface can be measured directly. They are to be retrieved from pH potentiometric or electrokinetic data on the basis of certain theoretical concepts and models.

1. pH Potentiometric Titration of Reactive Surface Groups

The most straightforward and widely applied routine for quantification of reactive surface groups possessing either basic or acidic properties and thus capable of binding or elimination of protons or hydroxyl ions is probably pH potentiometric titration. If it is known that there are no ions other than protons (hydroxyl ions) that can react with the surface to any appreciable extent—a rather exceptional situation, as will be shown later—the number, n_R , of reacted surface groups per

AGGREGATE



GLOBULA

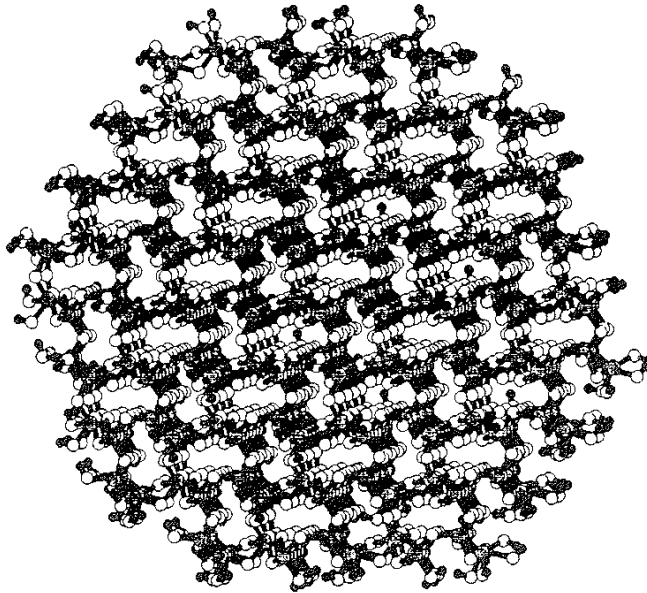


FIG. 3 Aggregated structure of silica gel composed of 84 spherical globulas $\text{Si}_{705}\text{O}_{1560}\text{H}_{300}$, each having a radius of 42 Å and the structure of β -cristobalite.

unit area of the surface is equal to the numbr of protons (hydroxyl ions) bonded or released at that area [9]:

$$n_R = \frac{N_A V}{m S_{\text{sp}}} \left[[\text{H}^+]_0 - [\text{H}^+]_{\text{eq}} - K_W \left(\frac{1}{[\text{H}^+]_0} - \frac{1}{[\text{H}^+]_{\text{eq}}} \right) \right] \quad (9)$$

where N_A is the Avogadro number, V the volume of the solution, m the mass of the dispersed solid, K_W the water dissociation constant, $[\text{H}^+]_0$ the initial concentration of protons determined by the amount of titrant added, and $[\text{H}^+]_{\text{eq}}$ the equilibrium concentration due for measurement. For insoluble solids in the absence of concurrent ion adsorption, n_R can be identified as the number of elementary charges, e , per unit surface area: that is, en_R can be treated as the surface charge density.

As follows from the above definition, n_R can be either positive or negative. As water is normally present in abundance, the negative adsorption of protons is thermodynamically equivalent to their desorption or to the adsorption of hydroxyl ions.

2. Electrokinetic Measurements

In principle, both the potential and charge density at the surface of a porous solid can be calculated from electrokinetic data such as the electro-osmotic transfer rate or the conductivity of a porous plug. Interpretation of this type of experimental data is based on the solution of the so-called electrokinetic equations [10–13]

$$\eta \nabla \times \nabla \times \mathbf{v} - \nabla p + \rho \nabla \psi = 0 \quad (10a)$$

$$\nabla \cdot \mathbf{v} = 0 \quad (10b)$$

$$\nabla \cdot \left(n_i \mathbf{v} - D_i \nabla n_i - \frac{e z_i n_i D_i}{kT} \nabla \psi \right) = 0, \quad i = 1, 2, \quad (10c)$$

and

$$\nabla^2 \psi = -\frac{\rho}{\epsilon \epsilon_0} = -\frac{e}{\epsilon \epsilon_0} \sum_i z_i n_i \quad (10d)$$

Equations (10a) and (10b) describe the dynamics of a viscous incompressible charged liquid in the external electric potential field $E = -\nabla \psi$ under the pressure gradient ∇p . Equation (10c) expresses the continuity requirement for ion fluxes, and Eq. (10d) is the Poisson equation for the potential ψ . Here, n_i is the number density of the i th ion species, D_i its diffusion coefficient, z_i the charge number, η the viscosity of the liquid, and ρ the volume charge density; the n_i 's are assumed to meet some mass balance requirements, and a possible departure from the equilibrium values is neglected. After imposing certain boundary conditions specifying the geometry of the system under study and the behavior of the solution at the surface and in the bulk, system (10) becomes determinate and allows the velocity vector field and the electric field to be calculated. These quantities can then be used to calculate the electro-osmotic velocity and streaming current, the quantities that can be measured experimentally. Since both the electro-osmotic velocity and streaming current are related to the surface potential, the latter can be found as well.

Unfortunately, an explicit solution to Eqs. (10) can be obtained for only a very few simple geometries. In most cases of practical interest, a numerical solution is required. To simplify the problem, some additional assumptions are involved: The potential is usually considered to be uniform and the double layer to be thin. However, introduction of the charge regulation, with its inherent inhomogeneous potential distributions and overlapping double layers, would mean avoidance of the above simplifications, thus putting the problem in the range of formidable and not yet solved ones.

Another problem rests in the difference between the surface potential that appears in a charge regulation model and the experimentally determined electro-

kinetic potential, or zeta potential. This is a consequence of uncertainty in the location of the hydrodynamic shear plane [13].

These difficulties explain why up to now the most valuable practical result is that obtained by Smoluchowski at the beginning of the century. As applied to the electro-osmotic transfer rate, v_{eo} it reads [14]

$$v_{eo} = -\frac{\varepsilon\varepsilon_0\zeta_{eo}}{\eta}\mathbf{E} \quad (11)$$

where ζ_{eo} is the zeta potential, which is thought to be equal to the value of ψ at the shear plane. Applicability of the above equation is limited to thin and weakly conducting double layers. The superscript “eo” is used to emphasize that the corresponding quantities come from an electro-osmotic experiment, for the results obtained with different electrokinetic techniques may differ appreciably.

Once the zeta potential has been found, it can be used to calculate the surface charge density using the Grahame equation,

$$\sigma_{eo} = \frac{4en_0}{\kappa} \sinh \frac{e\zeta_{eo}}{2kT} \quad (12)$$

But again, the σ_{eo} obtained in this way cannot be directly compared to the charge density that appears in the charge regulation model.

Notwithstanding the existing limitations of the interpretation of experimental results, electrokinetic measurements are a valuable tool for locating, paradoxically in the present context, the uncharged state of ionizable surfaces. As shown later, no proper interpretation of pH potentiometric charge titration data is possible without knowledge of the conditions under which the net surface charge becomes zero, commonly specified by indicating the point of zero charge or the isoelectric point.

III. THERMODYNAMIC BACKGROUND OF CHARGE REGULATION

Classical thermodynamics offers a unique tool for analysis of basic concepts of charge regulation from quite a general point of view. Consider the course of events occurring when an insoluble and undeformable solid is set in contact with a liquid solution. After a relatively short relaxation period needed for reorientation of solvent molecules in the potential field of the solid surface, one or more quasi-steady physicochemical processes, such as adsorption or surface hydroxylation, may still be in progress until global equilibrium is achieved. Each process can be depicted as motion along the corresponding reaction coordinate, ξ_j , with speed proportional to the affinity, A , [15]. At constant temperature, pressure, and system dimensions—rather limiting constraints chosen here for the sake of simplicity—the change in the Gibbs free energy of the whole system is given by

$$dG = sd\gamma - \sum_i A_j d\xi_j \quad (13)$$

where s is the area of the solid/solution interface, usually taken equal to the net surface area of the dispersed solid measured in dry conditions, and γ is the interfacial tension. The physical meaning of the latter quantity is stipulated later.

In equilibrium, $dG = 0$; hence

$$A_j = s \left(\frac{\partial \gamma}{\partial \xi_j} \right)_{T,p,s} = s \sum_i v_{ij} \left(\frac{\partial \gamma}{\partial n_i} \right)_{T,p,s}, \quad v_{ij} = \frac{\partial n_i}{\partial \xi_j} \quad (14)$$

where n_i is the number of moles of the i th component and v_{ij} its stoichiometric coefficient in the j th process. Then, by using the standard relations between the affinity, A_j , and the chemical potentials, μ_i , of components involved in the process,

$$A_j = - \sum_i v_{ij} \mu_i \quad (15)$$

and between the chemical potentials and the mole fractions, x_i , of the components,

$$\mu_i = \mu_i^0 + RT \ln x_i \quad (16)$$

the following generalized form of the mass action law is easily obtained:

$$\prod_i x_i^{v_{ij}} = K_j^0 \exp \left[- \frac{s}{RT} \sum_i v_{ij} \left(\frac{\partial \gamma}{\partial n_i} \right)_{T,p,s} \right] \quad (17)$$

where K_j^0 is the so-called intrinsic equilibrium constant of the process, expressed through the standard chemical potentials, μ_i^0 , by

$$RT \ln K_j^0 = - \sum_i v_{ij} \mu_i^0 \quad (18)$$

Although preferable from a theoretical viewpoint, the use of mole fractions as units of concentration may be inconvenient in the case of heterogeneous systems. Since, however, mass balance is usually implied, concentration units can be changed as appropriate.

It is expedient to express $d\gamma$ via the increments, dn_i :

$$d\gamma = \sum_j \frac{A_j}{s} d\xi_j = \sum_i \sum_j \frac{\mu_i}{s} \left(\frac{\partial n_i}{\partial \xi_j} \right) d\xi_j = - \sum_i \frac{\mu_i}{s} dn_i \quad (19)$$

The same result can be arrived at in another way. Introduce a so-called adsorption phase, which is composed of adsorbed components and the solid itself, referred to as the adsorbent. Next, it is necessary to define excess quantities. To do so, a reference system is required [16]. Normally, the latter is taken to be composed of the same components, and under the same conditions, as the main system in study but without adsorption. Then the excess quantities, Q^s , are defined as

$$Q_i^s = Q_i - Q_i^0 \quad (20)$$

where Q_i is some quantity measured in the main system and Q_i^0 is the same quantity measured in the reference system. Chemical potentials of all components except adsorbent can be chosen to be the same in both systems. Then, according to general

thermodynamic principles, the change, dU^s , in the total energy of the adsorption phase is

$$dU^s = \mu_a^s dn_a^s + \sum_{i \neq a} \mu_i^s dn_i^s = \gamma ds + \sum_{i \neq a} \mu_i dn_i^s \quad (21)$$

where

$$\mu_a^s = \mu_a - \mu_a^0; \quad \gamma = \mu_a^s / S_M; \quad s = n_a^s S_M \quad (22)$$

and, for $i \neq a$, $\mu_i = \mu_i^s$ by definition of the reference system. The subscript a indicates the adsorbent. Here S_M is an ill-defined quantity (referring to the surface area of 1 mol of adsorbent) whose exact value is immaterial.

By introduction of the corresponding thermodynamic potential,

$$U^s = U^s(s, n_i^s) \equiv \gamma s + \sum_i \mu_i n_i^s \quad (23)$$

differentiation, and comparison with Eq. (21), the following result is obtained:

$$s d\gamma + \sum_i n_i^s d\mu_i = 0 \quad (24)$$

which is nothing other than a generalization of the Gibbs–Duhem equation, transforming itself into the Gibbs adsorption isotherm on substituting $\Gamma_i = n_i^s / s$.

By introducing another well-known thermodynamic potential,

$$G^s = G^s(\gamma, n_i^s) \equiv U^s - \gamma s = \sum_i \mu_i n_i^s \quad (25)$$

writing the equilibrium condition as $dG = dG^s + dG^0 = 0$, and taking into account that $n_i = n_i^s + n_i^0$ and so $dn_i = dn_i^s$, one gets

$$\sum_i \mu_i dn_i + \sum_i n_i^s d\mu_i = 0 \quad (26)$$

from which, after comparison with Eq. (24), the same result as expressed in Eq. (19) follows at once.

Now that Eq. (17) is available and well substantiated, it is possible to proceed with its application to the problem of charge regulation. The underlying idea here is that for many solids, especially those containing ionizable surface groups, brought into contact with an aqueous electrolytic solution, the main contribution to γ is made by the free electrostatic energy, F_{el} , of the solid/solution interface,

$$\gamma \approx \gamma_{el} = F_{el} / s \quad (27)$$

where F_{el} can be calculated according to the Derjaguin formula [17],

$$F_{el} = \frac{\epsilon \epsilon_0}{2} \int_V (\nabla \psi)^2 dV - \int_V dV \int_0^p \psi d\rho \quad (28)$$

or using the thermodynamically equivalent Debye charging procedure [18],

$$F_{el} = \int_s ds \int_0^\sigma \psi d\sigma \quad (29)$$

In the former case, the knowledge of the spatial distribution of potential is required, whereas in the latter case, knowledge of the surface potential will suffice.

After substitution of Eqs. (27) and (28) for γ , Eq. (17) turns into

$$K_j = \prod_i x_i^{v_{ij}} = K_j^0 \exp \left[-\frac{1}{RT} \sum_i v_{ij} \left(\frac{\partial F_{el}}{\partial n_i} \right)_{T,p,s} \right] \quad (30)$$

where the apparent equilibrium constants, K_j , have been introduced. Then, making use of the evident identity,

$$\left(\frac{\partial F_{el}}{\partial n_i} \right)_{T,p,s} = e N_A z_i \psi \quad (31)$$

which follows from Eq. (29) on noting that

$$\left(\frac{\partial F_{el}}{\partial n_i} \right)_{T,p,s} = \left(\frac{\partial F_{el}}{\partial \sigma} \right)_{T,p,s} \frac{\partial \sigma}{\partial n_i} \quad (32)$$

one gets a more familiar expression for Eq. (30):

$$K_j = \prod_i x_i^{v_{ij}} = K_j^0 \exp \left[-\frac{e\psi}{kT} \sum_i' v_{ij} z_i \right] \quad (33)$$

where the prime reminds us that the sum should be taken over surface-attached components only. The latter equation together with the mass conservation principle constitute the basis of charge regulation.

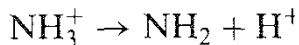
Before proceeding further, it is of concern to demonstrate the logic of the basic equation (30) in explaining equilibrium properties of a few real processes. Consider, for instance, two proteolytic reactions that occur at the surface of amine-modified silica in contact with aqueous electrolytes:

Example 1. Protonation of surface amino groups,



Here $v_{\text{NH}_3^+} = +1$, and $\partial F_{el}/\partial n_{\text{NH}_3^+} > 0$, hence K_j is expected to be a decreasing function of the degree of protonation or the amount of protonated amino groups.

Example 2. The reverse reaction is



Here $v_{\text{NH}_3^+} = -1$, and $\partial F_{el}/\partial n_{\text{NH}_3^+} > 0$; therefore this time K_j is expected to increase together with $n_{\text{NH}_3^+}$. This result is somewhat trivial, through, for the equilibrium constant of the reverse reaction is just the reciprocal of that for the direct reaction.

Of course, the above conclusions are so evident that there would not probably be any need to resort to Eq. (30). They are intended to demonstrate its general consistency.

IV. SURFACE IONIZATION

A. Protolytic Properties of Partly Oxidized Silicon Nitride: Heuristic Ideas

Perhaps the easiest way to understand how charge regulation works lies through consideration of a particular system. Take partly oxidized silicon nitride, for example. In contact with an aqueous solution, its surface acquires an electric charge on account of the protolytic reactions [19]



Such a set of reactions responsible for charging the surface constitutes a charge regulation model. Writing down the mass action law for each of the reactions,

$$K_1 = \frac{\{\text{SiO}^-\}[\text{H}^+]}{\{\text{SiOH}\}} = K_1^0 \exp\left[\frac{e\psi}{kT}\right] \quad (35a)$$

$$K_2 = \frac{\{\text{NH}_3^+\}}{\{\text{NH}_2\}[\text{H}^+]} = K_2^0 \exp\left[\frac{-e\psi}{kT}\right] \quad (35b)$$

where braces are used to designate the so-called surface concentrations (mol/m²), expressing the surface charge density σ via $\{\text{NH}_3^+\}$ and $\{\text{SiO}^-\}$,

$$\sigma = eN_A(\{\text{NH}_3^+\} - \{\text{SiO}^-\}) \quad (36)$$

and imposing the mass balance requirements

$$\{\text{NH}_2\} + \{\text{NH}_3^+\} = c_{\text{NH}_2}^{\text{tot}}, \quad \{\text{SiO}^-\} + \{\text{SiOH}\} = c_{\text{SiOH}}^{\text{tot}} \quad (37)$$

one gets after rearrangement

$$\sigma = eN_A \left[\frac{c_{\text{NH}_2}^{\text{tot}}[\text{H}^+]K_2^0}{[\text{H}^+]K_2^0 + \exp[e\psi/kT]} - \frac{c_{\text{SiOH}}^{\text{tot}}K_1^0 \exp[e\psi/kT]}{[\text{H}^+] + K_1^0 \exp[e\psi/kT]} \right] \quad (38)$$

Then, on adding a potential-to-charge relation,

$$\psi = f(\sigma) \quad (39)$$

where f is some, in general implicit, function of σ whose mathematical expression depends on the choice of the electrical double layer model and the geometry of the system, a determinate system of equations results. Alternatively, substituting Eq. (39) into (38) yields a transcendental equation for σ that can be solved numerically, provided that $K_1^0, K_2^0, c_{\text{NH}_2}^{\text{tot}}, c_{\text{SiOH}}^{\text{tot}}$, and $[\text{H}^+]$ are known. Practically, this is rarely so; hence another approach proves to be more usable: $K_1^0, K_2^0, c_{\text{NH}_2}^{\text{tot}}$ and $c_{\text{SiOH}}^{\text{tot}}$ are fitted to approximate some experimental data, typically a dependence of σ or zeta potential on $\text{pH} = -\log[\text{H}^+]$ [9,19–22].

Particular implementation of a charge regulation model depends largely on the form of Eq. (39). In the so-called low potential, or Debye, approximation, the latter

assumes the simplest linear form. A few explicit formulas [23] are given below. Henceforth, for the sake of convenience, the reduced potential u measured in units of kT/e and reduced linear dimensions measured in units of $1/\kappa$ are used.

Plane:

$$u = \frac{\kappa\sigma}{2en_0} \quad (40)$$

Long cylindrical cavity of radius r :

$$u = \frac{\kappa\sigma I_0(r)}{2en_0 I_1(r)} \quad (41)$$

Long empty cylinder with internal radius r_{in} and external radius r_{out}

$$u(r) = \begin{cases} \alpha I_0(r), & 0 \leq r \leq r_{\text{in}} \\ \beta K_0(r), & r_{\text{out}} \leq r < \infty \end{cases} \quad (42a)$$

$$\alpha D = \left(\varphi K_1(r_{\text{out}}) + \frac{\varepsilon_s K_0(r_{\text{out}})}{\varepsilon_b r_{\text{out}}} \right) \sigma_{\text{in}} - \frac{\varepsilon_s}{\varepsilon_b r_{\text{in}}} \sigma_{\text{out}} \quad (42b)$$

$$\beta D = \frac{\varepsilon_s I_0(r_{\text{in}})}{\varepsilon_b r_{\text{out}}} \sigma_{\text{in}} + \left(\frac{\varepsilon_s I_0(r_{\text{in}})}{\varepsilon_b r_{\text{in}}} + \varphi I_1(r_{\text{in}}) \right) \sigma_{\text{out}} \quad (42c)$$

$$D = \varepsilon_0 \varepsilon_s \left(\frac{I_0(r_{\text{in}}) K_1(r_{\text{out}})}{r_{\text{in}}} + \frac{I_1(r_{\text{in}}) K_0(r_{\text{out}})}{r_{\text{out}}} \right) + \varepsilon_0 \varepsilon_b I_1(r_{\text{in}}) K_1(r_{\text{out}}) \varphi \quad (42d)$$

$$\varphi = \ln(r_{\text{out}}/r_{\text{in}}) \quad (42e)$$

Here, I_n and K_n ($n = 0, 1$) are modified Bessel functions, ε_b is the dielectric constant of the bulk solution, and ε_s is that of the solid. In Eq. (42e) the surface charge density on the internal and external walls of the cylinder may not be the same, which is emphasized by the subscripts.

Theoretically, Debye's approximation is valid only for potentials so low that the exponentials in Eq. (38) can be expanded in power series retaining terms up to and including quadratics. Without such an expansion, it will still work for high potentials; however, in this case the magnitude of charge density is severely underestimated, whereas the magnitude of the surface potential is overestimated.

In general, large potentials necessitate the use of a nonlinear potential-to-charge relation. Unfortunately, the latter can be written explicitly for a plane geometry only, in which case

$$u = 2 \operatorname{arcsinh} \left(\frac{\kappa\sigma}{4en_0} \right) \quad (43)$$

For more complex geometries, it is sometimes possible to obtain approximate analytic expressions [24]. However, in general, the desired potential-to-charge relationship must be obtained via numerical solution of the Poisson–Boltzmann equation. In particular, for a long cylindrical cavity, the case most relevant to this study, the desired relation can be obtained by solving the system [25],

$$\frac{1}{r} \frac{d}{dr} \left(r \frac{du}{dr} \right) = \sinh u, \quad \left. \frac{du}{dr} \right|_{r=0} = 0 \quad (44a)$$

$$\kappa r \sigma - 2en_0 \int_0^r r' \sinh u(r') dr' = 0 \quad (44b)$$

where Eq. (44a) is the Poisson–Boltzmann equation for potential, and (44b) is just a mathematical expression of the electroneutrality condition.

On substituting (44a) for $\sinh u$ to (44b) and integrating by parts, another equivalent formulation is obtained:

$$\left. \frac{du}{dr} \right|_s = \frac{\kappa \sigma}{2en_0} \quad (45)$$

which is, indeed, a direct consequence of Gauss's theorem.

To give some more ideas of how the choice of a potential-to-charge relation can affect the behavior of a charge regulation model, Fig. 4 compares spatial distributions of the potential within cylindrical cavities of different sizes under different

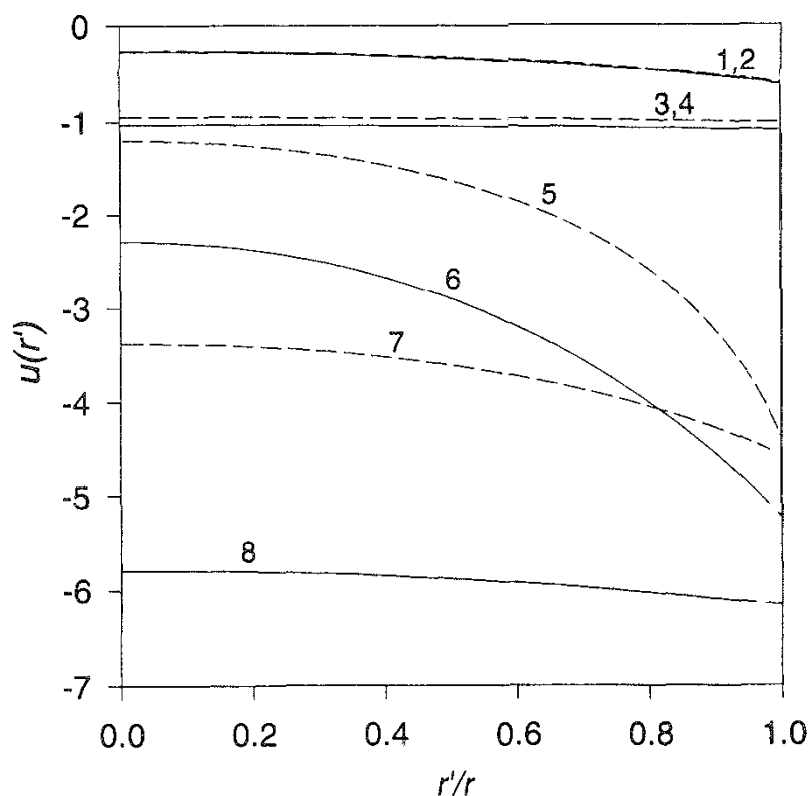


FIG. 4 Radial distribution of potential inside cylindrical pores with charge-regulated walls. The charge-regulation model used in the calculation was based on the reaction set (58) with the following model parameters: $c_{\text{SiOH}}^{\text{tot}} = 4.6 \times 10^{-6} \text{ mol/m}^{-2}$, $K_d = 1.5 \times 10^{-8} \text{ mol/dm}^3$, and $K_{as}^0 = 1.0 \text{ dm}^3/\text{mol}$ [28]. Curves 3,4,7, and 8 correspond to $r = 0.5$, and curves 1,2,5, and 6 correspond to $r = 2.0$ (radius is in units of $1/\kappa$, and the ionic strength is 0.01 M). (—) Linear potential-to-charge relation (Debye–Hückel); (---) nonlinear potential-to-charge relation (Poisson–Boltzmann).

conditions, calculated using the charge regulation model based on the reaction set (34) with potential-to-charge relations established by Eqs. (41) and (44), respectively. The model parameters were taken to simulate the properties of amine-coated silica gel [25] with equivalent amounts of silanols and amino groups.

As can be seen, the use of Debye's approximation beyond the limits of its applicability results in serious errors. Another important conclusion that can be drawn from Fig. 4 is that when double layers overlap, both the surface charge density and surface potential become dependent on pore size.

B. Distribution of Surface Potential and Surface Charge over Pore Sizes

1. Relation with the Porous Structure Parameters

As follows from Eq. (29), γ_{el} represents the density of the free electrostatic energy, a quantity that depends on pore size. Consequently, the equilibrium state of surface reactions accompanied by charge transfer also becomes pore size dependent. The same concerns, of course, all the "charge-regulated" quantities, including u , a , and surface concentrations of reaction components [9,22,25]. For instance, by substituting the equation

$$u(\sigma_r, r') = \frac{e\sigma_r I_0(r')}{kT\epsilon\epsilon_0\kappa I_1(r)} \quad (46)$$

which describes the radial distribution of potential within a cylindrical pore of radius r , into Derjaguin's formula, Eq. (28), and making simple quadratures, one gets

$$\gamma_{el} = \frac{\kappa\epsilon\epsilon_0(kT)^2}{2\pi e^2 r} \int_0^r \left[u^2(\sigma_r, r') + \left(\frac{du(\sigma_r, r')}{dr'} \right)^2 \right] r' dr' = \frac{kT\sigma_r u(\sigma_r, r)}{2e} \quad (47)$$

where the subscript r is added to emphasize the pore size dependency of the corresponding quantities. This result can also be obtained by using Debye's charging process, Eq. (29).

Now let $\Lambda(r)$ be the pore size distribution normalized as follows:

$$\Lambda(0) = \Lambda(\infty) = 0; \quad \int_0^\infty \Lambda(r) dr = \kappa^3 V_p \quad (48)$$

where V_p is the specific pore volume. Then it is easy to see that

$$F_{el} = \frac{2}{\kappa^2 S_{sp}} \int_0^\infty \gamma_{el} \frac{\Lambda(r)}{r} dr \quad (49)$$

determines the average free electrostatic energy of the solid whose specific surface area is given by

$$S_{sp} = \frac{2}{\kappa^2} \int_0^\infty \frac{\Lambda(r)}{r} dr \quad (50)$$

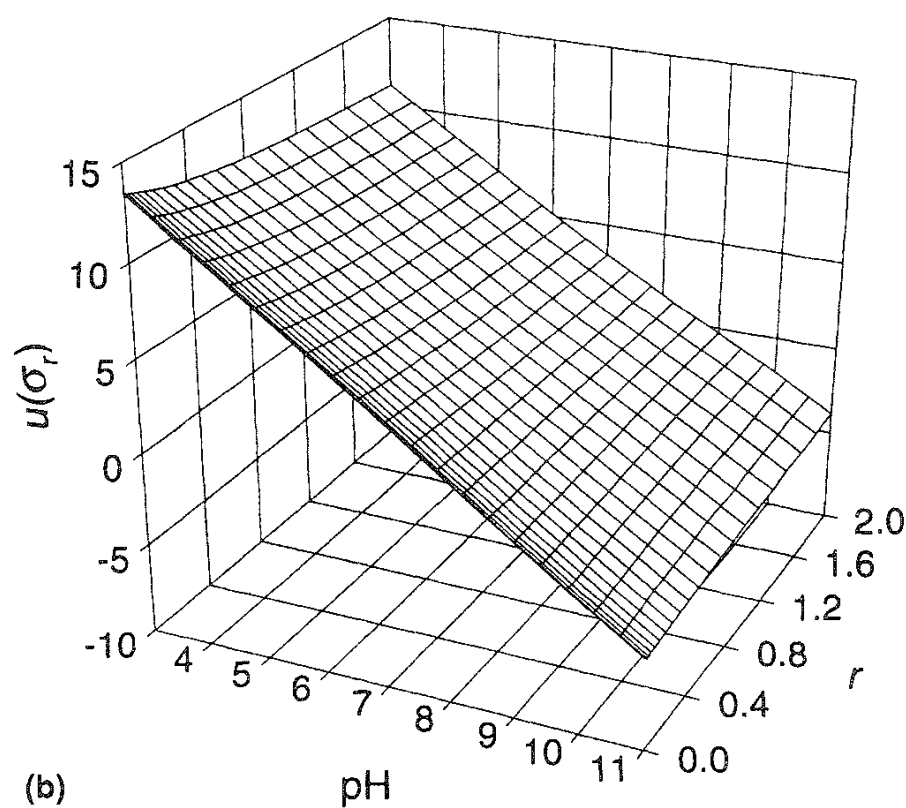
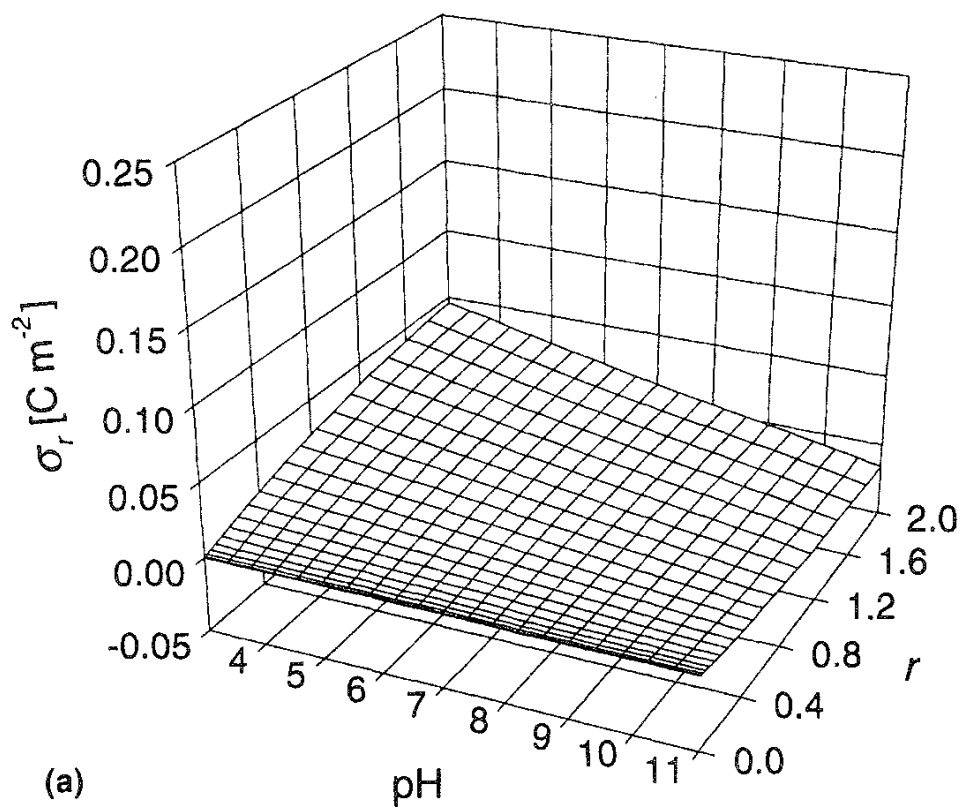
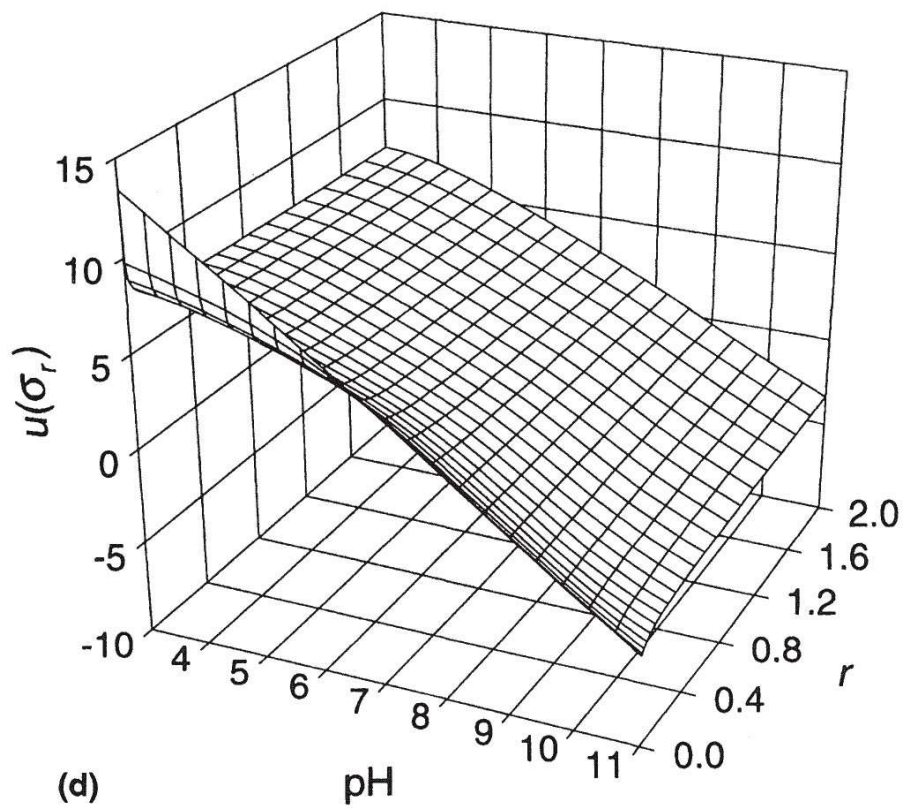
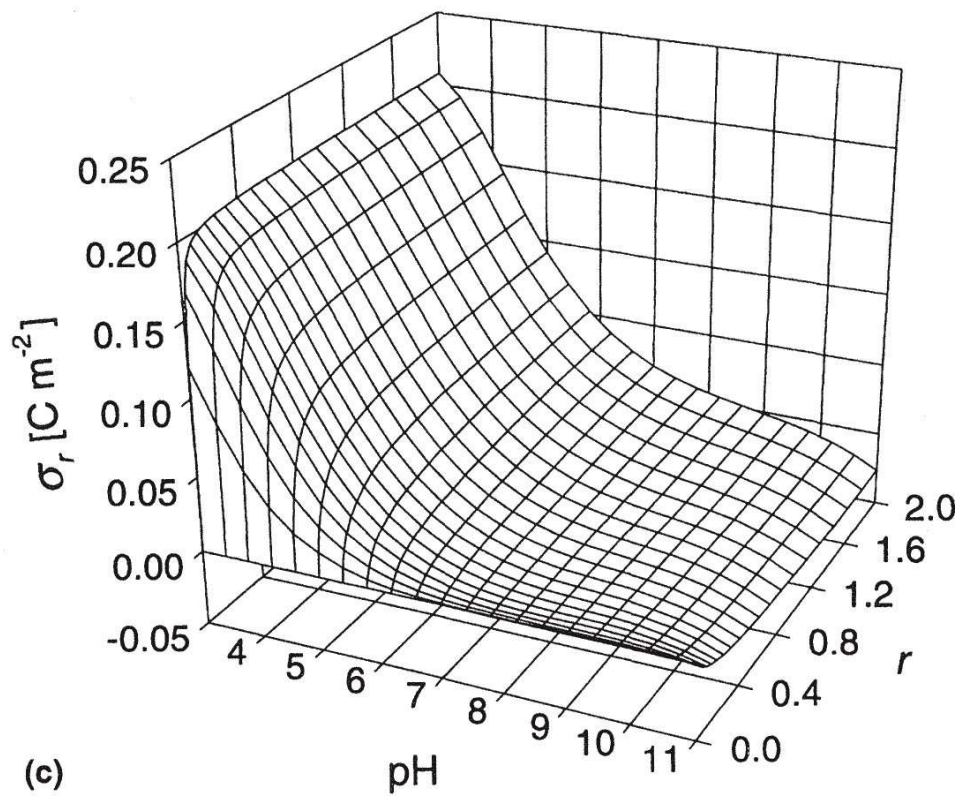


FIG. 5 (a, c) Surface charge density and (b, d) surface potential as functions of pH and pore size. (a, b) Linear potential-to-charge relation (Debye–Hückel); (c, d) nonlinear potential-to-charge relation (Poisson–Boltzmann). The charge regulation model used in the calculation was based on reaction set (34) with the following model parameters: $K_1^0 = 2.4 \times 10^{10} \text{ dm}^3/\text{mol}$, $K_2^0 = 5.1 \times 10^{-8} \text{ mol/dm}^3$ [25], $c_{\text{NH}_3}^{\text{tot}} = c_{\text{SiOH}}^{\text{tot}} = 2.3 \times 10^{-6} \text{ mol/m}^2$, and ionic strength 0.01 M.



The averages, $\langle K_j \rangle$, of the local equilibrium constants K_j are determined by

$$\langle K_j \rangle = \exp(\ln K_j) = \exp \left[\frac{2}{\kappa^2 S_{sp}} \int_0^\infty \ln K_j \frac{\Lambda(r)}{r} dr \right] \quad (51)$$

By solving the charge regulation problem for different r values, distributions of surface charge density and surface potential over pore sizes are obtained (see Fig. 5).

2. Asymptotic Behavior of Surface Charge Density and Surface Potential in Small Pores

The results in Fig. 5 show that as the pore size tends to zero, the surface charge density also approaches zero, whereas the surface potential takes on a finite non-zero value. This can be proven analytically [9,25]. From Eq. (44), it follows that

$$\sigma_r = \frac{2en_0}{\kappa r} \int_0^r r' \sinh u \, dr' \cong \frac{en_0 r}{\kappa} \sinh u, \quad r \rightarrow 0 \quad (52)$$

which, by virtue of Eq. (36), can be rewritten as

$$\sinh u = \frac{\kappa N_A}{n_0 r} (\{NH_3^+\} - \{SiO^-\}) \equiv f(u) \quad (53)$$

The right-hand side of Eq. (53) is a function of u , as can be seen after retrieving the concentrations of protonated amino groups and deprotonated silanols from Eq. (35). By taking into account the evident relations,

$$f(-\infty) = \frac{\kappa N_A c_{NH_2}^{tot}}{n_0 r} \rightarrow +\infty; \quad f(+\infty) = -\frac{\kappa N_A c_{SiOH}^{tot}}{n_0 r} \rightarrow -\infty \quad \text{as } r \rightarrow 0 \quad (54)$$

and the fact that $\sinh(-\infty) = -\infty$ and $\sinh(+\infty) = +\infty$, the existence of a finite real root of the transcendental equation $\sinh u = f(u)$ is established. The finiteness of the root necessitates equality of $\{NH_3^+\}$ to $\{SiO^-\}$, thus simplifying the task of finding that root to solving the quadratic equation

$$A \exp 2u + B \exp u + C = 0 \quad (55)$$

where

$$\begin{aligned} A &= c_{SiOH}^{tot} K_1^0 \\ B &= K_1^0 K_2^0 [H^+] (c_{SiOH}^{tot} - c_{NH_2}^{tot}) \\ C &= -c_{NH_2}^{tot} K_2^0 [H^+]^2 \end{aligned}$$

3. Influence of Electrostatic Saturation on Charge Regulation

It is known that the dielectric constant of the solution close to the surface of a charged colloidal particle is lower than that in the bulk because of the electrostatic saturation effect [26]. Therefore, the hydration energy is also lower, and ions tend to leave this region and move to a region with a higher dielectric constant [27].

General thermodynamic principles declare that the above-mentioned effect is not only limited to the redistribution of the ions in the electrical double layer but also exerts an influence on the acid–base and ion-exchange properties of surface-ionizable groups and thereby on the entire process of formation of the surface charge [25,28].

When the hydration effects are taken into account, the Poisson–Boltzmann equation governing the potential distribution takes on the form [27,28]

$$\nabla \cdot (\varepsilon \nabla u) = -\varepsilon_b \rho \quad (56a)$$

$$\rho = \sum_i z_i \exp[-(z_i u + h_i)] \quad (56b)$$

$$h_i = \frac{\kappa^2}{16\pi n_0 a_i} \left(\frac{\varepsilon_b}{\varepsilon} - 1 \right) \quad (56c)$$

$$\varepsilon = \eta^2 - \frac{3}{bE} (\varepsilon_b - \eta^2) \left(\coth(bE) - \frac{1}{bE} \right) \quad (56d)$$

$$E = -\nabla u \quad (56e)$$

where u is the potential, ε is the coordinate-dependent dielectric constant of the solution close to the surface, ε_b is the dielectric constant of the bulk solution, a_i is the radius of the i th ion, η is the refractive index of water, and $b = b\kappa kT/e$, where $b_0 = 1.41 \times 10^{-8}$ m/V. Other symbols have their conventional meanings. The above equations together with the electroneutrality condition

$$\kappa r \sigma_r + en_0 \int_0^r r' \rho(r') dr' = 0 \quad (57)$$

establish a one-to-one potential-to-charge relation that can be used in place of Eq. (39).

Correspondingly Eq. (33) is replaced by [28]

$$K_j = K_j^0 \exp \left[-u \sum_i' v_{ij} z_i - \frac{\kappa^2}{16\pi n_0} \left(\frac{\varepsilon_b}{\varepsilon} - 1 \right) \sum_i' \frac{v_{ij} z_i^2}{a_i} \right] \quad (58)$$

where the primes over the summations recall as usual that the summation is limited to surface-attached components.

Figure 6 compares the pH dependencies of surface charge density and surface potential calculated either neglecting or allowing for the above-mentioned effect.

C. Application of Charge Regulation Model for Determination of Equilibrium Constants of Surface Reactions

The charge regulation model can be used successfully for interpreting pH potentiometric titration data, thus enabling the determination of intrinsic equilibrium constants of surface reactions and the prediction of surface composition under various conditions. The following example demonstrates this.

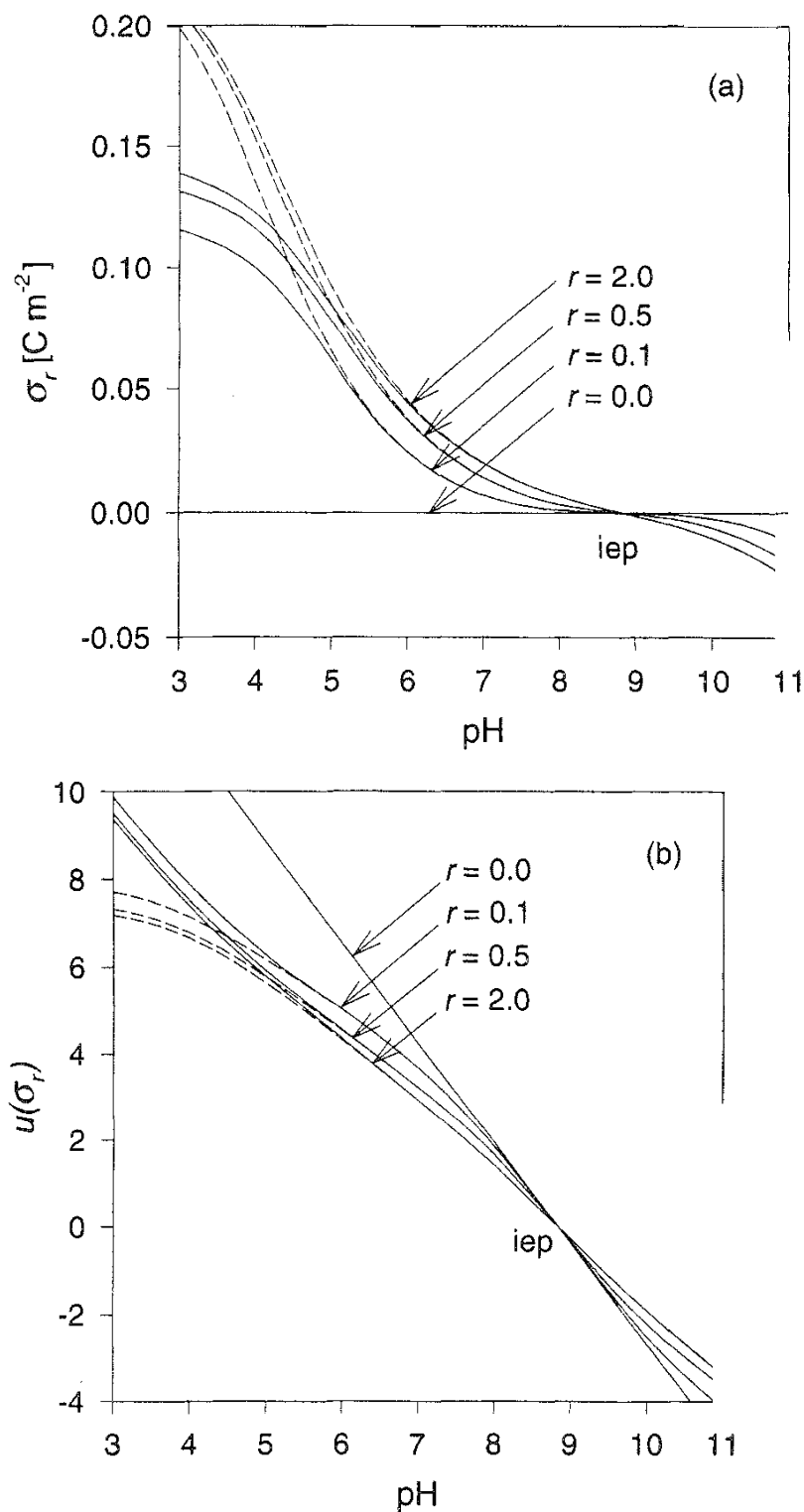
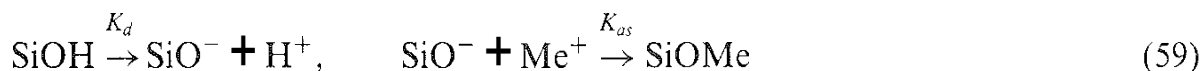


FIG. 6 Influence of electrostatic saturation on the pH dependencies of (a) surface charge density and (b) surface potential for different degrees of overlapping of the electrical double layers. (—) Electrostatic saturation allowed for; (---) electrostatic saturation neglected. The charge regulation model used in this calculation was based on reaction set (34) with the following model parameters: $K_1^0 = 2.4 \times 10^{10} \text{ dm}^3/\text{mol}$, $K_2^0 = 5.1 \times 10^{-8} \text{ mol/dm}^3$ [25], $c_{\text{NH}_4}^{\text{tot}} = c_{\text{SiOH}}^{\text{tot}} = 2.3 \times 10^{-6} \text{ mol/m}^2$, $a_{\text{Na}^+} = 1.612 \text{ \AA}$, $a_{\text{Cl}^-} = 2.371 \text{ \AA}$, and ionic strength 0.01 M NaCl [28]. The potential was calculated from either Eq. (44) or Eq. (56). Pore radii are given in units of $1/\kappa$ and are inversely proportional to the degree of overlapping.

Consider the titration of reactive silanols at the surface of a porous silica gel [25]. Typical titration data are shown in Fig. 7 by discrete points. One may want to approximate these data by a titration curve calculated according to the charge regulation model based on the minimal reaction set



For a given pore size r , the solution to this charge regulation problem is found from the system

$$\frac{\sigma_r}{eN_A} = \{\text{SiO}^-\}_r = \frac{c_{\text{SiOH}}^{\text{tot}} K_d}{[\text{H}^+] + K_d(1 + K_{as}[\text{Me}^+])} \quad (60)$$

where

$$K_d = K_d^0 \exp u(\sigma_r); \quad K_{as} = K_{as}^0 \exp[-u(\sigma_r)]$$

with the potential-to-charge relation established by Eq. (44). Since protons are in fact being removed from the surface, it is possible to speak of their negative adsorption,

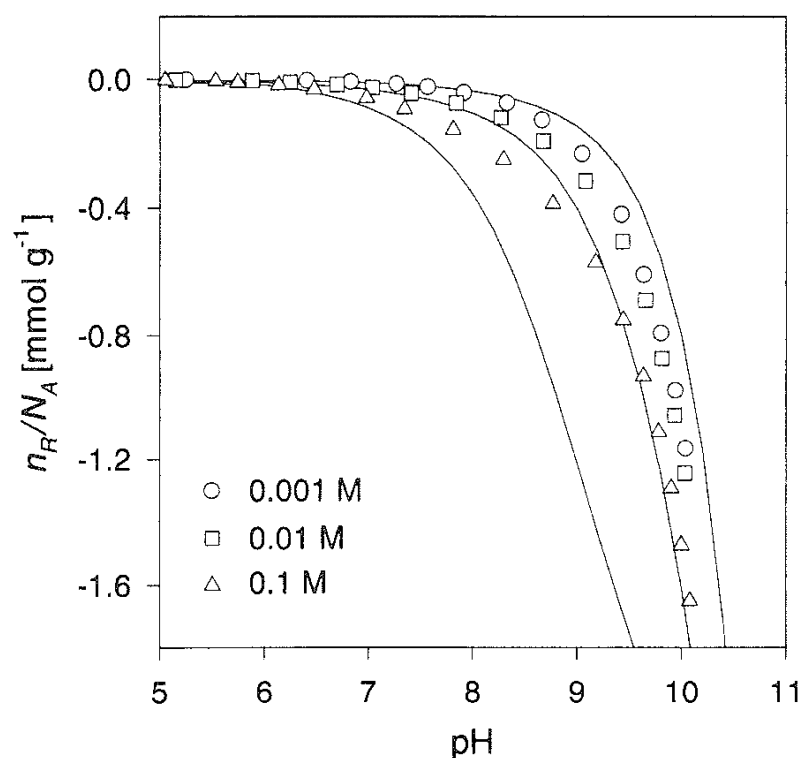


FIG. 7 Titration data for mesoporous silica gel. The characteristics of the sample are specified in the caption to Fig. 1. Ionic strength: (○) 0.001 M, (□) 0.01 M, and (△) 0.1 M NaCl. Discrete points are the experimental results; solid lines are the best-fit curves calculated according to the charge regulation model based on reaction set (59) with the following parameters: $c_{\text{SiOH}}^{\text{tot}} = 4.6 \times 10^{-6} \text{ mol/m}^2$, $K_d^0 = 1.05 \times 10^{-8} \text{ mol/dm}^3$, $K_{as}^0 = 1.0 \text{ dm}^3/\text{mol}$, $a_{\text{NA}^+} = 1.612 \text{ \AA}$, $a_{\text{Cl}^-} = 2.371 \text{ \AA}$. (From Ref. 28.)

$$-A_r = \{\text{SiO}^-\}_r + \{\text{SiOMe}\}_r = \{\text{SiO}^-\}_r(1 + K_{as}[\text{Me}^+]) \quad (61)$$

However, what can be determined experimentally is only an average of A_r over all pore sizes,

$$\langle A \rangle = \int_0^\infty A_r \frac{\Lambda(r)}{r} dr \quad (62)$$

where $\Lambda(r)$ is the pore size distribution defined in Eq. (48). The above equation can be rewritten in a finite-difference representation reflecting the discreteness of experimental data,

$$\begin{aligned} \langle A \rangle &= Y \sum_i A_{r_i} \frac{1}{r_i} \left(\frac{\Delta V_i}{\Delta r_i} \right) \Delta r_i \\ Y^{-1} &= \frac{1}{2} \sum_i \left[\frac{\Delta V_{i+1}}{\Delta r_{i+1}} \left(1 - \frac{r_i}{r_{i+1}} \right) - \frac{\Delta V_i}{\Delta r_i} \left(1 - \frac{r_{i+1}}{r_i} \right) \right] \end{aligned} \quad (63)$$

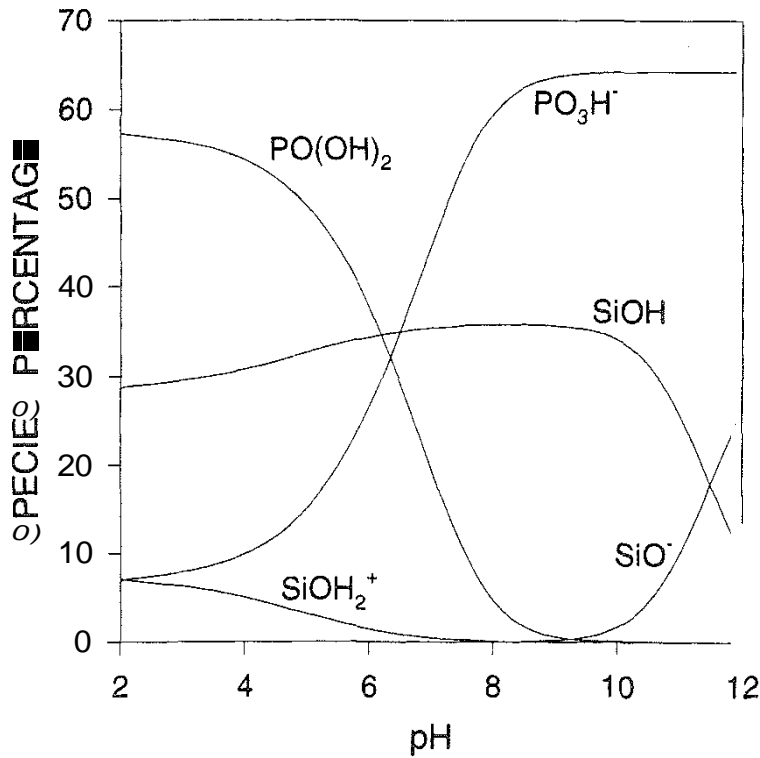
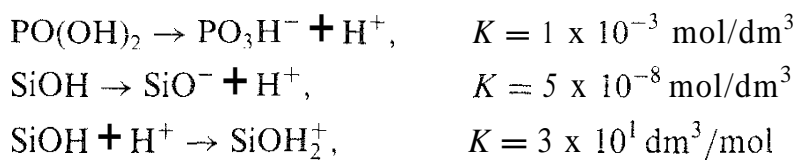


FIG. 8 Surface speciation of phosphate-doped silica gel ($S_{sp} = 187 \text{ m}^2/\text{g}$, loading of phosphate 1.2 mmol/g), retrieved from titration data by applying the charge regulation model based on the reaction set



(From Ref. 29.)

Finally, to compare (A) with the amount, n_R , of reacted silanols determined experimentally [cf. Eq. (9)], a correction for dissolution of silica gel at high pH should be made:

$$-n_R = (A) - \frac{v \prod}{m[\text{H}^+]} \quad (64)$$

where v is the volume of the solution, m is the mass of the sample, and \prod is the product of the solubility of orthosilicic acid and its dissociation constant. Now, K_p^0 and K_{as} , as well as some other parameters of interest, can be used as fitting parameters and evaluated by minimizing the difference, usually expressed as the squared deviation, between the theoretical and experimental results [25,28].

Knowledge of intrinsic equilibrium constants of surface reactions allows calculation of surface specification as a function of pH and ionic strength of the solution, sometimes leading to quite unexpected results. As an example, Fig. 8 demonstrates the percentage of different species at the surface of phosphate-doped silica gel [29]. It is the charge regulation that allows protonated silanols to exist in appreciable amounts up to pH as high as 6–7 (for pure silica gel, the amount of protonated silanols becomes negligible at a pH of about 4 [30]), at the same time dramatically reducing the dissociation ability of phosphate groups. Thus, the charge regulation model proves to be effective in the analysis and modeling of protolytic and ionic equilibria at charged interfaces.

REFERENCES

1. J. O'M. Bockris., B. E. Conway, and E. Yeager (eds.), *Comprehensive Treatise of Electrochemistry*. Vol. 1, *The Double Layer*, Plenum, New York, 1980.
2. T. W. Healy and L. R. White, *Adv. Colloid Interface Sci.* 9:303 (1978).
3. R. O. James and G. A. Parks, in *Surface and Colloid Science* (E. Matijevic, ed.), Wiley-Interscience, New York, 1982, p. 119.
4. J. Westall and H. Hohl, *Adv. Colloid Interface Sci.* 12:265 (1980).
5. E. S. Reiner and C. J. Radke, *Adv. Colloid Interface Sci.* 47:59 (1993).
6. S. J. Gregg and K. S. W. Sing, *Adsorption, Surface Area and Porosity*, 2nd ed., Academic, London, 1982.
7. K. K. Unger, *Porous Silica*, Elsevier, Amsterdam, 1988.
8. A. V. Neimark, in *Characterization of Porous Solids* (F. Rodriguez-Reinozo, J. Rouquerol, K. S. W. Sing, and K. K. Unger, eds.), Elsevier, Amsterdam, 1991, p. 67.
9. B. V. Zhmud and J. Sonnefeld, *J. Chem. Soc., Faraday Trans.* 91:2965 (1995).
10. P. H. Wiersema, A. L. Loeb, and J. Th. G. Overbeek, *J. Colloid Interface Sci.* 22:78 (1966).
11. S. S. Dukhin and B. V. Derjaguin, *Electrophoresis*, Nauka, Moscow, 1979.
12. R. W. O'Brien, *J. Colloid Interface Sci.* 92:204 (1983).
13. R. W. O'Brien, *J. Colloid Interface Sci.* 110:477 (1986).
14. R. J. Hunter, *Zeta Potential in Colloid Science*, Academic, London, 1981.
15. I. Prigogine and R. Defay, *Chemical Thermodynamics*, Longmans Green, London, 1954.

16. A. A. Lopatkin, *Theoretical Foundations of Physical Adsorption*, Moscow Univ. Press, Moscow, 1983.
17. B. V. Derjaguin, *Theory of the Stability of Colloids and Thin Films*, Nauka, Moscow, 1996.
18. R. S. Harned, and B. B. Owen, *The Physical Chemistry of Electrolytic Solutions*, 3rd ed., Reinhold, New York, 1958.
19. L. Bergstrom and E. Bostedt, *Colloids Surf.* 9:183 (1990).
20. A. A. Golub, A. I. Zubenko, and B. V. Zhmud, *J. Colloid Interface Sci.* 179:482 (1996).
21. J. Sonnefeld, *Colloid Surf. A* 108:27 (1996).
22. B. V. Zhmud and A. A. Golub, *Colloid Surf. A.* 105:173 (1995).
23. R. J. Hunter, *Foundations Of Colloid Science*, Clarendon Press, Oxford, 1987.
24. V. V. Panjukov, *J. Colloid Interface Sci.* 110:556 (1986).
25. B. V. Zhmud, *J. Colloid Interface Sci.*, 183:111 (1996).
26. F. Booth, *J. Chem. Phys.* 19:391 (1951).
27. Y. Gur, I. Ravina, and A. J. Babchin, *J. Colloid Interface Sci.* 64:333 (1978).
28. B. V. Zhmud, W. A. House, and J. Sonnefeld, *J. Chem. Soc., Faraday Trans.* 93:3129 (1997).
29. B. V. Zhmud, E. B. Sevastyanova, and A. A. Golub, *Zh. Fiz. Khim.* 71:692 (1997).
30. S. M. Ahmed, *Can. J. Chem.* 44:1663 (1966).

Surface Ionization and Complexation

ZHENGHE XU Department of Chemical and Materials Engineering, University of Alberta, Edmonton, Alberta, Canada

QINGSONG ZHANG Hewlett Packard, Palo Alto, California

JAMES A. FINCH Department of Mining and Metallurgical Engineering, McGill University, Montreal, Quebec, Canada

- I. Introduction
- II. Surface Charging Mechanisms
 - A. Unequal hydration
 - B. Surface hydrolysis
 - C. Adsorption
 - D. Isomorphous replacement
- III. A Hybrid Triple-Layer Model
- IV. Site-Binding Model
- V. Balance Equations
- VI. Determination of Site-Binding Constants
- VII. Prediction of Surface Charge Density
- VIII. Effect of Ion Adsorption on the Zeta Potential
- IX. Prediction of Surface Species
- X. Current Status
- XI. Summary
- References

I. INTRODUCTION

Nanosized particles and porous materials play an important role in many technological applications. They have been used widely as biological sensors, integrated electronic devices, catalyst supports, and adsorbents for detoxification of industrial effluents and domestic water, decoloring of processing water, and purification of pharmaceuticals and proteins. In [Chapter 3](#), Xu et al. showed some typical applications of functionalized superparamagnetic particles in biological cell separation and industrial effluent detoxification. Porous media, on the other hand, constitute an

important class in catalyst, membrane, and supported adsorbent technology. For example, a tailored pore size in a membrane allows selective binding of specific targets or the separation of biological cells based on geometric fit, i.e., cell size.

It is well known that a solid surface of either nanosized particles or porous materials, often becomes charged when brought into contact with a polar medium such as an aqueous electrolyte solution, although the charging mechanism varies according to the system from preferential dissolution to ionization, hydrolysis, specific adsorption, isomorphous replacement, tempering, and surface polarization [1–7]. The charging process is a complex physicochemical process and involves, in general, more than one charging mechanism. Regardless of the mechanism, the charges developed on a solid surface impose an electrostatic force on nearby charged species (e.g., electrolytes or biological cells). As a result, an electrical double layer is developed, usually consisting of a layer of compact surface charge and a diffuse region of charged species in solution. The surface charge along with the electrical double layer controls the interactions and behavior of these particles and porous media with targets or ligands.

The surface charge density and hence the surface electrical potential are determined by the nature of the surface and solution physicochemistry. As shown in Fig. 1, the surface potential [measured by the zeta potential, (ζ), the potential at the slip plane] of corundum (Al_2O_3) depends on the solution pH and the type and concen-

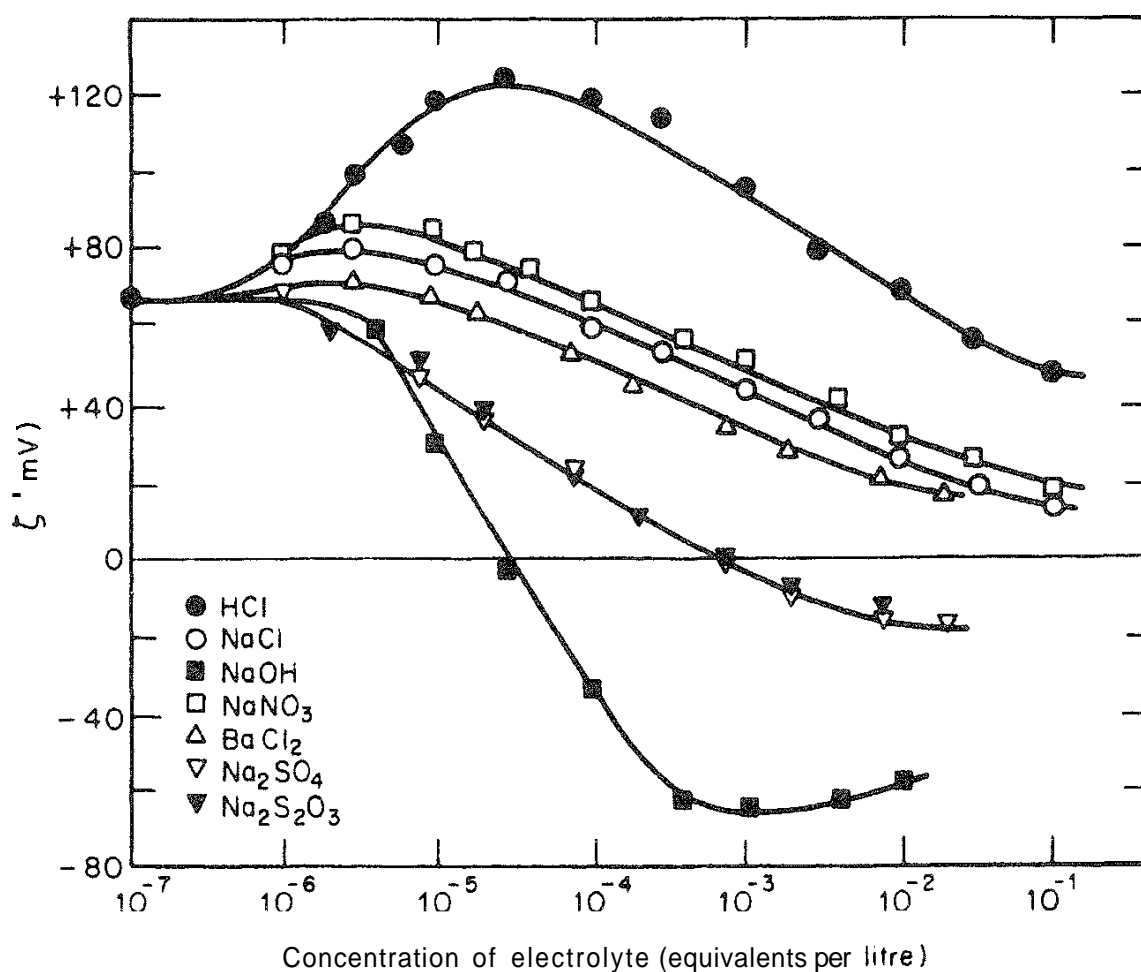


FIG. 1 Zeta potential of corundum in solutions of various electrolytes. (After Ref. 7.)

tration of metal ions present in addition to the nature of the surface itself [8]. As a result, the interaction of nanoparticles and porous media with targets such as metal ions is anticipated to be affected by changing either surface properties or solution conditions. It is therefore important to understand the charging mechanism and to be able to predict the variations of surface charge (the sign and magnitude) in response to changes in solution.

In this chapter, a brief summary is presented of various charging mechanisms, each with a typical example. The progress on the development of a surface complexation model to describe quantitatively the adsorption of cationic or anionic species is then reviewed, with emphasis on contributions from our research laboratory. A general approach to modeling the charged particles and predicting surface species distribution is described. Finally, a few examples are given to illustrate the applications of the modeling approach to an understanding of molecular adsorption at a mineral surface.

II. SURFACE CHARGING MECHANISMS

A. Unequal Hydration

When an ionic solid crystal, such as AgI, is brought into contact with pure water, it often becomes negatively charged although the solid particle is electrically neutral. The negative surface charge indicates the existence of excess surface anions (I^-). The asymmetrical distribution of surface cations and anions may be attributed to unequal hydration between cations and anions. A stronger hydration of a cation (Ag^+) results in a lower activity of that cation in the solution phase and hence a surface deficiency. The surface charge can in this case be predicted by comparing the hydration free energy of cations and anions. Provided that the concentration of Ag^+ is increased to above $10^{-5.6}$, the AgI surface becomes positively charged because of the increased activity of Ag^+ in the solution and hence excess Ag^+ on the surface. In this example, Ag^+ and I^- are referred to as potential-determining ions (pdi's). Most inorganic solids suspended in an aqueous solution in which they have some solubility are charged according to this mechanism. Other examples include CaF_2 , $BaSO_4$, $PbSO_4$, and $CaWO_4$.

B. Surface Hydrolysis

It is well known [3] that natural silica particles are negatively charged in pure water, which can be attributed to surface hydrolysis followed by the pH-dependent dissociation of surface hydroxyl groups. When a silica matrix is broken in air, the surface concentration of SiO^- and Si^+ are the same to meet the requirement of electrical neutrality. When the fractured surface is brought into contact with water, these charged sites, called unsaturated sites, are readily hydrolyzed to form neutral surface species of $SiOH$, releasing either O^-H or H^+ . Adjusting the pH, i.e., changing H^+ and O^-H activity, will cause the neutral surface species to dissociate, giving rise to a net surface charge. In this case, H^+ and O^-H are pdi's and the pH at which the particle is neutral (i.e., surface charge density $\sigma = 0$) is called the point of zero charge (pzc). Negative surface charge is created by an acidic dissocia-

tion of surface hydroxyl groups, which occurs at pH above its pzc, while positive surface charge results from protonation of neutral SiOH groups at pH below its pzc. For most oxides, the surface charge originates from this charging mechanism. Unoxidized sulfide minerals are charged by this mechanism, although mineral oxidation may involve more than one charging mechanism. The other examples in this category include surfaces containing groups such as sulfates, sulfonates, and carboxyl and/or hydroxyl groups that are readily charged when the free energy of the system favors their dissociation [8].

C. Adsorption

In some cases, the adsorption of specific site-binding ions, such as Ca^{2+} and Mg^{2+} , is responsible for the surface charge of a previously uncharged surface. The surface charge of lipid bilayers of zwitterionic head groups in the presence of Ca^{2+} is due to the adsorption of Ca^{2+} on $-\text{COO}^-$ sites vacated by H^+ or Na^+ [9]. Obviously, the surface charge due to this mechanism requires specifically adsorbing ions in aqueous solutions. As a result, this charging mechanism can be readily tested. The preferential adsorption of charged species in some cases is responsible for surface charge. The surface charge at air/water and hydrocarbon/water interfaces in the presence of simple electrolytes has been attributed to the preferential adsorption of anions at these interfaces [10–12]. It is interesting to note that the adsorption of specifically adsorbing ions not only makes certain neutral surfaces charged but can also change the sign of the surface charge for a charged surface. A well-known example is hematite. In the presence of Ca^{2+} , the originally negatively charged hematite becomes positively charged as long as the concentration of Ca^{2+} is sufficiently high. The charging mechanism of salt-type minerals, such as apatite and calcite, is a combination of surface hydrolysis followed by preferential dissociation and adsorption of specifically adsorbing ions.

D. Isomorphous Replacement

The surface charge of clay particles serves as an example of a charging mechanism of this kind. To illustrate, consider the charging process of mica, a layered structure mineral in which 25% of the Si^{4+} ions are substituted by Al^{3+} ions, resulting in a positive charge deficiency. The excess negative charge in the matrix is compensated for by interstitial cations, such as K^+ or Na^+ , in order to keep the mineral neutral. These interstitial ions are usually small, weakly bonded to the matrix, and mobile. When mica is placed in water, the interstitial ions within the surface regions transfer into the water through a strong hydration force, leaving a net negative charge on the basal plane of the mica, which is pH-independent [13]. The hydrolysis of unsaturated bonds such as broken $\text{Si}-\text{O}$ and $\text{Al}-\text{O}$ bonds on the edges, followed by the dissociation of hydrated species creates, on the other hand, a pH-dependent surface charge. Therefore, H^+ and OH^- may also act as pzi's. For a clay mineral system, the surface charge density cannot be reduced to zero, although an apparent point of zero charge may exist. In this case, the basal plane and edge may still carry the charge of opposite signs although the overall effect shows a pzc.

The charging mechanisms described above do not cover a complete spectrum but rather focus on mechanisms often encountered in practice. A number of theoretical models have been developed to predict the sign of surface charge and point of zero charge. Examples are the Parks–deBruyn original minimum solubility treatment [14], Parks' adsorption model [15], the Lai–Fuerstenau site distribution model [16], the Yoon–Salman–Donnay fractional charge model [17], and, more recently, Miller's hydration model [18]. With these models, a variety of interfacial phenomena can be readily explained. In the following section, we demonstrate the use of a site-binding model incorporated with electrical double layer theories in predicting electrokinetics and understanding adsorption phenomena of ionic species on a charged surface.

III. A HYBRID TRIPLE-LAYER MODEL

To use the surface complexing phenomenon in various technological applications, it is essential to develop a predictive tool using a surface complexation model. For a charged surface, the electrostatic field of the particle is known to affect the distribution of ions in the interfacial region and the probability of a given species reacting with the surface. Therefore, the contribution of electrostatic free energy to the surface binding of various species must be considered. To incorporate the surface charge effect on the surface complexing process, a few models have been used including the diffuse double-layer model (DLM), the constant-capacitance model (CCM), the basic Stern model (BSM), the triple-layer model (TLM) [19], and recently the four-layer model (FLM) [20]. With these models, the effect of surface charge on surface complexation has two aspects: (1) ion distribution (usually Boltzmann's distribution of ionic species given by $\exp[-ze\psi/kT]$, where z is the charge of the adsorbing ions; e , elemental charge; ψ , electrical potential at the location of adsorbing ion; k , the Boltzmann constant; and T , temperature), and (2) electrostatic contribution ($\Delta G_{\text{elec}} = ZF\psi_0$) to the intrinsic (chemical) free energy of adsorption. The TLM in combination with surface complexation has been used extensively in developing a predictive tool for understanding the acid–base and metal-binding properties of oxide colloids and is considered to be satisfactory for most metal oxide and hydroxide systems [21–22]. It has been shown that only the triple-layer model incorporated with proper surface complex reactions can reproduce both the surface charge (σ_0)–pH and surface potential (ψ_0)–pH relationships [23–25]. However, a recent comparison among various models [25] showed that the TLM cannot give a satisfactory description of all the major adsorption phenomena such as charging curves, pH and salt dependency of cation adsorption, and hydrogen–cation exchange simultaneously. In this study, we describe a different approach based on, but not limited by, the existing triple-layer model shown schematically in Fig. 2.

In this model, there exist two charge-free layers and a diffuse double layer. The potential determining ions are located on a surface, designated by subscript 0, and are responsible for developing surface charge (σ_0). The surface potential at this plane (ψ_0) drops linearly across the inner Helmholtz layer to ψ_β at the inner Helmholtz plane (denoted by β), where most specifically adsorbing ions along

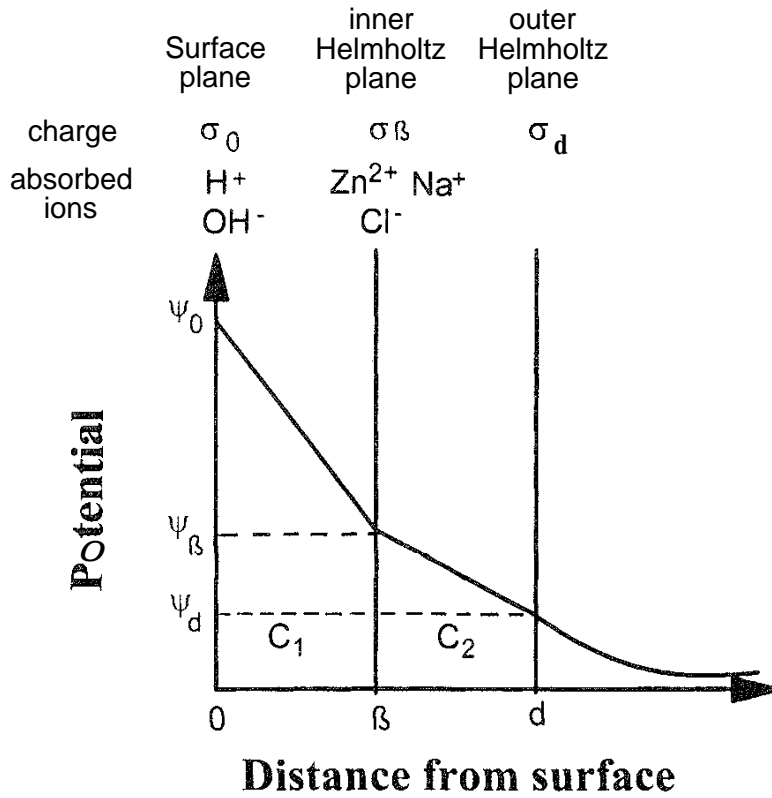


FIG. 2 Structure of electrical double layer around a sphalerite particle used in triple-layer model.

with pair formers are located. (Note: A fraction of specifically adsorbing ions, such as zinc ions, may locate on the surface and hence contribute to surface charge.) Further out in the solution phase, a second charge-free layer is present due to the adsorption of specific adsorbing ions along with ion pairs, with a further linear drop in the potential across this layer but at a reduced gradient. The plane dividing the compact layer and diffuse layer is referred to as the outer Helmholtz plane, where the diffuse layer starts (denoted by d). The potential at the outer Helmholtz plane coincides with the potential at the end of the diffuse double layer (ψ_d).

Based on the classical electrical double layer theory, the potential drop across the inner Helmholtz layer ($\psi_0 - \psi_\beta$) is related to the surface charge (σ_0) by

$$\sigma_0 = C_1(\psi_0 - \psi_\beta) \quad (1)$$

where C_1 is the integral capacitance of the inner Helmholtz layer, given by $\epsilon_0 \epsilon_r / x_\beta$, in which ϵ_0 and ϵ_r are the dielectric constant in a vacuum and relative dielectric constant, respectively, and x_β is the thickness of the layer. The potential drop across the outer Helmholtz layer, on the other hand, is given by

$$\sigma_d = C_2(\psi_d - \psi_\beta) \quad (2)$$

in which C_2 is the integral capacitance of the outer Helmholtz layer. Finally, according to the Gouy–Chapman–Stern diffuse layer theory, the potential at the outer Helmholtz plane is related to the charge density by [26–27]

$$\sigma_d = -0.1174z\sqrt{c} \sinh(19.46z \psi_d) \quad \text{C/m}^2 \quad (3)$$

in which c and z are the bulk concentration and charge, respectively, of the symmetrical electrolyte counterions in the diffuse layer. Based on the definition of differential capacitance of the diffuse double layer, C_2 in Eq. (2) can be expressed as

$$C_2 = -\frac{d\sigma_d}{d\psi_d} = 2.285z\sqrt{c} \cosh(19.46z\psi_d) \text{ F/m}^2 \quad (4)$$

Equations (1)–(4) are the foundations of electrical double layer theory and are often used in modeling the adsorption of metal ions at interfaces of charged solid and electrolyte solutions. In a typical TLM, the outer layer capacitance is often fixed at a lower value (i.e., $C_2 = 0.2 \text{ F/m}^2$), whereas inner layer capacitance (C_1) can be adjusted to between 1.0 and 1.4 F/m^2 [25]. It should be noted that the three-plane model (TPM) is a variation of the classical triple-layer model, in which the outer layer capacitance is not fixed. Although the physical presentations of the TLM and TPM are identical as shown in Fig. 2, i.e., both involve a surface layer (0), an inner Helmholtz plane (β), and an outer Helmholtz plane (d) where the diffuse double layer starts, a one-step protonation process (i.e., 1 pK approach) is, in general, assumed in the TPM, in contrast to a two-step protonation process (i.e., 2 pK approach) in the TLM. Another distinct difference is that pair-forming ions are assumed to be on the outer Helmholtz plane in the TPM but on the inner Helmholtz plane in the TLM. In our study, the outer layer capacitance is allowed to vary while the pair-forming ions are placed on the inner Helmholtz plane with a complete set of surface complexation reactions being considered. Therefore, our approach represents a hybrid of the TPM and TLM.

IV SITE-BINDING MODEL

To successfully model the surface charge and surface potential requires an accurate description of surface complexing reactions. For illustration purposes, we use sphalerite, a sulfide mineral, as an example to show the surface site-binding model [28,29]. The first step in the model development is to identify the surface species. In the present case these are $\equiv \text{ZnSH}^+$, $\equiv \text{SZnOH}^-$, and $\equiv \text{SH}_2$, with \equiv representing the surface. The second step involves considerations of all species present in the inner Helmholtz plane for the system of interest. For sphalerite in a simple electrolyte solution (NaCl), as in our example, the species includes $\equiv \text{SZnOH}^- - \text{Zn}^{2+}$, $\equiv \text{SZnOH}^- - \text{Na}^+$, and $\equiv \text{ZnSH}^+ - \text{Cl}^-$. With all the species being identified, the complexing reactions associated with these species need to be specified and the mass action law applied. These are summarized in Table 1 for the current example.

The constants K_1 – K_6 in Table 1 are site-binding constants, and the subscript s represents concentration of surface species, which is related to the corresponding bulk concentration $[C]$ through $[C]_s = [C] \exp\{-ze\psi/kT\}$, i.e., Boltzmann's distribution. Replacing all surface concentrations in Eqs. (1)–(6) by this relation, and rearranging them, the concentration of individual species can then be expressed in terms of the concentrations of two basic surface species ($\equiv \text{SZn}$ and $\equiv \text{ZnS}$), the bulk concentrations of ionic species (Zn^{2+} , Na^+ , and Cl^-), and the electrical potential at the locations of ions through corresponding site-binding constants. These relations are summarized in Table 2 for ease of reference.

TAE Summary of Surface Species and Corresponding Surface Complexation Reactions for Sphalerite in NaCl Solutions

| Species | Reactions | Mass action law | Eq. |
|--|---|--|-------|
| $\equiv \text{S}\ddot{\text{S}}$ | $\equiv \text{S}\text{Zn} + 2\text{H}^+ = \equiv \text{SH}_2 + \text{Zn}^{2+}$ | $K_1 = \frac{[\equiv \text{SH}_2][\text{Zn}^{2+}]_s}{[\equiv \text{SZn}][\text{H}^+]_s^2}$ | (5a) |
| $\equiv \text{SZnOH}^-$ | $\equiv \text{SZn} + \text{H}_2\text{O} = \text{SZnOH}^- + \text{H}^+$ | $K_2 = \frac{[\equiv \text{SZnOH}^-][\text{H}^+]_s}{[\equiv \text{SZn}][\text{H}_2\text{O}]}$ | (6a) |
| $\equiv \text{ZnSH}^+$ | $\equiv \text{ZnS} + \text{H}^+ = \equiv \text{ZnSH}^+$ | $K_3 = \frac{[\equiv \text{ZnSH}^+]}{[\equiv \text{ZnS}][\text{H}^+]_s}$ | (7a) |
| $\equiv \text{SZ}\ddot{\text{O}}\text{H}^- - \text{Zn}^{2+}$ | $\equiv \text{SZ}\ddot{\text{O}}\text{H}^- + \text{Zn}^{2+} = \equiv \text{SZ}\ddot{\text{O}}\text{H}^- - \text{Zn}^{2+}$ | $K_4 = \frac{[\equiv \text{SZnOH}^- - \text{Zn}^{2+}]}{[\equiv \text{SZnOH}^-][\text{Zn}^{2+}]_s}$ | (8a) |
| $\equiv \text{SZ}\ddot{\text{O}}\text{H}^- - \text{Na}^+$ | $\equiv \text{SZ}\ddot{\text{O}}\text{H}^- + \text{Na}^+ = \equiv \text{SZ}\ddot{\text{O}}\text{H}^- - \text{Na}^+$ | $K_5 = \frac{[\equiv \text{SZnOH}^- - \text{Na}^+]}{[\equiv \text{SZnOH}^-][\text{Na}^+]_s}$ | (9a) |
| $\equiv \text{ZnSH}^+ - \text{Cl}^-$ | $\equiv \text{ZnSH}^+ + \text{Cl}^- = \equiv \text{ZnSH}^+ - \text{Cl}^-$ | $K_6 = \frac{[\equiv \text{ZnSH}^+ - \text{Cl}^-]}{[\equiv \text{ZnSH}^+][\text{Cl}^-]_s}$ | (10a) |

TABLE 2 Expressions of Surface Species in Terms of Basic Surface Components ($\equiv\text{SZn}$ and $\equiv\text{ZnS}$), Bulk Concentration of Ionic Species (Zn^{2+} , Na^+ , and Cl^-), and Electrical Potential

| Species | Expression | Eq. |
|---|---|-------|
| $\equiv\text{SH}_2$ | $[\equiv\text{SH}_2] = \frac{K_1[\equiv\text{SH}_2][\text{Zn}^{2+}]}{[\equiv\text{SZn}][\text{H}^+]^2}$ | (5b) |
| $\equiv\text{SZnOH}^-$ | $[\equiv\text{SZnOH}^-] = \frac{K_2[\equiv\text{SZn}]}{[\text{H}^+]} \exp\left[\frac{e\psi_0}{kT}\right]$ | (6b) |
| $\equiv\text{ZnSH}^+$ | $[\equiv\text{ZnSH}^+] = K_3[\equiv\text{SZn}][\text{H}^+] \exp\left[\frac{e\psi_0}{kT}\right]$ | (7b) |
| $\equiv\text{SZnOH}^- - \text{Zn}^{2+}$ | $[\equiv\text{SZnOH}^- - \text{Zn}^{2+}] = K_2 K_4 \frac{[\equiv\text{SZn}][\text{Zn}^{2+}]}{[\text{H}^+]} \exp\left[\frac{e\psi_0}{kT}\right] \exp\left[\frac{-2e\psi_\beta}{kT}\right]$ | (8b) |
| $\equiv\text{SZnOH}^- - \text{Na}^+$ | $[\equiv\text{SZnOH}^- - \text{Na}^+] = K_2 K_5 \frac{[\equiv\text{SZn}][\text{Na}^+]}{[\text{H}^+]} \exp\left[\frac{e\psi_0}{kT}\right] \exp\left[\frac{-e\psi_\beta}{kT}\right]$ | (9b) |
| $-\text{Cl}^-$ | $[-\text{Cl}^-] = K_3 K_6 [\equiv\text{ZnS}][\text{H}^+][\text{Cl}^-] \exp\left[\frac{e\psi_0}{kT}\right] \exp\left[\frac{e\psi_\beta}{kT}\right]$ | (10b) |

V BALANCE EQUATIONS

After establishing the surface complexing reactions [Eqs. (5)–(10), Tables 1 and 2] the charge densities at various planes can be derived by using speciation concentrations. The surface charge, for example, is given by the summation of all ionic species on the surface, i.e.,

$$\sigma_0 = B\{[\equiv \text{ZnSH}^+] + [\equiv \text{ZnSH}^+ - \text{Cl}^-] - [\equiv \text{SZnOH}^-] - [\equiv \text{SZnOH}^- \text{Na}^+] - [\equiv \text{SZnOH}^- - \text{Zn}^{2+}]\} \quad (11)$$

where B is a conversion factor from surface concentration (mol/L) to surface charge density (C/m^2), and is given by $B = F/(Sa c')$, in which F , Sa and c' are the Faraday constant, the specific surface area (m^2/g) and the solid concentration (g/L), respectively. Similarly, at the β plane, the specifically adsorbed charge is

$$\sigma_\beta = B\{[\equiv \text{SZnOH}^- - \text{Na}^+] + 2[\equiv \text{SZnOH}^- - \text{Zn}^{2+}] - [\equiv \text{ZnSH}^+ - \text{Cl}^-]\} \quad (12)$$

The corresponding species concentrations in Eqs. (11) and (12) are given by Eqs. (5b)–(10b) (Table 2). Considering electrical neutrality of the system, the accumulated charges in the compact layers must be compensated for by an equivalent amount of opposite charges (σ_d) in the diffuse layer, i.e.,

$$\sigma_s + \sigma_\beta + \sigma_d = 0 \quad (13)$$

Assuming that surface species are distributed among the total number of available surface sites, N_s (sites/ m^2), one final condition that has to be satisfied is the surface mass balance given by

$$N_s e = B\{[\equiv \text{ZnS}] + [\equiv \text{SZn}] + [\equiv \text{SH}_2] + [\equiv \text{ZnSH}^+] + [\equiv \text{ZnSH}^+ - \text{Cl}^-] + [\equiv \text{SZnOH}^-] + [\equiv \text{SZnOH}^- - \text{Na}^+] + [\equiv \text{SZnOH}^- - \text{Zn}^{2+}]\} \quad (14)$$

VI. DETERMINATION OF SITE-BINDING CONSTANTS

One of the major uses of setting up these fundamental relations and constraints is to determine site-binding constants of surface complexing reactions (K_1 – K_6). These constants are the foundation for various applications, such as predicting the surface charge density and potentials, identifying adsorption characteristic of metal ions on solids, and calculating the distribution of surface species. In our hybrid TLM approach, the basic information required to solve this complex problem is a set of experimental $\psi_{0/d}(\text{pH})$ or $\sigma_0(\text{pH})$ (at least as many data points as the parameters to be estimated minus balance constraints imposed, i.e., five for the above example). In this chapter we use $\psi_{0/d}(\text{pH})$ as our input variables. Although it is possible to measure ψ_0 using ion-sensitive field effect transistors [30], a common approach is to use the zeta potential (ζ) as an approximation of ψ_d [7,28–29,31] due to its access experimentally. The possible error involved with this approximation was addressed in detail earlier [32]. The effect of shifting the slip plane, where ζ is measured, a known distance Z into the solution on the fitted site-binding constants can be examined using the exact solution of the Poisson equation [33].

The measured zeta potentials of sphalerite at different electrolyte concentrations were fitted with the above model using a numerical approach, and the fitted site-binding constants are summarized in Table 3. It is evident that the fitted equilibrium constants are independent of electrolyte concentrations, as expected for a thermodynamic variable. Also shown in this table is a relatively constant integral capacitance of the inner Helmholtz layer (0.68 ± 0.01 F/m²). This value is in the range of reported values (0.2–2.4 F/m²) for various sulfide, oxide, and hydroxide materials [19,34–37]. A slightly larger pair formation constant was obtained for sodium ions ($pK_5 = -3.45$) than for chloride ions ($pK_6 = -3.05$), although both bond to the surface by electrostatic interactions. Similar asymmetrical pair formation constants of Na⁺ and NO₃[−] were also reported [34]. A larger binding constant representing stronger binding appears to be associated with smaller cations (Na⁺ = 0.095 nm) than with anions (Cl[−] = 0.181 nm) [9]. This difference in pair binding constants causes a shift of iep from pzc, and the self-consistency, i.e., $\text{pH}_{\text{iep}} = (\text{p}K_{a1} + \text{p}K_{a2})/2$ as often assumed in the conventional TLM, breaks [38]. This accounts, partially, for the observed poor description of the pH dependency of metal ion binding encountered with the conventional TLM [25].

With these site-binding constants being determined, the ζ value of sphalerite in electrolyte solutions can be calculated as a function of pH, and the results are shown in Fig. 3 by solid lines (only three NaCl concentrations are shown for clarity). The excellent fit of the prediction with the experimental results is illustrated by all the points lying on the predicted curve. These results testify to the significant improvement achieved by our hybrid TLM over the conventional TLM which cannot predict accurately both pH and ionic strength dependence of surface potentials. The improvement is due in part to allowing the variations of differential capacitance across the diffuse double layer, given by Eq. (4), in contrast to the conventional TLM, in which the capacitance of the outer Helmholtz layer is assumed to be independent of electrolyte concentrations.

VII PREDICTION OF SURFACE CHARGE DENSITY

In the above example, a hybrid TLM was developed for a sphalerite in NaCl solutions. This approach can be readily applied to other systems. To illustrate its versatility, experimental data on the boehmite water interface, generously provided

TABLE 3 Best-Fit Parameters for Sphalerite in NaCl Solutions

| [NaCl](M) | pK_1 | pK_2 | pK_3 | pK_4 | pK_5 | pK_6 | C_1 (F/m ²) |
|-----------|--------|--------|--------|--------|--------|--------|---------------------------|
| 10^{-1} | −1.45 | 4.53 | −1.16 | −3.25 | −3.51 | −3.05 | 0.70 |
| 10^{-2} | −1.45 | 4.52 | −1.15 | −3.24 | −3.49 | −3.05 | 0.68 |
| 10^{-3} | −1.43 | 4.50 | −1.13 | −3.23 | −3.49 | −3.05 | 0.68 |
| 10^{-4} | −1.43 | 4.51 | −1.14 | −3.22 | −3.48 | −3.06 | 0.67 |
| 10^{-5} | −1.44 | 4.50 | −1.13 | −3.24 | −3.48 | −3.05 | 0.66 |
| Average | −1.44 | 4.51 | −1.14 | −3.24 | −3.49 | −3.05 | 0.68 |
| Std dev | 0.01 | 0.01 | 0.01 | 0.01 | 0.01 | 0.01 | 0.01 |

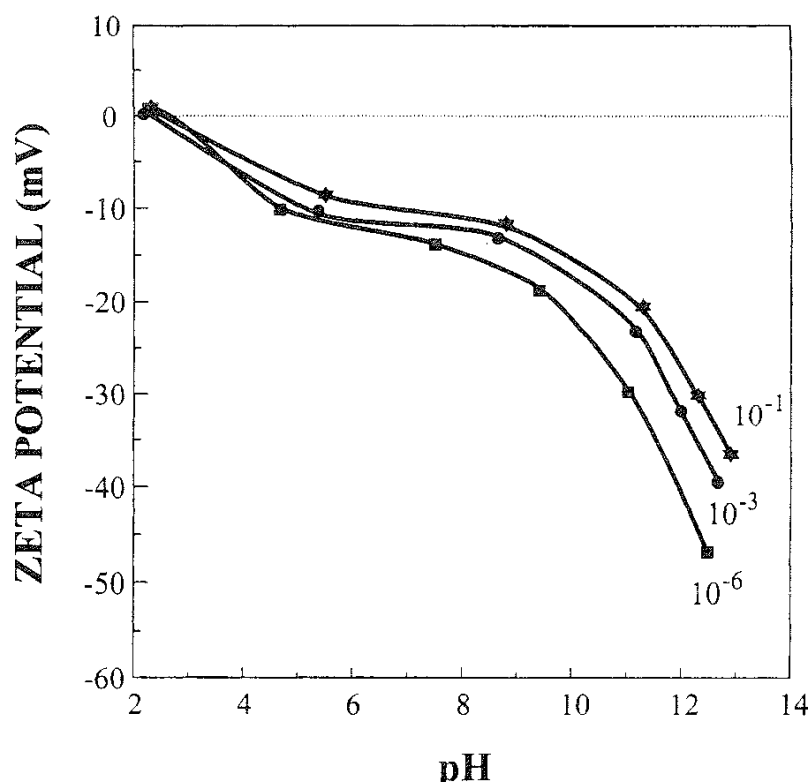


FIG. 3 Comparison between the predicted using hybrid triple-layer model and measured zeta potentials of sphalerite particles in NaCl solutions.

by Wood et al. [35], were examined. The fitted parameters are given in Table 4, along with those obtained by Wood et al. with the conventional TLM. Although the fitted parameters from both approaches are comparable as shown in Table 4, a better fitting by our hybrid TLM is seen clearly in Fig. 4. An important improvement in the numerical procedure used here over those published previously is that experimental data on surface charge density are not required in the fitting process. With the fitted site-binding constants, on the other hand, $\sigma_0\{\text{pH}, [\text{KNO}_3]\}$ can be calculated. For boehmite in KNO_3 solutions, the calculated $\sigma_0\{\text{pH}, [\text{KNO}_3]\}$ is also shown in Fig. 4. The excellent agreement between the measured and calculated $\sigma_0\{\text{pH}, [\text{KNO}_3]\}$ seen in this figure further supports our hybrid TLM.

TABLE 4 Best-Fit Parameters for Boehmite in KNO_3 Solutions

| KNO_3 (M) | $\text{p}K_1$ | $\text{p}K_2$ | $\text{p}K_3$ | $\text{p}K_4$ | C_1 (F/m ²) |
|--------------------|---------------|---------------|---------------|---------------|---------------------------|
| 10^{-1} | 6.4 | 11.5 | 7.2 | 9.8 | 0.60 |
| | 6.3 | 10.9 | 7.8 | 9.5 | 0.55 |
| Wood et al. [35] | 6.3 | 11.9 | 7.5 | 9.6 | 0.59 |

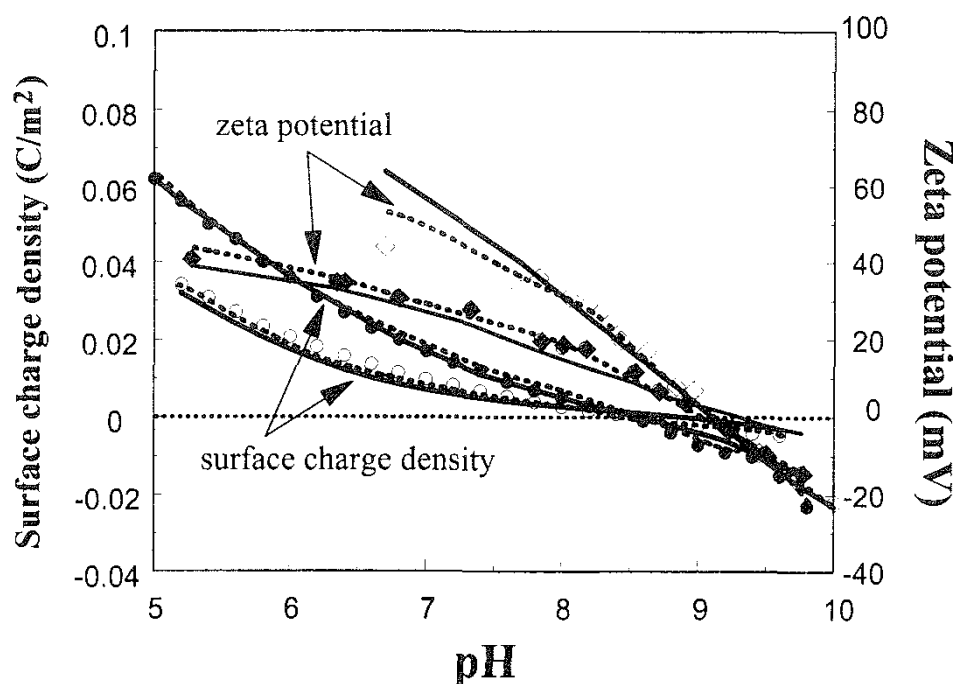


FIG. 4 Comparison between the predicted, using triple-layer and hybrid triple-layer models, and measured surface charge density and zeta potential of boehmite in KNO_3 solutions.

VIII. EFFECT OF ION ADSORPTION ON THE ZETA POTENTIAL

The hybrid TLM described above can be further extended to the adsorption of metal ions on metal oxide, hydroxide, or sulfide surfaces. As an example, the adsorption of ferrous ions on sphalerite, which causes unintentional activation of sphalerite [39,40], is examined. Additional species to be considered include FePH^+ and Fe(OH)_2 , while Fe(OH)_3^- and Fe(OH)_4^{2-} are not considered because of their relatively low concentrations in the pH range of current interest ($\text{pH} > 8$). It has been noted that the ferrous species on the sphalerite surface oxidizes to the corresponding ferric species. Therefore, the redox reaction on a sphalerite surface needs to be considered by including the corresponding ferric hydroxy species in surface complexing reactions. The reactions considered in addition to those shown in Table 1 are given in Table 5.

Similarly, the surface binding constants can be obtained numerically from the above surface complexation model in combination with the electrical double layer theories, including one additional constraint, total iron balance [29]. Assuming that all the binding constants (K_1 – K_9) are unknown in our hybrid TLM, the best-fit parameters to the experimental ζ (pH) relation are given in Table 6. Also shown in this table are the fitted parameters for sphalerite in NaCl solutions. It is interesting to note the excellent agreement between the binding constants K_1 – K_6 obtained in the presence and absence of ferrous ions, further reinforcing the fidelity of our hybrid TLM. The excellent fit between the predicted and measured ζ (pH) relations has been reported elsewhere [29].

ABLE 5 Additional Iron-Containing Surface Species and Corresponding Surface Complexation Reactions for Sphalerite in NaCl solutions Containing Ferrous Ions

| reaction | Mass action law | Eq. |
|--|--|-------|
| $\text{SZnOH}^- + \text{FeOH}^+ - e = \equiv \text{SZnOH}^- - \text{FeOH}^{2+}$ | $K_7 = \frac{[\text{SZnOH}^- - \text{FeOH}^{2+}]}{[\equiv \text{SZnOH}^-][\text{FeOH}^+]_s}$ | (15a) |
| $\text{nOH}^- + \text{FeOH}^+ + \text{OH}^- - e = \equiv \text{SZnOH}^- - \text{Fe}(\text{OH})_2^+$ | $K_8 = \frac{[\equiv \text{SZnOH}^- - \text{Fe}(\text{OH})_2^+]}{[\equiv \text{SZnOH}^-][\text{OH}^-]_s[\text{FeOH}^+]_s}$ | (16a) |
| $\equiv \text{SZnOH}^- + \text{FeOH}^+ + 2\text{OH}^- - e = \equiv \text{SZnOH}^- - (\text{FeOH})_3$ | $K_9 = \frac{[\equiv \text{SZnOH}^- - \text{Fe}(\text{OH})_3]}{[\equiv \text{SZnOH}^-][\text{FeOH}^+]_s[\text{OH}^-]_s^2}$ | (17a) |

TABLE 6 Best-Fit Surface Binding Constants and Integral Capacitance Using the Hybrid TLM for Sphalerite in 0.01 M NaCl Solutions with (I ppm) and Without Ferrous Ions

| System | pK_1 | pK_2 | pK_3 | pK_4 | pK_5 | pK_6 | pK_7 | pK_8 | pK_9 | C_1 (F/m ²) |
|---------|--------|--------|--------|--------|--------|--------|--------|--------|--------|------------------------------|
| With Fe | -1.40 | 4.52 | -1.15 | -3.25 | -3.49 | -3.05 | -3.27 | -3.40 | -0.54 | 0.65 |
| No Fe | -1.45 | 4.52 | 1.15 | -3.24 | -3.49 | -3.05 | — | — | — | 0.68 |

With the surface binding constants being determined the adsorption of ferrous ions on sphalerite can be predicted with the use of commercial packages such as MINEQL, developed by Westall et al. [41], or SOILCHM, developed by Sposito and Coves [42]. Here we focus on the effect of ferrous ion adsorption on the sphalerite zeta potential. Using the best-fit surface binding constants (K_1 – K_9), the zeta potentials of sphalerite as a function of ferrous ion concentration at various pH values are calculated and the results are given as solid lines in Fig. 5, along with the measured ζ values under the same conditions. Here, the excellent agreement between the two is evident. For all pH values studied, a similar effect of ferrous ions on ζ of sphalerite was observed, i.e. the zeta potential increases initially with ferrous

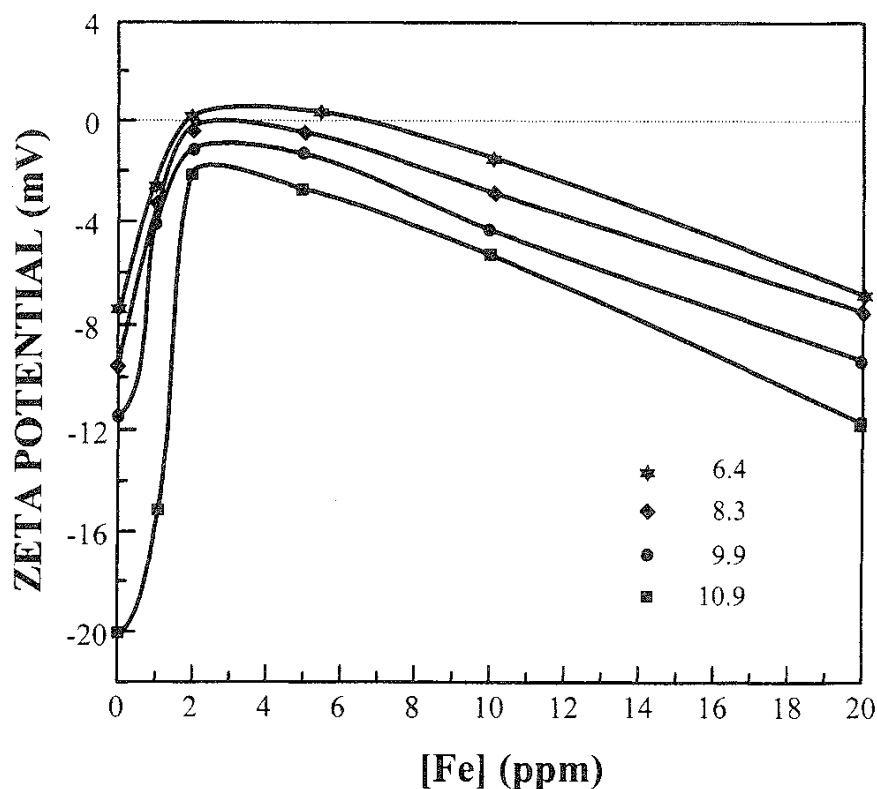


FIG. 5 Effect of ferrous ion addition on zeta potentials of sphalerite: prediction versus measurement.

ion concentration, reaching a maximum at 2 ppm, and followed by a slight decrease with a further increase in ferrous ion concentration. This type of calculation provided valuable insight into the role of ferrous ions in sphalerite activation [39].

IX. PREDICTION OF SURFACE SPECIES

The species generated on nanoparticles or porous media play an important role in a variety of technological applications. For instance, some biological enzymes will react only with (protonated) cationic surface sites, while other metal ions may react with anionic surface ligands only. Changing the pH of the system often transfers these sites from one molecular form to another. It is therefore crucial to be able to predict and identify the surface species. With the hybrid TLM, reliable surface binding constants can be obtained, from which the surface species concentration can be calculated readily. As an example, we calculated the surface concentration of various iron-containing species on a sphalerite surface as a function of pH, and the results are given in Fig. 6. Also calculated are the ferrous species distributions in solution with (Fig. 7a) and without (Fig. 7b) sphalerite. Figure 6 shows that the concentration of ferrous species on sphalerite is relatively low compared with that in solution. The main species on the surface at pH 8–10 is $\equiv\text{SZnOH}^- - \text{FeOH}^{2+}$, which may be responsible for unintentional activation of sphalerite by iron. Also shown in Fig. 6 is that $\equiv\text{SZnOH}^- - \text{FeOH}^{2+}$ reaches a maximum at $\text{pH} \sim 10$, as does the zeta potential of sphalerite [29]. These findings correspond to the sphalerite flotation observed around pH 10 with xanthate collector in the presence of ferrous ions [39], strongly

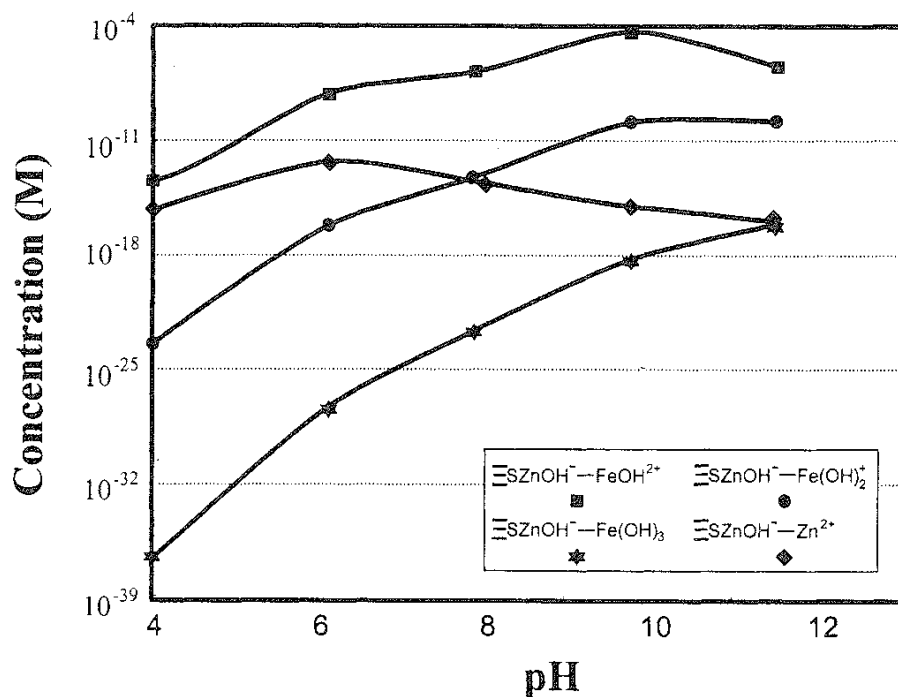


FIG. 6 Predicted surface distribution of iron-containing species relevant to sphalerite flotation.

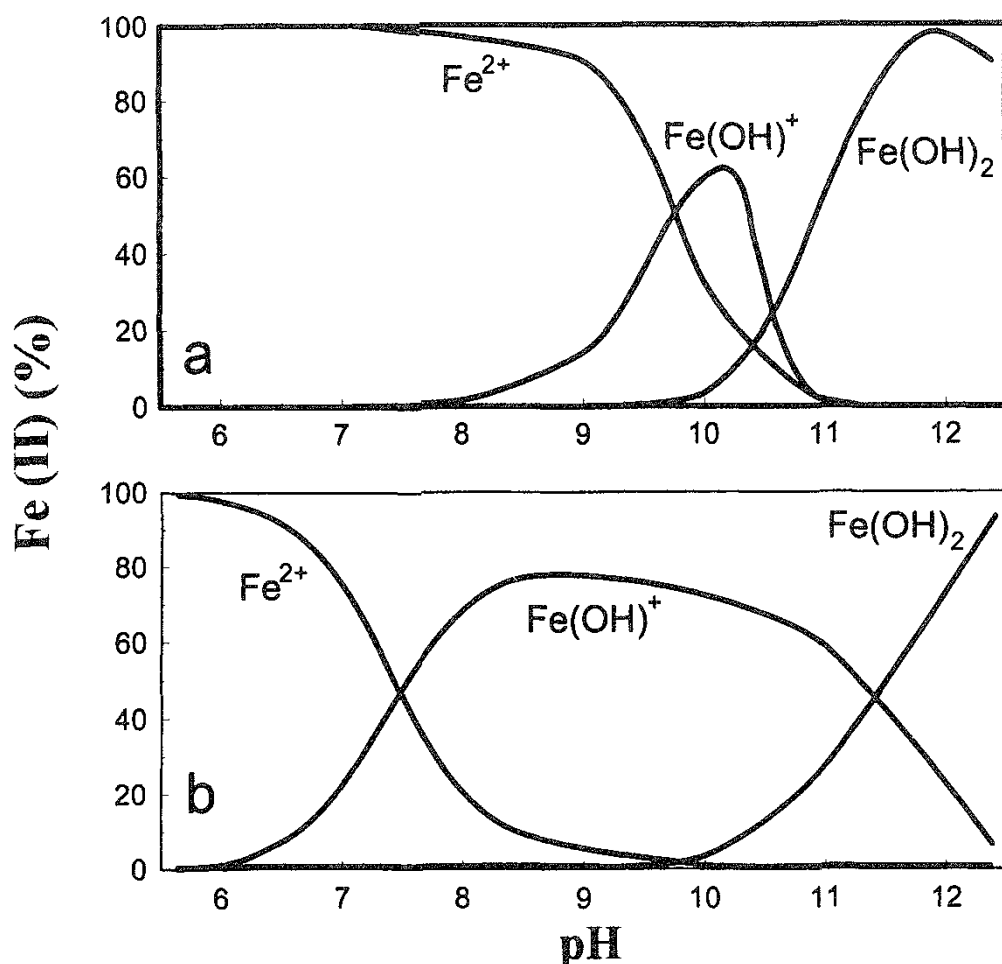


FIG 7 Predicted effect of sphalerite on distribution of iron-containing species in solution (a) with (b) without sphalerite.

suggesting that $\equiv\text{SZnOH}^- \cdots \text{FeOH}^{2+}$ is the principal species responsible. This conclusion is in general agreement with that from the previous work by X-ray photoelectron spectroscopy and Fourier transform infrared spectroscopy [40].

Comparing the ferrous species distributions in Fig. 7a with those in Fig. 7b, we see the similar main features. However, species concentration changes gradually in the presence of sphalerite, suggesting that the concentrations of ferrous species are buffered by sphalerite. This finding may provide an alternative avenue to buffer species by adding fine solids.

X. CURRENT STATUS

In the previous sections, we have demonstrated that a hybrid approach integrating the useful features of the triple-layer model and the three-plane model allows accurate description of the zeta potential (pH) for a range of electrolyte concentrations and excellent prediction of the surface charge density vs. pH relationship. As noted, the effect of replacing ψ_d by ζ in the TLM needs to be further examined by

investigating the effect of shifting the slip plane on the fitted parameters. A sensitivity study using the $\psi_d(Z)$ relation proposed by Blesa and Kallay [43] will be useful.

The current hybrid TLM remains based on all the ions in the compact layers being located at a single plane. However, due to the variations in size of various ions, such as Cl, Na, and Zn, in our case the assumption needs to be further justified by using a recently developed four-layer or yet to be developed five-layer model. Introducing more layers for ions of various sizes is equivalent to redistributing the charges at various planes and hence involves more capacitors in series. The integral capacitance in our model is actually an equivalent of two capacitors (described by the four-layer model) in series. The pH dependence of adsorption can be examined by varying the position of the planes in which various ions adsorb. Due to the practical importance of surfactant adsorption in many disciplines, the development of a new model is urged to include the adsorption of ionic species such as surfactant, at both the inner (β) and outer (d) Helmholtz planes where activated sites are present. In this case, the hybrid triple-layer model needs to be further refined to account for the contributions of charges from the adsorbed ionic surfactant species.

XI. SUMMARY

In this chapter, a novel hybrid triple-layer model was described. Three significant differences between the hybrid and conventional triple-layer models were noted:

1. No assumption was made with regard to 1 pK or 2 pK approach in contrast to the conventional triple-layer model in which an assumption of $\text{iep} = (\text{p}K_{a1} + \text{p}K_{a2})/2$, valid only for a system of symmetrical binding of pair-formation ions, is often involved,
2. The capacitance of the outer Helmholtz layer was allowed to vary (following the differential capacitance of the diffuse double layer), in contrast to being fixed in the conventional TLM.
3. The surface charge density was not required as input; rather it was calculated from the fitted equilibrium constants of surface complexing reactions. An improved fit was clearly demonstrated with the hybrid triple-layer model compared to the conventional one.

The sphalerite–ferrous surface binding constants in NaCl solutions were determined. Applications of the hybrid triple-layer model in predicting electrokinetics, surface charge density, metal ion adsorption, and surface solution speciation were described and illustrated with examples.

REFERENCES

1. P. L. De Bruyn and G. E. Agar. in *Froth Flotation* (D. W. Fuerstenau, ed.), AIME, New York, 1962, pp. 91–138.
2. J. A. Topps and D. W. Fuerstenau, *J. Colloid Interface Sci.* 19:61 (1964).
3. P. Somasundaran and K. P. Ananthapadmanabhan, *Trans. Indian Inst. Metals* 32:177 (1979).

4. M. C. Fuerstenau, J. D. Miller, and M. C. Kuhn, *Chemistry of Flotation*, SME, AIME, New York, 1985.
5. D. Myers, *Surface, Interfaces, and Colloids—Principles and Applications*, VCH, New York, 1991.
6. E. P. Honig and J. H. Th. Hengst, *J. Colloid Interface Sci.* 31:545 (1969).
7. H. J. Modi and D. W. Fuerstenau, *J. Phys. Chem.* 61:640 (1957).
8. M. E. Labib, *Colloids Surf.* 29:293 (1988).
9. J. N. Israelachvili, *Intermolecular and Surface Forces*, 2nd ed., Academic, San Diego, 1992.
10. A. N. Frumkin, *Z. Phys. Chem.* 109:34 (1924).
11. R. H. Yoon and J. L. Yordan, *J. Colloid Interface Sci.* 113:430 (1986).
12. D. A. Haydon, *Biochim. Biophys. Acta* 50:450 (1961).
13. H. van Olphen, *An Introduction to Clay Colloid Chemistry*, Interscience, New York, 1963.
14. G. A. Parks and P. L. deBruyn, *J. Phys. Chem.* 66:967 (1962).
15. G. A. Parks, *Chem. Rev.* 65:177 (1965).
16. R. Lai and D. W. Fuerstenau, *AIME Trans.* 260:104 (1976).
17. R. H. Yoon, T. Salman, and G. Donnay, *J. Colloid Interface Sci.* 70:483 (1979).
18. J. D. Miller, M. R. Yalamanchili, and J. J. Keller, *Langmuir* 8:1464 (1992).
19. J. A. Davis and J. O. Leckie, *J. Colloid Interface Sci.* 67:90 (1978).
20. R. Charmas, W. Piasecki, and W. Rudzinski, *Langmuir*, 11:3199 (1995).
21. A. P. Robertson and J. O. Leckie, *J. Colloid Interface Sci.* 188:144 (1997).
22. L. E. Katz and K. M. Hayes, *J. Colloid Interface Sci.* 170:477 (1995).
23. G. R. Wright and R. J. Hunter, *Aust. J. Chem.* 26:1183 (1973).
24. J. C. Westall and H. Hohl, *Adv. Colloid Interface Sci.* 12:265 (1980).
25. P. Venema, T. Hiemstra, and W. H. Riemsdijk, *J. Colloid Interface Sci.* 181:45 (1996).
26. R. J. Hunter, *Foundations of Colloid Science*, Oxford. New York, 1986.
27. W. Stumm and J. J. Morgan, *Aquatic Chemistry*, 3rd ed., Wiley-Interscience, New York, 1996.
28. Q. Zhang, Z. Xu, and J. A. Finch, *J. Colloid Interface Sci.* 169:414 (1995).
29. Q. Zhang, Z. Xu and J. A. Finch, *J. Colloid Interface Sci.* 175:61 (1995).
30. P. Bergveld, *IEEE Trans. Biomed. Eng.* 17:70 (1970).
31. D. Fornasiero and J. Ralston, *J. Colloid Interface Sci.* 151:225 (1992).
32. W. Rudzinski, R. Charmas, S. Partyka, F. Thomas, and J. Y. Bottero, *Langmuir* 8:1154 (1992).
33. R. Charmas, W. Piasecki, and W. Rudzinski, *Langmuir* 11:3199 (1995).
34. D. Fornasiero, V. Eijt, and J. Ralston, *J. Colloid Interface Sci.* 62:63 (1992).
35. R. Wood, D. Fornasiero, and J. Ralston, *Colloid Surf.* 51:389 (1990).
36. L. K. Koopal, W. H. van Riemsdijk, and G. H. Bolt, *J. Colloid Interface Sci.* 118:117 (1987).
37. A. W. M. Gibb and L. K. Koopal, *J. Colloid Interface Sci.* 134:122 (1990).
38. R. J. Crawford, I. H. Harding, and D. E. Mainwaring, *J. Colloid Interface Sci.* 181:561 (1996).
39. Q. Zhang, S. R. Rao, and J. A. Finch, *Colloids Surf.* 169:414 (1995).
40. S. H. R. Brienne, Q. Zhang, I. S. Butler, Z. Xu, and J. A. Finch, *Langmuir* 10:3582 (1994).

41. J. C. Westall, J. L. Zachary, and F. Morel, Technical Note 18, Water Quality Laboratory. Department of Civil Engineering, MIT, 1976.
42. G. Sposito and J. Coves, *SOILCHEM Manual*. University of California, Berkeley, 1988.
43. M. A. Blesa and N. Kallay, Adv. Colloid Interface Sci. 28:111 (1988).

The Surface Charge of Alkali Halides in Their Saturated Solutions

JAN D. MILLER and SRINIVAS VEERAMASUNENI Department of
Metallurgical Engineering, University of Utah, Salt Lake City, Utah

- I. Introduction
- II. Simplified Lattice Ion Hydration Theory
- III. Nonequilibrium Electrophoretic Measurements
 - A. Electrokinetic phenomena — electrophoresis
 - B. Laser-Doppler electrophoresis
 - C. Results and discussion
- IV. Extended Lattice Ion Hydration Theory
 - A. Case A (KF, RbF, CsF, CsCl, CsBr, and CsI)
 - B. Case B (LiF, NaF, LiCl, NaCl, LiBr, NaBr, LiI, NaI, and KI)
 - C. Case C (KCl, RbCl, KBr, RbBr, and RbI)
 - D. The sign of the surface charge
- V. Oxygen Defect States
- VI. Conclusions
- References

I. INTRODUCTION

The importance of surface charge in understanding important phenomena such as adsorption, crystallization, and coagulation/dispersion has been well established for many different systems [1–3]. Until recently the significance of surface charge at high ionic strengths was questioned. It is now evident that in such systems it is very important. For example, the flotation of alkali halide particles from their saturated solution is controlled in many instances by the sign of the surface charge of the alkali halide particles.

The significance of surface charge in alkali flotation systems was very controversial when it was first introduced in 1967 by Roman et al. [4]. Critics argued that

in such systems the double layer is collapsed and electrostatic particle interaction forces do not become significant except at very close separation distances. Furthermore, Roman et al. [4] failed to show any direct experimental evidence to validate the hypothesis. Conventional electrophoresis could not be used to study soluble salts because of the difficulty in obtaining colloidal sized particles and also because of the high conductivity of the solutions [5]. In addition, the streaming potential technique was evaluated without success. Later, Pizarro [6] had similar problems in providing experimental evidence regarding the role of surface charge in the flotation of alkali oxyanion salt systems. Since then, the advent of the laser-Doppler electrophoretic technique has made possible the characterization of certain interesting systems including soluble salt systems that were hitherto not investigated due to the lack of an appropriate experimental technique.

Based on nonequilibrium electrokinetic measurements for alkali halides by laser-Doppler electrophoresis reported by Miller et al. [7], the sign of the surface charge of alkali halides in their saturated brines has been established. The surface charge results thus determined are generally as expected from simplified lattice ion hydration theory. However, there are seven exceptions—LiF, NaCl, KCl, KBr, RbBr, KI, and RbI—when the results from nonequilibrium electrophoretic measurements by laser-Doppler electrophoresis are compared with the predictions from lattice ion hydration theory. Previously it was observed [7,8] that in almost each case inaccurate predictions occur when the difference between cationic and anionic gaseous hydration energies is small. However, more recent theoretical analysis [9] has shown that when the surface is considered to be partially hydrated, dependent on the properties of the lattice ions such as the ionic radius (steric effect) and the hydration number (hydration effect), the sign of the surface charge of all alkali halides except for KCl can be accurately predicted by this extended lattice ion hydration theory.

Finally, it has been shown by Yalamanchili and Miller [10] that oxygen defects present in the KCl lattice can strongly influence its surface charge characteristics and the negative deviation of KCl from theory can be explained by the presence of oxygen defects. Further, Veeramasuneni et al. [11] showed that oxygen defects deliberately introduced into positively charged NaCl can reverse the surface charge.

The fundamental aspects of, and some recent contributions to, the analysis of surface charge of alkali halides in their saturated solutions include simplified lattice ion hydration theory, nonequilibrium electrophoresis [7], extended lattice ion hydration theory [9], and oxygen defect states [10,11], and these issues are discussed in the following sections.

II. SIMPLIFIED LATTICE ION HYDRATION THEORY

Surface charge at mineral surfaces can be generated by one or more mechanisms. The most commonly encountered charging mechanisms include dissociation of surface acid groups [12–14], lattice substitution [15–17], preferential hydration of surface lattice ions, and preferential adsorption phenomena [18–20]. In some cases, a surface may be charged by the orientation of dipoles or by surface polarization. Of particular concern in the case of alkali halides is the preferential hydration of

surface lattice ions. De Bryn and Agar [15] first described this mechanism for nonreactive ionic solids in terms of lattice ion hydration theory.

The simplified lattice ion hydration theory describes surface charge development by nonreactive ionic solids placed in water. This theory applies to ionic solids that do not react with water to form weak surface acid groups (hydrolysis) and to ionic solids that do not undergo surface oxidation reactions. Either reaction type would modulate the surface charge that the solid develops in water. The only reaction of consequence then is the hydration of lattice ions, and the differential hydration of these lattice ions at the surface of the solid determines the sign of the surface charge.

The theory as first proposed by deBruyn and Agar [15] was for simple uni-univalent salts in which the cation and anion are at interchangeable lattice positions, which is to say that their lattice energies are equivalent. In this elementary case, the surface charge can be estimated simply from a comparison of the hydration free energies of the corresponding gaseous ions. Until recently, this concept has been demonstrated only for certain silver halides as shown in Table 1, where the surface charge of the silver halides predicted by lattice ion hydration theory based on gaseous ion hydration free energies [21] is compared with experimentally determined surface charges. It can be noted from Table 1 that there is excellent agreement between theoretical predictions and experimental results. The sign of the surface charge of silver halides, except for AgF, has been measured experimentally by many researchers. However, recently, for the first time, nonequilibrium electrokinetic measurements for AgF made with the laser-Doppler electrophoretic technique were reported [22]. Now, with the electrophoretic mobility measurements for AgF, the lattice ion hydration theory has been substantiated for all silver halides (see Table 1). It can be noted from Table 1 that, unlike the other silver halides, silver fluoride is positively charged in its saturated solution as determined by nonequilibrium electrophoretic measurements and as expected from simplified lattice ion hydration theory. Until recently, the analysis of other halide salts was not possible.

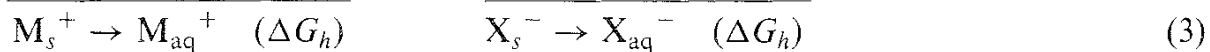
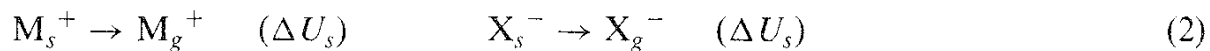
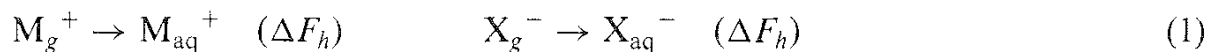
The process of charge generation by hydration of lattice ions should be represented more rigorously by considering the lattice energy of surface ions, which in turn is dependent on the crystal structure and preferential plane of cleavage

TABLE 1 Sign of Surface Charge for Silver Halides

| Salt | $-\Delta G_h^-$ (kJ/mol) | $-\Delta G_h^+$ (kJ/mol) | Sign of surface charge | |
|------|-----------------------------|-----------------------------|------------------------|----------|
| | | | Predicted | Exptl. |
| AgF | 458.6 | 441.0 | Positive | Positive |
| AgCl | 347.3 | 441.0 | Negative | Negative |
| AgBr | 318.0 | 441.0 | Negative | Negative |
| AgI | 279.1 | 441.0 | Negative | Negative |

Source: Ref. 22

[21,23,24]. For uni-univalent ionic solids such as the alkali halides the energetics can be represented, for the solid MX, as follows:



If the hydration energy (ΔG_h) of the surface lattice cation is more negative than the hydration energy of the surface lattice anion, as described by reactions (3), then the surface of MX will carry a negative charge. The converse is also true. The complete analysis requires knowledge of the hydration free energies for gaseous ions [reactions (1)] and the lattice energy for surface ions [reactions (2)]. The hydration free energy, ΔF_h , for individual gaseous ions can be determined from the Born expression [25–27] given by

$$\Delta F_h = -\frac{Nz^2e^2}{2r} \left(1 - \frac{1}{\epsilon}\right) \quad (4)$$

where

N = Avogadro's number

z = valence of the ion

e = charge on the ion

r = radius of the ion

ϵ = dielectric constant of the water

The lattice energy for surface ions can be determined from Born–Mayer theory [25] as expressed by the equation

$$\Delta U_s = \frac{NAe^2z^2}{R_0} \left(\frac{1}{n} - 1\right) \quad (5)$$

where

ΔU_s = lattice energy

A = Madelung constant for the crystal

R_0 = characteristic unit cell dimension

n = a parameter related to the repulsive forces in the crystal that is evaluated from compressibility measurements

Equations (4) and (5) can be used to obtain the hydration free energy (ΔG_h) of the surface cation or anion [Reaction (3)] as follows:

$$\Delta G_h = \Delta F_h + \Delta U_s \quad (6)$$

Depending on whether the hydration free energy of the cation or the hydration free energy of the anion is more negative, the corresponding surface ion will hydrate to a greater extent, leaving the surface either positively or negatively charged as mentioned above. Of course, for symmetric uni-univalent nonreactive ionic solids having a structure in which cation and anion are interchangeable, the ΔU_s terms are

equivalent, and the free energy of hydration for the gaseous ions can be used to determine the sign of the surface charge. This is the essence of the simplified lattice ion hydration theory.

For valence-asymmetric nonreactive ionic solids such as calcium fluoride, the analysis of the sign of the surface charge becomes tedious and cannot be done simply by comparing the gaseous ion hydration free energies of anion and cation for a particular solid. In this regard, Miller and Calara [21,23,24] extended the simplified lattice ion hydration theory to more complex ionic solids by considering the lattice energy effects. These authors developed a computational technique for the calculation of surface Madelung constants and binding energies of surface ions for semi-infinite solids. The calculated binding energy of surface ions together with the gaseous ion hydration free energy allows for the calculation of the hydration energy of surface ions. Thus, the sign of the surface charge can be predicted for complex ionic solids from the relative magnitudes of the ionic surface hydration energies. The positive surface charge for CaF_2 in its saturated solution was explained on this basis. In summary, the utility of the lattice ion hydration theory has been demonstrated both for simple ionic solids [15,22] and for complex ionic solids when the lattice energy must be taken into consideration by calculation of surface Madelung constants [21,23,24].

In view of the above, the lattice ion hydration theory has been shown to be useful to predict the sign of the surface charge of alkali halides in their saturated solutions.

III. NONEQUILIBRIUM ELECTROPHORETIC MEASUREMENTS

A Electrokinetic Phenomena—Electrophoresis

There are four basic types of electrokinetic techniques that can be used to evaluate the zeta potential under a given set of conditions. The common feature of these electrokinetic measurements is the relative motion between a charged surface and its surrounding fluid, with an electric field either applied or generated from the movement. Perhaps the most familiar type and most widely used electrokinetic technique is electrophoresis, which involves the movement of charged particles under the influence of an applied electric field [28].

The second technique, known as electro-osmosis, causes a fluid in contact with a stationary charged surface to move in response to an applied electric field. The third technique, which can be regarded as the converse of electro-osmosis, is known as the streaming potential technique. The streaming potential involves the measurement of the electric potential generated when a liquid is forced under pressure to move in contact with a stationary charged surface. Finally, the sedimentation potential technique is a method that is, in a way, the converse of electrophoresis. A sedimentation potential arises across the suspension when charged particles settle in a stationary liquid. Adamson (29) explained the basic principles of these electrokinetic techniques in a nutshell as shown in [Table 2](#).

The electrophoretic technique is of particular interest because it has been used for measuring the electrophoretic mobilities of alkali halide particles. In this case, charged particles suspended in the electrolyte are transported toward the electrode of opposite charge when an electric field is applied across the electrolyte. However,

TABLE 2 Electrokinetic Phenomena

| Potential | Nature of solid surface | |
|-----------|-------------------------|-------------------------|
| | Stationary surface | Moving surface |
| Applied | Electro-osmosis | Electrophoresis |
| Induced | Streaming potential | Sedimentation potential |

Source: Ref. 29

viscous forces oppose this movement, and when an equilibrium is reached between electrical attraction and viscous drag, the particle moves with a constant velocity. This velocity depends on the voltage gradient, the dielectric constant, and the particle's zeta potential. The particle's velocity divided by the electric field is generally known as its electrophoretic mobility.

The zeta potential (ζ) can be determined from the electrophoretic mobility by using the Henry equation in which the electrophoretic mobility is seen to be a function of the double layer thickness, $f(\kappa a)$:

$$u = \zeta(\varepsilon/\eta) f(\kappa a) \quad (7)$$

where

u = electrophoretic mobility

ε = dielectric constant

η = viscosity of the medium

a = particle radius

κ = double layer thickness

For large values of κa , i.e., for high electrolyte concentrations, Smoluchowski modified the Henry equation as

$$u = (\varepsilon/\eta) \zeta \quad (8)$$

This equation can be used to simply calculate the zeta potential from the measured electrophoretic mobility. For small values of κa , Eq. (7) becomes

$$u = \frac{2}{3} \left(\frac{\varepsilon}{\eta} \right) \zeta \quad (9)$$

For many years, electrophoretic measurements have been carried out using a simple optical microscope to observe the individual particles moving between two electrodes when a potential gradient is imposed. The actual electrophoretic mobilities are determined by manually timing the movement of particles over a fixed measuring distance. This microscopic method, which is still being used by some researchers, suffers from several limitations:

- First of all, the method is very slow and tedious. For this reason, a trained operator must devote considerable time and effort to accumulate a meaningful set of data from which a mean mobility can be calculated. Operator fatigue and eyestrain are real factors that could affect the outcome of these experiments.

2. The technique is particularly strenuous and is limited to particles that are visible. Particles with an unfavorable refractive index may be virtually invisible.
3. Electro-osmosis is always a problem in classical microscopic methods, and extreme care must be taken to precisely locate the stationary layer before each measurement.
4. Electrophoretic mobility measurements are limited to low ionic strength solutions due to electrode polarization and conductivity limitations, which, if not satisfied, can lead to sample heating and the generation of thermally induced convective flow in the sample cell.
5. Finally, only dilute samples of suspended particles can be used, in order to allow individual particles to be clearly observed during the measurement.

In spite of some improvements made in the classical optical microscopic method, such as the use of video cameras to relieve eyestrain and the use of laser light illumination for better particle visibility, the disadvantages mentioned above remain in large part.

B. Laser-Doppler Electrophoresis

The availability of low power lasers that provide bright and coherent light sources together with sophisticated signal analysis instrumentation have led to the development of an electrophoretic light scattering method to measure electrophoretic mobilities of particles in suspension. This method combines the principles of electrophoresis with laser-Doppler velocimetry, a method used for measuring the speed of moving particles by analyzing the Doppler shifts of scattered light from such moving particles. The new generation of laser-Doppler instruments have transformed electrophoresis from a tedious technique to one that can be applied routinely to obtain fast, accurate data without extensive operator training. Laser-Doppler electrophoretic measurements offer several advantages over classical microscopic methods.

1. Advantages of Laser-Doppler Electrophoresis

Laser-Doppler electrophoretic measurements can be made very rapidly, in a matter of few seconds rather than a few hours, and over a wide range of particle concentrations. Systems suitable for these measurements typically have particle concentrations of up to 10,000 ppm. These features are very important in systems that are either chemically or physically unstable or settle rapidly.

Small values of the electrophoretic mobility [even smaller than $0.1 (\mu\text{s})/(\text{v}/\text{cm})$] can be measured using the laser-Doppler electrophoretic technique. This aspect is particularly important when the mobilities involved are small in magnitude and are in the region close to the point of zero charge.

The traditional microscopic method is complicated by the electro-osmotic velocity due to the negatively charged glass walls of the cell. There is only one particular region between the wall and the center of the cell, which is called the stationary layer, where the particles move with a velocity that is due solely to their charge. It is difficult to consistently focus the microscope in this layer with classical methods. However, the laser-Doppler electrophoretic technique overcomes this difficulty by accurately measuring the particle's velocity in the stationary layer.

Sample heating and electrode polarization are greatly reduced in laser-Doppler electrophoresis instruments due to certain features incorporated in the technique. These features facilitate electrophoretic measurements even in solutions with high salt concentrations.

Laser-Doppler electrophoretic measurements are made on a much larger number of particles compared to other techniques, resulting in the determination of mobility distributions rather than single-point mobilities. Operator bias is completely eliminated because the operator does not select the particles to be measured.

2. Alkali Halide Particles

The advent of laser-Doppler electrophoresis instrumentation allows for the characterization of the electrophoretic properties of many interesting systems that were previously experimentally inaccessible. In particular, systems that change with time can now be studied. In view of this, laser-Doppler electrophoresis was used to determine the electrophoretic mobilities of soluble salt particles (alkali halides and other soluble salts) and thus predict the sign of their surface charge in saturated brines. Of course, zeta potential measurements in a saturated brine are impossible because the double layer is collapsed and consequently a zeta potential does not exist. However, a surface charge may still be present. To describe the electrokinetic behavior of soluble salt particles, nonequilibrium electrophoretic mobility measurements of the alkali halide salt particles were made after injection of the particles into fresh water. Such measurements are dynamic in the sense that the salt particles are dissolving in the aqueous phase during the course of the electrophoretic mobility measurement. It is important, however, that these measurements should give a relative indication of the sign of the surface charge of the salt particles in their saturated brine provided the rate of release is the same for both cation and anion.

3. Principles of Operation

Zetasizer 3 (Malvern Instruments Ltd., London, UK) with the AZ4 standard cell was used for measuring electrophoretic mobilities by laser-Doppler electrophoresis. The schematic of the Zetasizer 3 is shown in [Fig. 1](#). Two coherent laser beams of red light produced by splitting the output of a low-power He-Ne laser are focused and made to intersect within the quartz capillary cell at a point of zero convective flow. As a result, a pattern of interference fringes is formed, and the particles scatter light as they move across the fringes under the influence of the applied electric field. The intensity of the scattered light varies with a frequency that is related to the velocity of the particles. A fast photomultiplier tube together with a digital correlator is used to analyze the signals, and the distribution of zeta potentials and/or distribution of electrophoretic mobilities is thus determined. The sign of the electrophoretic mobility and thus the sign of the surface charge is determined by referencing the observed Doppler frequency of the light scattered by the particles moving through the fringes to the modulation frequency applied to one of the laser beams.

The accurate measurement of low electrophoretic mobilities of particles is thus accomplished by modulating one of the laser beams. This is done by reflecting one of the beams off a mirror that is attached to a piezoelectric crystal. A varying voltage is applied to the crystal, causing it to move. The modulation frequency,

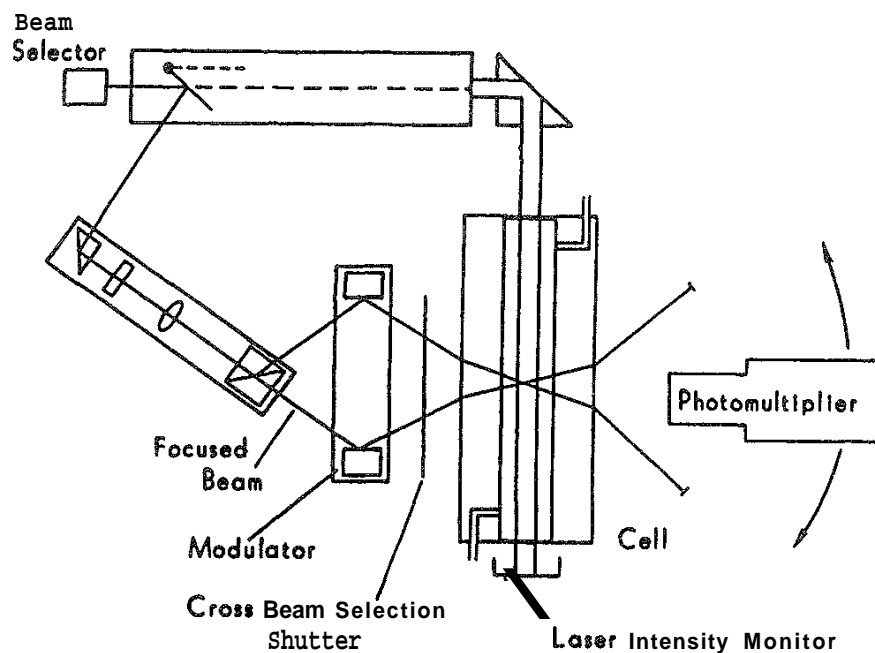


FIG. 1 Schematic arrangement of Zetasizer 3. (From Ref. 7.)

which is between 100 and 1000 Hz, is always present in the signal, so that if the particles have no net velocity the scattered light collected by the photomultiplier will have exactly that frequency. In this way, particles with low or zero mobility can be accurately measured.

The nonequilibrium measurements for alkali halide particles take only a few seconds. Since the measurement is done on a large number of dissolving particles, a distribution of electrophoretic mobilities is obtained, and a distinct electrokinetic characterization of the alkali halide particles is expected.

Figure 2 presents a schematic diagram of the AZ4 standard cell. This cell consists of a 4mm diameter quartz capillary. The platinum electrodes are in compartments at each end of the cell. A semipermeable membrane separates the electrodes from the suspension sample to prevent contamination of the electrodes by the sample. The electrode chambers are filled with an electrolyte that is at least as conducting as the sample itself. Polarization of the electrodes is reduced by simply reversing the direction of the applied electric field at about 2 Hz. The measurement of particle velocity from many field reversals is added to obtain a good signal-to-noise ratio. A technique called "duty cycling", which allows the voltage to be switched off for a short time between cycles is used to avoid heating of the suspension sample, especially for high conductivity solutions [30]. Switching off the applied voltage allows the heat in the sample to dissipate. The problem of electro-osmosis is overcome by measuring the velocity of particles at a point in the cell where the electro-osmotic velocity is zero.

4. Experimental Procedure for Laser-Doppler Electrophoresis

Electrophoretic mobility measurements for various soluble salts were performed by the laser-Doppler electrophoretic technique. The Zetasizer 3 with AZ4 standard cell was used for measuring the electrophoretic mobilities.

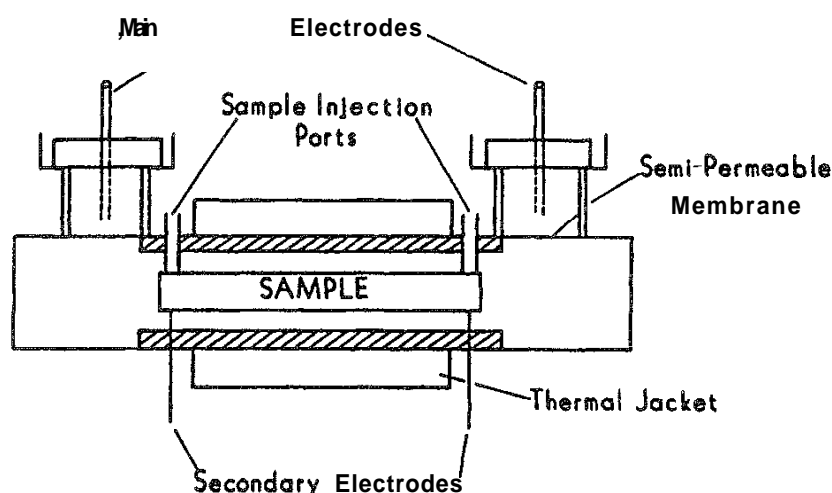


FIG. 2 Schematic diagram of the capillary electrophoresis cell for the Zetasizer 3. (From Ref. 7.)

The soluble salts were sized by dry sieving, and the 65 x 100 mesh fraction was used in this study for nonequilibrium electrophoretic mobility measurements. The electrode chambers were filled with an appropriate electrolyte of required ionic strength. The electrophoretic mobilities of the alkali halides were measured in the following manner:

1. The salt particles were added to 150 mL of high purity water in a beaker.
2. The amount of salt added (from 0.5 to 2.5 g depending on density and solubility) was such that the Zetasizer 3 system would signal when an ideal level of particles was present in the solution after injection.
3. The suspension was stirred gently for a moment (~ 1 s), then quickly injected into the cell, and the electrophoretic mobility was measured.

Each measurement required approximately 15 s. The starting size of the salt particles is a critical factor. If the salt particles are too small, they dissolve before the measurement can be completed. On the other hand, if they are too large, sedimentation occurs in the capillary. Great care was taken to avoid the injection of air bubbles into the cell. The experiment was performed at least three times for each salt under the same conditions to determine the reproducibility of the measurements.

In the case of reference equilibrium measurements which were possible for LiF and NaF, the salts (-400 mesh) were allowed to equilibrate at natural pH for at least 60 min prior to electrophoretic measurements.

C. Results and Discussion

The nonequilibrium electrophoretic mobilities of selected alkali halides were measured during dissolution by laser-Doppler electrophoresis. As stated, the measurements were made during a time interval of 10–15 s. The results were found to be quite reproducible with respect to the sign of the electrophoretic mobility.

The laser-Doppler electrophoretic measurements give a distribution of electrophoretic mobilities. For example, typical electrophoretic mobility distributions for NaCl and KCl are shown in Fig. 3. Note that, although small in magnitude, NaCl exhibits an electrophoretic mobility of $+0.17 \pm 0.14$ ($\mu\text{m/s}/(\text{V/cm})$), which is distinctly positive, while the electrophoretic mobility for KCl, -0.47 ± 0.26 ($\mu\text{m/s}/(\text{V/cm})$), is distinctly negative.

The distributions of electrophoretic mobilities are determined for a sample containing a large number of particles, which is quite impossible by optical microscopic methods. The mobility distributions obtained by laser-Doppler electrophoresis represent a comprehensive and accurate assessment of the mobility spectrum of all the constituent particles in the sample. More important, the sensitivity of the technique is such that particles ranging in size from a few nanometers to several micrometers can be measured. Table 3 presents the experimental results for 21 different alkali halides. In all cases excellent reproducibility was achieved with respect to the sign of the electrophoretic mobility, when ultrapure ($\geq 99.9\%$) salts were used. As many as nine replicate measurements were made, and it should be emphasized that for a given salt the measured electrophoretic mobility was consistently of the same sign. The electrophoretic mobilities reported in Table 3 were determined by taking into account the composite data from all the replicate measurements. For example, in the case of NaI, the experiment was performed nine times, resulting in nine different electrophoretic mobility distributions. The data from these nine measurements were combined, and a grand distribution for the electrophoretic mobility of NaI was calculated.

Of course, the ultimate demonstration of the validity of these nonequilibrium measurements is the measurement of the corresponding equilibrium electrophoretic

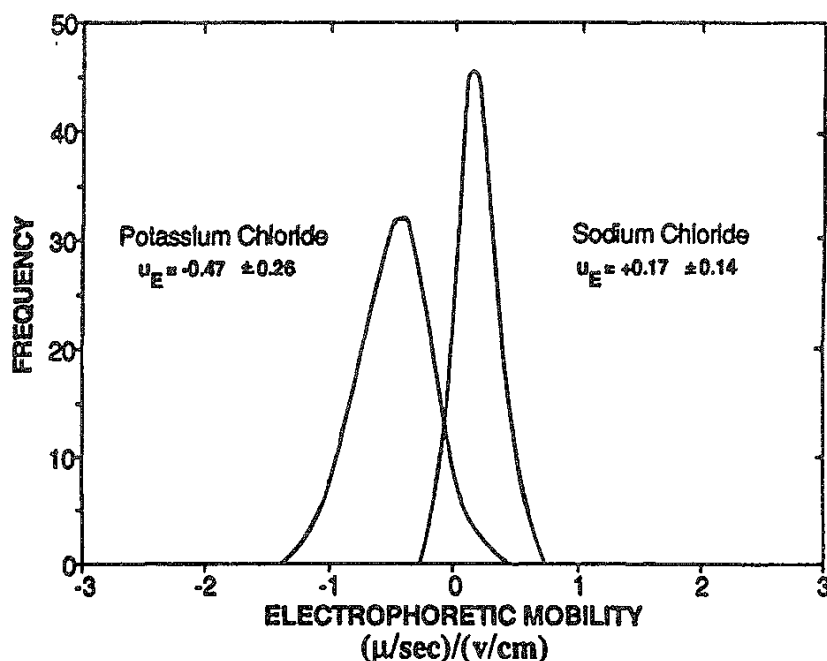


FIG. 3 Nonequilibrium electrophoretic mobility distributions for KCl and NaCl. (From Ref. 7.)

TABLE 3 Results from Laser-Doppler Electrophoretic Experiments--Nonequilibrium Conditions

| Alkali halide | No. of observations | Electrophoretic mobility [(μ /s)/(V/cm)] |
|-------------------------------|---------------------|--|
| Fluoride | | |
| LiF | 5 | $+0.22 \pm 0.15$ |
| NaF | 4 | $+0.16 \pm 0.12$ |
| KF | 5 | $+0.08 \pm 0.07$ |
| RbF | 9 | $+0.10 \pm 0.06$ |
| CsF | 3 | $+0.58 \pm 0.19$ |
| Chloride | | |
| LiCl | 4 | -0.64 ± 0.24 |
| NaCl | 5 | $+0.19 \pm 0.10$ |
| KCl | 6 | -0.43 ± 0.19 |
| RbCl | 3 | $+0.22 \pm 0.16$ |
| CsCl | 4 | $+0.40 \pm 0.24$ |
| Bromide | | |
| LiBr | 7 | -0.33 ± 0.17 |
| NaBr | 3 | -0.32 ± 0.16 |
| RbBr | 3 | -0.47 ± 0.24 |
| KBr | 5 | -0.09 ± 0.06 |
| CsBr | 3 | $+0.07 \pm 0.05$ |
| Iodide | | |
| LiI | 4 | -0.76 ± 0.24 |
| NaI | 9 | -0.72 ± 0.19 |
| KI | 4 | $+0.08 \pm 0.06$ |
| RbI | 4 | -0.25 ± 0.14 |
| CsI | 3 | $+0.05 \pm 0.04$ |
| NaI \cdot 2H ₂ O | 4 | $+0.04 \pm 0.03$ |

Source: Ref. 7.

mobilities that was possible for LiF and NaF. The results are presented in Table 4 and show the nonequilibrium electrophoretic mobilities to be equivalent in sign to the equilibrium electrophoretic mobilities. Again, the electrophoretic mobilities reported in Table 4 were determined from the composite electrophoretic mobility data.

It should be mentioned that diffusiophoresis, the movement of particles in suspension under the influence of an externally imposed solution concentration gradient, can affect the nonequilibrium measurements of alkali halide particles. When a particle of an alkali halide salt is dissolving in solution, it is possible that a concentration gradient will be established in the volume adjacent to the outer boundary of the double layer. The concentration gradient thus established can influence the measured electrophoretic mobilities by laser-Doppler electrophoresis. However, in the case of alkali halide particles, the slope of the concentration

TABLE 4 Comparison of Nonequilibrium Electrophoretic Mobilities with Equilibrium Electrophoretic Mobilities for Two Alkali Halide Salts

| Salt | Solubility | Electrophoretic mobility" [(μ /s)/V/cm)] | |
|------|-----------------------------|--|----------------------|
| | | Nonequilibrium | Equilibrium |
| LiF | 0.27 g/100 cm ³ | +0.22 \pm 0.15 (5) | +0.16 \pm 0.12 (3) |
| NaF | 4.22 g, 100 cm ³ | +0.16 \pm 0.12 (4) | +0.12 \pm 0.08 (4) |

"Number of observations reported in parentheses

Source: Ref. 7.

gradient varies with time because of the rapid dissolution of these particles in solution. Therefore, due to the small concentration gradient close to the particle's surface, the influence of diffusiophoresis on measured electrophoretic mobilities is expected to be of little significance. Furthermore, the results from equilibrium electrophoretic mobility measurements for LiF and NaF (no diffusiophoresis) suggest that at least the sign of the surface charge, if not the magnitude, as measured by laser-Doppler electrophoresis is not affected by diffusiophoresis due to concentration gradients in the outer layers of the double layer. Further, it is interesting that the measured electrophoretic mobility for NaI is negative, whereas that for the thermodynamically stable NaI·2H₂O is positive. It would appear that the hydration of lattice ions does have a significant influence on the surface charge of alkali halides and other soluble salts [31].

IV. EXTENDED LATTICE ION HYDRATION THEORY

As described in the previous section, nonequilibrium electrokinetic measurements using laser-Doppler electrophoresis have established the sign of the surface charge for 21 alkali halide salts. These surface charge results for alkali halides are generally as expected from simplified lattice ion hydration theory with some exceptions, specifically LiF, KCl, NaCl, KBr, RbBr, KI, and RbI, as shown in Table 5. Thus the sign of the surface cannot be predicted solely from consideration of the hydration energies of the gaseous ions that constitute the ionic lattice. Accurate prediction of the surface charge must include consideration of the partial hydration of surface lattice ions. In this regard, ion-dipole interaction energies have been taken into consideration for three cases, based on steric and hydration effects, in order to predict more accurately the surface charge of alkali halides. The calculations indicate that the sign of the surface charge of alkali halides can be accurately predicted from an extended lattice ion hydration theory that involves the partial hydration of surface lattice ions [9].

One deficiency in the simplified lattice ion hydration theory is that the surface state, indicated by M_s^+ in the equation $M_s^+ \rightarrow M_{aq}^+$, is an anhydrous state in a vacuum, and, in fact, this surface ion should be considered to be partially hydrated in order to more accurately represent the system. The additional reaction that needs

TABLE 5 Sign of the Surface Charge for Selected Alkali Halides

| | Negative gaseous ion hydration free energies (kJ/mol) | | | Sign of surface charge | |
|-------------------------|--|--------|------------|------------------------|---------------------|
| | Cation | Anion | Δ^a | Predicted ^b | Exptl. ^c |
| Fluoride | | | | | |
| LiF | 470.70 | 461.08 | 9.62 | — | + |
| NaF | 371.54 | 461.08 | 89.54 | + | + |
| KF | 298.32 | 461.08 | 162.76 | + | + |
| RbF | 276.56 | 461.08 | 184.52 | + | + |
| CsF | 244.35 | 461.08 | 216.73 | + | + |
| Chloride | | | | | |
| LiCl | 470.70 | 347.27 | 123.43 | — | — |
| NaCl | 371.54 | 347.27 | 24.27 | — | + |
| KCl | 298.32 | 347.27 | 48.95 | + | — |
| RbCl | 276.56 | 347.27 | 70.71 | + | + |
| CsCl | 244.35 | 347.27 | 102.92 | + | + |
| Bromide | | | | | |
| LiBr | 470.70 | 318.40 | 152.30 | — | — |
| NaBr | 371.54 | 318.40 | 53.14 | — | — |
| KBr | 298.32 | 318.40 | 20.08 | + | — |
| RbBr | 276.56 | 318.40 | 41.89 | + | — |
| CsBr | 244.35 | 318.40 | 74.05 | + | + |
| Iodide | | | | | |
| LiI | 470.70 | 279.07 | 191.63 | — | — |
| NaI | 371.54 | 279.07 | 92.47 | — | — |
| KI | 298.32 | 279.07 | 19.25 | — | + |
| RbI | 276.56 | 279.07 | 2.51 | + | — |
| CsI | 244.35 | 279.07 | 34.72 | + | + |
| NaI · 2H ₂ O | NA | NA | NA | NA | + |

^a Δ = Difference between cation and anion gaseous hydration free energies.

^b Simplified lattice ion hydration theory.

^c Electrophoretic mobility measurements by laser-Doppler electrophoresis.

Source: Ref. 7.

to be considered is $M_s^+ \rightarrow M_{s(\text{partial hydration})}^+$, and the overall reaction that more accurately represents the system of interest would be $M_{s(\text{partial hydration})}^+ \rightarrow M_{\text{aq}}^+$. The results from this current theoretical analysis suggest that the surface ions must be considered to be partially hydrated, dependent on the properties of the lattice ions such as ionic radius (steric effect) and hydration number (hydration effect), and on this basis the sign of the surface charge of all alkali halides except for KCl can be accurately predicted. This analysis, which involves the inclusion of ion-dipole interactions together with the simplified lattice ion hydration theory, is referred to as the extended lattice ion hydration theory. The physical process of charge generation as described by the extended lattice ion hydration theory can be

represented by considering the relative energies of the following reactions for a uni-univalent ionic solid, MX:



where subscripts $s(ph)$, $s(f)$, g , and aq represent partially hydrated surface state, free (vacuum) surface state, gaseous state, and aqueous state, respectively. $\Delta U_s(M^+)$, $\Delta F_h(M^+)$, and $w_{i-d}(M^+)$ are the surface binding energy, the gaseous hydration free energy, and ion-dipole interaction energy, respectively, of the cation M^+ . Further $\Delta G_h(M^+)$ is the hydration free energy of the surface ion,

$$\Delta G_h(M^+) = \Delta U_s(M^+) + \Delta F_h(M^+) + w_{i-d}(M^+) \quad (14)$$

Similarly, for the anion X^- ,

$$\Delta G_h(X^-) = \Delta U_s(X^-) + \Delta F_h(X^-) + w_{i-d}(X^-) \quad (15)$$

Depending on whether $\Delta G_h(M^+)$ or $\Delta G_h(X^-)$ is more negative, the corresponding ion will hydrate to a greater extent, and the surface will acquire the charge of the other ion. Here, as in the case of simplified lattice ion hydration theory, the cation and anion are considered to be interchangeable, and thus the lattice energies of surface cation and anion are equivalent. Finally, the surface charge is established according to the extended lattice ion hydration theory by comparing both the gaseous ion hydration free energies and ion-dipole interaction energies for partial hydration of surface lattice ions.

Many molecules possess an electric dipole. For example, in the HCl molecule the chlorine atom tends to draw the hydrogen's electron toward itself, and this molecule therefore has a permanent dipole. Such molecules are called polar molecules. Permanent dipole moments occur only in asymmetric molecules and arise from the unequal distribution of electrons in the covalent bonds. Thus, it is not surprising that a characteristic dipole moment can be assigned to each type of covalent bond. The dipole moment of such a polar molecule is defined as

$$u = ql \quad (16)$$

where l is the distance between the centers of two charges, $+q$ and $-q$. The electrostatic pair interaction (interaction energy) between a charged atom and a polar molecule presented by Israelachvili [32] is

$$w_{i-d} = -\frac{zeu \cos \theta}{4\pi\epsilon_0\epsilon r^2} \quad (17)$$

where u is the dipole moment, r is the distance between the centers of charge of the ion and a polar molecule, θ is the angle subtended by the dipole and the line joining the centers of charge of the ion and the polar molecule, z is valence, e is electronic charge, ϵ_0 is permittivity of free space, and ϵ is dielectric constant [32]. As mentioned above, Eq. (17) gives the free energy for the interaction of a charge and a

point dipole in some medium of known dielectric properties. Then, by definition, when a cation is near a dipolar molecule, maximum attraction (i.e., maximum negative energy) will occur when the dipole points away from the ion ($\theta = 0^\circ$), whereas if the dipole points toward the ion ($\theta = 180^\circ$) the interaction energy is positive and the force is repulsive.

In the present work, Eq. (17) was used to calculate the ion–dipole interaction energies for the alkali halide water dipole system. Here, water was treated as a simple spherical molecule of radius 0.14 nm with a point dipole of moment 1.85 D. Also, based on steric and hydration effects, three cases—A, B, and C—were used to calculate the ion–dipole interaction energies. (See Table 6.) Case A considers the alkali halides KF, RbF, CsF, CsCl, CsBr, and CsI, which have an alkali ion radius close to that of the water molecule and a ratio of hydration numbers of alkali ion to halide ion of less than 2. Case B considers the alkali halides LiF, NaF, LiCl, LiBr, NaBr, LiI, NaI, and KI, which have an alkali ion radius less than that of the water molecule and a ratio of hydration numbers of alkali ion to halide ion of more than 2. Finally, case C considers the alkali halides KCl, RbCl, KBr, RbBr, and RbI, which have an alkali ion radius close to that of the water molecule and a ratio of

TABLE 6 Steric and Hydration Effects for Alkali and Halide Ions

| Case | Steric effect | Hydration effect | Alkali halide | Properties of alkali halides | | |
|------|--|--|---------------|------------------------------|------------|---------------|
| | | | | r^-/r^+ | r^+ (nm) | n_h^+/n_h^- |
| A | Small; $r^+ \sim r_w$; $r^-/r^+ < 1.4$ | Small; $n_h^+/n_h^- \leq 2$ | KF | 0.88 | 0.151 | 1.5–2.0 |
| | | | RbF | 0.826 | 0.161 | 1.0–1.5 |
| | | | CsF | 0.764 | 0.174 | 0.5–1.0 |
| | | | CsCl | 1.04 | 0.174 | 1.0–2.0 |
| | | | CsBr | 1.126 | 0.174 | 1.0–2.0 |
| | | | CsI | 1.26 | 0.174 | 1.0–2.0 |
| B | Significant; $r^+ < r_w$; $r^-/r^+ > 1.4$ | No; behavior limited by steric effect | LiF | 2.254 | 0.059 | 2.5–3.0 |
| | | | NaF | 1.3 | 0.102 | 2.0–2.5 |
| | | | LiCl | 3.068 | 0.059 | 5.0–6.0 |
| | | | NaCl | 1.775 | 0.102 | 4.0–5.0 |
| | | | LiBr | 3.322 | 0.059 | 5.0–6.0 |
| | | | NaBr | 1.922 | 0.102 | 4.0–5.0 |
| | | | LiI | 3.729 | 0.059 | 5.0–6.0 |
| | | | NaI | 2.157 | 0.102 | 4.0–5.0 |
| C | Small $r^+ \sim r_w$; $r^-/r^+ < 1.4$ | Significant $n_h^+/n_h^- > 2$ | KI | 1.457 | 0.151 | 3.0–4.0 |
| | | | KCl | 1.199 | 0.151 | 3.0–4.0 |
| | | | RbCl | 1.124 | 0.161 | 2.0–3.0 |
| | | | KBr | 1.298 | 0.151 | 3.0–4.0 |
| | | | RbBr | 1.217 | 0.161 | 2.0–3.0 |
| | | | RbI | 1.366 | 0.161 | 3.0–4.0 |

Source: Ref. 9

hydration numbers of alkali ion to halide ion of more than 2. A detailed description of these three cases showing the ion–dipole interaction energy calculations is presented in the following sections.

A. Case A (KF, RbF, CsF, CsCl, CsBr, and CsI)

Six alkali halide salts KF, RbF, CsF, CsCl, CsBr, and CsI—have an alkali ion radius close to that of the water molecule and a ratio of hydration numbers of alkali ion to halide ion of less than 2. These alkali halides were classified into one group, and calculations based on steric and hydration effects were made to analyze their surface charge. The steric effect, which is related to the size of the alkali ion, halide ion, and water molecule, has little influence on the partial hydration of these six alkali halides due to the fact that the radii of alkali ion, halide ion, and water molecule are very close to one another. The other effect, the hydration effect, mainly depends on the ratio of alkali ion hydration number to halide ion hydration number. In this case, since the ratio is less than 2, the influence of hydration is also negligible. The situation for case A is summarized in Table 6.

Figure 4 shows a schematic representation of case A. The angles θ_1 and θ_2 in Fig. 4 represent the angles subtended by the dipole to the line joining the ion and the polar molecule. The angles θ_1 and θ_2 used to calculate the interaction energy were obtained by taking the inverse cosine of the ratio of the sides of the respective triangles as shown in Fig. 4. The lengths of these sides were obtained from the available radius values for alkali ion, halide ion, and water molecule. These angles were then used in Eq. (17) to calculate the ion–dipole interaction energy values. Both attractive and repulsive components of interaction energy were calculated using Eq. (17). For example, an attractive interaction energy was calculated for an alkali ion–water dipole with an angle $\theta = 0^\circ$, and a repulsive interaction energy was calculated for the same dipole with an angle $\theta = \theta_1$. The total ion–dipole interaction energy for alkali ion–water dipole (w_{i-d}^+) is obtained simply by adding the attractive and repulsive components. Similarly, an attractive interaction energy was calculated for halide ion–water dipole with an angle $\theta = 0^\circ$, and a repulsive interaction energy was calculated for the same system with an angle $\theta = \theta_2$. The total ion–dipole interaction energy for halide ion–water dipole (w_{i-d}) is obtained

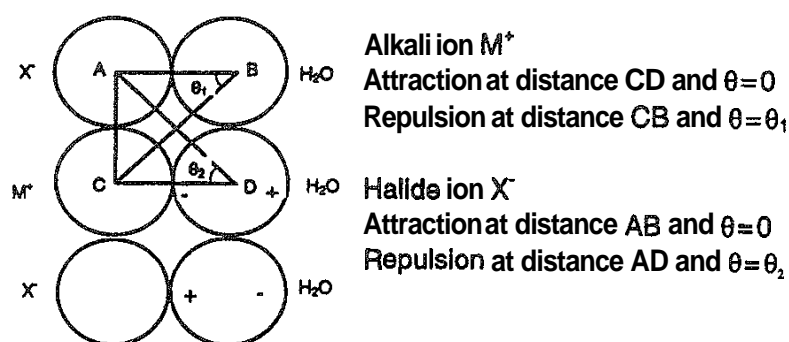


FIG. 4 Case A, suggested for KF, RbF, CsF, CsCl, CsBr, and CsI, alkali halides having an alkali ion radius close to that of the water molecule and a ratio of hydration numbers of alkali ion to halide ion of less than 2. (From Ref. 9.)

TABLE 7 Ion–Dipole Interaction Energies for Alkali Halides KF, RbF, CsF, CsCl, CsBr, and CsI According to Case A

| Alkali halides | Ion-dipole interaction energy (kJ/mol) | | | | | | $\Delta w_{i-d} =$ $w_{i-d}^+ - w_{i-d}^-$ (kJ/mol) |
|-------------------|--|-----------|-------------|-------------------------|-----------|-------------|---|
| | Alkali ion/water dipole | | | Halide ion water dipole | | | |
| | Attraction | Repulsion | w_{i-d}^+ | Attraction | Repulsion | w_{i-d}^- | |
| KF | −62.61 | 23.67 | −38.94 | −71.13 | 22.91 | −48.23 | 9.28 |
| RbF | −58.52 | 22.43 | −36.09 | −71.13 | 21.4 | −49.73 | 13.64 |
| CsF | −53.77 | 20.88 | −32.89 | −71.13 | 19.66 | −51.47 | 18.58 |
| CsCl | −53.77 | 15.54 | −38.23 | −51.45 | 15.64 | −35.81 | −2.42 |
| CsBr | −53.77 | 14.26 | −39.51 | −46.96 | 14.58 | −32.38 | −7.13 |
| CsI | −53.77 | 12.54 | −41.23 | −40.91 | 13.0 | −27.91 | −13.32 |

Source: Ref. 9.

simply by adding the attractive and repulsive components. Table 7 presents the results for interaction energies calculated for alkali ion–water dipole and halide ion–water dipole systems. Finally, the ion–dipole interaction energy for an alkali halide/water system (Δw_{i-d}) can be estimated simply from a comparison of the ion–dipole interaction energies of the corresponding alkali ion/water dipole and halide ion/water dipole systems. For example, if the interaction energy of the alkali ion/water dipole system is more negative than the interaction energy of the halide ion/water dipole system, then the partial hydration of surface lattice ions will cause the surface to be more negative. The converse is also true. However, for case A, as is evident from Table 7, the difference between the ion–dipole interaction energies of the alkali ion/water dipole and halide ion/water dipole systems is small. So the ion–dipole interactions will have little influence on the sign of the surface charge as predicted by the simplified lattice ion hydration theory.

B. Case B (LiF, NaF, LiCl, NaCl, LiBr, NaBr, LiI, NaI, and KI)

Nine alkali halide salts—LiF, NaF, LiCl, NaCl, LiBr, NaBr, LiI, NaI, and KI—have an alkali ion radius less than that of the water molecule and a ratio of hydration numbers of alkali ion to halide ion of more than 2. These alkali halides were classified into one group, and calculations based on steric and hydration effects were made to analyze their surface charge. The steric effect, which is related to the sizes of the alkali ion, halide ion, and water molecule, has a remarkable influence on the partial hydration of these nine alkali halides. The other effect, the hydration effect, which depends mainly on the ratio of alkali ion hydration number to halide ion hydration number, has limited significance in this case due to the very high steric effect. These characteristic features are presented in Table 6.

Figure 5 shows a schematic representation of case B. Table 8 presents the results from the calculation of interaction energies for the alkali ion/water dipole and halide ion/water dipole systems. Both attractive and repulsive components of interaction energy were calculated using Eq. (17). The ion–dipole interaction energy for any alkali halide/water system can be estimated simply from a comparison of the ion–dipole interaction energies of the corresponding alkali ion/water and halide ion/water dipole systems. As is evident from Table 8, the difference in ion–dipole interaction energies between alkali ion/water dipole and halide ion/water dipole

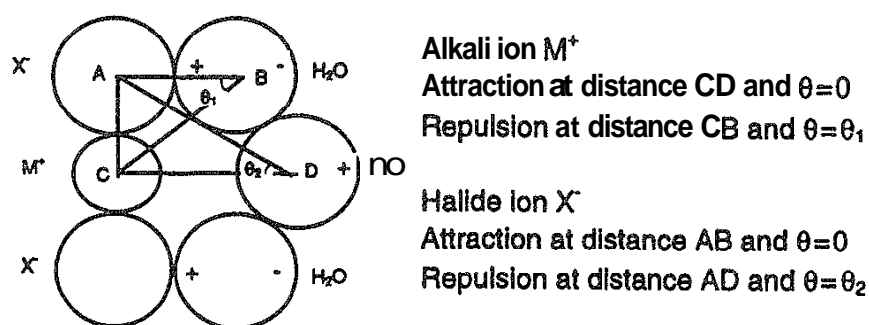


FIG. 5 Case B, suggested for LiF, NaF, LiCl, NaCl, LiBr, NaBr, LiI, NaI, and KI, alkali halides having an alkali ion radius less than that of the water molecule and a ratio of hydration numbers of alkali ion to halide ion of more than 2. (From Ref. 9.)

TABLE 8 Ion--Dipole Interaction Energies for Alkali Halides LiF, NaF, LiCl, NaCl, LiBr, NaBr, LiI, NaI, and KI According to Case B

| Alkali halides | Ion-dipole interaction energy (kJ/mol) | | | | | | $\Delta w_{i-d} = w_{i-d}^+ - w_{i-d}^-$ (kJ/mol) |
|----------------|--|-----------|-------------|-------------------------|-----------|-------------|---|
| | Alkali ion/water dipole | | | Halide ion/water dipole | | | |
| | Attraction | Repulsion | w_{i-d}^+ | Attraction | Repulsion | w_{i-d}^- | |
| LiF | -27.89 | 38.87 | 10.98 | -71.13 | 21.41 | -49.72 | 60.7 |
| NaF | -25.49 | 31.0 | 5.51 | -71.13 | 17.9 | -53.23 | 58.74 |
| LiCl | -22.24 | 26.54 | 4.3 | -51.45 | 16.08 | -35.37 | 39.67 |
| NaCl | -20.27 | 21.71 | 1.44 | -51.45 | 13.6 | -37.85 | 39.29 |
| LiBr | -20.67 | 23.71 | 3.04 | -46.96 | 14.73 | -32.23 | 35.27 |
| NaBr | -18.95 | 19.67 | 0.72 | -46.96 | 12.54 | -34.42 | 35.14 |
| LiI | -18.57 | 20.24 | 1.67 | -40.91 | 12.97 | -27.94 | 29.61 |
| NaI | -17.0 | 16.94 | -0.06 | -40.91 | 11.07 | -29.84 | 29.78 |
| KI | -15.33 | 13.81 | -1.52 | -40.91 | 9.28 | -31.63 | 30.11 |

Source: Ref. 9.

systems is positive. These calculations suggest that the halide ion has a more attractive (more negative) ion–dipole interaction energy value than the alkali ion due to the steric effect; the halide ion is much larger than the alkali ion. Finally, the ion–dipole interaction energy values calculated for the nine alkali halide salts were found to have a significant influence on the relative hydration tendency and hence on the sign of the surface charge predicted by the simplified lattice ion hydration theory.

C. Case C (KCl, RbCl, KBr, RbBr, and RbI)

Five alkali halide salts—KCl, RbCl, KBr, RbBr, and RbI—have an alkali ion radius close to that of a water molecule and a ratio of hydration numbers of alkali ion to halide ion of more than 2. These alkali halides were classified into one group, and calculations based on steric and hydration effects were made to analyze their surface charge. The steric effect, which is related to the sizes of the alkali ion, and water molecule, has very little influence on the hydration of these five alkali halides. The other effect, the hydration effect, which depends mainly on the ratio of alkali ion hydration number to halide ion hydration number, is significant in this case. These properties are presented in Table 6.

Figure 6 shows a schematic representation of case C. Table 9 presents the results from the calculation of interaction energies for the alkali ion/water dipole and halide ion/water dipole systems. Both attractive and repulsive components of interaction energy were calculated using Eq. (17). As discussed before, the ion–dipole interaction energy for an alkali halide/water system can be estimated simply from a comparison of the ion–dipole interaction energies of the corresponding alkali ion/water dipole and halide ion/water dipole systems. As is evident from Table 9, the difference in ion–dipole interaction energies between alkali ion/water dipole and halide ion/water dipole systems is negative. These results suggest that the alkali ion has more attractive (more negative) ion–dipole interaction energy values than the halide ion since the hydration number of the alkali ion is higher than that of the halide ion. The higher hydration number of the alkali ion is responsible for the accommodation of a greater number of water dipoles in the absence of any steric

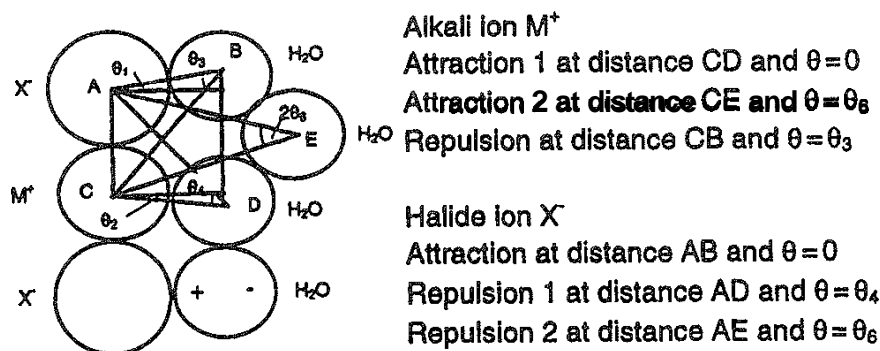


FIG. 6 Case C, suggested for KCl, RbCl, KBr, RbBr, and RbI, alkali halides having an alkali ion radius close to that of the water molecule and a ratio of hydration numbers of alkali ion to halide ion of more than 2. (From Ref. 9.)

TABLE 9 Ion--Dipole Interaction Energies for Alkali Halides KCl, RbCl, KBr, RbBr, and RbI According to Case C

| Alkali halide | Ion--dipole interaction energy (kJ/mol) | | | | | | |
|---------------|---|--------|-------|-------------------------|--------|--------|---|
| | Alkali ion/water dipole | | | Halide ion/water dipole | | | $\Delta w_{i-d} = w_{i-d}^+ - w_{i-d}^-$ (kJ/mol) |
| | Att. 1 | Att. 2 | Rep. | w_{i-d}^+ | Att. | Rep. 1 | Rep. 2 |
| KCl | -62.61 | -23.8 | 16.87 | -69.54 | -51.45 | 17.13 | 10.27 |
| RbCl | -58.52 | -19.41 | 15.94 | -61.99 | -51.45 | 16.15 | 19.74 |
| KBr | -62.61 | -20.8 | 15.3 | -68.11 | -46.96 | 15.73 | 21.48 |
| RbBr | -58.52 | -19.95 | 14.54 | -63.93 | -46.96 | 14.91 | 20.6 |
| RbI | -58.52 | -15.59 | 12.58 | -61.53 | -46.96 | 13.19 | 16.54 |

Att = attraction; **Rep** = repulsion.

Source: Ref. 9.

effect. Finally, the ion–dipole interaction energy values calculated according to this case for these five alkali halide salts were found to have a significant influence on the relative hydration tendency and hence on the sign of the surface charge predicted by the simplified lattice ion hydration theory.

D. The Sign of the Surface Charge

Table 10 compares the results obtained for the extended lattice ion hydration theory with the results for the nonequilibrium electrophoretic mobility measurements. It is evident that the extended lattice ion hydration theory provides for an

TABLE 10 Sign of Surface Charge of Alkali Halides — Extended Lattice Ion Hydration Theory

| Alkali halide | ΔG_h^g (kJ/mol) | Δw_{i-d} (kJ/mol) | $\Delta G_h^g =$ $\Delta G_h^g + \Delta w_{i-d}$ (kJ/mol) | Sign of surface charge | |
|------------------|----------------------------|------------------------------|---|------------------------|--------------------|
| | | | | Predicted ^a | Exptl ^b |
| Fluoride | | | | | |
| LiF | −9.62 | 60.7 | 51.08 | + | + |
| NaF | 89.54 | 58.74 | 148.28 | + | + |
| KF | 162.76 | 9.28 | 172.04 | + | + |
| RbF | 184.52 | 13.64 | 198.16 | + | + |
| CsF | 216.73 | 18.58 | 235.31 | + | + |
| Chloride | | | | | |
| LiCl | −123.43 | 39.67 | −83.76 | − | − |
| NaCl | −24.27 | 39.29 | 15.02 | + | + |
| KCl | 48.95 | −45.49 | 3.46 | + | − |
| RbCl | 70.71 | −46.43 | 24.28 | + | + |
| CsCl | 102.92 | −2.42 | 100.5 | + | + |
| Bromide | | | | | |
| LiBr | −152.3 | 35.27 | −117.03 | − | − |
| NaBr | −53.14 | 35.14 | −18 | − | − |
| KBr | 20.08 | −58.36 | −38.28 | − | − |
| RbBr | 41.89 | −52.48 | −10.91 | − | − |
| CsBr | 74.05 | −7.13 | 66.92 | + | + |
| Iodide | | | | | |
| LiI | −191.63 | 29.61 | −162.02 | − | − |
| NaI | −92.47 | 29.78 | −62.69 | − | − |
| KI | −19.25 | 30.11 | 10.86 | + | + |
| RbI | 2.51 | −44.3 | −41.79 | − | − |
| CsI | 34.72 | −13.32 | 21.4 | + | + |

^aExtended lattice ion hydration theory.

^bNonequilibrium electrophoretic mobility measurements by laser-Doppler electrophoresis

Source: Ref. 9.

excellent explanation of the experimental results. In particular, the addition of the interaction energy values to account for the partial hydration of surface lattice ions showed a significant effect on the total energy (gaseous ion hydration free energy plus ion–dipole interaction energy) values of the seven exceptions (LiF, NaCl, KCl, KBr, RbBr, KI, and RbI) that, according to simplified lattice ion hydration theory, had deviated from the results of nonequilibrium electrophoretic measurements by laser-Doppler electrophoresis. For example, LiF, which has a difference of -9.62 kJ/mol between cation and anion gaseous hydration free energies, was predicted to have a negative sign of surface charge by the simplified lattice ion hydration theory. However, by considering partial hydration of surface ions with an interaction energy of 60.7 kJ/mol according to surface ion–dipole interactions, the total energy is found to be 51.08 kJ/mol , and a positive sign is predicted for the surface charge, which is in excellent agreement with the experimental data. These calculations indicate that the sign of the surface charge of alkali halides except for KCl can be accurately predicted by the extended lattice ion hydration theory, which involves the additional consideration of surface ion–dipole interactions.

To further examine the validity of the above calculations, a sensitivity analysis was carried out, particularly for the seven exceptions that had deviated from the simplified lattice ion hydration theory. Slight changes in the angles and the consideration of other possible interactions for the calculations of ion–dipole interaction energies were the main features of the sensitivity analysis. In almost all cases only a very small change in the energy values was observed, and, most important, there was no change in the sign of the surface charge of the alkali halides except that of KCl. From [Table 10](#) it is evident that the energy value of KCl is very small, 3.46 kJ/mol , and this might account for the change in the sign of the surface charge of KCl from negative to positive during the sensitivity analysis. Further, it is interesting to note that Yalamanchili and Miller [10] showed that oxygen defects present in the crystal lattice can strongly influence the surface charge characteristics of KCl. At a low oxygen concentration ($< 60\text{ ppm}$), KCl is positively charged, and as the oxygen content increases, the sign of the surface charge changes from positive to negative. Therefore, the small energy values (gaseous ion hydration free energy plus ion–dipole interaction energy) may allow for the energy associated with oxygen defects to account for the anomalous behavior of KCl. In general, excellent agreement in the sign of surface charge is now observed between theoretical predictions and experimental data for the alkali halide salts in their saturated brines. Further refinement in the calculation of ion–dipole interaction energies for the partial hydration of surface ions may include consideration of different orientations for water dipoles, dielectric boundary effects, and dipole–dipole interactions.

V. OXYGEN DEFECT STATES

In order to understand the anomalous behavior of KCl, the effect of oxygen defect states on its surface charge was studied in detail by Yalamanchili and Miller [10]. The possible types of defects that can be present in ionic crystals are many [33]. As is well known, the most common types of defects that are always present in ionic crystals are Frenkel and Schottky defects. A Frenkel defect forms when an ion

leaves the normal lattice site and occupies some interstitial position. A Schottky defect forms when an ion leaves the lattice site and migrates to the surface or, more simply, when a lattice site is vacant. These defects can be significant even in pure crystals of ideal composition. It has been demonstrated that these defect states exhibit substantial mobility in the crystal lattice. Two other types of defects that can be present are dislocations and stacking faults, which are important from the viewpoint of mechanical properties and crystal growth.

The presence of defects has been found to influence the bulk as well as surface characteristics of alkali halides. Basically, these defects alter the charge neutrality on the cleavage planes, leading to a change in the surface properties of uni-univalent alkali halides. In this regard, oxygen defects have been either introduced into or removed from the crystal lattice in order to examine their influence on the surface properties of KCl and NaCl. The KCl and NaCl salts were selected for these studies because they have been shown to be very stable hosts for various types of defects and also represent the most important alkali halide salts that deviate from the simplified lattice ion hydration theory.

As a first step, an ultrapure laser quality KCl crystal was grown at the University of Utah crystal growth laboratory. The Czochralski method [34] was employed to grow the KCl crystal from a starting material with five nines purity. The properties of the University of Utah laser quality KCl crystal were compared to those of the optical quality KCl crystal obtained from Optovac, Inc. and the KCl reagent grade powder as shown in Table 11. It can be seen from this table that the University of Utah KCl crystal has a positive charge as predicted by lattice ion hydration theory, whereas the Optovac KCl crystal and KCl reagent grade powder exhibit a negative surface charge. The oxygen levels as determined by neutron activation indicate that the Optovac KCl has a higher oxygen content than the University of Utah KCl as

TABLE 11 Nonequilibrium Electrokinetic Properties of KCl from Various Sources

| KCl source | Crystal growth/quality | Sign of surface charge | Oxygen ^a (ppm) |
|----------------------|--|------------------------|---------------------------|
| U of U crystal | Czochralski method; laser quality; 99.999% KCl starting material; chlorine purging | Positive | 60 ± 8.6 |
| Optovac crystal | Not known; optical quality; 99.5% KCl starting material; no purging | Negative | 345 ± 13 |
| Reagent grade powder | Not applicable | Negative | Not measured |

^aIRT Corporation, San Diego.
Source: Ref. 10.

shown in Table 11. The higher oxygen levels in Optovac KCl appear to be due to the use of relatively less pure KCl as a starting material for crystal growth and the crystal growth procedure employed. For example, if the crystal is grown under ambient atmosphere, oxygen in the atmosphere could react with the KCl melt, forming various defect states that are discussed in the following paragraphs. Unfortunately, Optovac, Inc. was unwilling to share information regarding their crystal growth procedures. However, it is most likely that one or all the reasons mentioned above could account for the presence of higher levels of oxygen in Optovac KCl crystals. Nevertheless, it seems that the difference in oxygen levels in the University of Utah and Optovac crystals is responsible for the difference in the electrokinetic behavior of these KCl crystals.

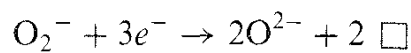
Oxygen can be present in the KCl crystal in two different forms, namely, O_2^- and O^{2-} centers [35]. If the crystals are grown in an ambient atmosphere, KCl melt reacts with oxygen to form KO_2 (O_2^- centers) as follows:



When excess potassium is introduced into KCl, KO_2 present within the lattice is converted to K_2O (O^{2-} centers) according to the reaction



Equation (19) can also be represented as



The symbol \square in Eq. (20) represents a vacancy in the crystal lattice. The introduction of excess potassium ions into the KCl lattice creates F centers (e^- at anion vacancies) in the crystal lattice as mentioned in the previous section. Therefore Eq. (20) can be rewritten as



It is clear from Eq. (21) that the number of O_2^- defects will be reduced by the presence of F centers in the crystal lattice, thereby forming the O^{2-} defect pairs.

The presence of O_2^- and O^{2-} defects can be characterized by their typical absorption frequencies in the UV/Vis region [35,36]. Figures 7 and 8 show the absorption spectra of the Optovac KCl and the University of Utah KCl, respectively, in the UV/Vis region. The presence of O_2^- defects in the Optovac KCl can be clearly seen from Fig. 7, as indicated by the band positions at 205 and 244 nm. On the other hand, Fig. 8 shows that the University of Utah KCl crystal is free of O_2^- defects, as indicated by the absence of any absorption bands in the region of 200–250 nm. Fisher et al. [35] reported that both O_2^- and O^{2-} defects in KCl have a characteristic absorption band in the range of 200–250 nm. It should be mentioned that O_2^- defects could easily be converted into O^{2-} defects if the crystal were exposed to prolonged radiation even in the natural environment. However, neither the University of Utah nor Optovac crystals show any characteristic absorption due to O^{2-} defects. Typically, O^{2-} defects have multiple absorption bands at 440, 286, 215, and 194 nm [37], and clearly these multiple bands are absent in Figs. 7 and 8,

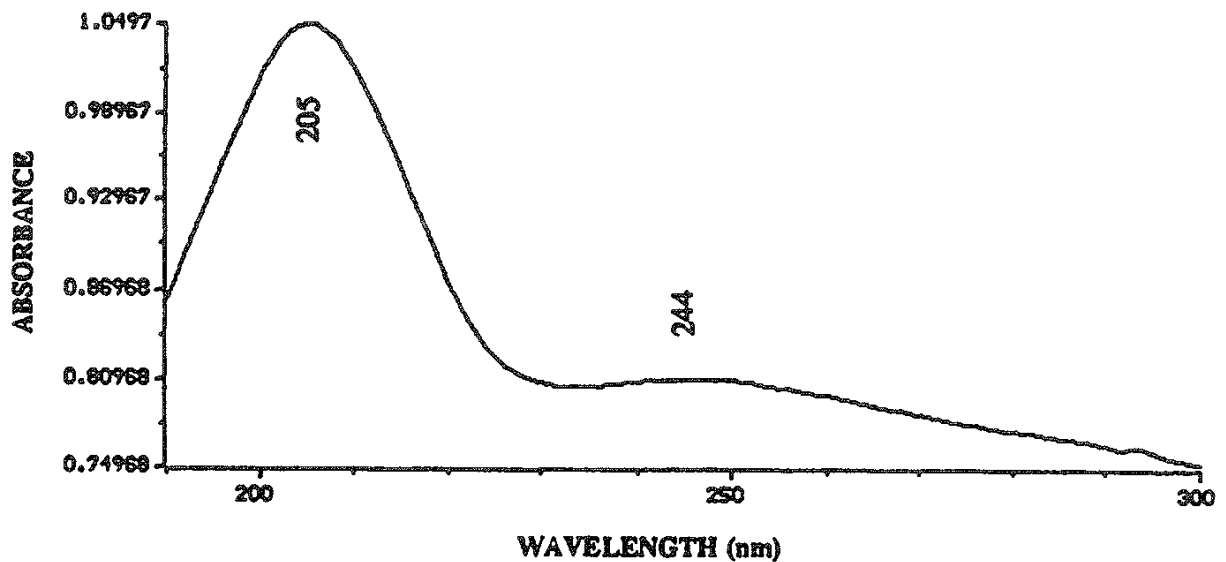


FIG. 7 Absorption spectrum of Optovac KCl crystal showing the absorption due to oxygen (O_2^-) defects. (From Ref. 10.)

which indicate that the University of Utah and Optovac crystals had not been exposed to long-term radiation, as they are free of O_2^- defects.

Therefore it can be concluded that the absorption bands in Fig. 7 for the Optovac KCl are due to the presence of O_2^- defects, while Fig. 8 indicates that the University of Utah KCl crystal is free of any oxygen defects, which was expected, as the University of Utah crystal was grown with extreme care to avoid oxygen contamination.

In any case, the UV/Vis spectra for Optovac KCl and University of Utah KCl and their nonequilibrium electrophoretic mobility results suggest that O_2^- defects

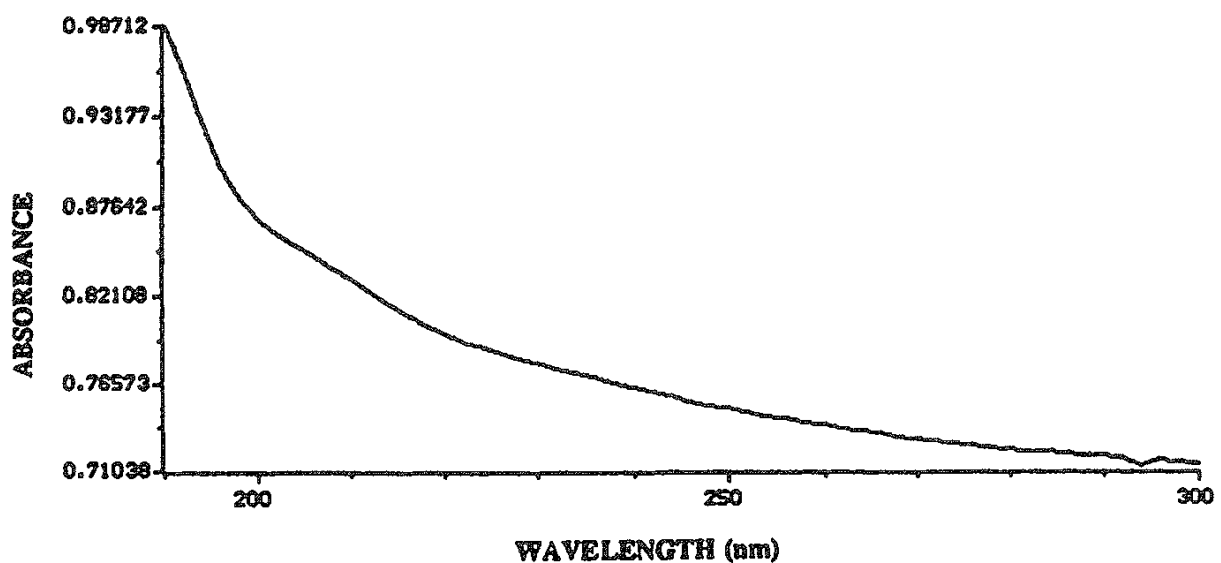


FIG. 8 Absorption spectrum of the University of Utah KCl crystal showing the absence of absorption due to oxygen defects. (From Ref. 10.)

strongly influence the surface properties and are responsible for the deviation of normal KCl from predictions of lattice ion hydration theory.

The concentration of oxygen defects was varied to examine their influence on the electrokinetic properties of KCl. Optovac and reagent grade KCl particles were thermally treated in a nitrogen atmosphere containing less than 1 ppm oxygen in a tube furnace. Similarly, the KCl crystal grown at the University of Utah was thermally treated in an oxygen atmosphere. Table 12 presents the results from these thermal treatment experiments. It can be noted from this table that when the University of Utah KCl particles were thermally treated at 650°C for about 27 h in an oxygen atmosphere, the sign of the surface charge was reversed from positive to negative due to oxygen incorporation into the crystal lattice. In the case of Optovac and reagent grade KCl, the sign of the surface charge reversed from negative to positive when these particles were thermally treated in the presence of nitrogen having less than 1 ppm oxygen. The sign of surface charge reversal in the case of the University of Utah KCl indicates that oxygen has diffused into the crystal, as suggested by the increase in oxygen level from 61 ± 8 ppm to 147 ± 9 ppm, thus accounting for the change in the electrokinetic behavior. These results show that when KCl is relatively free of oxygen defects, its electrokinetic behavior is predicted according to lattice ion hydration theory. However, it is clear from these studies that KCl deviates from lattice ion hydration theory when oxygen defects are introduced into the crystal lattice.

Similar observations can be made for both Optovac and reagent grade KCl particles. Both Optovac and reagent grade KCl (samples with high oxygen content) exhibited a negative surface charge before thermal treatment. When these KCl particles were thermally treated in the presence of nitrogen having less than 1 ppm oxygen, the sign of the surface charge of these particles reversed from negative to positive as expected from lattice ion hydration theory. Presumably, oxygen present in the crystal has diffused out during the thermal treatment due to low oxygen pressure in the atmosphere above the bed of KCl particles. In fact, the UV/Vis spectrum of a KCl plate (Optovac, 5 x 5 x 1 mm), thermally treated at about 650°C in the presence of a nitrogen (oxygen < 1 ppm) atmosphere, revealed that oxygen had indeed been removed from the KCl plate, as indicated by the absence of

TABLE 12 Thermal Treatment Experiments—Effect of Oxygen

| KCl source | Temp/atm (°C) | Time (h) | Electrophoretic mobility | Oxygen (ppm) |
|------------|---------------------|-------------|-----------------------------|-----------------|
| U of U | As prepared | — | $+0.18 \pm 0.10$ | 60 ± 8.6 |
| | 650/O ₂ | 27 | -0.26 ± 0.17 | 147 ± 9.0 |
| Optovac | As received | — | -0.46 ± 0.20 | 345 ± 13.0 |
| | 650, N ₂ | 27 | $+0.34 \pm 0.16$ | Not measured |
| Reagent | As received | — | -0.42 ± 0.19 | Not measured |
| | 650/N ₂ | 27 | $+0.32 \pm 0.16$ | Not measured |

Source: Ref. 10

characteristic absorption bands associated with O_2^- defects in the range of 200–250 nm as shown in Fig. 9.

The change in the electrokinetic behavior of Optovac KCl has been monitored with respect to the thermal treatment time. It took approximately 30 h of thermal treatment (650°C , $\text{O}_2 < 1$ ppm) for the change in the electrokinetic behavior of KCl to occur as shown in Fig. 10. These observations further substantiate the fact that oxygen defect states are responsible for the deviation of KCl from behavior expected according to lattice ion hydration theory.

Based on these results, it seems that the deviation of KCl from the sign of the surface charge predicted according to theory can be explained in terms of defect states present in the crystal lattice, which would account for the anomalous electrokinetic behavior of KCl. In this regard, to further understand the effect of oxygen defect states on the surface charge of alkali halides, NaCl was studied in detail by Veeramasuneni et al. [11]. Oxygen imperfections were intentionally created in an NaCl single crystal in order to examine the influence of oxygen defects on its electrokinetic properties. The surface charge of the NaCl crystal with oxygen (~ 4000 ppm) grown at the University of Utah crystal growth laboratory was found to be negative. On the other hand, optical quality NaCl crystal without oxygen was found to be positively charged. These results suggest that oxygen defects deliberately introduced into positively charged NaCl can reverse the surface charge. Bubble attachment studies [11] also show that the results for the Optovac NaCl (positively charged) were quite opposite to those observed for the University of Utah NaCl (negatively charged).

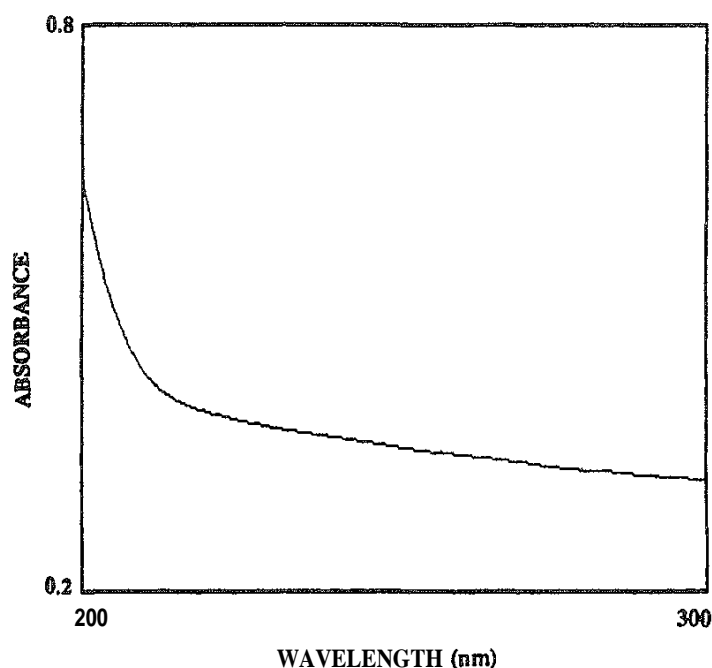


FIG. 9 Absorption spectrum of Optovac KCl thermally treated at 650°C in a nitrogen (oxygen < 1 ppm) atmosphere for 30 h. (From Ref. 10.)

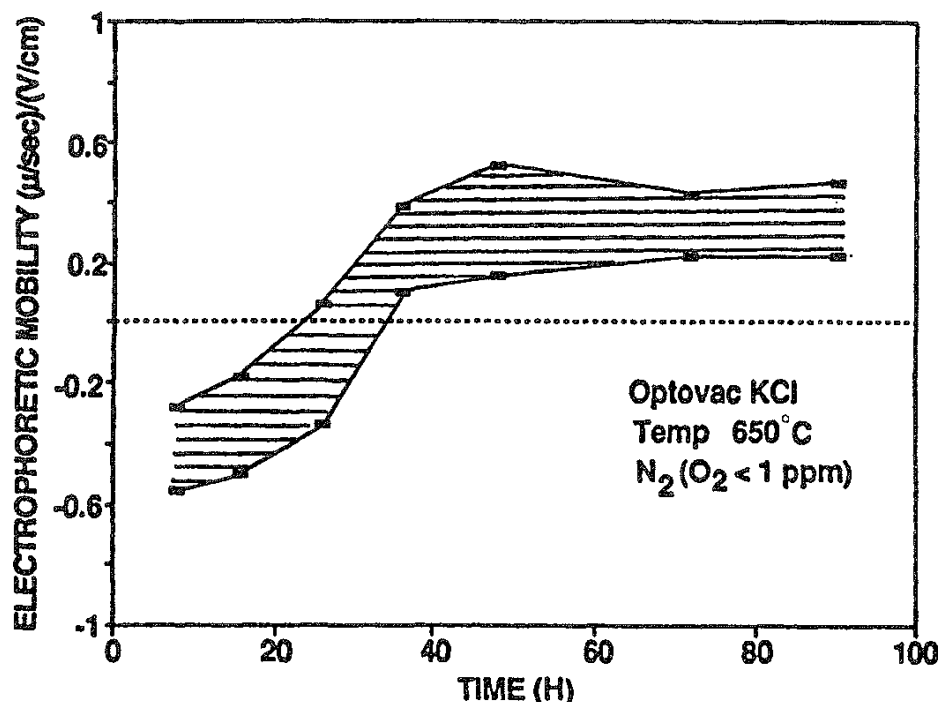


FIG. 10 Nonequilibrium electrophoretic mobility of Optovac KCl thermally treated at 650°C in a nitrogen (oxygen < 1 ppm) atmosphere as a function of time. (From Ref. 10.)

In any case, UV/Vis spectra for University of Utah NaCl and Optovac NaCl and the results from nonequilibrium electrophoretic mobility measurements suggest that the negative surface charge of the University of Utah NaCl is due to the presence of O_2^- defects. It has been demonstrated that oxygen defects can be created in alkali halides to make them negatively charged, thus confirming the previously reported results for oxygen defects in KCl. These results demonstrate that oxygen defect states in NaCl and KCl crystal lattices can change the sign of the surface charge and alter the flotation response of these salts and that of other alkali halide salts is expected.

VI. CONCLUSIONS

Recent contributions have clearly improved our understanding of the fundamentals of various phenomena related to the surface charge of alkali halides in their saturated solutions. For the first time, nonequilibrium electrophoretic mobility measurements for alkali halide salts have been made by laser-Doppler electrophoresis. The measurements, which were made during the initial stages of salt dissolution, were found to be reproducible, and their utility was confirmed by measurement of the corresponding equilibrium electrophoretic mobilities for LiF and NaF. More important, the nonequilibrium electrophoretic mobility measurements allow for the sign of surface charge to be predicted for alkali halides in their saturated solutions. In general, the results can be explained with the simplified lattice ion hydration theory.

The necessity of considering the partial hydration of surface lattice ions in the analysis of the surface charge of alkali halides has been demonstrated. The seven exceptions (LiF, NaCl, KCl, KBr, RbBr, KI, and RbI) whose surface charge, based on simplified lattice ion hydration theory, deviated from experimental measurements were found to be in good agreement with the extended lattice ion hydration theory, which accounts for partial hydration of surface lattice ions by consideration of ion–dipole interaction energies. Sensitivity analysis further confirmed the validity of this approach. Thus, the sign of the surface charge of alkali halides predicted from extended lattice ion hydration theory, which considers partial hydration of surface lattice ions, together with the simplified lattice ion hydration theory was found to be in excellent agreement with nonequilibrium electrophoretic measurements by laser-Doppler electrophoresis.

The deviation of the electrokinetic behavior of KCl from that predicted by lattice ion hydration theory has been found to be due to the presence of oxygen defect states in KCl. The surface charge of a laser quality KCl crystal with very low oxygen content is positive and conforms to the behavior expected according to lattice ion hydration theory. On the other hand, optical quality and reagent grade particulate KCl crystals with relatively high oxygen content are negatively charged and do not conform to the behavior expected according to lattice ion hydration theory. Thermal treatment of these KCl crystals in appropriate atmospheres showed that the sign of the surface charge is controlled by the oxygen content of the KCl crystal. Experimental results suggest that for an oxygen content in excess of about 150 ppm, deviation of KCl from behavior expected according to lattice ion hydration theory should be anticipated. Finally, the results suggest that oxygen defects can be created in alkali halides to make them negatively charged as demonstrated for NaCl and KCl salts.

ACKNOWLEDGMENTS

Support by the DOE Basic Science Division, grant DE-FG-03-93ER14315, for this work is gratefully acknowledged. Thanks are also extended to Dr. M. R. Yalamanchili and Dr. Yuehua Hu for their suggestions and helpful discussions.

REFERENCES

1. M. C. Fuerstenau, J. D. Miller, and M. C. Kuhn, *Chemistry of Flotation*, SME/AIME, Littleton, CO, 1985.
2. E. J. W. Verwey and J. Th. G. Overbeek, *Theory Of the Stability of Lyophobic Colloids*, Elsevier, Amsterdam, 1948.
3. R. J. Pugh, in *Colloid Chemistry in Mineral Processing* (J. S. Laskowski and J. Ralston, eds.), Elsevier, Amsterdam, 1992, p. 243.
4. R. J. Roman, M. C. Fuerstenau, and D. Seidel. *Trans. AIME* 241:56 (1968).
5. R. J. Roman. Ph. D. Thesis, Colorado School of Mines, Golden, CO, 1956.
6. R. S. Pizarro, M. S. Thesis, Colorado School of Mines, Golden, CO, 1967.
7. J. D. Miller, M. R. Yalamanchili, and J. J. Kellar, *Langmuir* 8:1464 (1992).
8. M. R. Yalamanchili, Ph. D. Thesis, University of Utah, Salt Lake City, 1993.

9. S. Veeramasuneni, Y. Hu, and J. D. Miller, *Surf. Sci.* 382:127 (1997).
10. M. R. Yalamanchili and J. D. Miller, *J. Colloid Interface Science* 163:137 (1994).
11. S. Veeramasuneni, M. R. Yalamanchili, and J. D. Miller, *J. Colloid Interface Sci.* 182:275 (1996).
12. K. B. Quast and D. J. Readett, *Adv. Colloids Interface Sci.* 27:169 (1987).
13. R. H. Yoon, T. Salman, and G. Doonay, *J. Colloid Interface Sci.* 70:483 (1979).
14. M. E. Labib, *Colloids Surf.* 29:293 (1988).
15. P. L. deBruyn and G. E. Agar, in *Froth Flotation — 50th Anniversary Volume* (M. C. Fuerstenau, ed.), AIME, New York, 1962, p. 91.
16. F. F. Aplan and D. W. Fuerstenau, in *Froth Flotation — 50th Anniversary Volume* (M. C. Fuerstenau, ed.), AIME, New York, 1962, p. 170.
17. H. van Olphen, *An Introduction to Clay Colloid Chemistry*, Interscience, New York, 1963, p. 90.
18. I. Iwasaki, S. R. B. Cooke, and A. F. Colombo, *U.S. Bureau of Mines, RI 5593* U.S. Department of the Interior, 1960, p. 1.
19. I. Iwasaki, S. R. B. Cooke, and H. S. Choi, *Trans. AIME* 217:238 (1960).
20. I. Iwasaki, S. R. B. Cooke, and Y. S. Kim, *Trans. AIME* 241:453 (1962).
21. J. D. Miller and J. V. Calara, in *Flotation, A. M. Gaudin Memorial Volume* (M. C. Fuerstenau, ed.), AIME, New York, 1976, p. 66.
22. Y. Hu, Y. Lu, S. Veeramasuneni, and J. D. Miller, *J. Colloid Interface Sci.* 190:224 (1997).
23. J. V. Calara and J. D. Miller, *J. Chem. Phys.* 65:843 (1976).
24. J. V. Calara and J. D. Miller, in *Colloid and Interface Science, Proceedings of International Conference — 50th Colloid and Surface Science Symposium* (M. Kerker, ed.), Academic, New York, 1976, p. 157.
25. J. P. Hunt, *Metal Ions in Solutions*, W. A. Benjamin, New York, 1965.
26. Y. Marcus, *Ion Salvation*, Wiley, New York, 1985, p. 123.
27. G. A. Krestov, *Thermodynamics of Solvation: Solution and Dissolution, Ions and Solvents, Structure and Energetics*, Ellis Horwood Ser. Phys. Chem., Ellis Horwood, New York, 1991, p. 106.
28. R. J. Hunter, *Zeta Potential in Colloids Science*, Academic, New York, 1981.
29. A. W. Adamson, *Physical Chemistry of Surfaces*, 4th ed., Wiley, New York, 1982.
30. Anon., *Malvern Instruments Zetasizer User's Manual*, IM060, 1990, Issue 2.
31. M. Hancer, Y. Hu, M. C. Fuerstenau, and J. D. Miller, *Proceedings of the XX International Mineral Processing Congress* (H. Hoberg, ed.), GDMB, Clausthal-Zellerfeld, Germany, 1997, p. 715.
32. J. N. Israelachvili, *Intermolecular and Surface Forces*, 2nd ed., Academic, New York, 1992, p. 235.
33. W. S. Fyfe, *Geochemistry of Solids*, McGraw-Hill, New York, 1964, p. 151.
34. H. C. Gatos, in *Crystal Growth: A Tutorial Approach* (W. Bardsley, D. T. Hurle, and J. B. Mullin, eds.), North-Holland, New York, 1979, pp. 1–16.
35. F. Fischer, H. Grundig, and R. Hilsch, *Z. Phys.* 189:79 (1966).
36. D. Wandt, W. Gellerinan, and F. Luty, *J. Appl. Phys.* 61:864 (1987).
37. F. Luty, in *Physics of Color Centers* (W. B. Fowler, ed.), Academic, New York, 1968, p. 182.

Ionic Adsorbates on Hydrophobic Surfaces

RICHARD L. ZOLLARS Department of Chemical Engineering, Washington State University, Pullman, Washington

- I. Introduction
- II. Historical Perspective
- III. Structure Within the Adsorbed Layer
 - A. Experimental verification
 - B. Observations of hydrophobic interactions
- IV. Adsorption with Attractive Electrostatic Interactions
- V. Adsorption with Repulsive Electrostatic Interactions
- VI. Adsorption of Mixed Surfactants
- VII. Predictive Models of Surfactant Adsorption
- VIII. Summary
- References

I. INTRODUCTION

Surfactants are used in a wide variety of applications such as ore flotation, cleaning, polymerization processes, and pharmaceuticals and agriculture. The usual role for the surfactant is to modify interfacial properties, whether they be liquid/liquid, solid/liquid, or gas/liquid interfaces. To be effective in any of these applications, however, the surfactant must adsorb strongly at the interface. In addition to its concentration at the interface, the conformation of the surfactant at the interface is also an important factor. While the influence of solution properties such as concentration, ionic strength, and pH on surfactant adsorption are well known, the properties of the other phase also exert a significant influence.

Perhaps the most varied combinations occur in solid–liquid systems because of the variety of properties possessed by the solid phase. The most obvious property of the solid phase to affect surfactant adsorption is the hydrophilic or hydrophobic

character of the surface. But even within either of these groups, variations in the polarity of the surface have also been found to exert a significant influence on adsorption. Since solid surfaces may also possess an electric charge, the electrostatic interactions between the surface and the surfactant are a third major factor influencing both the amount absorbed and the conformation of the absorbed material.

This chapter reviews results for the adsorption of ionic surfactants onto hydrophobic surfaces. Even with this limitation there are many possible combinations. Both anionic and cationic surfactants are considered. The hydrophobic surfaces may be either uncharged or positively or negatively charged. Thus, the electrostatic interactions between the adsorbing surface and the surfactant may be either non-existent, attractive, or repulsive. Finally, the adsorbing materials may be either a single species or a combination of surfactants. This review is not a comprehensive overview of all of the published material on this topic. Rather it presents representative results concerning the adsorption of ionic surfactants onto hydrophobic surfaces.

II. HISTORICAL PERSPECTIVE

An early investigation of the adsorption of ionic surfactants onto hydrophobic surfaces is the work by Maron et al. on soap titration [1]. Although conceived as a method for the measurement of the average particle size of a synthetic latex, soap titration begins to shed some light on adsorption phenomena. The surface tension of a sample of the suspension to be analyzed is measured as a function of the amount of surfactant added. This analysis is repeated for a second sample that contains a different concentration of suspended solids. The difference between the amounts of surfactant needed to reach saturation, as measured by reaching the critical micelle concentration (cmc), for the two samples must be the amount of surfactant needed to saturate the additional surface area present in the sample with the higher suspended solids concentration. If the surface area occupied by a single surfactant molecule at saturation is a constant, this amount of surfactant can be converted to latex surface area and ultimately to an average particle size.

Following the work by Maron and coworkers, a number of publications appeared investigating various aspects of the technique and therefore also of surfactant adsorption. Brodnyan and Brown [2] used surface coverage areas for both anionic and nonionic surfactants measured independently of the soap titration to determine the average particle size of a latex. This was compared with the average particle size measured by ultracentrifugation and found to agree. Brodnyan and Brown took this as a verification of the technique and also as proof that the assumption of monolayer coverage by the surfactant at saturation was valid. This investigation also demonstrated that nonionic surfactants could be used as well as anionic surfactants. A number of other investigations also appeared seeking improvements in the technique (improved detection of the cmc [3], corrections for the amount of surfactant dissolved in the aqueous phase [4]), but none questioned the basic underlying assumptions.

Although other investigators had verified that the adsorption area of the surfactants was a constant independent of the adsorbing surface [5], this assumption

began to be questioned. Paxton [6] reported that the adsorption area for sodium dodecylbenzene sulfonate (SDBS) varied depending not only on the ionic strength of the solution but also on the polymer forming the latex particles. Piirma and Chen [7] also observed a variation in the adsorption area of two anionic surfactants adsorbed onto polystyrene or poly(methyl methacrylate) latices. In addition, they also observed a steady increase in the adsorption area for sodium dodecyl sulfate (SDS) as the composition of a copolymer latex went from 100% styrene to 100% methyl methacrylate (from less to more polar). Another important observation was the effect of adding solvents for the polymer to the system. When various solvents for the polymer forming the latex particles were added, the adsorption area for both potassium oleate and sodium dodecyl sulfate increased, leading to the suggestion that a solvent-swollen particle surface allowed greater penetration of the surfactant tail into the particles.

The observation that the adsorption area for a surfactant depended not only on the surfactant but also on the adsorbing surface was further confirmed in a number of investigations. Vijayendran [8] studied the adsorption of sodium dodecyl sulfate onto a number of different polymeric latices and onto various water/hydrocarbon interfaces. In so doing he was able to demonstrate the impact of the polarity of the solid/liquid interface in determining the adsorption area of the surfactant. By assuming a Langmuir type of adsorption isotherm, Vijayendran was able to separate the polar from the dispersive contributions to the polymer surface energy.

In a series of articles, Kronberg and coworkers studied the adsorption of non-ionic surfactants onto a polymeric latex. A Flory-Huggins approach was used to analyze the adsorption of a series of nonylphenol-polyoxypropylene-polyoxyethylene surfactants onto a polystyrene latex that indicated that the driving force for adsorption was primarily due to the surfactant structure (EO chain length) [9]. Extending this work, Kronberg and Stenius [10,11] used the thermodynamic model they had developed to analyze the adsorption of nonylphenol-polyoxyethylene surfactants of varying EO chain length. From this analysis they determined that adsorption measurements could be used to determine the latex polarity and that for this situation, 80% of the adsorption free energy was due to the structure of the surfactant, with the remaining 20% arising from the characteristics of the adsorbing surface. They also postulated that the adsorbed surfactant would be oriented with the hydrophobic moiety pointed toward the polymeric latex surface. This allowed surfactant-surfactant interactions to replace some of the water-hydrophobic moiety interactions, thus reducing the overall free energy and leading to adsorption. Finally, Kronberg [12] examined the applicability of the Langmuir adsorption isotherm for surfactant adsorption and found that two fundamental assumptions in the Langmuir isotherm were violated: (1) There were significant interactions between adsorbed species and (2) it is not possible to have a solvent-surface contact replaced by a surfactant-surface contact due to the differences in the sizes of the two species. However, the effects of these two differences work in opposite directions so that typical surfactant isotherms do indeed appear to follow the Langmuir model.

The result of these investigations leaves the following view of adsorption of ionic surfactants onto hydrophobic surfaces. Measured adsorption isotherms (Langmuir type) and comparisons between particle sizes as measured by soap titration and

other techniques led to the conclusion that adsorption leads to monolayer coverage by the surfactant. This monolayer is adsorbed on the surface with the hydrophobic moiety of the surfactant pointed toward the hydrophobic surface and the hydrophilic moiety pointed toward the aqueous phase. While the structure of the surfactant plays a major role in determining the amount adsorbed (or adsorption area per surfactant molecule) the characteristics of the adsorbing surface also play a significant role in the adsorption process. Various investigators have noted the possibility of cooperative adsorption phenomena resulting from hydrophobe–hydrophobe interactions between adsorbed surfactant molecules. Many questions remain unanswered, however. Some of these are: What is the structure of the adsorbed surfactant layer? Can this structure be explained by known colloidal phenomena? What is the effect of electrostatic interactions between the adsorbing surface and the surfactant? What happens when there is more than one surfactant present? Can the adsorption phenomena be modeled for all of the possible surfactant/surface systems?

III. STRUCTURE WITHIN THE ADSORBED LAYER

Intuitively one would expect that a surfactant would adsorb onto a hydrophobic surface with its hydrophobic portion pointed toward the hydrophobic surface and the hydrophilic portion pointed toward the aqueous phase. This adsorption is driven by the "hydrophobic attraction" between these two hydrophobic moieties. For a hydrophilic surface, adsorption should take place with the opposite orientation, as observed by Furlong and Aston [13].

When ionic surfactants adsorb onto an uncharged, hydrophobic surface, the charge at the solid surface increases, giving the surface a more hydrophilic character. As the adsorption continues, the concentration of charged groups at the outer edge of the adsorbed layer becomes great enough to block any further adsorption due to the electrostatic repulsions between the adsorbed surfactant and the surfactant molecules approaching the surface. This is opposite the expectation for adsorption onto hydrophilic surfaces [14]. In this latter situation, surfactants are expected to first adsorb with the hydrophilic portion in contact with the solid surface, frequently as a result of electrostatic attractions. This leaves the surface covered with an adsorbed layer with its hydrophobic ends exposed and thus looking very much like a hydrophobic surface. Subsequent adsorption will then occur onto this adsorbed layer, with the hydrophobic ends of the next layer of surfactants oriented toward the first layer. The final result, at saturation, is an adsorbed bilayer at the surface. Further adsorption is blocked by electrostatic interactions between the hydrophilic ends of the surfactants.

A. Experimental Verification

While data from many surfactant adsorption experiments would support the assumption that monolayer adsorption occurs, direct measurements of the adsorbed layer structure were not reported until recently. Herder [15] used a combination of contact angle measurements and surface force measurements to show that this is the situation for the adsorption of phosphine oxide onto a mica surface

made hydrophobic by the deposition of dimethyldioctadecylammonium bromide using Langmuir-Blodgett deposition. Using infrared-visible sum-frequency spectroscopy. Ward et al. [16] studied the adsorption of dodecanol onto an uncharged hydrophobic surface (a monolayer of octadecanethiol on gold). By using an uncharged surface-active material and a compact monolayer of hydrophobic material, this experiment ensures the lack of any electrostatic interactions between the adsorbing species and the surface. Their results show that the dodecanol is adsorbed with the terminal methyl group of the dodecanol oriented toward the hydrophobic surface. When similar experiments are conducted using dodecanol dissolved in an organic solvent, the dodecanol adsorbs onto the surface with the alkyl chain lying parallel to the surface.

In a study of the adsorption of sodium dodecyl sulfate onto graphite, Wanless and Ducker [17] found that the situation was more complex. Using atomic force microscopy, they were able to observe periodic structures developing on the surface with increasing surfactant concentration. For low bulk concentrations of surfactant (0.35 cmc), the adsorbed material was observed to be homogeneous. At higher bulk concentrations, periodic ridges, assumed to be hemicylinders, were observed. As the surfactant concentration increased still further, no change in the morphology was observed, although the spacing between the ridges decreased. These observations were counter to those observed for an analogous double-chain surfactant where the adsorbed layer remained homogeneous at all bulk surfactant concentrations.

Using ellipsometry, Tiberg [18] was able to measure adsorbed film thickness and use these measurements to deduce orientations for a series of polyoxyethylene glycol alkyl ethers adsorbed onto either a clean silicon surface (hydrophilic) or a silicon surface treated with dimethyloctylchlorosilane (hydrophobic). When the ethers were adsorbed onto the hydrophilic surface, surface micelles and bilayers were observed. On the uncharged hydrophobic surface, however, submonolayer coverage increasing to monolayer coverage was observed. At low coverage the adsorbed surfactants were observed to tilt toward the surface, a tilt that decreased continuously with increasing surface coverage. The claim was also made that the adsorption onto a hydrophobic surface appeared to be a noncooperative process. The observation that monolayer coverage results when surfactants are adsorbed onto a hydrophobic surface was also confirmed by Walthermo et al. [19], who studied the adsorption of alkyl glucosides onto a mica surface that had been rendered hydrophobic by using a Langmuir-Blodgett technique to deposit a layer of dimethyldioctadecylammonium bromide onto the surface.

B. Observations of Hydrophobic Interactions

The tendency for a hydrophobic material to adsorb onto a hydrophobic surface is frequently described in terms of a "hydrophobic interaction (attraction)." While entropic arguments for the presence of such a phenomenon are easy to make, the fact that long-range attractive forces between hydrophobic surfaces have been observed cannot be accounted for by typical DLVO theory [20]. A number of explanations of this phenomenon have been advanced, such as enhanced hydrogen bonding, electrostatic correlation forces, film stability, dissolved gases, and density fluctuations, but none has been successful in explaining all of the features of this

force that have been observed. Kekicheff and Spalla [21] conducted a series of experiments in a surface force apparatus using carefully degassed samples but still observed a long-range attractive force, thus indicating that dissolved gases are not the underlying cause of the attractive force. They also measured the refractive index between the surfaces in the same apparatus using multiple-beam interferometry and found an absence of density fluctuations, indicating that these too are not the source of the attractive hydrophobic forces.

Of interest in adsorption phenomena, however, is the work of Tsao et al. [22]. In their paper the hypothesis is made that the long-range attractive force arises from electric fields generated by lateral structures present on the hydrophobic surfaces. Furthermore, such a field is generated on one surface, with the second surface responding to the field of the first surface through its polarizability. Lateral interactions are also important when considering adsorption phenomena, since they are often cited as giving rise to enhanced adsorption through associations between the hydrophobic portions of the adsorbed surfactant molecules. These interactions may become stronger when a molecule is adsorbed, as van Lent et al. [23] reported that the interactions between polymeric species within grafted polymer layers are stronger than the interactions that occur between molecules within a grafted layer and free polymer molecules.

These results indicate that the presence of mono- or bilayer coverage depends on both the surfactant and the adsorbing surface. Within these layers there is an ordering of the adsorbed molecules due to lateral hydrophobic interactions. The presence of the adsorbed layer gives rise to a long-range attractive force. This force not only affects other nearby surfaces but could also attract surfactant molecules. In all of these studies the adsorbing surface has been electrically neutral. In the following sections, electrostatic effects on adsorption are considered.

IV. ADSORPTION WITH ATTRACTIVE ELECTROSTATIC INTERACTIONS

A number of adsorption studies have been conducted in which an ionic surfactant has been adsorbed onto a hydrophobic surface containing bound electric charges of the opposite sign. In this situation the first surfactant molecules adsorbed are assumed to adsorb via the attractive electrostatic forces present and thus to adsorb with their hydrophilic head groups pointed toward the surface. Since the hydrophobic tails will thus extend toward the aqueous phase, the particle becomes progressively more and more hydrophobic, as a result of both the hydrophobic tail orientation and the neutralization of the surface charges. Ultimately a second layer of surfactant starts to adsorb, this time with the hydrophobic portion of the molecule interacting with the hydrophobic portion of the electrostatically bound surfactants and the head groups pointing toward the aqueous phase. This type of behavior was observed by Connor and Ottewill [24] for the adsorption of cationic surfactants onto a polystyrene latex containing carboxyl groups on the surface and by Kayes [25] for a series of trimethylammonium bromides onto polystyrene latices. The amount of surfactant adsorbed was determined by measuring the amount remaining in solution after equilibration with the latex, using liquid scintillation

counting. The electrophoretic mobility of the particles was also measured at the same time. When the cationic surfactants were adsorbed onto an uncharged polystyrene latex, a Langmuir-type isotherm was observed. When adsorbed onto a charged surface, however, a well-defined "knee" was observed in the isotherm. A comparison of the adsorption results with the electrophoretic mobility measurements showed that the knee occurred at the point where the surface charge of the particles reversed. Thus they concluded that up to the knee in the isotherm, adsorption occurred via ionic interactions between the surfactant head group and the bound surface charges. Above the knee the adsorption isotherm closely resembled that observed for adsorption onto an uncharged latex surface. The fact that the adsorbed concentration was affected by the ionic strength of the aqueous phase also led Connor and Ottewill to suggest that lateral interactions between the adsorbed surfactant molecules were present and that the adsorbed molecules were not in a completely vertical orientation at low ionic strength even when the surface was saturated.

An investigation similar to that reported by Connor and Ottewill was recently published by Gonzalez et al. [26] except that in this latter investigation anionic surfactants (alkyl sulfonates) were adsorbed onto a cationic polystyrene latex. Again the amount of surfactant adsorbed was determined by measuring the difference in aqueous phase surfactant concentration before and after equilibration with the latex (via the methylene blue method) along with measurements of the electrophoretic mobility of the latex particles. Again a jump in the adsorption isotherm was observed at the point of charge reversal for the latex particles, which was attributed to a changeover in adsorption from a head-down orientation due to head group–surface group electrostatic interactions to a head-outward orientation due to hydrophobic interactions between the surfactant tail group and either the particle surface or previously adsorbed material. Unlike the investigation by Connor and Ottewill, however, this investigation found higher concentrations of the anionic surfactants adsorbed at the latex particle surface. The investigators explained this by hypothesizing a multiple-step mechanism for adsorption. They hypothesized that the first molecules to adsorb may do so either by electrostatic or hydrophobic interactions and by lying flat on the latex surface. At higher surface coverages the adsorbed surfactant molecules begin to move to a partially vertical orientation with the hydrophilic groups pointing toward the aqueous phase. As the cmc was approached there appeared to be interactions between the adsorbed surfactant molecules, finally leading to a leveling off of the adsorbed amount.

Zhao and Brown [27,28] in a more recent pair of articles studied the adsorption of both cationic (alkyltrimethylammonium bromide) and anionic (sodium dedecyl sulfate) surfactants onto polystyrene latex particles modified to have aromatic amino groups on the surface. Conductimetric titrations of the latex particles indicated that they possessed both cationic groups (the amino groups) and anionic groups (sulfate residues from the initiator). The amount of surfactant adsorbed was determined by surface tension measurements (drop weight method), while the conformation of the adsorbed surfactant was inferred from measurements of the hydrodynamic diameter by dynamic light scattering. In both cases, arguments are made for including the effect of the roughness of the particle surface in considering adsorption phenomena. The ionic groups on the polystyrene chains are known to

impart a surface-active character to the chains that results in a "hairy" surface rather than a hard, billiard ball-like surface. After examining the changes in the hydrodynamic diameter of the latex particles, Zhao and Brown postulate that the initial adsorption is a combination of both a hydrophobic interaction between the polystyrene chains in the hairy layer and the hydrophobic tails of the surfactants, and either a hydrogen bonding interaction (for SDS) or an electrostatic interaction (for the cationic surfactants) between the surfactant head group and the surface group of the opposite charge. At higher surfactant concentrations, the adsorption process then becomes dominated by hydrophobic associations, ultimately resulting in globular micelles strung along polystyrene chains that extend out from the surface due to the electrostatic repulsions between head groups of the surfactants adsorbed along the chain.

The assertion that both hydrophobic and electrostatic (or hydrogen bonding) interactions occur during the initial phases of adsorption appears to arise because the amount of surfactant adsorbed at the point where their adsorption isotherms show a break is higher than the number of oppositely charged groups at the particle surface. This does not agree with the observation by Connor and Ottewill of a one-to-one correlation between initial surfactant adsorption and surface groups of the opposite sign. Zhao and Brown also claim that the adsorbed amount continued to increase even after the cmc had been reached, which could be explained by having globular micelles attached along an extended polymer chain. Again, this is counter to many other investigations where the final plateau adsorption level is usually observed to occur very near the cmc. It is also interesting that the maximum amount of surfactant adsorbed in any of the results shown in the two papers by Zhao and Brown corresponds to an adsorption area of between 0.20 and 1.0 nm^2 per molecule. These values are not significantly different from the adsorption areas at saturation reported for SDS and alkyltrimethylammonium ions, which are typically in the $0.20\text{--}0.40\text{ nm}^2/\text{molecule}$ range. Considering that the cross-sectional area of a methylene chain has been reported to be 0.23 nm^2 , the adsorption area reported by Zhao and Brown would appear to argue more for monolayer coverage rather than for such structures as globular micelles strung along an extended polymer chain.

The potential for tail-to-tail interactions in the adsorbed surfactant was clearly demonstrated in an article by Kandori et al. [29]. They studied the adsorption of sodium dodecyl sulfate, cetyltrimethylammonium bromide (CTAB), and sodium bis(2-ethylhexyl)sulfosuccinate (Aerosol OT) onto both an anionic and a zwitterionic latex. They found, as did Connor and Ottewill, that a one-to-one relationship existed between adsorbed amount and surface charge for the case of adsorption of an ionic surfactant onto a surface of opposite charge. They also determined, through zeta potential measurements, that for both CTAB and Aerosol OT there appeared to be two surfactant molecules adsorbed to the tail of each molecule adsorbed in the head-down conformation. This is interesting in view of the fact that Aerosol OT is a two-tailed surfactant, thus giving rise to twice as many tails for subsequent adsorption when it is adsorbed in the head-down conformation. The result by Kandori would thus indicate that the limiting factor for the second layer of adsorbed material is not the number of tails available but is perhaps the interactions between the head groups on this second adsorbed layer.

V. ADSORPTION WITH REPULSIVE ELECTROSTATIC INTERACTIONS

For the situation where both the ionic surfactant and the adsorbing surface have charged groups of the same sign, there will be a repulsive electrostatic force tending to prevent the surfactant from adsorbing onto the surface. Any adsorption must then take place via hydrophobic interactions between the surface and the hydrophobic portion of the surfactant. Since adsorption must occur through the hydrophobic portion of the surfactant, the expected conformation of the adsorbed surfactant molecule would have the head group pointing toward the aqueous phase. This conformation would seem to preclude multilayer coverage, giving rise instead to an adsorbed monolayer. This is the conclusion reached by Keesom et al. [30] as a result of studying the adsorption of sodium dodecyl sulfate onto a polycarbonate surface. The results of this investigation show that the adsorbed materials are oriented with the hydrophobic end toward the surface and the head groups oriented toward the aqueous phase with a surface coverage of less than a full monolayer. The observation that less than monolayer coverage may occur was also made by Becher et al. [31] for the adsorption of sodium dodecylbenzene sulfonate onto atrazine and cyanazine, two hydrophobic crystalline herbicides.

In contrast to these observations are the results reported by Brown and Zhao [32,33] for the adsorption of sodium dodecyl sulfate onto polystyrene and polystyrene-butadiene latex particles. In these investigations the amount of surfactant adsorbed is determined by measuring the surfactant concentration in the aqueous phase before and after equilibration with the latex via surface tension measurements (drop weight method), while changes in the hydrodynamic diameter were measured via dynamic light scattering. They continue to report two-stage adsorption isotherms, although this result has not been reported by other investigators. As with their reports for adsorption of a surfactant onto a surface containing a group of opposite charge, Brown and Zhao report that the initial adsorption is via hydrophobic interactions between the surfactant tail group and the latex particle surface. As adsorption proceeds, however, Brown and Zhao report that the adsorbed surfactant molecules begin to form micelles and hemimicelles at the sites of the previously adsorbed species. Computing the adsorption area at saturation from their results yields values between 0.30 and 0.40 nm²/molecule. Since this is very close to the results for monolayer coverage by sodium dodecyl sulfate reported by many other investigators, the claim of multilayer adsorption seems unlikely.

The most complete studies of surfactant adsorption onto hydrophobic surfaces containing the same charge are those by Ali et al. [34], Hoeft and Zollars [35], and Brouwer and Zsom [36]. In all of these studies a series of polystyrene latices were used with varying surface charge densities. The adsorption of alkyl sulfates, usually sodium dodecyl sulfate, onto these latices then allowed the direct study of the effect of the electrostatic interactions between the surfactant and the surface. In these studies the amount of sodium dodecyl sulfate adsorbed at saturation was found to decrease with increasing surface charge density of the same sign, as shown in Fig. 1. Unlike the investigation reported by Brown and Zhao, the adsorption isotherms were all Langmuir-type isotherms, indicating the presence of only monolayer cover-

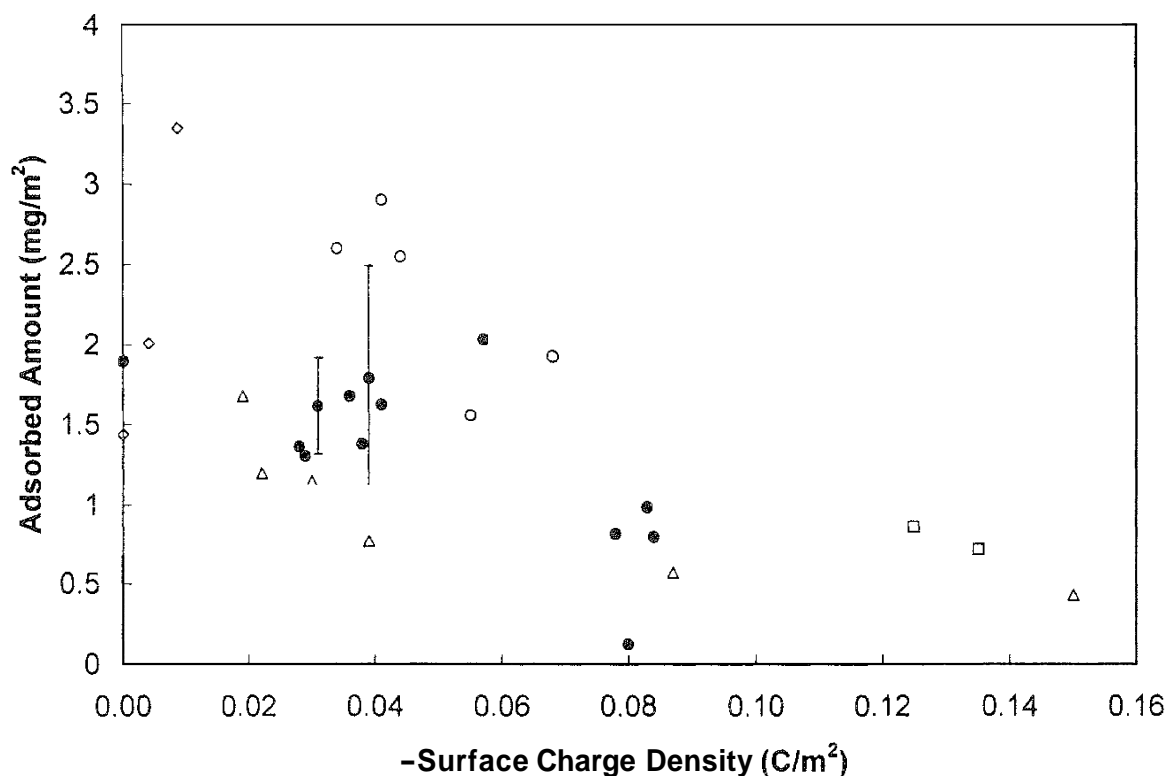


FIG. 1 Amount of sodium dodecyl sulfate adsorbed onto polystyrene latex surfaces as a function of surface charge density. (●) Hoeft [44]; (◇) Ali et al. [34]; (○) Hoeft and Zollars [35]; (△) Brouwer and Zsom [36]; (□) Gwin [37].

age. In this situation the decrease in adsorbed amount is easy to explain. As surfactant is adsorbed, the surface charge density of the particle will increase due to a combination of the groups bound to the surface and the head groups on the adsorbed surfactant molecules. As the surface charge of the same sign increases there are increasingly stronger electrostatic repulsions between the surfactant molecules and the adsorbing surface acting to prevent the adsorption from occurring. In fact, as observed by Gwin [37], when the surface charge on the latex particle surface becomes large enough, no observable adsorption takes place. Similar changes in adsorbed amount with surface charge density were also reported for sodium octyl sulfate and sodium decyl sulfate in the investigation by Hoeft and Zollars. This study also showed that the amount of surfactant adsorbed at a constant surface charge density increased with increasing alkyl chain length of the surfactant as would be expected for increasingly more hydrophobic species.

When all of the data for the adsorption of sodium dodecyl sulfate onto a polystyrene latex particle containing bound sulfate groups is examined (Fig. 1), the relationship between adsorbed amount and surface charge appears to be more complex than described above. Except for an offset between the data from Brouwer and Zsom (possibly due to inaccuracies in the measurement of the surface charge density resulting from not pretreating the latex with a dilute acid), the amount of sodium dodecyl sulfate adsorbed appears to first increase with increasing surface charge density followed by a decrease, a region of relatively little change

from -0.03 to -0.07 C/m^2 , followed by a further decrease with higher surface charge densities. Tuin and Stein [38] also observed that surface charge density had little effect on the adsorption of sodium dodecylbenzene sulfonate onto polystyrene latex particles for surface charge densities between 0.02 and 0.10 C/m^2 . These changes have been explained as arising from changes in the adsorbed surfactant conformation resulting from the electrostatic interactions. When charged groups are first introduced onto the latex surface, the electrostatic repulsions will cause the adsorbed surfactant molecules to change to a more extended conformation to reduce the electrostatic interactions with the particle surface. This results in two changes. First, more of the polystyrene surface will be exposed, allowing for further surfactant adsorption. Second, with fewer surfactant hydrophobe-particle surface contacts, the potential for more hydrophobic interactions between the surfactant molecules is increased, which can also increase surfactant adsorption. These rearrangements of the adsorbed surfactant molecules could give rise to increases in the amount adsorbed or act to counter the tendency for reduced adsorption arising from increased electrostatic repulsions.

VI. ADSORPTION OF MIXED SURFACTANTS

Since hydrophobic interactions appear to play a significant role in determining surfactant adsorption it is possible that these interactions may also alter the manner in which a mixture of surface-active materials might adsorb. In a very early investigation, Orr and Breitman [39] found that when mixtures of anionic and nonionic surfactants were adsorbed onto a polymeric latex particle there was a decrease in the adsorption area per molecule for the anionic surfactants. Hay et al. [40], however, observed a decrease in total adsorption for sodium dodecyl sulfate and *O*-*n*-octyltetraethylene glycol onto graphitized carbon.

In general, however, it is observed that the presence of a nonionic surface-active material will increase the adsorption of ionic surfactants. This was directly observed using in situ sum-frequency spectroscopy for the adsorption of sodium dodecyl sulfate and dodecanol by Bain et al. [41], where more highly ordered films are observed for dodecanol-sodium dodecyl sulfate mixtures than for pure sodium dodecyl sulfate. The reason for this is usually given as a screening of the electrostatic interactions between the head groups on the sodium dodecyl sulfate by the nonionic material, allowing for a closer approach by the head group while still maintaining strong hydrophobic interactions within the adsorbed layer. This, in turn, allows more compact adsorbed layers and greater adsorption.

A possible reason for the decreased adsorption of some nonionic materials has been suggested by Claesson et al. [42]. In a study of the adsorption of sodium dodecyl sulfate and ethyl(hydroxyethyl) cellulose onto hydrophobized silica surfaces, they found that the amount of adsorbed cellulosic derivative was reduced when sodium dodecyl sulfate is also adsorbed. A possible reason for this is again the effect of hydrophobic associations. The sodium dodecyl sulfate, being more surface-active, will tend to adsorb onto the hydrophobic surface more strongly. It will also associate with the ethyl(hydroxyethyl) cellulose in solution, rendering this nonionic material more hydrophilic. With both the adsorbing surface and the

nonionic material becoming more hydrophilic in the presence of the sodium dodecyl sulfate, the driving force for adsorption is reduced.

For much bulkier surfactants the orderly arrangements observed for simpler surfactants appear to disappear. Johal et al. [43] used sum-frequency spectroscopy to observe the coadsorption of a series of trichain surfactants and dodecanol. Their data indicated that the best model for the coadsorption was one consisting of an ordered dodecanol monolayer with scattered monomers or small clusters of disordered trichain molecules.

Hoeft [44] also studied the cooperative and competitive adsorption of ionic surfactant mixtures onto hydrophobic surfaces. When shorter alkyl chain surfactants (sodium octyl sulfonate and sodium decyl sulfonate) are adsorbed, the decyl will displace the octyl surfactant. For mixtures of sodium dodecyl sulfonate and sodium octyl sulfonate, however, there appears to be an association between the surfactant molecules leading to enhanced adsorption of the sodium dodecyl sulfonate with no depletion of the octyl sulfonate adsorption. This is shown in Fig. 2, where the lines indicate the expected adsorption determined using a two-component Langmuir adsorption isotherm with the adsorption parameters determined by analyzing the data from adsorption of each species individually. Also shown in Fig. 2 is the concentration of surface-active materials in the aqueous phase at equilibrium. In each of these experiments the total molar concentration and amount of surfactant solution added to the latex was a constant, as was the amount of latex. Thus a lower value for the bulk concentration corresponds to greater adsorption.

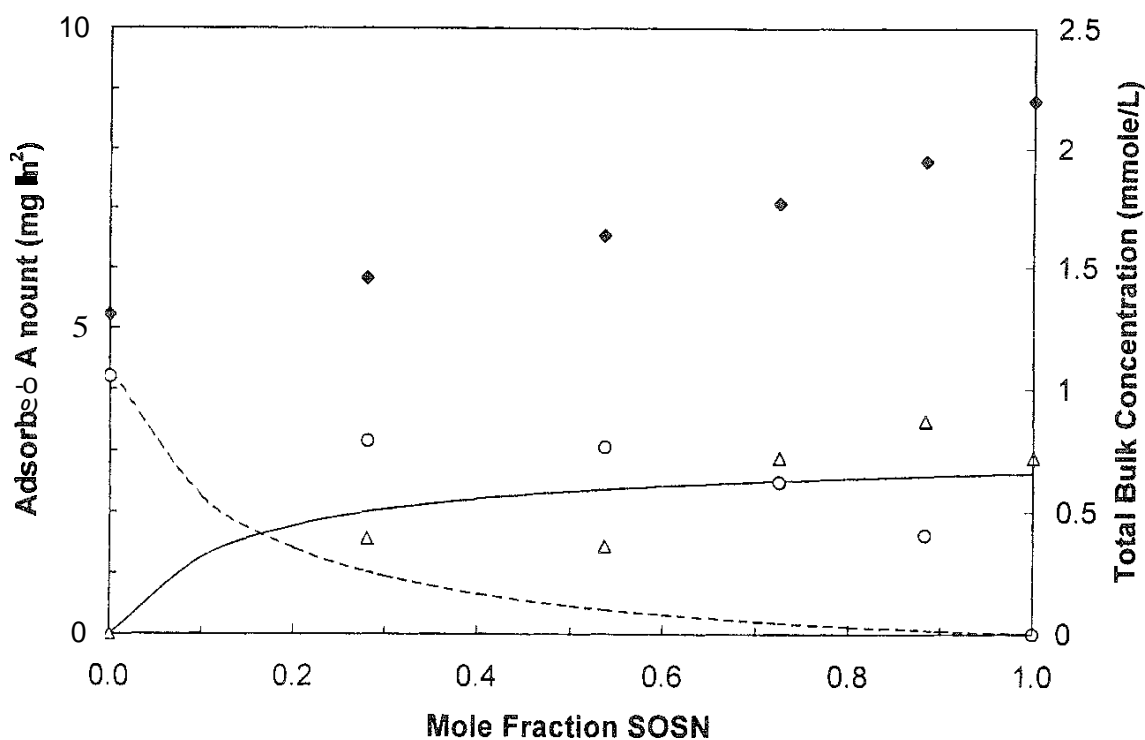


FIG. 2 Adsorption of (Δ) sodium octyl sulfonate and (\circ) sodium dodecyl sulfonate onto polystyrene latex particles, (\blacklozenge) bulk surfactant concentration, —, (---) value predicted from Langmuir model.

VII PREDICTIVE MODELS OF SURFACTANT ADSORPTION

The investigations reported above generally rely on established models, such as the Langmuir isotherm, for the analysis of their data. The difficulty with this approach is that each model contains parameters that are specific to the surfactant–surface–solution–temperature combination used during the experimentation. This makes it virtually impossible to develop a model capable of predicting surfactant adsorption because of the large number of possible combinations of surfactants, surfaces, and solutions. An exception to this are the self-consistent field models proposed by Scheutjens and various coworkers. The models all started with a common approach — a Flory–Huggins type of analysis of the solution phase in contact with the surface. In this approach the solution is modeled as a quasi-lattice, with each site in the lattice being occupied either by a solvent molecule or by a segment of the surface-active material. By developing interaction parameters for segment–solvent, segment–surface, and solvent–surface interactions, the free energy of the system can be calculated and minimized to yield the concentration profile of the surfactant segments as a function of distance from the surface. This profile can be used to predict both the amount of surfactant adsorbed and the average conformation of the adsorbed material.

As first developed [45,46], the model allowed only a single surface-active material composed of only one type of segment. In subsequent publications the limitations of the original model were relaxed to allow for the presence of more than one type of segment within the surfactant chain [47], the presence of more than one surface [48], the formation of lipid bilayers and vesicles [49–51], the formation of micelles [52], and the inclusion of charged groups [53]. The predictions show the generally expected behavior for adsorbing species with the hydrophobic moieties predominantly toward a hydrophobic surface, the hydrophilic groups generally concentrated toward the aqueous phase, and, for larger chains, adsorption via either loops, trains, or tails. This model has also been used to predict that the absorption of a nonionic surfactant onto a hydrophobic surface will occur as a monolayer [54].

Koopal and Ralston, after incorporating electrostatic effects, were unable to solve the general problem but instead presented solutions to two extremes of behavior, adsorption where the molecules were adsorbed either flat on the surface or perpendicular to it. Hassan and Zollars [55] were able to overcome this difficulty and present predictions for the adsorption of an ionic surfactant onto a surface with charges of the same sign. Using this model it is possible to predict conditions where local maxima and minima do appear in the adsorption isotherm, as observed by Hoeft and Zollars. When the adsorbed amount, as predicted by the model, was compared with experimental data, however, the predicted amount was low by about an order of magnitude. One of the key parameters affecting the prediction of the amount adsorbed is the lattice spacing. In their calculations Hassan and Zollars used a spacing of 0.4 nm. Reducing this value would give greater values for the adsorbed amount but would also magnify the electrostatic effects resulting in numerical instabilities in the problem solution. Therefore, although the work by Hassan and Zollars indicates the potential for the interplay of electrostatics with

adsorbed conformation and adsorbed amount, a definitive answer will have to await more robust numerical techniques.

VIII. SUMMARY

From reviewing all of these sources a picture begins to emerge about the current state of knowledge about the adsorption of ionic surfactants onto hydrophobic surfaces. For adsorption onto an uncharged surface the adsorbed molecules associate with the surface via a hydrophobic interaction. This results in molecules being adsorbed in a tail-down conformation. At low concentrations the molecules appear to lie flat on the surface but become progressively more vertical as the concentration increases. In this vertical position significant lateral interactions between the adsorbed molecules occur, leading to increased adsorption and, ultimately, monolayer formation. On surfaces that themselves possess a structure, such as graphite; this may also induce a structure in the adsorbed layer (adsorption epitaxy?) along the individual grains of the surface as observed by Wanless and Ducker [17].

When ionic surfactants adsorb onto a hydrophobic surface that also contains charged groups of the same sign as the surfactant, electrostatic interactions begin to play a role. At low surface charge densities the initial adsorption will take place as in the case of adsorption onto an uncharged surface, with the surfactant lying nearly flat on the surface. As the surface charge density is increased, the adsorbed surfactant will be forced into a more vertical orientation. In this orientation the potential exists for greater adsorption due to the opportunity for more hydrophobic associations via either surface–surfactant or surfactant–surfactant contacts. At still higher surface charge densities the electrostatic repulsions become so strong that no observable adsorption occurs.

For the adsorption of ionic surfactants onto hydrophobic surfaces of opposite charge, a couple of different scenarios are possible. At low surface charge densities, the initial adsorption may take place primarily through hydrophobic associations as in the case of an uncharged surface, with an occasional adsorbed molecule occurring in a head-down orientation due to electrostatic attractions between the surface group and the surfactant head group. Once the surface charge has been neutralized, subsequent adsorption should occur as if on an uncharged surface. This should result in monolayer coverage with the potential for some structuring of the layer around the sites where a surfactant molecule has adsorbed in the head-down orientation. At high surface charge densities, the initial absorption should occur predominantly via electrostatic attractions between the surface groups and the surfactant head groups. As the adsorption proceeds, the surface will become more and more hydrophobic due to the tails of the adsorbed surfactant extending toward the aqueous phase and charge neutralization. Ultimately the surface will become so hydrophobic that another adsorbed layer will start to form due to hydrophobic associations between the surfactant tails. This ultimately leads to the formation of an adsorbed bilayer,

When more than a single surfactant species is present, the situation becomes more complex again. It seems clear, however, that whether the presence of other surface-active species increases or decreases the tendency for adsorption depends

very strongly on the structure of the materials. More strongly hydrophobic materials, especially nonionic materials, appear to cause greater adsorption of an ionic species. This is probably due to hydrophobic interactions between the species and screening of the ionic groups on the surfactant by the nonionic material. As Hoeft observed, however, synergistic effects may also be present between two ionic species.

REFERENCES

1. S. H. Maron, M. E. Elder, and I. N. Ulevitch, *J. Colloid Sci.* 9:89 (1954).
2. J. G. Brodnyan and G. L. Brown, *J. Colloid Sci.* 15:76 (1960).
3. A. M. Maurice, *J. Colloid Interface Sci.* 30:473 (1985).
4. K. J. Abbey, J. R. Erickson, and R. J. Seidewand, *J. Colloid Interface Sci.* 66:203 (1978).
5. R. J. Orr and L. Breitman, *Can. J. Chem.* 38:668 (1960).
6. T. R. Paxton, *J. Colloid Interface Sci.* 31:19 (1969).
7. I. Piirma and S.-R. Chen, *J. Colloid Interface Sci.* 74:90 (1980).
8. B. R. Vijayendran, *J. Appl. Polym. Sci.* 23:733 (1979).
9. B. Kronberg, P. Stenius, and Y. Thorsell, *Colloids Surf.* 12:113 (1984).
10. B. Kronberg, and P. Stenius, *J. Colloid Interface Sci.* 102:410 (1984).
11. B. Kronberg and P. Stenius, *J. Colloid Interface Sci.* 102:418 (1984).
12. B. Kronberg, *J. Colloid Interface Sci.* 96:55 (1983).
13. D. N. Furlong and J. R. Aston, *Colloids Surf.* 4:121 (1982).
14. A. M. Gaudin and D. W. Fuerstenau, *Trans AIME* 202:958 (1955).
15. C. E. Herder, *J. Colloid Interface Sci.* 143:1 (1991).
16. R. N. Ward, P. B. Davies, and C. D. Bain, *J. Phys. Chem.* 97:7141 (1993).
17. E. J. Wanless and W. A. Ducker, *J. Phys. Chem.* 100:3207 (1996).
18. F. Tiberg, *J. Chem. Soc., Faraday Trans.* 92(4):531 (1996).
19. Å. Waltermo, P. M. Claesson, and I. Johansson, *J. Colloid Interface Sci.* 183:506 (1996).
20. W. A. Ducker, Z. Xu, and J. N. Israelachvili, *Langmuir*, 10:3279 (1994).
21. P. Kekicheff and O. Spalla, *Langmuir* 10:1584 (1994).
22. Y.-H. Tsao, D. F. Evans, and H. Wennerstrom, *Langmuir* 9:779 (1993).
23. B. van Lent, R. Israels, J. M. H. M. Scheutjens, and G. J. Fleer, *J. Colloid Interface Sci.* 137:380 (1990).
24. P. Connor and R. H. Ottewill, *J. Colloid Interface Sci.* 37:642 (1971).
25. J. B. Kayes, *J. Colloid Interface Sci.* 56:426 (1976).
26. F. G. Gonzalez, M. A. C. Vilchez, and R. Hidalgo-Alvarez, *Colloid Polym. Sci.* 269:406 (1991).
27. J. Zhao and W. Brown, *J. Phys. Chem.* 99:15215 (1995).
28. J. Zhao and W. Brown, *Langmuir* 12:1141 (1996).
29. K. Kandori, H. Ishiguro, K. Kon-no, A. Kitahara, *Langmuir* 5:1258 (1989).
30. W. H. Keesom, R. L. Zelenka, and C. J. Radke, *J. Colloid Interface Sci.* 125:575 (1988).
31. P. Becher, S. E. Trifiletti, and P. C. Petty, *J. Dispersion Sci. Tech.* 2:53 (1981).
32. W. Brown and J. Zhao, *Macromolecules* 26:2711 (1993).

33. W. Brown and J. Zhao, *Langmuir* 10:3395 (1994).
34. S. I. Ali, J. C. Steach, and R. L. Zollars, *Colloids Surf* 26:1 (1987).
35. C. E. Hoeft and R. L. Zollars, *J. Colloid Interface Sci.* 177:171 (1996).
36. W. M. Brouwer and R. L. J. Zsom, *Colloids Surf*, 24:195 (1987).
37. J. L. Gwin. M.S. Thesis, Washington State University, 1988.
38. G. Tuin and H. N. Stein, *Langmuir* 10:1054 (1994).
39. R. J. Orr and L. Breitman, *Can. J. Chem.* 38:668 (1960).
40. M. J. Hay, J. W. Mactaggart, and C. H. Rochester, *J. Chem. Soc., Faraday Trans.* 82:1805 (1986).
41. C. D. Bain, P. B. Davis, and R. N. Ward, *Langmuir* 10:2060 (1994).
42. P. M. Claesson, M. Malmsten, and B. Lindman, *Langmuir* 7:1441 (1991).
43. M. S. Johal. R. N. Ward, and P. B. Davies, *J. Phys. Chem.* 100:274 (1996).
44. C. E. Hoeft. PhD. Thesis, Washington State University, 1993.
45. J. M. H. M. Scheutjens and G. J. Fleer, *J. Chem. Phys.* 83:1619 (1979).
46. J. M. H. M. Scheutjens and G. J. Fleer, *J. Chem. Phys.* 84:178 (1980).
47. B. van Lent and J. M. H. M. Scheutjens, *Macromolecules* 22:1931 (1989).
48. G. J. Fleer and J. M. H. M. Scheutjens, *J. Colloid Interface Sci.* 111:504 (1986).
49. F. A. M. Leermakers and J. M. H. M. Scheutjens, *J. Chem. Phys.* 89:3264 (1988).
50. F. A. M. Leermakers and J. M. H. M. Scheutjens, *J. Phys. Chem.* 93:7417 (1989).
51. F. A. M. Leermakers and J. M. H. M. Scheutjens, *J. Chem, Phys.* 89:6912 (1988).
52. F. A. M. Leermakers and J. M. H. M. Scheutjens, *J. Colloid Interface Sci.* 136:231 (1990).
53. L. K. Koopal and J. Ralston, *J. Colloid Interface Sci.* 112:362 (1986).
54. M. R. Böhmer and L. K. Koopal, *Langmuir* 6:1478 (1990).
55. M. H. Hassan and R. L. Zollars, *J. Colloid Interface Sci* 146:299 (1991).

Adsorption of Metal Ions onto Humic Acid

HIDESHI SEKI and AKIRA SUZUKI Department of Marine Bioresources
Chemistry, Hokkaido University, Hakodate, Japan

- I. Introduction
- II. Metal Complexing Ability of Humic Acid
 - A. Acid–base properties of humic acid
 - B. Metal–humic acid complexation
- III. Adsorption of Metal Ions by Immobilized Humic Acid
 - A. Preparation of composite biopolymer adsorbent
 - B. Metal adsorption ability of HA-M
- IV. Adsorption of Metal Ions onto Insolubilized Humic Acid
 - A. Preparation of insolubilized HA
 - B. Effect of insolubilization on metal–HA complexation
- V. Practical Application of IHA
 - A. Cadmium–midgut gland complexation
 - B. Removal of cadmium from MG by competitive adsorption
- References

I. INTRODUCTION

Metal recovery by adsorption from dilute aqueous solutions is an emerging field of interest from the standpoints of both resource conservation and environmental remediation. Many biopolymers derived from microbes and plants are known to bind metals strongly. The use of biopolymers as adsorbents for the recovery or removal of metals from aqueous environments has been a topic of extensive research in recent years [1–8]. Biopolymers such as cellulose, alginate, carrageenans, lignins, proteins, and chitin derivatives are industrially attractive for a number of reasons. Biopolymers are capable of removing heavy metal ions at parts per

billion concentrations [2]. Moreover, they are readily available and ecologically acceptable.

Humic substances, which are biopolymers widely and abundantly present in natural waters and soils, also have a high complexing ability with various heavy metal ions. These compounds are formed by the random condensation of breakdown products of terrestrial and aquatic plants and extracellular metabolites of phytoplankton. Concentrations of metals in marine and fresh waters are often higher than predicted from the solubility products of corresponding hydroxide and carbonate compounds. The complexation of metal ions with dissolved humic substances is responsible for the apparent supersaturation of metals in natural waters [9–21]. Water-soluble humic substances are usually divided into two fractions, humic acid (HA) and fulvic acid (FA). HA is defined in operational terms as the fraction of humic substance soluble in alkaline solutions and insoluble in acidic solutions, while FA is the fraction soluble in both alkaline and acidic solutions. A general method for the fractionation of humic substances is illustrated in Fig. 1. HA is easily obtained as a precipitate in acidic solution ($\text{pH} < 1.5$). Although HA appears to be an attractive adsorbent for the recovery of heavy metal ions, there is little information on its practical application as adsorbent. It is difficult to use humic acid as the adsorbent because of its high solubility in water.

We have studied the use of HA as adsorbent. A composite biopolymer adsorbent in which HA was immobilized by a combination of calcium alginate gel membrane and activated carbon powder was developed [6,8]. Furthermore, another HA was made by a thermal process [7]. Based on a metal complexation model [7,8], the effect of immobilization and insolubilization on the metal complexing ability of HA is discussed in the following sections.

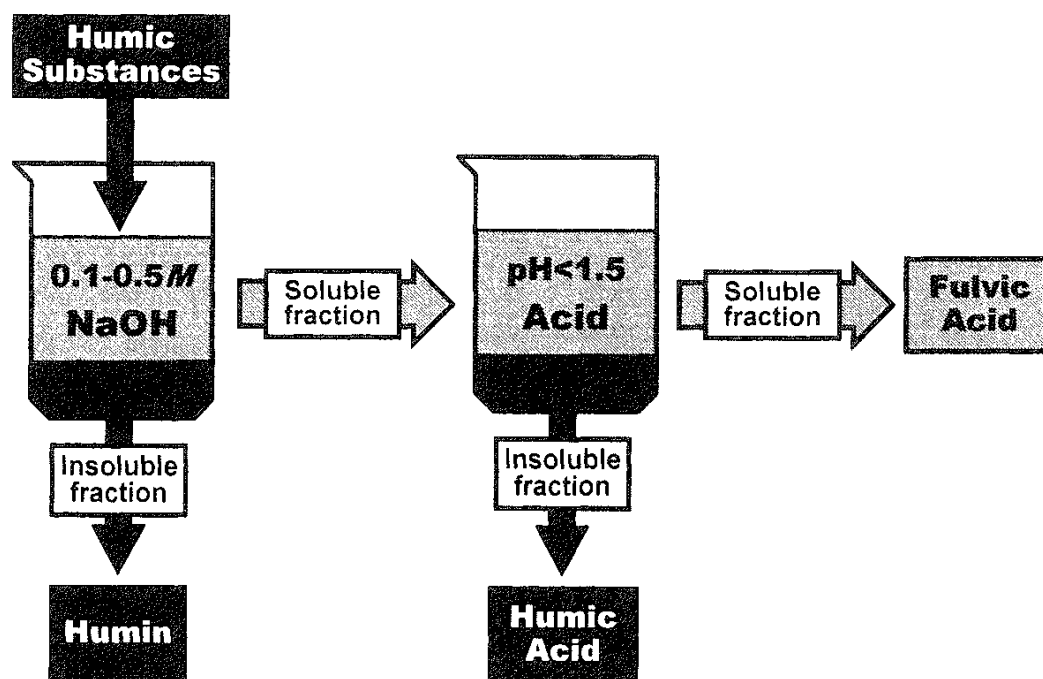


FIG. 1 Method for fractionating humic substances.

II. METAL COMPLEXING ABILITY OF HUMIC ACID

A Acid-Base Properties of Humic Acid

Acidic groups on HA, which serve as effective electron donors in the binding with metal ions, also bind protons in aqueous environments. Therefore, determining the equilibrium parameters of the acid dissociation (e.g., the number and dissociation constants) is important to estimating the metal complexing ability of HA.

1. Total Number of Acidic Groups on Humic Acid

The total number of acidic groups on HA was determined by a conductometric titration [22]. A typical conductometric titration curve of commercial HA (Aldrich Chemical Co.) with HNO_3 is shown in Fig. 2. The intersection of two straight lines defines the end point of the titration. The total number of acidic groups was determined from the titration curve to be $3.40 \times 10^{-3} \text{ mol/g}$. Since the HA used here was in the form of sodium salt, no end point was obtained from the titration with NaOH .

2. Dissociation Constants of Acidic Groups on HA

To determine the dissociation constants of the acidic groups, an adsorption isotherm for the adsorption of protons by HA was obtained from the potentiometric titration of HA as shown in Fig. 3. The ordinate, X_H , represents the equilibrium number of protons bound to acidic groups of 1 g of HA. The number of protons bound to acidic groups on HA was determined from the difference between the bulk proton concentrations in the absence and presence of HA. The ionic strength of the system was adjusted to 0.1 mol/dm^3 by the addition of NaNO_3 .

The potentiometric titration curves of HA are usually broad and ill-defined, reflecting the varying properties of acidic groups on HA [23,24]. Wilson and Kinney [25] investigated the acid-base properties of lake water and marine humic substances and determined a two-step dissociation process. Schnitzer and

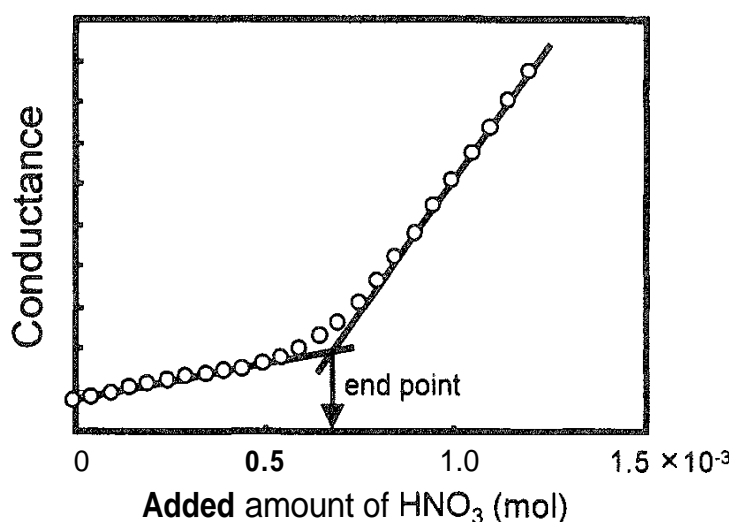


FIG. 2 Conductometric titration curve for 300 cm^3 of a solution containing 0.2 g of HA with 0.1 mol/dm^3 HNO_3 at 30°C . (From Ref. 7.)

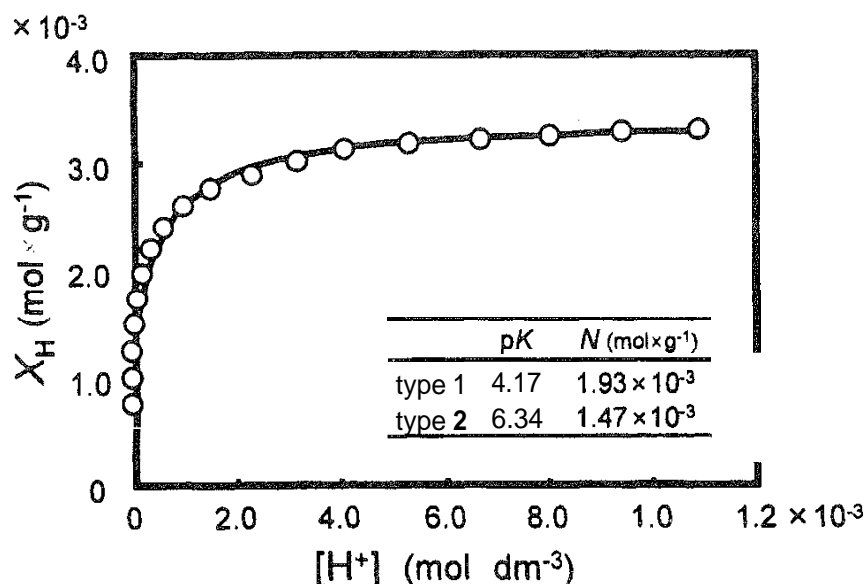
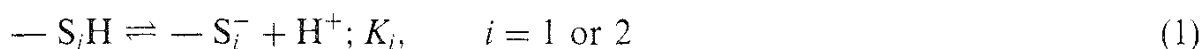


FIG. 3 Adsorption isotherm of proton adsorption to HA at 30°C. Initial concentrations of HA and NaNO₃ were 0.67 g/dm³ and 0.1 mol/dm³, respectively. The solid line represents the theoretical curve calculated with Eq. (3).

Khan [26] accounted for the acidic properties of humic compounds in terms of a range of aromatic carboxyl groups and to a lesser extent phenolic hydroxyl groups. In this case, the acid dissociation reactions of HA can be written as



where $-S_i$ represents acidic groups of type i on HA. The acid dissociation constant K_i is defined as

$$K_i = \alpha_i[H^+]/(1 - \alpha_i) \quad (2)$$

where α_i is the degree of dissociation of type i acidic groups. X_H can then be expressed as

$$X_H = N_1(1 - \alpha_1) + N_2(1 - \alpha_2) = \frac{N_1[H^+]}{K_1 + [H^+]} + \frac{N_2[H^+]}{K_2 + [H^+]} \quad (3)$$

where N_1 and N_2 are the numbers of type 1 and 2 acidic groups, respectively. Their sum should be equal to the total number of acidic groups determined from the conductometric titration,

$$N_1 + N_2 = 3.40 \times 10^{-3} \text{ mol/g} \quad (4)$$

We applied a nonlinear least squares method to determined the four constants K_1 , K_2 , N_1 , and N_2 in Eq. (3). The constants that gave the best fit with the experimental data are listed in Fig. 3. The solid line in Fig. 3 represents the theoretical curve calculated from Eq. (3) using the constants. Figure 4 shows a comparison of the proton-binding capacity of HA with that of some inorganic adsorbents such as silica gel (Silikagel H and Aerosol 200), hydrous titanium oxide (HTiO), γ -alumina, hydrous throrium oxide (HThO), and magnetite. It is evident that the number of

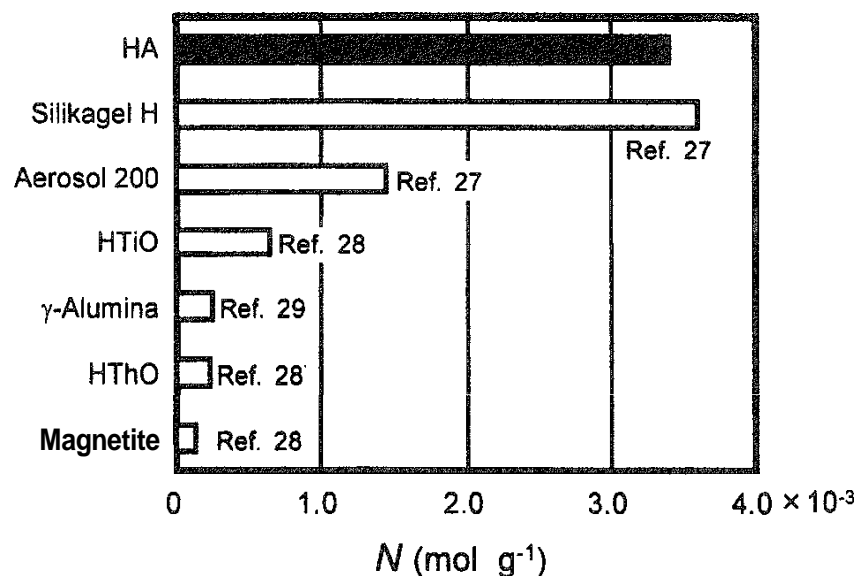
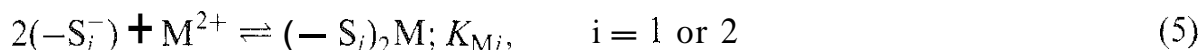


FIG. 4 Comparison of the proton-binding capacity of HA and inorganic adsorbents.

acidic groups on HA, which may serve as the metal complexing sites, is higher than that of most conventional inorganic adsorbents.

B. Metal-Humic Acid Complexation

The acid dissociation constants of type 1 and 2 acidic groups differ by about two orders of magnitude. Therefore, the complexation of divalent metal ions with HA can be written as



where M^{2+} represents the divalent metal ion. The complexation constant K_{Mi} is defined as

$$K_{Mi} = \frac{\theta_i}{\{(1 - \theta_i)\alpha_i\}^2[M^{2+}]} = \frac{\theta_i}{\{(1 - \theta_i)K_i/(K_i + [H^+])\}^2[M^{2+}]} \quad (6)$$

or

$$\theta_i = (P_i - \sqrt{P_i^2 - 4})/2 \quad (7)$$

where

$$P_i \equiv 2 + \{K_{Mi}[M^{2+}]\{K_i/(K_i + [H^+])\}^2\}^{-1}$$

where θ_i represents the fraction of type i acidic groups complexed with metal ions. The number of metal ions complexed with 1 g of HA, X_{MH} , is expressed as

$$X_{MH} = (N_{M1}\theta_1 + N_{M2}\theta_2)/2 \quad (8)$$

where N_{M1} and N_{M2} represent the numbers of type 1 and 2 acidic groups available for metal complexation, respectively.

The pH dependence of the number of cadmium and lead ions complexed with HA is presented in Figs. 5 and 6, respectively. A nonlinear least squares method was applied to find K_{M1} , K_{M2} , N_{M1} , and N_{M2} . The constants that gave the best fit with the experimental data are listed in the figures. The solid lines in the figures represent the theoretical curves calculated from Eqs. (7) and (8) using the fitted constants. The number of acidic groups available for metal complexation, N_{Mi} , is in reasonable agreement with the number of acidic groups on HA determined by potentiometric titration, N_i . This means that all the acidic groups on HA are available for metal complexation. The metal complexing capacity of HA, $(N_{M1} + N_{M2})/2 = 1.7 \times 10^{-3} \text{ mol/g}$, is large enough to use HA as an adsorbent material.

III. ADSORPTION OF METAL IONS BY IMMOBILIZED HUMIC ACID

As mentioned above, humic acid is an attractive adsorbent material for the recovery of valuable and toxic heavy metals from aqueous environments. However, it is difficult to use HA itself as the adsorbent because of its high solubility in water. Ho and Miller [30] investigated the interaction of uranium ions and HA at the hematite/water interface. They demonstrated that the presence of HA enhanced the adsorption of uranium on hematite to a remarkable extent. In their study, HA was adsorbed on hematite particles prior to the uranium adsorption experiments. The hematite particles can therefore be regarded as the HA-immobilized adsorbent. Heitkamp and Wagener [31] immobilized HA on anion-exchange resins as carriers, and they tried to use them for the recovery of uranium from seawater. Since the carriers are usually inert materials in adsorption, the HA/carrier ratio is very important. In those studies, the percentage of HA in the total adsorbent was

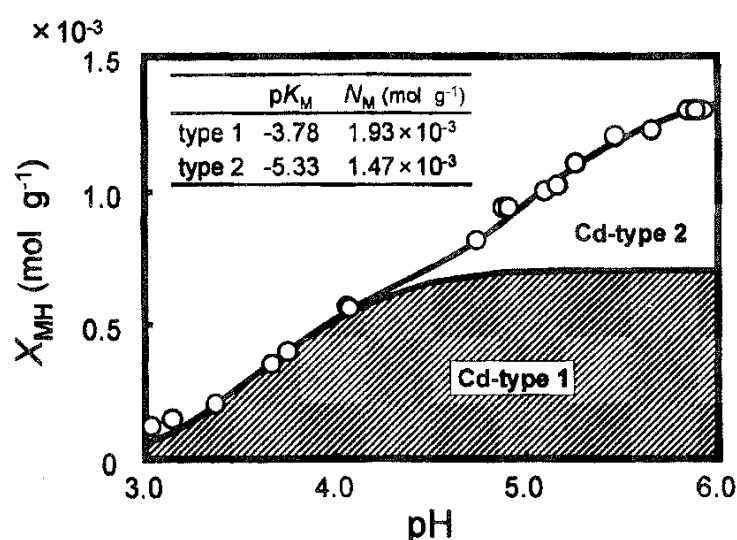


FIG. 5 pH dependence of Cd-HA complexation at 30°C. Initial concentrations of HA, NaNO_3 , and $\text{Cd}(\text{NO}_3)_2$ were, respectively, 1.0 g/dm^3 and 1×10^{-1} and $3.0 \times 10^{-3} \text{ mol/dm}^3$. The solid lines represent the theoretical curves calculated with Eqs. (7) and (8). (From Ref. 7.)

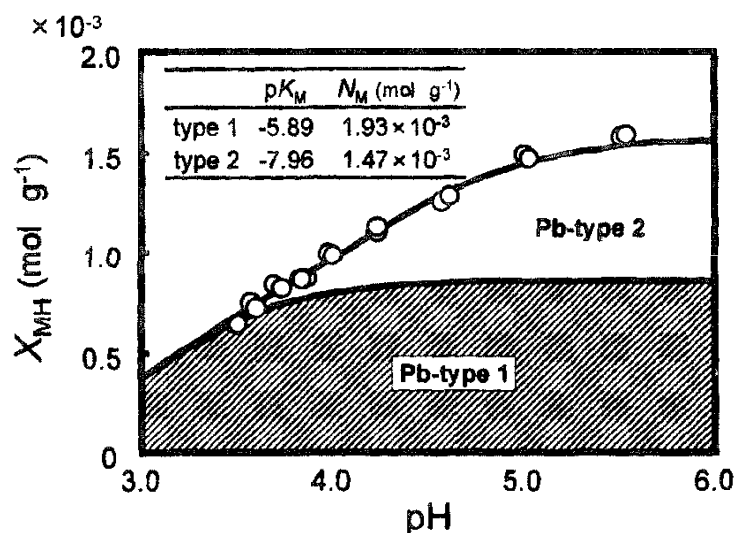


FIG. 6 pH dependence of Pb-HA complexation at 30°C. Initial concentrations of HA, NaNO₃, and Pb(NO₃)₂ were, respectively, 0.2 g/dm³ and 1×10^{-1} and 4.0×10^{-4} mol/dm³. The solid lines represent the theoretical curves calculated with Eqs. (7) and (8). (From Ref. 7)

3.5% [30], 25% [31] on a dry weight basis. We developed a membranous composite biopolymer adsorbent in which HA was almost completely immobilized by a combination of calcium alginate gel membrane and activated carbon powder. The adsorbent comprised as much as 40% HA [8].

A. Preparation of Composite Biopolymer Adsorbent

An aqueous solution containing HA, alginic acid (AA), and activated carbon powder (ACP) was well mixed. It was extruded, dropwise, onto a plastic plate and dried at 60°C. Then it was gelated in an excess of CaCl₂ solution for 1 h. The membranes of HA-entrapped calcium alginate had a diameter of about 5 mm and a thickness of about 0.3 mm. Using this immobilizing method, we obtained a membranous adsorbent (HA-M) consisting of 40% HA, 20% AA, and 40% ACP on a dry weight basis.

B. Metal Adsorption Ability of HA-M

1. Metal Complexing Ability of AA

Many biopolymers are known to bind metal ions strongly. Alginic acid used as the immobilizing agent also has a complexing ability with divalent metal ions. Many studies have been carried out on the application of AA to the aqueous phase separation of heavy metals, and the possibility of AA as the adsorbent material has been suggested [1–5]. HA-M comprises 20% AA on a dry weight basis. Therefore, it can be expected that AA plays an important role in metal adsorption by HA-M.

The metal complexing ability of AA was evaluated in the same manner as that of HA [8]. AA, which is a main cell-boundary constituent of brown algae, is a linear polysaccharide composed of β -D-mannuronic acid and α -L-glucuronic acid. The acidic property of AA is due to the presence of carboxylic groups [32]. Therefore, AA can be regarded as an adsorbent containing only one type of metal-binding site. The total number and the acid dissociation constant of acidic (carboxylic) groups on AA were determined from the conductometric and potentiometric titrations to be $N_A = 4.08 \times 10^{-3} \text{ mol/g}$ and $K_A = 6.15 \times 10^{-4} \text{ mol/dm}^3$, respectively. The subscript A is used to designate the parameters for AA. The acid dissociation constant of carboxylic groups on AA was about one order of magnitude larger than that of type 1 acidic (carboxylic) groups on HA.

The complexation of divalent metal ions with biopolymers that contain only one type of metal binding site can be written as



The fraction of acidic groups complexed with metal ions, θ , and the number of metal ions complexed with 1 g of biopolymer, X_M , can be expressed as

$$\theta = (P - \sqrt{P^2 - 4})/2 \quad (10)$$

where

$$P \equiv 2 + \{K_M[M^{2+}]\{K/(K + [H^+])\}^2\}^{-1}$$

and

$$X_M = N_M \theta / 2 \quad (11)$$

where N_M represents the number of acidic groups available for metal complexation on 1 g of biopolymer. The metal-AA complexation experiments were carried out using the membranous calcium alginate gel (containing no HA or ACP) as the adsorbent. The equilibrium parameters for the metal-AA complexation, K_{MA} and N_{MA} , were determined in the same manner as those for HA, and they listed in Table 1. The number of carboxylic groups available for metal complexation on AA, N_{MA} , is about 30% smaller than the total number of carboxylic groups on AA determined from the conductometric titration, N_A . Liang et al. [33] reported that the primary mechanism of gelation of alginate was the dimerization of polyfuluronate sequences, with specific site binding of calcium ions between alginate chains. This process reached completion at a calcium level of about 30% of the total cation requirement of the alginate. Therefore, it can be considered that about 30% of the

TABLE 1 Equilibrium Parameters for Metal-AA Complexation

| | N_{MA} (mol/g) | pK_{MA} |
|---------|------------------------|-----------|
| Cadmium | 3.04×10^{-3} | -3.17 |
| Lead | 3.02×10^{-3a} | -5.13" |

^a Data from Ref. 8.

carboxyl groups on the membranous calcium alginate gel were occupied by calcium ions during the gelation process. The metal complexing capacity of AA, $N_{MA}/2 = 1.5 \times 10^{-3}$ mol/g, is comparable to that of HA (1.7×10^{-3} mol/g).

2. Adsorption of Metal Ions on HA-M

The number of metal ions adsorbed to 1 g of HA-M, X_{MC} , can be expressed as

$$X_{MC} = f_A X_{MA} + f_H X_{MH} \quad (12)$$

where f_A and f_H represent the weight fractions of AA and HA, respectively, in the adsorbent. Since the equilibrium parameters for metal-AA and metal-HA complexation were already obtained, we can calculate X_{MC} by using Eqs. (7), (8), and (10)–(12). Figure 7 shows a comparison between the experimentally found number of metal ions adsorbed onto 1 g of HA-M, X_{MCexp} , and the number calculated from the equations, X_{MCcal} . The data agree well with those calculated. This means that the complexation constants and the numbers of available acidic groups for complexation of metal-HA and metal-AA systems were scarcely influenced by immobilization. The metal adsorption capacity of HA-M, which comprises as much as 40% HA and 20% AA, was about 1×10^{-3} mol/g on a dry weight basis.

IV. ADSORPTION OF METAL IONS ONTO INSOLUBILIZED HUMIC ACID

The heating of raw humic acid above a certain temperature causes dehydration (condensation) between the acidic groups and lowers its solubility in water (Fig. 8). Therefore we tried to prepare an HA insolubilized by heating (IHA).

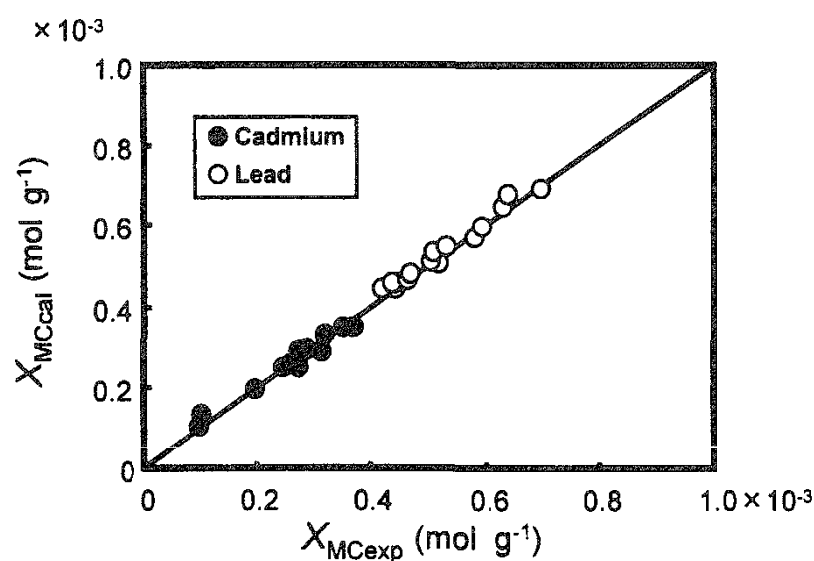


FIG. 7 Comparison of the experimental amount of metal adsorption onto HA-M and the amounts calculated with Eqs. (7), (8), (10), (11), and (12).

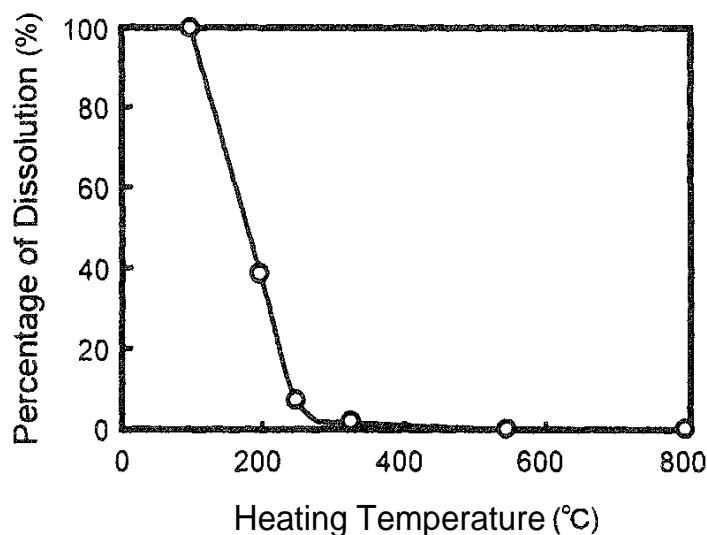


FIG. 8 Effect of heating temperature on the percentage of IHA dissolution in distilled water at 30 °C.

A. Preparation of Insolubilized HA

Humic acid was pretreated with excess CaCl_2 solution and converted to a calcium salt [34]. It was made insolubilized by heating at 300–350°C for 1 h. Heating at higher temperature or for a longer period reduced the acidic groups on HA to a considerable extent [35]. The HA thus obtained (IHA) was ground in an agate mortar with a pestle and washed repeatedly with 1 M HNO_3 solution and hot distilled water. Finally, IHA was converted from the hydrogen form to the sodium form by soaking in 1 M NaNO_3 solution, rinsed with distilled water, and dried at 80°C. IHA prepared in this way was virtually insoluble in water up to pH 10 at 30°C, and there was only 7% dissolution even in boiling water [36].

B. Effect of Insolubilization on Metal–HA Complexation

Humic acid is insolubilized by condensation of acidic groups such as aromatic carboxyl groups and phenolic hydroxyl groups, which are probably the sites of metal complexation. Therefore, it may be presumed that the number of acidic groups and the acid dissociation constant of IHA are lowered by heating compared with those of HA. The number and acid dissociation constants of type 1 and 2 acidic groups on IHA were determined by potentiometric titration [7]. Surprisingly, the acid dissociation constants were scarcely influenced by insolubilization. However, 25% of the type 1 acidic groups and 22% of the type 2 acidic groups on HA were lost by the condensation reaction ($N_1 = 1.45 \times 10^{-3} \text{ mol/g}$ and $N_2 = 1.15 \times 10^{-3} \text{ mol/g}$).

The equilibrium parameters for the metal–IHA complexation were determined in the same manner as those for HA. The parameters obtained are listed in Table 2 [7]. The insolubilization process scarcely influenced the complexation constants, K_{M1} and K_{M2} . The number of type 1 acidic groups available for metal complexation, N_{M1} almost coincided with the number of acidic groups determined by poten-

TABLE 2 Equilibrium Parameters for Metal–IHA Complexation

| | $N_{M1}(\text{mol/g})$ | $N_{M2}(\text{mol/g})$ | pK_{M1} | pK_{M2} |
|---------|------------------------|------------------------|-----------|-----------|
| Cadmium | 1.45×10^{-3} | 0.90×10^{-3} | -3.70 | -5.40 |
| Lead | 1.45×10^{-3} | 0.96×10^{-3} | -5.80 | -7.64 |

Source Ref. 7

tiometric titration, N_1 . However, 20% of the type 2 acidic groups were unavailable for metal complexation. The metal complexation capacity of IHA was about 1.2×10^{-3} mol/g on a dry weight basis.

V. PRACTICAL APPLICATION OF IHA

The internal organs of most marine organisms contain valuable materials such as EPA, DHA, proteins, and essential amino acids [37–39]. However, one of the "big three" toxic heavy metals, cadmium, is concentrated in the internal organs of marine organisms throughout the food chain. Many studies have been carried out to study the accumulation of cadmium in the internal organs of edible marine organisms such as mussels [40–43], snails [44,45], crabs [46–49], whelk [50], scallops [51], and squid [52,53]. For example, cadmium concentration in the mid gut gland (MG) of the scallop *Patinopecten yessoensis*, which is one of the most popular edible shellfish, is as high as 200 $\mu\text{g/g}$ on a dry weight basis [54]. For the effective use of these valuable materials, the cadmium removal process should be established. Cadmium in the internal organs can be removed by treatment in acidic solutions. Cadmium ions are released as a result of the protonation of metal-binding proteins in the organs. Therefore, the proton concentration of the acidic solution must be kept at a high level, and the subsequent treatment of cadmium-containing, low pH wastewater is required. Moreover, treatment in a strongly acidic solution may denature these valuable biomaterials.

In a recent study, we proposed a new method (competitive adsorption method) for the removal of toxic heavy metal ions from acid-sensitive biomaterials, and applied it to the removal of cadmium from the MG of the scallop *Patinopecten yessoensis* [54]. In this method, a competitive adsorbent (IHA) is added to a weakly acidic solution containing MG to lower the cadmium concentration in the liquid phase. The lowering of the cadmium concentration in the liquid phase promotes the release of cadmium ions from MG, and the released cadmium ions are immediately adsorbed by IHA. In this manner the competitive adsorption method enables the simultaneous removal of cadmium from the scallop midgut and from the liquid phase under mild acidic conditions.

A. Cadmium–Midgut Gland Complexation

Accumulation of heavy metals by several organisms has been shown to be associated with the production of special proteins. The internal organs of marine organisms accumulate not only cadmium but also copper and zinc. Fractionation of metal-binding proteins of squid liver by gel permeation chromatography revealed

that the cytosolic cadmium, copper, and zinc are bound to different proteins [52, 53]. Assuming that a similar relation holds in the present MG, MG can be regarded as an adsorbent containing only one type of cadmium-binding site. Therefore we carried out cadmium adsorption experiments on MG in an attempt to determine the acid dissociation constant K_G , the complexation constant K_{MG} , and the number of metal complexing sites, N_{MG} , for the Cd–MG system in the same manner as those for AA. The parameters that gave the best fit with the experimental data were obtained as $K_G = 8.47 \times 10^{-11} \text{ mol/dm}^3$, $K_{MG} = 8.89 \times 10^{12} \text{ dm}^3/\text{mol}$, and $N_{MG} = 5.21 \times 10^{-5} \text{ mol/g}$, respectively. We obtained good agreement between the experimental amounts of cadmium adsorbed onto MG and the values predicted with Eqs. (10) and (11). The correlation coefficient between the experimental and predicted values was 0.972.

B. Removal of Cadmium from MG by Competitive Adsorption

Competitive adsorption experiments were carried out in the following procedure. A polyethylene mesh bag (7 x 9.5 cm) containing IHA and a certain amount of MG were added to an NaNO_3 (0.1 mol/dm^3) solution. The pH of the solution was adjusted to the desired value with HNO_3 . The solution was stirred for the time necessary to attain equilibrium, and then the polyethylene mesh bag containing IHA was removed from the system. MG was separated from the liquid phase in a centrifuge at 10,000 rpm for 10 min, and the cadmium concentrations of the supernatant and MG were measured. The MG used in these experiments contained about $1.8 \times 10^{-6} \text{ mol/g}$ ($\sim 200 \text{ ppm}$) of cadmium on a dry weight basis.

From the material balance on cadmium, the equilibrium concentration of free cadmium ion in the competitive adsorption system can be expressed as

$$[\text{Cd}^{2+}] = [\text{Cd}]_T - (m_G X_{MG} + m_I X_{MI})/V \quad (13)$$

where m_G and m_I represent the amounts of MG and IHA added to the system, respectively, X_{MG} and X_{MI} are the amounts of cadmium ions complexed with MG and IHA, respectively, and $[\text{Cd}]_T$ is the total cadmium concentration in the system. Sliced MG was used in these competitive adsorption experiments. Since 46% of the cadmium binding protein in MG was constantly dissolved in the liquid phase, we modified Eq. (13) to

$$C_L = [\text{Cd}]_T - (0.54m_G X_{MG} + m_I X_{MI})/V \quad (14)$$

where C_L represents the cadmium concentration (the sum of the free cadmium ions and the cadmium ions complexed with the dissolved protein) in the liquid phase. The pH dependence of C_L in the competitive adsorption systems containing 30 g/dm^3 of MG and 1.0, 2.0, or 4.0 g/dm^3 of IHA is presented in Fig. 9. For comparison, the results of acid treatment (in the absence of IHA) are also plotted in Fig. 9. A successive approximation method was applied to numerically estimate C_L from Eqs. (7), (8), (10), (11), and (14). The experimental data (symbols) agreed well with the predicted values (solid lines). The pH dependence curves of C_L have minimum values at $\text{pH} \sim 5$. The competitive adsorption method enabled the simultaneous removal of toxic cadmium from both the liquid and MG phases at pH 5. The increase in C_L in the $\text{pH} < 5$ region was attributed to the increase of free cadmium

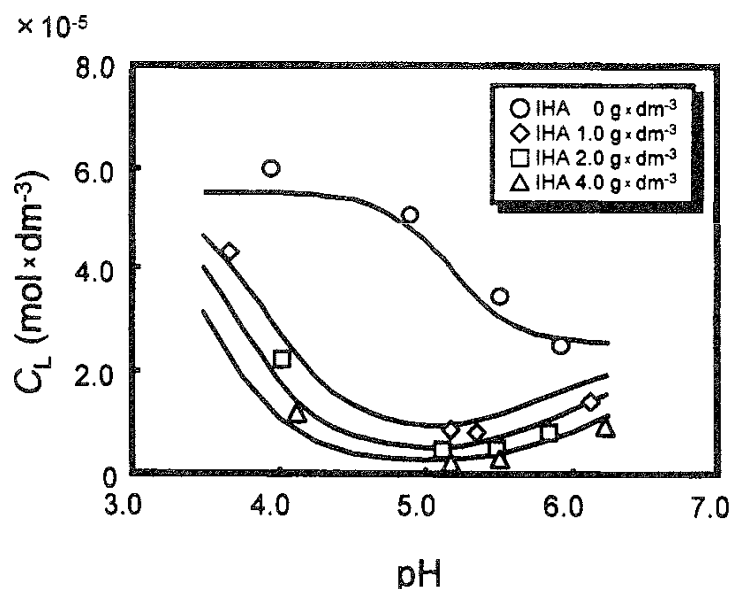


FIG. 9 pH dependence of cadmium concentration in the liquid phase in the competitive adsorption system at 30°C. Initial concentrations of MG, NaNO₃, and IHA were 30 g/dm³, 0.1 mol/dm³, and 0–4 g/dm³, respectively. The solid lines represent the theoretical curves calculated from Eqs. (7), (8), (10), (11), and (14). (From Ref. 54.)

ion, while the increase in the pH > 5 region was attributed to the increase in the amount of cadmium–protein complex dissolved in the liquid phase.

REFERENCES

- D. Chen, Z. Lewandowski, F. Roe, and P. Surapaneni, *Biotechnol. Bioeng.* **41**:755 (1993).
- J. R. Deans and B. G. Dixon, *Water Res.* **26**:469 (1992).
- L. K. Jang, W. Brand M. Resong, and W. Mainieri, *Environ. Prog.* **9**:269 (1990).
- L. K. Jang, G. G. Geesey, S. L. Lopez, S. L. Eastman, and P. L. Wichlacz, *Water Res.* **24**:889 (1990).
- L. K. Jang, S. L. Lopez, and S. L. Eastman, *Biotechnol. Bioeng.* **37**:266 (1991).
- H. Seki, A. Suzuki, and I. Kashiki, *J. Colloid Interface Sci.* **134**:59 (1990).
- H. Seki and A. Suzuki, *J. Colloid Interface Sci.* **171**:490 (1995).
- H. Seki and A. Suzuki, *Ind. Eng. Chem. Res.* **35**:1378 (1996).
- Y. Sugimura, Y. Suzuki, and Y. Miyake, *J. Oceanogr. Soc. Jpn.* **34**:93 (1978).
- Y. Sugimura, Y. Suzuki, and Y. Miyake, *Deep-sea Res.* **25**:309 (1978).
- G. Sposito, *Environ. Sci. Technol.* **15**:396 (1981).
- R. A. Saar and J. H. Weber, *Anal. Chem.* **52**:2095 (1980).
- R. A. Saar and J. H. Weber, *Environ. Sci. Technol.* **16**:510A (1982).
- J. Buffle, F. Greter, and W. Haerdi, *Anal. Chem.* **49**:216 (1977).
- S. Ramamoorthy and D. J. Kushner, *Nature* **256**:398 (1975).
- R. A. Torres and G. R. Choppin, *Radiochim. Acta* **35**:143 (1984).
- M. S. Caceci, *Radiochim. Acta* **39**:51 (1985).
- W. P. Cacheris and G. R. Choppin, *Radiochim. Acta* **42**:185 (1987).
- G. R. Choppin, *Radiochim. Acta* **44/45**:23 (1988).

20. A. Maes, J. De Brabandere, and A. Cremers, *Radiochim. Acta* 44/45:51 (1988).
21. V. Moulin, P. Robouch, P. Vitorge, and B. Allard, *Radiochim. Acta* 44/45:33 (1988).
22. R. O. James and G. A. Parks, in *Surface and Colloid Science*, Vol. 12 (E. Matijevic, ed.), Plenum. New York. 1982, pp. 119–216.
23. A. M. Pommer and I. A. Breger, *Geochim. Cosmochim. Acta* 20:30 (1960).
24. D. S. Gamble, *Can. J. Chem.* 50:2680 (1972).
25. D. E. Wilson and P. Kinney, *Limnol. Oceanogr.* 22:281 (1977).
26. M. Schnitzer and S. U. Khan, *Humic Substances in the Environment*, Marcel Dekker. New York, 1972. p. 327.
27. P. W. Schindler, B. Fürst, R. Dick, and P. U. Wolf, *J. Colloid Interface Sci.* 55:469 (1976).
28. A. R. Gupta and B. Venkataramani, *Bull. Chem. Soc. Jpn.* 61:1357 (1988).
29. H. Hohl and W. Stumm, *J. Colloid Interface Sci.* 55:281 (1976).
30. C. H. Ho and N. H. Miller, *J. Colloid Interface Sci.* 106:281 (1985).
31. D. Heitkamp and K. Wagener, *Ind. Eng. Chem, Process Des. Dev.* 21:781 (1982).
32. L. K. Jang, N. Harpt, T. Uyen, D. Grasmick, and G. G. Geesey, *J. Polym. Sci., Part B* 27:1301 (1989).
33. J. N. Liang, E. S. Stevens, S. A. Frangou, E. R. Morris, and D. A. Rees, *Int. J. Biol. Macromol.* 2:204 (1980).
34. M. Nakagawa, *Kinzoku* 43:66 (1973). [In Japanese]
35. H. Seki, Thesis, Hokkaido University, Hokkaido, 1994.
36. H. Seki and A. Suzuki, *Bull. Fac. Fish. Hokkaido Univ.* 43:185 (1992). [In Japanese]
37. K. Hayashi, *Bull. Jpn. Soc. Sci. Fish.* 52:1559 (1986).
38. K. Hayashi, *Nippon Suisan Gakkaishi* 54:1449 (1988).
39. K. Hayashi, *Nippon Suisan Gakkaishi* 55:1383 (1989).
40. F. Frankenhe, F. Noel-Lambot, and A. Disteche, *Comp. Biochem. Physiol.* C66:179 (1980).
41. J. M. Frazier, S. S. George, J. Overnell, T. L. Coombs, and J. Kägi, *Comp. Biochem. Physiol.* C80:257 (1985).
42. F. Noel-Lambot, *Experientia* 32:324 (1976).
43. A. Viarengo, M. N. Moore, G. Mancinelli, A. Mazzucotelli, R. K. Pipe, and S. V. Farrar, *Mar. Biol.* 94:251 (1987).
44. R. Dallinger, E. Carpena, G. J. Dalla Via, and P. Cortesi, *Arch. Environ. Contain. Toxicol.* 18:554 (1989).
45. W. J. Langston and M. Zhou, *Mar. Biol.* 92:505 (1986).
46. K. Lerch, D. Ammer, and R. W. Olafson, *Comp. J. Biol. Chem.* 257:2420 (1982).
47. J. Overnell, *Comp. Biochem. Physiol.* C77:237 (1984).
48. J. Overnell, *Comp. Biochem. Physiol.* C77:245 (1984).
49. J. Overnell and E. Trehwella, *Comp. Biochem. Physiol.* C64:69 (1979).
50. Y. Dohi, K. Ohba, and Y. Yonehama, *Biochim. Biophys. Acta* 745:50 (1983).
51. H. C. Stone, S. B. Wilson, and J. Overnell, *Comp. Biochem. Physiol.* C85:259 (1986).
52. V. Castillo and Y. Maita, *Bull. Fac. Fish. Hokkaido Univ.* 42:26 (1991).
53. T. Tanaka, Y. Hayashi, and M. Ishizawa, *Experientia* 39:746 (1983).
54. H. Seki and A. Suzuki, *J. Colloid Interface Sci.* 190:206 (1997).

26

Hydrous Metal Oxides as Adsorbents for Aqueous Heavy Metals

RUSSELL CRAWFORD and IAN H. HARDING Centre for Applied Colloid and BioColloid Science, Swinburne University of Technology, Melbourne, Australia

DAVID E. MAINWARING Department of Applied Chemistry, Royal Melbourne Institute of Technology, Melbourne, Australia

| | |
|---|------------|
| I. Introduction | |
| A. The use of hydrous metal oxides as adsorbents | |
| B. Surface characterization | |
| C. Removal of heavy metals from solution | |
| II. Experimental Techniques | |
| A. Reagents | |
| B. Background electrolyte | |
| C. Metal ion solutions | |
| D. Colloidal substrates | |
| E. Precipitation, adsorption, and coprecipitation studies | |
| F. Determination of metal ion removal | |
| III. Precipitation, Adsorption, and Coprecipitation | |
| IV. Comparison of HCO and HFO as Substrates | |
| A. Adsorption | |
| B. Coprecipitation | |
| V. The Influence of Competing Metal Ions | |
| A. Cr(III) with HFO | |
| B. Zn(II) with HFO | |
| C. Ni(II) with HFO | |
| D. Zn(II) with HCO | |
| E. Ni(II) with HCO | |
| VI. The Influence of a Complexing Ligand | |
| A. The influence of ammonia on the solution chemistry of aqueous heavy metals | 699 |
| B. The influence of ammonia on the adsorption of Zn(II) | 700 |
| C. The influence of ammonia on the coprecipitation of Zn(II) | 703 |
| VII. Modeling of Adsorption and Coprecipitation | 703 |
| A. Introduction | 703 |
| | 675 |

| | |
|--|-----|
| B. The James–Healy model for metal ion adsorption | 705 |
| C. The significance of the chemical free energy contribution to adsorption | 706 |
| VIII, Conclusions | 706 |
| A. Precipitation, adsorption, and coprecipitation | 706 |
| B. Comparison of HCO and HFO as substrates | 707 |
| C. The influence of competing metal ions | 707 |
| D. The influence of a complexing ligand | 707 |
| E. Modeling of adsorption and coprecipitation | 707 |
| References | 707 |

I. INTRODUCTION

The removal of heavy metal ions from both natural water supplies and industrial wastewater streams is becoming increasingly important as awareness of the environmental impact of such pollutants is fully realized. In particular, the likelihood of such metal ions precipitating out of solution and/or coating other materials can have a profound effect on both aqueous and nonaqueous environments. There is considerable evidence in the literature that the primary mechanism for transportation of metal contaminants in aquatic systems is the movement of suspended particulate material containing the adsorbed pollutant metals [1,2]. It is also known that a strong correlation exists between the concentration of trace metals in the (aquatic) environment and the extent to which those metal ions adsorb onto colloidal substrates present in the environment [2,3]. A similar correlation between the concentration of trace metals in the (aquatic) environment and their precipitation behavior is not so clear. There is, then, a well-founded need to study adsorption-related phenomena in order to understand and predict the behavior of toxic metals in the environment.

Industrial companies are increasingly being required to account for the fate of all chemical species, whether deliberately added or present as by-products, at all stages of industrial, mining, and manufacturing processes. The processes of precipitation, adsorption, and coprecipitation, apart from directly controlling the economics of many chemical processes, are also often involved in the cleanup of industrial wastewater [4–6]. Thus there is also a well-founded need to study adsorption-related phenomena in order to understand and predict the behavior of toxic metals in industry.

Metal ions that are prevalent in industrial effluent and have a considerable environmental impact include Cr(III), Zn(II), and Ni(II) [7]. Waste solutions of these metals are routinely found at levels that are in excess of acceptable disposal limits. Such waste solutions are produced, for example, by electroplating and metal pretreatment [Cr(III), Zn(II), Ni(II)], printed board manufacture [Cr(III), Ni(II)], leather tanning and wool scouring [Cr(III)], and anodizing [Cr(III), Zn(II)], among others [7,8]. These three metal ions are studied in detail in this chapter.

A. The Use of Hydrous Metal Oxides as Adsorbents

As will be discussed shortly, the structure of amorphous hydrous metal oxides is open to conjecture. They almost certainly comprise submicrometer porous particles and/or small nanosized primary particles that aggregate into larger submicrometer sized structures [10]. The influence this porosity and/or ultrasmall particle size has on adsorption-related phenomena has not been well documented but should be investigated

Amorphous hydrous metal oxides not only represent a class of adsorbents that are commonly encountered in the environment [2], they are also commonly used as adsorbents in industrial wastewater treatment [4–6]. They are easy to prepare, inexpensive, and common in nature. As such, they are appropriate substrates to choose for fundamental studies of adsorption phenomena.

Two common examples are the amorphous hydrous oxides of iron(III) and chromium(III). For simplicity, these are referred to hereafter as HFO and HCO, respectively.

HFO and HCO are used as the substrates in this study.

The amorphous hydrous oxide of Fe(III) (HFO) has been studied extensively as a substrate for metal ion adsorption, including the metal ions of interest here [Cr(III), Zn(II), Ni(II)] [7,11–27]. Pertinent observations relevant to HFO as an adsorbent for Cr(III), Zn(II), and/or Ni(II) include the following:

1. The localized structure (determined by X-ray absorption fine structure) of adsorbed Cr(III) depends on the history of the Cr(III) ion, i.e., on whether it was adsorbed onto or coprecipitated with the HFO surface [11].
2. Metal ions present in an industrial waste were successfully treated using adsorbing colloid flotation, dependent on the pH. Some metal ions could be treated at lower pH values than others, with the order being Cr(III) > Zn(II) > Ni(II) [7]. This is the same order found for their hydrolysis in solution and reflects a well-known pattern for adsorption phenomena (see Sec. I.C.2).
3. Coprecipitates of chromium and iron hydroxides appear to enhance the removal of metal ions [13,28,29].
4. Adsorbed metal ions such as Ni(II) [16], Co(II) [23], and Cd(II) [23] may inhibit the crystallization of HFO into crystalline forms such as goethite and hematite [16]. Other metal ions, such as Pb(II) [23], apparently do not.

The amorphous hydrous oxide of Cr(III) (HCO) has been studied extensively as a source of sols of uniform particle size and shape [30] and as an electrophoresis standard [31]; however, it has not been studied extensively as an adsorbent of metal ions. Sen [32] found that chromium (III) hydroxide generally has a larger adsorption capacity than the hydroxides of other triple-charged metals. Simon et al. [33] reported that coprecipitation of Cd(II) with chromium(III) hydroxide removed Cd(II) from solution at a pH that was two units lower than that obtained using aluminum(III) hydroxide as the coprecipitating hydroxide. Similarly, Packter and Panesar [34] used Cr(III) and Mg(II) mixtures to show enhanced removal for both ions compared with the individual metal systems. HCO has also been used as an adsorbing surface to effectively adsorb the proteins ovalbumin, γ -globulin, and lysozyme as a separation technique [35].

B. Surface Characterization

The surface characteristics of HFO and HCO would be expected to play a dominant role in their use as adsorbents for metal ions. In particular, one would expect the surface area of the substrate to play a dominant role in determining the extent of adsorption. Intuitively, one would expect the adsorption to be enhanced if either the porosity of the substrate was increased (and hence its available surface area increased) or the particle size was decreased (and hence the available surface area per mass increased). Electrokinetic properties would also be expected to be important, with a negative surface providing the best substrate for positively charged metal ions.

1. Particle Size and Morphology

The average particle sizes of the HFO and HCO used here were measured using dynamic light scattering and found to be 420 and 260 nm, respectively [25]. It should be remembered, however, that these sizes probably reflect the average sizes of aggregates composed of nanosized particles and/or porous material. In terms of adsorption phenomena, the significance of particle size lies in its relationship to surface area. The smaller particles (HCO) are assumed to have a larger surface area (per mass) and therefore a greater capacity to adsorb (all other things being equal). As we show in this chapter, to a first approximation this is the case.

2. Surface Area

For metal ion adsorption studies, the surface area of the adsorbent that is of interest is the area that contains ionizable surface sites that are capable of interacting reversibly with (metal) ions in solution. It is usually assumed to be the exterior surface and/or the surface of large macropores. Ionizable surface sites may also, however, exist in the interior of a porous adsorbent solid or may not be immediately available due to the coagulation of primary particles. Such sites may interact at a slower rate than readily accessible surface sites, giving rise to slow adsorption kinetics [36]. Measurement of surface area by the BET (N_2) method is generally considered suitable for measuring the exterior surface area of a substrate.

BET surface areas require drying samples in a vacuum oven at elevated temperatures, and therefore it is probable that some fine structure that is present in aqueous solution is lost [10]. The BET surface area should therefore be considered a lower estimate of the surface area of porous or amorphous materials. Nevertheless, a simple BET (N_2) surface area should give an indicative estimate of the surface area available for adsorption.

The surface areas of the two substrates used in this study were measured using the nitrogen BET method on a Micromeritics ASAP 2000 and found to be 225 and 316 m²/g for HFO and HCO, respectively [21].

As expected, the BET surface areas are much larger than would be indicated by their particle size if they were hard sphere particles. Thus the surface areas indicate either a porous particle and/or an aggregate comprising ultrasmall, nanosized particles. As also expected, the BET surface area is greater for HCO than for HFO. This difference in surface area must be taken into consideration when discussing any intrinsic difference in the efficiency of adsorption between the two substrates.

3. Electrokinetic Properties

The isoelectric points (iep's) of the two substrates used in this study were measured [25] by using a DELSA 440 and found to be at pH 8.2 for HFO and at pH 9.2 for HCO. Both Ni(II) and Zn(II) are completely adsorbed at pH values considerably less than either of these values (see Sec. III, Figs. 3–51, indicating that the surface is positively charged during adsorption. Electrostatic forces, in this case, are unfavorable to adsorption, and there must be a strong specific interaction for adsorption to occur.

C. Removal of Heavy Metals from Solution

1. Interdependence of pH, Metal Ion, and Substrate

(a) *Role of pH.* One common method of obtaining an adsorption isotherm is to keep the total amounts of adsorbent and adsorbate constant and vary the pH (typically from a low pH to a high pH). The results of such an experiment are shown in Fig. 1 for the adsorption of several aqueous heavy metals onto silica (SiO_2). From this figure, the influence of pH is apparent. At low pH values, there is little adsorption. At intermediate pH values, which depend on the particular metal ion being adsorbed, adsorption increases from near zero to near complete adsorption over a relatively small pH range. At high pH values, the metal ion is completely removed

There are two possible reasons for this trend. As the pH is increased, the substrate surface becomes more negative (or less positive) and thus more favorable for adsorp-

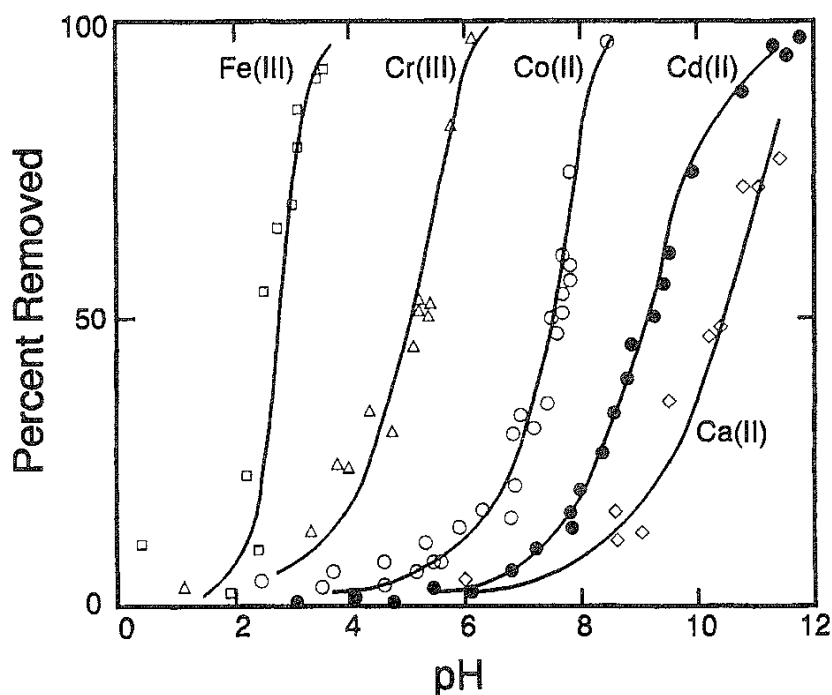


FIG. 1 Adsorption curves at 25°C for SiO_2 as a function of pH for metal ions at various concentrations of 6.7 ppm Fe(III), 10.4 ppm Cr(III), 19.9 ppm Co(II), 2.5 ppm Cd(II), and 5.6 ppm Ca(II). (From Ref. 37.)

tion of a positively charged metal ion. At the same time, however, the metal ion itself undergoes hydrolysis as the pH is increased, and it is often argued that hydrolysis is required before a metal ion can become "activated" to adsorption [37–39].

(b) Role of the Metal Ion. One of the strongest pieces of supporting evidence to suggest that hydrolysis is required for a metal ion to undergo adsorption is given by the data in Fig. 1. If hydrolysis is required, then the minimum pH at which adsorption takes place (for a given metal ion) should reflect the hydrolytic behavior of that metal ion. In Fig. 1, the order of adsorption is $\text{Fe(III)} > \text{Cr(III)} > \text{Co(II)} > \text{Cd(II)} > \text{Ca(II)}$. Corresponding p^*K_1 values (the onset of hydrolysis in solution) for the metal ions are also, in order, $\text{Fe(III)} > \text{Cr(III)} > \text{Co(II)} > \text{Cd(II)} > \text{Ca(II)}$ (1.71, 3.94, 9.25, 9.92, and 12.78, respectively [40,41]). A similar relationship between metal ion adsorption and the hydrolytic characteristics of the metals was observed, for example, by Benjamin and Leckie [18] and Rodda et al. [42]. McKenzie [43], however, observed several discrepancies in this trend when using birnessite, hematite and goethite substrates, as did Kinniburgh and Jackson [44] when using iron hydroxide and aluminum hydroxide gel substrates,

There is, then, assumed to be a strong correlation between adsorption and hydrolysis. This does not, however, prove that hydrolysis is required for adsorption to occur. Rather, the correlation may simply reflect the similarity of binding a metal ion to a hydroxide surface functional group and binding a metal ion to a hydroxide ion in solution.

(c) Role of the Substrate. Many inorganic oxides have been used in adsorption trials for the purposes of assessing their effectiveness. Some oxides do appear to exhibit a greater affinity for particular metal ions over others [32,33,44]; however, this effect is, in general, minimal.

For example, Harding and Healy [37] and Duker et al. [24] showed for Cd(II) and Zn(II) , respectively, that the characteristics of adsorption of a given metal ion onto a wide range of oxide substrates can be described by a general curve when the results are normalized by surface area. Oxides that are exceptions are solids with high dielectric constants, such as TiO_2 , and solids that undergo redox reactions, such as CuO . The roles of porosity and/or ultrasmall particle size were not investigated, and it remains to be shown whether or not HFO and HCO will prove to have specific affinity for metal ion adsorption.

The importance of surface area should not be overlooked. Kooner [45] reported that by increasing the surface area of goethite from 30 to $120 \text{ m}^2/\text{L}$, a corresponding increase (from 40% to 80%) of the percent removal of an initially 5 ppm Pb(II) solution could be achieved (at pH 5.5). Benjamin and Leckie [18] reported that adsorption of Cd(II) onto HFO also increased with surface area; in this case from 0% to 90% (at pH 6.5) by increasing the total iron concentration (and hence the surface area) from 1.3×10^{-4} to $1.3 \times 10^{-2} \text{ M}$.

Although these effects appear dramatic, they should be kept in perspective by considering the importance of pH. From Fig. 1, for example, it can be seen that an increase of 50% in metal ion adsorption can also be achieved by increasing the pH value by as little as 0.25 pH unit (if the right initial pH is chosen to demonstrate the point). The choices of pH and metal ion remain dominant factors over the surface area of the substrate

2. Effect of Complexing Agents

The presence of the OH group on metal ion hydrolysis products probably allows hydrogen bonding to occur between the hydrolysis species and the substrate surface. This, then, gives rise to the aforementioned correlation between adsorption and hydrolysis. Substitution of the OH groups with ligands that are not capable of forming hydrogen bond structures allows the contribution of these groups to the adsorption process to be studied. The role of complexed metal ions, which involve hydroxide and another ligand, is not clear [46,47] and requires further investigation.

James and Healy [48] found that Co(II) hydrolysis species adsorb strongly onto SiO₂, yet Stumm et al. [49] found that Co(NH₃)₆³⁺ did not. Fuerstenau and Osseo-Asare [50–52] studied the adsorption of Cu(II), Ni(II), and Co(II) onto titania, hematite, alumina, and quartz in ammoniacal solutions and found that the conventional sigmoidal adsorption curve was replaced by an adsorption profile that increased initially with increased pH, declined in adsorption as the ammine complexes formed, and then increased at high pH as the hydroxide ligands replaced the ammonia ligands. This effect was also reported by Luo and Huang [53], who studied Cu(II) adsorption onto iron(III), aluminum(III), and tin(IV) oxides in ammonia solution for the pH range 5–9.

The effects of ligands other than ammonia have also been extensively studied. Music and Ristic [54] showed that Zn(II) adsorption in the presence of EDTA or glycine decreases with increasing concentration. Rauf et al. [55] observed similar results for Eu(III) adsorption onto MnO₂ from H₂SO₄/CH₃OH binary mixtures in the presence of EDTA. Bowers and Huang [56] reported similar results for Pb(II)/EDTA adsorption onto SiO₂ and mordenite but found that the presence of a second metal ion [such as Fe(III)] introduced competition for the complexing agent.

In general, species complexed with multidentate ligands may exhibit enhanced adsorption due to multipoint anchoring or surface precipitation of the complexed metal [46,57] or may still inhibit adsorption. Duker et al. [24] reported that Zn(II) adsorption in the presence of fulvic acid was either enhanced or inhibited depending on the substrate, indicating that the ligand–substrate interaction is also important. The role of a porous and/or ultrafine substrate such as HFO or HCO in the presence of a ligand such as ammonia is not clear and will be investigated here.

Apart from using ammine complexes as a probe for adsorption mechanisms, there is a need to develop treatment procedures for ammonia-containing metal wastes. Ammonia-containing metal wastes are encountered in, for example, mining by-products, which may be subject to ammoniacal leaching either directly or after treatment [51,58,59]. Leather tannery effluent also contains high levels of Cr(III), often in the presence of ammonia, the pollutant that causes the most difficulty in Cr(III) effluent treatment [8].

3. Precipitation, Adsorption, and Coprecipitation

The distinction between simple precipitation, coprecipitation, and adsorption of aqueous heavy metal ions is not always clear, and in particular the terms "adsorption" and "coprecipitation" are often used interchangeably. Figure 2a is a schematic diagram illustrating the differences among the three mechanisms, and Fig. 2b illustrates their relative effectiveness.

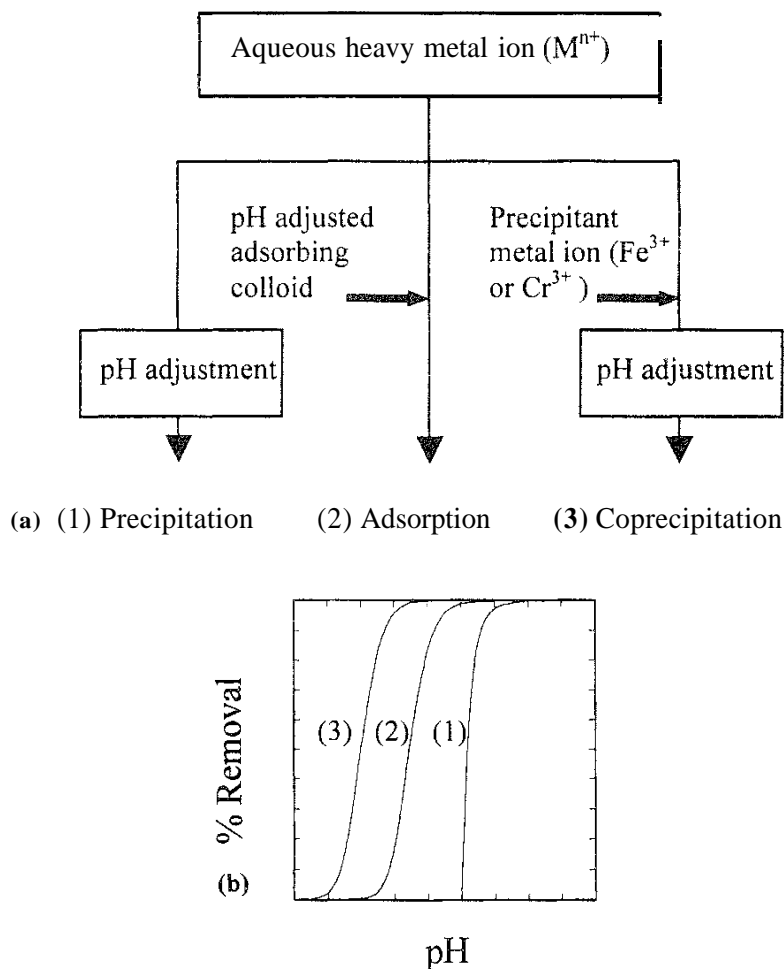


FIG. 2 Schematic representation of the three processes responsible for the removal of heavy metal ions from solution.

(a) *Precipitation.* It is well known [60] that increasing the pH of a solution of heavy metal ions will eventually result in the formation of an insoluble metal hydroxide precipitate. This simple mechanism is commonly used for removing metal ions in waste treatment processes [5,6] with no further sophistication required. If the removal from solution is presented on a percent removal versus pH graph, simple hydroxide precipitation typically results in a sharp sigmoidal removal profile [61,62] as depicted by curve 1 of Fig. 2b. It is the least efficient of the three mechanisms and requires a high pH to effect removal.

At very high pH levels, redissolution of the metal hydroxide may occur [60]. However, this is not often considered, as it is the initial removal that is of interest, and even when thermodynamically favored, redissolution of the precipitate is often slow to occur.

(b) *Adsorption* Aqueous heavy metals can be removed via adsorption processes if a solid substrate surface is present and, when presented on a percent removal versus pH graph, also typically results in a sigmoidal curve, commonly not as steep as that observed for simple hydroxide precipitation [39,48,63]. This is schematically depicted by curve 2 in Fig. 2b. Adsorption processes show significant metal ion removal at a lower pH than those obtained by direct precipitation [42,48,63–65].

(c) *Coprecipitation.* Metal ion coprecipitation processes are different from adsorption processes in that the solid substrate is formed by simultaneously increasing the pH of both the precipitating hydroxide and the metal ion to be removed from solution. In this fashion, the colloid forms in the presence of the adsorbate rather than being preformed in a separate step. The percent removal versus pH curve for coprecipitation studies is similar in shape to that of adsorption curves, again commonly not as steep as that observed for simple hydroxide precipitation [34,66]. This is schematically depicted by curve 3 in Fig. 2b.

Coprecipitation processes tend to be more effective than adsorption processes at removing aqueous heavy metal ions from solution. This could be due to a much larger effective surface area becoming available as various "layers" of the colloid form. Alternatively, it may result from the formation of mixed metal hydroxide complexes (either in solution or as a solid) that exhibit greater adsorption characteristics than those of the individual metal ions.

II. EXPERIMENTAL TECHNIQUES

A. Reagents

All reagents used to prepare solutions were of analytical reagent (AR) quality unless otherwise specified.

B. Background Electrolyte

The electrolyte concentration used in adsorption and coprecipitation experiments was dominated by the high concentration of nitrate required to prepare the colloidal substrates (precipitated from a solution of the appropriate metal nitrate, 250 ppm with respect to the metal), the concentration of the adsorbing or coprecipitating metal ion nitrate solutions (50 ppm with respect to the metal), and the base required for adjustment of the pH. It is difficult to estimate the resultant electrolyte concentration, because an unknown amount of the electrolyte would be occluded into and/or adsorbed onto the colloidal phase and thus lost to the solution. The total background electrolyte concentration used was determined to be the equivalent of 0.0175 M KNO_3 by calibration of the colloidal suspension's conductivity with standard KNO_3 solutions. It was found that the conductance of these solutions did not change over the pH range 3–11.

All solutions were prepared to give the equivalent of 0.0175 M KNO_3 background electrolyte solution, except for those experiments involving adsorption and coprecipitation of metal ions from ammoniacal solutions, where a 0.5 M NH_4NO_3 background electrolyte was used.

C. Metal Ion Solutions

Metal ion solutions were prepared from the nitrates to provide stock solutions that, when diluted, produced concentrations of 50 ppm with respect to the adsorbing or coprecipitating metal under investigation and 250 ppm with respect to the metal ion

used to prepare the colloidal substrate [either Fe(III) or Cr(III)]. The total volume of each batch precipitation, adsorption, or coprecipitation experiment was 400 cm³.

The concentration of each adsorbing/coprecipitating metal ion was chosen to be 50 ppm, as this was the approximate concentration found in industrial effluent with significant metal ion contamination [7].

D. Colloidal Substrates

Two types of solid substrate surfaces were used in this study: amorphous hydrous iron(III) oxide (HFO) and amorphous hydrous chromium(III) oxide (HCO). Both substrates were prepared by slowly increasing the acidic pH of either an iron(III) nitrate or chromium(III) nitrate solution of concentration 250 ppm with respect to the metal ion in question. Metal ion adsorption or coprecipitation experiments using amorphous hydrous metal oxide substrates are generally described in terms of the concentration (ppm) of metal ion that was used to form the colloidal adsorbent rather than its corresponding specific surface area (m²/L) [64,65].

E. Precipitation, Adsorption, and Coprecipitation Studies

The extent to which metal ions were removed from solution was assessed by performing experiments carried out in three modes: direct precipitation, adsorption, and coprecipitation. In all cases, the initial pH of the starting metal nitrate solution (~3) was low (i.e., pH 3.5 or less). Atomic absorption analysis confirmed that no appreciable quantities of insoluble hydroxide precipitates were present in the metal nitrate solutions at these low pH values.

Direct precipitation profiles of single metal ions were obtained by increasing the pH of nitrate solutions of the metal ion in question. The pH and extent of precipitation were measured after equilibration at the final pH for 40 min. The experiment was repeated with a fresh sample for each pH measured.

In the adsorption experiments, the colloidal substrate (either HFO or HCO) was prepared by increasing the pH of an iron(III) or chromium(III) nitrate solution of concentration 250 ppm with respect to metal ion, and allowed to equilibrate for a period of 5 min. When studying the removal behavior of single metal ions, the metal ion of interest was then added to the pH-adjusted colloidal suspension and equilibration was allowed to take place, after which time the equilibrium pH of the suspension and extent of adsorption were measured.

When studying the removal behavior of the various metals in multiple metal systems, the metal ions under investigation were premixed in a separate container before being added to the reaction vessel containing the pH-adjusted colloidal substrate. This procedure was followed in order to avoid the possibility of preferential adsorption of any of the metal types that may have occurred if the metal ions were added to the suspensions separately. Again, the experiment was repeated with a fresh sample for each pH measured; equilibration time was 40 min.

In the coprecipitation experiments, the pH of the solution containing both the iron(III) or chromium(III) nitrate solution and the metal ion(s) under investigation was increased. Again, the pH and extent of coprecipitation were measured after

equilibration (40 min) had taken place and the experiment was repeated with a fresh sample for each pH measured.

A series of adsorption and coprecipitation experiments were also performed in the presence of an initially 0.5M NH_4NO_3 solution. The procedures adopted for adsorption and coprecipitation of metal ions under these conditions were the same for those performed in 0.0175M KNO_3 background electrolyte.

F. Determination of Metal Ion Removal

The metal ion removal achieved during the various precipitation, adsorption, or coprecipitation experiments was evaluated by determining the concentration of the metal remaining in solution after equilibration had taken place. Each sample for analysis was removed from the reaction vessel, filtered through a 0.22 μm Millipore nitrocellulose filter into a glass vial containing two drops of concentrated nitric acid, and analyzed using a Varian SpectrAA-20 atomic absorption spectrometer with a nitrous oxide/acetylene flame. The quantity of metal ion precipitated, adsorbed, and/or coprecipitated was assumed to be given by a simple mass balance, i.e., the mass added less the mass found in solution.

III. PRECIPITATION, ADSORPTION, AND COPRECIPITATION

Figures 3–5 show the uptake of Cr(III), Zn(II), and Ni(II), respectively, using HFO as the substrate (when required). The symbols marked on this graph, as with all subsequent graphs, refer to experimental data; however, the lines do not. Rather, the lines are given by the "best fit" of the theory to be discussed in Sec. VII.

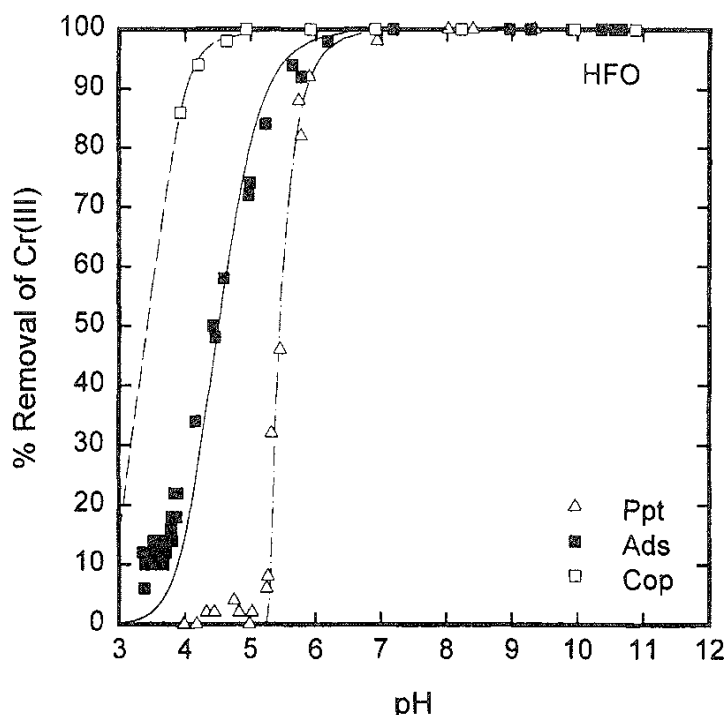


FIG. 3 Adsorption and coprecipitation of Cr(III) (50 ppm) with HFO [250 ppm with respect to Fe(III)] compared to precipitation of Cr(III) (50 ppm) alone.

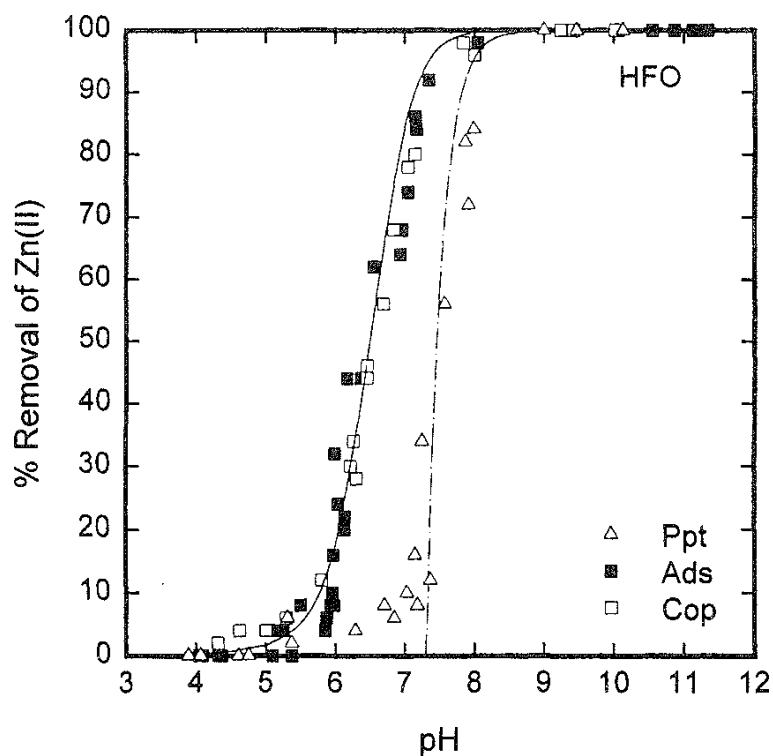


FIG. 4 Adsorption and coprecipitation of Zn(II) (50 ppm) with HFO [250 ppm with respect to Fe(III)] compared to precipitation of Zn(II) (50 ppm) alone,

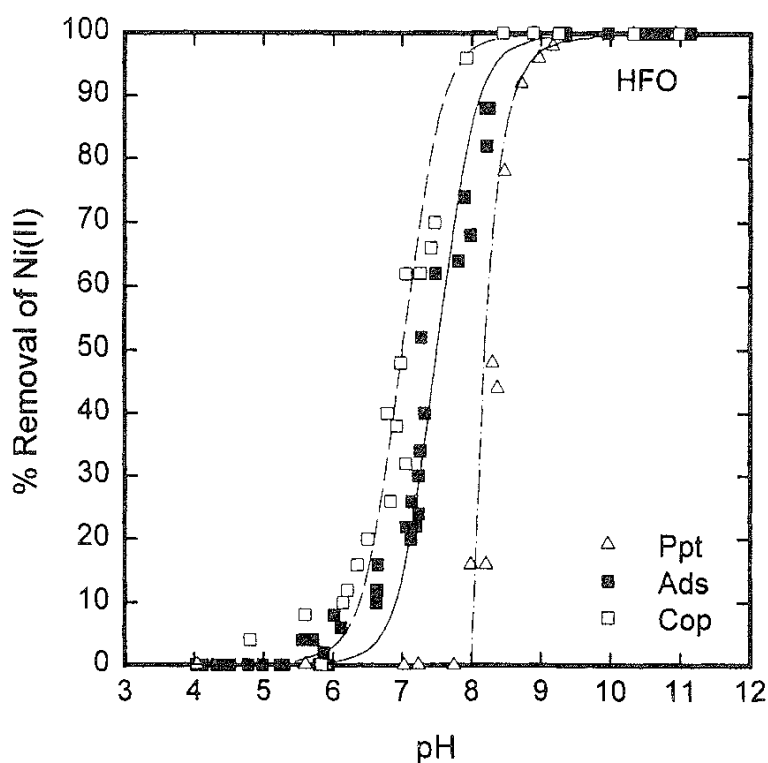


FIG. 5 Adsorption and coprecipitation of Ni(II) (50 ppm) with HFO [250 ppm with respect to Fe(III)] compared to precipitation of Ni(II) (50 ppm) alone.

The concentration of Cr(III) in aqueous phase changes from the initial Cr(III) concentration (i.e., 0% removal) to nearly zero (i.e., 100% removal) over a narrow pH range (Fig. 3). This pattern is characteristic for aqueous metal removal by adsorption or precipitation mechanisms [39,50,62,63,67]. James and Healy [39], for example, showed that the adsorption of Cr(III) onto SiO₂ changes from approximately zero at pH 3.5 to 50% at pH 4.5 and 100% at pH 6.1. The pH range for adsorption of Cr(III) onto HFO, given in Fig. 3, is very similar. Comparable results were obtained by Chang et al. [68] for Cr(III) adsorption onto γ -Al₂O₃.

The removal of Zn(II) (Fig. 4) follows the same qualitative pattern as the one seen for Cr(III). The adsorption curve shows an increase in adsorption ranging from zero at pH 6.0 to nearly 100% at pH 7.2. This pH range is consistent with the results obtained by Duker et al. [24], Benjamin [61], and Benjamin and Leckie [18] for Zn(II) adsorption onto HFO and by Rodda et al. [42] for Zn(II) adsorption onto synthetic goethite. The results are not, however, consistent with those of Kinniburgh et al. [17]. The pH range over which adsorption took place for Zn(II) onto HFO oxide gel was found by the latter authors to be approximately one pH unit lower than the results presented here.

The pH range over which Ni(II) was removed by adsorption in this study (Fig. 5) is 6.8–8.2, which is similar to that found by Barrow et al. [69] for Ni(II) adsorption onto goethite, but again dissimilar to that obtained by Kinniburgh et al. [17] for Ni(II) adsorption onto HFO gel.

For both adsorption and coprecipitation mechanisms, the expected correlation between hydrolysis and adsorption (or coprecipitation) is seen in Figs. 3–5. Cr(III), which hydrolyzes at the lowest pH of the three metal ions, was also removed by adsorption and coprecipitation at the lowest pH. Conversely, Ni(II), which hydrolyzes at the highest pH, was removed by adsorption and coprecipitation at the highest pH.

In all three cases, the expected trend is observed: Coprecipitation results in removal at a lower pH than does adsorption, which in turn results in removal at a lower pH than simple precipitation. In the case of Zn(II), however, the difference between adsorption and coprecipitation is barely perceptible. For the cases of Ni(II) and Cr(III), the enhancement of coprecipitation over the adsorption is very significant and is worth discussing further.

Corey [70] argued that the main difference between adsorption and coprecipitation lies in the geometry of the adsorbent surface, that coprecipitation should be considered a three-dimensional process leading to a greater effective removal capacity than simple adsorption. Such an argument would predict considerably increased removal, at any given pH, for coprecipitation over adsorption. Alternatively, the increased removal may simply reflect an increase in available surface area as the HFO is formed. However, it was earlier argued that such an increase would not necessarily result in a significant shift along the pH axis. For this to occur, the increase in effective surface area probably needs to be of two or three orders of magnitude.

Meng and Letterman [71], Sion et al. [72], and Taylor [73], among others, presented evidence for the formation of mixed hydroxides of well-defined stoichiometry and solution behavior that differs from that of either hydroxide alone. One may

thus speculate that the existence of such mixed hydroxide species during coprecipitation leads to enhanced removal compared to adsorption. Such species may also help to explain one of the unusual aspects of the data presented in Figs. 3–5, this being the degree of enhancement of coprecipitation over adsorption.

For the case of Zn(II) the enhancement is minimal, yet Zn(II) falls between Cr(III) and Ni(II) both in terms of the pH at which hydrolysis occurs and in terms of the pH at which adsorption occurs. One would expect Cr(III) to show the greatest enhancement (as it does), because its removal is closest to the precipitation edge for HFO. Therefore, one would expect a large amount of Fe(III) to be still in solution with Cr(III) is being coprecipitated. According to this argument, however, one would expect Zn(II) to show the least enhancement because its removal is at the highest (i.e., furthest away) pH. This trend may support the concept of mixed hydroxide species forming during coprecipitation in that such mixed hydroxide species would probably differ in their affinity for one another. Thus in the case of Fe(III) and Zn(II) there may not be such a complex, or rather the complex formed may not have any special affinity for Zn(II), and hence there is minimal enhancement of removal.

IV. COMPARISON OF HCO AND HFO AS SUBSTRATES

A. Adsorption

Experiments to remove metal ions from solution similar to those discussed in Sec. III were performed using Zn(II) and Ni(II) with HCO as the adsorbing or coprecipitating colloid. It is not possible to perform adsorption studies of Fe(III) with HCO, because the HFO forms at a lower pH than the HCO.

Adsorption or coprecipitation studies do not appear to have been performed using HCO as the substrate, and hence comparisons between the data obtained in this study with previous literature values are not possible.

The adsorption of Zn(II) and Ni(II) onto HCO is compared with that for HFO in Fig. 6. Again, the lines in Fig. 6 refer to the "best fit" of the model to be discussed in Sec. VII. This is the case with all remaining graphs in this chapter.

Amorphous hydrous iron(III) oxide (HFO) has often been used as an adsorbing substrate not simply because of the ease with which it can be prepared but also because of its recognized efficiency as an adsorbent [77]. The above comparison shows that HCO is an even more efficient adsorbing substrate than HFO. Moreover, the difference between HFO and HCO is significantly greater than the minor variation that would be predicted by, for example, Harding and Healy [37] on the basis of their slightly different surface areas. This indicates that HCO is atypical of hydroxides and oxides and has a specific affinity, at least for Zn(II) and Ni(II).

The origin of any such special affinity is not clear; however, it may relate to the solution chemistry of Cr(III). Chromium(III) has an unusual solution chemistry in that it has a slower ligand exchange rate than the other transition metals due to its stable d_3 electron configuration [74,75]. This could well result in structure at the HCO surface that enhances adsorption by, for example, preventing adsorbed ions from readily desorbing and thus effectively shifting the equilibria to favor greater adsorption.

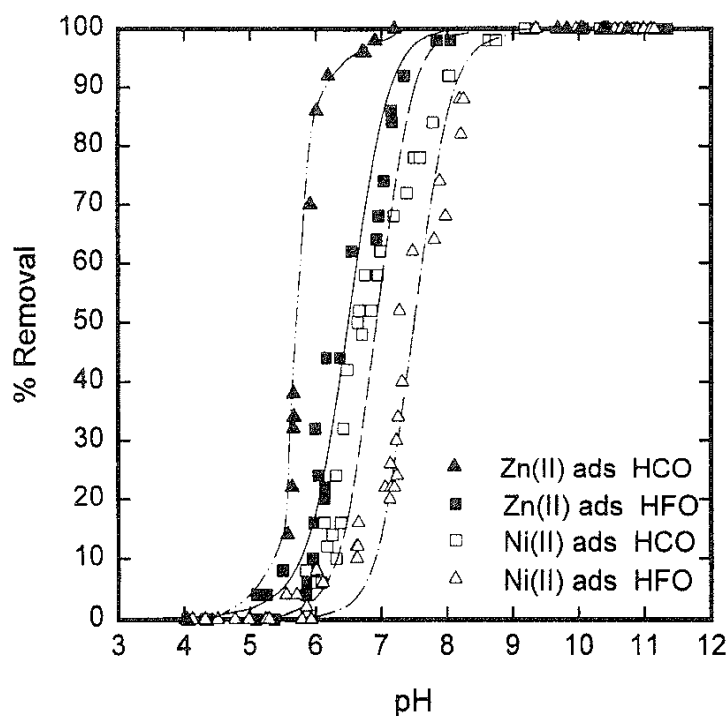


FIG. 6 Adsorption of Zn(II) (50 ppm) or Ni(II) (50 ppm) with HFO [250 ppm with respect to Fe(III)] or HCO [250 ppm with respect to Cr(III)].

B. Coprecipitation

The coprecipitation of Zn(II) and Ni(II) with HCO is compared with that for HFO in Fig. 7. Again, HCO is seen as a far stronger adsorbent (or more correctly a coprecipitant) than HFO. For the case of both Ni(II) and Zn(II), the coprecipitation curves initially reflect the formation of HCO and may thus indicate a simple entrainment process as the removal mechanism. This pattern continues at high pH for Zn(II) removal, but Ni(II) removal is shifted slightly to higher pH values. Of the two metal ions, Ni(II) is removed at slightly higher pH values than Zn(II), and this seems to be enough (at high pH values) to shift the mechanism from entrainment (or at least a mechanism that is dependent on the formation of HCO) to genuine coprecipitation.

The ability of HCO to remove Zn(II) and Ni(II) more efficiently (at any given pH) than HFO has considerable implications for the application of adsorption phenomena in the presence of Cr(III). Sanciolo et al. [7], for example, showed that metal ion removal using adsorbing colloid flotation is more efficient in waste effluent samples containing Cr(III), the efficiency depending on the Cr(III) concentration. The results obtained in this study suggest that this may be due to the enhancement of adsorption and coprecipitation by the formation of HCO.

V. THE INFLUENCE OF COMPETING METAL IONS

The influence of a second or third metal ion on the adsorption and coprecipitation removal of metal ions is given in this section, initially using HFO, and then HCO, as the adsorbing or coprecipitating colloid.

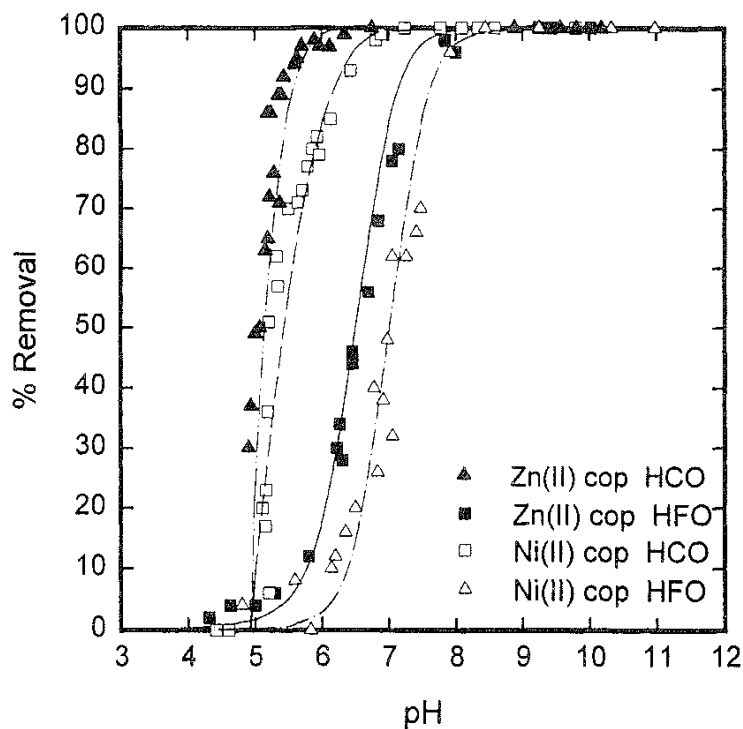


FIG. 7 Coprecipitation of Zn(II) (50 ppm) or Ni(II) (50 ppm) with HFO [250 ppm with respect to Fe(III)] or HCO [250 ppm with respect to Cr(III)].

In single-metal systems, the adsorption or coprecipitation of the metal ion [25] alters the surface chemical characteristics of the substrate. In multiple metal systems, then, the surface seen by a second or third adsorption metal ion is different from the original surface. This one might expect to see significant changes in the removal behavior. Furthermore, if the metal ions have similar hydrolytic behavior, they may interact in solution prior to, or in combination with, adsorption. Thus simple adsorption experiments may involve coprecipitation among the adsorbing metal ions, even if the substrate is added preformed.

The following sections detail adsorption and coprecipitation experiments involving HFO and HCO as the substrate and Cr(III), Zn(II), and Ni(II), in their various permutations, as the competing metal ions.

A. Cr(III) with HFO

The removal, by adsorption, of Cr(III) onto HFO in different solution environments is illustrated in Fig. 8. The four adsorption curves follow the same removal profile, designated as curve 1, indicating that a similar mechanism is operating in all cases. The presence of Ni(II) and/or Zn(II) has little influence over the adsorption profile of Cr(III) onto HFO. This presumably is because the Cr(III) adsorbs at a lower pH than either Ni(II) or Zn(II) and thus the substrate surface, at the pH values of interest, is unaffected.

The removal by coprecipitation of Cr(III) with HFO in different solution environments is illustrated in Fig. 9. The four coprecipitation curves again follow a

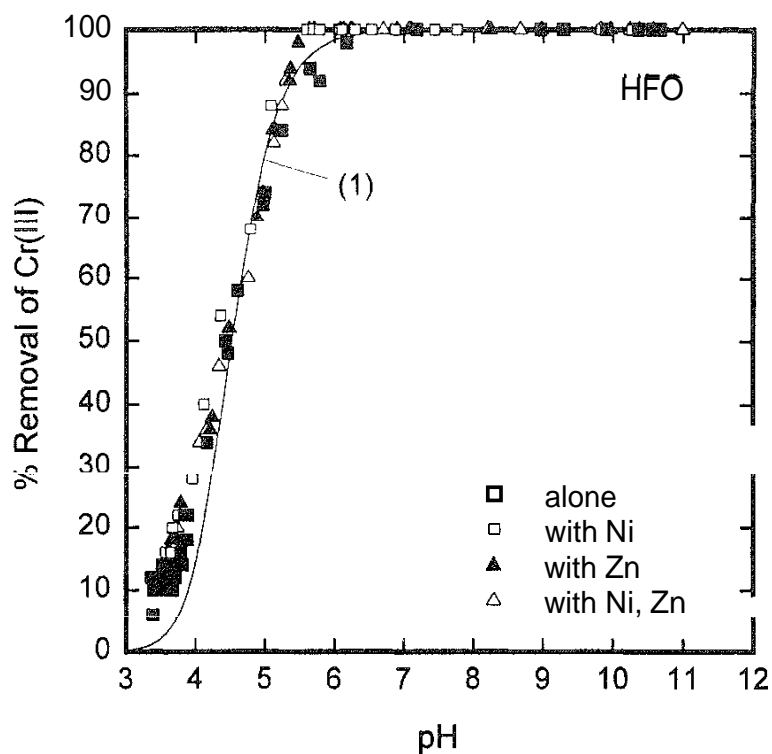


FIG. 8 Adsorption of Cr(III) (50 ppm) alone with HFO [250 ppm with respect to Fe(III)] and with either 50 ppm Zn(II) or 50 ppm Ni(II) or both.

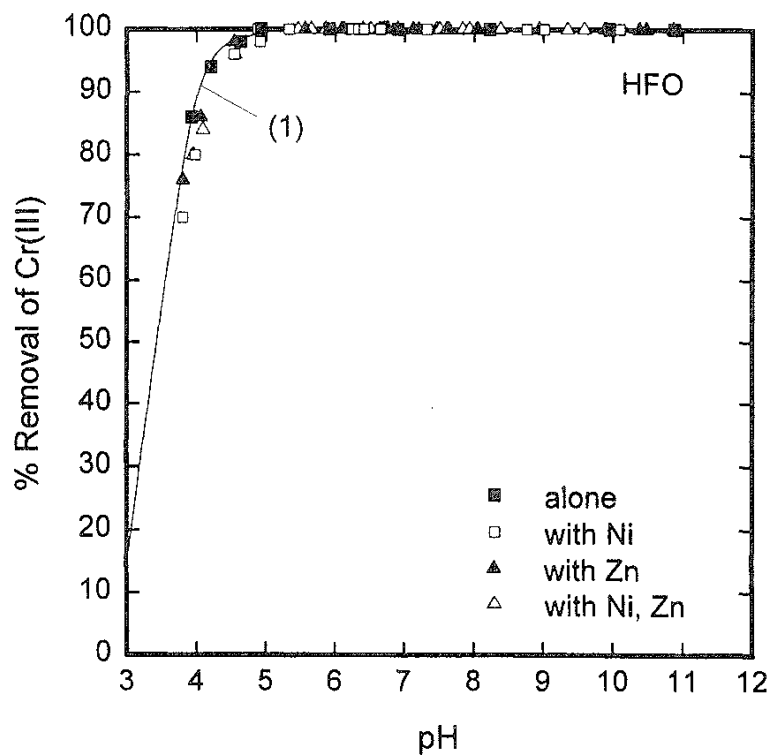


FIG. 9 Coprecipitation of Cr(III) (50 ppm) alone with HFO [250 ppm with respect to Fe(III)] and with either 50 ppm Zn(II) or 50 ppm Ni(II) or both.

single profile, curve 1, again indicating that a similar mechanism is operating in all cases. The presence of Ni(II) and/or Zn(II) has little influence over the coprecipitation profile of Cr(III) onto HFO.

B. Zn(II) with HFO

The removal by adsorption of Zn(II) onto HFO in different solution environments is illustrated in Fig. 10. The presence of Ni(II) has little effect on the adsorption of Zn(II); however, the presence of Cr(III) considerably enhances the adsorption of Zn(II). Enhancement of adsorption is rarely seen in metal ion adsorption experiments, and even in this study the enhancement may reflect coprecipitation (which has been shown to be more efficient than adsorption) rather than adsorption as the removal mechanism. The four sets of adsorption data follow two distinct trends, one in the presence (curve 1) and one in the absence (curve 2) of Cr(III).. Again, the curves represent the best fit model using to be discussed in Sec. VII. In this case, since there are two curves, there are also two sets of modeling parameters.

Closer inspection of the data in Fig. 10 shows that there is a slight decrease in Zn(II) removal in the presence of Ni(II), probably simply due to competition for surface sites and subsequent decreasing of the surface area available for adsorption. Experimental accuracy, however, does not allow a genuine distinction to be made.

The removal by coprecipitation of Zn(II) with HFO in different solution environments is illustrated in Fig. 11. It can be seen that at pH values greater than about 7, the four curves are approximately equivalent and are designated curve 1. There

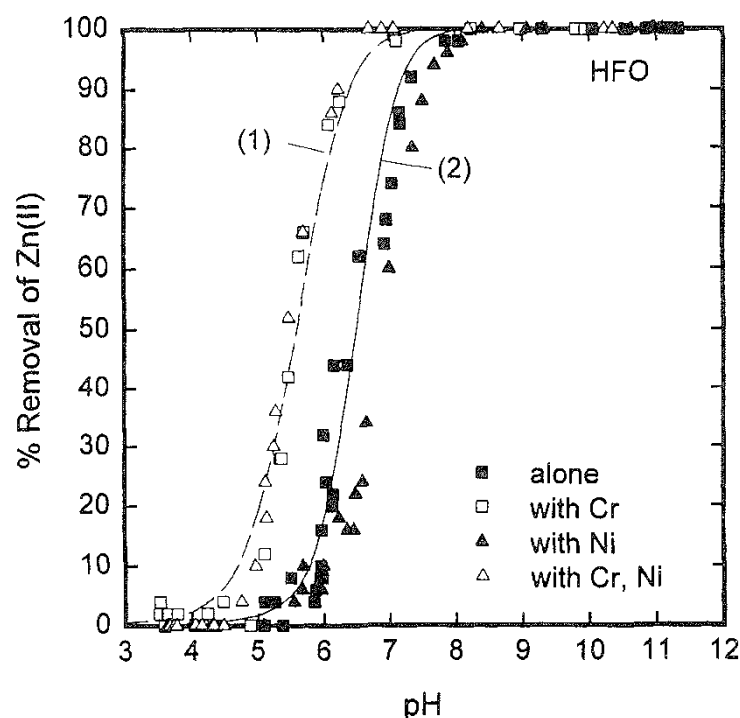


FIG. 10 Adsorption of Zn(II) (50 ppm) alone with HFO [250 ppm with respect to Fe(III)] and with either 50 ppm Cr(III) or 50 ppm Ni(II) or both.

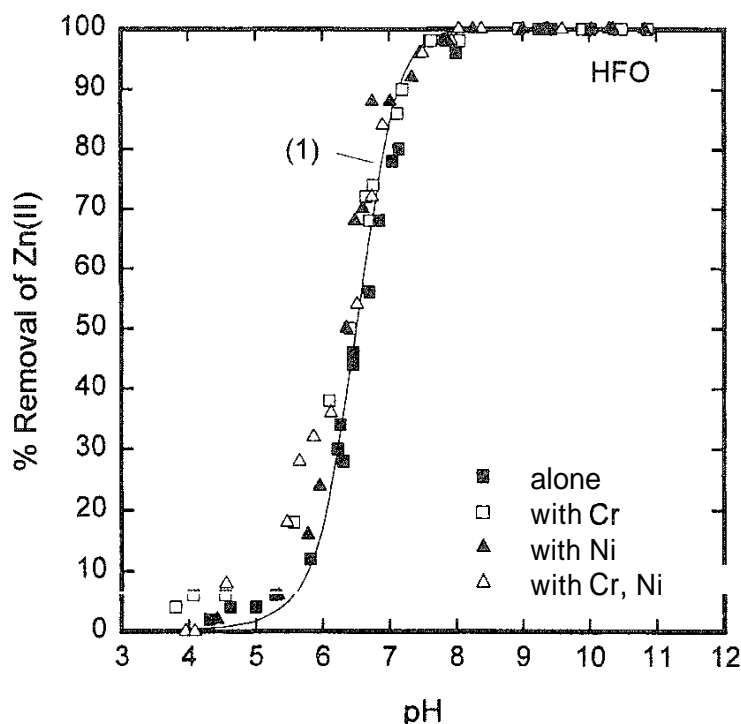


FIG. 11 Coprecipitation of Zn(II) (50 ppm) alone with HFO [250 ppm with respect to Fe(III)] and with either 50 ppm Cr(III) or 50 ppm Ni(II) or both.

is, however, a slight deviation at pH values less than 7. Again, the presence of Cr(III) enhances metal ion removal; however, the enhancement is small and occurs only at low degrees of metal ion removal.

C. Ni(II) with HFO

The removal by adsorption of Ni(II) onto HFO in different solution environments is illustrated in Fig. 12. Two distinct curves are obtained, one in the presence (curve 1) and one in the absence (curve 2) of Cr(III). The presence of Zn(II) has little effect on the adsorption of Ni(II), despite the fact that Zn(II) has almost completed its adsorption at the onset of Ni(II) adsorption. There is a common argument (see, e.g., Netzer and Hughes [76]) that metal ions compete for surface sites and that adsorption of one metal ion should inhibit the adsorption of a second. Benjamin and Leckie [19], on the other hand, argued that different metals may adsorb onto different surface sites and that the adsorption of one metal can have little influence over later adsorption of a second metal. The data shown in Fig. 12 support this latter idea, although the lack of sensitivity to the presence of Zn(II) could be simply due to the lack of sensitivity to changes in surface area. Whatever the case, adsorption of Zn(II) appears to have little effect on the subsequent adsorption of Ni(II) onto HFO.

The presence of Cr(III), however, considerably enhances the adsorption of Ni(II), whether Zn(II) is present or not. As shown in Sec. IV.B, Cr(III) coprecipitates with Ni(II) to remove it at a lower pH than by adsorption onto HFO. The data shown in Fig. 12 probably reflect coprecipitation of Cr(III) with Ni(II).

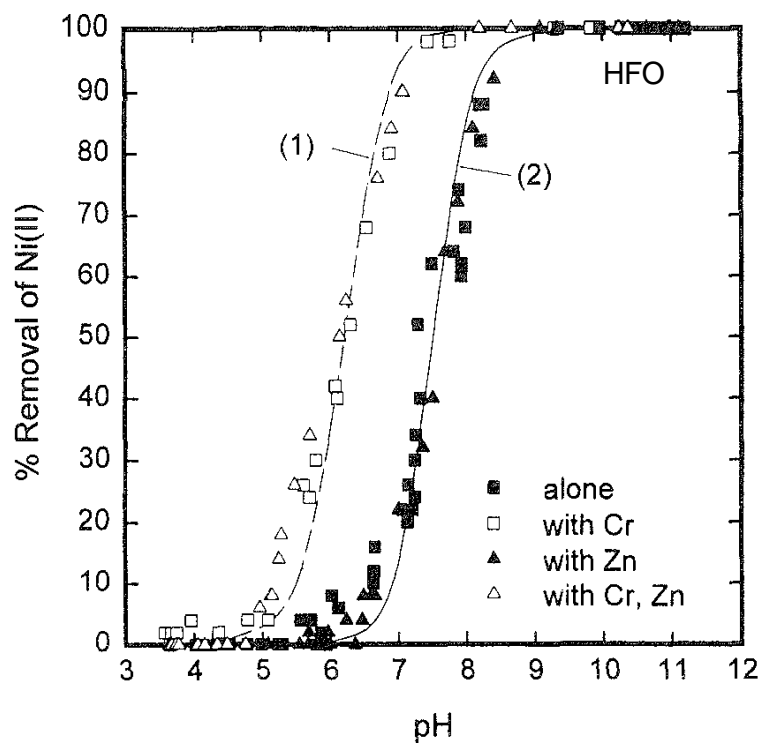


FIG. 12 Adsorption of Ni(II) (50 ppm) alone with HFO [250 ppm with respect to Fe(III)] and with either 50 ppm Cr(III) or 50 ppm Zn(II) or both.

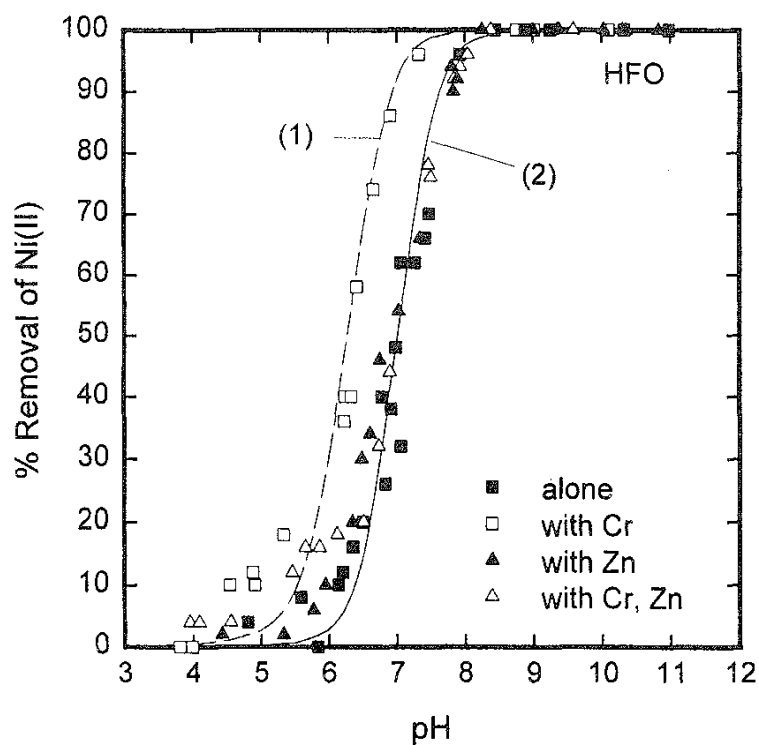


FIG. 13 Coprecipitation of Ni(II) (50 ppm) alone with HFO [250 ppm with respect to Fe(III)] and with either 50 ppm Cr(III) or 50 ppm Zn(II) or both.

The removal by coprecipitation of Ni(II) with HFO in different solution environments is illustrated in Fig. 13. Two distinct curves are obtained; however, the difference in this case is not simply the presence or absence of Cr(III). In contrast to the adsorption results, Ni(II) coprecipitation with HFO in the presence of *both* Cr(III) and Zn(II) displays a profile that is similar to that observed with HFO in the absence of these ions, yet the presence of Cr(III) without Zn(II) still enhances Ni(II) adsorption. The most likely explanation for this latter result is that the removal of Ni(II) is enhanced by the presence of Cr(III) due to Cr(III)/Ni(II) coprecipitation.

The data in Fig. 12 suggest that the Zn(II) coprecipitates with Cr(III) at a lower pH than does the Ni(II), effectively removing the Cr(III) from solution. The consequence of this is that the enhanced removal of the Ni(II) by coprecipitation with Cr(III) is not observed. This result was not observed in the earlier adsorption experiments because in those cases sufficient Cr(III) was present to coprecipitate with both Zn(II) and Ni(II). In this coprecipitation experiment, however, a much smaller quantity of Cr(III) was available for coprecipitation with Zn(II) and Ni(II) as a greater proportion had already coprecipitated with Fe(III).

D. Zn(II) with HCO

The removal by adsorption of Zn(II) onto HCO in different solution environments is illustrated in Fig. 14. The presence of Ni(II) does not affect the removal of Zn(II) by adsorption onto HCO, and a single curve (curve 2) is obtained. It is important to

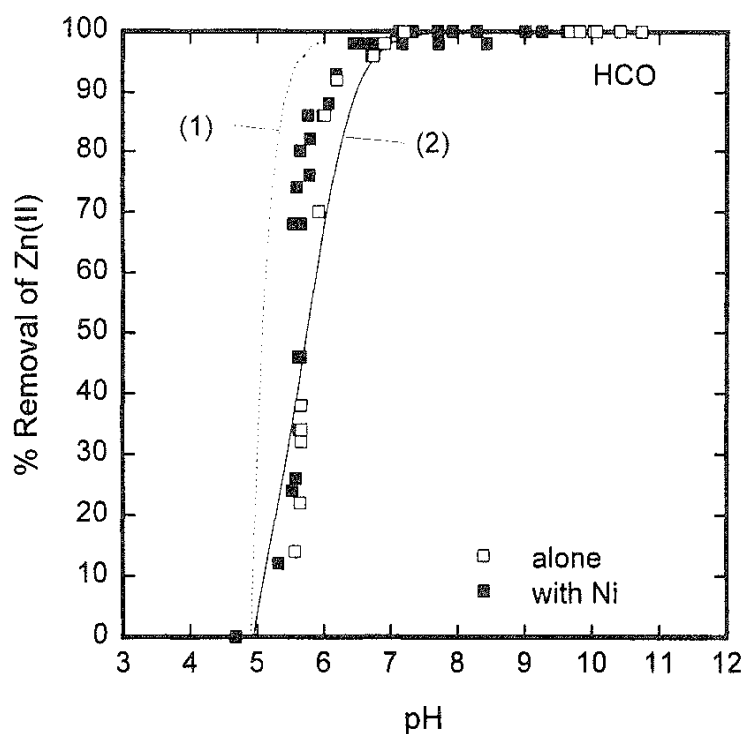


FIG. 14 Adsorption of Zn(II) (50 ppm) alone with HCO [250 ppm with respect to Cr(III)] or with 50 ppm Ni(II).

note that at pH 5.5, where Zn(II) adsorption has commenced, Cr(III) is not fully precipitated, and this would inhibit any enhanced removal at low pH. When modeling the data, the reduction in overall surface area caused by incomplete formation of the HCO was taken into account. The precipitation curve appropriate to 250 ppm Cr(III) (curve 1) is included for comparison in Fig. 14.

The removal by coprecipitation of Zn(II) with HCO in different solution environments is illustrated in Fig. 15. The presence of Ni(II) has no effect on the removal of Zn(II) by coprecipitation with HCO, and again a single curve results (curve 2). Again, however, any enhanced removal at low pH would be masked by the incomplete precipitation of Cr(III). The precipitation curve appropriate to 250 ppm Cr(II) (curve 1) is also included for comparison in Fig. 15.

E. Ni(II) with HCO

The adsorption of Ni(II) onto HCO in different solution environments is illustrated in Fig. 16. Ni(II) adsorption in the absence of Zn(II) follows the expected shape (modeled by curve 2); however, the curve corresponding to Ni(II) removal in the presence of Zn(II) is of an unusual shape. At a pH less than approximately 6.5, Ni(II) removal is enhanced by the presence of Zn(II) and can be modeled by assuming that there is interaction between Zn(II) and Ni(II) (curve 1). At higher pH values, Ni(II) removal is, if anything, slightly inhibited and can be modeled by assuming such inhibition (curve 3).

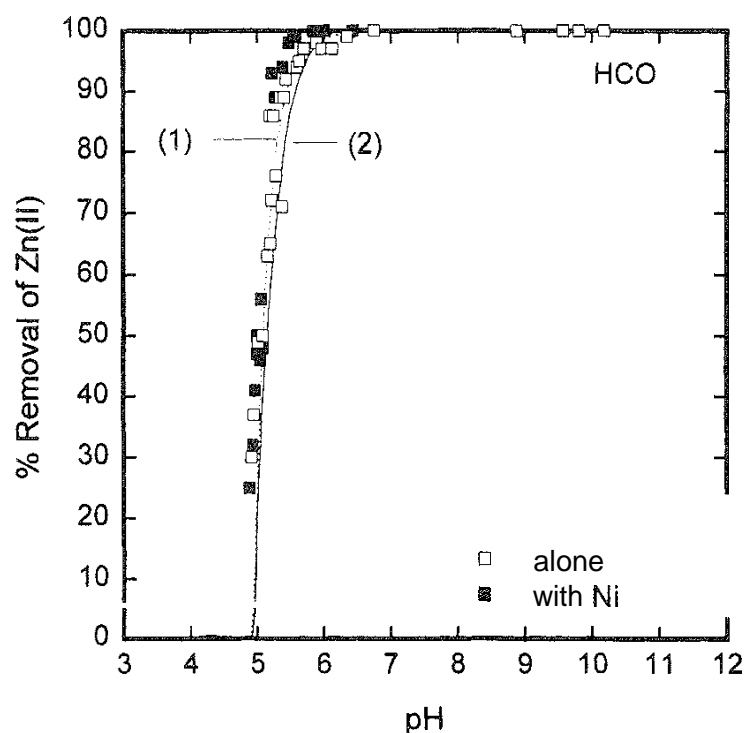


FIG. 15 Coprecipitation of Zn(II) (50 ppm) alone with HCO [250 ppm with respect to Cr(III)] or with 50 ppm Ni(II).

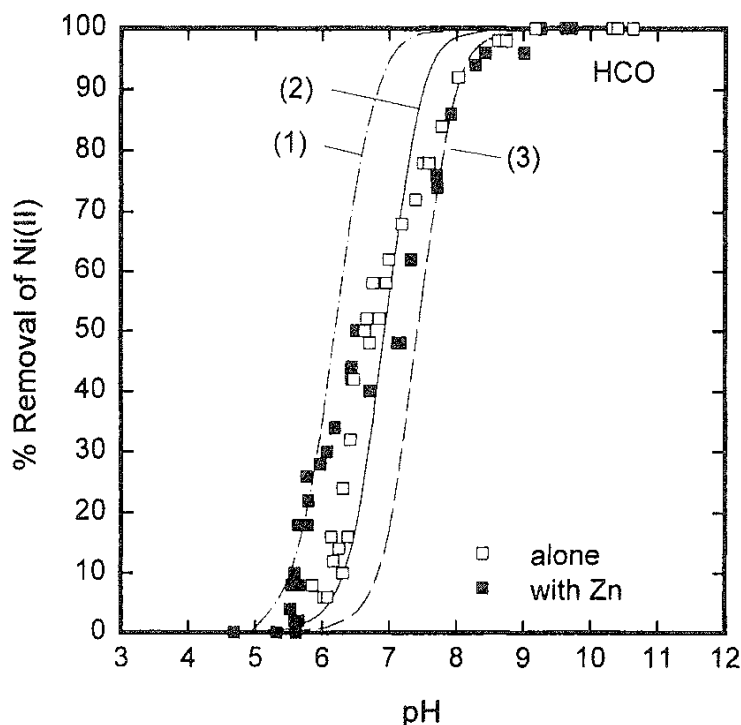


FIG. 16 Adsorption of Ni(II) (50 ppm) alone with HCO [250 ppm with respect to Cr(III)] or with 50 ppm Zn(II).

The enhancement seen at low pH is very unusual and is difficult to attribute to simple coprecipitation mechanisms operating in tandem with adsorption. Ni(II) could not coprecipitate with Cr(III) because the HCO was preformed. Any effects due to Cr(III) remaining in solution or being stripped from the surface to form a coprecipitate with Ni(II) would be seen in the data for Ni(II) adsorption onto HCO [in the absence of Zn(II)], and there would be no enhancement in the presence of Zn(II). If Ni(II) were to coprecipitate with Zn(II), then one would expect to observe enhanced removal of Ni(II) in the presence of Zn(II) onto HFO, which was not the case.

It is possible, however, that a mixed Cr(III), Zn(II), and Ni(II) precipitate forms and that this mixed precipitate is responsible for the enhanced adsorption. It was earlier argued that the enhanced removal of Ni(II) in the presence of Zn(II) and Cr(III) by HFO could be due to coprecipitation of a mixed hydroxy species, although it was not strictly necessary to invoke such a phenomenon. In this case [Ni(II) adsorption onto HCO in the presence of Zn(II)], the concept of a mixed hydroxide precipitate is more likely.

The removal by coprecipitation of Ni(II) with HCO in different solution environments is illustrated in Fig. 17. In both cases the removal of Ni(II) is similar (curve 2) and initially follows the precipitation curve for the 250 ppm Cr(III) alone (curve 1). Subsequent metal ion removal follows a curve possessing a shape characteristic of an adsorption or coprecipitation process. Zn(II) has little, if any, effect on the percentage removal by coprecipitation of Ni(II) with HCO.

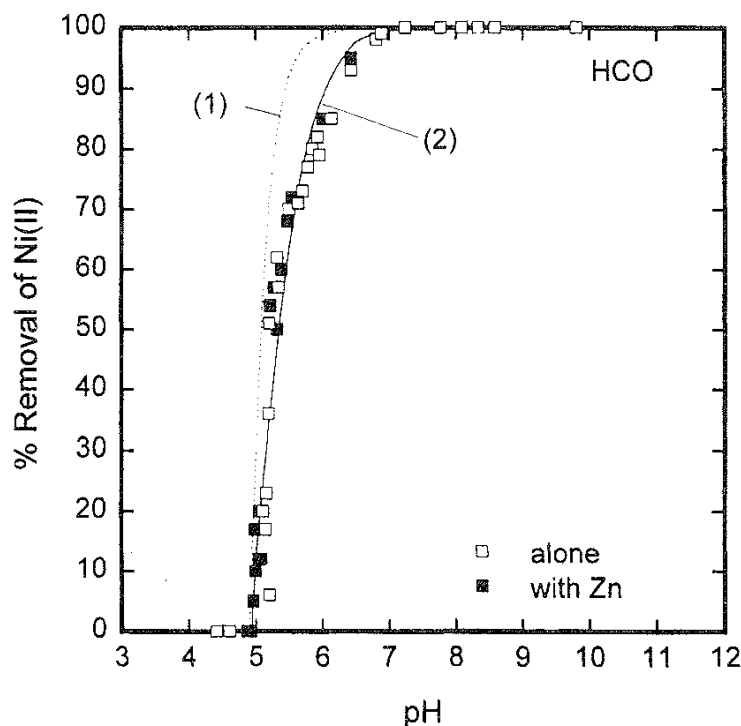


FIG. 17 Coprecipitation of Ni(II) (50 ppm) alone with HCO [250 ppm with respect to Cr(III)] or with 50 ppm Zn(II).

VI. THE INFLUENCE OF A COMPLEXING LIGAND

The influence of a complexing ligand (ammonia) on the adsorption and coprecipitation of Zn(II) using HFO and HCO is reported here. Before discussing the results, however, it should be noted that direct comparison between the results presented here and those of earlier sections is made difficult due to changes in the ionic strength. It is necessary to use a high concentration (0.5 M) of ammonia (added as ammonium nitrate) to effect significant complexing, particularly to effect competitive complexing with the hydroxide ligand. This necessitates the use of a much higher ionic strength than was used in the studies reported in the previous sections. When discussing the significance of results, the effect of ionic strength should therefore be considered.

Hayes and Leckie [77] reported that changing the ionic strength of the background electrolyte has a negligible effect on the adsorption of specifically adsorbed ions such as Cu(II), Pb(II), Ni(II), and Cd(II). However, for divalent alkaline earth cations such as Mg(II), Ca(II), and Ba(II), the ionic strength had a dramatic effect.

Ionic strength effects have been shown to be negligible in the case of the adsorption of 5 ppm Pb(II) and Zn(II) onto goethite in 0.01 and 0.1 M NaNO₃ solutions [45] and that of Cr(III) onto γ -Al₂O₃ [68]. Chang et al. [78], however, reported decreased adsorption of 1×10^{-6} M Zn(II) onto TiO₂ as the concentration of the NaCl background electrolyte was increased from 0.002 to 0.1 M. Schindler et al. [79] reported a similar decrease in adsorption with increase in electrolyte concentration for Cu(II), Cd(II), and Pb(II) onto kaolinite. Barrow et al. [69] also reported a decrease in the adsorption of Cd(II) and Ni(II) onto goethite with increasing

background electrolyte concentration 0.01–1.0M $\text{Ca}(\text{NO}_3)_2$; however, a negligible effect was noted for Zn(II) under the same conditions. $\text{Ca}(\text{NO}_3)_2$ is an unusual choice for a "background" electrolyte because, being nonsymmetrical, it has a different effect on the surface of goethite on either side of the isoelectric point, although most of the adsorption data reported were obtained at pH levels lower than the isoelectric point of goethite.

The influence of ionic strength on the adsorption of metal ions is attributed to two main effects, the effect on the solubility of the ions in solution and the effect on the electrical potential of the surface [69]. Baes and Mesmer [60] described methods to adjust dissociation constants to allow for differing ionic strength, and generally the activity of heavy metal hydrolysis products decreases with increasing ionic strength. Increasing the ionic strength also decreases the absolute values of the electrical potential in the plane at which adsorption takes place [44]. For metal ions such as Zn(II) that adsorb at relatively low pH onto oxide surfaces, the decrease in positive potential of the surface increases adsorption by an amount that approximately offsets the decreased activity of the hydrolysis species of Zn(II), for example $\text{Zn}(\text{OH})^+$ [69]. For such metals, changes in electrolyte concentration have little effect on the adsorption profile. For metals that adsorb at higher pH, the pH range usually extends into a region where the substrate surface becomes negative, and as increasing the ionic strength decreases the negative surface potential, the adsorption of the metal ion also decreases. The extent to which this occurs, however, is subject to debate.

The concentration of the background electrolyte has also been shown to have an effect on the degree to which metal ions are included in coprecipitate structures. Pingitore [80] showed, by performing coprecipitation studies in both the presence and absence of 0.48M NaCl, that the presence of NaCl at this concentration reduces substantially the amount of Ba(II) that can be incorporated into a Ba(II)/Ca(II) coprecipitate.

A. The Influence of Ammonia on the Solution Chemistry of Aqueous Heavy Metals

To help understand the influence of ammonia on adsorption and coprecipitation, it is useful to first look at the influence of ammonia on the solution chemistry of the metal ions to be removed. The concentration of the ammonia ligand is pH-dependent, forming the ammonium ion (NH_4^+) at low pH. It is assumed that the ammonium ion does not, itself, complex with positively charged metal ions and serves mainly to limit the amount of free ammonia available at any given pH.

Ammonia may form a series of complexes with any given metal ion that have a variable number of ammonia ligands per metal ion. Each of these complexes may further interact with the hydroxide ion to form a series of complexes having a variable number of ammonia ligands and a variable number of hydroxide ligands per metal ion. The metal ion itself will interact with hydroxide ions and any electrolyte (NO_3^-) that may be present to form a suite of these complexes as well. Fortunately, a complete set of equilibrium constants have been obtained for the Zn(II) system, and these are given in [Table 1](#).

TABLE 1 Zn(II) Hydrolysis and Ammonia Complexation in 0.5 M Ammoniacal Solution at 25°C^a

| Equilibrium | Constant |
|---|----------------------------|
| $\text{Zn}_{(\text{aq})}^{2+} + \text{H}_2\text{O} \rightleftharpoons \text{Zn}(\text{OH})_{(\text{aq})}^+ + \text{H}_{(\text{aq})}^+$ | $p^*K_1 = 9.20$ |
| $\text{Zn}(\text{OH})_{(\text{aq})}^+ + \text{H}_2\text{O} \rightleftharpoons \text{Zn}(\text{OH})_{2(\text{aq})} + \text{H}_{(\text{aq})}^+$ | $p^*K_2 = 10.11$ |
| $\text{Zn}(\text{OH})_{2(\text{aq})} + \text{H}_2\text{O} \rightleftharpoons \text{Zn}(\text{OH})_{3(\text{aq})}^- + \text{H}_{(\text{aq})}^+$ | $p^*K_3 = 10.91$ |
| $\text{Zn}(\text{OH})_{3(\text{aq})}^- + \text{H}_2\text{O} \rightleftharpoons \text{Zn}(\text{OH})_{4(\text{aq})}^{2-} + \text{H}_{(\text{aq})}^+$ | $p^*K_4 = 11.65$ |
| $\text{Zn}(\text{OH})_{2(\text{ppt})} \rightleftharpoons \text{Zn}_{(\text{aq})}^{2+} + 2\text{OH}_{(\text{aq})}^-$ | $p^*K_{\text{so}} = 16.45$ |
| $\text{Zn}_{(\text{aq})}^{2+} + \text{NO}_{3(\text{aq})}^- \rightleftharpoons \text{Zn}(\text{NO}_3)_{(\text{aq})}^+$ | $pK_1 = -0.46$ |
| $\text{Zn}_{(\text{aq})}^{2+} + 2\text{NO}_{3(\text{aq})}^- \rightleftharpoons \text{Zn}(\text{NO}_3)_{2(\text{aq})}$ | $p\beta_{12} = 0.95$ |
| $\text{Zn}_{(\text{aq})}^{2+} + \text{NH}_3 \rightleftharpoons \text{Zn}(\text{NH}_3)_{(\text{aq})}^{2+}$ | $pK_1 = -2.17$ |
| $\text{Zn}(\text{NH}_3)_{(\text{aq})}^{2+} + \text{NH}_3 \rightleftharpoons \text{Zn}(\text{NH}_3)_{2(\text{aq})}^{2+}$ | $pK_2 = -2.24$ |
| $\text{Zn}(\text{NH}_3)_{2(\text{aq})}^{2+} + \text{NH}_3 \rightleftharpoons \text{Zn}(\text{NH}_3)_{3(\text{aq})}^{2+}$ | $pK_3 = -2.30$ |
| $\text{Zn}(\text{NH}_3)_{3(\text{aq})}^{2+} + \text{NH}_3 \rightleftharpoons \text{Zn}(\text{NH}_3)_{4(\text{aq})}^{2+}$ | $pK_4 = -1.95$ |
| $\text{Zn}_{(\text{aq})}^{2+} + \text{NH}_3 + \text{OH}_{(\text{aq})}^- \rightleftharpoons \text{Zn}(\text{NH}_3)(\text{OH})_{(\text{aq})}^+$ | $p\beta_{11} = -9.23$ |
| $\text{Zn}_{(\text{aq})}^{2+} + 2\text{NH}_3 + \text{OH}_{(\text{aq})}^- \rightleftharpoons \text{Zn}(\text{NH}_3)_2(\text{OH})_{(\text{aq})}^+$ | $p\beta_{12} = -10.80$ |
| $\text{Zn}_{(\text{aq})}^{2+} + 3\text{NH}_3 + \text{OH}_{(\text{aq})}^- \rightleftharpoons \text{Zn}(\text{NH}_3)_3(\text{OH})_{(\text{aq})}^+$ | $p\beta_{13} = -12.00$ |
| $\text{Zn}_{(\text{aq})}^{2+} + \text{NH}_3 + 2\text{OH}_{(\text{aq})}^- \rightleftharpoons \text{Zn}(\text{NH}_3)(\text{OH})_{2(\text{aq})}$ | $p\beta_{21} = -11.50$ |
| $\text{Zn}_{(\text{aq})}^{2+} + 2\text{NH}_3 + 2\text{OH}_{(\text{aq})}^- \rightleftharpoons \text{Zn}(\text{NH}_3)_2(\text{OH})_{2(\text{aq})}$ | $p\beta_{22} = -13.60$ |
| $\text{Zn}_{(\text{aq})}^{2+} + \text{NH}_3 + 3\text{OH}_{(\text{aq})}^- \rightleftharpoons \text{Zn}(\text{NH}_3)(\text{OH})_{3(\text{aq})}^-$ | $p\beta_3 = -14.50$ |

^a Annotation as used by Sill  n and Martell [40,41].

The easiest way to use the constants presented in Table 1 is to graphically plot concentrations of the various species as a function of pH. Given the number of species involved, this is best performed by using three separate graphs, as shown in Fig. 18. This figure will be referred to when discussing the species likely to be present at any given pH value. For example, at pH 6, the species in highest concentration are $\text{Zn}(\text{NO}_3)^+$ and Zn^{2+} (Fig 18a), and these species are relatively independent of pH near that pH. The species $\text{Zn}(\text{NH}_3)^{2+}$ (Fig. 18b) and $\text{Zn}(\text{NH}_3)(\text{OH})^+$ (Fig. 18c) are not present in high concentration, but the shapes of their curves indicate that they become more and more important as the pH is increased.

B. The Influence of Ammonia on the Adsorption of Zn(II)

The data obtained from the adsorption of Zn(II) onto HFO in the presence of 0.5 M $\text{NH}_4^+/\text{NH}_3$ are given in Fig. 19. It can be seen that the shape of the removal curve is complex, showing several reversals of direction with respect to pH. In this respect, the results are similar to those obtained by Osseo-Asare and Fuerstenau

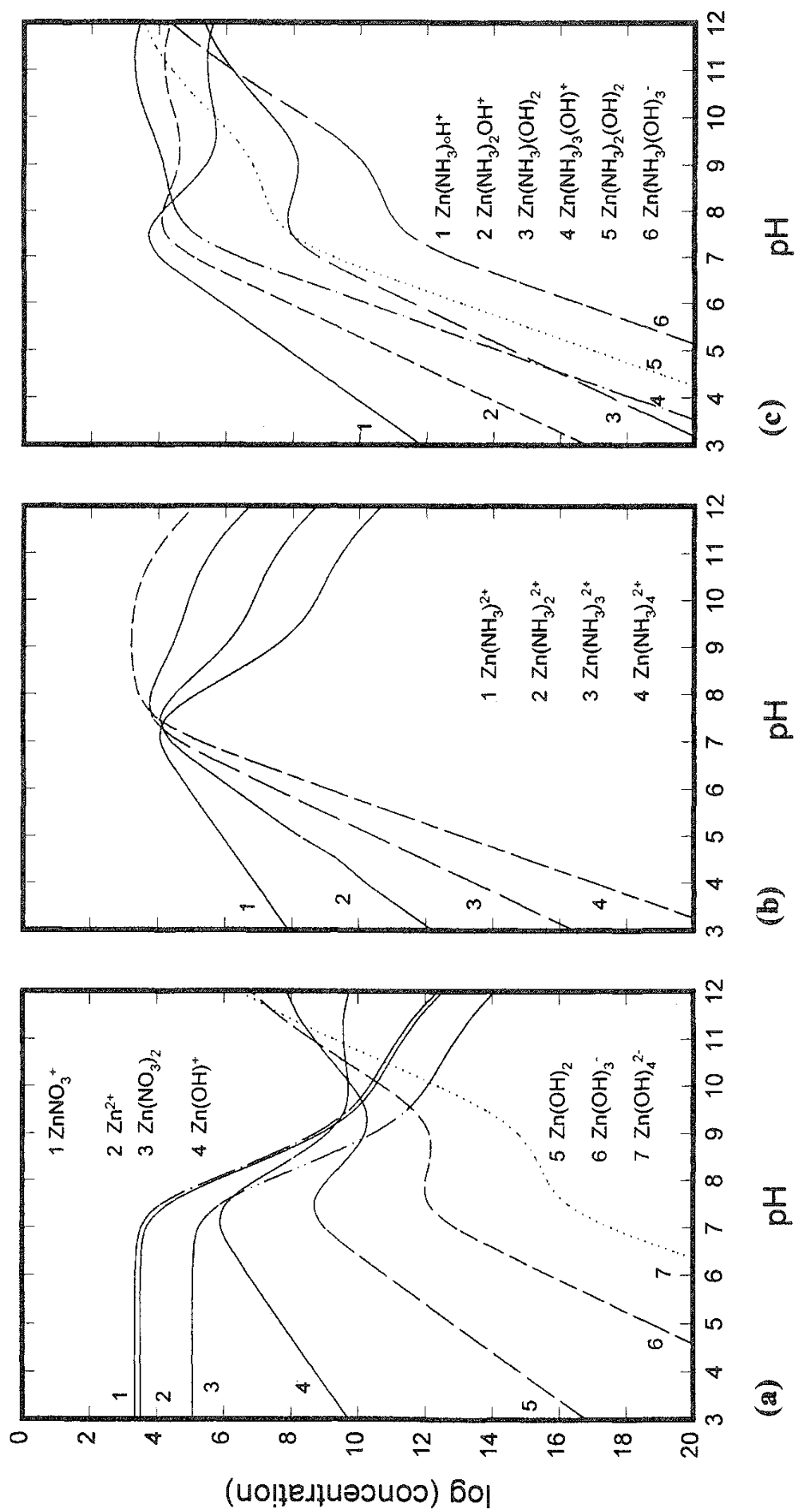


FIG. 18 The concentration of the various hydrolytic, ammine, and hydroxyammine complexes of $\text{Zn}(\text{II})$ as a function of pH for a 50 ppm $\text{Zn}(\text{II})$ solution in 0.5 M $\text{NH}_4^+/\text{NH}_3$ solution at 25°C.

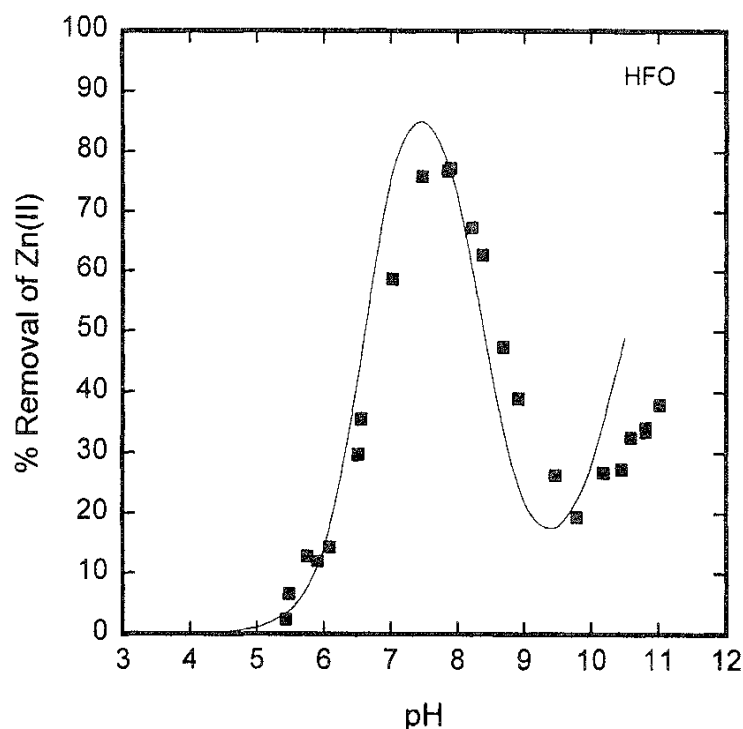


FIG. 19 Adsorption of Zn(II) (50 ppm) onto HFO [250 ppm with respect to Fe(III)] in 0.5 M $\text{NH}_4\text{NO}_3/\text{NH}_3$.

[51,52] for adsorption of several aqueous metals onto a variety of oxide substrates. Guan et al. [27] performed a similar experiment using Zn(II) adsorption onto SiO_2 but did not see such reversals of direction. In their case, however, this may reflect a difference in the way the results were obtained and, in particular, the way they were plotted. They obtained equilibrium concentration-dependent, rather than pH-dependent, adsorption curves and so may have missed this trend.

The results given in Fig. 19 show that the Zn(II) adsorption removal begins at approximately pH 5 [as was observed for Zn(II) adsorption onto HFO in 0.0175 M KNO_3 solution] and increases with pH until approximately pH 7.5. This pH corresponds to the point at which sufficient ammonia is present to form ammine complexes with the aqueous metal ion. Inspection of the Zn(II) speciation diagram (Fig. 18) shows that the concentrations of Zn(II) ammine complexes become dominant at this pH. At pH levels corresponding to high levels of Zn(II) ammine species, the removal of Zn(II) decreases. At a pH of 9.8, however, the concentrations of Zn(II) hydrolysis species and mixed Zn(II) liydroxammine species become significant. At this point, an increase in the Zn(II) removal is observed.

The removal of Zn(II) by adsorption onto HCO in ammoniacal solutions is illustrated in Fig. 20. The data around pH 6-7 do not follow the characteristic sigmoidal curve, with the percent removal decreasing sharply followed by an immediate sharp increase. The data are modeled as two distinct curves (see Sec. VI) to highlight the probable cause of this apparent deviation from normal adsorption behavior. Curve 1 represents the removal assuming that a coprecipitation mechanism is operating. Curve 2 represents the removal assuming that an adsorption mechanism is operating.

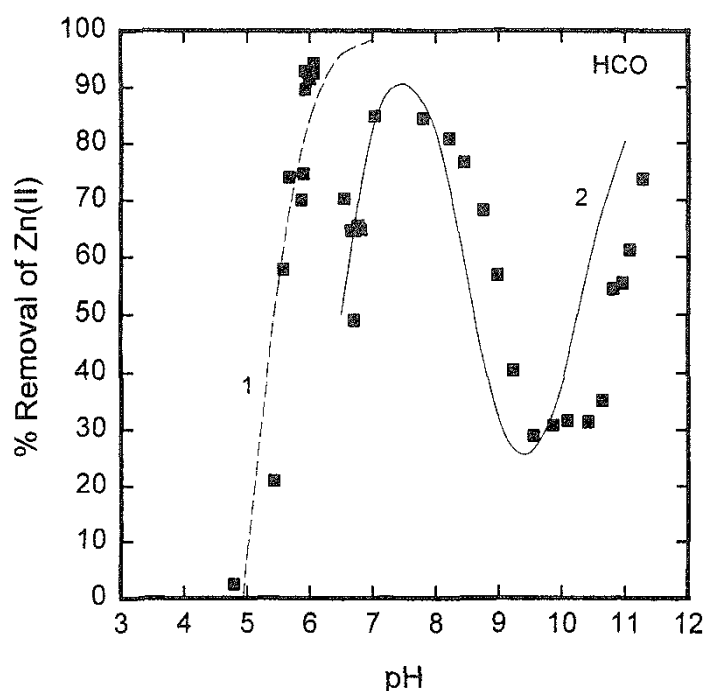


FIG. 20 Adsorption of Zn(II) (50 ppm) onto HCO [250 ppm with respect to Cr(III)] in 0.5 M $\text{NH}_4\text{NO}_3/\text{NH}_3$.

C. The Influence of Ammonia on the Coprecipitation of Zn(II)

The removal of Zn(II) by coprecipitation with HFO in ammoniacal solutions is illustrated in Fig. 21, and its removal by coprecipitation with HCO in ammoniacal solution, in Fig. 22. In the case of HFO, the pattern is similar to that observed for adsorption. Coprecipitation, in this case, results in only a slight increase in removal. In the case of HCO, however, the pattern is quite different, with removal considerably enhanced at all pH values. These results indicate that the coprecipitation mechanism is very effective and can overcome the effect of a complexing ligand to promote heavy metal removal over a wide range of pH values and conditions.

VII. MODELING OF ADSORPTION AND COPRECIPITATION

A. Introduction

A large number of models exist for modeling the adsorption of metal ions onto colloidal substrates, and most of them can be adapted to include coprecipitation. They all involve "fitting" parameters (e.g., the equilibrium constant for adsorption or the chemical specific free energy for adsorption) in order to match experimental and theoretical results. Therefore, there remains some skepticism over the ability of current theories to fully account for the adsorption process. Nevertheless, these "fitting" parameters are generally held constant as a function of pH. Thus the *trend* in adsorption (or coprecipitation) with pH is a guide to the success of the model. It is not the purpose of this chapter to detail all the adsorption models or to compare them. Rather, one model is used to test its robustness in modeling precipitation,

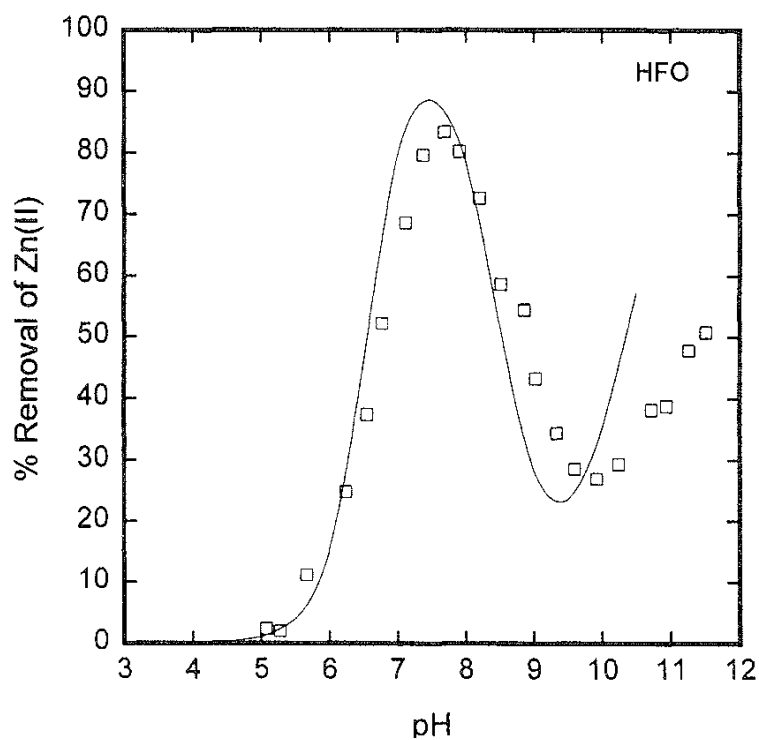


FIG. 21 Coprecipitation of Zn(II) (50 ppm) onto HFO [250 ppm with respect to Fe(III)] in 0.5 M $\text{NH}_4\text{NO}_3/\text{NH}_3$

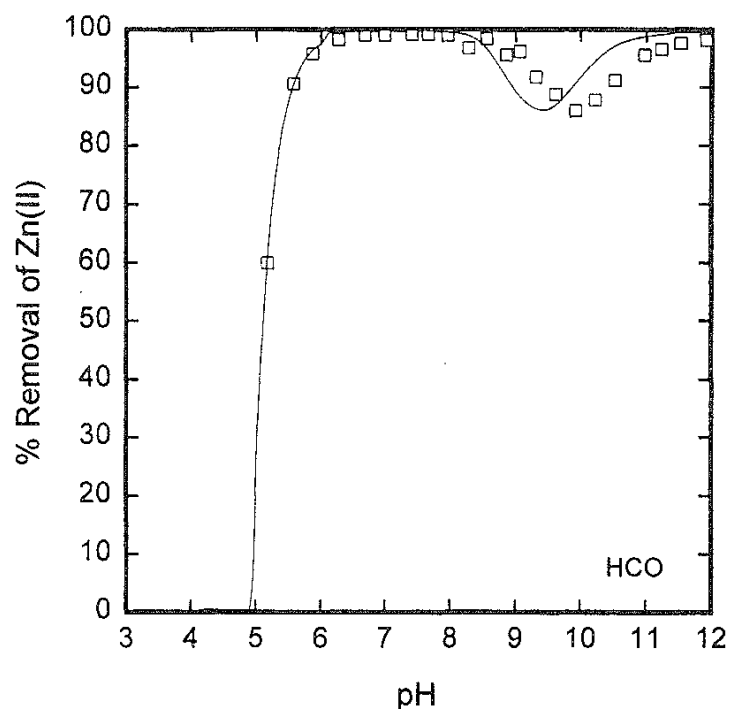


FIG. 22 Coprecipitation of Zn(II) (50 ppm) onto HCO [250 ppm with respect to Cr(III)] in 0.5 M $\text{NH}_4\text{NO}_3/\text{NH}_3$.

adsorption, and coprecipitation under conditions of simple metal ion removal and metal ion removal in the presence of competing metal ions and a complexing agent. The model chosen is a modified form [26] of the James–Healy model [39] for metal ion adsorption.

B. The James–Healy Model for Metal Ion Adsorption

The James–Healy model [39] has been used extensively to model the adsorption behavior of a series of aqueous heavy metals onto a variety of substrates. However, there is still considerable uncertainty in many of its underlying concepts. The model is based on determining the free energy of adsorption for all potential adsorbing species i ($\Delta G^\circ_{\text{ads},i}$). For example, in the study of Zn(II) adsorption in the presence of a KNO_3 background electrolyte, such species are the free metal ion, its hydrolysis species, and its nitrate complexes. For each species, $\Delta G^\circ_{\text{ads},i}$ is divided into three components: $\Delta G^\circ_{\text{solv},i}$, $\Delta G^\circ_{\text{elec},i}$, and $\Delta G^\circ_{\text{chem},i}$. The first component, $\Delta G^\circ_{\text{solv},i}$ is associated with the replacement of part of the solvation sheath that surrounds a charged ion in solution, with a solid surface. The second component, $\Delta G^\circ_{\text{elec},i}$, is associated with bringing a charged ion into close proximity to a charged surface. The third component, $\Delta G^\circ_{\text{chem},i}$, is associated with specific chemical interactions not accounted for in the first two terms. Such specific interactions may include hydrogen bonding, crystal field stabilization, hydration forces, and chemical bonding. It was also originally envisaged that it could account for errors in the calculation of $\Delta G^\circ_{\text{solv},i}$ and $\Delta G^\circ_{\text{elec},i}$, but aspects of all three terms remain open to further definition.

The James–Healy model [39] has been used to model the adsorption of Fe(III), Cr(III), Co(II), and Ca(II) onto SiO_2 [39], of Co(II) onto TiO_2 [39], of Cd(II) onto amphoteric polystyrene latexes [62,67], of Cd(II) onto TiO_2 and goethite [37], of Cu(II), Pb(II), and Zn(II) onto synthetic goethite [55], of Cu(II), Ni(II), Co(II), and Co(III) ammine complexes onto Al_2O_3 , Fe_2O_3 , SiO_2 and TiO_2 [50,52], of Ca(II) onto ZnS [82], and of mercury complexes onto SiO_2 [47]. In each of these cases, the model was used in the original form proposed by James and Healy [39], although recent advances in physical chemistry can improve the algorithms used to calculate the various free energy components.

There has been little improvement to the calculation of $\Delta G^\circ_{\text{solv}}$, used by James and Healy [39] despite the simplicity of the approach, which involves a discrete, rather than a continuous, change in solvation energy. Although this may be considered a weakness, it is appropriate because there is increasingly more evidence that interfacial properties are of a discrete nature [83].

By contrast, there is considerable evidence to suggest that the Nernst equation, used to calculate the surface potential and thus $\Delta G^\circ_{\text{elec},i}$, is inappropriate in the case of hydrous metal oxides [84,85]. Crawford et al. [25,26,28] proposed the use of zeta potentials rather than surface potential to calculate $\Delta G^\circ_{\text{elec},i}$ (and also $\Delta G^\circ_{\text{solv},i}$) and this forms the basis of the modified model used throughout this chapter.

Of the greatest concern is the uncertainty associated with the origin of $\Delta G^\circ_{\text{chem},i}$. This term is used largely as a fitting parameter, although there are some indications of its phenomenological basis. MacNaughton and James [47], for example, showed that complexation of a metal ion with a unidentate ligand, such as chloride, pre-

vents the adsorption of that metal ion; however, use of the James–Healy model can predict this only if $\Delta G^\circ_{\text{chem},i}$ for the complex is set at, or near, zero. Fuerstenau and Osseo-Asare [50,52] showed that optimal modeling results are obtained if different $\Delta G^\circ_{\text{chem},i}$ values are assigned to the different hydrolysis products of metal ions, (i.e., aqueous metal hydroxide species), although this is not necessary to obtain reasonable agreement between theory and data. Importantly, Rodda et al. [42] suggested that the use of differing $\Delta G^\circ_{\text{chem},i}$ terms lessens the credibility of a theoretical model.

In general, a significant (negative) $\Delta G^\circ_{\text{chem},i}$ indicates that adsorption is greater than that predicted on the basis of electrostatic and solvation forces. Species that exhibit this are the hydrolysis products of the metal ion. Species complexed with simple ligands, other than hydroxide, do not adsorb [50,52] and cannot be given a significant $\Delta G^\circ_{\text{chem},i}$ value.

C. The Significance of the Chemical Free Energy Contribution to Adsorption

For each species involved in each experiment given in this chapter, a $\Delta G^\circ_{\text{chem},i}$ value was determined by modeling the data with the modified James–Healy model. In some cases, several sets of data could be used, although in most cases the choice of $\Delta G^\circ_{\text{chem},i}$ was clear. Details of this can be found elsewhere [26,81].

The philosophy behind modeling is to assume that $\Delta G^\circ_{\text{chem},i}$ is independent of pH, concentration, and the presence of other metal ions. It was, however, dependent on the particular metal species and the particular substrate. Where possible, $\Delta G^\circ_{\text{chem},i}$ was kept constant for a given suite of metal–ligand complexes.

Several interesting features have arisen from the modeling process. $\Delta G^\circ_{\text{chem},i}$ for zinc nitrate complexes, for example, need to be considerably smaller than for the free metal ion (Zn^{2+}) and could be set to zero. $\Delta G^\circ_{\text{chem},i}$ for zinc hydroxyammine (mixed) complexes, however, must be smaller than for zinc hydroxy complexes but cannot be set to zero. All of the modeling shown in this chapter is consistent with the general rule that hydroxide must be present to have significant specific interaction and that any other complex (such as ammonia) diminishes this interaction without stopping it.

The agreement between experimental data and modeled curves shown throughout this chapter is very good, indicating that the model is quite robust.

VIII. CONCLUSIONS

A. Precipitation, Adsorption, and Coprecipitation

The adsorption and coprecipitation profiles for Zn(II) removal using HFO are very similar. There is a small but significant difference between adsorption and coprecipitation for Ni(II) and a large difference for Cr(III) using the same substrate. In all cases, coprecipitation was as efficient as or more efficient than adsorption, which was in turn more efficient than precipitation alone.

In all cases, Cr(III) was removed at a lower pH than Zn(II), which was removed at a lower pH than Ni(II), consistent with their hydrolytic behavior.

B. Comparison of HCO and HFO as Substrates

In all cases, HCO was a more efficient adsorbent than HFO.

C. The Influence of Competing Metal Ions

Adsorption and coprecipitation of Cr(III) with HFO was independent of the presence of Ni(II) and/or Zn(II) because Cr(III) precipitates at a lower pH than either Ni(II) or Zn(II) and apparently at a pH lower than or similar to that of any mixed precipitate involving any combination of these three metals.

The adsorption and coprecipitation of Zn(II) with either HFO or HCO was relatively unaffected by the presence of Ni(II), although there may be a slight suppression of removal, possibly due to simple competition for surface sites.

The adsorption of Ni(II) onto HCO, however, provided an unusual profile in the presence of Zn(II). Adsorption was enhanced at low pH but not at high pH. Ni(II) adsorption onto HFO in the presence of Zn(II) did not show this unusual removal profile.

D. The Influence of a Complexing Ligand

The adsorption and coprecipitation removal profiles for Zn(II) with HFO and HCO in the presence of 0.5M $\text{NH}_4\text{NO}_3/\text{NH}_3$ solution were measured. The onset of ammine complex formation inhibited the adsorption and coprecipitation of Zn(II) onto both HFO and HCO.

E. Modeling of Adsorption and Coprecipitation

The modified James–Healy model for metal ion adsorption could be used to model all the results (precipitation, coprecipitation, adsorption, single metals, multiple metals, complexing ion) as illustrated throughout this chapter.

REFERENCES

1. B. T. Hart, *Hydrobiologia* 91:299 (1982).
2. E. A. Jenne, Trace element sorption by sediments in soils: sites and processes, in *Symposium on Molybdenum on the Environment* (W. Chapell and K. Peterson, eds.), Marcel Dekker, New York, 1977, Vol. 2, p. 425.
3. K. B. Krauskopf, *Geochim. Cosmochim. Acta* 9:1 (1956).
4. H. P. Mott, K. E. Hartz, and D. R. Yunge, *Environ. Eng.* 133:476 (1987).
5. S. Gutcho, *Waste Treatment with Polyelectrolytes and Other Flocculants*, Noyes Data Corporation, Park Ridge, NJ, 1977.
6. R. S. Ramalho, *Introduction to Waste Water Treatment Processes*, Academic, New York, 1977.
7. P. Sanciolo, I. H. Harding, and D. E. Mainwaring, *Sep. Sci. Technol.* 27:375 (1992).
8. C. A. Money and R. W. Cranston, Reductions in Tannery Effluent by Implementation of the Sirolime Process with Liquor Recycling and a Rapid

- Processing Technology, Melbourne Board of Works Industry Waste Grants Scheme Report, CSIRO Division of Wool Technology, Melbourne, 1990, p. 9.
- M. Sittig, Wastewater sources, in *Electroplating and Related Metal Finishing: Pollutant and Toxic Materials Control*, Pollution Technol. Rev. No. 46, Noyes Data Corporation, Park Ridge, NJ, 1978, p. 136.
10. J. A. Davis and J. O. Leckie, *J. Colloid Interface Sci.* 67:90 (1978).
 11. L. Charlet and A. A. Manceau, *J. Colloid Interface Sci.* 148:443 (1992).
 12. C. Namasivayam and K. Ranganathan, *Environ. Pollut.* 82:255 (1993).
 13. C. Namasivayam and K. Ranganathan, *Ind. Eng. Chem. Res.* 34:869 (1995).
 14. B. M. Sass and D. Rai, *Inorg. Chem.* 26:2228 (1987).
 15. S. Mustafa and I. Haq, *Environ. Technol. Lett.* 9:1379 (1988).
 16. R. M. Cornell, R. Giovanoli, and W. Schneider, *J. Chem. Technol. Biotechnol.* 53:73 (1992).
 17. D. G. Kinniburgh, M. L. Jackson, and J. K. Syers, *Soil Sci. Soc. Am. J.* 40:796 (1976).
 18. M. M. Benjamin and J. O. Leckie, *J. Colloid Interface Sci.* 79:209 (1981).
 19. M. M. Benjamin and J. O. Leckie, *J. Colloid Interface Sci.* 83:410 (1981).
 20. E. Bruninx and E. Van Meyl, *Anal. Chim. Acta* 80:85 (1975).
 21. R. J. Crawford, I. H. Harding, and D. E. Mainwaring, *Langmuir* 9:3050 (1993).
 22. R. J. Crawford, I. H. Harding, and D. E. Mainwaring, *Langmuir* 9:3057 (1993).
 23. C. C. Ainsworth, J. L. Pilon, P. L. Gassman, and W. G. Van der Sluys, *Soil Sci. Soc. Am. J.* 58:1615 (1994).
 24. A. Duker, A. Ledin, S. Karlsson, and B. Allard, *Appl. Geochem.* 10:197 (1995).
 25. R. J. Crawford, I. H. Harding, and D. E. Mainwaring, *J. Colloid Interface Sci.* 181:561 (1996).
 26. R. J. Crawford, D. E. Mainwaring, and I. H. Harding, *Colloids Surf.* 126:167 (1997).
 27. Y. Guan, J. J. Kellar, and K. N. Han, *Min. Met. Proc.*, August 1994, p. 130.
 28. G. R. Wiese and T. W. Healy, *J. Colloid Interface Sci.* 51:427 (1975).
 29. M. R. Houchin and L. J. Warren, *J. Colloid Interface Sci.* 100:278 (1984).
 30. A. Bell and E. Matijevic, *J. Inorg. Nucl. Chem.* 37:907 (1975).
 31. R. Sprycha and E. Matijevic, *Colloids Surf.* 47:195 (1990).
 32. K. C. Sen, *Z. Anorg. Allgem. Chem.* 182:118 (1929).
 33. J. Simon, W. Schulze, and R. Reinke, *Z. Anal. Chem.* 264:4 (1973).
 34. A. Packter and K. S. Panesar, *Cryst. Res. Technol.* 20:1181 (1985).
 35. J. E. Johnson and E. Matijevic, *Colloid Polym. Sci.* 270:353 (1992).
 36. R. O. James and G. A. Parks, in *Surface and Colloid Science*, Vol. 12 (E. Matijevic, ed.), Wiley-Interscience, New York, 1982, p. 119.
 37. I. H. Harding and T. W. Healy, *Prog. Water Technol.* 11:265 (1979).
 38. R. O. James, P. J. Stiglich, and T. W. Healy, *Faraday Discuss, Chem. Soc.* 59:142 (1975).
 39. R. O. James and T. W. Healy, *J. Colloid Interface Sci.* 40:65 (1972).
 40. L. G. Sillén and A. E. Martell, *Stability Constants*, Chem. Soc. (London) Spec. Publ. 17, Metcalfe and Cooper, London, 1964.
 41. L. G. Sillén and A. E. Martell, *Stability Constants*, Suppl. 1, Chem. Soc. (London) Spec. Publ. 25, Metcalfe and Cooper, London, 1971.

42. D. P. Rodda, B. B. Johnson, and J. D. Wells, *J. Colloid Interface Sci.* **161**:57 (1993).
43. R. M. McKenzie, *Aust. J. Soil Res.* **18**:61 (1980).
44. D. G. Kinniburgh and M. L. Jackson, Cation adsorption by hydrous metal oxides and clay, in *Adsorption of Inorganics at Solid-Liquid Interfaces* (M. A. Anderson and A. J. Rubin, eds.), Ann Arbor Science, Ann Arbor, MI, 1981, p. 91.
45. Z. S. Kooner, *Environ. Geol.* **21**:242 (1993).
46. C. P. Huang, and Y. T. Lin, in *Adsorption from Solution* (P. H. Tewari, ed.), Plenum, New York, 1981, p. 61.
47. M. G. MacNaughton and R. O. James, *J. Colloid Interface Sci.* **47**:431 (1974).
48. R. O. James and T. W. Healy, *J. Colloid Interface Sci.* **40**:53 (1972).
49. W. Stumm, H. Hohl, and F. Dalang, *Croat. Chem. Acta* **48**:491 (1976).
50. D. W. Fuerstenau and K. Osseo-Asare, *J. Colloid Interface Sci.* **118**:524 (1987).
51. K. Osseo-Asare and D. W. Fuerstenau, *Int. J. Miner. Process.* **6**:85 (1979).
52. K. Osseo-Asare and D. W. Fuerstenau, *Int. J. Miner. Process.* **7**:219 (1980).
53. C. Luo and S. Huang, *Sep. Sci. Technol.* **28**:1253 (1993).
54. S. Music and M. Ristic, *J. Radioanal. Nucl. Chem.* **162**:351 (1992).
55. M. A. Rauf, M. T. Hussain, and S. M. Hasany, *Sep. Sci. Technol.* **28**:2237 (1993).
56. A. R. Bowers and C. P. Huang, *Water Res.* **21**:757 (1987).
57. A. Beveridge and W. F. Pickering, *Water Res.* **17**:215 (1983).
58. D. W. Fuerstenau and K. N. Han, *Miner. Process. Technol. Rev.* **1**:1 (1983).
59. K. C. Nathsarma and P. V. R. Bhaskara Sarma, *Hydrometallurgy* **33**:197 (1993).
60. C. F. Baes and R. E. Mesmer, *The Hydrolysis of Cations*, Krieger, 1986.
61. M. M. Benjamin, *Environ., Sci. Technol.* **17**:686 (1983).
62. I. H. Harding and T. W. Healy, *J. Colloid Interface Sci.* **107**:362 (1985).
63. R. O. James and T. W. Healy, *J. Colloid Interface Sci.* **40**:42 (1972).
64. M. M. Benjamin and J. O. Leckie, *Environ. Sci. Technol.* **15**:1050 (1981).
65. M. M. Benjamin and J. O. Leckie, *Environ. Sci. Technol.* **16**:162 (1982).
66. T. Aoki and M. Munemori, *Bull. Univ. Osaka Prefect., Ser. A.* **33**:181 (1984).
67. I. H. Harding and T. W. Healy, *J. Colloid Interface Sci.* **107**:371 (1985).
68. K. Chang, C. F. Lin, D. Lee, S. Lo, and T. Yasunaga, *J. Colloid Interface Sci.* **165**:169 (1994).
69. N. J. Barrow, J. Gerth, and G. W. Brümmer, *J. Soil. Sci.* **40**:437 (1989).
70. R. B. Corey, in *Adsorption of Inorganics at Solid-Liquid Interfaces* (M. A. Anderson and A. J. Rubin, eds.), Ann Arbor Sci., Ann Arbor, MI, 1981, p. 161.
71. X. Meng and R. D. Letterman, *Environ. Sci. Technol.* **27**:970 (1993).
72. J. Sion, W. Schultzl, and M. Voltz, *Z. Anal. Chem.* **257**:108 (1971).
73. H. F. W. Taylor, *Min. Mag.* **39**:377 (1973).
74. D. Benson, *Mechanisms of Inorganic Reactions in Solution*, McGraw-Hill, London, 1968.
75. S. E. Fendorf, M. Fendorf, D. Sparks, and R. Gronsky, *J. Colloid Interface Sci.* **153**:37 (1992).
76. A. Netzer and D. E. Hughes, *Water Res.* **18**:927 (1984).
77. K. F. Hayes and J. O. Leckie, *J. Colloid Interface Sci.* **115**:564 (1987).
78. C. C. Y. Chang, J. A. Davis, and J. S. Kuwabara, *Estuarine, Coastal Shelf Sci.* **24**:419 (1987).
79. P. W. Schindler, P. Liechti, and J. C. Westall, *Neth. J. Agric. Sci.* **35**:219 (1987).

80. N. E. Pingitore, Models of coprecipitation of Ba^{2+} and Sr^{2+} with calcite, in *Surface and Colloid Science* (ACS Symp. Ser. 323) (J. A. Davis and K. F. Hayes, eds.), American Chemical Society, Washington, DC, 1986, p. 577.
81. R. J. Crawford, Ph.D. Thesis. University of Melbourne, 1995.
82. M. S. Moignard, R. O. James, and T. W. Healy, *Aust. J. Chem.* 30:733 (1977).
83. J. M. Israelachvili and S. J. Kott, *J. Colloid Interface Sci.* 129:461 (1989).
84. T. W. Healy, D. Chan, and L. R. White, *Pure Appl. Chem.* 52:1207 (1980).
85. T. W. Healy, D. E. Yates, L. R. White, and D. Chan. *J. Electroanal. Chem.* 80:57 (1977).

Adsorption of Ions onto Alumina

EDWIN BAUMGARTEN Institut für Physikalische Chemie und Elektrochemie,
Heinrich-Heine-Universität, Düsseldorf, Germany

- I. Introduction
- II. Theoretical Considerations and Modeling
- III. Experimental Considerations
- IV. Investigations of Adsorption of Various Ions
 - A. Adsorption of H^+ and OH^-
 - B. Adsorption of cations
 - C. Elemental anions and oxo anions
 - D. Complex ions
 - E. Organic ions
- V. Concluding Discussion
- References

I. INTRODUCTION

Adsorption of ions onto alumina is a problem of great interest in very different fields. As can be seen from the journals mentioned in the reference list, it is important in geochemistry as well as in limnology, in pollution control as well as in catalyst preparation or soil chemistry, and sometimes even in unexpected disciplines such as nuclear techniques. The different applications lead to different questions and experimental conditions. For example, the "normal" concentrations are low in limnology and the pH is restricted to nearly neutral conditions. In contrast, in catalysis there are rather high concentrations and the pH, in principle, is variable, though sometimes not even discussed, probably as a consequence of the use of older technical impregnation techniques in which nonequilibrium conditions were applied.

As a consequence we must expect to find a mosaic, or perhaps a puzzle, of information, a puzzle with many missing elements. In order to get an overview of ion adsorption on alumina in spite of the difficulties, in Sec. III we discuss the basic physicochemical principles, which are necessarily the basis for any serious model calculations. As modeling of the adsorption process is treated in a separate chapter of this book, it is not treated in great detail here.

A small section (Sec. III) is dedicated to the experimental methods of special importance. Various adsorption systems are treated in Sec. IV. Section IV.A deals with proton and hydroxyl adsorption onto aluminas and also onto aluminum hydroxides, as the principles turned out to be the same for any of these hydrated surfaces. In Sec. IV.B the adsorption of "normal" cations is discussed, generally following the position in the periodic table but mentioning other ions used earlier in the same investigation. A discussion of "normal" anions (elemental ions and oxoanions) follows in Sec. IV.C. Complex ions — cations and anions — are discussed together (Sec. IV.D), as some cations may be converted into anions and vice versa by changes in pH. Aquo complexes are treated as "normal" ions. A short review of the adsorption of some organic ions follows in Sec. IV.E. In Sec.V, some general aspects of ions adsorption onto alumina, as obtained from the puzzle, complete the chapter.

II. THEORETICAL CONSIDERATIONS AND MODELING

In quantitative descriptions of adsorption it is usually expected that equilibrium is reached, and thus the laws of thermodynamics may be used to describe the system, so the equation

$$\Delta G_R = 0 \quad (1)$$

where ΔG_R is the free enthalpy of reaction, must be valid for any reaction, leading to

$$\Delta G_R^\circ = \Delta H_R^\circ - T \Delta S_R^\circ = -RT \ln K = -RT \ln \left[\prod a_i \right] \quad (2)$$

where

ΔG_R° = standard free enthalpy of reaction

ΔH_R° = standard enthalpy of reaction

ΔS_R° = standard entropy of reaction

R = gas constant

T = reaction temperature

K = equilibrium constant

$\prod a_i$ = product of activities of substances i

The activities of the substances are related to the concentrations by

$$a_i = f_i c_i \quad (3)$$

where f_i is the activity coefficient (in the case of ions, f_{\pm} for ion pairs).

The following relation between the activity coefficient and ionic strength J is derived from the extended Debye–Hückel theory for dissolved ions.

$$\ln f_{\pm} = \frac{-A |z_+ z_-| \sqrt{J}}{1 + B\sqrt{J}} + CJ \quad (4)$$

where $J = \frac{1}{2} \sum c_i z_i^2$ is the ionic strength and z_i is the charge of ion i .

For surface phases the electrostatic effects are usually considered directly, using models with different numbers of layers for the positions of different ions relative to the solid surface [1–3], leading to the capacitance parameter. A description of surface activity coefficients is given by Liu et al. [4].

For a complete model all reactions have to be considered:

1. Speciation reactions within the liquid phase
2. Speciation reactions in the surface phase
3. Equilibria between the phases

It follows that the number of parameters is great, and the information obtainable from experiments is usually insufficient for a determination of all of them.

The problem may get even more complicated if equilibrium is not reached quickly enough for all partial reactions. On the other hand, kinetics measurements may help to construct a realistic model.

In the case of the alumina adsorption system, one may investigate the oxide/acid–base system separately. This is necessary because aluminas are amphoteric oxides of remarkable solubility with a number of different species in solution, and the possible adsorption of protons and hydroxyls at the surface leads to the development of surface charges.

Each surface site may be taken to consist of an H_2O unit with one H replaced by surface Al; in this case the adsorption enthalpy will depend on coverage for high loads, especially if the aluminum atom carries two hydroxyl groups. Alternatively, the completely coordinated aluminum ions may be seen as centers, and these may be compared with dissolved $\text{Al}(\text{OH})_3$ species dissociating stepwise.

Besides the mononuclear and partially hydrolyzed species $[\text{Al}^{3+}, \text{AlOH}^{2+}, \text{Al}(\text{OH})_2^+, \text{Al}(\text{OH})_3, \text{Al}(\text{OH})_4]$, the solution phase also contains polynuclear species. The latter may be formed by condensation of some of the mononuclear species, especially the nearly neutral ones, to form intermediates to precipitation [5]. On the other hand, the charged surface species may be seen as intermediates to dissolved species.

In a similar way, the speciation and possible precipitation of adsorptive ions have to be discussed before adsorption itself may be investigated. In practical systems other equilibria may also play a notable role. for example, that of H_2O and CO_2 forming HCO_3^- and CO_3^{2-} and its consequential effect on acid–base balance and precipitation.

Finally, the adsorption will depend on the standard free enthalpy of adsorption:

$$\Delta G_{\text{ad}}^{\circ} = \Delta H_{\text{ad}}^{\circ} - T \Delta S_{\text{ad}}^{\circ} \quad (5)$$

$\Delta H_{\text{ad}}^{\circ}$ will cause the greatest differences between different adsorbed ions, leading to physisorption in the case of small values and to chemisorption, with the formation of chemical bonds, for large values. Partial models may be constructed for weak or strong interactions.

$\Delta S_{\text{ad}}^{\circ}$ is influenced most strongly by the changing structure of the hydrate spheres of adsorbed and desorbed ions during the adsorption process.

Any real model calculations require more or less simplification. As only a very few measurements were made at different temperatures, only equilibrium constants or the corresponding $\Delta G^{\circ}(T)$ values can be derived. Activity coefficients are often disregarded by measuring at nearly constant ionic strength obtained by the addition of a sufficient number of background ions. Here the equilibrium constants will contain an "activity factor." Further simplifications will depend on the particular system.

The typical sigmoidal curve for the adsorbed part of an ion as a function of pH is often used to define the pH_{50} , i.e., the pH value at which 50% of the total amount of any ion is adsorbed. This value — helpful for a comparison of different ions — depends on the initial concentration or on the concentration at pH_{50} , called C_{50} .

III. EXPERIMENTAL CONSIDERATIONS

In contrast to investigations of adsorption from the gas phase, the number of methods applicable to adsorption from the liquid phase is very small. On the one hand this is caused by the fact that not all methods using either electrons or ions can be applied in situ. In addition the adsorbents are normally powders with no plane surfaces. As a consequence the results of quantitative adsorption measurements are usually calculated from the difference between the liquid concentrations before and after the adsorption process. In principle, any analytical method may be used provided it has sufficient sensitivity; pH measurements with a glass electrode and atomic adsorption spectroscopy (AAS) are standard, but complexometry and ion-selective electrodes can also be used. Radiochemical methods are useful in the case of small final concentrations. If electrochemical methods are used, one has to consider that activities, not concentrations, are obtained. In the case of partially soluble adsorbents, such as transition aluminas, their concentration should also be determined, as well as those of all other constituents of the solution, e.g., CO_3^{2-} .

A detailed review of the spectroscopic methods applied to investigate ion adsorption was given by Scheidegger and Sparks [6]. Electron spin resonance (ESR) is one of the situ methods that can give qualitative and quantitative information about metal ions with unpaired electrons. Complexation at the surface may cause line shifts.

Electrokinetic measurements, i.e., observation of the motion of the adsorbent particles in an electric field, depending on pH, provide independent information on the point of zero charge (pzc) related to the adsorption constants for H^+ and OH^- .

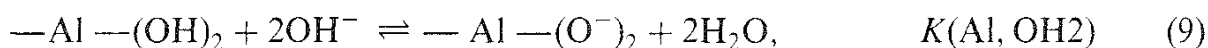
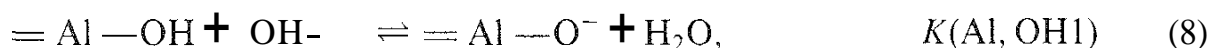
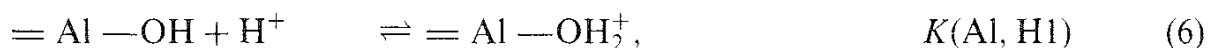
Ex situ investigations can be carried out with all the methods usually applied to gas-phase adsorption problems, provided they do not require flat surfaces. These methods are of limited value, as separation from the liquid phase will generally influence the composition of the surface unless the adsorption enthalpy is very great, which means that a stable surface compound may be formed. Under this condition all additional information may be useful.

IV. INVESTIGATIONS OF ADSORPTION OF VARIOUS IONS

A. Adsorption of H^+ and OH^-

The adsorption of protons and hydroxyl ions is of fundamental importance, as it greatly influences the properties of the adsorption system. Moreover, the investigation of this "simple" system may provide information about the distribution (numbers and adsorption enthalpies and entropies) of the surface sites. In order to describe the system, we first need some values determined independently: the concentration of the alumina suspension and the specific surface of the solid. Both values will vary to a certain degree with dissolution of the oxide, an effect that will be small in concentrated suspension. The dissolution process leads to a "living" surface, one on which the adsorption centers are continuously formed and destroyed; this makes rather doubtful the information about the energy of surface centers taken from investigations of oxides dehydrated at higher temperatures. It can be expected that the high energy centers will be destroyed first by the dissolution process.

The main parameters describing the system, in addition to suspension concentration and specific surface area, are the concentration of adsorption sites on the solid surface and the equilibrium constants in the adsorption equations, provided Langmuir-type adsorption, i.e., only one type of adsorption centers with constant adsorption enthalpy, is assumed:



(The formulas represent the formal addition of one or two protons or hydroxyls, not necessarily the correct structures! The water activity is not included in the constants.)

In principle, the surface speciation of alumina may be compared with that of the Al species in water solution (here the lattice Al_2O_3 structure is replaced by OH in the liquid phase) (Fig. 1) or the surface hydroxyl groups may be compared with those of water (the surface aluminum ion is replaced by a proton).

The solubility of alumina strongly increases with decreasing pH. so dissolved Al^{3+} and $Al(OH)^{2+}$ will tend to stay dissolved because of the high charge, whereas neutral and weakly charged species tend to condense. Thus in the pH region where most other ions are adsorbed, Al^{3+} and $Al(OH)^{2+}$ are present in low concentrations only [8]. Taking water as a model substance for $=Al-OH$, only one type of center can be present, but the adsorption enthalpy of such a center should depend on the coverage if neighboring charged centers are present on the surface. Under these conditions only one positive and one negative species can exist, in contrast to Fig. 1a.

The treatment of the surface reaction gets more difficult if centers of different acidity or basicity are considered. Contescu et al. [9,10] discuss experimental results

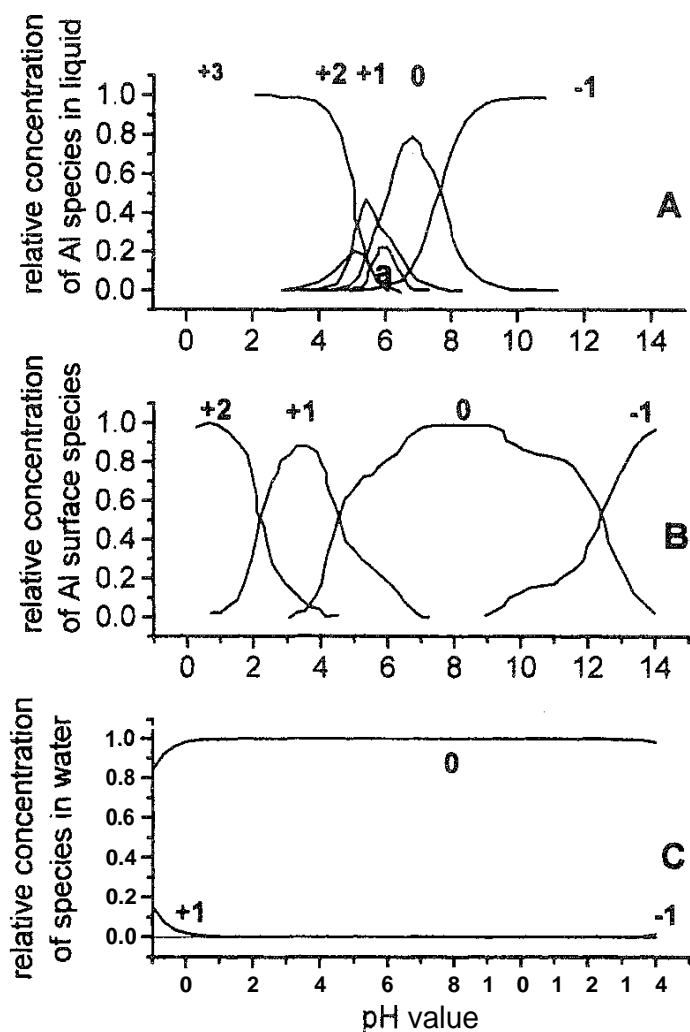


FIG. 1 Relative concentrations of species vs. pH. (A) Speciation of aluminum in liquid-phase (water) (from Ref. 5). Numbers are valences of species. Polynuclear species = $\text{Al}_{13}\text{O}_4(\text{OH})_{24}^{7+}$. (B) Speciation of aluminum in the surface phase (from Ref. 7). (C) Speciation of H_2O liquid phase.

indicating heterogeneous surfaces, and Hiemstra et al. [11–13] developed a surface model (MUSIC) to describe such systems.

The basis for the investigation of equilibria is generally the titration of a suspension of the adsorbent with acid or base. Figure 2 shows some examples that also give an idea about the reproducibility obtained with γ -aluminas of different origins. A problem may arise from the kinetics of the processes. Brunelle [16] observed concentration changes for 24 h when adding HCl to $\gamma\text{-Al}_2\text{O}_3$, so different titration rates may influence the result.

Schulthess and Sparks [3,7,17] pointed out that erroneous results were often obtained because the consumption of acid or base as a consequence of dissolution processes was not considered. In the case of alumina this seems to be of great importance and will vary with the solubility and the speciation of the dissolved aluminum ions, depending on pH. They proposed a back-titration of the supernatant liquid to correct values. In Fig. 3 a comparison is given of the difference between proton and hydroxy surface concentrations Γ^+ and Γ^- , respectively,

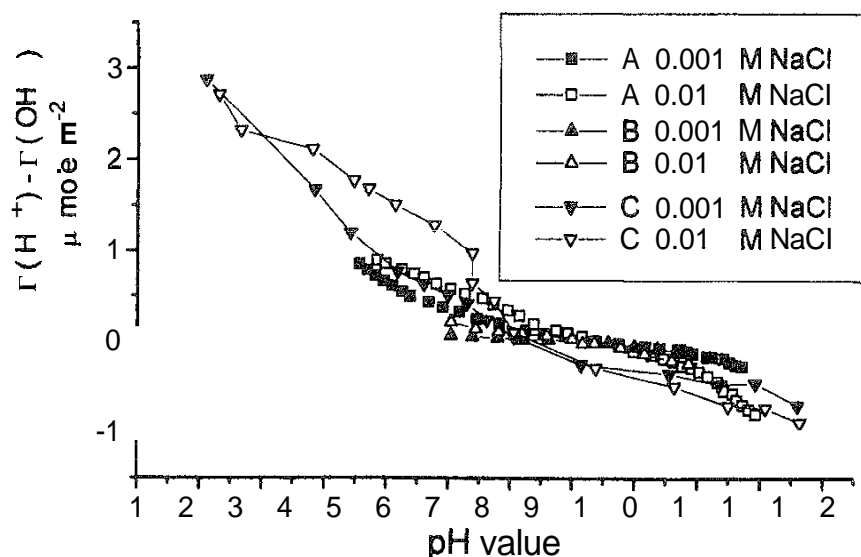


FIG. 2 Difference of H^+ and OH^- coverage as a function of pH. Measurements at different NaCl concentrations by various authors. A, Ref 14; B, Ref 15; C, Ref 7.

obtained directly by the titration method (Fig. 3a) and from model calculations (Fig. 3b) [18,19].

Koopal reports [20] that surface charge (σ_s) vs. pH, and its derivative with respect to pH ($d\sigma_s/dpH$) vs. pH can often be described on the basis of pseudo-homogeneity. In the case of transition aluminas (and of gibbsite) this may, at least partially, be caused by the fact that these oxides are remarkably soluble, which will lead to more homogeneous surfaces, as the most active centers, having the highest energies, will dissolve first.

The adsorption of protons and hydroxyls necessarily leads to charges on the surface, which are balanced by counterions of opposite charge in the solution. Assumptions about the structure of the charged layers, which also contain other adsorbed species, lead to different models (i.e., double- or triple-layer models).

The point of zero charge (solution pH at which the surface is uncharged) is related to the constants $K(Al, H1)$ and $K(Al, OH1)$ by

$$pzc = [pK(Al, OH1) - pK(Al, H1) + pL_w]/2 \quad (10)$$

where

$$pK = -\log K$$

$$pL_w = pH + pOH = -\log(a_H a_{OH}) \cong 14.0$$

provided that no surface sites are occupied by other ions. In the presence of background ions, an extrapolation to zero concentration is possible. $pK(Al, H2)$ and $pK(Al, OH2)$ can be disregarded at this pH; in most publications they are not used at all, but they are introduced here as they are to be expected theoretically. The pzc can be determined independently from electrokinetic measurements provided the isoelectric point (iep) is equal to the pzc. This reduces the number of constants to be derived from the titration experiments, or it gives a tool to test the reliability of the titration method, provided the pzc results are trustworthy themselves.

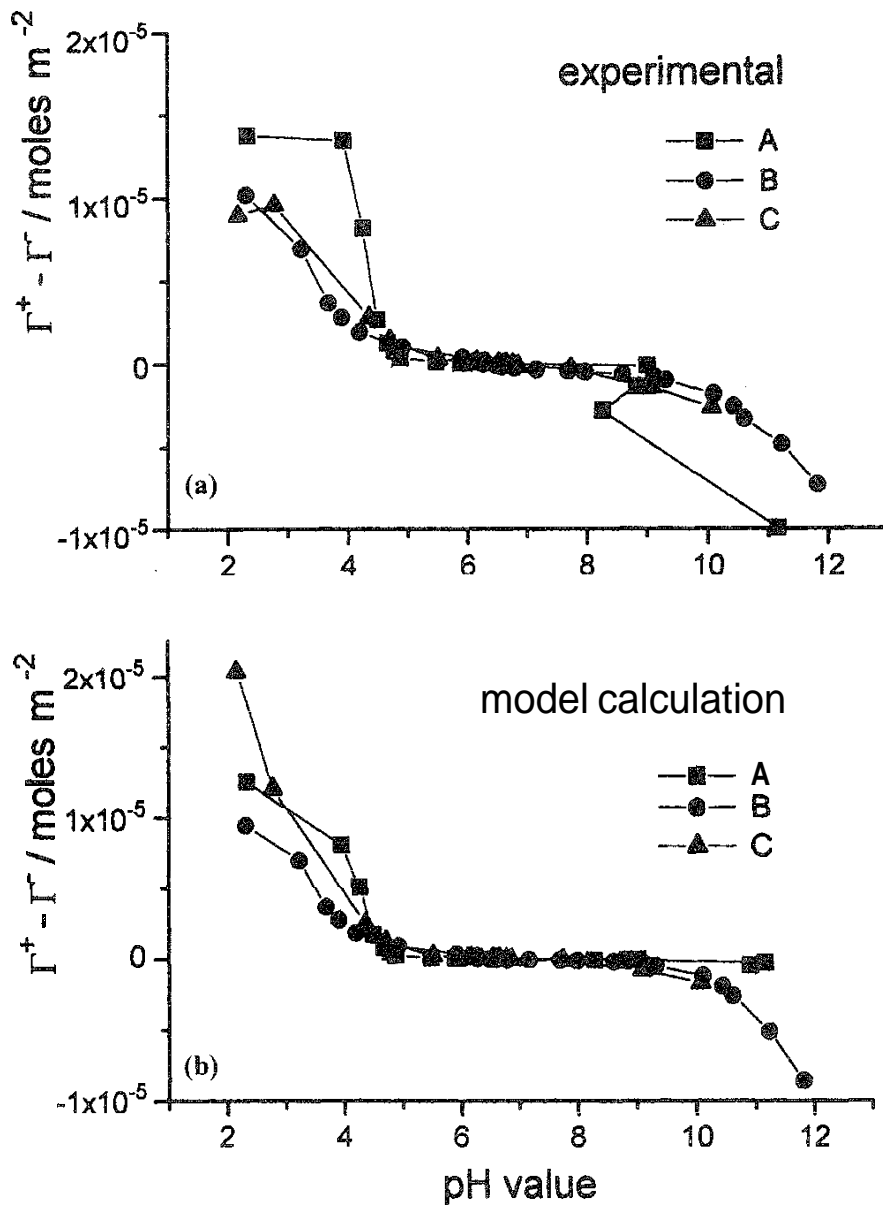


FIG. 3 Difference of H^+ and OH^- coverage as a function of pH. All measurements with same γ -alumina prepared according to Torkar [21]. BET areas (m^2/L): A. 180 (from Ref. 18); B. 244 (from Ref. 19); C, 170 (From Ref. 18).

At this point one may ask whether a second constant can be defined in analogy to the ion product in the liquid water phase:

$$p_{LW} = p_{K1} + p_{K2} + 2p_{H_2O}$$

Such a product was indeed used in logarithmic form as DPK [22–24], but in contrast to water, which mainly consists of neutral water species even in acidic and basic solution (i.e., $[H_2O] \cong \text{const}$), the neutral alumina surface phase is only stable near pH 7 [25]. This shown in Fig. 4, in addition to Fig. 1, for systems differing mainly in the BET surfaces. So DPK is a constant for $pH = pzc$ only. But, as even under these conditions it is not certain that $\Theta_{=AlOH} = 1$, it is more reasonable to describe the system by using the equilibrium constants.

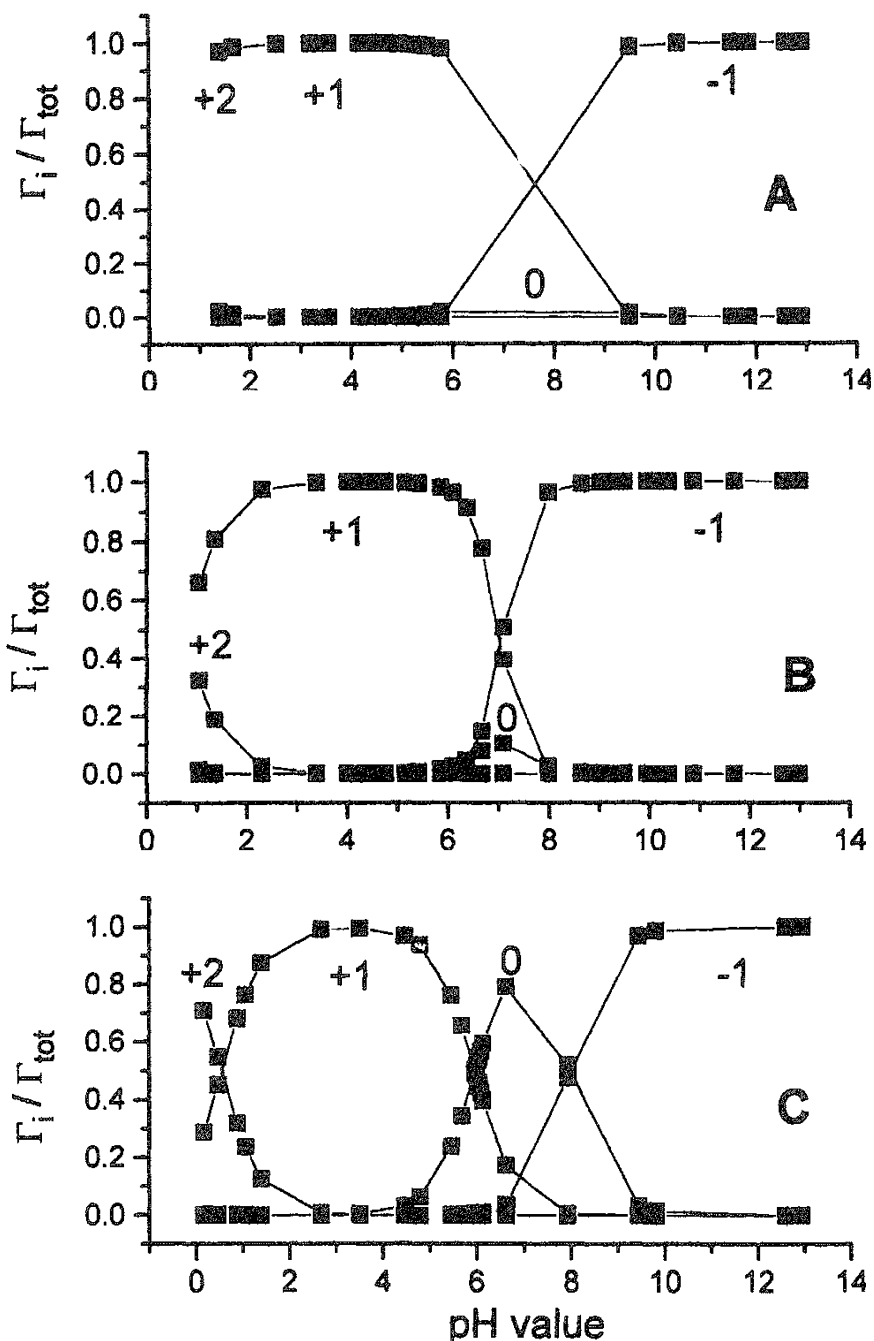


FIG. 4 Speciation of Al in the liquid phase, obtained by model calculations [18] from experiments with γ -alumina, prepared according to Torkar [21]. A, C, from Ref. 18; B from Ref. 19. Numbers are valences of Al species.

Lewis-Russ [26] reviewed methods for determining pzc values, and [Table 1](#) contains values for different aluminas from the literature. It can be seen that the pzc values vary by about 5 units, and thus they cannot be used to replace direct methods of obtaining equilibrium constants. The pzc values, if obtained by acid-base titration, reflect uncertainties even for the corresponding adsorption constants. Therefore constants should be determined with the same material and under the same experimental conditions if the values are to be used in model calculations for

TABLE 1 Point of Zero Charge (pzc) of Al₂O₃ Determined by Various Authors

| Ref. | pzc | Oxide | Method | Background ion |
|-------|------|-------------------------|--|-------------------------------|
| 27 | 8.3 | γ | Titsation | 0.1 M NaCl |
| 28 | 6.45 | γ | Titration | 1 M NaClO ₄ |
| 29 | 9.1 | Hydroxide | Electroacoustics | 3 M NaCl |
| 30,31 | 6.94 | γ | Electrophoresis | — |
| 32 | 9.1 | α | Titration, ion adsorption, electrophoresis | — |
| 33 | 4.45 | — | — | None |
| 3 | 9.8 | — | — | 0.01/0.03/0.07/ 0.3 M NaCl |
| 34 | 7.2 | γ | — | — |
| 35,36 | 8.50 | γ | Triple-layer model | None |
| 35,37 | 8.9 | α | Triple-layer model | None |
| 30,38 | 8.4 | Nat. prod. ^a | Electrophoresis | — |
| 30,39 | 9.45 | Nat. prod. ^a | Streaming potential | — |

^aNat. prod. = natural product

adsorption of other ions. Table 2 contains some adsorption constants for protons and hydroxyl ions. Other values cannot be compared directly, as they do not contain electrostatic terms, i.e., they are not intrinsic values.

The concentration of surface centers is often taken to be equal to the number of hydroxyl groups in a monolayer on the surface [40–42]; other values were obtained by acid–base titration [7,43], tritium exchange [44], and equilibration experiments combined with model calculations ("long time titrations") [18,46,47]. Table 3 gives an overview of numbers of centers determined by various researchers. Most values are found between 1.0×10^{-5} and 3.2×10^{-5} mol/m²; only that of Schulthess [7] (1.7×10^{-6} mol/m²) was clearly lower, possibly because of the back-titration technique. So the assumption that the number of centers is equal to the number of surface OH groups seems to be acceptable, though in principle different numbers of

TABLE 2 pK Values for Protonation and Hydroxylation of Alumina

| Ref. | Oxide | pK(Al, H1) | pK(Al, OH1) | Constant type |
|-------|----------|------------|-------------|---------------|
| 27 | γ | 7.2 | 9.5 | Intrinsic |
| 28 | γ | 4.45 | 8.45 | Intrinsic |
| 35,36 | γ | 5.7 | 7.9 | Intrinsic |
| 35,36 | γ | 5.2 | 7.9 | Intrinsic |
| 35,36 | α | 6.90 | 10.90 | — |
| 15 | — | 4.47 | 11.5 | — |
| 15 | — | 5.13 | 11.1 | — |

TABLE 3 Number of Centers on Alumina

| Ref. | Oxide | Method | A_s (m ² /g) | n_c (mol/m ²) |
|------|---|-------------------------|---------------------------|-----------------------------|
| 43 | γ -Al ₂ O ₃ | Titration | 155 | 3.20×10^{-5} |
| 7 | γ -Al ₂ O ₃ , type C | Titration | 100 | 1.70×10^{-5} |
| 44 | γ -Al ₂ O ₃ | H ³ exchange | 123 | 1.33×10^{-5} |
| 19 | γ -Al ₂ O ₃ | Exp + mod | 244 | 9.56×10^{-6} |
| 46 | γ -Al ₂ O ₃ | Exp + mod | 180 | 1.48×10^{-5} |
| 47 | γ -Al ₂ O ₃ | Exp + mod | 170 | 2.32×10^{-5} |
| 40 | γ -Al ₂ O ₃ | OH groups | 123 | 2.07×10^{-5} |
| 41 | γ -Al ₂ O ₃ | OH groups | | 2.01×10^{-5} |
| 42 | γ -Al ₂ O ₃ | OH groups | — | 2.22×10^{-5} |

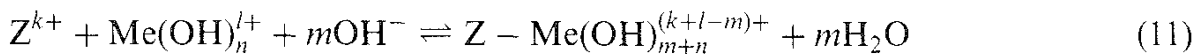
centers for OH[−] and H⁺ might be expected. Centers different in number and adsorption energy may exist for H⁺ adsorption, as mentioned before.

In addition to Fig. 1, further surface speciation data are shown in Fig. 5. Figure 5a shows the relative abundance obtained by Sivaraj et al. [25]; Fig. 5b shows the number of centers obtained with the same model calculation for all measurements by Baumgarten et al. [18] and Judat [19]. Figure 6 shows adsorption isotherms for H⁺ and OH[−] from data of Ref. 18 assuming Langmuir-type isotherms and equal numbers of centers for H⁺ and OH[−] ions. The model used assumes pseudohomogeneous surfaces. The speciations in the liquid and the surface phase are calculated from the respective equilibrium constants. Modified solubility products, with the activity of the solid proportional to the coverage with neutral sites and possible consideration of charges, serve to calculate the interphase equilibria.

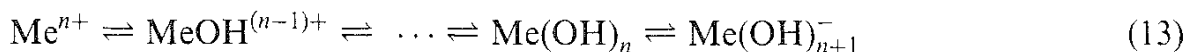
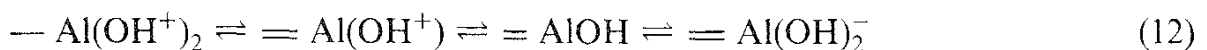
B. Adsorption of Cations

The numbers of publications about the adsorption of different cations onto alumina are very different depending on the practical importance of the adsorption process. A lot of work is done with hazardous ions, or ions of known catalytic activity, with the ions themselves or after their reduction to finely dispersed metal particles. On the other hand, the literature about other ions, being of scientific interest only, is limited.

Any specific adsorption of ions takes place in competition with that of H⁺ or OH[−] ions, provided it takes place at the same centers:



where Z^{k+} denotes a free surface center. Here both surface speciation and speciation of the metal ions in solution must be known, with Eq.(12) being equivalent to Eqs.(6)–(9):



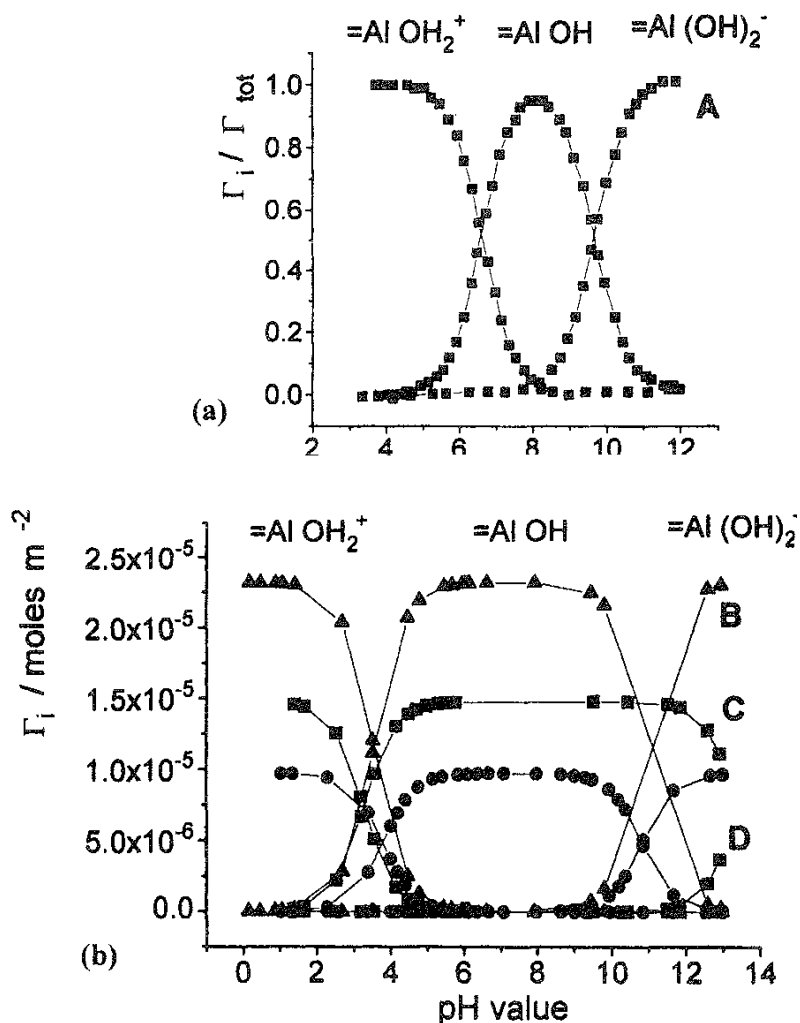


FIG. 5 Alumina surface speciation assuming one positively and one negatively charged species each. (a) Relative amounts of species, data from Ref. 25. (b) Absolute coverages, with numbers of centers obtained by model calculation [18]. B, from Ref. 18; C, from Ref. 19; D, from Ref. 18.

One adsorption equilibrium, according to reaction (11), must be given. As usually background electrolytes (normally alkali metal nitrates or halides) are used to obtain constant ion strength, these ions may compete for centers because of their high concentrations. The possible formation of precipitates consisting of hydroxides; aluminates, and, if CO_2 is not completely excluded, carbonates has to be considered. Often it is difficult to exclude these processes.

Alkali metals are examples of ions of limited direct interest. In most adsorption experiments their salts are used as "background electrolyte," to avoid greater changes in the activity coefficient during the reactions by keeping the ion strength nearly constant. Comparison of adsorption measurements of other ions in the presence of different amounts of alkali ions or metal ions reveal that, indeed, their influence is limited (Fig. 7). A direct measurement of the amount adsorbed, as a difference between the added concentration and the concentration after the adsorption process, is thus difficult as the difference is very small. As stronger

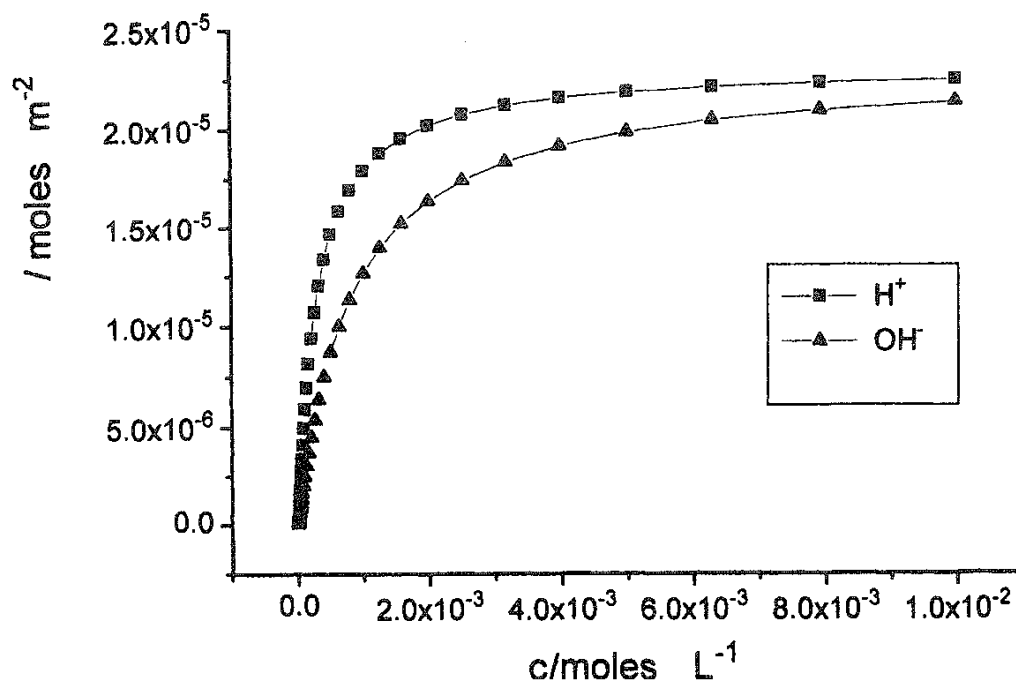


FIG. 6 Adsorption isotherms of H^+ and OH^- , calculated from Ref. 18, assuming Langmuir adsorption and equal numbers of adsorption centers.

covalent forces are absent, electrostatic forces will be dominant. Another effect may be of greater importance here, too: As there is no evidence of strong specific interaction, one has to consider the corresponding anion also; if the anion is adsorbed specifically, i.e., in the inner layer of the double- or triple-layer system, the corresponding cation will be enriched in the outer layer(s), compensating for the negative surface charge.

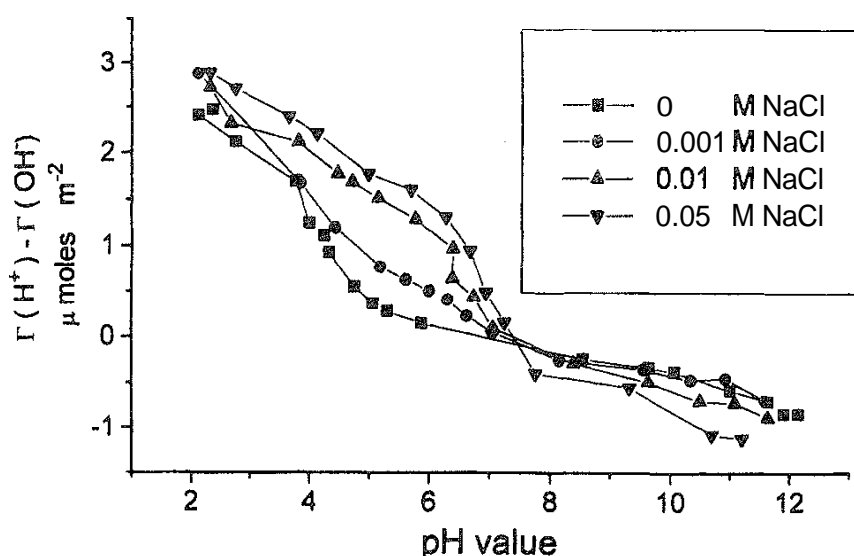


FIG. 7 Influence of different concentrations of Na^+ on H^+ and OH^- adsorption as a function of pH. (From Ref. 7.)

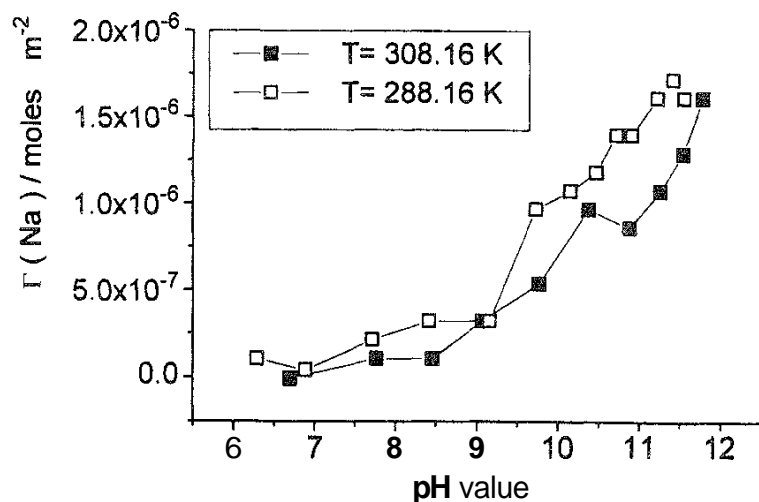


FIG. 8 Adsorption of Na^+ at different temperatures from a solution containing 0.1 M NaCl as a function of pH. (Calculated from Ref. 48.)

Figure 8 shows the adsorption of sodium ions at two temperatures from a 0.1 M NaCl solution as a function of pH as calculated from Ref. 48. The degree of adsorption is very low compared to specifically adsorbed (chemisorbed) ions. Deng [49] used various NMR techniques (MAS, CP-MAS, quadrupolar nutation NMR) to investigate Na^+ adsorption on γ -alumina and reported the occurrence of two adsorption species, $=\text{Al}-\text{O}-\text{Na}$ and $=\text{Al}-\text{OH}-\text{Na}^+$, in addition to "adsorbed" Na_2CO_3 at coverages $\Theta > 1$. Some information on Cs, indicating adsorption comparable to that of Na, is given in Ref. 48. An equilibration of Na-doped alumina with KNO_3 (0.001–0.1 M) (Fig. 9) [45] seems to indicate much higher adsorption, but probably equilibrium was not attained. Shiao et al. [50] discuss the distribution

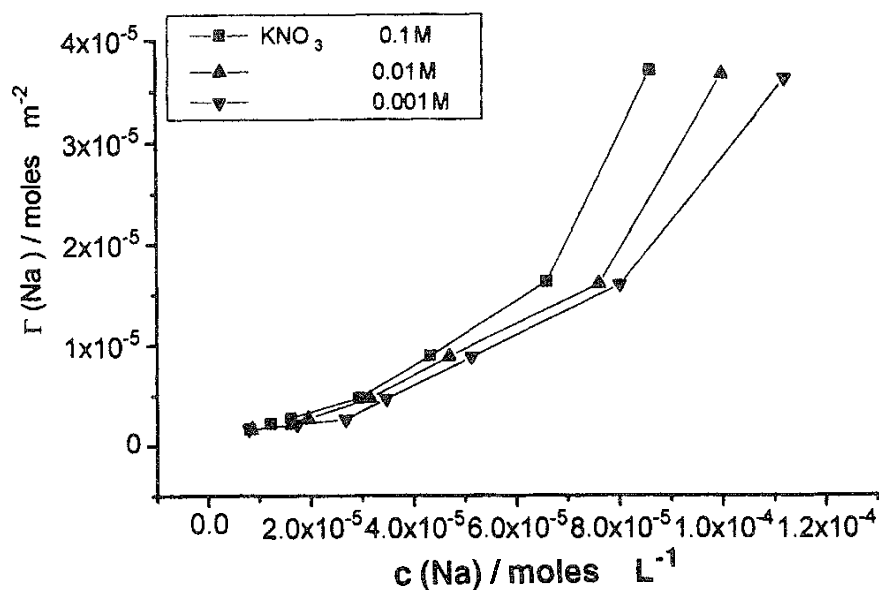


FIG. 9 Surface coverage with Na^+ and dissolved Na^+ concentration after equilibrating Na-containing alumina with KNO_3 solutions. (From Ref. 45.)

of ions between the surface and the liquid phase in 0.05 M NaCl. Assuming a BET surface of 100 m²/g, this value — on the order of 10⁻⁷ mol/m² — looks reasonable at pH 8 and a liquid concentration of 0.1 M. In contrast, Sr²⁺ shows a 100-fold increased distribution coefficient, and Eu³⁺ a 10³-fold one.

The adsorption of alkaline earths onto γ -Al₂O₃ was described by Huang and Stumm [14]. Examples of adsorption depending on pH are shown in Fig.10. Adsorption onto a slightly negative surface may lead to a reversal of the surface charge, i.e., the surface speciation curves are shifted to higher pH values by alkaline earth ions compared to those of pure alumina. From the corresponding experiments it was concluded that the ions are chemisorbed, or at least bound in an inner surface layer. The logarithms of the equilibrium constants for the reaction



are: Mg, -5.43; Ca, -6.06; Sr, -6.27; Ba, -6.59. Adsorption on fresh alumina gel was described by Kinniburgh et al. [51]. As expected, the adsorption tendency is the same as for alumina, though a direct comparison is not possible because no specific surface can be defined. The results are discussed in terms of pH₅₀ values.

Measurements with Ba and Ra on α -Al₂O₃ [53] show that pH₅₀ is constant for concentrations below 1 x 10⁻⁷ mol/L, while it increases linearly with log *c* above this concentration. At low concentration the pH₅₀ value for both is 10, increasing about one unit per decade of concentration for Ba above 10⁻⁷ mol/L.

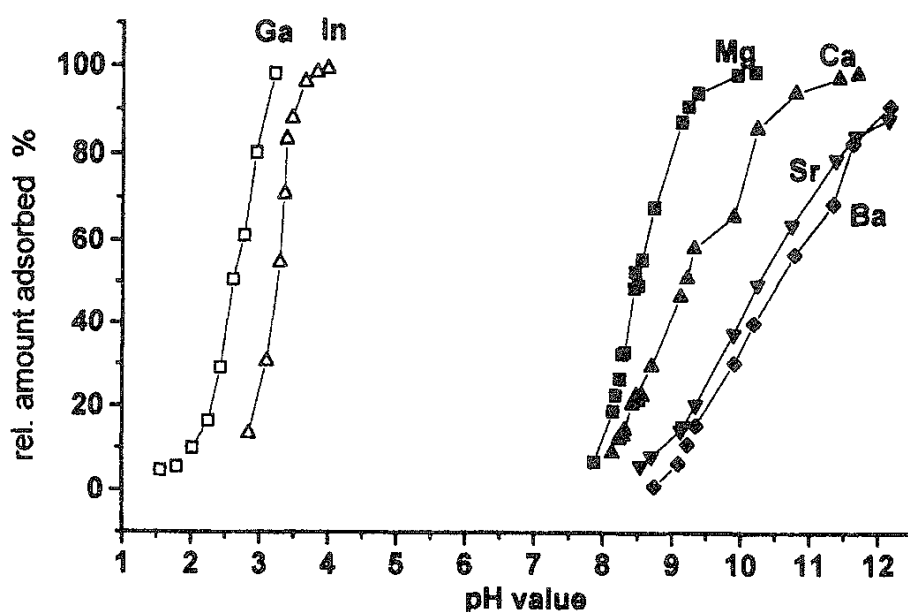


FIG. 10 Adsorption of main group ions. Mg, Ca, Sr, Ba: 2.5×10^{-4} M in 1 M NaNO₃ on Al(OH)₃ (0.093 M Al) (from Ref. 51). Ga, In: 3.0×10^{-3} M in 0.01 M NaNO₃ on γ -Al₂O₃ (4.0 g/L) (from Ref. 52).

The adsorption of Ga and In ($c_0 = 3 \times 10^{-3} \text{M}$) on $\gamma\text{-Al}_2\text{O}_3$ was investigated by Lin et al. [52]. Under these conditions the observed pH_{50} values were 2.65 (Ga) and 3.25(In) (Fig. 10). Lin et al. derived the following equilibrium constants (in logarithmic form):

| | Ga | In |
|----------------------------|-------|-------|
| SOM^{2+} | 10.3 | 8.87 |
| $(\text{SO})_2\text{M}^+$ | 3.15 | 1.63 |
| SOM-OH^+ | 1.73 | 0.26 |
| $(\text{SO})_2\text{M-OH}$ | -5.21 | -6.67 |

From kinetic results they conclude a two-step mechanism:

1. Proton release from the surface
2. Coordination of the metal ion

This description of the main group ions of the first three columns of the periodic table shows that with the exception of alkali metal ions all these ions are adsorbed specifically; the same is true of other ions, especially the heavy metal ions, which generally are of greatest practical interest. The other main group elements form anions or oxoanions directly. In the case of equal valence, the transition metal ions resemble each other more than the main group elements do, so more generalization should be possible.

Adsorption kinetics will be discussed first. Figure 11A shows the equilibration of the alumina system after the addition of HCl [16]. Figure 11B shows that the adsorption of Cu, with liberation of protons [47], takes about 24 h to reach equilibrium. Figure 11C gives kinetic data for the adsorption of Co, Fe, and Ni ions [54], evidently in equilibrium after about 1 h. On the other hand, pressure jump experiments of Cu adsorption used a time scale of 10^{-2} – 10^{-1} s [55]. These results are mentioned to demonstrate that reactions taking place in the adsorption system may have rates that differ by several orders of magnitude.

Figure 12 gives an example of the partial irreversibility of the adsorption of copper ions. Lowson and Evans [53] give other examples of poor reversibility. A reasonable choice of reaction time is a serious problem. We will discuss the transition metal ions, beginning with the first column, containing Cu, Ag, and Au, but, as mentioned earlier, we will also discuss other ions treated in the same publication in order to enable comparisons. Because of their relevance, measurements of interaction with $\text{Al}(\text{OH})_3$ and AlOOH are also discussed. Figure 13 shows the pH dependence of transition metal ion adsorption on hydroxide and oxide.

Electron spin resonance studies [56–58] reveal that Cu is adsorbed in dispersed form in tetragonally distorted octahedral symmetry, with the signal intensity increasing linearly until a monolayer is reached ($6.3 \times 10^{-6} \text{ mol/m}^2$) at 4% Cu on $\gamma\text{-Al}_2\text{O}_3$ [58]. the dehydration process changes the spectra but can be reversed by adding water. This indicates a strong local fixation of Cu, which withstands drying and subsequent wetting without forming clusters. Rudin and Motschi [59] used ESR and ENDOR with $\delta\text{-Al}_2\text{O}_3$ and proposed a structure of Cu bound to two Al atoms via oxygens and four H_2O ligands. Chang et al. [55] compared pressure

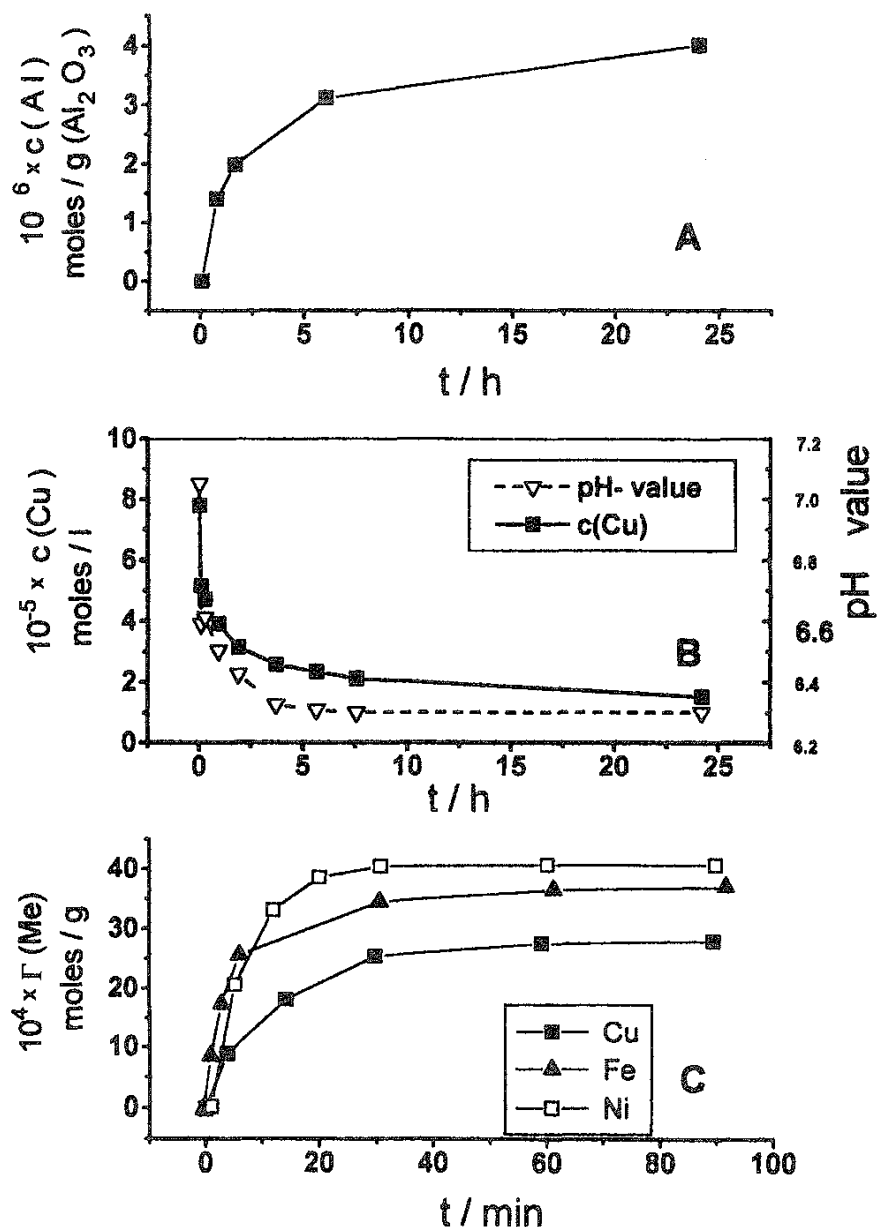


FIG. 11 Kinetics of equilibration. (A) Dissolution of $\gamma\text{-Al}_2\text{O}_3$ after addition of HCl. (From Ref. 16.) (B) Consumption of Cu and pH change during Cu adsorption on $\gamma\text{-Al}_2\text{O}_3$. (From Ref. 47.) (C) Adsorption of different metals at $\gamma\text{-Al}_2\text{O}_3$. (From Ref. 54.)

jump experiments with sorption data and found $\log K^{\text{int}}$ of deprotonated surface = Al-OH groups with Cu^{2+} of 9.71 and 9.59 L mol.

Hachiya et al. [60,61] found a linear relationship between the logarithms of intrinsic adsorption constants and the hydrolysis constant of the metal ions for Cu, Pb, Zn, Co, and Mn. They described pressure jump experiments [61] with $\gamma\text{-Al}_2\text{O}_3$, showing a fast and a slow process — attributed to two surfaces sites — with Cu^{2+} , Mn^{2+} , Zn^{2+} , Co^{2+} , and Pb^{2+} . The relaxation times decreased with metal ion and proton concentrations. The kinetic constants for adsorption and desorption are $k_1^{\text{int}} = (7.24 \pm 2.0) \times 10^3$ and $k_{-1}^{\text{int}} = (3.1 \pm 0.9) \times 10^5 \text{ mol}^{-1} \text{ L s}^{-1}$. The order of the adsorption rate constants corresponds to that of the water release reaction from the aquo complex in the liquid phase.

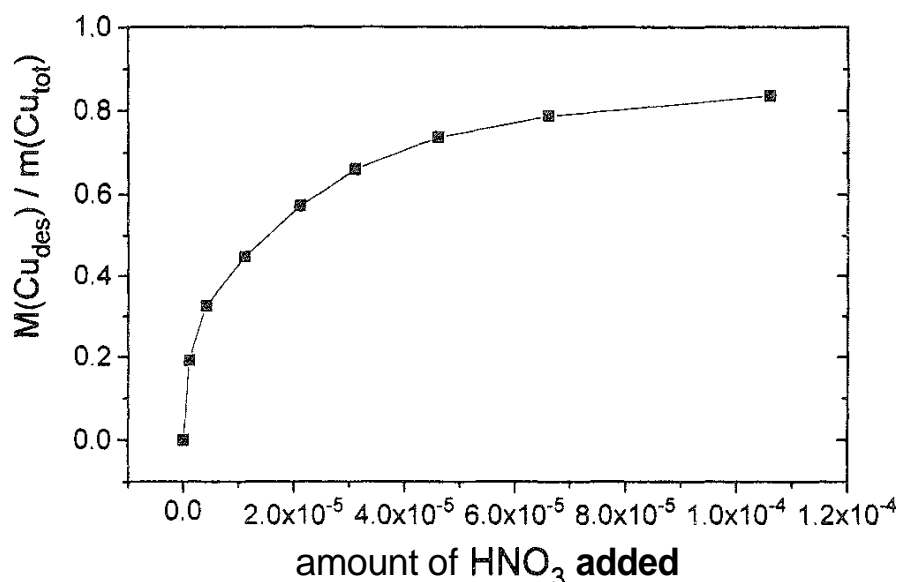
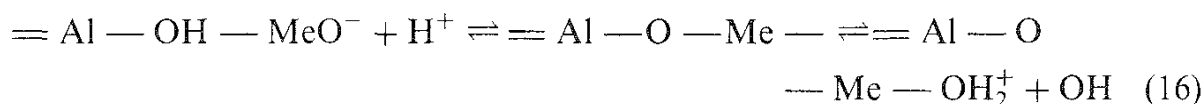
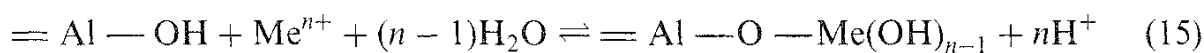


FIG. 12 Reversibility of the adsorption process. Desorption of Cu adsorbed on 0.1 g of γ -Al₂O₃, by addition of different amounts of HNO₃, $A_t = 60$ min. (From Ref. 47.)

Baumgarten and Kirchhausen-Duesing [47] compared precipitation and adsorption of Cu, Co, Ni, and Cr at γ -Al₂O₃ and interpreted the results on the basis of a model, considering dissolution of alumina. The adsorption is described by



The pK_{ad} and pK_s values (negative logarithms of the adsorption constant and the solubility product) are given in Table 4. In the case of Co and Ni it is difficult to separate the effects of precipitation and adsorption.

Further results were obtained with Al(OH)₃ and AlOOH. Mustafa et al. [62] discussed adsorption isotherms of divalent Cu, Zn, Ni, and Co ions on aluminum hydroxide at different temperatures and derived the thermodynamic values shown in Table 5.

TABLE 4 Negative Decadic Logarithms of Adsorption Constants (pK_{ad}) and Solubility Products (pK_s)

| Ion | pK_{ad} | pK_s |
|------------------|------------------|--------|
| Cu ²⁺ | -18.23 | 19.09 |
| Co ²⁺ | -17.06 | 19.25 |
| Ni ²⁺ | -15.77 | 18.04 |
| Cr ³⁺ | -30.83 | 31.76 |

Source: Refs. 17 (pK_{ad}) and 47 (pK_s).

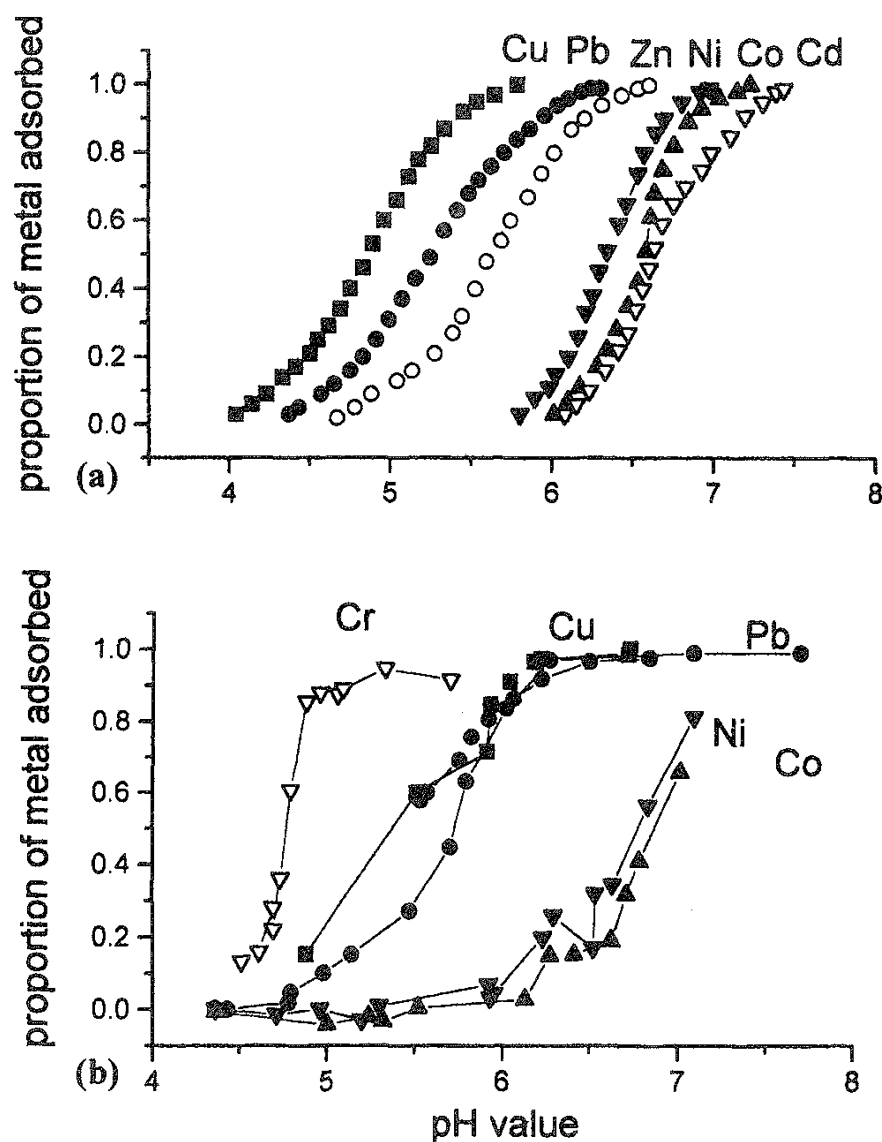


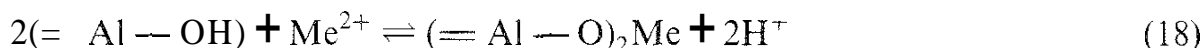
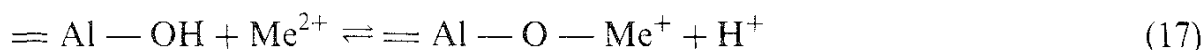
FIG. 13 Degree of adsorption of transition metals as a function of pH. (a) 1.25×10^{-4} mol/L on alumina hydrogel (0.093 mol Al/L). (From Ref. 51.) (b) $(7.9\text{--}8.4) \times 10^{-5}$ mol/L on γ -Al₂O₃ (2 g/L, BET area 170 m²/g). (From Refs. 19 and 47.)

TABLE 5 Thermodynamic Data for Adsorption on Al(OH)₃

| Ion | ΔH° (kJ/mol) | ΔS° [J/(mol K)] |
|------------------|---------------------------|------------------------------|
| Cu ²⁺ | 11.18 | 114 |
| Zn ²⁺ | 19.20 | 143 |
| Co ²⁺ | 21.80 | 153 |
| Ni ²⁺ | 27.81 | 188 |

Source: Ref. 62.

Pavlova and Sigg [63] measured equilibrium constants for the reactions



The constants are given in Table 6. Copper adsorption at "low pH" in contrast to that of Ca, Mg, and Mn, is mentioned by McBride [64]. Different pH_{50} values for the adsorption of Cu on hydroxide (5.0), gibbsite (5.5), and boehmite (5.7) [65] may be caused by the different numbers of centers.

The second transition ion group contains Zn, Cd, and Hg, which are known to be strong poisons. Besides the works cited already. Huang and Rhoads [66] give curves for the removal of Zn^{2+} of different initial concentrations by different amounts of $\gamma\text{-Al}_2\text{O}_3$. Brady [28] shows the temperature dependence of Cd and Pb adsorption. The speciation of Zn and Cd in the liquid phase — necessary for model calculations — is reported in Refs. 4 and 67 with remarkable differences, especially for the MeOH^+ species. Liu et al. [4] observed a linear relation of the logarithms of adsorbed and dissolved amounts of Zn^{2+} and Cd^{2+} . Kalatsei et al. [68] report extremely slow equilibration of Zn with alumina in the presence of NH_3 . Lowson and Evans [53] studied the adsorption of Zn and Cd ions from very dilute solutions on $\alpha\text{-Al}_2\text{O}_3$.

Aluminum hydroxide was used as an adsorbent in a number of publications. Coprecipitation of $\text{Cd}(\text{OH})_2$ and $\text{Al}(\text{OH})_3$ was measured by Simon et al. in the absence [69] and presence [70] of NH_3 . Shiao et al. [50] demonstrate that cadmium distribution coefficients between liquid and surface are practically uninfluenced by the NaNO_3 concentration, while NaCl has a remarkable influence. According to Shimada et al. [71] and Packter and Derry [1], coprecipitation leads to the formation of Zn aluminates. Besides investigating various ions [62], Mustafa and co-workers describe sorption on $\alpha\text{-Al}(\text{OH})_3$ [72,72], especially that of Zn, at different temperatures. They observed Langmuir isotherms and derived thermodynamic data. Kinetic studies were carried out by Simon et al. [74] using polarographic techniques. In their experiments equilibrium was reached after 3 h with two consecutive first-order reactions, in contrast to the findings of Lo and Leckie

TABLE 6 Negative Decadic Logarithms of Adsorption Constants [Eq. (14)]

| Ion | $\text{p}K_1$ | $\text{p}K_2$ |
|------------------|---------------|---------------|
| Cu^{2+} | -2.1 | -7.0 |
| Pb^{2+} | -2.2 | -8.1 |
| Ni^{2+} | -3.6 | -9.2 |
| Zn^{2+} | -3.1 | -7.9 |
| Cd^{2+} | -3.8 | -10.0 |
| Co^{2+} | -3.5 | -11.6 |

Source: Ref. 63.

[75–77], who also observed two reactions on amorphous alumina, but with much slower equilibration, probably because of the pore system of the adsorbent. Even desorption processes were slow, but they depended on the solution pH.

Of the next three groups — (Sc, Y, La), (Ti, Zr, Hf), and (V, Nb, Ta), yttrium was investigated by Kosmulski [78] in a work about adsorption thermodynamics that also treated Ni and Gd. The adsorption behavior of one other rare earth ion was measured: Adsorption of Eu turned out to be a function of pH and the concentration of NaCl (0.5–5.0 M) [50]. One publication about the adsorption isotherms of Pr, Nd, and Er is of little value, as the pH was not measured [79].

Of the members of Group VIB, Mo and W were investigated only as oxoanions; the adsorption of only cationic Cr^{3+} is described. Static and kinetic measurements done by Wehrli et al. [80] and Chang et al. [81] showed fast and slow reactions, the slow one with a linear relation between $\log k$ and pH, measured polarographically [80]. The pressure jump technique and equilibrium measurements with different NaNO_3 concentrations were evaluated with the triple-layer model, assuming various adsorption equilibria. Different assumptions on the adsorbed species gave equally good fits.

Typical adsorption behavior was observed by Baumgarten and Kirchhausen-Duesing [47] for Cr (Fig. 13b). Here the rest concentration at a given pH is clearly lower in the presence than in the absence of alumina (pure precipitation). ESR measurements [82] show a broad signal ($g_{\text{eff}} = 2.06$), which is interpreted as merely adsorption onto the surface without incorporation into the surface; a change of color from green to violet was observed as a consequence of ligand exchange. Zaki et al. [83] used UV diffuse reflectance and X-ray diffraction and found highly dispersed chromate species on γ -alumina.

Some work has been done with Mn in addition to that mentioned already [64,84,85]. The kinetics of adsorption on $\gamma\text{-Al}_2\text{O}_3$ was measured for different initial concentrations, showing equilibrium after 30 min [54]. A similar time to equilibrium was found by Roy et al. [86]: 100 min. In static experiments they showed redissolution at high pH, probably by oxidative formation of MnO_2^{2-} and MnO_2H^- . ESR measurements [87] indicate two forms, one reversibly adsorbed and one irreversibly adsorbed. Lowson and Evans [53] showed that the influence of the anion (Cl^- , NO_3^- , SO_4^{2-}) on the adsorption of Mn^{2+} is almost negligible. The desorption of adsorbed Mn brought about by lowering the pH value is incomplete.

In the Group VIIIB uncomplexed Fe attracted little interest, probably because of the two possible valence states. The pH dependence of Ni adsorption by $\gamma\text{-Al}_2\text{O}_3$ was shown by de Bokx et al. [88]; they even stated that “surface aluminate” is formed in the case of low Ni coverage, while higher coverage leads to the formation of an NiO phase. They give a diagram showing a linear relationship between the logarithms of the intrinsic equilibrium constants and the hydrolysis constant. Shiao et al. [50] show equal precipitation of Co on two different $\gamma\text{-Al}_2\text{O}_3$ samples. Isotherms obtained for the Co/ $\gamma\text{-Al}_2\text{O}_3$ system at different pH values are shown by Spanos and Lycourghiotis [89]. Adsorption isotherms of Co and Ni on a- $\text{Al}(\text{OH})_3$ given by Mustafa et al. [62] were evaluated as Langmuir isotherms but cannot be compared directly with those mentioned before, as the number of centers is unknown here.

Baumgarten and Kirchhausen-Duesing [47] investigated Co and Ni adsorption onto $\gamma\text{-Al}_2\text{O}_3$ (as well as that of Cu and Cr) and evaluated the data on the basis of a surface complexation model. Spanos and Lycourghiotis [90] discuss the mechanism of Co^{2+} and Ni^{2+} deposition onto pure and F-doped $\gamma\text{-Al}_2\text{O}_3$.

Towle et al. [91] interpret their EXAFS and TEM results of the $\text{Co}/\text{Al}_2\text{O}_3$ (Linde A alumina powder) system as a surface precipitation of $\text{Co}(\text{OH})_2$ with many vacancies, while Scheidegger et al. [92] report, also on the basis of EXAFS, the formation of mixed cation phases. Finally, Brown et al. [93] show in situ EXAFS and X-ray absorption measurements with the result that Co (and Pb) adsorb at pH 6.8 on $\gamma\text{-Al}_2\text{O}_3$ as inner-sphere complexes without forming three-dimensional precipitates or diffusing into the oxide, but multinuclear species are formed on the oxide.

According to Mieth and Schwarz [94], Ni adsorption on $\gamma\text{-Al}_2\text{O}_3$ is complete after 60 min.

C. Elemental Anions and Oxo Anions

Anions have attracted much less interest than cations. Some of them, such as nitrate, are not specifically adsorbed, i.e., they are not able to replace surface OH groups. Cl^- is adsorbed to a maximum of $2.7 \times 10^{-6} \text{ mol/m}^2$ at pH 2.5 from a 0.1 M NaCl solution [48]. Figure 14 shows the pH dependence of adsorption for some anions. It must be stressed that, in contrast to the figures for cations, the adsorption of anions cannot be compared directly, as the measuring conditions are

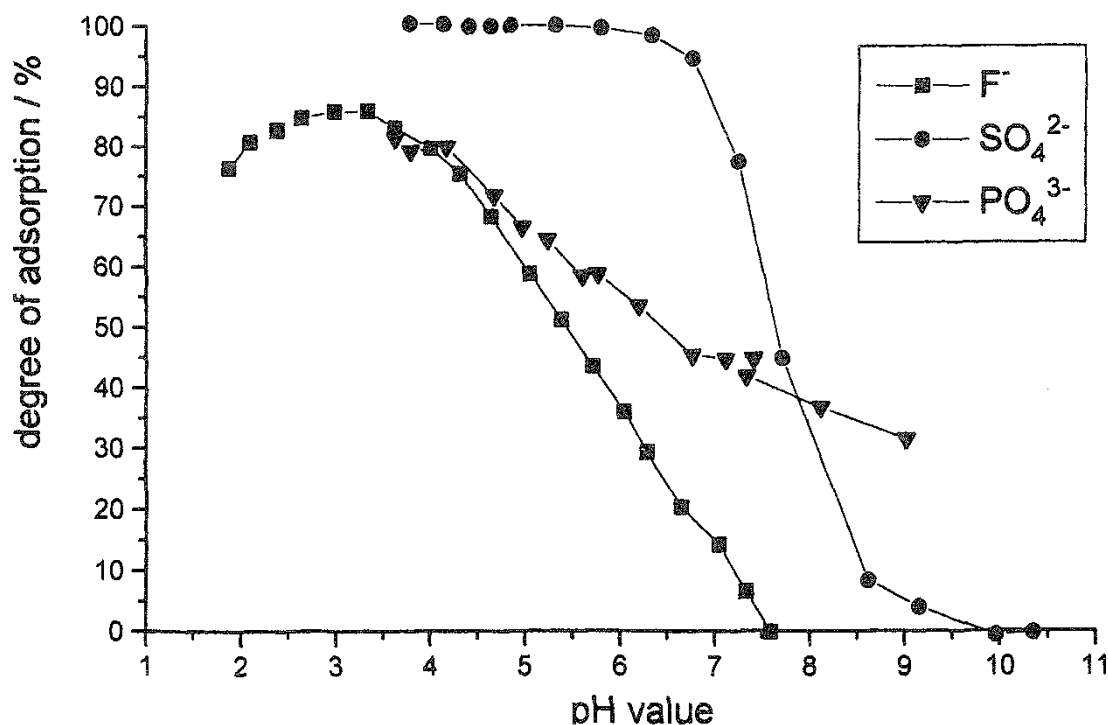


FIG 14 Adsorption of anions. F^- : From Ref. 95, conditions not given. SO_4^{2-} : $c_0 = 0.1 \text{ M}$; 0.01 M KCl ; $10 \text{ g Al}_2\text{O}_3/\text{L}$. (From Ref. 96.) PO_4^{3-} : $c_0 = 1 \times 10^{-5} \text{ M}$; 0.1 M KCl ; $1 \text{ g Al}_2\text{O}_3/\text{L}$. (From Ref. 97.)

very different. However, it can be seen that the pH dependence differs from that of cations, as expected: The greatest amount is adsorbed at low pH. In contrast to Cl^- mentioned before, F^- , SO_4^{2-} , and PO_4^{3-} are adsorbed nearly completely at low pH, indicating specific adsorption. Petkovic et al. [98] investigated adsorption of NO_3^- , Cl^- , Br^- , and I^- onto colloidal boehmite by titration in the respective potassium salt solutions and obtained the following values of negative logarithms of intrinsic surface complexation constants (TLM): 5.6 (NO_3^-), 5.4 (Cl^-), 5.5 (Br^-), and 5.5 (I^-). They concluded, because of the equal values, that the adsorption is not specific. A comparison with other aluminas or Na^+ instead of K^+ shows remarkable differences.

Borate sorption investigated by Toner and Sparks [99] shows the maximum values at about pH 8.5 with a slow decrease to lower pH values and a strong decrease to higher ones. Saeki and Matsumoto [100] discuss selenite adsorption onto various adsorbents. $\alpha\text{-Al}_2\text{O}_3$ ($A_s = 5.3 \text{ m}^2/\text{g}$) evidently had too small a surface to give meaningful results. with $\text{Al}(\text{OH})_3$ ($A_s = 126 \text{ m}^2/\text{g}$) the maximum adsorption (80%) was found at pH 6, decreasing to 20% at both pH 3 and pH 10.

Sharma et al. [101] show adsorption isotherms of ammonium metavanadate for different pH values. They also describe the desorption of permanganate, chromate, and metavanadate at different pH values in the presence of different background ions. EXAFS was used to investigate the adsorption of metal oxoanions (Re, Mn, Cr, Mo, W) on γ -alumina [102]. It shows that molybdate and tungstate are adsorbed more strongly than the other oxoanions. Tungstate adsorption, especially its mechanistic aspect, is treated by Karakonstantis et al. [103]. Adsorption of molybdate was investigated by Spanos et al. [104,105]; adsorption isotherms are shown for different conditions. UV-Vis spectroscopy was used by Pizzio et al. [106] to follow the adsorption of meta- and paratungstates on $\gamma\text{-Al}_2\text{O}_3$.

D. Complex Ions

In principle, all ions form complexes in solution, normally aquo complexes. Here we discuss complexes with ligands other than H_2O . They are treated together, whether cations or anions, as their charge depends on the number and charge of the ligands for a given central ion.

The inorganic ligands that were investigated are NH_3 , Cl^- , and CN^- . Brunelle [16] gives an overview of the tendency of elements of Groups 7A, 8, and 1B to form cationic or anionic complexes and uses the adsorption of cationic or anionic complexes for catalyst preparation [107].

Amino ligands, not changing the charge, were used in the following investigations. Spielbauer et al. [108] described ammino aquo complexes, using Pd speciation in the liquid phase described by Rasmussen and Jorgensen [109] containing NH_3 for comparison. They interpret their results on the basis of the triple-layer model (TLM) of Davis et al. [110], unfortunately without experimental values above pH 11.5, where the adsorbed amount should decrease according to the model calculation.

Contescu et al. [111] gave adsorption isotherms for $[\text{Pd}(\text{NH}_3)_4]^{2+}$ for pH 8 and 10, and one for pH 10.6 was given by Schwarz et al. [112]. Fuerstenau and Osseo-Assare [113] showed the adsorption of Cu, Ni, and Co amines ($1 \times 10^{-3} \text{ M}$) at

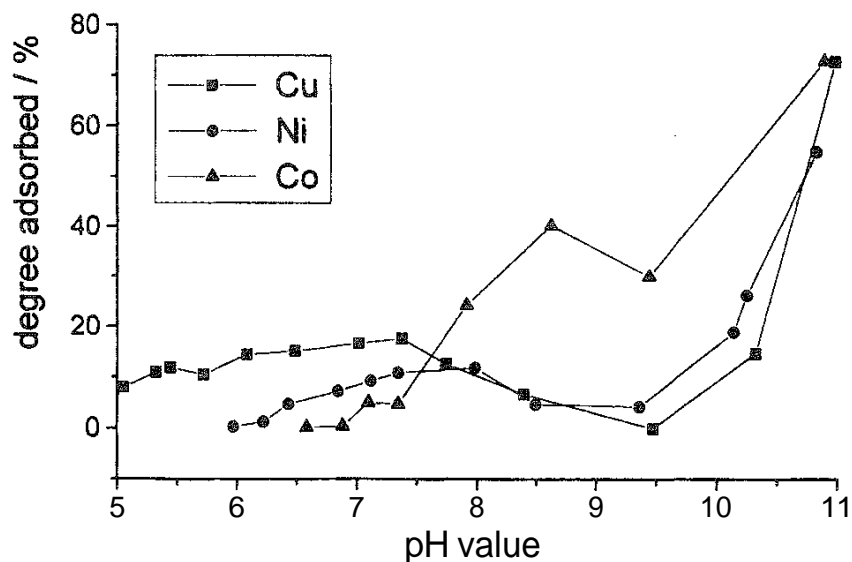


FIG. 15 Adsorption of ammine complexes. Cu, Ni, Co: 1×10^{-3} M on $(\gamma + \eta)$ Al_2O_3 in the presence of 0.1 M $(\text{NH}_3 + \text{NH}_4^+)$; 160m^2 $\text{Al}_2\text{O}_3/\text{L}$. (From Ref. 113.)

different pH values by alumina ($160\text{m}^2/\text{L}$) in the presence of 0.5 M total ammonia. Figure 15 gives results for alumina (Linde A, Union Carbide, $15\text{m}^2/\text{g}$). The results are interpreted on the basis of an extended double-layer model. Interaction of alumina (γ and η , $186\text{m}^2/\text{g}$) with $\text{Pd}(\text{NH}_3)_n\text{Cl}_{4-n}$ complexes formed at different pH values was investigated by Contescu and Vass [114]. Experimental isotherms are compared with calculated Langmuir-type isotherms (Fig. 16). In another paper [115] Contescu and Vass gave kinetic data on adsorption of palladium tetrahalide

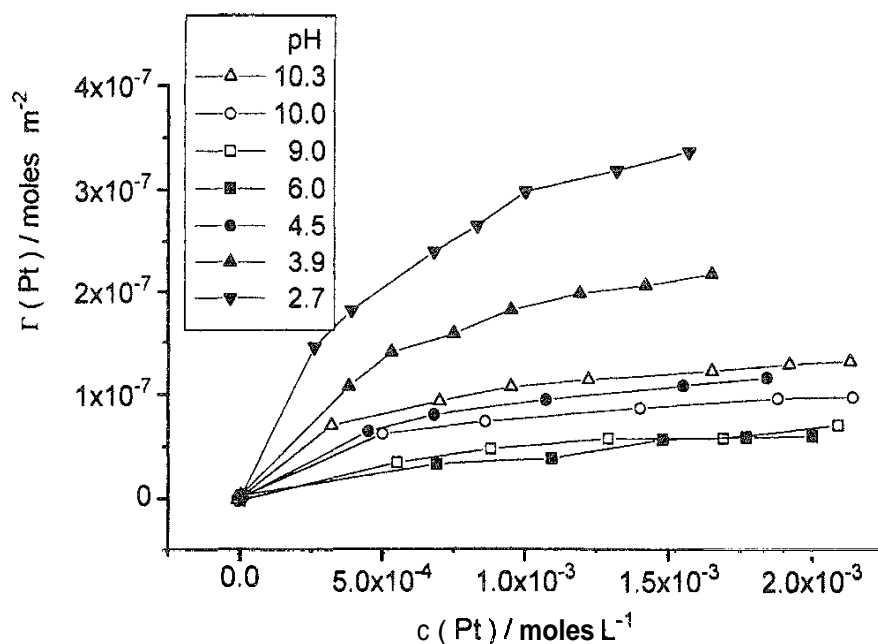


FIG. 16 Adsorption isotherms for Pt complexes on $(\gamma + \eta)$ Al_2O_3 , depending on pH. (Starting from pH 1.92, ammonia was added to reach higher pH values.) (From Ref. 114.)

anions (Cl, Br) and proposed chemisorption by ligand exchange. Adsorption kinetics for $[\text{PdCl}_4]^{2-}$ was shown by Nicolescu et al. [54]; equilibrium was reached after about 90 min. According to Mang et al. [116] $[\text{PtCl}_6]^{2-}$ sorption on $\gamma\text{-Al}_2\text{O}_3$ is maximal at pH 4. A simulation assuming ligand exchange gives better results than a purely electrostatic one. Cadmium coprecipitation with aluminum is reduced in the presence of NH_3 [70].

Cheng and Huang [117] discussed the adsorption of ferri- and ferrocyanide, giving adsorption as a function of pH and distribution coefficients depending on liquid concentration. Geldsetzer [46] studied the adsorption of $[\text{Cu}(\text{CN})_4]^{3-}$, $[\text{Ni}(\text{CN})_4]^{2-}$, $[\text{Pt}(\text{CN})_6]^{2-}$, and $[\text{PtCl}_6]^{2-}$ on γ -alumina. The kinetics of Co tetrasulfophthalocyanine was described by Belikhmaer and Filicheva [118].

E. Organic Ions

Organic ions have attracted the most interest in the form of cationic and anionic surfactants, though other organic ions may be a limnological problem too. Martell and Motekaitis [119] reviewed the adsorption of aliphatic acids (maleic, gluconic, citric, and D,L-tartaric acid), salicylic acid, catechol, and a number of sulfone acids (3,5-disulfocatechol, 1,8-dihydroxy-4,5-disulfonaphthalene, 5-sulfosalicylic acid)- and nitrogen-containing complex ligands (NTA, EDTA, DTPA). Equilibrium constants are given for the relevant equilibria. An example of the application of organic acids (oxalic acid, salicylic acid, glycine) is aimed for better dispersion of Pd on a catalyst carrier by coadsorption [120]. The adsorption of a cationic surfactant (TTAC = *n*-tetradecyltrimethylammonium chloride) is shown in the form of an adsorption isotherm for pH 10 by Huang and Somasundaran [121]; that of anionic surfactants (4- C_{11} -paraxylenesulfonate and sodium octylbenzenesulfonate) by Hankins et al. [122] and Fu et al. [123] (Fig. 17). The maximum load of 2×10^{-6} – $\times 10^{-6}$ mol/m² shows that the whole surface is covered, assuming that an area of 0.28–0.83 nm² is covered by one molecule. The anionic surfactants show the same normal pH dependence as an inorganic anion, with greater adsorption at lower pH values ($\text{pH}_{50} \cong 10$).

The adsorption of nitrophenols onto alumina pretreated with various acids is shown in Refs. 124 and 125, unfortunately without giving the final pH values.

V. CONCLUDING DISCUSSION

First, one point may be mentioned, which was not discussed before: If the intention is to prepare a surface with an ionic adsorption layer, as for catalyst preparation, then adsorption from the gas phase may be an alternative. In this way organic ions may be adsorbed onto an alumina surface dehydrated at a higher temperature. Infrared spectra reveal that a surface aluminum salt was formed under these conditions [126,127]. Halogenated surfaces can be formed in the same way [128]. Complexes can be adsorbed in this way too, though normally neutral complexes are used here because of the better volatility.

Although it is not the intent of this chapter to thoroughly discuss model calculations, they also have to be regarded to a certain extent. In recent years a number of

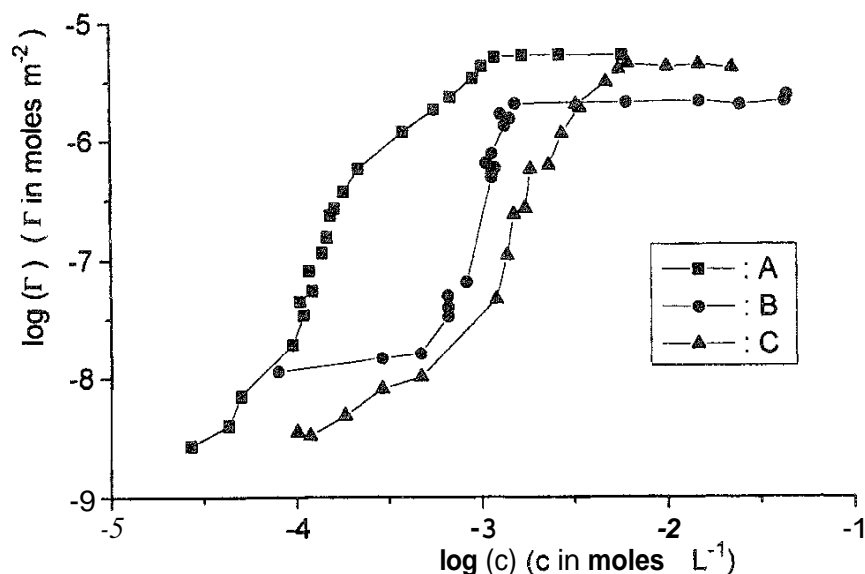


FIG. 17 Adsorption isotherms of surfactants on α -alumina (0.03M NaCl). A, 4- C_{11} -paraxylene sulfonate (pH 8–9; $T = 316$ K). (From Ref. 122.) B, TTAC (n -tetradecyltrimethylammonium chloride; pH 10; $T = 295$ K). (From Ref. 121.) C, $C_{8\phi S}$ (sodium p -octylbenzenesulfonate; pH 8.2, $T = 323$ K). (From Ref. 123.)

models have been developed that are broadly based on the surface complexation model of Farley et al. [129], which, in agreement with the spectroscopic results, shows a chemical interaction at the surface. Some recent extensions of this model try to close the gap between adsorption, precipitation, and coprecipitation with different assumptions — surface precipitation, surface coprecipitation, the formation of a continuously variable surface layer [130,131], or competitive precipitation of pure or mixed oxides [$Me(OH)_n$, $Me(Al(OH)_4)_n$] [18,47]. A revised physical model based on very different assumptions was published recently by Agashe and Regalbuto [132]. All models give fairly good fits to experimental values. Robertson and Lecky [133] demonstrate that equilibrium constants are "conditional," i.e., they vary with the experimental conditions, which means either that not all experimental data were sufficiently considered or they were not correctly implanted into the model.

The fact that different models lead to a sufficient fit of quantitative experimental data shows that additional information must be used for discrimination. Spectroscopic data reveal the formation of chemical bonds between adsorbed ions and the surface, which led to certain convergence to surface complex models, and extended to considering multilayer adsorption in the case of high ion concentration in the solution.

A serious problem is the fact that for most models the number of model parameters is great and the information obtained from the experiments comparatively poor. Many parameters have to be taken from other sources or have to be estimated (or even disregarded, because it is supposed that they have small influence in an estimation). Activity coefficients in the liquid phase are usually omitted by using a "sufficient" concentration of background electrolyte. The surface activity coefficients are usually not mentioned at all. In most models only one type of adsorption

center is assumed, often with a maximal surface concentration equal to the monolayer OH concentration. Some reactions are disregarded, such as the formation of doubly charged surface species, in spite of the fact that analogous species are found in the liquid phase. The speciation in the liquid phase, if regarded at all, is taken from the literature, though even these values may be erroneous. The remaining parameters, depending on the specific model and the choice of fixed parameters, generally allow fitting the experimental data, as they are not rich in information. Therefore even an incorrect model may give a good fit.

As a consequence the experimental conditions should be standardized as much as possible to allow the comparison of data obtained by different groups. Thus, in the case of equilibrium adsorption experiments as an example, the following conditions might be standardized, with the proposed values in parentheses:

1. Background ions (KNO_3 , 0.1 M)
2. Adsorbents [$\gamma\text{-Al}_2\text{O}_3$, standard method of preparation, larger common stock, constant area per volume ($100\text{ m}^2/\text{L}$)]
3. Constant conditioning time of oxide with all ingredients except for the metal salt solution (1 h)
4. Adsorbent $[\text{Me}(\text{NO}_3)_n]$, total conc. $1 \times 10^{-2}\text{ M}$
5. Analytical techniques.
 - a. pH measurements: types of electrodes, calibration
 - b. Metal analysis (AAS, etc.)
6. Measuring temperature ($T = 298\text{ K}$)
7. Equilibration time (1 h)
8. CO_2 exclusion (N_2 bubbling during conditioning, at low pH)

Only one condition should be varied at a time, to allow comparison. The primary experimental results might be published, e.g., on the Internet, for an easier exchange of data.

Some standardization may also be proposed for the model calculations. A great number of species are accepted in different models, but as it is irrelevant from the standpoint of thermodynamics which reaction is chosen to calculate the concentration of one species from that of any other species, different reactions are used, and thus different model parameters are obtained. A unified reaction scheme would facilitate comparison of results.

ACKNOWLEDGMENT

I gratefully acknowledge the valuable assistance of Mrs. U. Koehler and Mr. D. Judat in preparing this manuscript,

REFERENCES

1. A. Packter and A. Derry, *Cryst. Res. Technol.* 21:1281 (1986).
2. L. Ghosh, K. P. Das, and D. K. Chattoraj, *J. Surf. Sci. Tech.* 2:25 (1986).
3. C. P. Schulthess and D. L. Sparks, *Soil Sci. Soc. Am. J.* 52:92 (1988).
4. J. Liu, S. M. Howard, and K. N. Han, *Langmuir* 9:3635 (1993).

5. Ch. F. Baes, Jr. and R. E. Mesmer, *The Hydrolysis of Cations*, Wiley, New York, 1976.
6. A. M. Scheidegger and D. L. Sparks, *Soil Sci.* 161:813 (1996).
7. C. P. Schulthess and D. L. Sparks, *Soil Sci. Soc. Am. J.* 51:1136 (1987).
8. P. P. Wu, J. R. Feldkamp, J. L. White, and St. L. Hem, *J. Colloid Interface Sci.* 110:601 (1986).
9. C. Contescu, J. Jagiello, and J. A. Schwarz, *Langmuir* 9:1754 (1993).
10. C. Contescu, A. Contescu, and J. A. Schwarz, *J. Phys. Chem.* 98:4327 (1994).
11. T. Hiemstra, W. H. van Riemsdijk, and G. H. Bolt, *J. Colloid Interface Sci.* 133:91 (1989).
12. T. Hiemstra, J. C. M. deWit, and W. H. van Riemsdijk, *J. Colloid Interface Sci.* 133:105 (1989).
13. T. Hiemstra, P. Venema, and W. H. van Riemsdijk, *J. Colloid Interface Sci.* 184:680 (1996).
14. Ch.-P. Huang and W. Stumm, *J. Colloid Interface Sci.* 43:409 (1973).
15. W. Janusz and J. Szczypa, *Mater. Sci. Forum* 25–26:427 (1988).
16. J. P. Brunelle, *Pure Appl. Chem.* 50:1211 (1978).
17. C. P. Schulthess and D. L. Sparks, *Soil Sci. Soc. Am. J.* 50:1406 (1986).
18. E. Baumgarten, F. Geldsetzer, and U. Kirchhausen-Duesing, *J. Colloid Interface Sci.* 173:104 (1995).
19. D. Judat, Diploma Work, Düsseldorf, 1996.
20. L. K. Koopal, *Electrochim. Acta* 41:2293 (1996).
21. K. Torkar, *Monat. Chem.* 91:450 (1960).
22. T. W. Healy and L. R. White, *Adv. Colloid Interface Sci.* 9:303 (1978).
23. J. S. Noh and J. A. Schwarz, *J. Colloid Interface Sci.* 130:157 (1989).
24. R. J. Hunter. *Foundations of Colloid Science*, Vol 1, Clarendon Press, Oxford, UK, 1987.
25. Ch. Sivaraj, C. Contescu, and J. A. Schwarz, *J. Catal.* 132:422 (1991).
26. A. Lewis-Russ, *Adv. Agron.* 46:199 (1991).
27. H. Hohl and W. Stumm, *J. Colloid Interface Sci.* 55:281 (1976).
28. P. V. Brady, *Geochim. Cosmochim. Acta* 58:1213 (1994).
29. W. N. Rowlands, R. W. O'Brien, R. J. Hunter, and V. Patrick, *J. Colloid Interface Sci.* 188:325 (1997).
30. G. A. Parks and P. L. de Bruyn, *J. Phys. Chem.* 66:967 (1962).
31. S. N. Tewari and S. Ghosh, *Acad. Sci. India (Allahabad) Proc.* A21:41 (1952).
32. J. A. Yopps and D. W. Fuerstenau, *J. Colloid Sci.* 19:61 (1964).
33. P. G. Koutsoukos and A. S. Lycourghiotis, *Colloids Surf.* 55:297 (1991).
34. St. J. Scierka, M. Houalla, A. Proctor, and D. M. Hercules, *J. Phys. Chem.* 99:1537 (1995).
35. J. Lutzenkirchen, P. Magnico, and Ph. Behra, *J. Colloid Interface Sci.* 170:326 (1995).
36. K. F. Hayes, G. Redden, E. Ela, and J. O. Leckie, *J. Colloid Interface Sci.* 142:448 (1991).
37. C. P. Huang, Ph.D. Thesis, Harvard University, 1971.
38. P. G. Johansen and A. S. Buchanan, *Aust. J. Chem.* 10:398 (1957).
39. H. J. Modi and D. W. Fuerstenau, *J. Phys. Chem.* 61:640 (1957).
40. J. B. Peri, *J. Phys. Chem.* 69:211 (1965).

41. H. Knozinger and P. Ratnasamy, *Cat. Rev. - Sci. Eng.* 7:31 (1978).
42. D. Hollenberg, Dissertation, Düsseldorf, 1980.
43. H. Tamura, N. Katayama, and R. Furuichi, *Environ. Sci. Technol.* 30:1198 (1996).
44. R. Sprycha and J. Szczypa, *J. Colloid Interface Sci.* 102:288 (1984).
45. L. Vordonis, P. G. Koutsoukos, and A. Lycourghiotis, *J. Catal.* 98:296 (1986).
46. F. O. Geldsetzer, Dissertation, Dusseldorf, 1994.
47. E. Baumgarten and U. Kirchhausen-Duesing, *J. Colloid Interface Sci.* 194:1 (1997).
48. M. Kosmulski, *Colloids Surf. A* 83:237 (1994).
49. F. Deng, Y. Du, C. Ye, Y. Kong, *Solid State N. M. R.* 2:317 (1993).
50. S. Y. Shiao, Y. Egozy, and R. E. Meyer, *J. Inorg. Nucl. Chem.* 43:3309 (1981).
51. D. G. Kinniburgh, M. L. Jackson, and J. K. Syers, *Soil Sci. Soc. Am, J.* 40:796 (1976).
52. C.-F. Lin, K.-S. Chang, C.-W. Tsay, D.-Y. Lee, S. L. Lo, T. Yasunaga, *J. Colloid Interface Sci.* 188:201 (1997).
53. R. T. Lowson and J. V. Evans, *Aust. J. Chem.* 37:2165 (1984).
54. I. V. Nicolescu, V. Parvulescu, V. Parvulescu, and E. Angelescu, *Rev. Roum. Chim.* 35:145 (1990).
55. K.-S. Chang, C.-F. Lin, D.-Y. Lee, and S.-L. Lo., *Chemosphere* 27:1397 (1993).
56. V. Hronsky and M. Rakos, *Czech. J. Phys. B* 33:1347 (1983).
57. O. Cozar, V. Znamirovski, and M. Gridan, *Rev. Roum. Phys.* 27:389 (1982).
58. Y. Zhang, X. Zeng, and T. Cheng, *React. Kinet. Cata. Lett.* 43:387 (1991).
59. M. Rudin and H. Motschi, *J. Colloid Interface Sci.* 98:385 (1984).
60. K. Hachiya, M. Sasaki, Y. Saruta, N. Mikami, and T. Yasunaga, *J. Phys. Chem.* 88:23 (1984).
61. K. Hachiya, M. Sasaki, T. Ikeda, N. Mikami, and T. Yasunaga, *J. Phys. Chem.* 88:27 (1984).
62. S. Mustafa, M. Safdar, S. Yar, and A. Naeem Khan, *Phys. Chem.* 12:63 (1993).
63. V. Pavlova and L. Sigg, *Water Res.* 22:1571 (1988).
64. M. B. McBride, *Soil. Sci. Soc. Am. J.* 42:27 (1978).
65. M. B. McBride, *Clays Clay Min.* 30:21 (1982).
66. C. P. Huang, and E. A. Rhoads, *J. Colloid Interface Sci.* 131:289 (1989).
67. C. P. Schulthess and C. P. Huang, *Soil. Sci. Soc. Am. J.* 54:679 (1990).
68. E. A. Kalatsei, A. P. Dushina, I. P. Alekseeva, and V. B. Aleskovskii, *Zh. Obsch. Khim. SSSR* 42:1883 (1972).
69. J. Simon, W. Schulze, and M. Völtz, *Z. Anal. Chem.* 257:108 (1971).
70. J. Simon, W. Schulze, and M. Völtz, *Z. Anal. Chem.* 257:184 (1971).
71. H. Shimada, Y. Maru, T. Yasuoka, and S. Mitsuzawa, *Proc. Sch. Sci. Tokai Univ.* 28:27 (1993).
72. S. Mustafa, M. Safdar, and S. Yar Hussain, *J. Surf. Sci. Technol.* 5:267 (1989).
73. S. Mustafa, M. Safdar, and G. Nawab, *Phys, Chem.* 9:79 (1990).
74. J. Simon, W. Schulze, and M. Völtz, *Z. Anorg. Allgem. Chem.* 394:233 (1972).
75. S. L. Lo and J. O. Leckie, *Proc. Natl. Sci. Counc. ROC(A)* 13:332 (1989).
76. S. L. Lo and J. O. Leckie, *J. Chin. Inst. Eng.* 12:579 (1989).
77. K. S. L. Lo and J. O. Leckie, *Water Sci. Technol.* 28:39 (1993).
78. M. Kosmulski, *J. Colloid Interface Sci.* 192:215 (1997).

79. M. Saleem, M. Afzal, F. Mahmood, and A. Ali, *Adsorp. Sci. Technol.* 9:17 (1992).
80. B. Wehrli, S. Ibric, and W. Stumm, *Colloids Surf.* 1990:77.
81. K.-S. Chang, C.-F. Lin, D.-Y. Lee, S.-L. Lo, and T. Yasunaga, *J. Colloid Interface Sci.* 165:169 (1994).
82. T. Böttjer and G. Lehmann, *Z. Phys. Chem, NF* 166:233 (1990).
83. M. I. Zaki, S. A. A. Mansour, F. Taha, and G. A. H. Mekhemes, *Langmuir* 8:727 (1992).
84. D. Judat, private communication.
85. H. Bilinski, S. Kozar, and M. Branica, *J. Colloid Interface Sci.* 3:211 (1976).
86. R. Roy, M. A. Cogneau, R. Debuyst, and D. J. Apers, *Bull. Soc. Chim. Belg.* 82:75 (1973).
87. L. Burlamacchi and P. L. Villa, *React, Kinet. Catal. Lett.* 3:199 (1975).
88. P. K. de Bokx, W. B. A. Wassenberg, and J. W. Geus, *J. Catal.* 104:86 (1987).
89. N. Spanos and A. Lycourghiotis, *Langmuir* 10:2351 (1994).
90. N. Spanos and A. Lycourghiotis, *J. Chem. Soc., Faraday Trans.* 89:4101 (1993).
91. St. N. Towle, J. R. Bargar, G. E. Brown, Jr., and G. A. Parks, *J. Colloid Interface Sci.* 187:62 (1997).
92. A. M. Scheidegger, G. M. Lamble, and D. L. Sparks, *J. Colloid Interface Sci.* 186:118 (1997).
93. G. E. Brown, Jr., G. A. Parks, and C. J. Chrisholm-Brause, *Chimia* 43:248 (1989).
94. J. A. Mieth and J. A. Schwarz, *Appl. Catal.* 55:137 (1989).
95. W. Stumm and R. Wollast, *Rev. Geophys.* 28:53 (1990).
96. L. M. He, L. W. Zelazny, V. C. Baligar, K. D. Ritchey, and D. C. Martens, *Soil Sci. Soc. Am. J.* 60:442 (1996).
97. A. Violante, C. Colombo, and A. Buondonno, *Soil Sci. Soc. Ain. J.* 55:65 (1991).
98. M. D. Petkovic, S. K. Milonjic, and V. T. Dondur, *Separ. Sci. Technol.* 29:627 (1994).
99. C. V. Toner IV and D. L. Sparks, *Soil Sci. Soc. Am. J.* 59:395 (1995).
100. K. Saeki and S. Matsumoto, *Commun. Soil Sci. Plant Anal.*, 25:2147 (1994).
101. E. M. Sharma, G. L. Mundhara, S. Jha, and J. S. Tiwari, *J. Indian Chem. Soc.* 69:566 (1992).
102. F. M. Mulcahy, M. J. Fay, A. Proctor, M. Houalla, and D. M. Hercules, *J. Catal.* 124:231 (1990).
103. L. Karakonstantis, Ch. Kordulis, and A. Lycourghiotis, *Langmuir* 8:1318 (1992).
104. N. Spanos, L. Vordonis, Ch. Kordulis, and A. Lycourghiotis, *J. Catal.* 124:301 (1990).
105. N. Spanos and A. Lycourghiotis, *J. Catal.* 147:57 (1994).
106. L. R. Pizzio, C. V. Caceres, and M. N. Blanco, *Adsorp. Sci. Technol.* 9:36 (1992).
107. J. P. Brunelle and A. Sugier, *C. R. Acad. Sci. Paris* 276:1545 (1973).
108. D. Spielbauer, H. Zeilinger, and H. Knözinger, *Langmuir* 9:460 (1993).
109. L. Rasmussen and C. K. Jorgensen, *Acta Chem. Scand.* 2212313 (1968).
110. J. A. Davis, R. O. James, and J. O. Leckie, *J. Colloid Interface Sci.* 63:480 (1978).
111. C. Contescu, J. Hu, and J. A. Schwarz, *J. Chem. Soc., Faraday Trans.* 8914091 (1993).
112. J. A. Schwarz, C. T. Ugbor, and R. Zhang, *J. Catal.* 138:38 (1992).

113. D. W. Fuerstenau and K. Osseo-Asare, *J. Colloid Interface Sci.* *118*:524 (1987).
114. C. Contescu and M. I. Vass, *Appl. Catal.* *33*:259 (1987).
115. C. Contescu and M. I. Vass, *React. Kinet. Catal. Lett.* *43*:393 (1991).
116. Th. Mang, B. Breitscheidel, P. Polanek, and H. Knozinger, *Appl. Catal. A*: *106*:239 (1993).
117. W. P. Cheng and C. Huang, *J. Colloid Interface Sci.* *181*:627 (1996).
118. Y. A. Belikhmaer and O. D. Filicheva, *Russ. J. Coord. Chem.* *20*:43 (1994).
119. A. E. Martell and R. J. Motekaitis, *Proc. 194th Annu. Meeting Am. Chem. Soc. (Envir. Chem. and Toxicol. of Aluminum) 1987* (T. Lewis, ed.).
120. C. Contescu and M. I. Vass, *React. Kinet. Catal. Lett.* *43*:399 (1991).
121. L. Huang and P. Somasundaran, *Colloids Surf.* *117*:235 (1996).
122. N. P. Hankins, J. H. O'Haver, and J. H. Harwell, *Ind. Eng. Chem. Res.* *35*:2844 (1996).
123. E. Fu, P. Somasundaran, and Q. Xu, *ACS Symp. Ser.* *501*:366 (1992).
124. S. Jha, G. L. Mundhara, R. M. Sharma, and J. S. Tiwari, *Adsorp. Sci. Technol.* *9*:92 (1992).
125. R. M. Sharma, G. L. Mundhara, S. Jha, and J. S. Tiwari, *Colloids Surf.* *66*:259 (1992).
126. E. Baumgarten, R. Wagner, and C. Lentjes-Wagner, *J. Catal.* *104*:307 (1987).
127. E. Baumgarten and B. Dedek, *J. Mol. Catal.* *62*:37 (1990).
128. E. Baumgarten and A. Zachos, *Spectrochim. Acta* *37A*:757 (1981).
129. K. J. Parley, D. A. Dzombak, and F. M. M. Morel, *J. Colloid Interface Sci.* *106*:226 (1985).
130. L. E. Katz and K. F. Hayes, *J. Colloid Interface Sci.* *170*:477–490 (1995).
131. L. E. Katz and K. F. Hayes, *J. Colloid Interface Sci.* *170*:491 (1995).
132. K. B. Agashe and J. R. Regalbuto, *J. Colloid Interface Sci.* *185*:174 (1997).
133. A. P. Robertson and J. O. Leckie, *J. Colloid Interface Sci.* *188*:444 (1997).

Protein Adsorption onto Latex Particles

JEFFREY LEAVER Molecular Recognition Group, Hannah Research Institute, Ayr, Scotland

- I. Introduction
- II. Protein Structure
- III. Polystyrene Latex Particles
- IV. Interaction of Proteins with Polystyrene Latex
 - A. Adsorption
 - B. Conformation of adsorbed protein
 - C. Stability of adsorbed protein layers
 - D. Controlling protein adsorption
- V. Conclusions
- References

I. INTRODUCTION

Proteins, like other surface-active macromolecules, readily adsorb onto interfaces, particularly if the surfaces are hydrophobic. This property has important implications in a number of diverse technological areas. For example, within the food processing industry, protein-stabilized emulsions, where separation of the immiscible oil and water phases is prevented by stabilizing individual droplets with an interfacial layer of protein and surfactants, are, in terms of their commercial value, the most important class of food colloids. Similarly, food foams are usually stabilized by a combination of proteins and low molecular weight surfactants adsorbed at the air/water interface. On the negative side, fouling of processing equipment, particularly of heat exchangers, resulting from the deposition of proteins on solid surfaces decreases efficiency and increases the need for frequent cleaning. In biomedicine, fouling and rejection of implants, membranes, and contact lenses are problems, but immunoassays based on immobilized antibodies and antigens are

of increasing importance. In dentistry, control of plaque formation is a major interest, as is targeted drug delivery within the pharmaceutical industry. Protein purification via chromatography where protein molecules adsorb to, and are specifically released from, solid surfaces and the manufacture of specific enzyme-based bioelectrodes are of great interest in the bioprocessing industry.

In order to control protein adsorption, to enhance it in some cases and prevent it in others, it is necessary to understand the various stages involved in the process. The interaction of protein molecules with polystyrene (PS) latex particles having a well-defined surface has proved to be a very useful model system with which to study the interfacial behavior of proteins. Other colloidal systems, including silica and metal particles, have also been used in these investigations, and although this review concentrates mainly on interactions between proteins and latex particles, other systems are also mentioned where appropriate. Before looking at the interactions of proteins with PS latex particles in detail, it is worthwhile to take a brief overview of the two major components in the system.

II. PROTEIN STRUCTURE

Proteins are linear chains of amino acids in which individual residues are linked by peptide bonds between the carboxyl group of one amino acid and the amino group of the next. This is the primary sequence of the protein. The side chains of some of the amino acids undergo enzyme-catalyzed modifications such as glycosylation and phosphorylation, which serve to alter the functionality of the protein. Folding of the polypeptide chain as a result of hydrogen bonding between $C=O$ and $N-H$ groups of the amino acids gives rise to α -helices and β -sheets and sheets, with structured regions being linked by flexible loops. This is the secondary structure. Other types of secondary structure have also been identified, but in globular proteins these forms predominate. Compared to peptide bond energies (> 200 kJ/mol), these hydrogen bonds are relatively weak (around 10 kJ/mol).

The extent of ordered structure in different protein species is very variable. Some proteins, and in the context of this chapter the caseins are a prime example, adopt a relatively open, expanded-coil conformation. In contrast, globular proteins are almost spherical, with a packing density at the interior of the molecule being equal to that found in crystals and close to the theoretical value for close-packed spheres. This high packing density means that short-range interactions such as hydrogen bonding and van der Waals forces are important in stabilizing the secondary structure. In general, hydrophobic amino acid residues tend to be buried in the interior of the protein, whereas hydrophilic charged groups are located on the outside of the protein in contact with the aqueous phase. However, polar and apolar amino acids are fairly equally distributed at the surface of globular proteins.

An additional type of covalent bond, the disulfide bridge, can form between individual cysteine residues and is also important in determining the stability of many proteins. Proteins with disulfide bridges usually contain at least two, proteins containing single disulfide bridges being relatively rare. Both inter- and intramolecular disulfide bridges are found; the addition of thiol-containing reagents such as

2-mercaptoethanol (2-ME) and dithiothreitol reduces disulfide bridges and destabilizes the protein.

Denaturation, or unfolding, of globular proteins can be induced by exposing the protein to high temperature or pressure, extreme pH, high concentrations of salts, organic solvents, surfactants, urea, or guanidine hydrochloride. In addition, as discussed later, some proteins are also denatured by adsorption to interfaces. In general, globular proteins behave as random coils when dissolved in 6 M guanidine hydrochloride.

III. POLYSTYRENE LATEX PARTICLES

Since polystyrene latex particles are generally hard spheres, protein adsorption to them is solely a surface phenomenon. Methods for the production of polystyrene latex particles have been reviewed by Piskin et al. [1].

The diameter of polystyrene particles can range from less than 0.1 μm to more than 1000 μm . By varying the polymerization conditions, it is possible to produce polystyrene latex particles in a broad range of sizes and degrees of monodispersity. Larger beads are usually produced by suspension polymerization. In this process, agitation breaks the monomer phase into individual droplets suspended within the dispersion phase, which also contains a surfactant to stabilize the droplets. An initiator is also incorporated into the monomer phase, and by varying both the rate of agitation and the temperature, polymerization is induced. The polystyrene particles produced by this technique typically have mean diameters between 50 and 1000 μm , with a relatively broad distribution. Emulsion polymerization, where surfactant-stabilized monomer micelles are polymerized by initiator molecules dissolved in the dispersion phase, is used to produce extremely uniform, very small, spherical particles with diameters up to 0.1 μm . In phase inversion polymerization, the monomer, initiator, and stabilizer are all dissolved in an inert solvent. When the growing polymer chains reach a certain critical size, phase inversion occurs, and the chains aggregate to form stable monodisperse particles. The size range of particles produced by this method is between those of particles produced by the other techniques.

The polarity and density of charged groups on the surface of PS latex particles can be varied by altering the chemical composition of the monomer mix. Alternatively, it is also possible to change the surface by allowing acrylate monomers to adsorb to preformed particles and subsequently polymerizing these in situ.

The surface charge density of beads can be determined by measuring their average zeta potentials and electrophoretic mobilities or by conductometric titration. Size, polydispersity, and smoothness are usually determined by microscopy or photon correlation spectroscopy.

IV. INTERACTION OF PROTEINS WITH POLYSTYRENE LATEX

The various stages in the interaction of a protein molecule with a surface are shown schematically in Fig. 1. Initially, protein molecules in the bulk phase approach the latex surface. Adsorption may then occur, and in some instances this is followed by

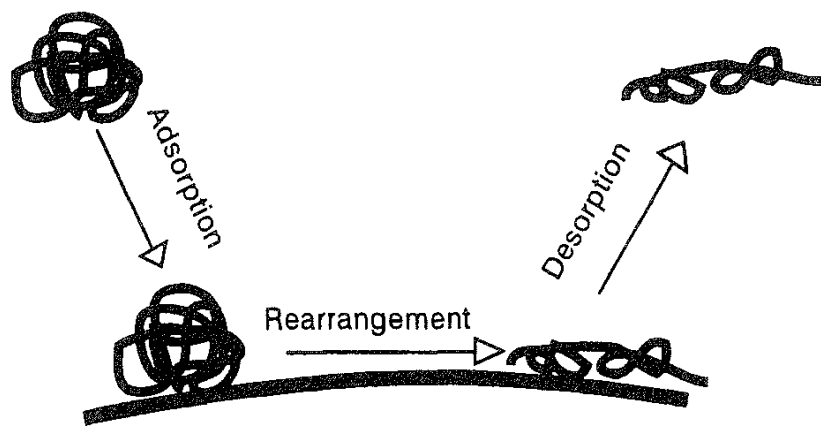


FIG. 1 Schematic picture illustrating the various stages in the interaction of a protein molecule with the surface of a PS latex particle.

rearrangement of the protein structure; both of these steps are controlled through a combination of ionic and hydrophobic interactions and hydrogen bonding. Finally, in some systems the structurally modified protein molecules may be released back into the bulk phase. These stages are now considered in more detail.

A. Adsorption

1. Dimensions of Adsorbed Protein Layers

The two parameters of the adsorption process that are the easiest to quantify and are therefore most frequently reported are the thickness of the adsorbed protein layer and the density of the protein on the surface. The increase in the thickness of the adsorbed protein layer and in surface coverage as a function of added protein are shown schematically in Figs. 2A and 2B, respectively.

(a) Protein Layer Thickness. The thickness of the adsorbed layer is listed for a variety of proteins on PS latex in Table 1. Although protein layer thickness on polystyrene latex particles has most frequently been determined by light scattering using photon correlation spectroscopy (PCS), small-angle X-ray scattering (SAXS) has also been used. Random-coil proteins such as the caseins give relatively thick layers (10–15.5 nm), whereas compact, globular proteins such as 3-lactoglobulin produce much thinner layers. The actual thickness of the adsorbed layer is dependent on a number of variables, including pH, surface charge on the particles, charge on the protein, and extent of denaturation of the protein. These are discussed in more detail later.

(b) Surface Loading. Maximum values of Γ , the protein surface coverage, for a variety of proteins are listed in Table 2. Γ is usually expressed in milligrams of protein adsorbed per square meter of surface. By measuring the proportion of the protein adsorbed at increasing concentrations of protein, the adsorption isotherm and hence the affinity of a protein for the surface can be determined. The amount of adsorbed protein is most commonly determined by the solution depletion technique, in which protein adsorbed onto the latex particles is separated from un-

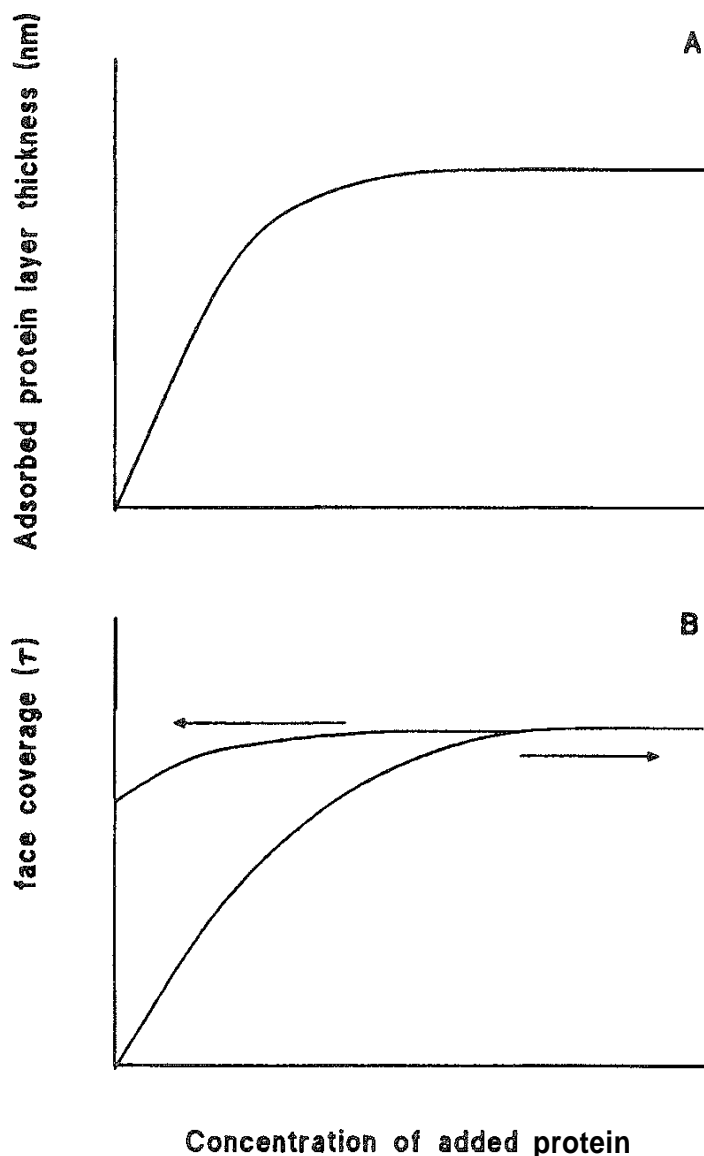


FIG. 2 Schematic diagram showing (A) the increase in layer thickness as a function of added protein and (B) the adsorption and desorption isotherms.

adsorbed protein by either centrifugation or filtration and the concentration of protein in the liquid phase is determined spectrophotometrically. An alternative method in which the amount of protein bound to the latex particles was determined directly using a modified Lowry procedure has been reported [17]. As with protein layer thickness, Γ values vary widely depending on the same variables. Plateau values of Γ for the adsorption of IgG from various species onto a wide variety of surfaces under various conditions are listed by Hidalgo-Alvarez and Galisteo-Gonzalez [18].

Protein adsorption to PS latex has also been determined by sedimentation field flow fractionation (SdFFF). The maximum surface coverages of β -casein and β -lactoglobulin on negatively charged PS latex calculated using this method were similar at around 1 mg/m^2 [19]. This figure, which was confirmed by amino acid analysis of the material irreversibly bound to the surface, was significantly lower

TABLE 1 Maximum Layer Thickness of Proteins on Polystyrene Latex Particles

| Protein | Surface charge | Thickness' (nm) | pH | Additions | Ref. |
|-----------------------------------|----------------|-----------------|-------------|-----------|------|
| β -Casein | — | 10-15 | 7.0 | Urea | 2 |
| | — | 11.1 | | | 3 |
| | — | 15.5 | | | 4 |
| | — | 14 | 7.2 | | 5 |
| | — | 15.5 | | | 6 |
| | — | 10* | | | |
| | — | 11.5 | | | |
| β -Casein, dephosphorylated | — | 11 | | 4,5 | |
| α_{s1} -Casein | — | 11.5 | 7.0 | Urea | 3 |
| | — | 10.5 | | | |
| α_{s2} -Casein | — | 8.5 | | | |
| κ -Casein, nonglycosylated | — | 11 | | | 7 |
| | — | 13 | | 2-ME | |
| | + | 10 | | 2-ME | |
| κ -Casein, glycosylated | — | 14 | | | |
| | — | 15 | | 2-ME | |
| | + | 12 | | 2-ME | |
| β -Lactoglobulin | — | 3.8, 2, 2* | 4.6, 7.2, 9 | | 8 |
| κ -Casein | — | 8.3 | | | 3 |
| | — | 13.7 | 7.0 | 2-ME | |
| Phosvitin | — | 15 | | | 4 |
| | — | 5 | | Urea | |

^aAll thicknesses determined by PCS except for those marked*. where SAXS was used

than that measured by solution depletion techniques, the difference being explained by the authors as being due to loosely associated protein that is not detected by the SdFFF method. Adsorption of IgG to latex particles at pH 7.0 determined using SdFFF showed that adsorption times were less than 10 min and the maximum value of Γ was 4.75 mg/m² [20].

2. Influence of pH and Charge on Protein Adsorption

Proteins are multivalent electrolytes with the side chains of their aspartic acid, glutamic acid, cysteine, tyrosine, histidine, lysine, and arginine residues being involved in acid–base equilibria. The net charge on a protein is therefore dependent on pH. At the isoelectric point (pI), the net charge on the molecule is zero, and at pH values below and above their pI, proteins are positively and negatively charged, respectively. The interaction of a protein with a surface will therefore vary with pH, and, in general, the maximum value of Γ is attained at or near the pI of the protein. Obviously, electrostatic interactions between the surface and the protein and between adjacent adsorbed protein molecules are therefore important.

TABLE 2 Maximum Surface Coverage (T) of Proteins on Polystyrene Latex Particles

| Protein | Surface charge | Max coverage Γ (mg/m ²) | pH | Ref. |
|--------------------------------------|----------------|--|--------------------|------|
| β -Casein | — | 3.1 | 7.0 | 5 |
| | — | 2.8 | 7.2 | 6 |
| O-Casein, dephosphorylated | — | 3.3 | 7.0 | 5 |
| κ -Casein, nonglycosylated | — | 5.0 | | 7 |
| | + | 3.0 | 7.0 | |
| κ -Casein, glycosylated | — | 3.0 | | |
| | + | 1.7 | | |
| RNAse | — | 1.9 | | 9 |
| a-Lactalbumin | — | 2 | 7.0 | |
| Lysozyme | — | 3.8 | | |
| | — | 4.1, 3.3, 1.8 | 4.5, 5.5, 3.3 | 10 |
| | — | 5.0, 3.5, 2.1 | | |
| Fibrinonectin | — | > 5 | 7.4 | 11 |
| Fibrinogen | — | 9.4 | | |
| Immunoglobulin | — | 5.8 | | |
| | — | 1.7, 2.8, 2.6, 1.7 | 3.0, 5.0, 7.0, 9.0 | 12 |
| Lipolase | + | 2.3 | 8.0 | 13 |
| | — | 0.1–0.6 | | |
| Savinase | — | 1.8 | 8.0 | 14 |
| | + | 0–0.2 | | |
| Bovine serum albumin | — | 1.2 | 6.5 | 15 |
| | — | 1.3, 9.4, 8.5, 0 | 3.5, 5.0, 6.0, 7.0 | 1 |
| | — | 1.8 | 7.0 | 10 |
| β -Lactoglobulin | — | 1.6, 1.3, 0.9 | 4.65, 7.2, 9.0 | 8 |
| F(ab') ₂ | — | 2.9, 2.8, 2.5 | 4.0, 7.0, 8.0 | 16 |
| | + | 4.2, 6.3, 3.6 | | |

One way to demonstrate the influence of electrostatic interactions on the interaction of proteins with surfaces is to use different forms of the same protein modified so as to change the net charge on the molecules. β -Casein contains five phosphoserine residues, each of which increases the net negative charge on the molecule by one unit. Enzymatic dephosphorylation cleaves off these phosphate residues and reduces the electronegativity of the protein. As shown in Tables 1 and 2, reduced repulsion between the protein and the negatively charged latex and between adjacent protein chains resulted in the formation of a thinner protein layer and a slight increase in the packing density of the adsorbed dephosphorylated protein.

κ -Casein, which has a net negative charge at pH 7.0, formed a thinner layer on a positively charged latex than on a negatively charged one. Naturally occurring

glycosylation of this protein increases its net negative charge by one unit for each sialic residue attached to the polypeptide chain and, as expected, also increases the thickness of the adsorbed protein layer on a negatively charged surface (Table 1).

Another way to investigate electrostatic interactions is to change the surface characteristics. Kawaguchi et al. [21] prepared a series of PS latices of the same particle size but different surface structures and measured the adsorption of human serum albumin (HSA), γ -globulin, cytochrome, myoglobin, and horseradish peroxidase. In general, hydrophilic surfaces had little affinity for proteins. Generally, increasing the hydrophobicity or the surface charge increased the affinity of proteins for the surface. Electrostatic interactions were found to be more important in determining the adsorption of polar and relatively small protein molecules. If adsorption of a protein onto a surface was largely determined by electrostatic interactions, it would be expected that these should be maximal in the region where the protein and the surface are oppositely charged. However, measurements of the adsorption of HSA and γ -globulin onto carboxylated surfaces showed that this was not the case [21]. This may be due either to conformational changes in the protein structure induced by adsorption to the surface, which weakens electrostatic interactions between the protein and the surface, or to deionization of groups on the surface of the protein, or to both.

In addition to the polarity of the surface, the density of charged groups on the surface also affects protein adsorption [22]. At carboxyl group densities less than 1 nm^{-2} , adsorption of bovine serum albumin to PS latex was both dominated by hydrophobic interactions and relatively sensitive to pH. At densities above two carboxyl groups per square nanometer, hydrogen bonding predominated irrespective of pH. The surface coverage of lysozyme and apolactalbumin (α -lactalbumin from which the calcium ion bound at the high affinity binding site has been removed and which is therefore less stable than the native protein) on negatively charged PS latices has also been shown to be dependent on the density of charged groups on the surface of the support. At pH 7, the adsorption of lysozyme, which is positively charged at this pH, is higher on a more negatively charged latex whereas that of apolactalbumin, which is negatively charged, is lower, demonstrating the importance of electrostatic interactions to protein adsorption [23]. Gallisteo and Norde [23] also showed that the maximum value of Γ was pH-dependent, being highest at a pH value just below the pI of the individual protein and decreasing at pH values to either side of the pI . As expected, the influence of the density of negative charge on the surface loading of these two proteins was also pH-dependent, with loading on the more highly negatively charged surface being greater at pH values below the pI of each protein.

As part of a study aimed at the rational development of immunoassays, the influence of surface characteristics on the interaction of $F(ab')_2$ fragments obtained by peptic digest of rabbit polyclonal IgG has been investigated [12]. The latex particles differed in their hydrophilic character and in the nature and density of their surface ionic groups. The most important force governing the adsorption of the protein onto the surface was shown to be hydrophobic interactions, although in low ionic strength buffers electrostatic interactions were also found to play a part. On anionic latices, maximum Γ values were obtained at pH

5, which was very close to the pI of these fragments (pH 5.3). At this pH, where the molecules have no net charge, molecular folding is at its most compact, and they can therefore pack closer together on the surface. On cationic latex, maximum adsorption was shifted to pH 7.0, showing the importance of electrostatic interactions at low ionic strength.

3. Effect of Inorganic Ions

According to the Derjaguin–Landau–Verwey–Overbeek (DLVO) theory, the stability of colloidal dispersions is determined by the surface potential, which is the sum of the attractive van der Waals forces and the repulsive electrostatic force arising from the diffuse electrical double layer around the surface of charged particles. Decreasing the surface potential by increasing the ionic strength reduces electrostatic repulsion and promotes aggregation.

The adsorption of lysozyme and apolactalbumin was enhanced by low ionic strength, particularly around the pI of the protein [23], and the surface coverage of HSA and γ -globulin on amphoteric polystyrene latex was lower at higher ionic strength irrespective of pH [21]. The influence of ionic strength on the colloidal stability of PS latex coated with either $F(ab')_2$ fragments from IgG or bovine serum albumin has been investigated [24,25]. At low surface coatings of protein, the particles behaved as expected, with increasing ionic strength promoting aggregation. At high surface concentrations of $F(ab')_2$, although aggregation occurred at moderate ionic strength, at high ionic strength the coated particles did not aggregate. The explanation offered for these observations was that the hydration repulsion force arising from counterions adsorbed onto the protein dominated interactions between particles at short range.

Adding NaCl to negatively charged PS latex precoated with β -casein resulted in a 4–5nm reduction in the thickness of the protein layer [5]. This was due to suppression of ionization of the negatively charged groups located in the hydrophilic tail region of the protein and on the surface of the latex, reducing electrostatic repulsion. Increasing the NaCl concentration further caused aggregation of the coated particles. When low concentrations of β -casein were added to latex in the presence of 50mM NaCl, aggregation occurred [4,5]. This was due to bridging flocculation, where suppression of ionization of the charged groups on the protein and the surface permitted protein molecules to span between partially coated latex particles.

Calcium ions have also been shown to decrease the thickness of preadsorbed β -casein layers on negatively charged PS latex [5]. The maximum decrease in layer thickness was 6nm. The concentration of calcium ions required to achieve this reduction in adsorbed protein layer thickness was around 1% of the NaCl concentration. Comparison with the behavior of preadsorbed layers of dephosphorylated β -casein, where the reduction in layer thickness was less, indicated that the calcium ions were largely binding to negatively charged phosphate groups in the tail region, reducing repulsion between this portion of the molecule and the surface and also between adjacent protein tails. Higher concentrations of calcium ions caused aggregation of the coated particles.

B. Conformation of Adsorbed Protein

The conformation that protein molecules adopt at an interface is not necessarily the same as that which they possess in solution. A variety of physical and biochemical methods have therefore been employed to determine the conformation of both random coil and globular proteins when adsorbed to latex particles. Since they are relatively lacking in extensive secondary structure, the results obtained with the former are simpler to interpret, and these are therefore considered first.

1. Random Coil Proteins

The caseins, the major milk proteins, are classic examples of random coil proteins. They are generally good emulsifiers, and the interfacial conformation of β -casein in particular has been studied in some detail both in model emulsions and on polystyrene latex. p-Casein has a high content of proline residues, which serve to disrupt the formation of ordered regions of secondary structure, and the molecule has a relatively open random coil conformation. In addition, it has a distinctly amphiphilic character. The N-terminal 21 amino acid region, which includes a cluster of four phosphoserine residues, has a net charge of -12 at pH 6.6 and is therefore markedly hydrophilic. The remaining large hydrophobic domain has no net charge at this pH. In solution, at temperatures above about 5°C , the molecules undergo a highly cooperative reversible self-association to form polymers with a structure similar to that of a detergent micelle. As measured by PCS, at pH 7.0 this protein formed a monolayer about 15 nm thick on negatively charged PS latex (Table 1). Dephosphorylation using acid phosphatase reduced the net negative charge on the protein, specifically in the N-terminal region, and resulted in the formation of an adsorbed protein layer only 11 nm thick. Addition of the proteolytic enzyme trypsin to latex particles precoated with either form of the protein resulted in a biphasic decrease in the layer thickness as the adsorbed protein was hydrolyzed. The rate of the initial rapid decrease in layer thickness was greater with the dephosphorylated form of the protein, although the rate of the second, slower phase and the thickness of the residual layer (about 5 nm) were the same [26,27]. It appears that the negatively charged N-terminal region of both types of the protein forms a tail that projects from the negatively charged surface, with the remaining hydrophobic portion of the molecule lying close to the surface (Fig. 3A). Removal of the phosphate groups reduces the electrostatic repulsion between the tail and the surface and also between adjacent protein tails, decreasing layer thickness and coincidentally permitting easier access of trypsin molecules to susceptible bonds in this region. The same conformation has been proposed for this protein at the oil/water interface on the basis of proteolytic experiments [28] and also at the air/water interface on the basis of small-angle neutron scattering measurements [29,30]. Small-angle X-ray scattering (SAXS) of the protein on PS latex showed that most of the protein lies close to the surface, with part of the polypeptide chain extending out into the aqueous phase [8]. Neutron reflection studies of this protein adsorbed onto a chemically modified silicon surface also indicated a two-layer conformation with a dense layer 2.3 nm thick and a surface coverage of 1.9mg/m^2 lying close to the surface and an external layer with a thickness of 3.5 nm and a protein volume fraction of 12% extending into the aqueous phase [31].

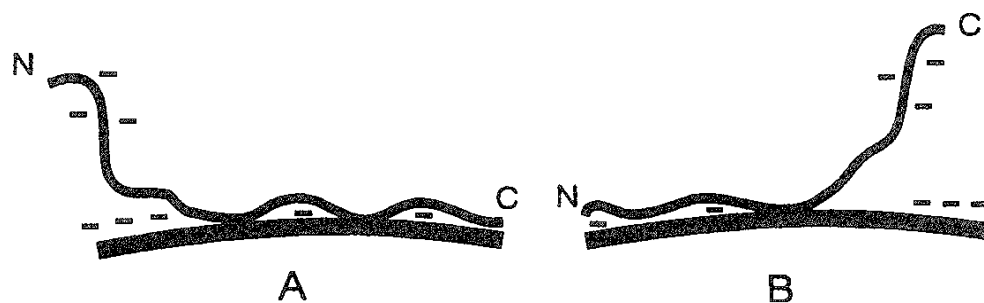


FIG. 3 The probable conformation adopted by β -casein (A) and κ -casein (B) at pH 7.0 on the surface of a negatively charged PS latex particle. N and C indicate the terminals of the proteins.

The conformation of another milk protein, κ -casein, on PS latex particles has also been investigated [3,7,32]. Much of the surface of the casein micelles, the submicrometer-sized particles, which contain approximately 80% of the proteins present in milk, is thought to be formed by the κ -casein component. This protein has a highly electronegatively charged C-terminal tail that projects into the aqueous phase in the form of a "hairy layer." Through a combination of electrostatic and steric repulsion, this layer prevents individual micelles from aggregating. In the manufacture of cheese, proteolysis by the enzyme chymosin at a specific phenylalanine-methionine bond leads to the release of the charged tail, the caseinomacropetide (CMP). This reduces repulsion between individual micelles, allowing aggregation to occur. κ -Casein adsorbs readily onto both positively and negatively charged PS latices, the surface coverage and layer thickness being dependent on the surface charge and the form of the protein (Tables 1 and 2). Addition of 2-mercaptoethanol to κ -casein prior to adsorption onto latex particles increased the thickness of the adsorbed layer as a result of reduction of the intermolecular disulfide bridges (Table 1). Addition of chymosin to κ -casein-coated latex particles caused a 10 nm decrease in the thickness of the adsorbed protein layer [32]. This was similar to the 7–8 nm chymosin-catalyzed decrease in the hydrodynamic radius of casein micelles determined using the same PCS technique [33]. The peptide released from the surface of the coated latex particles was shown to be CMP, indicating that κ -casein binds to negatively charged PS latex particles with the same orientation it adopts in the micelles, i.e., with the C-terminal tail projecting into the aqueous phase (Fig. 3B). In the presence of calcium ions, the proteolyzed particles aggregated, the rate of aggregation being dependent on both the concentration of calcium ions and the degree of glycosylation of the protein. Again, this is very similar to the behavior of micelles in milk, and PS latex aggregation appears to be due to unhydrolyzed κ -casein molecules forming bridges between individual PS particles.

2. Globular Proteins

Due to their more highly folded structure, globular proteins can potentially undergo more extreme conformational changes when adsorbed to surfaces, and interpretation of these structural changes is consequently more complex. At the

simplest level, if the molecular dimensions of a protein are known, then, purely on the basis of the measurements of the maximum surface coverage, information on the orientation of the molecules on the surface can be obtained (Fig. 4). IgGs and their $F(ab')_2$ fragments apparently adsorb onto hydrophobic surfaces in an end-on orientation but provided the proteins have a high charge density opposite that of the surface, the orientation on negatively charged hydrophilic latex switches to side-on in order to maximize electrostatic interactions [34].

More detailed information on the conformation of adsorbed proteins has been obtained by using a variety of physical techniques. Although fluorescently labeled HSA and γ -globulin molecules have been shown to undergo conformational changes consistent with the loss of internal fluidity when adsorbed onto polystyrene/acrolein latexes [35], in general the application of spectroscopic techniques to the analysis of protein conformation at solid interfaces is complicated by the scattering and adsorption of light caused by the particles themselves. This can be reduced either by using very small particles that adsorb and/or scatter light to a much smaller degree or by using particles that display negligible adsorption and scattering. Using the latter approach, circular dichroism (CD) and fluorescence anisotropy were used to detect changes in the conformation of the proteolytic enzyme subtilisin 309 resulting from its adsorption to a novel hydrophobic perfluoroalkoxy fluorocarbon latex [36]. At $\Gamma = 0.5 \text{ mg/m}^2$, the fluorescence of the adsorbed protein was quenched and an increase in the α -helix content was detected by CD. This finding was in contrast to the decrease in α -helix content that is usually detected when proteins adsorb onto hydrophilic silica particles. At $\Gamma = 2 \text{ mg/m}^2$, which represents full surface coverage, the fluorescence and α -helix content of the adsorbed protein were essentially the same as in solution, indicating that in this instance the extent of conformational changes in the structure of adsorbed proteins is dependent on the density of packing of the molecules on the surface.

In addition to spectroscopic techniques, microcalorimetry, which measures transition enthalpies (ΔH) and transition temperatures (T_o) as proteins undergo cooperative unfolding, has also been applied to the study of conformational changes resulting from protein adsorption. Since PS latex particles show no thermal transitions over the temperature range of interest for protein structural analysis, their presence does not interfere with this technique. HSA, a three-domain protein whose

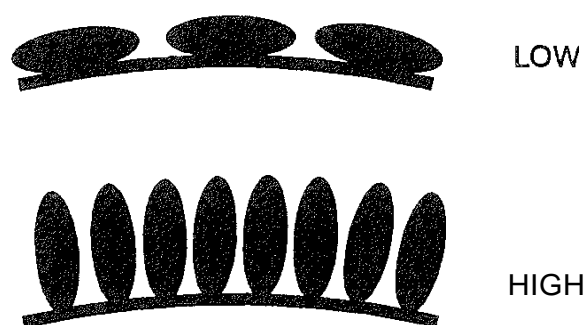


FIG. 4 Schematic diagram showing a protein molecule adsorbing to the surface of a latex particle in the side-on conformation at low protein loading and the end-on conformation at high protein loading.

structure unfolds readily at low concentrations of the denaturant guanidine hydrochloride (GuHCl), also unfolds readily on the surface of PS latex, as evidenced by the complete absence of thermal transitions as determined by microcalorimetry of HSA-coated polystyrene latex (Fig. 5) [37]. Similarly, hen lysozyme, which is structurally a more stable protein, unfolding at much higher concentrations of GuHCl, does not undergo a thermal transition when adsorbed onto PS latex. However, when this protein was adsorbed onto contact lenses made from anionic hydrogels, a thermal transition was clearly seen. Even here there were differences compared with the behavior of the protein in solution. The T_m was 6°C lower, the peak was broader, and the transition enthalpy was smaller than that measured in solution, indicating that some change had occurred in the structure. Adsorption of streptavidin, which is stable to denaturation even at very high concentrations of GuHCl, onto PS latex particles had little effect on the appearance of the thermograms compared with that of the protein in solution, indicating that association with the surface had little effect on protein structure. Egg white lysozyme and bovine milk α -lactalbumin both lost most of their ordered secondary structure upon adsorbing onto hydrophobic negatively charged polystyrene latex [38,39]. α -Lactalbumin adsorbed onto negatively charged latex particles did not undergo the native-to-apo transition that the soluble protein undergoes at low pH. Adsorption of α -lactalbumin onto the hydrophilic surface of hematite dispersions also resulted in almost complete loss of secondary structure, again indicating the relative instability of this protein. In contrast, most of the secondary structure of lysozyme, which is a more stable protein, was retained on this surface. Proton

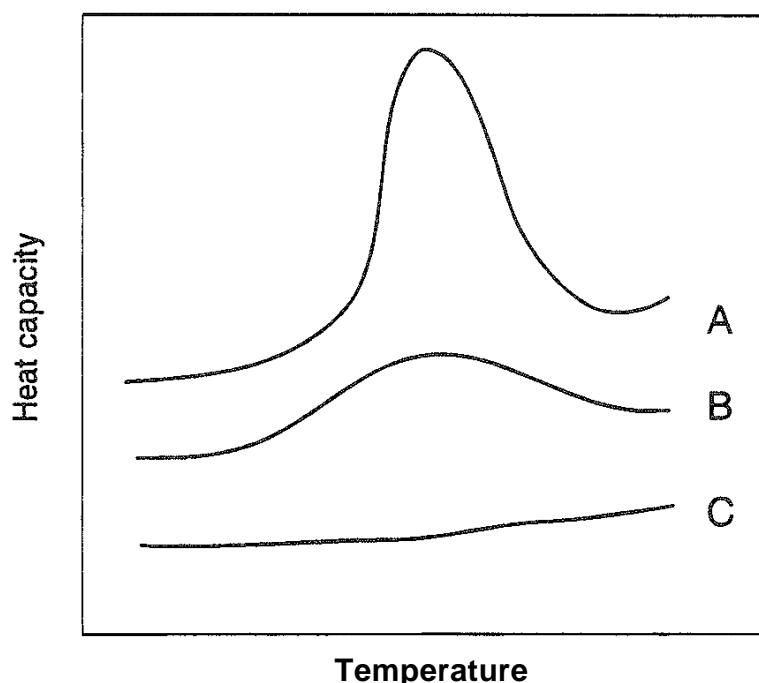


FIG. 5 Idealized thermograms of (A) a globular protein in solution, (B) the same protein adsorbed onto PS latex particles with partial retention of secondary folding, and (C) the same protein adsorbed onto latex particles with extensive loss of secondary folding.

titration measurements showed an increase in the average pK of carboxyl groups in both of these proteins, suggesting that some carboxyl groups are relatively close to the latex surface and/or that unfolding of the protein structure during adsorption diminishes electrostatic repulsion between the remaining carboxylic groups. Microcalorimetric measurements of the globular milk protein β -lactoglobulin showed that a significant amount of secondary structure was retained after adsorption onto negatively charged PS latex [19].

C-reactive protein (CRP), which is thought to play an important role in immunomodulation, has been adsorbed onto latex beads and shown to bind a variety of plasma proteins, including some, such as the immunoglobulins, that are not bound by the soluble form of the protein [40]. This alteration in specificity may be caused either by conformational changes in the adsorbed protein or by an increase in the number of binding events due to an increase in the density of the reacting species, or by a combination of the two. The results obtained with the PS latex-immobilized model system strongly support the hypothesis that CRP *in vivo* possesses lectin function only when it is immobilized on the surface of inflamed tissue cell membranes, allowing it to bind bacterial polysaccharides, etc., rendering them susceptible to phagocytosis.

Although almost all of these studies have dealt with the adsorption of single protein species onto surfaces, in biological systems surfaces are usually exposed to mixtures of proteins. Little work has been reported on whether different species of proteins segregate and form patches on the surface. Brynda et al. [41] measured excitation energy transfer between fluorescein donors attached to bovine serum albumin molecules and tctrainethylrhodanine acceptors attached to other molecules of the same protein when the molecules were adsorbed onto hydrophobized silica slides, which would be expected to have surface properties similar to those of polystyrene latex particles. Unlike the situation in solution, when denaturation resulted in aggregation, the surface-adsorbed protein molecules did not appear to aggregate as a result of the loss of their secondary structure. When the adsorption of mixtures of BSA with IgG was studied, there was no evidence of patch formation. Instead, molecules of the different protein species appeared to adopt a random distribution on the surface.

C. Stability of Adsorbed Protein Layers

The more stable globular proteins such as lysozyme, α -lactalbumin, and ribonuclease, which appear to retain most or all of their native structure when adsorbed onto PS latex particles, would be expected to be desorbed more readily by dilution than proteins such as IgG, serum albumin, and hemoglobin, which appear to lose most of their secondary structure. Haynes and Norde [38] investigated the desorption of lysozyme and α -lactalbumin from negatively charged PS latex. At pH 7.0, dilution did not result in any detectable change in the concentration of bound protein, indicating that binding under these conditions is irreversible by dilution. Adsorbed lysozyme was also not displaced by changing pH over the range 2–12 or by increasing the temperature to 95°C. The behavior of α -lactalbumin was similar, except that above pH 11.5, where both the protein and the surface have a large

negative charge, displacement did occur. Adsorption of $F(ab')_2$, which belongs to the latter group of proteins, was also not reversed by dilution [12].

SdFFF measurements of the desorption of IgG as a result of dilution indicated that slow desorption of bound protein to a level of about 20% of the original loading occurred over the first 2 h after dilution. Negligible desorption occurred over the following 6 h [20]. Dilution has also been reported to cause significant release of radiolabeled IgG from negatively charged polystyrene latex [42]. The homogeneous exchange reaction between radiolabeled IgG molecules in the bulk solution and those adsorbed onto the surface of negatively charged polystyrene latex was found to follow first-order kinetics, with an apparent exchange rate constant of $(2.3 \pm 0.4) \times 10^{-5} \text{ cm/h}$ [42]. IgG has also been shown to desorb from negatively charged PS latex on redispersion at pH values between 5 and 8 [43]. In addition, a significant amount of the preadsorbed IgG was displaced by incubation with monomeric bovine serum albumin.

Adsorbed proteins can be displaced by small surface-active molecules such as detergents. Although this has been widely reported in publications dealing with protein-stabilized emulsions, little appears to have been published dealing with the same proteins adsorbed onto latex particles. Figure 6 shows the desorption of β -casein from negatively charged PS latex particles and the accompanying decrease in protein layer thickness as a result of the addition of increasing concentrations of the nonionic detergent Tween 20 (unpublished data).

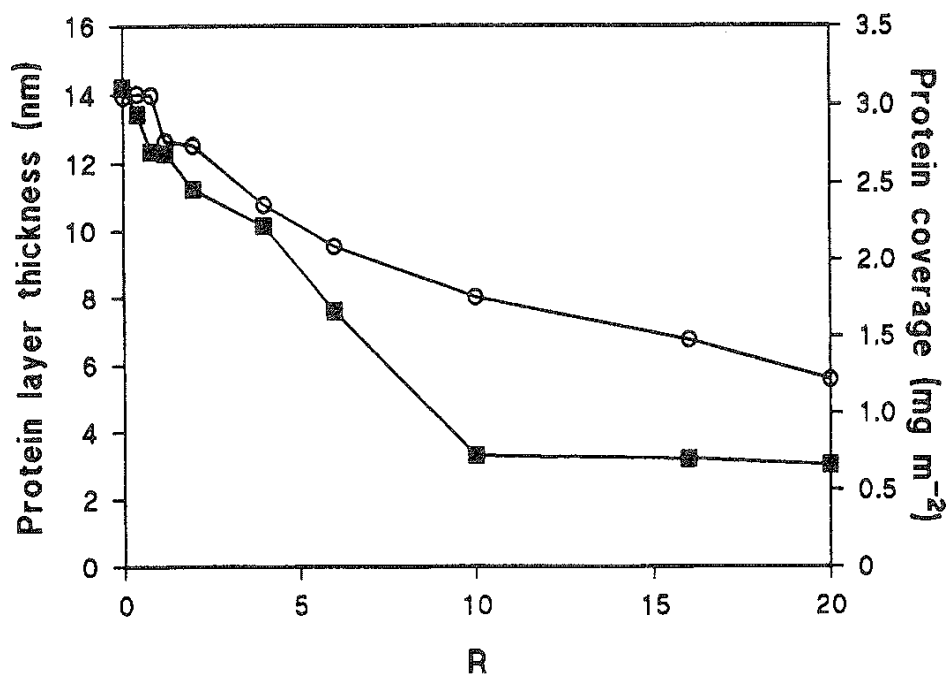


FIG. 6 The displacement of bovine β -casein from the surface of a negatively charged PS latex by the nonionic detergent Tween 20, showing that protein displacement is accompanied by a decrease in the thickness of the adsorbed protein layer. (○) Protein coverage; (■) hydrodynamic layer thickness. R is the molar ratio of detergent to protein.

Those conformational changes that fluorescently labeled human serum albumin and γ -globulins undergo when adsorbed onto polystyrene/acrolein latexes were not reversed on desorption [17]. This therefore acts as a useful marker for the exchange of adsorbed molecules with nonadsorbed molecules. Even when the amount of latex in a sample was very low compared to the total amount of protein, i.e., the percentage of adsorbed protein was small at any one time, eventually all of the protein was found to have undergone this conformational change, indicative of a relatively active exchange process.

D. Controlling Protein Adsorption

1. Decreasing Protein Adsorption

The adsorption of serum proteins in general, and of fibrinogen in particular, onto surfactant-treated polystyrene latex is accompanied by displacement of surfactant molecules [43]. Using a series of polyoxyethylene-containing block copolymer surfactants, the stability of the adsorbed surfactant layer to displacement by protein was shown to be dependent on a combination of its surface concentration, layer thickness, and surface dynamics. Pluronic (polyoxyethylene-containing) surfactants adsorbed onto the surface of PS particles made the hydrophobic surface hydrophilic, minimizing protein adsorption and increasing the blood circulation half-life from a few minutes to more than 13 h [37,45]. The most stable coating was not displaced by incubation with either HSA or human fibrinogen. However, incubation with whole plasma resulted in the displacement of 30% of the surfactant [44,46]. Coating PS latex beads with poly(vinyl alcohol) also decreased nonspecific protein adsorption [47].

2. Increasing the Specificity of Protein Adsorption

Various methods have been adopted to alter the selectivity of the relatively non-specific adsorption of protein molecules onto polystyrene latex. By activating the end of the pluronic surfactant molecules and forming, for example, the 2-pyridyl disulfide derivative, it was possible to make the surface specific for thiol-containing proteins and peptides, which could subsequently be desorbed by addition of low molecular weight thiol-containing compounds [47]. Cibacron Blue F3G-A covalently attached to poly(vinyl alcohol)-coated PS microspheres specifically adsorbed BSA up to a concentration of 60mg of protein per gram of latex beads [48].

Phospholipids adsorb onto positively charged amidine PS latex initially as a monolayer but subsequently as lipid bilayers [49]. By incorporating the cholera toxin receptor monosialoganglioside (GM1) into these bilayers, specific binding of cholera toxin has been achieved [50].

V. CONCLUSIONS

Proteins adsorbed onto polystyrene latex particles have proved to be good models for the interfacial behavior of proteins in processed foods. The behavior of caseins on latex particles appears to be very similar to that at the oil/water interfaces of emulsions, at the air/water interface of foams, and at the surface of casein micelles.

Investigations into the behavior of mixtures of proteins together with other low molecular weight food grade emulsifiers to move the model system closer to real processed foods would be an obvious development of these studies.

In the area of fouling and implant rejection, progress has been made in understanding how proteins interact with these PS latex surfaces and how this interaction can be controlled. Again, the model will be improved as the complexity of the system is increased. The demonstration that the surface of latex particles can be modified either chemically or by adsorption of cell surface constituents opens up new possibilities for the use of such systems in understanding a host of complicated cellular events including the development of colloid-based drug delivery systems.

Latex agglutination kits are becoming increasingly important in their own right as diagnostic tools. It is therefore very likely that in the future much more effort will be expended in optimizing the interaction of antibodies and antigens with the support in order to improve their range and effectiveness.

ACKNOWLEDGMENTS

Core funding for the Hannah Research Institute is provided by The Scottish Office Agriculture, Environment and Fisheries Department.

REFERENCES

1. E. Piskin, A. Tuncel, A. Denizli, and H. Ayhan, *J. Biomater. Sci. Polym. Ed.* 5:341 (1994).
2. D. G. Dalgleish and J. Leaver, in ***Food Polymers, Gels and Colloids*** (E. Dickinson, ed.), Royal Society of Chemistry, Cambridge, UK, 1991. pp. 113–122.
3. D. G. Dalgleish, *Colloids Surf. B: Biointerfaces* 1:1 (1993).
4. D. G. Dalgleish, *Colloids Surf.* 46:141 (1990).
5. D. V. Brooksbank, C. M. Davidson, D. S. Horne, and J. Leaver. *J. Chem. Soc., Faraday Trans.* 89:3418 (1993).
6. A. R. Mackie, J. Mingins, and A. N. North, *J. Chem. Soc., Faraday Trans.* 87:3043 (1991).
7. J. Leaver, D. V. Brooksbank, and D. S. Horne, *J. Colloid Interface Sci.* 162:463 (1994).
8. A. R. Mackie, J. Mingins, and R. Dann, in ***Food Polymers, Gels and Colloids*** (E. Dickinson, ed.), Royal Society of Chemistry, Cambridge, UK, 1991, pp. 96–112.
9. A. Kondo and K. Higashitani, *J. Colloid Interface Sci.* 150:344 (1992).
10. W. Norde, *Cells Mater.* 5:97 (1995).
11. M. D. Bale, D. F. Mosher, L. Wolfahrt, and R. C. Sutton, *J. Colloid Interface Sci.* 125:516 (1988).
12. J. L. Ortega Vinuesa, M. J. Galvez Ruiz, and R. Hildago-Alvarez, *Langmuir* 12:3211 (1996).
13. S. Duinhoven, R. Poort, G. van der Voert, W. G. M. Agterof, W. Norde, and J. Lyklema, *J. Colloid Interface Sci.* 170:351 (1995).
14. S. Duinhoven, R. Poort, G. van der Voert, W. G. M. Agterof, W. Norde, and J. Lyklema, *J. Colloid Interface Sci.* 170:340 (1995).

15. J. Revilla, A. Elaissari, P. Carriere. and C. Pichot, *J. Colloid Interface Sci*, *180*:405 (1996).
16. J. L. Ortega Vinuesa and R. Hildago-Alvarez, *J. Biomater. Sci. Polym*, Ed. 6:269 (1994).
17. S. Slomkowski and T. Basinska, *ACS Symp. Ser.* *492*:328 (1992).
18. R. Hidalgo-Alvarez and F. Galisteo-Gonzalez, *Heterog. Chem. Rev.* *2*:249 (1995).
19. K. D. Caldwell, J. Li, J.-T. Li, and D. G. Dalgleish, *J. Chromatogr.* *604*:63 (1992).
20. Y. Jiang, J. C. Giddings, and R. Beckett, in *Proteins at Interfaces II: Fundamentals and Applications* (T. A. Horbett and J. L. Brash, eds.), American Chemical Society, Washington, DC, 1995, pp. 405–419.
21. H. Kawaguchi, H. Amagasa, T. Hagiya, N. Kimura, and Y. Ohtsuka, *Colloids Surf.* *13*:295 (1985).
22. J.-Y. Yoon, H.-Y. Park, J.-H. Kim, and W.-S. Kim, *J. Colloid Interface Sci.* *177*:6134 (1996).
23. F. Gallisteo and W. Norde. *Colloids Surf. B: Biointerfaces* *4*:375 (1995).
24. J. A. Molina-Bolivar, F. Galisteo-Gonzalez, and R. Hidalgo-Alvarez, *Colloids Surf. B: Biointerfaces* *8*:73 (1996).
25. J. A. Molina-Bolivar, F. Galisteo-Gonzalez, and R. Hidalgo-Alvarez, *Phys. Rev.* *55*:4522 (1996).
26. J. Leaver and D. S. Horne, in *Food Colloids and Polymers: Stability and Mechanical Properties* (E. Dickinson and P. Walstra, eds.), Royal Society of Chemistry. Cambridge, UK, 1993, pp. 332–340.
27. D. G. Dalgleish and J. Leaver, *J. Colloid Interface Sci.* *141*:288 (1991).
28. J. Leaver and D. G. Dalgleish, *Biochem. Biophys. Acta* *1041*:217 (1990).
29. E. Dickinson, D. S. Horne, J. S. Phipps, and R. M. Richardson, in *Food Colloids and Polymers: Stability and Mechanical Properties* (E. Dickinson and P. Walstra, eds.) Royal Society of Chemistry, Cambridge, UK, 1993, pp. 396–401.
30. E. Dickinson. D. S. Home, and R. M. Richardson, *Food Hydrocolloids* *7*:497 (1993).
31. G. Fragneto, R. K. Thomas, A. R. Rennie, and J. Penfold, *Science* *267*:657 (1995).
32. J. Leaver and D. S. Horne, *J. Colloid Interface Sci.* *181*:220 (1996).
33. P. Walstra, V. A. Bloomfield, G. J. Wei, and R. Jenness, *Biochim. Biophys. Acta* *669*:258 (1977).
34. J. Buijs, J. W. Th. Lichtenbelt, W. Norde. and J. Lyklema, *Colloids Surf. B: Biointerfaces*, *5*:11 (1995).
35. S. Slomkowski, D. Kowalczyk, T. Basinska, and F. W. Wang, *ACS Symp. Ser.* *548*:449 (1994).
36. M. C. L. Maste, E. H. W. Pap, A. van Hoek, W. Norde, and A. J. W. G. Visser, *J. Colloid Interface Sci.* *180*:632 (1996).
37. G. Yan, J.-T. Li, S.-C. Huang, and K. D. Caldwell, *ACS Symp, Ser.* *602*:256 (1995).
38. C. A. Haynes and W. Norde, *J. Colloid Interface Sci.* *169*:313 (1995).
39. C. A. Haynes, E. Sliwinsky, and W. Norde, *J. Colloid Interface Sci.* *164*:394 (1994).
40. E. Kottgen, B. Hell. A. Kage, and R. Tauber, *J. Immunol.* *149*:445 (1992).
41. E. Brynda, V. Hylady, and J. D. Andrade, *J. Colloid Interface Sci.* *139*:374 (1990).

42. V. Ball, P. Huetz, A. Elaissari, J.-P. Cazenave, J.-C. Voegel, and P. Schaaf, *Proc. Natl. Acad. Sci. USA* *91*:7330 (1994).
43. J. M. Peula, R. Hidalgo-Alvarez, and F. J. de las Nieves, *J. Biomater. Sci. Polym. Ed.* *7*:231 (1995).
44. J.-T. Li and K. D. Caldwell, *Colloids Surf. B; Biointerfaces* *7*:9 (1996).
45. M. E. Norman, P. Williams, and L. Illum, *Biomaterials* *13*:841 (1992).
46. T. I. Armstrong, M. C. Davies, and L. Illum, *J. Drug Targeting* *4*:389 (1997).
47. A. Tuncel, A. Denizli, D. Purvis, C. R. Lowe, and E. Piskin, *J. Chromatogr.* *634*:161 (1993).
48. J.-T. Li, J. Carlsson, J.-N. Lin, and K. D. Caldwell, *Bioconjugate Chem.* *7*:592 (1996).
49. A. M. Carmona-Ribeiro and T. M. Herrington, *J. Colloid Interface Sci.* *156*:19 (1993).
50. S. M. Sicchierolli and A. M. Carmona-Ribeiro, *J. Phys. Chem.* *100*:16771 (1996).

Adsorption of Pharmaceutical Organic Compounds onto Porous Materials

KEIJI YAMAMOTO Department of Pharmaceutical Technology, Chiba University, Chiba, Japan

SIRIPORN OKONOGI Department of Pharmaceutical Technology, Chiang Mai University, Chiang Mai, Thailand

- I. Introduction
- II. Adsorption onto Porous Materials
- III. Improving Dissolution
- IV. Effect of Adsorption on Chemical Stability
- V. Fluorescence Spectroscopic Studies of Interaction
- VI. Therapeutic Use of Porous Materials
- VII. Conclusions
- References

I. INTRODUCTION

When poorly water soluble drugs are administered in solid dosage forms, the dissolution rate is often considered a rate-limiting factor in the adsorption process. The rate of dissolution of these drugs depends on the effective surface area and the energy state within the drug crystals [1]. The amorphous form of the drug can exhibit a much higher dissolution rate and better bioavailability than the crystalline form. Various techniques have been used to reduce the crystallinity or to obtain the amorphous form of a crystalline drug [2]. The formation of an amorphous solid is usually achieved by freeze drying, spray drying, solid dispersion, condensation from the vapor, and milling. The rapid cooling of indomethacin liquid causes the glass formation of the drug [3]. Egawa et al. [4] reported that amorphous cefalexin prepared by pulverization and lyophilization showed different dissolution behavior. According to Yamaguchi et al. [5], the amorphous 16-membered macrolide compound prepared by different conditions of spray drying showed different degrees of solubility and stability.

When a system consists of multiple components, as pharmaceutical formulations do, it is feasible that amorphous solid-state solutions can form in analogy to liquid solutions. It has been reported that some crystalline medicinal compounds in mixtures with adsorbents or porous powders gradually became amorphous during storage. These phenomena are believed to be caused by the adsorption of organic medicinal molecules onto the surface of porous powders, as organic compounds have relatively higher vapor pressure than inorganic compounds.

In this chapter we review the adsorption phenomena that can be commonly encountered in pharmaceuticals. As our interest was focused on the changes in molecular states and pharmaceutical properties before and after adsorption, the techniques used were a little different from those of mainstream adsorption research works. The purpose of this chapter is to report general information concerning the gaseous adsorption of pharmaceutical organic compounds onto porous materials. The adsorption technique may have numerous pharmaceutical applications that remain to be explored.

II. ADSORPTION ONTO POROUS MATERIALS

The changes in the X-ray diffraction patterns of mixtures of 30% flufenamic acid (FFA) and 70% of either florite R or florite S after storage at 0% RH and 40°C are shown in Fig. 1 [6]. In the mixture of FFA and florite R, the intensities of X-ray diffraction peaks due to FFA crystals gradually decreased with period of storage, and a halo pattern was observed after 5 weeks. In contrast, these X-ray diffraction peaks were still observed in the FFA–florite S mixture even after storage for 8

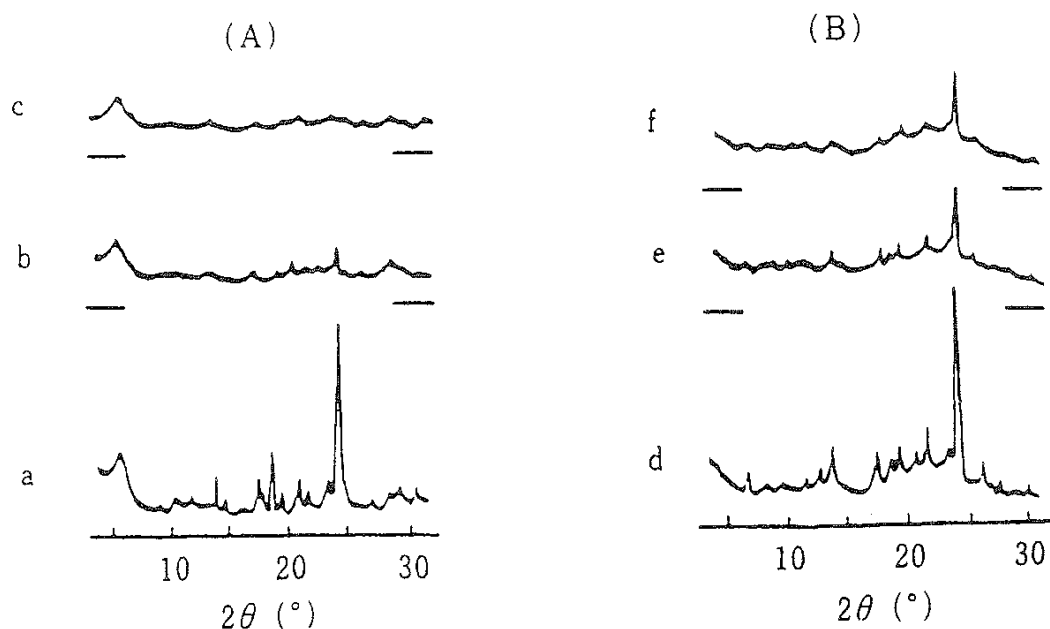


FIG. 1 Changes in X-ray diffraction patterns of mixtures of 30% FFA and 70% of either florite R (A) or florite S (B) after storage at 0% RH and 40°C. Florite R: (a) Fresh mixture; (b) stored for 4 weeks; (c) stored for 5 weeks. Florite S: (d) Fresh mixture; (e) stored for 4 weeks; (f) stored for 8 weeks. (From Ref. 6.)

weeks, though the crystallinity of the FFA was reduced. The X-ray diffraction data indicated that florite R has a greater capability to induce the transformation of FFA into the amorphous state than does florite S. This was attributed to the difference in the chemical compositions of florite R and florite S, florite R being composed primarily of porous calcium silicate and florite S of porous silicon dioxide,

The differential scanning calorimetric (DSC) curves of freshly prepared mixtures of FFA and either florite R or florite S in various mixing ratios are shown in Fig. 2. In the first run of the mixtures of FFA and florite R, those with 30% FFA showed a broad endothermic peak between 90 and 135°C. The mixtures containing 60% FFA showed two overlapping endothermic peaks; the first peak was broad and observed at low temperature, and the second peak was due to the melting of FFA crystals. By increasing the mixing ratio of FFA, the area of the broad peak was reduced while the second peak became more predominant. None of the mixtures showed any peak in the second run. In the first run of the mixtures of FFA and florite S, the mixtures that were 30-60% FFA showed a sharp endothermic peak due to the melting of FFA at 135°C. In the second run, they showed two endothermic peaks, the first peak attributable to the disordered FFA in the pores and the second to melting of the crystalline FFA.

The DSC results confirmed that florite R had the greatest ability to induce the transformation of FFA into the amorphous state. They also indicated that FFA

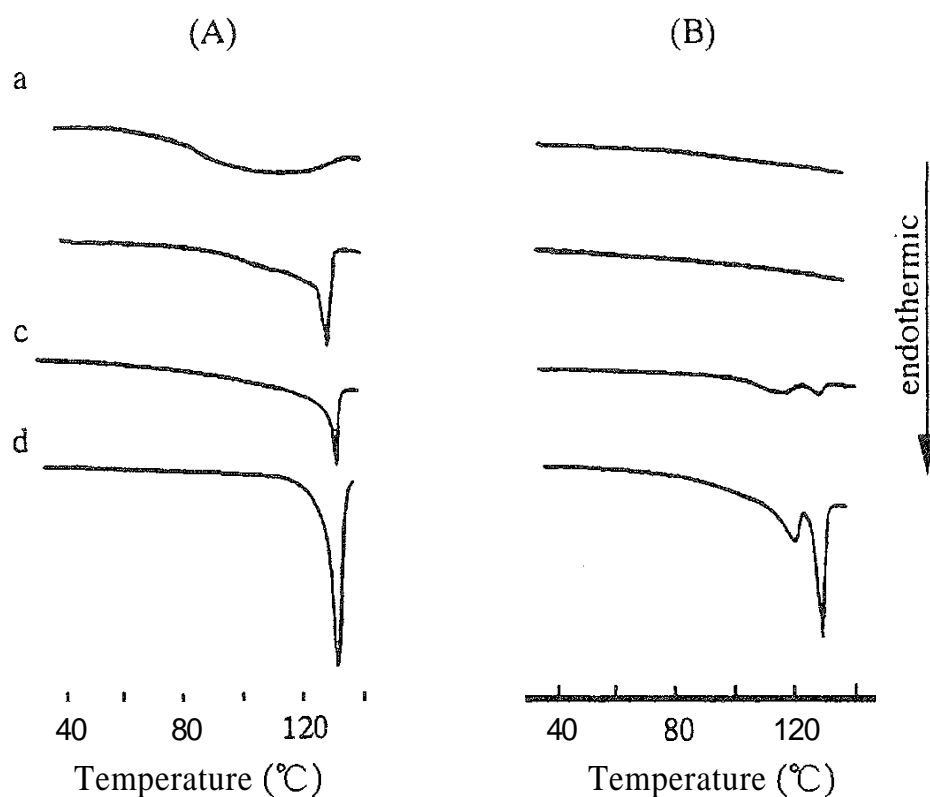


FIG. 2 DSC curves of mixtures of FFA and either florite R or florite S in various mixing ratios. (A) First run; (B) second run. (a) 30% FFA in florite R; (b) 60% FFA in florite R; (c) 30% FFA in florite S; (d) 60% FFA in florite S. (From Ref. 6.)

had the following three phases in the mixture with porous powders: a crystalline state that gave a sharp endothermic peak, a disordered state that gave a broad endothermic peak at low temperature, and an amorphous state that gave no peak. The IR spectroscopic results indicated that in the mixtures of FFA and florite R, storage or grinding induced the transformation of FFA into the amorphous ionic state, while in the corresponding mixtures of FFA and florite S there was no change in the molecular state of the drug.

The powder X-ray diffraction patterns of porous crystalline cellulose (PCC) – 10% ethenzamide (EZ) mixtures before and after storage of the mixtures for 1 month at 40°C and 0, 40.0, and 97.0% relative humidity are shown in Fig. 3 [7]. In the freshly prepared mixture (A), X-ray diffraction peaks were observed at $2\theta = 14.5, 19.3,$ and 25.3° that were attributable to EZ crystals. Following storage at 0 and 40.0% RH (represented by patterns B and C in Fig. 3), the X-ray diffraction peaks of EZ crystals disappeared. It was found that the mixing of EZ with PCC under dry conditions led to the transformation of crystalline EZ into the amorphous state. EZ molecules would be adsorbed physically onto the pore surface of PCC. In the case of 97.0% RH (Fig. 3D), X-ray diffraction peaks of EZ crystals were still observed; EZ remained in the crystalline state under this condition. Matsumura et al. [8] reported that coexisting water vapor caused a decrease in the adsorption of methanol onto porous materials. At 97.0% RH, the maximum pore diameter for water condensation was calculated as 42 nm. All capillaries of PCC were filled with water at 97.0% RH, and molecules of EZ had little chance to adsorb onto the surface of PCC. These results indicated that the indispensable condition for amorphization of EZ by mixing with PCC was storage under dry conditions.

Controlled pore glass (CPG) is used as a support for enzymes in size-exclusion chromatography [9]. The adsorption of biological materials onto glass surfaces is a

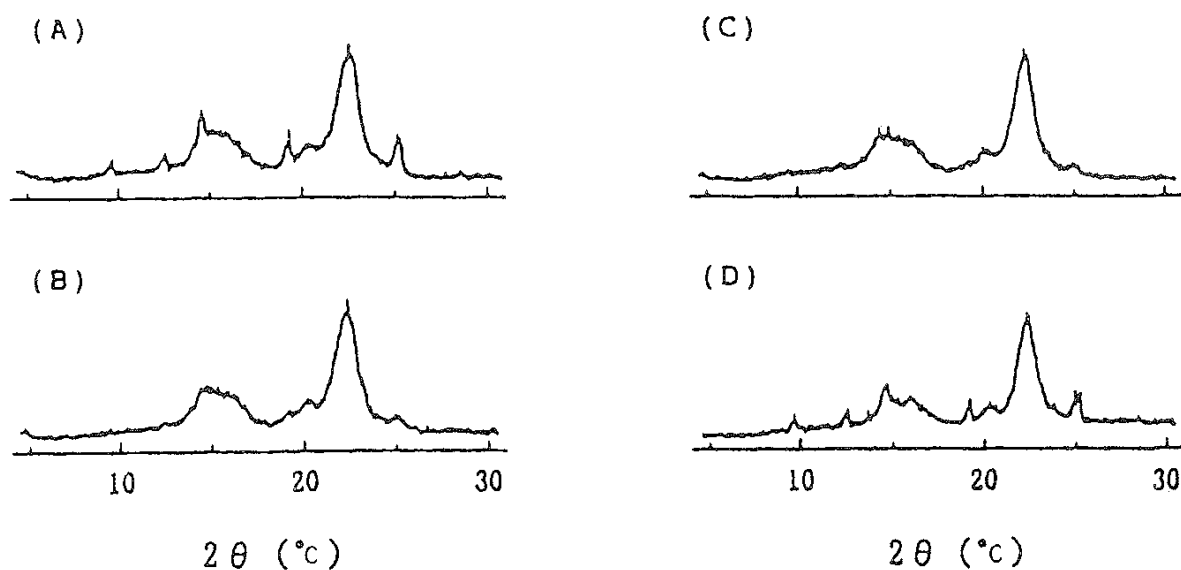


FIG. 3 Powder X-ray diffraction patterns of mixtures of 10% EZ and 90% PCC after storage at 40°C for 1 month at various relative humidities. (A) Fresh mixture; (B) 0% RH; (C) 40.0% RH; (D) 97.0% RH. (From Ref. 7.)

well-known phenomenon, e.g., the blood clotting reaction, macrophage adhesion, an antigen-coated column, and low adhesion of transformed cells [10]. Surface silanol groups on CPGs and pore size distribution have received keen interest because of their important roles in interface interaction in chromatography and substrate adsorption in catalytic processes.

Nakai and coworkers [11] investigated the molecular properties of benzoic acid, ethyl *p*-aminobenzoate, and benzophenone mixed with porous glass powder by DSC, powder X-ray diffraction, and gas adsorption measurements. The mixtures had anomalous properties compared with the mixtures with glass beads; that is, (1) a low concentration mixture (about 5%) did not show the melting peak and X-ray diffraction peaks associated with the pharmaceutical crystals, (2) a high concentration mixture (about 20%) showed only a broad endothermic peak at a lower temperature than the melting point, and (3) a higher concentration mixture (more than 40%) showed an endothermic peak of the melting point together with the broad peak at a lower temperature. The DSC peak area at the melting point increased with an increase of drug concentration while the broad peak area remained unchanged. Mixing with medicinal compounds caused a decrease of surface area and a change in the pore diameter distribution of the porous glass. From these results it was concluded that the drugs took three phases in the mixture; phase 1, crystal structure; phase 2, disordered structure; and phase 3, probably adsorbed on the pore walls. The amount of material in each of these phases was calculated from DSC curves.

As crystalline drugs generally have very low vapor pressure at room temperature, almost no drugs noticeably sublime except for volatile drugs such as naphthalene. However, when the drugs are mixed with porous powder, the capillaries can provide a sink condition for the diffusion of the drug molecules in the mixture. The rate of diffusion of benzoic acid was calculated for a mixture of 50 mg benzoic acid and 950 mg CPG at 300 K. The diffusion equation

$$N = -D \frac{\partial C}{\partial x} \quad (1)$$

is of the form

$$N = -D \frac{C_s}{X} \quad (2)$$

at steady-state under sink condition, where D is the diffusion constant of benzoic acid in the air, N is the flux. C is the concentration of benzoic acid at distance x in the diffusion layer, C_s is the saturated concentration of benzoic acid in the air, and X is the mean distance between the surfaces of benzoic acid crystals and the CPG particles.

The following data were used for the calculation of the diffusion rate. $D = 0.1 \text{ cm}^2 \text{ s}^{-1}$ in air at 300 K and 1 atm, $X = 0.01 \text{ cm}$, and $C_s = 4.4 \times 10^{-10} \text{ mol/cm}^3$ at 300 K. The C_s value was calculated from the vapor pressure of benzoic acid of $8 \times 10^{-3} \text{ mmHg}$ by assuming an ideal gas. Equation (2) gives

$$N = 4.4 \times 10^{-9} \text{ mol/}(\text{cm}^2 \cdot \text{s}) \quad \text{or} \quad 5.36 \times 10^{-7} \text{ g/}(\text{cm}^2 \cdot \text{s})$$

The specific surface area of benzoic acid was calculated to be $474\text{cm}^2/\text{g}$ by using the equation $S_v = 6/\rho d$, the value of 1.266 for the density, and $1 \times 10^{-2}\text{cm}$ for the mean particle diameter. Therefore, the surface area was 24cm^2 for the initial amount of benzoic acid of 50 mg. Thus, the diffusion rate of benzoic acid is calculated to be

$$N = 46\text{mg/h}$$

Although this calculation was rather too simple, a considerably large value comparable to the total amount added was obtained, which could explain the rapid disappearance of crystals of benzoic acid.

Drug molecules that penetrate into the capillaries have higher sticking probabilities (adsorption rates) than those colliding with flat surfaces because they undergo a great number of collisions with the capillary walls [12]. Thus, these molecules easily lose their kinetic energy during the collisions and rapidly become fixed on the walls, which provide the sink condition at the surface of the porous powders.

To verify that these phenomena take place via the gaseous phase, Konno et al. [13] studied the rate of amorphization using crystalline substances with various vapor pressures. Benzoic acid and its derivatives were used as the crystalline substances, and activated carbon as the adsorbent. After each crystalline substance was mixed with activated carbon in a porcelain mortar, the changes in the X-ray diffraction patterns during storage were examined, and the time required for the crystal peaks to disappear was determined. The relationship between the vapor pressure of the crystalline substances and the time required to become amorphous, plotted on a logarithmic scale, is shown in Fig. 4. At atmospheric pressure and 25°C , benzoic acid, which has the highest vapor pressure of the substances used, became amorphous within only 1 h, whereas p-hydroxybenzoic acid, whose vapor

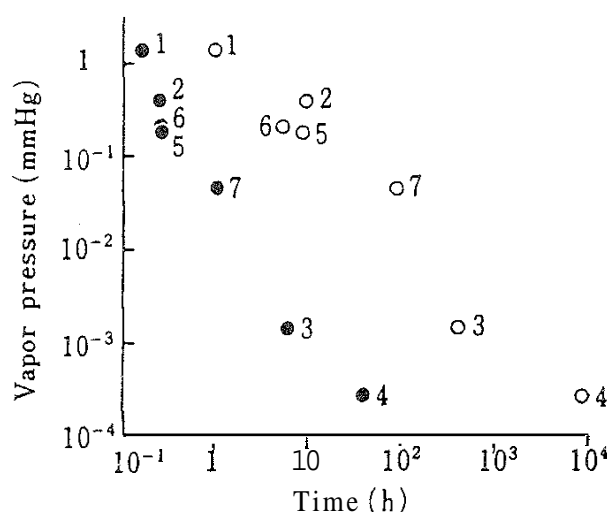


FIG. 4 Plots of vapor pressure of the crystalline substances versus the time required to become amorphous in mixtures with activated carbon. (○) At 25°C and atmospheric pressure; (●), at 40°C and reduced pressure. 1, Benzoic acid; 2, o-hydroxybenzoic acid; 3, m-hydroxybenzoic acid; 4, p-hydroxybenzoic acid; 5, o-chlorobenzoic acid; 6, m-chlorobenzoic acid; 7, p-chlorobenzoic acid. (From Ref. 13.)

pressure is the lowest, changed after 8600 h. Thus, it was observed that the higher the vapor pressure, the faster the change to the amorphous state. A similar tendency was recognized at reduced pressure at 40°C. The results suggest that the phenomenon of the gradual loss at room temperature (25°C) of the crystalline properties of some organic pharmaceuticals mixed with adsorbents takes place via the gaseous phase and is induced by the vapor pressure of the pharmaceuticals themselves

Activated carbon, the residue from the destructive distillation of various organic materials, was found to be capable of forming an amorphous solid. After storage of a mixture of aspirin and activated carbon at 25°C for 7 days, the aspirin changed from crystalline to amorphous. In the condition of reduced pressure, the amorphization, the transfer of organic molecules to adsorbent surface took place more rapidly as the mean free path of the organic molecules was much longer than at atmospheric pressure [13].

In the presence of porous and nonporous silicon dioxides, organic crystallites were converted into the amorphous state. Kim et al. [14] reported the kinetic of the transformation of the crystalline drug in the presence of various types of silicas using DSC.

The relative enthalpy change obtained with the 1:1 drug-silica mixtures after storage at 25°C is shown in Fig. 5. These thermal data clearly indicate that the rate of crystalline transformation into the amorphous state was markedly dependent on the types of silica employed. The mixtures with a mesoporous silica, such as silica

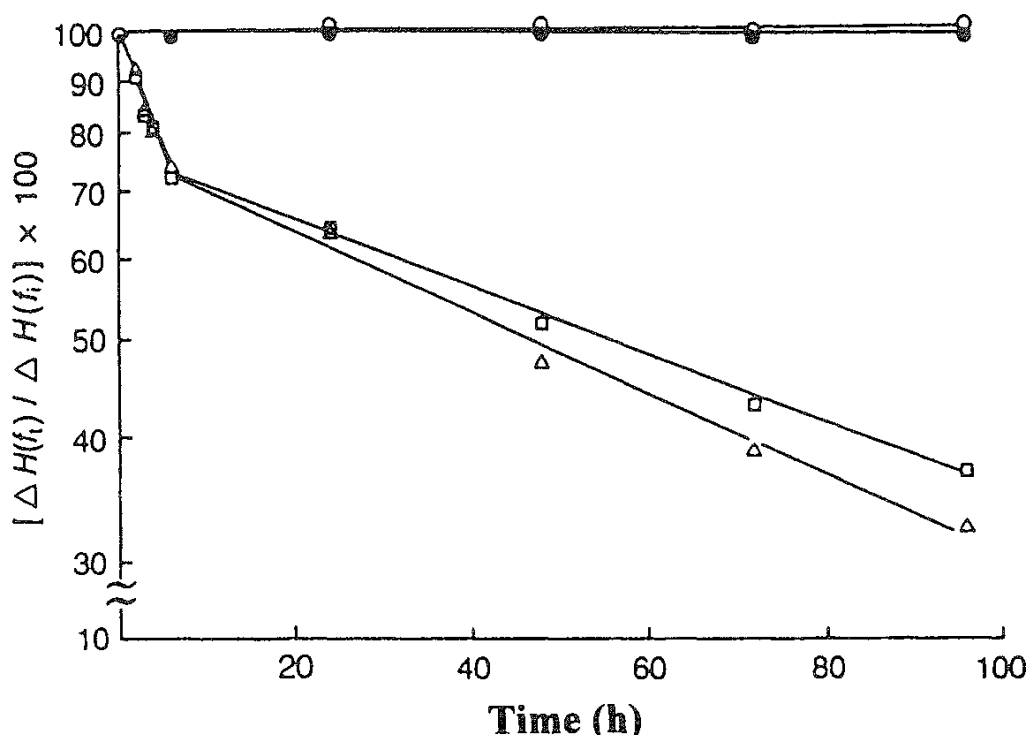


FIG. 5 The change in endothermic transition energy with time for 1:1 mixtures of drug and porous or nonporous silicon dioxide at 25°C (○) Drug + silica 63 (porous); (●) drug + fumed silicon dioxide M-5 (nonporous); (□) drug + silica 244 (porous); (Δ) drug + silica 74 (porous). (From Ref. 14.)

74 (mean pore diameter 15 nm) and silica 244 (mean pore diameter 20 nm), yielded a fast rate of crystal transformation at 25°C. In contrast, the crystalline drug mixed with either a microporous silica such as silica 63 (mean pore diameter 2.0 nm) or a nonporous fumed silicon dioxide remained intact and did not convert into the amorphous state. Thus, the pore openings on the silica surface were considered to be an important factor for the transformation of the crystalline drug into the amorphous phase in the binary mixture systems. The crystal conversion process for the drug in the silica 74 and silica 244 mixtures was biphasic; the initial process (up to 6 h) generally followed first-order kinetics, and thereafter the slope changed. The results indicate that the crystal modification in the initial stage occurred at a markedly faster rate than that observed in the later phase of the conversion process.

Colloidal silicas are well known for their large surface area and highly polar silanol groups on the surface, which are capable of hydrogen bonding and electrostatic interactions with various organic compounds, in particular molecules that contain hydroxyl groups such as alcohols. The adsorption interactions between the surface hydroxyl groups of silica and drug molecules that also contain hydroxyl groups are well documented [15]. For example, physical adsorption studies of trimethyl carbinol on silica showed that the interaction is based on hydrogen bonding with surface hydroxyl groups. Considering these physicochemical properties of colloidal silicon dioxide, it is quite reasonable to assume that drug molecules having an —OH or —COOH moiety can be hydrogen-bonded to the silica surface.

III. IMPROVING DISSOLUTION

The primary use of the amorphous state in pharmaceuticals is to increase bioavailability by increasing the rate and extent of drug dissolution. This relatively new pharmaceutical technique plays an important role in increasing the dissolution and absorption of drugs in dosage forms. An example of the use of porous materials to improve the dissolution rate was reported by Ali et al. [6]. The dissolution profiles of FFA from newly prepared and stored mixtures with either florite R or florite S in pH 1.2 solution at 37°C are shown in Fig. 6. The stored mixture of FFA and florite S exhibited a greater dissolution rate than the fresh mixture owing to the presence of the drug in an amorphous state. The observed concentration of FFA after the first 10 min is attributed to the stable crystalline state of FFA. However, when florite R was used, the stored mixture showed the greatest enhancement in the dissolution rate of FFA due to the existence of FFA in an amorphous ionic state. The decrease in the concentration of FFA after its initial fast dissolution may be due to the conversion of the calcium flufenamate to the molecular form.

A clearer improvement of dissolution was shown in the mixtures with magnesium aluminum silicate (MAS) [16]. The dissolution profiles of FFA into various dissolution media are shown in Fig. 7. The dissolution profiles of FFA mixtures with MAS stored at a reduced pressure were compared with those of fresh mixtures. Since FFA was an acid with a pK_a value of 3.9, the amount of FFA dissolved changed markedly in this pH region. Furthermore, in mixtures with MAS stored at a reduced pressure, the concentration of FFA became higher than in the case of

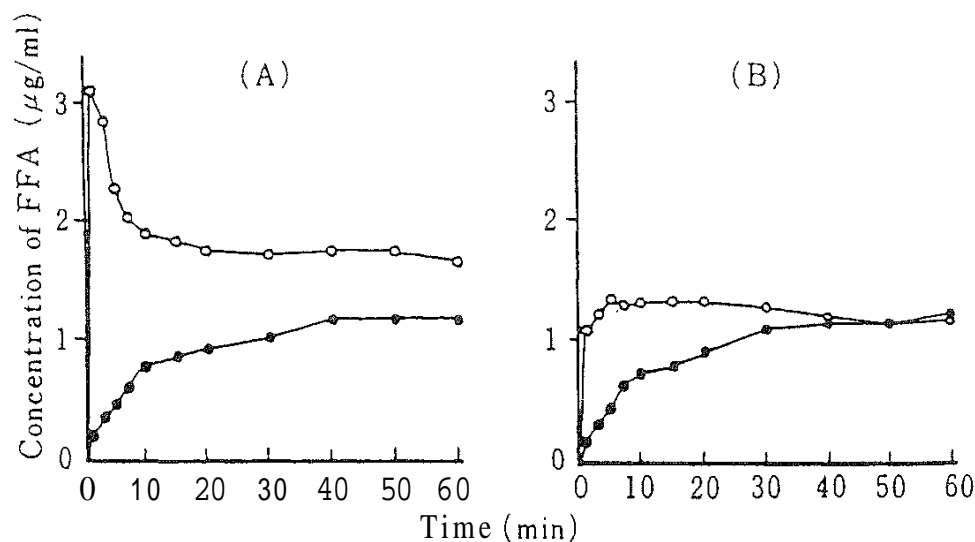


FIG. 6 Dissolution profiles of FFA from mixtures with either florite R or florite S in pH 1.2 solution at 37°C. (A) Mixture of 20% FFA and 80% florite R; (B) mixture of 20% FFA and 80% florite S. (●) Fresh mixture; (○) mixture stored for 10 days at 0% RH and 40°C. (From Ref. 6.)

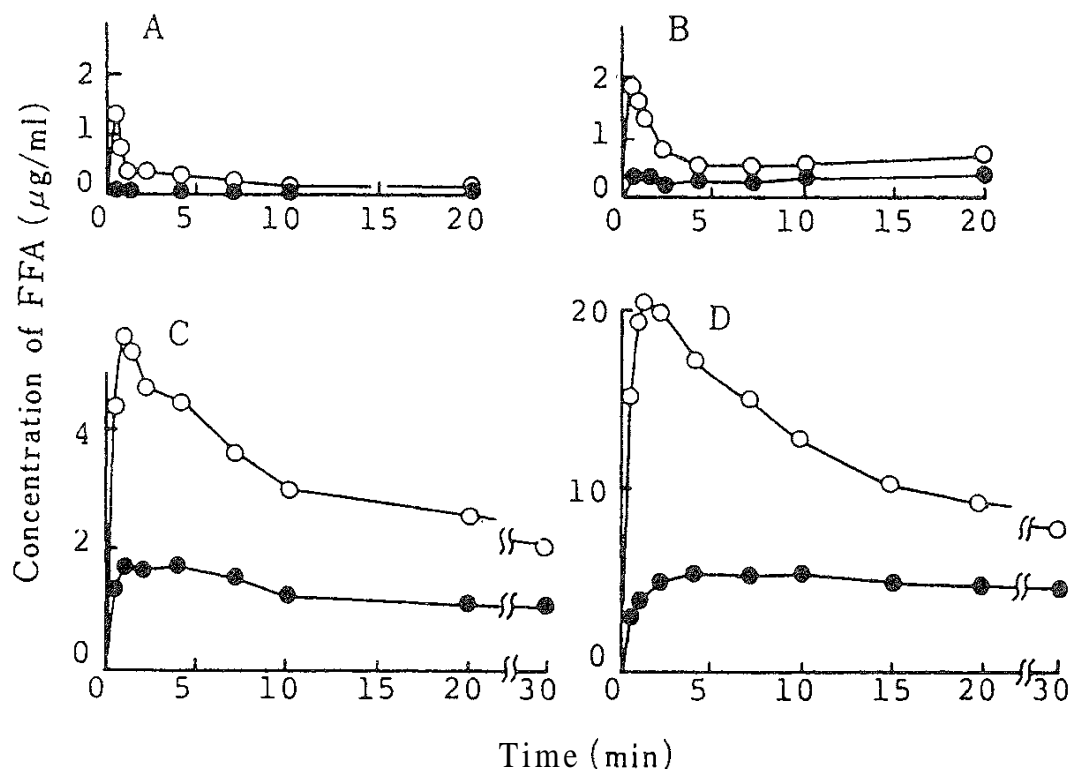


FIG. 7 Dissolution profiles of FFA from mixtures with MAS into various dissolution media at 37°C. (●) 20% FFA, fresh; (○) 20% FFA, stored for 5 h at a reduced pressure at 60°C. A, pH 1.2 solution (JP 1st fluid); B, pH 3.0 citrate buffer solution; C, pH 4.0 acetate buffer solution; D, pH 5.0 acetate buffer solution. (From Ref. 16.)

freshly prepared mixtures, and the concentration then decreased gradually, showing a typical supersaturation phenomenon. The longer the supersaturated state continued, the higher the pH value of the medium was. Takayama et al. [17] reported that the dissolution profiles of FFA from a solid dispersion system showed the same supersaturation pattern. The decrease of FFA concentration was due to a phase transition to stable forms accompanied by crystallization.

Naproxen, a nonsteroidal anti-inflammatory drug, is practically insoluble in water. For pharmaceutical application, improvement in the dissolution properties has been expected. Dissolution properties of naproxen in the JP first fluid (pH 1.2) were studied according to the JP paddle method (Fig. 8) [18]. A mixture with CPG 120 showed a dissolution curve similar to that of intact naproxen crystals. It is noteworthy that the dissolution of naproxen was significantly improved in the heated sample with CPG 120, especially in the initial stage of dissolution. In

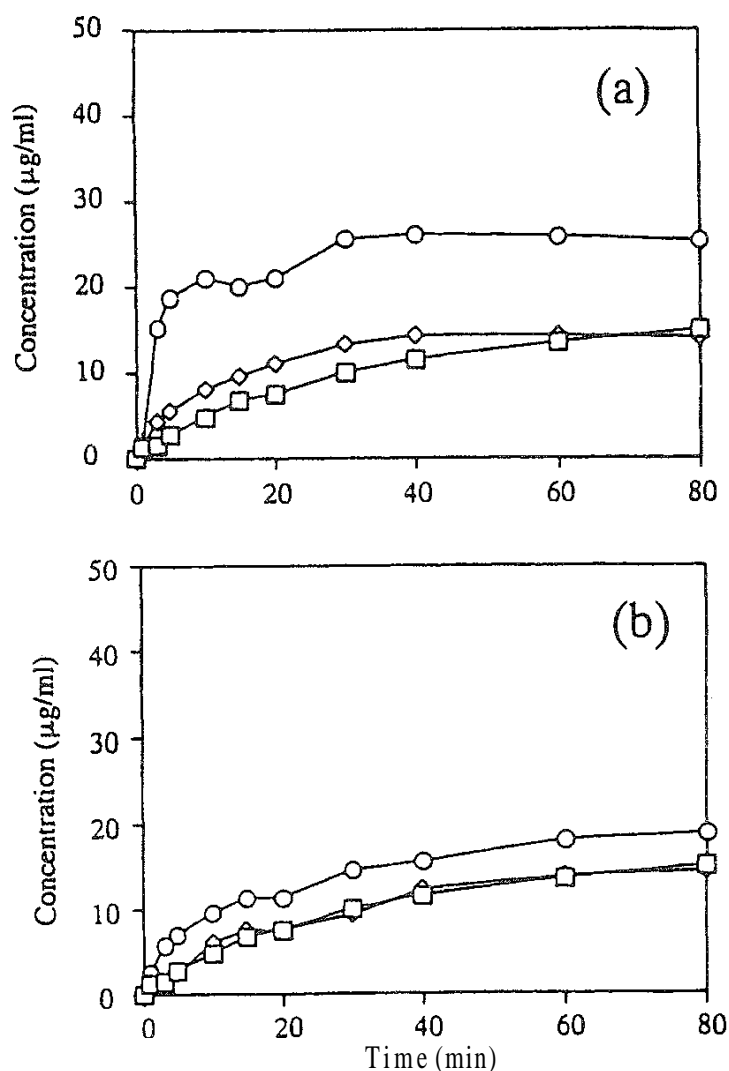


FIG. 8 Dissolution patterns of naproxen in JP first fluid at 37.0°C. (a) Naproxen-CPG 120 system; (b) naproxen-CPG 1000 system. (□) Naproxen crystals; (◇) fresh mixture of 10% naproxen crystal and 90% CPG; (○) same mixture after heating at 90°C for 3 h. Each point represents the mean value ($n = 3$). (From Ref. 18.)

contrast, only slight improvement of naproxen dissolution was observed in the heated sample with CPG 1000. Consequently, the improved dissolution of naproxen results from the molecular dispersion of naproxen on the CPG surface and is affected by the pore structure of CPG.

IV. EFFECT OF ADSORPTION ON CHEMICAL STABILITY

The need to ensure product quality and hence stability of the drug concerned in the product is obvious. Decomposition leads to a decrease in drug potency, and the decomposition products may be unpleasant or toxic. Stability is therefore an important issue with pharmaceutical products.

The hydrolytic decomposition of aspirin has been widely studied in aqueous media. It has been shown that the rate of hydrolysis of solid aspirin is proportional to the relative humidity of the atmosphere [19]. The effect of additives on this hydrolysis has been investigated, and the presence of additives has been found to affect the decomposition rate of aspirin.

The kinetics of aspirin hydrolysis were studied in CPG mixtures containing 5% aspirin. The pore diameters of CPG varied from 75 to 3000 Å. Plots of the first-order rate constants at 50°C under the two different relative humidities versus the pore diameter of CPG are shown in Fig. 9 [20]. In the CPG mixtures where the pore diameter was less than 300 Å, the rate constants of aspirin decomposition were independent of CPG pore diameters in the cases of both 0% RH and 79% RH. However, the rate constant in the mixtures with CPG of large pore size decreased with increasing CPG pore diameter. The pore diameter profiles of the rate constant indicate that the stability of aspirin was closely related to changes in the crystal-

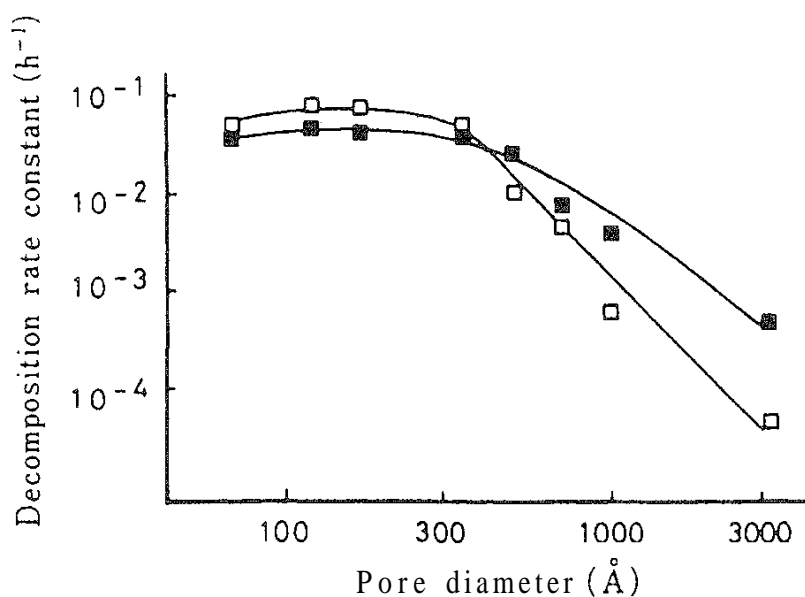


FIG. 9 Effect of CPG's pore diameter (log scale) on the first-order rate constant for the decomposition of aspirin at 50°C. Aspirin concentration is 5%. (□) 0% RH; (■) 79% RH. (From Ref. 20.)

linity of aspirin in the mixtures. That is, greater and similar decomposition rate constants were observed in the mixture of small pore diameter (less than 300 Å), where aspirin was in a completely amorphous state.

Figure 9 also reveals that the decomposition rate constants observed at 0% RH were greater than those at 79% RH in samples from CPG 75 to CPG 350. In the cases of the CPG 1000 and CPG 3000 mixtures, the decomposition at 79% RH was faster than that at 0% RH. Although hydrolysis in the solid state was generally accelerated by humidification, the opposite situation was observed in the mixtures with small-pore CPGs. The decomposition rate constant in the CPG 75 mixture at 0% RH and 50°C was determined as $4.90 \times 10^{-2} \text{ h}^{-1}$, indicating a half-life of 14.1 h for aspirin decomposition.

The RH dependency of the first-order rate constant of aspirin decomposition in the CPG 170 mixture at 50°C is illustrated in Fig. 10. An anomalous linear relationship was obtained between the RH and the rate constants; as the RH was raised, the rate constant decreased. Leeson and Mattocks [21] proposed the mechanism of aspirin decomposition in the solid state as follows. After the formation of a water layer on aspirin particles, aspirin was dissolved into the water layer. The aspirin then decomposed in the solution. In the crystalline state, the amount of adsorbed water increased at a high RH; therefore, faster aspirin decomposition was observed. On the other hand, the stability of aspirin in the solid dispersed system was affected by many factors such as hygroscopicity of additives, pH on the surface, specific surface area, and dispersed state. El-Banna et al. [22] reported that the aspirin in the coprecipitated samples with povidone or urea had slightly higher degradation rates due to its increased water sorption ability. In the case of a urea solid dispersion,

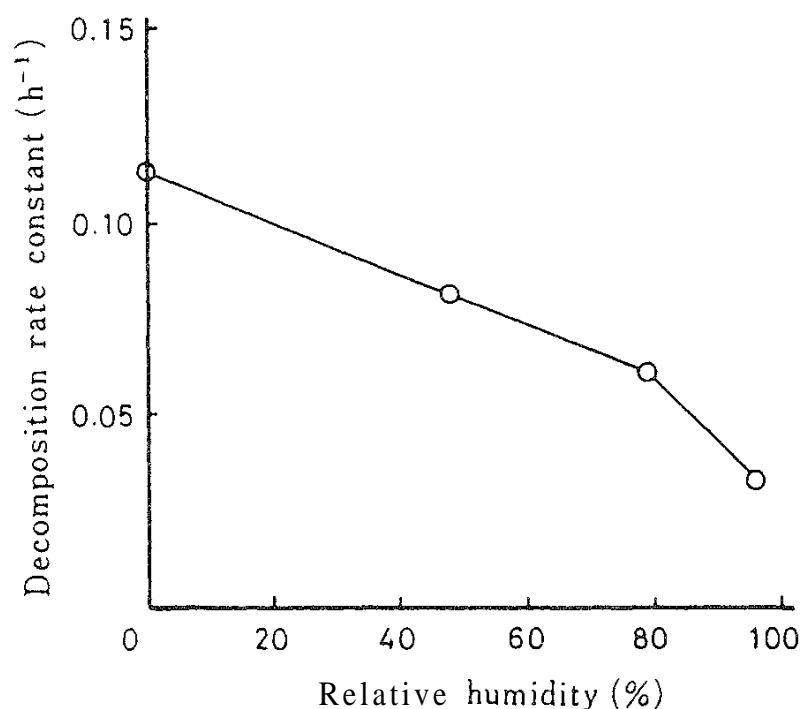


FIG. 10 Effect of RH on the first-order rate constant for the decomposition of aspirin mixed with CPG 170 at 50°C. Aspirin concentration is 1%. (From Ref, 20.)

urea could also be dissolved into a thin water layer and imparted a slight alkalinity to this film.

By way of contrast, Gore and Banker [23] showed an enhanced aspirin stability after the addition of colloidal silica at a high RH. They interpreted these results in terms of the action as due to an internal moisture scavenger. The water molecules were entrapped by the silanol groups of colloidal silica. The surface of CPG was also covered by silanol groups as well as by colloidal silica; however, the concentration of aspirin in these experiments was as low as 3%, differing from the high concentrations (85–99%) used by Gore and Banker. Therefore, the simple mechanism of preferential water vapor adsorption of the CPG surface should not be applied to the explanation of anomalous behavior of aspirin decomposition in the CPG 170 mixtures. The competitive adsorption of aspirin and water molecules onto the CPG surface was considered a suitable concept to explain the RH dependence of aspirin decomposition in the CPG mixture.

The aspirin concentration in the CPG 170 mixture varied from 0.3 to 30%. The condition at 50°C and 0% RH was used to study aspirin decomposition kinetics. In the mixtures in which the concentration was less than 2.0%, the rate constants were large and steady. In those with concentrations of more than 2.0%, increasing concentrations of aspirin caused a decrease in the decomposition rate constant. In the aspirin concentration range of 0.3–2.0%, both the independence of the rate constant from the aspirin concentration and the good linearity of first-order plots were observed. The results suggest that the aspirin molecules were dispersed homogeneously in CPG 170 in low aspirin concentration mixtures and that a sufficient amount of water was adsorbed to hydrolyze aspirin on the CPG 170 surface. The decrease of the aspirin decomposition rate at concentrations greater than 2.0% should be ascribed to the remaining crystalline portion of aspirin in the mixture as well as to the time-consuming process of the change from crystalline to amorphous aspirin.

Matsumoto et al. [24] investigated to the stability of aspirin in mixtures of aspirin and PCC at various temperatures and humidities. They calculated the intrinsic rate constants of aspirin hydrolysis from the relationship between the apparent first-order hydrolysis rate constant and the amount of water adsorbed at each temperature. The apparent first-order rate constant of aspirin and the amount of adsorbed water in the heated mixture of PCC and aspirin at different temperatures are listed in [Table 1](#). It was suggested that the apparent first-order decomposition rate constants of aspirin in the heated mixtures were closely related to the amount of adsorbed water.

The relationship between the amount of adsorbed water and the apparent first-order rate constant of aspirin in the heated mixtures at various temperatures is also shown in [Fig. 11](#). The amount of adsorbed water was defined as the number of moles of adsorbed water per kilogram of the mixture. At each temperature, the apparent first-order rate constant of aspirin increased with increases in the amount of adsorbed water, and a linear relationship was observed. From [Fig. 11](#), the following equation can be derived.

$$k_{\text{app}} = k(C_{\text{H}_2\text{O}} - \alpha) \quad (3)$$

TABLE 1 Apparent First-Order Decomposition Rate Constants of Aspirin and Amounts of Adsorbed Water in PCC–Aspirin Mixtures at 30, 40, and 50°C

| Temp. (°C) | RH (%) | Apparent rate constant (day ⁻¹) | Amount of adsorbed water (%) |
|---------------|-----------|--|---------------------------------|
| 30 | 11.8 | 2.25×10^{-3} | 2.13 |
| | 36.3 | 4.66×10^{-3} | 3.56 |
| | 52.0 | 6.65×10^{-3} | 4.45 |
| | 67.9 | 9.63×10^{-3} | 6.11 |
| 40 | 11.6 | 5.97×10^{-3} | 2.11 |
| | 32.3 | 1.11×10^{-2} | 3.25 |
| | 49.2 | 1.60×10^{-2} | 4.10 |
| | 66.8 | 2.38×10^{-2} | 5.64 |
| 50 | 11.4 | 1.55×10^{-2} | 1.90 |
| | 28.4 | 2.53×10^{-2} | 2.96 |
| | 46.3 | 3.83×10^{-2} | 3.71 |
| | 65.0 | 5.88×10^{-2} | 5.17 |

Source: Ref. 24

where k_{app} is the apparent first-order rate constant of aspirin in the heated PCC–aspirin mixture, k is the intrinsic rate constant of aspirin, C_{H_2O} is the amount of adsorbed water, and a is the intercept on the abscissa. The values of k and a obtained from Eq. (3) at each temperature are listed in Table 2. As the values of k were independent of the amount of water, they are the intrinsic hydrolysis rate constants of aspirin at each temperature. The values of a at 30, 40, and 50°C were

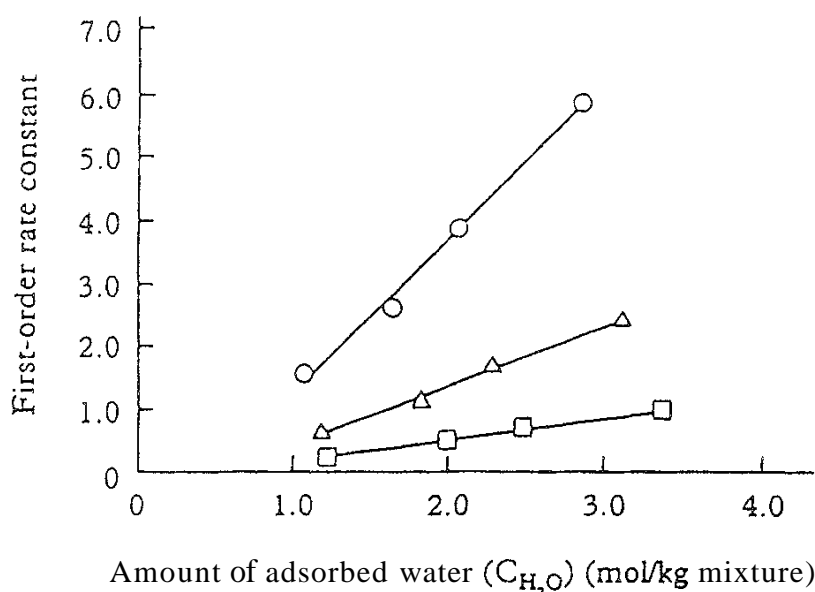


FIG. 11 Relationship between the amount of adsorbed water and apparent first-order decomposition rate constants of aspirin in PCC–aspirin mixtures at various temperatures. (\square) 30°C; (\triangle) 40°C; (\circ) 50°C. (From Ref. 24.)

TABLE 2 Values of Intrinsic Hydrolysis Rate Constant of Aspirin (k) and Critical Amount of Water (a) in PCC–Aspirin Mixtures at 30, 40, and 50°C

| Temp. (°C) | k ($\times 10^{-3}$ kg mole/day) | 1 (mol/kg) | Amount of adsorbed water (%) |
|---------------|--------------------------------------|----------------------|---------------------------------|
| 30 | 3.37 | 0.534 | 0.999 |
| 40 | 9.17 | 0.547 | 0.999 |
| 50 | 24.4 | 0.493 | 0.994 |

Source: Ref. 24.

in good agreement, and they can be considered the critical amounts of water when aspirin hydrolysis takes place in the heated mixtures.

Edwards [25] investigated the hydrolysis of aspirin in aqueous solution at 17°C and demonstrated that the aspirin is hydrolyzed by general acid–base catalysis and water molecules for ionic and nonionic aspirin, comprising six simultaneous reactions involving H_3O^+ , OH^- , and H_2O for ionic and nonionic aspirin. The intrinsic hydrolysis rate constant in the heated mixture was comparable with the hydrolysis rate constants of the two-element reactions of nonionic aspirin and H_2O or ionic aspirin and H_2O in aqueous solution. As aspirin molecules would be adsorbed onto the pore surface of PCC in the molecular state, as a possible mechanism of aspirin hydrolysis in the mixture with PCC it was suggested that the aspirin is dispersed monomolecularly in the heated mixture and reacts with water molecules rather than by acid–base catalysis.

V. FLUORESCENCE SPECTROSCOPIC STUDIES OF INTERACTION

The photophysical behavior of molecules can provide information about molecular orientation and association in the adsorbed state. The molecular state of drug molecules should be related strongly to drug stability and bioavailability. The solid-state emission and excitation spectra and the fluorescence decay of pyrene, which was adsorbed onto porous additives, were investigated by Yamamoto [26]. PCC and Inertsil ODS-80TM were used as the porous additives. Mixtures of pyrene and porous additive were prepared at definite mixing ratios (pyrene content 0.10–10%) by simple blending and were kept at 298 K for various lengths of time. For a 1.0% pyrene–PCC system, the monomer emission peak was observed and the intensity increased for 3 days, while the excimer intensity changed slightly (Fig. 12). The fluorescence patterns changed with duration of storage time. In the case of the 1.0% pyrene–ODS-80TM system, the changes in monomer and excimer occurred in the same way, but the rate of change was faster than that of the PCC system. We propose two steps for this adsorption process: the adsorption of drug molecules onto the surface of porous additives and the formation of the ground-state dimer. The ability to form the ground-state dimer would be associated with the surface hydrophobicity of the additives.

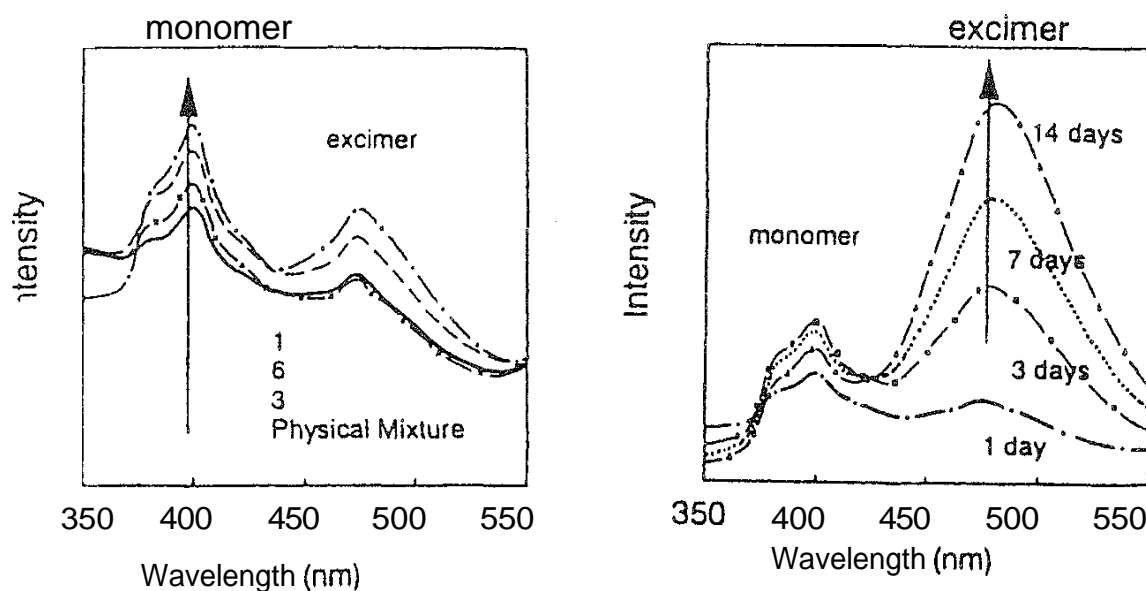


FIG. 12 Change in fluorescence spectrum of 1% pyrene-PCC mixture by storage at 25°C, $\lambda_{\text{ex}} = 300.0 \text{ nm}$. Left: Changes within 1 day. Right: Changes within 2 weeks. (From Ref. 25.)

VI. THERAPEUTIC USE OF POROUS MATERIALS

Drug delivery applications of drug-loaded porous materials are considered to be advantageous for chemotherapy. Therapeutic agents incorporated into porous materials include antibiotics, antineoplastics, and hormones. Hydroxyapatite $[\text{Ca}_{10}(\text{PO}_4)_6(\text{OH})_2]$ is an important mineral component of hard tissue such as teeth and bone. Therefore, when used in implanted artificial hard tissue, hydroxyapatite has a high affinity for natural hard tissue in situ and can be molded to fill spaces created by physical damage to the bones and/or teeth. Yamamura and Yostuyanagi [27] applied hydroxyapatite beads to bone filler with drug-delivering ability and reported the release of adriamycin from the beads.

On the other hand, self-setting calcium phosphate cement is transformed into hydroxyapatite and sets within 0.5 h in situ. The cement system is easy to handle during clinical application and after setting. It possesses excellent bioaffinity for the hard tissues and in effect serves as artificial bone. Otsuka et al. [28] investigated a drug delivery system for antibiotics, polypeptides, and an anti-inflammatory drug from the pharmaceutical perspective, using a self-setting calcium phosphate cement as a new way to deliver drugs to bone. They demonstrated the controlled release of 6-mercaptopurine (6-MP), an anticancer agent, from a self-setting calcium phosphate cement over a period of 100 h. The results suggest that a skeletal drug delivery system with self-setting calcium phosphate cement could be developed into an effective treatment for localized bone cancers in patients following surgery.

Shimada et al. [29] reported a new drug delivery system using small silica particles that can adsorb bleomycin and are easily transferred to the lymphatics to deliver a large dose of anticancer agents to the regional lymph nodes. As shown in Table 3, transplanted tumors had increased in size at the time of sacrifice in the

TABLE 3 Anticancer Effect of Bleomycin–Small Silica (BLM-SI) and Bleomycin Solution (BLM-SOL) on Transplanted Tumor and Metastatic Lymph Nodes

| | Tumor size (mm) at injection | Tumor size (mm) at sacrifice | Lymph node metastasis |
|----------------------|---------------------------------|---------------------------------|--------------------------|
| BLM-SI ($n = 11$) | 13.1 ± 2.1 | 6.3 ± 3.0^a | 1/11(9%) ^a |
| BLM-SOL ($n = 11$) | 11.8 ± 2.5 | 19.6 ± 3.5^a | 7/11(64%) ^a |
| Control ($n = 11$) | 12.0 ± 2.1 | 29.1 ± 9.2 | 11/11(100%) |

^a $p < 0.01$ significantly different to control

Source: Ref. 28.

control and bleomycin solution groups. In contrast, the size of the tumor significantly decreased in the bleomycin–small silica group ($p < 0.01$, $p < 0.05$). Lymph node metastasis occurred in all the animals of the control group, but the incidence of such metastasis was 64% (7/11) in the bleomycin solution group and only 9% (1/11) in the bleomycin–small silica group. A new drug delivery system using silica particles might be useful for the control of tumor and lymph node metastasis.

VII. CONCLUSIONS

When mixed with porous materials, organic medicinal molecules changed their arrangement in the crystal lattice from the crystalline state to a disordered phase, accompanying changes in pharmaceutical properties. This transformation proceeded through the sublimation of organic molecules from the crystals and adsorption onto the porous materials via the gaseous phase. The adsorption equilibrium depended on the temperature, water content, and surface properties of the porous materials. The resulting solid phase consisted of continuous disordered states involving a liquid-like molecular arrangement near the surface, an amorphous portion including a vitreous state, and imperfect crystals where the crystal growth was highly inhibited in the pore. Since solid dosage forms such as tablets, capsules, and pills are multicomponent systems containing the active ingredient, diluents, binders, lubricants, and other pharmaceutical additives, it is important to recognize that adsorption phenomena have a great influence on the effectiveness, stability, and safety of dosage forms.

REFERENCES

1. S. Byrn, R. Pfeiffer, M. Ganey, C. Hoiberg, and G. Poochikian, *Pharm. Res.* 12:945 (1995).
2. B. C. Hancock and G. Zografi, *J. Pharm. Sci.* 86:1 (1997).
3. E. Fukuoka, M. Makita, and S. Yainamura, *Chem. Pharm. Bull.* 34:4314 (1986).
4. H. Egawa, S. Maeda, E. Yonemochi, T. Oguchi, K. Yamamoto, and Y. Nakai, *Chem. Pharm. Bull.* 40:819 (1992).

- T. Yamaguchi, M. Nishimura, R. Okamoto, T. Takeuchi, and K. Yamamoto, *Int. J. Pharm.* 85:87 (1992).
- A. S. Ali, K. Yamamoto, A. M. El-Sayed., F. S. Habib, and Y. Nakai, *Chem. Pharm. Bull.* 40:1289 (1992).
7. K. Matsumoto, Y. Nakai, E. Yonemochi, T. Oguchi, and K. Yamamoto, *Int. J. Pharm.* 108:167 (1994).
8. Y. Matsumura, K. Yamabe, and H. Takahashi, *Carbon* 23:263 (1985).
9. T. Yazawa, *Hyomen* 33:503 (1995).
10. R. Schnabel and P. Langer, *Glastech. Ber.* 62:56 (1989).
11. E. Yonemochi, M. Kojima, A. Nakatsuji, S. Okonogi, T. Oguchi, Y. Nakai, and K. Yamamoto, *J. Colloid Interface Sci.* 173:186 (1995).
12. N. K. Adam, *The Physics and Chemistry of Surfaces*. Oxford Univ. Press, Oxford, 1938, p. 274.
13. T. Konno, K. Kinuno, and K. Kataoka, *Chem. Pharm. Bull.* 34:301 (1986).
14. K. H. Kin, M. J. Frank, and N. L. Henderson, *J. Pharm. Sci.* 74:283 (1985).
15. H. Rupprecht, M. J. Biersack, G. Kindl. and H. Liebl, *Pharm. Ind.* 38:1009 (1976).
16. T. Konno and K. Kinuno. *Chem. Pharm. Bull.* 37:2481 (1989).
17. K. Takayama, H. Imaizumi, N. Nambu. and T. Nagai, *Chem. Pharm. Bull.* 30:3701 (1982).
18. T. Oguchi, Y. Tozuka, S. Okonogi, E. Yonemochi, and K. Yamamoto, *Yakuzaigaku* 57:168 (1997).
19. J. T. Carstensen, F. Attarchi, and X. Hou, *J. Pharm. Sci.* 74:741 (1985).
20. E. Yonemochi, M. Matsumura. T. Oguchi, K. Yamamoto, and Y. Nakai, *Chem. Pharm. Bull.* 39:1027 (1991).
21. L. J. Leeson and A. M. Mattocks, *J. Am. Pharm. Assoc.* 47:329 (1958).
22. H. M. El-Banna, N. A. Daabis, and A. A, El-Fattah, *J. Pharm. Sci.* 67:1631 (1982).
23. H. Y. Gore and G. S. Banker, *J. Pharm. Sci.* 68:197 (1979).
24. K. Matsumoto, Y. Nakai, E. Yonemochi, T. Oguchi, and K. Yamamoto, *Drug Stability* 1:92 (1996).
25. L. J. Edwards, *Trans. Faraday Soc.* 46:723 (1950).
26. K. Yamamoto, *Pacific Basin Workshop on Adsorption Science and Technology*, Kisarazu, Japan, 1997.
27. K. Yamamura and T. Yotsuyanagi, *Int. J. Pharm.* 79:R1 (1992).
28. M. Otsuka, Y. Matsuda, J. L. Fox, and W. I. Higuchi, *J. Pharm. Sci.* 84:733 (1995).
29. M. Shimada, S. Natsugoe, and T. Aikou, *Anticancer Res.* 15:109 (1995).